TURBULENT WALL PRESSURE FLUCTUATIONS UNDER SEPARATED SUPERSONIC AND HYPERSONIC FLOWS

J. D. REVELL and R. E. GLEASON

NORTHROP CORPORATION

FOREWORD

This research effort was performed by Northrop Corporation, Norair Division, Hawthorne, California, for the Aero-Acoustics Branch, Vehicle Dynamics Division, AF Flight Dynamics Laboratory, Wright-Patterson AFB, Ohio under Contract AF 33(657)-11712, "Noise from Separated Flow." It is part of a continuing effort to predict and control the aero-acoustic environment of flight vehicles and is part of the Research and Technology Division, Air Force Systems Command's exploratory development program. The work was directed under Project 1471, "Aero-Acoustic Problems" and Task 147102, "Prediction and Control of Noise," with Mr. P. H. Hermes (FDDA) as technical monitor.

This research effort was conducted from 13 June 1963 to 1 March 1965 by the Structures and Auxiliary Systems Group of the Research and Technology Section of Norair. A Norair Report No. NOR 65-4 has been assigned for internal control. In addition to the authors, contributing personnel from Northrop included W. E. Anderson and R. W. Lucas. Authors are J. D. Revell and R. E. Gleason.

Manuscript of this report was released by the authors May 1965 for publication as an AFFDL Technical Report.

This report has been reviewed and is approved.

Walter J. Mykytow

WALTER J. MYKYTOW
Asst. for Research & Technology
Vehicle Dynamics Division

ABSTRACT

The objective of this project was to conduct an exploratory theoretical and limited experimental program to obtain the parameters that are important in the occurrence, magnitude, frequency content, and effective areas of forcing functions arising from separated flow, wakes, base pressure fluctuations, and oscillating shock waves.

Two models were used to obtain pressure fluctuation data generated by the above mentioned phenomena from wind tunnel tests. These models were purposely constructed to generate separated flows, oscillating shock waves, and base pressure fluctuations.

The fluctuating pressure data obtained during the tests have been reduced in the form of one-third octave band spectra. These reduced data are compiled in the Appendix.

Analyses of these data have been made, and are given in the report. Comparisons have been made of the effects of Mach number, angle of attack, frequency, and Strouhal number on the sound pressure levels generated.

TABLE OF CONTENTS

		PAGE
I	INTRODUCTION	1
II	GENERAL DISCUSSION OF SEPARATED FLOW AND WALL TURBULENT PRESSURE FLUCTUATIONS	3
	THE TURBULENT WALL PRESSURE FLUCTUATION PROBLEM	3
	COMPRESSIBILITY EFFECTS ON TURBULENCE AND WALL PRESSURE FLUCTUATIONS	6
	DISCUSSION OF SPECIAL EFFECTS IN COMPRESSIBLE BOUNDARY LAYERS AND WAKES	7
	TURBULENT PRESSURE FLUCTUATIONS FOR BODIES OF REVOLUTION AT FINITE α	11
	AXIAL FLOW AND CROSS FLOW INTERACTION AT FINITE α	13
III	DISCUSSION OF MODELS AND INSTRUMENTATION	25
	MODELS	25
	INSTRUMENTATION	25
IV	TEST CONDITIONS	53
V	EXPERIMENTAL RESULTS AND DISCUSSION	64
	TUNNEL OPERATING CONDITIONS AND BACKGROUND NOISE	64
	RESULTS FOR THE AXISYMMETRIC MODEL	74
	RESULTS FOR THE FLAT PLATE MODELS	118
	REFERENCES	179
	APPENDIX - ONE-THIRD OCTAVE BAND SPECTRA	183

ILLUSTRATIONS

FIGURE		PAGE
1	SCHEMATIC OF A SHOCKWAVE BOUNDARY LAYER INTERACTION	7
2	TURBULENCE SHOCK INTERACTION	9
3	EQUIVALENT CYLINDRICAL PROBLEM FOR DETERMINING THE AFT FLARE STANDOFF DISTANCE	9
4	VISCOUS CROSS FLOW WAKE	12
5	MODEL NUMBER 1	26
6	MODEL NUMBER 1 INSTRUMENTATION	27
7	MODEL NUMBER 2	28
8	MODEL NUMBER 2 INSTRUMENTATION FOR TUNNEL "A" TESTS	29
9	MODEL NUMBER 2 INSTRUMENTATION FOR TUNNEL "C" TESTS	30
10	AXISYMMETRIC MODEL WITHOUT TRANSDUCERS INSTALLED	31
11	TWO-DIMENSIONAL MODEL, FLAT CONFIGURATION	32
12	TWO-DIMENSIONAL MODEL, 30° FLAP	33
13	AXISYMMETRIC MODEL INSTALLED IN TUNNEL "A"	34
14	AXISYMMETRIC MODEL INSTALLED IN TUNNEL "A"	35
15	TWO-DIMENSIONAL MODEL INSTALLED IN TUNNEL "A"	36
16	TWO-DIMENSIONAL MODEL WITH BOUNDARY LAYER PROFILE RAKE	37
17	INSTRUMENTATION SYSTEM BLOCK DIAGRAM	39
18	TRANSDUCER CALIBRATION SYSTEM	40
19	CALIBRATION CURVE, TRANSDUCER #1	41
20	CALIBRATION CURVE - TRANSDUCER #2	42
21	CALIBRATION CURVE - TRANSDUCER #3	43
22	CALIBRATION CURVE - TRANSDUCER #4	44
23	CALIBRATION CURVE - TRANSDUCER #5	45
24	CALIBRATION CURVE - TRANSDUCER #6	46
25	CALIBRATION CURVE - SPARE LEAD - TRANSDUCER #6	47

ILLUSTRATIONS (Cont.)

FIGURE		PAGE
26	CALIBRATION CURVE - TRANSDUCER #7	48
27	STAGNATION TEMPERATURE AND PRESSURE DURING DYNAMIC RECORDING TESTS	65
28	FLOW CONDITIONS DURING WIND TUNNEL TESTS	66
29	BASIC NOISE LEVEL OF WIND TUNNEL (CORRECTED FOR q_∞ CHANGE)	67
30	STROUHAL NUMBER RANGE FOR CLEAN PLATES VS. PRESENT TEST RANGE FOR A 22 IN. LONG PLATE	68
31	RMS PRESSURE FLUCTUATIONS ON A CLEAN FLAT PLATE VS. MACH NUMBER	69
32	BOUNDARY LAYER MACH NUMBER PROFILES FOR AXISYMMETRIC MODEL (1)	75
33	DENSITY PROFILE IN BOUNDARY LAYER, AXISYMMETRIC MODEL	77
34	VELOCITY PROFILE IN BOUNDARY LAYER, AXISYMMETRIC MODEL	78
35	NORMALIZED VELOCITY PROFILE IN BOUNDARY LAYER, AXISYMMETRIC MODEL	79
36	NORMALIZED DENSITY PROFILE IN BOUNDARY LAYER, AXISYMMETRIC MODEL	80
37	DISPLACEMENT THICKNESS INTEGRAND AXISYMMETRIC MODEL	81
38	MOMENTUM THICKNESS INTEGRAND AXISYMMETRIC MODEL	82
39	DISPLACEMENT THICKNESS AND MOMENTUM THICKNESS VS. MACH NUMBER AXISYMMETRIC MODEL (BASED ON GRAPHICAL INTEGRATION AND LOCAL BOUNDARY LAYER EDGE CONDITIONS)	83
40	MACH NUMBER COMPARISON AT $\alpha = 0^\circ$ $R_e/L = 1 \times 10^6$/FT. AXISYMMETRIC MODEL	85
41	REYNOLDS NUMBER COMPARISON AT M = 5.0, $\alpha = 0$ AXISYMMETRIC MODEL	86
42	REYNOLDS NUMBER COMPARISON AT M = 3.5, $\alpha = 0$ AXISYMMETRIC MODEL	87
43	REYNOLDS NUMBER COMPARISON AT M = 2.5, $\alpha = 0$ AXISYMMETRIC MODEL	88

ILLUSTRATIONS (Cont.)

FIGURE		PAGE
44	ANGLE OF ATTACK COMPARISON AT $M_\infty = 5.0$, $R_e/L = 1 \times 10^6$/FT.	89
45	ANGLE OF ATTACK COMPARISON AT $M_\infty = 3.5$, $R_e/L = 1 \times 10^6$ FT. AXISYMMETRIC MODEL	90
46	ANGLE OF ATTACK COMPARISON AT $M_\infty = 2.5$ $R_e/L = 1 \times 10^6$ FT. AXISYMMETRIC MODEL	91
47	AXISYMMETRIC MODEL. M = 2. $\alpha = \phi = 0$	93
48	AXISYMMETRIC MODEL. M = 2.5 $\alpha = \phi = 0$. $P_o = 3.5$	94
49	AXISYMMETRIC MODEL. M = 2.5 $\alpha = \phi = 0$. $P_o = 5.2$	95
50	AXISYMMETRIC MODEL. M = 2.5 $\alpha = \phi = 0$. $P_o = 32$	96
51	AXISYMMETRIC MODEL M = 3.5 $\alpha = \phi = 0$. $P_o = 9.3$	97
52	AXISYMMETRIC MODEL M = 3.5 $\alpha = \phi = 0$. $P_o = 56$	98
53	AXISYMMETRIC MODEL M = 5 $\alpha = \phi = 0$. $P_o = 11$	99
54	AXISYMMETRIC MODEL M = 5 $\alpha = \phi = 0$. $P_o = 18$	100
55	AXISYMMETRIC MODEL. M = 5 $\alpha = \phi = 0$. $P_o = 150$	101
56	ANGLE OF ATTACK EFFECTS ON 1/3 OCTAVE AND OVERALL SPL AXISYMMETRIC	103
57	ANGLE OF ATTACK EFFECTS ON 1/3 OCTAVE AND OVERALL SPL AXISYMMETRIC	104
58	NON-DIMENSIONAL FREQUENCY SPECTRA DERIVED FROM 1/3 OCTAVE ANALYSIS, AXISYMMETRIC MODEL. TRANSDUCER #3 (LENGTH DIMENSION BASED ON h = 2 INCHES	105
59	NON-DIMENSIONAL FREQUENCY SPECTRA DERIVED FROM 1/3 OCTAVE ANALYSIS, AXISYMMETRIC MODEL. TRANSDUCER #3 (LENGTH DIMENSION BASED ON δ^*)	105
60	NON-DIMENSIONAL FREQUENCY SPECTRA DERIVED FROM 1/3 OCTAVE ANALYSIS. AXISYMMETRIC MODEL. TRANSDUCER #3 (LENGTH DIMENSION BASED ON θ)	106
61	DIMENSIONAL FREQUENCY SPECTRA DERIVED FROM 1/3 OCTAVE ANALYSIS, AXISYMMETRIC MODEL. TRANSDUCER #3, h = 2 INCHES	106

ILLUSTRATIONS (Cont.)

FIGURE		PAGE
62	AXISYMMETRIC MODEL (CYLINDRICAL SHELL) VIBRATION FREQUENCIES ℓ = 27", h = 1/8", R = 3.75", STEEL	108
63	NON-DIMENSIONAL STROUHAL FREQUENCY SPECTRUM NORMALIZED TO MEAN SQUARED PRESSURE FLUCTUATION, AXISYMMETRIC MODEL TRANSDUCER NO. 3	114
64	NON-DIMENSIONAL STROUHAL FREQUENCY SPECTRUM NORMALIZED TO MEAN SQUARED PRESSURE FLUCTUATION USING MOMENTUM THICKNESS AS A LENGTH DIMENSION, AXISYMMETRIC MODEL TRANSDUCER NO. 3	115
65	NON-DIMENSIONAL FREQUENCY SPECTRA DERIVED FROM 1/3 OCTAVE ANALYSIS, AXISYMMETRIC MODEL. ($h = r_b - r_{STING}$)	116
66	DIMENSIONAL FREQUENCY SPECTRA DERIVED FROM 1/3 OCTAVE ANALYSIS, AXISYMMETRIC MODEL. TRANSDUCER #6, D = 11.5 INCHES, $h = r_b - r_{STING}$ = 4.69 INCHES, r/r_b = .825	116
67	BASE PRESSURE DIMENSIONLESS FREQUENCY SPECTRA FOR VARIOUS MACH NUMBERS α = 0, $R_e/L = 1 \times 10^6$ Ft. D_b = 11.5" CHANNEL 6 r/r_b = 0.825	117
68	DISPLACEMENT THICKNESS AND MOMENTUM THICKNESS VS MACH NUMBER. FLAT PLATE MODELS (BASED ON GRAPHICAL INTEGRATION AND FREE STREAM CONDITIONS)	119
69	EFFECT OF MACH NUMBER ON THE NON-DIMENSIONAL BOUNDARY LAYER DISTRIBUTIONS (30° FLAP CONFIG. y = 0, α = 0 Re/L = 10^6/Ft.)	120
70	EFFECT OF MACH NUMBER ON THE BASIC BOUNDARY LAYER DISTRIBUTIONS (30° FLAP) CENTER RAKE (y = 0), α = 0, Re/L = 1×10^6/ft.	121
71	CORRECTION FOR "TRUE" VELOCITY BASED ON CROCCOS' THEOREM* FOR STAGNATION TEMPERATURE AND COMPARISON WITH EXPERIMENT *U(Z) BASED ON $T_t(Z) = T_w + \bar{u}\,(T_o - T_w)$ U'(Z) BASED ON $T_t(Z) = T_o$ (FROM AEDC CALCULATIONS)	122
72	ANGLE OF ATTACK EFFECT ON THE NON-DIMENSIONAL BOUNDARY LAYER DISTRIBUTIONS (30° FLAP M = 2, $Re/L = 1 \times 10^6$/Ft y = 0")	123
73	EFFECT OF MACH NUMBER ON THE NON-DIMENSIONAL BOUNDARY LAYER DISTRIBUTIONS (60° FLAP) CENTER RAKE (y = 0), α = 0, $Re/L = 1 \times 10^6$/Ft	124
74	EFFECT OF MACH NUMBER ON THE BASIC BOUNDARY LAYER DISTRIBUTIONS (60° FLAP) CENTER RAKE: (y = 0), α = 0 $Re/L = 1 \times 10^6$ FT	125

ILLUSTRATIONS (Cont.)

FIGURE		PAGE
75	SPANWISE VARIATION OF NON-DIMENSIONAL BOUNDARY LAYER DISTRIBUTIONS (30° FLAP CONFIG) M = 2, α = 0 Re/L = $1x10^6$/FT	126
76	MACH NO. COMPARISON, FLAT PLATE MODEL (0° FLAP), α = 0, Re/L = $1x10^6$/FT.	128
77	MACH NUMBER COMPARISON (30° FLAP) α = 0, Re/L = $1x10^6$/FT. FLAT PLATE MODEL	129
78	MACH NUMBER COMPARISON (60° FLAP) α = 0, R_e/L = $1x10^6$/FT. FLAT PLATE MODEL	130
79	TWO-DIMENSIONAL MODEL, CLEAN CONFIGURATION, M = 2, P_o = 4, T_o = 90F, α = 0, ϕ = -90°	132
80	TWO-DIMENSIONAL MODEL, CLEAN CONFIGURATION, M = 2, P_o = 19.2, T_o = 90F, α = 0, ϕ = -90°	133
81	TWO-DIMENSIONAL MODEL, CLEAN CONFIGURATION, M = 2, P_o = 19.2, T_o = 90F, α = ϕ = 0	134
82	TWO-DIMENSIONAL MODEL, CLEAN CONFIGURATION, M = 3.5, P_o = 4.5 T_o = 110F, α = 0, ϕ = -90°	135
83	TWO-DIMENSIONAL MODEL, CLEAN CONFIGURATION, M = 5, P_o = 11, T_o = 115F, α = 0, ϕ = -90°	136
84	TWO-DIMENSIONAL MODEL, CLEAN CONFIGURATION, M = 5, P_o = 18, T_o = 105F, α = 0, ϕ = -90°	137
85	TWO-DIMENSIONAL MODEL, 30° FLAP, M = 2, P_o = 3, T_o = 90F, α = 0, ϕ = -90°.	138
86	TWO-DIMENSIONAL MODEL, 30° FLAP, M = 2, P_o = 4, T_o = 90F, α = 0, ϕ = -90°	139
87	TWO-DIMENSIONAL MODEL, 30° FLAP, M = 3.5 P_o = 4.5, T_o = 90F, α = 0, ϕ = -90°	140
88	TWO-DIMENSIONAL MODEL, 30° FLAP, M = 3.5 P_o = 9.3, T_o = 100F, α = 0, ϕ = -90°	141
89	TWO-DIMENSIONAL MODEL, 30° FLAP, M = 5, P_o = 11, T_o = 100F, α = 0, ϕ = -90°	142
90	TWO-DIMENSIONAL MODEL, 30° FLAP, M = 5, P_o = 18, T_o = 100F, α = 0, ϕ = -90°	143
91	TWO-DIMENSIONAL MODEL, 60° FLAP, M = 2, P_o = 3, T_o = 90F, α = 0, ϕ = -90°	144

ILLUSTRATIONS (Cont.)

FIGURE		PAGE
92	TWO-DIMENSIONAL MODEL, 60° FLAP, M = 2, P_o = 4, T_o = 90F, α = 0, ϕ = -90°	145
93	TWO-DIMENSIONAL MODEL, 60° FLAP, M = 3.5, P_o = 4.5, T_o = 120F, α = 0, ϕ = -90°	146
94	TWO-DIMENSIONAL MODEL, 60° FLAP, M = 3.5, P_o = 9.3, T_o = 120F, α = 0, ϕ = -90°	147
95	TWO-DIMENSIONAL MODEL, 60° FLAP, M = 5, P_o = 11.2, T_o = 100F, α = 0, ϕ = -90°	148
96	TWO-DIMENSIONAL MODEL, 60° FLAP, M = 5, P_o = 18, T_o = 100F, α = 0, ϕ = -90°	149
97	OVERALL SPL VS DISTANCE OF TRANSDUCER FROM L.E. OF MODEL FOR α = 0, FLAT PLATE CONFIGURATION	151
98	ANGLE OF ATTACK EFFECTS ON 1/3 OCTAVE AND OVERALL SPL, FP 0, MACH NO. 10, CHANNEL 3, TUNNEL C	153
99	ANGLE OF ATTACK EFFECTS ON 1/3 OCTAVE AND OVERALL SPL, FP 30 MACH NO. = 10, CHANNEL 3, TUNNEL C	154
100	ANGLE OF ATTACK EFFECTS ON 1/3 OCTAVE AND OVERALL SPL, FP 60, MACH NO. = 10, CHANNEL 3, TUNNEL C	155
101	ANGLE OF ATTACK EFFECTS ON 1/3 OCTAVE AND OVERALL SPL FLAT PLATE MODEL 0	156
102	ANGLE OF ATTACK EFFECTS ON 1/3 OCTAVE AND OVERALL SPL FLAT PLATE MODEL 0	157
103	ANGLE OF ATTACK EFFECTS ON 1/3 OCTAVE AND OVERALL SPL FLAT PLATE MODEL 30	158
104	ANGLE OF ATTACK EFFECTS ON 1/3 OCTAVE AND OVERALL SPL FLAT PLATE MODEL 30	159
105	ANGLE OF ATTACK EFFECTS ON 1/3 OCTAVE AND OVERALL SPL FLAT PLATE MODEL 60	160
106	ANGLE OF ATTACK EFFECTS ON 1/3 OCTAVE AND OVERALL SPL FLAT PLATE MODEL 60	161
107	NON-DIMENSIONAL FREQUENCY SPECTRA DERIVED FROM 1/3 OCTAVE ANALYSIS MODEL FP 30°	163
108	NON-DIMENSIONAL FREQUENCY SPECTRA DERIVED FROM 1/3 OCTAVE ANALYSIS. MODEL: FP 30°	164

ILLUSTRATIONS (Cont.)

FIGURE		PAGE
109	NON-DIMENSIONAL FREQUENCY SPECTRA DERIVED FROM 1/3 OCTAVE ANALYSIS MODEL: FP 60° h = 4, δ^* = VAR, θ = VAR TRANSDUCER 4	165
110	NON-DIMENSIONAL FREQUENCY SPECTRA DERIVED FROM 1/3 OCTAVE ANALYSIS MODEL: FP 60° h = 4" δ^* = VAR. θ = VAR. TRANSDUCER CH. NO. 3 AT x = 18" AFT L.E.	166
111	COMPARISON OF 1/3 OCTAVE SPL, CORRECTED FOR FREE STREAM DYNAMIC PRESSURE TO 1 psi 60° FLAP CONFIGURATION, α = 0, R_e/L = 1×10^6/FT.	167
112	NON-DIMENSIONAL STROUHAL FREQUENCY SPECTRUM NORMALIZED TO THE MEAN SQUARED PRESSURE FLUCTUATION. FLAT PLATE MODEL, 60° FLAP	170
113	NARROW BAND VALUES OF (CORRELATION AREA) PLATE AREA EVALUATED AT f_{nm} VS $_m$ (BASED ON LOW SPEED NORMALIZED CROSS SPECTRAL DENSITIES FOR TURBULENT BOUNDARY LAYER PRESSURE. ASSUMED CONVECTION SPEED U_c = 2000 FT/SEC	176

TABLES

TABLE		PAGE
1	VALUES OF QUARTER WAVE LENGTH FREQUENCIES BEHIND DETACHED FLARE OR FLAP SHOCK	10
2	TUNNEL A TEST - INSTRUMENTATION CALIBRATION DATA AXISYMMETRIC MODEL	49
3	TUNNEL A TEST - INSTRUMENTATION CALIBRATION DATA TWO-DIMENSIONAL MODEL	49
4	TUNNEL C TESTS - INSTRUMENTATION CALIBRATION DATA TWO-DIMENSIONAL MODEL	51
5	TEST CONDITIONS TUNNEL A	54
6	TEST CONDITIONS TUNNEL C	62
7	CALCULATED 1/3 OCTAVE MEAN SQUARE VIBRATORY VELOCITY ERROR OF A SHOCK MOUNTED PIEZOELECTRIC CRYSTAL ON A CYLINDRICAL SHELL FOR Q=100	111
8	NATURAL VIBRATION FREQUENCIES OF THE FLAT PLATE MODEL CALCULATED FROM SIMPLY SUPPORTED PLATE THEORY	169
9	FREQUENCIES INSIDE $6860 \leq f \leq 8630$ cp AND $(A_{nn}/b1)$ VALUES	175

I INTRODUCTION

The work described in this report is an exploratory experimental investigation of fluctuating wall pressures under separated supersonic flows. One of the primary engineering objectives of such studies is to evaluate forcing functions for random structural vibratory response for vehicle structure adjacent to such separated flows. The vibratory response of the structure leads to structural fatigue, equipment failures, external acoustic radiation (as does the turbulence itself) and transmission of noise to the interior which may produce unacceptable internal noise levels in terms of speech communication interference, or passenger annoyance in the case of transport aircraft.

Separated flows arise locally on an aerospace vehicle whenever structural weight, and the size and volume of bulky payload items make ideal aerodynamic streamlining impractical. This is especially the case with blunt, hypersonic re-entry vehicles, where drag is not the primary design consideration. Also, a lifting re-entry vehicle is often a payload on a large booster during the launch phase, such that there is a sudden discontinuity in the diameter between the payload and the upper stage adjacent to it; this would lead to separated flow past the payload during the launch phase. During the re-entry phase, the deflection of aerodynamic control surfaces through large angles, and the large angles of attack which often accompany re-entry trajectories further contribute phases of flight which are characterized by separated flows. For supersonic aircraft, the deflection of flaps for "trimming" of aerodynamic pitching moments gives rise to a separated wake which may impinge upon fuselage structure downstream. We thus see the possibilities for separated flows to exist under some circumstances for vehicles which are, in general, well designed aerodynamically.

Fluctuating pressures under turbulent boundary layers have been measured for low speed flow with great care, most notably by Willmarth (Refs. 44-47, 49), Willmarth and Woolridge (Ref. 1), and Serafini (Ref. 34). Additional measurements are reported by Bull (Ref. 48), Tack, Smith and Lambert (Ref. 47), Harrison (Ref. 50), Skudrzyk and Haddle (Ref. 51). Wall pressures adjacent to low speed turbulent pipe flow have been measured by Bakewell, et al (Ref. 43), Bakewell (Ref. 35) and Von Winkle (Ref. 52).

With regard to supersonic boundary layers, there appears to be only the measurements of Kistler and Chen (Ref. 17). Also, Kistler (Ref. 13) has measured the fluctuating pressures under a separated supersonic boundary layer ahead of a forward facing step; this flow field is the one most similar to the flow fields of the present experiments.

With regard to theory, fundamental considerations are given by Batchelor (Ref. 53), and Townsend (Ref. 2). Specific studies directed toward the incompressible turbulent boundary layer wall pressure problem have been made by Kraichnan (Refs. 54 and 55), Lilley and Hodgson (Ref. 57), and Lilley (Ref. 56). The only supersonic boundary layer theory for wall pressure fluctuations appears to be that of Lilley (Ref. 21), although Phillips' work (Ref. 22) is closely related. The common denominator of the above work is the flat plate or pipe flow having a steep wall shear layer and (excepting Ref. 13) a nearly zero streamwise pressure gradient. The theory and measurements have all been confined to unseparated flows at zero angle of attack in the case of the flat plates, and afford no data for external flows past bodies of revolution. There is, thus, a scarcity of turbulent wall pressure fluctuation data at any Mach number for bodies of revolution, especially at angle of attack; however, the flat plate and pipe flow results

* * * * * * * * * * * * * * * *

are expected to be reasonably applicable for $\alpha = 0$ for unseparated flows. Base pressure data are also practically non-existent except for the measurements of Eldred (Ref. 12) for low speed flow. For separated flows, we apparently have only the work of Kistler (Ref. 13, cited above); hence, there is an urgent need for data on many kinds of representative separated flows over a range of Mach number, angle of attack, and Reynolds number. This need provided the genesis of the present work, which is exploratory in nature (covering many types of flows) as opposed to the very exhaustive studies in regards to boundary flow on flat plates which have pioneered the experimental technique, and illuminated problems such as the resolution of pressure by transducers of finite size (see especially Refs. 42 and 45).

Section II of the present work discusses some of the many additional physical mechanisms affecting supersonic wall pressure fluctuations. Some of these are steady flow effects, such as shock wave boundary layer interactions and compressibility effects on the turbulent mixing region, either directly or indirectly through changes in the exterior inviscid flow (causing changes in the boundary layer pressure gradient). All of these factors have quantitative effects on the low speed (vorticity mode) turbulent pressure fluctuations. In high speed flows, other effects enter which are discussed. Also, an analytical study of pressure fluctuations for bodies of revolution at angle of attack in incompressible flow is presented, which is believed to be original, in order to obtain some understanding of the factors which would alter the pressure fluctuations at finite angles of attack.

Sections III and IV discuss the model design and instrumentation, and Section V discusses the experimental results along with a further elucidation of possible experimental errors due to random vibratory response of the transducers.

II GENERAL DISCUSSION OF SEPARATED FLOW AND WALL TURBULENT PRESSURE FLUCTUATIONS

THE TURBULENT WALL PRESSURE FLUCTUATION PROBLEM

We begin by following Ref. 2, page 24, to establish some important features of incompressible wall turbulent pressure fluctuations. The three Navier-Stokes (momentum) equations (Ref. 2, page 24) can be written as

$$\frac{\partial u_i}{\partial t} + u_j \frac{\partial u_i}{\partial x_j} = -\frac{1}{\rho}\frac{\partial (P+p)}{\partial x_i} + \nu \nabla^2 u_i \quad [i,j = 1,2,3] \tag{1}$$

and the continuity equation for incompressible flow yields (using the summation convention for repeated indices)

$$\frac{\partial u_i}{\partial x_i} = \frac{\partial u_1}{\partial x_1} + \frac{\partial u_2}{\partial x_2} + \frac{\partial u_3}{\partial x_3} = 0 \tag{2}$$

At the high Reynolds' numbers of aerodynamic interest, we neglect the viscous terms in Eq. (1). Then differentiation of Eq. (1) with respect to x_i and applying Eq. (2) leads directly to the result (noting that ρ = constant; also,

$$\partial^2 u_i/\partial x_i \partial t = 0 \text{ and } \partial/\partial x_i\,(u_j\ \partial u_i/\partial x_j) = \partial^2(u_i u_j)/(\partial x_i \partial x_j)$$

$$\frac{\partial^2 (P+p)}{\partial x_i^2} = \nabla^2 (P+p) = -\frac{1}{\rho}\frac{\partial^2 \left[\rho (u_i u_j)\right]}{\partial x_i\ \partial x_j} \tag{3}$$

Eq. (3) is a classical Poisson equation relating the steady plus fluctuating pressure $(P + p)$ to the product, $u_i u_j$ $(k,j = 1,2,3)$ of velocity components. The solution of Eq. (3) is (Ref. 2, page 24),

$$P(\vec{x}) + p(\vec{x},t) + \frac{\rho}{4\pi}\int_{\text{turbulence volume}} \frac{\partial^2}{\partial y_i\, \partial y_j}\left[u_i(\vec{y},t)\, u_j(\vec{y},t)\right]\frac{dV(\vec{y})}{[\vec{r}]} \tag{4}$$

where u_i is the total velocity consisting of the mean flow $U_i(\vec{y})$ and a fluctuation field $v_i(\vec{y},t)$, $\vec{r}$ is the radius vector between the field point $\vec{x}$ at which p is measured and the variable source point $\vec{y}$ in the turbulence. The repeated indices j and i are to be summed giving nine terms in all. If the result Eq. (4) is squared and averaged over a long time, noting that the mean of the fluctuation $\langle u \rangle$ is zero, we find that the mean square fluctuation pressure is

$$\left\langle (p^2(\vec{x},t)\right\rangle = \frac{\rho^2}{16\pi^2}\int \frac{dV(\vec{y})}{r^2}\int dV(\vec{y})^1 \left\langle \frac{\partial^2 (u_i u_j)}{\partial y^1{}_i\, \partial y^1{}_j}\ \frac{\partial^2 (u_k u_l)}{\partial y_k\ \partial y_l}\right\rangle \tag{5}$$

In general, the fluctuations at the points $\vec{y}$ and $\vec{y}^1$ are only correlated within a small interval $\vec{z}$ where:

$$\left|\vec{z}\right| = \left|\vec{y}^{\,1} - \vec{y}\right| \simeq \delta \tag{6}$$

and δ is some small measure of the flow mixing region thickness (e.g. boundary layer, "wake", or mixing layer thickness).

It is convenient to introduce the so-called "correlation volume," ν whose size is of order δ^3, (see Refs. 6, 18-20 for examples in the related sound radiation problem). From Eq. (5), we find

$$\left\langle p^2(\vec{x},t)\right\rangle \cong \frac{\rho^2}{16\pi^2}\, V_o \left\langle \left(\frac{\partial^2 u_i u_j}{\partial y_i\, \partial u_j} \right)^2 \frac{1}{r^2_{av}} \right\rangle \nu \tag{7}$$

We carry this further as follows:

(1) Using some estimates of Townsend (Ref. 2, page 94) and applying dimensional analysis, one assumes that a dominant term of the 81 terms implied by Eq. (7) can be estimated by putting

$$u_i \sim U_\infty \quad \text{or} \quad (U_\infty - U_{min}) = U_s \tag{8}$$

$$v_i \sim U_s \sqrt{\frac{2.5\,\delta}{L}} \sim U_s \sqrt{\frac{\delta}{L}} \qquad \text{(Ref. 2, p. 94)} \tag{9}$$

and if L is a characteristic body dimension

$$r_{ave} \sim L$$

$$V_o \sim L^2 \delta \qquad \text{(planar flow)} \tag{10}$$

We remark that ν is defined precisely by the exact value of the second integral in Eq. (5). Physically, it represents the volume of fluid within which the second partial derivatives of the instantaneous Reynolds stresses are statistically correlated. We shall use the abbreviation of Corcos (Ref. 23) and define

$$X(\vec{y},t) \equiv \frac{\partial^2 \left[u_i(\vec{y},t)\, u_j(\vec{y},t) \right]}{\partial y_i\, \partial y_j} \tag{11}$$

(2) In the presence of a strong shear flow with a mean velocity component only in the streamwise (1) direction and varying only in the (2) direction (perpendicular to the wall), then the bracketed sum of 81 terms in Eq. (7) is dominated by the mean shear interaction yielding 4 equal terms. (See for example, Refs. 20 through 23.) This will be true in the central region even of a wake-like separated flow for which $\frac{\partial U_1}{\partial y_2}$ is zero at the wall. We then find

$$X^2(\vec{y},t) = \left(\frac{\partial^2 u_i u_j}{\partial y_i \partial y_j}\right)^2 \simeq \left(2\frac{\partial u_1}{\partial y_2}\frac{\partial v_2}{\partial y_1}\right)^2 \simeq \left(2\frac{U_s}{\delta}\frac{U_s}{L}\sqrt{\frac{\delta}{L}}\right)^2 \simeq \left[2U_s^2/(L^{3/2}\delta^{1/2})\right]^2 \quad (12)$$

Using Eqs. (8 to 12) in Eq. (7)

$$\langle p^2(x,t)\rangle \sim \frac{1}{\pi^2}\left(\frac{\rho U_\infty^2}{2}\right)^2 \frac{\delta^3}{L^3} \quad (13)$$

or

$$P_{rms} = \sqrt{\left[p^2(x,t)\right]} \sim \frac{q_\infty}{\pi}\left(\frac{\delta}{L}\right)^{3/2} \quad (14)$$

The above order of magnitude analysis serves to emphasize the following points:

(1) Incompressibility implies that the turbulent wall pressure is determined by the turbulent velocity field. This dependence involves integration over the entire volume of turbulence. It is, therefore, not uniquely determined by the local wall shear stress which, in fact, vanishes (by definition for a "separated flow" at the separation point, Ref. 5, page 31).

(2) It is seen that the root mean square pressure increases rapidly with the thickness/length ratio of the turbulent flow (for a planar surface). We thus expect more intense turbulent pressure fluctuations for a "separated flow". The separated region commences downstream of the separation point and is attended by a rapid thickening of the boundary layer as the flow proceeds downstream. Also, because separated flows have zero wall shear, we choose to scale our pressure fluctuations to $q_\infty = 1/2(\rho U_\infty^2)$.

(3) It appears to be easier to measure statistical quantities related directly to the wall turbulent pressure fluctuations of p (x,t) in view of the complexity of the right hand side of Eq. (5), even for incompressible flow (see Ref. 21 for example). There is, of course, fundamental interest in calculating turbulent pressure from the velocity gradients whenever sufficiently complete turbulence velocity wave number spectra are available for a given flow (see Refs. 21 and 22).

COMPRESSIBILITY EFFECTS ON TURBULENCE AND WALL PRESSURE FLUCTUATIONS

Since we will be very much concerned with the compressible case, we examine some of the possible complications.

(1) The general effects of viscosity, heat conduction and compressibility lead also to density and temperature fluctuations and, in general, there exist three fluctuation modes:

(a) vorticity (of which we have been implicitly speaking)
(b) acoustic
(c) entropy

Chu and Kovasznay (Ref. 7) have carried out a lengthy investigation of the interaction of these three modes by perturbing the Navier-Stokes, energy continuity and state equations. Their objective was to investigate problem areas in the interpretation of hot wire anemometers, but their results have implications for us in the "sound-vorticity" interactions leading to vorticity convection and the "sound-entropy" mode yielding sound generation. The problem of sound generation by vorticity has been treated explicitly by Powell (Ref. 24) and implicitly by Lighthill (Refs. 18, 19 and 20). We will not concern ourselves here with sound radiation, but merely recognize this as having a significant quantitative effect on our wall pressure measurements in compressible flow. The present measurements will give the sum of all three component fluctuation modes. These effects represent additional degrees of freedom of the problem which cannot be inferred merely from compressible boundary layer effects on the low speed (vorticity mode) results. The addition of these modes is expected to increase the intensity level of pressure fluctuations.

(2) We also expect a strong quantitative influence of decreased wall to free stream density on the incompressible contribution directly as seen from Eq. (5) and indirectly due to changes in the mean velocity gradients (see Eq. 11) . Also, changes in the external pressure gradient influence the rate of growth of the boundary layer and its tendency to separate. The general effects of these factors will be discussed below.

(3) The strong gradients of density, sound speed and velocity cause acoustic impedance gradients which will cause refraction of the acoustic part of the pressure. Such effects in the forward parts of the turbulent flow would have a pronounced influence on the downstream pressure. It may likewise alter the transmission of tunnel noise through the boundary layer selectively at high frequencies, as in other layered media problems (see Ref. 39).

(4) Aerodynamically generated sound in one part of the turbulent flow will be scattered by the downstream turbulent flow, affecting the wall pressure fluctuations at downstream points. The scattering of sound waves by atmospheric turbulence is an example of a fundamentally similar problem (though the nature of the turbulence involved is vastly different for the large Reynolds numbers involved in the geophysical problem)! This subject has been treated by Tartarski (Ref. 40), and has a vast literature which will not be discussed here.

DISCUSSION OF SPECIAL EFFECTS IN COMPRESSIBLE BOUNDARY LAYERS AND WAKES

Density

A lower density exists near the wall which would tend to lower the direct vorticity mode contribution [Eq. (5)].

Free Stream Pressure Gradient

This quantity depends on the entire inviscid, exterior flow field; the inviscid flow field depends on the entire body geometry and local protuberance geometry. It is well known from boundary layer theory that a positive pressure gradient ($\frac{\partial p}{\partial x} > 0$) in the direction of the flow increases the rate of growth of the boundary layer and will eventually cause separation (see Schlichting Ref. 5, pp. 113). Conversely, an accelerated external flow with a negative pressure gradient causes a thinning of the boundary layer and favors reattachment of "separated" flows.

The effects, therefore, of positive pressure gradients are to increase the level of turbulent pressure fluctuations even for "unseparated" flows. This is true also for low speed flows, but the pressure gradients are strongly influenced by compressibility of the exterior inviscid flow (see Liepmann and Roshko (Ref. 4) for example). The most pronounced examples of pressure gradient effects lie in the shock wave-boundary layer interaction problem, and at hypersonic speeds, changes are manifested in the exterior inviscid flow due to interaction of the thickened boundary layer with the leading edge shock (see Hayes and Probstein, Ref. 12, Chapter 9).

Shock Wave Boundary Layer Interactions

This is basically an extreme adverse pressure gradient since the shockwave pressure rise always is smooth because viscous effects eliminate the discontinuities associated with an ideal shock wave. Furthermore, the subsonic region of a supersonic boundary layer transmits the pressure rise upstream of the external shock position, which causes a readjustment of the steady flow and affects the strength and location of the external shock. An extensive literature exists on the magnitude of shock pressure rise required to separate turbulent boundary layers (see, for example, Ref. 26).

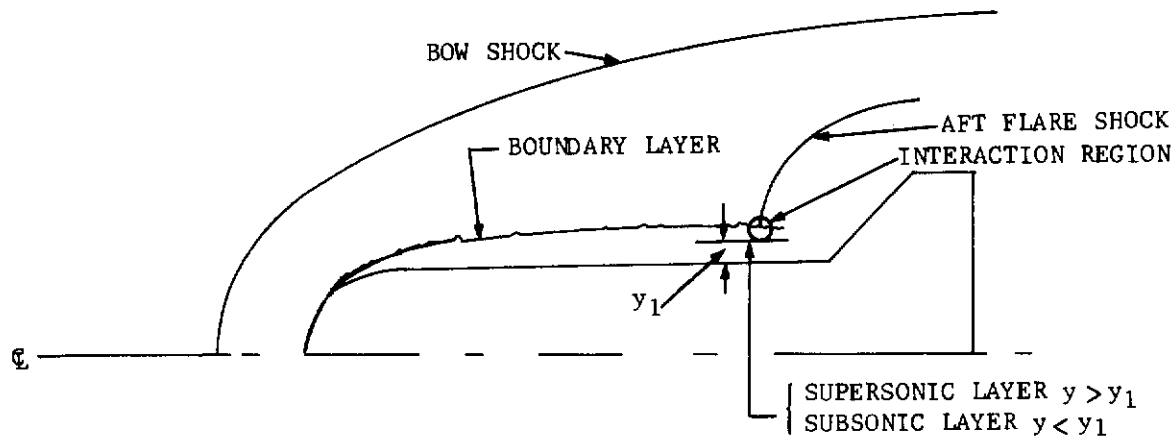

FIGURE 1 SCHEMATIC OF A SHOCKWAVE BOUNDARY LAYER INTERACTION

Oscillating Shock Waves

Under some circumstances, a shock wave-boundary layer interaction can lead to a hydrodynamic instability which, in this case, is referred to as an oscillating shock wave instability. This is like other hydrodynamic stability problems such as the classical laminar boundary layer instability problem investigated by Tollmein and Schlichting [see Schlichting (Ref. 5, page 383) and Lin (Ref. 27, page 13, and Chapter 5] in the following sense: small disturbances to a steady flow, obeying the basic equations of fluid motion and linearized with respect to the disturbances, exhibit positive exponential (unstable) amplification under certain conditions. At sufficiently large amplitudes non-linear effects limit the oscillation intensities (though these non-linear effects are not predicted by first order instability theory). In the case of laminar boundary layers, the interest is in boundary layer transition (from laminar to turbulent flow), and the linear instability theory yields qualitative correlation with experimental results for natural transition (see Ref. 5).

A simplified hydrodynamic stability approach to laminar boundary layer shock wave instability has been applied by Trilling (Ref. 28) who has derived criteria for the pressure coefficient increment required for a neutrally stable shock wave oscillation; no theory has been developed for turbulent boundary layer shock wave interaction instability. In general, the laminar boundary layer theory is of academic interest for the high Reynolds numbers associated with the maximum dynamic pressures where the pressure fluctuations are the greatest. Furthermore, it is well known from previous experimental work that laminar boundary layers will easily separate for a normal shock pressure rise at any local Mach number greater than 1.03 (see Gadd, Ref. 41, for example). Therefore, any laminar layer induced shock wave oscillation will tend to quicken the onset of transition to turbulent flow. This will then invalidate the laminar stability criteria, and any oscillating shock frequency criteria would have to be based on a theory involving possible unstable interaction between the shock wave and a turbulent boundary layer.

The effect of an oscillating shock wave situation would be to greatly amplify the wall pressure fluctuations in narrow frequency bands associated with the eigen-frequencies of the hydrodynamic stability problem (see Ref. 27, pages 32-45, where the characteristic wave lengths for instability of traveling wave hydrodynamic disturbances are considered for laminar flow between two parallel planes). Except for some possible extension of Trillings' work, no theory exists for predicting an oscillating shock wave instability due to a free turbulent boundary layer-shock wave interaction. It is, therefore, desirable to set up an experiment wherein forced shock wave oscillations occur due to an upstream wake. Ribner (Ref. 29) has shown, for example, that a random turbulent velocity fluctuation interacting with a shock wave can yield amplification of the turbulence. In the present experiments, therefore, a forward flare wake was set up which would interact with a detached shock wave ahead of the aft flare, thereby causing forced oscillations of the aft flare detached shock due to the upstream turbulent velocity fluctuations. Because the detached shock wave ordinarily assumes a fixed standoff position with respect to the aft flare, one might possibly expect additional discrete frequency amplification such that the standoff distance was equal to one quarter to a wave length (based on some average sonic velocity in the region aft of the shock) by analogy to the organ pipe with one end closed (see Rayleigh Ref. 30, page 51, e.g.). We indicate this possibility in Figure 2 which is considered as another possible instability mode. This analysis,

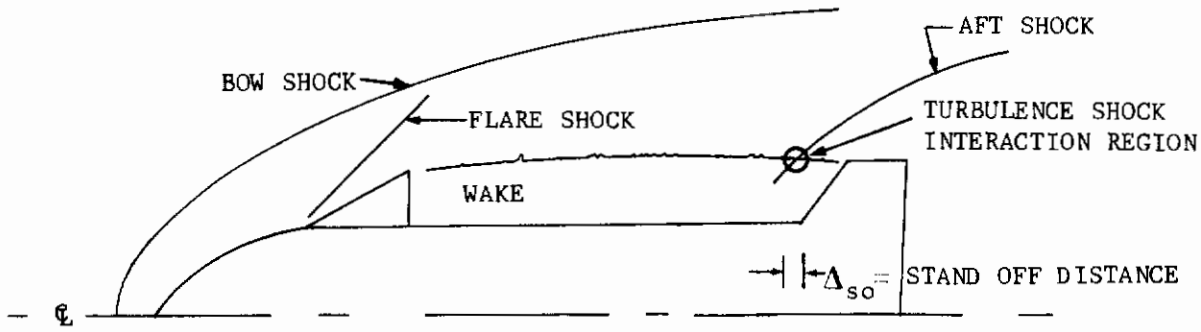

FIGURE 2 TURBULENCE SHOCK INTERACTION

of course, is in lieu of a rigorous shock perturbation analysis.

We would expect possibly that if c_2 is the sound speed behind the aft flare shock, then

$$f \cong \frac{c_2}{\lambda} = \frac{(c_2/h)}{4(\Delta_{so}/h)} \tag{15}$$

In terms of Strouhal, number

$$S = \frac{fh}{U_\infty} = \frac{1}{4}\left(\frac{c_2}{U_\infty}\right)\frac{1}{(\Delta_{so}/h)} = \frac{1}{4}\sqrt{\frac{T_2}{T_\infty}}\,\frac{1}{(M_\infty \Delta_{so}/h)} \tag{16}$$

To evaluate Eq. (16), one must estimate the shock wave standoff distance ratio, Δ_{so}/h. When the protuberance height, h, is small compared to the radius of the cylindrical body (as is nearly the case with the axisymmetric model of the present tests) then the detached aft flare shock appears locally as a two-dimensional (plane) shock. Because of this, one would idealize the shock wave standoff distance problem on the basis of the detachment distance ahead of a circular cylinder (2 dimensional) rather than on the basis of a spherical (3 dimensional) shock. We would use the protuberance height, h, as the radius of the equivalent cylinder, R_b, (see Figure 3).

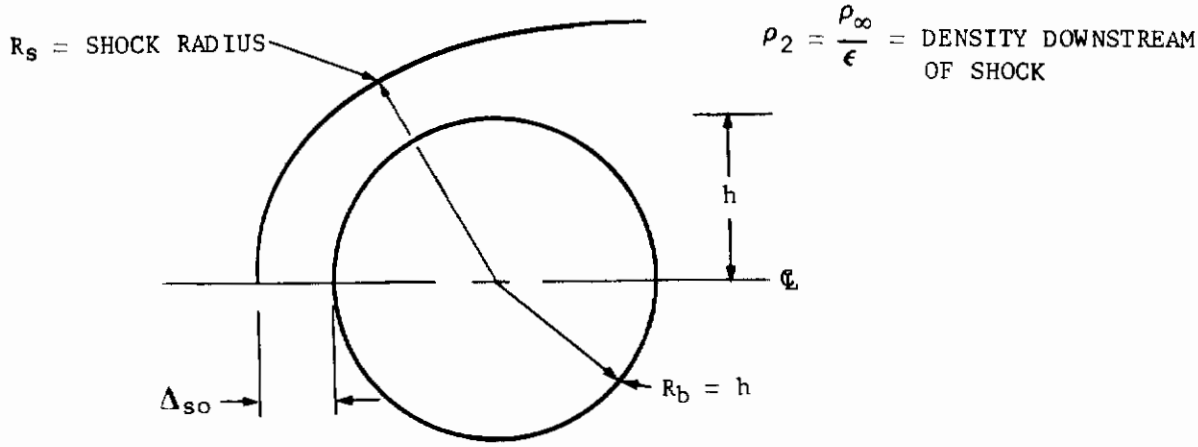

FIGURE 3 EQUIVALENT CYLINDRICAL PROBLEM FOR DETERMINING THE AFT FLARE STANDOFF DISTANCE

An approximate expression, valid for small density ratio $\epsilon = \rho_\infty / \rho_2$, for the standoff distance is (see Hayes and Probstein, Ref. 22, page 152)

$$\Delta_{so} = R_s - R_b = \frac{1}{2}\epsilon R_s \left[\ell n\left(\frac{4}{3\epsilon}\right) + \epsilon \ell n\left(\frac{4}{3\epsilon}\right) + 0\left(\epsilon^2 \ell n \frac{1}{\epsilon} + \ldots\right)\right] \tag{17}$$

Eq. (17) can be used in Eq. (16) by noting that

$$\begin{aligned} R_s &= R_b + \Delta_{so} \\ R_b &\simeq h \end{aligned} \tag{18}$$

Then, using the two term approximation,

$$\begin{aligned} \Delta_{so} &= \frac{\epsilon}{2}(h + \Delta_{so})\left[\ell n\left(\frac{4}{3\epsilon}\right)(1 + \epsilon + \ldots)\right] \\ \frac{\Delta_{so}}{h} &\simeq \left\{\frac{\epsilon}{2}\ \ell n\left(\frac{4}{3\epsilon}\right)(1+\epsilon)\right\} \Big/ \left\{1 - \frac{\epsilon}{2}\ \ell n\left(\frac{4}{3\epsilon}\right)(1+\epsilon)\right\} \end{aligned} \tag{19}$$

The value of ϵ may be estimated from standard gas dynamic normal shock tables (see i.e., Ref. 31); the results at lower supersonic Mach numbers are somewhat erroneous because the density ratio ϵ is larger. The following tabulation shows the calculated quantities of interest at the test Mach numbers.

TABLE 1 VALUES OF QUARTER WAVE LENGTH FREQUENCIES BEHIND DETACHED FLARE OR FLAP SHOCK

		(1)	(2)	(3)	(4)	(5)	(6)	(7)	(8)	(9)
M	T_{t_∞} °R	c_2 (ft/sec)	h_1 (ft)	$\frac{\Delta_{so}}{h}$	f_1 (cps)	U_∞ (ft/sec)	fh_1/U_∞	h_2^1 (ft)	f_2 (cps)	fh_2/U_∞
2.0	550	1150	.167	.483	3.570	1692	.354	.333	1785	.354 *
2.5	550	1150	.167	.411	4,190 *	1890	.370 *			
3.5	580	1182	.167	.333	5,330	2200	.404	.333	2665	.404 *
5.0	630	1232	.167	.294	6,280	2500	.419	.333	3140	.419
10.0	1800	2090	.167	.264	11,860	4500	.438	.333	5930	.438

*Test conditions enclosed in box.

The above frequencies are only suggestive, since several important factors are not accounted for by this simple quarter wave length criterion.

(1) The open end approximation (free pressure boundary condition) at the shock must be replaced by the Rankine Hugoniot relations with perturbations.

(2) Because of the viscous wake from the forward flare, the Mach number ahead of the detached shock ahead of the forward flare is non-uniform and generally lower than the free stream mach number. From Figure 32 we find M(z,x) = 1.25 to 2.25 ahead of the flare locally just beyond the flare edge (z = 2 inches). The Mach numbers here are so low that the shock detachment standoff distance estimate is probably inaccurate for the axisymmetric case.

(3) Also because of the viscous wake impinging on the detached aft flare shock, there are present all three modes of upstream fluctuations, e.g., entropy, vorticity and sound (see Ref. 7). Therefore, the relative proportion of the acoustic fraction of the pressure is uncertain.

With these remarks, we conclude our discussion of the factors relating to turbulent pressure fluctuations for zero angle of attack and consider angle of attack effects, especially for the axisymmetric model.

TURBULENT PRESSURE FLUCTUATIONS FOR BODIES OF REVOLUTION AT FINITE α

We begin by developing the zero angle of attack case for a body of revolution in contrast to the planar case, treated previously.

In the wake of the flare, the characteristic velocity scale is U_∞ and the characteristic length is taken as h. Then the characteristic frequency will be U_∞/h. The flow shear layer thickness δ will be of the order of h. We proceed along the lines of the previous discussion and then estimate (using Eqs. 7, 8 and 11) that the hydrodynamic part of the pressure fluctuation will be of the following order.

$$\Delta p_{rms} \sim \frac{1}{4\pi r} \left(\frac{2 \rho U_s^2}{L^{3/2} \delta^{1/2}} \right) \sqrt{\nu_{corr} V_{turb}} \qquad (20)$$

We proceed as in the case of Eq. (14) but we use estimates of ν_{corr} and V_{turb} appropriate to the axisymmetric case. For a body of radius R, length L, and protuberance height h, we put

$$\nu_{corr} \sim \delta^3 \sim h^3 \; ; \quad \alpha = 0 \qquad (21)$$

and the turbulence volume is estimated as

$$V_{turb} = 2\pi R \, (L - x_{ff}) \sim 2\pi R h (L - x_{ff}) \qquad (22)$$

where x_{ff} is the position of the trailing edge of the forward flare. We consider that the average source to field point radius, r, is of order $(L - x_{ff})$. Then from Eq. 20 we have, (assuming $U_s \sim U_\infty$, $\delta \sim h$),

$$\Delta p_{rms} \sim \frac{\left(\frac{\rho U_\infty^2}{2\pi}\right)\sqrt{h^3\, 2\pi R h\,(L-x_{ff})}}{(L-x_{ff})^{5/2}\, h^{1/2}} \tag{23}$$

or

$$\Delta p_{rms} \sim \left(\frac{\rho U_\infty^2}{\sqrt{2\pi}}\right) \frac{(h^3 R)^{1/2}}{(L-x_{ff})^2} \qquad \text{for } \alpha = 0$$

Eq. (23) is an axisymmetric counterpart of Eq. (12) when the turbulence is dominated by the mean shear interaction. The reader is warned that this argument is not as strong for separated flows as it is in the case of unseparated shear flows [see Corcos (Ref. 23) for an expansion of the term in Eq. (11) of the mean and fluctuating velocity components].

We now consider the flow structure at angle of attack due to viscous cross flow. A characteristic cross flow velocity is

$$w_\alpha = U_\infty \sin\alpha \tag{24}$$

The characteristic frequency is then of order $U_\infty \sin\alpha/D$ where D is the body diameter. The correlation volume will be of the order R^3 and the total volume of turbulence in the cross flow wake, $V_{turb, \alpha}$ will be a triangular prismatic region such as depicted in the sketch 1, having length $L - x_{ff}$, with $D = 2R$, and a base, $(L - x_{ff}) \tan\alpha$

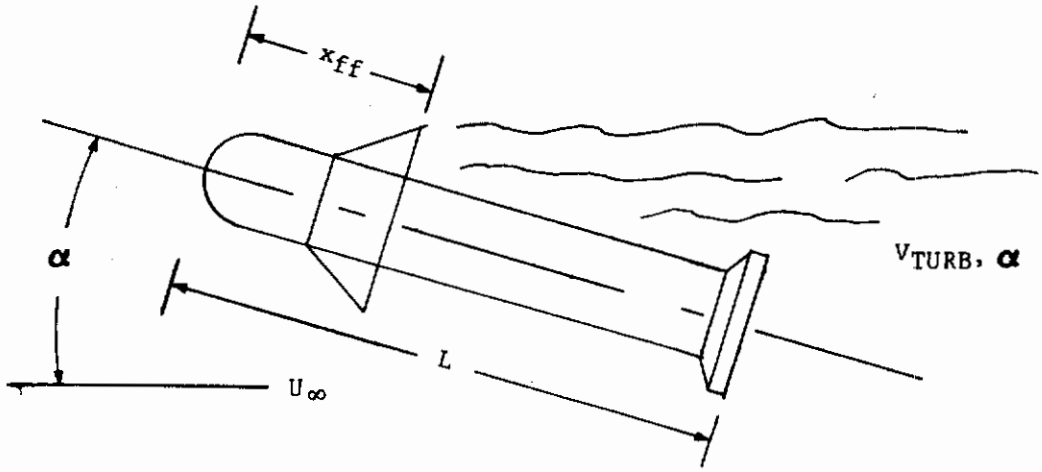

FIGURE 4 VISCOUS CROSS FLOW WAKE

$$V_{turb, \alpha} = \frac{1}{2}(L-x_{ff})^2\, 2R \tan\alpha \tag{25}$$

Then, assuming $\nu_{corr} \sim R^3$, $r \sim (L - x_{ff})$, $\delta \sim R$ and using Eqs. (24, 25 and 20), we find

$$\Delta p_{rms} \sim \frac{\frac{\rho (U_\infty \sin\alpha)^2}{4\pi} \sqrt{\frac{1}{2} R^3 (L-x_{ff})^2 R \tan\alpha}}{(L-x_{ff})^{5/2} R^{1/2}}$$

or

$$\Delta p_{rms} \sim \left(\frac{\rho U_\infty^2}{4\pi\sqrt{2}}\right) \sin^2\alpha \, (\tan\alpha)^{1/2} \left(\frac{R}{(L-x_{ff})}\right)^{3/2} ; \text{ for large } \alpha \qquad (26)$$

With regard to the angle dependence, it could be argued that dimensional analysis cannot distinguish between ρU_∞^2 and ρw_α^2. On the other hand, empirical aerodynamic representations of viscous cross force on cylindrical bodies have been successfully represented as a $\sin^2\alpha$ dependence or simply α^2 for small α. The present theory would suggest

$$F_{\text{viscous cross flow}} \sim \Delta p_{rms} \, D^2 \qquad (27)$$

$$\sim \sin^2\alpha \sqrt{\tan\alpha}$$

$$\sim \alpha^{2.5} \text{ for } \alpha << 1$$

This theory, however, ignores any curvature of the wake edge in defining the turbulence volume for use in Eq. (25). Eq. (26) is based on the formal integral of the Poisson equation for incompressible turbulent pressure. We shall now present a more rigorous and general theory.

AXIAL FLOW AND CROSS FLOW INTERACTION AT FINITE α

Eqs. (20) and (26) afford a framework for evaluating turbulent pressure fluctuations on a body of revolution at $\alpha = 0$ and at large finite α respectively. The increment due to angle of attack would, however, have an interaction due to cross correlation between the axial and cross flow generated turbulent fluctuations which would not reduce to a simple $\alpha^{2.5}$ dependence. First, we represent the three absolute velocity components as $[u_i^T(x,t): \; i = 1,2,3]$ and split them into axial and cross flow terms

$$u_i^T(\vec{x},t) = u_i^T(\vec{x},t) \cos\alpha + v_i^T(\vec{x},t) \sin\alpha \qquad (28)$$

We then define the double velocity correlation function as

$$R_{ij} \equiv \left[u_i^T(x,t) \, u_j^T(x,t)\right] \qquad (29)$$

$$= \left[\left(u_i^T u_j^T\right) + 2\tan\alpha \left(u_i^T v_j^T\right) + \tan^2\alpha \left(v_i^T v_j^T\right)\right] \cos^2\alpha \qquad (30)$$

We now use the mean shear dominance as a simplifying hypotheses again (Eq. 11) but in the present case, we separate the axial and cross flow components

$$u_i^T(\vec{y},t) \equiv u_i^T + v_i^T \equiv (U_i \cos\alpha + V_i \sin\alpha) + (u_i \cos\alpha + v_i \sin\alpha) \quad (31)$$

$$= \cos\alpha\left[(U_i + V_i \tan\alpha) + (u_i + v_i \tan\alpha)\right] \quad (32)$$

where (U_i, V_i) are the steady flow velocities and (u_i, v_i) are the turbulent velocities. Then we find that if as assumed in Eq. (11) using the notation of Corcos (Ref. 23)

$$X(\vec{y},t) \equiv \frac{\partial^2\left(u_i^T u_j^T\right)}{\partial y_i\, \partial y_j} \simeq 2\frac{\partial W_1}{\partial y_2}\frac{\partial w_2}{\partial y_1} \; ; \; W_1 = U_1 + V_1 \tan\alpha \; ; \; w_2 = u_2 + v_2 \tan\alpha \quad (33)$$

then

$$X(\vec{y},t) = \frac{\partial^2(u_i u_j)}{\partial y_i\, \partial y_j} \simeq 2\left(\frac{\partial U_1}{\partial y_2} + \frac{\partial V_1}{\partial y_2}\tan\alpha\right)\left(\frac{\partial u_2}{\partial y_1} + \frac{\partial v_2}{\partial y_1}\tan\alpha\right)\cos^2\alpha$$

$$\simeq 2\cos^2\alpha\left[\left(\frac{\partial U_1}{\partial y_2}\frac{\partial u_2}{\partial y_1}\right) + \tan\alpha\left(\frac{\partial V_1}{\partial y_2}\frac{\partial u_2}{\partial y_1} + \frac{\partial U_1}{\partial y_2}\frac{\partial v_2}{\partial y_1}\right) + \sin\alpha\left(\frac{\partial V_1}{\partial y_2}\frac{\partial v_2}{\partial y_1}\right)\right] \quad (34)$$

We will now proceed in a general way to develop $X(\vec{y},t)$ by using Eqs. (30 and 32) and collecting coefficients of $\tan\alpha$, which is not restricted by Eqs. (33 and 34):

$$X(\vec{y},t) = \left[X_0(\vec{y},t) + X_1(\vec{y},t)\tan\alpha + X_2(\vec{y},t)\tan^2\alpha\right]\cos^2\alpha \quad (35)$$

where X_0, X_1, and X_2 are the coefficients of $(1, \tan\alpha, \tan^2\alpha)$ in the case of Eq. (34).

We shall now rewrite Eq. (5) of Section II in the following form since the variations in $|x - \vec{\eta}|$ are small because $\left(X(\vec{y},t)\, X(\vec{\eta},t)\right)$ is only finite as $\vec{y} \to \vec{\eta}$.

$$\left\langle p_{rms}^2(\vec{x},t)\right\rangle = \frac{\rho^2}{16\pi^2}\int\frac{dV(\vec{y})}{|\vec{x}-\vec{y}|^2}\int dV(\vec{\eta})\left\langle X(\vec{y},t)\, X(\vec{\eta},t)\right\rangle \quad (36)$$

We shall now use Eq. (35). First we develop the covariance functions required by Eq. (36). We put

$$\left\langle X(\vec{y},t)\, X(\vec{\eta},t)\right\rangle = \left\langle\left[X_0(\vec{y},t) + X_1(\vec{y},t)\tan\alpha + X_2(\vec{y},t)\tan^2\alpha\right]\right.$$
$$\left.\times\left[X_0(\vec{\eta},t) + X_1(\vec{\eta},t)\tan\alpha + X_2(\vec{\eta},t)\tan^2\alpha\right]\right\rangle\cos^4\alpha \quad (37)$$

Let us define the space correlation functions

$$S_{ij}(\vec{y},\vec{\eta}) = \left\langle X_i(\vec{y},t)\, X_j(\vec{\eta},t) \right\rangle ; \; (i,j = 0,1,2) \tag{38}$$

$$T_{ij}(\vec{y},\vec{\eta}) = \left\langle X_i(\vec{\eta},t)\, X_j(\vec{y},t) \right\rangle \tag{39}$$

Then expanding Eq. (37) and using Eqs. (38 and 39), we find

$$\begin{aligned} R_x(\vec{y},\vec{\eta}) \equiv \left\langle X(\vec{y},t)X(\vec{\eta},t) \right\rangle \equiv \Big\{ & S_{00} + (S_{01} + T_{10}) \tan\alpha \\ & + (S_{20} + S_{11} + T_{20}) \tan^2\alpha + (S_{12} + T_{21}) \tan^3\alpha \\ & + S_{22} \tan^4\alpha \Big\} \cos^4\alpha \end{aligned} \tag{40}$$

Let us abbreviate Eq. (40) by

$$R_x(\vec{y},\vec{\eta}) = \sum_{k=0}^{4} R_k \tan^k\alpha \cos^4\alpha \tag{41}$$

where $\{R_k\}$ are the coefficients of $\tan^k\alpha$ in Eq. (40). It is evident that since $\vec{y}$ and $\vec{\eta}$ are two adjacent points and $X_i(\vec{y},t)$ and $X_i(\vec{\eta},t)$ are the same functions of $\vec{y}$ and t, then

$$\left\langle X_i(\vec{y},t)\, X_j(\vec{\eta},t) \right\rangle \equiv \left\langle X_i(\vec{\eta},t)\, X_j(\vec{y},t) \right\rangle \tag{42}$$

since $\vec{\eta}$ is only a dummy variable for $\vec{y}$. Therefore,

$$S_{ij} = T_{ij} \tag{43}$$

and Eqs. (40 and 41) may be simplified. Accordingly

$$\begin{aligned} R_0 &= S_{00} \\ R_1 &= S_{01} + S_{10} = 2\,S_{01} \\ R_2 &= S_{20} + S_{11} + S_{20} = 2\,S_{20} + S_{11} \\ R_3 &= S_{12} + S_{21} = 2\,S_{12} \\ R_4 &= S_{22} \end{aligned} \tag{44}$$

We again emphasize that Eqs. (37 through 44) are generally valid, independent of any assumptions such as Eq. (33 and 34) used to simplify X or its power series development in α.

We can now write Eq. (36) as

$$\left[p_{rms}^2\right] = \frac{\rho^2}{16\pi^2}\left(\sum_{k=0}^{4}\tan^k\alpha \int_{V\ turb} \frac{dV(\vec{y})}{|\vec{x}-\vec{y}|^2}\ \nu_k\right)\cos^4\alpha \qquad (45)$$

where the correlation volume associated with R_k is rigorously defined by

$$\nu_k \equiv \int_{\text{turbulence vol.}} dV\,(\vec{\eta})\,R_k\,(\vec{y},\vec{\eta}) \qquad (46)$$

The contributions to Eq. (4) will only come from a small neighborhood $|\eta - y| \leq k\delta$ where δ is the mixing region thickness and K is of order unity. We may now apply dimensional analysis by estimating the ν_k as all of the order $\nu_k \sim R_k\ \delta^3$, $r \sim (L - x_{ff})$, and we shall refine our estimate of V_{turb} for small angles of attack. We will then write the approximate expression

$$\left[p^2_{rms}\,(\vec{x})\right] \cong \frac{\rho^2}{16\pi^2}\,\frac{V_{turb}\,\delta^3}{|\vec{x}-y_{av}|^2}\left(\sum_{k=0}^{4} R_k \tan^k\alpha\right)\cos^4\alpha \qquad (47)$$

Before calculating V_{turb}, we must estimate the orders of magnitudes of the R_k. At small angles of attack, the quantities R_0 and R_1 will be of greatest importance, and R_0 will make contributions to the α dependence due to the angle of attack dependence of V_{turb} and δ. From Eqs. (44, 38, 35 and 34) we find the following relations if we now again restrict ourselves to the limitations of Eqs. (33 and 34):

$$\begin{aligned} R_0 = S_{00} &= \left[X_0\,(\vec{y},t)\,X_0\,(\vec{\eta},t)\right] \\ &= 4\left[\left(\frac{\partial U_1}{\partial y_2}\,(\vec{y},t)\,\frac{\partial u_2}{\partial y_1}\,(\vec{y}_1,t)\right)\left(\frac{\partial U_1}{\partial \eta_2}\,(\vec{\eta},t)\,\frac{\partial u_2}{\partial \eta_1}\,(\vec{\eta},t)\right)\right] \qquad (48) \\ &= 4\,\tilde{R}_0(\vec{y},\vec{\eta})\left[\left(\frac{\partial U_1}{\partial y_2}(\vec{y},t)\ \frac{\partial u_2}{\partial y_1}\ (\vec{y},t)\right)^2\right] \end{aligned}$$

where $\tilde{R}_0(\vec{y},\vec{\eta})$ is a dimensionless space correlation coefficient (= 1 for $\vec{y} = \vec{\eta}$) and approaching zero as $|\vec{y} - \vec{\eta}| \to \infty$. We may estimate the order of magnitude of

$$\left[\left(\frac{\partial U_1}{\partial y_2}\ \frac{\partial u_2}{\partial y_1}\right)^2\right]$$

from Eqs. (8) and (9) with $\frac{\partial}{\partial y_1} \sim \frac{1}{L - x_{ff}}$, $\frac{\partial}{\partial y_2} \sim \frac{1}{\delta}$

$$\left\langle \left(\frac{\partial U_1}{\partial y_2} \; \frac{\partial u_2}{\partial y_1} \right)^2 \right\rangle \sim \left(\frac{U_\infty}{\delta} \; \frac{U_\infty}{L-x_{ff}} \sqrt{\frac{\delta}{L-x_{ff}}} \right)^2$$

$$\sim \left[U_\infty{}^2 / (L-x_{ff})^{3/2} \, \delta^{1/2} \right]^2 \qquad (49)$$

$$\sim \left[U_\infty{}^4 / (L-x_{ff})^3 \delta \right]$$

which agrees with Eq. (12) derived for $\alpha = 0$. We now consider R_1. From Eqs. (44, 38, 35 and 34) we find

$$R_1 = 2 S_{01} = 2 \left\langle \left(X_0 (\vec{y}, t) \, X_1 (\vec{\eta}, t) \right) \right\rangle$$

$$= 8 \left\langle \left(\frac{\partial U_1}{\partial y_2} \; \frac{\partial u_2}{\partial y_1} \right) \left(\frac{\partial V_1}{\partial \eta_2} \; \frac{\partial u_2}{\partial \eta_1} + \frac{\partial U_1}{\partial \eta_2} \; \frac{\partial v_2}{\partial \eta_1} \right) \right\rangle \qquad (50)$$

Now again we estimate

$$\frac{\partial V_1}{\partial \eta_2} \sim \frac{U_\infty}{\delta}; \; \frac{\partial v_2}{\partial \eta_1} \sim \frac{U_\infty}{L-x_{ff}} \sqrt{\frac{\delta}{L-x_{ff}}} \sim \frac{\partial u_2}{\partial \eta_1} \qquad (51)$$

The assumptions (51) are reasonable since the total cross flow velocity at infinity is $U_\infty \sin\alpha$; therefore, $|\vec{V} + \vec{v}| \sim U_\infty$. Then by Eqs. (51, 50 and 49) we find that

$$R_1 \sim 16\, \tilde{R}_1\, (\vec{y},\vec{\eta}) \left| U_\infty^4 / (L-x_{ff})^3 \delta \right| \tag{52}$$

where

$$\tilde{R}_1\, (\vec{y},\vec{\eta}) = \frac{\tilde{R}_0(\vec{y},\vec{\eta})}{2} \left[\left(\frac{\partial V_1/\partial y_1}{\partial U_1/\partial y_1} \right) + \frac{\left| (\partial u_2(\vec{y},t)/\partial y_1)(\partial v_2(\vec{\eta},t)/\partial \eta_1) \right|}{\left| (\partial u_2(\vec{y},t)/\partial y_1)(\partial u_2(\vec{\eta},t)/\partial \eta_1) \right|} \right] \tag{53}$$

$$\sim \tilde{R}_0\, (\vec{y},\vec{\eta}) \sim 1 \tag{54}$$

We must now calculate δ^3 and V_{turb} and develop each of them in a power series in $\tan\alpha$. These quantities along with R_0 and R_1 from Eqs. (49 and 52) will give the leading terms of the $\tan\alpha$ expansion for small α when substituted in Eq. (47).

We now proceed to estimate δ, δ^3 and V_{turb}:

For $\alpha = 0$ as before

$$V_{\substack{\alpha=0 \\ ,corr}} \sim \delta^3 \sim h^3 \tag{55}$$

For large α as in Eq. (26)

$$V_{\substack{\alpha \\ ,corr}} \sim \delta^3 \sim R^3 : (x-x_{ff}) \tan\alpha \gg R \tag{56}$$

For small α such that $(x - x_{ff}) \tan\alpha \ll R$, let us assume that the flow thickness δ is given by

$$\delta(x, \theta, \alpha) \sim \left| h + (x - x_{ff}) \tan\alpha \cos\theta \right| \tag{57}$$

where θ is the circumferential angle measured from the top center (lee side) of the body.

Similarly, our total volume of turbulence for the three angle of attack regimes will be from Eq. (22)

$$V_{turb} = 2\pi Rh\,(L-x_{ff})\,; \qquad \alpha = 0 \tag{22}$$

For large α we have Eq. (25) again

$$V_{turb} = \frac{1}{2}(L-x_{ff})^2\, 2\, R \tan\alpha \tag{25}$$

When $\alpha = 90^\circ$, we have the situation as with Aeolian tones where the cylinder wake can be thought of as having a finite length of perhaps 5D = 10R and

$$V_{turb} \sim (L-x_{ff})\,(2R)\,L_{wake}$$

$$\sim 20\,(L-x_{ff})R^2 \quad ; \quad \alpha = 90^\circ \tag{58}$$

For the small angle of attack range such that $(L - x_{ff}) \sin\alpha \leq R$, we can estimate the cross flow wake volume as an unsymmetrical cone whose upper half base area is an ellipse whose semi-major and semi-minor axes are $[R + h + (L - x_{ff}) \sin\alpha]$ and $(R + h)$ respectively, minus a hole of radius R. On the windward side, we have simply a semi-annular region of area $1/2\ \pi[(R + h)^2 - R^2]$. Then we have for small α,

$$V_{turb} = \frac{1}{3}(L-x_{ff})\left\{\frac{\pi(R+h)^2}{2} + \frac{\pi}{2}\left[(R+h) + (L-x_{ff})\tan\alpha\right](R+h) - \pi R^2\right\}$$

$$= \frac{1}{3}(L-x_{ff})\left\{\pi(2Rh+h^2) + \frac{\pi}{2}(R+h)(L-x_{ff})\tan\alpha\right\} \tag{59}$$

The order of magnitude of δ is given by putting $\theta = 0$, $x = L$ in Eq. (57),

$$\delta(L,\alpha) \sim \left[h + (L-x_{ff})\tan\alpha\right] \tag{60}$$

Then using Eqs. (60, 59, 52 and 49) in Eq. (47) we obtain with $|\overrightarrow{x - y}| \sim (L - x_{ff})$

$$\left[p_{rms}^2(\vec{x})\right] \sim \frac{\rho^2\left[h + (L-x_{ff})\tan\alpha\right]^3 \pi(L-x_{ff})}{3 \times 16\pi^2(L-x_{ff})^2}\left\{(2Rh + h^2) + \frac{1}{2}(R+h)(L-x_{ff})\tan\alpha\right\}$$

$$\times \left(\frac{U_\infty^4}{(L-x_{ff})^3\left[h + (L-x_{ff})\tan\alpha\right]}\right)\left[4 + 16\tan\alpha + 0(\alpha^2) + \ldots\right]\cos^4\alpha$$

or,

$$\left[p_{rms}^2(\vec{x})\right] \sim \left(\frac{\rho U_\infty^2}{2}\right)^2\left(\frac{1}{3\pi}\right)\frac{\left[h + (L-x_{ff})\tan\alpha\right]^2}{(L-x_{ff})^4}\left\{(2Rh + h^2) + \frac{1}{2}(R+h)(L-x_{ff})\tan\alpha\right\}$$

$$\times \left\{1 + 4\tan\alpha + 0(\alpha^2) + \ldots\right\}\cos^4\alpha \tag{61}$$

We, thus, finally obtain our desired result

$$\sqrt{\left\langle p_{rms}^{\,2}\,(\vec{x})\right\rangle} \sim \left(\frac{\rho U_\infty^{\,2}}{2}\right) \frac{1}{(3\pi)^{1/2}} \frac{\left[h + (L-x_{ff}) \tan\alpha\right]}{(L-x_{ff})^2} \left\{ 2Rh + h^2) + \frac{(R+h)(L-x_{ff}) \tan\alpha}{2} \right\}^{1/2} \tag{62}$$

$$x \left\{ 1 + 4\tan\alpha + 0(\tan^2\alpha) + \ldots \right\}^{1/2} \cos^2\alpha$$

We can see that three distinct factors contribute to the angle of attack dependence: (1) the change of δ, (2) the change of V_{turb} and (3) the change of the Reynolds stresses due to the cross flow velocity components.

It is possible to develop the trigonometric functions into a power series in α; however this expansion would introduce unnecessary errors compared to Eq. (62) and would obscure the non-linear behavior at large values of α. However, to evaluate the behavior at large α, we would also need the terms R_3 and R_4 from Eq. (44). Eq. (62) does have the implicit assumption of Townsend's order of magnitude estimate of the turbulence velocity for a shear flow Eq. (9)

$$|v_i| \sim U_\infty \sqrt{\frac{\delta}{L-x_{ff}}} \tag{9}$$

where we have allowed δ to vary with α. Also, when $\alpha \to 90^o$ we use $\delta \sim R$ in Eq. (62). We also recall that the assumption was made that the mean shear turbulence interaction dominated X (y,t), reducing the nine (9) fundamental terms of Eqs. (12 and 33) to twice the value of a single dominant term. Let us close our theoretical discussion by reviewing the validity of this assumption.

Recall that by definition

$$X^T(\vec{y},t) = \sum_{i=1}^{3} \sum_{j=1}^{3} \frac{\partial^2 (u_i^T\, u_j^T)}{\partial y_i y_j} \tag{63}$$

where u_i^T is the total velocity.

We shall use the summation of repeated indices convention of Cartesian tensor theory hereafter to avoid writing of summation signs. We expand Eq. (62)

$$X^T = \frac{\partial}{\partial y_i} \left[u_i^T \frac{\partial u_j^T}{\partial y_j} + u_j^T \frac{\partial u^T{}_i}{\partial y_j} \right] \tag{64}$$

Recall that for incompressible flow, the continuity Eq. (2) yields

$$\frac{\partial u_i^T}{\partial y_i} = \frac{\partial u_j^T}{\partial y_j} = 0 \tag{2}$$

Then (64) reduces to

$$X^T = \frac{\partial}{\partial y_i}\left(u_j^T \frac{\partial u_i^T}{\partial y_j}\right) = u_j^T \frac{\partial}{\partial y_j}\left(\frac{\partial u_i^T}{\partial y_i}\right) + \left(\frac{\partial u_i^T}{\partial y_i}\right)\left(\frac{\partial u_j^T}{\partial y_i}\right) \tag{65}$$

We again spply the continuity relation to Eq. (65); the first term vanishes and

$$X^T = \left(\frac{\partial u_i^T}{\partial y_j}\right)\left(\frac{\partial u_j^T}{\partial y_i}\right) \tag{66}$$

If we now split U_i^T into a steady plus a fluctuating part, we write

$$u_i^T(\vec{y},t) \equiv U_i(\vec{y}) + u_i(\vec{y},t) \; ; \; |u_i| << |U_i| \tag{67}$$

which is justified by Eq. (8) above. Then substituting Eq. (67) in Eq. (66) and expanding we find

$$X^T(t) = \left(\frac{\partial U_i}{\partial y_j} + \frac{\partial u_i}{\partial y_j}\right)\left(\frac{\partial U_j}{\partial y_i} + \frac{\partial u_j}{\partial y_i}\right)$$

$$= \left(\frac{\partial U_i}{\partial y_j}\frac{\partial U_j}{\partial y_i}\right) + \left(\frac{\partial u_i}{\partial y_j}\frac{\partial U_j}{\partial y_i} + \frac{\partial U_i}{\partial y_j}\frac{\partial u_j}{\partial y_i}\right) \tag{68}$$

$$+ \left(\frac{\partial u_i}{\partial y_j}\frac{\partial u_j}{\partial y_i}\right)$$

The first term of Eq. (68) is a steady state term and is not in interest. In the second term, i and j are dummy summation indices. Therefore,

$$\frac{\partial u_i}{\partial y_j}\frac{\partial U_j}{\partial y_i} \equiv \frac{\partial U_i}{\partial y_j}\frac{\partial u_j}{\partial y_i} \tag{69}$$

and the fluctuating part of X^T is

$$X(\vec{y},t) = 2\frac{\partial u_j}{\partial y_i}\frac{\partial u_i}{\partial y_j} + \frac{\partial u_i}{\partial y_j}\frac{\partial u_j}{\partial y_i} \tag{70}$$

If the wake or shear layer is one which is spreading slowly, then the mean velocity has only a streamwise component, $\{U_i\} = \{U_1, 0, 0\}$. (71)

This assumption neglects the cross flow components, U_2 and U_3.

Furthermore, the continuity Eq. (2) is linear. Therefore,

$$\frac{\partial u_i^T}{\partial y_i} \equiv \frac{\partial U_i}{\partial y_i} + \frac{\partial u_i}{\partial y_i} = 0 \tag{72}$$

This requires that separately

$$\frac{\partial U_i}{\partial y_i} = 0 \; ; \; \frac{\partial u_i}{\partial y_i} = 0 \tag{73}$$

Proceeding from Eqs. (73 and 71) we obtain

$$\frac{\partial U_i}{\partial y_i} \equiv \frac{\partial U_1}{\partial X_1} = 0 \tag{74}$$

Eq. (74) implies (with an error of order $\tan\alpha$) that

$$U_1 = U_1(y_2, y_3) \text{ only} \tag{75}$$

If y_2 and y_3 are directions of Cartesian coordinates perpendicular to the body axis, then the dominant terms in Eq. (70) are

$$X(\vec{y},t) \simeq 2\left(\frac{\partial U_1}{\partial y_2}\frac{\partial u_2}{\partial y_1} + \frac{\partial U_1}{\partial y_3}\frac{\partial u_3}{\partial y_1}\right) \tag{76}$$

where the neglected terms give an error

$$\epsilon_x = \sum_{j=1}^{3}\sum_{i=1}^{3} \frac{\partial u_i}{\partial y_j}\frac{\partial u_j}{\partial y_i} \tag{77}$$

We can estimate Eq. (76) as follows. Let the shear layer mean velocity profile be

$$U_1 = U_\infty \cos\alpha\, f\left(\frac{y_n}{h + (L-x_{ff})\tan\alpha\,\cos\theta}\right); \quad \text{for } \theta \le \frac{\pi}{2} \tag{78}$$

where

$$y_n = r - R$$

Then in terms of Cartesian coordinates

$$\cos\theta = \frac{y_3}{\sqrt{y_3^2 + y_2^2}} = \frac{y_3}{r} \tag{79}$$

we find by differentiation with respect to y_3 holding y_2 constant:

$$\frac{\partial U_1}{\partial y_3} = \frac{U_\infty \cos\alpha}{\delta} f'\left(\frac{y_n}{\delta}\right)\left\{\cos\theta - \frac{(L-x_{ff})}{\delta}\tan\alpha\,\sin^2\theta\right\} \tag{80}$$

By a similar analysis, we find

$$\frac{\partial U_1}{\partial y_2} = \frac{\partial U_1}{\partial r}\sin\theta - \frac{\cos\theta}{r}\frac{\partial U_1}{\partial \theta} \tag{81}$$

Using Eqs. (78 and 81), we find

$$\frac{\partial U_1}{\partial y_2} = \frac{U_\infty \cos\alpha}{\delta} f'(y_n/\delta)\left\{\sin\theta - \sin\theta\,\cos\theta\,\frac{(L-x_{ff})\tan\alpha}{\delta}\right\} \tag{82}$$

Then both $\frac{\partial U_1}{\partial y_2}$ and $\frac{\partial U_1}{\partial y_3}$ are of the same order of magnitude. We now consider the turbulence components. From Eq. (9), the Cartesian components would be

$$\begin{Bmatrix} u_2 \\ u_3 \end{Bmatrix} \sim U_\infty \sqrt{\frac{\delta}{(L-x_{ff})}} \begin{Bmatrix} \sin\theta \\ \cos\theta \end{Bmatrix} \tag{83}$$

Then from Eqs. (83, 82 and 80), since both terms in Eq. (76) are of comparable magnitude, we find

$$X(\bar{y},t) \sim \frac{4\,U_\infty^2 \cos\alpha\, f'(y_n/\delta)}{\delta^{1/2}(L-x_{ff})^{3/2}} \tag{84}$$

This confirms the previous order of magnitude analysis except for a factor of 2 in the lifting body of revolution case and an error of order $\tan \alpha$ due to the assumption $\partial U_1 / \partial y_1 = 0$.

Finally, we note that

$$\epsilon_x = \frac{\partial u_i}{\partial y_j} \frac{\partial u_j}{\partial y_i} \sim \left(\frac{U_\infty}{\delta} \sqrt{\frac{\delta}{(L-x_{ff})}} \right) \left(\frac{U_\infty}{(L-x_{ff})} \sqrt{\frac{\delta}{(L-x_{ff})}} \right) \tag{85}$$

$$\sim U_\infty / (L-x_{ff})^2$$

$$\sim \sqrt{\delta / (L-x_{ff})}\ X(\vec{y},t)$$

which justifies neglect of the squared fluctuation terms.

III DISCUSSION OF MODELS AND INSTRUMENTATION

MODELS

Two models were used to obtain the experimental data by a series of tests conducted in the AEDC 40-inch Supersonic Tunnel (A), and the 50-inch Mach 10 Tunnel (C). Model number 1 was an axisymmetric model with a diameter of 7.5 inches and a length of 36.75 inches. A forward flare and an aft flare were attached to this model for the purpose of creating separated flows, oscillating shock waves, and base pressure fluctuations. Figure 5 shows the general overall geometry and dimensions of this model. The basic model is the AEDC 7.5 inch diameter HV Ballistic Type Force Model No. HB-1, which was loaned by ARO, Inc. for use in this program. The basic model was modified by the addition of the forward skirt and the aft skirt, static pressure taps, thermocouples, and pressure transducers. Figure 6 shows the location of the instrumentation that was used for this model.

Model number 2 was a two-dimensional model having a length of 22.03 inches, and a width of 10 inches. This model had the provision of being run as a flat plate or as a flat plate with flaps. Two different rearward facing flaps were used. One made an aft facing angle of 30°, and the other made an aft facing angle of 60°. Each of the two flaps were made to have the same vertical protuberance height from the top surface of the model. This height was 4 inches. Figure 7 shows the general geometry and dimension of this model.

The upper surface plate of this model was removable to afford access to the instrumentation and the wiring.

The interior of the model was machined out to make room for instrumentation wiring, and copper tubing for conducting cooling water through the model. Cooling of the model was done only during the tunnel C testing.

Model number 2 was also instrumented with static pressure taps, thermocouples, and transducers. Figure 8 shows the location of the instrumentation that was used for this model during the testing in tunnel A. Provision was made in the model to use seven transducers during tunnel A testing. However, since two transducers became inoperative during the testing of the axisymmetric model, only five transducers were used for the two-dimensional model tests.

Figure 9 shows the location of the instrumentation that was used for model 2 during the tunnel C tests. It will be noted that this instrumentation is identical with that for the tunnel A tests (Figure 8) except for the location and number designation of the transducers. As mentioned in the instrumentation subsection of this report, recalibration and renumbering of the transducers was accomplished between the tunnel A tests and tunnel C tests.

The two dimensional model was tested in tunnel A without cooling the transducers. Prior to the tunnel C tests, the transducers were removed from the model and mounted in water jackets through which cooling water was circulated during the testing in tunnel C.

Figures 10, 11, and 12 show pictures of the two models prior to the installation of the transducers. Figures 13, 14, 15, and 16 show the two models mounted in tunnel A.

INSTRUMENTATION

The instrumentation that was used to accomplish this program is discussed in detail in reference 10. Pertinent excerpts from this reference are included herein for the purposes of clarity and coherence.

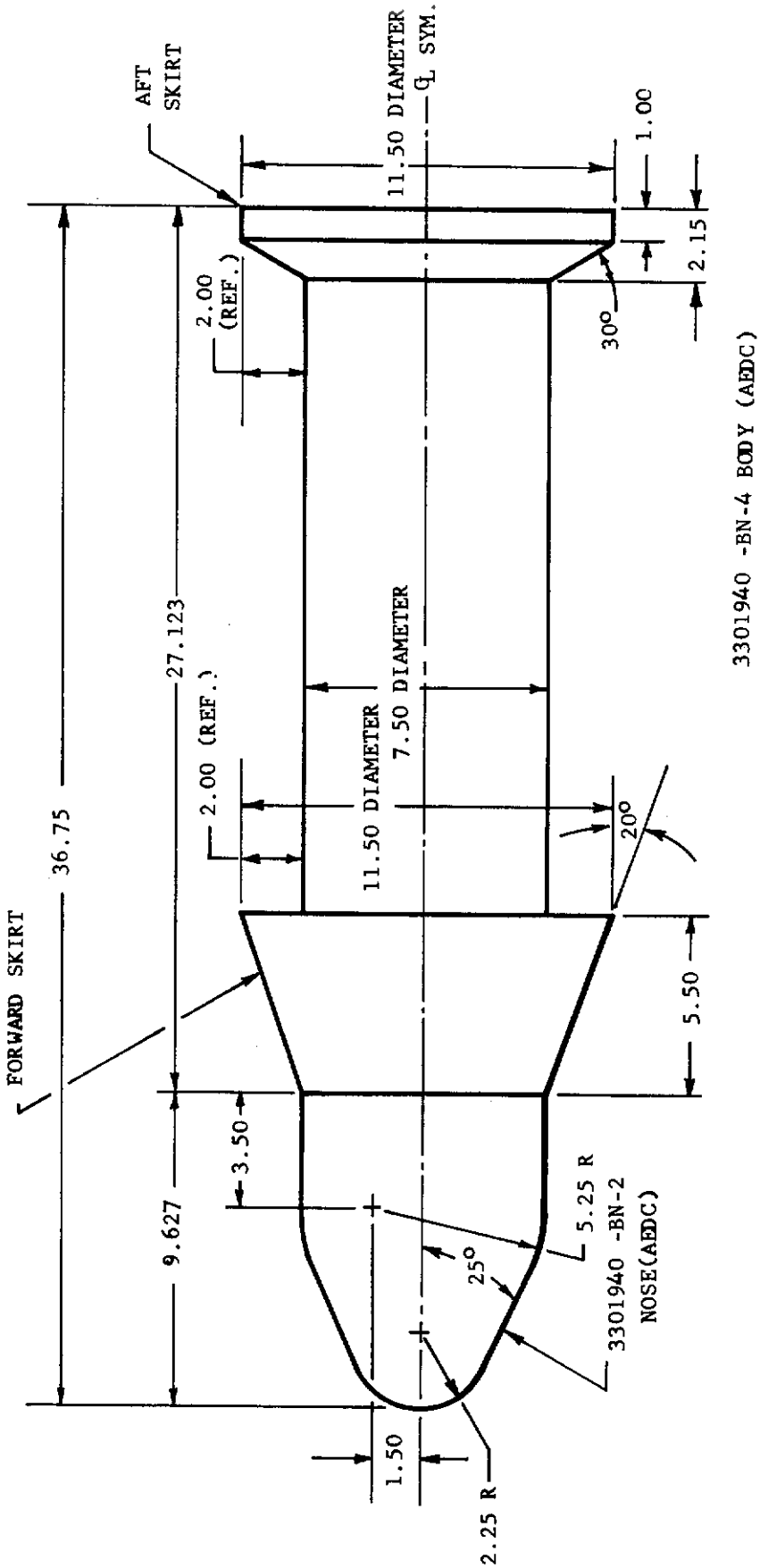

FIGURE 5 MODEL NUMBER 1

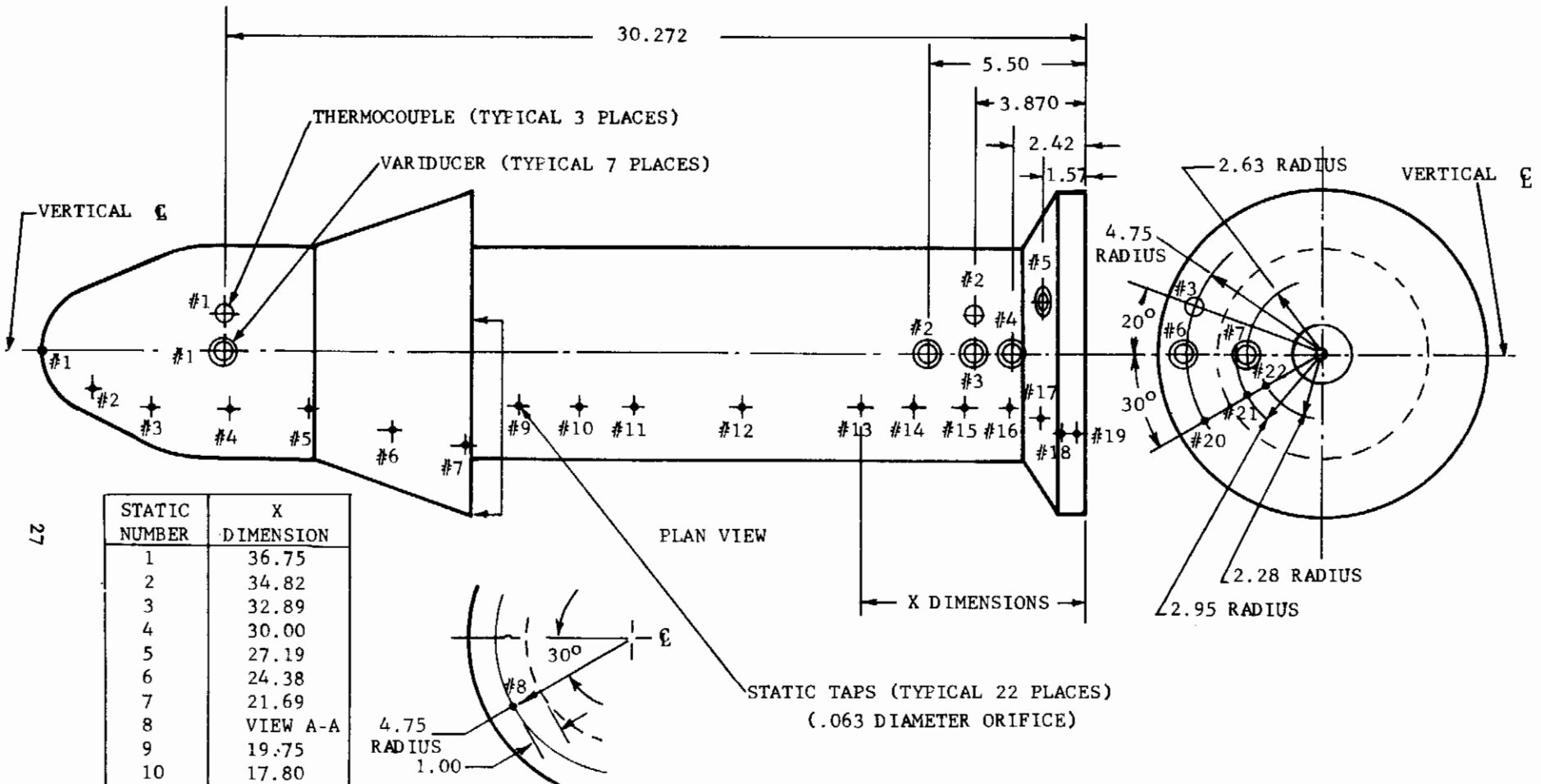

STATIC NUMBER	X DIMENSION
1	36.75
2	34.82
3	32.89
4	30.00
5	27.19
6	24.38
7	21.69
8	VIEW A-A
9	19.75
10	17.80
11	15.80
12	12.00
13	7.90
14	6.00
15	4.18
16	2.63
17	1.58
18	.95
19	.31
20	END VIEW
21	END VIEW
22	END VIEW

FIGURE 6 MODEL NUMBER 1 INSTRUMENTATION

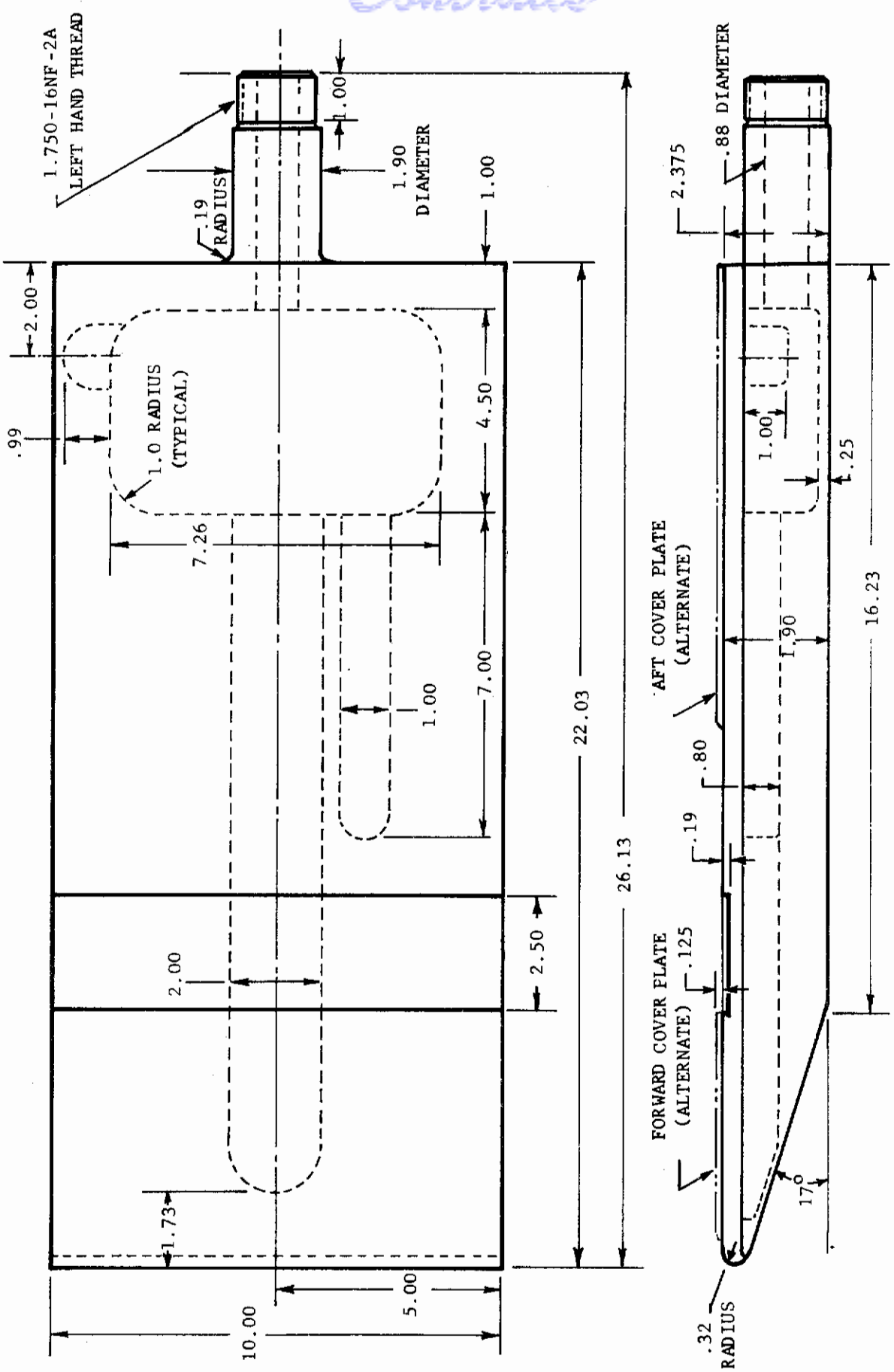

FIGURE 7 MODEL NUMBER 2

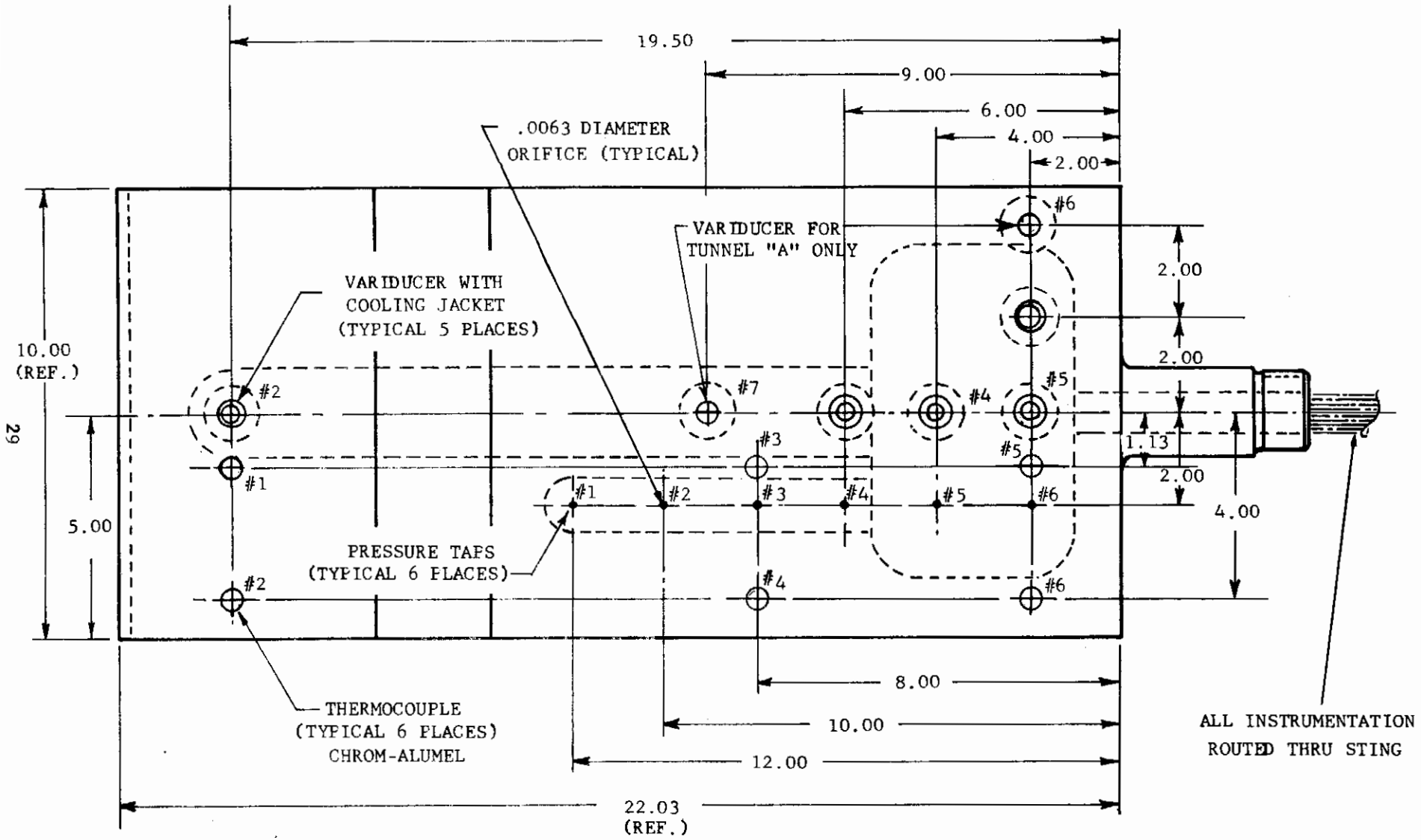

PLAN VIEW

FIGURE 8 MODEL NUMBER 2 INSTRUMENTATION FOR TUNNEL "A" TESTS

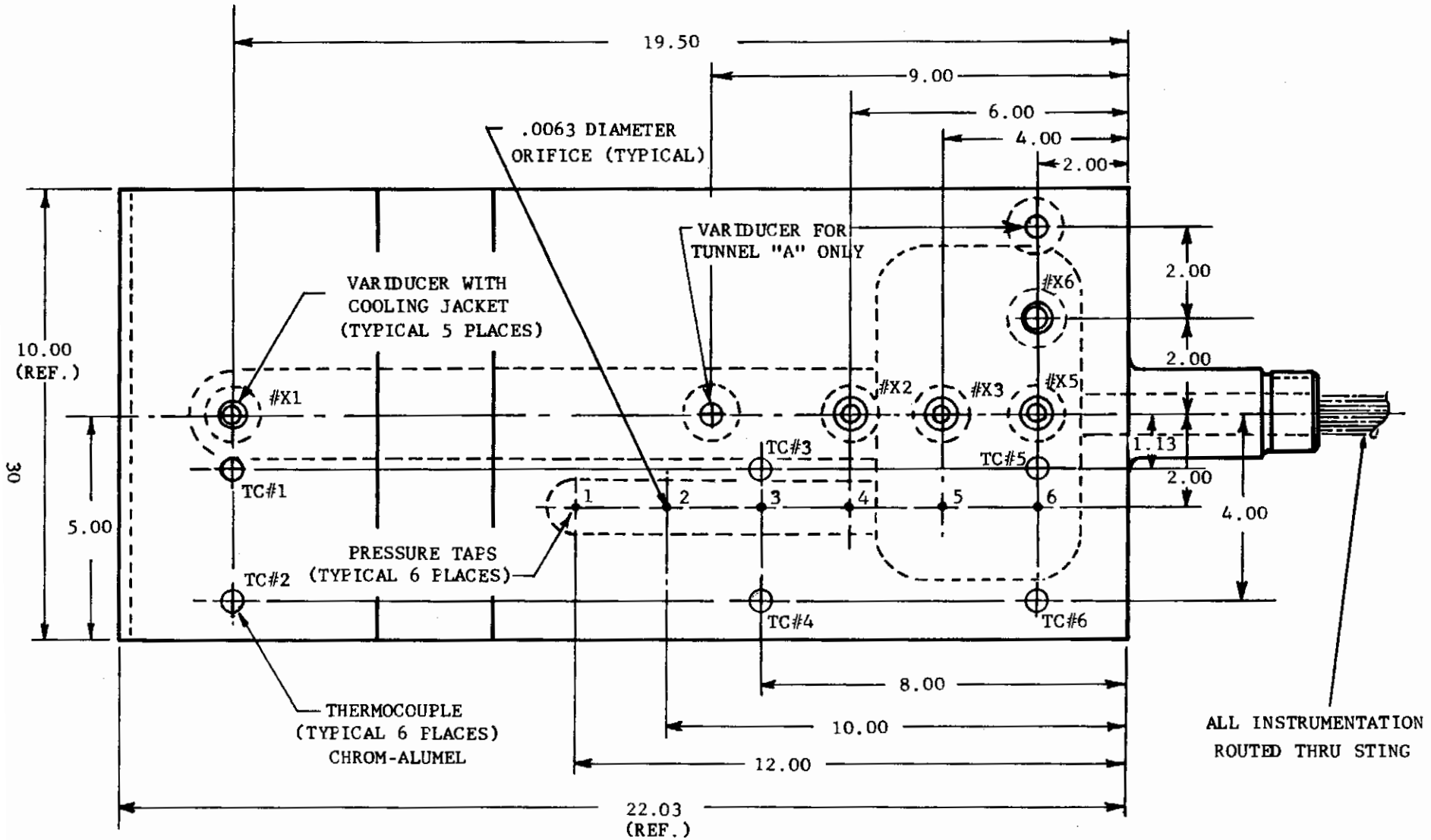

PLAN VIEW

FIGURE 9 MODEL NUMBER 2 INSTRUMENTATION FOR TUNNEL "C" TESTS

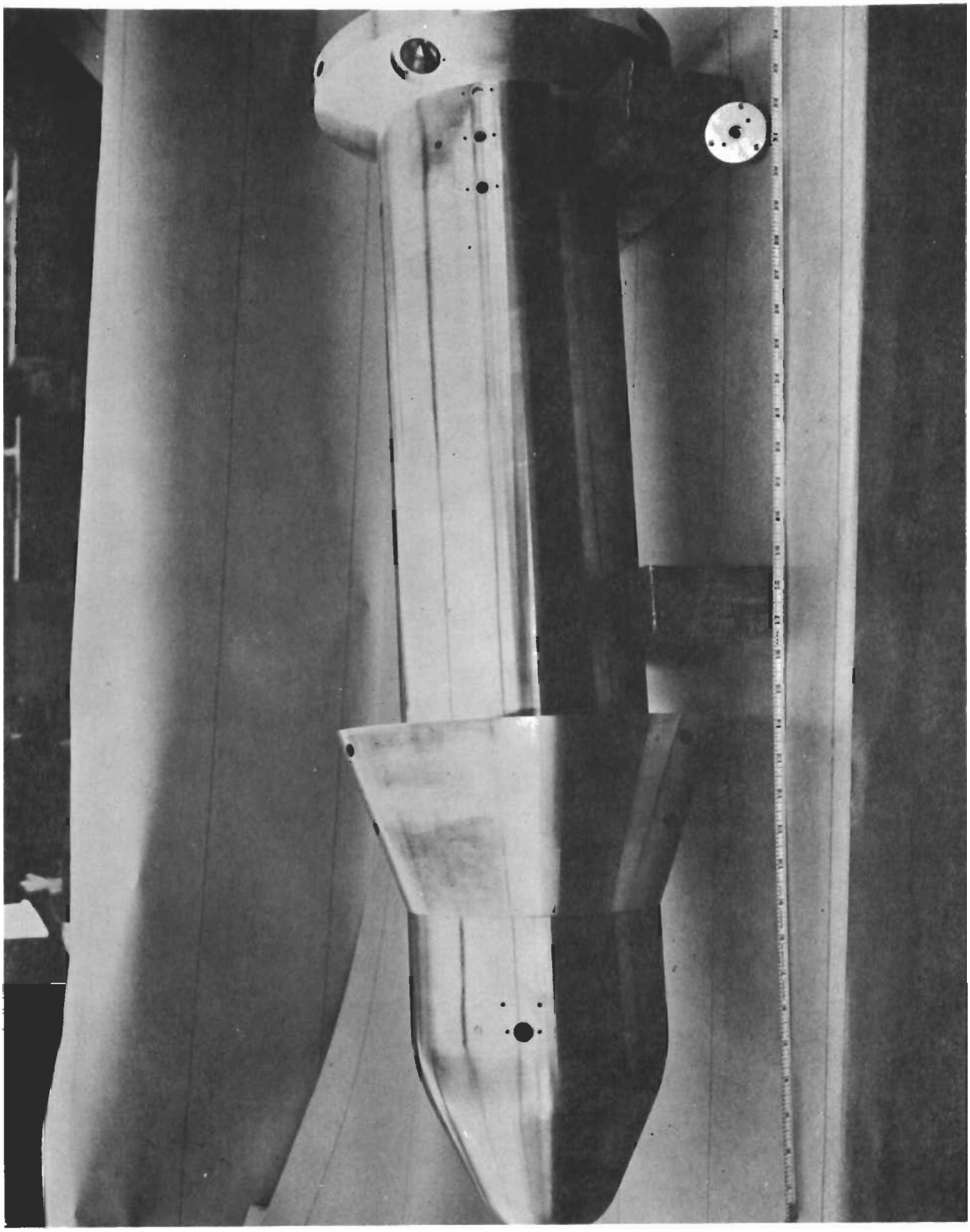

FIGURE 10 AXISYMMETRIC MODEL WITHOUT TRANSDUCERS INSTALLED

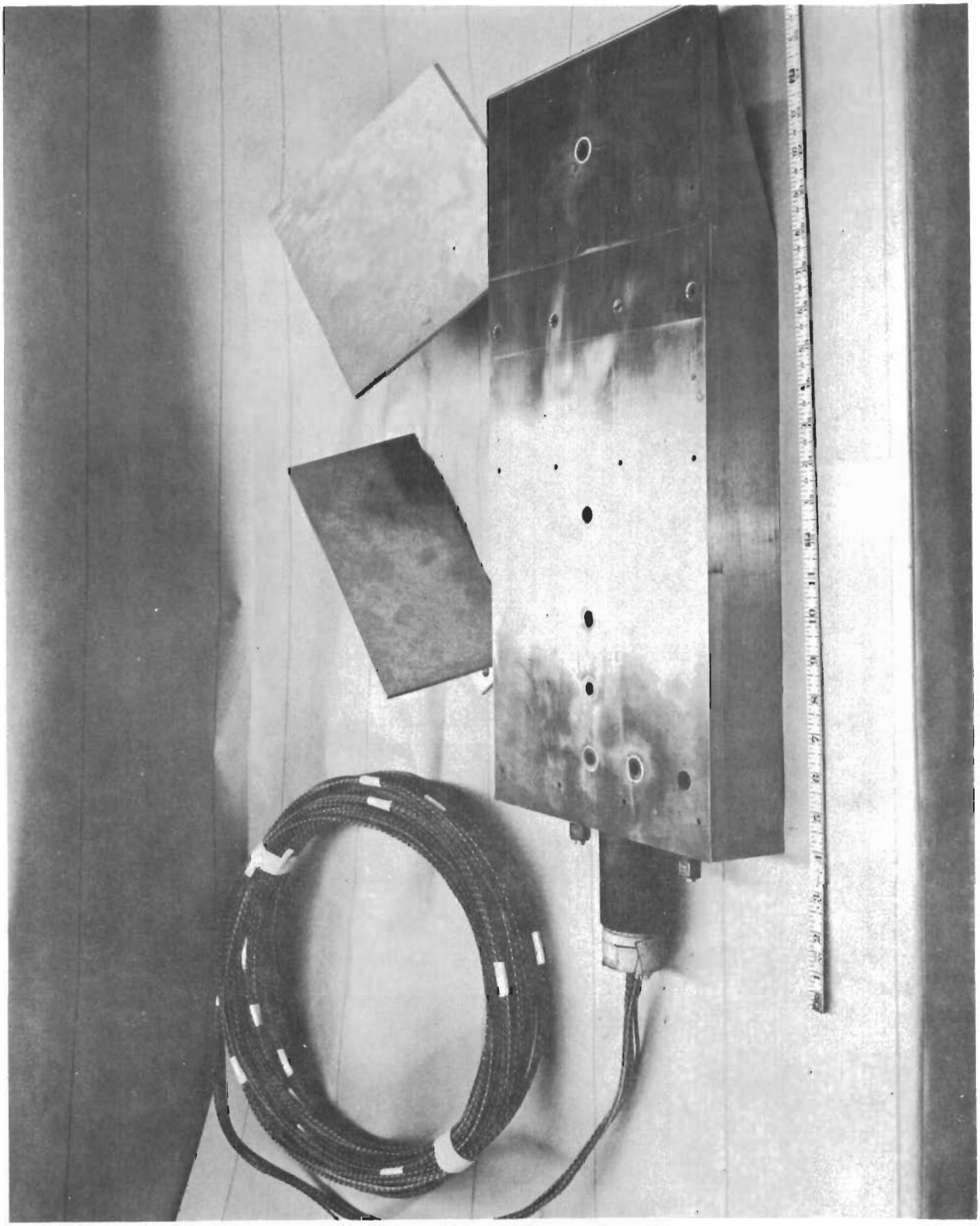

FIGURE 11 TWO-DIMENSIONAL MODEL, FLAT CONFIGURATION

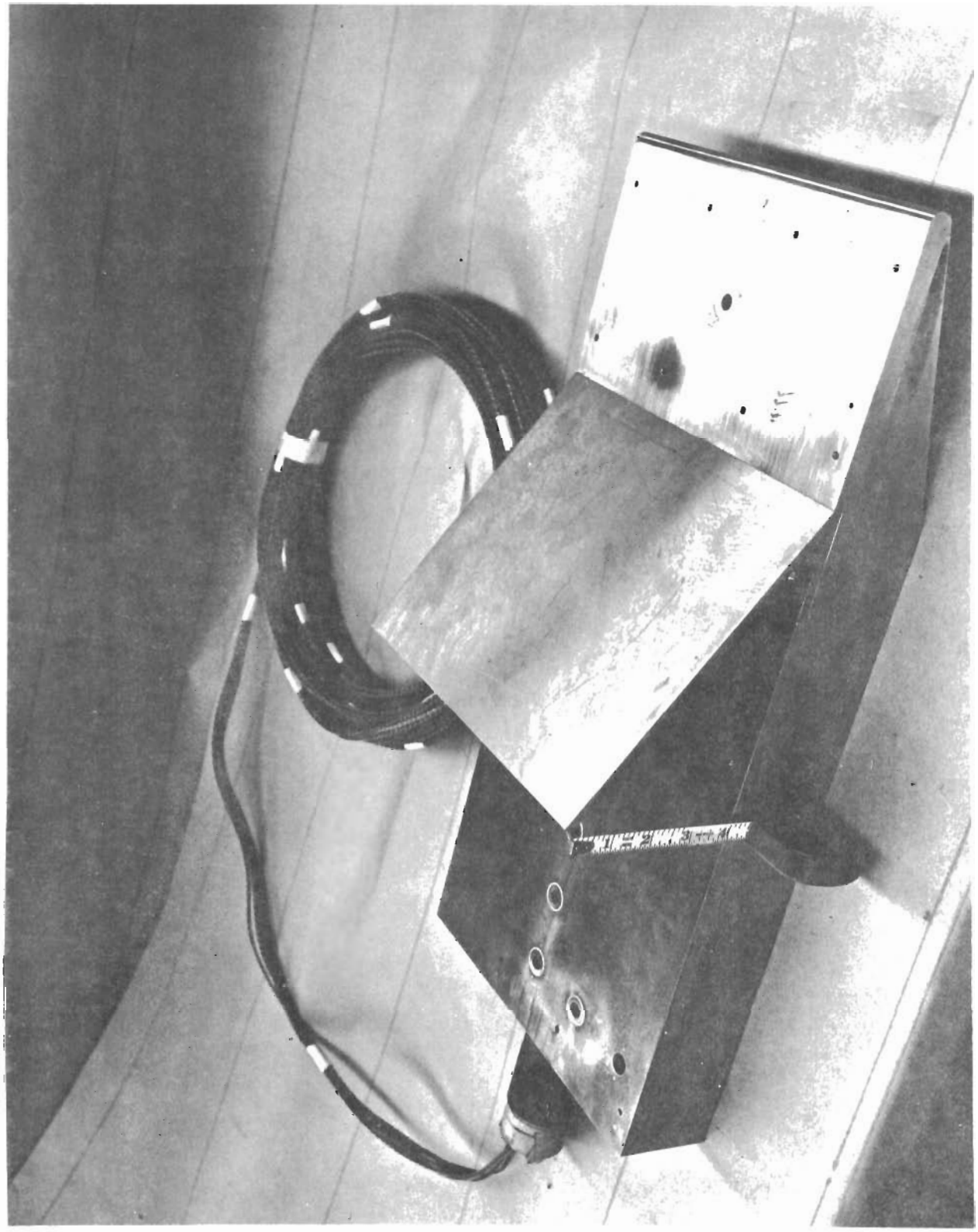

FIGURE 12 TWO-DIMENSIONAL MODEL, 30° FLAP

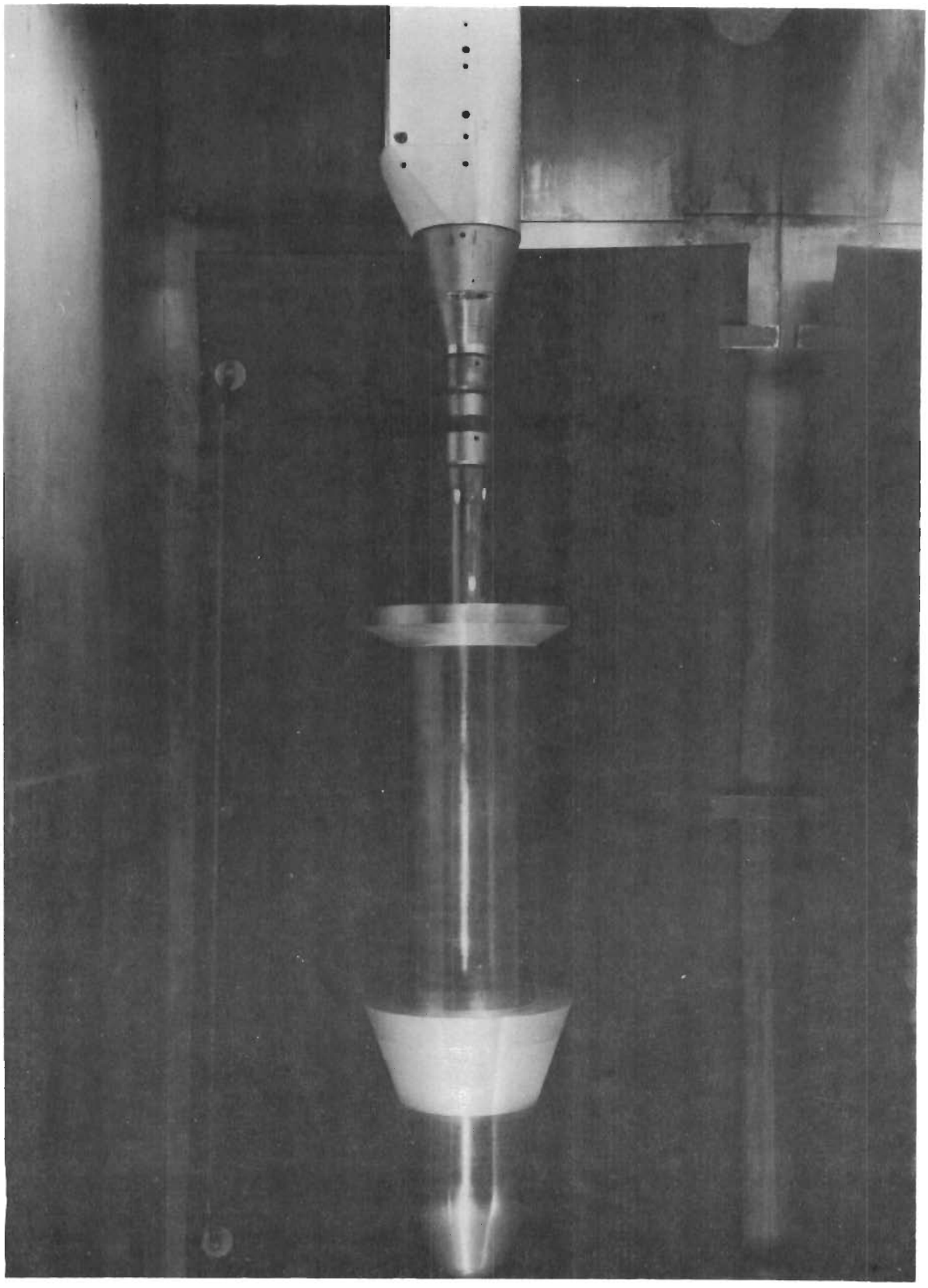

FIGURE 13 AXISYMMETRIC MODEL INSTALLED IN TUNNEL "A"

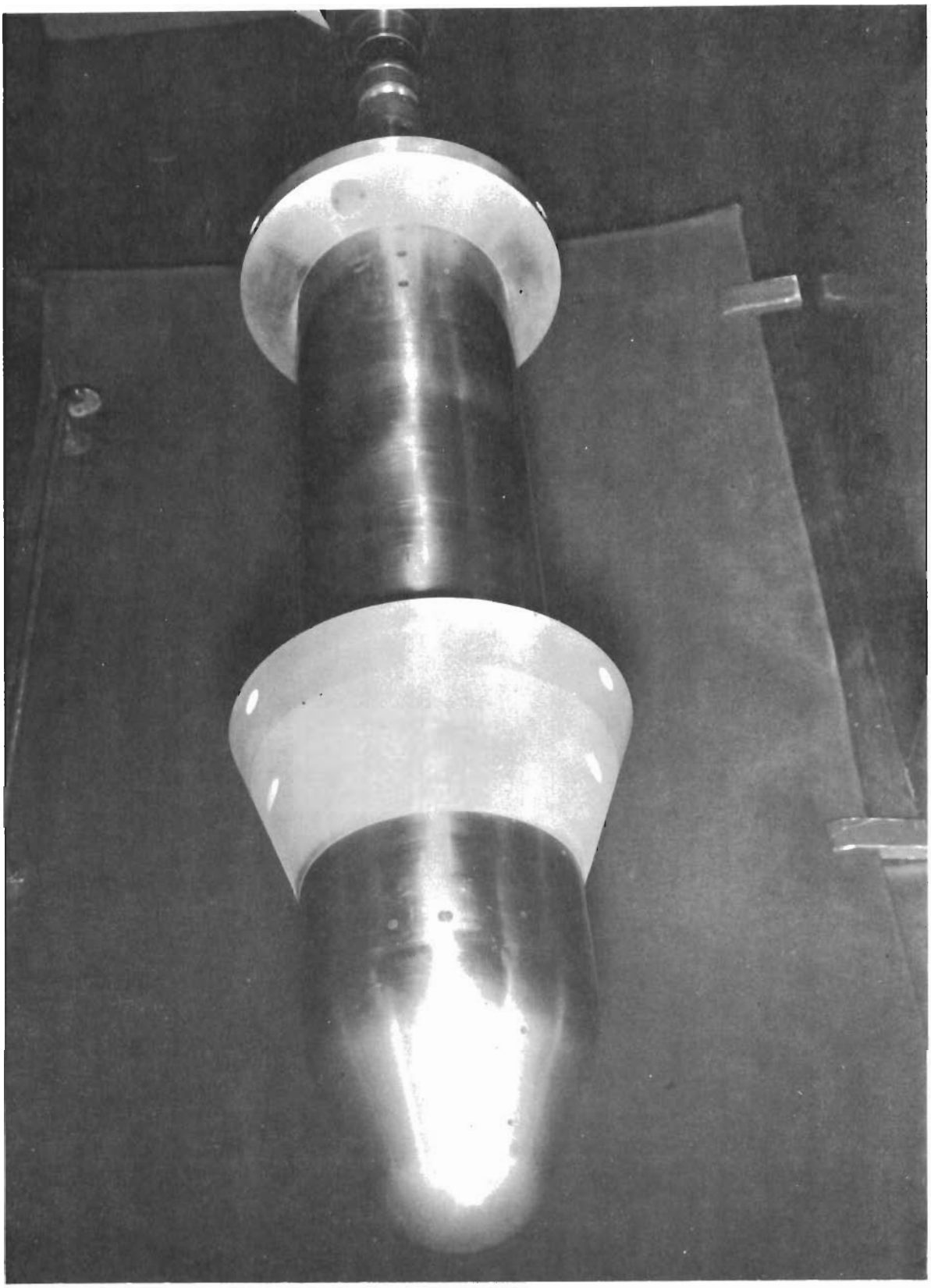

FIGURE 14 AXISYMMETRIC MODEL INSTALLED IN TUNNEL "A"

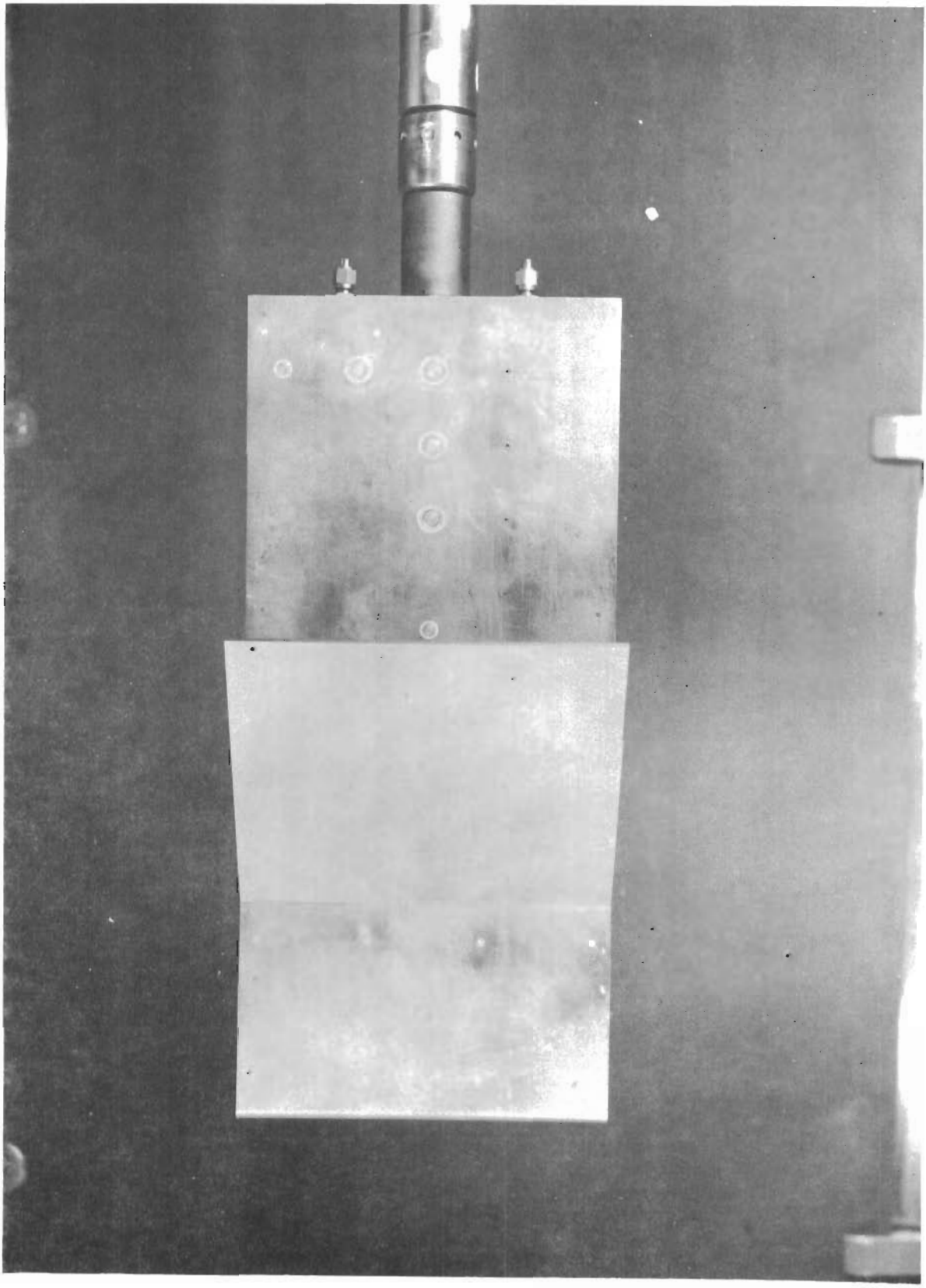

FIGURE 15 TWO-DIMENSIONAL MODEL INSTALLED IN TUNNEL "A"

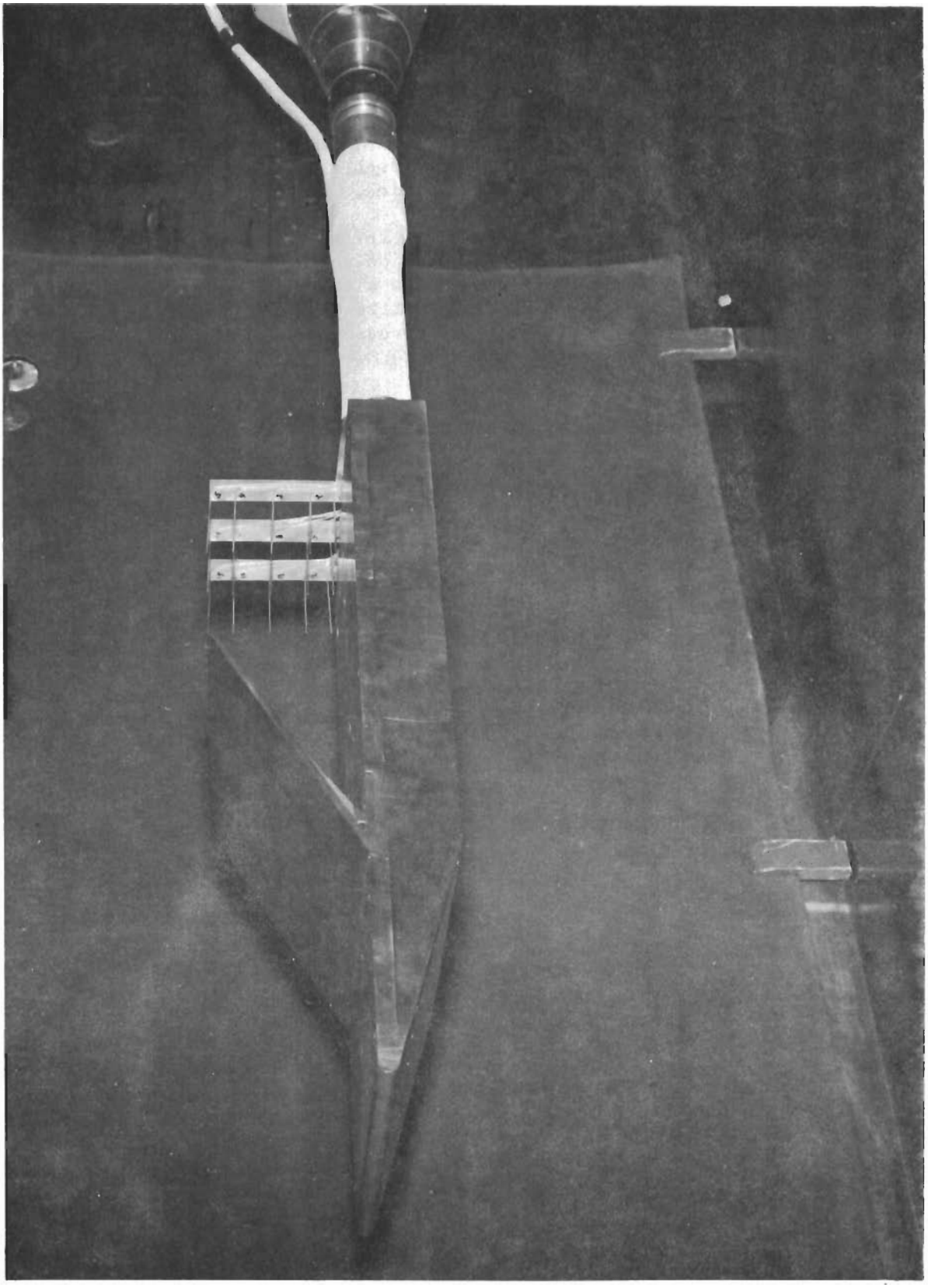

FIGURE 16 TWO-DIMENSIONAL MODEL WITH BOUNDARY LAYER PROFILE RAKE

The block diagram at the instrumentation system is shown in Figure 17. The pressure transducers that were used were the Sensonics V25-1 Variducer. These are lead zirconate titanate ceramic piezoelectric transducers with a charge sensitivity of 21 picocoulombs/psi. The pressure range is 0 - 100 psi with a resolution of 0.005 psi. The resonant frequency of the transducer is near 350 kc. The frequency response of the crystal and amplifier system is approximately flat from 200 cps $< f <$ 50,000 cps. The transducer is 0.375 inches in diameter and 0.548 inches in length. The active crystal is 0.25 inches in diameter and 0.10 inches thick.

A calibration box was used with each transducer, for each channel of information. Its purpose was to provide a means of suppressing the dc voltage produced by the pyroelectric effect in the transducer crystal element, and also to provide a method of injecting an ac signal for calibration checks on the entire transducer system. The pyroelectric voltage from the transducer, if not suppressed, will build up in the charge amplifier and cause its sensitivity to vary.

The lower limit to the frequency response of approximately 200 cps applies to the short time constant mode of operation of the charge amplifiers. It was possible to extend the flat frequency response to about 50 cps by operating the charge amplifiers in the long time constant mode. However, when operating in the long time conconstant mode, it was found that drift due to pyroelectric effect was difficult to control. Therefore, nearly all of the data were recorded with the charge amplifiers operating in the short time constant mode. The amplifiers were very stable throughout all tests when operating in this mode.

The system calibration could be checked at any time, even during a run, by injecting the 1 kc oscillator into the calibration terminals and observing the system output on the oscilloscope.

Chromel-alumel thermocouples were used to determine model temperatures at selected positions. Static pressure taps were located along the models to determine the longitudinal distribution of static pressure from which local boundary layer edge conditions were determined. The location of the thermocouples and pressure taps are shown in Figure 6 and 8.

A boundary layer total pressure tube rake and a boundary layer temperature rake were used to obtain aerodynamic data that was needed to define the flow characteristics.

Calibration of the seven transducers was accomplished in the Northrop Norair Instrumentation Laboratory prior to the wind tunnel test at AEDC. Pressure was applied to each transducer using the system shown in Figure 18. The sensitivity curves for each transducer are shown in Figures 19 through 26.

These calibrations were used for the tests conducted in Tunnel A at AEDC, and are summarized in tables 2 and 3. The values of $Gain_{(cal.)}$ listed in these tables are the system gains that were determined during calibrations at Northrop Norair. The values of $Gain_{(test)}$ listed in these tables are the system gains of the total system at AEDC; that is, they are the gains of the system consisting of the models installed in tunnel A, through the charge amplifiers, to the output of the tape recorder located in the data room at the Von Karman Facility.

The values of K and K^1 listed in tables 2 and 3 are system constants that were used to reduce the recorded test data to the 1/3 octave band power spectral density plots of the appendix.

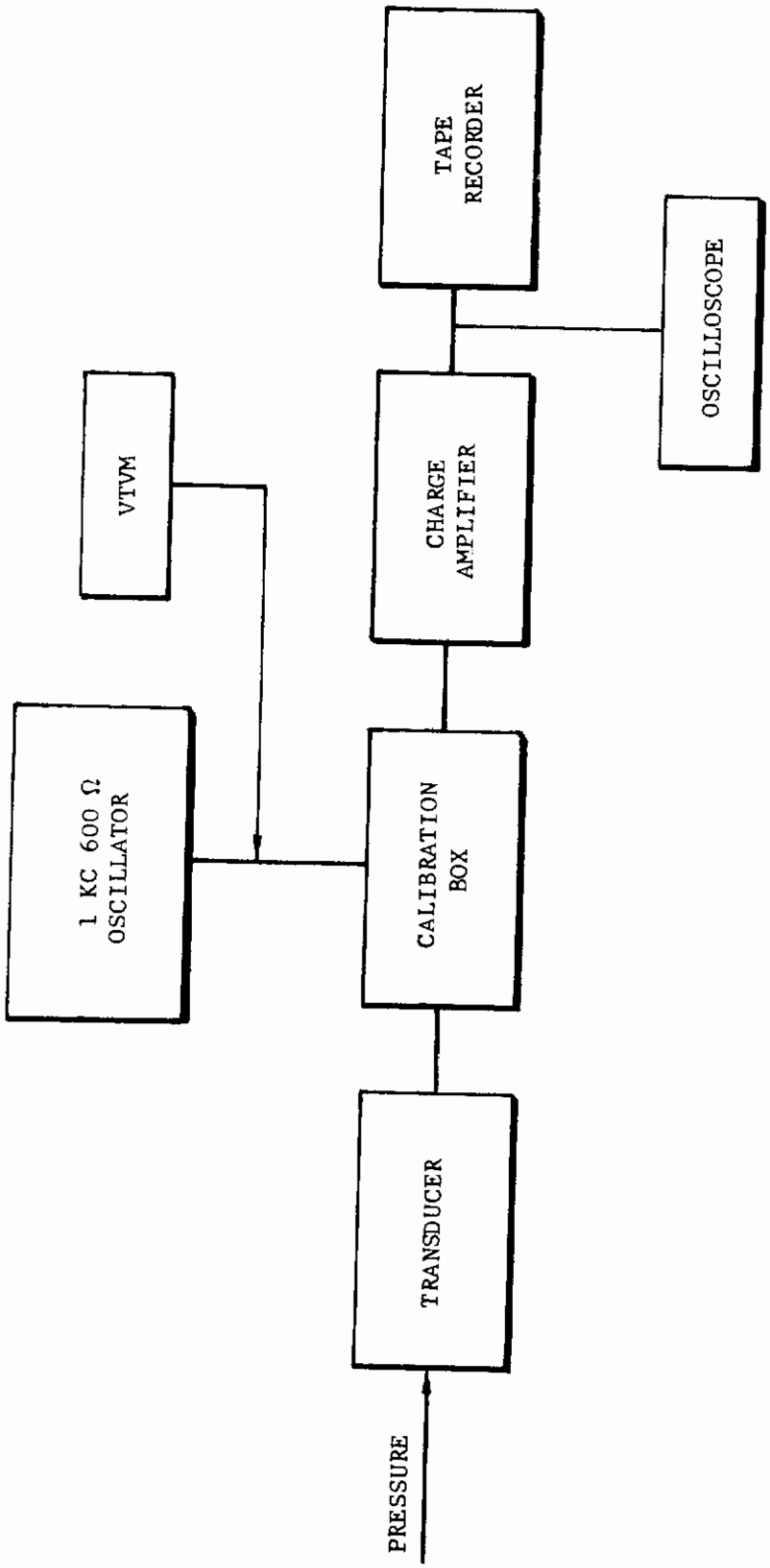

FIGURE 17 INSTRUMENTATION SYSTEM BLOCK DIAGRAM

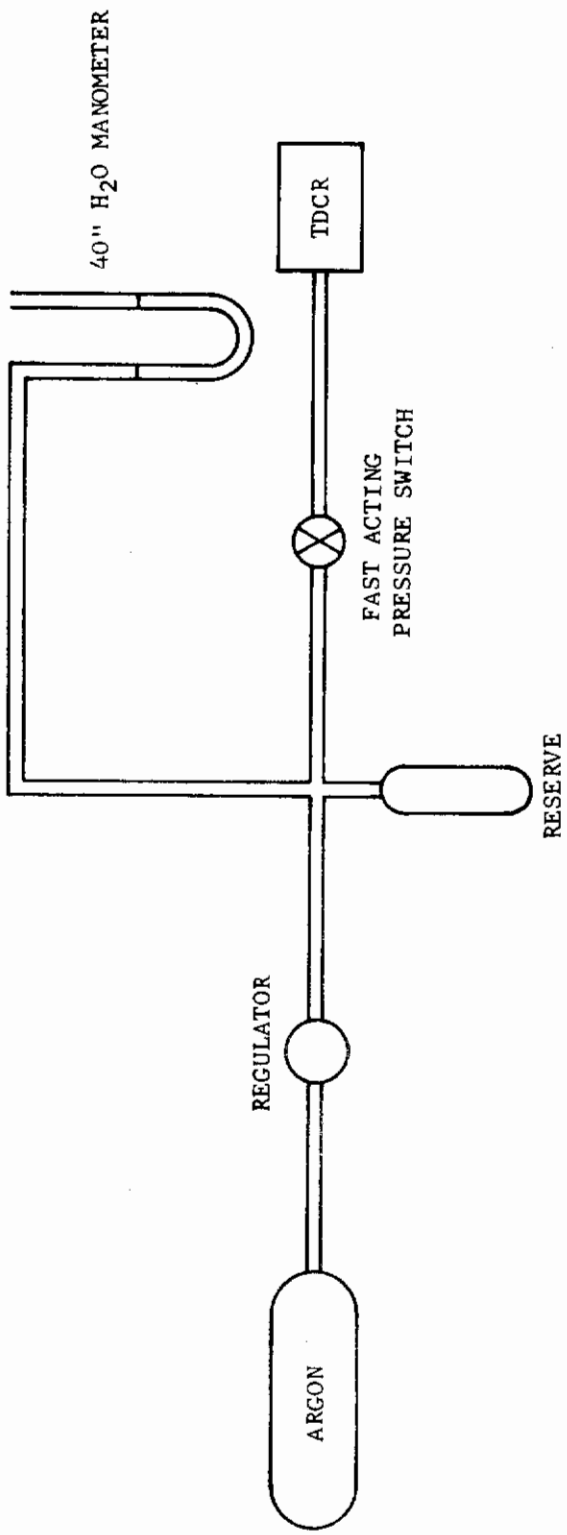

FIGURE 18 TRANSDUCER CALIBRATION SYSTEM

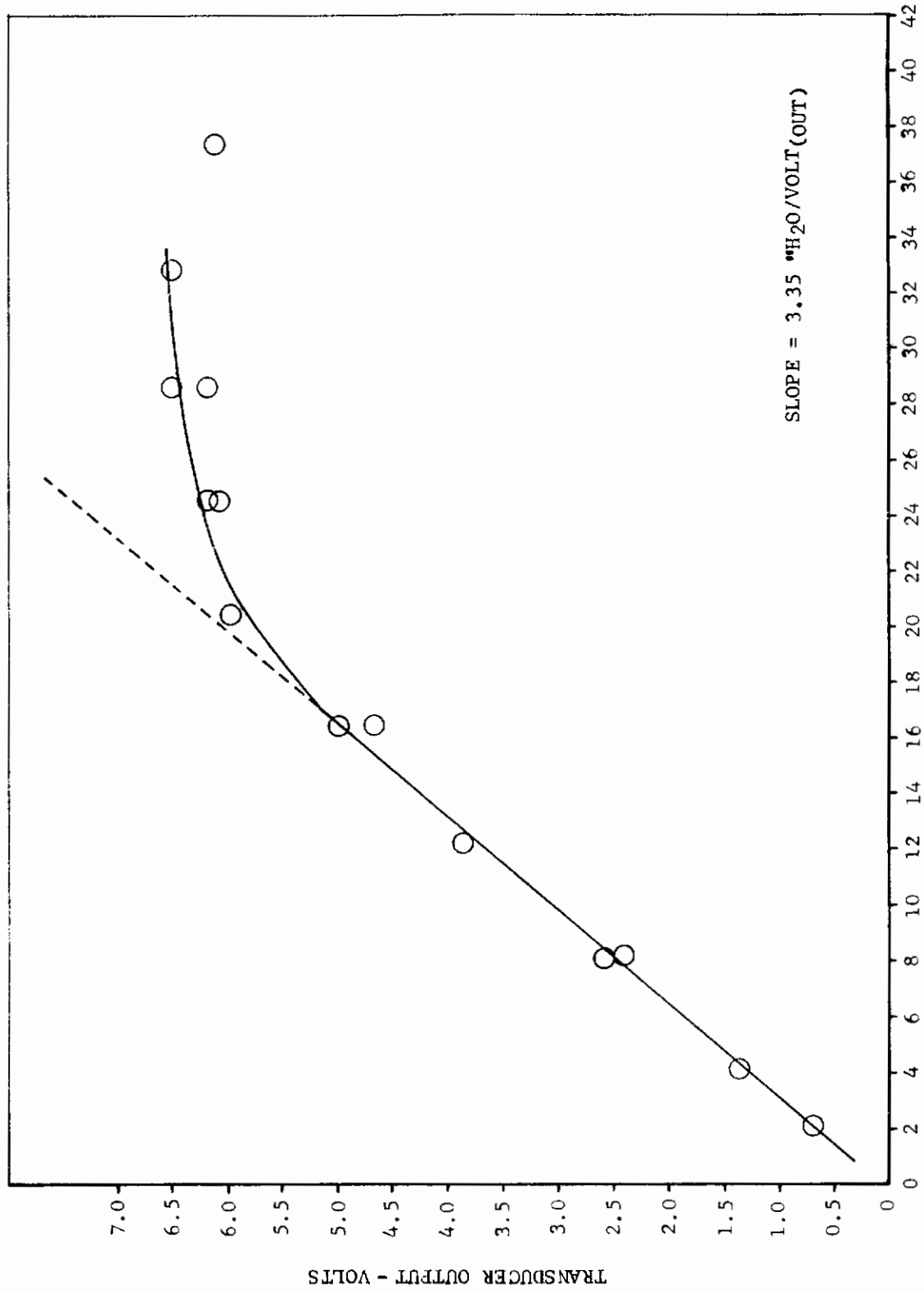

FIGURE 19 CALIBRATION CURVE, TRANSDUCER #1

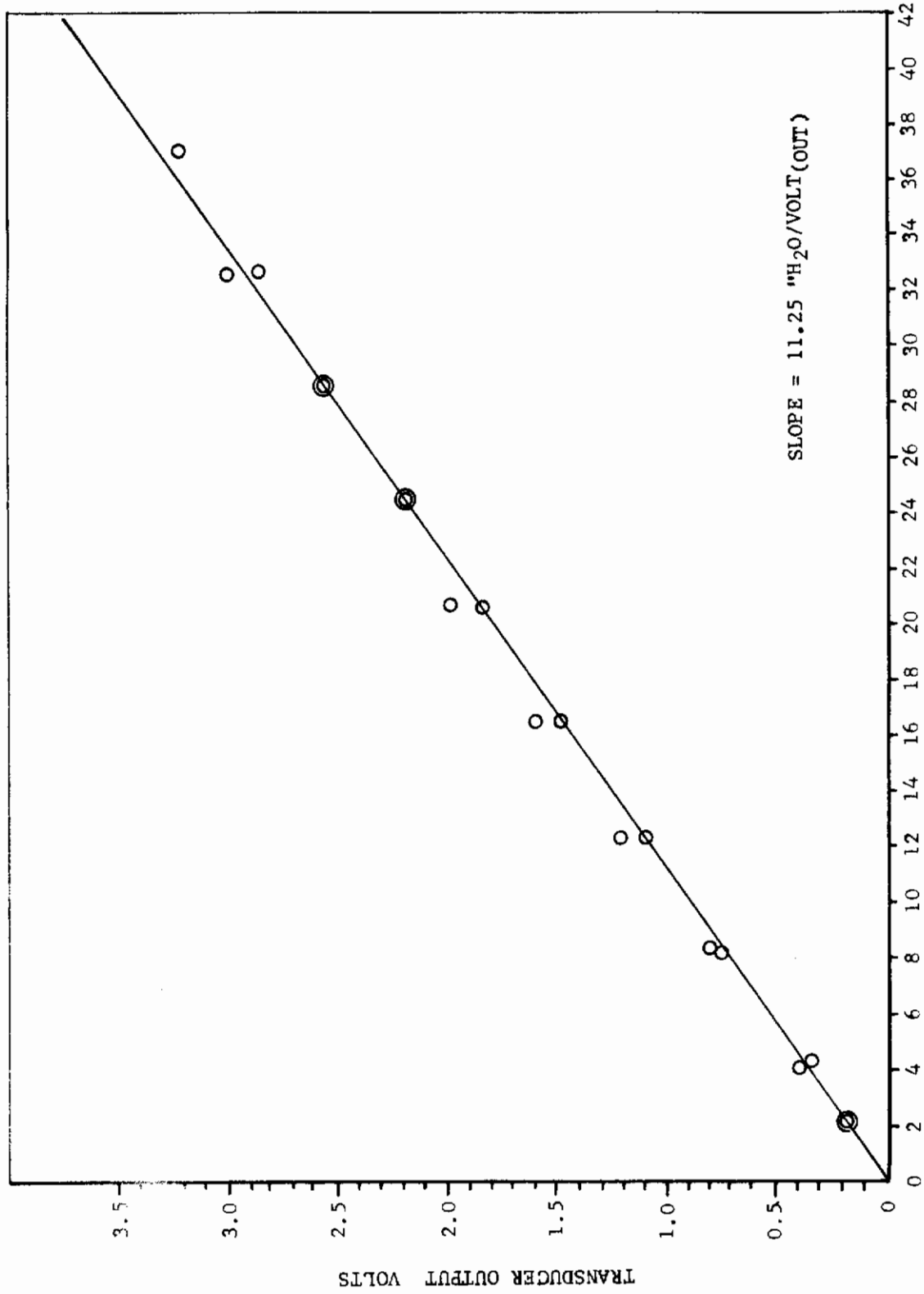

FIGURE 20 CALIBRATION CURVE - TRANSDUCER #2

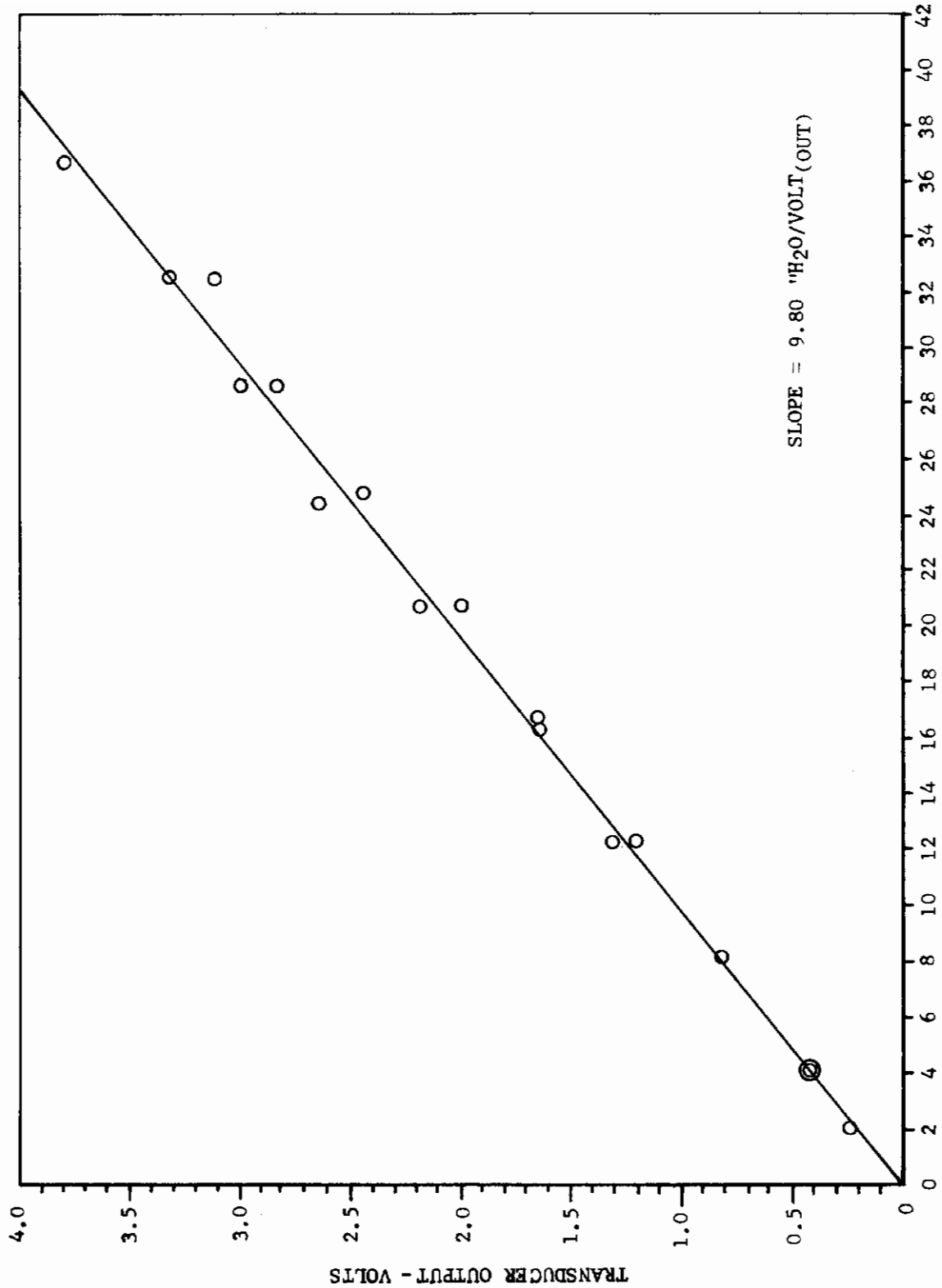

FIGURE 21 CALIBRATION CURVE - TRANSDUCER #3

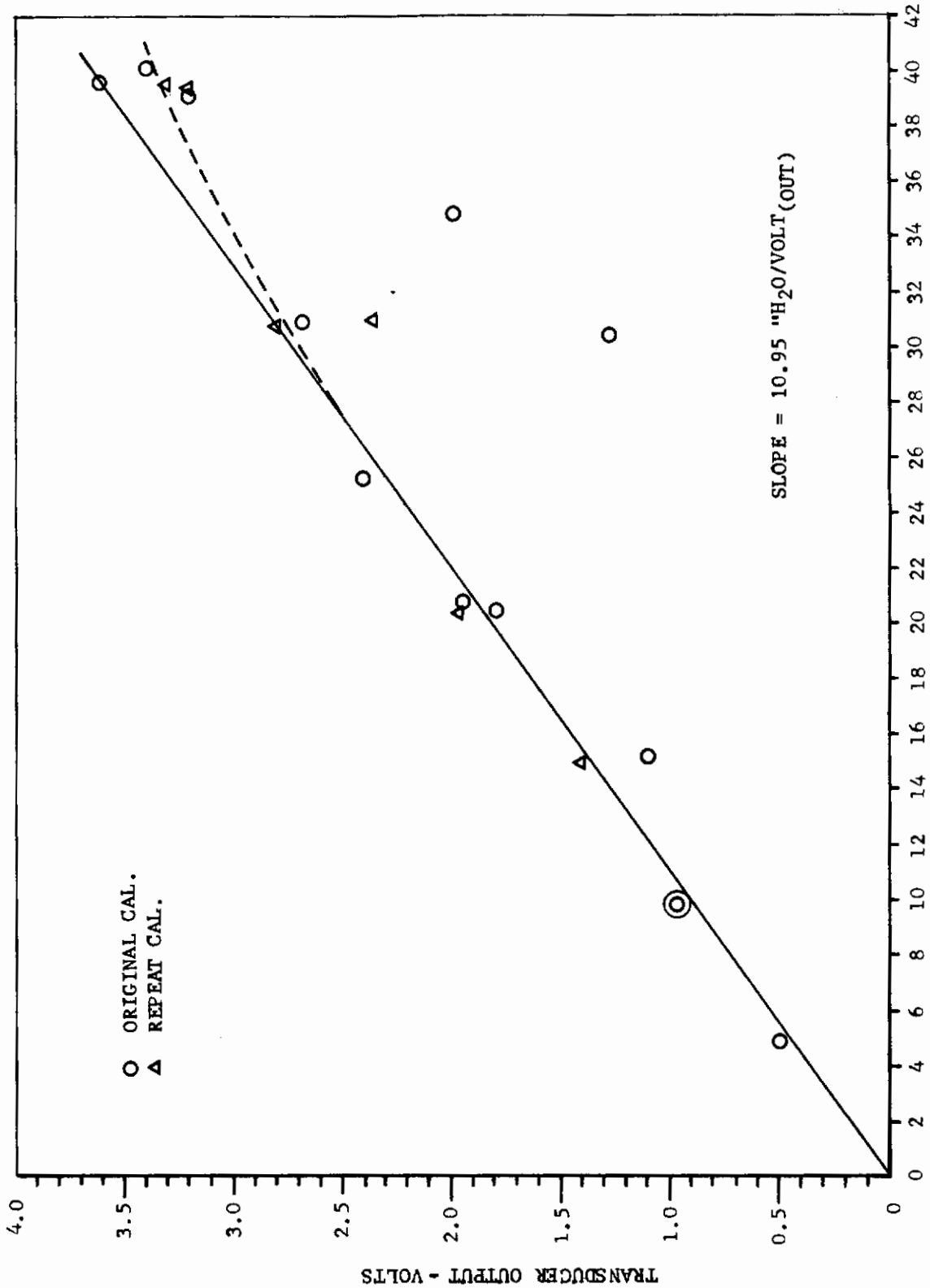

FIGURE 22 CALIBRATION CURVE - TRANSDUCER #4

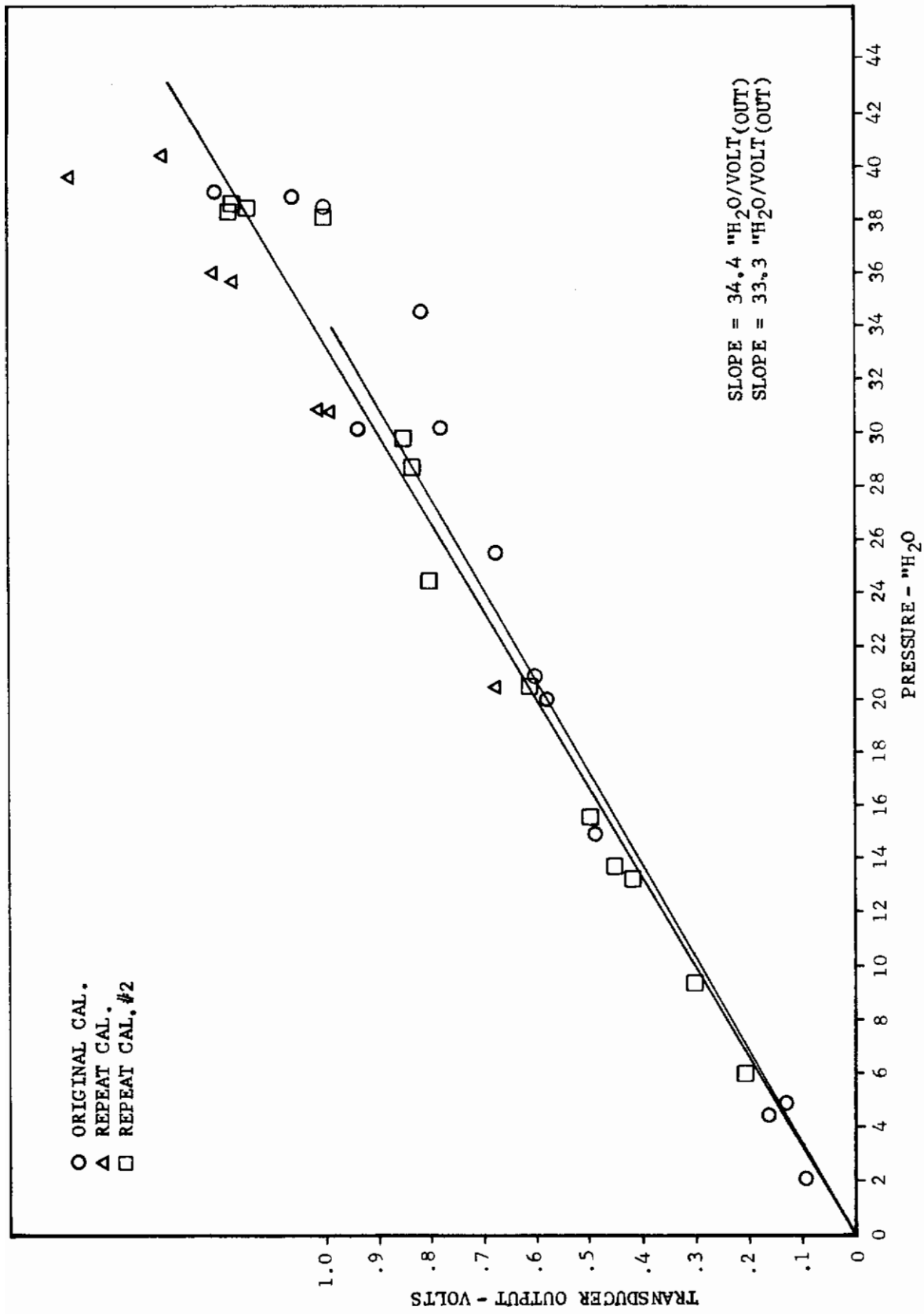

FIGURE 23 CALIBRATION CURVE - TRANSDUCER #5

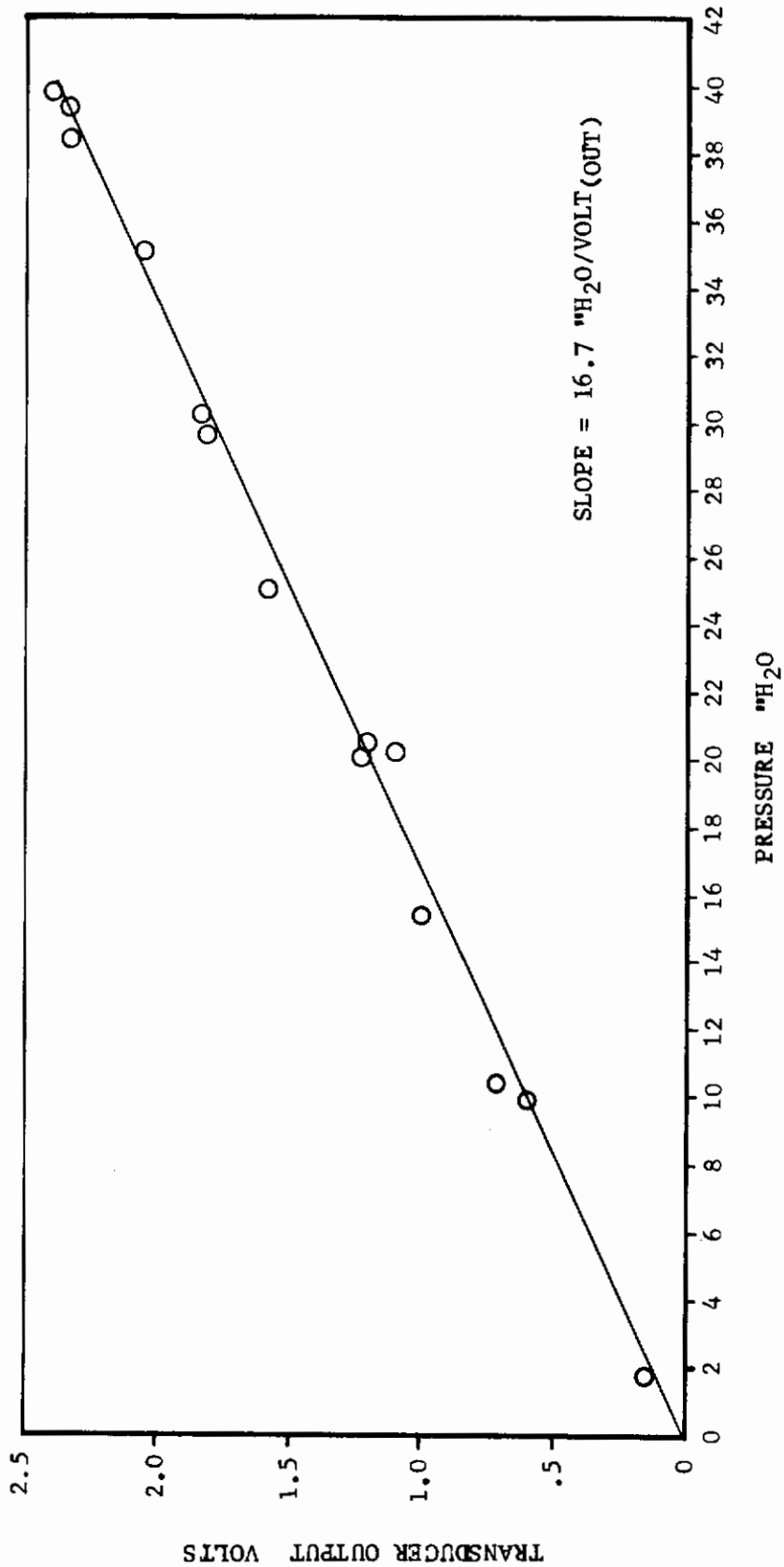

FIGURE 24 CALIBRATION CURVE - TRANSDUCER #6

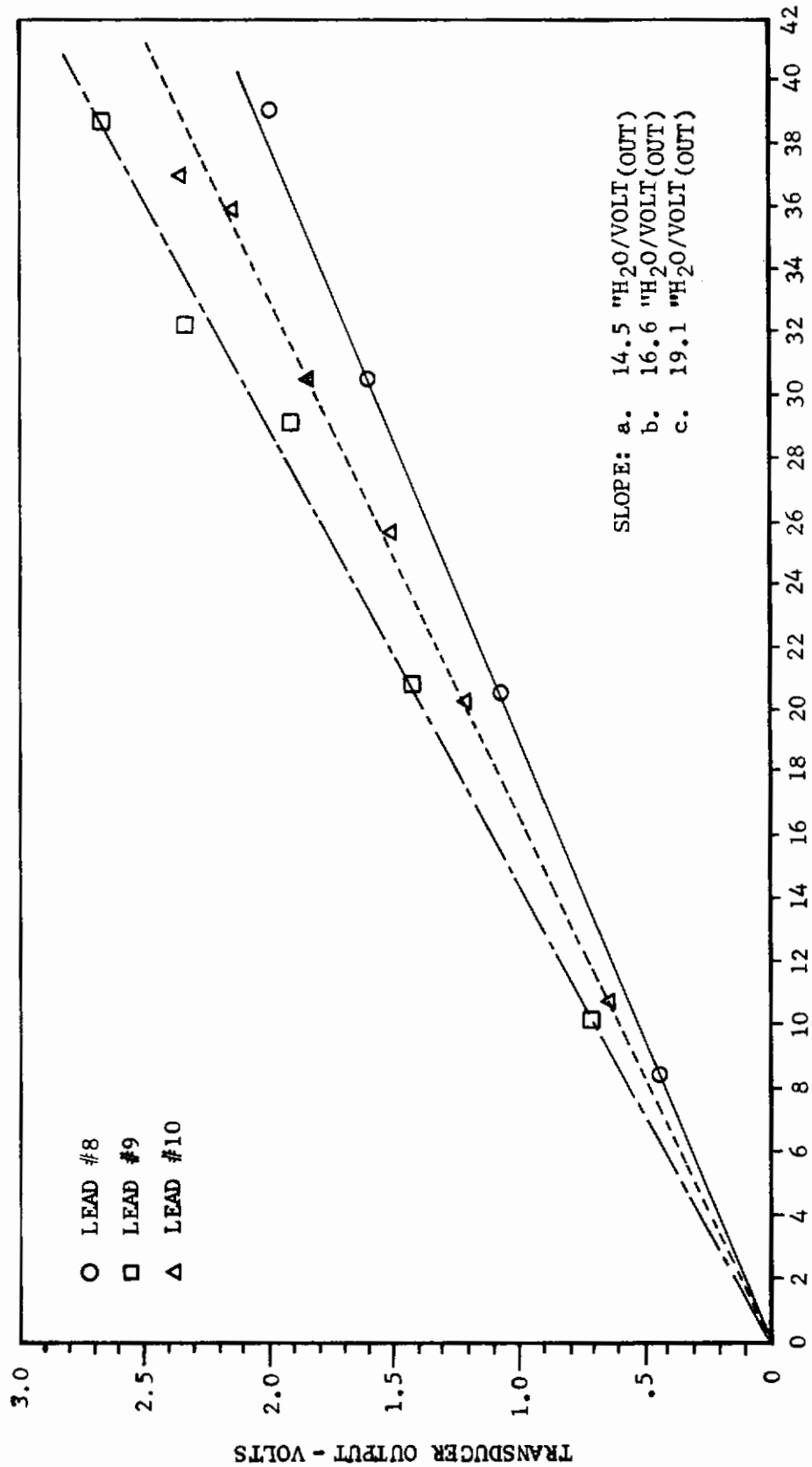

FIGURE 25 CALIBRATION CURVE - SPARE LEAD - TRANSDUCER #6

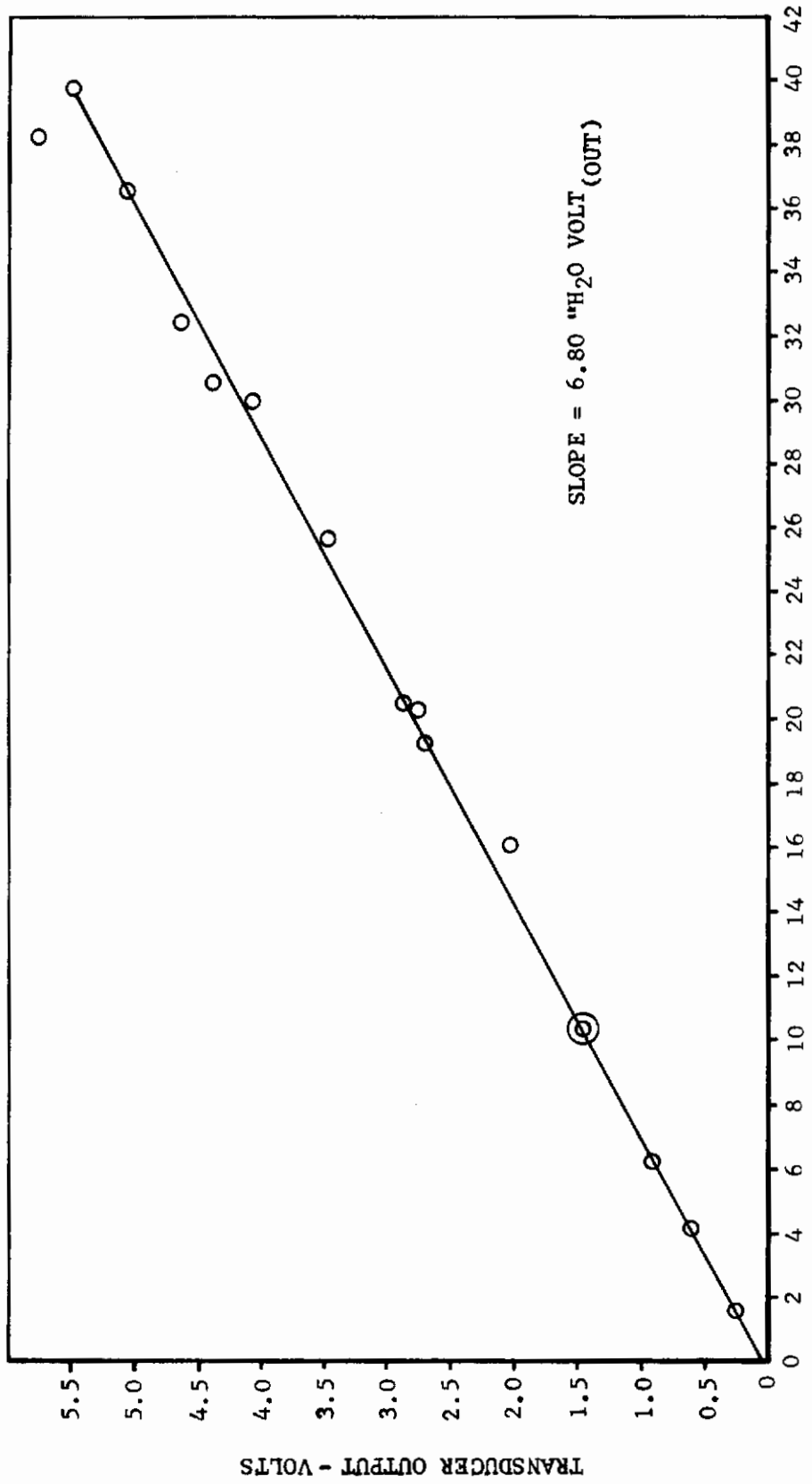

FIGURE 26 CALIBRATION CURVE - TRANSDUCER #7

TUNNEL A TESTS

INSTRUMENTATION CALIBRATION DATA

TABLE 2

AXISYMMETRIC MODEL

Transducer Number	Channel No. (Amplifier No.)	Transducer Sensitivity ("H_2O/Volt Output)	$Gain_{(cal.)}$	$Gain_{(test)}$	K db	K^1 db
1	1	3.35	125.0	189	148.4	148.5
2	2	11.25	122.0	196	158.7	158.5
3	3	9.80	132.0	218	158.2	157.1
4	4	10.95	97.3	200	156.5	156.2
5	5	33.30	107.2	211	167.1	166.3
6	6	16.70	97.3	214	160.2	159.3
7	7	6.80	143.5	204	155.7	155.2

TABLE 3

TWO-DIMENSIONAL MODEL

Transducer Number	Channel No. (Amplifier No.)	Transducer Sensitivity ("H_2O/Volt Output)	$Gain_{(cal.)}$	$Gain_{(test)}$	K db	K^1 db
2	2	11.25	122.0	187	158.7	155.8
4	4	10.95	97.3	191	156.5	156.5
5	5	33.30	107.2	201	167.1	166.8
6	6	16.70	97.3	204	160.2	159.7
7	7	6.80	143.5	193	155.7	155.7

The following formulas define K and K^1.

$$SPL = 20 \log_{10} \frac{p}{p_o}$$

$$\text{where } p_o = 2 \times 10^{-4} \frac{\text{dynes}}{\text{cm}^2}$$

For a pressure p in psi, this formula becomes:

$$SPL = 20 \log_{10} P(\text{psi}) + 170.5$$

Since our output was in voltage, the following formula defines our SPL:

$$SPL = 20 \log_{10} \text{volts out}_{(\text{test})} + K - 20 \log_{10} \frac{\text{Gain}_{(\text{test})}}{192}$$

$$K = 96 + 20 \log_{10} \text{Gain}_{(\text{cal})} + 20 \log_{10} \frac{"H_2O}{\text{volt out}}$$

$$K^1 = K - 20 \log 10 \frac{\text{Gain}_{(\text{test})}}{192}$$

Transducers one and three became inoperative during runs of the two-dimensional model in tunnel A. For this reason, table 3 shows calibration data for only the channels and transducers that were operating.

At the completion of the testing in tunnel A, the transducers were removed from the models and installed in water jackets in preparation for testing of the two-dimensional model in tunnel C. These water jackets were designed to keep the transducers within the operating temperature limit.

Excessive handling of the transducers during their installation in the water jackets made it necessary to recalibrate them prior to the tunnel C tests. Since positive identification of the transducers was not possible after installation in the water jackets, they were re-numbered during recalibration. This recalibration and re-numbering was accomplished at the VKF at AEDC. The calibration data is shown in table 4. The parameters that are listed in this table are defined in the preceding discussion of the tunnel A calibration data.

No corrections were applied to the frequency response of the transducers for the cancellation of transducer response because of its finite size, compared to the scale of the turbulence in the lateral direction and the wave length of the convected turbulence in the streamwise direction. Corcos (Ref. 42) presents tables and graphs for such corrections, based upon measurements for incompressible turbulent boundary layers. It will be seen in Section V that no significant response was found for a Strouhal number greater than 2, based upon the protuberance height, h. The error is potentially most serious for the axisymmetric model, where h = 2". Assuming a convection speed equal to 50% of the free stream velocity (which appears to be a lower bound, and is derived from the data for separated flow ahead of a forward facing step (Ref. 13), then we find

TUNNEL C TESTS

INSTRUMENTATION CALIBRATION DATA

TABLE 4

TWO-DIMENSIONAL MODEL

Transducer Number	Channel No. (Amplifier No.)	Transducer Sensitivity ("H_2O/Volt Output)	$Gain_{(cal.)}$	$Gain_{(test)}$	K	K^1
X1	1	5.20	192	218	156.0	154.9
X2	2	22.0	192	228	168.5	167.0
X3	3	20.9	192	236	168.0	166.2
X5	6	15.0	192	244	165.2	163.0
X6	7	22.0	192	226	168.5	167.1

$$\frac{\omega r}{U_c} = \frac{2\pi fh}{U_\infty} \frac{U_\infty}{U_c} \frac{r}{h}$$

$$\leq 2\pi(2) \frac{1}{0.5} \frac{0.125}{2}$$

$$\leq 1.57$$

where r is the radius of the transducer

For this case, Corcos finds the apparent spectral density is 25% of the correct value (6db low) which is a significant error; however, the spectral densities will be found in Section V to decrease with increasing frequency at a much more rapid rate than can be accounted for on the basis of the data of Ref. 42. For the flat plate model, h = 4 in., which implies $(\omega_r/U_c) \leq .885$, and the ratio of apparent to the correct value of spectral density is 50% (3db low). It will be seen further that for separated flows, the highest spectral densities occur for (fh/U_∞) below 1.0. In this case, the errors for the axisymmetric and flat plate models are, respectively, -3db and -1.24db.

Considering the above facts and the uncertain applicability of calculated corrections based upon low speed boundary layer turbulent pressures, no corrections were applied to the present spectral density data, since these errors cause the measured response to be low. This could partly compensate for any vibratory induced errors which would tend to cause errors on the high side, so that the data for the wide band RMS pressure fluctuation level would be reasonably correct. The vibration-induced errors are discussed in Section V in connection with the discussion of the non-dimensional frequency spectra.

IV TEST CONDITIONS

Fluctuating pressure data caused by separated flows, oscillating base pressures, wakes, and oscillating shock waves were obtained for each of two models. For the axisymmetric model, the pressures were obtained at Mach numbers of 2.5, 3.5 and 5 for free stream Reynolds numbers per foot of 0.5, 1 and 6 million. For the two-dimensional model, the pressures were obtained at Mach numbers of 2, 3.5, 5 and 10 for free stream Reynolds numbers per foot of 0.5, 1, 2, and 5 million.

Data was obtained for angles of attack of 0, 5, 10 and 15 degrees. Tables 5 and 6 list the test conditions that were run. Model configuration 1 is the axisymmetric model with the forward and aft flares attached, and model configuration 2 is the two-dimensional model. The runs with covers were made with the transducers covered with plates in order to isolate the fluctuating aerodynamic pressures from the model vibrations. The temperature rake and pressure rake data, to define the boundary layer profiles, were obtained in test runs subsequent to the dynamic pressure fluctuation runs.

At the beginning of the tests, comparisons were made of the transducer data obtained by operating the charge amplifiers in both the long time constant mode and the short time constant mode. All data from AEDC Group number 5 to the end of the testing was recorded with che charge amplifiers operating in the short time constant mode.

The figure numbers listed in tables 5 and 6 refer to the figures in the Appendix showing the one-third octave band spectra.

TABLE 5

TEST CONDITIONS TUNNEL A

MODEL CONFIGURATION	MACH NO. NOM.	P_o psia	T_o °F	α DEG.	ϕ DEG.	DATA RECORDED	REMARKS	FIG. NOS.	AEDC GROUP NOS.
1	5	11	105	0	0	DYN.	SHORT T.C.	1-7	1
		11	105				LONG T.C.	8-14	2
		18	110				SHORT T.C.	15-21	3
				5			LONG T.C.	22-28	4
				15			SHORT T.C.	29-35	5
							SHORT T.C. FOR RE-MAINDER	36-42	6
				0				43-49	7
					-90				8
		150	170		0			50-56	9
	2.5	3.5	92					57-63	10
		32	95					64-70	11
		5.2	90					71-77	12
				5				78-84	13
				15				85-91	14
				5					15
				0				92-98	16
					-90			99-105	17
	3.5	56	123	0	0			106-112	18
				5					19
				15					20
				0					21
		9.3	121					113-119	22
				5				120-126	23
				15				127-133	24
				0				134-140	25
					-90				26
1 (covers)		56	122		0				27
				5					28
				15					29
		9.3	120	0					30
				5					31
				15					32
	2.5	32	100	0	0				33
		3.5		0					34
				5					35
				15					36#1
1(covers and rake)		5.2	92	0	0	DYN. & PRESS			36#2
			92						37
		32	95						38
1		3.5	90			PRESS.			39
1		5.2	90			PRESS.			40

TABLE 5 (Continued)

TEST CONDITIONS TUNNEL A

MODEL CONFIGURATION	MACH NO. NOM.	P_o psia	T_o °F	α DEG.	ϕ DEG.	DATA RECORDED	REMARKS	FIG. NOS.	AEDC GROUP NOS.
1	2.5	5.2	90	5	0	PRESS.			41
					-30				42
					30				43
				15	0				44
					-30				45
					30				46
				0	0				47
		32							48
	3.5	9.3	120						49
				5					50
					-30				51
					30				52
				0	0				53
		56		0					54
				5					55
					-30				56
					30				57
				15	0				58
				15	-30				59
				15	30				60
				0	0				61
		9.3		15	0				62
					-30				63
	3.5	9.3	120	15	30				64
	5.0	18	110	0	0				65
				5					66
					-30				67
					30				68
				15	0				69
					-30				70
					30				71
				0	0				72
		11	105						73
		150	170						74
1 (covers and temp rake)		11	101			DYN. & TEMP.			75
		18	102						76
				5					77
				15					78
		150	170	0					79
1 (temp. rake)		11	110			TEMP.			80
		18							81
				5					82
					-20				83

TABLE 5 (Continued)

TEST CONDITIONS TUNNEL A

MODEL CONFIGURATION	MACH NO. NOM.	P_o psia	T_o °F	α DEG.	ϕ DEG.	DATA RECORDED	REMARKS	FIG. NOS.	AEDC GROUP NOS.
1 (temp. rake)	5.0	18	110	5	-30	TEMP.			84
				15	0				85
					-20				86
					-30				87
		150	170	0	0	TEMP.			88
	3.5	9.3	120						89
				5					90
					-20				91
					-30				92
				15	0				93
					-20				94
					-30				95
				0	0				96
		56							97
				5					98
					-20				99
					-30				100
				15	0				101
					-20				102
					-30				103
				0	0				104
	2.5	3.5	91						105
		5.2							106
				5					107
				5	-20				108
				5	-30				109
				15	0				110
					-20				111
					-30				112
				0	0				113
		32							114
2 (30° FLAP)	2.0	3	90	0	-90	DYN.		141-145	115
		3			0			146-150	116
		4						151-155	117
				5				156-160	118
				15				161-165	119
				0				166-170	120
	3.5	4.5	90	0	-90				121
				0	0				122
				5				171-175	123
				15					124
				0					125
									126
		9.3	122					176-180	127

TABLE 5 (Continued)

TEST CONDITIONS TUNNEL A

MODEL CONFIGURATION	MACH NO. NOM.	P_o psia	T_o °F	α DEG.	ϕ DEG.	DATA RECORDED	REMARKS	FIG. NOS.	AEDC GROUP NOS.
2 (30° Flap)	3.5	9.3	122	5	0	DYN.		181-185	128
			120	15				186-190	129
				0				191-195	130
					-90				131
	5.0	11	100		-90				132
					0			196-200	133
		18						201-205	134
				5				206-210	135
				15				211-215	136
				0	-90				137
					0			216-220	138
2 (60° Flap)		11						221-225	139
		18						226-230	140
				5				231-235	141
				15				236-240	142
				0				241-245	143
	3.5	4.5	120	0				246-250	144
		9.3		0				251-255	145
				5				256-260	146
				15				261-265	147
				0				266-270	148
	2.0	3	93	0				271-275	149
		4		0				276-280	150
				5				281-285	151
				15				286-290	152
				0				291-295	153
2 (clean)		3	90		-90				154
					0			296-300	155
		4						301-305	156
					5			306-310	157
					15			311-315	158
					0			316-320	159
		19.2	90	0	-90				160
					0			321-325	161
	3.5	4.5	110		0			326-330	162
		4.5			-90				163
		9.3	120		0			331-335	164
				5				336-340	165
				15				341-345	166
				0				346-350	167
	5.0	11	115		-90				168
					-90				169
					0			351-355	170
		18	105					356-360	171

TABLE 5

TEST CONDITIONS TUNNEL A

MODEL CONFIGURATION	MACH NO. NOM.	P_o psia	T_o °F	α DEG.	ϕ DEG.	DATA RECORDED	REMARKS	FIG. NOS.	AEDC GROUP NOS.
2 (clean)	5.0	18	105	5	0	DYN		361-365	172
				15				366-370	173
				0				371-375	174
2 (30° Flap and covers)		11	100						175
		18							176
				5					177
				15					178
				0					179
	3.5	4.5							180
		9.3							181
				5					182
				15					183
				0					184
	2.0	3							185
		4							186
				5					187
				15					188
				0					189
2 (60° Flap and covers)		3							190
		4							191
		4	100	5					192
		4		15					193
				0					194
	3.5	4.5	105						195
		9.3							196
				5					197
				15					198
				0					199
	5.0	11.2							200
		18							201
				5					202
				15					203
				0					204
2(Clean covers)		11.2	100			NONE			205
2(30° Flap, press. rake						PRESS.			206
		18							207
				5					208
				10					209
				15					210
				0					211
	3.5	4.5	120						212
				5					213
				15					214
				0					215
		9.3							216

TABLE 5 (Continued)

TEST CONDITIONS TUNNEL A

MODEL CONFIGURATION	MACH NO. NOM.	P_o psia	T_o °F	α DEG.	ϕ DEG.	DATA RECORDED	REMARKS	FIG. NOS.	AEDC GROUP NOS.
2(30° Flap, press. rake)	3.5	9.3	120	5	0	PRESS.			217
				10					218
				15					219
				0					220
	2.0	3	90						221
		4							222
				5					223
				10					224
	2.0			15					225
				0					226
2(60° Flap, press. rake)		3							227
		4							228
				5					229
				10					230
				15					231
				0					232
	3.5	4.5	120						233
				5					234
				15					235
				0					236
		9.3							237
				5					238
				10					239
				15					240
				0					241
	5.0	18	100	0					242
				5					243
				10					244
				15					245
				0					246
		11.2							247
2(30° Flap, Press. rake)		18	94	15					248
				0					249
		11.2							250
	3.5	9.3	120						251
				5					252
				10					253
				15					254
				0		PRESS.			255
		4.5							256
2(30° Flap, Temp. rake)	2.0	3	90			TEMP.			257
		4							258
				5					259
									260

TABLE 5 (Continued)

TEST CONDITIONS TUNNEL A

MODEL CONFIGURATION	MACH NO. NOM.	P_o psia	T_o °F	α DEG.	ϕ DEG.	DATA RECORDED	REMARKS	FIG. NOS.	AEDC GROUP NOS.
2(30° Flap, Temp. rake)	2.0	4	90	10	0	TEMP.			261
	↓	↓	↓	15	↓	↓			262
	↓	↓	↓	0	↓	↓			263
	3.5	4.5	120	↓	↓	↓			264
	↓	↓	↓	5	↓	↓			265
	↓	↓	↓	15	↓	↓			266
	↓	↓	↓	0	↓	↓			267
	↓	9.3	↓	↓	↓	↓			268
	↓	↓	↓	5	↓	↓			269
	↓	↓	↓	10	↓	↓			270
	↓	↓	↓	15	↓	↓			271
	↓	↓	↓	0	↓	↓			272
	5.0	18	100	↓	↓	↓			273
	↓	↓	↓	5	↓	↓			274
	↓	↓	↓	10	↓	↓			275
	↓	↓	↓	15	↓	↓			276
	↓	↓	↓	0	↓	↓			277
	↓	11.2	↓	↓	↓	↓			278
2(60° Flap, Temp. rake)	↓	18	↓	↓	↓	↓			279
	↓	18	↓	5	↓	↓			280
	↓	↓	↓	10	↓	↓			281
	↓	↓	↓	15	↓	↓			282
	↓	↓	↓	0	↓	↓			283
	↓	11.2	↓	↓	↓	↓			284
	3.5	4.5	120	↓	↓	↓			285
	↓	9.3	↓	↓	↓	↓			286
	↓	↓	↓	5	↓	↓			287
	↓	↓	120	10	↓	↓			288
	↓	↓	↓	15	↓	↓			289
	↓	↓	↓	0	↓	↓			290
	2.0	3	90	↓	↓	↓			291
	↓	4	92	↓	↓	↓			292
	↓	↓	↓	5	↓	↓			293
	↓	↓	↓	10	↓	↓			294
	↓	↓	↓	15	↓	↓			295
	↓	↓	↓	0	↓	↓			296
	↓	3	90	↓	↓	↓			297
	↓	4	↓	↓	↓	↓			298
	↓	↓	↓	5	↓	↓			299
	↓	↓	↓	10	↓	↓			300
	↓	↓	↓	15	↓	↓			301
	↓	↓	↓	0	↓	↓			302
	3.5	4.5	120	↓	↓	↓			303
	↓	9.3	↓	↓	↓	↓			304

TABLE 5 (Continued)

TEST CONDITIONS TUNNEL A

MODEL CONFIGURATION	MACH NO. NOM.	P_o psia	T_o °F	α DEG.	ϕ DEG.	DATA RECORDED	REMARKS	FIG. NOS.	AEDC GROUP NOS.
2(60° Flap, Temp. rake)	3.5	9.3	120	5	0	TEMP.			305
				10					306
				15					307
				0					308
	5.0	18	100						309
				5					310
				10					311
				15					312
				0					313
		11.2							314
2(30° Flap, Temp. rake)		18							315
				5					316
				10					317
				15					318
				0					319
		11.2	100						320
	3.5	4.5	120						321
		9.3							322
					5				323
					10				324
					15				325
					0				326
	2.0	3	90						327
		4							328
					5				329
					10				330
					15				331
					0				332
2(Clean, Temp. rake)			Vary						333
									334

TABLE 6

TEST CONDITIONS TUNNEL C

MODEL CONFIGURATION	MACH NO. NOM.	P_o psia	T_o °F	α DEG.	ϕ DEG.	DATA RECORDED	REMARKS	FIG. NOS.	AEDC GROUP NOS.
2 (Clean)	10	750	1350	0	0	DYN.		376-380	1
				5				381-385	2
				13.7				386-390	3
				0				391-395	4
2 (30° Flap)				0				396-400	5
				5				401-405	6
				13.7				406-410	7
				10				411-415	8
				0				416-420	9
2(60° Flap)				↓					10
				5				421-425	11
				10				426-430	12
				13.7				431-435	13
				0				436-440	14
		1650	1430	↓				441-445	15
				5					16
				13.7				446-450	17
				0				451-455	18
2(30° Flap)				0				456-460	19
				5				461-465	20
				13.7				466-470	21
				0				471-475	22
2 (Clean				0				476-480	23
				5				481-485	24
				13.7				486-490	25
				0				491-495	26
2 (Clean		750	1350	↓		PRESS.		496-500	27
Press. rake)									28
2(30° Flap,	10	750	1350	0					29
Press. rake)	10	750	1350	5					30
	10	750	1350	13.7					31
2(60° Flap,				↓					32
Press. rake)				5					33
				0					34
2(60° Flap,						TEMP.			35
Temp. rake)									36
						NONE	THERMO-COUPLES BAD.		37
2(30° Flap,						PRESS.			38
Press. rake)									
2(60° Flap,	10	750	1350	0		PRESS.			39
Press. rake)	↓	1650	1425	↓		↓			40

TABLE 6 (Continued)

TEST CONDITIONS TUNNEL C

MODEL CONFIGURATION	MACH NO. NOM.	P_o psia	T_o °F	α DEG.	ϕ DEG.	DATA RECORDED	REMARKS	FIG. NOS.	AEDC GROUP NOS.
2(30° Flap, Press. rake)	10	1650	1425	0	0	PRESS.			41
2(60° Flap, Press. rake)	10	1650	1425	5	0	↓			42
	↓	↓	↓	13.7	↓	↓			43
2(60° Flap, Temp. rake)	10	750	1350	0	0	TEMP.			44
2(30° Flap, Temp. rake)	10	750	1350	0	0	↓			45
	↓	↓	↓	5	↓	↓			46
2(60° Flap, Temp. rake)	10	750	1350	5	↓	↓			47
	↓	↓	↓	13.7	↓	↓			48
2(30° Flap, Temp. rake)	↓	1650	1435	0	↓	↓			49
2(60° Flap, Temp. rake)	↓	↓	↓	↓	↓	↓			50
									51

V EXPERIMENTAL RESULTS AND DISCUSSION

TUNNEL OPERATING CONDITIONS AND BACKGROUND NOISE

Tunnel A

Operating Conditions and Measured Tunnel Noise

Tunnel "A" is a supersonic tunnel having flexible hydraulically actuated nozzle wall contours giving the proper contours for smooth expansion of the flow from the nozzle throat to the 40" x 40" test section. The tests were conducted at a constant Reynolds number by suitable adjustment of the stagnation pressure according to the Mach number and stagnation temperature. Figure 27 shows the actual recorded values of stagnation temperature and pressure during the tests at Reynolds numbers of 0.6, 1.0, 2.0 and 6.0 x 10^6/ft. at various test Mach numbers. Figure 28 shows the associated values of free stream dynamic pressure, $q_\infty = 1/2\rho u_\infty^2$, and free stream velocity U_∞ in ft/sec. As is typical with wind tunnel operation, the stagnation temperature is nearly constant over the range of Mach number from 2 to 5; hence, the total kinetic energy is constant and the velocity increase with Mach number is only slight (1700 ft/sec. to 2390 ft/sec.). The variation of dynamic pressure shows a drop from 1.57 psi at Mach 2 to.62 psi at Mach 5 for operation at one million Reynolds number per ft. for which most of the dynamic data were recorded. Because the RMS sound pressure scales according to q_∞, the basic wind tunnel noise level corrected by subtracting 20 $\log_{10} q_\infty$ is presented in Figure 29. The basic noise level is based upon measurements (1) on a smooth flat plate (0^o flap) at various distances from the leading edge and (2), at the forward reference transducer for the axisymmetric model (Channel 1). The flow is judged to be laminar at Channel 2 on the flat plate model ($R_{ex} = 2.08 \times 10^5$) and transitional at Channel 1 on the axisymmetric model ($R_{ex} = 5.4 \times 10^5$, x = distance aft of the leading edge). As can be seen, the acoustic levels are quite high. If one had a transducer capable of measuring the entire frequency spectrum of the very thin boundary layer on the 22 inch long plate, one might expect a value of 126 db based on low speed results such as those of Willmarth and Woolridge (Ref. 1); however, as can be seen from Figure 30, the calculated boundary layer thickness on a 22 inch plate is of the order of 0.37 inches at the trailing edge, and the Strouhal number based upon the nominal thickness, δ, and associated with the maximum frequency of the spectra (20 kc) amounts to .27 to .35, as compared with the range of measurable spectra up to a Strouhal number of about 5. This range is inferred from the work of Kistler and Chen (Ref. 17) for supersonic flat plate boundary layers. Using the spectra of Ref. 2 as a guide, it is estimated that only 15% of the energy is measured for this flat plate turbulent boundary layer spectrum at the trailing edge (x = 22 in.) by the present experimental technique. Therefore, the apparent RMS Δp is reduced to 40% of its correct value by the 20,000 cps upper analysis limit. Figure 31 shows the basic tunnel noise data again in the form of RMS $\Delta p/q_\infty$, along with estimates from a smooth plate and the reduced level corresponding to the 20 kc cutoff in the data analysis. These estimates based on the trailing edge boundary layer thickness are still high for the forward locations (Channels 2 and 7 on the plate) where the boundary layer is laminar or transitional. We, therefore, regard the high levels recorded by Channels 5 and 6 as due to wind tunnel noise. Channel 5 appears high relative to Channel 6 which might suggest a calibration error on the high side. For this reason, the aft flare pressures on the axisymmetric model (which were measured by Channel 5 and which appear very high in comparison to other measurements), are viewed with some suspicion and the ($\Delta p/q_\infty$) values for Channel 5 might be high by a factor of 2. There does appear to be fair agreement between the forward reference Channel 1 of the axisymmetric model and the most forward channel (2) of the flat plate model; exact agreement would not be expected due to the different wave reflection situations of the two model configurations. Also shown in Figure 31 is the upper bound of Laufers supersonic wind tunnel radiated sound levels (Ref. 3).

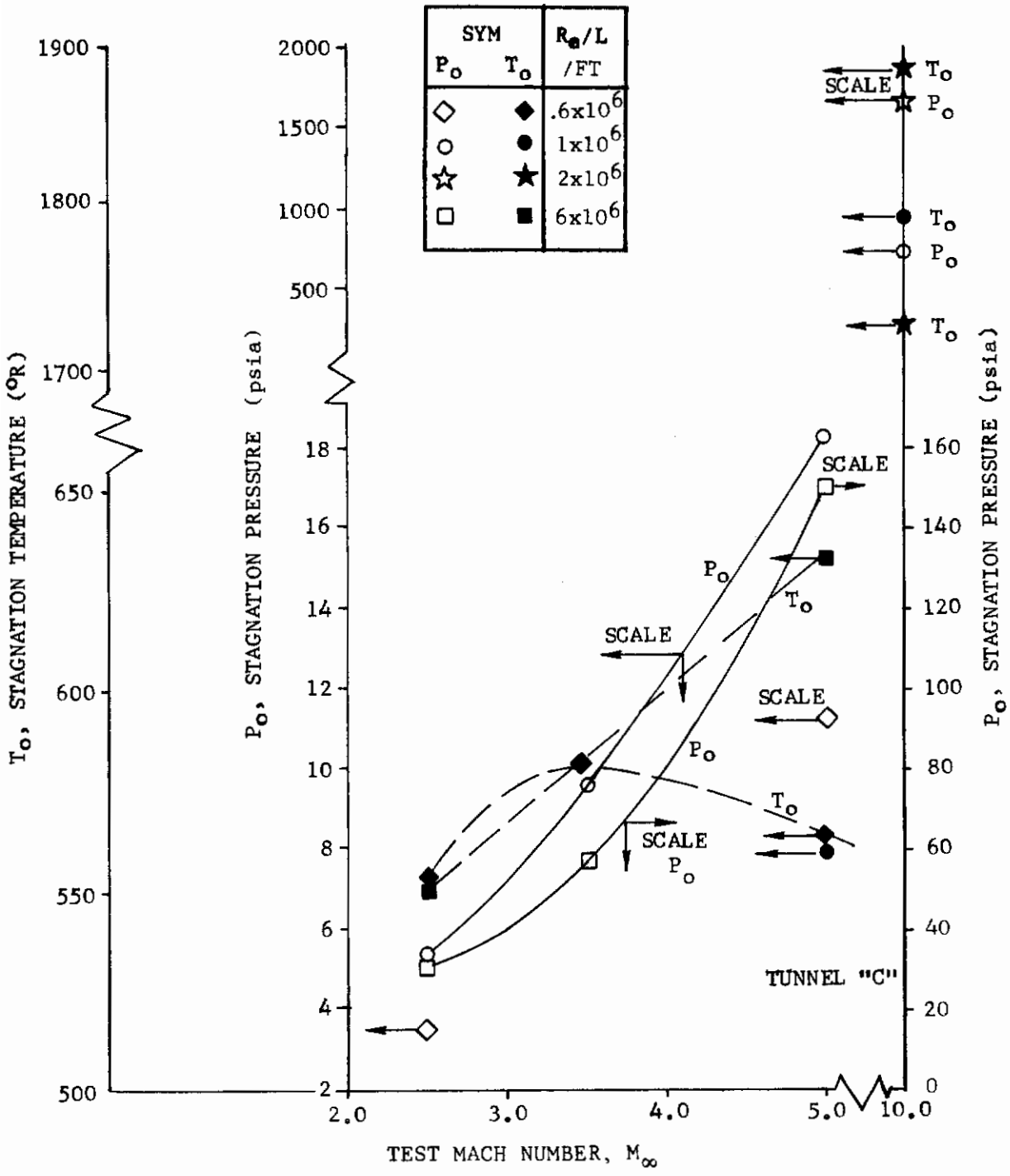

FIGURE 27 STAGNATION TEMPERATURE AND PRESSURE DURING DYNAMIC RECORDING TESTS

a. FREE STREAM DYNAMIC PRESSURE VS. MACH NUMBER

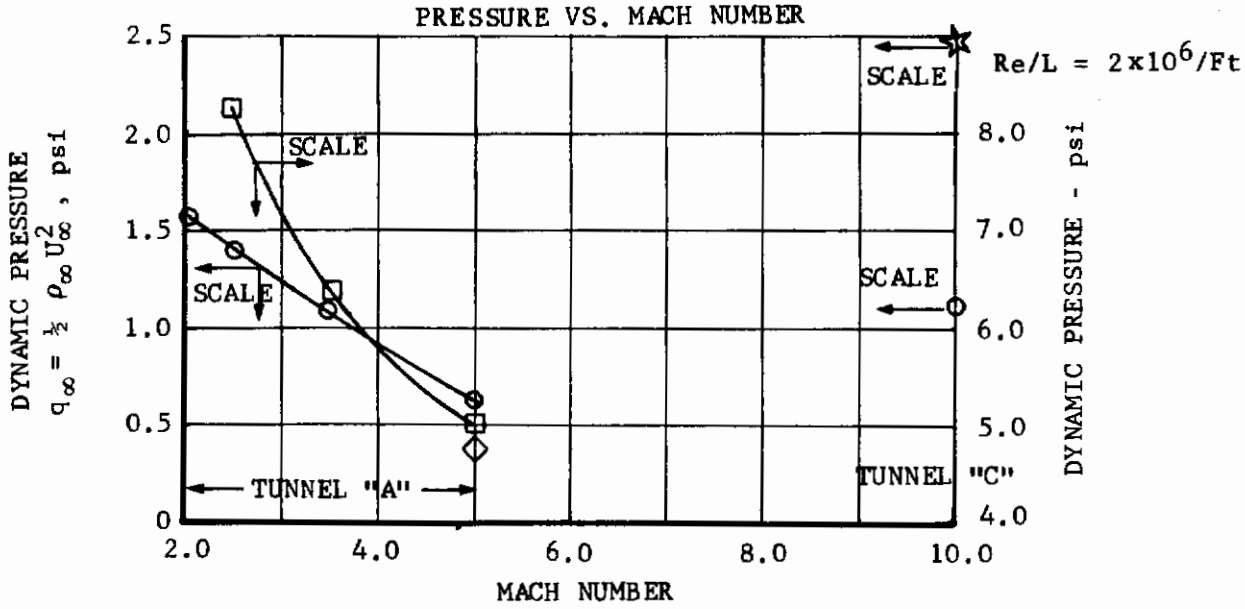

b. FREE STREAM VELOCITY VS. MACH NUMBER

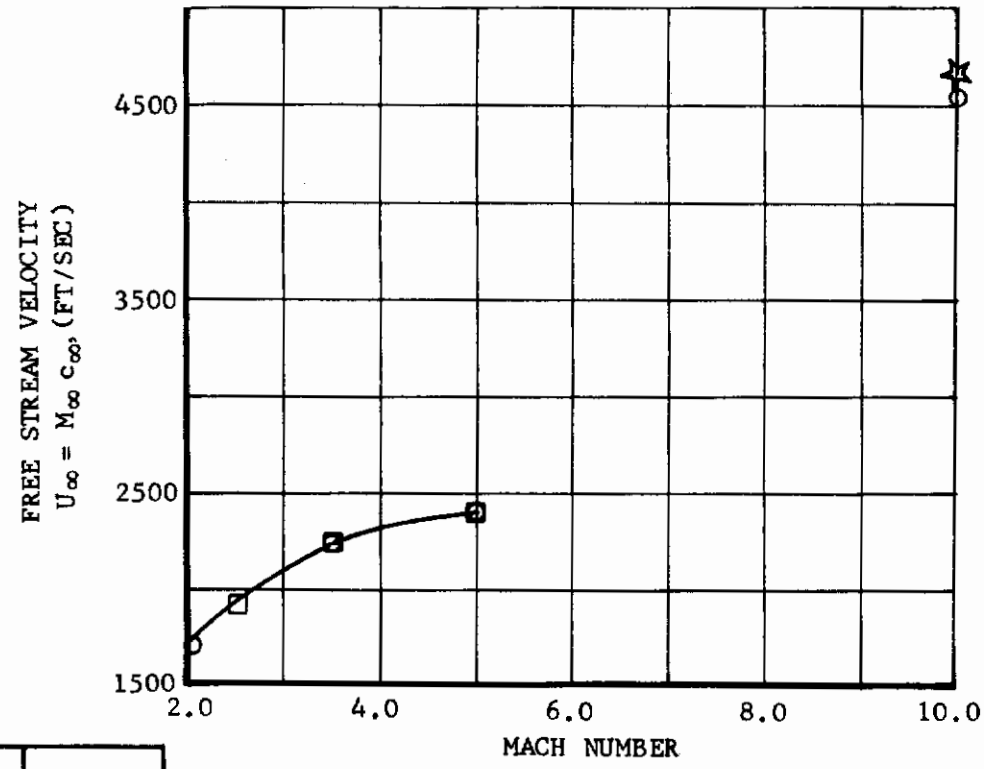

SYM	Re/L (FT^{-1})
◇	0.6×10^6
○	1.0
☆	2.0
□	6.0

FIGURE 28 FLOW CONDITIONS DURING WIND TUNNEL TESTS

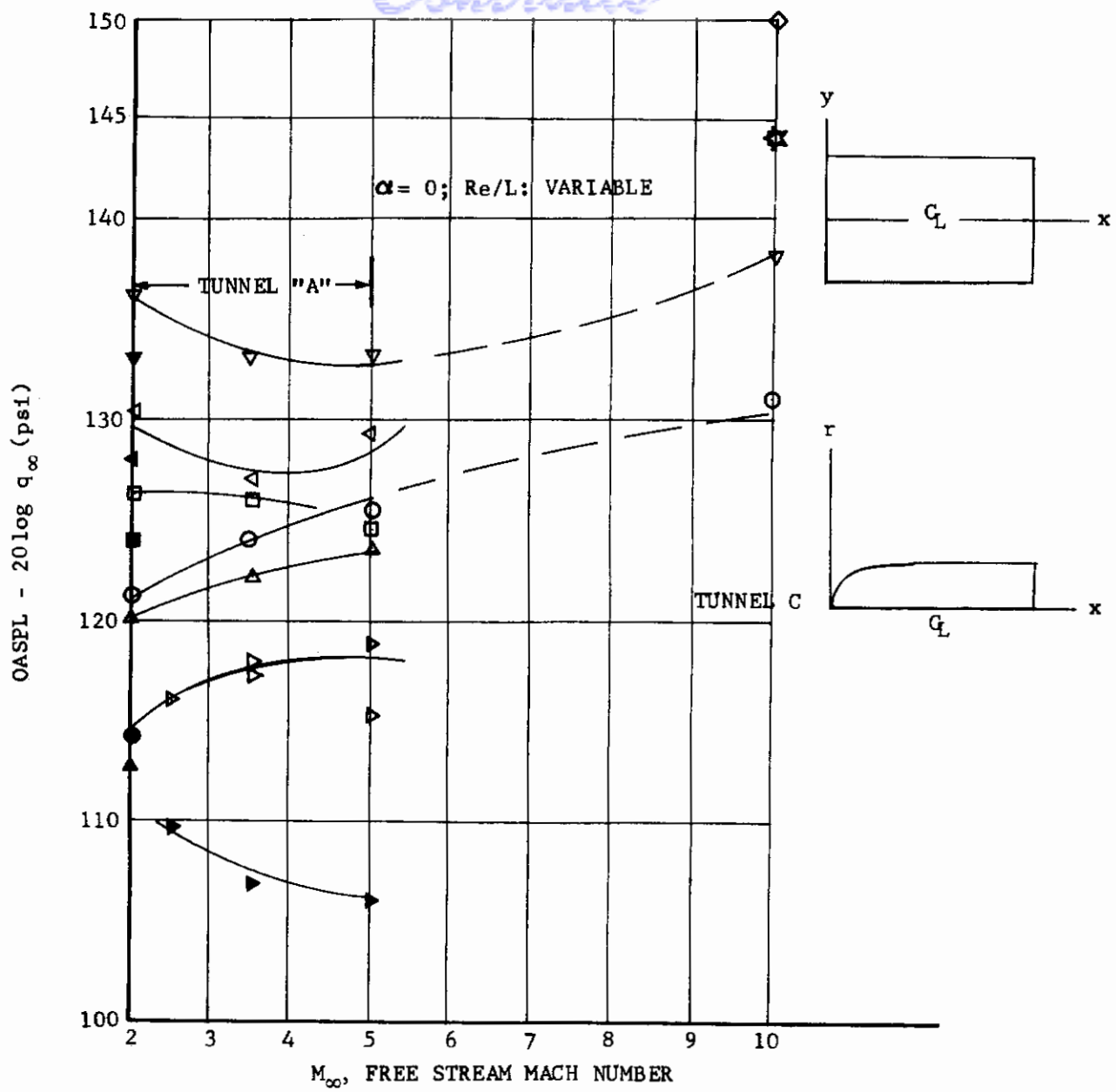

	LOCATION x IN	LOCATION y IN	TUNNEL A CHANNEL NO	TUNNEL C CHANNEL NO	Re/FT	SYM	Re/FT	SYM
FLAT PLATE MODEL	2.5	0	2	1	1×10^6	○	5×10^6	●
	13.0	0	7	—		△		▲
	16.0	0	—	2		◇		◆
	18.0	0	4	3		□		■
	20.0	0	5	6		▽		▼
	20.0	2	—	7		☆		★
	20.0	4	6	—		◁		◀
AXISYMMETRIC MODEL	x IN	r IN						
	6.48	3.75	1	—	1×10^6	▷	6×10^6	▶

FIGURE 29 BASIC NOISE LEVEL OF WIND TUNNEL (CORRECTED FOR q_∞ CHANGE)

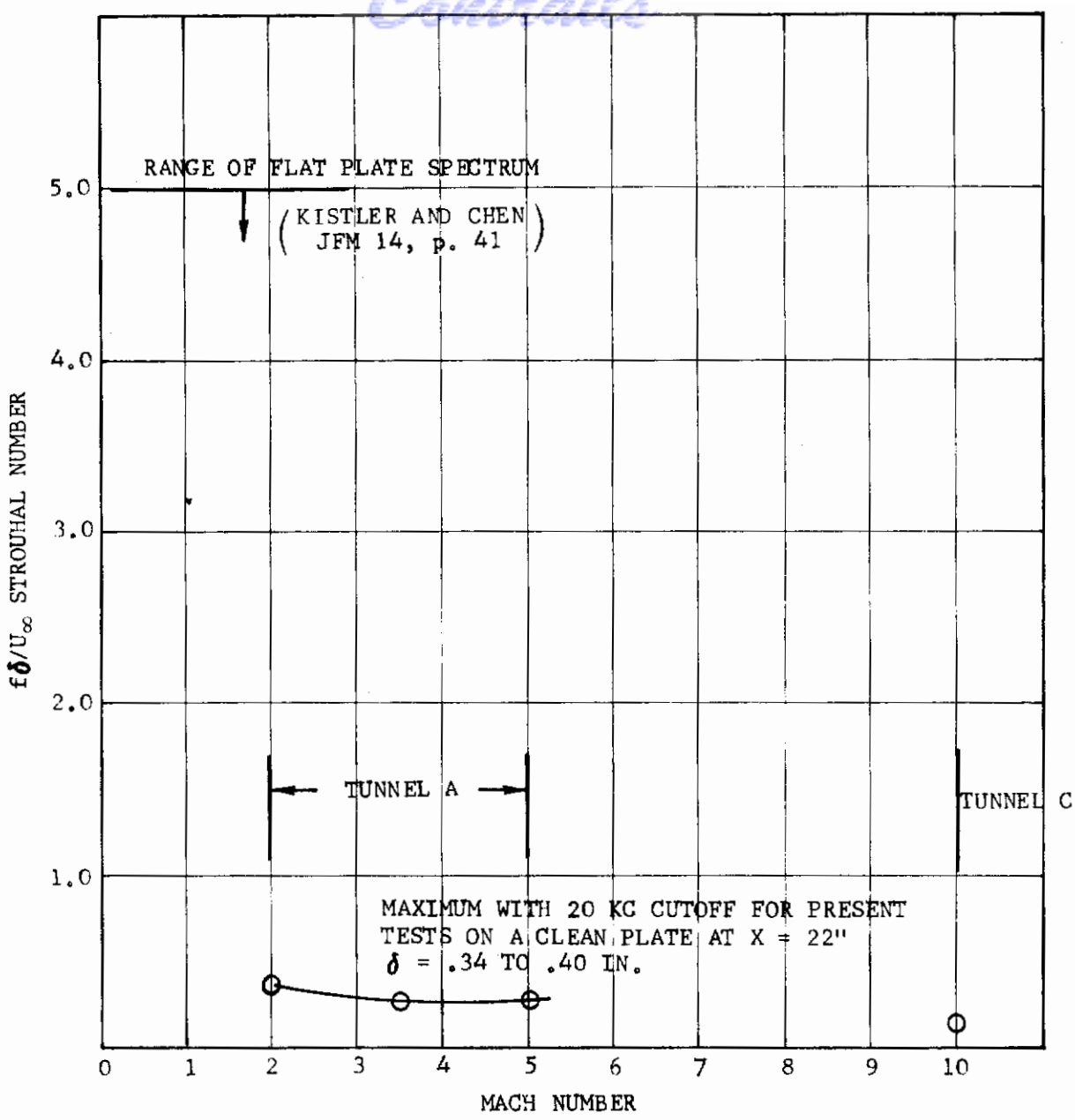

M_∞	R_e/L /FT	α	U_∞ FT/SEC	T_o °R	δ IN	δ^* IN	T_W °R
2.0	1×10^6	0	1710	552	.356	.0845	550
3.5	↓	↓	2225	582	.373	.140	↓
5.0			2375	563	.407	.201	(500-800)
10.0			4550	1810	.37	.140	

REMARK: δ & δ^* CALCULATED FROM VAN DRIEST THEORY AND TUCKER'S TABLES (NACA TN 2337 1951)

FIGURE 30 STROUHAL NUMBER RANGE FOR CLEAN PLATES VS. PRESENT TEST RANGE FOR A 22 IN. LONG PLATE

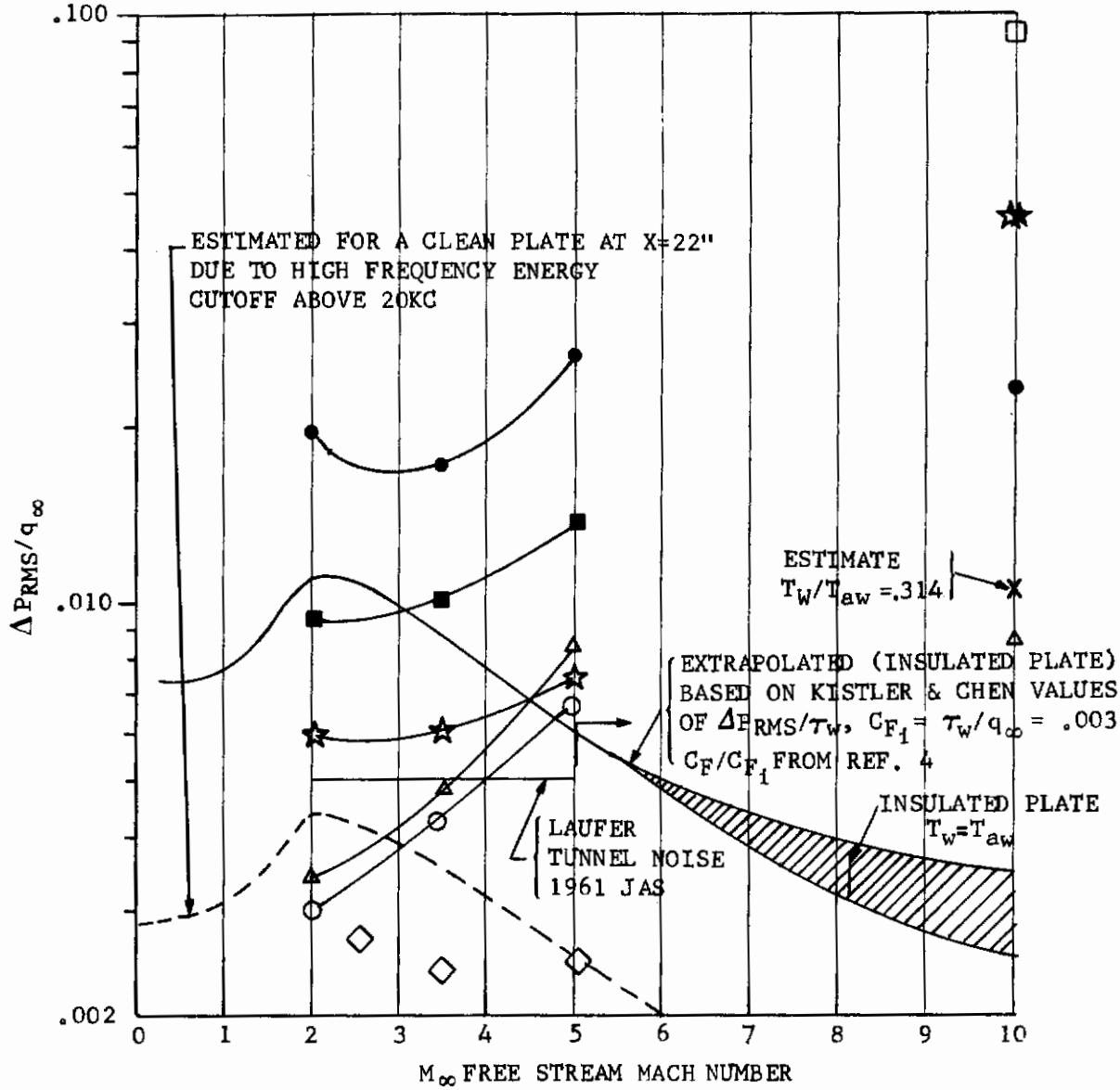

FLAT PLATE (0° FLAP)

SYM	XDCR LOCATION		XDCR CHANNEL TUNNEL	
	x	y	A	C
△	2.5"	0"	2	1
○	13.0"	↓	7	-
□	16.0"	↓	-	2
☆	18.0"	↓	4	3
●	20.0"	↓	5	6
★	↓	2"	-	7
■	↓	4"	6	-

AXISYMMETRIC REF. XDCR

	x	r
◇	6.5"	3.75"

FIGURE 31 RMS PRESSURE FLUCTUATIONS ON A CLEAN FLAT PLATE VS. MACH NUMBER

With regard to the above discussed estimate of the clean plate RMS ($\Delta p/q_\infty$), the following relation was used:

$$\frac{\Delta p_{rms}}{q_\infty} = \left(\frac{\Delta p_{rms}}{\tau_w}\right) C_{Fi} \left(\frac{C_F}{C_{Fi}} M_\infty\right) \qquad (86)$$

The values of C_F/C_{F_i} are taken from a correlation given in Ref. 4, p. 343, $C_{F_i} = \tau_w\ (M = o)/q_\infty \cong .003$ is from Ref. 5, p. 538. The values of $\Delta p_{rms}/\tau_w$ were taken from Ref. 3, p. 59, Figure 16.

As will be seen in the later discussion, an adequate signal to noise ratio prevailed for the 60° flap and axisymmetric models; however, the signal to noise ratio for the 30° flap configuration is questionable. Also, the high frequency portion of the base pressure frequency spectrum appeared to be masked by the background noise in the wind tunnel. The minimum noise levels associated with the forward most channels (2 and 7) of the plate and Channel 1 of the axisymmetric model are about what one would expect. The background noise levels of Channels 4, 6, and especially 5 appear higher than desirable; possibly these are affected by their location in the tunnel, and it must be borne in mind that no previous acoustic data are available for the open tunnel.

In order to obtain good wind tunnel acoustic data, it would be desirable to bleed off the sidewall turbulent boundary layers which will inevitably radiate noise according to Lighthill's theory (see Ref. 6, especially with regard to wind tunnel noise). Secondly, attempts should be made to reduce temperature and velocity fluctuations in the flow upstream of the nozzle, since the entropy and vorticity interactions can generate sound which will be swept downstream through the test section (see Ref. 7 and recall the discussion of section II). Devices such as turbulence screens and other flow smoothing techniques should be fully explored as a possible design modification of this facility if it is to be used for serious acoustic experimentation. Thirdly, it would be desirable to treat acoustically the walls of the tunnel to reduce the reflections and the lateral standing waves associated with the solid walls, though these are primarily of concern to the low frequency part of the spectrum.

Theoretical Considerations of Supersonic Tunnel Noise

One could evaluate the wall reflection effect by a generalization to three dimensions of Miles' treatment of unsteady supersonic flow in a wind tunnel (Ref. 8, p. 59). To illustrate the nature of such treatments, we consider an oscillating airfoil where $\bar{v}(x)$ is a prescribed airfoil vertical velocity at Z = 0 (center of the tunnel) and where the tunnel upper and lower walls are at $z = \pm Z_1$. Then Miles shows that, first the velocity disturbance potential ϕ is governed by

$$\frac{\partial^2\phi}{\partial x^2} + \frac{\partial^2\phi}{\partial z^2} - \frac{1}{c^2}\left(U^2 \frac{\partial^2\phi}{\delta x^2} + 2U \frac{\partial^2\phi}{\partial x \partial t} + \frac{\partial^2\phi}{\partial t^2}\right) = 0 \qquad (87)$$

The vertical velocity boundary conditions are

$$\frac{v}{U} = \frac{1}{U}\frac{\partial\phi}{\partial z} = \bar{v}(x) \qquad \text{at} \qquad z = 0,\ x > 0 \qquad (88)$$

$$\frac{\partial\phi}{\partial z} = 0 \qquad \text{at} \qquad z = \pm z_1 \text{ (solid walls)} \qquad (89)$$

The pressure fluctuation is given by

$$p(x, z, t) = -\rho \left(U \frac{\partial \phi}{\partial x} + \frac{\partial \phi}{\partial t} \right) \tag{90}$$

We remark that Eq. (90) includes both sound pressure and so-called pseudo sound, since Eq. (90) is valid even if the flow would be incompresible. (The reader is directed to Blokhintsev Ref. 9, p. 123 for a lucid discussion of this problem). In supersonic flow, the mathematical solution of the boundary value problem recognizing the presence of characteristic surfaces (Ref. 8, Chapter 3) yields the proper results if the streamwise initial conditions are specified. In particular, if the upstream flow is free of disturbances we can write the initial conditions on $\bar{x}$ as

$$x = 0: \qquad \phi(o, z, t) = \frac{\partial \phi}{\partial x} (o, \bar{z}, t) = 0 \tag{91}$$

Miles finds the solution to the above problem for the case of harmonic motion:

$$\phi(x, z, t) = \bar{\phi}(x, z) \ell^{i\omega t} \tag{92}$$

At the center of the tunnel, Z = 0. The result is

$$\phi(\bar{x}, o^+, t) = \frac{1}{\beta} \int_o^x g(\bar{x} - \bar{\xi})\, \bar{v}\, (\bar{\xi})\, d\bar{\xi} \tag{93}$$

where

$$(\bar{x}, \bar{z}) = (x/\ell, z/\ell)_\infty \tag{94}$$

$$g(\bar{x}) = \exp\left(- \frac{i k M^2 \bar{x}}{2} \right) \sum_{n=0}^{\infty} \frac{\left(2 - \delta_n^{\,o}\right)}{\left(\mu_n \bar{z}_1\right)} \sin\left(\mu_n \bar{x}\right) \tag{95}$$

$$\mu_n = \frac{kM}{\beta^2} \left[1 + \left(\frac{n\pi}{kMz_1} \right)^2 \right]^{1/2} \quad ; \quad \delta_n^{\,o} = \begin{cases} 1, & n = 0 \\ 0, & n \neq 0 \end{cases} \tag{96}$$

Now k is the so-called reduced frequency associated with an airfoil of length l

$$k = \frac{\omega \ell}{U} \tag{97}$$

In terms of the usual acoustic wave number

$$\alpha \equiv \omega / c \tag{98}$$

we have

$$kM\bar{x} = \left(\frac{\omega \ell}{U} \right) \left(\frac{U}{c} \right) \left(\frac{x}{\ell} \right) = \frac{\omega x}{c} = \alpha x \tag{99}$$

$$kM\bar{z}_1 = \frac{\omega z_1}{c} = \alpha z_1 \tag{100}$$

Miles interprets each of the terms of Eq. (94) as guided wave modes of the tunnel. In the case of an unbounded fluid, Eq. (94) is replaced by (Ref. 8, p. 50)

$$g(x) = \exp\left(-\frac{ikM^2x}{\beta^2}\right) J_o\,(kMx/\beta^2) \tag{101}$$

where J_o is the Bessel function of the first kind of order zero. What we observe from Equations (94) and (101) are the oscillatory character in the streamwise direction. When n is large, many wall reflections have occurred, and if the frequency is low enough and n is large enough, the second term in Eq. (95) dominates and μ_n reduces to

$$\underset{\left(\frac{n\pi}{\alpha z_1}\right) \gg 1}{\text{Lim}}\ (\mu_n) \longrightarrow \frac{kM}{\beta^2}\left(\frac{n\pi}{kM\bar{z}_1}\right) = \frac{n\pi}{\beta^2 z_1} \tag{102}$$

and

$$g(x) = \exp\left(-\frac{iM\alpha x}{\beta^2}\right) \sum_{n=0}^{\infty} \frac{\left(2-\delta_n{}^{o}\right)}{\left(\frac{n\pi}{\beta^2}\right)} \sin\left(\frac{n\pi x}{\beta^2 z_1}\right) \tag{103}$$

Equation (102) requires

$$\frac{\omega z_1}{c} \ll n\pi \tag{104}$$

or

$$\frac{f z_1}{c} \ll \frac{n}{2} \tag{105}$$

For a numerical example in Tunnel A, Z_1 = 20", c = 860 to 450 ft/sec., say 600 ft/sec. Therefore,

$$f \ll \frac{n}{2}\left(\frac{600 \times 12}{20}\right) = 180\ n\ \text{cps} \tag{106}$$

The condition (106) validates Eq. (103) for Tunnel "A". In this case, we see the rapid periodicity in the x direction. The value of β^2 varies from 3 to 24 from M = 2 to 5, so one quarter of a wave of the term $\sin \frac{n\pi x}{\beta^2 z_1}$ is defined by

$$x = z_1\beta^2/4n \geq \frac{3z_1}{4n} = \frac{15''}{n} \tag{107}$$

This concludes our theoretical discussion of wind tunnel noise, except to remark that the same factors apply in principle at hypersonic speeds; however, the number of possible mechanisms for generation of initial vorticity and entropy fluctuations at x = 0 are greatly increased due to the greater kinetic energy in the airstream at stagnation temperatures of the order of 1800R.

Tunnel C (Hypersonic Tests at Mach 10)

Figures 27 through 31 also display the conditions for the hypersonic tunnel "C". The hypersonic tests were conducted only at M = 10, at Reynolds numbers of 1 to 2 x 10^6/ft. The stagnation temperatures were 1790 to 1880R, respectively, and the stagnation pressures were 758 and 1650 psia, as seen in Figure 27. Figure 28 shows that the free stream dynamic pressures were 1.14 and 2.45 psi, and the velocities ranged from 4500 to 4600 ft/sec. Figure 29 again shows the overall SPL corrected to a dynamic pressure of 1 psi. The levels are evidently much higher than the flat plate results in Tunnel "A". The values range from 130 to 150 db at various longitudinal positions. It must be remarked that because of the shop work required to install the transducers in their water cooling jackets, it was necessary to recalibrate the transducers for the tunnel C tests. It is believed that the transducer calibration accuracy is within 10 to 15% relative to a "B and K" condenser microphone at a level of 131 db; therefore, the high levels of the clean flat plate tests are considered as indicative of a high wind tunnel noise level due to a combination of upstream turbulence and temperature fluctuations, their interactions with each other and with shock waves generated by the model, and radiated aerodynamic sound from the turbulent boundary layers on the side wall as discussed by Lighthill (Ref. 6). It is believed that temperature effects on the transducer response were unimportant since near the transducers, the model surface temperatures for the most part did not exceed 200 to 300F except the thermocouples at y = 1.13", x = 16" aft of the trailing edge achieved 340F at Re = 2 x 10^6/ft, To = 1875°R (Run 1/ group 19 at α = 0°). The effectiveness of the water cooling can be demonstrated by noting that the surface temperature at x = 16", y = 4" was 630F for the same condition. This is because the surface at the side edge was cooled only by heat conduction through the 1/2" thick upper plate, upon which the transducers were mounted, in the plane of the plate due to the spanwise thermal gradient. It is to be noted that these temperatures are considerably below the adiabatic wall temperature which would be of the order of 1696R for this condition based on a temperature recovery factor of 0.9 at M = 10.13 and T_o = 1875R. Frequent checking of the amplifier gains during the tests showed no evidence of change of voltage output for comparable tunnel pressure levels. This tends to confirm the lack of temperature sensitivity for the temperature range up to 300F (see Figure 8 of Ref. 10, Appendix A of Ref. 11). Anderson (Ref. 10) found that the pyroelectric effect could be suppressed by grounding the charge amplifiers before each run, and this was done faithfully prior to every dynamic data recording run. The charge amplifiers were operated only in the short time constant mode during the tunnel C tests and were drift free. As a result of these considerations, no temperature corrections to the sensitivities of the transducers were necessary in the data reduction procedure, and this is not deemed a reasonable cause for the apparent high SPL's measured in tunnel C on the clean plate configurations. As discussed in connection with Figure 30 and 31, the 20kc cutoff in frequency analysis would cause the RMS Δp due to the very thin turbulent boundary layer on the clean plate to be underestimated by 60% and from Figure 31 the extrapolation of Kistler and Chen data to M = 10 would produce a much lower level of RMS Δp than was apparently measured.

One would again have multiple reflections of supersonic waves due to the presence of wind tunnel (cylindrical) walls having a radius of 25". It is felt that the high background noise level is an exceptional handicap for acoustic testing in tunnel C and that noise and turbulence reduction design modifications should be seriously considered for this facility, although it is recognized that acoustical treatment which is compatible with the aerothermo-dynamic environment would present a formidable challenge for the wind tunnel designer.

It will be seen in the subsequent results that the 60° flap results seem to have an adequate signal to noise ratio because of the extremely intense fluctuations generated; however, the 30° flap results are partly doubtful on these grounds.

RESULTS FOR THE AXISYMMETRIC MODEL

Boundary Layer and Aerothermodynamic Conditions

Measured Static Data

The axisymmetric model provided the flow field for at least three distinct vehicle locations where fluctuating turbulent pressures are of interest.

(1) the wake of the forward flare on the cylindrical body (transducer channels 2, 3 and 4)

(2) the forward face of the aft flare (transducer channel 5)

(3) the base pressure regime (transducer channels 6 and 7)

The obvious length dimensions to use in the non-dimensional correlations of frequency spectra are the protuberance height for channels 2 through 5.

$$h = R_{base} - R_{body}$$

$$= 2 \text{ inches}$$

since

$$R_{base} = 5.75 \text{ inches}$$

$$R_{body} = 3.75 \text{ inches}$$

For the base pressures, the base diameter (11.50") was used in a previous low speed test by Eldred (Ref. 12); another possibility, due to the presence of the sting, ($R_{sting} = 1.06"$) would be

$$\hat{h} = R_{base} - R_{sting} = 4.69 \text{ inches}$$

The question inevitably arises as to how the results of the present tests might be correlated for application to other types of separated flows. Such a correlation could only be possible by finding a length scale derived from the spatial variation of the steady flow field or perhaps a turbulence scale based on velocity fluctuations if one could make simultaneous hot wire anemometer measurements. In the absence of the latter our attention is drawn to the boundary layer displacement and momentum thicknesses defined by (Ref. 5, p. 357).

$$\delta^* = \int_0^\infty \left(1 - \frac{\rho U}{\rho_e U_e}\right) dz \qquad (108)$$

and

$$\theta = \int_0^\infty \frac{\rho U}{\rho_e U_e} \left(1 - \frac{U}{U_e}\right) dz \qquad (109)$$

The values ρ_e and U_e were estimated for the axisymmetric model using the free stream stagnation pressure and the local wall static pressure and making the standard boundary layer assumption that the pressure is constant across the viscous boundary layer. Figure 32 shows the Mach number variation across the boundary layer for zero

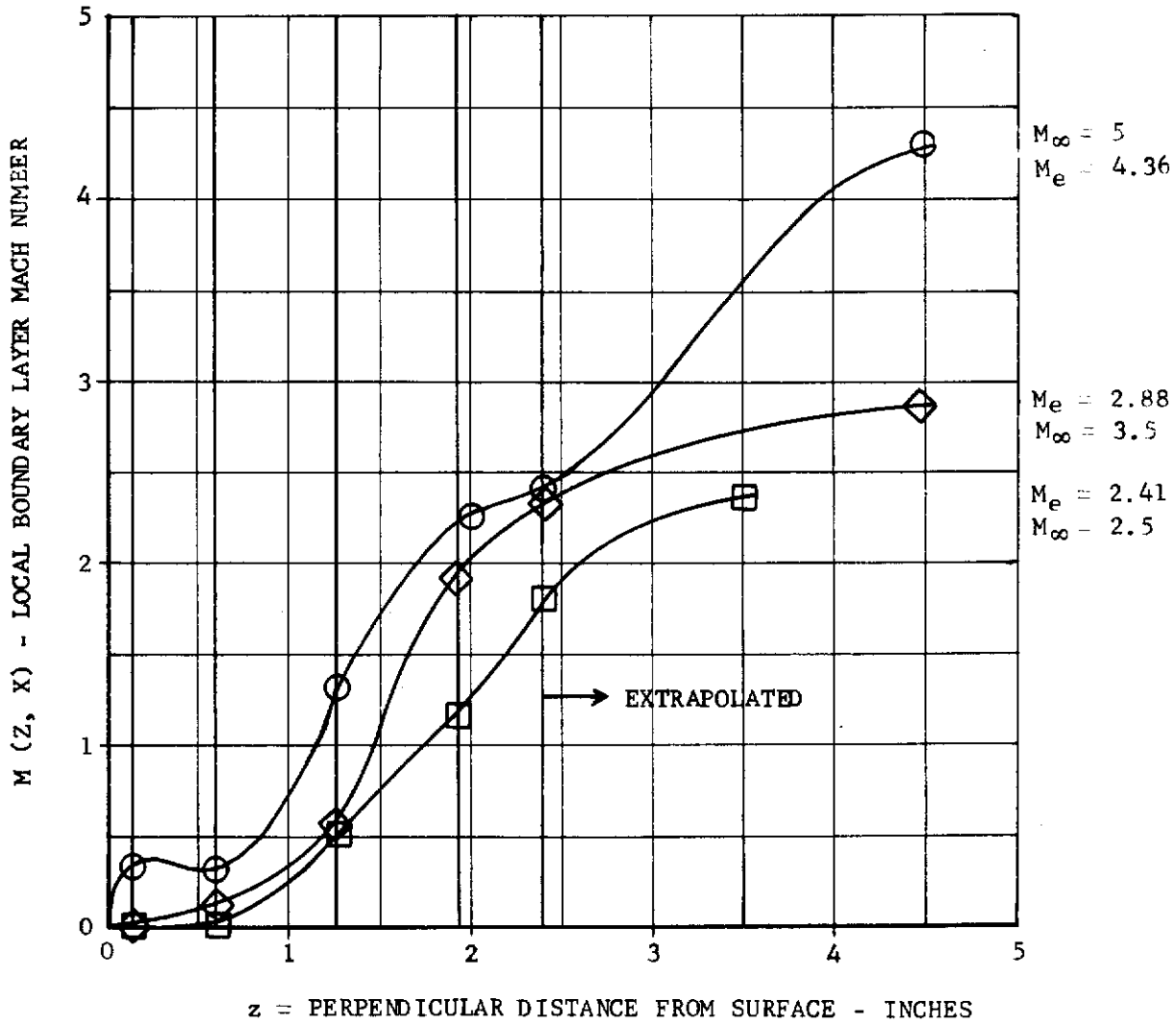

SYM	RUN/Gp	M_∞	R_e/L /FT	α
○	11/65	5	1×10^6	0
◇	10/49	3.5	↓	↓
□	9/40	2.5	↓	↓

FIGURE 32 BOUNDARY LAYER MACH NUMBER PROFILES FOR AXISYMMETRIC MODEL (1)

angle of attack (α =.0), at various Mach numbers for a Reynolds number of 1 x 10^6 ft. Figure 33 shows the density profiles, and Figure 34, the velocity profiles for the same conditions. Figure 35 shows the normalized velocity profile $U(z,x)/U_e(x)$ vs z; Figure 36 shows the normalized density profiles $\rho(z,x)/\rho e(x)$ vs z. Figure 37 shows the boundary layer displacement thickness integrand and Figure 38 shows the momentum thickness integrand. The results are plotted against Mach number in Figure 39. Graphical integration of Figures 37 and 38 was employed to evaluate δ^* and θ for subsequent use in non-dimensional frequency spectrum analyses. The graphical evaluations were only carried out for $\alpha = 0^o$. The values of δ^* so defined are larger than the values calculated by AEDC where $\rho_e U_e$ was replaced by $\rho_\infty U_\infty$ which was smaller due to the compression of the flow field by the body shock wave structure. Also, the numerical integration scheme of Reference 11 did not fully cover the viscous mixing region as can be seen from Figures 35 and 36 where the asymptotic fairing of the normalized velocity and density profiles indicates that viscous boundary layer nominal thickness ($U = .99U_\infty$) varied from 3.7 to 5.0 inches as compared to the protuberance height of 2 inches. The area under the extrapolated regions of Figure 37 and 38 represents the amount by which the numerical scheme of Ref. 11 underestimates δ^*or θ , even if the proper local free stream values ρ_e and U_e were used. In general, the tabulated values from AEDC provide a guide as to the effects of angle of attack, angle of roll, Reynolds number, and Mach number, insofar as the changes in the boundary layer flow manifest themselves within the inner 2.5 inches of the boundary layer; therefore, the ratios of the boundary layer quantities at other conditions to the tabulated values at $\alpha = 0$, Re/L = 1 x 10^6/ft can probably be applied to the values obtained by the graphical procedure, as a first order correction for the errors in the tabulated quantities at other conditions. Because the number of conditions were numerous, no attempt was made to include the boundary layer parameters at other than $\alpha = 0$ and Re/L = 1 x 10^6/ft. Furthermore, it will be seen that the angle of attack effects on the turbulent pressure fluctuations were not serious, amounting to about 6 db at most for channel 3; therefore, it was felt that the effort could be more profitably directed to other effects. The general effect, for example, at M = 3.5 was a decrease in θ and a slight increase in δ^* for α up to 15°. One possible area suggested for future research concerns angle of attack effects beyond $\alpha = 15^o$, where one would expect serious flow separation and strong cross flow effects. This would then justify more careful attention to the angle of attack effects on the boundary layer in order to find suitable parameters for generalizing the data. The large angle of attack studies were excluded from this exploratory test program to avoid the sting changes required to cover the range of angle attack beyond 15°.

Perhaps the most significant feature to note about the boundary layer flow is that it is more nearly described as a wakelike flow which is indeed caused by the separation from the bluff base of the forward flare. Now a very thin inner turbulent boundary layer would develop subsequent to reattachment, perhaps 4 to 8 inches aft of the forward flare. This would then result in an "inner" boundary layer growth length of about 8 to 12 inches between the reattachment point at the forward most transducer of the three on the cylindrical after body. This inner boundary layer would not exceed .12 inch and would have measurable influence only on the innermost tube of the boundary layer survey rake. We can probably expect a general behavior in the region forward of the aft flare like that ahead of a forward facing step such as was examined by Kistler (Ref. 13), although his value of h/δ was 1.33 at Re δ = 5 x 10^5 at M_∞ = 3.01 and 4.54. Kistler showed similar static pressure distributions to those measured by Bogdonoff (Ref. 14) and Chapman, Kuehn, and Larson (Ref. 15). The principle difference with the present flow ahead of the aft flare is that our value of h/δ varies from 0.40 to 0.54; thus, the protuberance due to the aft flare is submerged in the low energy boundary layer air. From Figure 32, one sees that for z less than 2 inches, that the boundary layer is almost entirely subsonic at M_∞ = 2.5 and is subsonic out to z = 1.1

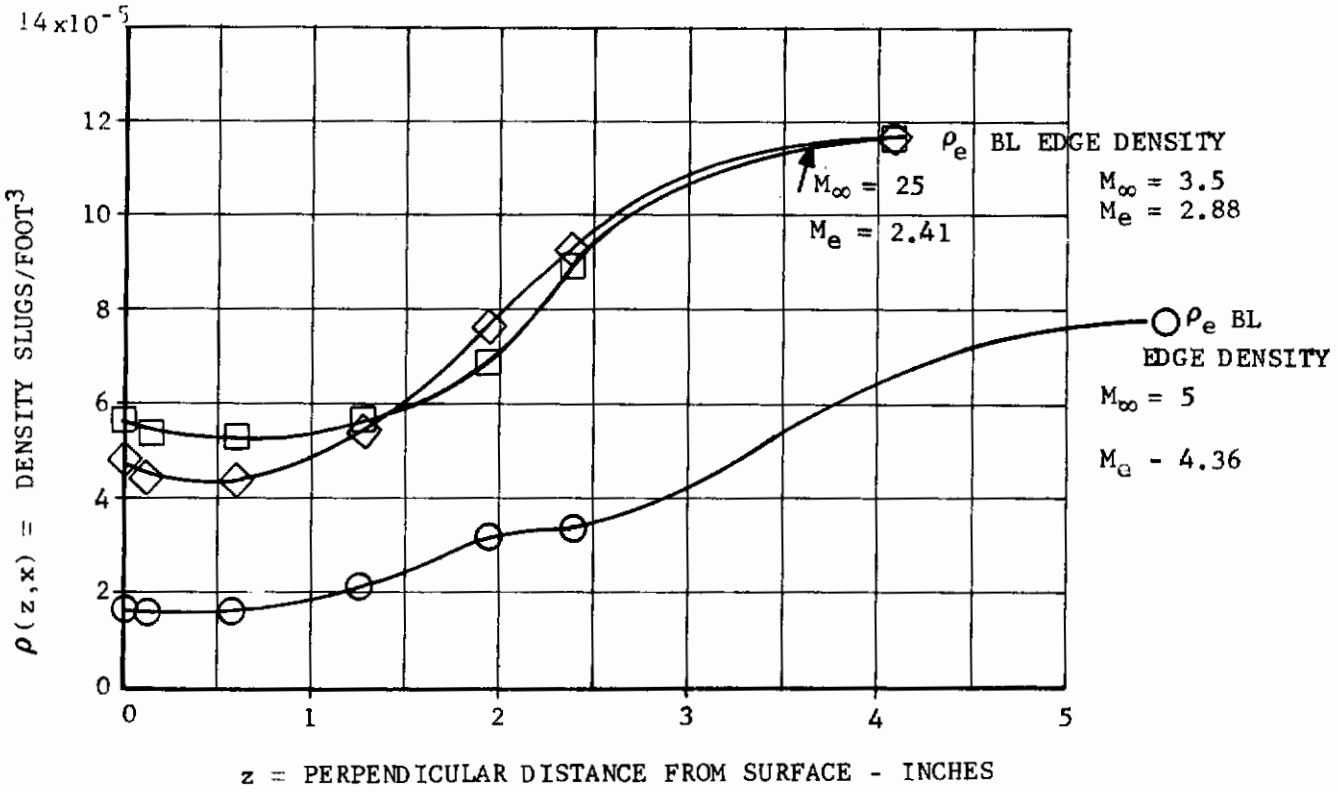

SYM	RUN/Gp	M_∞	R_e/L /FT	α	M_e
○	11/65	5	$1x10^6$	0	4.36
◇	10/49	3.5	↓	↓	2.88
□	9/40	2.5	↓	↓	2.41

FIGURE 33 DENSITY PROFILE IN BOUNDARY LAYER, AXISYMMETRIC MODEL

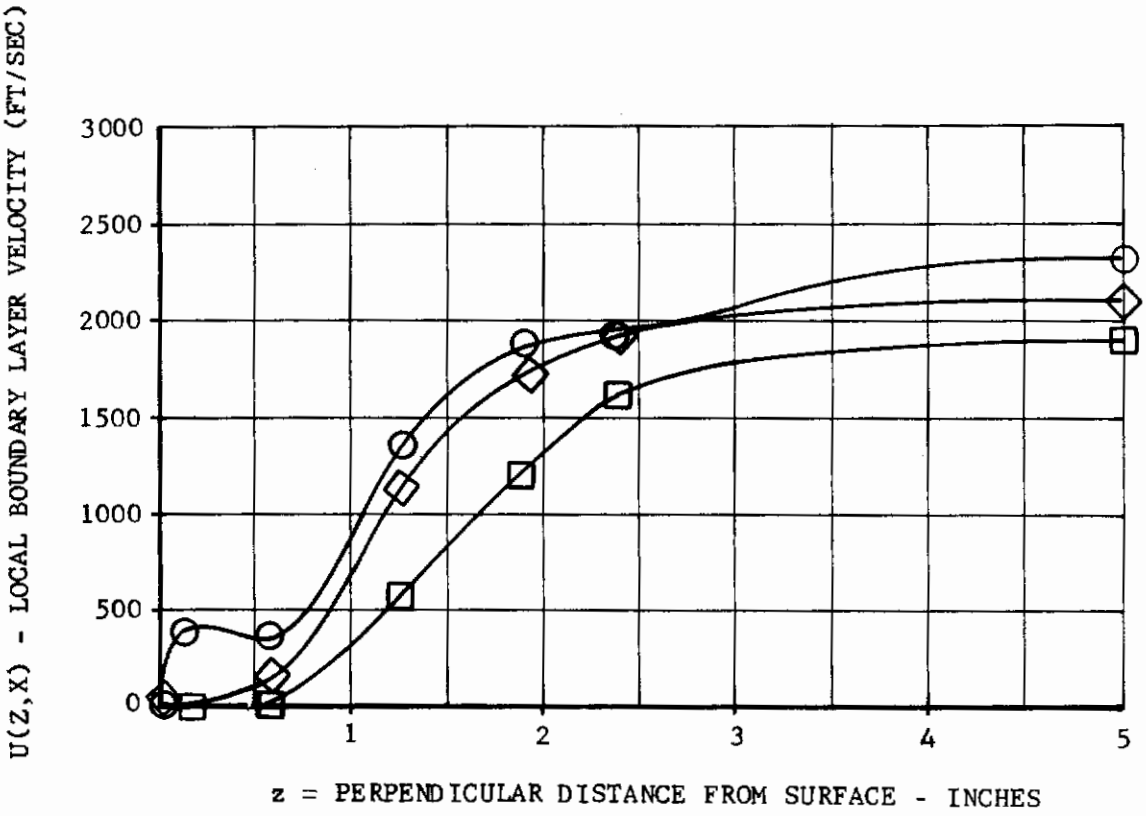

SYM	RUN/Gp	M_∞	R_e/L /FT	α	M_e
○	11/65	5	1×10^6	0	4.36
◇	10/49	3.5	↓	↓	2.88
□	9/40	2.5	↓	↓	2.41

FIGURE 34 VELOCITY PROFILE IN BOUNDARY LAYER, AXISYMMETRIC MODEL

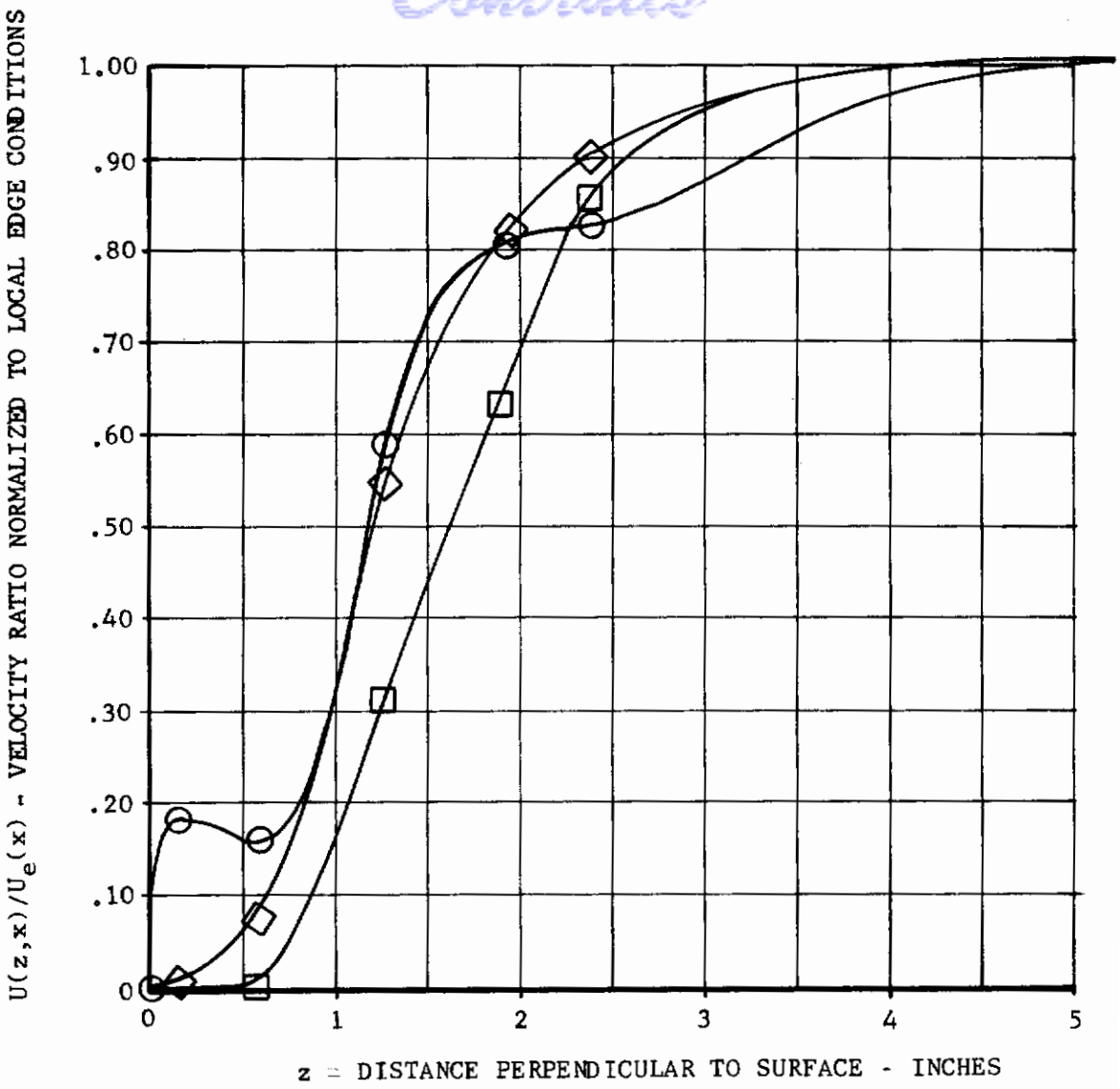

SYM	RUN/Gp	M_∞	R_e/L /FT	α	M_e	U_e FT/SEC
○	11/65	5	1×10^6	0	4.36	2310
◇	10/49	3.5	↓	↓	2.88	2100
□	9/40	2.5	↓	↓	2.41	1892

FIGURE 35 NORMALIZED VELOCITY PROFILE IN BOUNDARY LAYER, AXISYMMETRIC MODEL

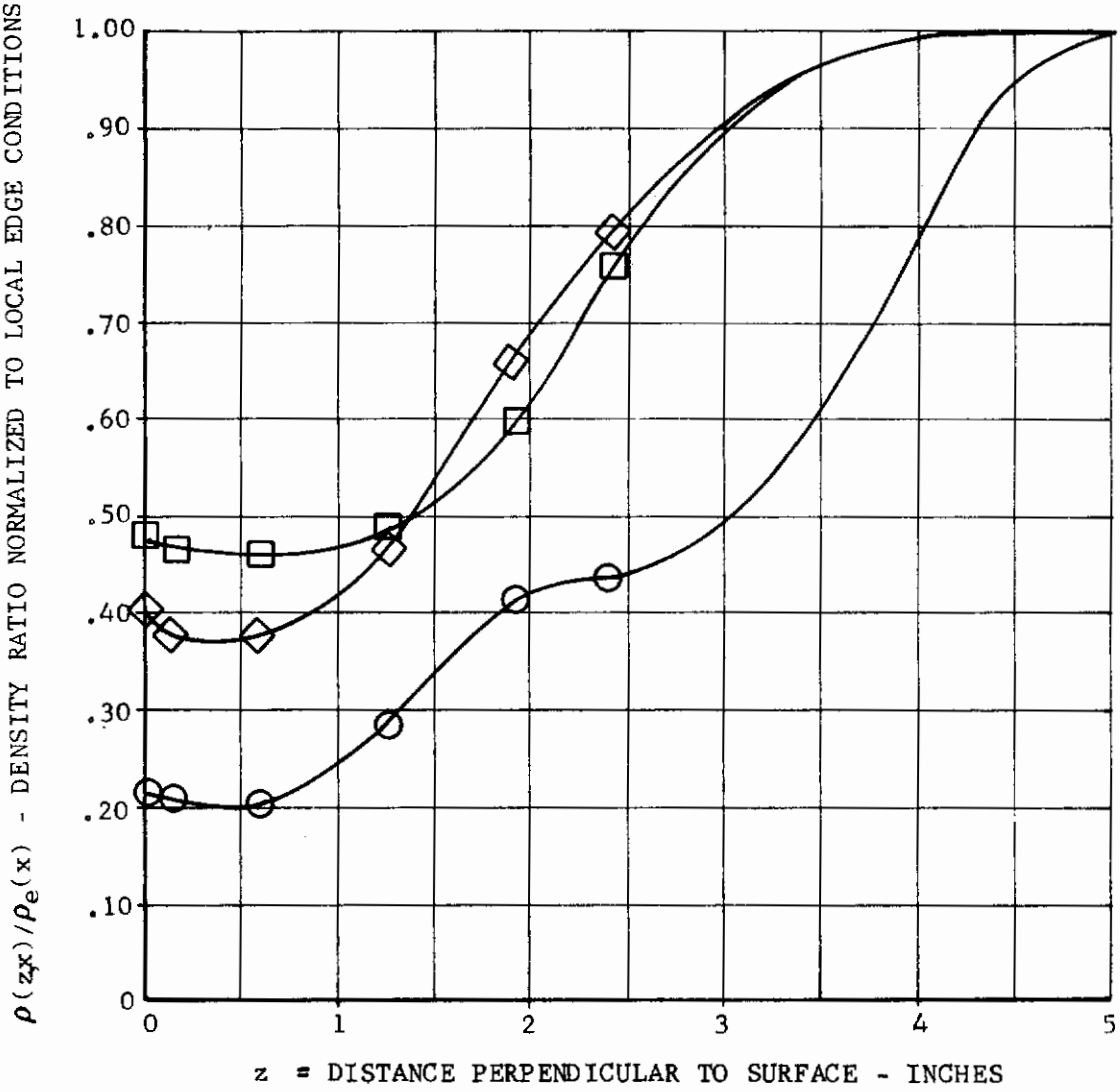

SYM	RUN/Gp	M_∞	R_e/L /FT	α	M_e	ρ_e SLUG/FT^3	U_e FT/SEC
○	11/65	5	1×10^6	0	4.36	7.75×10^{-5}	2310
◇	10/49	3.5	↓	↓	2.88	11.74	2100
□	9/40	2.5	↓	↓	2.41	11.74	1892

FIGURE 36 NORMALIZED DENSITY PROFILE IN BOUNDARY LAYER, AXISYMMETRIC MODEL

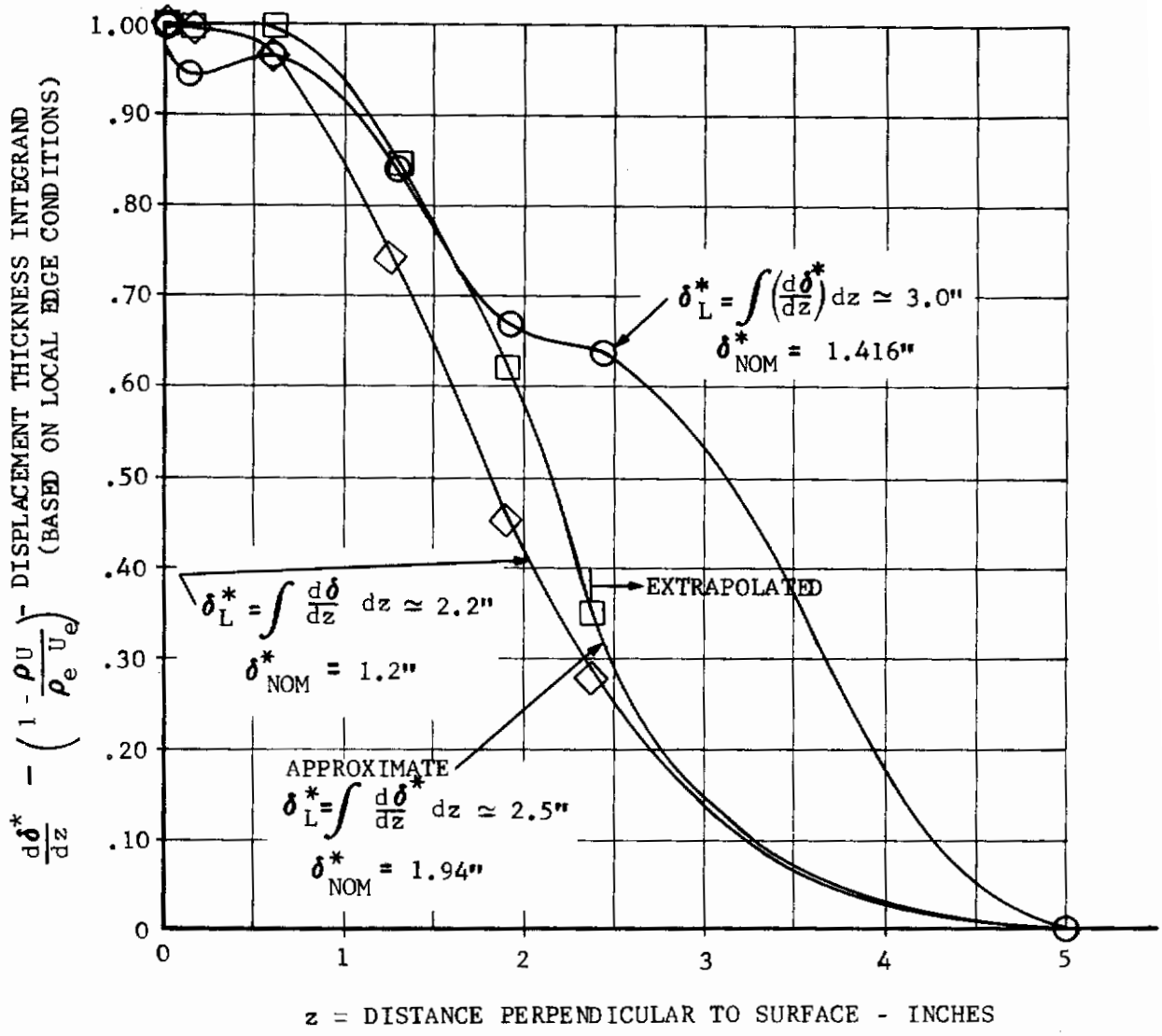

SYM	RUN/Gp	M_∞	R_e/L /FT	α	δ^*_L"	δ^*_{NOM}"	M_e
○	11/65	5	$1x10^6$	0	3.2	1.4	4.36
◇	10/49	3.5	↓	↓	2.2	1.2	2.88
□	9/40	2.5	↓	↓	2.5	1.94	2.41

FIGURE 37 DISPLACEMENT THICKNESS INTEGRAND AXISYMMETRIC MODEL

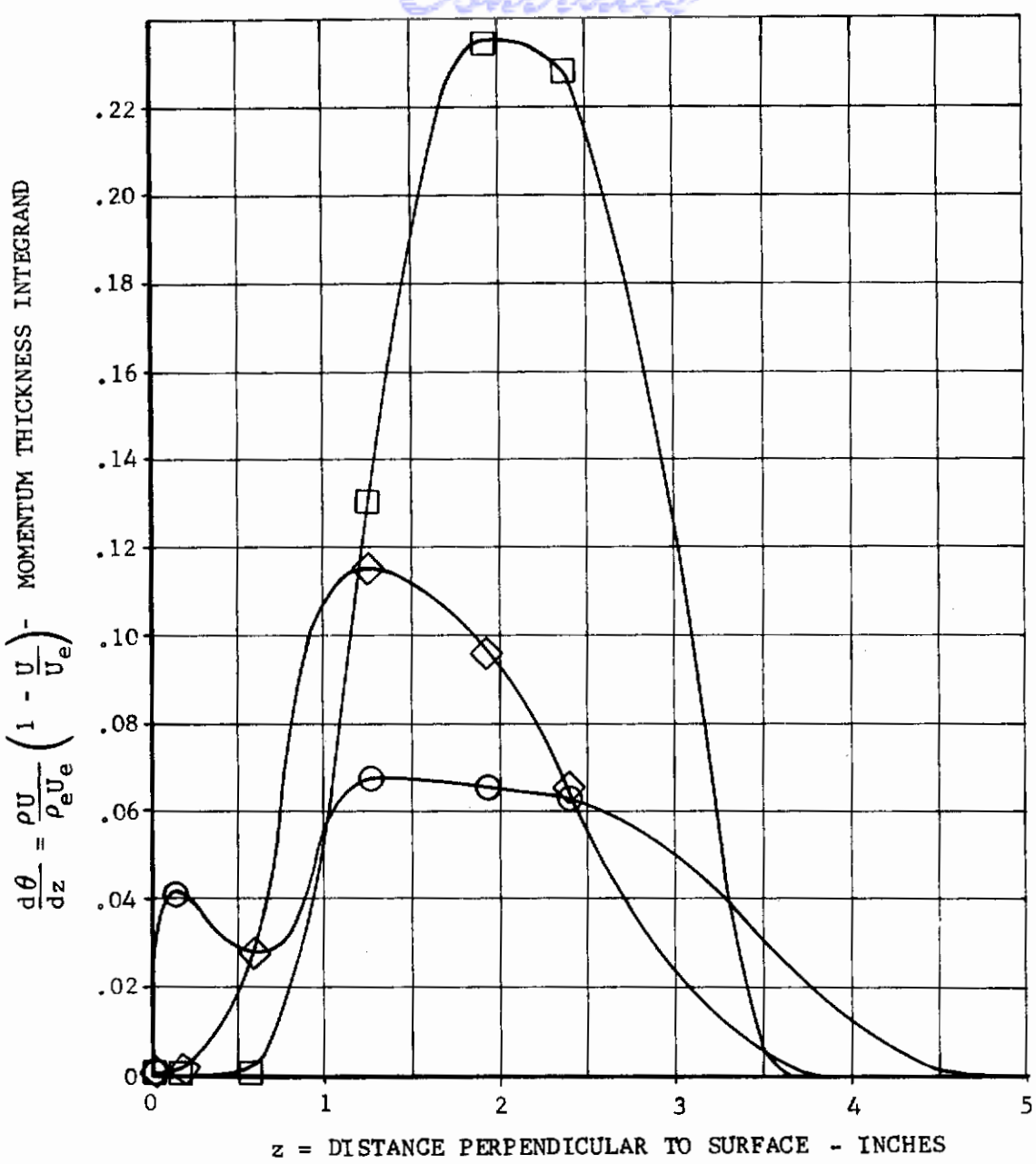

SYM	RUN/Gp	M_∞	R_e/L /FT	α	M_e	θ_{TRUE}	θ_{NOM}
○	11/65	5	1×10^6	0	4.36	.18	.39
◇	10/49	3.5	↓	↓	2.88	.22	.36
□	9/40	2.5	↓	↓	2.44	.44	.20

FIGURE 38 MOMENTUM THICKNESS INTEGRAND AXISYMMETRIC MODEL

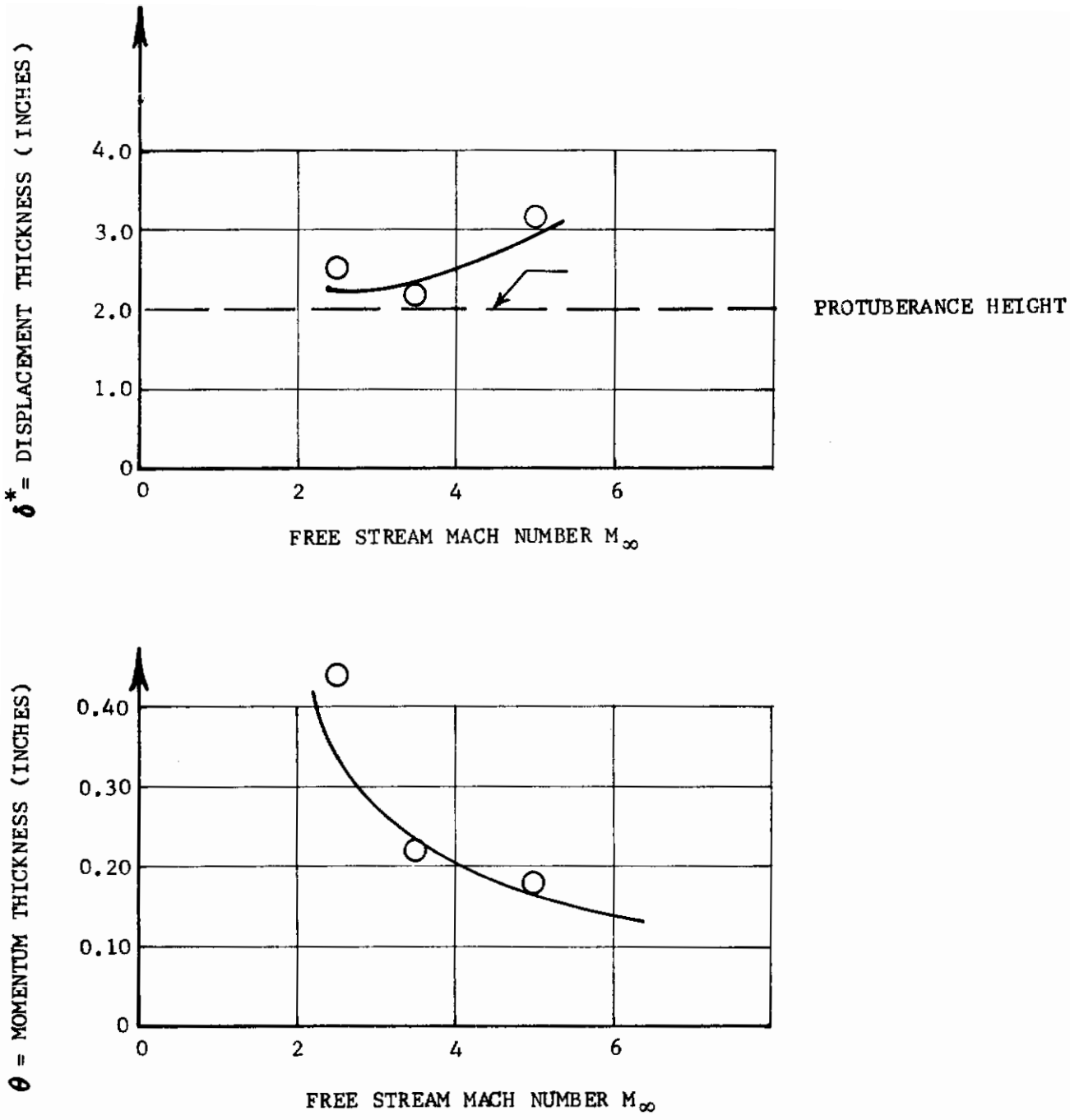

FIGURE 39 DISPLACEMENT THICKNESS AND MOMENTUM THICKNESS VS. MACH NUMBER AXISYMMETRIC MODEL (BASED ON GRAPHICAL INTEGRATION AND LOCAL BOUNDARY LAYER EDGE CONDITIONS)

inches even when $M_\infty = 5.0$. Therefore, the supersonic oblique shock turning mechanisms which pertain to the situation where $h/\delta > 1$ (Refs. 13, 14 and 15) apply only to the extreme outer portion of the free shock separated turbulent boundary layer in the present case. Since the amount of external oblique shock turning is less, and since there is more opportunity for the pressure rise to be signaled upstream through the subsonic part of the wake from the forward flare, we would expect a less severe shock induced separation (in this case, a thickening of the already separated wake) than was found in Kistlers' case where he found a continuously increasing value of RMS Δp, approaching 20 times the clean turbulent boundary layer values ahead of the shock interaction region. In our case, as will be seen below, the increase of RMS Δp is not so large, being only slight at $M_\infty = 5$ as one proceeds from transducer no. 2 to transducer no. 4. Transducer no. 5 on the forward face of the aft flare does show magnitudes higher by a factor of 4 to 5, compared with transducer no. 4 (see Figure 40). However, as was previously noted from Figures 29 and 31, there is some doubt concerning the data from channel 5 by perhaps 6 db, or 2:1 in RMS Δp. Applying this 6 db correction to Figure 40, the values of RMS $\Delta p/q_\infty$ on the flare would be about .04 at $M_\infty = 5$ compared to .006 for a clean plate according to Figure 31; this amounts to an increase of slightly more than 6 fold in contrast to the 20:1 factor which Kistler found when a thin boundary layer approaches a forward facing step. This supports the above contention that the interaction of the thick boundary layer with a sudden step is less severe than is the case with a thin boundary layer, free shock-induced separation.

We shall now consider the other static aerothermodynamic data derived from the surface static pressures before discussing the dynamic data further. Figure 40 shows the static pressure coefficient, the local free stream dynamic pressure and the local boundary layer edge Mach number. These quantities are based on assuming the local stagnation pressure, P_{te}, is equal to the free stream stagnation pressure, P_o, and assuming again the local wall static pressure $P_W(x)$ equals the boundary layer, P_e, and defining M_e based on this ratio. Figure 40 shows the lengthwise distributions with M_∞ as a parameter for $\alpha = 0$ and $Re/L = 1 \times 10^6$/ft. One can see that the pressure gradient is adverse positive approaching a stagnation point at the aft flare, which, as is well known, causes thickening of the boundary layer (Ref. 5, p. 341). One can also observe that the local values of q_e are higher in the compressed region ahead of the aft flare. This would imply higher density and Reynolds stresses and consequently, higher turbulent pressures, though the pressures depend on an integral over the entire volume of turbulence enclosed by the Mach forecone upstream of the point. (Recall the discussion of Section II.) Figures 41, 42 and 43 display Reynolds number effects on the static pressure distribution, local Mach number, and dynamic pressure at free stream Mach numbers of 5.0, 3.5 and 2.5. Evidently, the thinner boundary layers at the 6×10^6/ft. Reynolds numbers causes more sharply defined compression and expansion processes which are usually predicted from inviscid fluid theory for bodies having discontinuities. This effect appears most strongly at Mach numbers of 3.5 and 5.0. Figures 44, 45 and 46 show the angle of attack effects on the static pressure, local Mach number and local dynamic pressure. These effects show the expected flow expansion on the lee side of the body resulting in more negative pressures, higher Mach numbers and lower dynamic pressures with increasing angle of attack. It is interesting that the effect of α on static pressure is strong at $M_\infty = 5$ but only slight at $M_\infty = 3.5$ and 2.5 in the region just ahead of the aft flare, while the ratio of $(\Delta p)_{rms}/q_\infty$ at $\alpha = 14.7^\circ$ to $(\Delta p)_{rms}/q_\infty$ at $\alpha = 0$ is about 2:1 for all three Mach numbers. This increase might be explained in part by the incompressible angle of attack theory described in Section II.

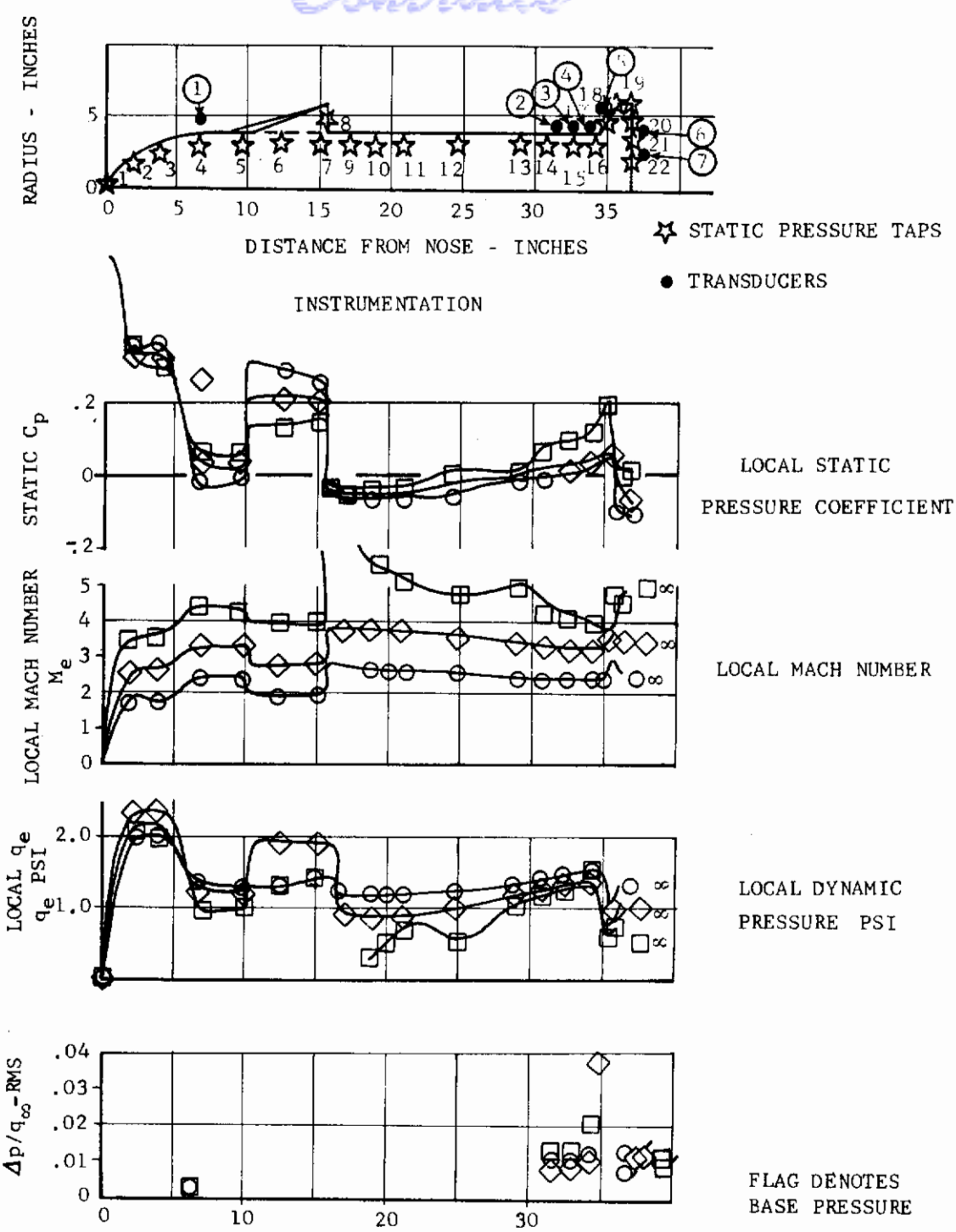

SYM	RUN/Gp	M_∞	R_e/L /FT	α	P_o PSIA	T_o ^oR	q_∞ PSI
○	4/12	2.48	$1x10^6$	0	5.35	550	9.39
◇	5/22	3.48	↓	↓	9.58	582	1.096
□	3/3	4.98	↓	↓	18.22	560	0.612

FIGURE 40 MACH NUMBER COMPARISON AT $\alpha = 0^o$ $R_e/L = 1x10^6$/FT. AXISYMMETRIC MODEL

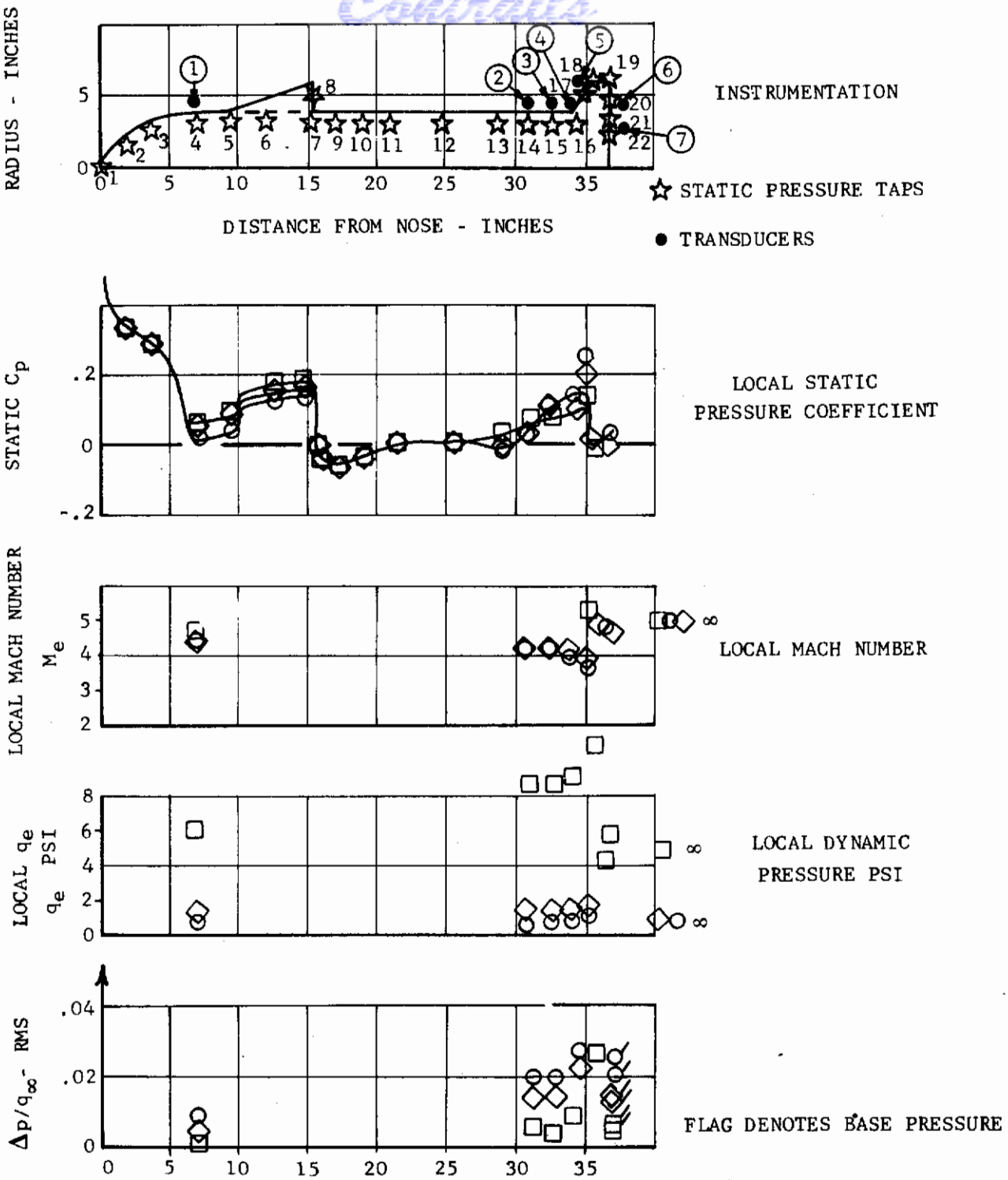

SYM	RUN/Gp	M_∞	R_e/L /FT	α	P_o PSIA	T_o ^oR	q_∞ PSI
○	3/1	5.0	$.6 \times 10^6$	0	11.3	563	.328
◇	3/3	↓	1×10^6	↓	18.22	560	.612
□	3/9	↓	6×10^6	↓	150.9	634	4.88

FIGURE 41 REYNOLDS NUMBER COMPARISON AT $M_\infty = 5.0$, $\alpha = 0$
AXISYMMETRIC MODEL

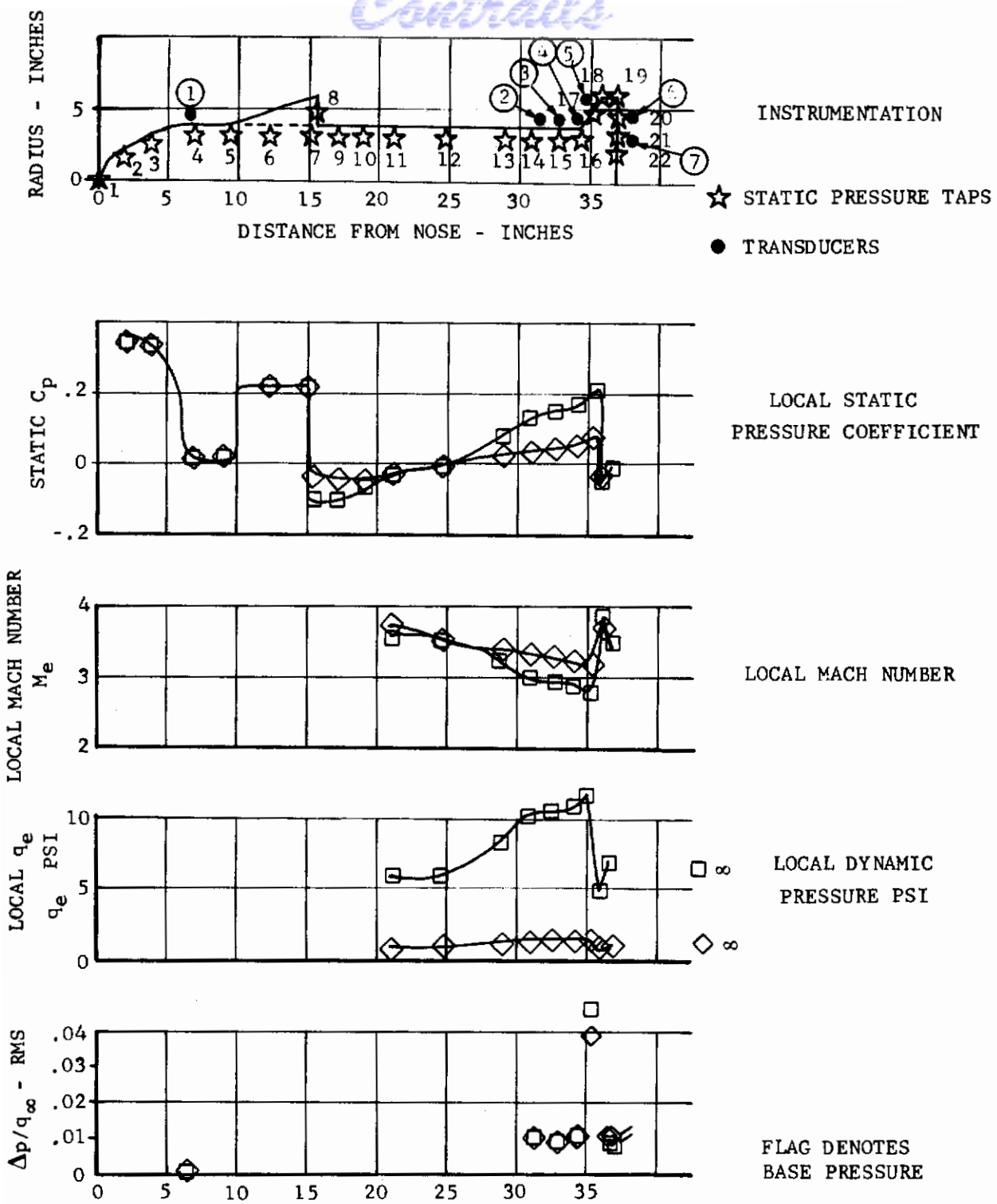

SYM	RUN/Gp	M_∞	R_e/L /FT	α	P_o PSIA	T_o ^oR	q_∞ PSI
◇	5/22	3.5	$1x10^6$	0	9.58	582	1.096
□	5/18	↓	$6x10^6$	↓	56.75	↓	6.38

FIGURE 42 REYNOLDS NUMBER COMPARISON AT $M_\infty = 3.5$, $\alpha = 0$
AXISYMMETRIC MODEL

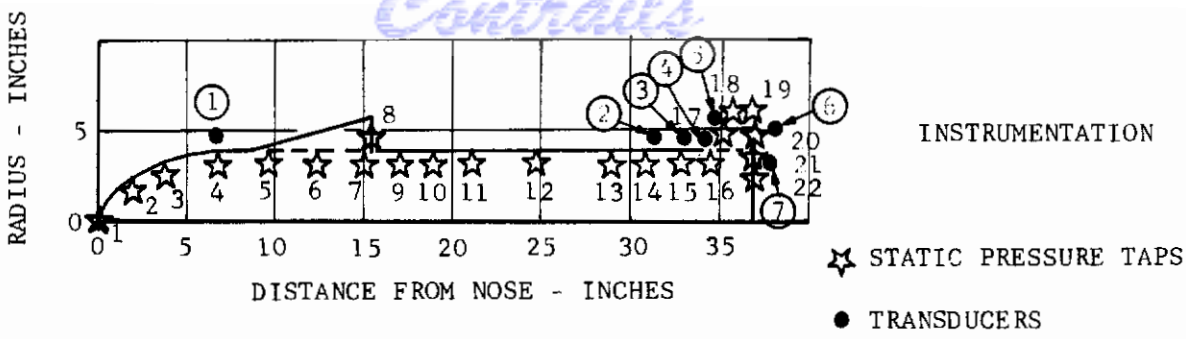

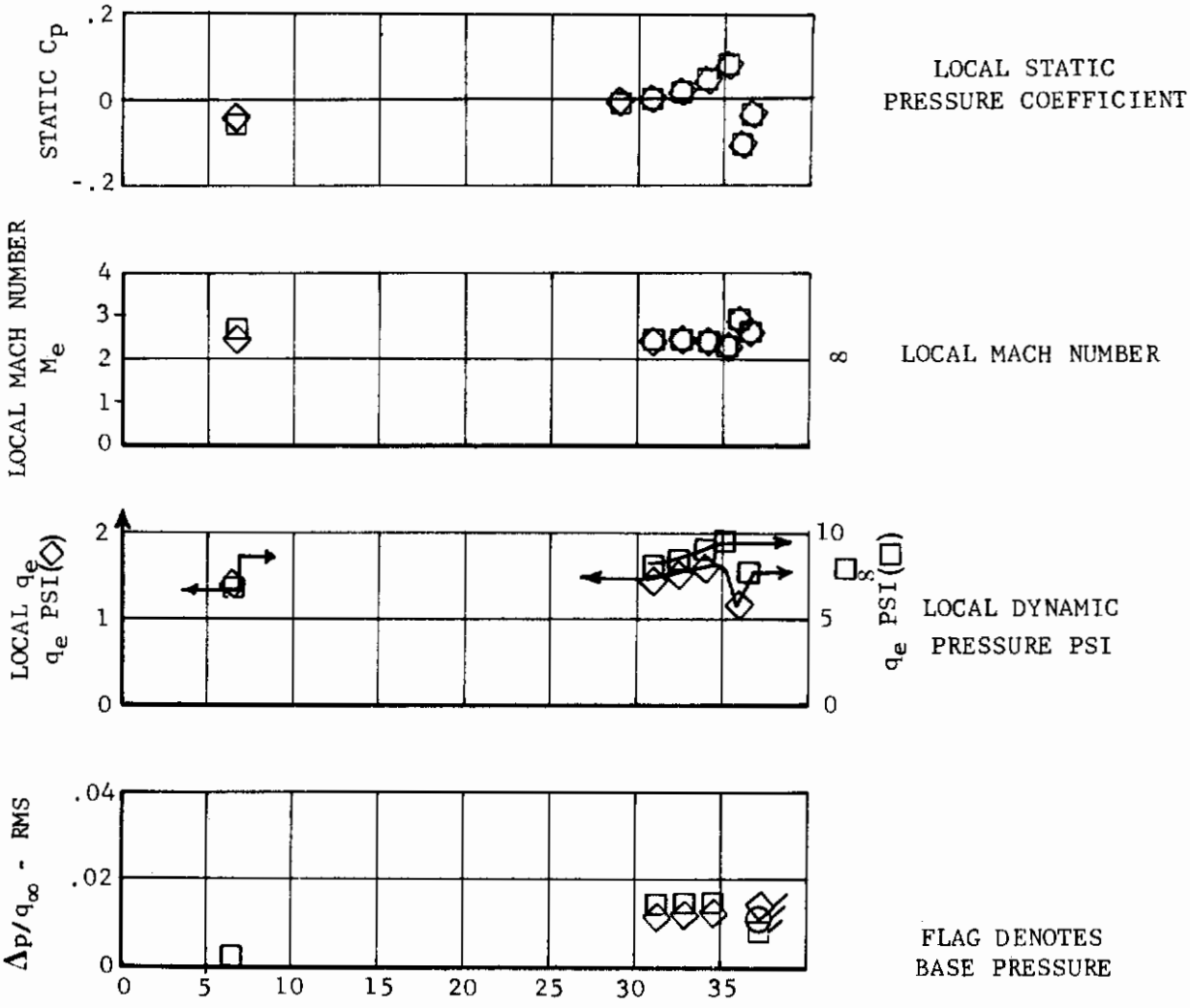

SYM	RUN/Gp	M_∞	R_e/L /FT	α	P_o PSIA	T_o °R	q_∞ PSI
◇	4/12	25	1×10^6	0	5.35	550	1.39
□	4/11	↓	6×10^6	↓	31.78	555	8.20

FIGURE 43 REYNOLDS NUMBER COMPARISON AT $M_\infty = 2.5$, $\alpha = 0$
AXISYMMETRIC MODEL

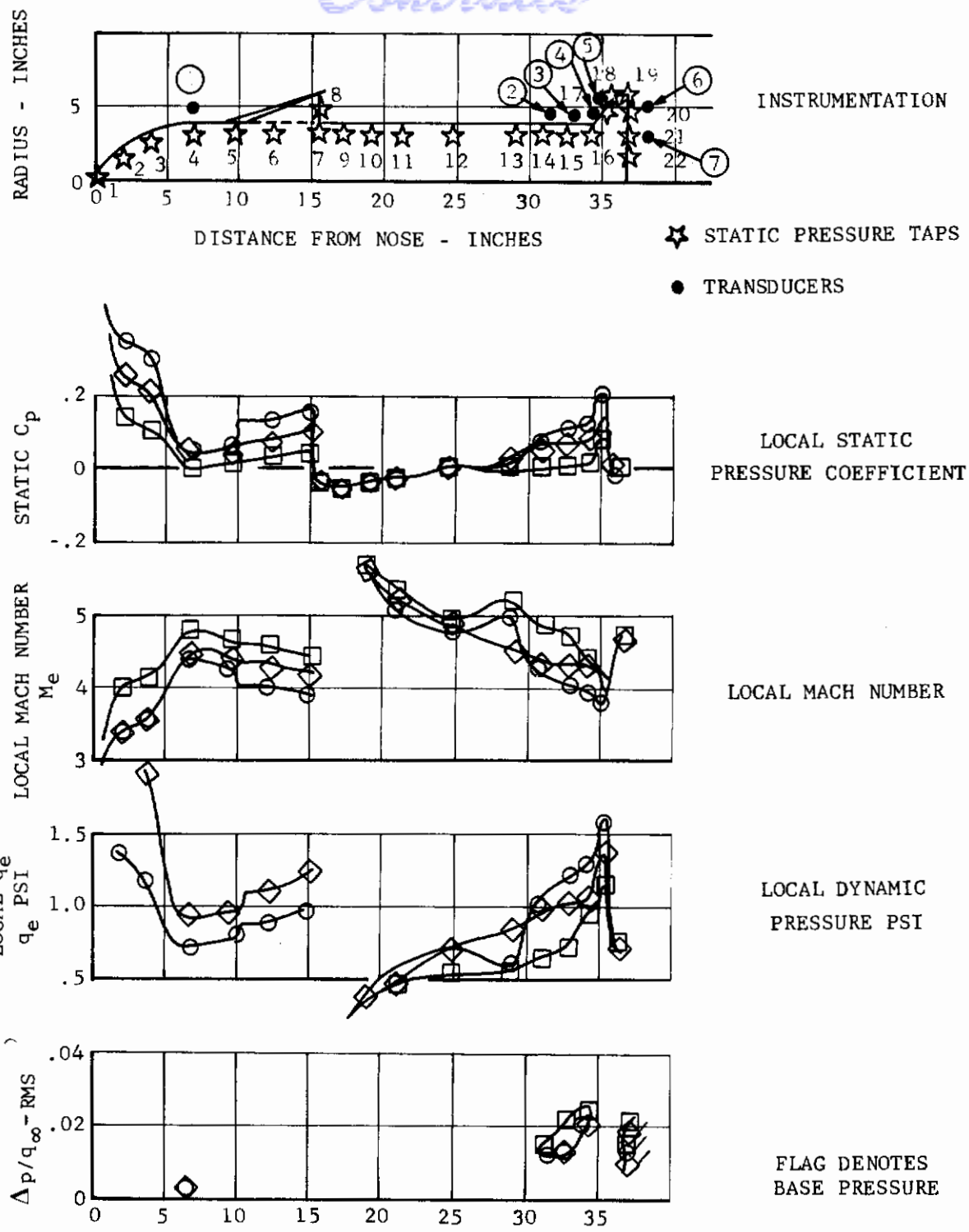

SYM	RUN/Gp	M_∞	R_e/L /FT	α	P_o PSIA	T_o °R	q_∞ PSI
○	3/3	4.98	1×10^6	0	18.22	563	.612
◇	3/5	↓	↓	5.0	18.24	559	.613
□	3/6	↓	↓	14.63	18.33	559	.6156

FIGURE 44 ANGLE OF ATTACK COMPARISON AT $M_\infty = 5.0$, $R_e/L = 1\times10^6$/FT. AXISYMMETRIC MODEL

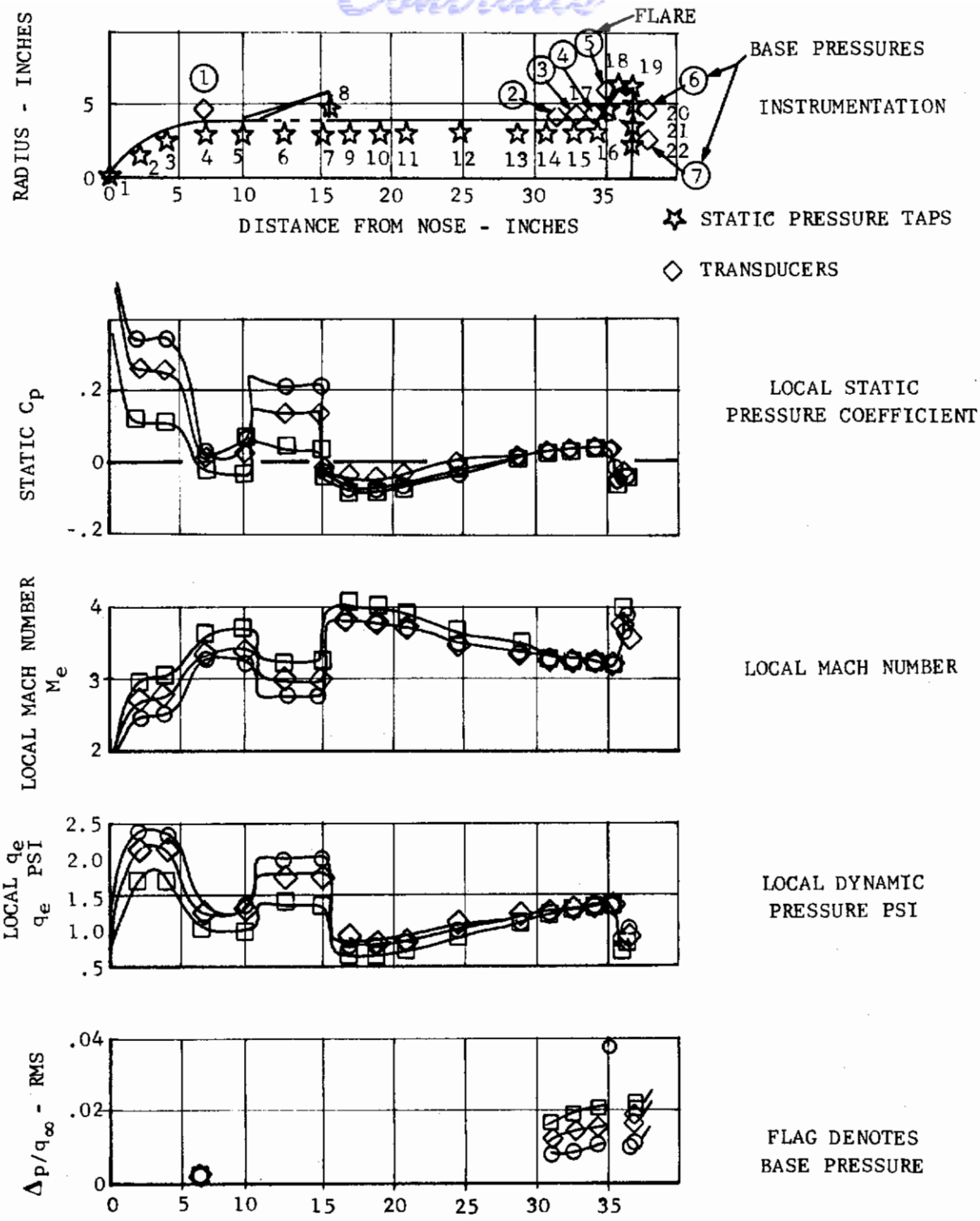

SYM	RUN/Gp	M_∞	R_e/L /FT	α	P_o PSIA	T_o ^oR	q_∞ PSI
○	5/22	3.48	$1x10^6$	0	9.58	582	1.096
◇	5/23	↓	↓	5.03	9.63	↓	1.102
□	5/24	↓	↓	14.62	9.66	↓	1.105

FIGURE 45 ANGLE OF ATTACK COMPARISON AT $M_\infty = 3.5$, $R_e/L = 1x10^6$/FT. AXISYMMETRIC MODEL

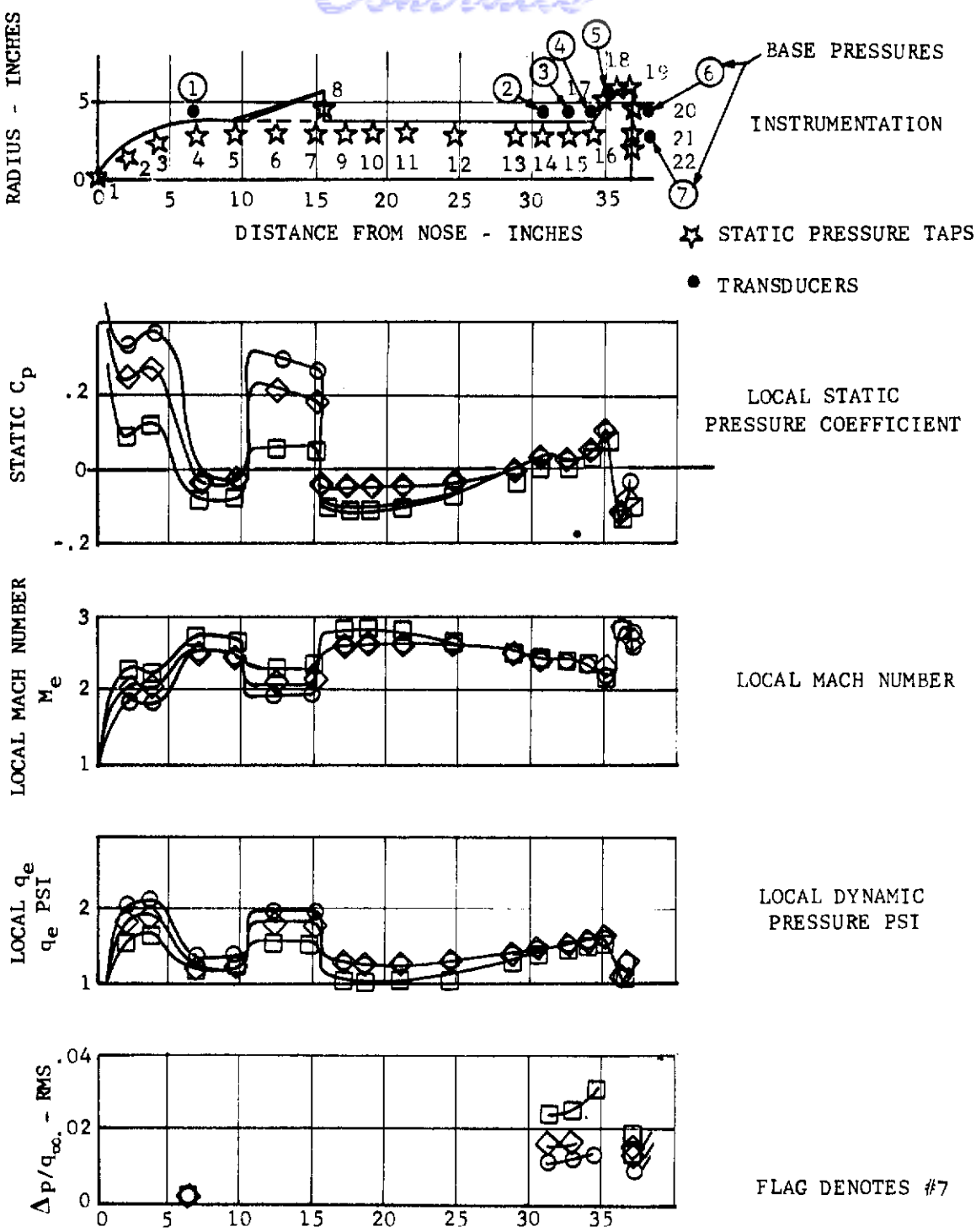

SYM	RUN/Gp	M_∞	R_e/L /FT	α	P_o PSIA	T_o ^oR	q_∞ PSI
○	4/12	2.48	$1x10^6$	0	5.35	550	1.392
◇	4/13	↓	↓	5.03	5.34	550	1.389
□	4/14	↓	↓	14.05	5.32	551	1.383

FIGURE 46 ANGLE OF ATTACK COMPARISON AT $M_\infty = 2.5$ $R_e/L = 1x10^6$ FT. AXISYMMETRIC MODEL

The static base pressure coefficients are rather weak functions of α up to 15°.

Visual Data; Schlieren Photographs

Figures 47 to 55 show Schlieren photographs of the axisymmetric configuration at zero angle of attack. It was from such visual evidence of shock reflection on the model that tests at $M_\infty = 2$ were precluded (see Figure 47) for the long axisymmetric model. Figures 48 to 55 show the effects of Reynolds number on the flow structure at $M_\infty = 2.5$, 3.5 and 5.0 respectively. The Schlieren process shows illumination intensity proportional to density gradient (Ref. 4) and is used primarily to show the qualitative flow features. The shock wave structure being characterized by steep gradients of density is clearly illustrated in almost all the pictures. The better pictures also show the boundary layer since there is a considerable decrease in density near the wall as one approaches the wall as has been already shown in Figure 14. In some cases, turbulent wake density fluctuations can be seen particularly at the higher pressure levels. The thickening of the thin boundary layer due to the 20° conical forward flare oblique shock is evident in most cases, as well as the weaker detached waves ahead of the aft flare, probably due to the relatively low Mach numbers prevailing in the wake of the forward flare as discussed previously.

RMS Pressure Fluctuation and Overall SPL

Forward Flare Wake and Aft Flare Face at Zero Angle of Attack

The basic data in the form of 1/3 octave and overall SPL's are given in the Appendix. For convenience, the overall SPL's have been converted to $\Delta p_{RMS}/q_\infty$ and plotted vs. distance along the model together with the static pressure coefficients (Cp), the local dynamic pressure, and local Mach number in Figures 40 to 46. The effects of Mach number at $R_e/L = 1 \times 10^6$/ft., $\alpha = 0$ (Figure 40) are not great except for transducer channel 4 just ahead of the aft flare showing a factor of 2 at $M_\infty = 5$ compared to values at $M_\infty = 2.5$ and 3.5. The high values measured on the flare by transducer channel 5 are considered high by a factor of approximately 2 as discussed previously in connection with tunnel background noise measurements on the flat plate. Figures 42 and 43 show that $\Delta p/q_\infty$ is essentially independent of Reynolds number at $\alpha = 0$ and $M_\infty = 3.5$ and 2.5 for R_e/L from 1×10^6/ft. to 6×10^6/ft. At $M_\infty = 5$ we find an apparent factor of 3 for $R_e/L = 0.6 \times 10^6$/ft compared with $Re/L = 6 \times 10$/ft. However, the RMS Δp was only of the order of .0016 psi at $Re/L = 0.6 \times 10^6$/ft., and the adequacy of the signal to noise ratio is considered as doubtful.

Base Pressure Fluctuations at Zero Angle of Attack

Transducer Channels 6 and 7 and the symbols plotted at the aft end of the model in Figures 40 through 46 represent base pressure fluctuations at $r/r_b = .825$ and .457 respectively. In general, the overall levels of the outer transducer were 1 to 3 db higher than the inner transducer. The values of RMS $\Delta p/q_\infty$ varied from .005 at $M_\infty = 5.0$ $Re/L = 6 \times 10^6$/ft to .025 at $M_\infty = 5.0$, $Re/L = 0.6 \times 10^6$/ft (Figure 41). Figure 40 shows that at $Re/L = 1 \times 10^6$/ft, $\alpha = 0$, that an average value of RMS $\Delta p/q$ is about .012 for $M_\infty = 2.5$, 3.5 or 5.0. This value approximates the results at high Reynolds number (6×10^6/ft) at $M_\infty = 3.5$ and 2.5 also, according to Figures 42 and 43.

Angle of Attack Effects at $Re/L = 1 \times 10^6$/ft

Forward Flare Wake and Aft Flare Face

Figures 44, 45 and 46 show the dependence upon angle of attack up to 14.7° of the RMS $\Delta p/q_\infty$ at $Re/L = 1 \times 10^6$/ft. for Mach numbers of 5.0, 3.5 and 2.5 respec-

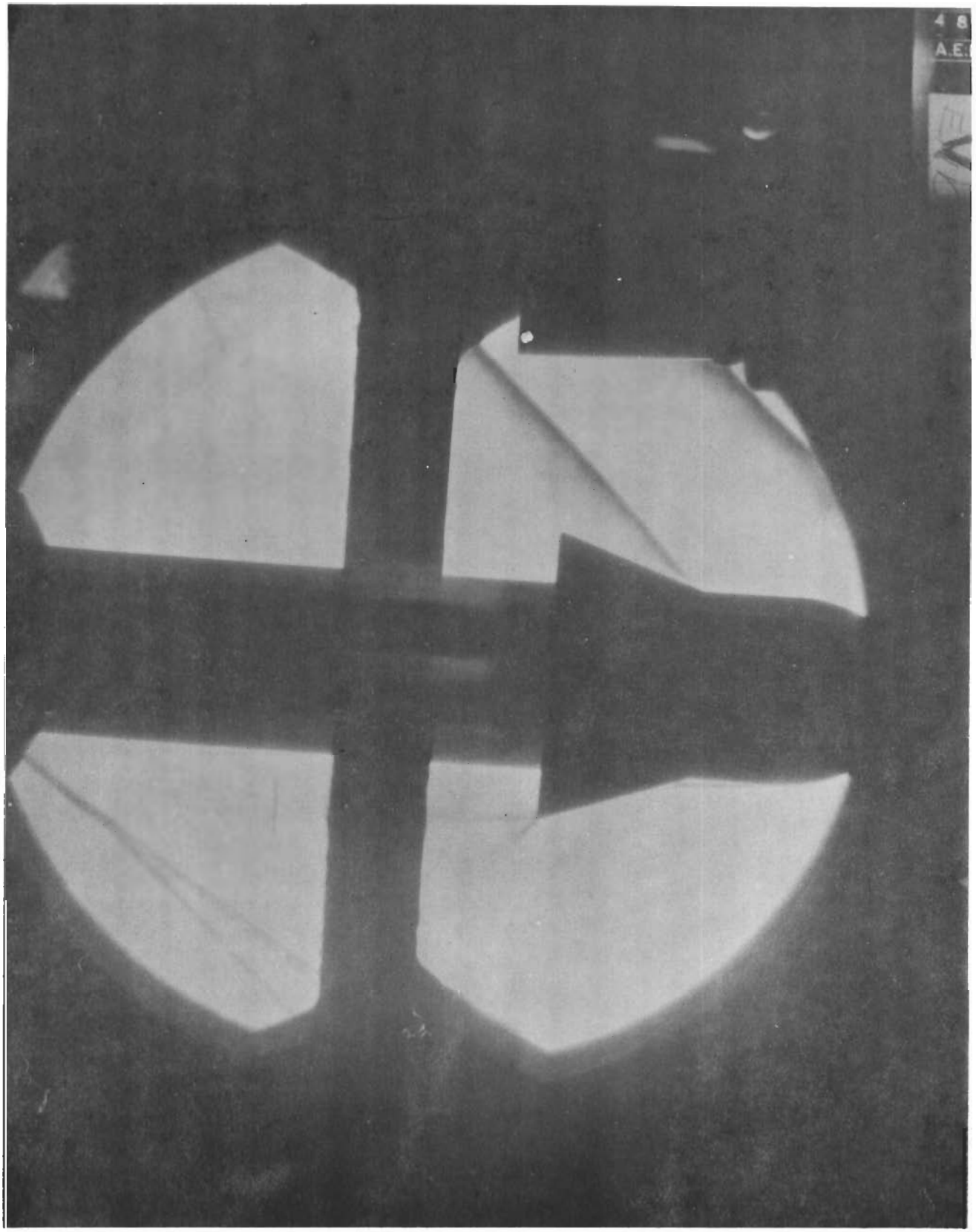

FIGURE 47 AXISYMMETRIC MODEL. M = 2. $\alpha = \phi = 0$

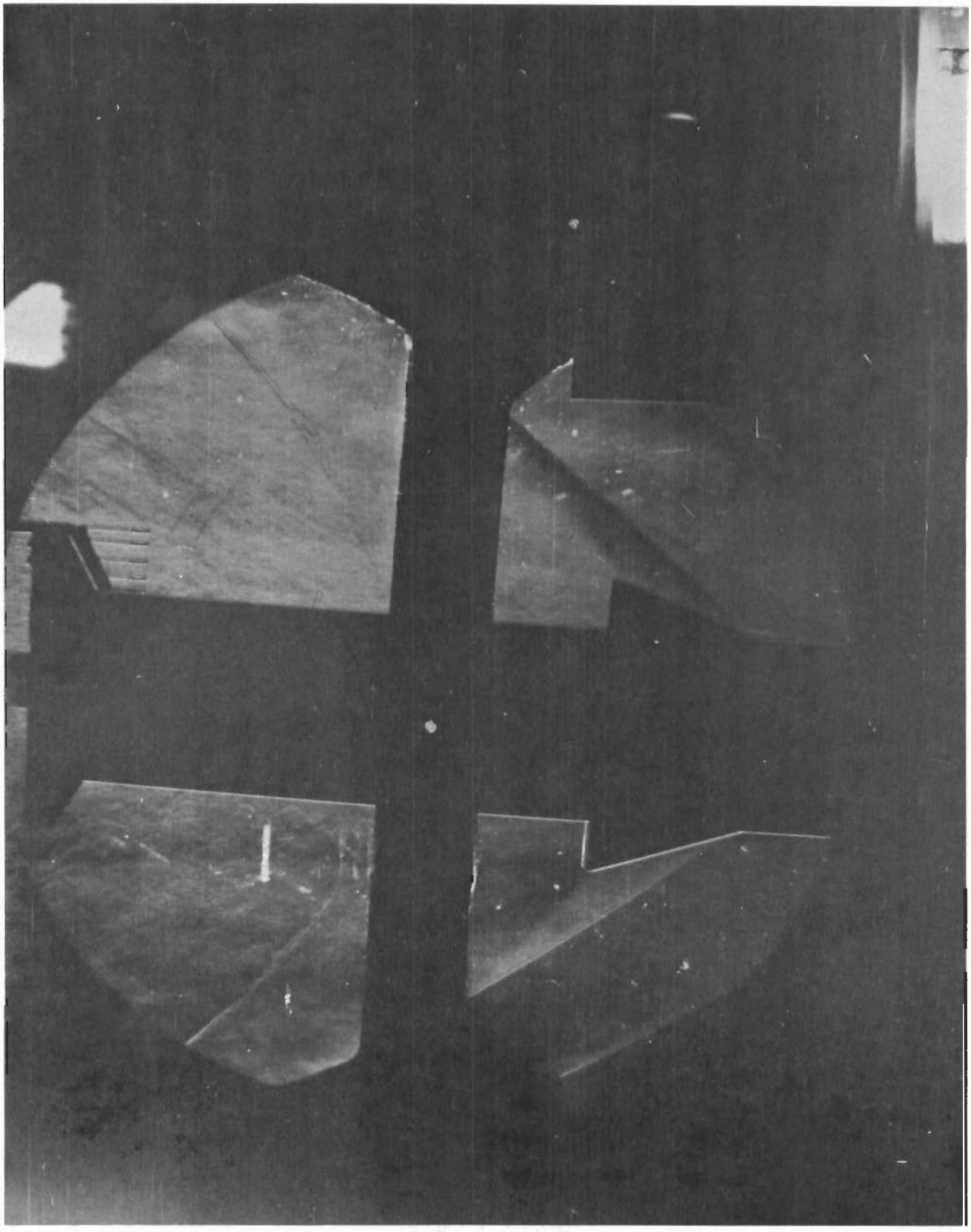

FIGURE 48 AXISYMMETRIC MODEL. $M = 2.5$ $\alpha = \phi = 0$. $P_o = 3.5$

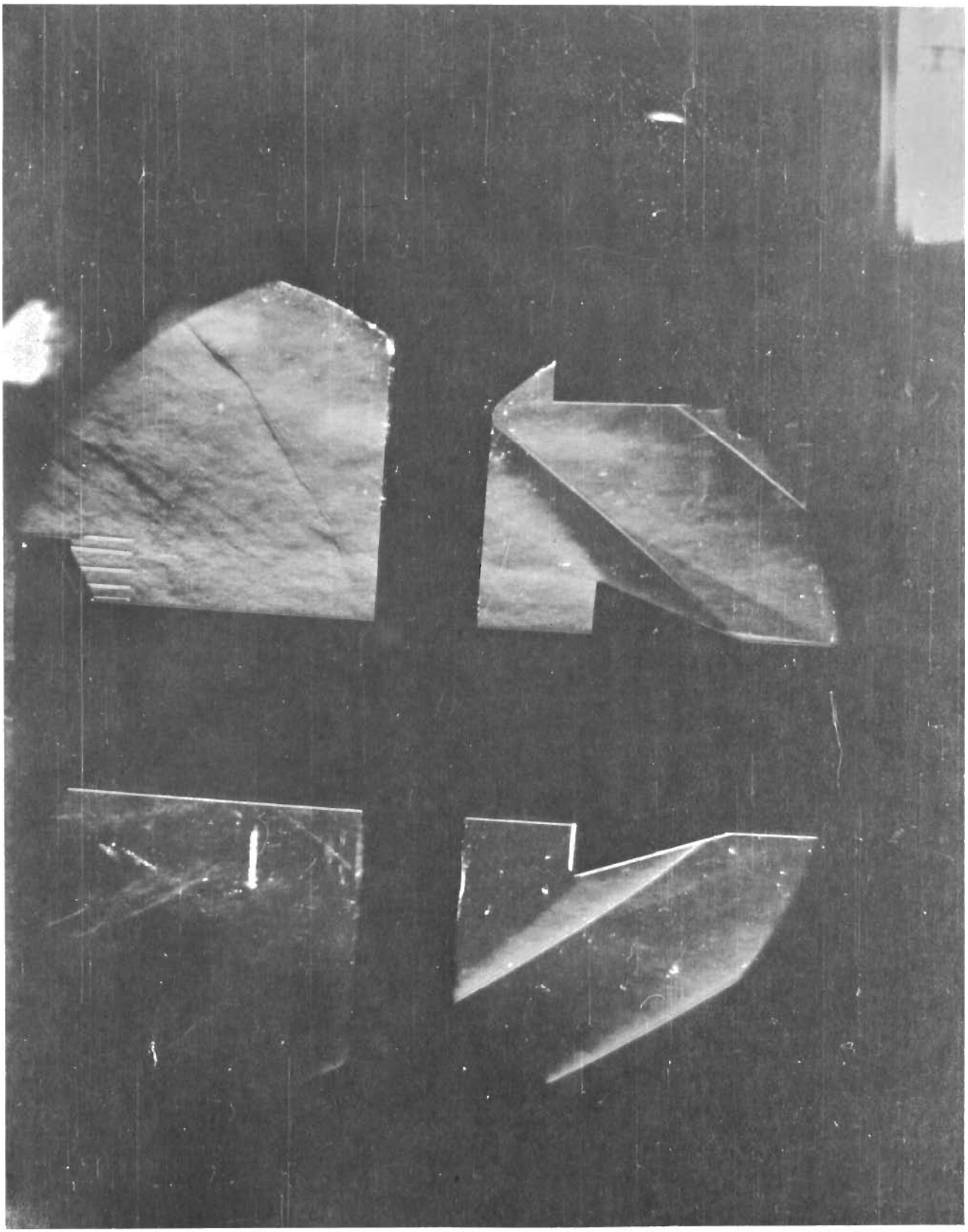

FIGURE 49 AXISYMMETRIC MODEL. M = 2.5 $\alpha = \phi = 0$. P_o = 5.2

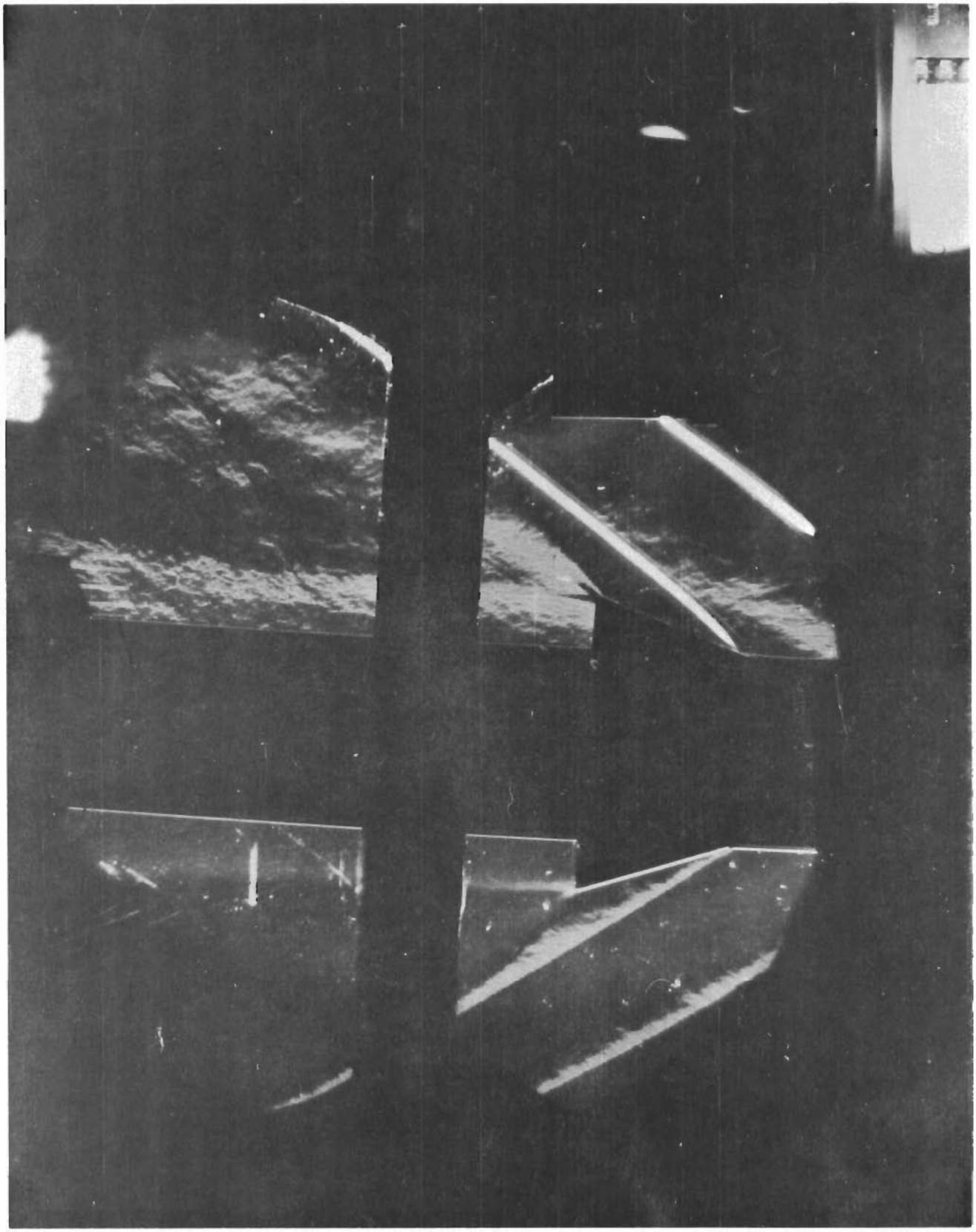

FIGURE 50 AXISYMMETRIC MODEL. M = 2.5 $\alpha = \phi = 0$. $P_o = 32$

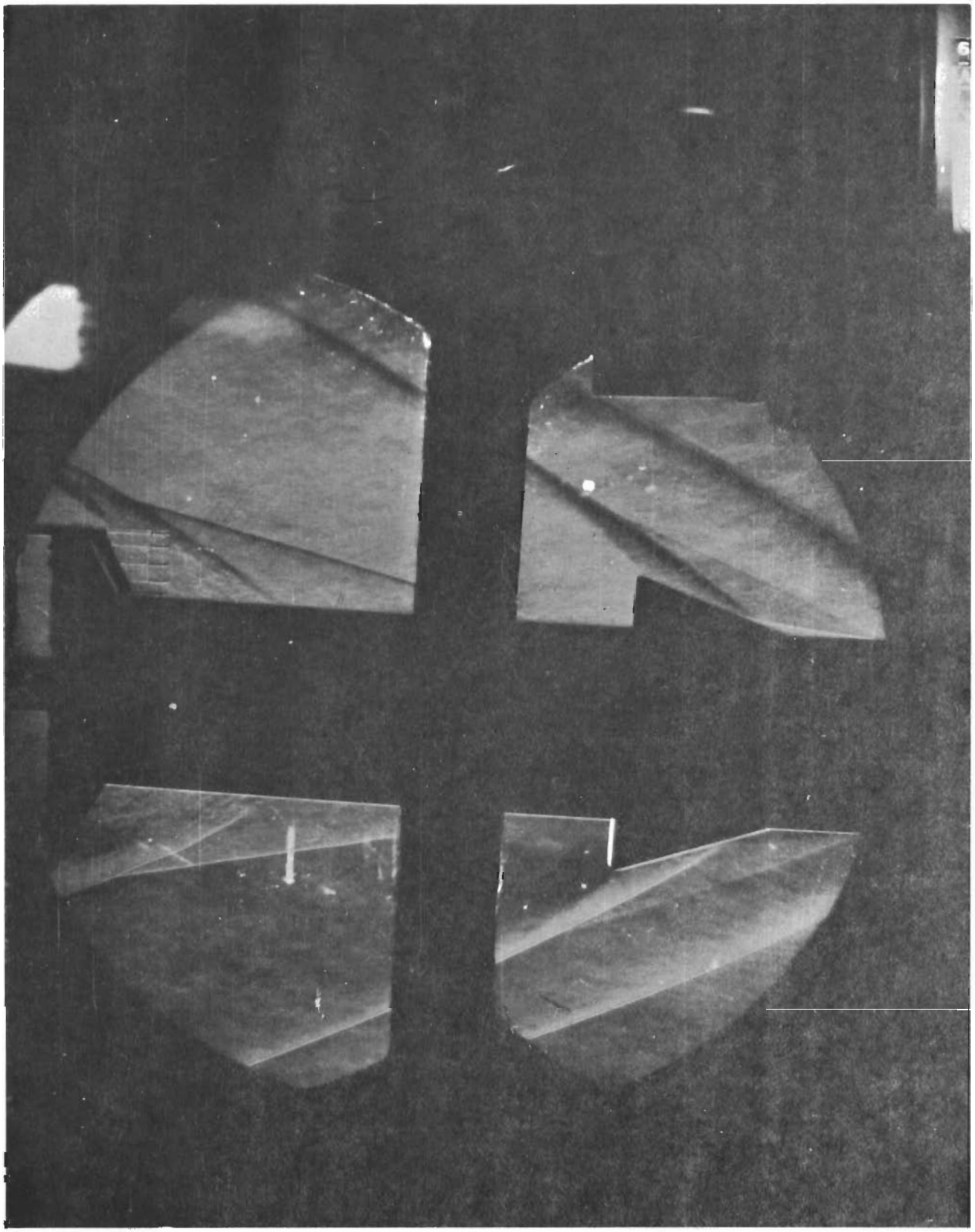

FIGURE 51 AXISYMMETRIC MODEL M = 3.5 $\alpha = \phi = 0.$ $P_o = 9.3$

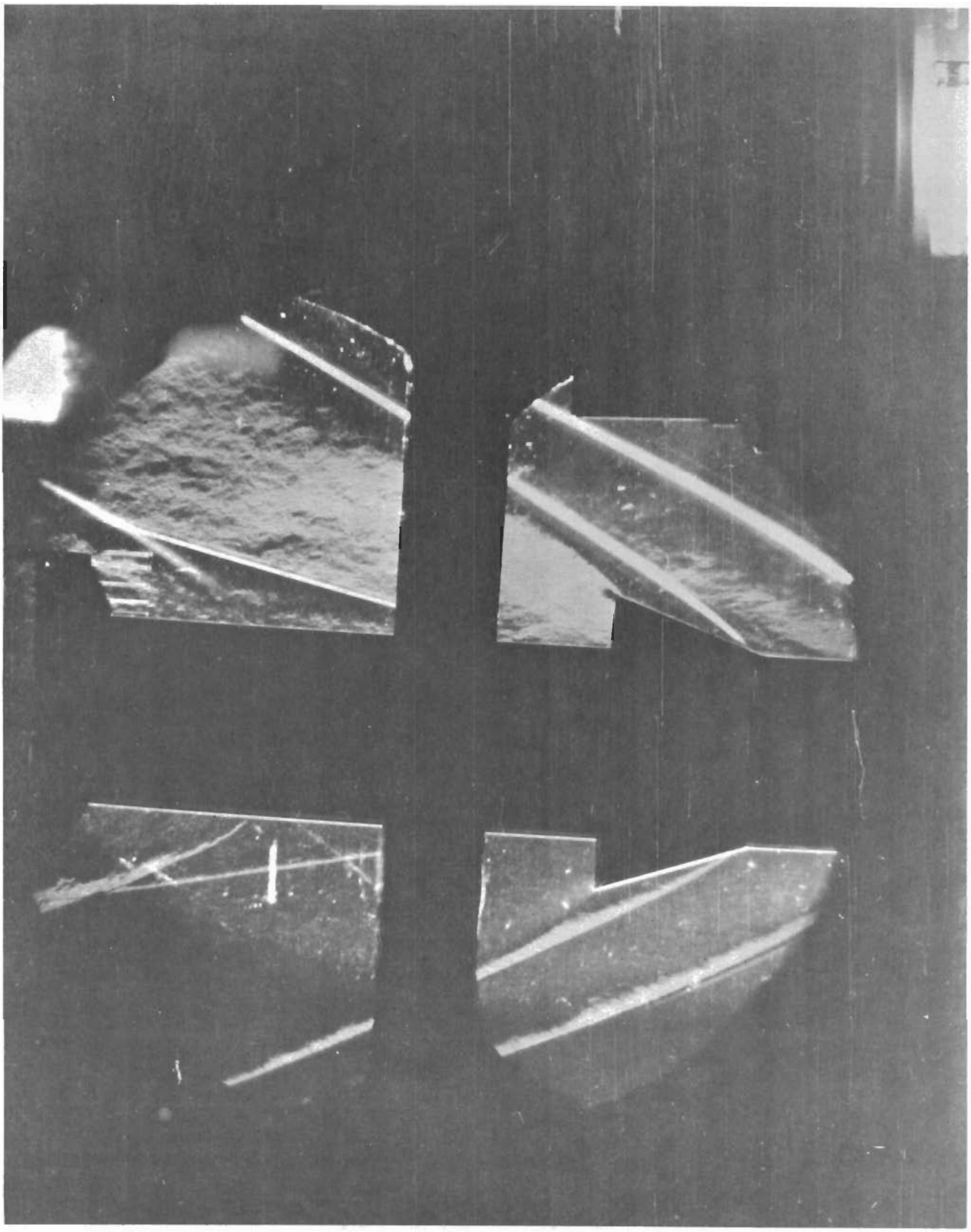

FIGURE 52 AXISYMMETRIC MODEL M = 3.5 $\alpha = \phi = 0.$ $P_o = 56$

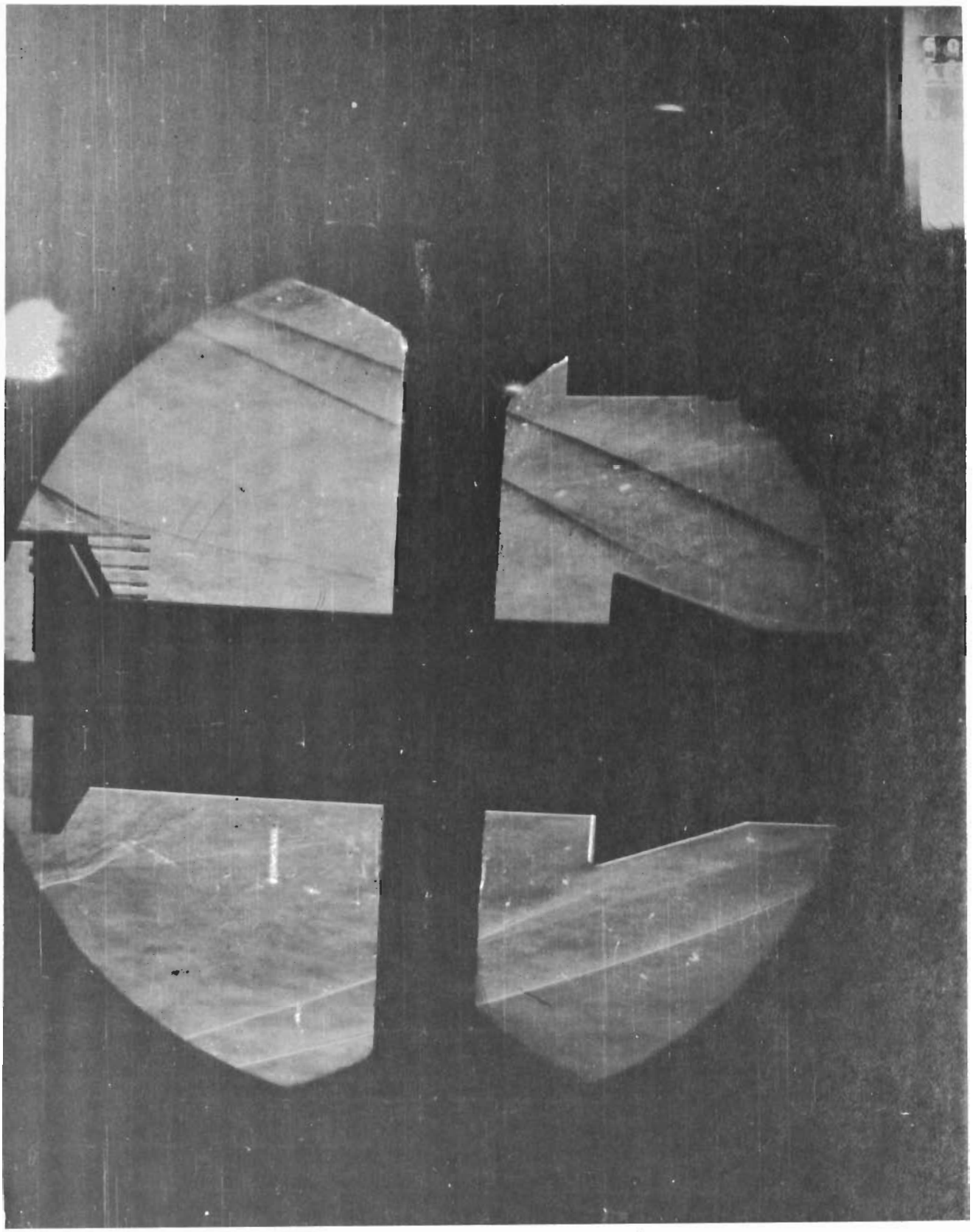

FIGURE 53 AXISYMMETRIC MODEL. M = 5 $\alpha = \phi = 0$. $P_o = 11$

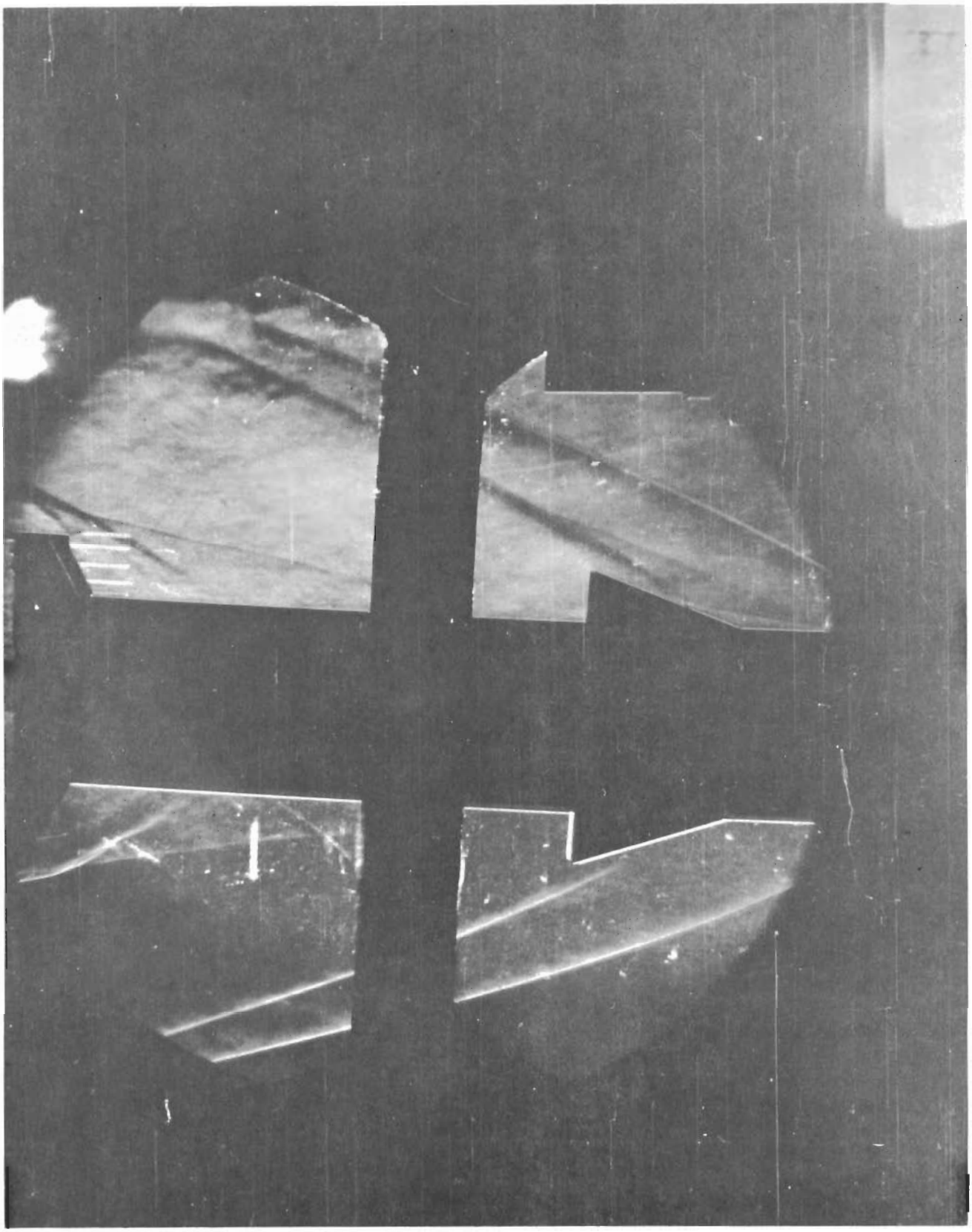

FIGURE 54 AXISYMMETRIC MODEL. M = 5 $\alpha = \phi = 0$. $P_o = 18$

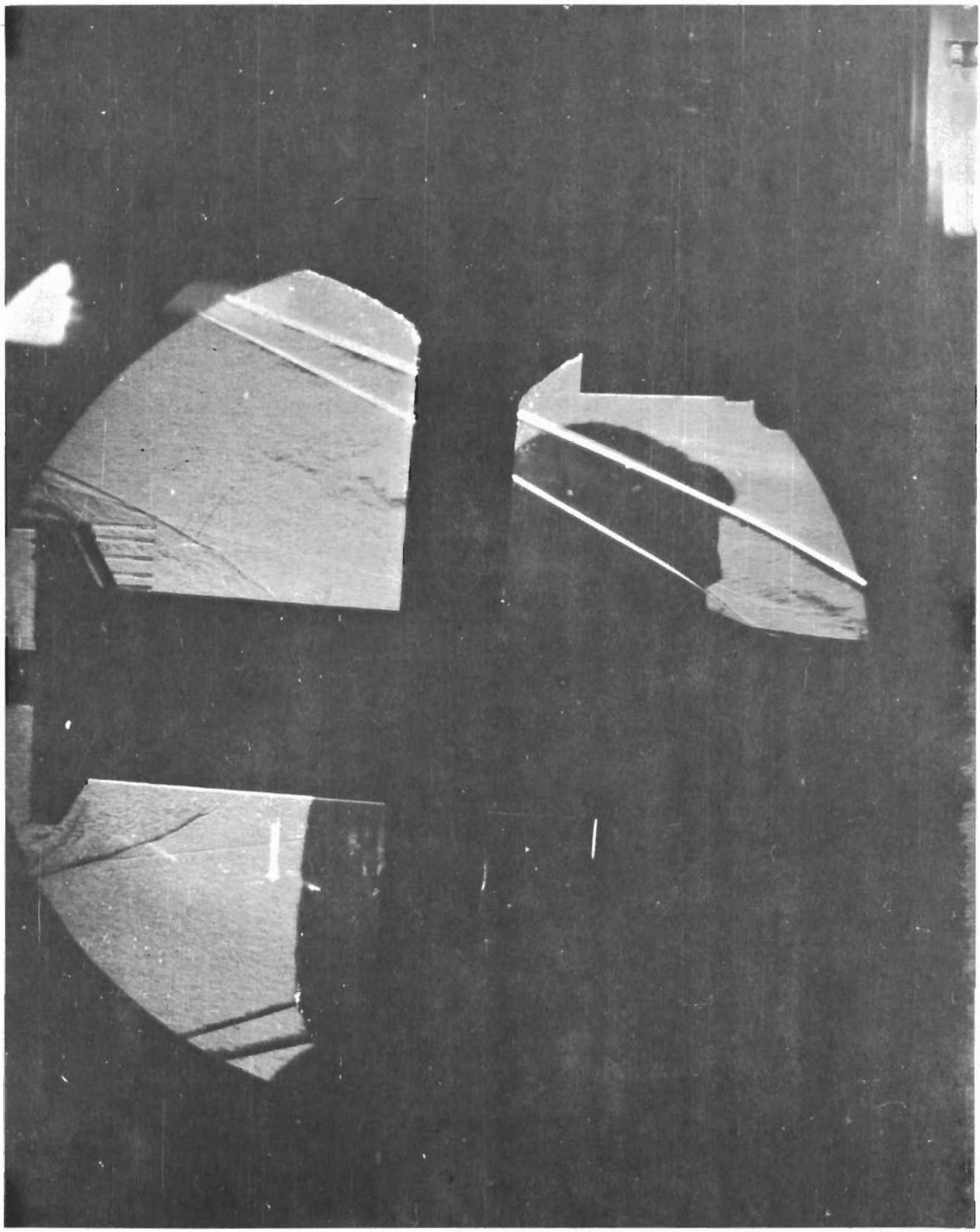

FIGURE 55 AXISYMMETRIC MODEL. M = 5 $\alpha = \phi = 0$. $P_o = 150$

tively. There appears to be little difference between results at α = 0 and 5 degrees at M_∞ = 5.0, but transducers 3, 4 and 5 (aft flare) show measurable increases at α = 14.7°. At Mach numbers of 3.5 and 2.5, these effects spread to a 2:1 ratio of RMS $\Delta p/q$ at α = 14.7° compared to values at α = 0°. At α = 15°, we find RMS $\Delta p/q_\infty$ decreases from .03 to .02 as the Mach number goes from 2.5 to 5.00 for locations just ahead of the aft flare.

Figures 56 and 57 show the angle of attack effects on overall SPL and selected 1/3 octave band SPL's for transducer 3 which is representative of data in the forward flare wake on the cylindrical portion ahead of the aft flare. We can see that the maximum increase in overall SPL is about 7 db between α = 0 and α = 15°. The data at M_∞ = 5.0 seem to show a slight dip at α = 5°, then a more rapid increase to higher levels at α = 15°. At Mach 2.5, the trend appears nearly linear, and at Mach 3.5 the curvature of the angle of attack variation appears even slightly opposite to the trend at Mach 5. It is felt that the number of angle of attack points for which data were taken are too few to take these small graphical curvatures too literally, and this would constitute a matter for future investigation. It would, of course, be desirable to extend the α range beyond 15° which would require difficult changes in the wind tunnel sting mounting arrangement for each 15° increment in α, as mentioned previously.

The theoretical considerations for incompressible flow at angle of attack, discussed in Section II, would seem to favor a greater than linear increase in RMS Δp, except for the counteracting expansion to lower density levels on the lee side at high Mach numbers for which the theory did not account.

As an introduction to the consideration of the frequency distribution of energy, we note that Figure 56 and 57 show the 1/3 octave band SPL's vs. α for transducer 3. There appears to be little difference in the angle of attack dependence among the various frequencies. We shall, therefore, use this as a partial justification for studying the non-dimensional frequency spectra at zero angle of attack only.

Nondimensional Frequency Spectra at Zero Angle of Attack

Forward Flare Wake

Figure 58 through 61 show various forms of nondimensional and dimensional frequency spectra derived from the 1/3 octave analyses presented in the Appendix. Transducer channel 3 is representative of channels 2, 3, 4 and 5. Figure 59 shows the form which is easiest for application using h as the unambiguous length dimension. The nondimensional spectra employed is

$$\tilde{W}_h = \frac{U_\infty \Delta \langle p^2 \rangle}{q_\infty^2 (\Delta f) h} \tag{110}$$

as a function of a Strouhal number based on h

$$\tilde{f}_h = \frac{fh}{U_\infty} \tag{111}$$

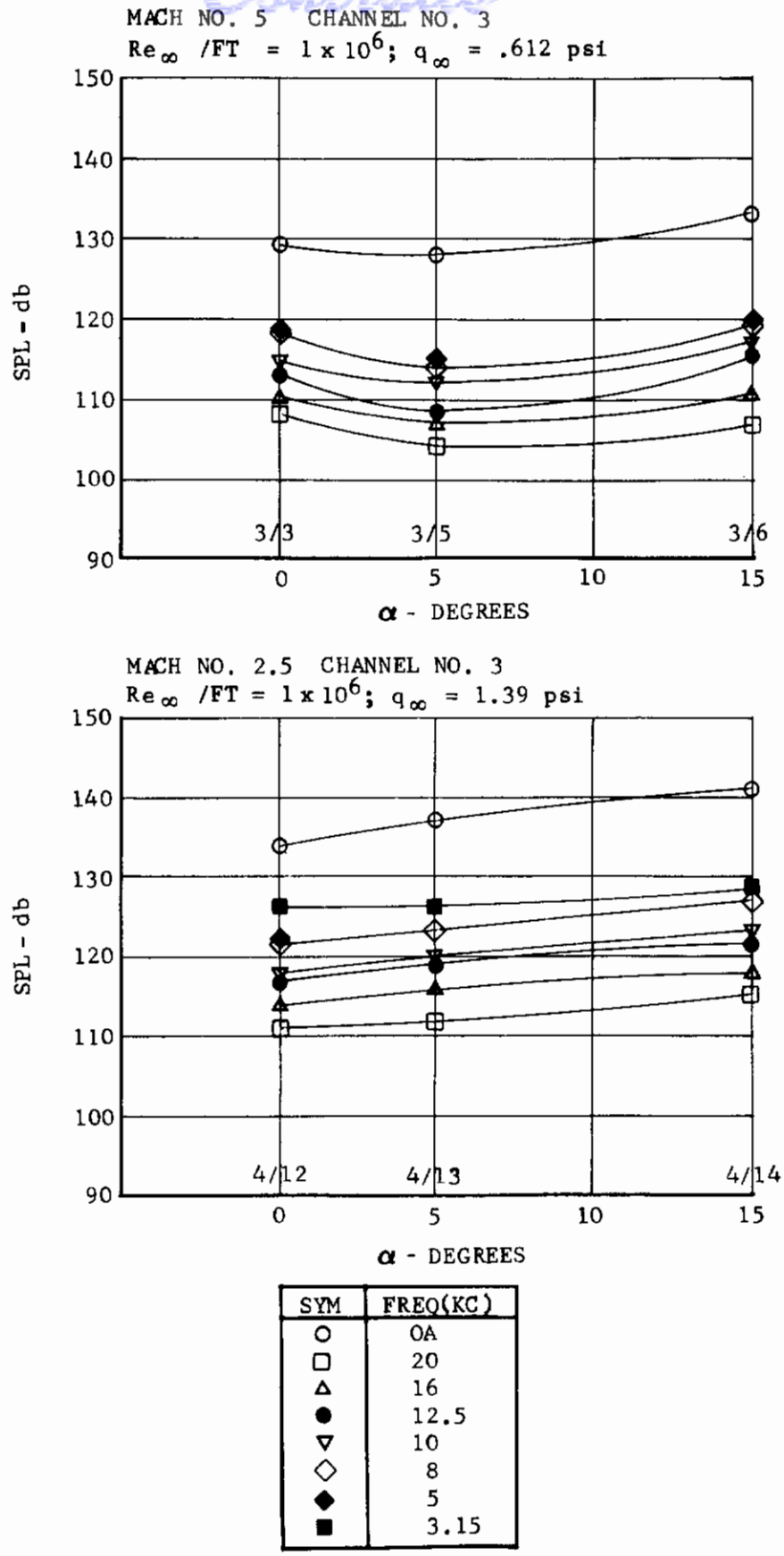

FIGURE 56 ANGLE OF ATTACK EFFECTS ON 1/3 OCTAVE AND OVERALL SPL AXISYMMETRIC

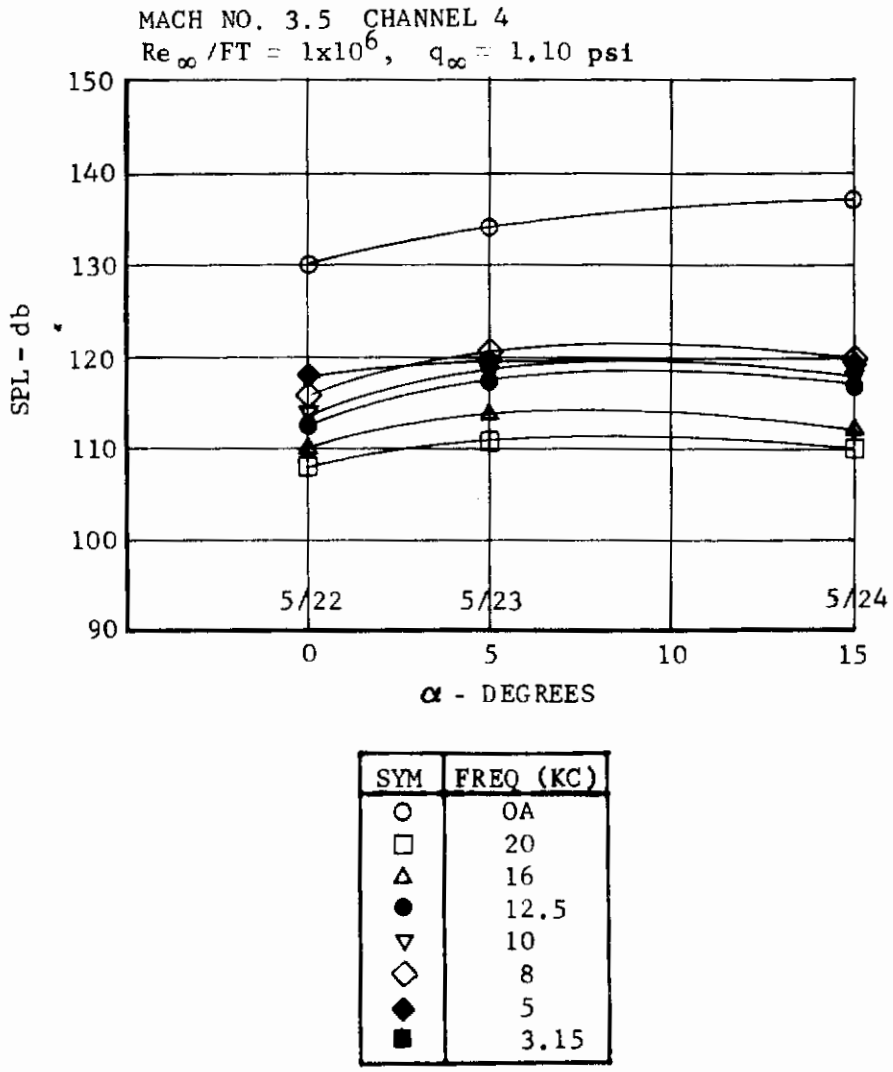

FIGURE 57 ANGLE OF ATTACK EFFECTS ON 1/3 OCTAVE AND OVERALL SPL AXISYMMETRIC

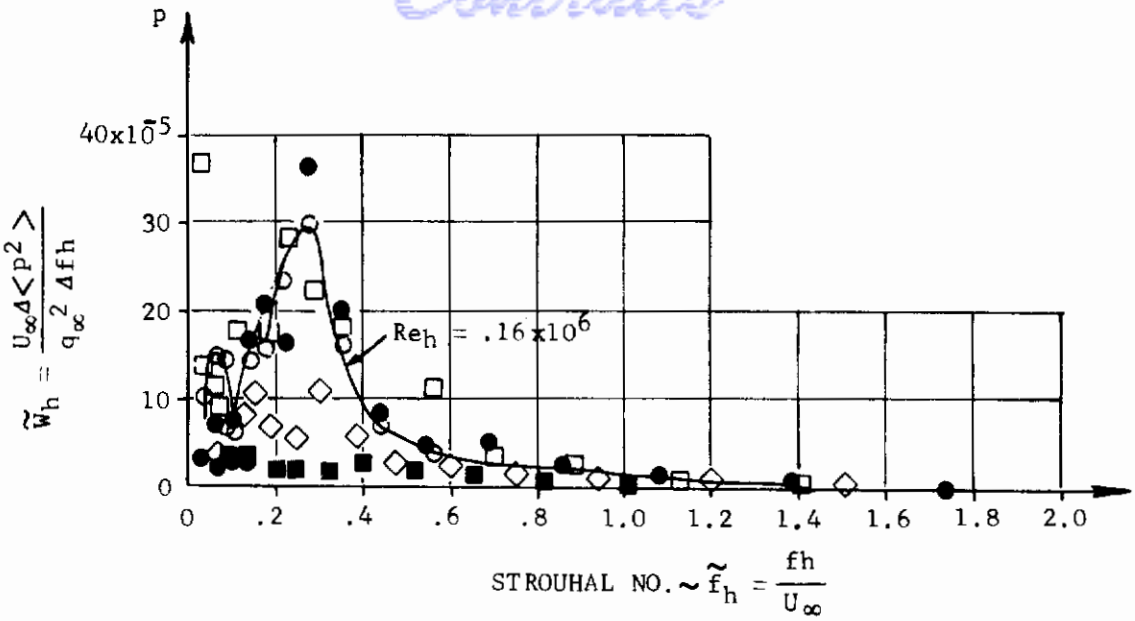

FIGURE 58 NON-DIMENSIONAL FREQUENCY SPECTRA DERIVED FROM 1/3 OCTAVE ANALYSIS, AXISYMMETRIC MODEL. TRANSDUCER #3 (LENGTH DIMENSION BASED ON h = 2 INCHES.

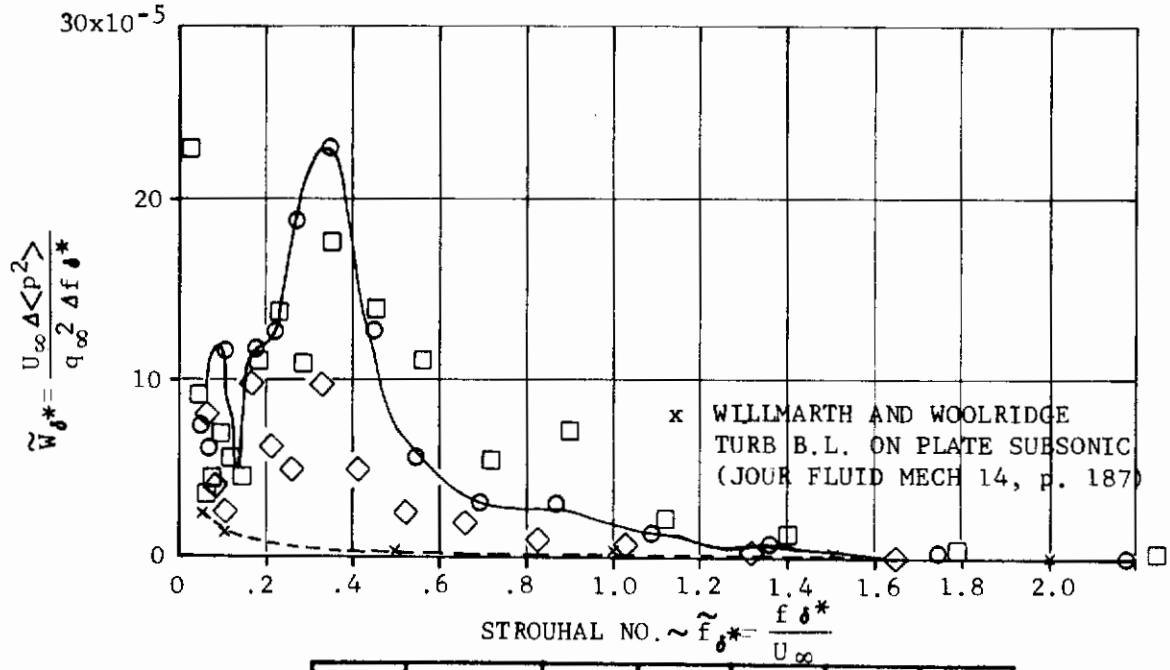

SYM	RUN/Gp	M_∞	R_e/L /FT^{-1}	α	δ^* IN	θ IN
○	4/12	2.5	$1x10^6$	0	2.5	.44
●	4/11	2.5	$6x10^6$	↓	—	—
◇	5/22	3.5	$1x10^6$	↓	2.2	.22
□	3/3	5.0	↓	↓	3.2	.18
■	3/9	5.0	$6x10^6$	↓	—	—

FIGURE 59 NON-DIMENSIONAL FREQUENCY SPECTRA DERIVED FROM 1/3 OCTAVE ANALYSIS, AXISYMMETRIC MODEL. TRANSDUCER #3 (LENGTH DIMENSION BASED ON δ^*)

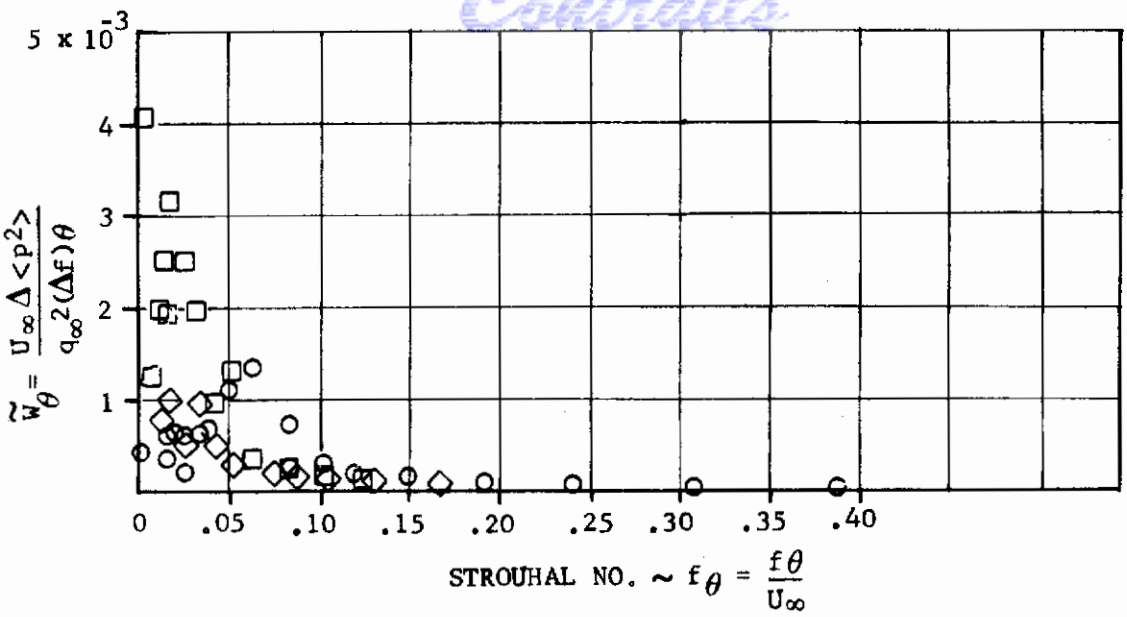

FIGURE 60 NON-DIMENSIONAL FREQUENCY SPECTRA DERIVED FROM 1/3 OCTAVE ANALYSIS, AXISYMMETRIC MODEL. TRANSDUCER #3 (LENGTH DIMENSION BASED ON θ)

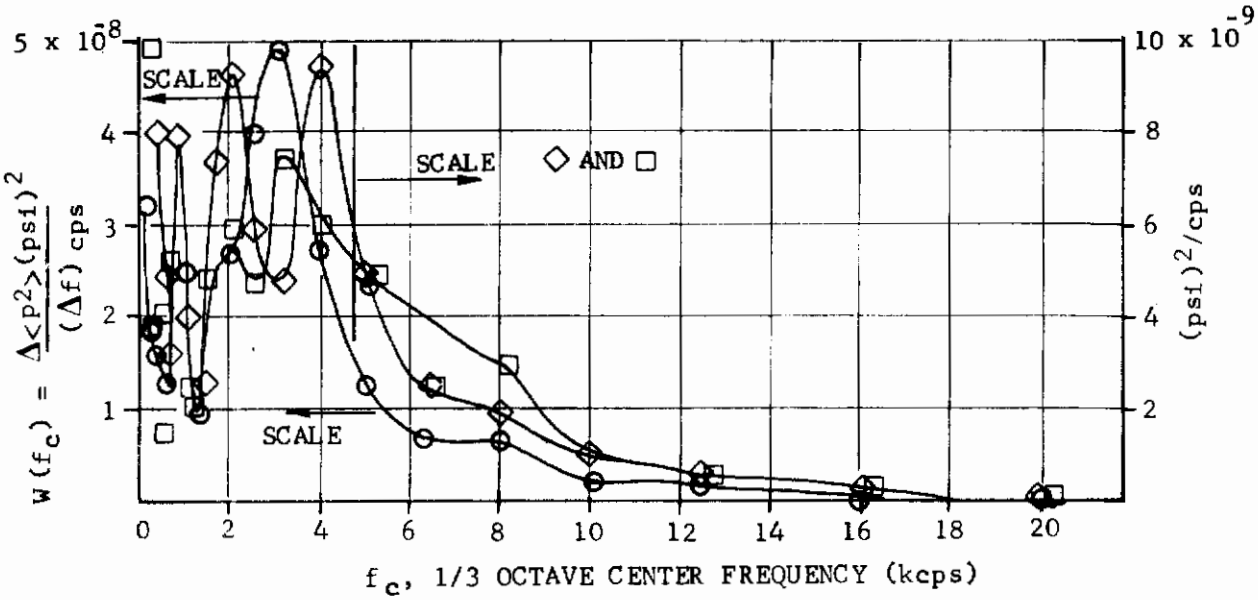

SYM	RUN/Gp	M_∞	R_e/L /FT^{-1}	α	δ^* (IN)	θ (IN)	q_∞ PSI
○	4/12	2.5	1×10^6	0	2.5	.44	1.38
◇	5/22	3.5	↓	↓	2.2	.22	1.09
□	3/3	5.0	↓	↓	3.2	.18	.62

FIGURE 61 DIMENSIONAL FREQUENCY SPECTRA DERIVED FROM 1/3 OCTAVE ANALYSIS, AXISYMMETRIC MODEL. TRANSDUCER #3, h = 2 INCHES

Similar definitions are employed in Figures 59 and 60, replacing h by δ^* and θ respectively. The results do not show any decisive advantage for the representations in terms of δ^* and θ, although it must be recalled that there was only a small variation in free stream velocity and δ^* is of the same order of magnitude as h for the Mach number range of the tests. The δ^* correlation seems to be preferable to the correlation in obtaining a smaller vertical scatter.

The low speed results of Willmarth and Woolridge on a flat plate are shown. As expected, the separated flow spectra are higher and more concentrated below $fh/U_\infty = 2$.

Figure 61 was presented to show the same data in dimensional form $\Delta(p^2)/\Delta f$ vs. f in cps. It is of interest to estimate the possible role of model shell vibrations in the interpretation of frequency spectra derived in this way. The shell frequencies range upwards from 543 cps for m = 1, n = 2, with an increasive density of resonant modes.

Evaluation of Vibration Induced Errors for the Axisymmetric Model

We shall digress briefly to evaluate vibration errors for the axisymmetric model which were of some concern because so many modes are in the frequency range of interest. These frequencies were estimated by assuming the model to be a simply supported steel cylindrical shell of length, 27 inches, radius, 3.75 inches and thickness, 1/8 inch. The assumed mode shape was

$$w_{mn}(x,\theta) = \sin\left(\frac{m\pi x}{\ell}\right)\cos n\theta \tag{112}$$

and the governing differential equation was taken to be the Donnell equation (see Ref. 32 for experimental comparison)

$$D\nabla^8 w + \frac{Eh}{R^2}\frac{\partial^4 w}{\partial x^4} + \rho h \nabla^4 \frac{\partial^2 w}{\partial t^2} = 0 \tag{113}$$

where the plate modulus is

$$D = \frac{Eh^3}{12(1-\nu^2)} \tag{114}$$

Numerical results plotted in Figure 62 indicate the presence of many vibration modes in the frequency range of interest. In Reference 33, a formula for the number of modes to be found in a given bandwidth is employed due to Heckl, (Ref. 36). This model density formula is used in vibratory spectra response to turbulent pressure given below. From the Donnell equation, one can express the frequency, f_{nm} associated with Eqs. (112 and 113) in a closed form as

$$f_{nm} = \frac{c_o}{2\pi R}\left\{\frac{(h/R)^2\left[(\lambda_m)^2 + n^2\right]^2}{1-\gamma^2} + \frac{(\lambda_m)^4}{\left[(\lambda_m)^2 + n^2\right]^2}\right\}^{1/2} \tag{115}$$

where $c_o = \sqrt{E/\rho}$ =5190 meters/sec. (cf. Heuter and Bolt, Ref. 16, p. 346) and

$$\lambda_m = \left(\frac{m\pi R}{\ell}\right) \tag{116}$$

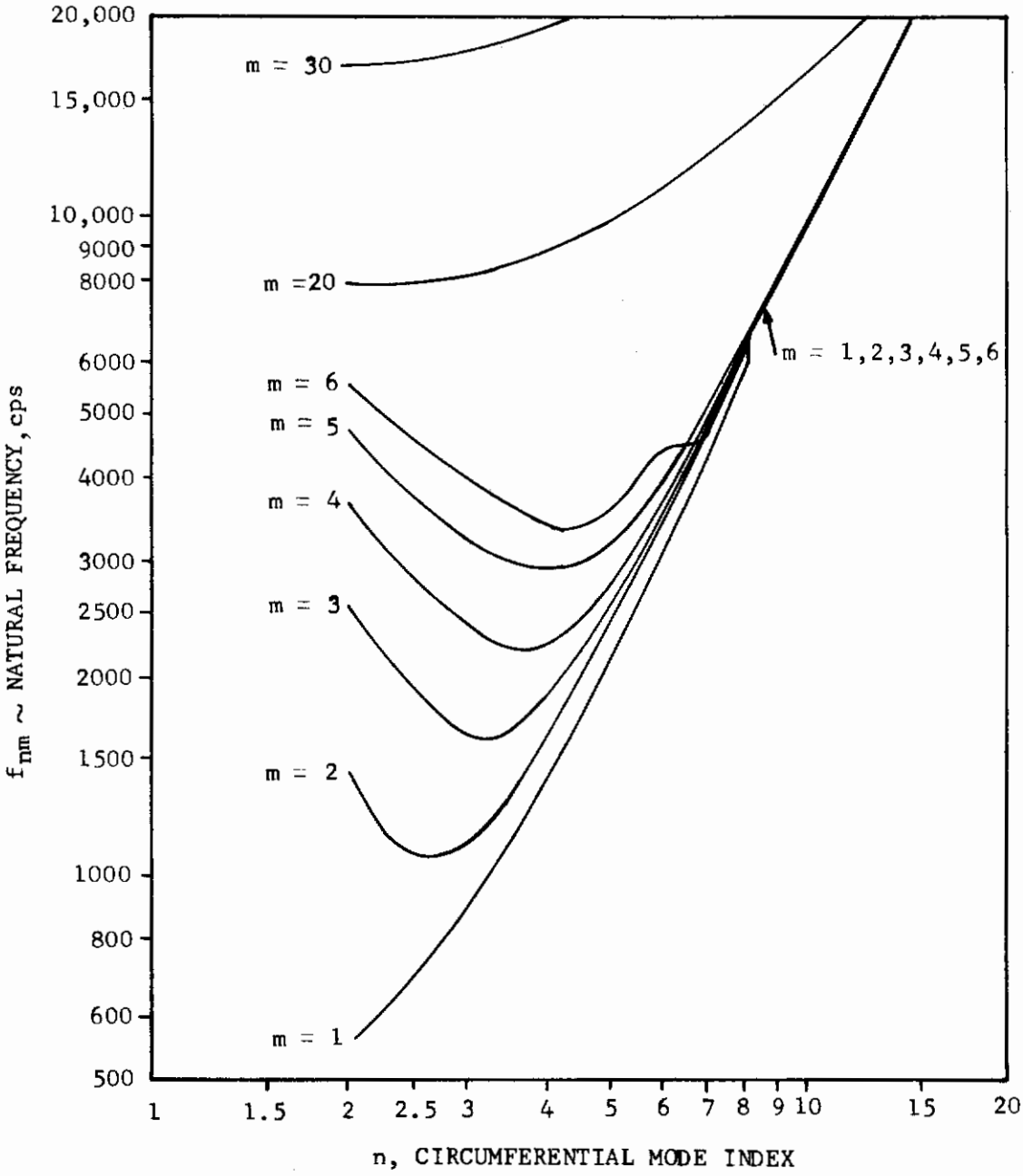

FIGURE 62 AXISYMMETRIC MODEL (CYLINDRICAL SHELL) VIBRATION FREQUENCIES
ℓ = 27", h = 1/8", R = 3.75", STEEL

Rattayya and Junger (Ref. 33) have estimated the random vibration response of a cylindrical shell due to subsonic turbulent pressure fluctuations, based on results of Refs. (1, 34 and 35). In order to indicate which of the many vibration modes are likely to participate, the coincidence principle is invoked, wherein the wave number of the convected turbulence, ω/U_c, equals the wave number for the axial vibration mode, thus, we require (Ref. 33) at coincidence:

$$\frac{\omega}{U_c} = \frac{\pi m_c}{\ell} \tag{117}$$

In general, U_c ranges from $0.8U_\infty$ to $0.6U_\infty$ (Refs. 1, 13, 17, 34, 35) so that Eq. (117) enables us to solve for the axial half wave index, m, which is most likely to be excited by a given flow velocity at a given frequency. We find at coincidence

$$m = m_c = \frac{2f\ell}{U_c} \tag{118}$$

As an example, for Tunnel "A", 1 = 27" = 4.33 ft., D = 7.5", U = 1900 to 2400 ft/sec., with a typical convection velocity, U_c = 1600 ft/sec. Then

$$m_c = \left(\frac{2 \times 4.33}{1600}\right) f = \frac{f}{192} \tag{119}$$

The implication of Eq. (119) is that the number of half waves excited increases by one for each increase of 192 cps in frequency. The question arises next as to which circumferential waves are likely to be excited. According to Ref. 33, the ratio of (circumferential wave length/axial wave length) must exceed one third. We define the circumferential and axial wave lengths by

$$\Lambda_\theta = 2R\theta_n = 2\pi R/n \tag{120}$$

$$\Lambda_x = 2\ell/m \tag{121}$$

then, adding an upper bound of $\Lambda_\theta \leq \frac{3}{2}\Delta_x$ we require

$$\frac{1}{3} \leq \frac{2\pi R}{n} \quad \frac{m}{2\ell} \leq \frac{3}{2}$$

which leads to the criterion

$$\frac{2m}{3}\left(\frac{\pi R}{\ell}\right) \leq n \leq 3m\left(\frac{\pi R}{\ell}\right) \tag{122}$$

Thus, the values of n and m defined by Eqs. (119 and 121) indicate the favored response modes. For the present model 1 = 27", R = 3.75" and Eq. 122 implies with $\pi R/1 = .436$

$$.291m \leq n \leq 1.308m \tag{123}$$

The response will, of course, seek the integers nearest to the values of m and n defined above. A further restriction on participating modes stems from the fact that for a given m defined by Eq. (119), that the natural frequencies associated with the higher values of n which satisfy Eq. (123) will be much greater than the assumed (driving) frequency in Eq. (119). Therefore, the response of these modes will be greatly less than those modes which are more nearly in resonance. Thus, the resonant coincident modes will be favored even when many other modes satisfy the wavelength compatibility condition as defined by Eq. (122). Ref. (33) shows that the coincidence principle follows directly from the evaluation of the covariance of the generalized force when the normalized turbulent pressure cross spectral density takes on the form established by Corcos (Ref. 23) appropriate to the convection of the turbulence pattern. In our notation, it is written as

$$\widetilde{W}_p(\xi,\eta;\omega) \equiv W_p(\xi,\eta;\omega)/Wp(o,o;\omega)$$

$$= \exp\left(-0.11\left|\frac{\omega\xi}{U_c}\right| - 0.60\left|\frac{\omega\eta}{U_c}\right|\right)\cos\frac{\omega\xi}{U_c} \qquad (124)$$

Because the product of $w_{mn}(x,\theta)\, w_{mn}(x+\xi,\ \theta+\theta^1)$ can, by use of Eq. (112), be written in the form of a function of x times cos $(\frac{m\pi\xi}{l})$, when this factor and Eq. 124 are then integrated over $-\infty<\xi<\infty$ to calculate the covariance of the generalized force, the factor $(\frac{\omega}{U_c} - \frac{m\pi}{l})$ goes to zero which eliminates the cancellation effect caused by the oscillatory behavior of the integral over ξ.

Analytical Estimate of Vibration Error for a Cylindrical Shell

In order to assess the magnitude of vibration induced errors, the analysis of Ref. 33 was carried out to calculate the mean squared vibratory velocity v_o^2, for a given 1/3 octave filter band width. Eq. (34) of Ref. 33 can be developed to the following form for the ratio (V_o^2/U_∞^2):

$$\frac{v_o^2(f)}{U_\infty^2} = \frac{\Delta f R}{U_\infty}(4.5\times10^{-5}\,Q)\left(\frac{U_\infty}{c_s}\right)^7\left(\frac{\rho_\infty}{\rho_s}\right)^2\left(\frac{c_s}{\omega h_s}\right)^6\left(\frac{h_s}{R}\right)^3\frac{F}{\left[1+\left(\frac{2U_\infty}{fR}\right)^3\right]} \qquad (125)$$

where

$$F = \begin{cases} \pi/2 - \arcsin\left|1-2\zeta\right|;\ \zeta = \dfrac{\omega R}{c_s} < 1 \\ \pi;\ \zeta \geq 1 \end{cases} \qquad (126)$$

and for a shell material of density, ρ_s, and elastic modulus E_s

$$c_s = \sqrt{\frac{E_s}{\rho_s}} \qquad (127)$$

and Q is the dynamic magnification factor for a 1 $\frac{\text{rad}}{\text{sec}}$ band width. For case of a shock mounted crystal, we take Q = 100 relative to the base of the crystal as a typical value. This equivalent to a Q of 200 for the shell, and a shock mount transmissibility of 50%. To evaluate the sensitivity of the crystal strain to vibratory motion of its mounting, it was assumed that the back face of the crystal

TABLE 7

CALCULATED 1/3 OCTAVE MEAN SQUARE VIBRATORY VELOCITY ERROR OF A SHOCK MOUNTED PIEZOELECTRIC CRYSTAL ON A CYLINDRICAL SHELL FOR Q=100.

Center Freq. 1/3 Octave cps	$v_o^2/U_\infty^2 Q$	$\frac{1}{Q}\sqrt{v_o^2/U^2}$	RMS Velocity $\sqrt{v_o^2/U^2}$ for $\sqrt{Q}=10$	Error Sensitivity $d\mathcal{E}/d\frac{V_o}{U_\infty}$ at $p_e=3.16 \times 10^{-3}$ psi	$\mathcal{E}$ RMS at 120db	$\mathcal{E}$ RMS at 130db
500	$.782 \times 10^{-14}$	8.84×10^{-8}	8.84×10^{-7}	$-.110 \times 10^{7}$	-.973	-.308
1,000	2.69×10^{-16}	1.64×10^{-8}	1.64×10^{-7}	$-.219 \times 10^{7}$	-.360	-.114
5,000	$.265 \times 10^{-16}$	$.515 \times 10^{-8}$	$.515 \times 10^{-7}$	$-.110 \times 10^{8}$	-.567	-.180
10,000	7.85×10^{-18}	$.280 \times 10^{-8}$	$.280 \times 10^{-7}$	$-.219 \times 10^{8}$	-.613	-.194
16,000	1.80×10^{-18}	$.134 \times 10^{-8}$	$.134 \times 10^{-7}$	$-.351 \times 10^{8}$	-.470	-.149

was constrained to move with a velocity equal to the vibrating shell, having a velocity, v_o. Because of the inertial loading, the crystal was given an erroneous strain in addition to that caused by the external pressure, p_e, we seek to measure. The strain in the crystal is governed by the following equations:

$$e_{11} = \frac{\partial \xi}{\partial x} \tag{128}$$

The displacement is expressed as

$$\xi = \xi_0 + \xi_1 \tag{129}$$

Then ξ_1, the strain displacement satisfies

$$\frac{\partial^2 \xi_1}{\partial x^2} - \frac{1}{c_c^2}\frac{\partial^2 \xi_1}{\partial t^2} = \frac{1}{c_c^2}\frac{\partial^2 \xi_0}{\partial t^2} \; ; \; 0 \le x \le \ell_c \tag{130}$$

The boundary conditions are

$$x = 0: \quad \xi_1 = 0 \tag{131}$$

$$x = \ell_c: \quad E_c \frac{\partial \xi_1}{\partial x} = p_e \tag{132}$$

The solution for ξ_1, is

$$\xi_1 = -\xi_0 \left[1 - \cos(k_c \ell_c)\right] + \left[\frac{p_e}{k_c E_c} + \xi_0 \sin(k_c \ell_c)\right] \frac{\sin k_c x}{\cos k_c \ell_c} \tag{133}$$

where

$$c_c = \sqrt{\frac{E_c}{\rho_c}} \quad ; \quad k_c = \omega/c_c = E_c \tag{134}$$

Then the vibratory strain error can be written as

$$d\epsilon/d\left(\frac{v_0}{U_\infty}\right) \equiv \left(\frac{\Delta p_e}{p_e}\right) = \frac{E_c}{p_e}\left(\frac{U_\infty}{c_c}\right)\left[\frac{1}{2}\left(\frac{\omega \ell_c}{c_c}\right)\right] \tag{135}$$

For the random vibration case, the mean squared response (assuming v_o and p_e are uncorrelated) is:

$$(p_e + \Delta p_e)^2 = p_e^2 + (\Delta p_e)^2 \tag{136}$$

The RMS vibration induced pressure error is then the product of Eq. (135) times the square root of Eq. (125). Numerical results are given in Table 7 over the frequency range of interest. We see that while the RMS velocity for the 1/3 octave band decreases with frequency according to Eq. (125), the velocity error sensitivity increases and the resultant RMS pressure error remains of the same order of magnitude over the range from 1000 to 16000 cps, though somewhat higher at 500 cps. The error sensitivity is inversely proportional to p_e for a given $v_o = d\xi_o/dt$ from Eq. (135); therefore, the error, $\mathscr{E}_{RMS}$, was shown for two typical values of measured p_e, corresponding to 1/3 octave band levels of 120 and 130 db. At 120 db, our vibratory error ranges from 22.8% to 61.3% which is undesirably high but the data should be acceptable from the point of view of design. At a level of 130 db, the errors would appear as acceptable. The analysis of Ref. 33 is based on low speed flat plate turbulent pressure spectra which correspond to a $\Delta p_{RMS}/q_\infty$ of about .006 and at $q_\infty = 1$ psi, we would have $\Delta p_{RMS} = .006$ psi. The overall SPL would correspond to about 126 db in this case, with a 1/3 octave level of the order of 116 db. Then our calculated error would have to be multiplied by a factor $\frac{(p_e)\ \text{apparent}}{.0019\sqrt{1 + \mathscr{E}^2}}$. This process can be iterated until convergence is obtained. The error estimate would be very close for 1/3 octave levels of 116 db. In any future test program, a specially designed axisymmetric model should be employed (rather than adapting an existing conventional aerodynamic test model as was done in the present test program). Because of the fairly low frequency range of the separated flow pressure fluctuations, it is believed that a stiffness controlled model could be successfully designed by making a smaller radius thick-walled stiffened cylindrical shell. This was not considered feasible in the initial design, because it was anticipated that the frequency spectrum of the pressure fluctuations might extend over such a wide range that successful stiffness control would be precluded.

Nondimensional Frequency Spectra Normalized to Mean Squared Pressure

We now continue our discussion of the non-dimensional frequency spectra, having established the general order of magnitude of experimental errors.

Figures 63 and 64 show the same transducer data normalized to the mean squared turbulent fluctuation pressure as derived from the overall SPL. This form of normalization was presented by Kistler and Chen (Ref. 17) for flat plate turbulent boundary layers in supersonic flow and their spectrum is shown for comparison. Also shown are Kistler's normalized spectrum for fluctuations in the separated region ahead of a forward facing step (Ref. 13). The present data agree surprisingly well with Ref. 13, and both Ref. 13 and the present data show the heavier concentration of spectal energy for Strouhal numbers under 0.40 as compared with flat plate boundary layer fluctuation spectra. Also, the separated flows have little energy beyond $f\delta/U_\infty = 2$, where the flat plate energy persists to $f\delta/U_\infty = 5$, probably due to the small scale eddies and high intensity fluctuations in the region of high mean shear near the wall. This region is not present in the present wake-like flows.

Since the spectrum of channel 3 was typical of the results for channels 3, 4 and 5 on the flare, no further discussion will be given.

Oscillating Shockwaves and Discrete Frequency Phenomena

In section II, it was indicated that amplification or resonance might occur for Strouhal numbers of 0.37 to 0.42 according to Table 1. One might be tempted to infer confirmation for this in the results of Figure 58 which show high spectral densities for the range .20 to .35 for fh/U_∞. Taking account of the lower local free stream Mach numbers ahead of the aft flare due to the forward flare wake, one would expect greater stand-off distances and lower frequencies bringing about good agreement in the neighborhood of $fh/U_\infty \simeq 0.30$. We note again that this mechanism is not the self induced instability discussed by Trilling (Ref. 28) but is a kind of forced resonant response of upstream turbulence interacting with a detached shock wave. The actual frequency range in Tunnel A corresponds to the range 2.5kc to 5kc for Mach numbers between 2.5 and 5.0. The previously discussed estimate of 1/3 octave band, averaged shell vibration induced response did not show any pronounced spectra peaks when subjected to the rather white flow noise typical of boundary layers; therefore, the spectra peaks might be at least partly of aerodynamic origin. The possibilities of a single shock mount resonance frequency and wind tunnel guided wave modes (discussed previously in Section V) cannot be excluded conclusively; however, the tunnel resonances are not likely to be important beyond 1 kc. At a velocity of 2000 ft/sec. and $h = 2''$, 1 kc corresponds to $fh/U_\infty = .08$. In the future, it would be of interest to test models of several sizes in view of the limited velocity variation for the supersonic range in order to give a wider variation of Strouhal number. We now consider the base pressure fluctuations.

Base Pressure Fluctuations

Figures 65, 66 and 67 present equivalent narrow band spectral densities derived from the 1/3 octave based data of the Appendix. The two sharp humps are somewhat dubious because it is estimated that the base pressure mounting plate has two vibration modes in the frequency range less than 10 kc. For solid clamped plates, these would be 6 kc and 10 kc. Because they are more nearly simply supported, the actual frequencies might be of the order of one-half of these values or 3 kc and 5 kc; furthermore, the center hold would tend to raise the frequencies possibly in the range of the humps of Figure 66 at 3-4 kc and 7-9 kc. In this range, the spectra would appear high by a factor of 2 to 3; however, despite these errors, the data is still considered useful for engineering purposes. Figure 65 shows a correlation using

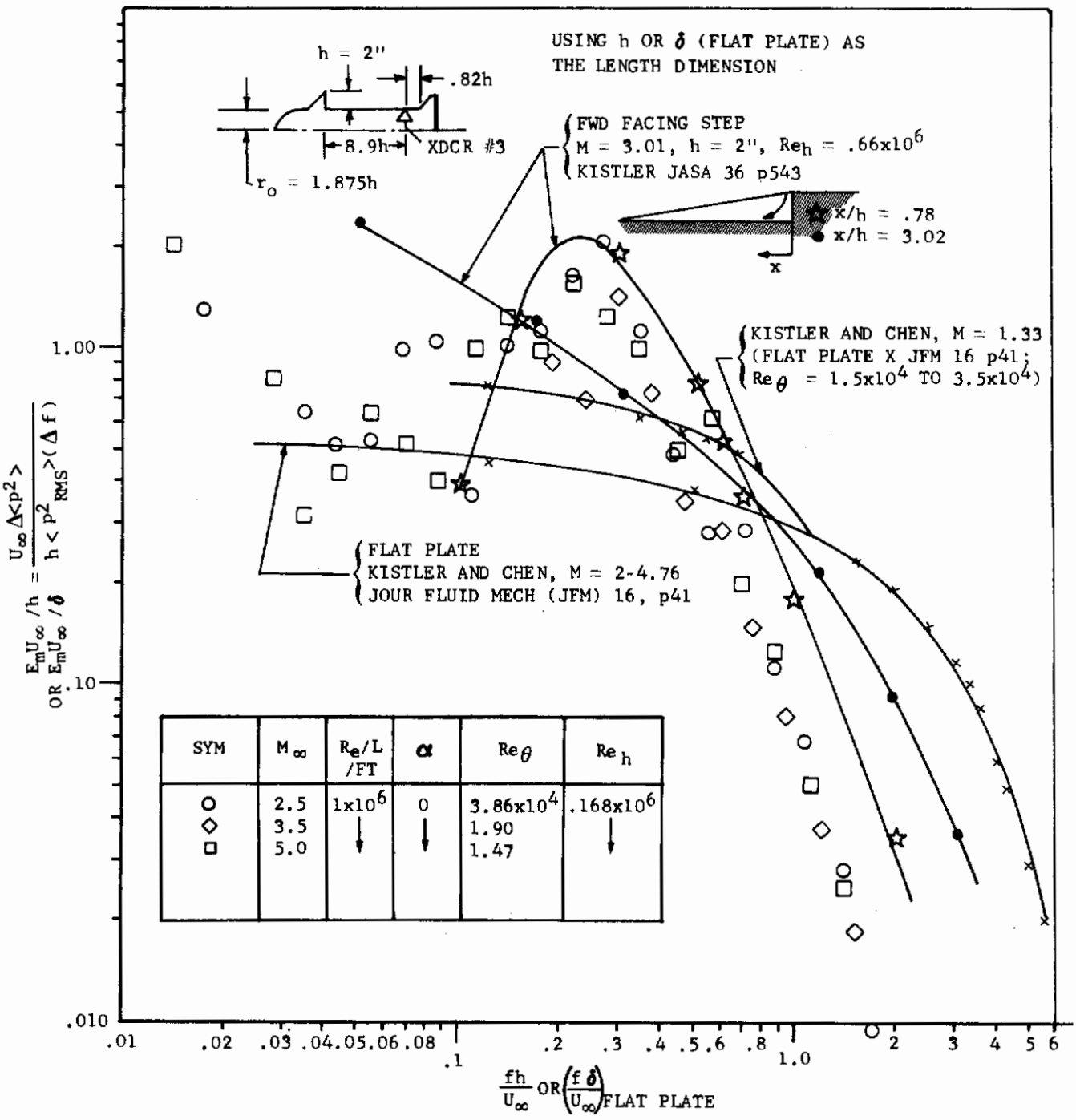

FIGURE 63 NON-DIMENSIONAL STROUHAL FREQUENCY SPECTRUM NORMALIZED TO MEAN SQUARED PRESSURE FLUCTUATION, AXISYMMETRIC MODEL TRANSDUCER NO. 3

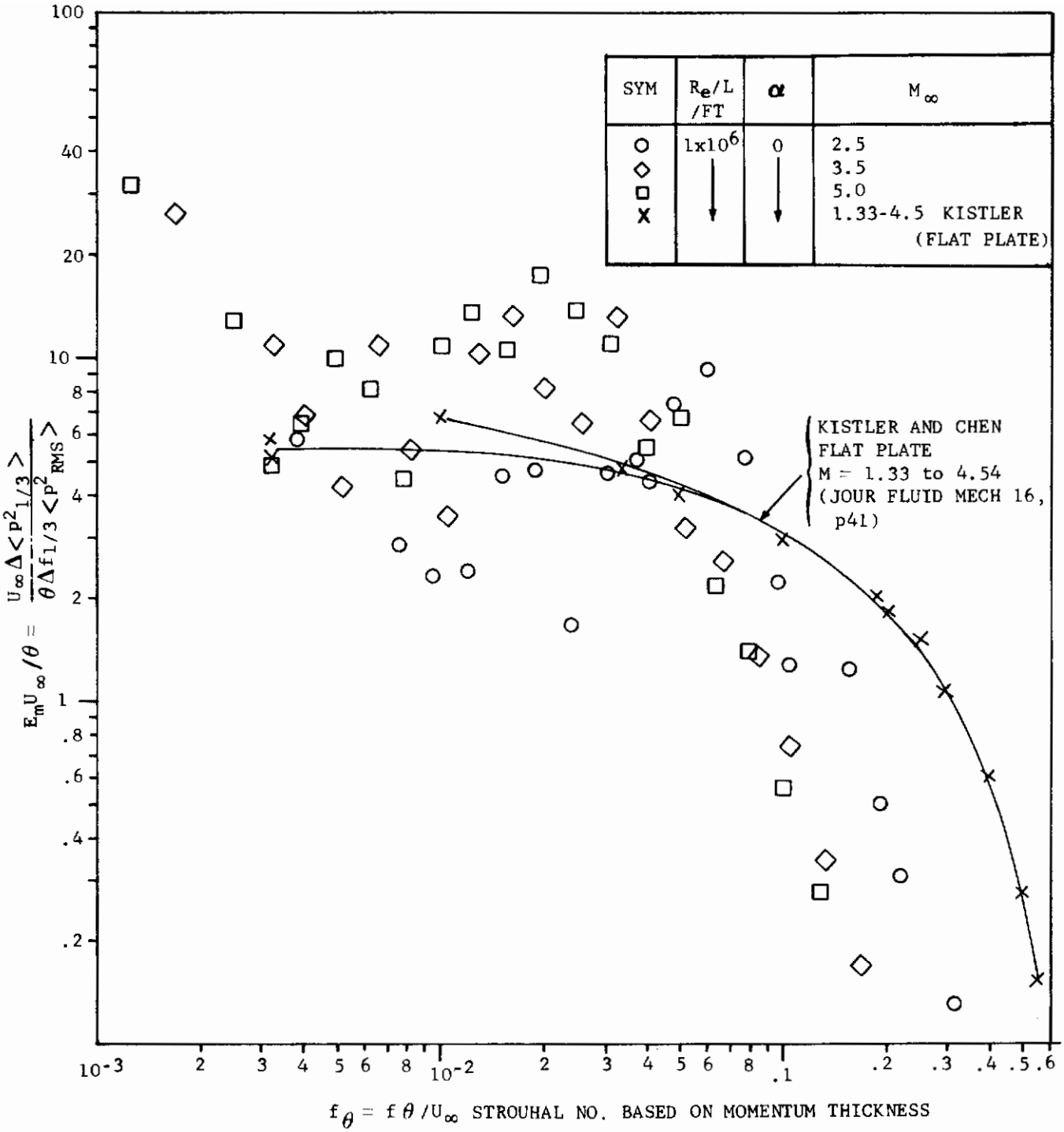

FIGURE 64 NON-DIMENSIONAL STROUHAL FREQUENCY SPECTRUM NORMALIZED TO MEAN SQUARED PRESSURE FLUCTUATION USING MOMENTUM THICKNESS AS A LENGTH DIMENSION, AXISYMMETRIC MODEL TRANSDUCER NO. 3

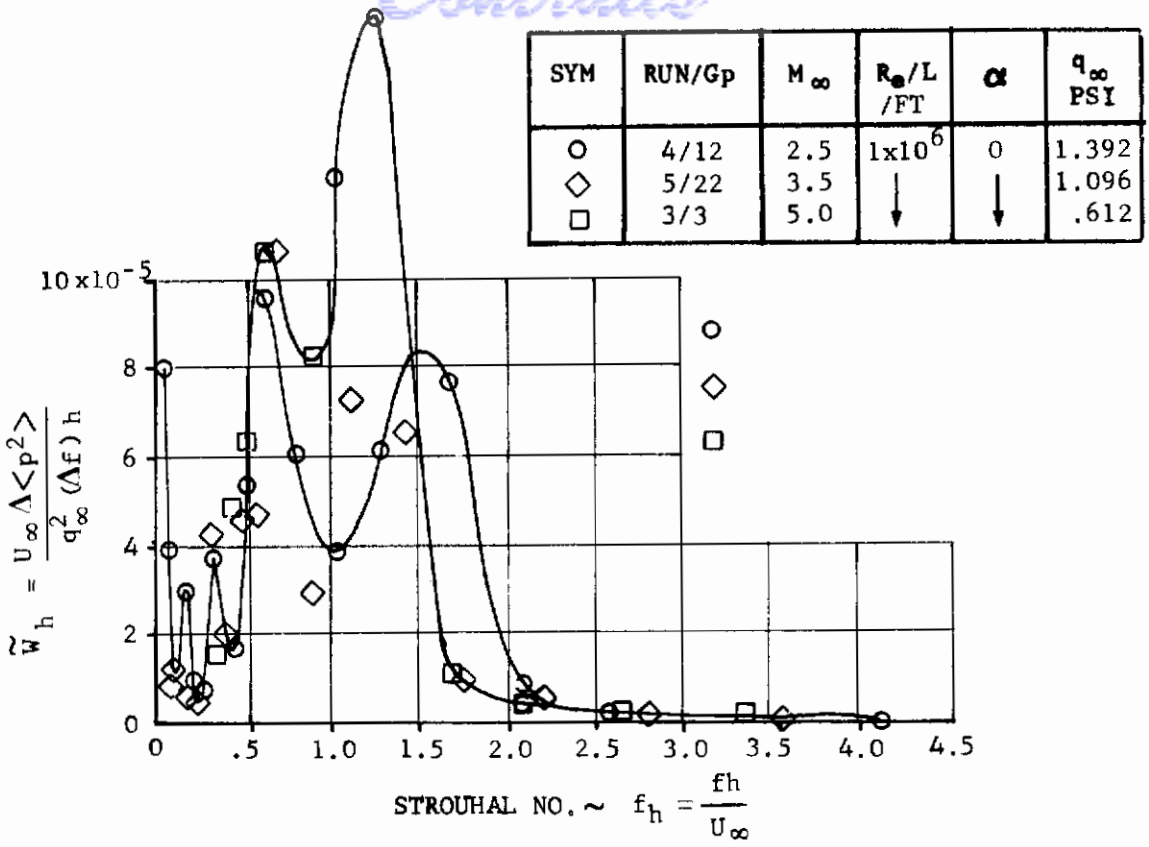

FIGURE 65 NON-DIMENSIONAL FREQUENCY SPECTRA DERIVED FROM 1/3 OCTAVE ANALYSIS, AXISYMMETRIC MODEL. ($h = r_b - r_{STING}$)

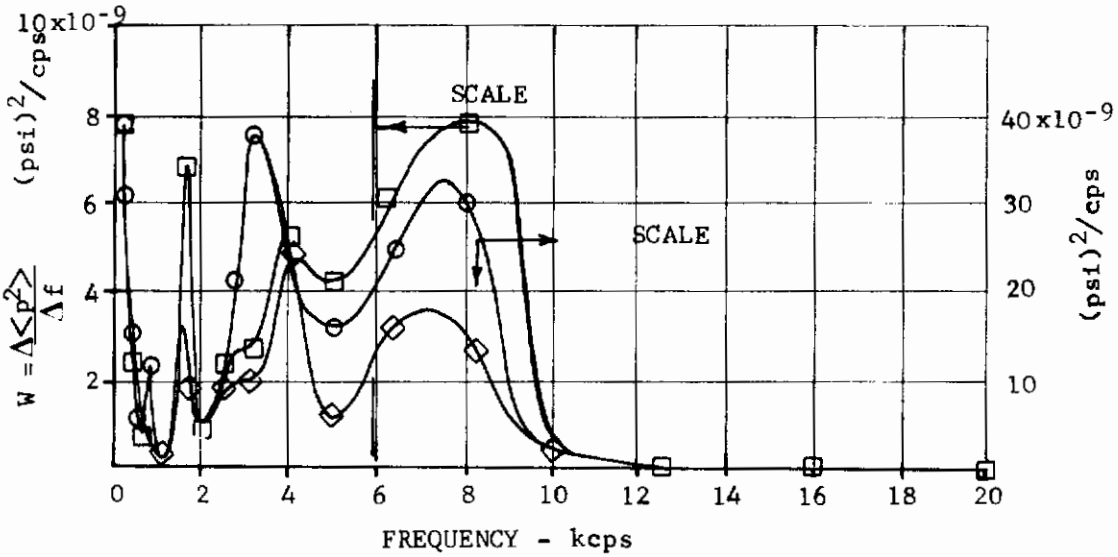

FIGURE 66 DIMENSIONAL FREQUENCY SPECTRA DERIVED FROM 1/3 OCTAVE ANALYSIS, AXISYMMETRIC MODEL. TRANSDUCER #6, D = 11.5 INCHES, $h = r_b - r_{STING}$ = 4.69 INCHES, r/r_b = .825

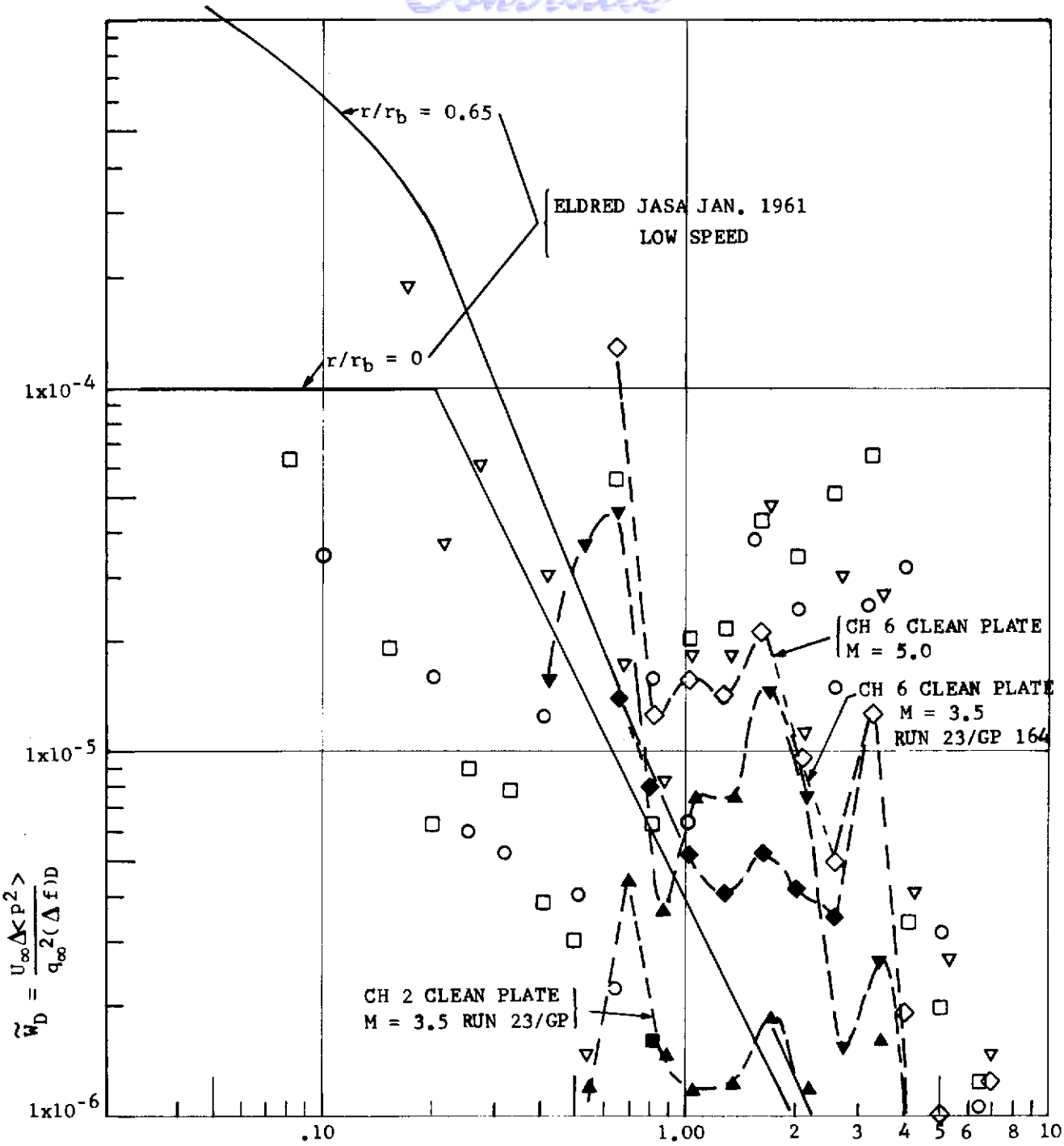

AXISYMMETRIC MODEL

SYM	CHANNEL	M
●	1	2.5
○	6	
△	1	3.5
▽	6	
■	1	5.0
□	6	

FLAT PLATE MODEL 0°

SYM	CHANNEL	M
☆	6	2.0
▲	2	3.5
▼	6	
◆	2	5.0
◇	6	

FIGURE 67 BASE PRESSURE DIMENSIONLESS FREQUENCY SPECTRA FOR VARIOUS MACH NUMBERS

$\alpha = 0$, Re/L = 1 x 10^6/ft. D_b = 11.5" CHANNEL 6 r/r_b = 0.825

a protuberance height based on $h = R_{base} - R_{sting}$ in an attempt to allow the finite center sting in the dimensionless Strouhal number correlation. Figure 67 shows a non-dimensional correlation using the gross diameter of the base (11.50 in. for these tests). Also shown in Figure 67 are lines representing Eldreds low speed based pressure tests (Ref. 12). The agreement for low Strouhal numbers is rather encouraging in view of the Mach numbers of the present tests. Also, because the wake thickness exceeds the flare protuberance height according to Figures 35 and 36; we have effectively a greater trailing edge boundary layer thickness to base diameter ratio, and probably a less steep mean velocity gradient in the shear layer between the base mixing region and the external stream than did Eldred. In the high Strouhal number region, $fD/U_\infty > 0.5$, the present data show large increases; however, it is to be noted that the background noise levels as measured by the same transducers on the clean plate configuration also exceed Eldred's spectrum level curve in Figure 67. This is regarded as a shortcoming of the present tests, due to the high wind tunnel background noise level; however, at supersonic speeds it does not follow that complete agreement with low speed results is to be expected, since there exist many flow noise producing interaction mechanisms (e.g., entropy, vorticity and acoustic) as discussed previously, and these behave as additional degrees of freedom. Experiments in a high speed low turbulence tunnel would be helpful with regard to this point.

RESULTS FOR THE FLAT PLATE MODEL

Boundary Layer and Aerothermodynamic Conditions

Measured Static Data

Figure 68 shows Mach number variation of the boundary layer displacement and momentum thicknesses for the 30° flap and 60° flap configurations. These were evaluated graphically from Figures 69 and 73 for $\alpha = 0$, $Re/L = 1 \times 10^6$/ft. Figure 70 shows the dimensional profiles of Mach number velocity and density for the 30° flap. Also shown in Figure 70 is the Mach 10 (Tunnel "C") velocity profile corrected for the measured stagnation temperature since the AEDC calculations were based upon assuming $T_t = T_o$ throughout the boundary layer. Figure 71 shows a comparison of the apparent boundary layer velocity based on assuming $T_t = T_o$ plotted against the true velocity ratio, based on local $T_t(z)$.

It is gratifying to note that for the Tunnel "A" tests, the calculated errors in velocity were negligible for stagnation temperature and model temperature range involved. In the case of Tunnel "C", there is a measurable difference which is, however, predictable using Crocos law for stagnation temperature variation across a boundary layer, derived for the special case of zero streamwise pressure gradient. Crocos law (Ref. 25, p. 327) gives

$$T_t(z) = T_w + \frac{U_{(z)}}{U_\infty} \left(T_0 - T_w \right) \qquad (136)$$

Figure 72 shows the angle of attack dependence of the dimensionless velocity profiles for the 30° flap. The angle of attack dependence of boundary layer data was not considered further because of the rather minor dependence of the fluctuating pressure on angle of attack for the range up to 15°. Figure 74 shows the free stream Mach number effect on the Mach number, density and velocity profiles in dimensional form to indicate the range of velocities and densities involved. Figure 75 shows the spanwise variation of the dimensionless boundary layer profiles for the 30° flap. Because of the complexity of the three-dimensional wake in the vicinity of the side edge, involving several vorticity components, no attempt has been made to explain the

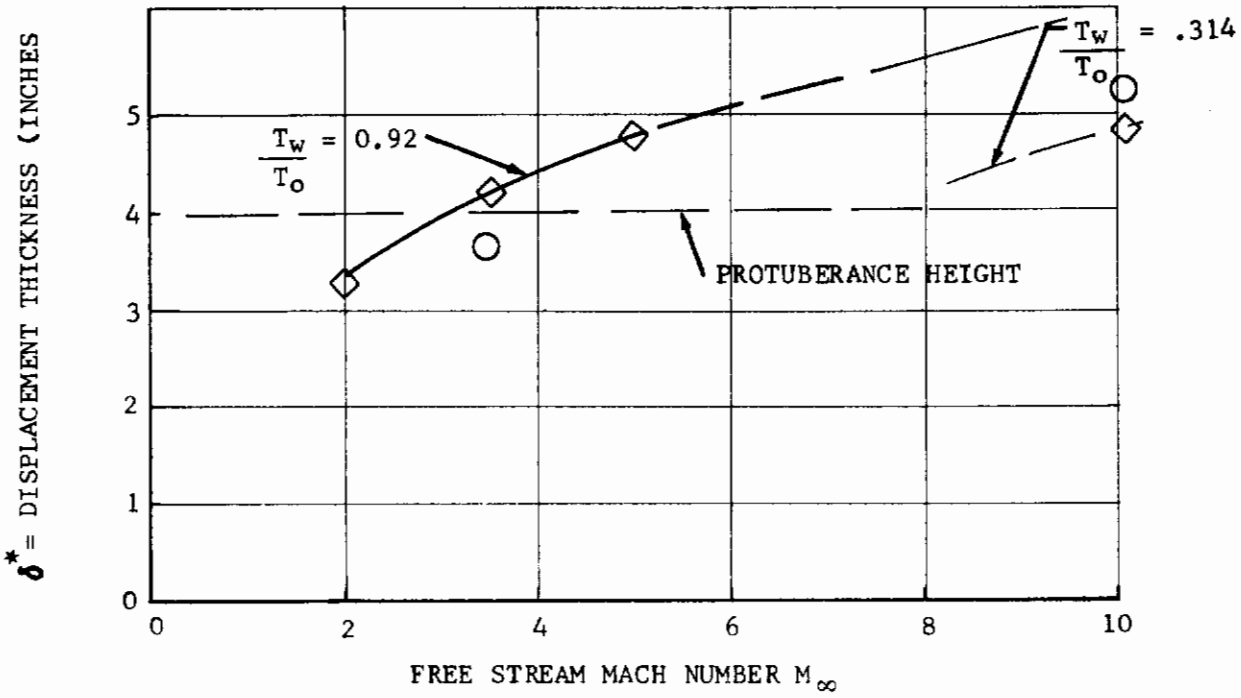

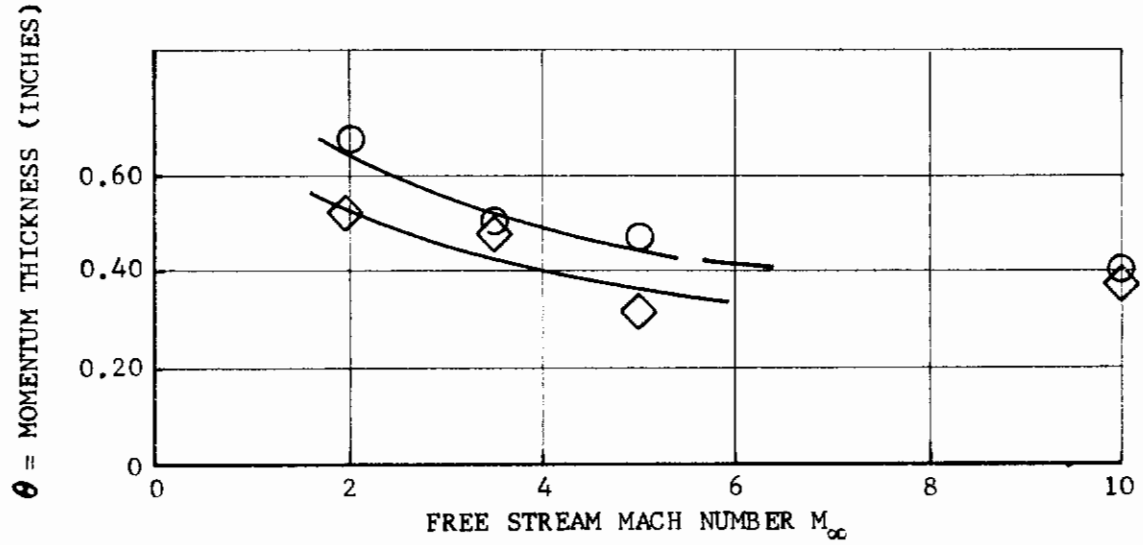

SYM	CONF	R_e/L /FT^{-1}	α	y /IN
◇	2(30°)	1×10^6	0	0
○	2(60°)			

FIGURE 68 DISPLACEMENT THICKNESS AND MOMENTUM THICKNESS VS MACH NUMBER. FLAT PLATE MODELS (BASED ON GRAPHICAL INTEGRATION AND FREE STREAM CONDITIONS)

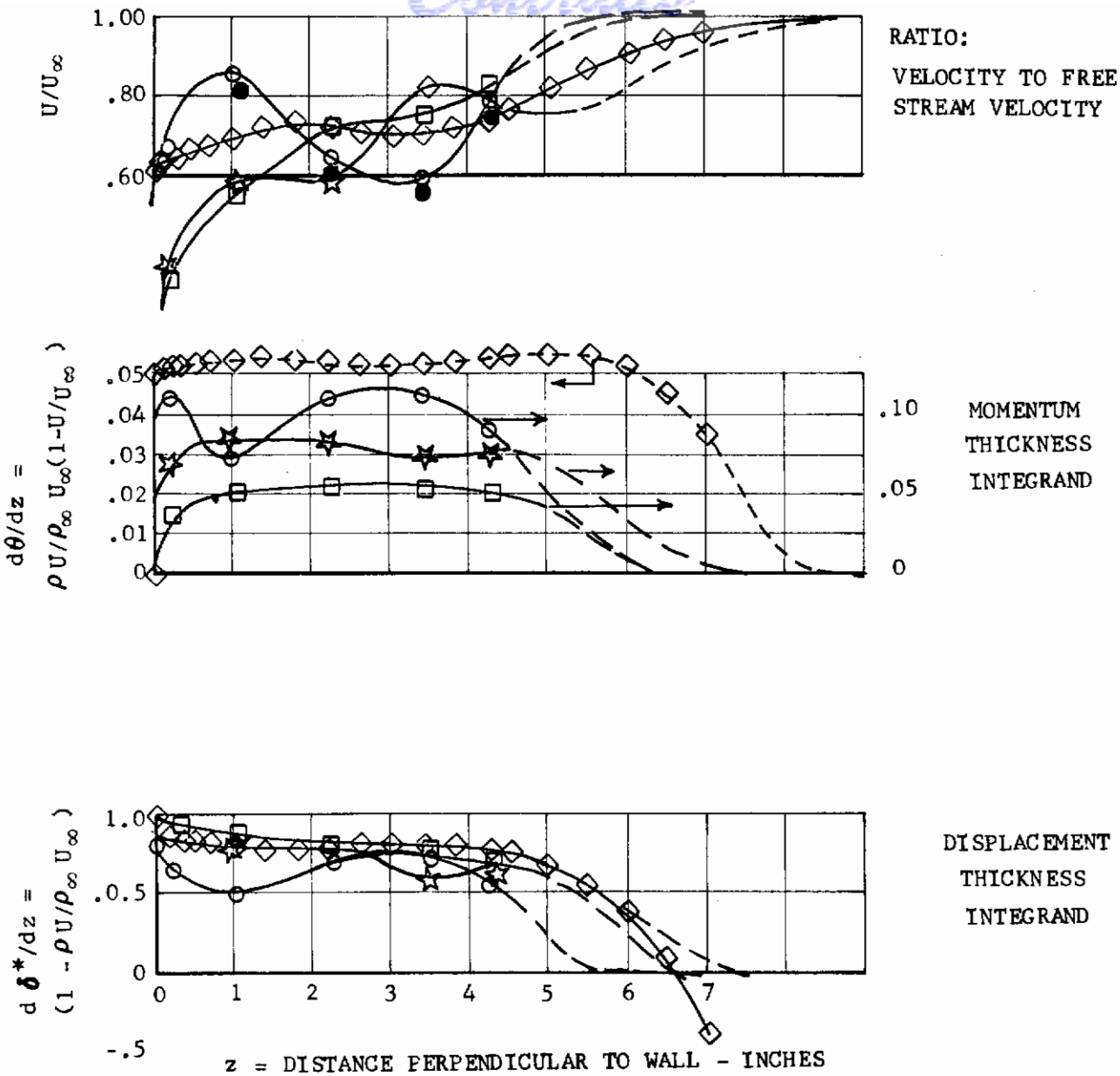

SYM	RUN/Gp	M_∞	R_e/L /FT	α	P_o PSIA	T_o °R	q_∞ PSI	U_∞ FT/SEC
●	34/226	1.98	$.6\times10^6$	0	4.238	550	1.533	1705
○	34/222	1.98	1×10^6	↓	9.638	582	1.102	2220
☆	33/216	3.48	↓	↓	18.48	561	.621	2370
□	32/207	4.98	↓	↓	↓	↓	↓	↓
◇	1/29	10.13	↓	↓	↓	↓	↓	↓
◇	3/38	↓	↓	↓	758.2	1797	1.137	4550

ASSUMPTIONS: P_e = LOCAL WALL PRESSURE AND $P_e = P_o = M_e$
$T_t = T_o$ = Const

FIGURE 69 EFFECT OF MACH NUMBER ON THE NON-DIMENSIONAL BOUNDARY LAYER DISTRIBUTIONS (30° FLAP CONFIG, y = 0, α = 0 Re/L = 10^6/Ft)

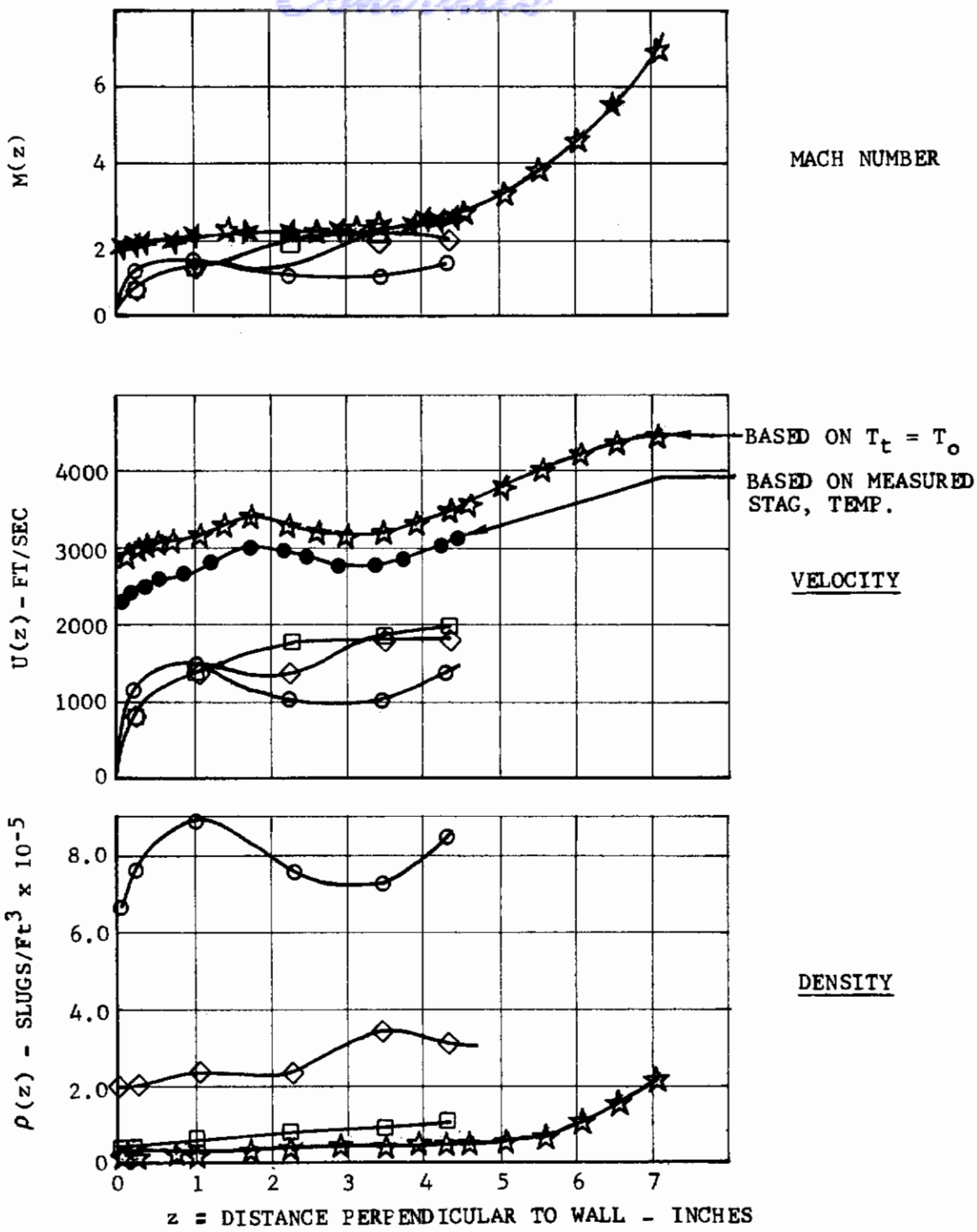

	SYM	RUN/Gp	M_∞	R_e/L /FT	α	P_o PSIA	T_o °R	q_∞ PSI	U_∞	y
TUNNEL A	○	34/222	2.0	1×10^6	0	4.24	550	1.533	1705	0
	◇	33/216	3.5	↓	↓	9.64	582	1.102	2220	
	□	32/207	5.0			18.17	561	.621	2370	
TUNNEL C	●	4/45	10.13			758.5	1795	1.138		
	★	1/29	10.13			763.0	1793	1.145	4550	22
	☆	3/38	10.13			758.2	1797	1.137		

FIGURE 70 EFFECT OF MACH NUMBER ON THE BASIC BOUNDARY LAYER DISTRIBUTIONS (30° FLAP) CENTER RAKE (y = 0), $\alpha = 0$, Re/L = 1 x 10^6/ft.

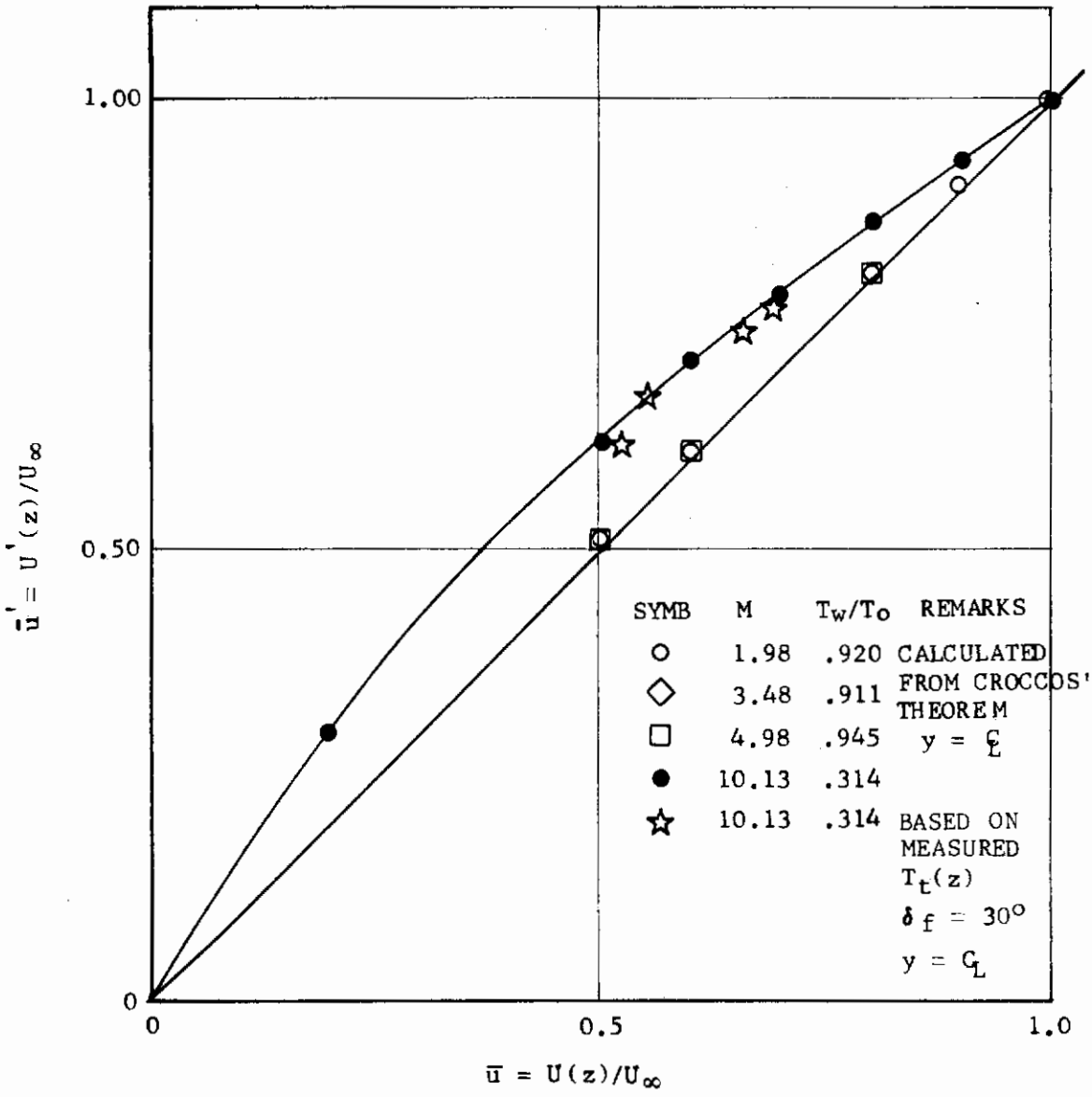

FIGURE 71 CORRECTION FOR "TRUE" VELOCITY BASED ON CROCCOS' THEOREM* FOR STAGNATION TEMPERATURE AND COMPARISON WITH EXPERIMENT

*U(Z) BASED ON $T_t(Z) = T_w + \bar{u}\ (T_o - T_w)$

U'(Z) BASED ON $T_t(Z) = T_o$ (FROM AEDC CALCULATIONS)

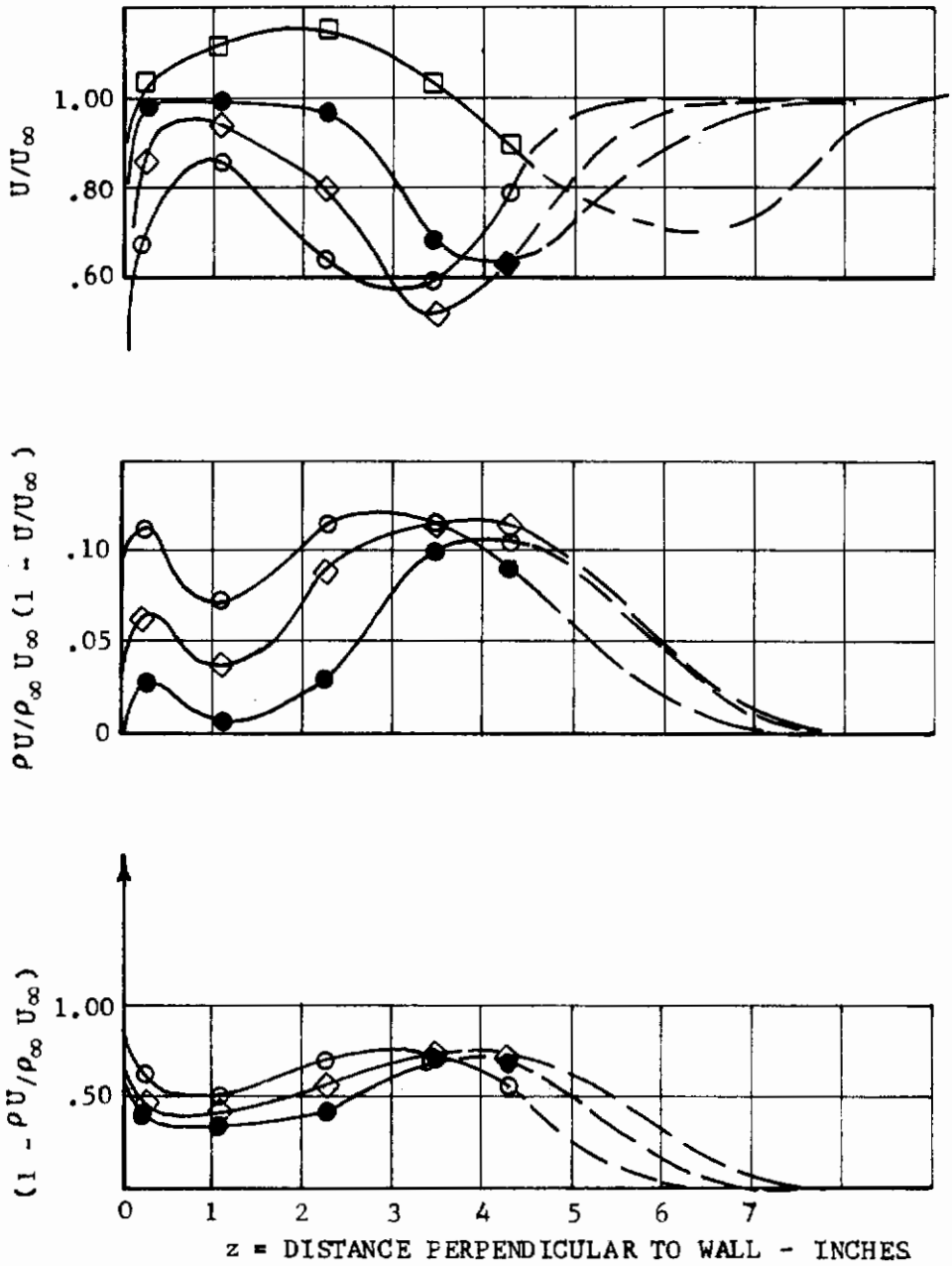

SYM	RUN/Gp	M_∞	R_e/L /FT	α	y
○	34/222	20	1×10^6	0	0
◇	34/223	↓	↓	5	↓
●	34/224			10	
□				14.7	

ASSUMPTIONS: P_e = LOCAL WALL PRESSURE
$T_t = T_o$ = CONST

FIGURE 72 ANGLE OF ATTACK EFFECT ON THE NON-DIMENSIONAL BOUNDARY LAYER DISTRIBUTIONS (30° FLAP M = 2, Re/L = 1 x 10^6/Ft y = 0")

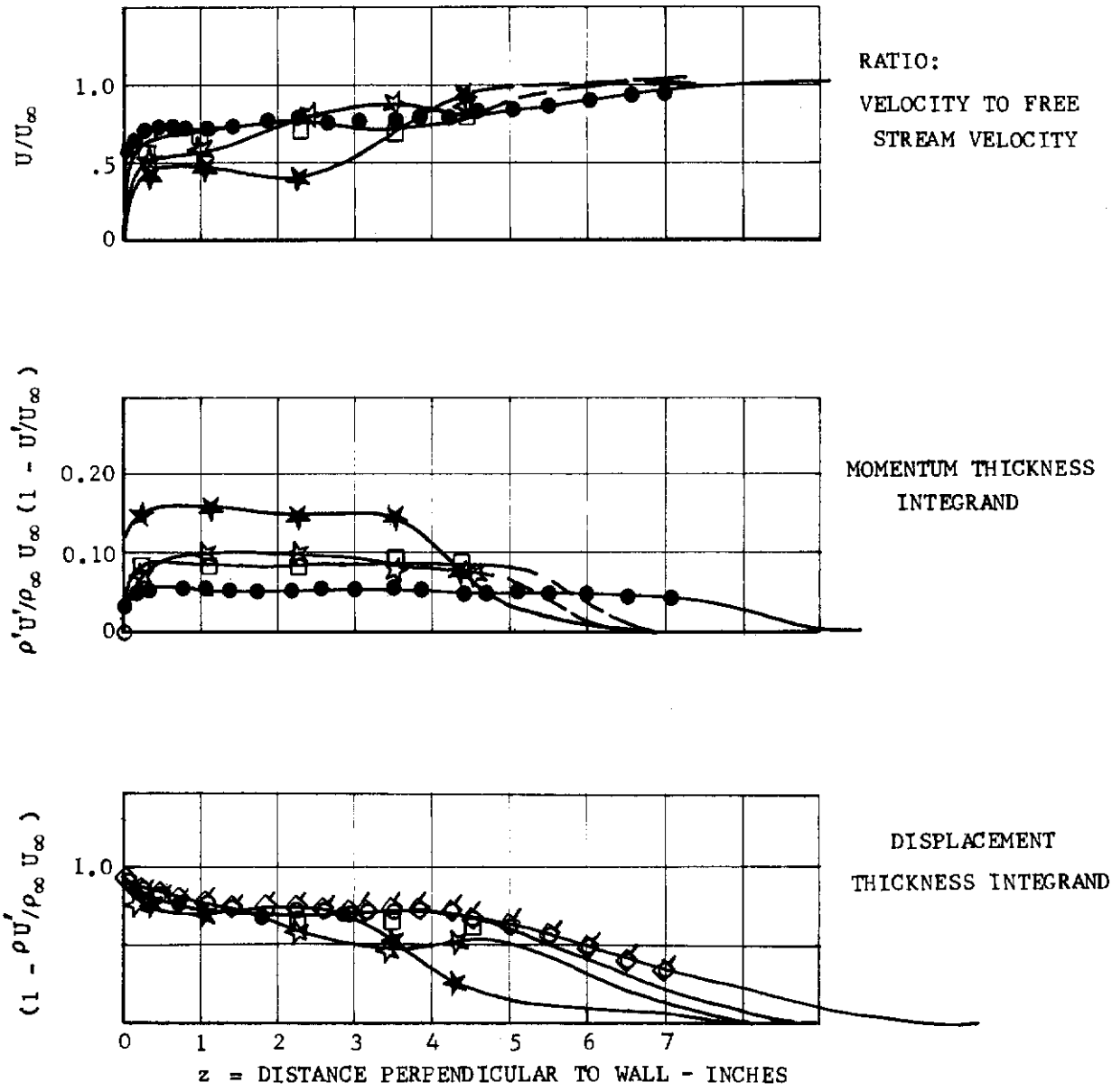

	SYM	RUN/Gp	M_∞	R_e/L	α	P_o PSIA	T_o °R	q_∞ PSI	y	U_∞ FT/SEC
Tunnel A ↓	★	35/228	2.0	1×10^6	0	4.21	552	1.525	0"	1700
	☆	36/237	3.5	↓	↓	9.67	583	1.106	↓	2260
	□	37/242	5.0	↓	↓	18.33	565	.615	↓	↓
Tunnel C ↓	●	1/34	10.0	↓	↓	749.2	1790	1.125	↓	↓
	◇	3/31	↓	↓	↓	↓	↓	↓	↓	↓
	○	3/40	↓	2×10^6	↓	757	1800	1.135	↓	↓

ASSUMPTIONS: P_e = LOCAL WALL PRESSURE

$T_t = T_o$ = CONST 0

FIGURE 73 EFFECT OF MACH NUMBER ON THE NON-DIMENSIONAL BOUNDARY LAYER DISTRIBUTIONS (60° FLAP)
CENTER RAKE (y = 0), α = 0, Re/L = 1 x 10^6/Ft

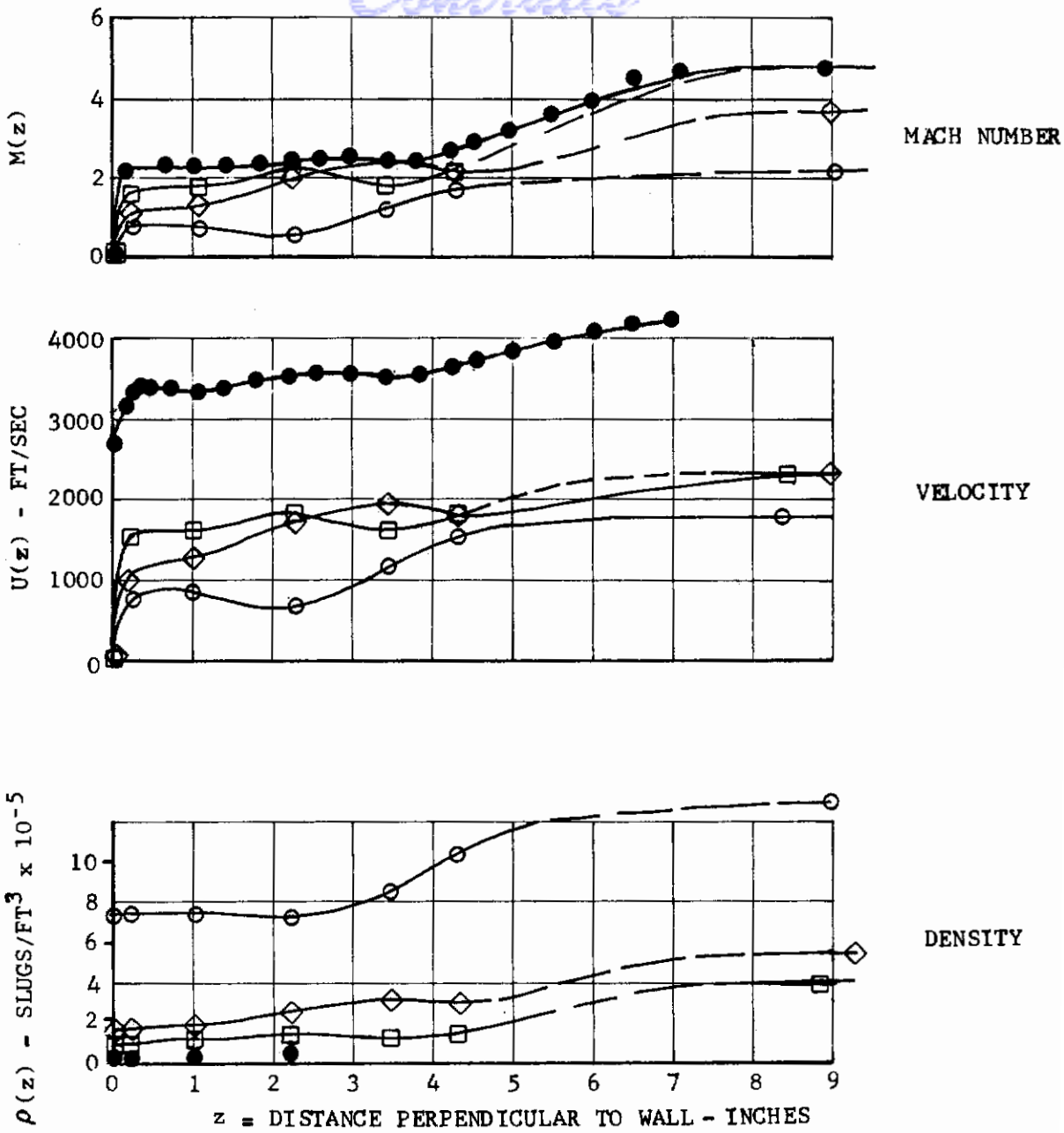

	SYM	RUN/Gp	M_∞	R_e/L /FT	α	P_o PSIA	T_o °R	q_∞ PSI	M_e
Tunnel A	○	35/228	1.98	1×10^6	0	4.20	552	1.52	2.14
	◇	36/237	3.48	↓	↓	9.67	583.5	1.106	3.65
	□	37/242	4.93			18.38	565.5	.615	4.68
Tunnel C	●	(1/34 3/39)	10.13			749.2	1790	1.125	
						757.0	1800	1.135	

FIGURE 74 EFFECT OF MACH NUMBER ON THE BASIC BOUNDARY LAYER DISTRIBUTIONS (60° FLAP) CENTER RAKE: (y = 0), α = 0 Re/L = 1×10^6/FT

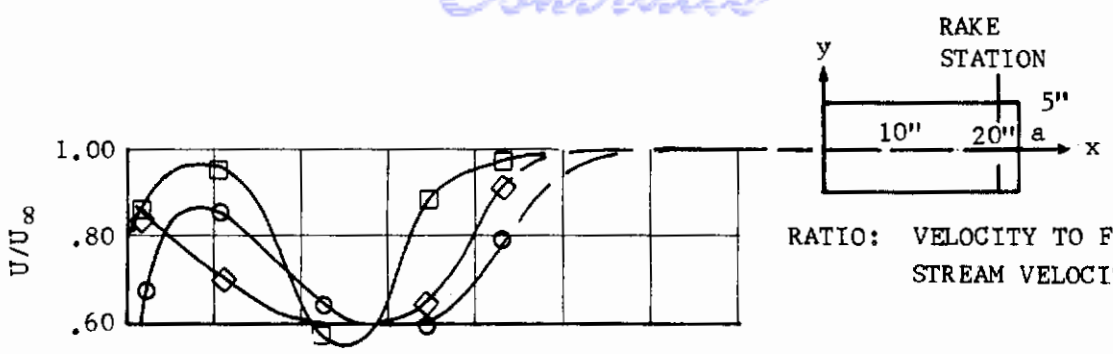

RATIO: VELOCITY TO FREE STREAM VELOCITY

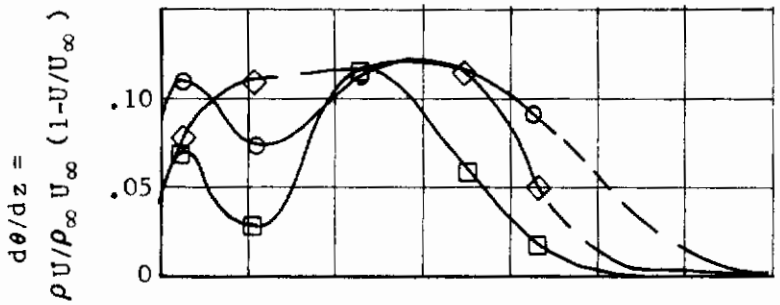

MOMENTUM THICKNESS INTEGRAND

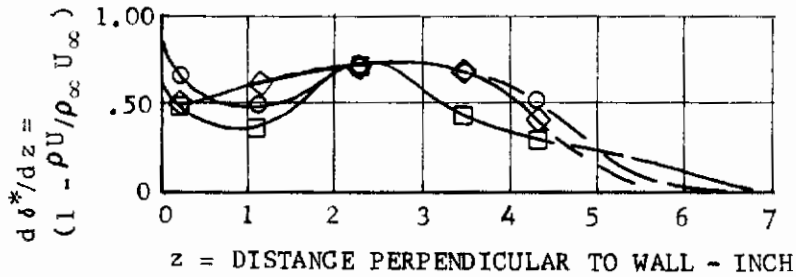

DISPLACEMENT THICKNESS INTEGRAND

z = DISTANCE PERPENDICULAR TO WALL - INCHES

SYM	RUN/Gp	M_∞	R_e/L	α	P_o PSIA	T_o ^oR	q_∞ PSI	y
○	34/222	1.98	$1x10^6$	0	4.238	550	1.533	0"
◇	↓	↓	↓	↓	↓	↓	↓	2"
□	↓	↓	↓	↓	↓	↓	↓	4"

ASSUMPTIONS: P_e = LOCAL WALL PRESSURE

$T_t = T_o$ = CONST

FIGURE 75 SPANWISE VARIATION OF NON-DIMENSIONAL BOUNDARY LAYER DISTRIBUTIONS (30° FLAP CONFIG) M = 2, α = 0 Re/L = 1 x 10^6/Ft

reasons for the structure of the steady boundary layer profiles, but rather they are presented in the interest of documentation of factors in the steady flow field that may be of interest when applying the pressure fluctuation data of the present tests to other aerodynamic situations where one might have access to data concerning the spanwise variation of boundary layer or wake profiles. We next consider the streamwise variations of static pressure and associated quantities.

Figures 76, 77 and 78 show the chordwise distribution of the static pressure coefficient, C_p. Also shown in Figure 76 are the variations of model surface temperature for the Tunnel "C" tests. The temperatures at y = -1.13 inches are in the water cooled region near the transducers and are seen to be less than 200F. The outer edge temperatures (y = 4 inches) are higher because heat conduction in the plane of the model surface is the only means by which heat can be transferred internally to cool this outer region. The main purpose of the surface thermocouples was to monitor the effectiveness of the water cooling system which was designed to produce a low temperature environment in the neighborhood of the transducer installations and in the interior cavity of the model where the electrical leads were housed. Figure 76 is typical of the surface temperature environment, and indicates the successful functioning of the water cooling system for the Tunnel "C" tests at Mach 10.

The static pressure distributions for the flat plate show C_p nearly zero as one would expect at $\alpha = 0$ (Figure 76). In the case of the 30° flap, the pressures behind and beneath the flap are strongly negative. These features are characteristic of a base pressure region, in this case downstream of the bluff flap protuberance. The pressure increase near the trailing edge is caused by recompression of the outer flow expansion region on the inviscid flow at the trailing edge of the flap. Figure 78 shows a similar pressure distribution for the 60° flap, this is because the reattachment of the separated flow is not much affected by the upstream conditions when the upstream boundary layer is thin compared to the dimension of the protuberance height. An attempt was made to calculate boundary layer edge Mach numbers; however, this effort was abandoned, because the large stagnation pressure losses associated with the strong oblique and curved detached shocks caused the boundary layer edge stagnation pressure to be uncertain at the downstream wake station. This was especially so for the Tunnel "A" tests, where the total pressure probes did not extend far enough out in the flow to detect the boundary between the inner "viscous" wake and the outer "entropy" wake. Even in the case of the Tunnel "C" tests at Mach 10, it was difficult to clearly distinguish between stagnation pressure losses, due to turbulent mixing in the wake on one hand, and due to strong shock loss variations caused by the rapidly changing shock wave angle beyond the edge of the protuberance. This was especially the case with the 30° flap Mach number profile (Figure 70), where the shock curvature commences closer to the model. In Figure 68, for the 60° flap, the Mach number appears to reach a plateau. It can be conjectured from the Schlieren photos (Figures 91 through 96 below) that the curvature of the detached shock ahead of the 60° flap is displaced outwards, so that the oblique plus normal shock stagnation pressure loss in the region $0 \leq z < 7$ inches was nearly constant. At $M_\infty = 10$, $M(z) \cong 5$, for $6 < z < 7$ inches from the wall, according to Figure 37. This low Mach number is a consequence of the considerable shock induced stagnation pressure loss. Because it was not possible to delineate an unambiguous "local free stream Mach number", the boundary layer quantities θ and δ^* were referred to conditions at infinity. These momentum and displacement thicknesses, therefore, reflect a certain amount of "non-viscous" stagnation pressure loss; because of this fact, we hold some reservations with regard to the use of these parameters in the non-dimensionalized frequency spectra, since one cannot expect these to be uniquely related to any turbulence scale. They do serve, however, to define more general parameters for characterizing wakes and "separated flows," where many different upstream flow mechanisms

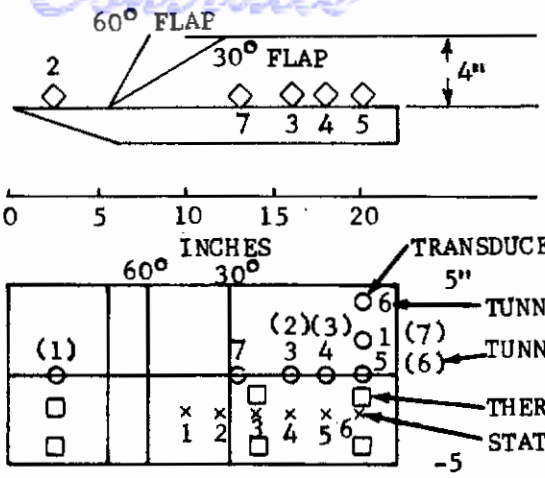

INSTRUMENTATION

STATIC PRESSURE COEFFICIENT

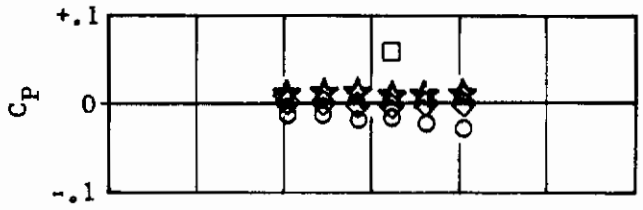

LOCAL WALL TEMPERATURE (°F)

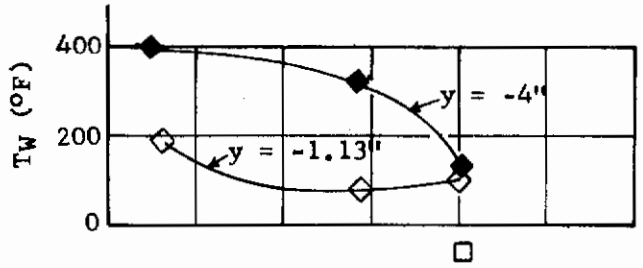

RMS $\Delta P/q_\infty$

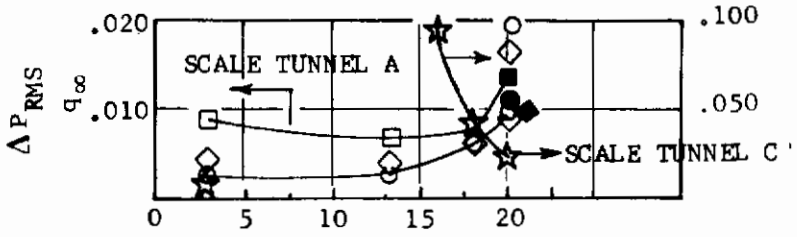

	SYM	RUN/Gp	M_∞	R_e/L /FT^{-1}	α	P_o PSIA	T_o °R	q_∞ PSI
TUNNEL A	○	22/156	1.98	1×10^6	0	4.30	552	1.555
	◇	23/164	3.48	↓	↓	9.71	582	1.109
	□	24/171	4.98			18.31	563	.615
TUNNEL C	☆	1/1C	10.13	1×10^6	0	758.5	1810	1.136
	●◆■	XDCR NO. 6						

FIGURE 76 MACH NO. COMPARISON, FLAT PLATE MODEL (0° FLAP), $\alpha = 0$, $Re/L = 1\times10^6$/FT.

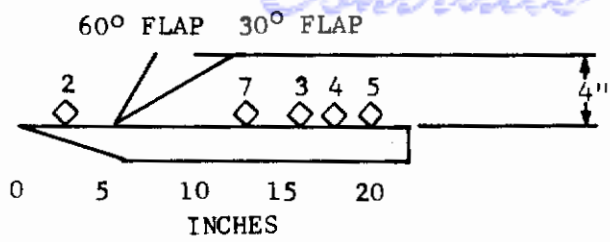

INSTRUMENTATION

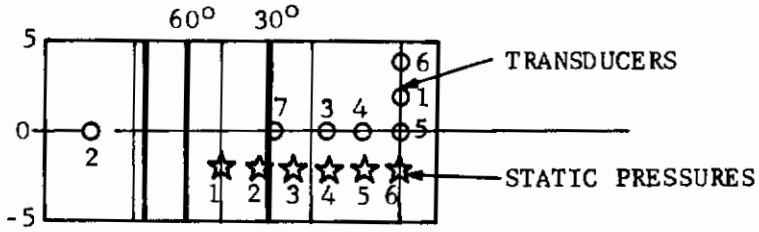

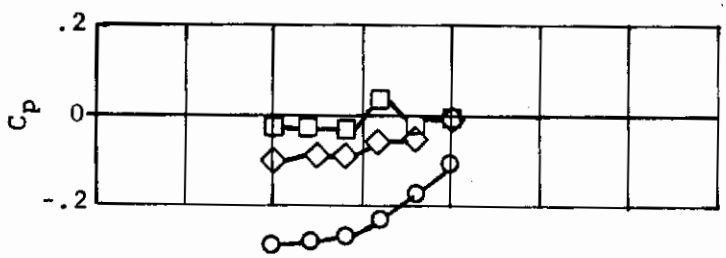

STATIC PRESSURE COEFFICIENT

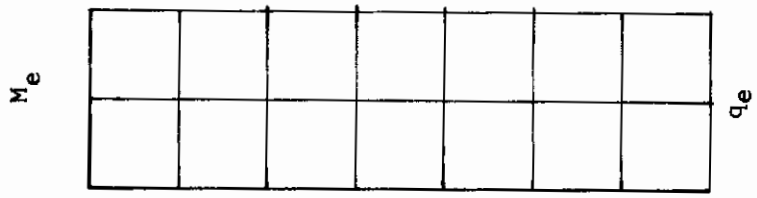

LOCAL MACH NUMBER AND DYNAMIC PRESSURE - q

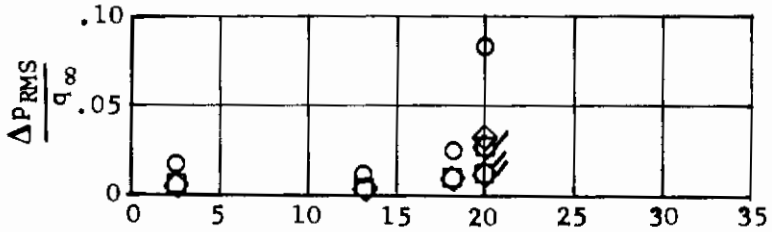

RMS $\Delta p/q_\infty$

FLAG DENOTES XDCR #6

SYM	RUN/Gp	M_∞	R_e/L /FT	α	P_o PSIA	T_o °R	q_∞ PSI
○	16/117	1.98	$1x10^6$	0	4.26	550	1.54
◇	17/127	3.48	↓	↓	9.65	584	1.10
□	18/134	4.98	↓	↓	18.60	561	.622

FIGURE 77 MACH NUMBER COMPARISON (30° FLAP) $\alpha = 0$, $R_e/L = 1x10^6$/FT. FLAT PLATE MODEL

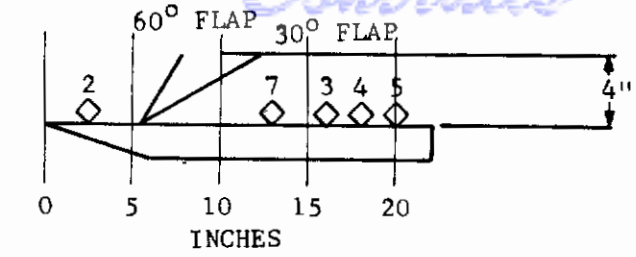

INSTRUMENTATION

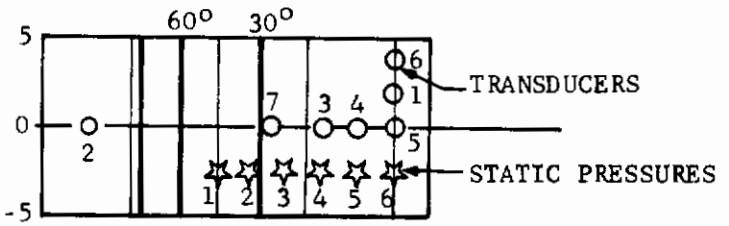

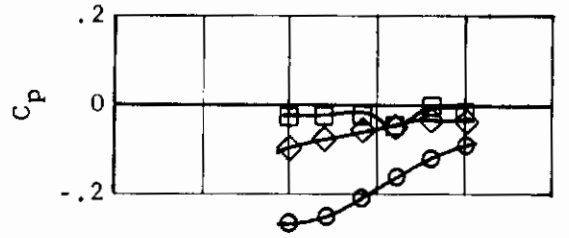

STATIC PRESSURE COEFFICIENT

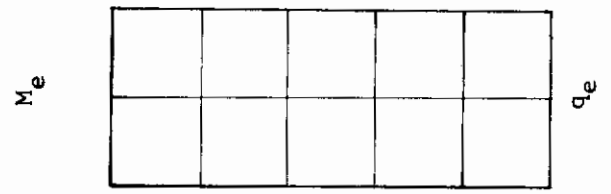

LOCAL MACH NUMBER
AND
DYNAMIC PRESSURE - q

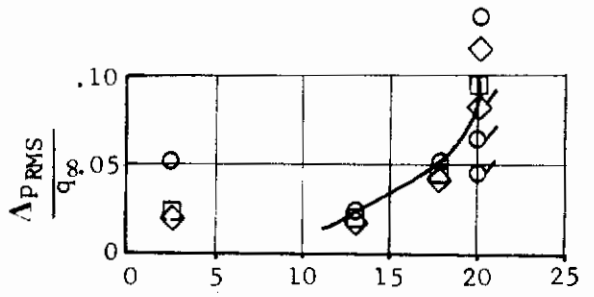

RMS $\Delta p/q_\infty$

FLAG DENOTES XDCR #6

SYM	RUN/Gp	M_∞	R_e/L /FT	α	P_o PSIA	T_o °R	q_∞ PSI
○	21/150	1.98	$1x10^6$	0	4.34	551	1.57
◇	20/145	3.48	↓	↓	9.73	582	1.12
□	19/140	4.98	↓	↓	18.61	567.5	.625

FIGURE 78 MACH NUMBER COMPARISON (60° FLAP) α = 0, $R_e/L = 1x10^6$/FT. FLAT PLATE MODEL

might have occurred which result in a similar mean velocity profile at a downstream station of interest. It is hoped that by providing this type of aerothermodynamic supporting data that the pressure fluctuation measurements can possibly be applied to other separated flows having similar downstream mean flow profiles.

Visual Data, Schlieren Photographs - Tunnel "A"

Figures (79 through 84) show the Schlieren photographs of the clean flat plate (0° flap) case for various Mach number and pressure conditions at zero angle of attack. Figure (85 through 90) show pictures of the flow past the 30° flap configuration at zero angle of attack for various Mach numbers and pressure levels. Figures (91 through 96) show similar pictures for the 60° flap configuration. We shall discuss the Tunnel "A" pictures. (Shadow-graph pictures were requested for the Tunnel "C" tests, but the pictures were deemed unsatisfactory by AEDC and are not available.)

The clean plate pictures, Figures (79 to 84) illustrate the nature of the free tunnel flow for the supersonic Tunnel "A" tests. Because the plate leading edge was blunted to reduce the heat transfer, a finite curved bow shock was obtained. Also, the wedge on the lower surface (used to increase the depth of the model to provide space for the internal instrumentation) caused a finite oblique compression shock, followed by a Prandtl-Meyer expansion region where the flow adjusts to the free stream direction. The possible importance of this lower surface wedge compression is that it tends to cause a cross flow past the side edges, tending to thicken the side edge boundary layer ahead of the flaps, and probably tending to increase the susceptibility of the boundary layer ahead of the flap to shock induced separation. One can see that the trailing edge boundary layer is of the order of 0.4 inches in thickness which confirms the calculations discussed in connection with the expected turbulent pressure fluctuations on the clean plate discussed earlier in Section V. The variations in background light intensity are gradients in the free stream density field. In comparing the photos, it must be remembered that the free stream density levels vary with Mach number and stagnation pressure level, so that it would be difficult to assess any percentage changes in the free stream density fluctuations, even on a qualitative basis. The side view Figure 81 shows a more rapid growth of the side edge boundary layer, probably caused by the cross flow due to the lower wedge compression discussed above.

For the 30° flap configurations, the flow structure is characterized by attached oblique shocks at M_∞ = 3.5 and 5.0. At Mach 2, there appears to be shock induced flow separation ahead of the flap (Figures 85 and 86). At Mach 2.0, the curved bow shock interacts with the oblique shock from the flap well outside the boundary layer survey region. Another feature of the flow at Mach 2.0 is a noticeable secondary oblique shock ahead of the oblique shock on the flap which is probably due to the displacement effect of the thick, shock-separated boundary layer ahead of the flap. The thickening of the boundary layer ahead of the flap gives rise to an outer viscous shear layer at the point where the upstream boundary layer on the flap separates from the trailing edge of the flap. This may have an effect on the intensity of turbulent pressure fluctuations downstream by alteration of the mean velocity gradients which play an important role in the turbulent pressure problem for incompressible flow (see Section II). The thickness of the upstream boundary layer is also an important parameter in the steady flow structure downstream of any blunt body and is important in the base pressure problem (Refs. 14, 15).

The 60° flap configuration was chosen because it leads to a detached shock wave at all supersonic Mach numbers. This fact is clearly evident in Figures (91 to 96). This detached shock wave interacts with the boundary layer upstream of the wedge causing extensive flow separation; this is especially violent at Mach 2.0 and persists for all Mach numbers. At the high Mach numbers, the detached shock standoff

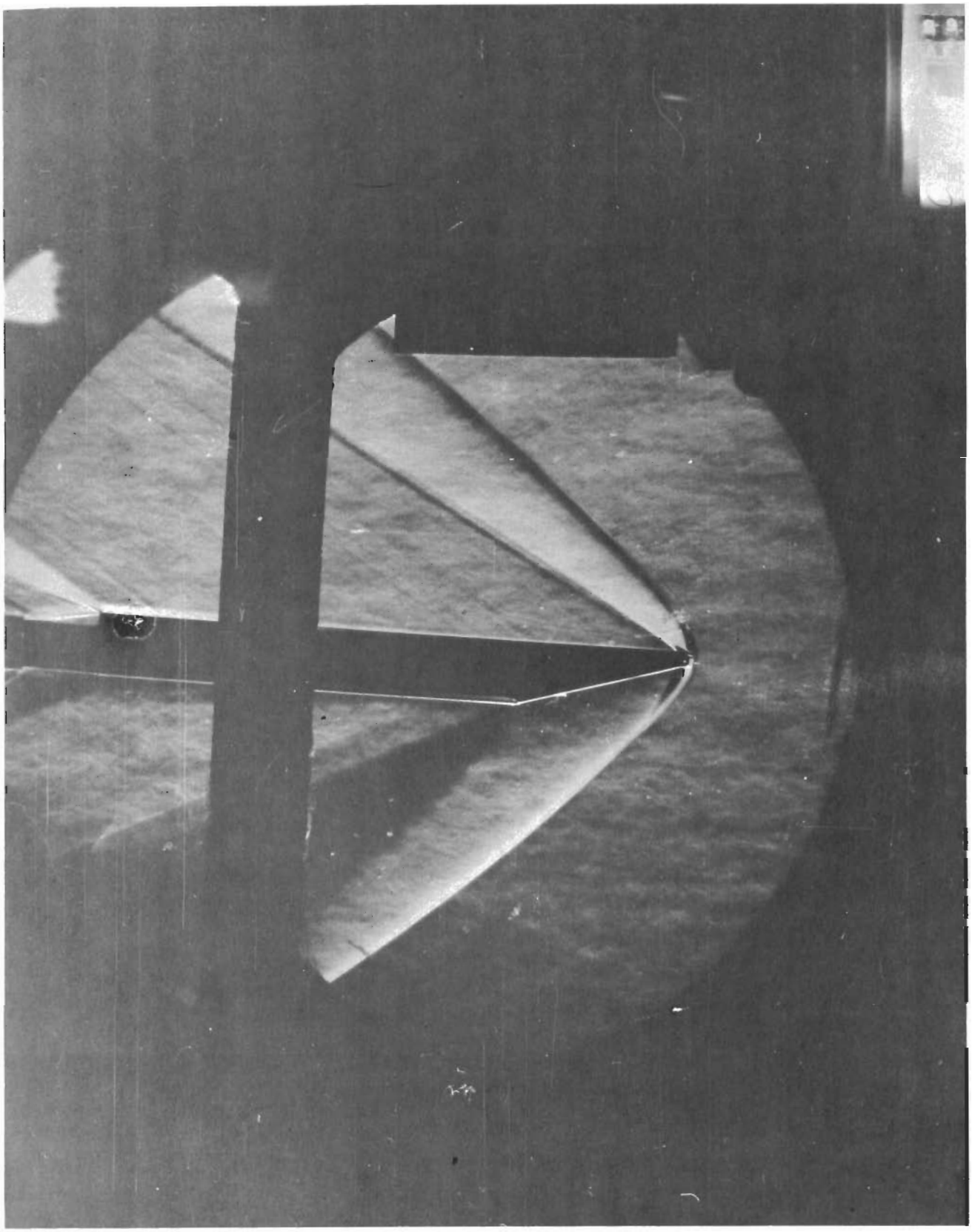

FIGURE 79 TWO-DIMENSIONAL MODEL, CLEAN CONFIGURATION, $M = 2$, $P_o = 4$, $T_o = 90F$, $\alpha = 0$, $\phi = -90^o$

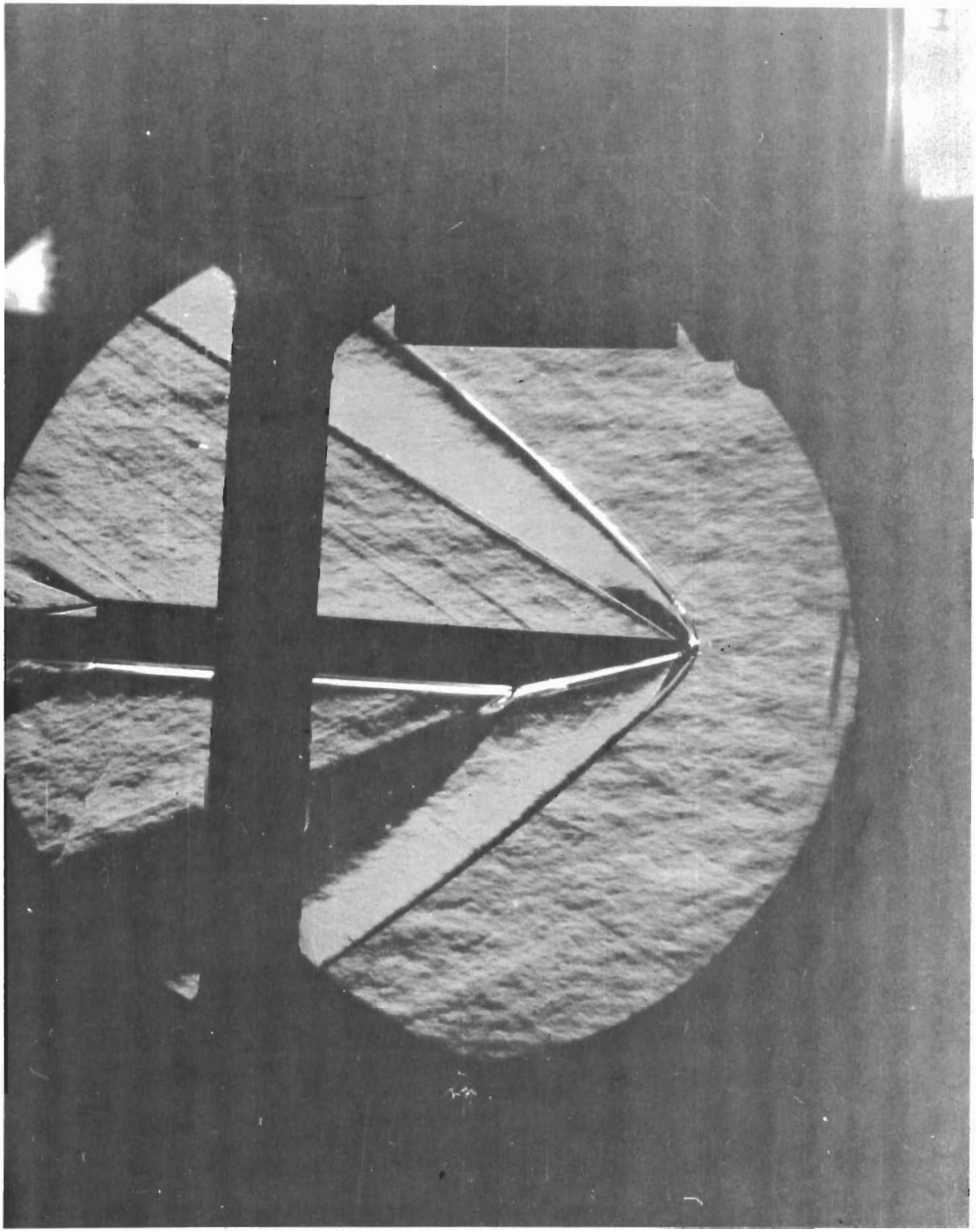

FIGURE 80 TWO-DIMENSIONAL MODEL, CLEAN CONFIGURATION, $M = 2$, $P_o = 19.2$, $T_o = 90F$, $\alpha = 0$, $\phi = -90^o$

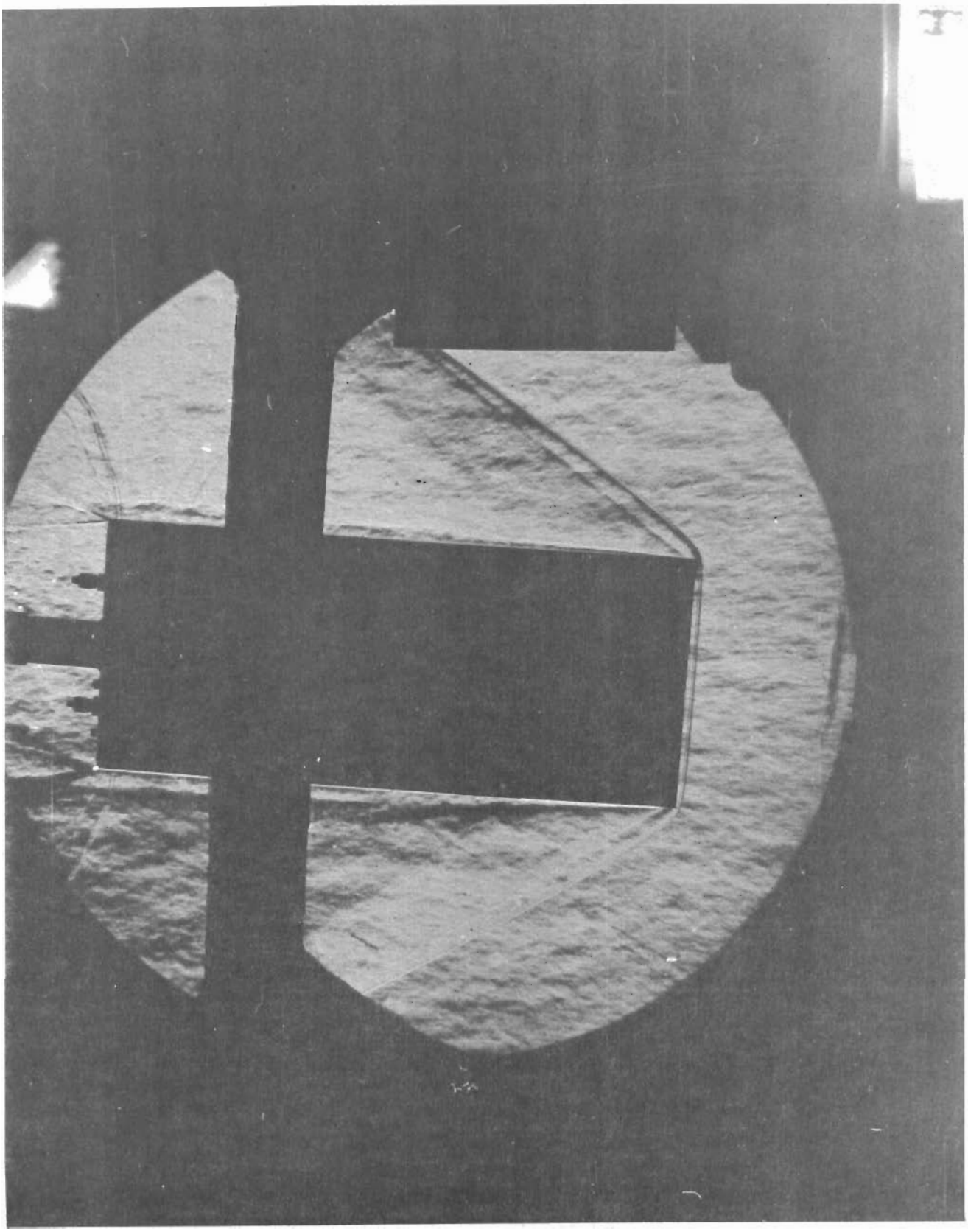

FIGURE 81 TWO-DIMENSIONAL MODEL, CLEAN CONFIGURATION, M = 2, P_o = 19.2, T_o = 90F, $\alpha = \phi = 0$

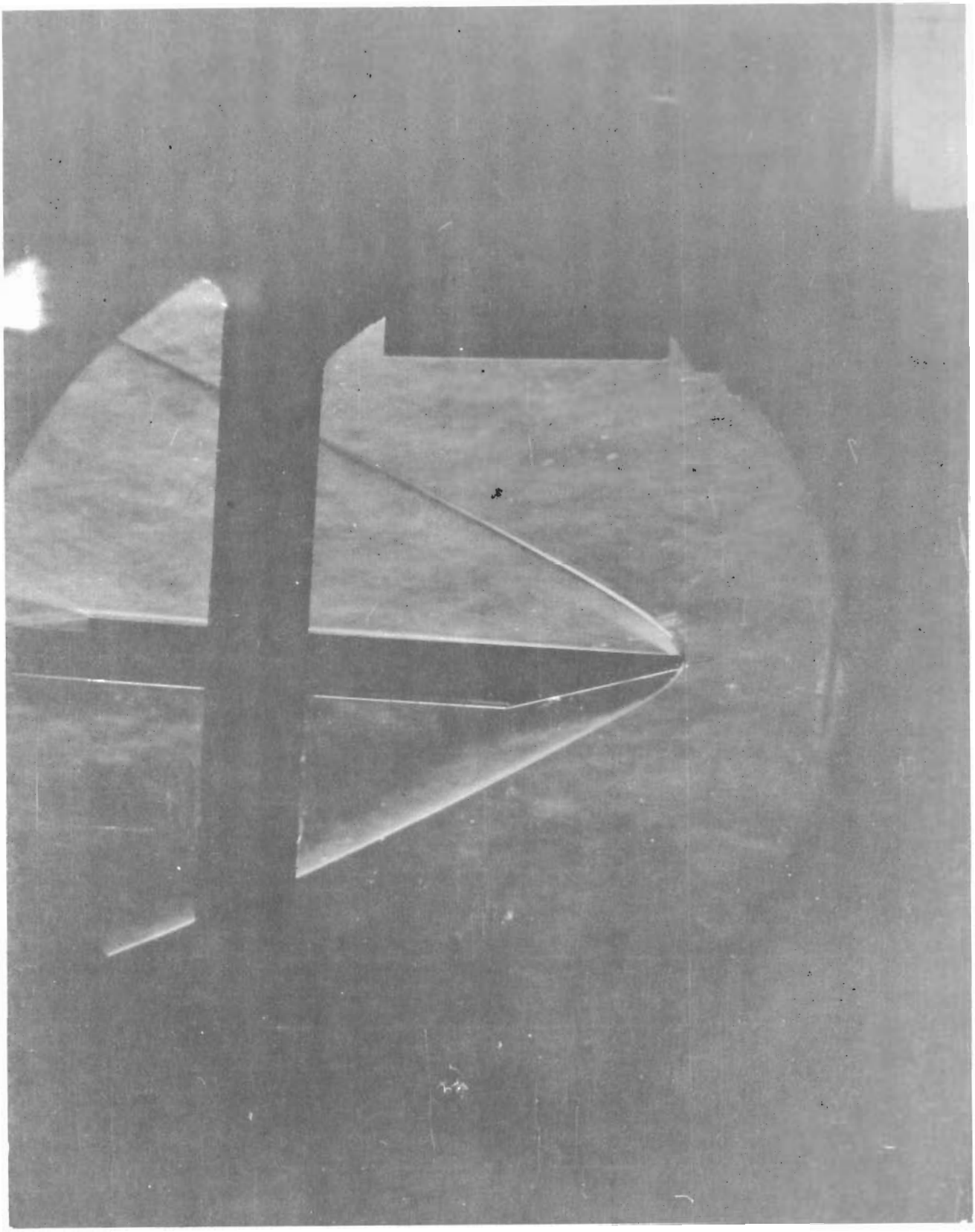

FIGURE 82 TWO-DIMENSIONAL MODEL, CLEAN CONFIGURATION, $M = 3.5$, $P_o = 4.5$ $T_o = 110F$, $\alpha = 0$, $\phi = -90^o$

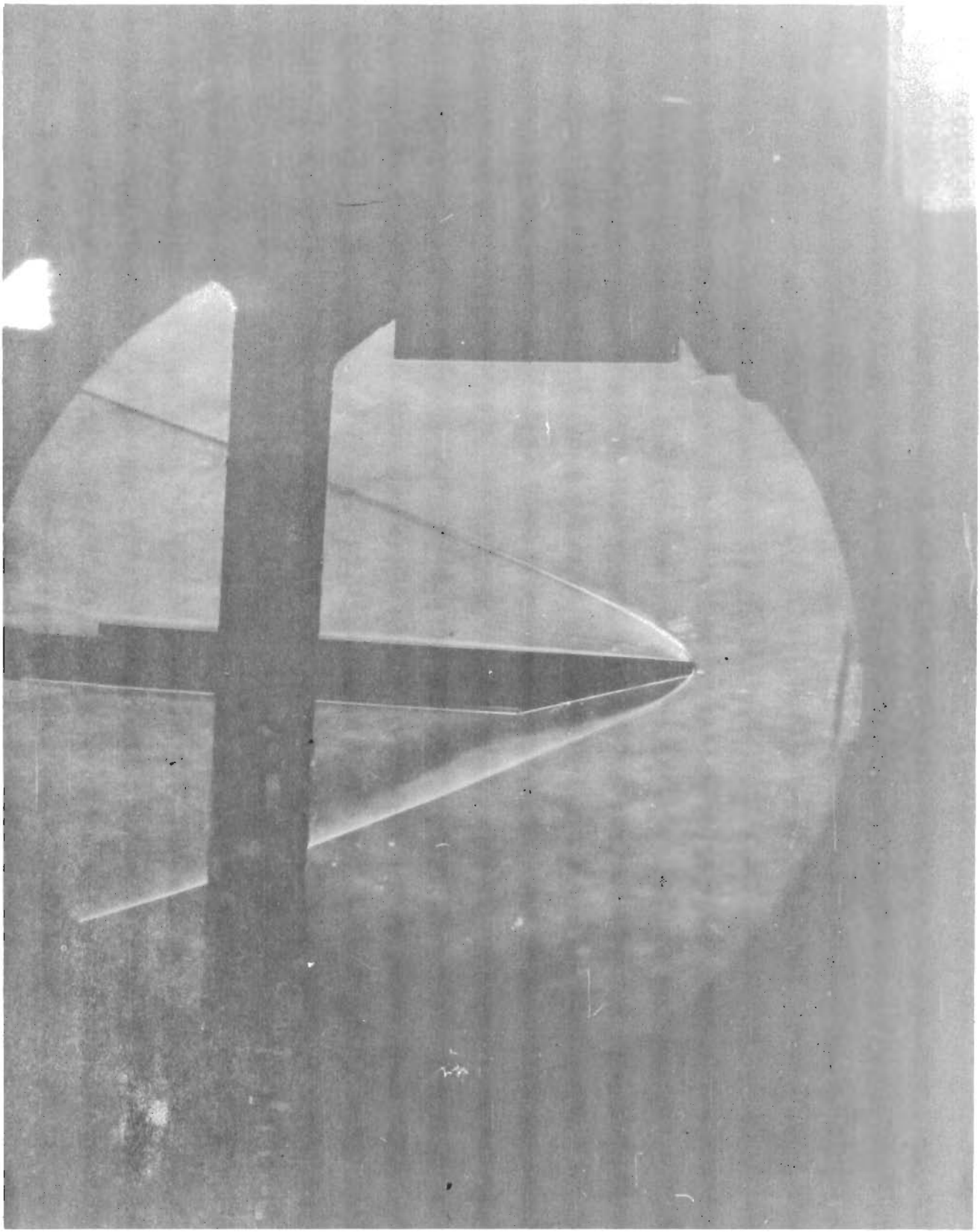

FIGURE 83 TWO-DIMENSIONAL MODEL, CLEAN CONFIGURATION, M = 5, P_o = 11, T_o = 115F, α = 0, ϕ = -90°

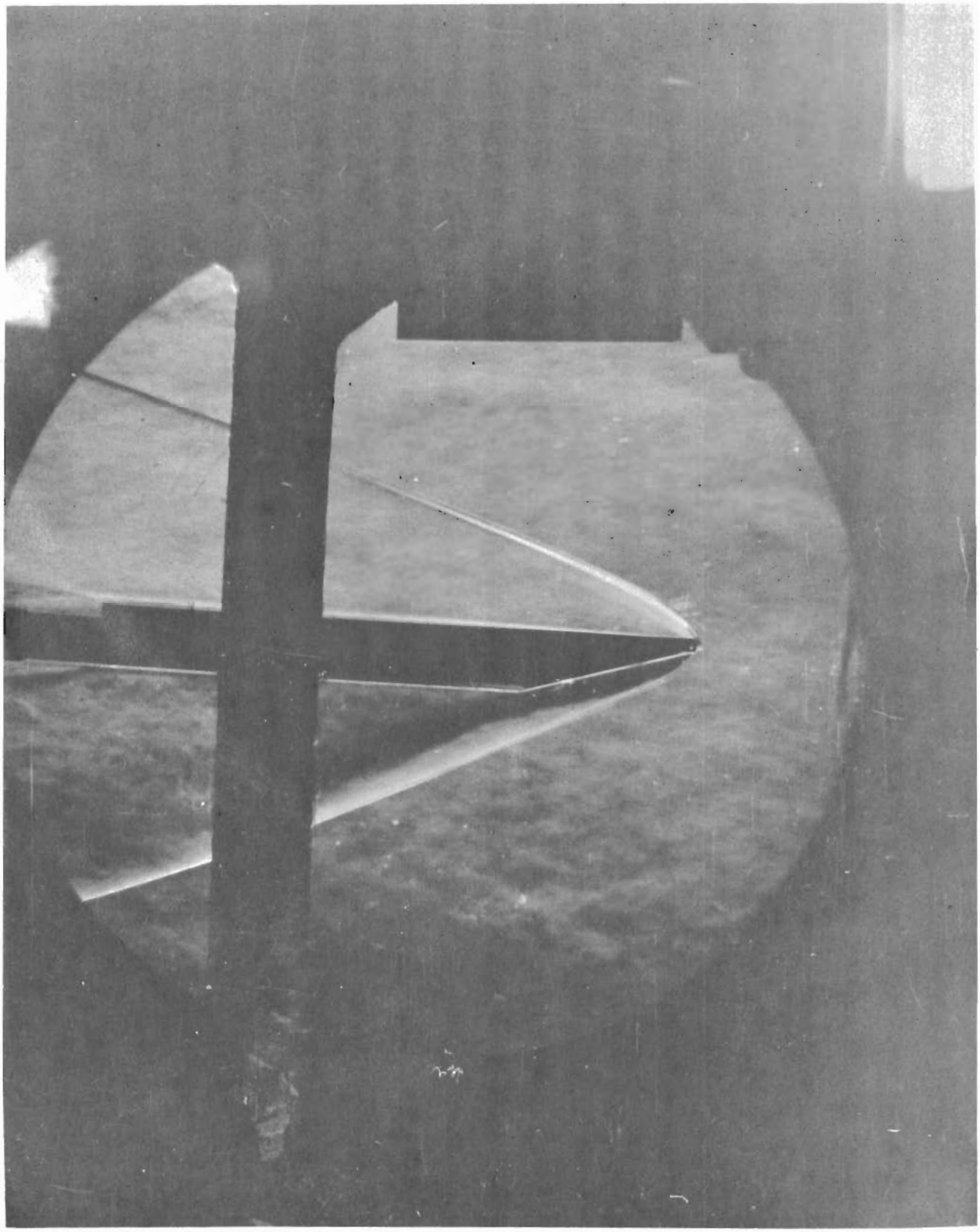

FIGURE 84 TWO-DIMENSIONAL MODEL, CLEAN CONFIGURATION, M = 5, P_o = 18, T_o = 105F, α = 0, ϕ = -90°

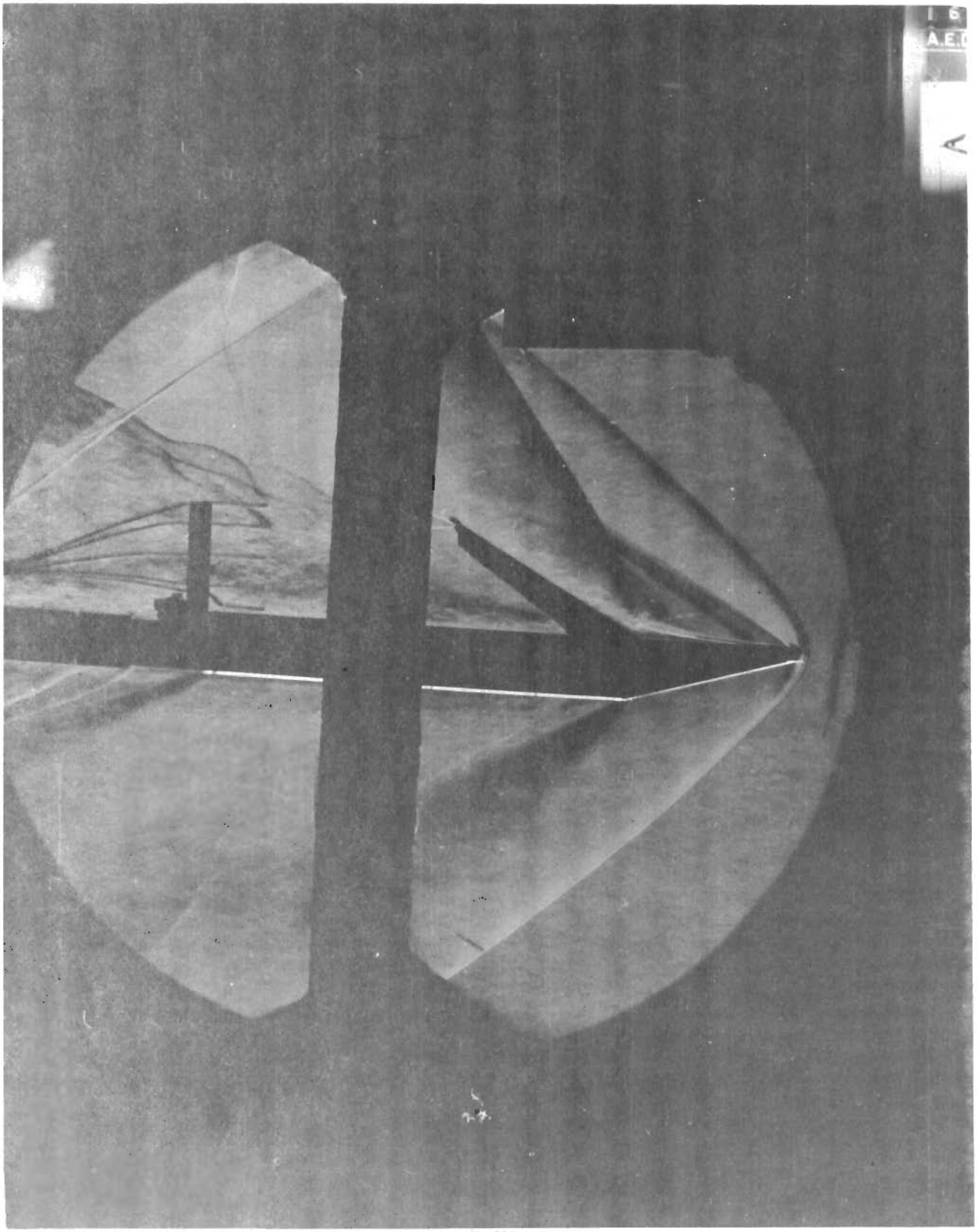

FIGURE 85 TWO-DIMENSIONAL MODEL, 30° FLAP, M = 2, P_o = 3, T_o = 90F, α = 0, ϕ = -90°

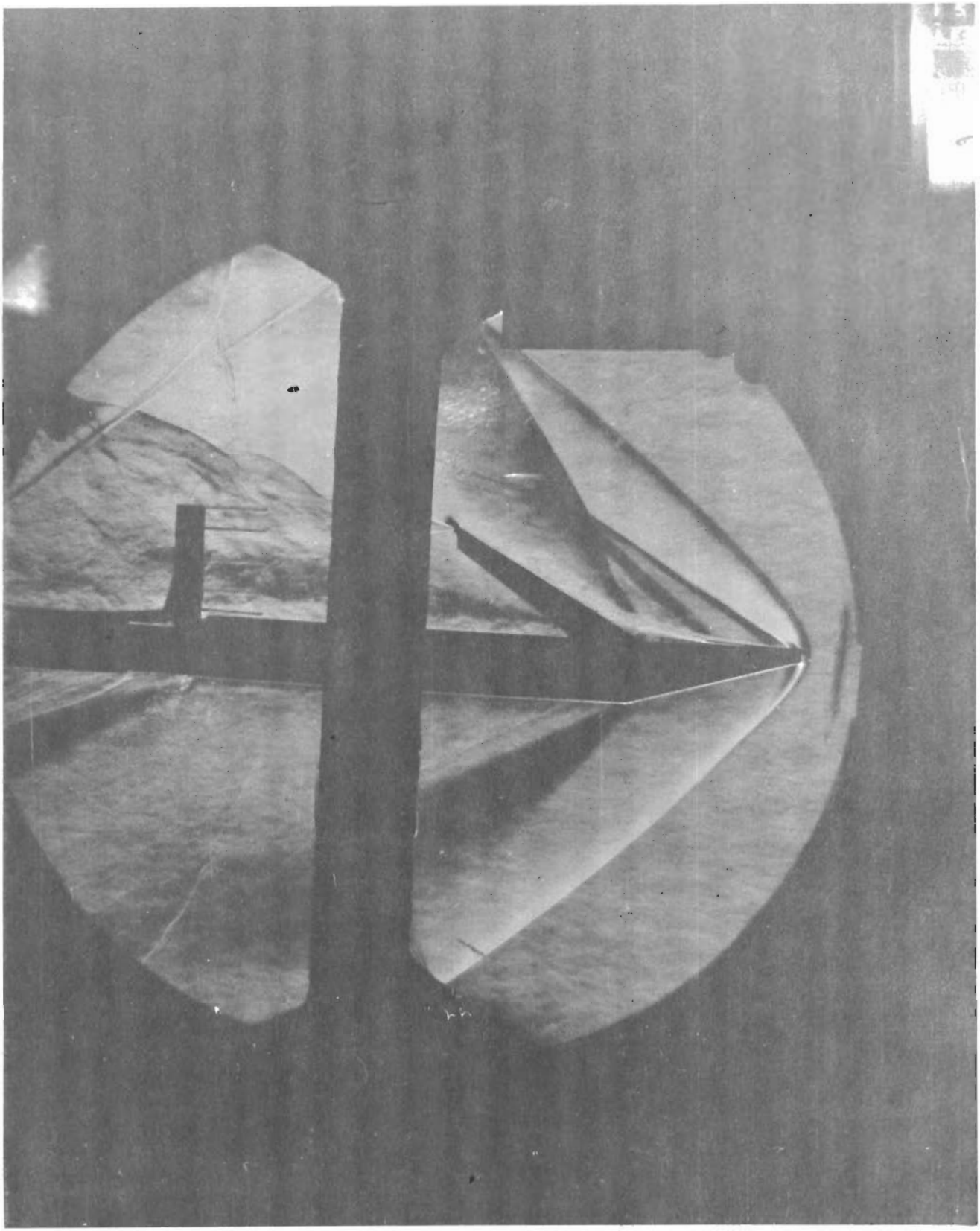

FIGURE 86 TWO-DIMENSIONAL MODEL, 30° FLAP, M = 2, P_o = 4, T_o = 90F, α = 0, ϕ = -90°

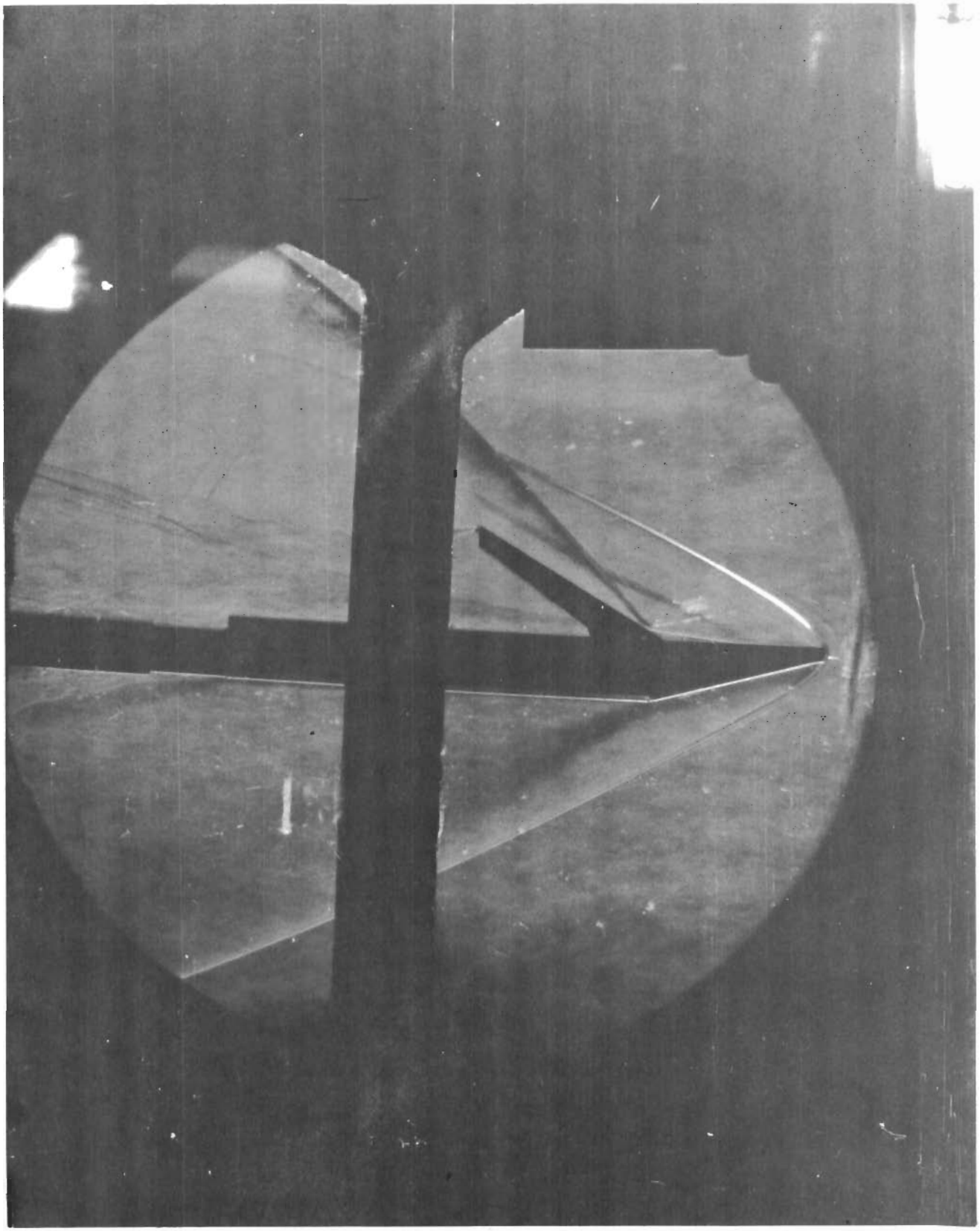

FIGURE 87 TWO-DIMENSIONAL MODEL, 30° FLAP, M = 3.5
P_o = 4.5, T_o = 90F, α = 0, ϕ = -90°

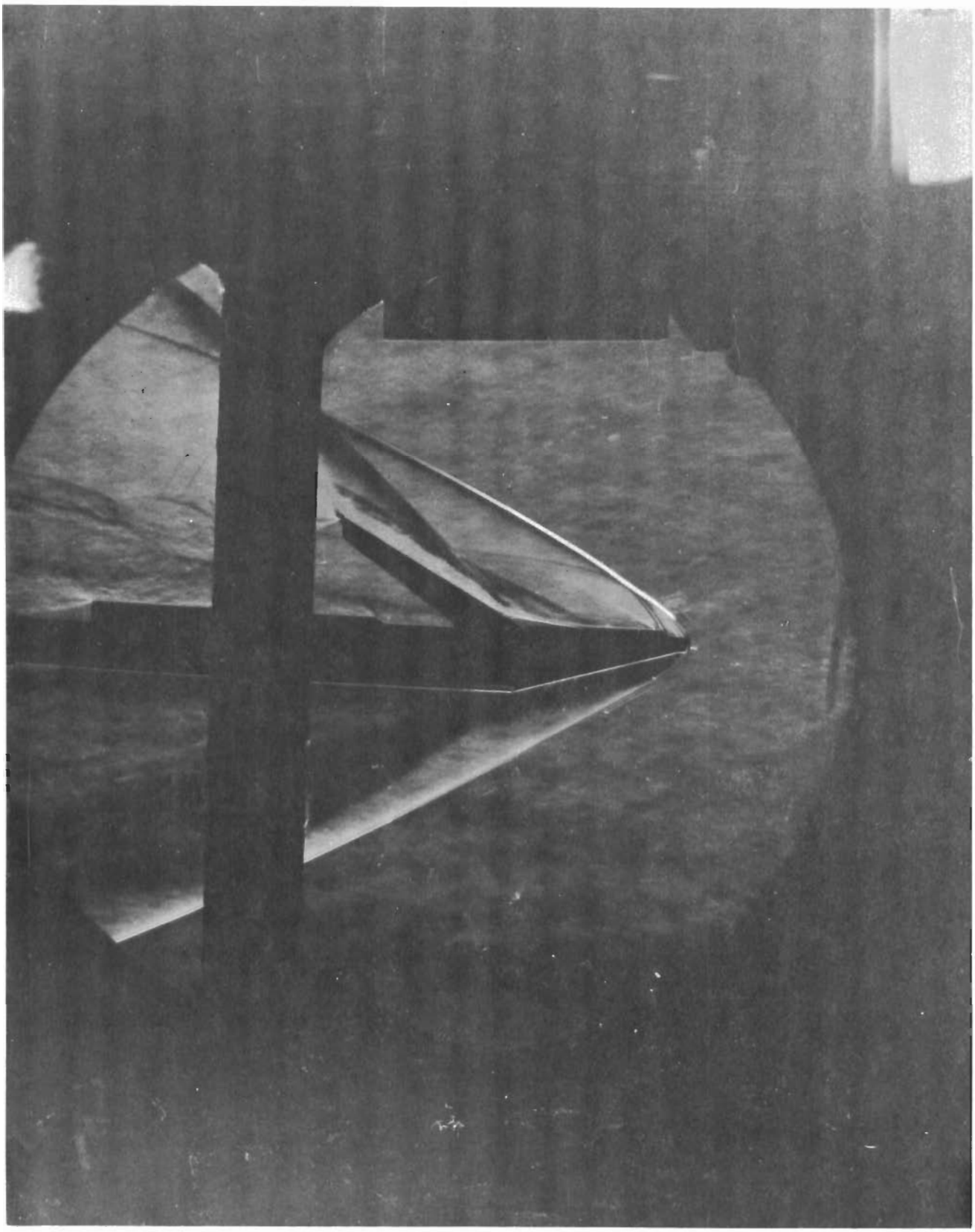

FIGURE 88 TWO-DIMENSIONAL MODEL, 30° FLAP, M = 3.5 P_o = 9.3, T_o = 100F, α = 0, ϕ = -90°

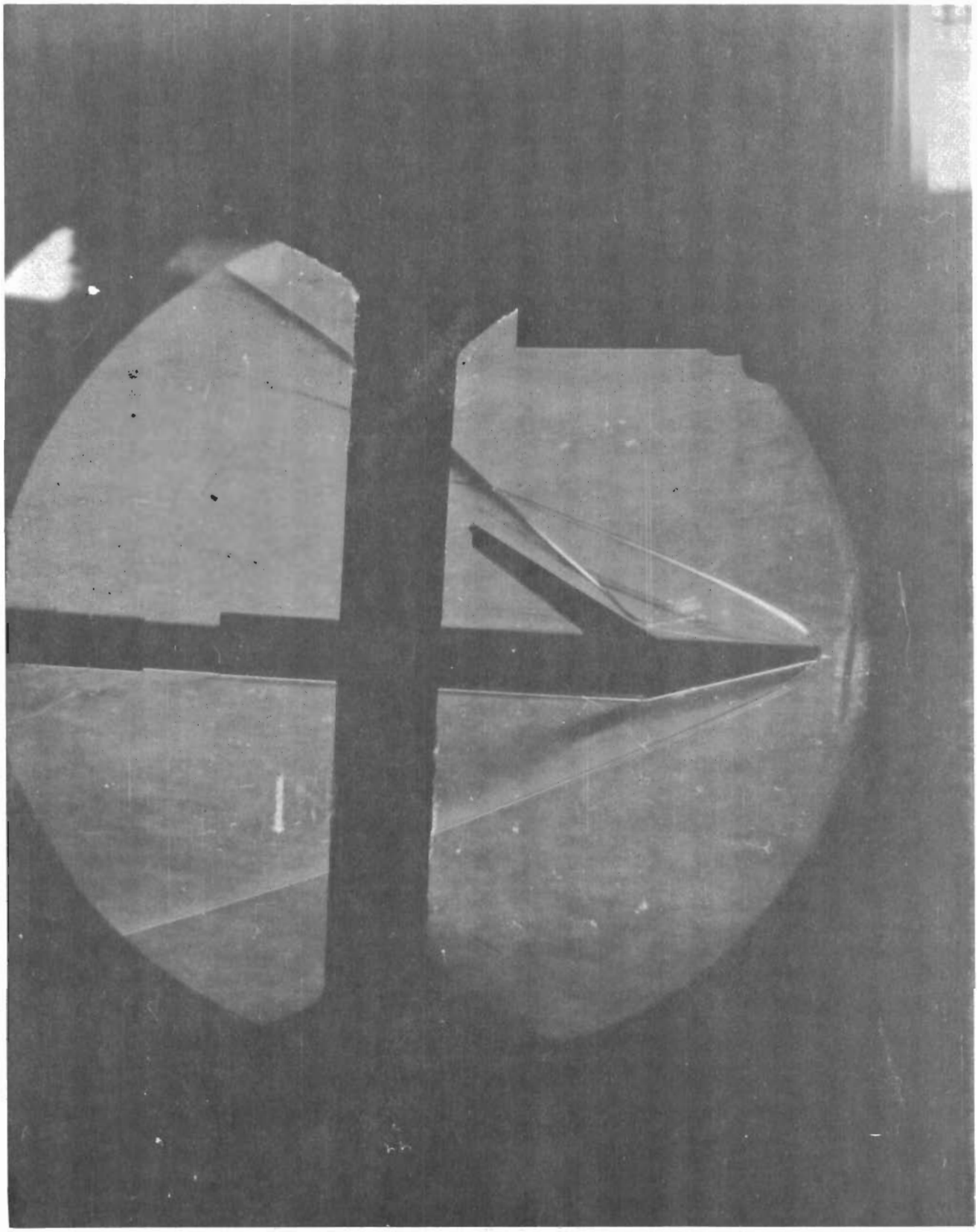

FIGURE 89 TWO-DIMENSIONAL MODEL, 30° FLAP, M = 5, P_o = 11, T_o = 100F, α = 0, ϕ = -90°

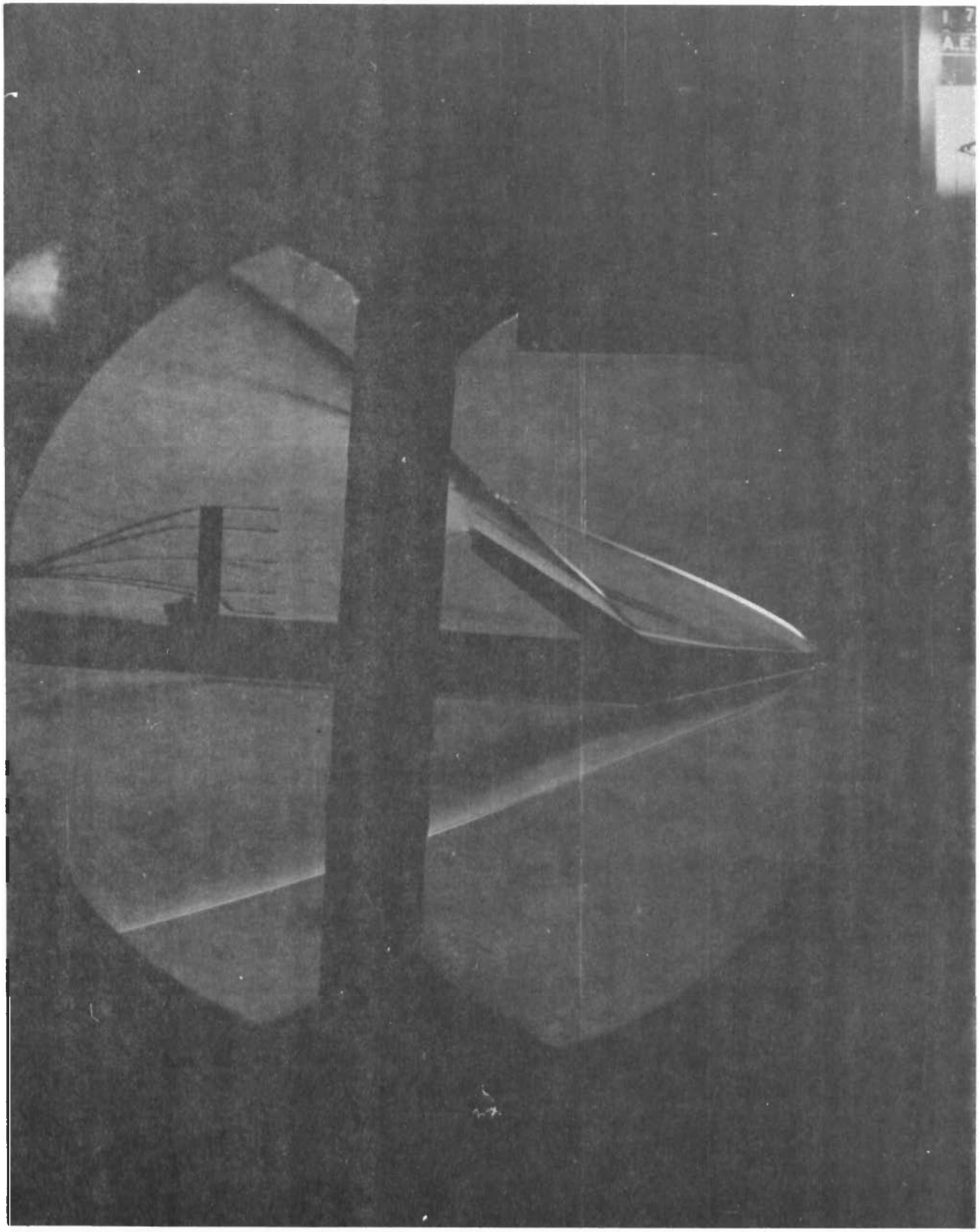

FIGURE 90 TWO-DIMENSIONAL MODEL, 30° FLAP, M = 5, P_o = 18, T_o = 100F, α = 0, ϕ = -90°

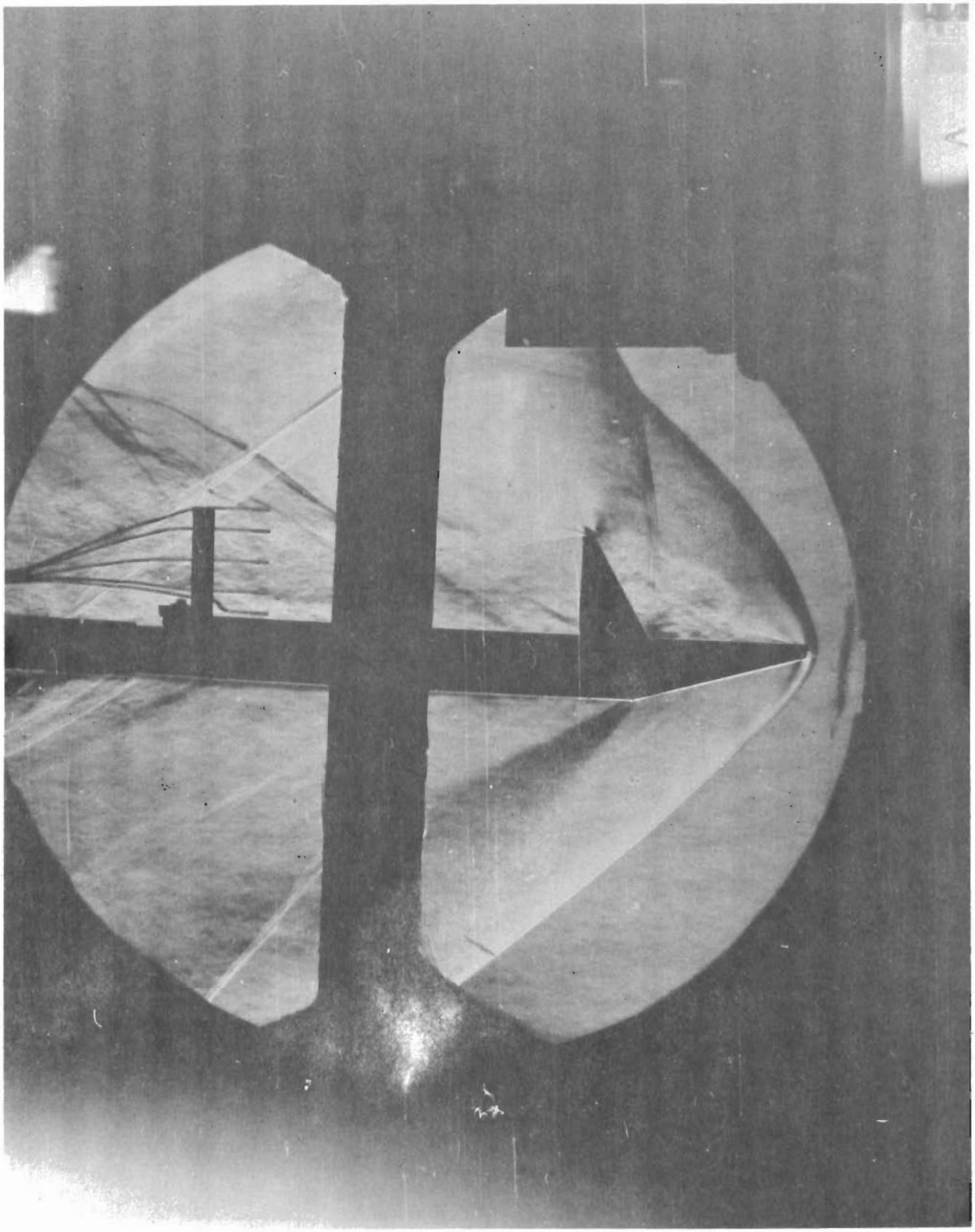

FIGURE 91 TWO-DIMENSIONAL MODEL, 60° FLAP, M = 2, P_o = 3, T_o = 90F, α = 0, ϕ = -90°

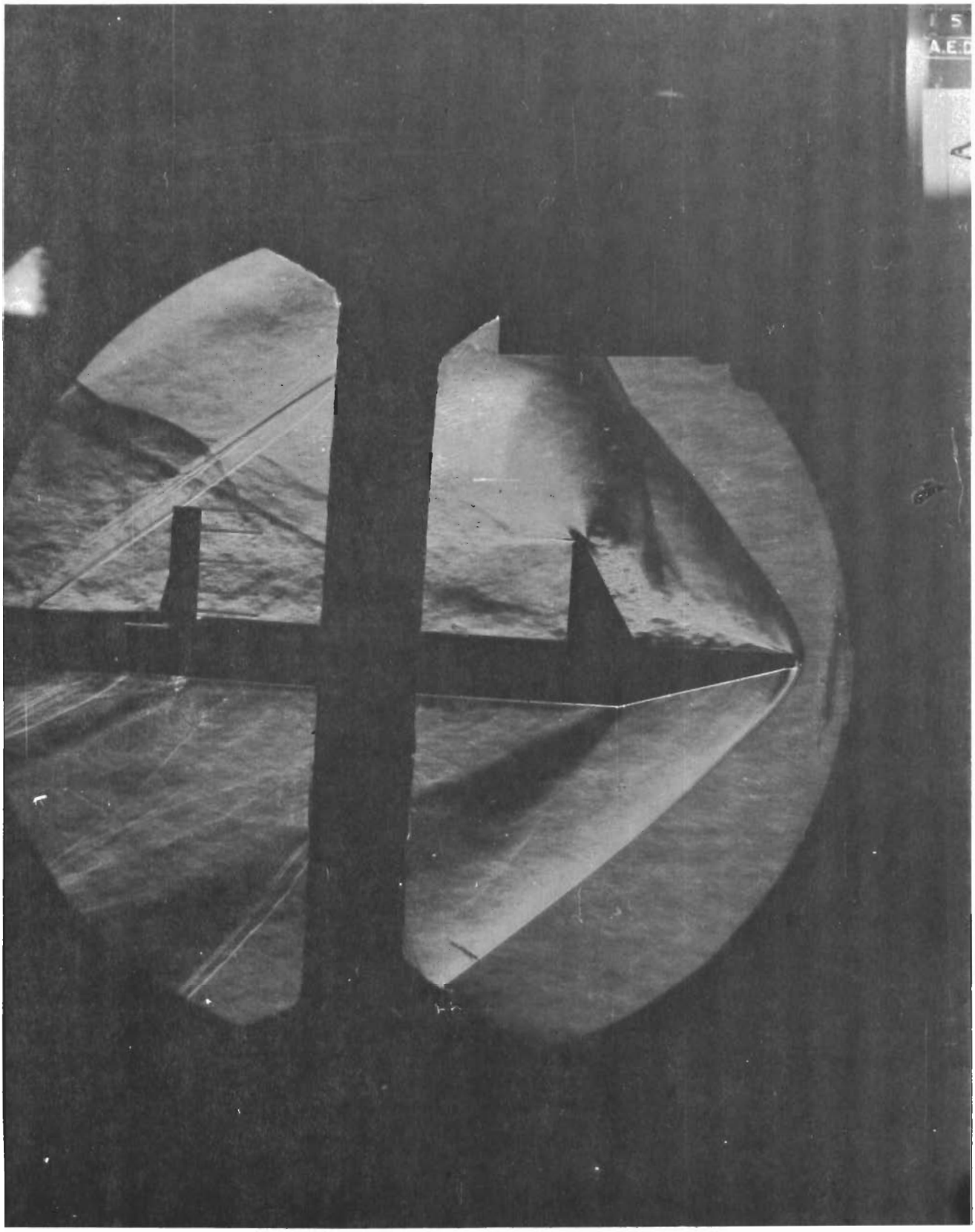

FIGURE 92 TWO-DIMENSIONAL MODEL, 60° FLAP, M = 2, P_o = 4, T_o = 90F, α = 0, ϕ = -90°

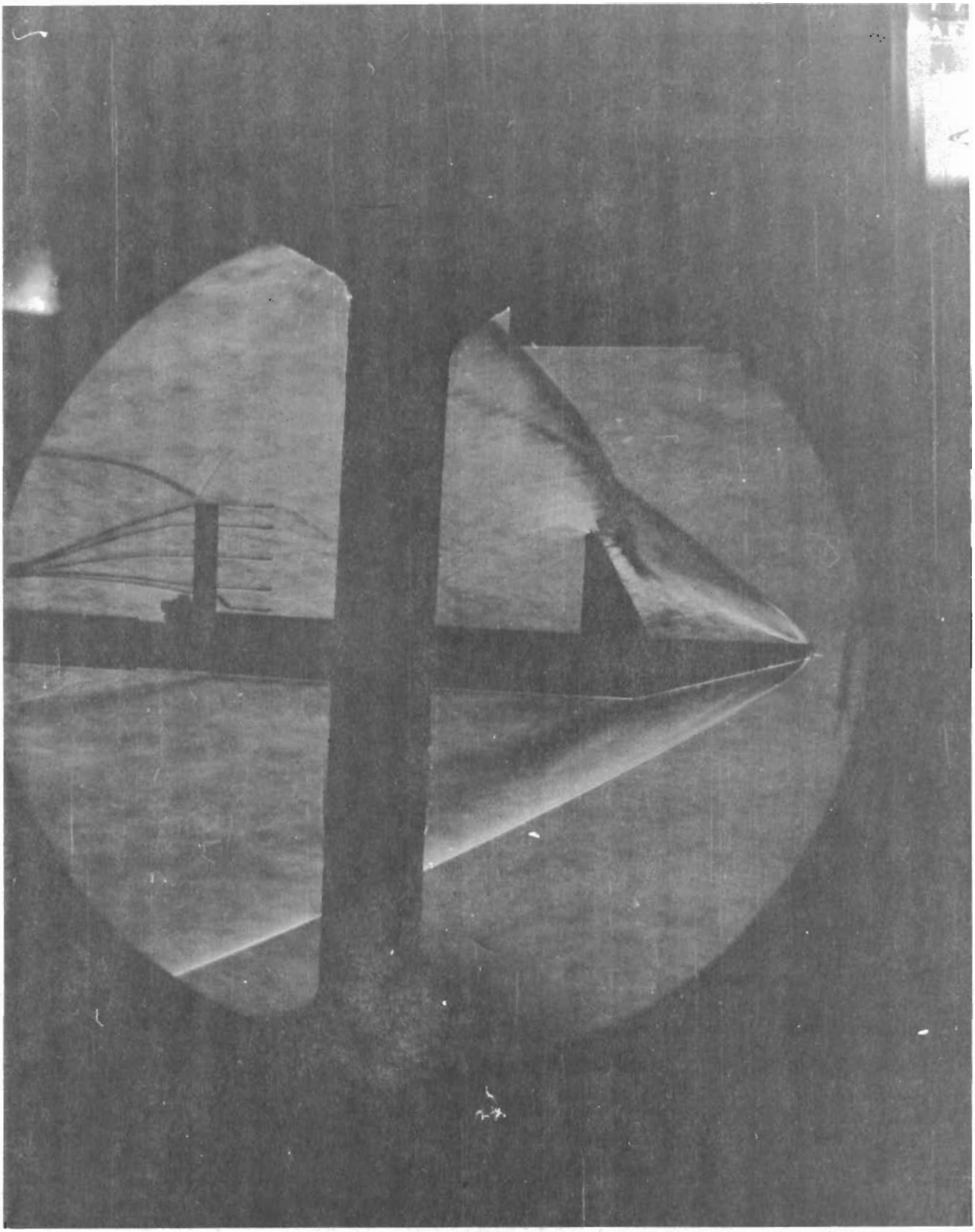

FIGURE 93 TWO-DIMENSIONAL MODEL, 60° FLAP, M = 3.5, P_o = 4.5, T_o = 120F, α = 0, ϕ = -90°

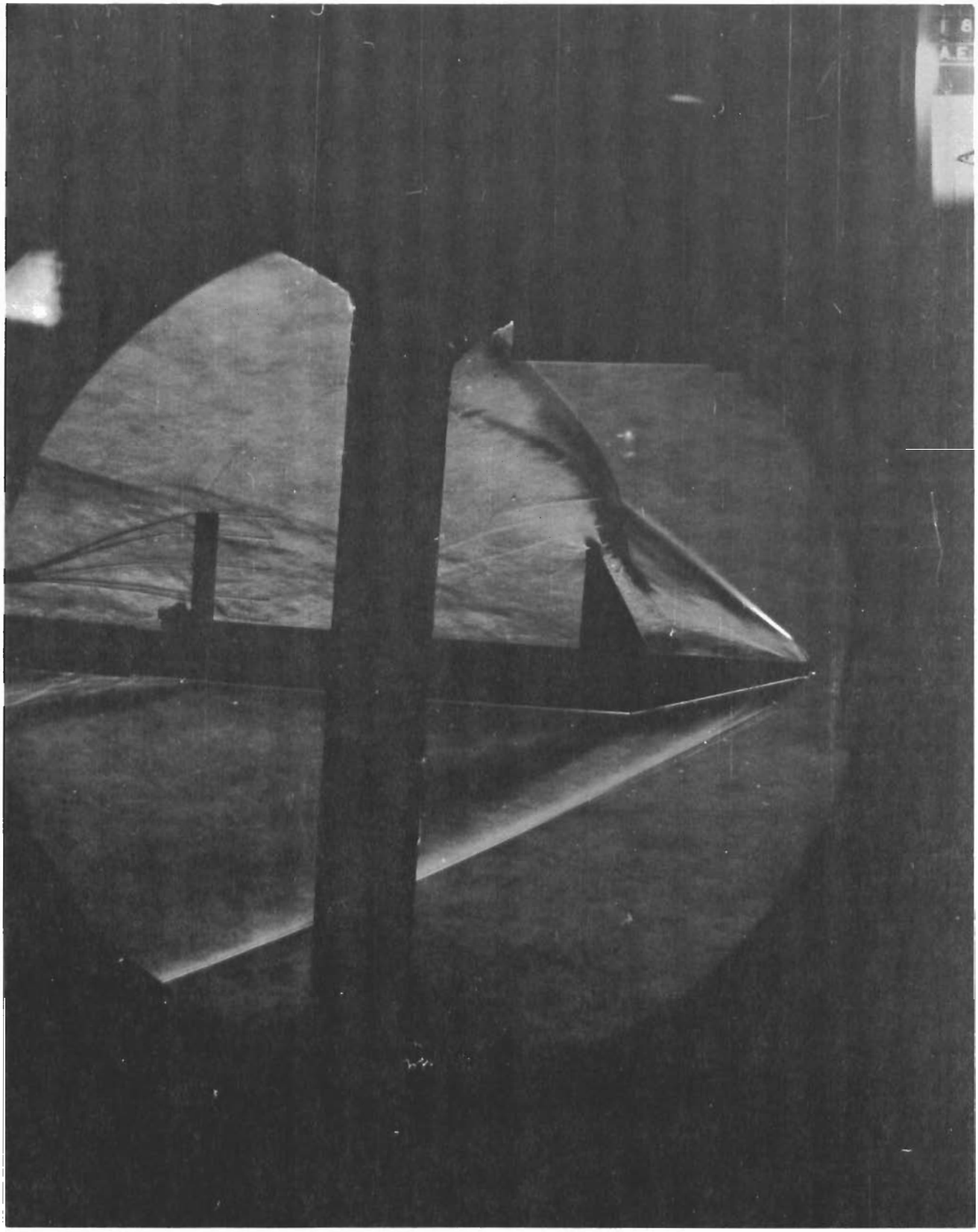

FIGURE 94 TWO-DIMENSIONAL MODEL, 60° FLAP, M = 3.5, P_o = 9.3, T_o = 120F, α = 0, ϕ = -90°

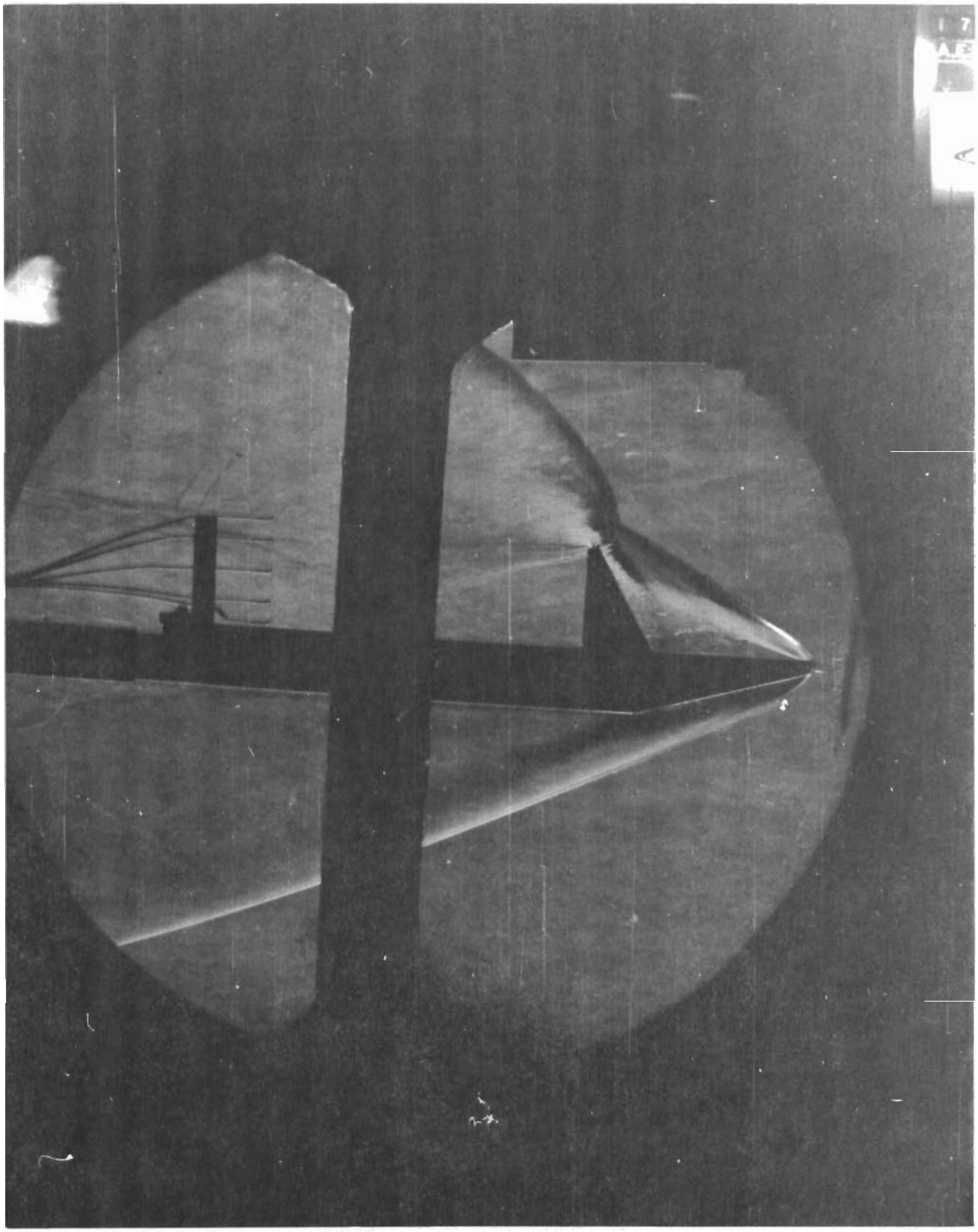

FIGURE 95 TWO-DIMENSIONAL MODEL, 60° FLAP, M = 5, P_o = 11.2, T_o = 100F, α = 0, ϕ = -90°

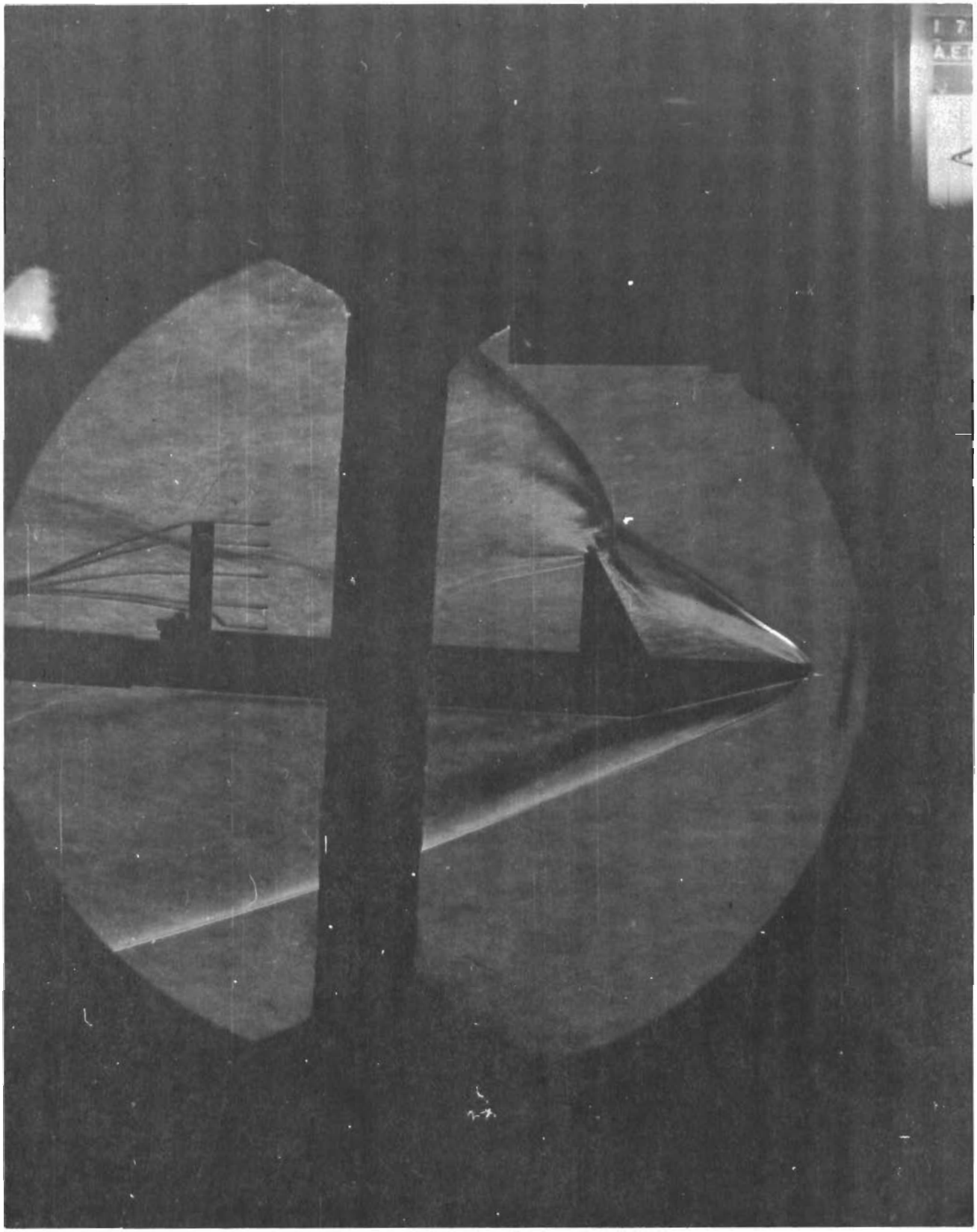

FIGURE 96 TWO-DIMENSIONAL MODEL, 60° FLAP, M = 5, P_o = 18, T_o = 100F, α = 0, ϕ = -90°

distance in the outer, inviscid part of the flow decreases as expected from theory. Also, the intersection of the bow shock and the detached, curved wedge shock moves in closer to the trailing edge of the flap as the Mach number increases. This intersection creates a vortex sheet (surface of tangential velocity discontinuity) because of the unequal shock strengths on the two sides of the sheet. This will, in turn, lead to an outer viscous mixing layer which will affect the outer structure of the turbulent wake downstream and may affect turbulent pressure fluctuation levels, especially at the higher Mach numbers. Because of this feature, it is especially disappointing that the shadowgraphs for Mach 10 were not successful. This feature of the flow would be even closer to the model surface at Mach 10 and would be much more intense due to the stronger shock waves involved. This behavior might be connected with the extremely high pressure fluctuations which were measured at Mach 10, as compared with the supersonic results up to Mach 5.0. A clarification of this possibility deserves further future investigation.

RMS Pressure Fluctuation and Overall SPL

Supersonic Results (Tunnel A: M = 2 to 5)

Figures 76,77 and 78 show the RMS $\Delta p/q_\infty$ at $\alpha = 0$, Re/L = 1 x 10^6/ft. plotted as a function of position along the model surface. The high values of the clean plate configuration (Figure 76) have already been discussed and are attributed primarily to wind tunnel noise, which evidently increases with free stream Mach number. Figure 77 shows the Mach number dependence of the RMS $\Delta p/q_\infty$ distribution for the 30° flap; the data for $M_\infty = 2.0$ appears somewhat higher having values ranging from $.02 \leq \Delta p_{RMS}/q_\infty \leq .035$. There exists doubt concerning the No. 5 transducer value, .086, in comparison with the value, .030 for No. 6, since the flow conditions are nearly the same, and because the No. 5 transducer readings were consistently high for the clean plate and axisymmetric case. There appears to be a steady increase in the fluctuation level as one proceeds towards the trailing edge. This may be explained partly by the increase of the static pressure level, probably with an attendant increase in the local q_e based on boundary layer edge conditions; however, the local boundary layer edge Mach number was not determined because of uncertainty of the stagnation pressure downstream from complicated shock structure ahead of the flap (see Figures85 through 90), as previously discussed. There is also evident a rapid streamwise thickening of the wake, and according to Section II, Eq. 14 one expects an increase in $\Delta p_{RMS}/q_\infty$ proportional to $\delta 3/2$ for incompressible flow which can only be considered as qualitative for the present purpose. It must be remarked that there is a signal to noise ratio problem with regard to the 30° flap data. This is displayed in Figure 97 where the overall SPL's (from which the $\Delta p_{RMS}/q_\infty$ where obtained) are compared for the 30°, 60° and no flap (flat) configurations. At Mach 2.0, there is a clear-cut 10db margin between the 30° flap and the no flap data (which is regarded as tunnel background noise). However, at Mach 3.5 and 5.0, there is no satisfactory signal to noise ratio.

Figure 78 shows the $\Delta p_{rms}/q_\infty$ for the 60° flap configuration, and we find intense fluctuation levels of the order of $.027 < \Delta p_{RMS}/q_\infty < .061$ (at the trailing edge for $M_\infty = 5.0$. For $M_\infty = 3.5$ the trailing edge value reaches .084. At Mach 2.0, the fluctuation levels ahead of the flap jumps to .050, probably as a result of the intense shock-induced separation discussed above in connection with the Schlieren photos. The trailing edge fluctuations are apparently lower at M = 2.0 than at either M = 3.5 or at M = 5; no explanation is offered for this. We again are doubtful of the high readings of the No. 5 transducer ($.096 < \Delta p_{RMS}/q_\infty < .134$).

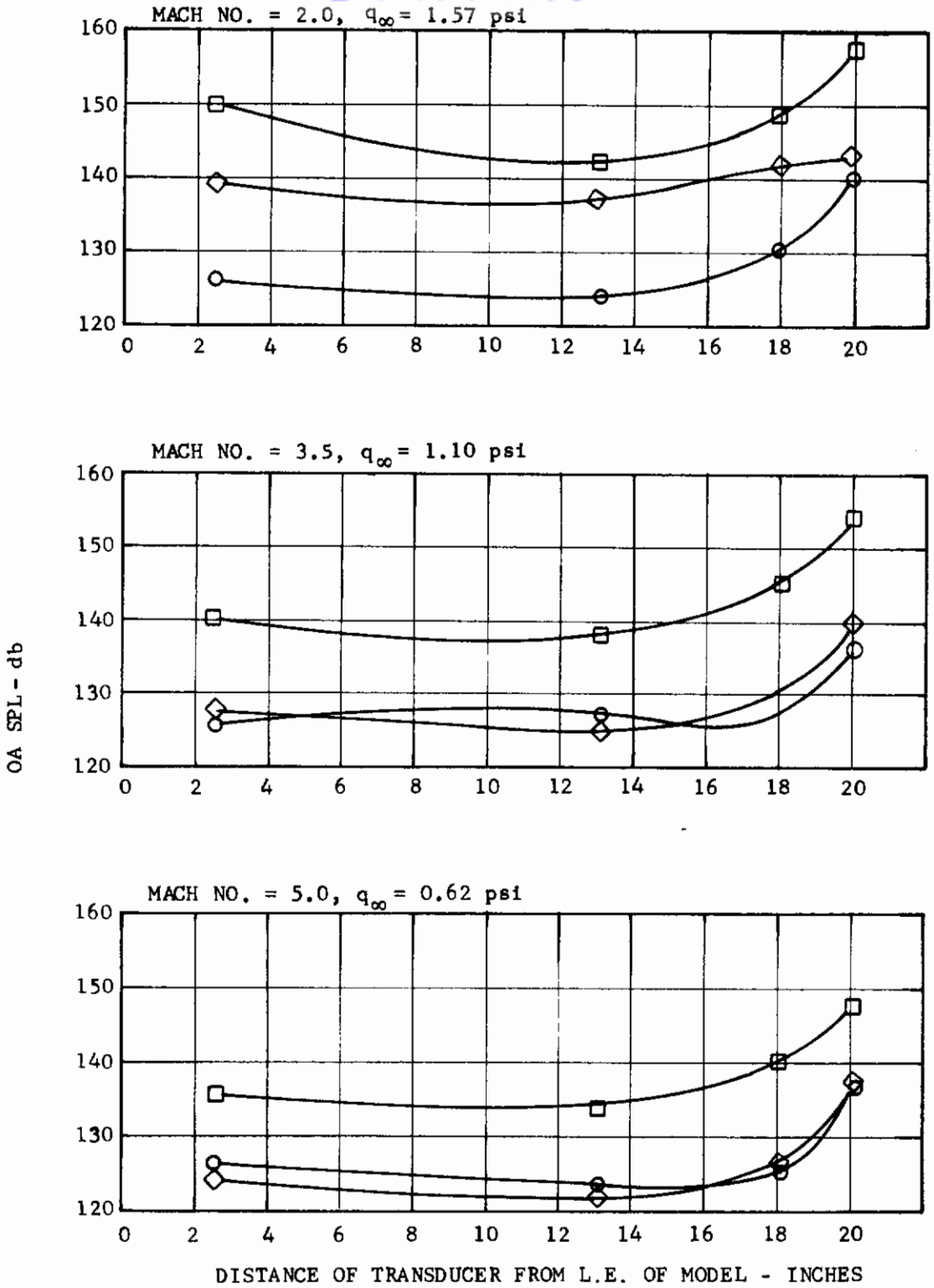

FIGURE 97 OVERALL SPL VS DISTANCE OF TRANSDUCER FROM L.E. OF MODEL FOR α = 0 , FLAT PLATE CONFIGURATION

Hypersonic Results (Tunnel "C": M = 10)

The top curve of Figures 98, 99 and 100 shows the overall SPL as a function of angle of attack for the no flap, 30° flap and 60° flap configurations respectively for transducer channel 3. (This is the same position as channel 4 of the supersonic tests, x = 18 inches aft of the leading edge, 5.5 inches aft of the 30° flap trailing edge, and 12 inches aft of the 60° flap trailing edge.) The data were presented in terms of SPL, since the Mach number and q were constant.)

We again find inadequate signal to noise level for the 30° flap configuration (compare Figures 98 and 99); apparently, the very high tunnel noise at Mach 10 masks the turbulent fluctuations for the 30° flap configuration. Figure 100 shows a 15 db margin for the noise of the 60° flap above the flat plate data level. For this case, some of the transducer channel data had "clipped" peaks and was not analyzed. We note the extremely high intensity 170 db measured at $\alpha = 0°$, Re/L = 2 x 10^6/ft q_∞ = 2.46 psi. This amounts to an RMS pressure of 1 psi, and this would cause severe acoustic fatigue problems for even very short structural exposure times at this level. Furthermore, acoustical non-linearities would tend to shift energy towards higher frequencies. These high fluctuation levels could indicate a structural problem area ahead of a control surface or wedge like, bluff protuberance on a lifting re-entry vehicle, if the trajectory permitted the rather modest dynamic pressure of 354 psf (2.46 psi) at Mach 10, especially for a reusable vehicle.

In view of these high fluctuation levels for the 60° flap, further hypersonic experiments appear to be warranted at various tunnel pressure levels. The success of the water cooling system in the present tests might permit experimentation with softer, more dissipative shock mount materials than the Teflon which was used in the present tests, which was selected for its ability to function at much higher model surface temperatures than were actually measured in the water cooled region.

Angle of Attack Effects on Pressure Fluctuations for the Flat Plate Models

Supersonic Tests (Tunnel "A:" M = 2 to 5)

Figures 101 through 106 show the angle of attack dependence of Channel 4 (x = 18" aft of leading edge). For the 30° flap, we have an adequate signal to noise ratio only for Mach 2, as seen from the Figures. Figures 103 and 104 show no significant trend with angle of attack for $0 < \alpha < 15°$. For the 60° flap, we appear to have a good signal to noise level. There appears to be a 3db drop at $\alpha = 15°$ at Mach 2.0 and about 6db drop at $\alpha = 15°$ for Mach 3.5 and 5.0. Evidently, the expansion of the steady flow on the lee side of the model at positive α causes a lower fluctuation level because the lowered density and Reynolds stresses. This works against the viscous cross-flow effects at positive angle of attack which apparently do not affect the turbulence level at the center of the plate strongly enough to compensate for the lower density of the expanded flow at small positive angles of attack.

In a future investigation, it would be desirable to extend these studies to large angles of attack, since at a high enough angle of attack the cross-flow should predominate the fluctuation level and change the frequency distribution of energy. This evidently does not occur below $\alpha = 15°$, as can be seen from the plots of 1/3 octave SPL at various frequencies (Figures 105 and 106).

Hypersonic Tests (Tunnel "C:" M - 10) - Channel 3 (x = 18")

We again refer to Figures 98, 99 and 100). Again, an inadequate signal to noise level exists for the 30° flap configuration, and this data will not be discussed further. The 60° flap shows a pronounced drop in SPL at $\alpha = 10°$, becoming flatter to

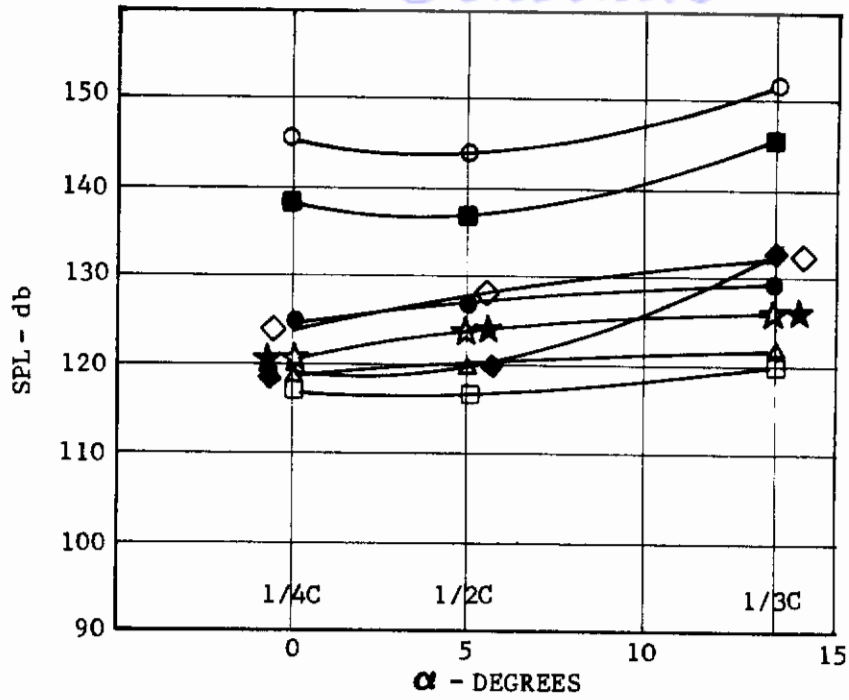

$Re_\infty/FT = 1.0 \times 10^6$
$q_\infty = 1.14$ psi

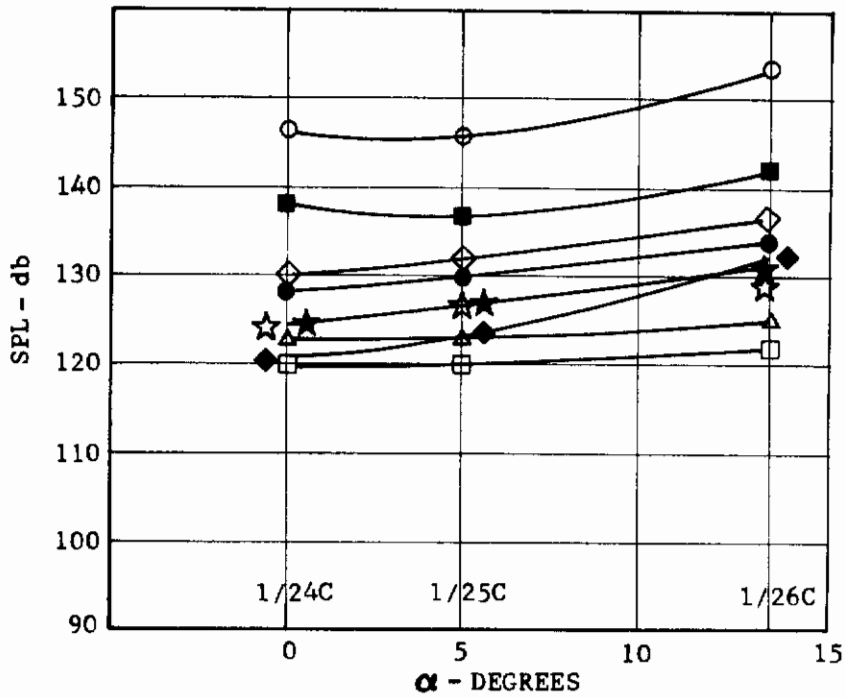

Re_∞/FT: 2.35×10^6
$q_\infty = 2.50$ psi

SYM	FREQ(KC)
○	OA
□	20
△	16
☆	12.5
★	10
●	8
◇	5
◆	3.15
■	0.8

FIGURE 98 ANGLE OF ATTACK EFFECTS ON 1/3 OCTAVE AND OVERALL SPL, FP 0, MACH NO. 10, CHANNEL 3, TUNNEL C

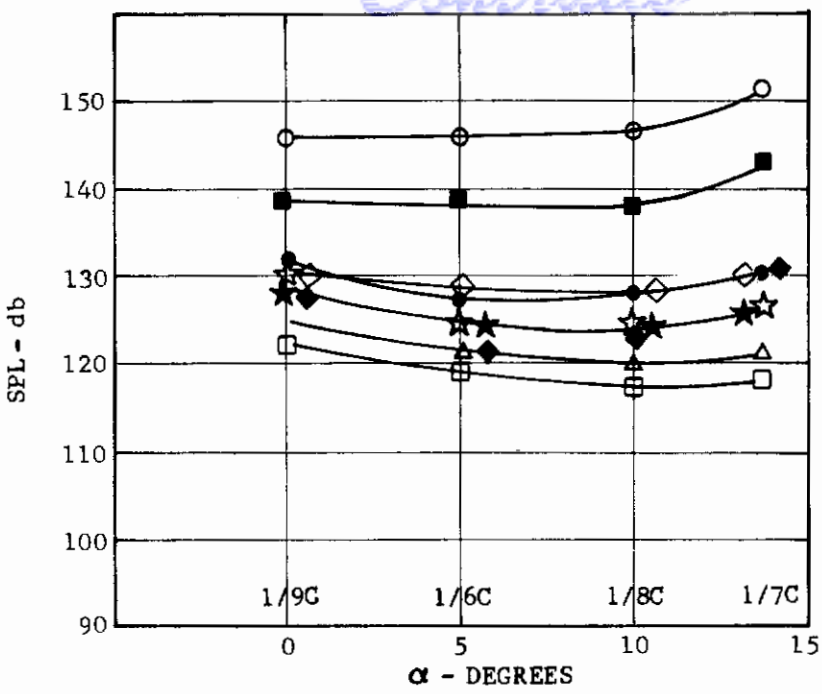

$R_{e_\infty}/FT = 1 \times 10^6$

$q_\infty = 1.14$ psi

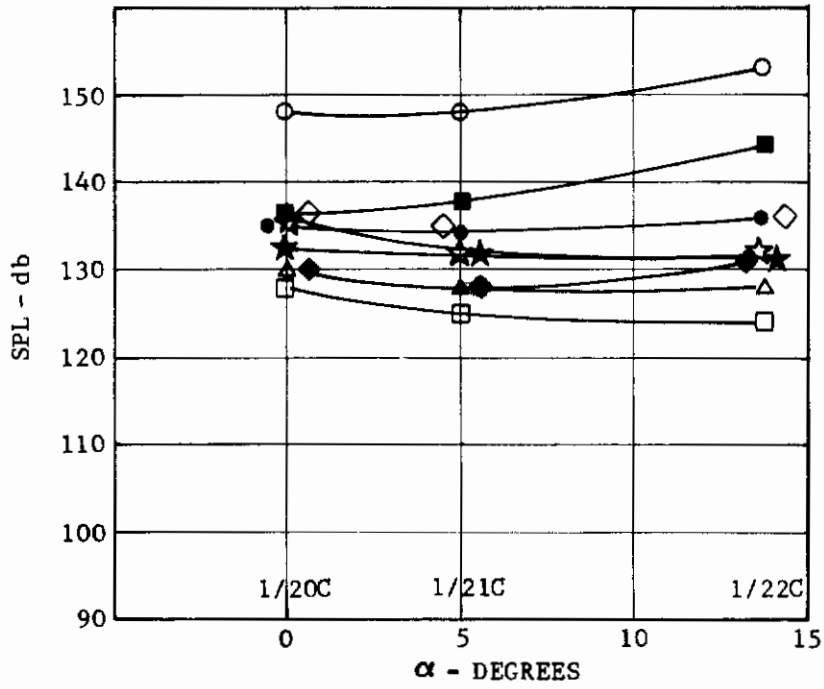

$Re_\infty /FT = 1 \times 10^6$

$q_\infty = 2.46$ psi

SYM	FREQ.(KC)
○	0A
□	20
△	16
☆	12.5
★	10
●	8
◇	5
◆	3.15
■	0.8

FIGURE 99 ANGLE OF ATTACK EFFECTS ON 1/3 OCTAVE AND OVERALL SPL , FP 30, MACH NO. = 10, CHANNEL 3 , TUNNEL C

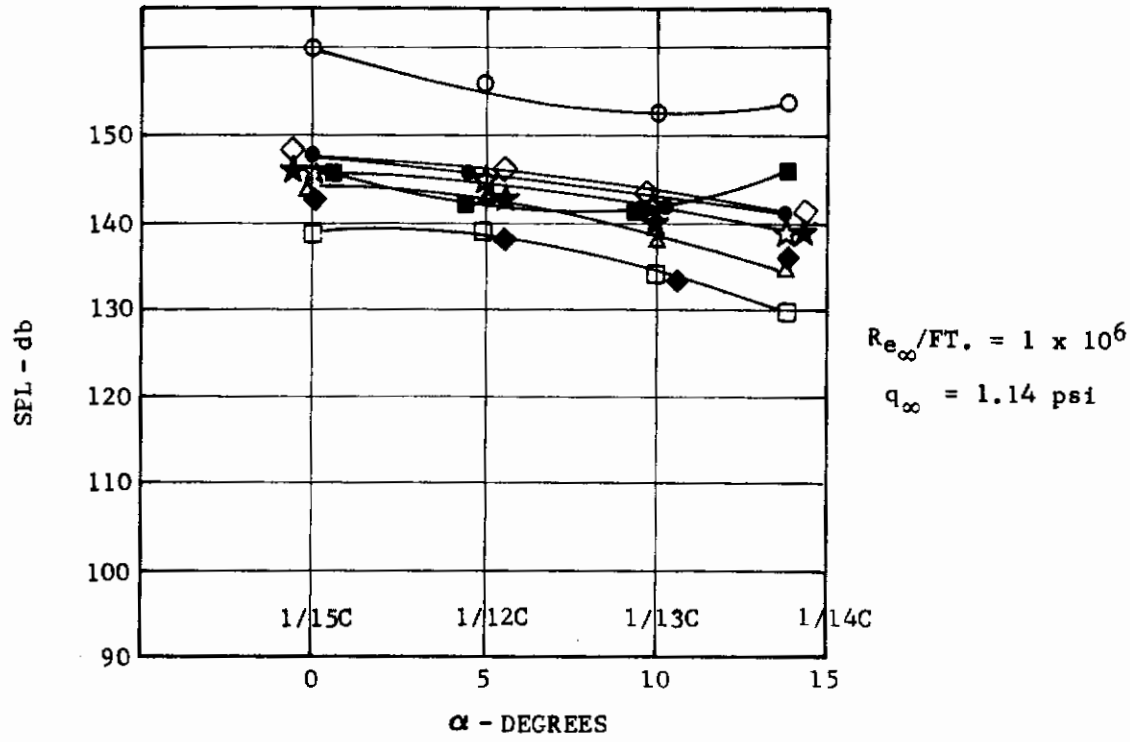

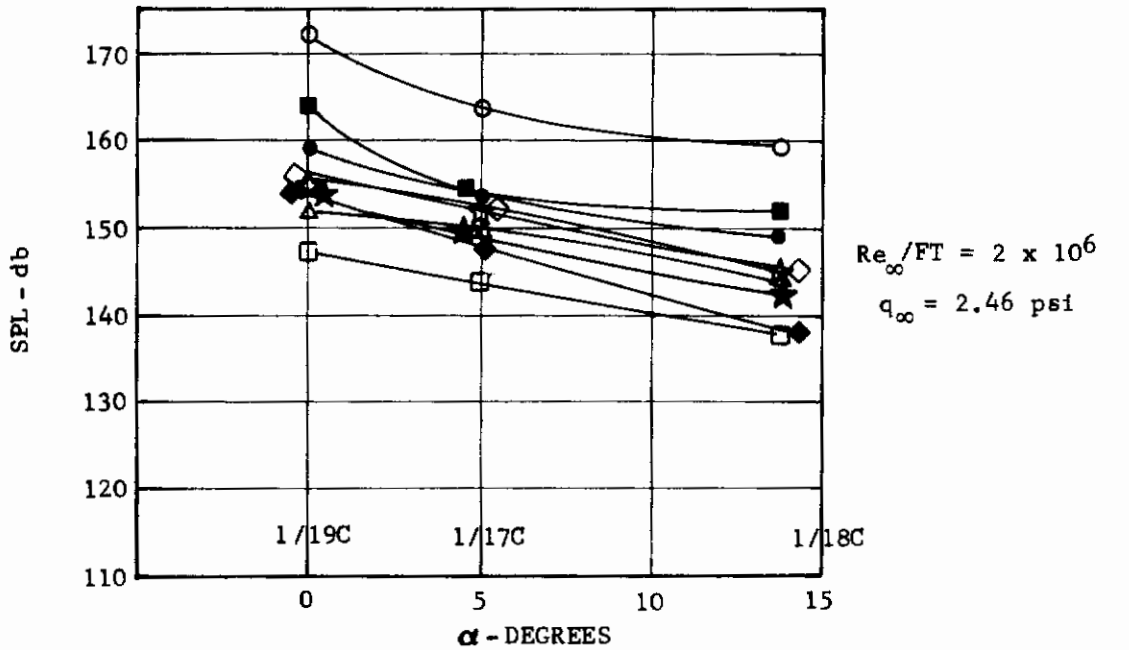

SYM	FREQ.(KC)
○	0A
□	20
△	16
☆	12.5
★	10
●	8
◇	5
◆	3.15
■	0.8

FIGURE 100 ANGLE OF ATTACK EFFECTS ON 1/3 OCTAVE AND OVERALL SPL, FP 60, MACH NO. = 10, CHANNEL 3, TUNNEL C

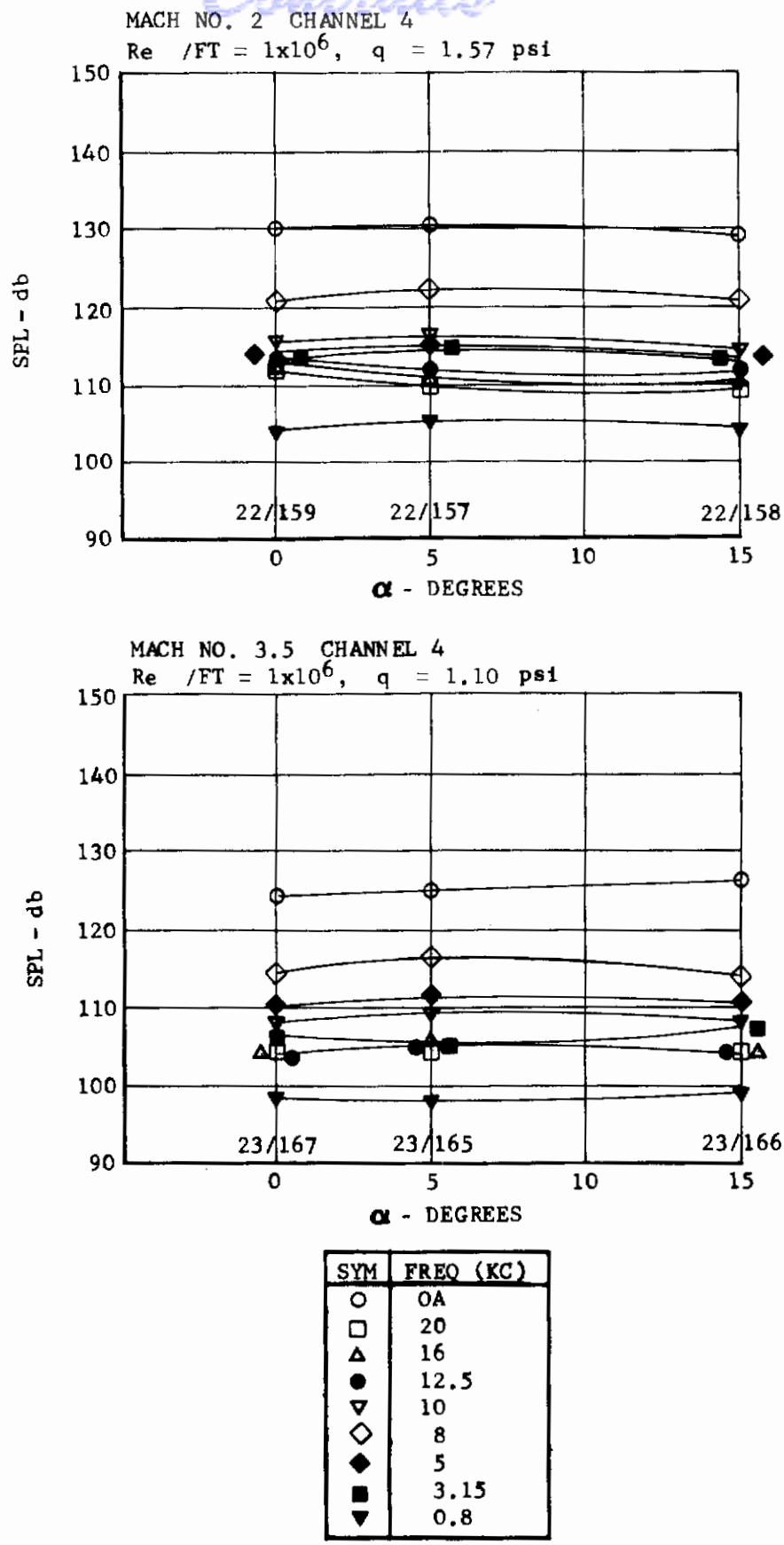

FIGURE 101 ANGLE OF ATTACK EFFECTS ON 1/3 OCTAVE AND OVERALL SPL FLAT PLATE MODEL O

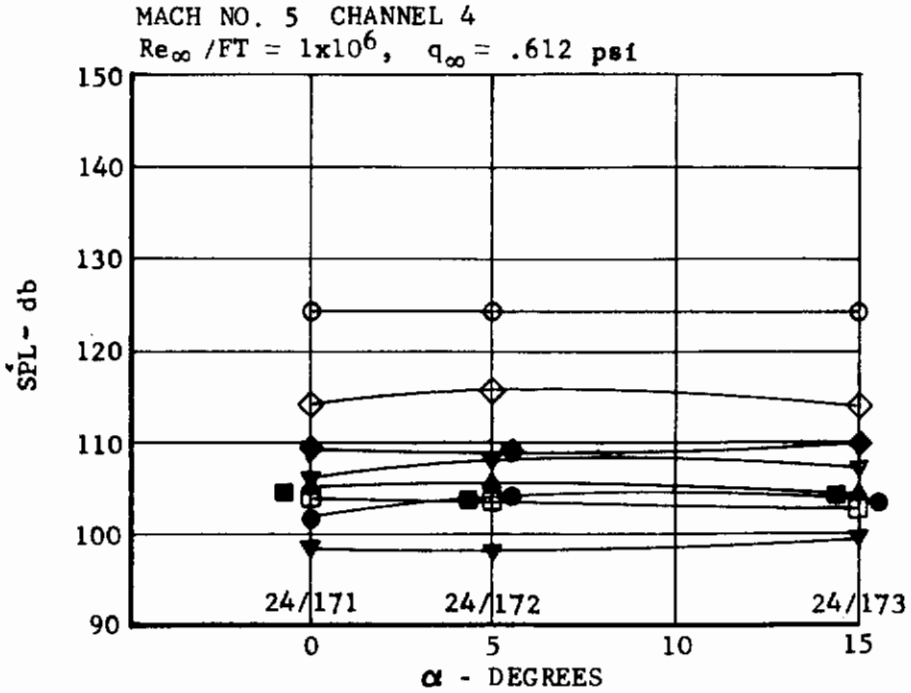

SYM	FREQ(KC)
○	OA
□	20
△	16
●	12.5
▽	10
◇	8
◆	5
■	3.15
▼	0.8

FIGURE 102 ANGLE OF ATTACK EFFECTS ON 1/3 OCTAVE AND OVERALL SPL
FLAT PLATE MODEL 0

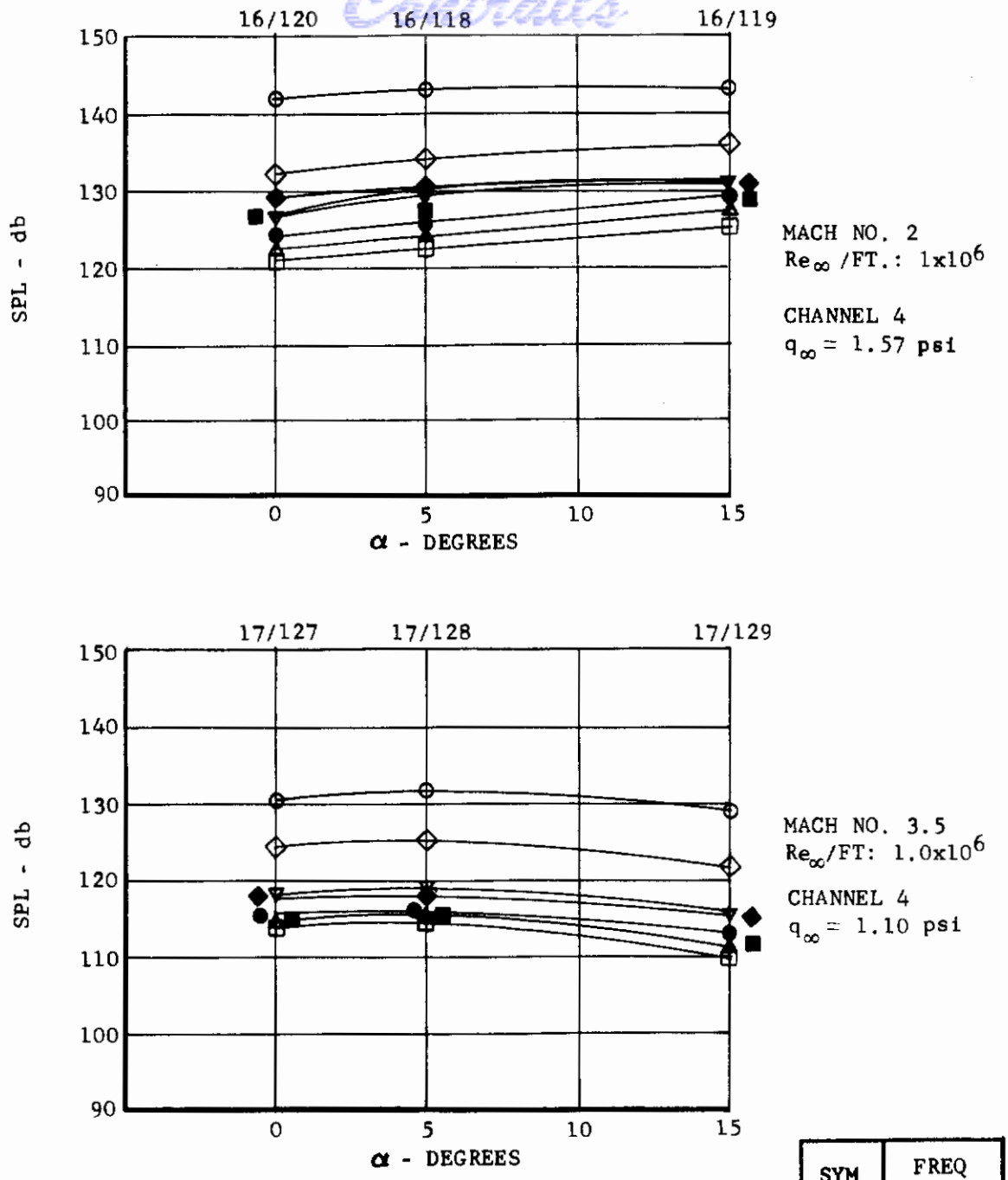

FIGURE 103 ANGLE OF ATTACK EFFECTS ON 1/3 OCTAVE AND OVERALL SPL FLAT PLATE MODEL 30

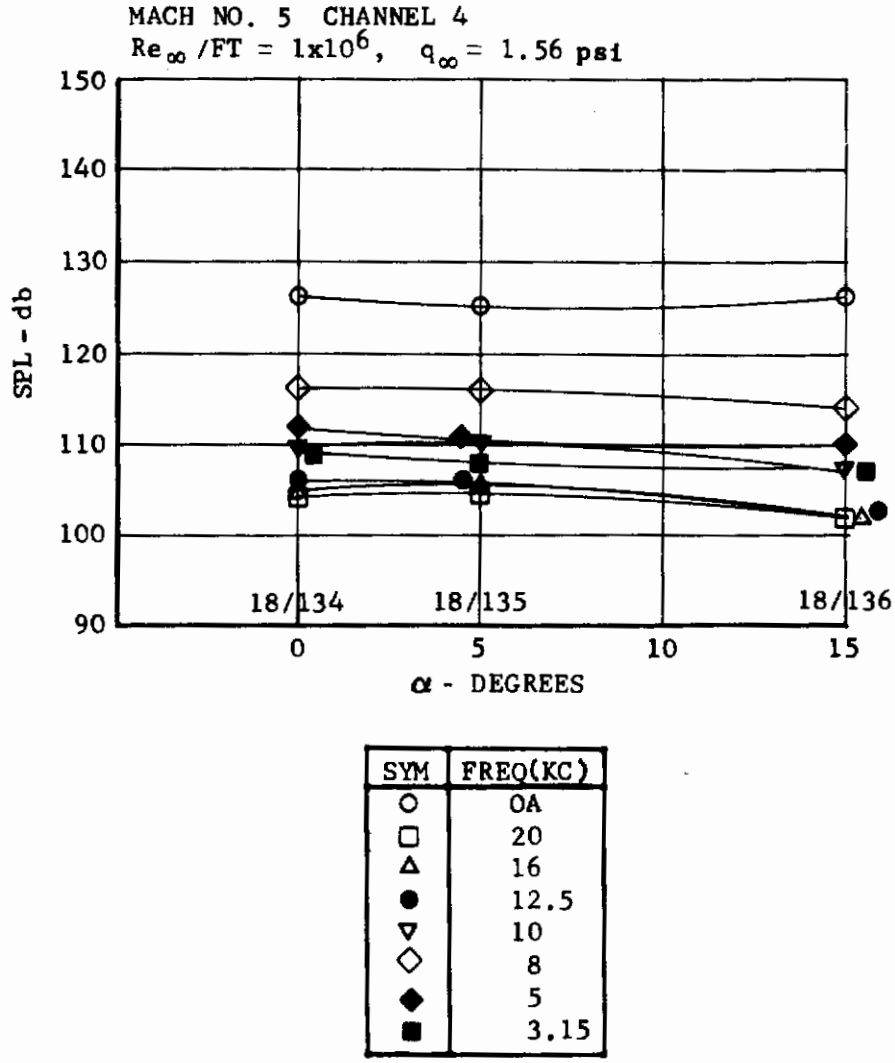

FIGURE 104 ANGLE OF ATTACK EFFECTS ON 1/3 OCTAVE AND OVERALL SPL
FLAT PLATE MODEL 30

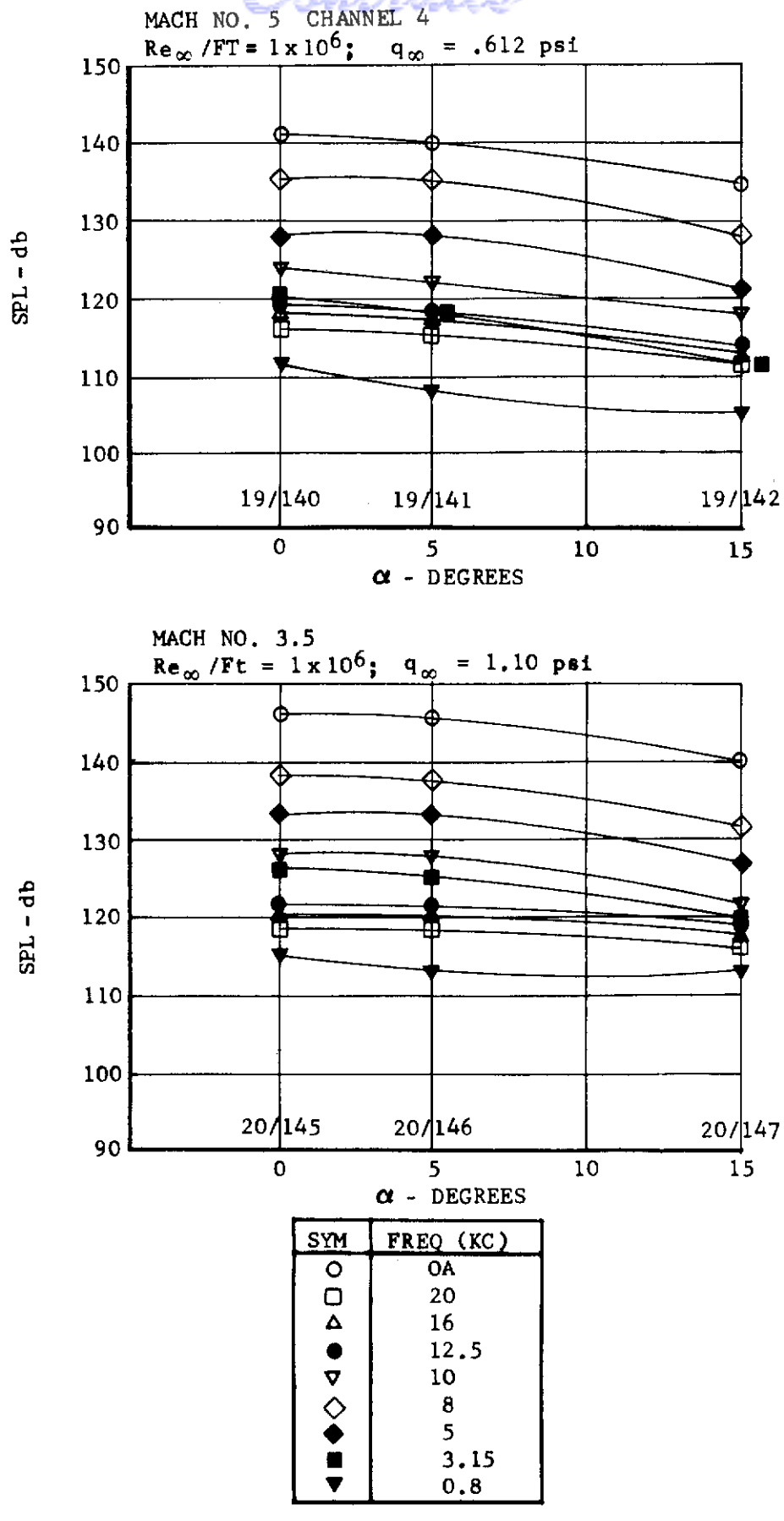

FIGURE 105 ANGLE OF ATTACK EFFECTS ON 1/3 OCTAVE AND OVERALL SPL FLAT PLATE MODEL 60

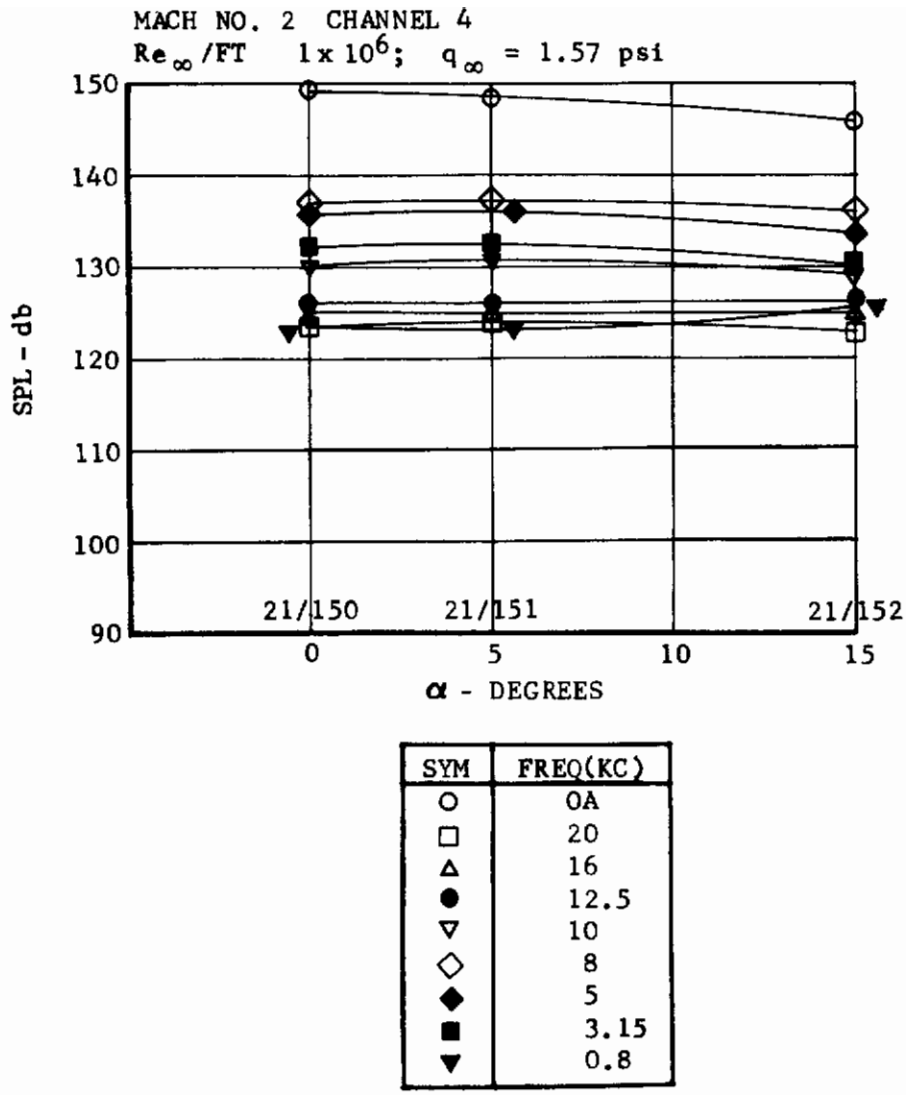

FIGURE 106 ANGLE OF ATTACK EFFECTS ON 1/3 OCTAVE AND OVERALL SPL FLAT PLATE MODEL 60

$\alpha = 15^{o}$. This perhaps indicates that the viscous cross flow is reversing the trend of decreasing fluctuation level which has been conjectured to be the result of lower density at small positive α. Again, no noticeable change in the frequency distribution with angle of attack can be seen.

For future work, studies at large angle of attack appear to be warranted at Mach 10.

Nondimensional Frequency Spectra

Discussion of Data

Figure 107 shows the dimensionless averaged frequency spectra for the 30° flap case, normalized in the form $\tilde{W}_h = U_\infty \Delta \langle p^2_{1/3} \rangle / (q^2_\infty \, h \Delta f_{1/3})$ vs (fh/U). Shown are the Willmarth and Woolridge low speed data (Ref. 1) converted to use a nominal boundary layer thickness eight times the displacement thickness which is valid for a 1/7th power boundary layer velocity profile in incompressible flow (Ref. 5). As mentioned previously, the data for the 30° flat plate are considered doubtful because of a poor S/N (signal to noise) ratio (relative to the background tunnel noise, as perceived by the smooth plate configuration. The data for Mach 2.0 may be reasonably correct from an S/N standpoint, and hopefully, parts of the spectrum may be correct for other Mach number conditions. Figure 108 shows the same data normalized with δ^* as the length dimension and a direct comparison with data of Ref. 1; the reader is, however, again cautioned with regard to the background noise level. From the Mach 2.0 data, the spectra of the separated flow is considerably higher than the flat plate data. This conclusion is believed valid, despite some doubt as to the absolute quantitative accuracy.

Figure 109 shows the 60° flap data, using h and the boundary layer displacement thickness, respectively, as the length dimensions plotted to linear scales. In this case, the displacement thickness appears to offer a slightly improved correlation; however, because of the narrow range of free stream velocities involved, this cannot be regarded as conclusive proof. Figure 110 shows a comparison of data taken at M = 5 in Tunnel A with those from Tunnel C at Mach 10, and neither h nor δ^* will succeed in universalizing these data on a Strouhal number basis. Figure 111 shows the data plotted simply in the form of 1/3 Octave SPL-20 log (q_∞) vs. frequency. This plot resolves the frequency variation for Tunnel A fairly well, since the spread in free stream velocities was small, and the SPL data scale nicely to q_∞. The Tunnel C data level at Mach 10 is definitely higher, even with corrections for q_∞. There does appear to be more energy at high frequencies; however, it is evident that the spectra shapes are not the same at Mach 10 as they are at Mach 2 to 5. In Section II it has been noted that many new noise generating modes (vorticity, entropy, and sound) are involved at supersonic speeds which are greatly emphasized at hypersonic speeds. In particular, Ribners work (Ref. 29) on the interaction of turbulence with shock waves shows that the turbulent velocity fluctuations of the order of 1% interacting with a normal shock could generate noise levels such as those measured in Tunnel C. In the case of the 60° flap, the turbulence in the shock separated boundary layer ahead of the flap could interact with the detached shock ahead of the flap. This might plausibly behave in a manner similar to the idealized problem treated by Ribner in which convected vorticity with a random direction of propagation encounters a plane shock wave; however, the actual flow in the present tests is too complex to expect any quantitative correlation. Also, the vorticity mode which dominates the low speed data measured by previous investigators, still plays an important role in the low supersonic tests as evidenced by the similarity to low speed data of the axisymmetric results on the cylindrical body in the forward flare wake and for the base pressure tests; therefore, there may exist a crucial transition between Mach 5 and Mach 10 beyond which other mechanisms overpower the low speed vorticity mode in determining turbulent wall pressure fluctuations.

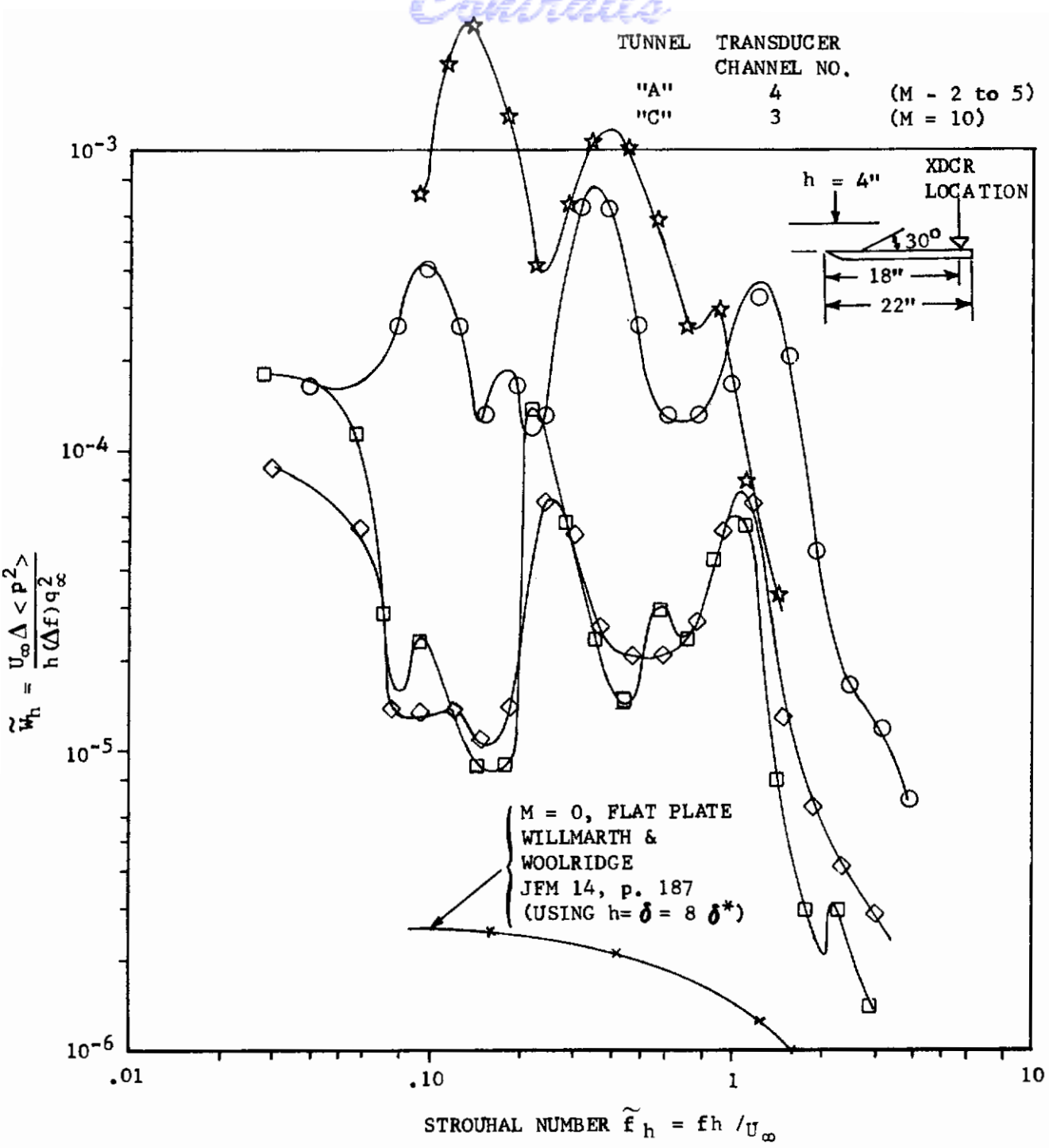

SYM	RUN/Gp	M_∞	R_e/L /FT	α	δ^* IN	θ IN	q_∞ PSI
○	16/119	2.0	1×10^6	0	3.3	.52	1.54
◇	17/127	3.5	↓	↓	4.2	.48	1.10
□	18/138	5.0			4.8	.32	.616
☆	1/5C	10.0			5.2	.40	1.14

FIGURE 107 NON-DIMENSIONAL FREQUENCY SPECTRA DERIVED FROM 1/3 OCTAVE ANALYSIS MODEL FP 30°

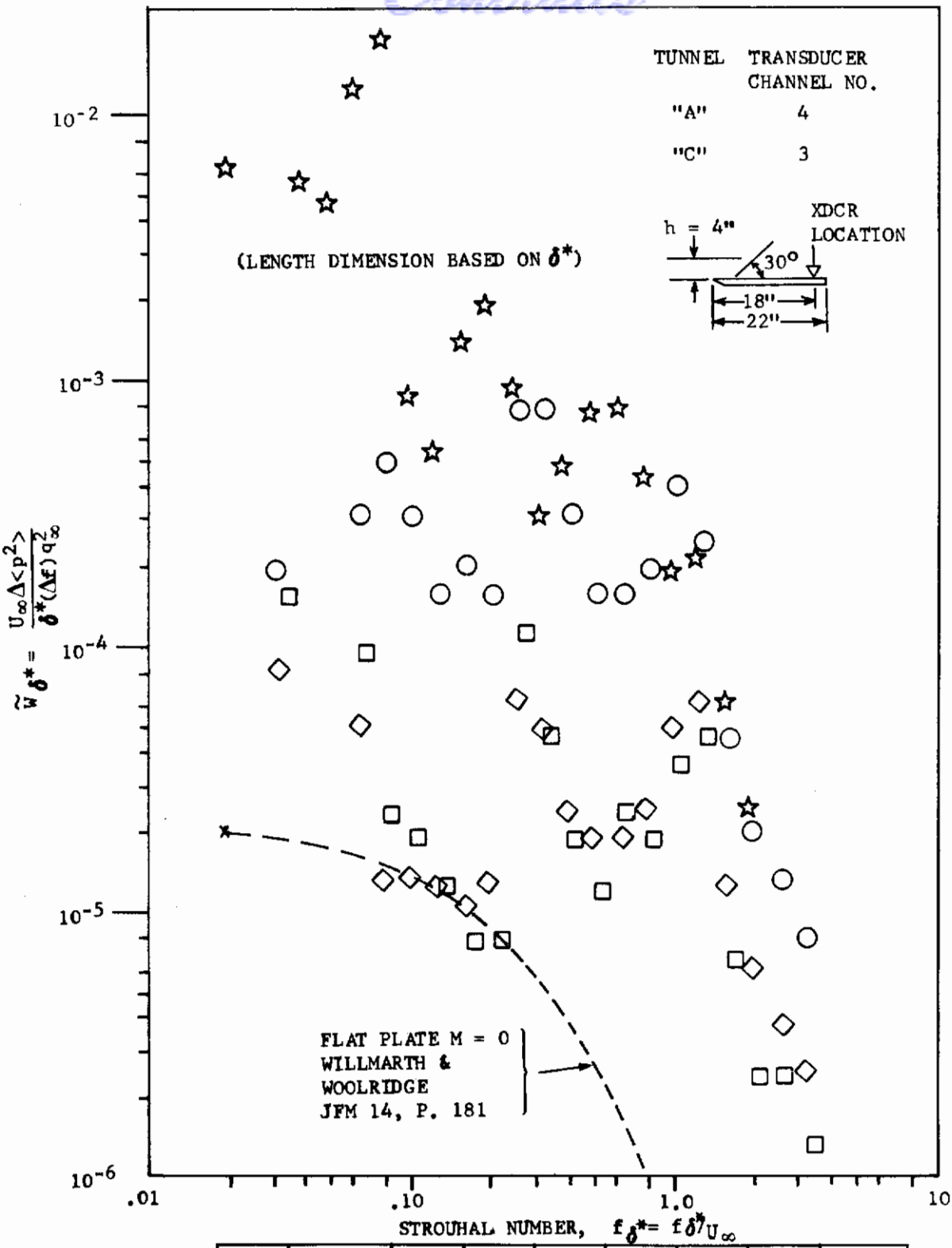

SYM	RUN/Gp	M_∞	R_e/L /FT	α	δ^* IN	θ IN	q_∞ PSI	R_{e_h}
○	16/117	2.0	1×10^6	0	3.3	.52	1.54	$.33\times10^6$
◇	17/127	3.5	↓	↓	4.2	.48	1.10	↓
□	18/138	5.0			4.8	.32	.62	
☆	1/5C	10.0			5.25	.40	1.14	

FIGURE 108 NON-DIMENSIONAL FREQUENCY SPECTRA DERIVED FROM 1/3 OCTAVE ANALYSIS MODEL FP 30°

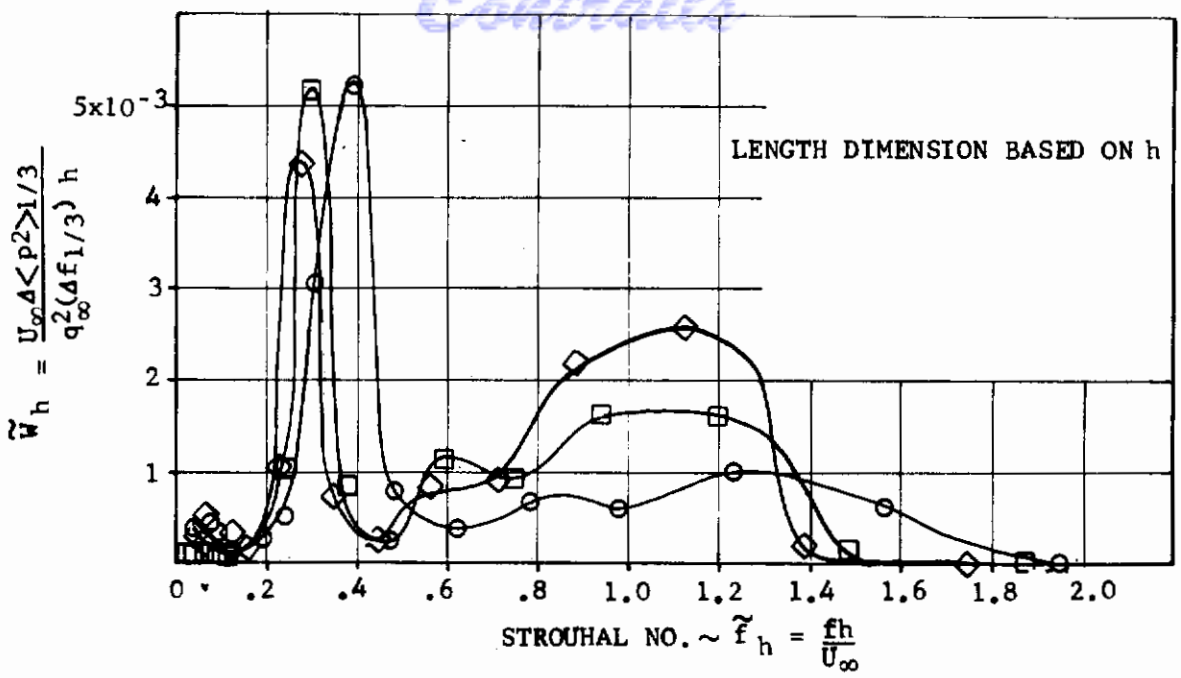

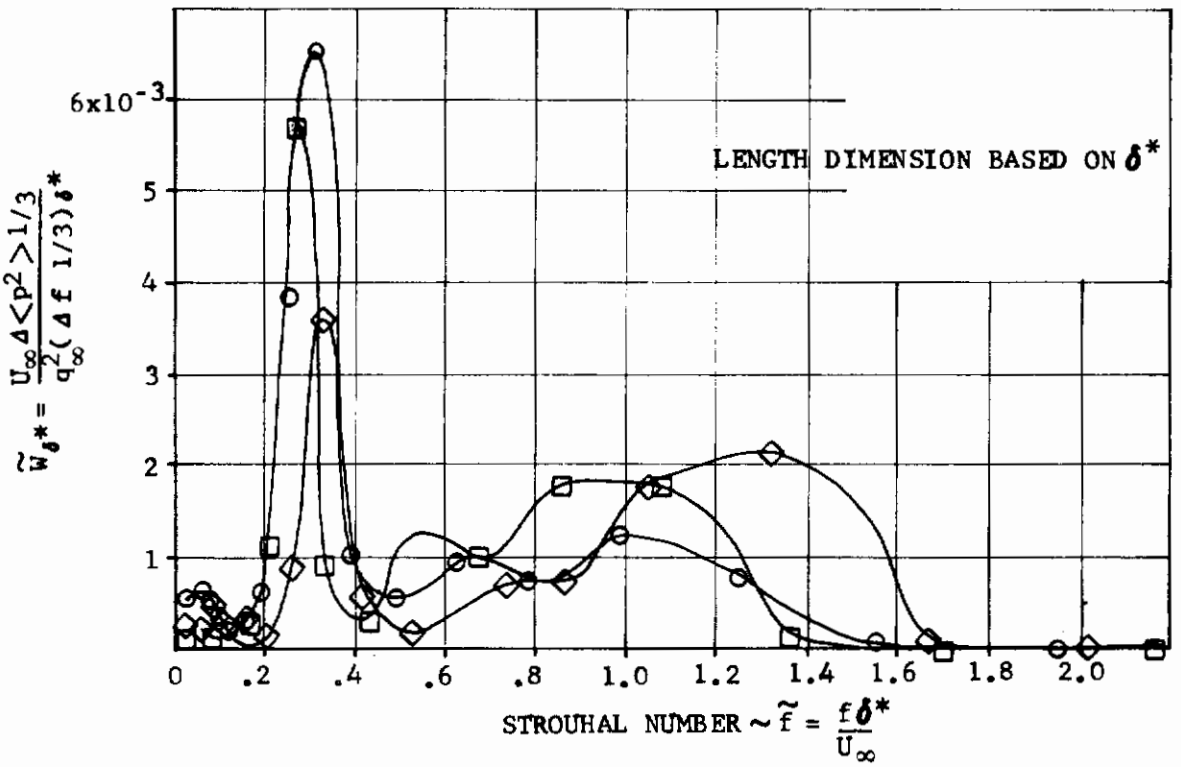

SYM	RUN/Gp	M_∞	R_e/L	α	δ^* (IN)	θ (IN)
◇	19/140	5.0	1×10^6	0	4.8	.47
□	20/145	3.5	↓	↓	3.6	.50
○	21/150	2.0			3.2	.68

FIGURE 109 NON-DIMENSIONAL FREQUENCY SPECTRA DERIVED FROM 1/3 OCTAVE ANALYSIS MODEL: FP 60° h = 4, δ^* = VAR, θ = VAR TRANSDUCER NO. 4

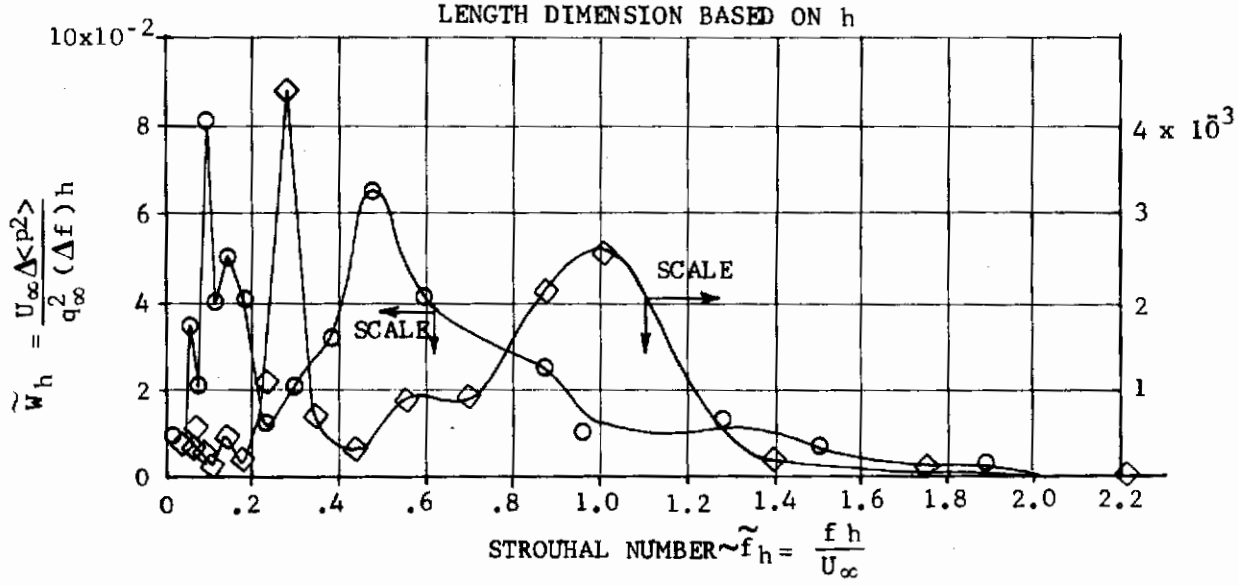

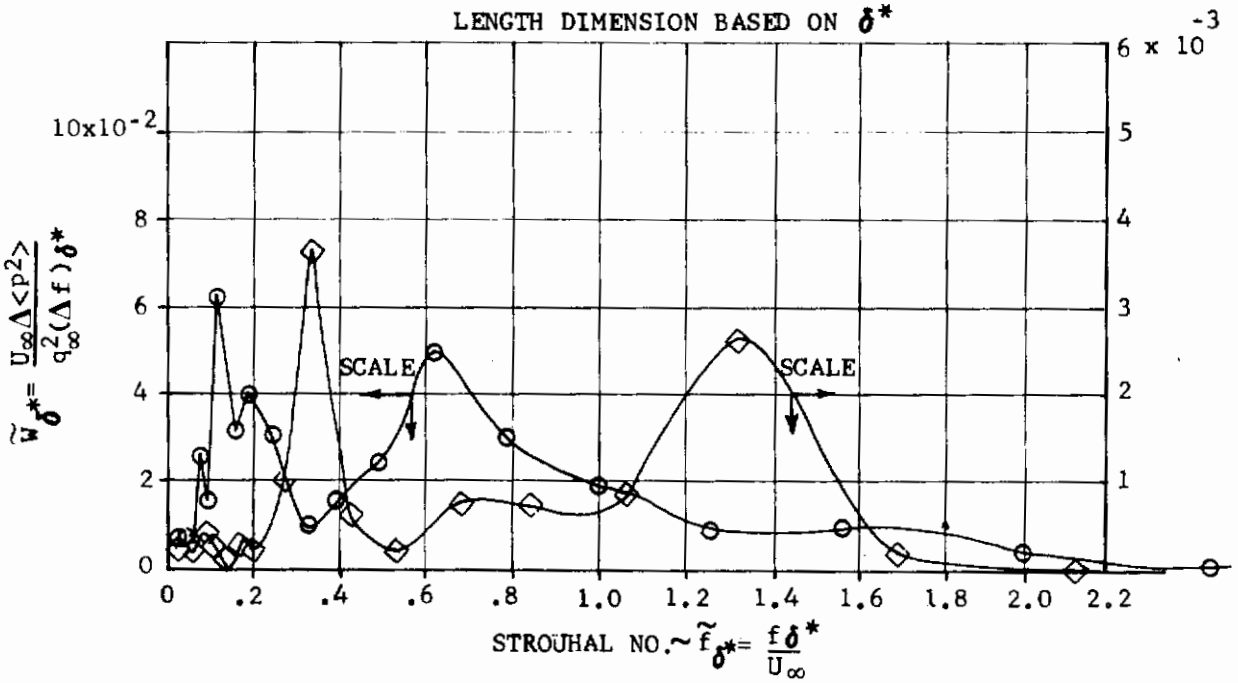

SYM	RUN/Gp	M_∞	R_e/L /FT^{-1}	α	δ^* (IN)	θ (IN)	XDCR CHAN
○	1/11C	10	$1x10^6$	0	5.25	.40	3
□	19/140	5	↓	↓	4.80	.47	4

FIGURE 110 NON-DIMENSIONAL FREQUENCY SPECTRA DERIVED FROM 1/3 OCTAVE ANALYSIS MODEL: FP 60° h = 4" δ^*= VAR. θ = VAR. TRANSDUCER CH. NO. 3 AT x = 18" AFT LE

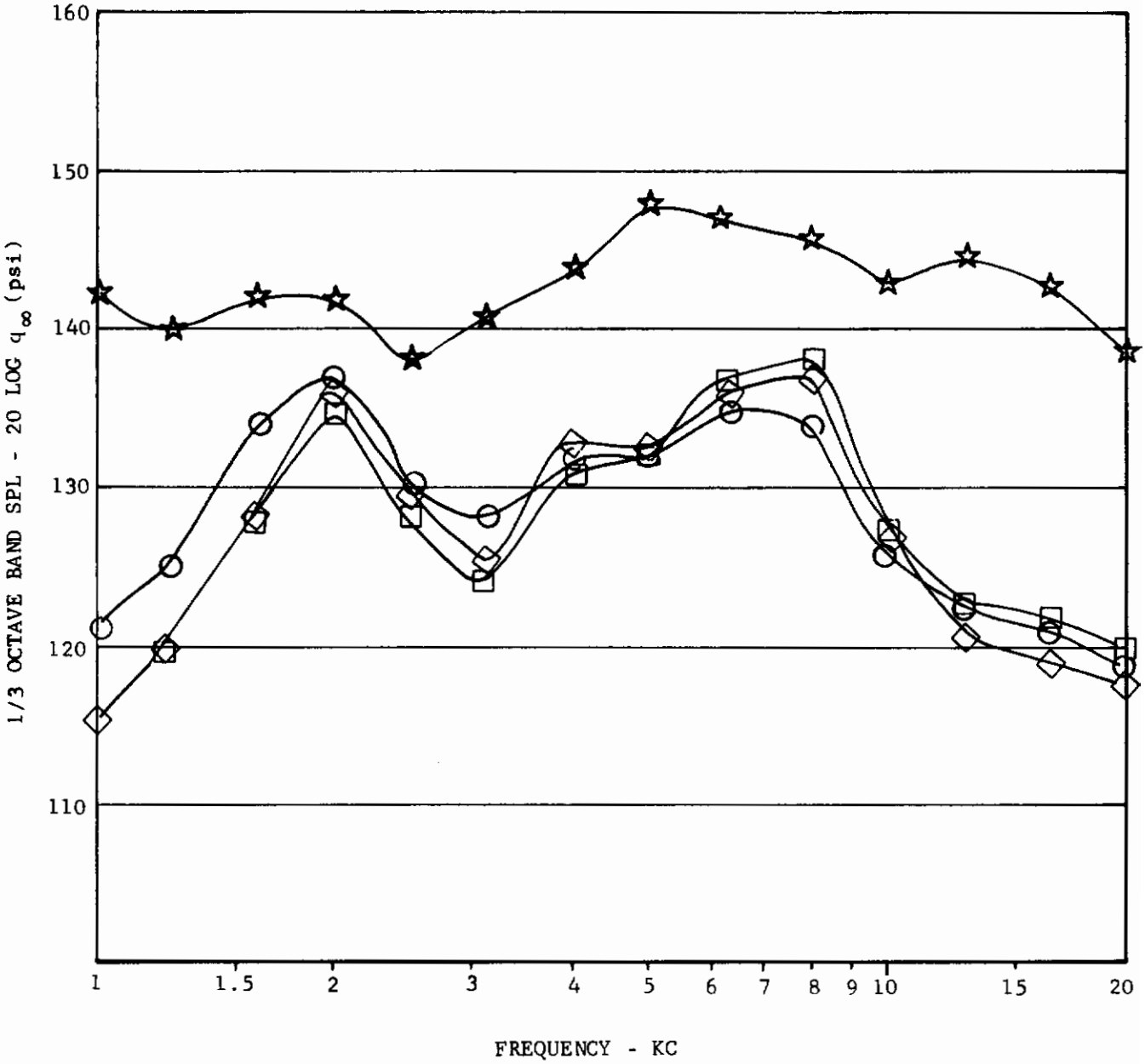

SYM	M_∞	q_∞ PSI	P_o PSIA	T_o °R	T_W °R	TUNNEL	CHANNEL
☆	10	1.138	750	1791	660	C	3
□	5	.624	18.6	567	519	A	4
◇	3.5	1.112	9.7	532	541	A	4
○	2	1.57	4.34	551	527	A	4

FIGURE 111 COMPARISON OF 1/3 OCTAVE SPL, CORRECTED FOR FREE STREAM DYNAMIC PRESSURE TO 1 psi 60° FLAP CONFIGURATION. α = 0, $R_e/L = 1 \times 10^6$/FT.

Figure 112 shows the 60° flap data normalized to the mean square pressure in the manner of Kistler and Chen (Ref. 17). Also shown are the supersonic plate results of Ref. 17. We again see a shift of the energy towards the low frequency range with strong attenuation beyond a Strouhal number of 2 (based on h). These results are in agreement with the axisymmetric results and those of Kistler for a forward facing step Ref. (13), which is encouraging. It is believed that the results of the present tests and those of Kistler (Ref. 13) indicate a general conclusion that turbulent wall pressure fluctuations under separated supersonic flows, when normalized to mean squared (RMS) pressure, are characterized by higher spectra, by perhaps a factor of 2 to 4, than the spectra of supersonic flat plate turbulent boundary layer. (See Figures 63 and 112). Since the square of RMS pressure is higher by a factor of 4 to 25 (Figures 78 and 40) than a typical plate value $(.006q_\infty)^2$, we can expect peak spectra of possibly 8 to 100 times higher than the spectra of clean turbulent boundary layers in the range $0.10 < fh/U_\infty < 1.0$. The results of the flat plate tests are considered better than those of the axisymmetric model with regard to possible errors due to vibratory response because there are far fewer vibration modes in the frequency range of interest. The mounting plate upon which the transducers were installed was idealized as a simply supported plate having length 22 inches, width 10 inches, and thickness ½ inch. If one considers only modes having at least one half wave in each direction, then there are 64 calculated natural frequencies below 20,000 cps as given by Table 8. These are obtained by substituting the simply supported plate mode shape, $w_{nm}(x,y)$ into the plate vibration equation |See Love (Ref. 38), p. 496.|

$$D\nabla^2\nabla^2 w_{nm} + \rho h \omega_{nm}^2 w_{nm} = 0 \qquad (137)$$

where

$$w_{nm}(x,y) = \sin\frac{m\pi x}{\ell} \sin\frac{m\pi y}{b} \; ; \; n, m = 1, 2, 3 \ldots \qquad (138)$$

The frequencies are given by the well known result of Eqs. (137 and 138) written in the form

$$f_{nm} = \frac{1}{2\pi}\frac{h}{\sqrt{12\,(1-\nu^2)}}\left(\frac{\pi}{\ell}\right)^2\sqrt{\frac{E}{\rho}}\left[m^2 + \frac{n^2\ell^2}{b^2}\right] \qquad (139)$$

Despite the numerous natural vibration frequencies below 20 kc, the random vibration response at the higher resonant frequencies is very small, due to the small area over which turbulent pressures are statistically correlated. This will be proven below.

Evaluation of Random Vibration Response Error

The forced vibratory response amplitude of the plate can be described in general by

$$w(x,y,\omega) = \sum_{n,m} \xi_{nm}(\omega)\, w_{nm}(x,y) \qquad (140)$$

$$\xi_{nm}(\omega) = \frac{Q_{nm}(\omega)}{M_{nm}\left(\omega_{nm}^2 - \omega^2\right) + i\left(M_{nm}\omega_{nm}^2 g\right)} \qquad (141)$$

TABLE 8

NATURAL VIBRATION FREQUENCIES OF THE FLAT PLATE
MODEL CALCULATED FROM SIMPLY SUPPORTED PLATE THEORY

f_{nm}(CPS)							
m \ n	1	2	3	4	5	6	7
1	573	2,000	4,370	7,700	11,960	17,200	23,400
2	869	2,292	4,670	8,000	12,350	17,500	
3	1,358	2,780	5,160	8,500	12,730	17,980	
4	2,040	3,470	5,950	9,170	13,410	18,650	
5	2,920	4,350	6,830	10,100	14,300	19,520	
6	4,000	5,470	7,810	11,400	15,400	20,600	
7	5,280	6,700	9,090	12,400	16,640	23,400	
8	6,750	8,180	10,560	13,890	18,100		
9	8,410	10,180	12,210	15,550	19,800		
10	10,380	11,700	14,080	17,400			
11	12,340	14,100	16,140	19,460			
12	14,580	16,100	18,400	21,750			
13	17,040	18,500	20,820				
14	19,700	21,120					
16	22,560						

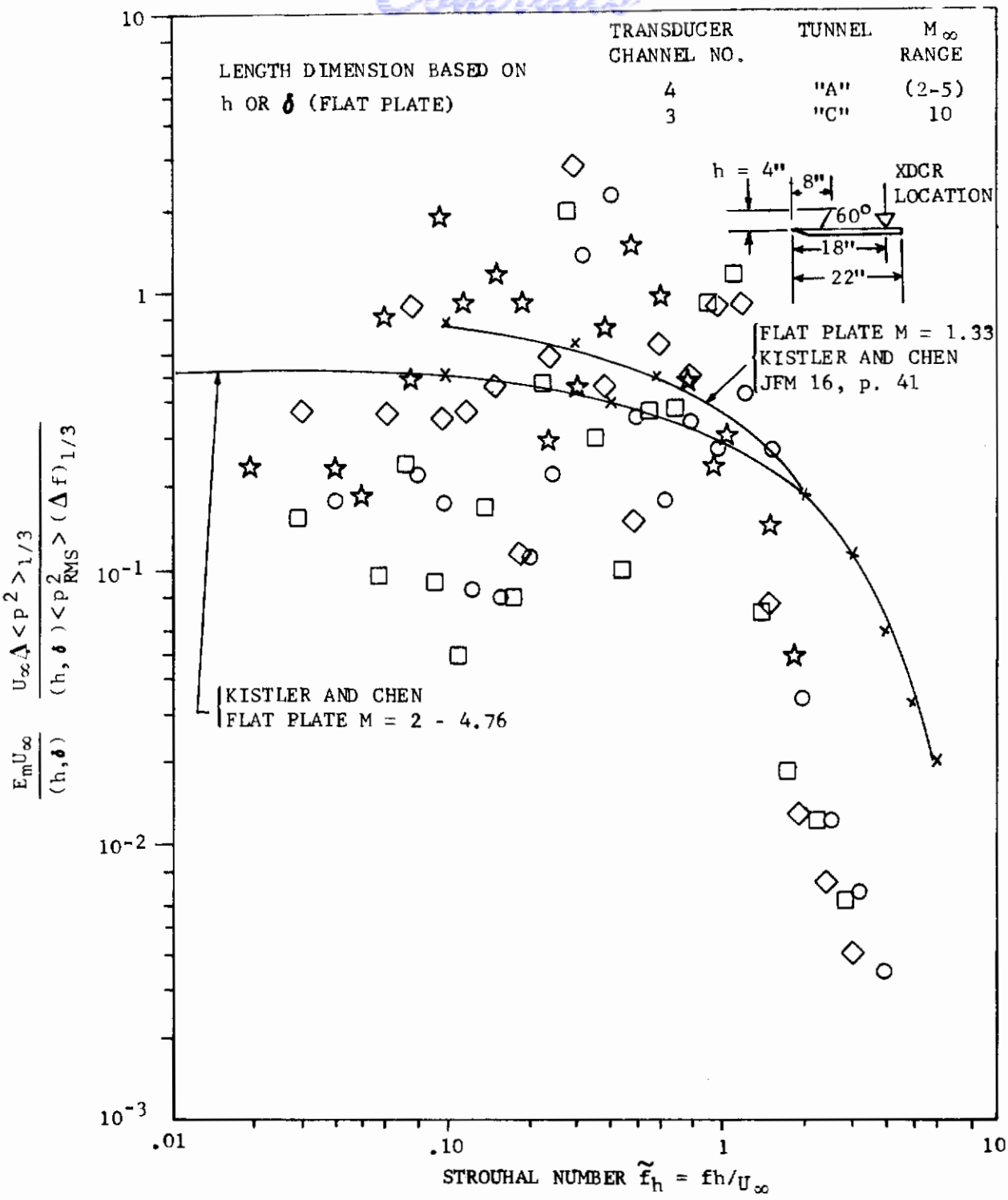

SYM	$Re/_L$ /FT	M_∞	α	SPL_{OA} db	R_{e_θ}	R_{e_h}
○	$1x10^6$	2.0	0	148		$.33x10^6$
◇	↓	3.5	↓	144	$4.37x10^4$	↓
□		5.0		140		
☆		10.0		158	$3.38x10^4$	

FIGURE 112 NON-DIMENSIONAL STROUHAL FREQUENCY SPECTRUM NORMALIZED TO THE MEAN SQUARED PRESSURE FLUCTUATION. FLAT PLATE MODEL, 60° FLAP

at resonance, $\omega = \omega_{nm}$, and

$$\xi_{nm}(\omega_{nm}) = \frac{Q_{nm}(\omega)}{\left(M_{nm}\,\omega_{nm}\right)^2 (ig)} \tag{142}$$

where g is the structural damping coefficient and Q_{nm} and M_{nm} are the generalized force and mass respectively defined by

$$Q_{nm}(\omega) = \int_{\text{Area}} w_{nm}(x,y)\, p(x,y,\omega)\, dA \tag{143}$$

$$M_{nm} = \int_{\text{Area}} w_{nm}^2(x,y)\, \rho h\, dA \tag{144}$$

For random excitation one can easily show that the cross spectra of ξ_{nm} is given by

$$R_{\xi}(\omega) \equiv \frac{\left|\xi_{nm}^2(\omega)\right|}{T} = \frac{\left[Q_{nm}^{*}\, Q_{nm}\right]}{T\left(M_{nm}\,\omega_{nm}^2\right)^2 g^2} = \frac{\frac{1}{2} W_Q(\omega)}{M_{nm}^2\,\omega_{nm}^4\, g^2} \tag{145}$$

where Q_{nm}^* is the complex conjugate of Q_{nm} and the brackets $\langle\,\rangle$ denote time averages of any statistical quantity to which it is applied. $Q_{nm}(\omega)$ is the Fourier transform of the time dependent generalized force

$$Q_{nm}(\omega) \equiv \int_0^T \hat{Q}_{nm}(t) \exp(-i\omega t)\, dt \tag{146}$$

$$= \int_{\text{Area}} w_{nm}(x,y)\, dA \int_0^T p(x,y,t)\, e^{-i\omega t}\, dt$$

We now develop an explicit formula for the vibratory response error averaged over the 1/3 octave band.

We define first the cross spectra of the generalized force

$$\Phi_q(\omega) \equiv \lim_{T\to\infty} \frac{1}{T} \left[Q_{nm}^{*}\, Q_{nm}\right] = \frac{1}{2} W_Q(\omega) \tag{147}$$

Also because in the time plane, $\hat{Q}_{nm}(t)$ is real, the physical spectra W_Q (defined for positive ω only) is related to the autocorrelation function $R_Q(\tau)$, which is even in τ, by

$$W_Q(\omega) \equiv 4 \int_0^{\infty} R_Q(\tau) \cos \omega\tau\, d\tau \;;\; 0 < \omega < \infty \tag{148}$$

$$R_Q(\tau) \equiv \left(Q^*(t)\, Q(t+\tau) \equiv \frac{1}{T} \int_0^T Q_{nm}(t)\, Q_{nm}(t+\tau)\, dt \right. \tag{149}$$

$$\hat{Q}_{nm}(t) \equiv \int_0^b dy \int_0^{\ell} w_{nm}(x,y)\, p(x,y,t)\, dx \tag{150}$$

Define the position vectors

$$\vec{r} = (x, y)$$

$$\vec{r}_1 = (x_1, y_1)$$

$$d\vec{r} = dx\, dy \tag{151}$$

$$d\vec{r}_1 = dx_1 dy_1$$

$$\vec{z} = \vec{r} - \vec{r}_1 = (\xi, \eta)$$

$$R_Q(\tau) = \int_{\text{Area}} d\vec{r} \int_{\text{Area}} w_{nm}(\vec{r})\, w_{nm}(\vec{r}_1) \times \int_0^T \frac{\left[p^*(\vec{r}, t)\, p(\vec{r}_1, t+\tau)\right]}{T} dt\, d\vec{r}_1 \tag{152}$$

Now 152 can be written

$$R_Q(\tau) = \int_0^b dy \int_0^\ell dx \sin^2\left(\frac{m\pi x}{\ell}\right) \sin^2\left(\frac{n\pi y}{b}\right) A_{corr}(\vec{r}, \tau) \left(p_{rms}^2\right) \tag{153}$$

where by definition then the correlation area is

$$A_{corr}(\vec{r}, \tau) \equiv \int_{\text{Area}} d\vec{z} \cos\left(\frac{m\pi\xi}{\ell}\right) \cos\left(\frac{n\pi\eta}{b}\right) R_p(\vec{z}, \tau) \tag{154}$$

Now we substitute Eqs. (154 and 153) with Eq. (148) and find

$$W_Q(\omega) = \left\langle p_{rms}^2 \right\rangle \int_0^b dy \int_0^\ell dx \sin^2\left(\frac{m\pi x}{\ell}\right) \sin^2\left(\frac{n\pi y}{b}\right) \tilde{A}_{corr}(\tilde{\omega}, x, y) \tag{155}$$

If we regard the turbulent pressures as homogeneous (though not necessarily isotropic) then $A_{corr}(\omega, x, y)$ is not a function of x and y and the narrow band correlation area is then defined by

$$A_{corr}(\vec{r}, \omega) \equiv 4 \int_0^\infty \cos\omega\tau\, d\tau\, A_{corr}(\vec{r}, \tau) \cong \text{constant} \tag{156}$$

and

$$R_p(\vec{z}, \tau) = \frac{1}{T} \int_0^T \left[p^*(\vec{r}, t)\, p(\vec{r}_1, t+\tau) \right] dt \tag{157}$$

$$W_p(\vec{z}, \omega) = 4 \int_0^\infty R_p(\vec{z}, \tau) \cos\omega\tau\, d\tau \tag{158}$$

$$= \left\langle p^2(0, \omega) \right\rangle \cos\left(\frac{\omega\xi}{U_c}\right) e^{-.11\left(\frac{\omega\xi}{U_c}\right) - .6\left(\frac{\omega\eta}{U_c}\right)} \tag{159}$$

Here we assume that the separated flow only affects the power spectrum $< p^2(o, \omega, >$ at least for the purposes of our error estimate. We have approximated the normalized narrow band space correlation of the pressure with the same expression used in Ref. 33. Carrying out the integrations in Eq. (155), one finds

$$W_Q(\omega) = \left\langle \left(p_{rms}^2\right) \right\rangle \; A_{corr}(\omega) \; \frac{b\ell}{4} \tag{160}$$

We now pursue the response calculation, having determined the cross spectra of the generalized force. The generalized mass from Eqs. 138 and 144 is

$$M_{nm} = \frac{\rho h b \ell}{4} = \frac{M}{4} \tag{161}$$

It turns out that the vibratory velocities are more convenient, so from Eq. 145 we calculate

$$R_{v_{nm}}(\omega_{nm}) \equiv \left\langle \omega_{nm}^2 \, \xi_{nm}^2 (\omega_{nm}) \right\rangle$$

$$\equiv \frac{\left\langle p_{rms}^2 \right\rangle \; A_{corr}(\omega) \; \frac{b\ell}{4}}{\omega_{nm}^2 \left(\frac{\rho h b \ell}{4}\right)^2 g^2} \tag{162}$$

We normalize the velocities to U_∞^2 and find that after integrating over the frequency band

$$\frac{\left(v_{nm}^2\right)}{U_\infty^2} = \frac{\left(p_{rms}^2\right)}{\left(\frac{\rho_\infty U_\infty^2}{4}\right)} \left[\frac{A_{corr}^{nm}(\omega)}{b\ell}\right] \left(\frac{\rho_\infty}{\rho_s}\right)^2 \left(\frac{U_\infty}{\omega_{nm} h_s}\right)^2 \widetilde{Q}_{Band}^2$$

$$= \frac{1}{4\pi^2} \left[\frac{\left\langle p_{rms}^2 \right\rangle}{q_\infty^2}\right] \left(\frac{\rho_\infty}{\rho_s}\right)^2 \left(\frac{U_\infty}{f_{nm} h_s}\right)^2 \widetilde{Q}_{Band}^2 \left[\frac{A_{corr}(\omega_{nm})}{b\ell}\right] \tag{163}$$

It is useful to define an admittance, Y_{nm}, such that

$$\frac{v_{nm}^2}{U_\infty^2} \equiv Y_{nm}^2 \; \frac{p_{rms}^2}{q_\infty^2} \tag{164}$$

$$Y_{nm}^2 = \frac{1}{4\pi^2} \left(\frac{\rho_\infty}{\rho_s}\right)^2 \left(\frac{U_\infty}{f_{nm} h_s}\right)^2 \widetilde{Q}_{Band}^2 \left[\frac{A_{corr}(\omega_{nm})}{b\ell}\right] \tag{165}$$

If there are several frequencies in the frequency band of interest, then

$$\frac{v^2(f)}{U_\infty^2} = \sum_{n,m} \frac{v_{nm}^2}{U_\infty^2} = Y_0^2 \; \frac{p_{rms}^2}{q_\infty^2} \tag{166}$$

Then

$$Y_0^2 = \sum_{n,m} Y_{nm}^2 \tag{167}$$

The vibration induced strain causes the piezoelectric crystal to read an erroneous pressure p'_{RMS} related to p_{RMS} by (Eq. 135)

$$\left(\frac{p'_{rms}}{p_{rms}}\right)^2 = \left\{ Y_0^2 \left(\frac{U_\infty}{c_c}\right)^2 \left(\frac{E_c}{q_\infty}\right)^2 \left(\frac{\omega \ell_c}{2c_c}\right)^2 + 1 \right\} \tag{168}$$

$$= \left\{ Y_0^2 \left(\frac{\rho_c}{\rho_\infty}\right)^2 \left(\frac{\omega_c \ell_c}{U_\infty}\right)^2 + 1 \right\} \tag{169}$$

From Eqs. (169 and 165) we find

$$\left(\frac{p'_{rms}}{p_{rms}}\right)^2 = \left\{ 1 + \sum_{n,m} \tilde{Q}_{Band}^2 \left(\frac{\rho_c}{\rho_s}\right)^2 \left(\frac{\ell_c}{h_s}\right)^2 \left[\frac{A_{corr}(\omega)}{b\ell}\right] \right\} \tag{170}$$

where $\tilde{Q}_{band}$ is a dynamic magnification factor integrated over a finite band width, Δf_B which is approximately:

$$\tilde{Q}_{Band}^2 \cong \frac{Q_{max}}{\left(\Delta f_B \sqrt{2}/2 f_{cB}\right)} \left\{ \tan^{-1}\left(Q_{max} \frac{\Delta f_B}{2 f_{cB}}\right) \sqrt{2} \right\} \tag{171}$$

$$Q_{max} = 1/g \tag{172}$$

When $\left(\frac{Q_{max} \Delta f_B}{\sqrt{2}\, f_{CB}}\right) \to 0$ then $\tilde{Q}_{Band} \to Q_{max}^2 = \frac{1}{g^2}$, as one would expect.

Numerical values for the present configuration are obtained by putting for the crystal thickness l_c = 10 in. Also, $\rho_c = 5.5 \times 10^3 kg/in^3 \rho_s = 7.8 \times 10^3 kg/m^3$, h_s = 0.50 in., $\Delta f_B / 2 f_{cB}$ = 0.128 (1/3 octave band) Q_{max} = 200. (This is probably pessimistic considering the presence of a shock mount, representing a rather sharply "tuned" response.) We find

$$\tilde{Q}_{1/3}^2 = 8.39\, Q_{max} = 1678 \tag{173}$$

and

$$\left(\frac{p'_{rms}}{p_{rms}}\right)^2 = \left\{ 1 + \sum_{n,m} 33.2 \left[\frac{A_{corr}(f_{nm})}{b\ell}\right] \right\} \tag{174}$$

Values of $\frac{A_{corr}(f_{nm})}{bl}$ are plotted vs. m at various n in Figure 113. To calculate the error for any 1/3 octave band, one finds first the values of f_{nm} lying in the given frequency band. Next, for the n and m corresponding to each f_{nm}, one finds $\frac{A_{corr}(f_{nm})}{bl}$ from Figure 113. Finally, these values are put into Eq. 174. As an example, consider the band

$$6860 \leq f \leq 8630 \; ; \quad f_c \cong 8000 \text{ cps}$$

From Table 8, we find the following frequencies in the selected analysis band (see Table 9).

TABLE 9 FREQUENCIES INSIDE $6860 \leq f \leq 8630$ cp and (A_{nm}/bl) VALUES

n	m	f_{nm}	$\frac{A_{nm}}{bl}$
1	9	8410	.00850
2	8	8180	.00850
3	6	7810	.00650
4	1	7700	.00345
	2	8000	.00340
	3	8500	.00320
		Sum	.03355

Then for this 1/3 octave band the vibratory error ratio is

$$\left(\frac{p'_{rms}}{p_{rms}}\right)^2 = \left\{1 + 33.2\,(.0335)\right\} = 1 + 1.115$$

$$\left(\frac{p'_{rms}}{p_{rms}}\right) = \sqrt{2.115} = 1.455 \text{ or } 3.25 \text{ db}$$

We then find a 3db error in this band, based on a dynamic magnification factor of 200 for narrow band response, which is probably too high for the shock mounted transducers; also, a given transducer will not always be at an anti-node of the vibration mode, which is a pessimistic aspect of the above calculation, probably of the order of two to one.

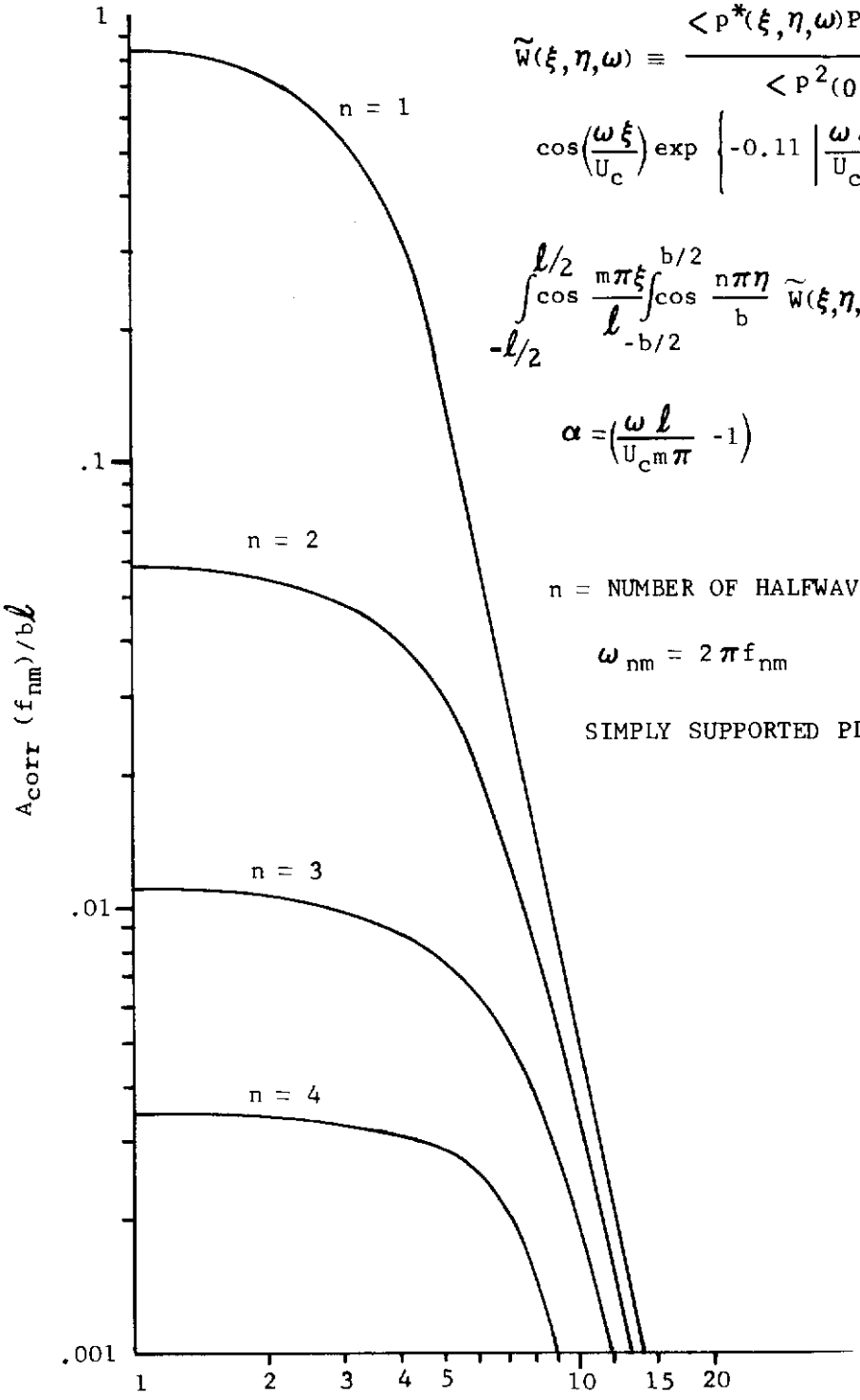

$$\tilde{W}(\xi,\eta,\omega) \equiv \frac{\langle p^*(\xi,\eta,\omega)P(0,0,\omega)\rangle}{\langle p^2(0,0,\omega)\rangle} =$$

$$\cos\left(\frac{\omega\xi}{U_c}\right)\exp\left\{-0.11\left|\frac{\omega\xi}{U_c}\right| - 0.6\left|\frac{\omega\eta}{U_c}\right|\right\} \quad A_{corr}(f_{nm}) =$$

$$\int_{-\ell/2}^{\ell/2}\cos\frac{m\pi\xi}{\ell}\int_{-b/2}^{b/2}\cos\frac{n\pi\eta}{b}\,\tilde{W}(\xi,\eta,\omega)\,d\eta\,d\xi = \frac{1.004}{\left[n^2+m^2\left[\alpha^2+.0866\right]\right]}$$

$$\alpha = \left(\frac{\omega\ell}{U_c m\pi} - 1\right)$$

n = NUMBER OF HALFWAVES IN THE SPANWISE DIRECTION

$\omega_{nm} = 2\pi f_{nm}$

SIMPLY SUPPORTED PLATE ℓ = 22 IN., b = 10 IN.

FIGURE 113 NARROW BAND VALUES OF (CORRELATION AREA)/PLATE AREA EVALUATED AT f_{nm} VS m (BASED ON LOW SPEED NORMALIZED CROSS SPECTRAL DENSITIES FOR TURBULENT BOUNDARY LAYER PRESSURE. ASSUMED CONVECTION SPEED U_c = 2000 FT/SEC

Cross Spectra and Spatial Correlation of Pressure Fluctuations

Measurements of cross spectra of spatially separated transducers were attempted, by means of multiplying the signals of a given pair of transducer channels, after adjusting their phase properly, and filtering the product using a 60 cps band width. These measurements were attempted for the flat plate model for selected Tunnel A and Tunnel C test points. In the case of Tunnel A streamwise correlations were tried for Channels 4 and 5 (x = 18 and 20 inches; y = 0). Transverse correlations were tried using Channels 5 and 6 (x = 20 inches; y = 0 and 4 inches). It was not possible to correlate with Channel 1 (x = 20 inches; y = 2 inches) because Channel 1 was inoperative during the flat plate tests in Tunnel A. The results of the present cross correlation tests were negative to the extent that it was felt that they should not be reported. This opinion is based upon studying the low speed results as summarized by Corcos in Ref. 23 and the fact that similar results were implied by the "convection velocities" measured by Kistler and Chen beneath a flat plate boundary layer in supersonic flow (Ref. 17) and by Kistler in the case of separated supersonic flow ahead of a forward facing step (Ref. 13). The principal measurable difference between supersonic flow measurements of Kistler in Refs. (13 and 17) and the subsonic measurements as summarized by Corcos (Ref. 23) seems to be that the convection speed represents a lower fraction of the free stream speed for the Mach number range of the present tests. For a supersonic boundary layer, Kistler and Chen data (Ref. 17) show that U_c/U_∞ = 0.6. One of the obvious theoretical factors bearing on this is that a moving eddy can have a subsonic influence on the wall only when the speed of the eddy relative to the wall is less than the local speed of sound in the boundary layer. In Ref. 17, some estimates are made in the case of an insulated, flat plate boundary layer. In Ref. 13, the convection velocities are even lower, on the order of 50% of free stream velocity for the separated flow ahead of a forward facing step. This factor might be partly attributed to a reduction of the local free stream velocity in the outer inviscid flow in the compression region ahead of the step; in this case, one could say that the ratio of convection velocity to local free stream velocity for the separated supersonic flow was not essentially different from the convection speed ratio for a convected pattern of turbulent pressure over a flat plate.

The difficulties of the present tests with regard to signal to noise ratio are believed to be acutely amplified with regard to evaluation of cross spectra, especially in the lateral direction. It is believed that an even thicker wake should be created for any future tests in conjunction with a larger sized transducer to achieve greater sensitivity without sacrificing frequency response, so that at least the low frequency portion of the cross spectra curve could be obtained. Also, it is believed that the minimum separation of transducers should be decreased. It would be desirable to be able to vary the position of a single transducer (e.g. like a roving microphone) rather than attempt to correlate the signals of two separate transducers, each with somewhat different individual calibrations. This, however, poses a very difficult model design problem for a supersonic wind tunnel test where permanently positioned instruments are much easier to install.

There appears to be one possibility for the estimation of cross spectra from the knowledge of the power spectra derived from the present tests. This possibility lies in the fact that the low speed cross spectra for turbulent boundary layers permits a normalization relative to the power spectra which does not depend on the thickness of the boundary layer (Ref. 23). If this is the case, the boundary layer thickness enters only into the power spectra. A similar situation may well exist for separated flows. Let us write the cross spectra in the form

$$W_p(\xi, \eta, \omega) = 4 \int_0^\infty \cos \omega\tau \int_0^T \left[p^*(\xi, \eta, t)\, p(0, 0, t+\tau) \right] \frac{dt}{T} d\tau \qquad (175)$$

and the power spectrum at $\xi = \eta = 0$ is $W_p(0,0,\omega)$. Then the normalized cross spectra is defined as

$$T(\xi,\eta,\omega) \equiv \frac{W_p(\xi,\eta,\omega)}{W_p(0,0,\omega)} \tag{176}$$

For low speed boundary layer flows, Corcos (Ref. 23) based on Willmarth and Woolridge's data Ref. (1) infers a form

$$T(\xi,\eta,\omega) = \cos\left(\frac{\omega\xi}{U_c}\right)\exp\left\{-a_\xi\left|\frac{\omega\xi}{U_c}\right| - a_\eta\left|\frac{\omega\eta}{U_c}\right|\right\} \tag{177}$$

It would be desirable in the future to see if a result such as Eq. (177) would be verified, and if the quantities (a_ξ, a_η and U_c) could be found for flow configurations such as the ones for which the present exploratory test program was conducted. In Ref. (33), Eq. (177) was employed to calculate random vibration response of cylindrical shells using $a_\xi = 0.11$ and $a_\eta = 0.60$. These quantities were used in our previous estimates of the random vibration errors in Section V. These values were based on earlier work of Bakewell (Ref. 43). Subsequent work of Bakewell (Ref. 35) with regard to the narrow band longitudinal space-time correlations suggest a value $a_\xi = 0.7$.

In a future test program, it might be desirable to concentrate on individual flow regimes such as that behind the forward flare wake in order to establish a tentative result such as Eq. (177). This has been the pattern of Refs. (1, 13, 17, 34, 35) which are representative of some of the most reliable of previous experimental results. In many cases, the investigations were justifiably restricted to a single Mach number. By contrast, the present exploratory program investigated a broad range of aerodynamic and configuration parameters, using a multiplicity of individual transducers designed to measure fluctuations covering a wide range of RMS level (from 125 db to 170 db).

REFERENCES

1. Willmarth, W. W. and Woolridge, C. E., "Measurements of the Fluctuating Pressure at the Wall Beneath a Thick Turbulent Boundary Layer", Jour. Fluid Mech., 14, p. 187 (1962).

2. Townsend, A. A., "The Structure of Turbulent Shear Flow", Cambridge U. Press, 1956.

3. Laufer, J., "Aerodynamic Noise in Supersonic Wind Tunnels," Jour. Aero Space Sci., 28, pp. 685-692, (1961).

4. Liepmann, H., and Roshko, A., "Elements of Gas Dynamics", J. Wiley & Sons, New York, (1957).

5. Schlichting, H., "Boundary Layer Theory", (Transl. by J. Kestin) 4th Ed., McGraw-Hill, New York (1960).

6. Lighthill, M. J., "Sound Generated Aerodynamically," (The Bakerian Lecture, 1961) Proc. Royal Soc., A267, pp. 147-182, (1952).

7. Chu, B. T., and Kovasznay, L. S. G., "Nonlinear Interactions in a Viscous, Heat Conducting Compressible Gas," Jour. Fluid Mech., 3, pp. 494-514, (1958).

8. Miles, J. W., "The Potential Theory of Unsteady Supersonic Flow," Cambridge U. Press, 1959.

9. Blokhintsev, D. I., "Acoustics of a Nonhomogeneous, Moving Medium," (Transl. from Russian) NACA TM No. 1399, (1956).

10. Anderson, W. E., "Instrumentation Report, Noise from Separated Flow," Report NOR 64-127, Northrop Corp., Norair Div., Hawthorne, Calif., (1964).

11. Revell, J. D. and Gleason, R. E., "Pretest Report for Wind Tunnel Test Program, Noise from Separated Flow to be Conducted at AEDC VKF, " Report NOR 64-148, Northrop Corp., Norair Div., Hawthorne, Calif., (1964).

12. Eldred, K. M., "Base Pressure Fluctuations," Jour. Acoust. Soc. Am. 33, pp. 59-63, (1961).

13. Kistler, A. L., "Fluctuating Wall Pressure Under a Separated Supersonic Flow," Jour. Acoust. Soc. Am., 36, pp. 543-550, (1964).

14. Bogdonoff, S. M., "Some Experimental Studies of the Separation of Supersonic Turbulent Boundary Layers," Heat Transfer and Fluid Mechanics Inst. Preprints of Papers, Univ. of Calif., Los Angeles, (1955).

15. Chapman, D. R., Kuehn, D. M., and Larson, K. H., "Investigation of Separated Flows in Supersonic and Subsonic Streams with Emphasis on the Effect of Transition," NASA Report 1356, (1958).

16. Heuter, T. F., and Bolt, R. H., "Sonics, Techniques for the Use of Sound and Ultrasound in Engineering and Science", John Wiley & Sons, New York, (1955).

REFERENCES (Cont.)

17. Kistler, A. L., and Chen, W. S., "A Fluctuating Pressure Field in a Supersonic Turbulent Boundary Layer," Jour. Fluid Mech., 16, Part I, pp. 41-64, (1963).

18. Lighthill, M. J., "Jet Noise," AIAA Jour., 1, pp. 1507-1517, (1963).

19. Lighthill, M. J., "On Sound Generated Aerodynamically, Part I: General Theory", Proc. Roy. Soc. (London) A211, pp. 564-587, (1952).

20. Lighthill, M. J., "On Sound Generated Aerodynamically, Part II: Turbulence as a Source of Sound," Proc. Roy. Soc. (London) A222, pp. 1-32 (1954).

21. Lilley, G. M., "Wall Pressure Fluctuation Under a Turbulent Boundary Layer at Subsonic and Supersonic Speeds," The College of Aeronautics, Cranfield (England) Note No. 140, March, 1963.

22. Phillips, O. M., "On the Generation of Sound by Supersonic Turbulent Shear Layers," Jour. Fluid Mech., 9, pp. 1-28 (1960).

23. Corcos, G. M., "The Structure of the Turbulent Pressure Field in Boundary Layer Flows," Jour. Fluid Mech., 18, (Part 3), pp. 353-378, (1964).

24. Powell, A., "Theory of Vortex Sound," Jour. Acoust. Soc. America, 36, pp. 177-195, (Jan. 1964).

25. Hayes, W. D. and Probstein, R. F., "Hypersonic Flow Theory", Academic Press, New York (1959).

26. Keuhn, D. M., "Experimental Investigation of the Pressure Rise Required for the Incipient Separation of Turbulent Boundary Layers in Two Dimensional Supersonic Flow," NASA Memo 1-21-59A, (1959).

27. Lin, C. C., "The Theory of Hydrodynamic Stability", Cambridge U. Press, (1955).

28. Trilling, L., "Oscillating Shock-Boundary-Layer Interaction," Jour. Aero/Space Sciences, 25, pp. 301-304, May 1958.

29. Ribner, H. W., "Shock-Turbulence Interaction and the Generation of Noise," NACA Report 1233 (Supersedes NACA TN 3255), (1955).

30. Rayleigh, J. W. S., "The Theory of Sound", Vol. II, Dover Publications, New York, (1945).

31. Ames Research Staff, "Equations, Tables and Charts for Compressible Flow," NACA Report 1135, (1953).

32. Weingarten, V. I., "Free Vibrations of Thin Cylindrical Shells," AIAA Journal 2, No. 4, pp. 717-721, (April 1964).

33. Rattayya, J. V., and Junger, M. C., "Flow Excitation of Cylindrical Shells and Associated Coincidence Effects," Jour. Acoust. Soc. Am., 36, No. 5, pp. 878-884, (May 1964).

34. Serafini, John S., "Wall Pressure Fluctuations and Pressure-Velocity Correlations in a Turbulent Boundary Layer," NASA TR R-165, (1963).

35. Bakewell, H. P., Jr., "Narrow-Band Investigations of the Longitudinal Space-Time Correlation Function in Turbulent Air Flow," Jour. Acoust. Soc. Am., 36, No. 1, pp. 146-148, (Jan. 1964).

REFERENCES (Cont.)

36. Heckl, M., "Vibrations of Point Driven Cylindrical Shells," Jour. Acoust. Soc. Am., 34, No. 10, pp. 1553-1557, (Oct. 1962).

37. Cady, W. G., "Piezoelectricity", (Vol. I) Revised Ed., Dover Publications, Inc., (1964).

38. Love, A. E. H., "Mathematical Theory of Elasticity," Dover Publications, Inc.) (4th Ed.), (1944).

39. Brekhovskikh, L. M., "Waves in Layered Media", (Trans. from Russian) Academic Press, (1960).

40. Tartarski, V. I., "Wave Propagation in a Turbulent Medium", (Trans. from Russian), McGraw-Hill Book Co., (1961).

41. Gadd, L. E., "Laminar Separation in Supersonic Flow," Jour. Aero Sci., 24, pp. 759-771, (October 1957).

42. Corcos, G. M., "Resolution of Pressure in Turbulence," Jour. Acoust. Soc. Am., 35, pp. 192-199 (February 1963).

43. Bakewell, H. P., Jr., Carey, G. F., Libuha, J. J., Schloemer, H. H., and Von Winkle, W. A., "Wall Pressure Fluctuations in a Turbulent Pipe Flow," U. S. Navy Underwater Sound Lab. Rept. No. 559 (August 1952) (See also, Jour. Acoust. Soc. Am., 35, p. 936 (1963).

44. Willmarth, W. W., "Wall Pressure Fluctuations in a Turbulent Boundary Layer," Jour. Acoust. Soc. Am., 28, pp. 1048-1053, (Nov. 1956).

45. Willmarth, W. W., "Space-Time Correlations and Spectra of Wall Pressure in a Turbulent Boundary Layer," NASA Memo 3-17-59 W, (1959).

46. Willmarth, W. W., "Small Barium Titanate Transducer for Aerodynamic or Acoustic Measurements," Rev. Sci. Inst., 29, pp. 218-222, (March 1958).

47. Tack, D. H., Smith, M. W., and Lambert, R. F. "Wall Pressure Correlations in Turbulent Air Flow, "Jour. Acoust. Soc. Am. 33, pp. 410-418, (April 1961).

48. Bull, M. K., "Properties of the Fluctuating Wall Pressure Field of a Turbulent Boundary Layer," University of Southampton, A.A.S.U. Report No. 234, (1963).

49. Willmarth, W. W. "Corrigendium: Measurement of Fluctuating Pressure at the Wall Beneath a Thick Turbulent Boundary Layer", Jour. Fluid Mech., 21, pp. 107-110, (January 1965).

50. Harrison, Mark, "Pressure Fluctuations on the Wall Adjacent to a Turbulent Boundary Layer, "Report 1260, David Taylor Model Basin, (December 1958).

51. Skudrzyk, E. J., and Haddle, G. P., "Noise Production in a Turbulent Boundary Layer by Smooth and Rough Surfaces," Jour. Acoust. Soc. Am., 32, pp. 19-34, (January 1960).

52. Von Winkle, W. A., "Some Measurements of Longitudinal Space-Time Correlations of Wall Pressure Fluctuations in Turbulent Pipe Flow", Inst. Engr. Research U. of Calif., Berkeley, Calif., (Sept. 1961).

53. Batchelor, G. K., The Theory of Homogeneous Turbulence", Cambridge University Press, (1956).

REFERENCES (Cont.)

54. Kraichnan, R. H., "Pressure Field Within Homogeneous Anisotropic Turbulence", Jour. Acoust. Soc. Am., 28, pp. 64-72, (January 1956).

55. Kraichnan, R. H., "Pressure Fluctuations in Turbulent Flow Over a Flat Plate," Jour. Acoust. Soc. Am., 28, pp. 378-390 (May 1956).

56. Lilley, G. M., "Pressure Fluctuations in an Incompressible Turbulent Boundary Layer, "Rep. 133, The College of Aeronautics (Cranfield), (June 1960).

57. Lilley, G. M., and Hodgson, T. H., "On Surface Pressures in Turbulent Boundary Layers," Note 101, The College of Aeronautics (Cranfield), (1960), (Also revised Rept. 276 AGARD, April 1960).

APPENDIX I

ONE-THIRD OCTAVE BAND

SPECTRA

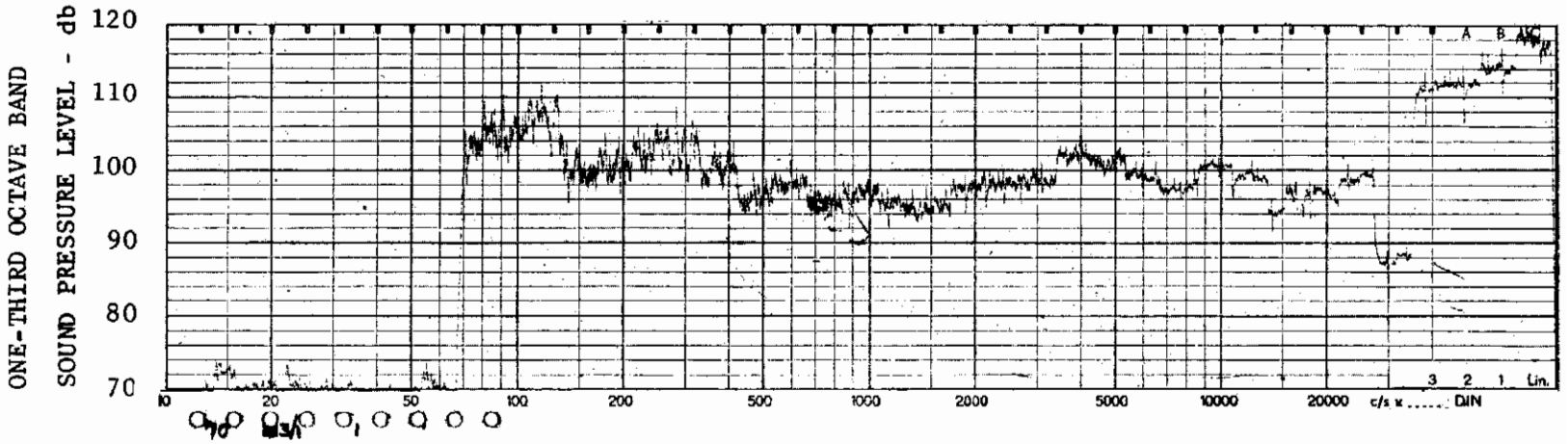

FIGURE 1 ONE-THIRD OCTAVE BAND SPECTRUM MODEL: AXISYM

CHANNEL: 1 MACH NO.: 5 α: 0 ϕ: 0 Re_∞/FT.: 0.5×10^6 AEDC GROUP NO.: 3/1

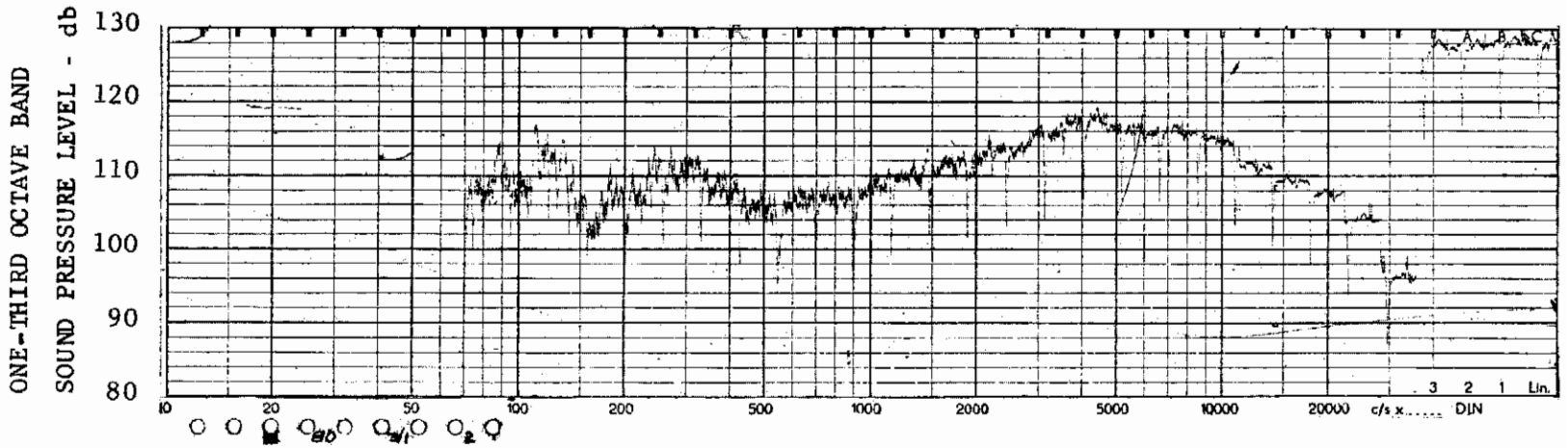

FIGURE 2 ONE-THIRD OCTAVE BAND SPECTRUM MODEL: AXISYM

CHANNEL: 2 MACH NO.: 5 α: 0 ϕ: 0 Re_∞/FT.: 0.5×10^6 AEDC GROUP NO.: 3/1

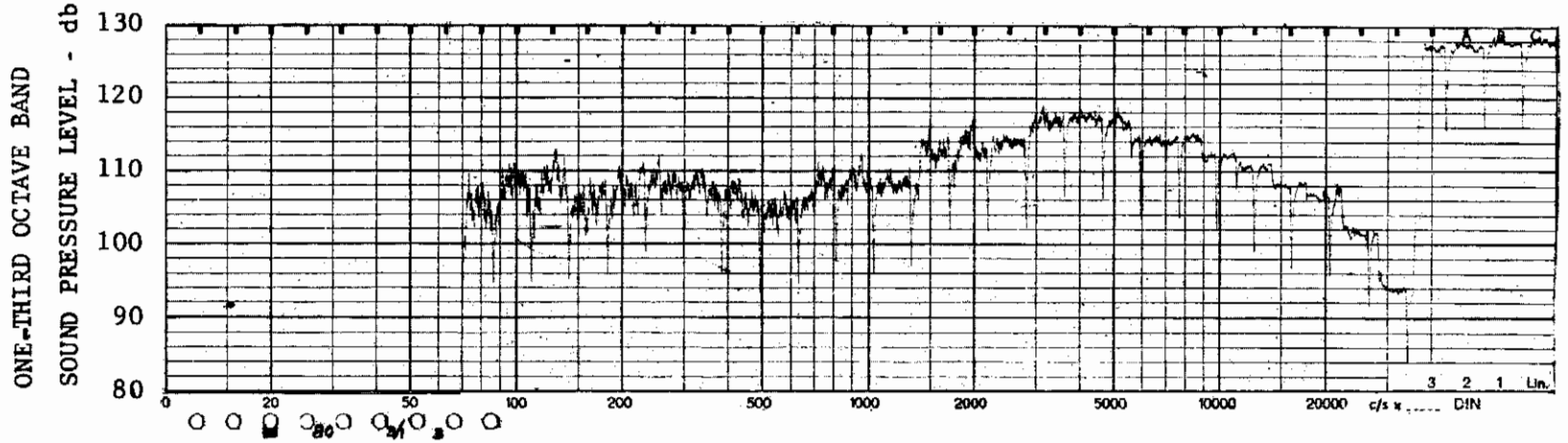

FIGURE 3 ONE-THIRD OCTAVE BAND SPECTRUM MODEL AXISYM

CHANNEL: 3 MACH NO.: 5 α: 0 ϕ: 0 Re_∞/FT.: 0.5×10^6 AEDC GROUP NO.: 3/1

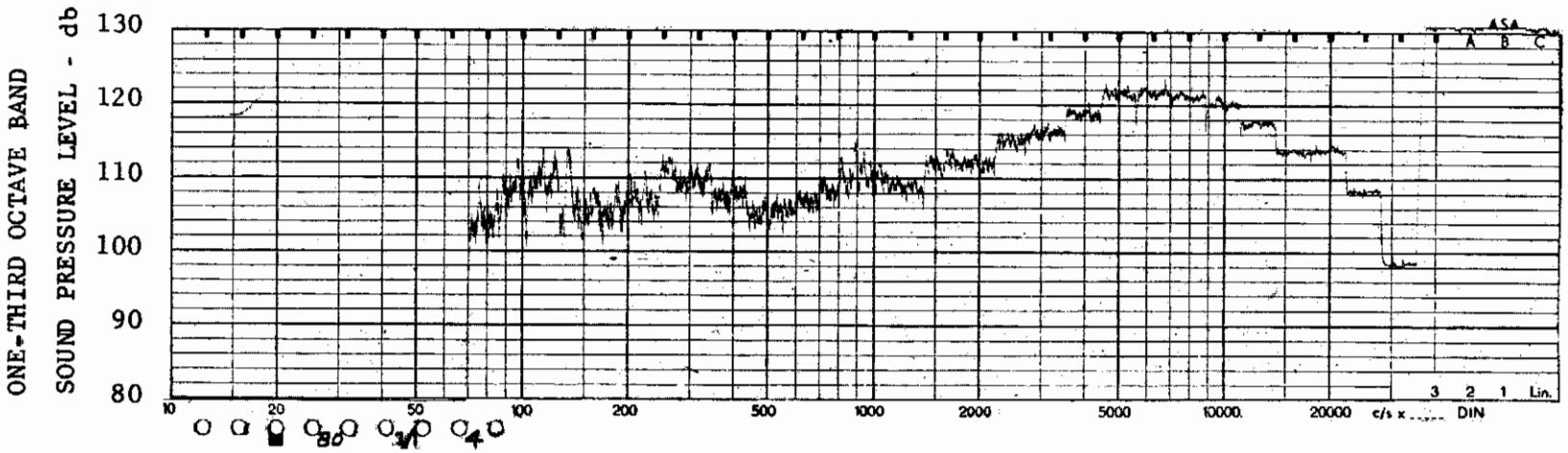

FIGURE 4 ONE-THIRD OCTAVE BAND SPECTRUM MODEL: AXISYM

CHANNEL: 4 MACH NO.: 5 α: 0 ϕ: 0 Re_∞/FT.: 0.5×10^6 AEDC GROUP NO.: 3/1

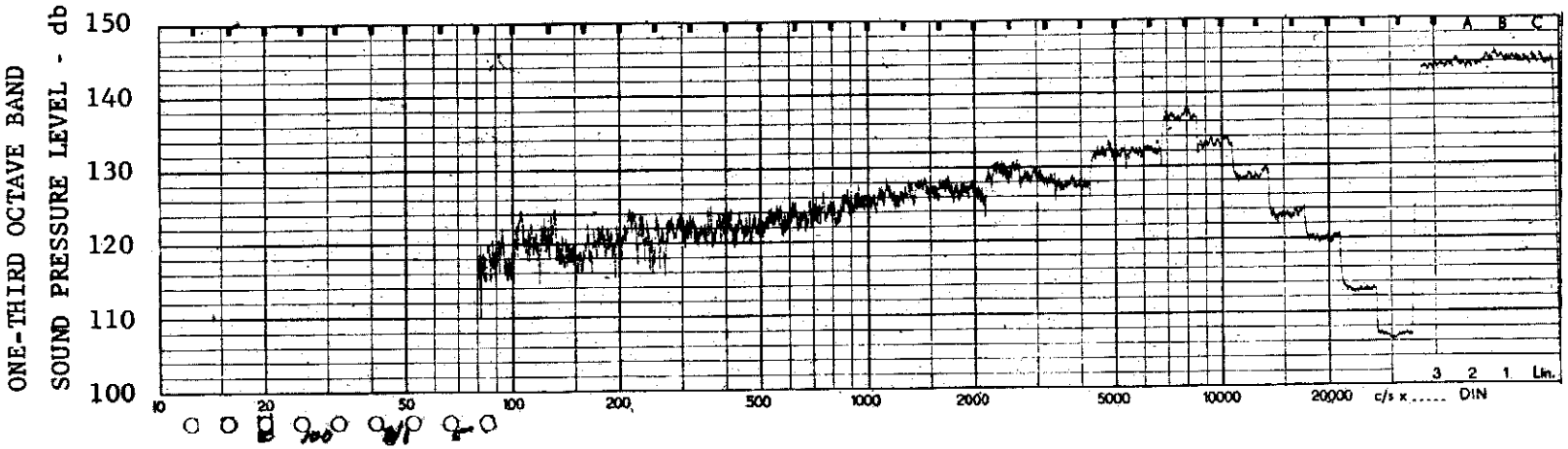

FIGURE 5 ONE-THIRD OCTAVE BAND SPECTRUM MODEL: AXISYM

CHANNEL: 5 MACH NO.: 5 α: 0 ϕ: 0 Re_∞/FT.: 0.5×10^6 AEDC GROUP NO.: 3/1

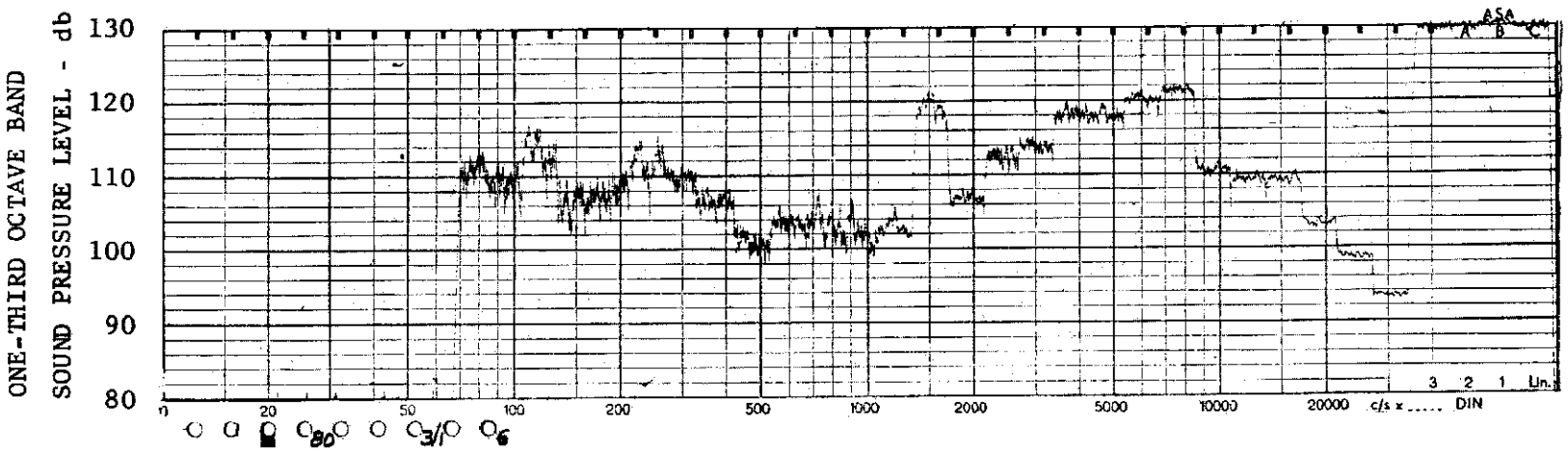

FIGURE 6 ONE-THIRD OCTAVE BAND SPECTRUM MODEL: AXISYM

CHANNEL: 6 MACH NO.: 5 α: 0 ϕ: 0 Re_∞/FT.: 0.5×10^6 AEDC GROUP NO.: 3/1

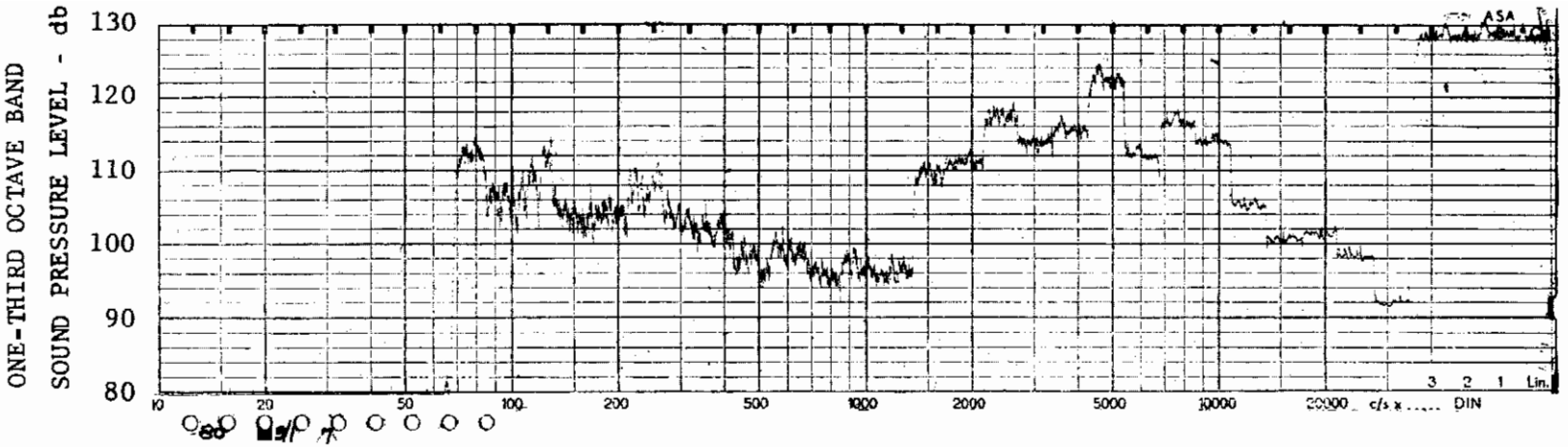

FIGURE 7 ONE-THIRD OCTAVE BAND SPECTRUM MODEL: AXISYM

CHANNEL: 7 MACH NO.: 5 α: 0 ϕ: 0 Re_∞/FT.: 0.5×10^6 AEDC GROUP NO.: 3/1

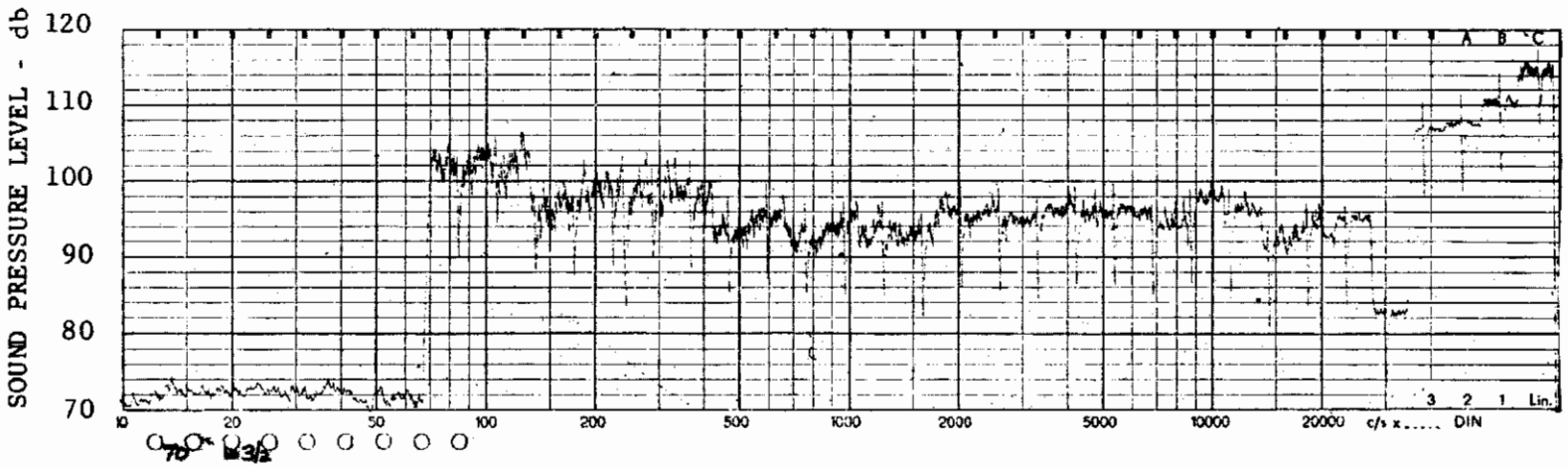

FIGURE 8 ONE-THIRD OCTAVE BAND SPECTRUM MODEL: AXISYM

CHANNEL: 1 MACH NO.: 5 α: 0 ϕ: 0 Re_∞/FT.: 0.5×10^6 AEDC GROUP NO.: 3/2

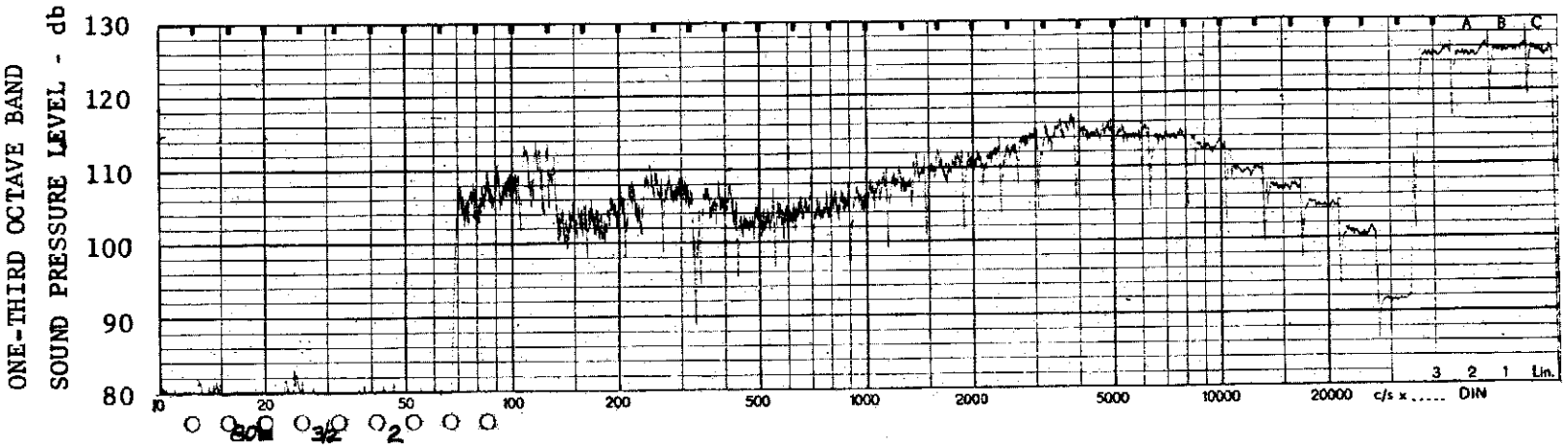

FIGURE 9 ONE-THIRD OCTAVE BAND SPECTRUM MODEL: AXISYM

CHANNEL: 2 MACH NO.: 5 α: 0 ϕ: 0 Re_∞/FT.: 0.5×10^6 AEDC GROUP NO.: 3/2

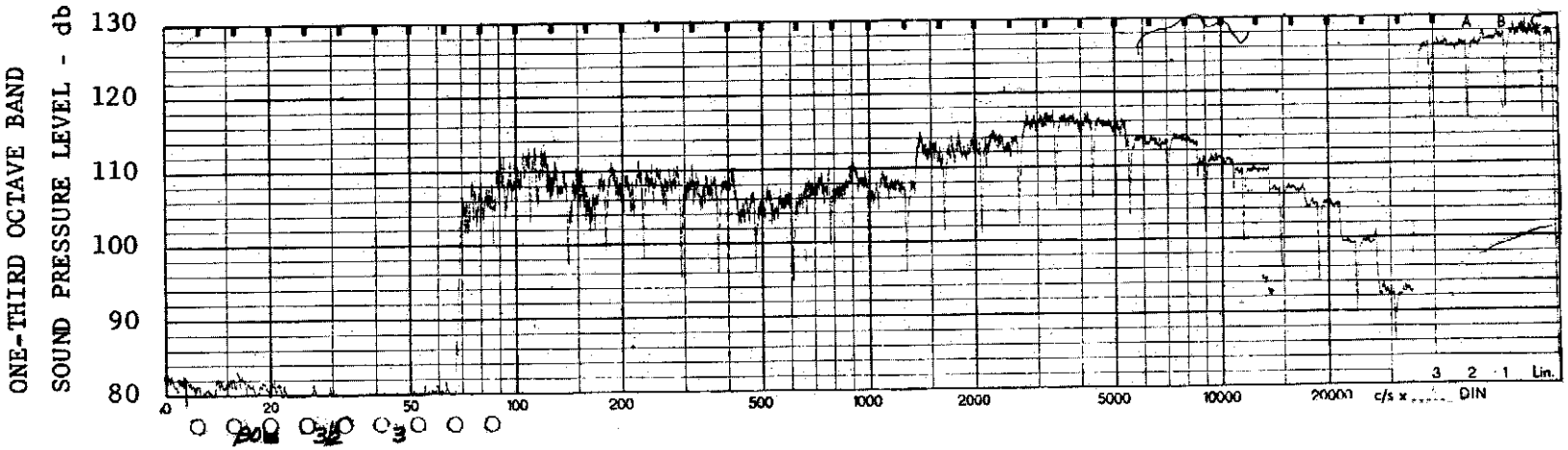

FIGURE 10 ONE-THIRD OCTAVE BAND SPECTRUM MODEL: AXISYM

CHANNEL: 3 MACH NO.: 5 α: 0 ϕ: 0 Re_∞/FT.: 0.5×10^6 AEDC GROUP NO.: 3/2

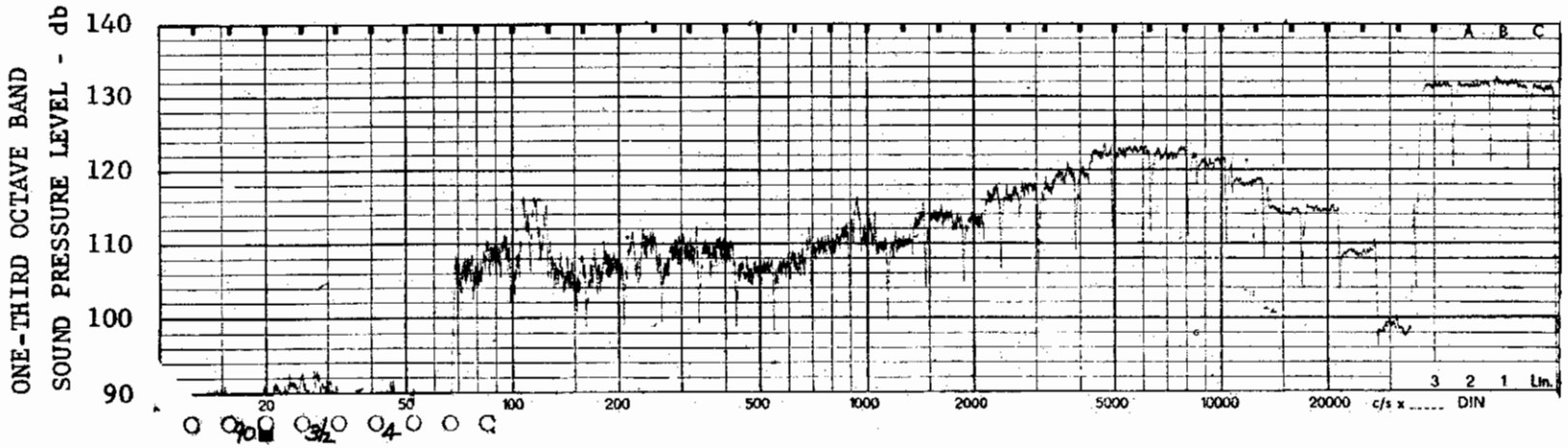

FIGURE 11 ONE-THIRD OCTAVE BAND SPECTRUM MODEL: AXISYM

CHANNEL: 4 MACH NO.: 5 α: 0 ϕ: 0 Re_∞/FT.. 0.5×10^6 AEDC GROUP NO.: 3/2

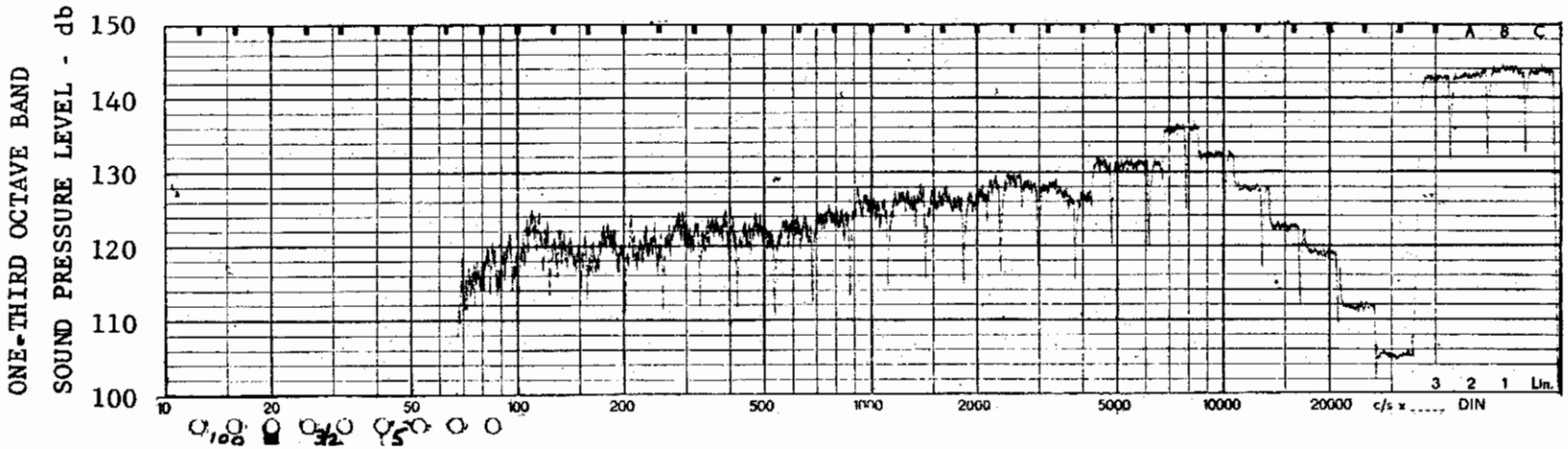

FIGURE 12 ONE-THIRD OCTAVE BAND SPECTRUM MODEL: AXISYM

CHANNEL: 5 MACH NO.: 5 α: 0 ϕ: 0 Re_∞/FT.: 0.5×10^6 AEDC GROUP NO.: 3/2

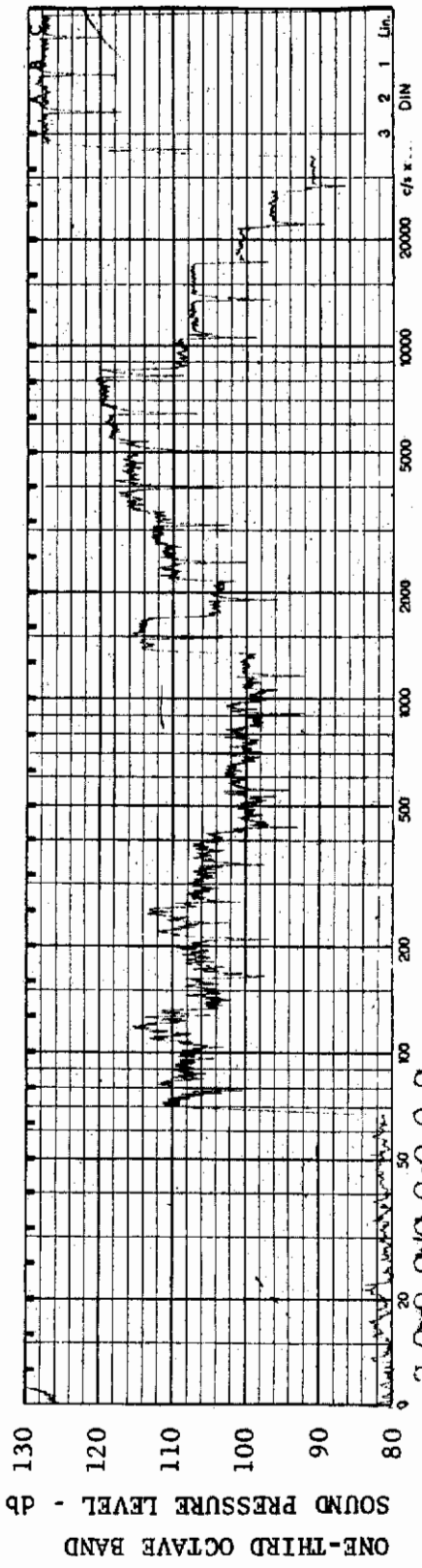

FIGURE 13 ONE-THIRD OCTAVE BAND SPECTRUM MODEL: AXISYM

CHANNEL: 6 MACH NO.: 5 α: 0 ϕ: 0 Re_∞/FT.: 0.5×10^6 AEDC GROUP NO.: 3/2

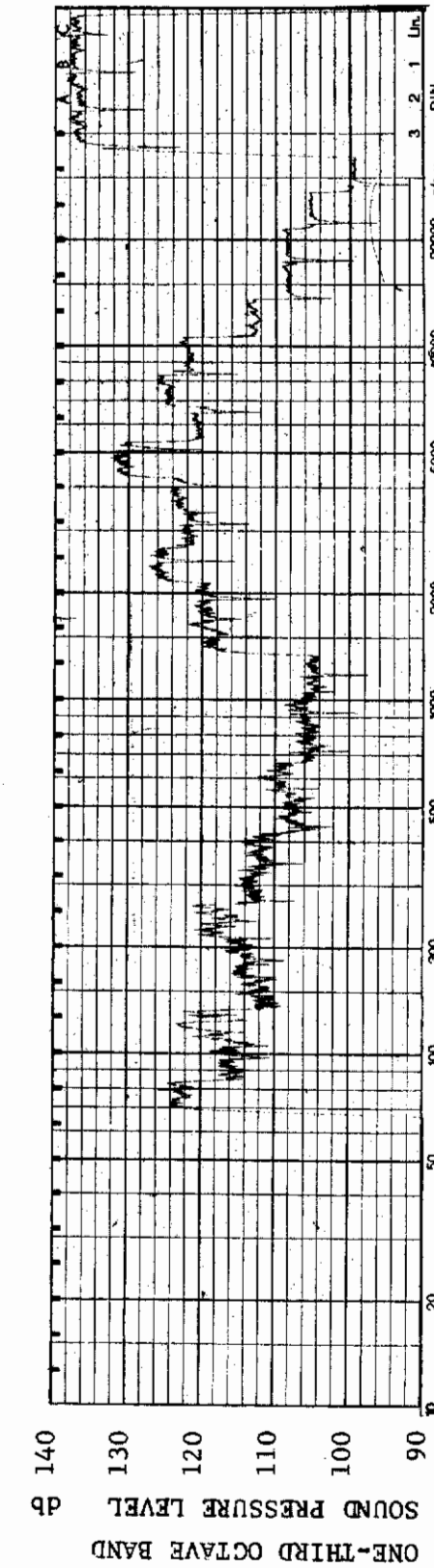

FIGURE 14 ONE-THIRD OCTAVE BAND SPECTRUM MODEL: AXISYM

CHANNEL: 7 MACH NO.: 5 α: 0 ϕ: 0 Re_∞/FT.: 0.5×10^6 AEDC GROUP NO.: 3/2

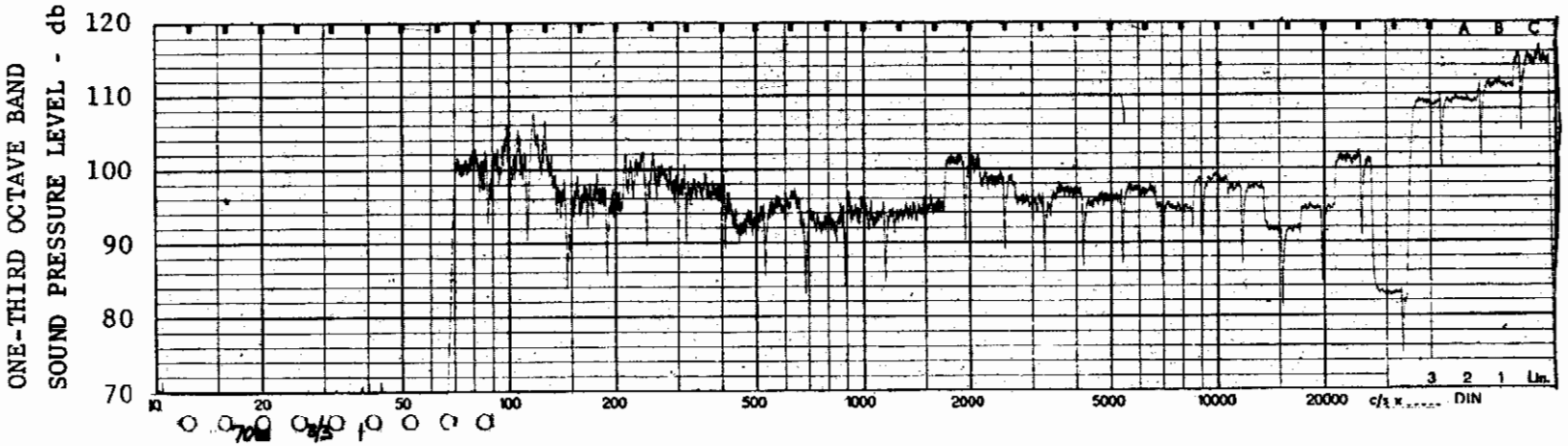

FIGURE 15 ONE-THIRD OCTAVE BAND SPECTRUM MODEL: AXISYM

CHANNEL: 1 MACH NO.: 5 α: 0 ϕ: 0 Re_∞/FT.: 1.0×10^6 AEDC GROUP NO.: 3/3

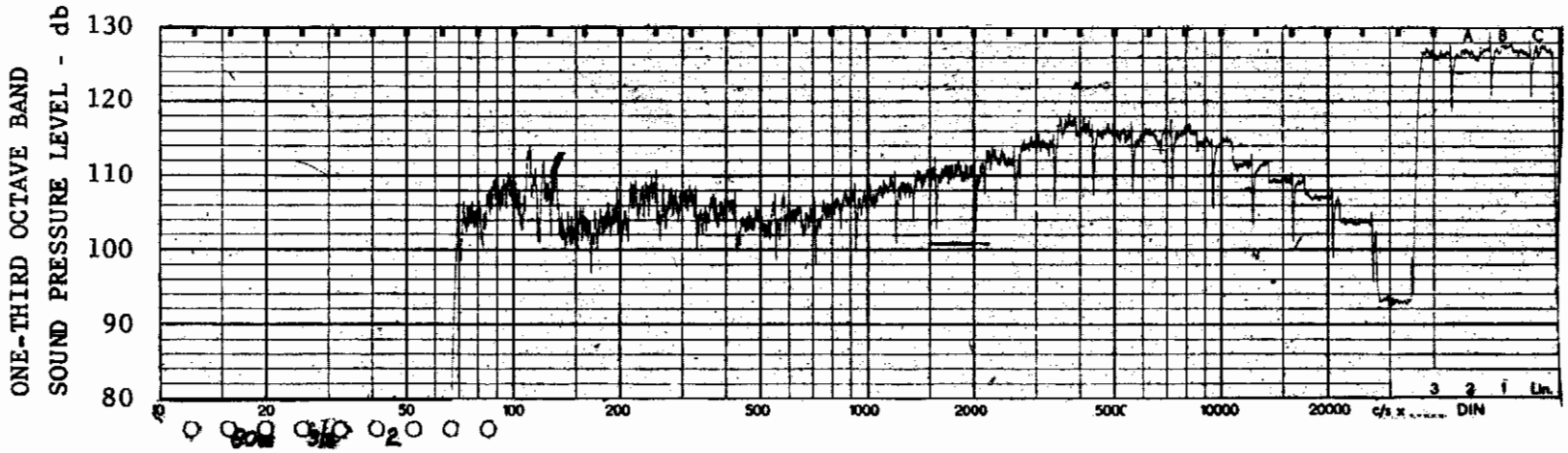

FIGURE 16 ONE-THIRD OCTAVE BAND SPECTRUM MODEL: AXISYM

CHANNEL: 2 MACH NO.: 5 α: 0 ϕ: 0 Re_∞/FT.: 1.0×10^6 AEDC GROUP NO.: 3/3

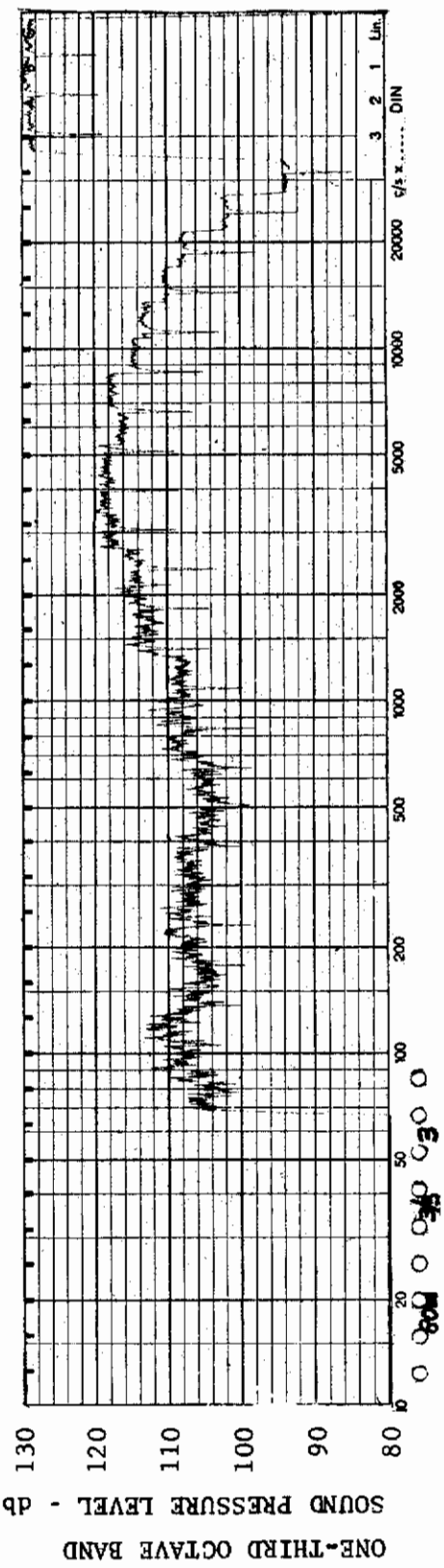

FIGURE 17 ONE-THIRD OCTAVE BAND SPECTRUM MODEL: AXISYM

CHANNEL: 3 MACH NO.: 5 α: 0 ϕ: 0 Re_∞/FT.: 1.0×10^6 AEDC GROUP NO.: 3/3

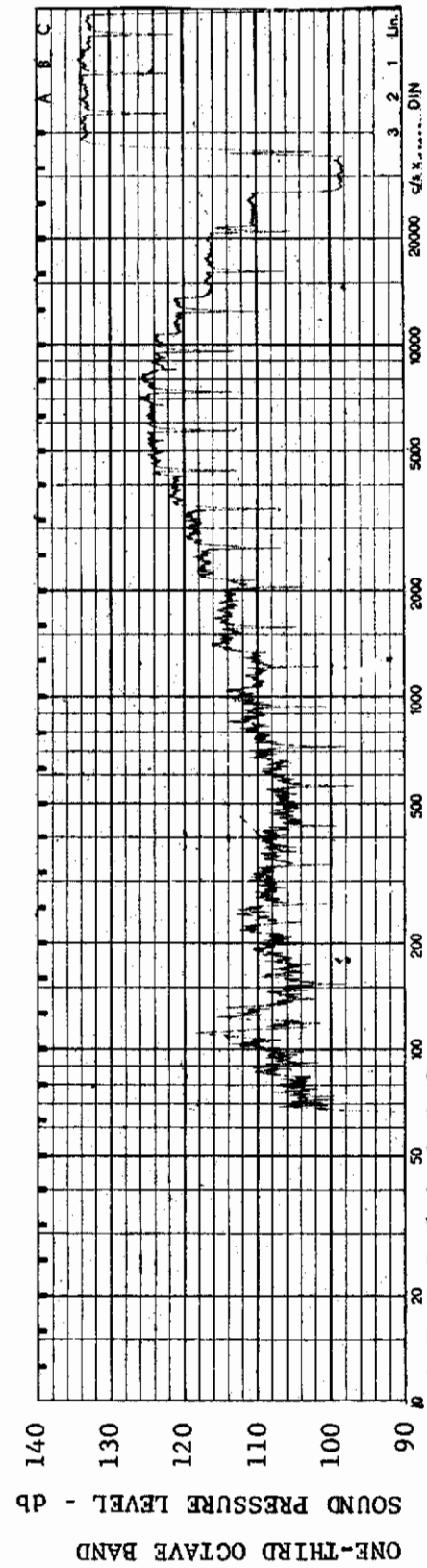

FIGURE 18 ONE-THIRD OCTAVE BAND SPECTRUM MODEL: AXISYM

CHANNEL: 4 MACH NO.: 5 α: 0 ϕ: 0 Re_∞/FT.: 1.0×10^6 AEDC GROUP NO.: 3/3

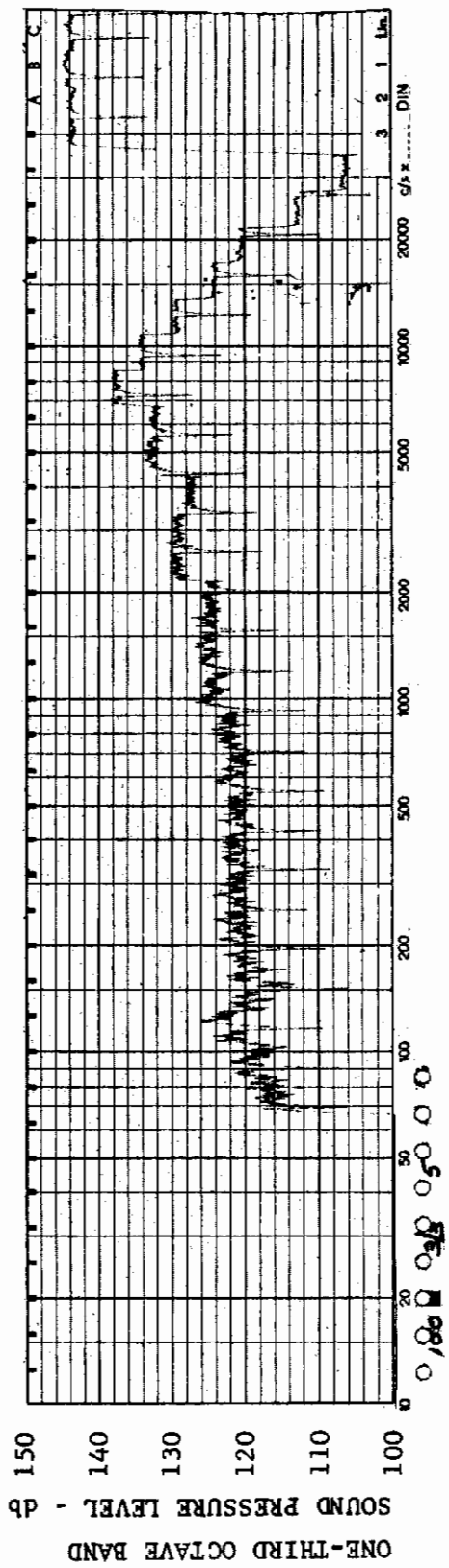

FIGURE 19 ONE-THIRD OCTAVE BAND SPECTRUM MODEL: AXISYM

CHANNEL: 5 MACH NO.: 5 α: 0 ϕ: 0 Re_∞/FT.: 1.0×10^6 AEDC GROUP NO.: 3/3

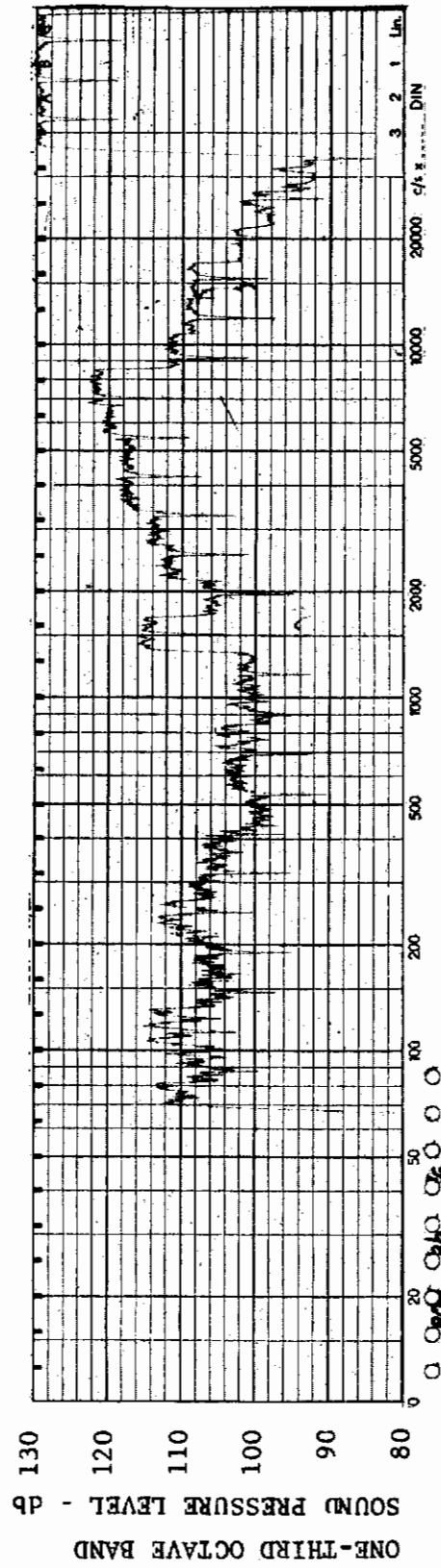

FIGURE 20 ONE-THIRD OCTAVE BAND SPECTRUM MODEL: AXISYM

CHANNEL: 6 MACH NO.: 5 α: 0 ϕ: 0 Re_∞/FT.: 1.0×10^6 AEDC GROUP NO.: 3/3

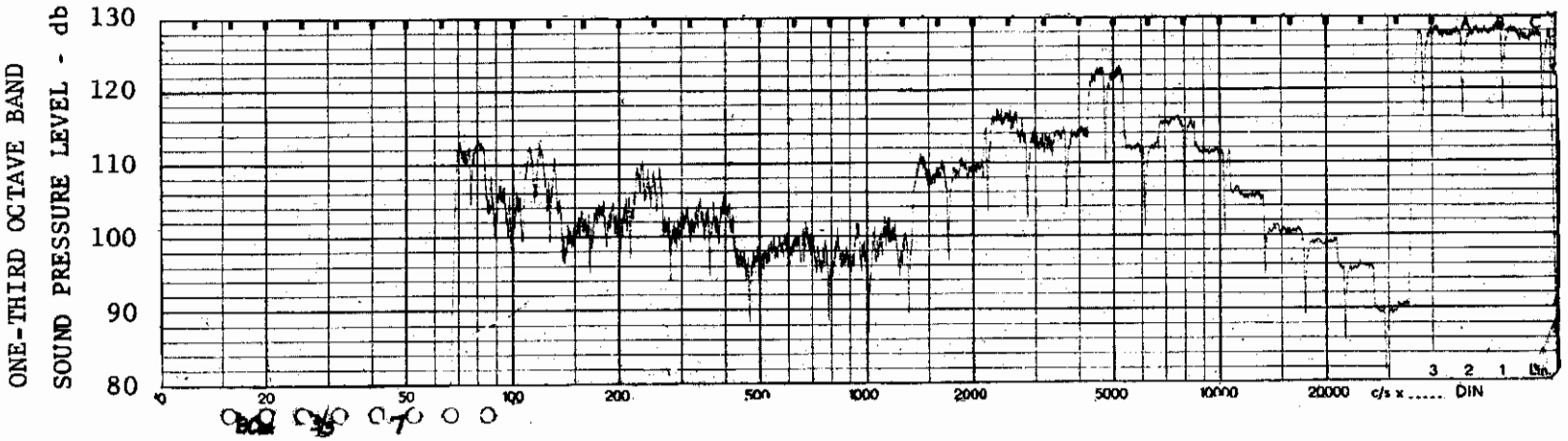

FIGURE 21 ONE-THIRD OCTAVE BAND SPECTRUM MODEL: AXISYM

CHANNEL: 7 MACH NO.: 5 α: 0 ϕ: 0 Re_∞/FT.: 1.0×10^6 AEDC GROUP NO.: 3/3

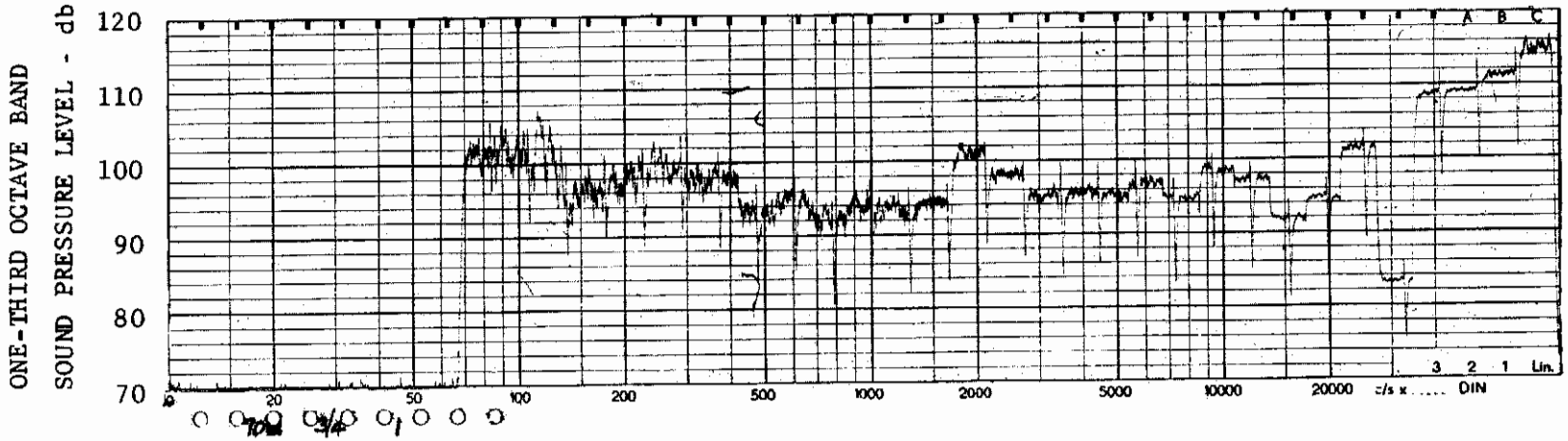

FIGURE 22 ONE-THIRD OCTAVE BAND SPECTRUM MODEL: AXISYM

CHANNEL: 1 MACH NO.: 5 α: 0 ϕ: 0 Re_∞/FT.: 1.0×10^6 AEDC GROUP NO.: 3/4

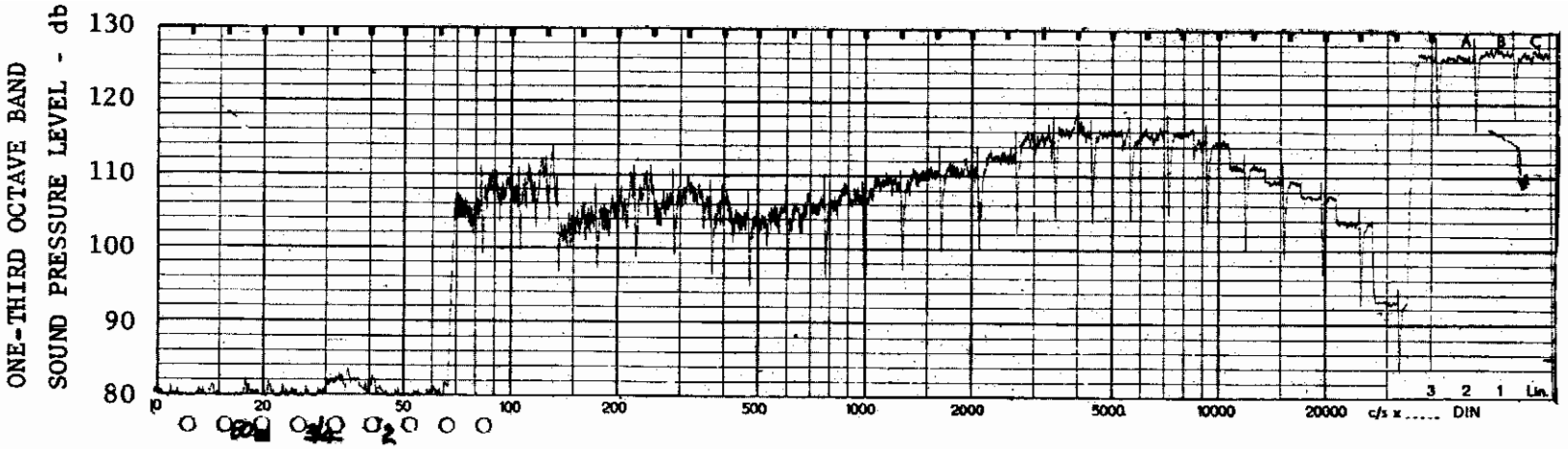

FIGURE 23 ONE-THIRD OCTAVE BAND SPECTRUM MODEL: AXISYM

CHANNEL: 2 MACH NO.: 5 α: 0 ϕ: 0 Re_∞/FT.: 1.0×10^6 AEDC GROUP NO.: 3/4

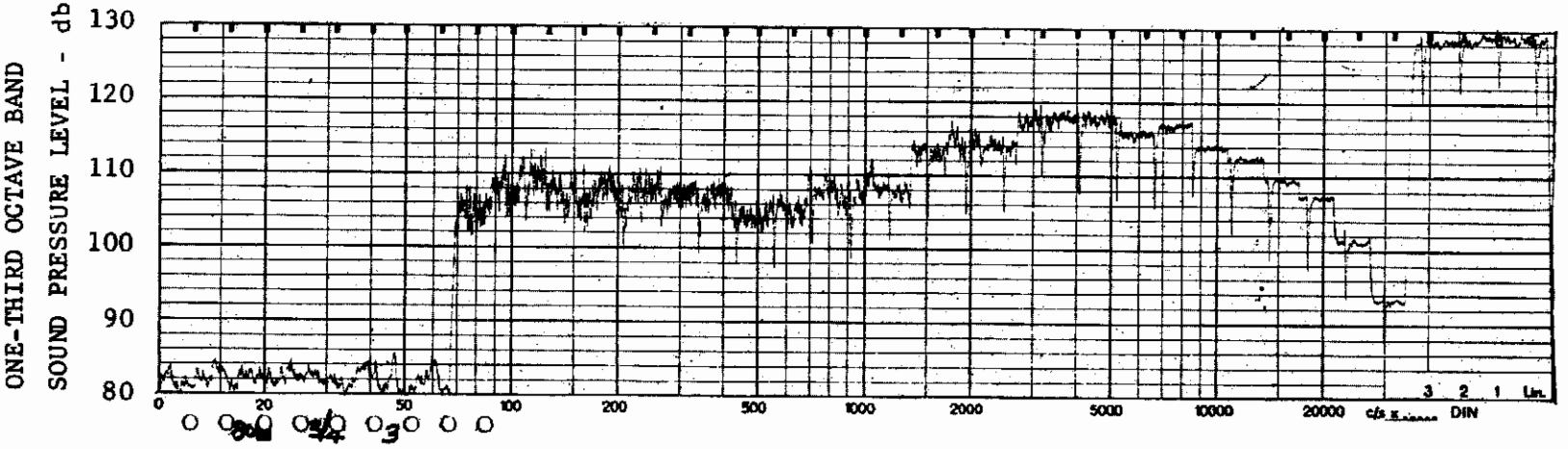

FIGURE 24 ONE-THIRD OCTAVE BAND SPECTRUM MODEL: AXISYM

CHANNEL: 3 MACH NO.: 5 α: 0 ϕ: 0 Re_∞/FT.: 1.0×10^6 AEDC GROUP NO.: 3/4

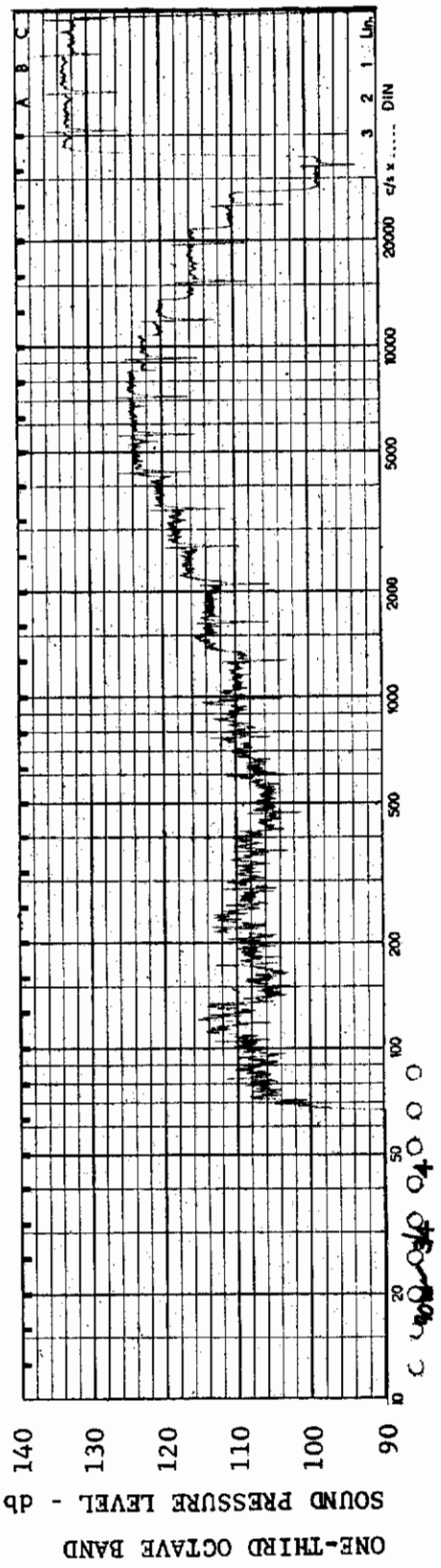

FIGURE 25 ONE-THIRD OCTAVE BAND SPECTRUM MODEL: AXISYM

CHANNEL: 4 MACH NO.: 5 α: 0 ϕ: 0 Re_∞/FT.: 1.0×10^6 AEDC GROUP NO.: 3/4

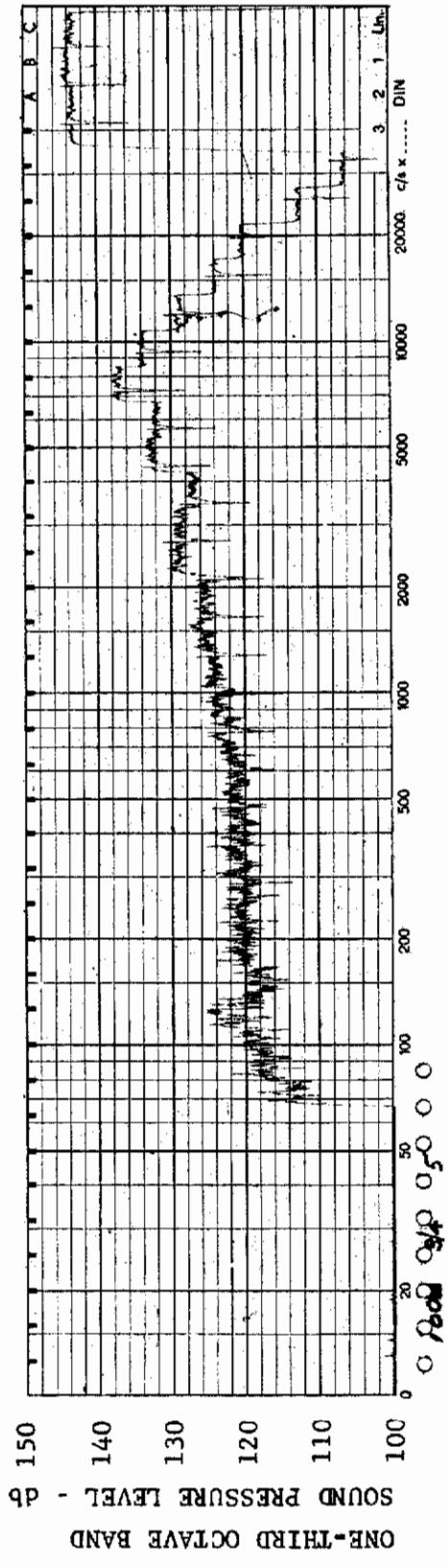

FIGURE 26 ONE-THIRD OCTAVE BAND SPECTRUM MODEL: AXISYM

CHANNEL: 5 MACH NO.: 5 α: 0 ϕ: 0 Re_∞/FT.: 1.0×10^6 AEDC GROUP NO.: 3/4

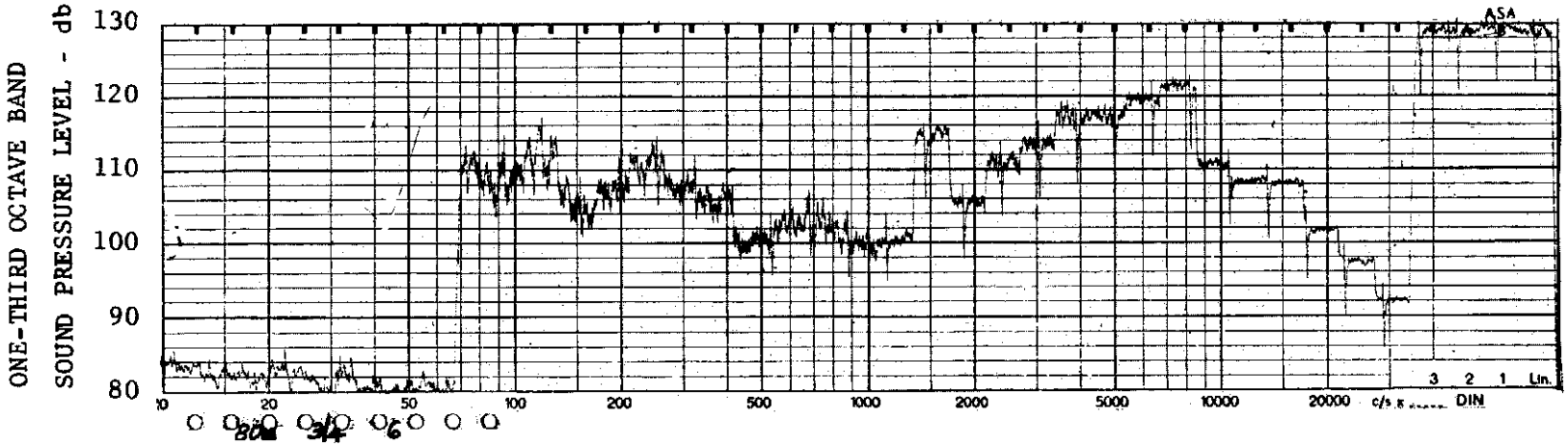

FIGURE 27 ONE-THIRD OCTAVE BAND SPECTRUM MODEL: AXISYM

CHANNEL: 6 MACH NO.: 5 α: 0 ϕ: 0 Re_∞/FT.: 1.0×10^6 AEDC GROUP NO.: 3/4

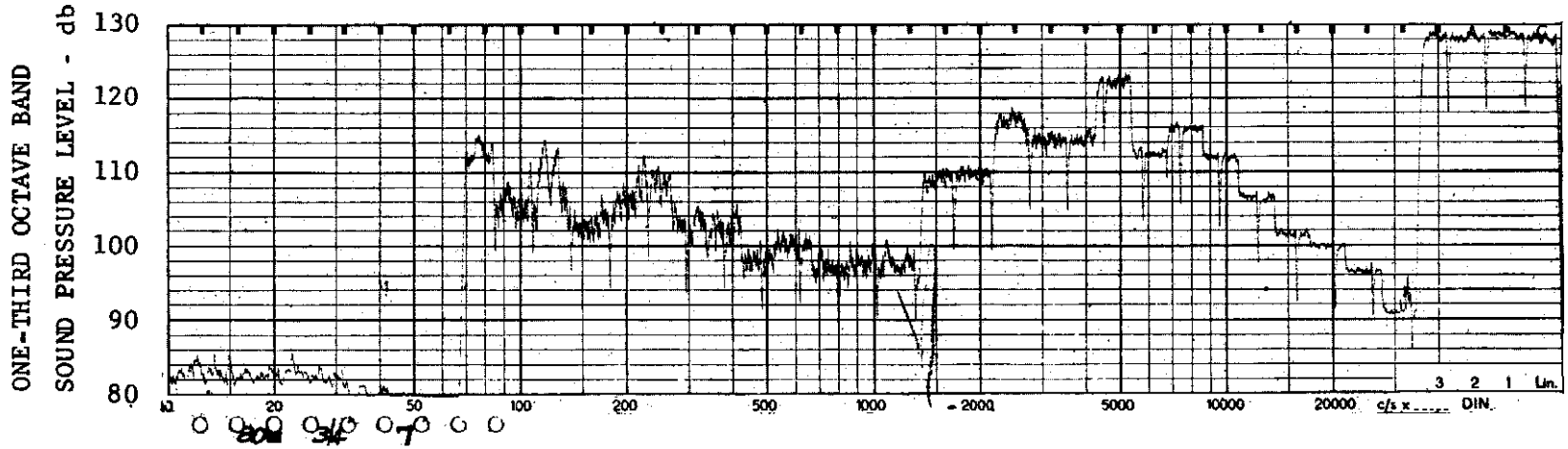

FIGURE 28 ONE-THIRD OCTAVE BAND SPECTRUM MODEL: AXISYM

CHANNEL: 7 MACH NO.: 5 α: 0 ϕ: 0 Re_∞/FT.: 1.0×10^6 AEDC GROUP NO.: 3/4

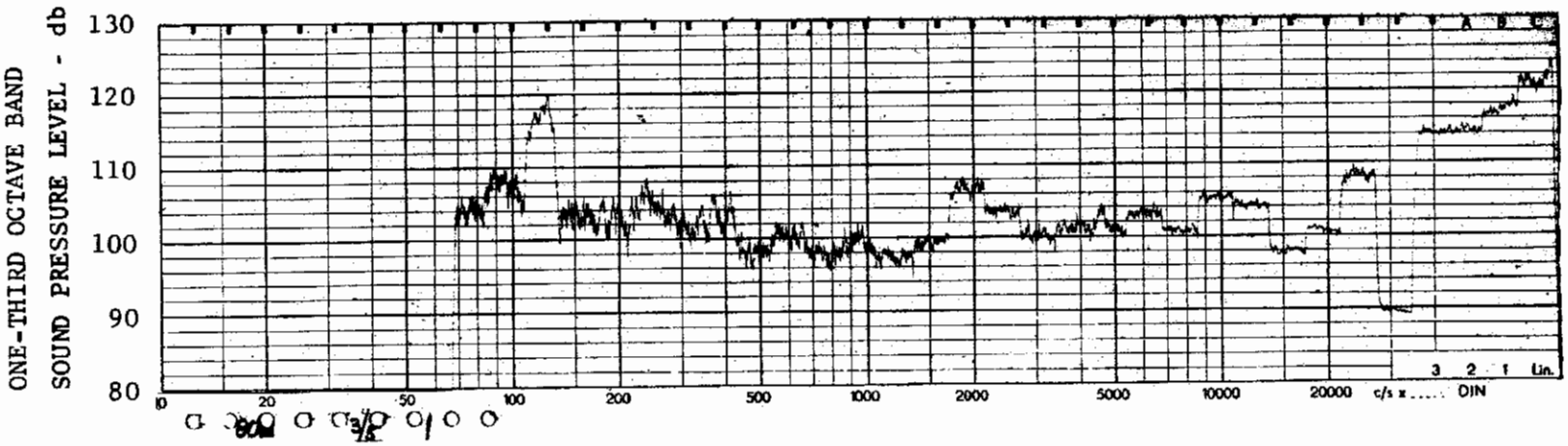

FIGURE 29 ONE-THIRD OCTAVE BAND SPECTRUM MODEL: AXISYM

CHANNEL: 1 MACH NO.: 5 α: 5° ϕ: 0 Re_∞/FT.: 1.0×10^6 AEDC GROUP NO.: 3/5

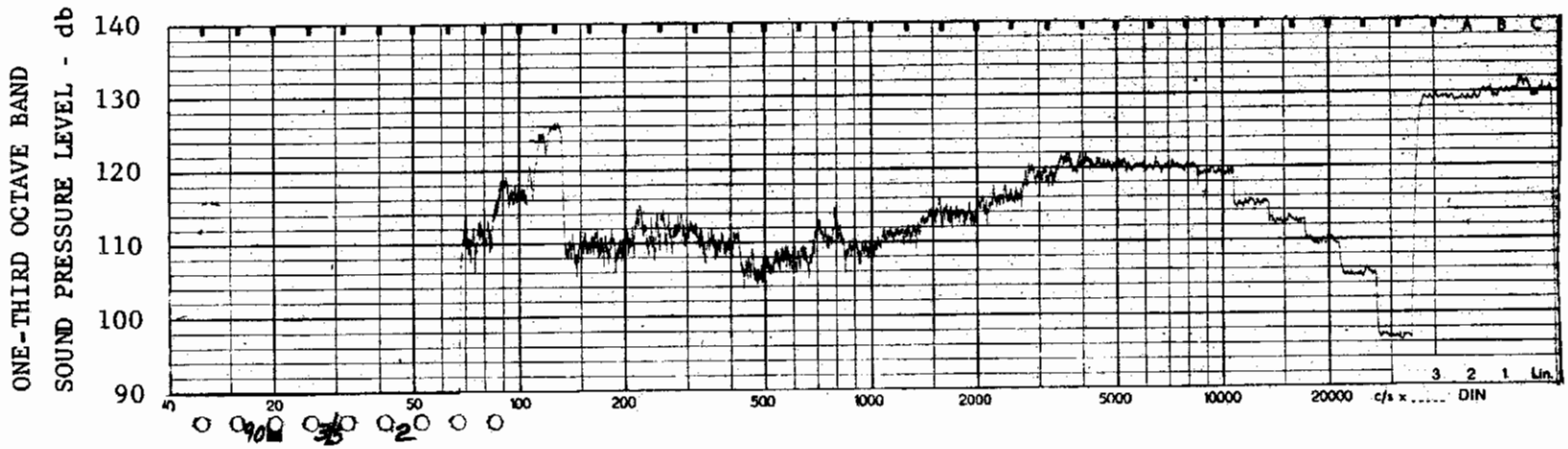

FIGURE 30 ONE-THIRD OCTAVE BAND SPECTRUM MODEL: AXISYM

CHANNEL: 2 MACH NO.: 5 α: 5° ϕ: 0 Re_∞/FT.: 1.0×10^6 AEDC GROUP NO.: 3/5

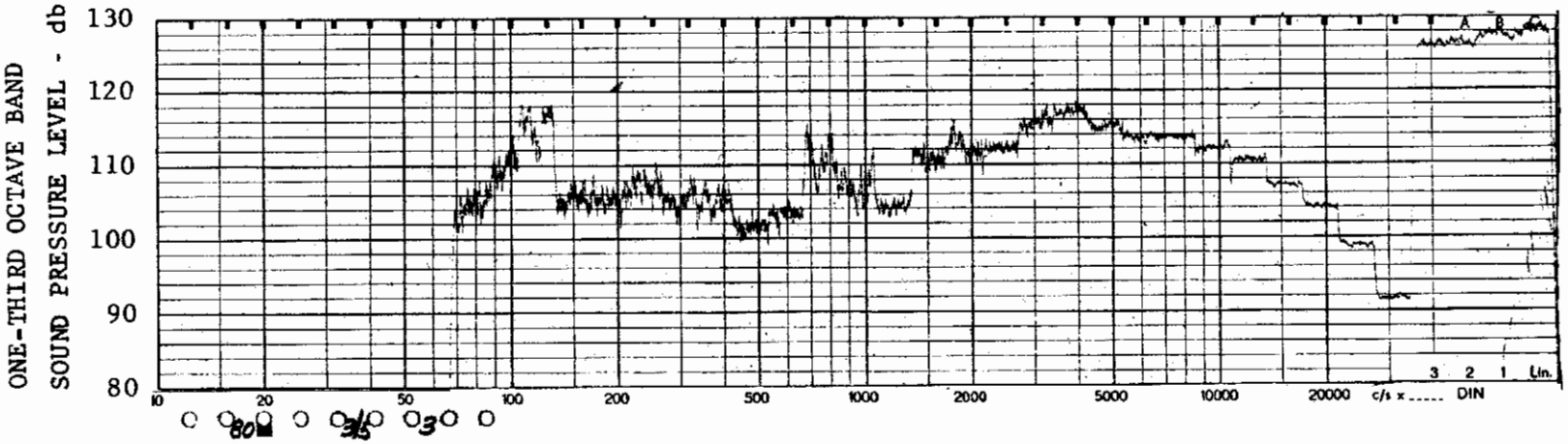

FIGURE 31 ONE-THIRD OCTAVE BAND SPECTRUM MODEL: AXISYM

CHANNEL: 3 MACH NO.: 5 α: 5° ϕ: 0 Re_∞/FT.: 1.0×10^6 AEDC GROUP NO.: 3/5

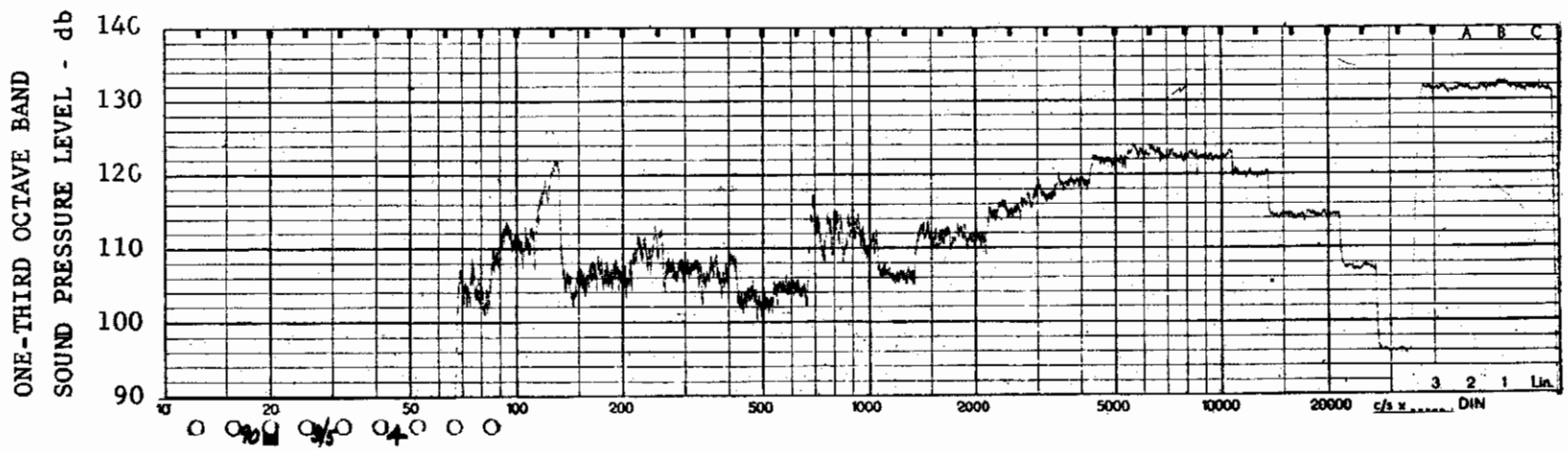

FIGURE 32 ONE-THIRD OCTAVE BAND SPECTRUM MODEL: AXISYM

CHANNEL: 4 MACH NO.: 5 α: 5° ϕ: 0 Re_∞/FT.: 1.0×10^6 AEDC GROUP NO.: 3/5

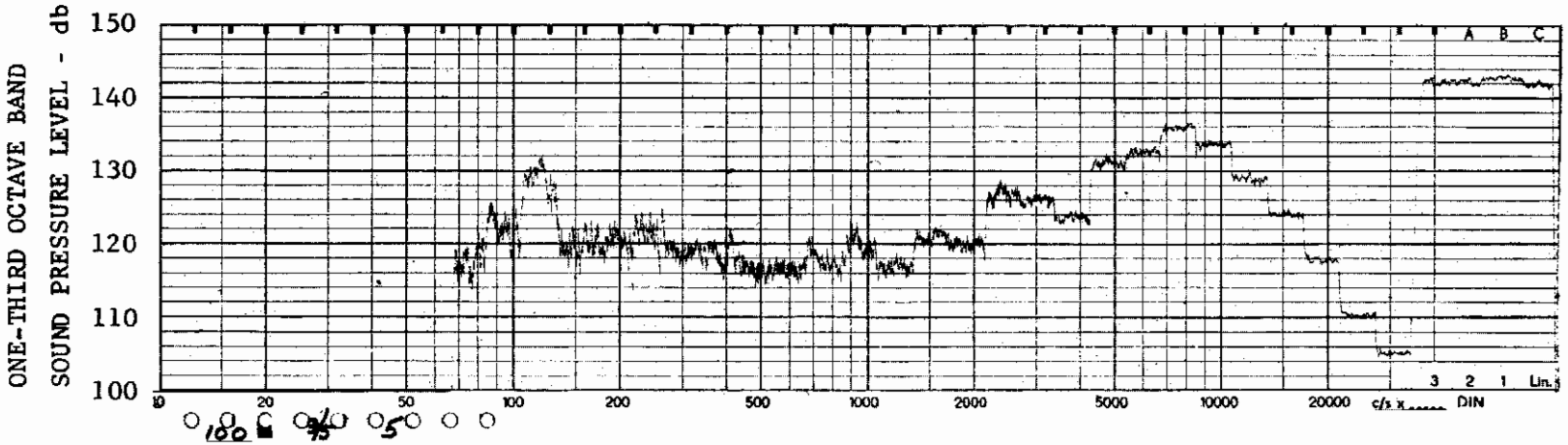

FIGURE 33 ONE-THIRD OCTAVE BAND SPECTRUM MODEL: AXISYM

CHANNEL: 5 MACH NO.: 5 α: 5° ϕ: 0 Re_∞/FT.: 1.0×10^6 AEDC GROUP NO.: 3/5

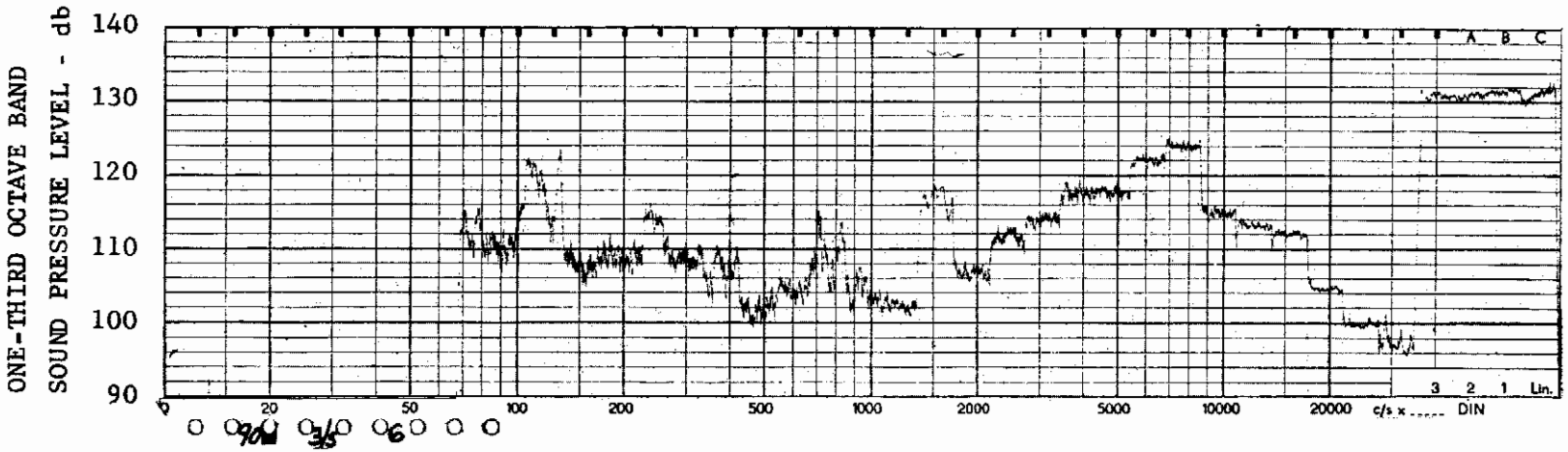

FIGURE 34 ONE-THIRD OCTAVE BAND SPECTRUM MODEL: AXISYM

CHANNEL: 6 MACH NO.: 5 α: 5° ϕ: 0 Re_∞/FT.: 1.0×10^6 AEDC GROUP NO.: 3/5

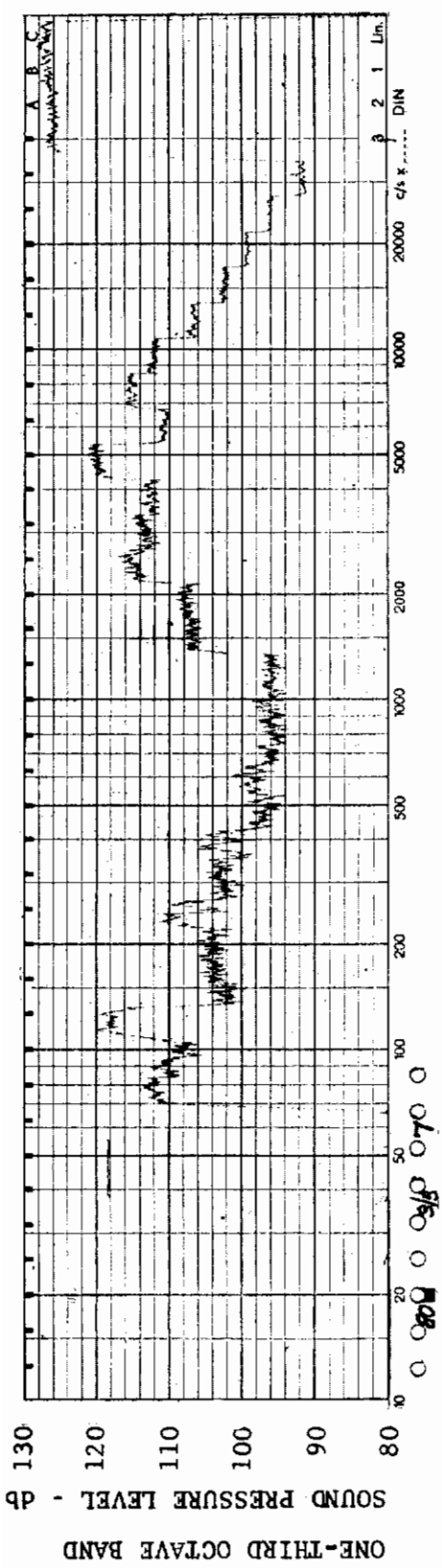

FIGURE 35 ONE-THIRD OCTAVE BAND SPECTRUM MODEL: AXISYM

CHANNEL: 7 MACH NO.: 5 α: 5° ϕ: 0 Re_∞/FT.: 1.0×10^6 AEDC GROUP NO.: 3/5

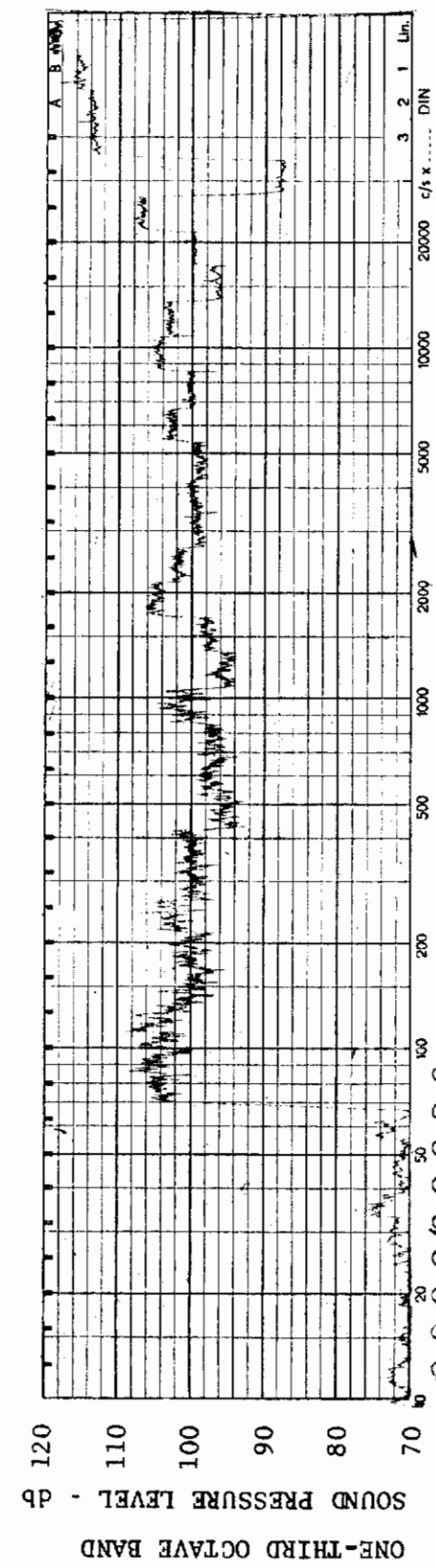

FIGURE 36 ONE-THIRD OCTAVE BAND SPECTRUM MODEL: AXISYM

CHANNEL: 1 MACH NO.: 5 α: 15° ϕ: 0 Re_∞/FT.: 1.0×10^6 AEDC GROUP NO.: 3/6

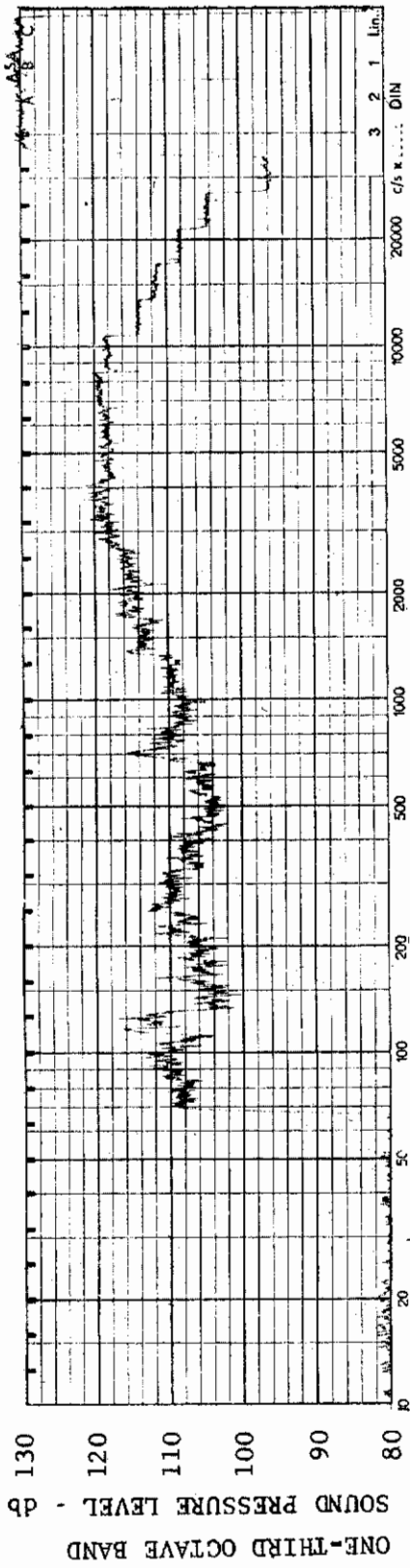

FIGURE 37 ONE-THIRD OCTAVE BAND SPECTRUM MODEL: AXISYM

CHANNEL: 2 MACH NO.: 5 α: 15° ϕ: 0 Re_∞/FT.: 1.0×10^6 AEDC GROUP NO.: 3/6

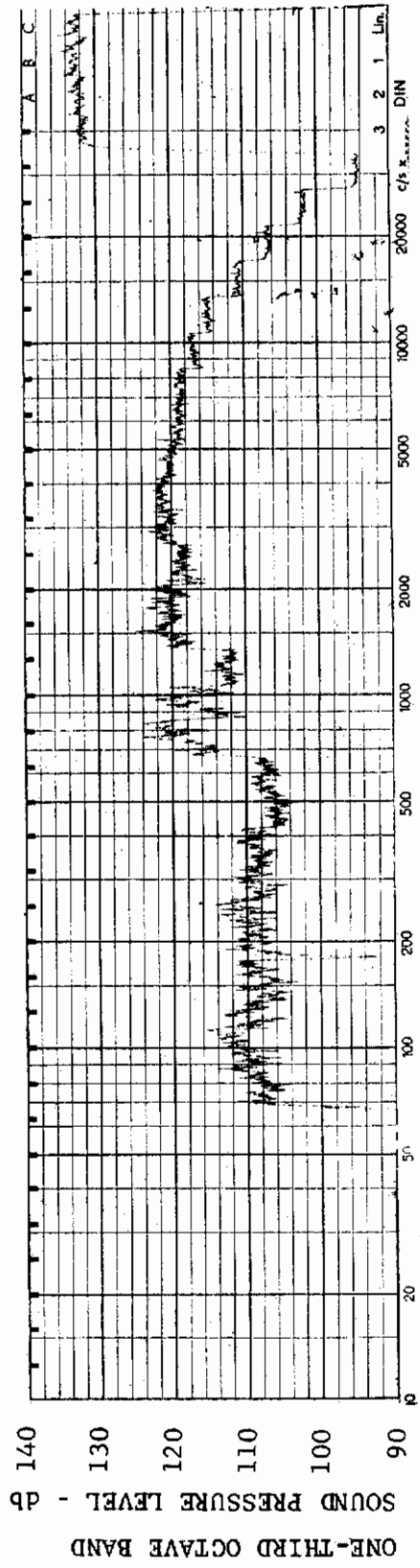

FIGURE 38 ONE-THIRD OCTAVE BAND SPECTRUM MODEL: AXISYM

CHANNEL: 3 MACH NO.: 5 α: 15° ϕ: 0 Re_∞/FT.: 1.0×10^6 AEDC GROUP NO.: 3/6

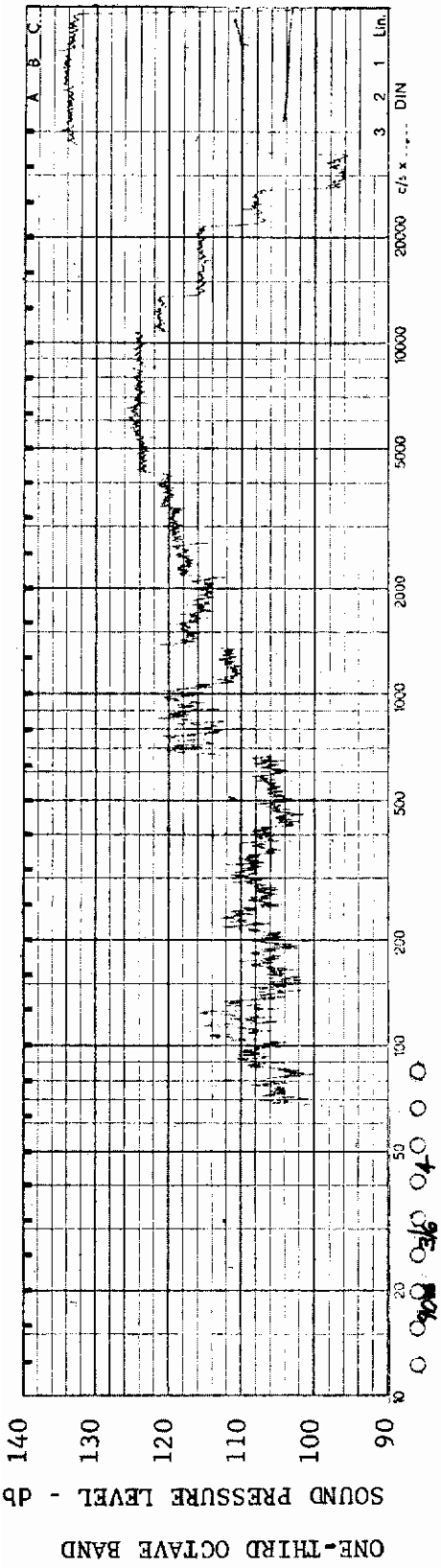

FIGURE 39 ONE-THIRD OCTAVE BAND SPECTRUM MODEL: AXISYM

CHANNEL: 4 MACH NO.: 5 α: 15° ϕ: 0 Re_∞/FT.: 1.0×10^6 AEDC GROUP NO.: 3/6

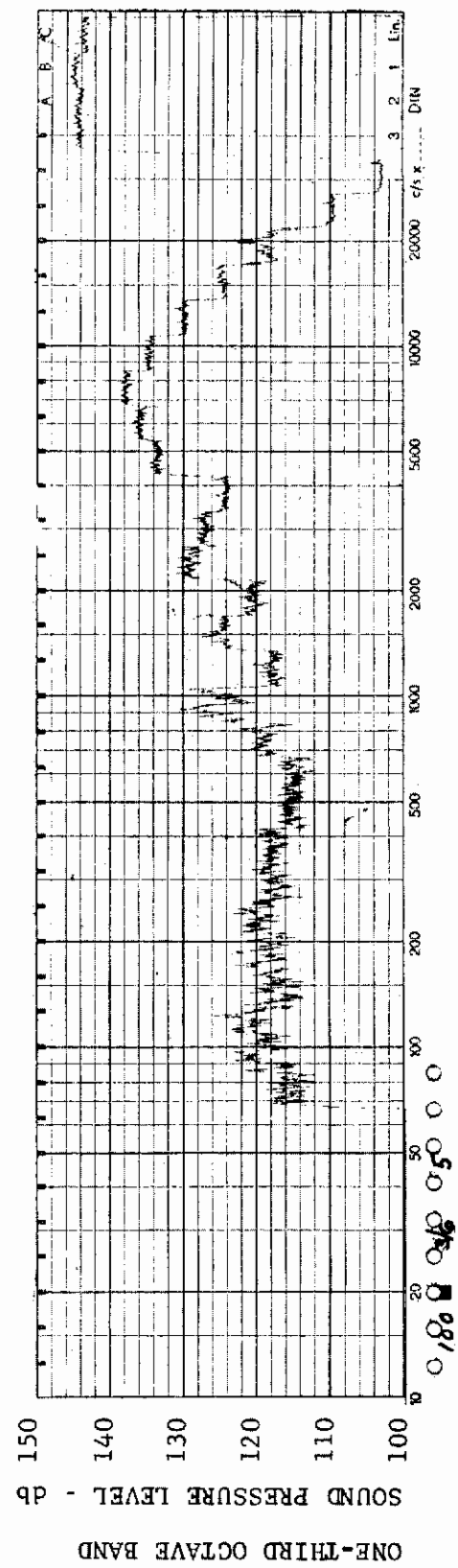

FIGURE 40 ONE-THIRD OCTAVE BAND SPECTRUM MODEL: AXISYM

CHANNEL: 5 MACH NO.: 5 α: 15° ϕ: 0 Re_∞/FT.: 1.0×10^6 AEDC GROUP NO.: 3/6

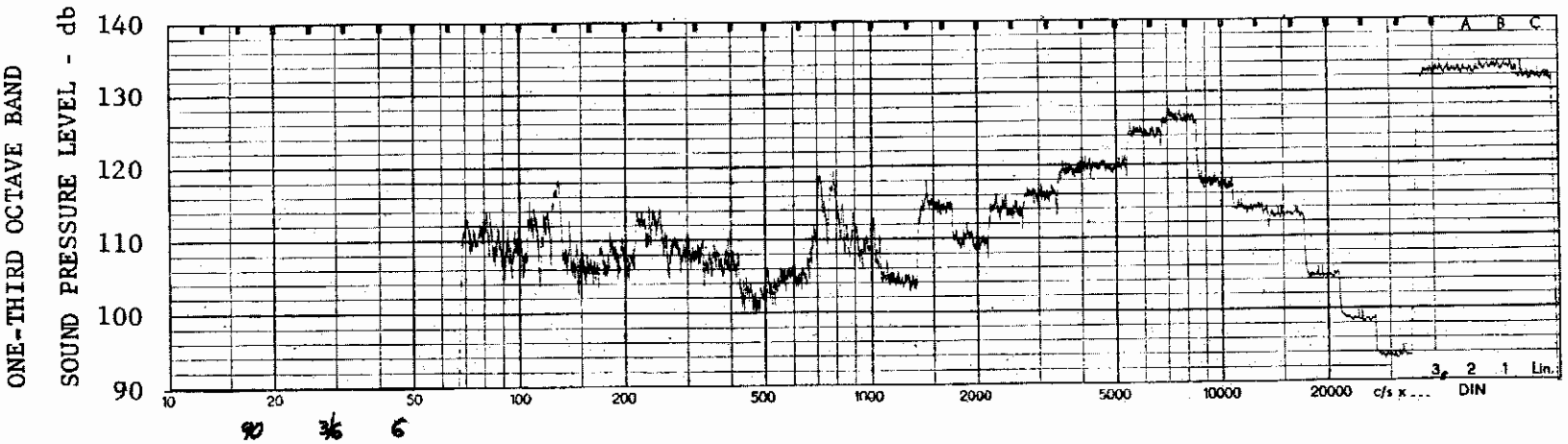

FIGURE 41 ONE-THIRD OCTAVE BAND SPECTRUM MODEL: AXISYM

CHANNEL: 6 MACH NO.: 5 α: 15° ϕ: 0 Re_∞/FT.: 1.0×10^6 AEDC GROUP NO.: 3/6

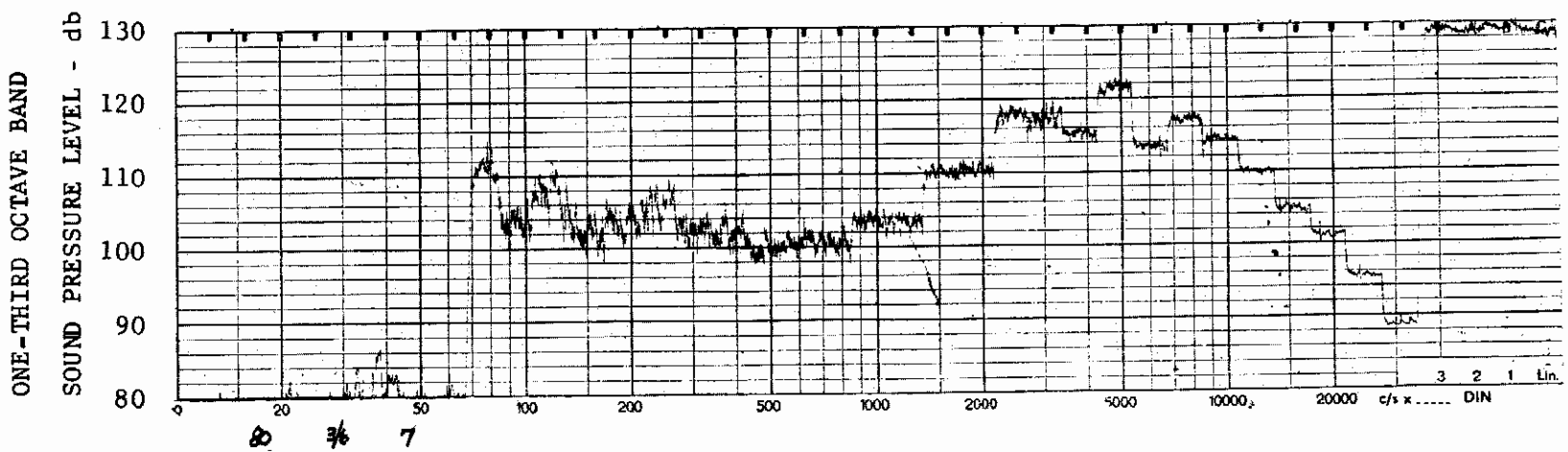

FIGURE 42 ONE-THIRD OCTAVE BAND SPECTRUM MODEL: AXISYM

CHANNEL: 7 MACH NO.: 5 α: 15° ϕ: 0 Re_∞/FT.: 1.0×10^6 AEDC GROUP NO.: 3/6

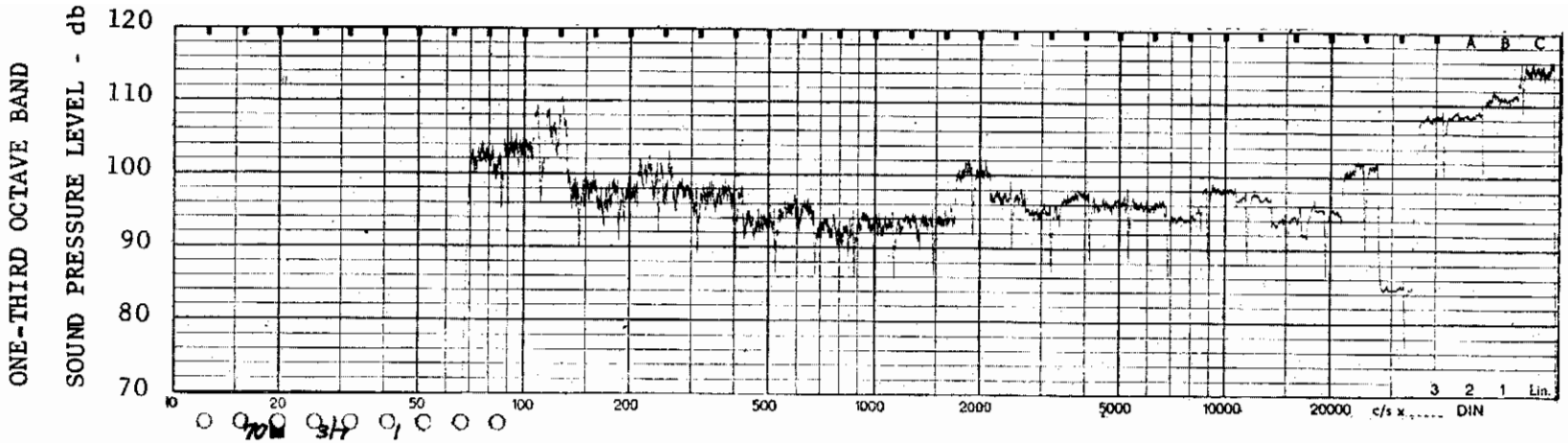

FIGURE 43 ONE-THIRD OCTAVE BAND SPECTRUM MODEL: AXISYM

CHANNEL: 1 MACH NO.: 5 α: 0 ϕ: 0 Re_∞/FT.: 1.0×10^6 AEDC GROUP NO.: 3/7

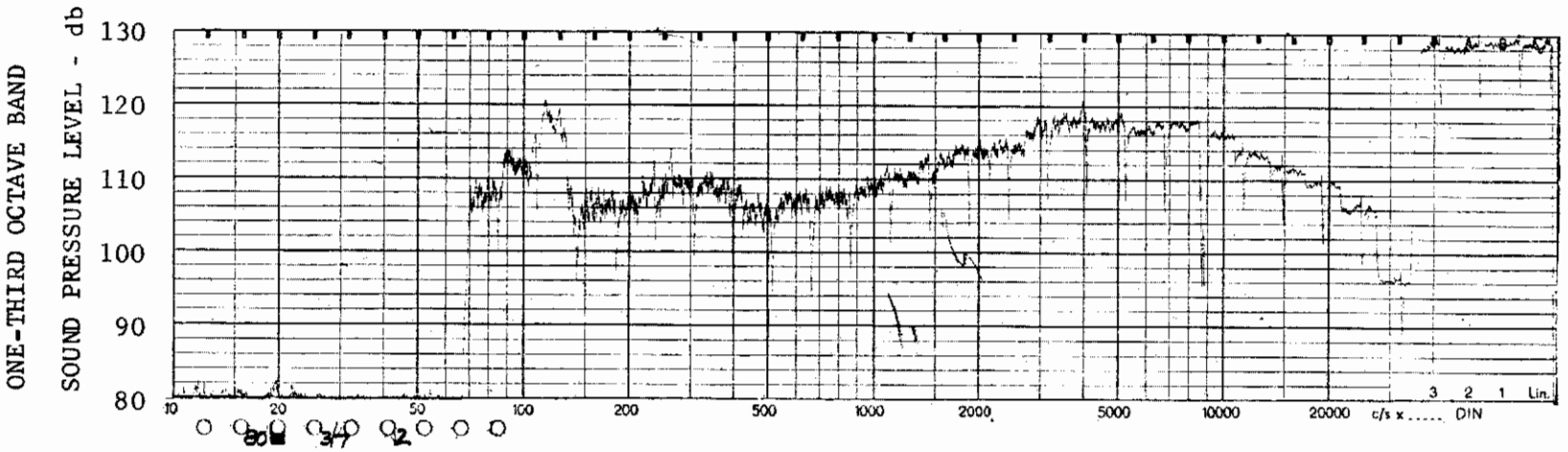

FIGURE 44 ONE-THIRD OCTAVE BAND SPECTRUM MODEL: AXISYM

CHANNEL: 2 MACH NO.: 5 α: 0 ϕ: 0 Re_∞/FT.: 1.0×10^6 AEDC GROUP NO.: 3/7

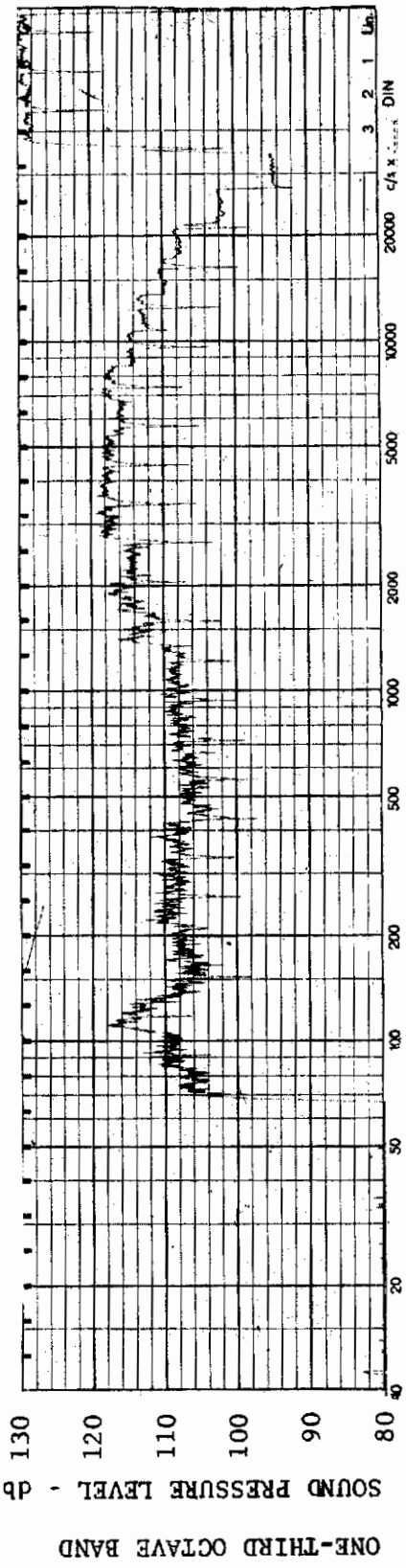

FIGURE 45 ONE-THIRD OCTAVE BAND SPECTRUM MODEL: AXISYM

CHANNEL: 3 MACH NO.: 5 α: 0 ϕ: 0 Re_∞/FT.: 1.0×10^6 AEDC GROUP NO.: 3/7

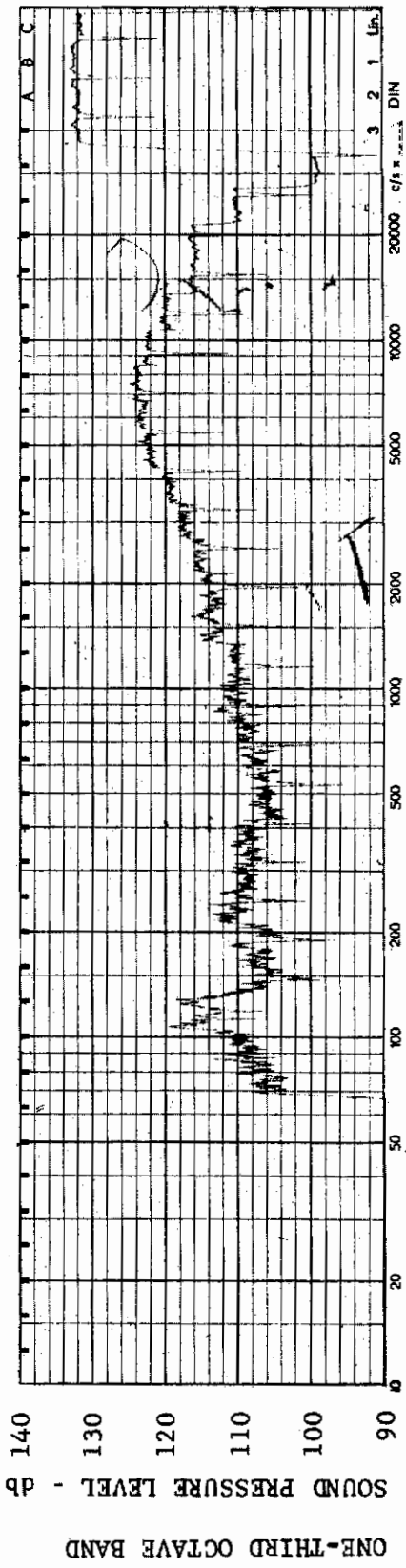

FIGURE 46 ONE-THIRD OCTAVE BAND SPECTRUM MODEL: AXISYM

CHANNEL: 4 MACH NO.: 5 α: 0 ϕ: 0 Re_∞/FT.: 1.0×10^6 AEDC GROUP NO.: 3/7

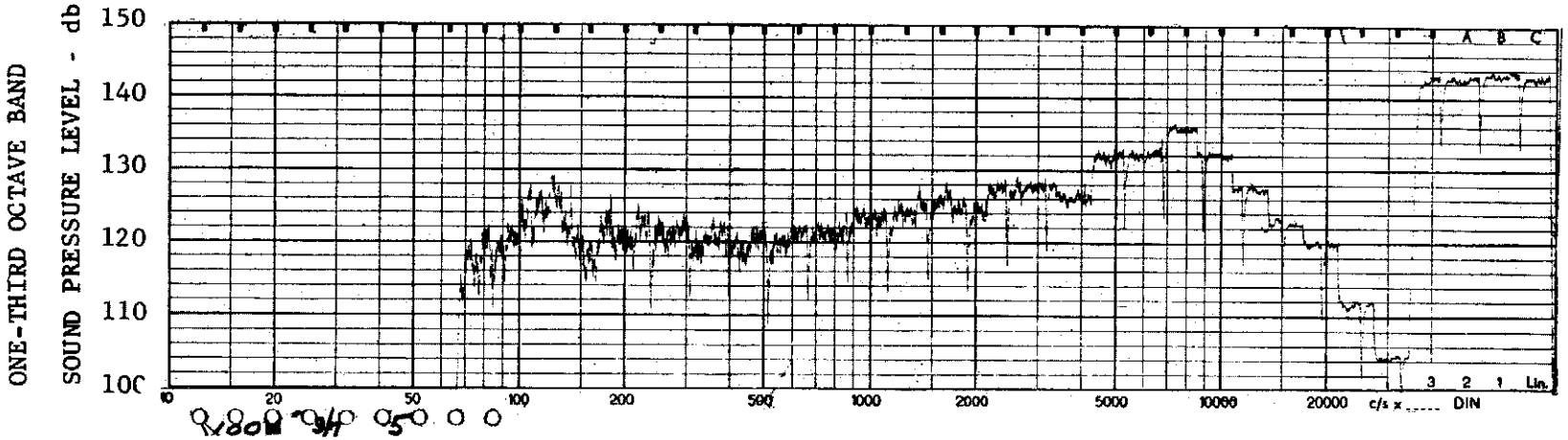

FIGURE 47 ONE-THIRD OCTAVE BAND SPECTRUM MODEL: AXISYM

CHANNEL: 5 MACH NO.: 5 α: 0 ϕ: 0 Re_∞/FT.: 1.0×10^6 AEDC GROUP NO.: 3/7

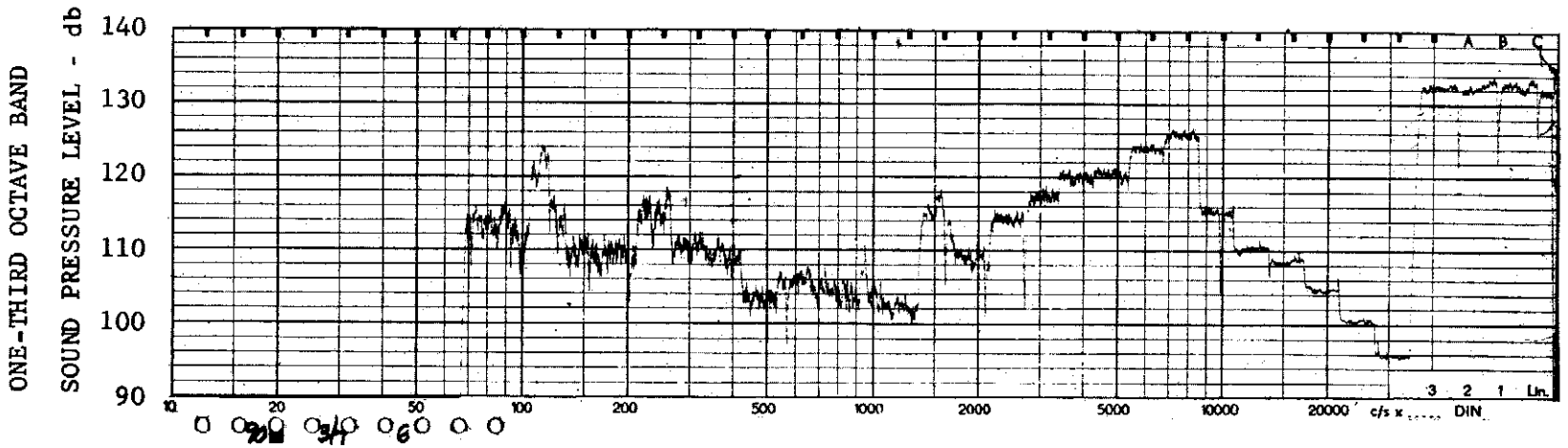

FIGURE 48 ONE-THIRD OCTAVE BAND SPECTRUM MODEL: AXISYM

CHANNEL: 6 MACH NO.: 5 α: 0 ϕ: 0 Re_∞/FT.: 1.0×10^6 AEDC GROUP NO.: 3/7

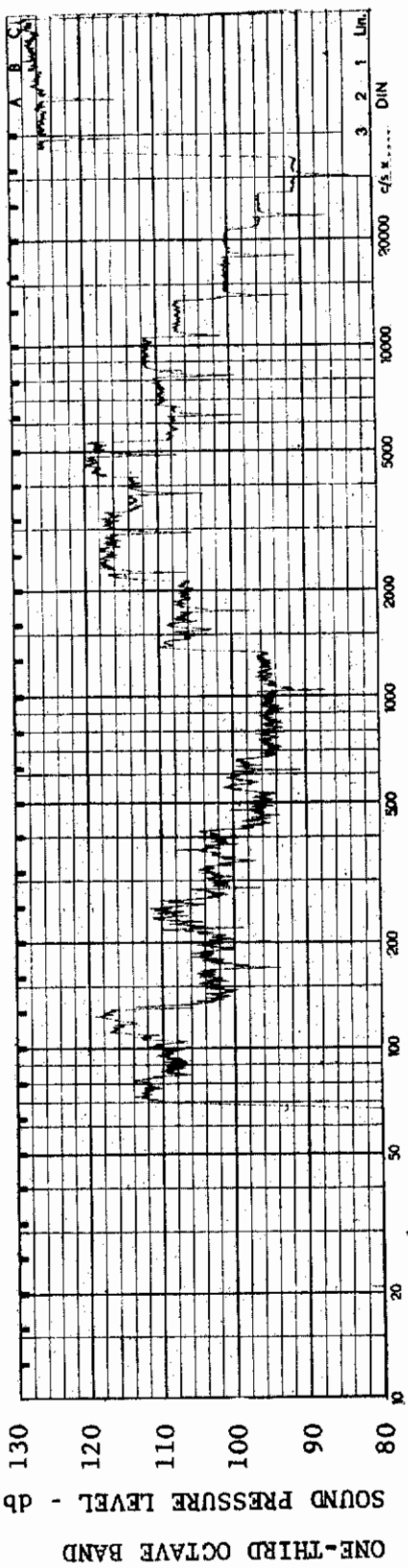

FIGURE 49 ONE-THIRD OCTAVE BAND SPECTRUM MODEL: AXISYM

CHANNEL: 7 MACH NO.: 5 α: 0 ϕ: 0 Re_∞/FT.: 1.0×10^6 AEDC GROUP NO.: 3/7

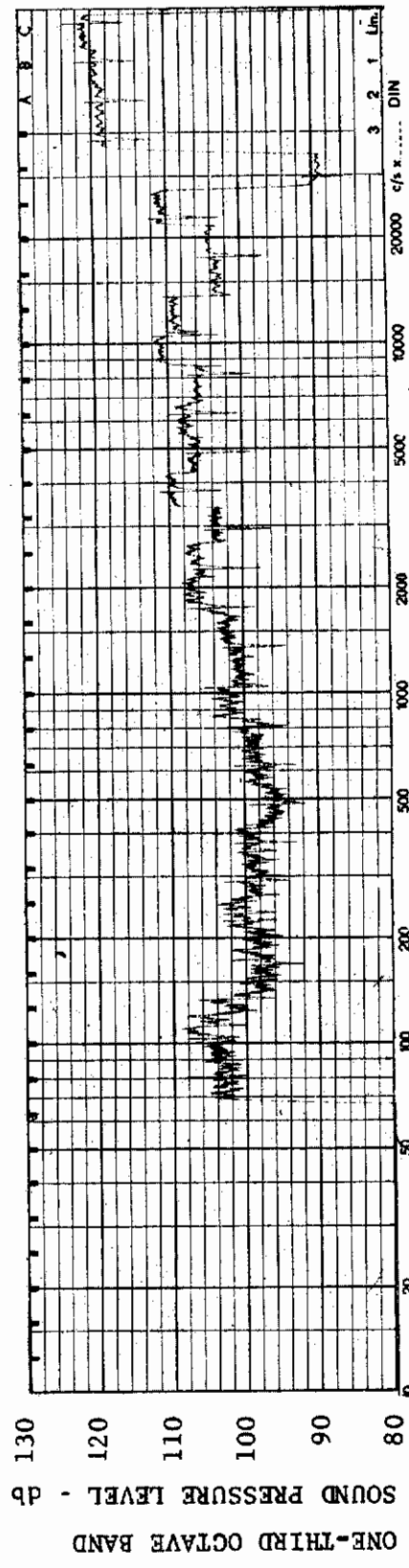

FIGURE 50 ONE-THIRD OCTAVE BAND SPECTRUM MODEL: AXISYM

CHANNEL: 1 MACH NO.: 5 α 0 ϕ: 0 Re_∞/FT.: 6.0×10^6 AEDC GROUP NO.: 3/9

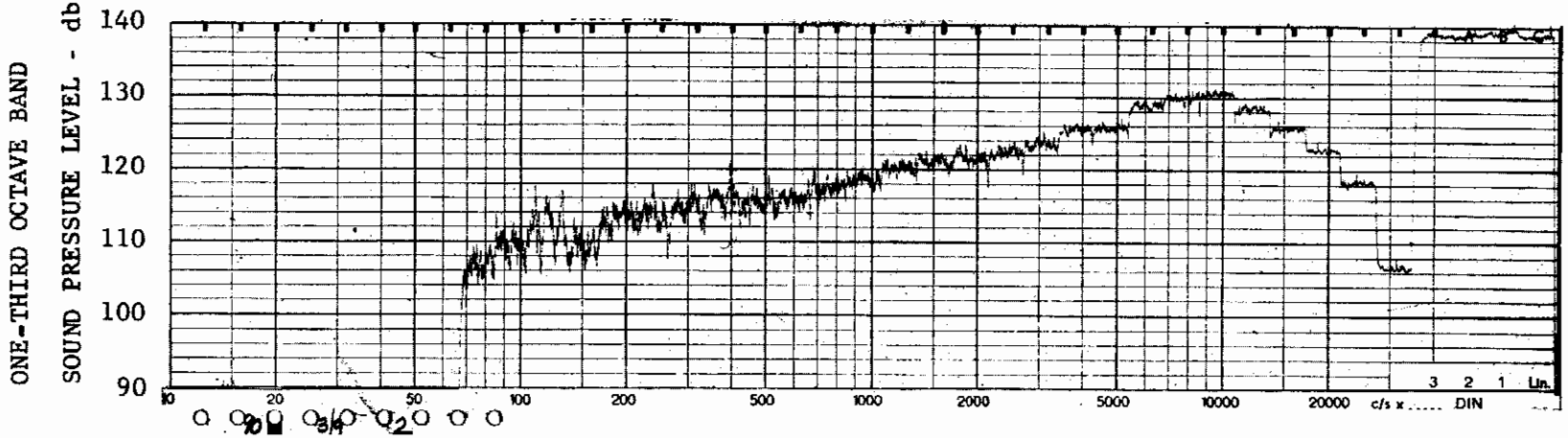

FIGURE 51 ONE-THIRD OCTAVE BAND SPECTRUM MODEL: AXISYM

CHANNEL: 2 MACH NO.: 5 α: 0 ϕ: 0 Re_∞/FT.: 6.0×10^6 AEDC GROUP NO.: 3/9

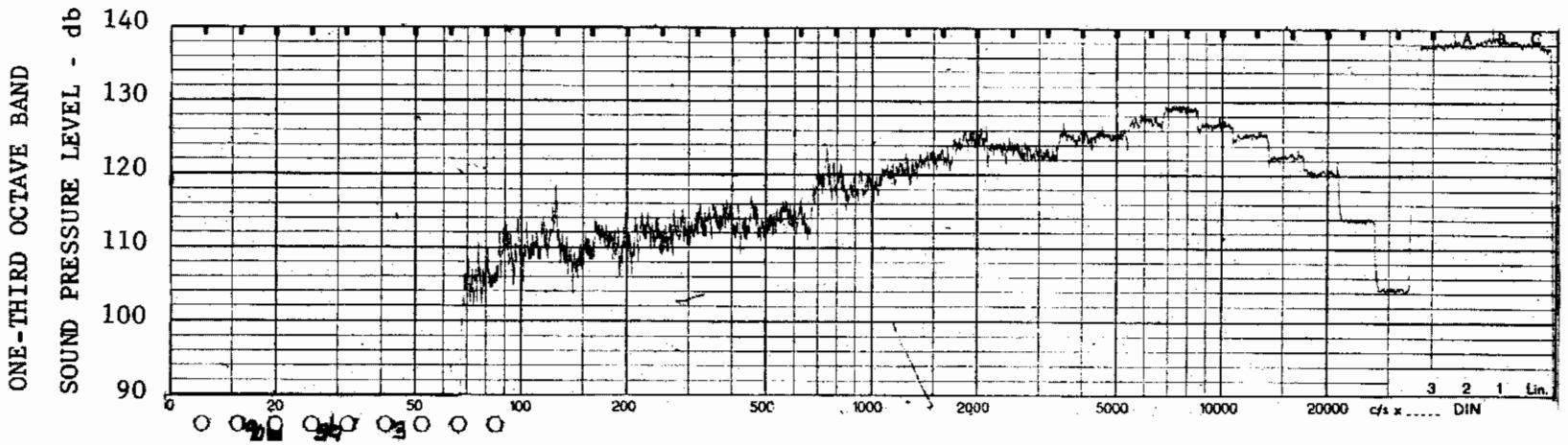

FIGURE 52 ONE-THIRD OCTAVE BAND SPECTRUM MODEL: AXISYM

CHANNEL: 3 MACH NO.: 5 α: 0 ϕ: 0 Re_∞/FT.: 6.0×10^6 AEDC GROUP NO.: 3/9

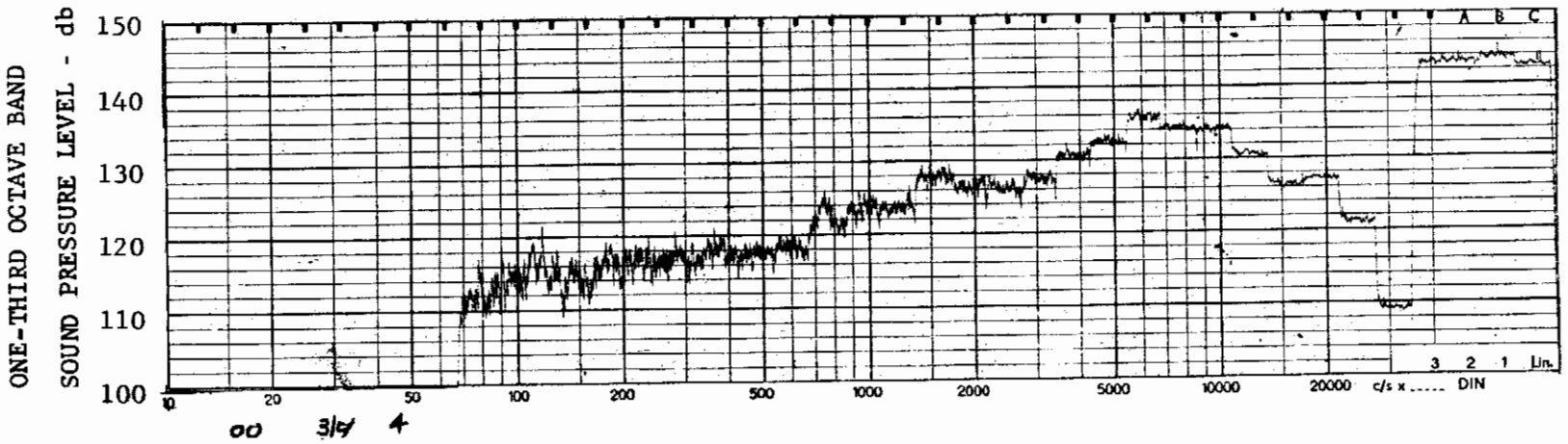

FIGURE 53 ONE-THIRD OCTAVE BAND SPECTRUM MODEL: AXISYM

CHANNEL: 4 MACH NO.: 5 α: 0 ϕ: 0 Re_∞/FT.: 6.0×10^6 AEDC GROUP NO.: 3/9

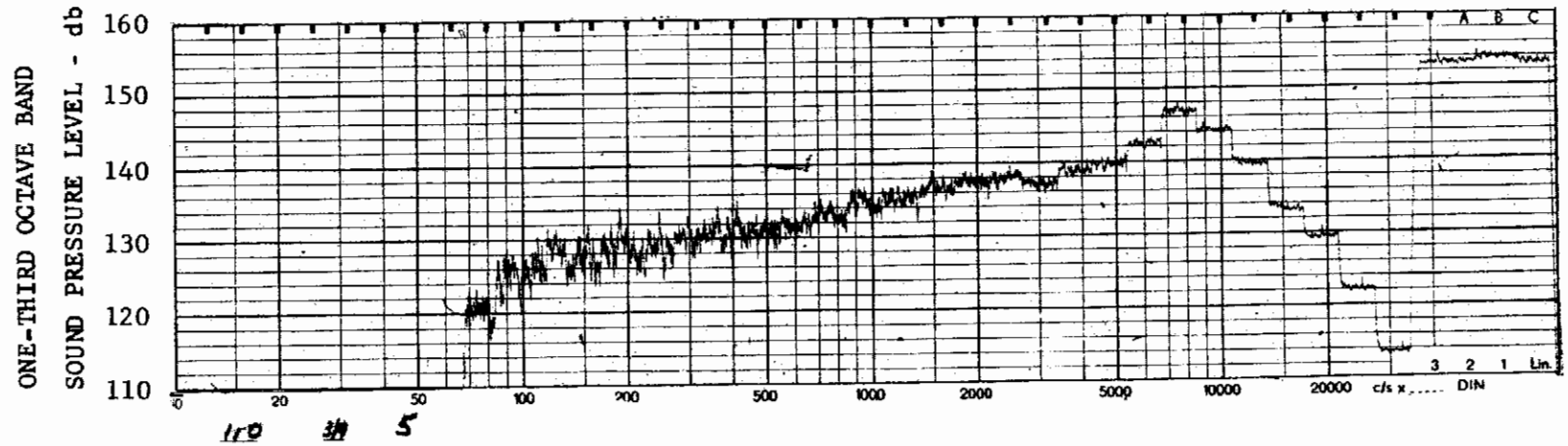

FIGURE 54 ONE-THIRD OCTAVE BAND SPECTRUM MODEL: AXISYM

CHANNEL: 5 MACH NO.: 5 α: 0 ϕ: 0 Re_∞/FT.: 6.0×10^6 AEDC GROUP NO.: 3/9

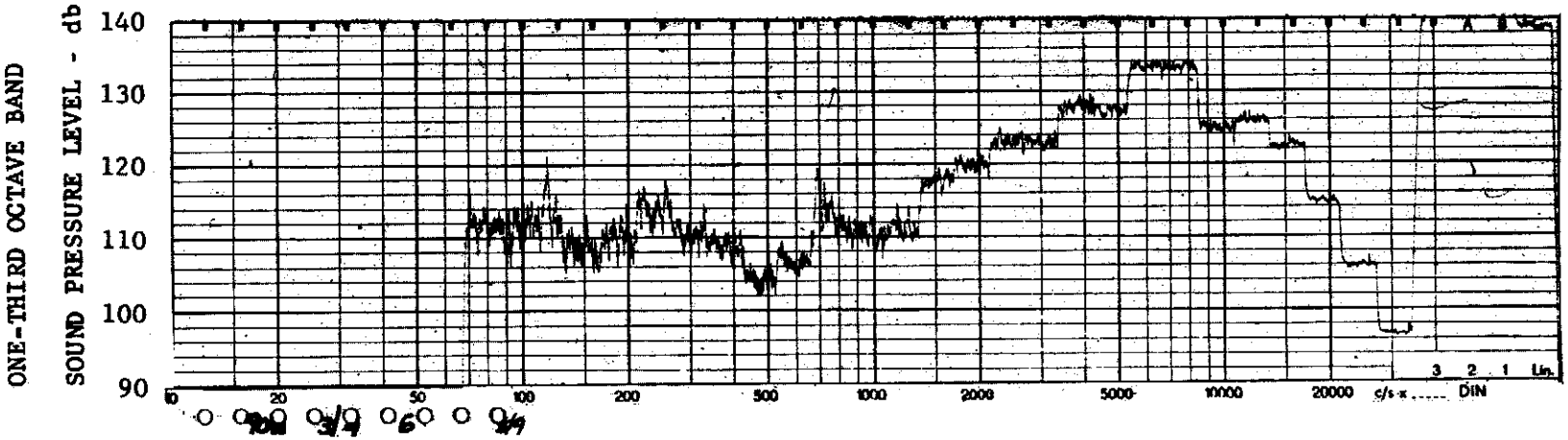

FIGURE 55 ONE-THIRD OCTAVE BAND SPECTRUM MODEL: AXISYM

CHANNEL: 6 MACH NO.: 5 α: 0 ϕ: 0 Re_∞/FT.: 6.0×10^6 AEDC GROUP NO.: 3/9

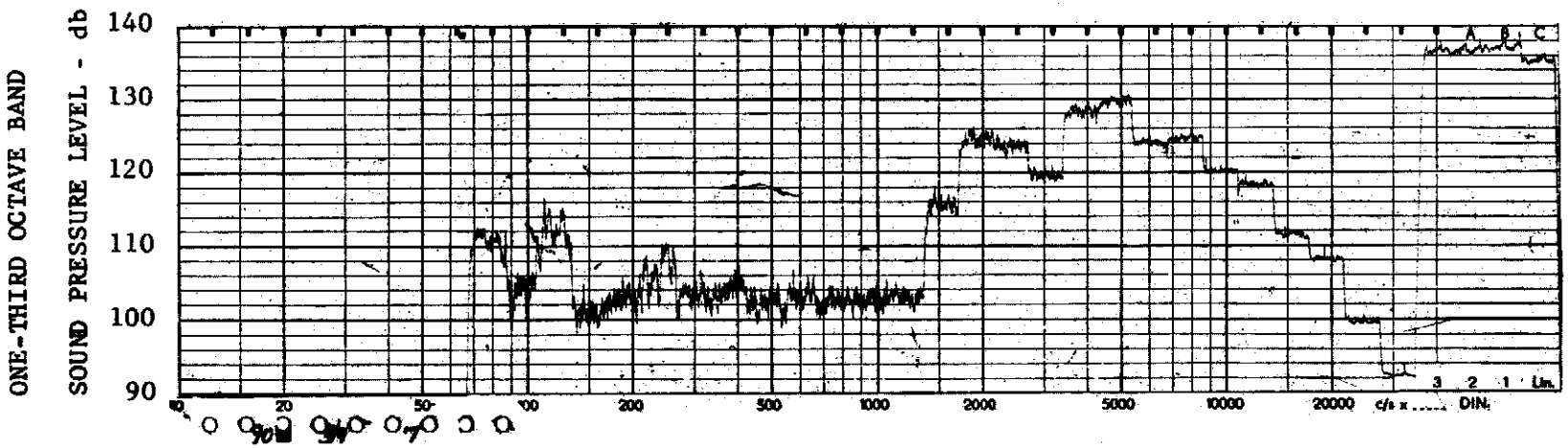

FIGURE 56 ONE-THIRD OCTAVE BAND SPECTRUM MODEL: AXISYM

CHANNEL: 7 MACH NO.: 5 α: 0 ϕ: 0 Re_∞/FT.: 6.0×10^6 AEDC GROUP NO.: 3/9

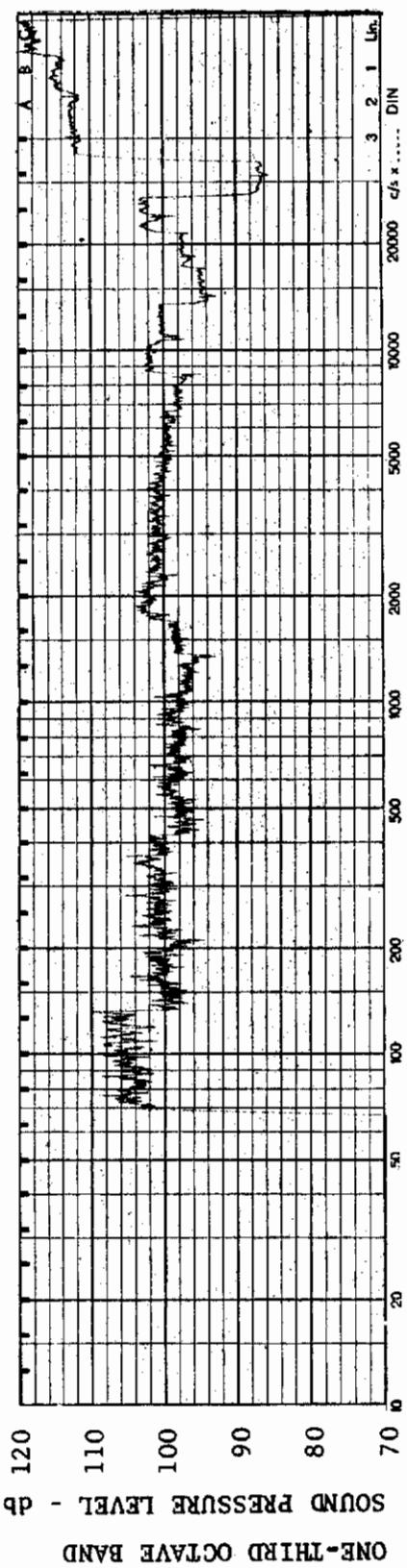

FIGURE 57 ONE-THIRD OCTAVE BAND SPECTRUM MODEL: AXISYM

CHANNEL: 1 MACH NO.: 2.5 α: 0 ϕ: 0 Re_∞/FT.: 0.5×10^6 AEDC GROUP NO.: 4/10

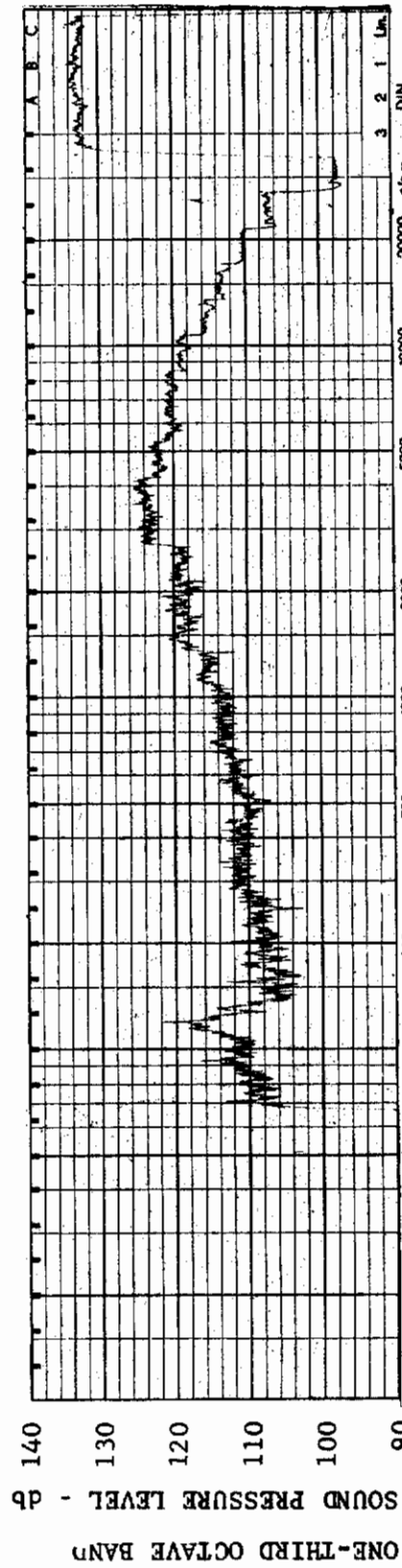

FIGURE 58 ONE-THIRD OCTAVE BAND SPECTRUM MODEL: AXISYM

CHANNEL: 2 MACH NO.: 2.5 α: 0 ϕ: 0 Re_∞/FT.: 0.5×10^6 AEDC GROUP NO.: 4/10

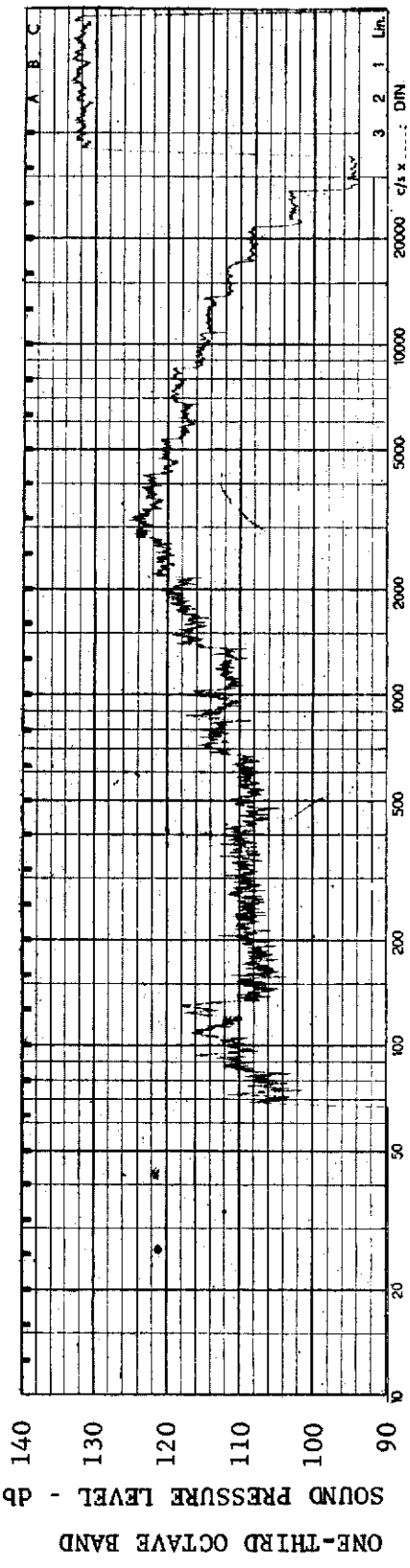

FIGURE 59 ONE-THIRD OCTAVE BAND SPECTRUM MODEL: AXISYM

CHANNEL: 3 MACH NO.: 2.5 α: 0 ϕ: 0 Re_∞/FT.: 0.5×10^6 AEDC GROUP NO.: 4/10

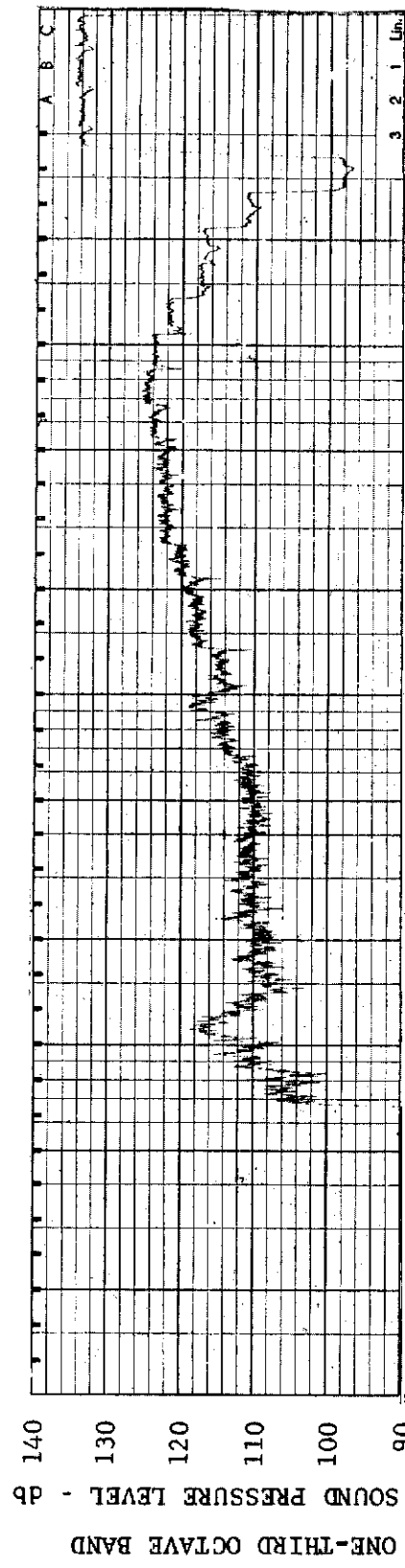

FIGURE 60 ONE-THIRD OCTAVE BAND SPECTRUM MODEL: AXISYM

CHANNEL: 4 MACH NO.: 2.5 α: 0 ϕ: 0 Re_∞/FT.: 0.5×10^6 AEDC GROUP NO.: 4/10

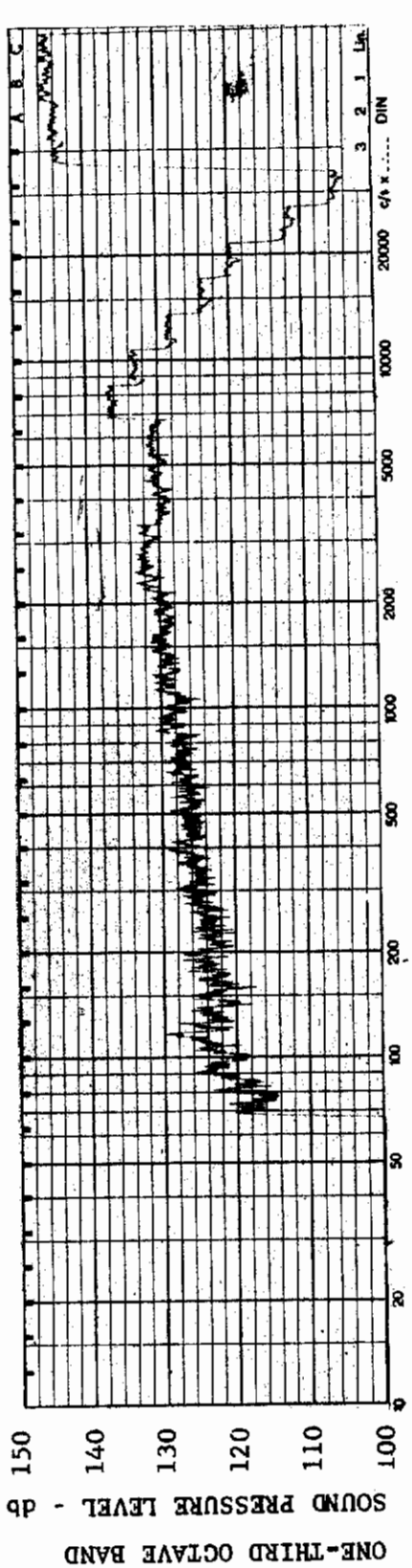

FIGURE 61 ONE-THIRD OCTAVE BAND SPECTRUM

MODEL: AXISYM

CHANNEL: 5 MACH NO.: 2.5 α: 0 ϕ: 0 Re_∞/FT.: 0.5×10^6 AEDC GROUP NO.: 4/10

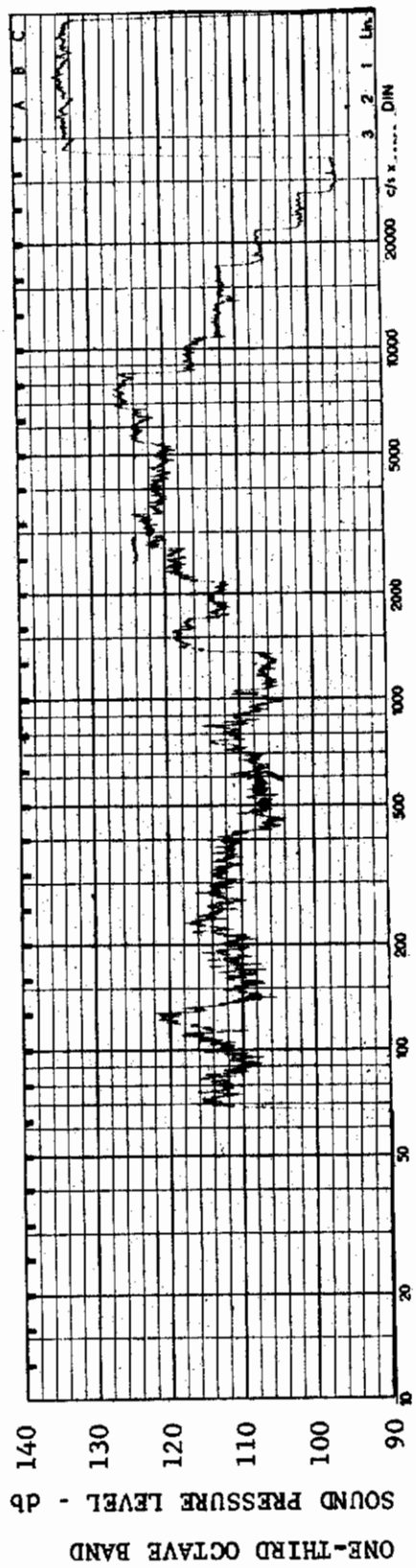

FIGURE 62 ONE-THIRD OCTAVE BAND SPECTRUM

MODEL: AXISYM

CHANNEL: 6 MACH NO.: 2.5 α: 0 ϕ: 0 Re_∞/FT.: 0.5×10^6 AEDC GROUP NO.: 4/10

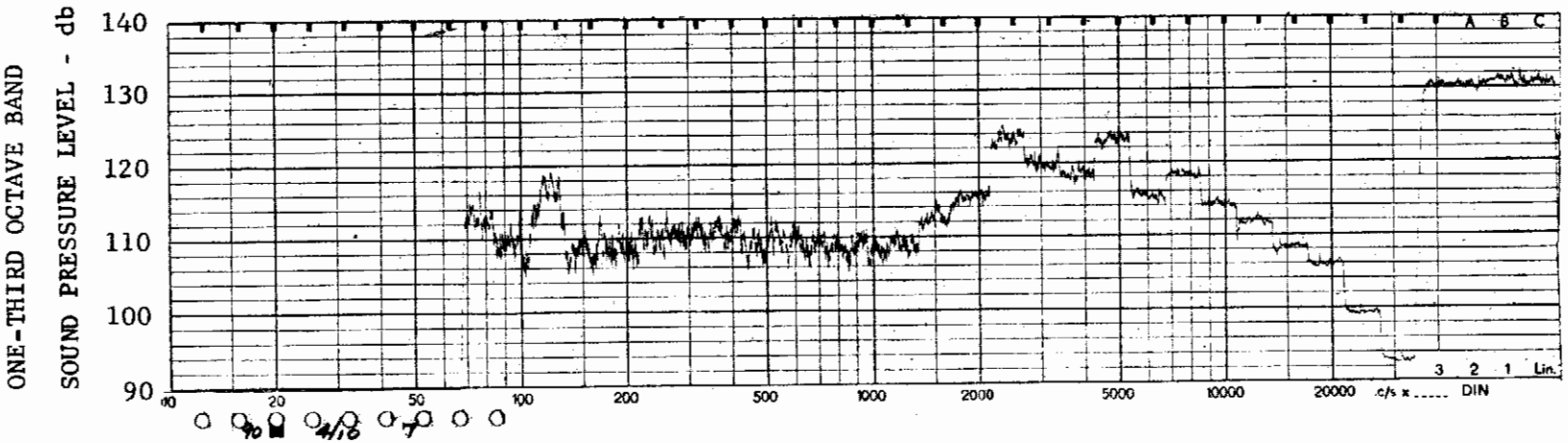

FIGURE 63 ONE-THIRD OCTAVE BAND SPECTRUM MODEL: AXISYM

CHANNEL: 7 MACH NO.: 2.5 α: 0 ϕ: 0 Re_∞/FT.: 6.5x10^6 AEDC GROUP NO.: 4/10

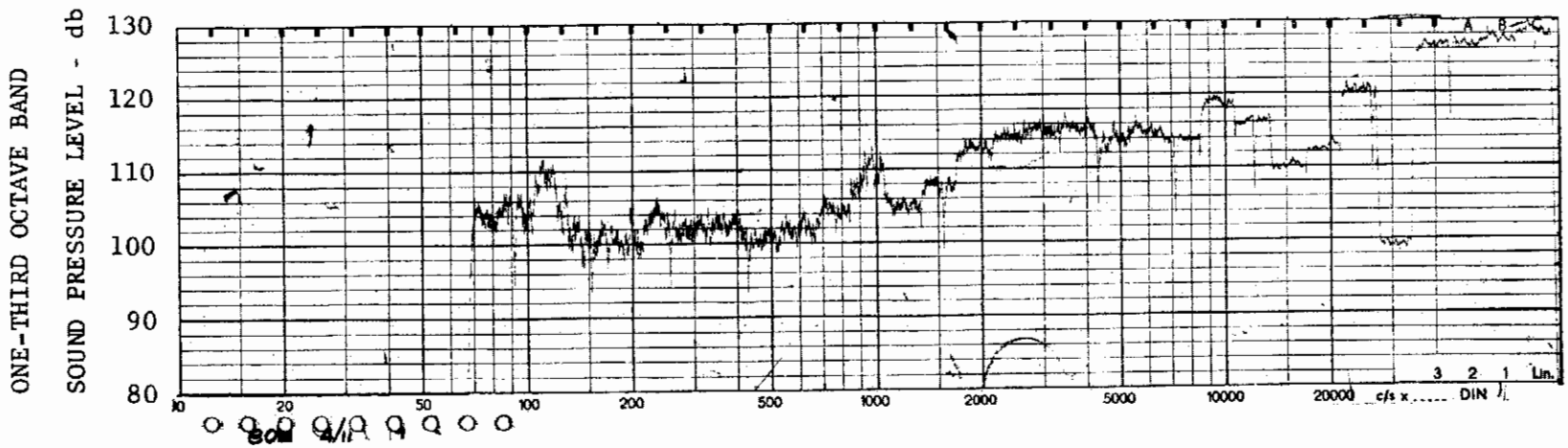

FIGURE 64 ONE-THIRD OCTAVE BAND SPECTRUM MODEL: AXISYM

CHANNEL: 1 MACH NO.: 2.5 α: 0 ϕ: 0 Re_∞/FT.: 6.0x10^6 AEDC GROUP NO.: 4/11

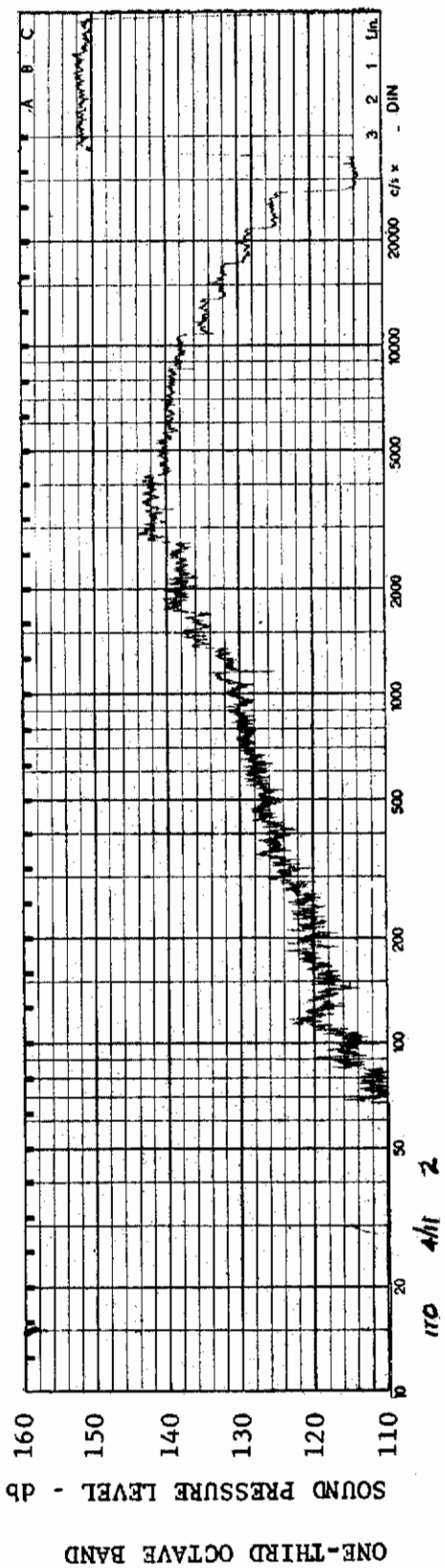

FIGURE 65 ONE-THIRD OCTAVE BAND SPECTRUM MODEL: AXISYM

CHANNEL: 2 MACH NO.: 2.5 α: 0 ϕ: 0 Re_∞/FT.: 6.0×10^6 AEDC GROUP NO.: 4/11

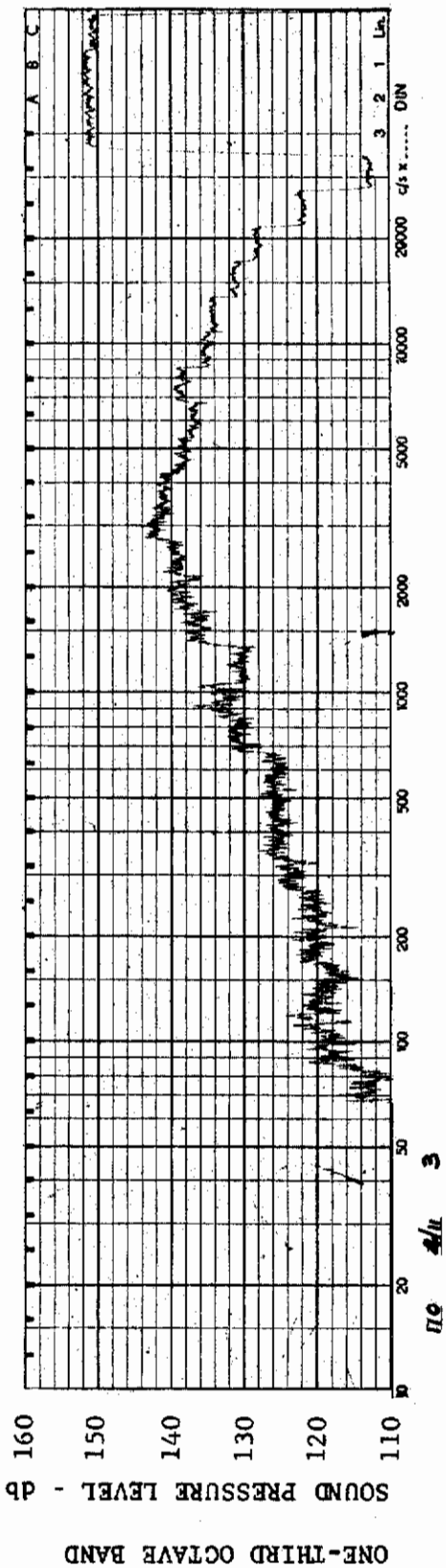

FIGURE 66 ONE-THIRD OCTAVE BAND SPECTRUM MODEL: AXISYM

CHANNEL: 3 MACH NO.: 2.5 α: 0 ϕ: 0 Re_∞/FT.: 6.0×10^6 AEDC GROUP NO.: 4/11

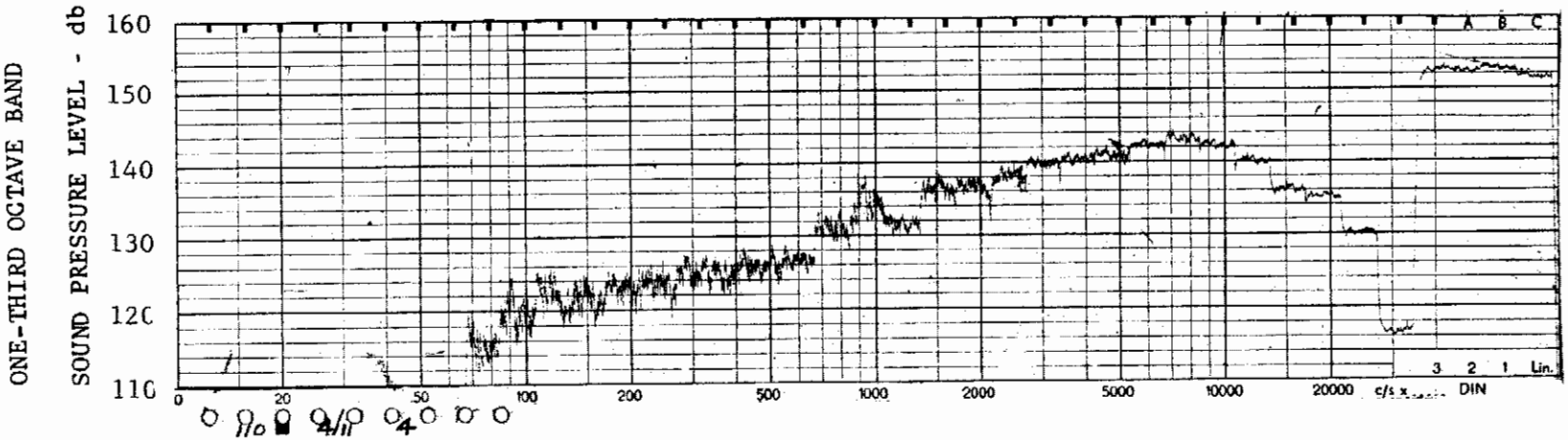

FIGURE 67 ONE-THIRD OCTAVE BAND SPECTRUM MODEL: AXISYM

CHANNEL: 4 MACH NO.: 2.5 α: 0 ϕ: 0 Re_∞/FT.: 6.0×10^6 AEDC GROUP NO.: 4/11

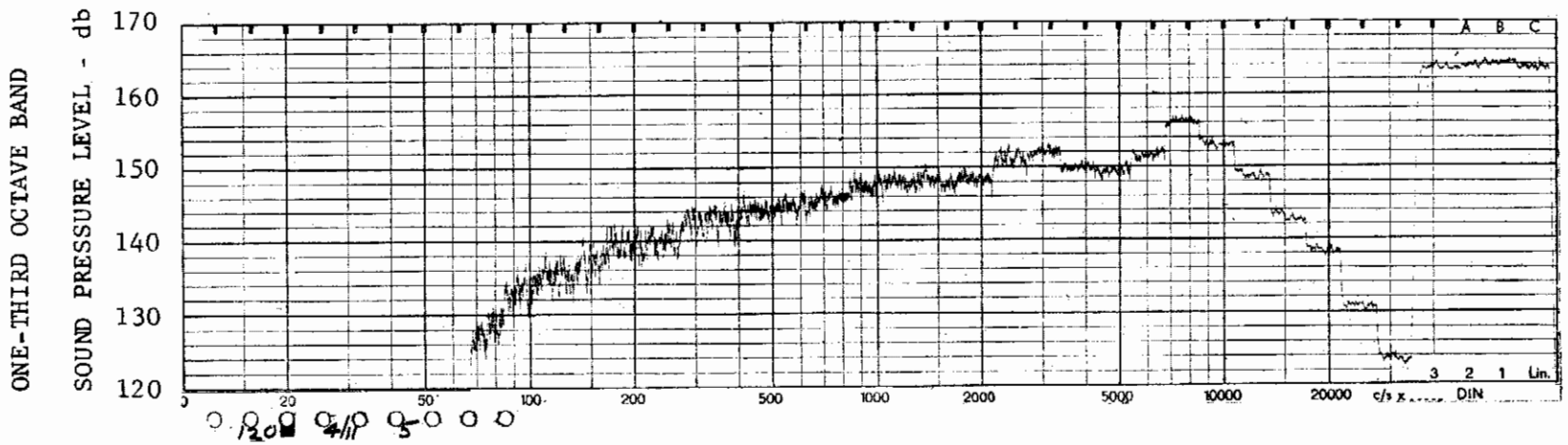

FIGURE 68 ONE-THIRD OCTAVE BAND SPECTRUM MODEL: AXISYM

CHANNEL: 5 MACH NO.: 2.5 α: 0 ϕ: 0 Re_∞/FT.: 6.0×10^6 AEDC GROUP NO.: 4/11

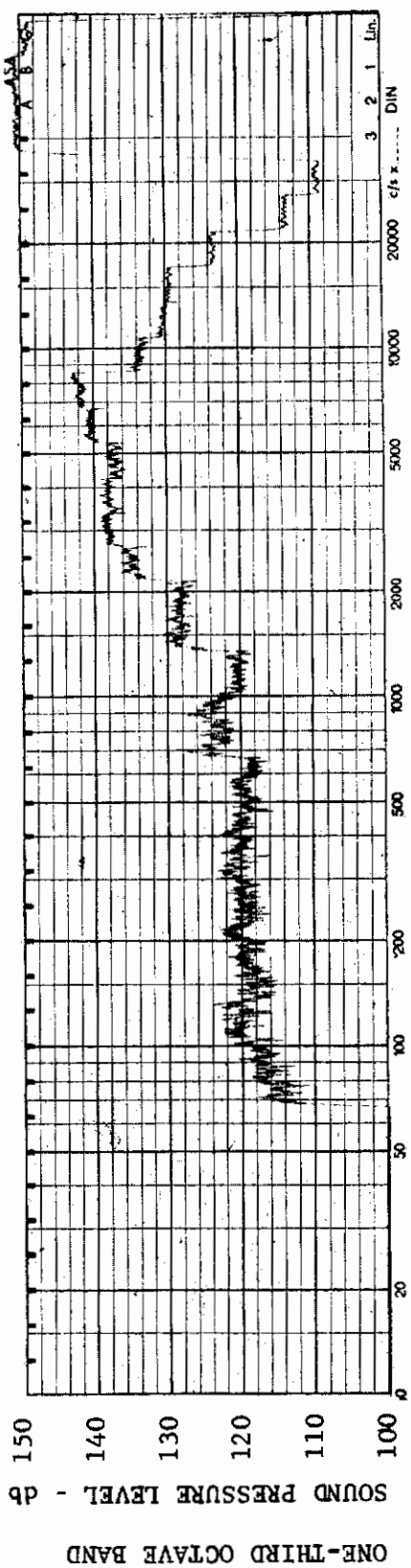

FIGURE 69 ONE-THIRD OCTAVE BAND SPECTRUM MODEL: AXISYM

CHANNEL: 6 MACH NO.: 2.5 α: 0 ϕ: 0 Re_∞/FT.: 6.0×10^6 AEDC GROUP NO.: 4/11

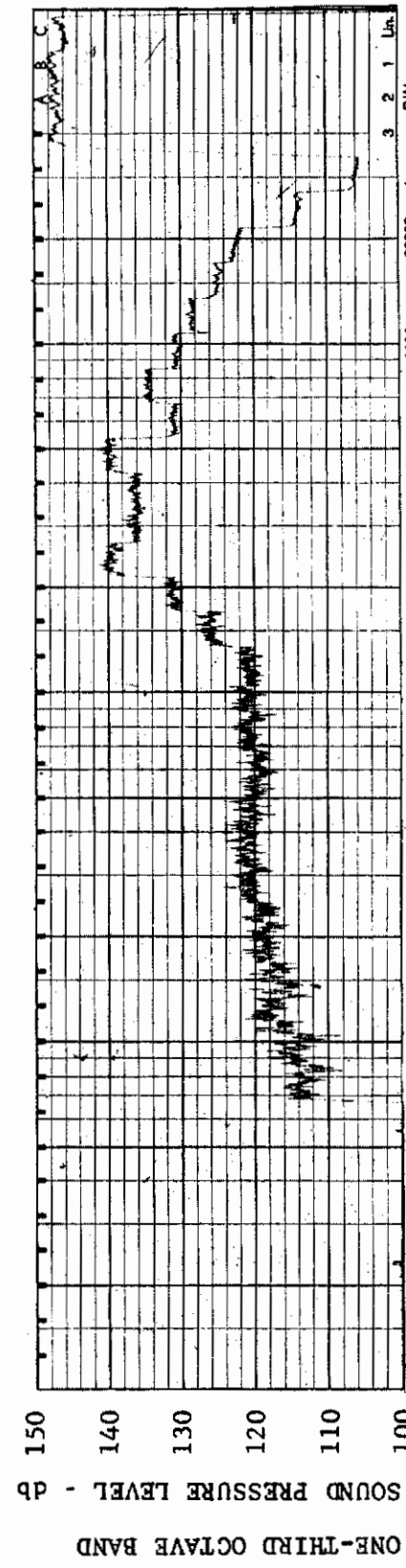

FIGURE 70 ONE-THIRD OCTAVE BAND SPECTRUM MODEL: AXISYM

CHANNEL: 7 MACH NO.: 2.5 α: 0 ϕ: 0 Re_∞/FT.: 6.0×10^6 AEDC GROUP NO.: 4/11

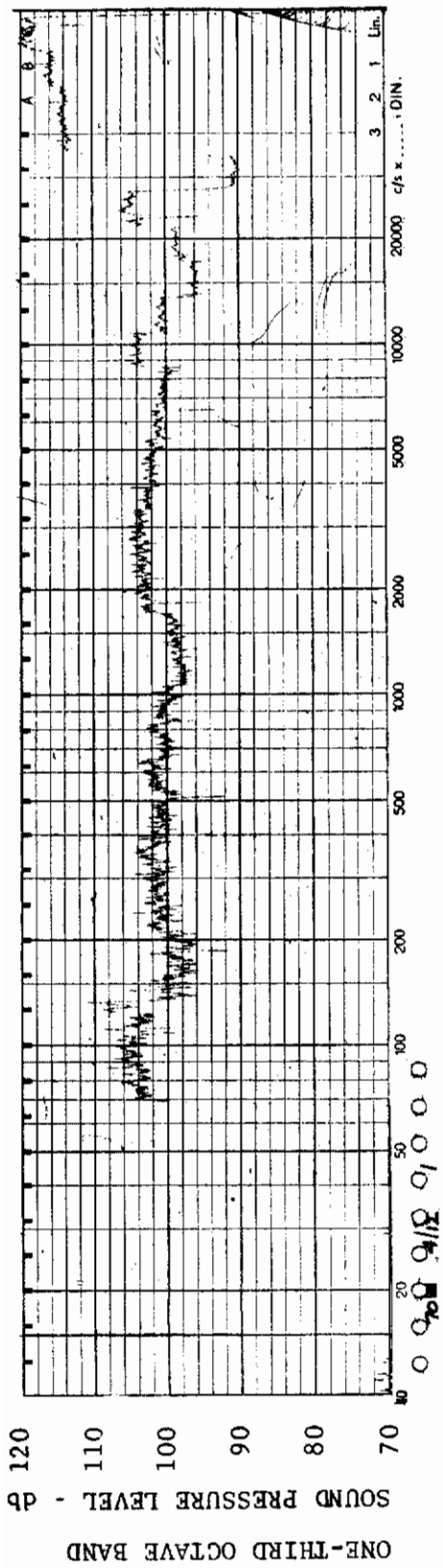

FIGURE 71 ONE-THIRD OCTAVE BAND SPECTRUM MODEL: AXISYM

CHANNEL: 1 MACH NO.: 2.5 α: 0 ϕ 0 Re_∞/FT.: 1.0×10^6 AEDC GROUP NO.: 4/12

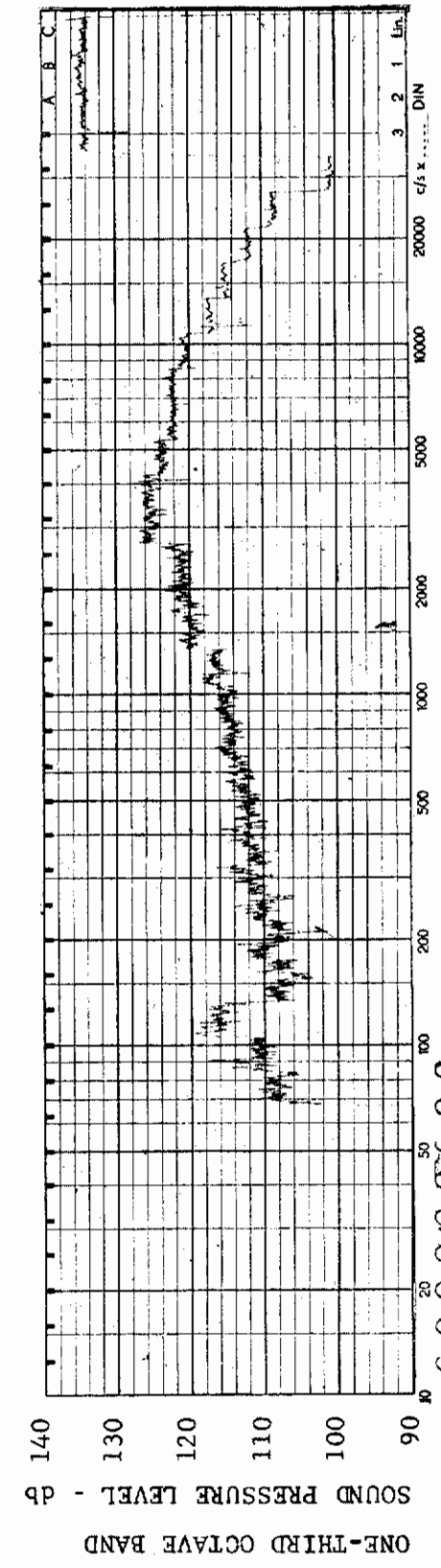

FIGURE 72 ONE-THIRD OCTAVE BAND SPECTRUM MODEL: AXISYM

CHANNEL: 2 MACH NO.: 2.5 α: 0 ϕ: 0 Re_∞/FT.: 1.0×10^6 AEDC GROUP NO.: 4/12

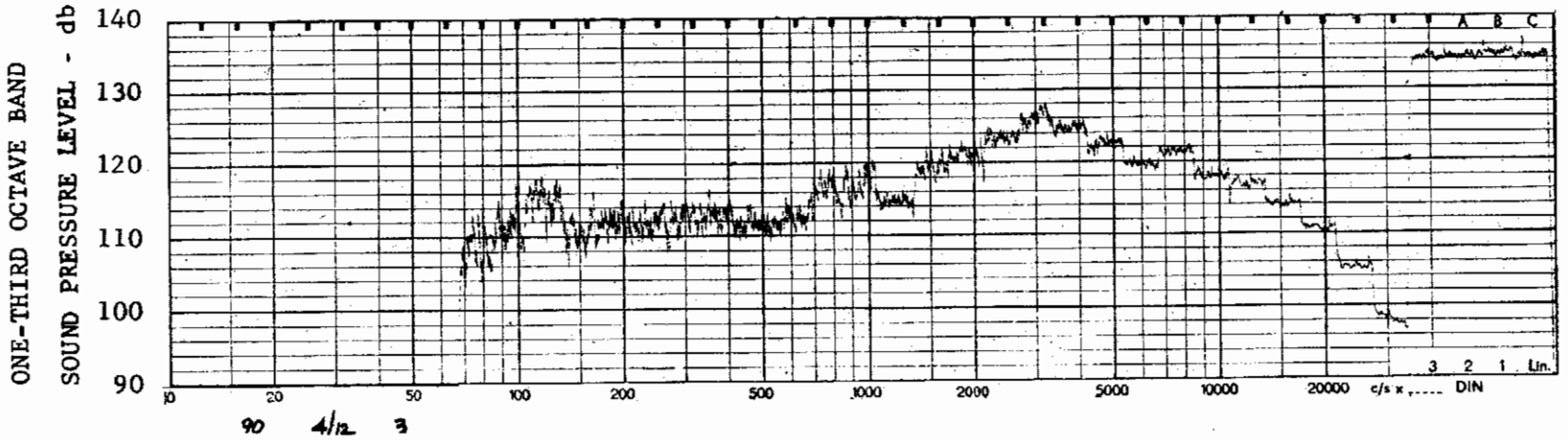

FIGURE 73 ONE-THIRD OCTAVE BAND SPECTRUM MODEL: AXISYM

CHANNEL: 3 MACH NO.: 2.5 α: 0 ϕ: 0 Re_∞/FT.: 1.0×10^6 AEDC GROUP NO.: 4/12

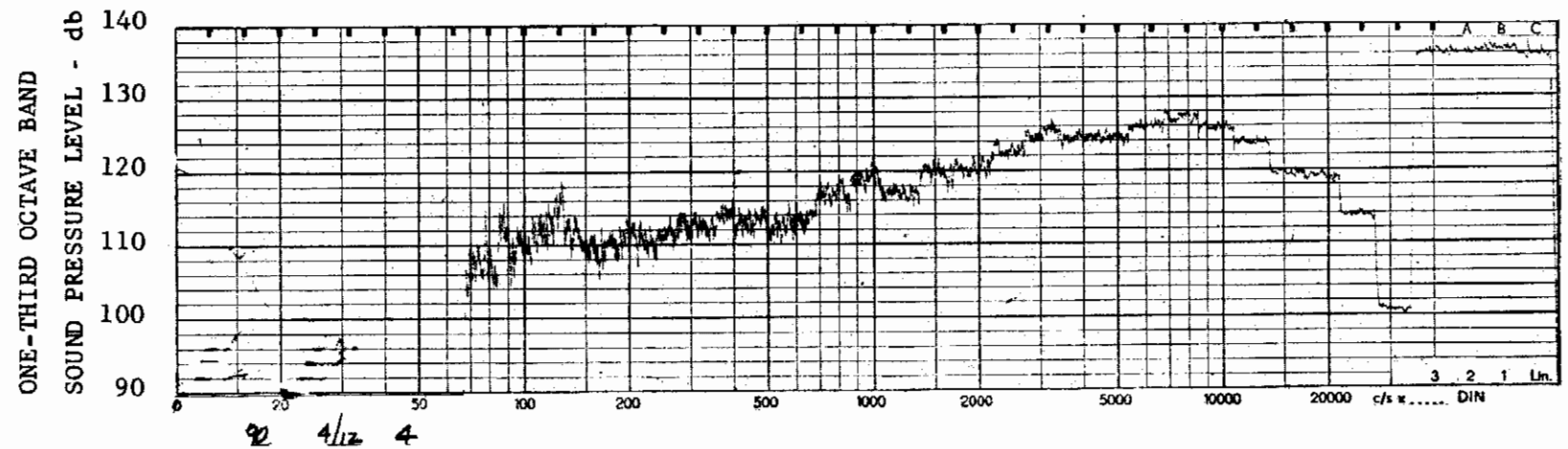

FIGURE 74 ONE-THIRD OCTAVE BAND SPECTRUM MODEL: AXISYM

CHANNEL: 4 MACH NO.: 2.5 α: 0 ϕ: 0 Re_∞/FT.: 1.0×10^6 AEDC GROUP NO.: 4/12

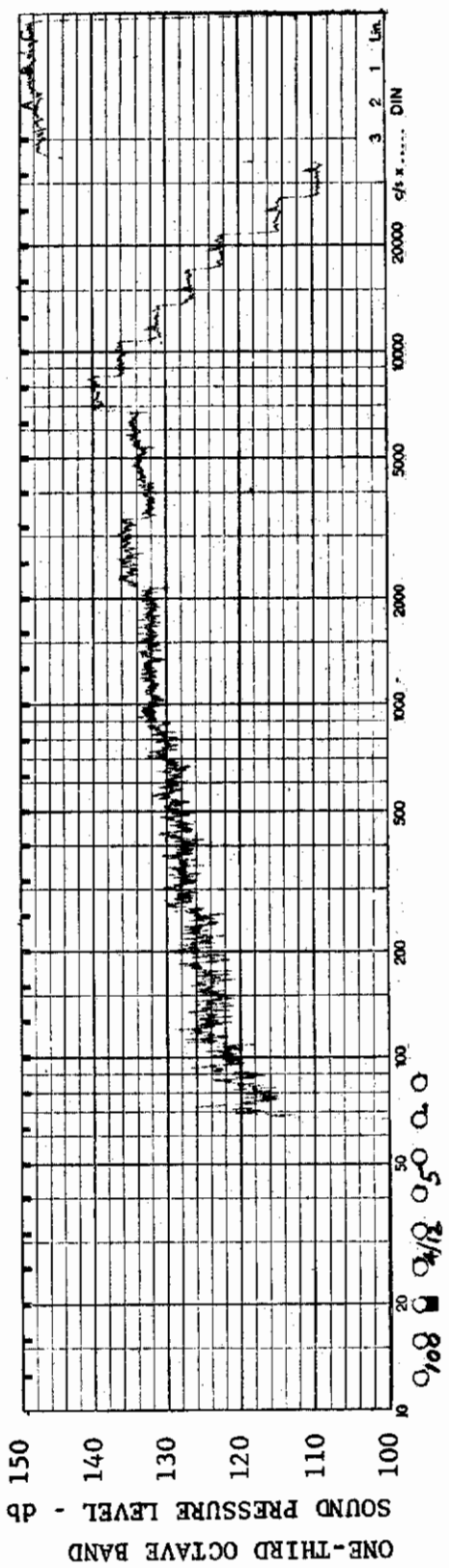

FIGURE 75 ONE-THIRD OCTAVE BAND SPECTRUM MODEL: AXISYM

CHANNEL: 5 MACH NO.: 2.5 α: 0 ϕ: 0 Re_∞/FT.: 1.0×10^6 AEDC GROUP NO.: 4/12

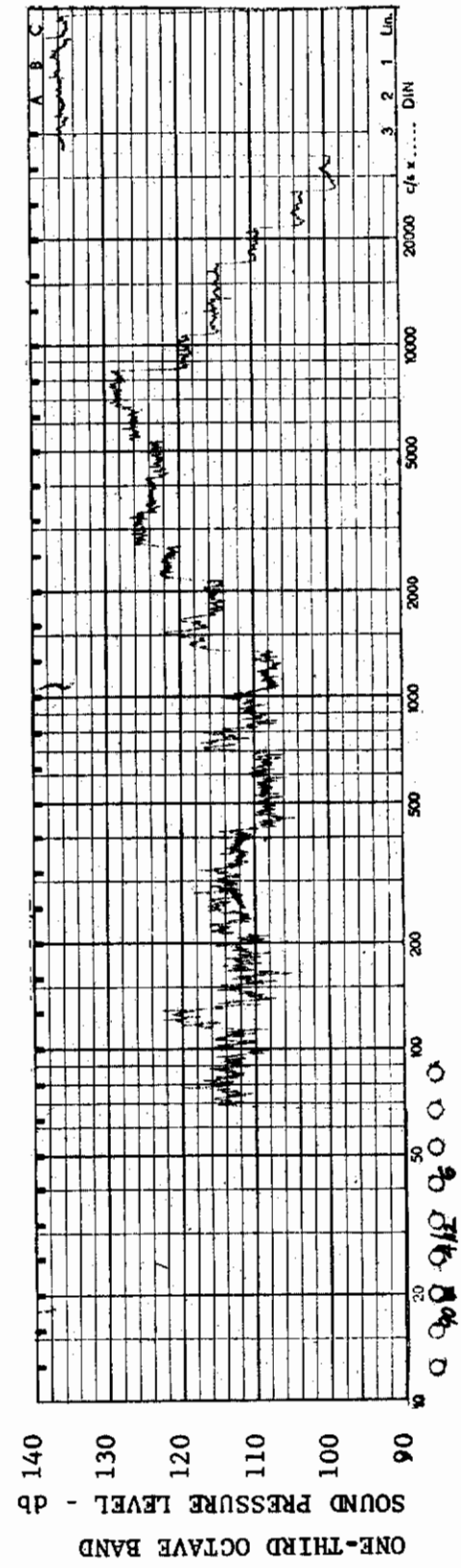

FIGURE 76 ONE-THIRD OCTAVE BAND SPECTRUM MODEL: AXISYM

CHANNEL: 6 MACH NO.: 2.5 α: 0 ϕ: 0 Re_∞/FT.: 1.0×10^6 AEDC GROUP NO.: 4/12

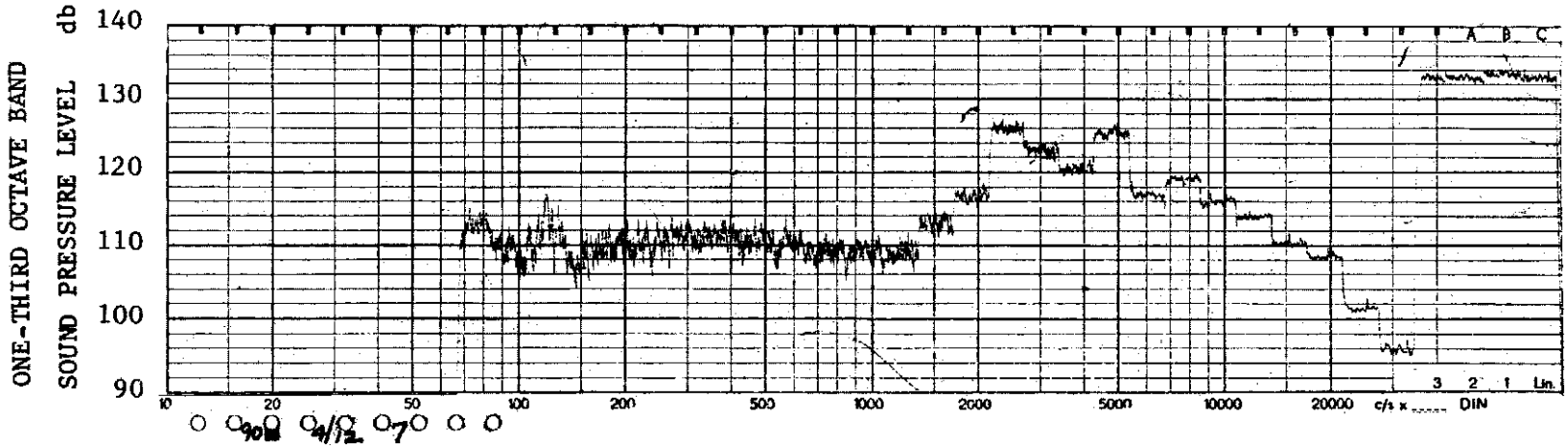

FIGURE 77 ONE-THIRD OCTAVE BAND SPECTRUM MODEL: AXISYM

CHANNEL: 7 MACH NO.: 2.5 α: 0 ϕ: 0 Re_∞/FT.: 1.0×10^6 AEDC GROUP NO.: 4/12

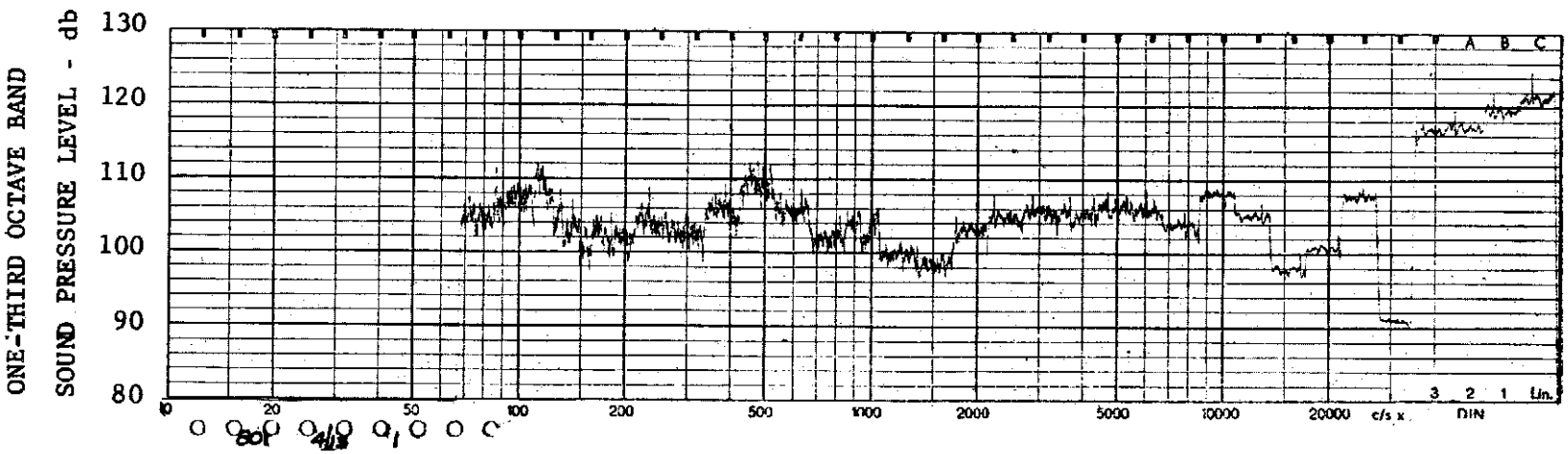

FIGURE 78 ONE-THIRD OCTAVE BAND SPECTRUM MODEL: AXISYM

CHANNEL: 1 MACH NO.: 2.5 α: 5° ϕ: 0 Re_∞/FT.: 1.0×10^6 AEDC GROUP NO.: 4/13

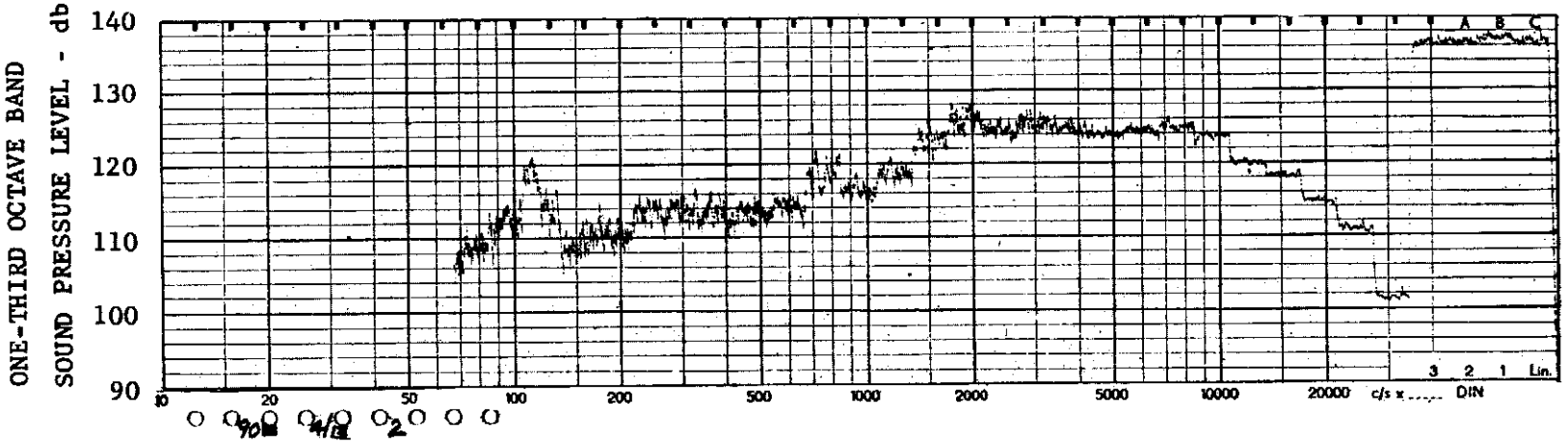

FIGURE 79 ONE-THIRD OCTAVE BAND SPECTRUM MODEL: AXISYM

CHANNEL: 2 MACH NO.: 2.5 α: 5° ϕ: 0 Re_∞/FT.: 1.0×10^6 AEDC GROUP NO.: 4/13

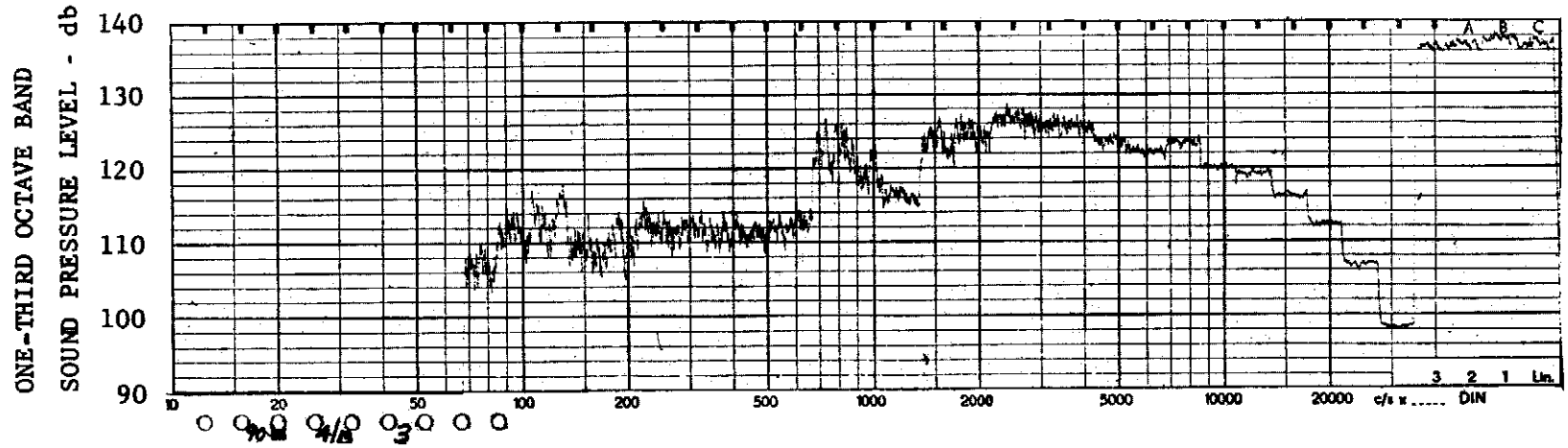

FIGURE 80 ONE-THIRD OCTAVE BAND SPECTRUM MODEL: AXISYM

CHANNEL: 3 MACH NO.: 2.5 α: 5° ϕ: 0 Re_∞/FT.: 1.0×10^6 AEDC GROUP NO.: 4/13

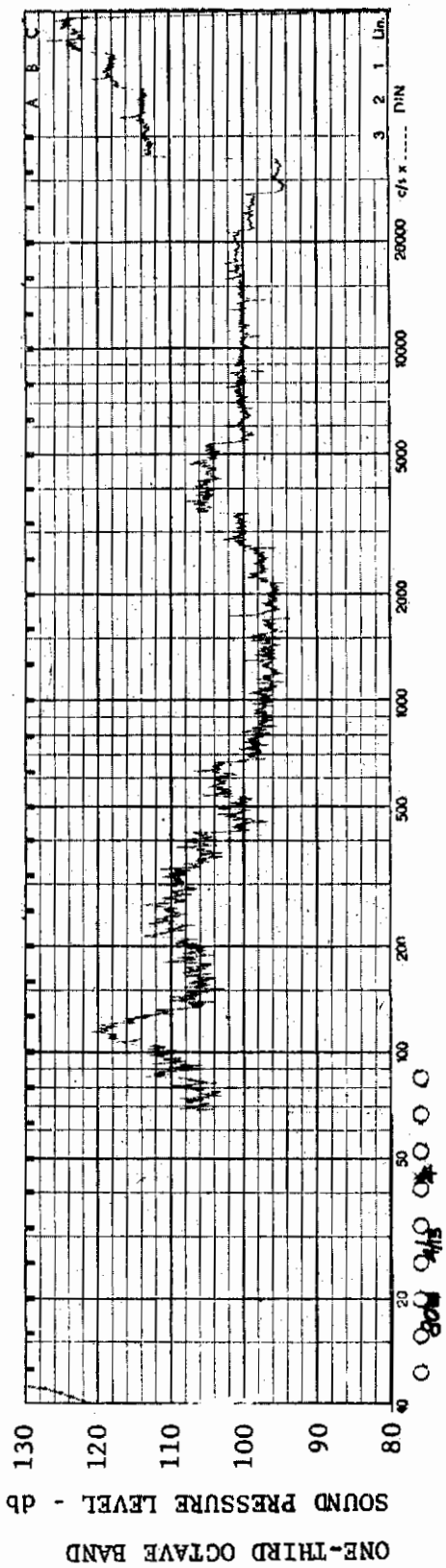

FIGURE 81 ONE-THIRD OCTAVE BAND SPECTRUM MODEL: AXISYM

CHANNEL: 4 MACH NO.: 2.5 α: 5° ϕ: 0 Re_∞/FT.: 1.0×10^6 AEDC GROUP NO.: 4/13

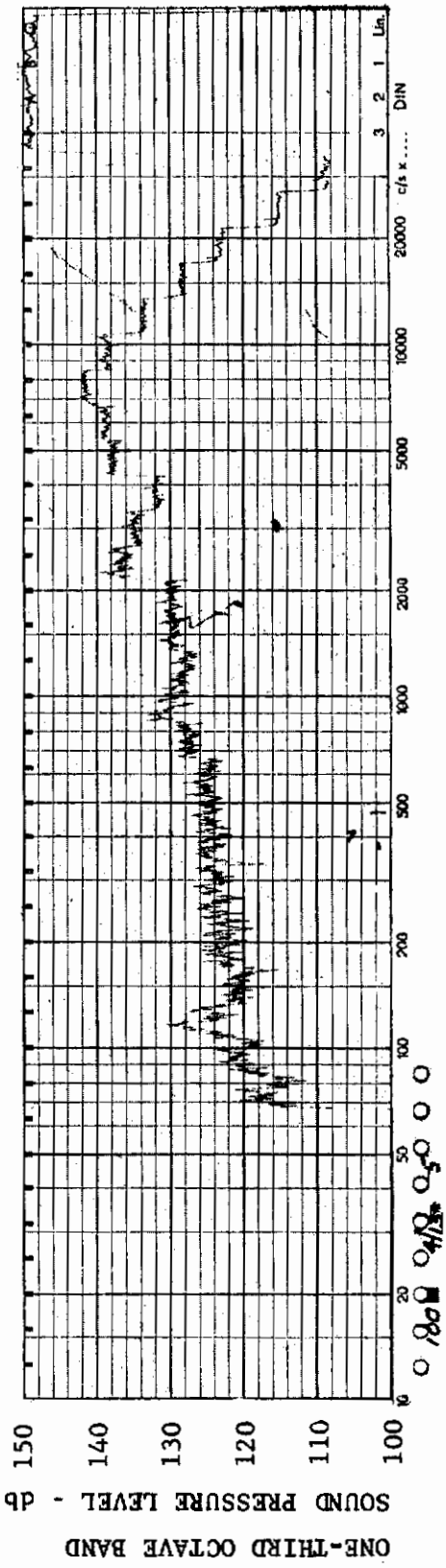

FIGURE 82 ONE-THIRD OCTAVE BAND SPECTRUM MODEL: AXISYM

CHANNEL: 5 MACH NO.: 2.5 α: 5° ϕ: 0 Re_∞/FT.: 1.0×10^6 AEDC GROUP NO.: 4/13

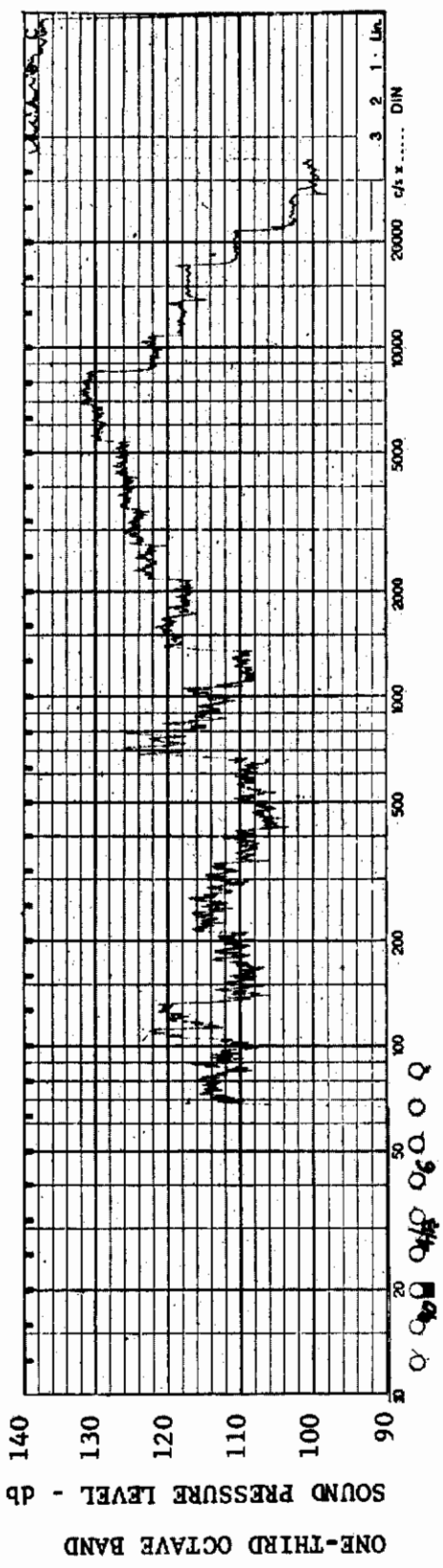

FIGURE 83 ONE-THIRD OCTAVE BAND SPECTRUM MODEL: AXISYM

CHANNEL: 6 MACH NO.: 2.5 α: 5° ϕ: 0 Re_∞/FT.: 1.0×10^6 AEDC GROUP NO.: 4/13

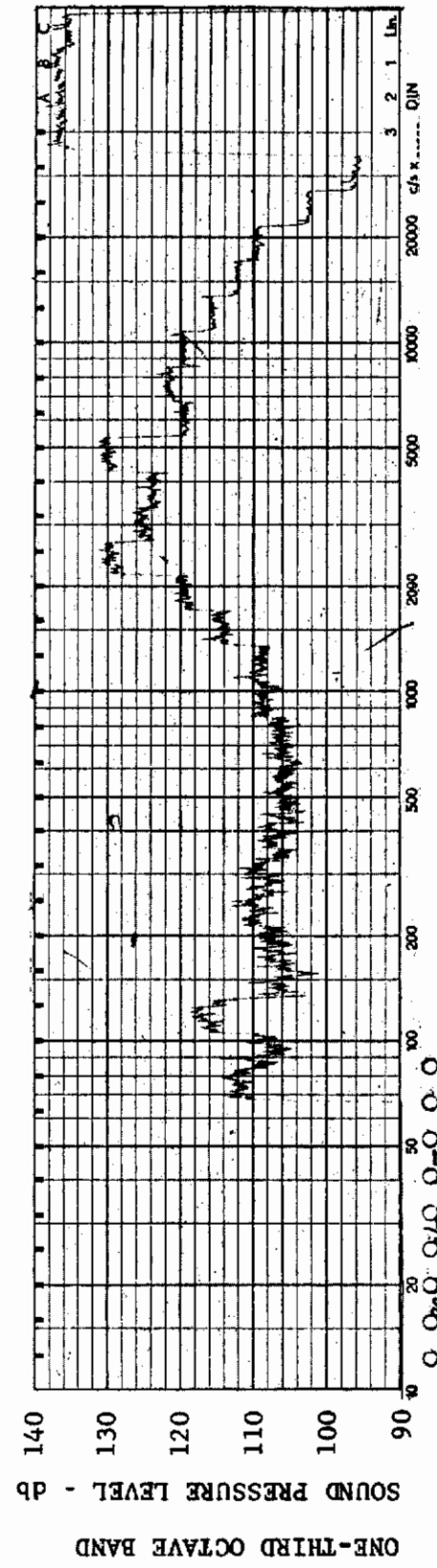

FIGURE 84 ONE-THIRD OCTAVE BAND SPECTRUM MODEL: AXISYM

CHANNEL: 7 MACH NO.: 2.5 α: 5° ϕ: 0 Re_∞/FT.: 1.0×10^6 AEDC GROUP NO.: 4/13

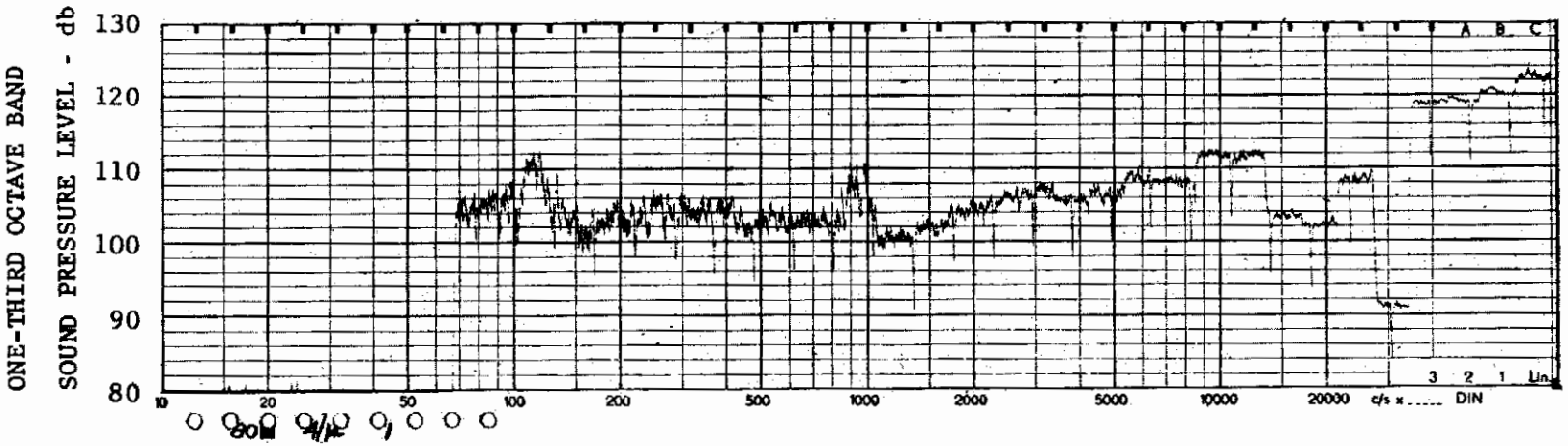

FIGURE 85 ONE-THIRD OCTAVE BAND SPECTRUM MODEL: AXISYM

CHANNEL: 1 MACH NO.: 2.5 α: 15° ϕ: 0 Re_∞/FT.: 1.0×10^6 AEDC GROUP NO.: 4/14

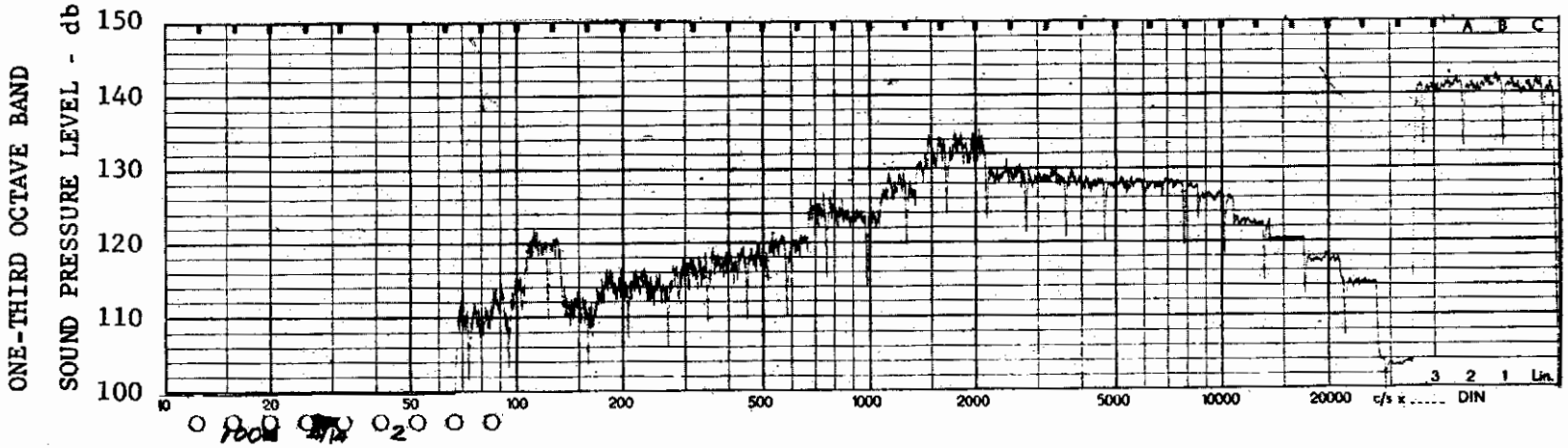

FIGURE 86 ONE-THIRD OCTAVE BAND SPECTRUM MODEL: AXISYM

CHANNEL: 2 MACH NO.: 2.5 α: 15° ϕ: 0 Re_∞/FT.: 1.0×10^6 AEDC GROUP NO.: 4/14

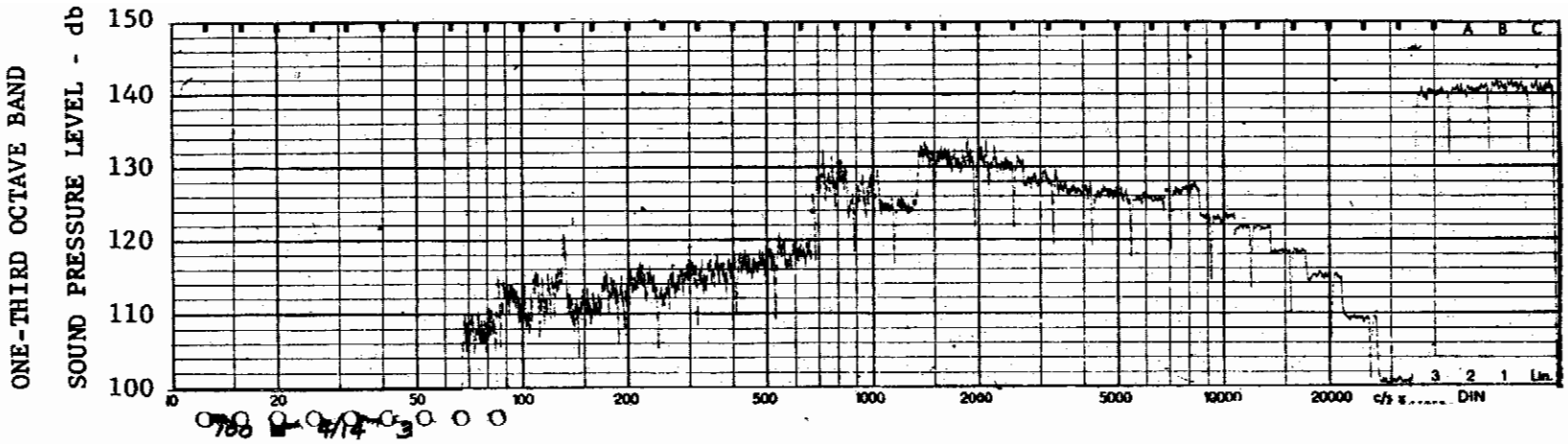

FIGURE 87 ONE-THIRD OCTAVE BAND SPECTRUM MODEL: AXISYM

CHANNEL: 3 MACH NO.: 2.5 α: 15° ϕ: 0 Re_∞/FT.: 1.0×10^6 AEDC GROUP NO.: 4/14

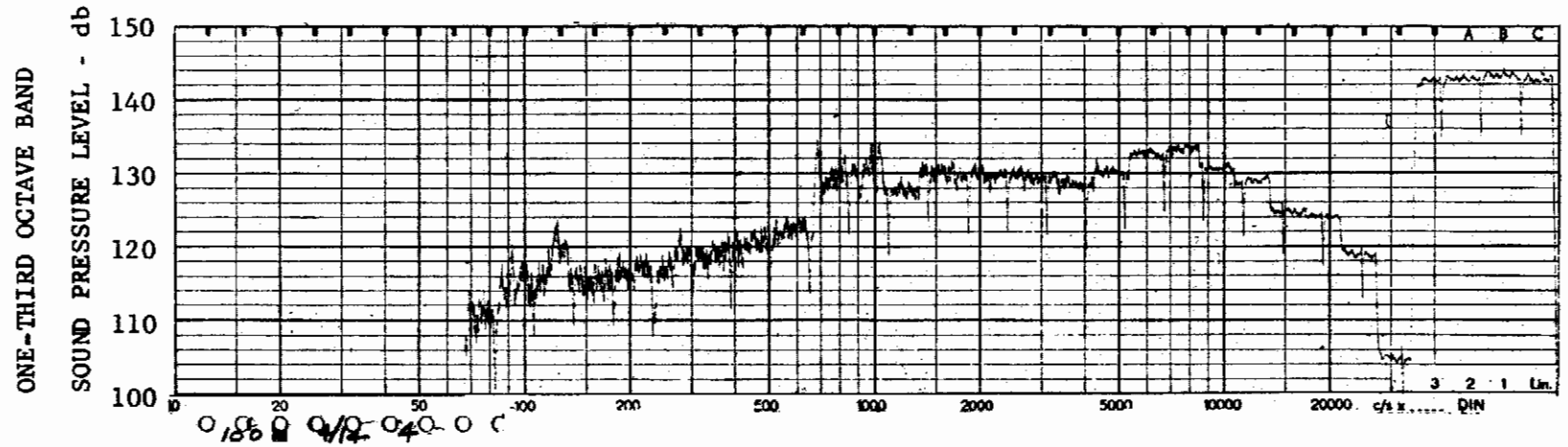

FIGURE 88 ONE-THIRD OCTAVE BAND SPECTRUM MODEL: AXISYM

CHANNEL: 4 MACH NO.: 2.5 α: 15° ϕ: 0 Re_∞/FT.: 1.0×10^6 AEDC GROUP NO.: 4/14

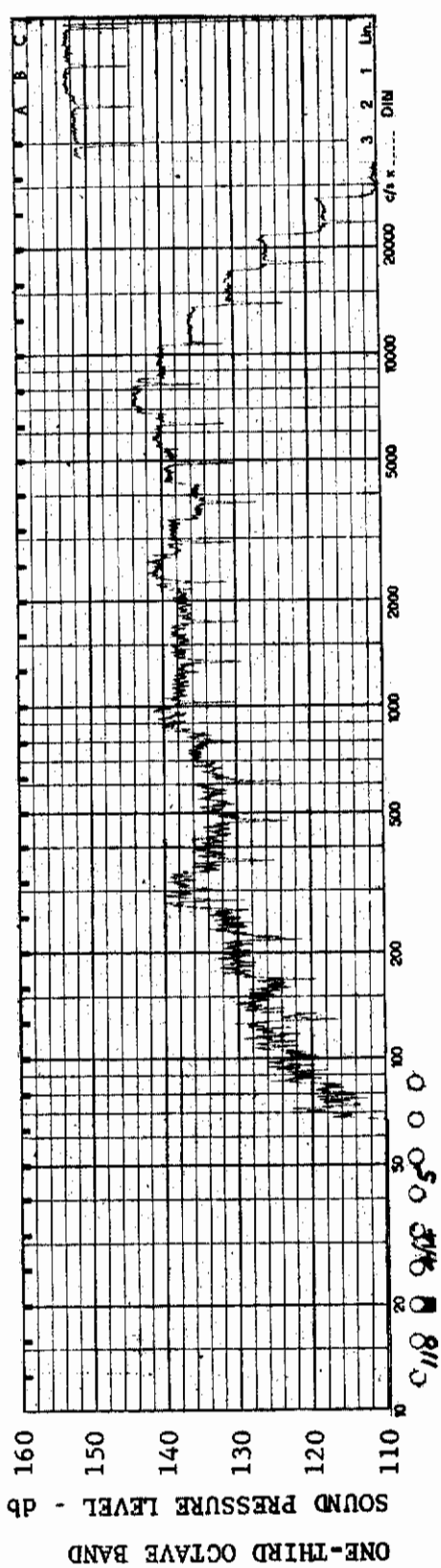

FIGURE 89 ONE-THIRD OCTAVE BAND SPECTRUM MODEL: AXISYM

CHANNEL: 5 MACH NO.: 2.5 α: 15° ϕ: 0 Re_∞/FT.: 1.0×10^6 AEDC GROUP NO.: 4/14

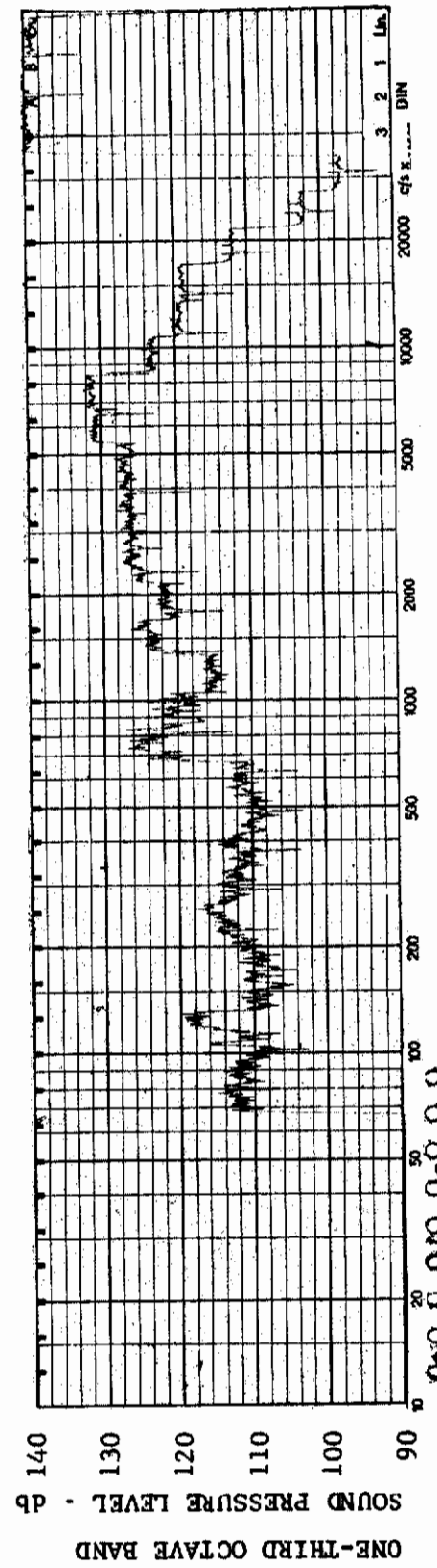

FIGURE 90 ONE-THIRD OCTAVE BAND SPECTRUM MODEL: AXISYM

CHANNEL: 6 MACH NO.: 2.5 α: 15° ϕ: 0 Re_∞/FT.: 1.0×10^6 AEDC GROUP NO.: 4/14

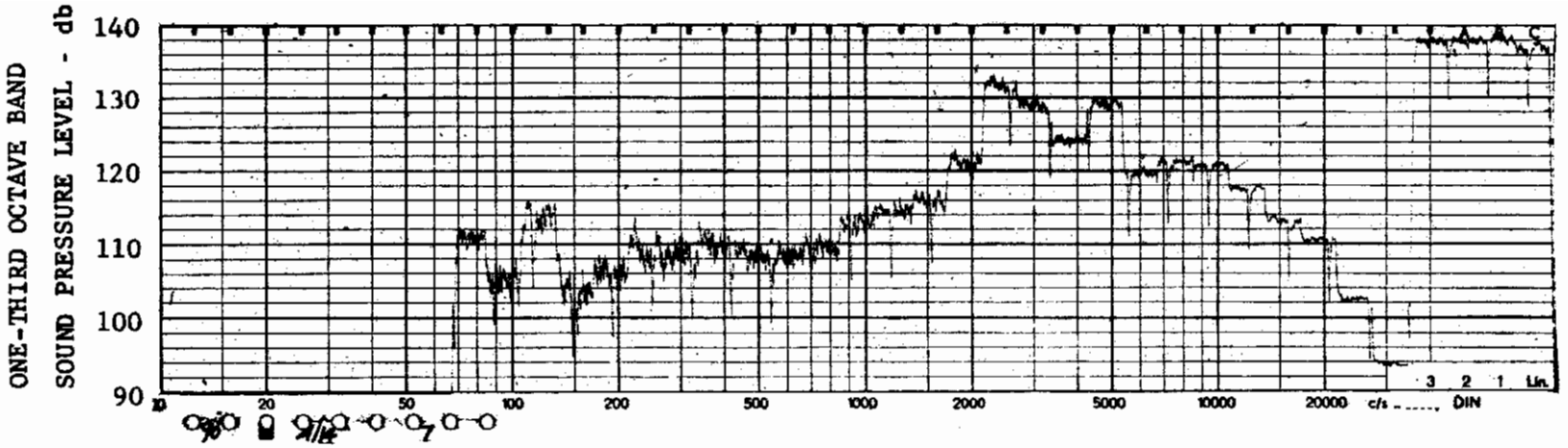

FIGURE 91 ONE-THIRD OCTAVE BAND SPECTRUM MODEL: AXISYM

CHANNEL: 7 MACH NO.: 2.5 α: 15° ϕ: 0 Re_∞/FT.: 1.0×10^6 AEDC GROUP NO.: 4/14

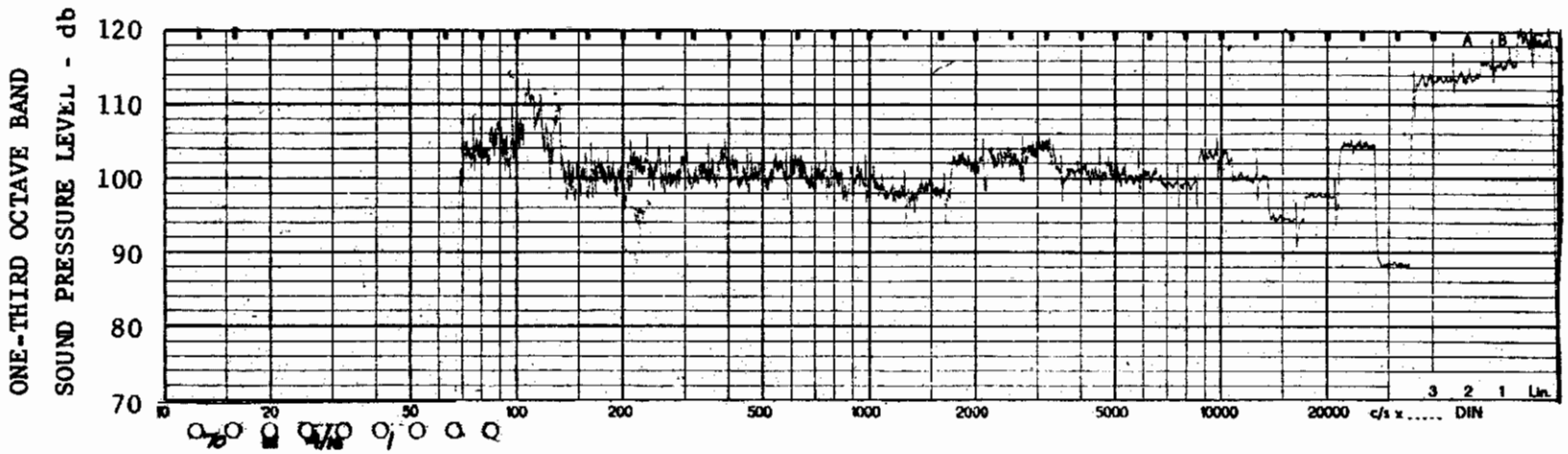

FIGURE 92 ONE-THIRD OCTAVE BAND SPECTRUM MODEL: AXISYM

CHANNEL: 1 MACH NO.: 2.5 α: 0 ϕ: 0 Re_∞/FT.: 1.0×10^6 AEDC GROUP NO.: 4/16

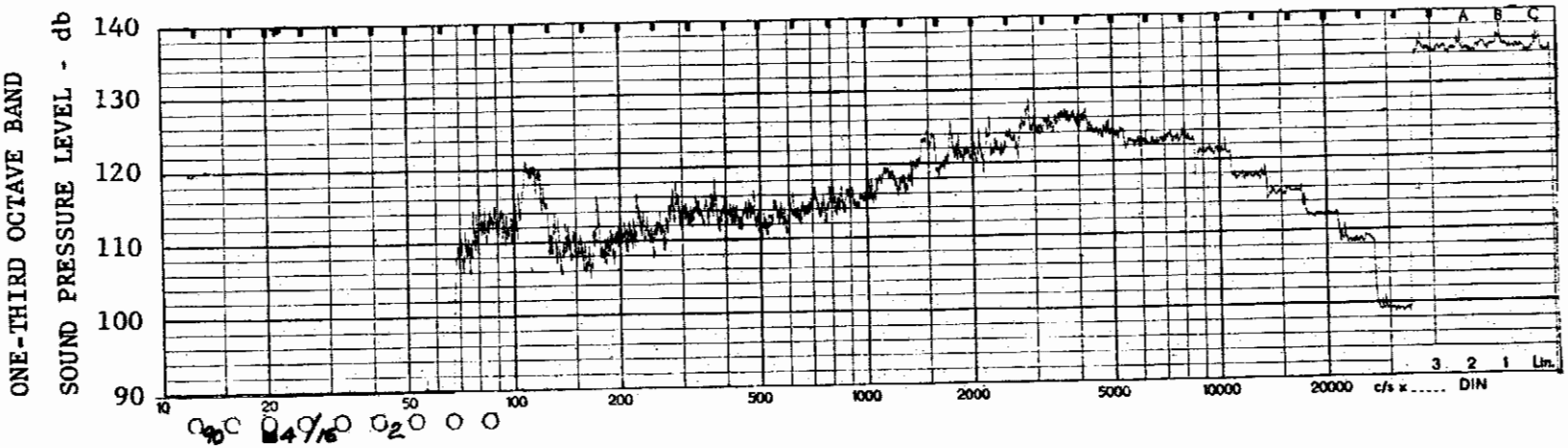

FIGURE 93 ONE-THIRD OCTAVE BAND SPECTRUM MODEL: AXISYM

CHANNEL: 2 MACH NO.: 2.5 α: 0 ϕ: 0 Re_∞/FT.: 1.0×10^6 AEDC GROUP NO.: 4/16

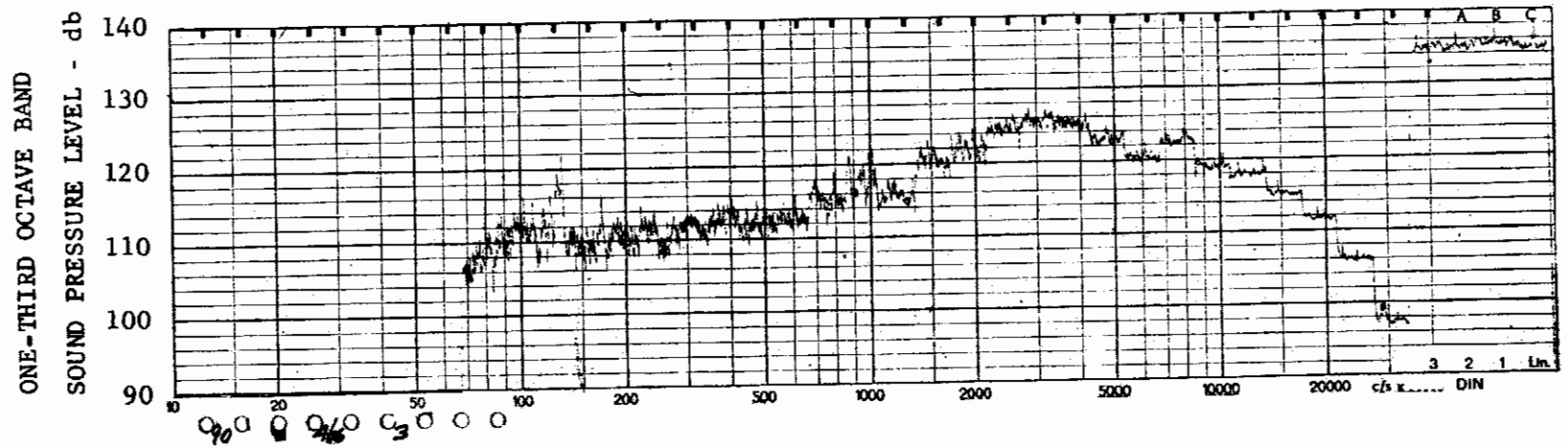

FIGURE 94 ONE-THIRD OCTAVE BAND SPECTRUM MODEL: AXISYM

CHANNEL: 3 MACH NO.: 2.5 α: 0 ϕ: 0 Re_∞/FT.: 1.0×10^6 AEDC GROUP NO.: 4/16

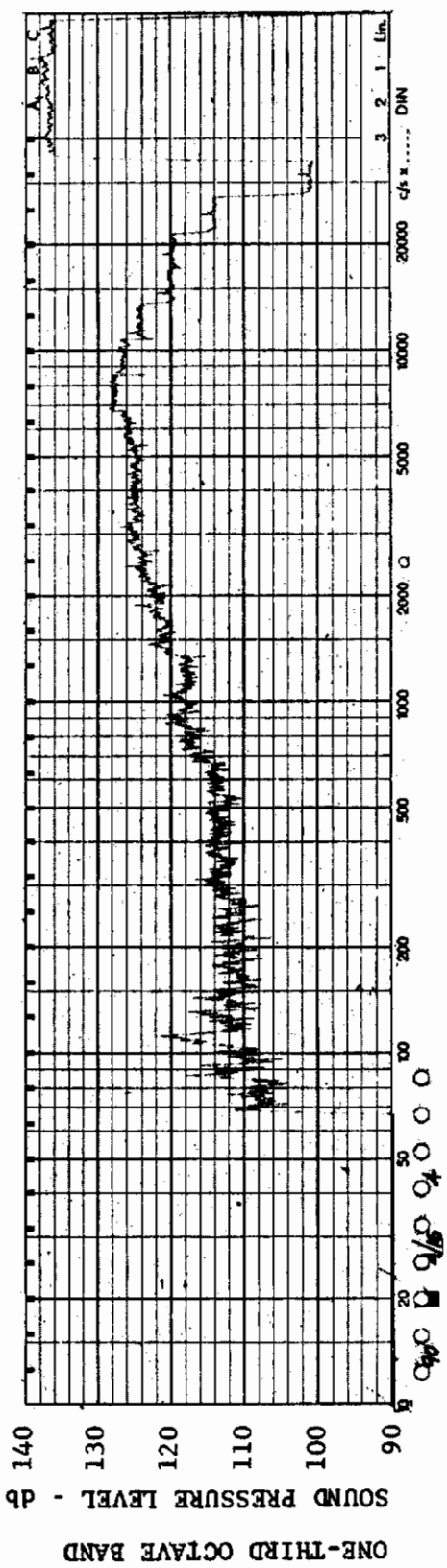

FIGURE 95 ONE-THIRD OCTAVE BAND SPECTRUM MODEL: AXISYM

CHANNEL: 4 MACH NO.: 2.5 α: 0 ϕ: 0 Re_∞/FT.: 1.0×10^6 AEDC GROUP NO.: 4/16

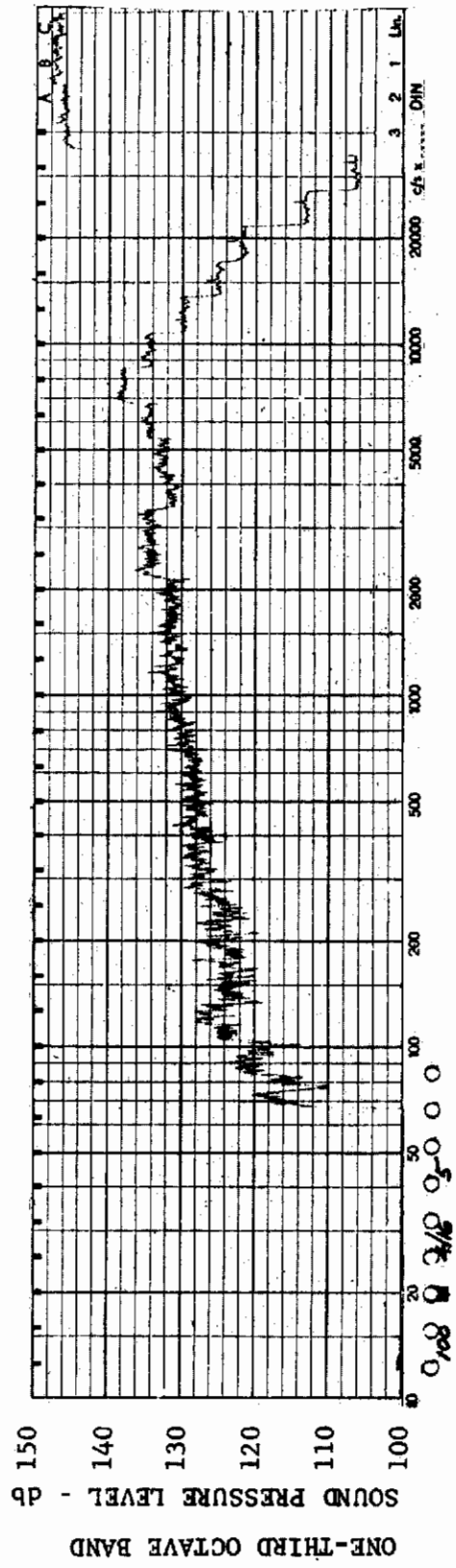

FIGURE 96 ONE-THIRD OCTAVE BAND SPECTRUM MODEL: AXISYM

CHANNEL: 5 MACH NO.: 2.5 α: 0 ϕ: 0 Re_∞/FT.: 1.0×10^6 AEDC GROUP NO.: 4/16

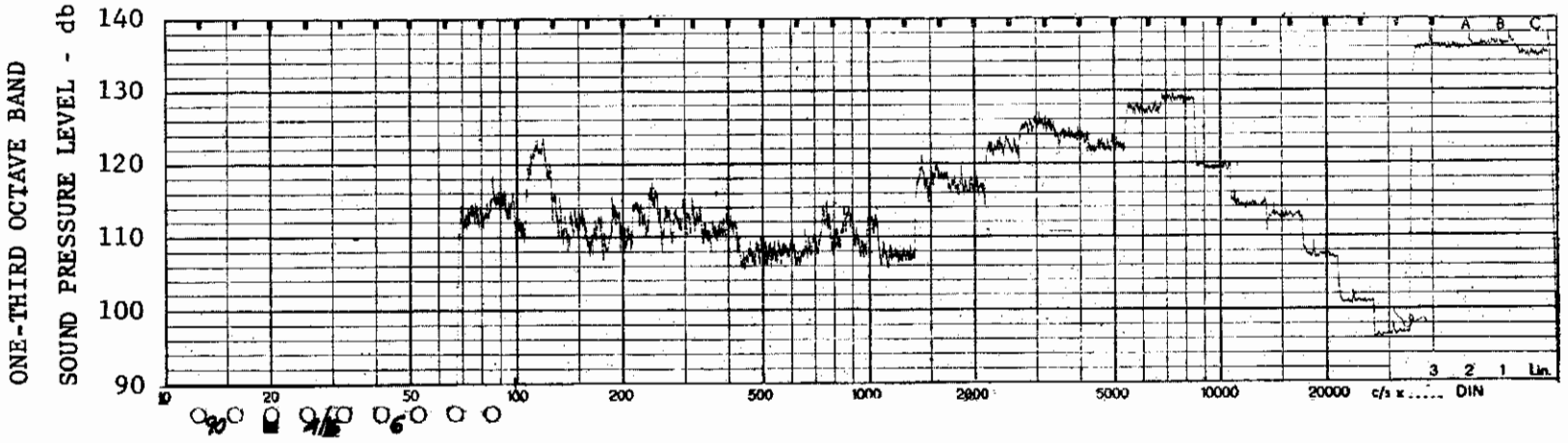

FIGURE 97 ONE-THIRD OCTAVE BAND SPECTRUM MODEL: AXISYM

CHANNEL: 6 MACH NO.: 2.5 α: 0 ϕ: 0 Re_∞/FT.: 1.0×10^6 AEDC GROUP NO.: 4/16

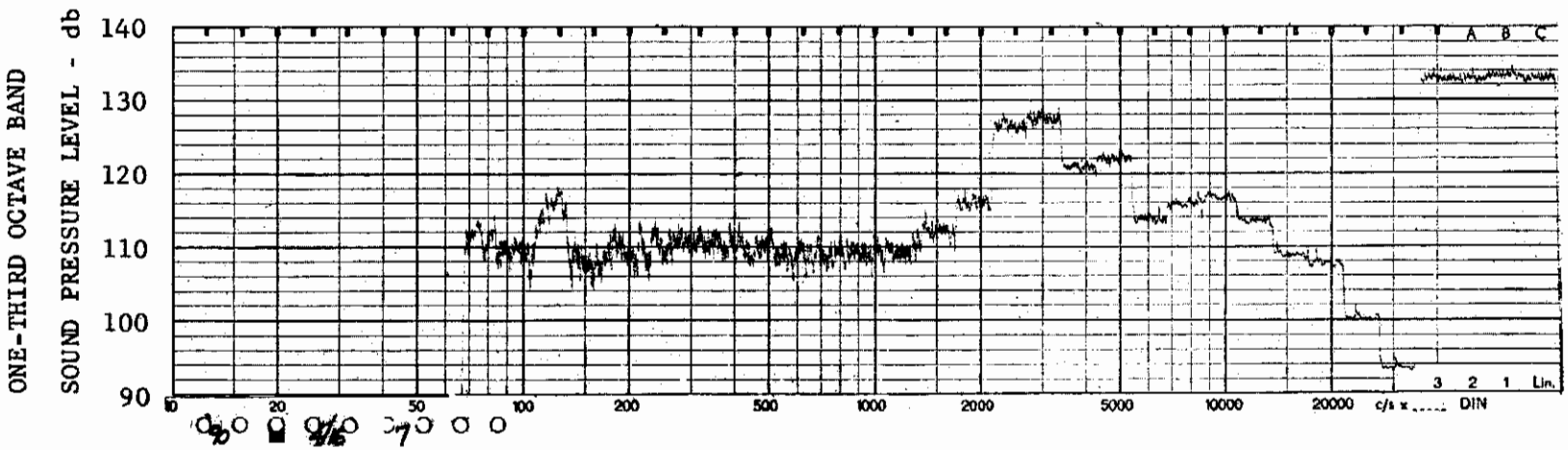

FIGURE 98 ONE-THIRD OCTAVE BAND SPECTRUM MODEL: AXISYM

CHANNEL: 7 MACH NO.: 2.5 α: 0 ϕ: 0 Re_∞/FT.: 1.0×10^6 AEDC GROUP NO.: 4/16

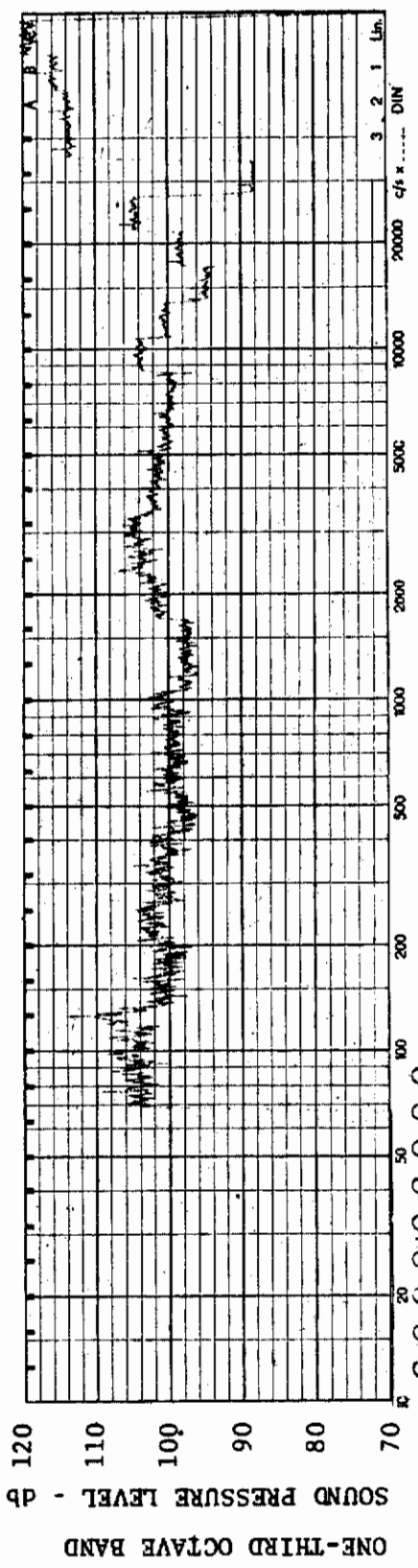

FIGURE 99 ONE-THIRD OCTAVE BAND SPECTRUM MODEL: AXISYM

CHANNEL: 1 MACH NO.: 2.5 α: 0 ϕ: -90° Re_∞/FT.: 1.0×10^6 AEDC GROUP NO.: 4/17

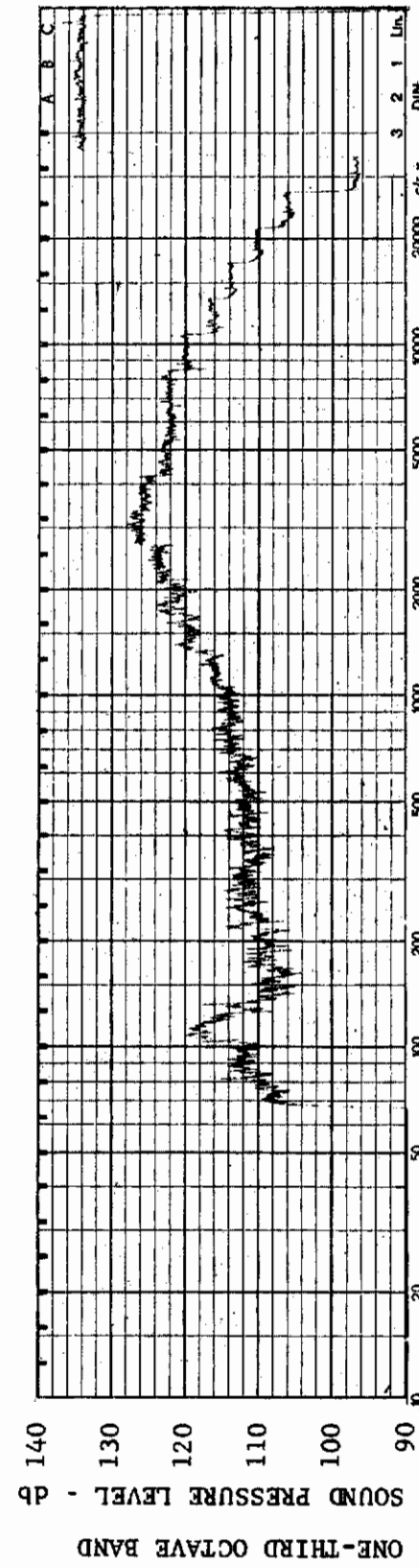

FIGURE 100 ONE-THIRD OCTAVE BAND SPECTRUM MODEL: AXISYM

CHANNEL: 2 MACH NO.: 2.5 α: 0 ϕ: -90° Re_∞/FT.: 1.0×10^6 AEDC GROUP NO.: 4/17

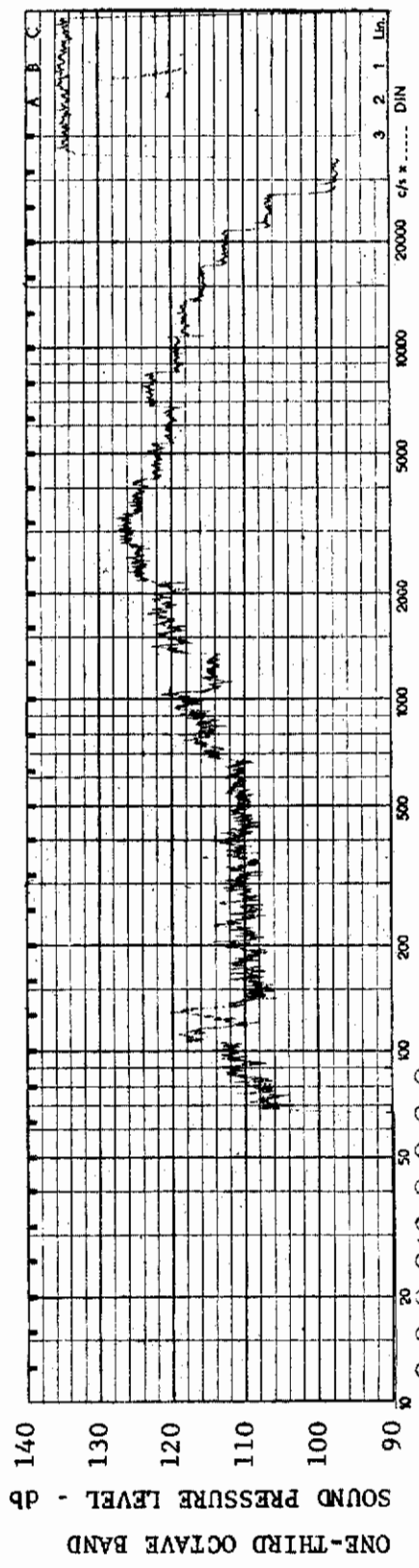

FIGURE 101 ONE-THIRD OCTAVE BAND SPECTRUM MODEL: AXISYM

CHANNEL: 3 MACH NO.: 2.5 α: 0 ϕ: -90° Re_∞/FT.: 1.0×10^6 AEDC GROUP NO.: 4/17

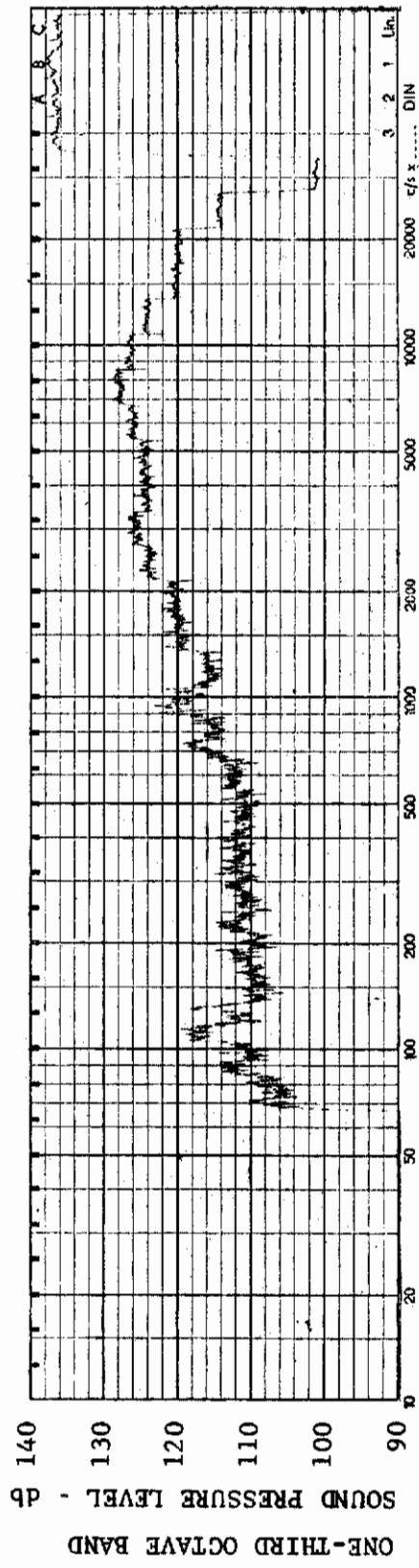

FIGURE 102 ONE-THIRD OCTAVE BAND SPECTRUM MODEL: AXISYM

CHANNEL: 4 MACH NO.: 2.5 α: 0 ϕ: -90° Re_∞/FT.: 1.0×10^6 AEDC GROUP NO.: 4/17

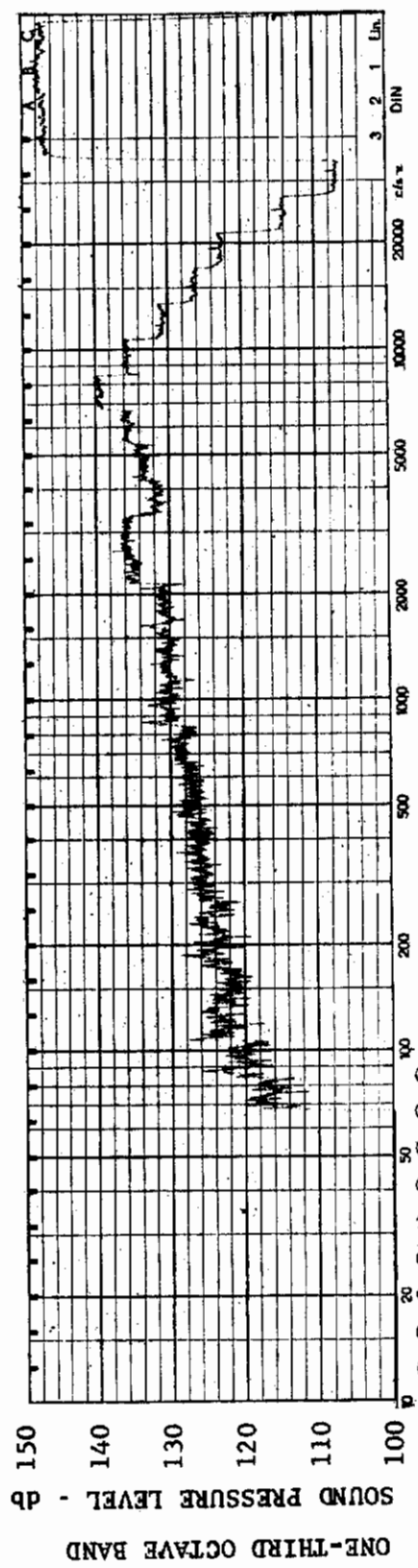

FIGURE 103 ONE-THIRD OCTAVE BAND SPECTRUM MODEL: AXISYM

CHANNEL: 5 MACH NO.: 2.5 α: 0 ϕ: -90° Re_∞ /FT.: 1.0×10^6 AEDC GROUP NO.: 4/17

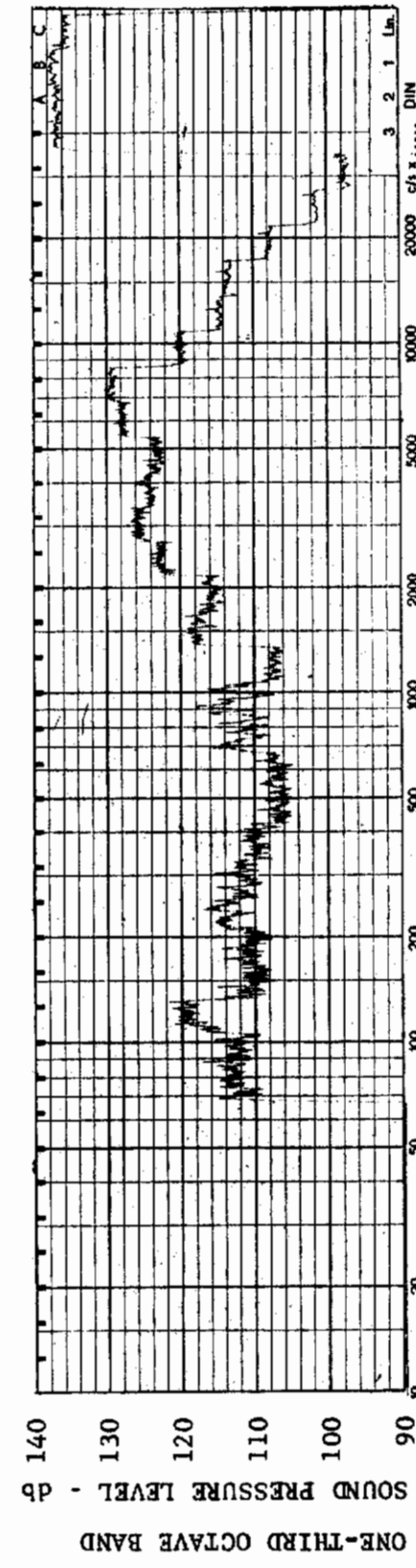

FIGURE 104 ONE-THIRD OCTAVE BAND SPECTRUM MODEL: AXISYM

CHANNEL: 6 MACH NO.: 2.5 α: 0 ϕ: -90° Re_∞ /FT.: 1.0×10^6 AEDC GROUP NO.: 4/17

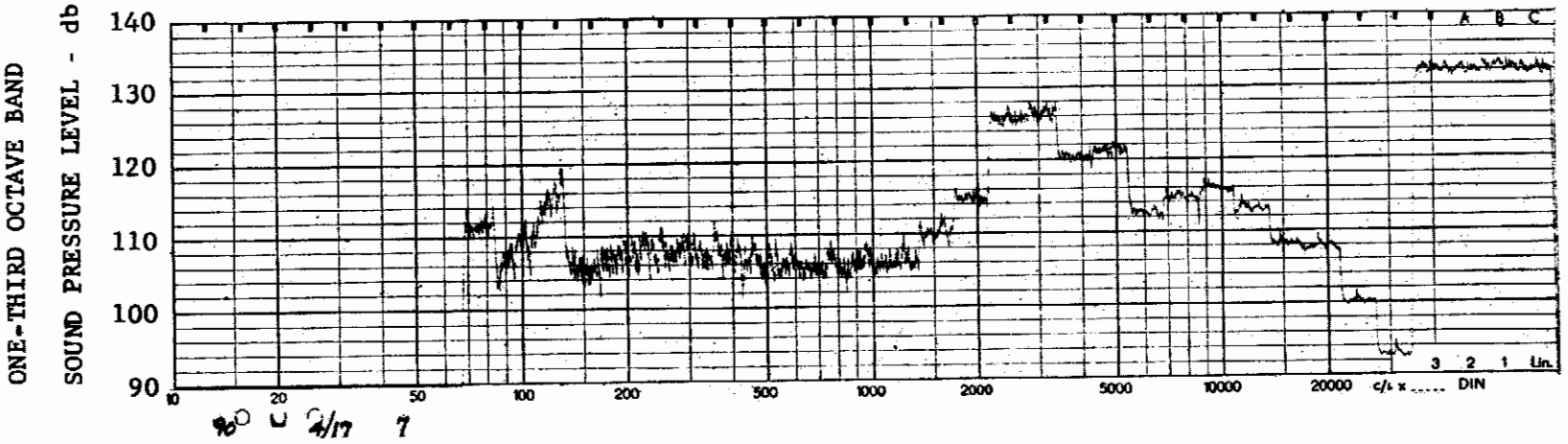

FIGURE 105 ONE-THIRD OCTAVE BAND SPECTRUM MODEL: AXISYM

CHANNEL: 7 MACH NO.: 2.5 α: 0 ϕ: -90° Re_∞/FT.: 1.0×10^6 AEDC GROUP NO.: 4/17

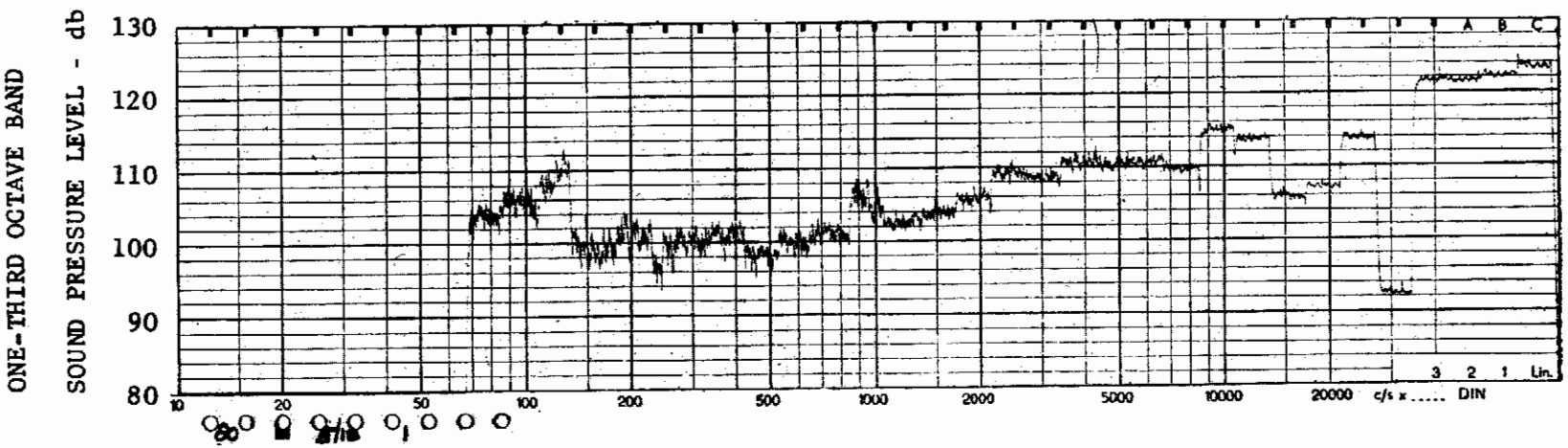

FIGURE 106 ONE-THIRD OCTAVE BAND SPECTRUM MODEL: AXISYM

CHANNEL: 1 MACH NO.: 3.5 α: 0 ϕ: 0 Re_∞/FT.: 6.0×10^6 AEDC GROUP NO.: 5/18

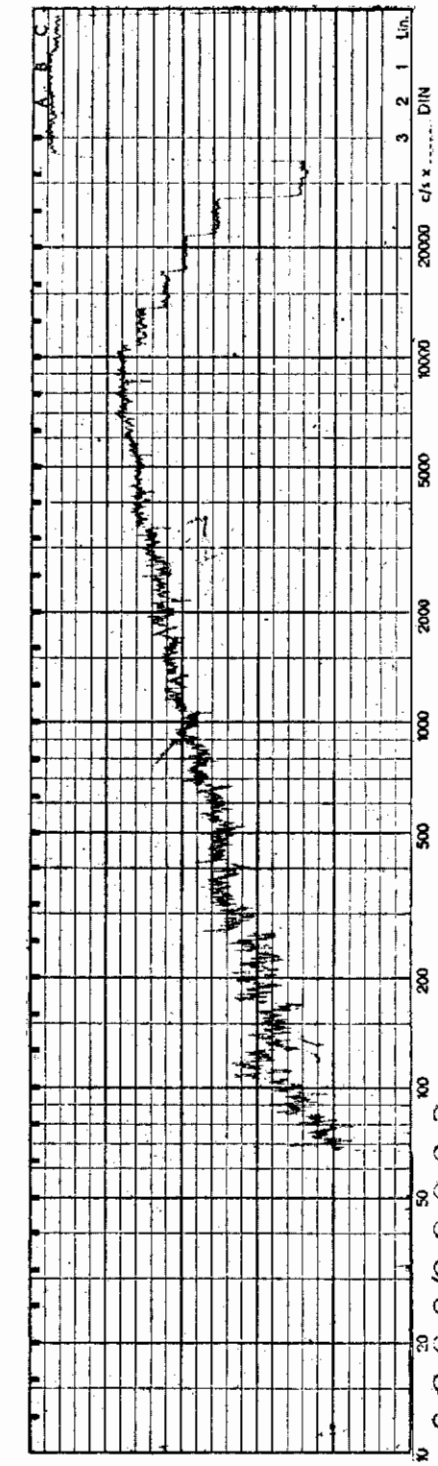

FIGURE 107 ONE-THIRD OCTAVE BAND SPECTRUM MODEL: AXISYM

CHANNEL: 2 MACH NO.: 3.5 α: 0 ϕ: 0 Re_∞/FT.: 6.0×10^6 AEDC GROUP NO.: 5/18

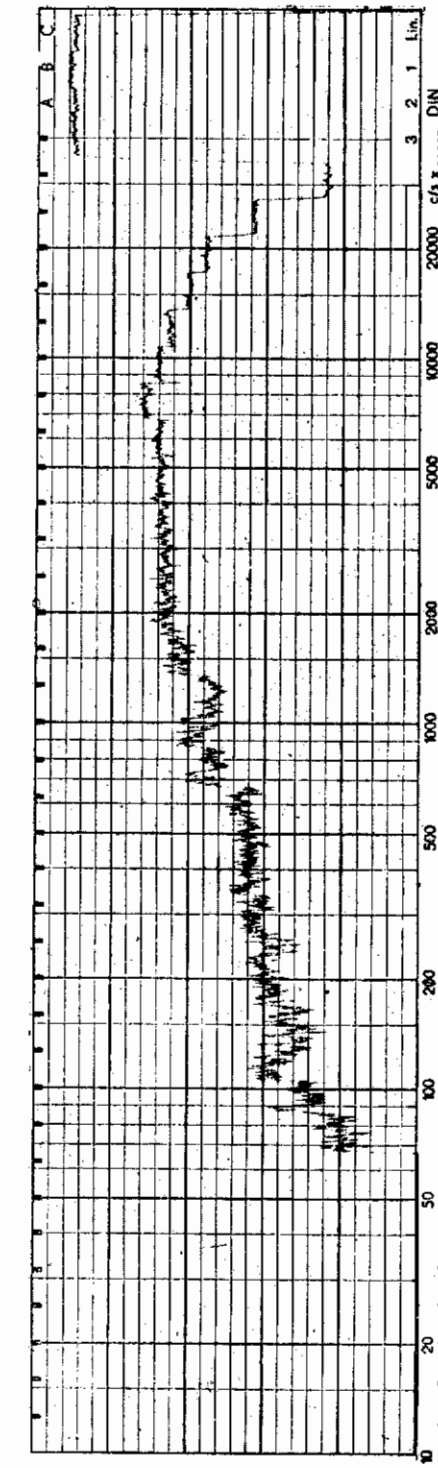

FIGURE 108 ONE-THIRD OCTAVE BAND SPECTRUM MODEL: AXISYM

CHANNEL: 3 MACH NO.: 3.5 α: 0 ϕ: 0 Re_∞/FT.: 6.0×10^6 AEDC GROUP NO.: 5/18

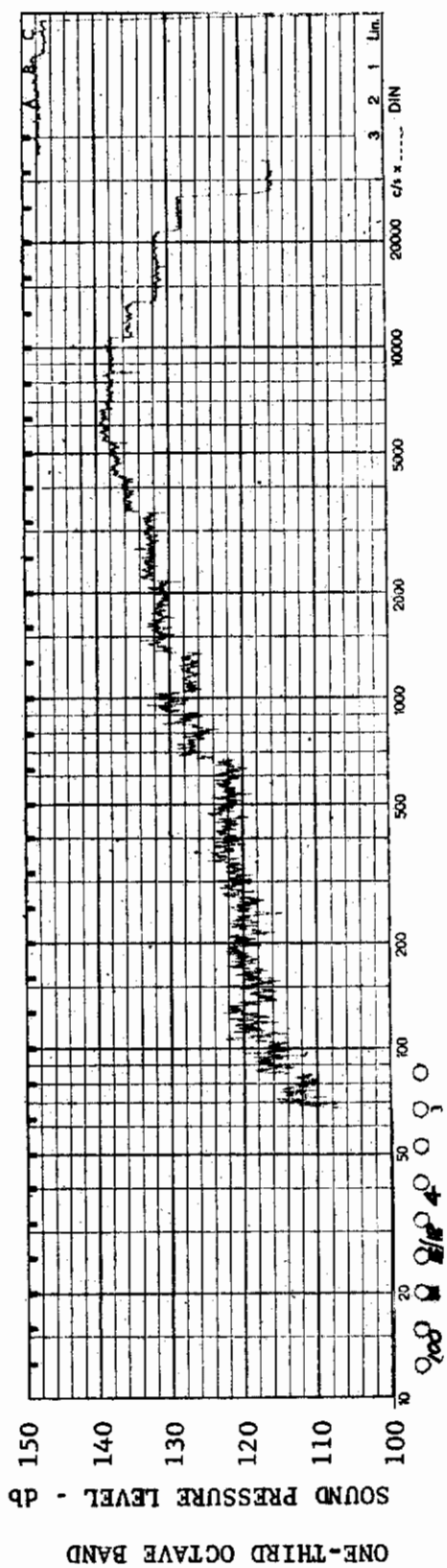

FIGURE 109 ONE-THIRD OCTAVE BAND SPECTRUM MODEL: AXISYM

CHANNEL: 4 MACH NO.: 3.5 α: 0 ϕ: 0 Re_∞/FT.: 6.0×10^6 AEDC GROUP NO.: 5/18

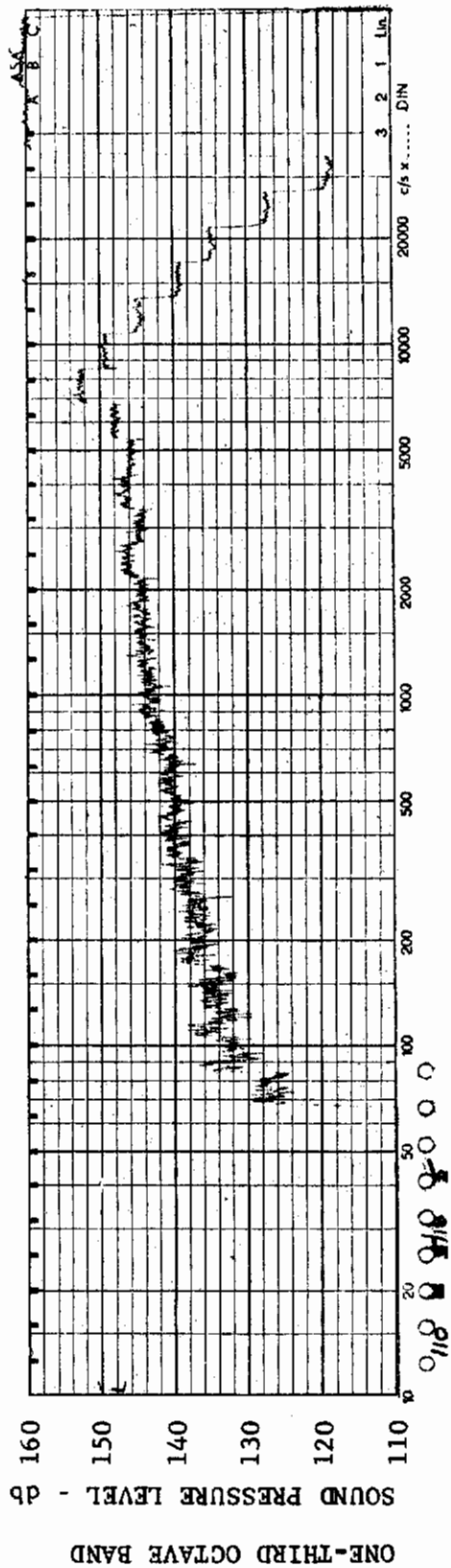

FIGURE 110 ONE-THIRD OCTAVE BAND SPECTRUM MODEL: AXISYM

CHANNEL: 5 MACH NO.: 3.5 α: 0 ϕ: 0 Re_∞/FT.: 6.0×10^6 AEDC GROUP NO.: 5/18

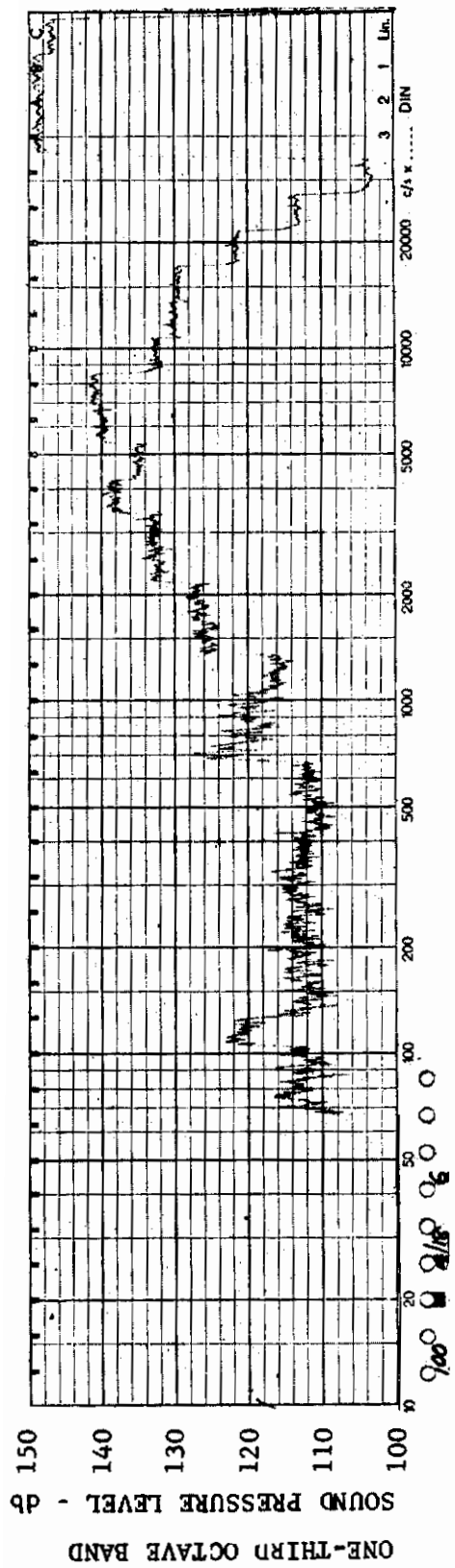

FIGURE 111 ONE-THIRD OCTAVE BAND SPECTRUM MODEL: AXISYM

CHANNEL: 6 MACH NO.: 3.5 α: 0 ϕ: 0 Re_∞/FT.: 6.0×10^6 AEDC GROUP NO.: 5/18

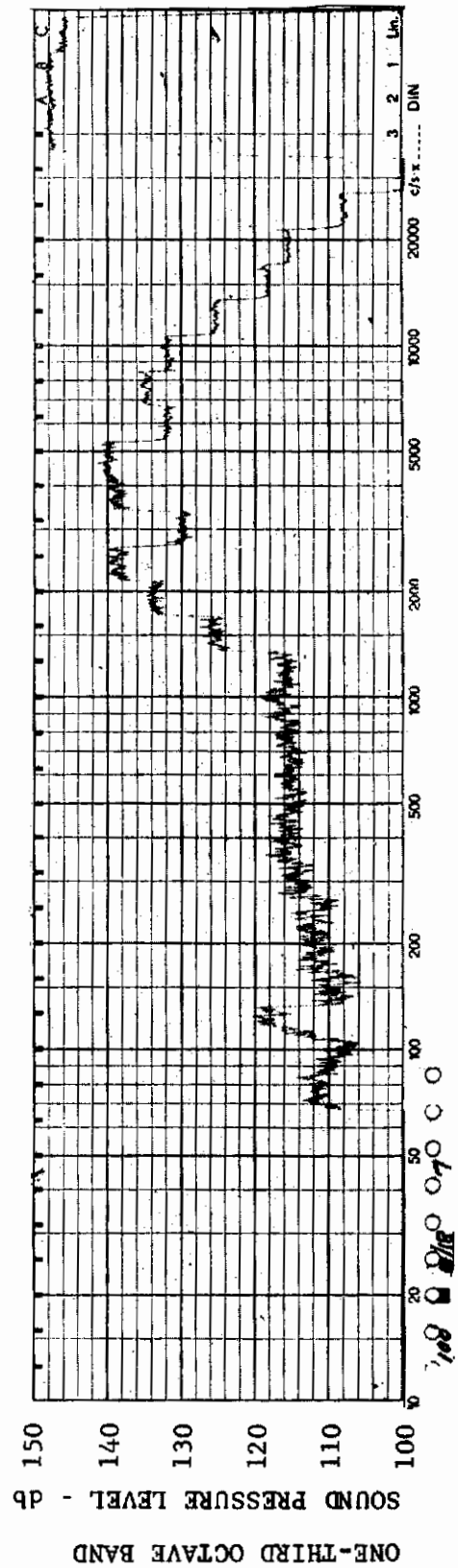

FIGURE 112 ONE-THIRD OCTAVE BAND SPECTRUM MODEL: AXISYM

CHANNEL: 7 MACH NO.: 3.5 α: 0 ϕ: 0 Re_∞/FT.: 6.0×10^6 AEDC GROUP NO.: 5/18

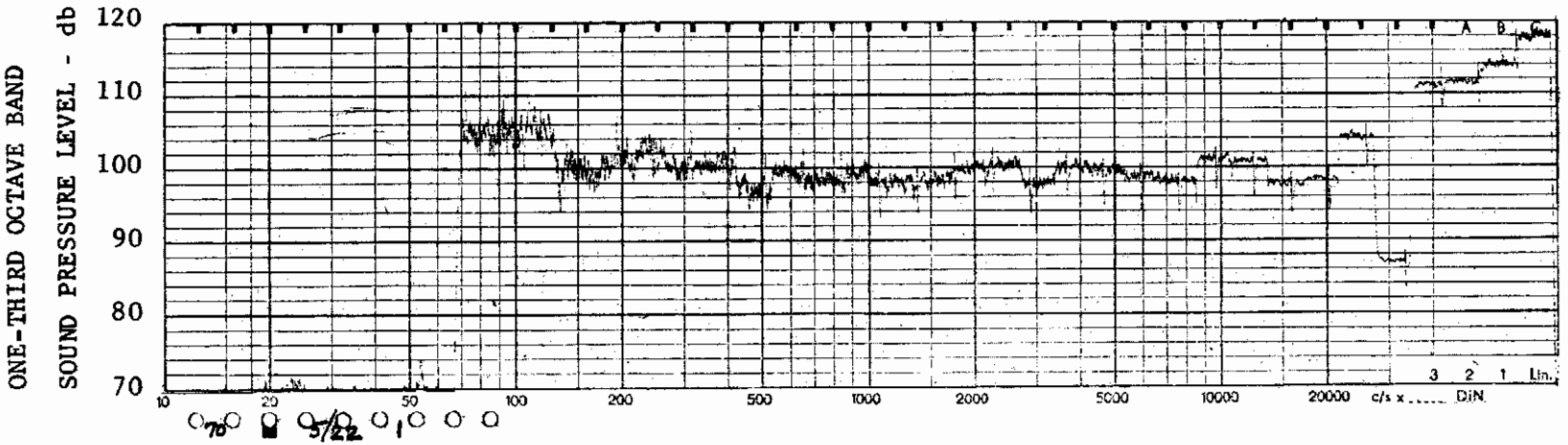

FIGURE 113 ONE-THIRD OCTAVE BAND SPECTRUM MODEL: AXISYM

CHANNEL: 1 MACH NO.: 3.5 α: 0 ϕ: 0 Re_∞/FT.: 1.0×10^6 AEDC GROUP NO.: 5/22

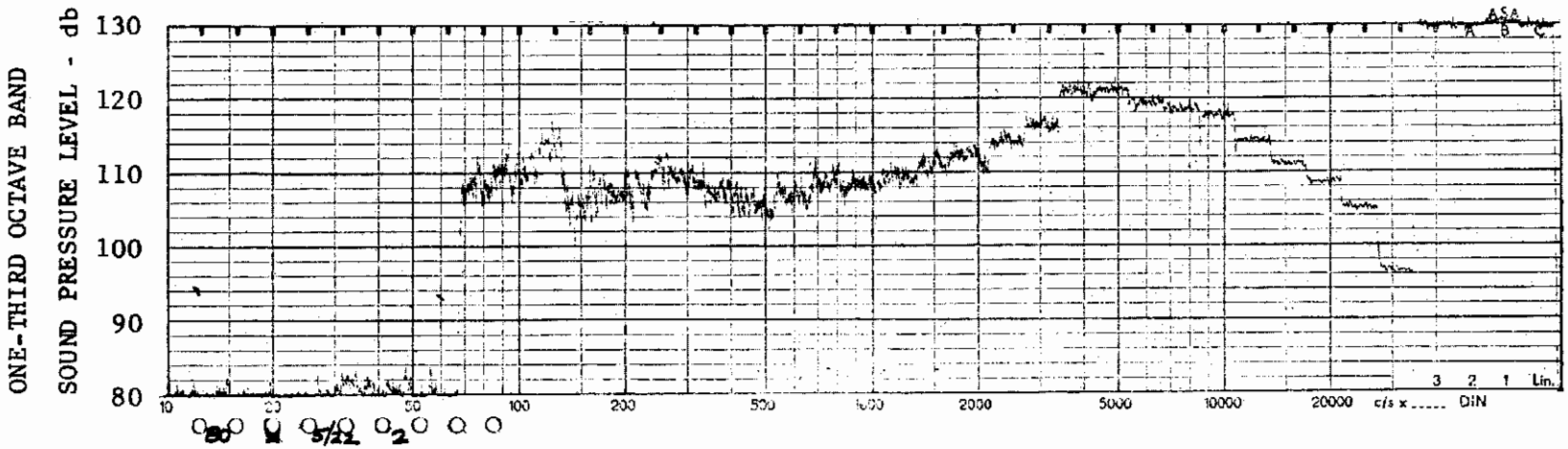

FIGURE 114 ONE-THIRD OCTAVE BAND SPECTRUM MODEL: AXISYM

CHANNEL: 2 MACH NO.: 3.5 α: 0 ϕ: 0 Re_∞/FT.: 1.0×10^6 AEDC GROUP NO.: 5/22

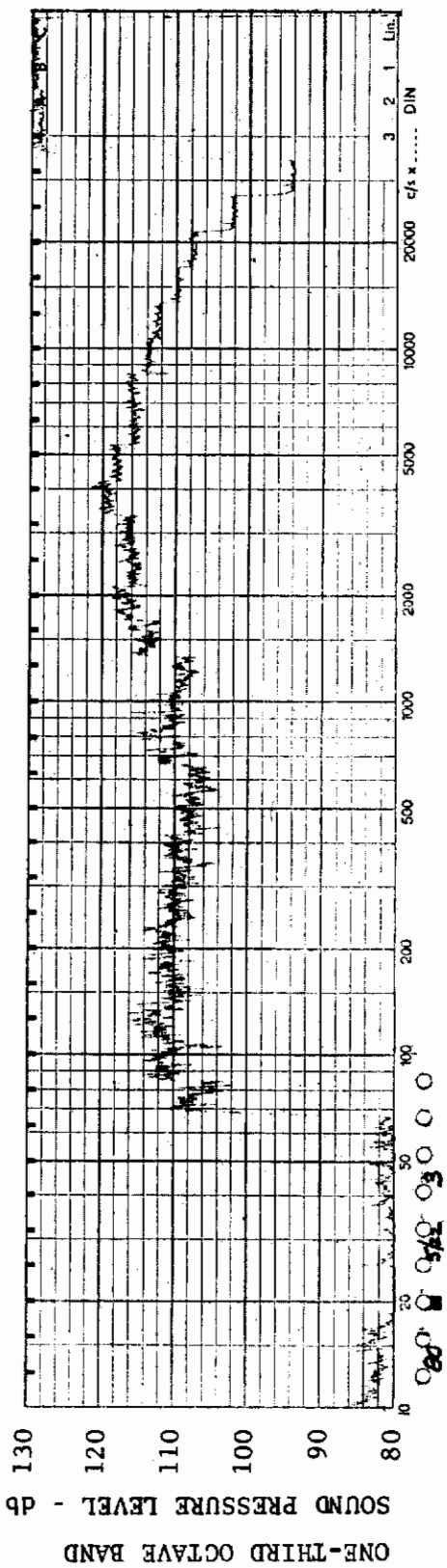

FIGURE 115 ONE-THIRD OCTAVE BAND SPECTRUM MODEL: AXISYM

CHANNEL: 3 MACH NO.: 3.5 α: 0 ϕ: 0 Re_∞/FT.: 1.0×10^6 AEDC GROUP NO.: 5/22

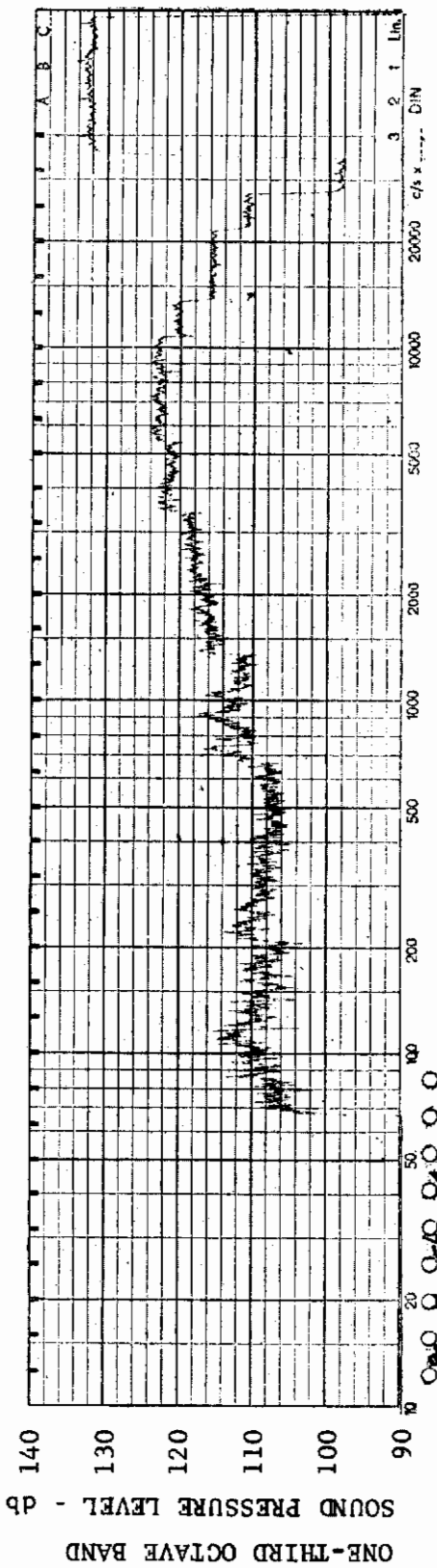

FIGURE 116 ONE-THIRD OCTAVE BAND SPECTRUM MODEL: AXISYM

CHANNEL: 4 MACH NO.: 3.5 α: 0 ϕ: 0 Re_∞/FT.: 1.0×10^6 AEDC GROUP NO.: 5/22

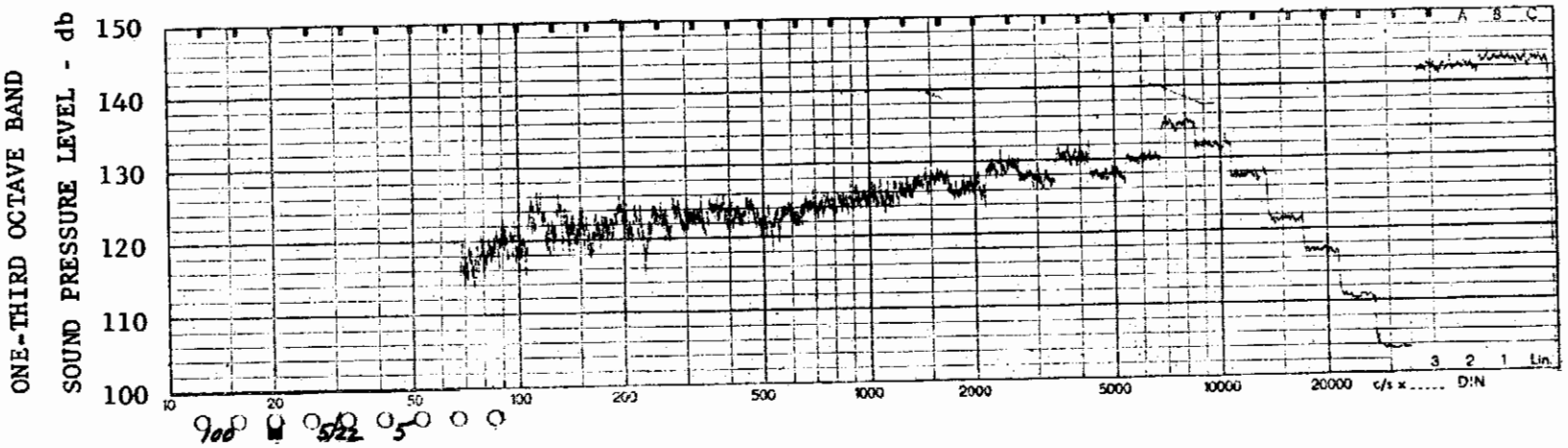

FIGURE 117 ONE-THIRD OCTAVE BAND SPECTRUM MODEL: AXISYM

CHANNEL: 5 MACH NO.: 3.5 α: 0 ϕ: 0 Re_∞/FT.: 1.0×10^6 AEDC GROUP NO.: 5/22

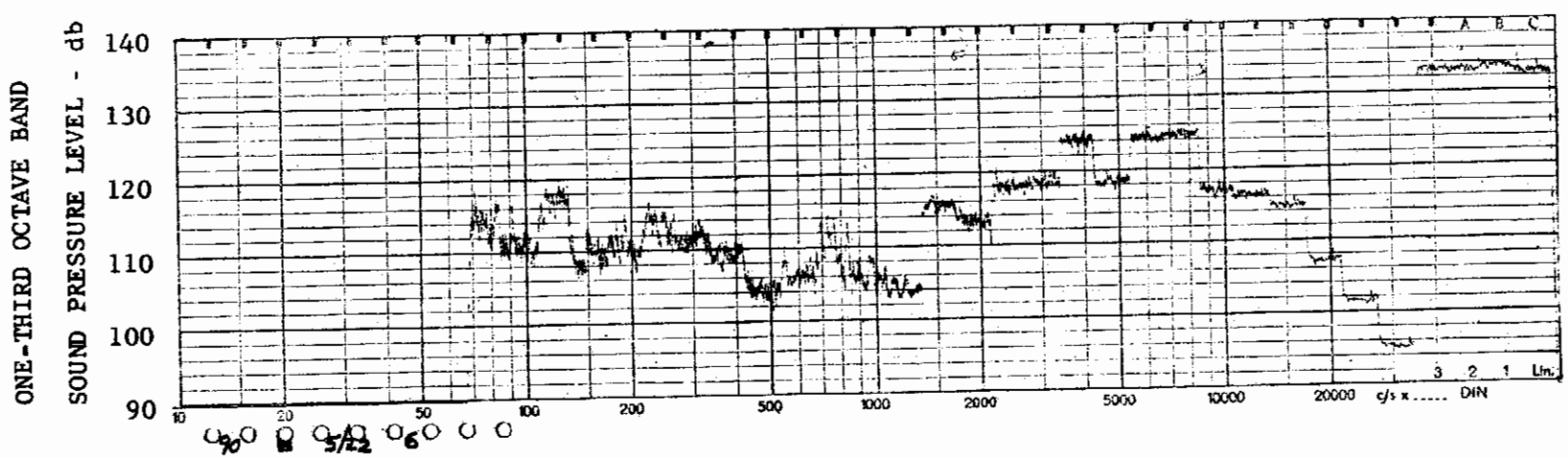

FIGURE 118 ONE-THIRD OCTAVE BAND SPECTRUM MODEL: AXISYM

CHANNEL: 6 MACH NO.: 3.5 α: 0 ϕ: 0 Re_∞/FT.: 1.0×10^6 AEDC GROUP NO.: 5/22

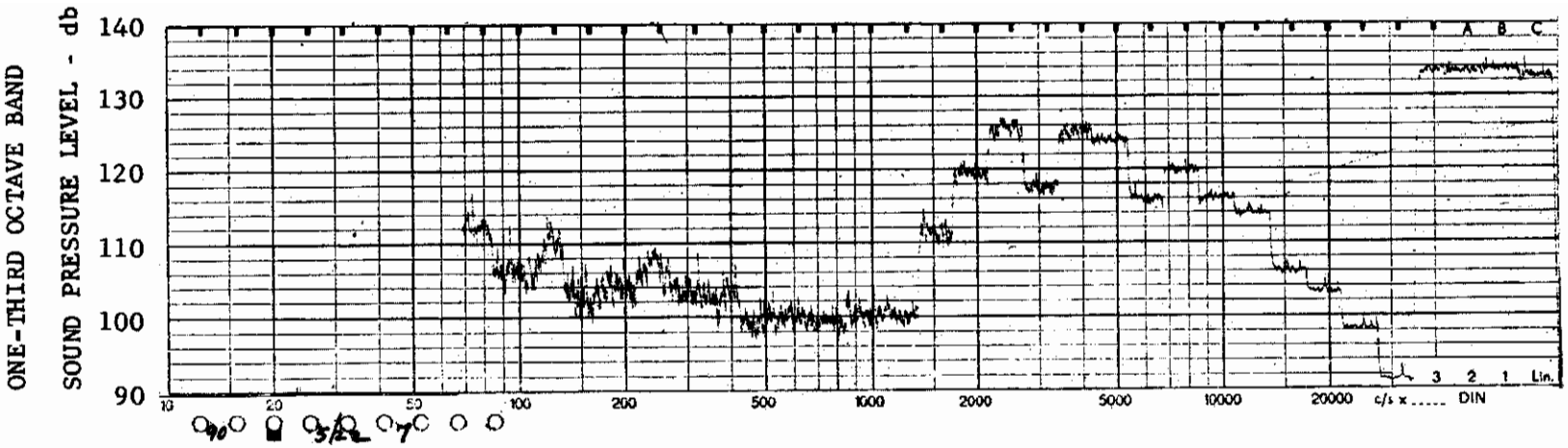

FIGURE 119 ONE-THIRD OCTAVE BAND SPECTRUM MODEL: AXISYM

CHANNEL: 7 MACH NO.: 3.5 α: 0 ϕ: 0 Re_∞/FT.: 1.0×10^6 AEDC GROUP NO.: 5/22

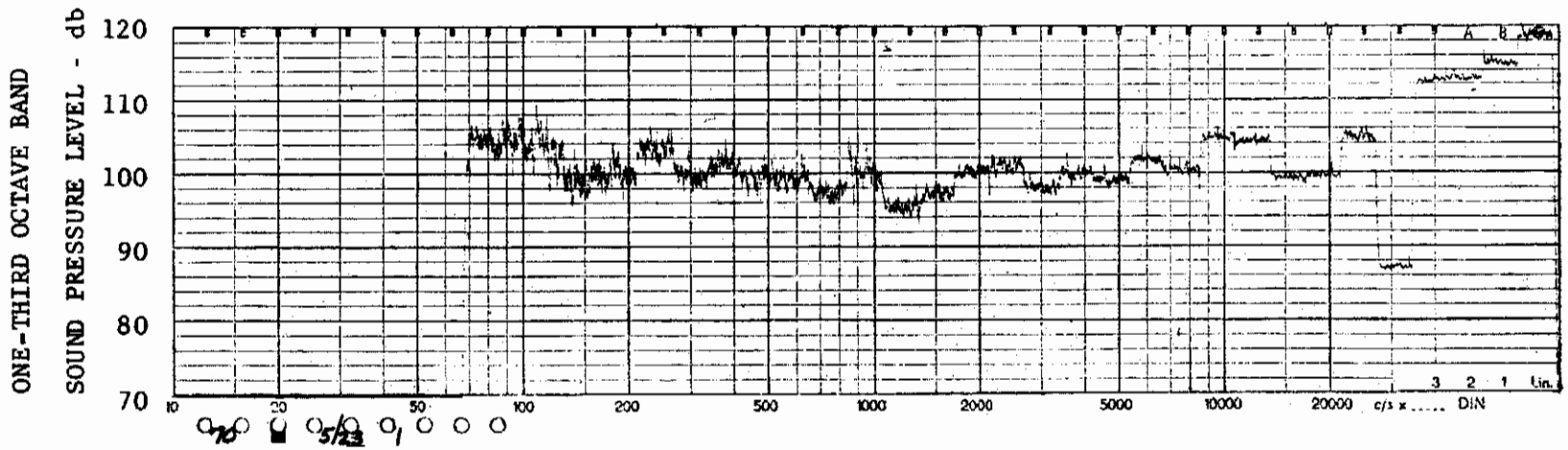

FIGURE 120 ONE-THIRD OCTAVE BAND SPECTRUM MODEL: AXISYM

CHANNEL: 1 MACH NO.: 3.5 α: 5° ϕ: 0 Re_∞/FT.: 1.0×10^6 AEDC GROUP NO.: 5/23

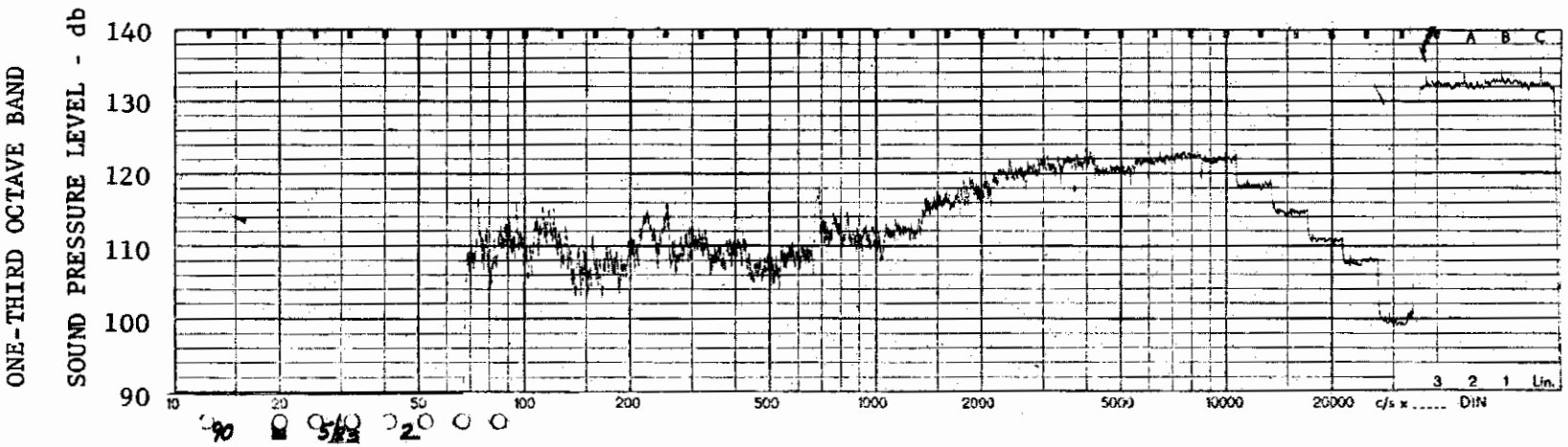

FIGURE 121 ONE-THIRD OCTAVE BAND SPECTRUM MODEL: AXISYM

CHANNEL: 2 MACH NO.: 3.5 α: 5° ϕ: 0 Re_∞/FT.: 1.0×10^6 AEDC GROUP NO.: 5/23

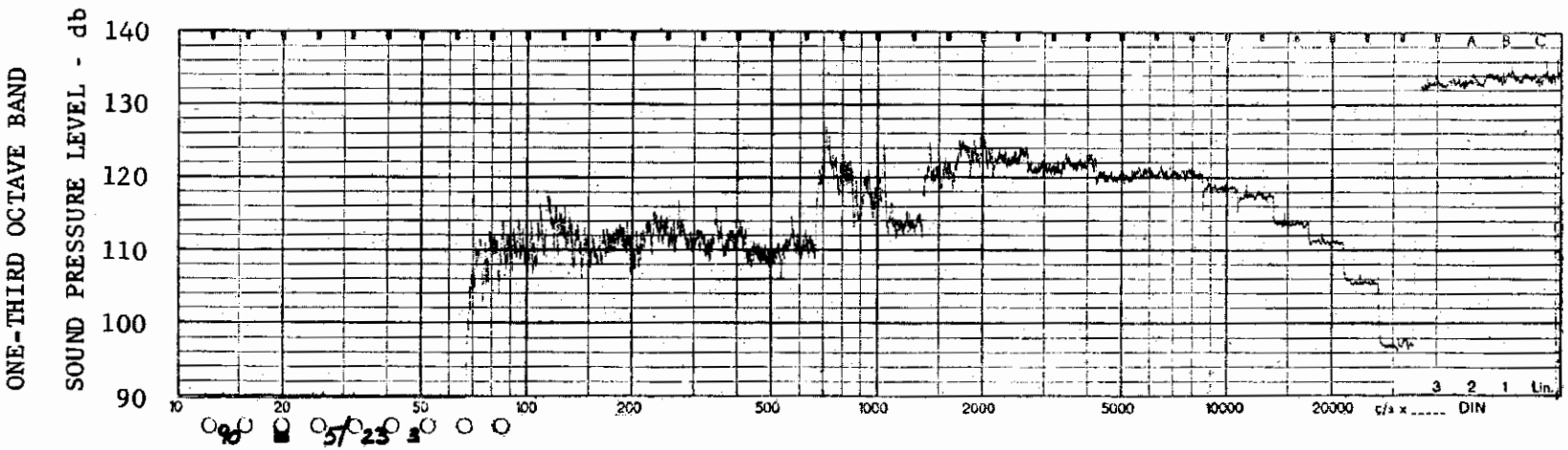

FIGURE 122 ONE-THIRD OCTAVE BAND SPECTRUM MODEL: AXISYM

CHANNEL: 3 MACH NO.: 3.5 α: 5° ϕ: 0 Re_∞/FT.: 1.0×10^6 AEDC GROUP NO.: 5/23

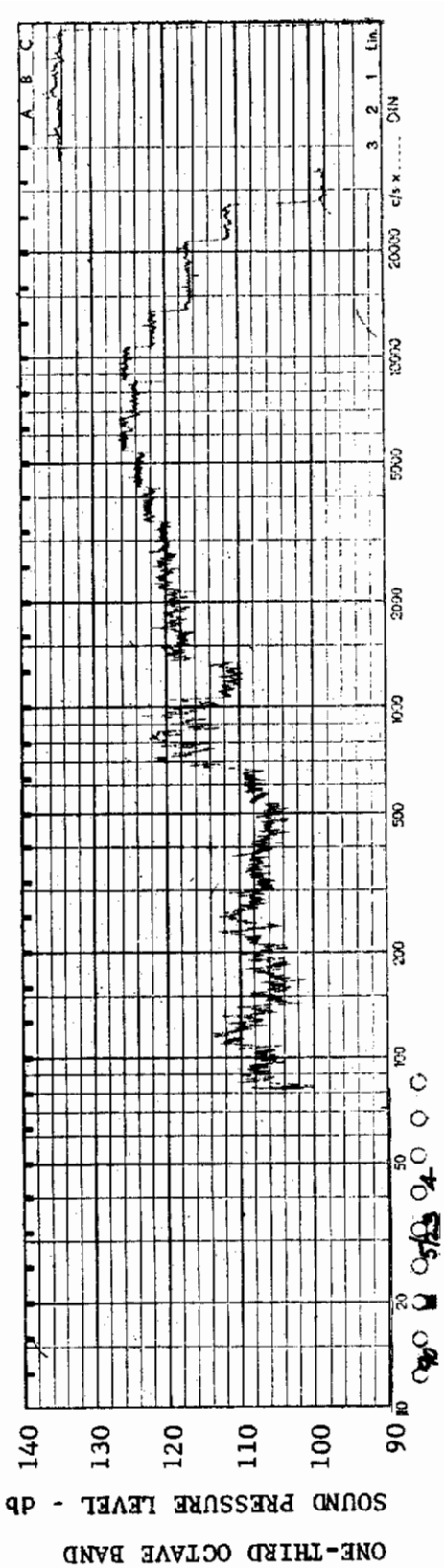

FIGURE 123 ONE-THIRD OCTAVE BAND SPECTRUM MODEL: AXISYM

CHANNEL: 4 MACH NO.: 3.5 α: 5° ϕ: 0 Re_∞/FT.: 1.0×10^6 AEDC GROUP NO.: 5/23

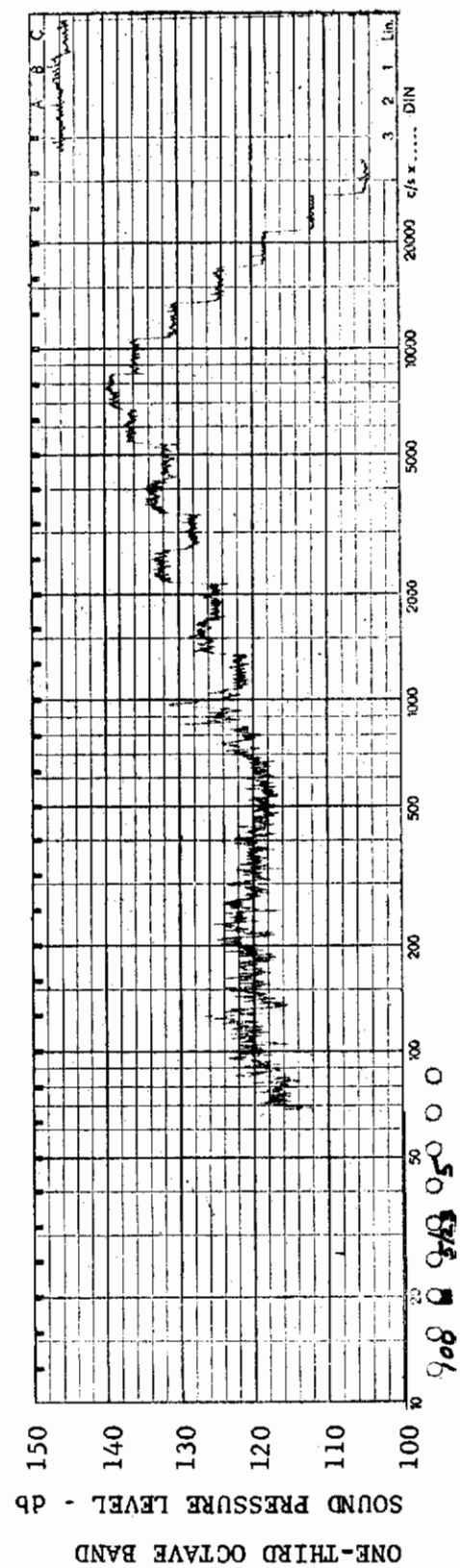

FIGURE 124 ONE-THIRD OCTAVE BAND SPECTRUM MODEL: AXISYM

CHANNEL: 5 MACH NO.: 3.5 α: 5° ϕ: 0 Re_∞/FT.: 1.0×10^6 AEDC GROUP NO.: 5/23

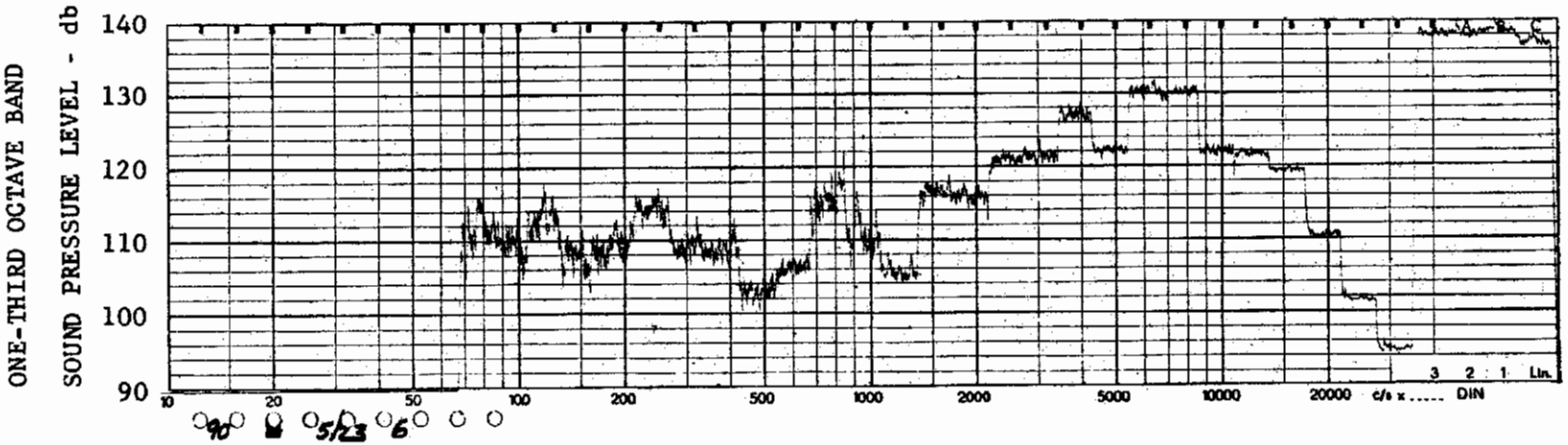

FIGURE 125 ONE-THIRD OCTAVE BAND SPECTRUM MODEL: AXISYM

CHANNEL: 6 MACH NO.: 3.5 α: 5° ϕ: 0 Re_∞/FT.: 1.0×10^6 AEDC GROUP NO.: 5/23

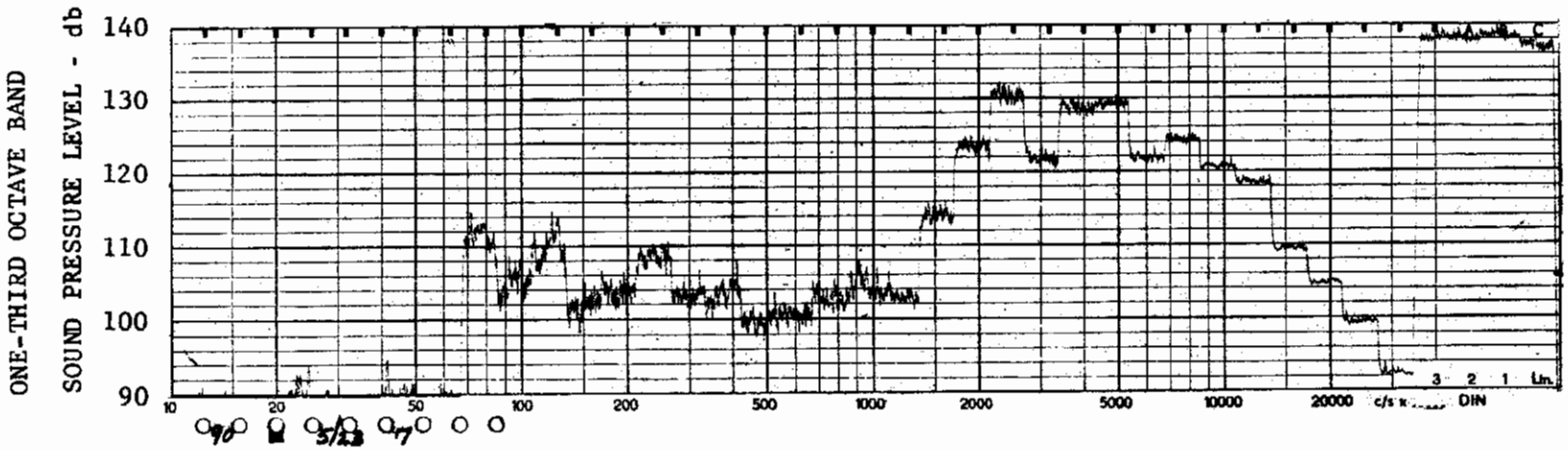

FIGURE 126 ONE-THIRD OCTAVE BAND SPECTRUM MODEL: AXISYM

CHANNEL: 7 MACH NO.: 3.5 α: 5° ϕ: 0 Re_∞/FT.: 1.0×10^6 AEDC GROUP NO.: 5/23

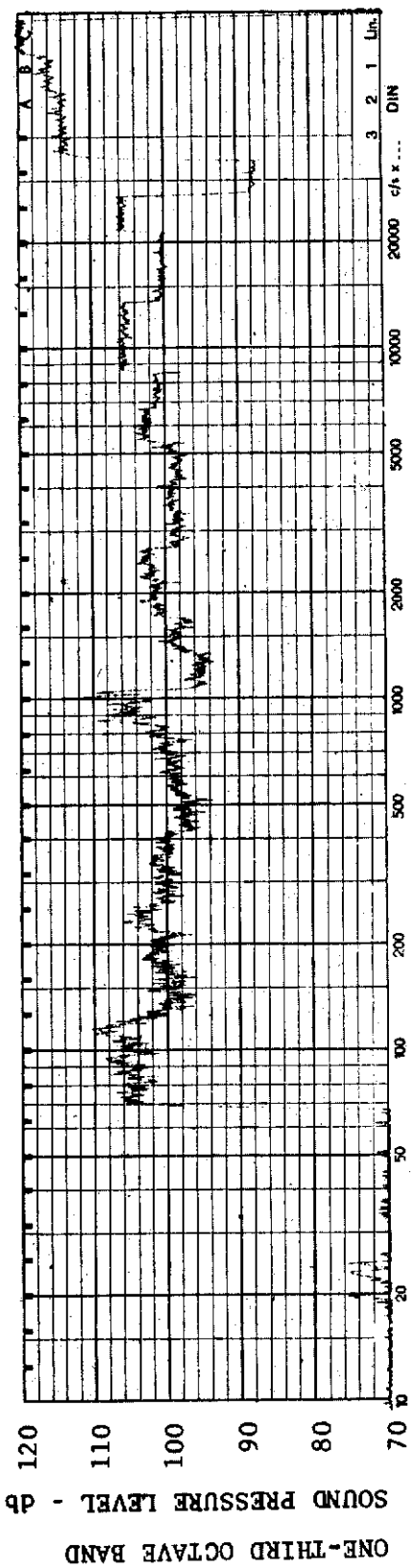

FIGURE 127 ONE-THIRD OCTAVE BAND SPECTRUM

MODEL: AXISYM

CHANNEL: 1 MACH NO.: 3.5 α: 15° ϕ: 0 Re_∞/FT.: 1.0×10^6 AEDC GROUP NO.: 5/24

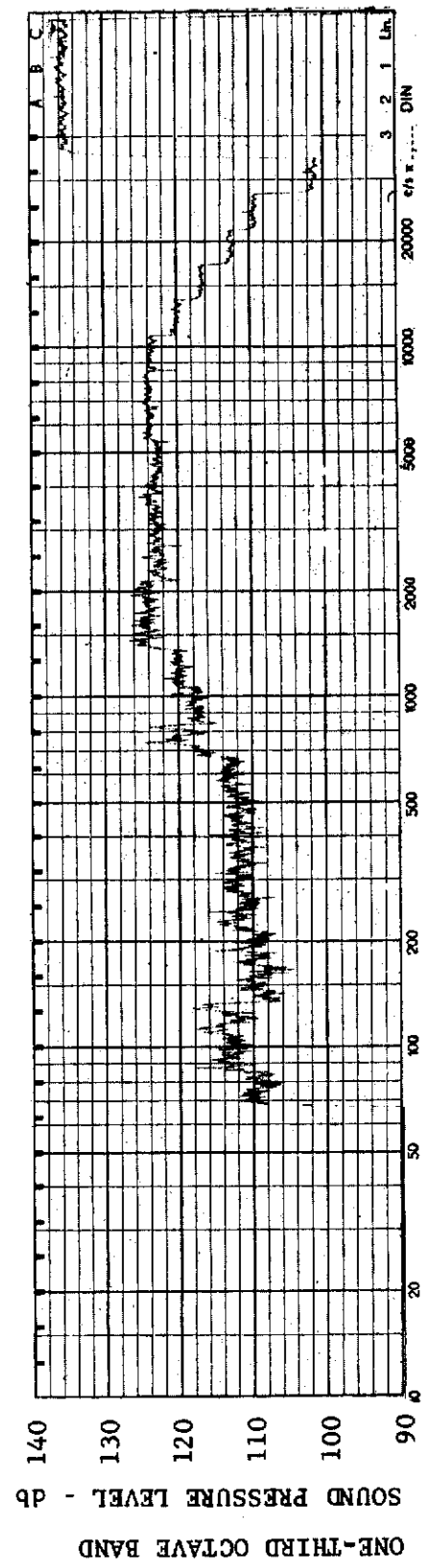

FIGURE 128 ONE-THIRD OCTAVE BAND SPECTRUM

MODEL: AXISYM

CHANNEL: 2 MACH NO.: 3.5 α: 15° ϕ: 0 Re_∞/FT.: 1.0×10^6 AEDC GROUP NO.: 5/24

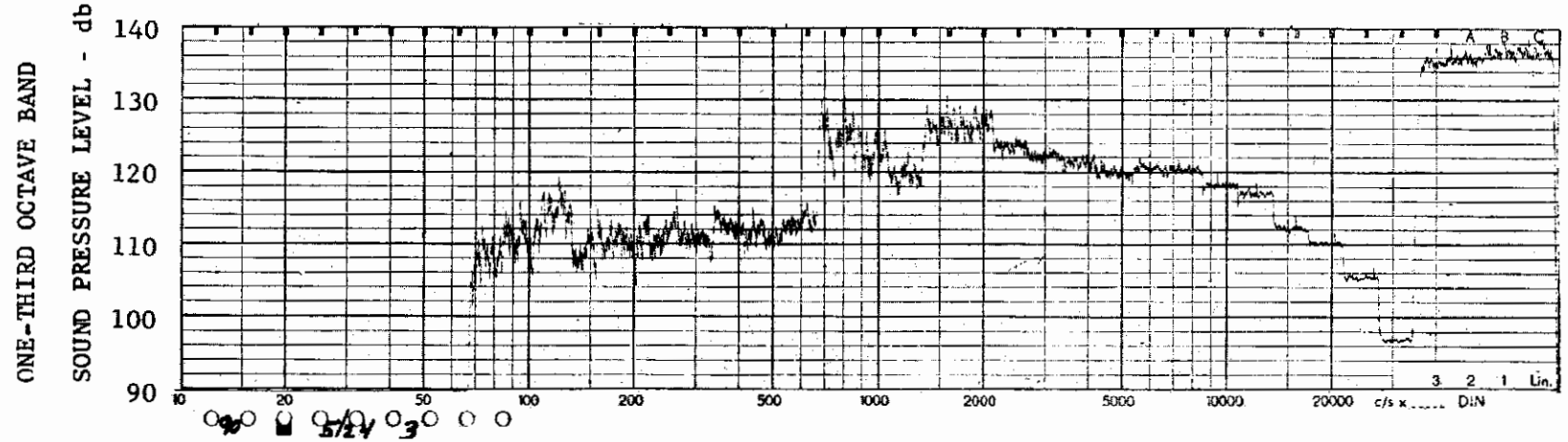

FIGURE 129 ONE-THIRD OCTAVE BAND SPECTRUM MODEL: AXISYM

CHANNEL: 3 MACH NO.: 3.5 α: 15° ϕ: 0 Re_∞/FT.: 1.0×10^6 AEDC GROUP NO.: 5/24

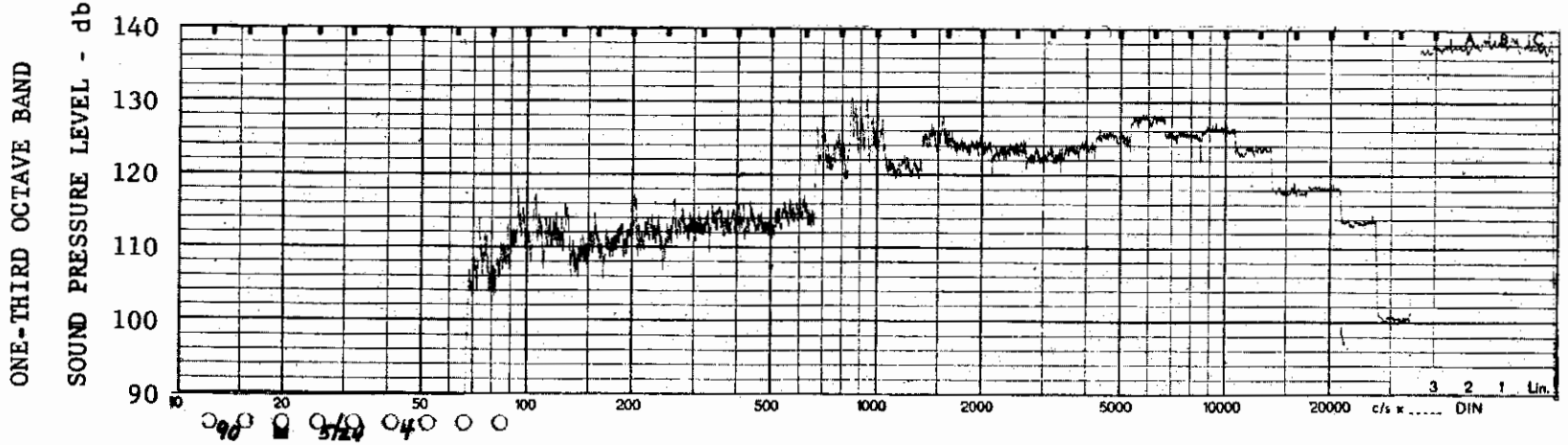

FIGURE 130 ONE-THIRD OCTAVE BAND SPECTRUM MODEL: AXISYM

CHANNEL: 4 MACH NO.: 3.5 α: 15° ϕ: 0 Re_∞/FT.: 1.0×10^6 AEDC GROUP NO.: 5/24

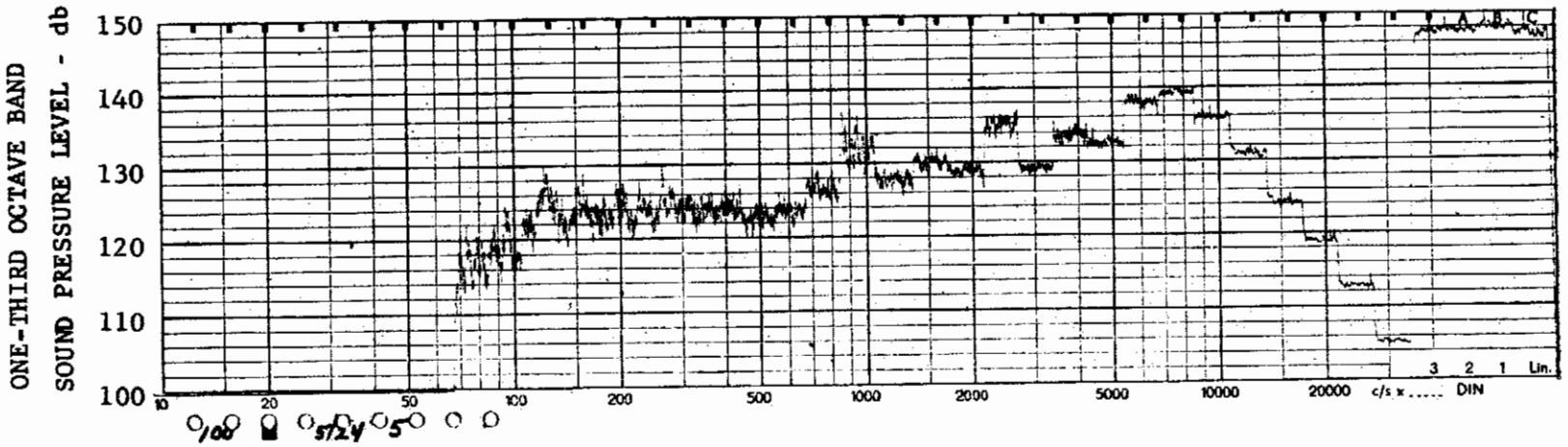

FIGURE 131 ONE-THIRD OCTAVE BAND SPECTRUM MODEL: AXISYM

CHANNEL: 5 MACH NO.: 3.5 α: 15° ϕ: 0 Re_∞/FT.: 1.0×10^6 AEDC GROUP NO.: 5/24

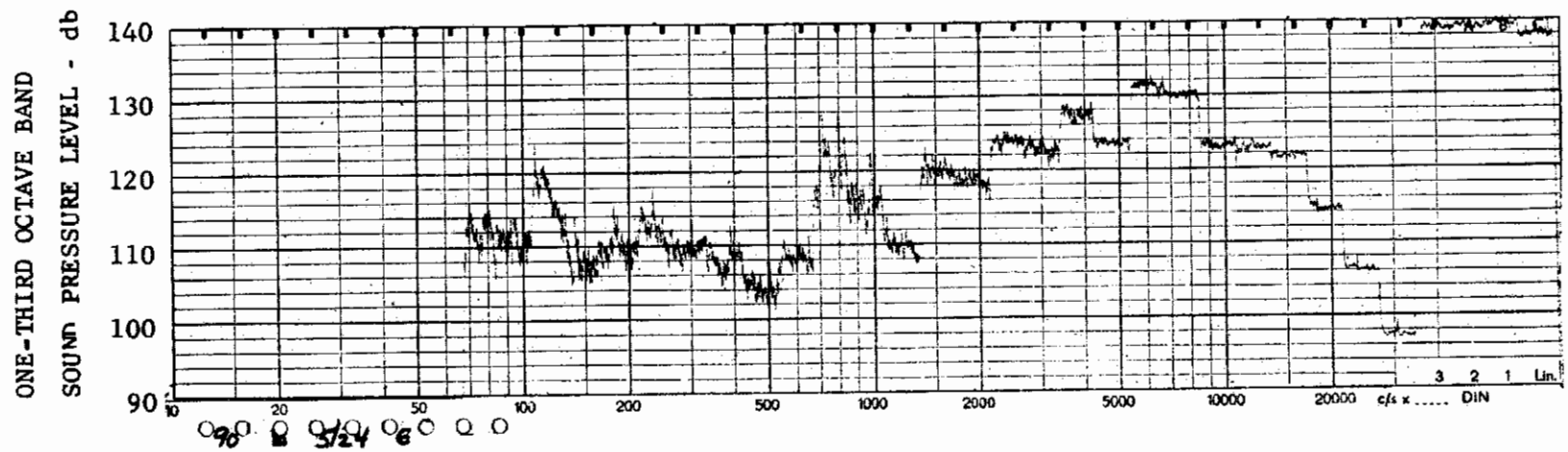

FIGURE 132 ONE-THIRD OCTAVE BAND SPECTRUM MODEL: AXISYM

CHANNEL: 6 MACH NO.: 3.5 α: 15° ϕ: 0 Re_∞/FT.: 1.0×10^6 AEDC GROUP NO.: 5/24

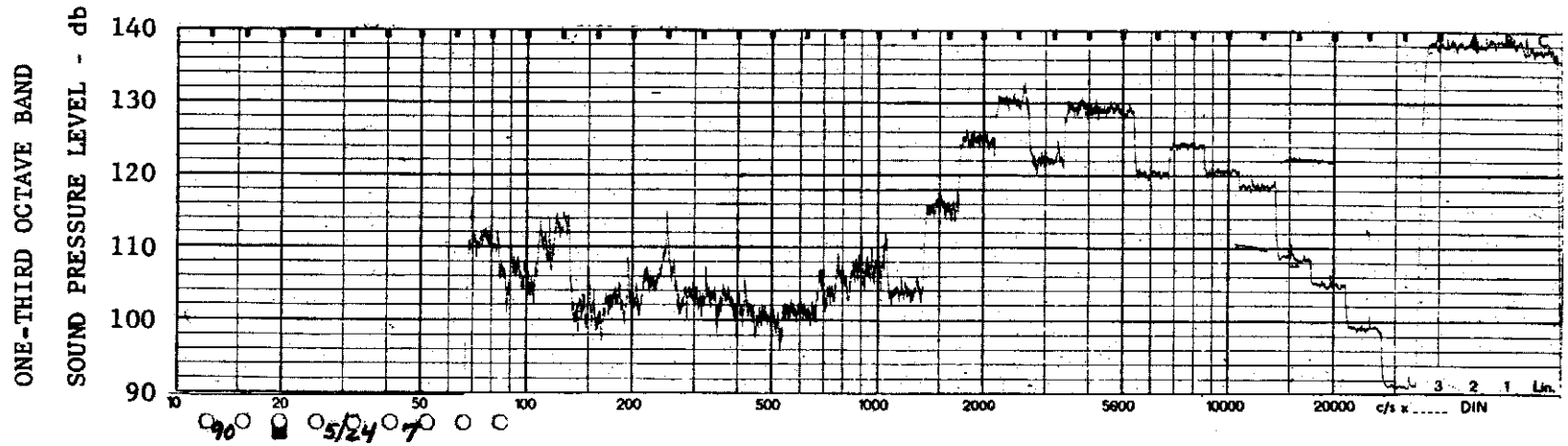

FIGURE 133 ONE-THIRD OCTAVE BAND SPECTRUM MODEL: AXISYM

CHANNEL: 7 MACH NO.: 3.5 α: 15° ϕ: 0 Re_∞/FT.: 1.0×10^6 AEDC GROUP NO.: 5/24

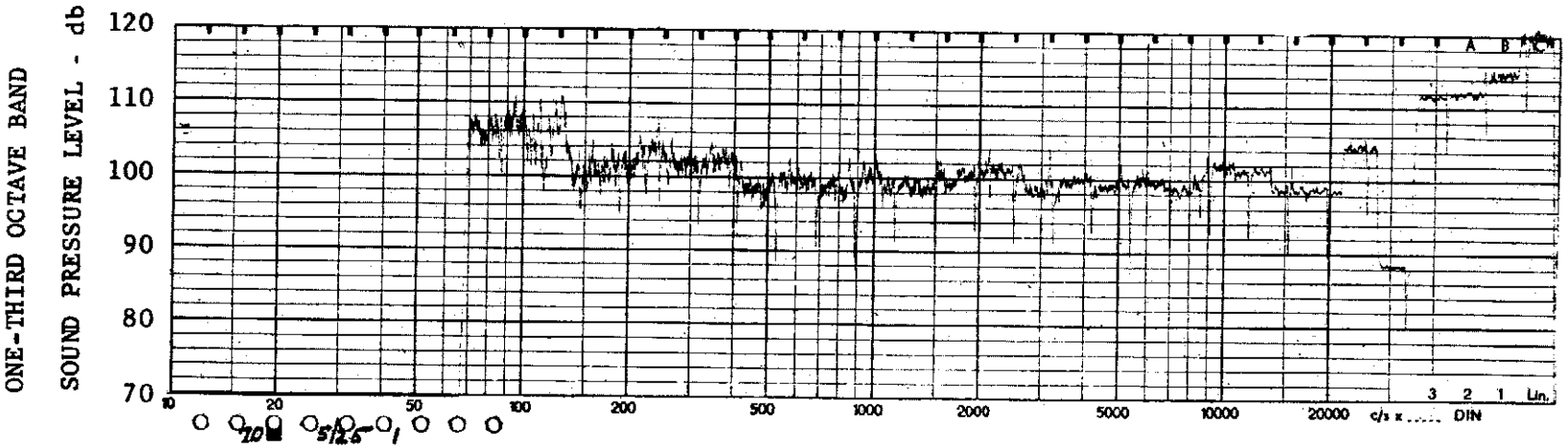

FIGURE 134 ONE-THIRD OCTAVE BAND SPECTRUM MODEL: AXISYM

CHANNEL: 1 MACH NO.: 3.5 α: 0 ϕ: 0 Re_∞/FT.: 1.0×10^6 AEDC GROUP NO.: 5/25

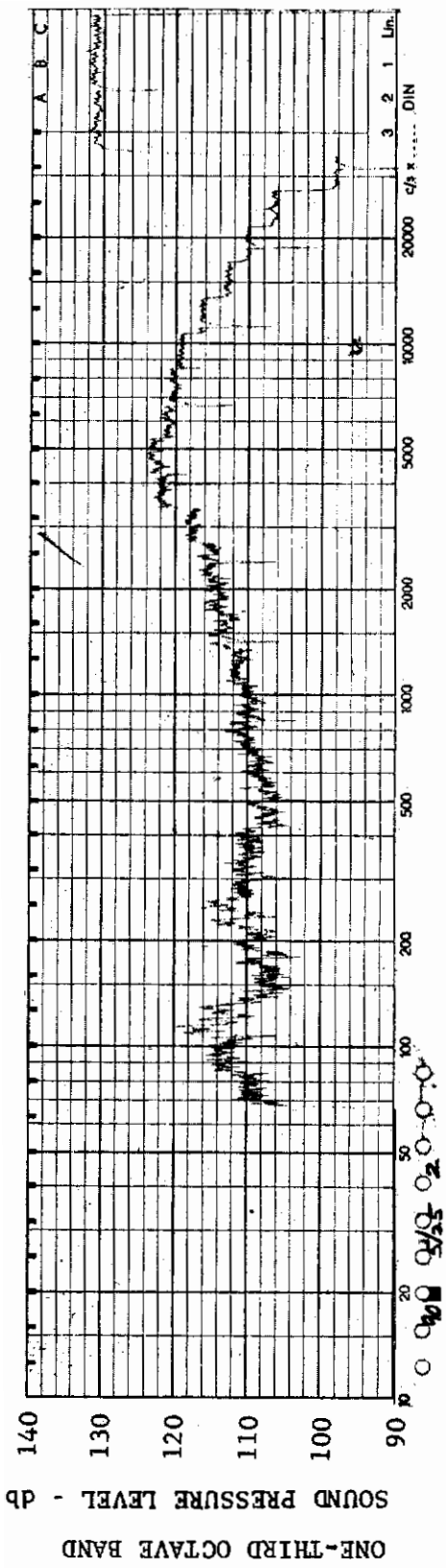

FIGURE 135 ONE-THIRD OCTAVE BAND SPECTRUM MODEL: AXISYM

CHANNEL: 2 MACH NO.: 3.5 α: 0 ϕ: 0 Re_∞/FT.: 1.0×10^6 AEDC GROUP NO.: 5/25

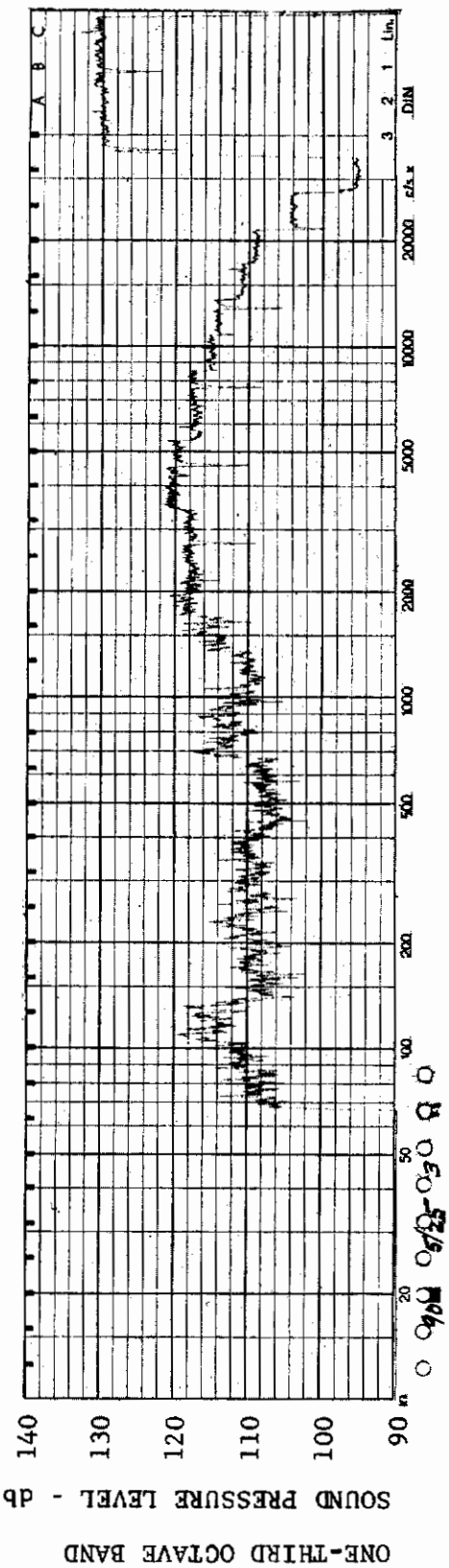

FIGURE 136 ONE-THIRD OCTAVE BAND SPECTRUM MODEL: AXISYM

CHANNEL: 3 MACH NO.: 3.5 α: 0 ϕ: 0 Re_∞/FT.: 1.0×10^6 AEDC GROUP NO.: 5/25

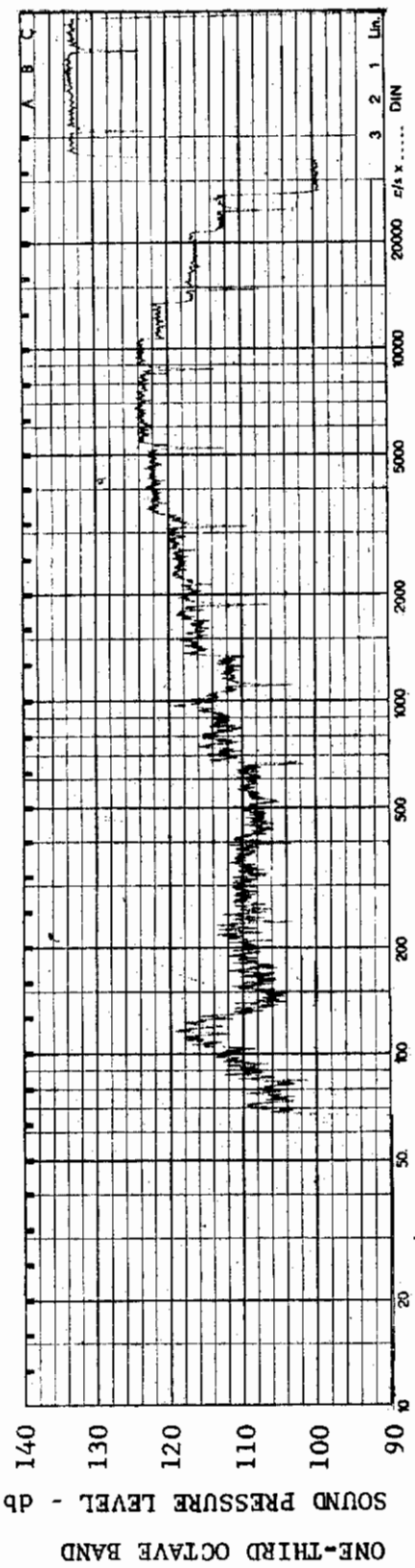

FIGURE 137 ONE-THIRD OCTAVE BAND SPECTRUM

MODEL: AXISYM

CHANNEL: 4 MACH NO.: 3.5 α: 0 ϕ: 0 Re_∞/FT.: 1.0×10^6 AEDC GROUP NO.: 5/25

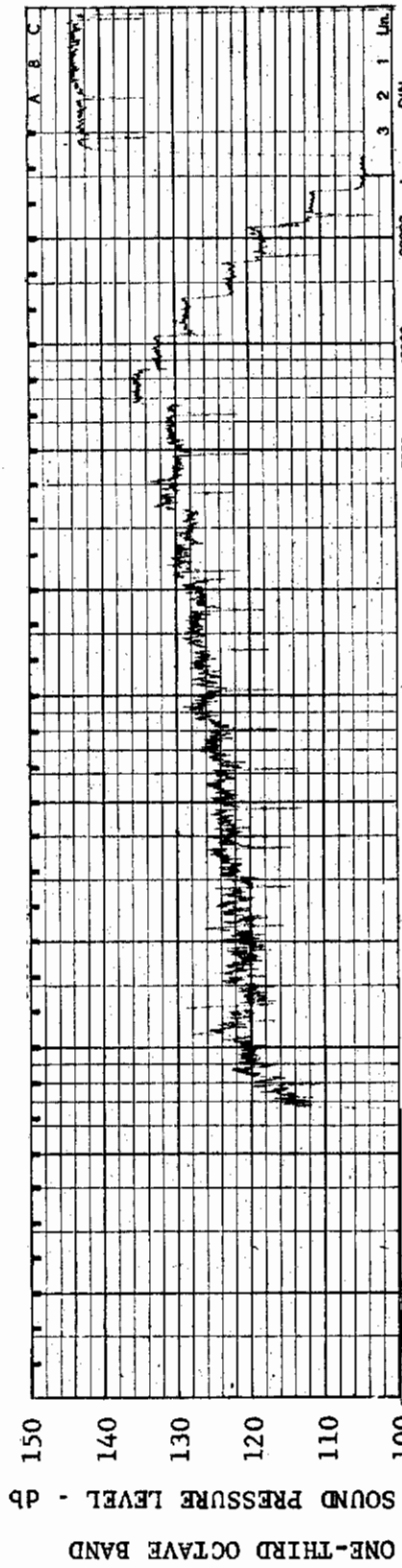

FIGURE 138 ONE-THIRD OCTAVE BAND SPECTRUM

MODEL: AXISYM

CHANNEL: 5 MACH NO.: 3.5 α: 0 ϕ: 0 Re_∞/FT.: 1.0×10^6 AEDC GROUP NO.: 5/25

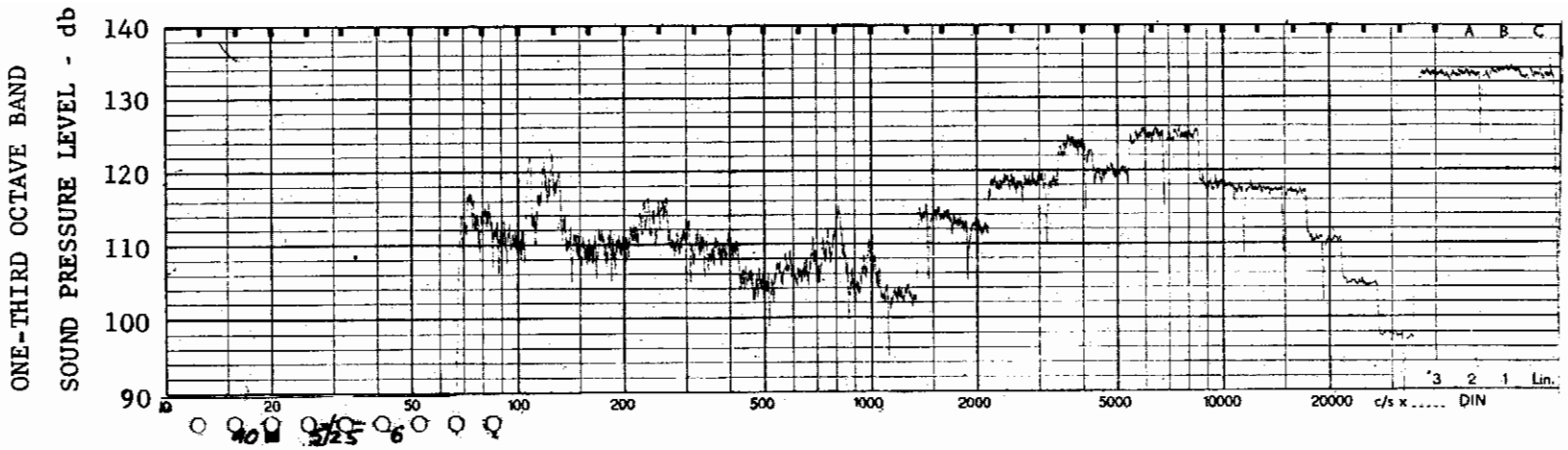

FIGURE 139 ONE-THIRD OCTAVE BAND SPECTRUM MODEL: AXISYM

CHANNEL: 6 MACH NO.: 3.5 α: 0 ϕ: 0 Re_∞/FT.: 1.0×10^6 AEDC GROUP NO.: 5/25

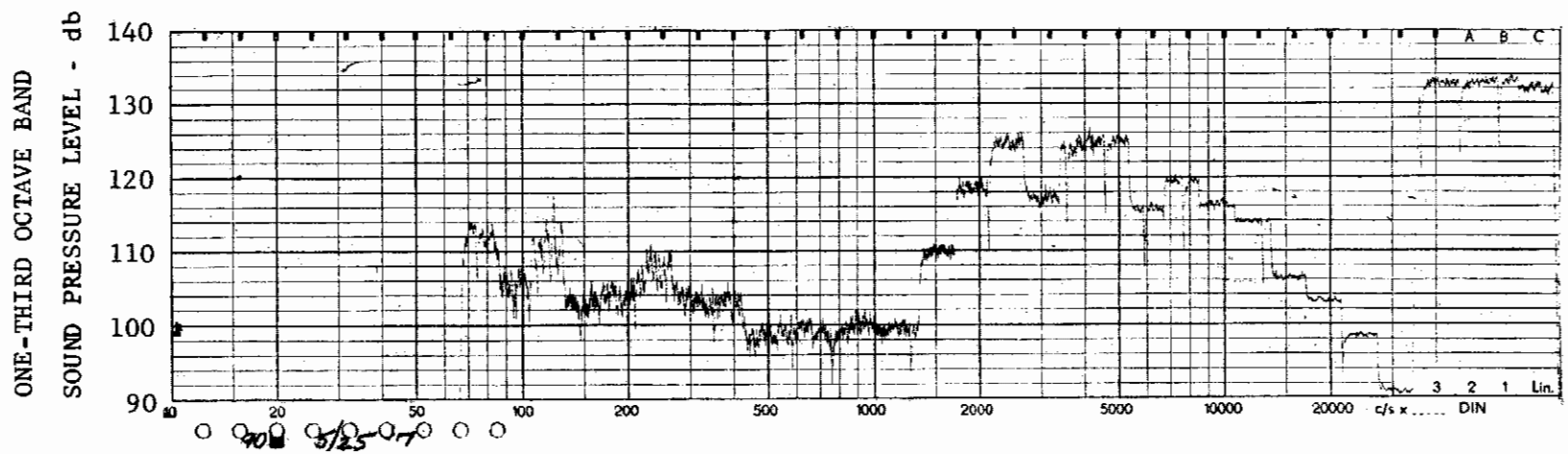

FIGURE 140 ONE-THIRD OCTAVE BAND SPECTRUM MODEL: AXISYM

CHANNEL: 7 MACH NO.: 3.5 α: 0 ϕ: 0 Re_∞/FT.: 1.0×10^6 AEDC GROUP NO.: 5/25

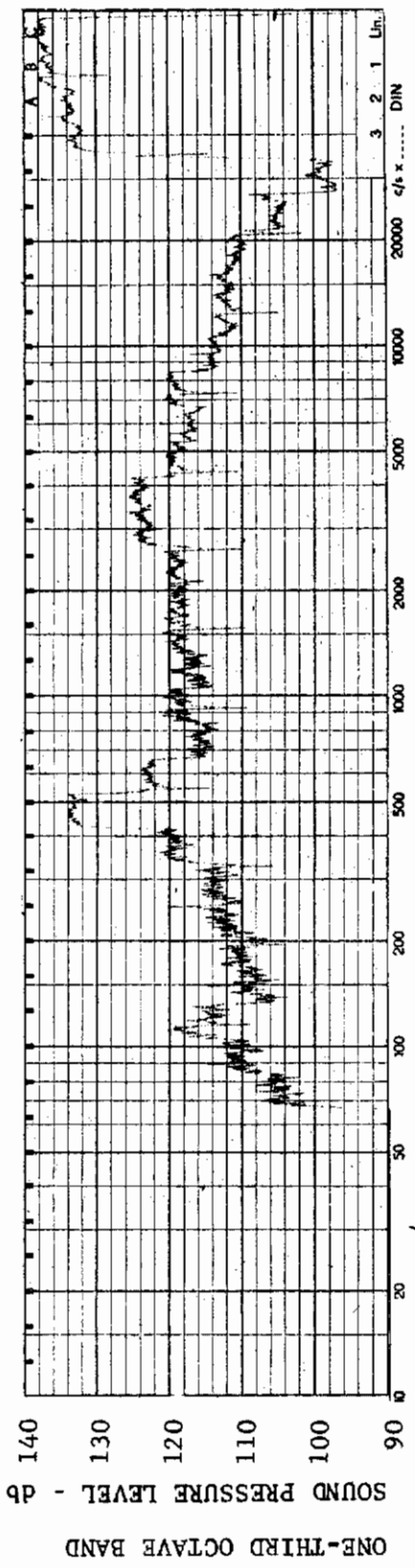

FIGURE 141 ONE-THIRD OCTAVE BAND SPECTRUM MODEL: FP 30

CHANNEL: 2 MACH NO.: 2 α: 0 ϕ: -90° Re_∞/FT.: 0.6×10^6 AEDC GROUP NO.: 16/115

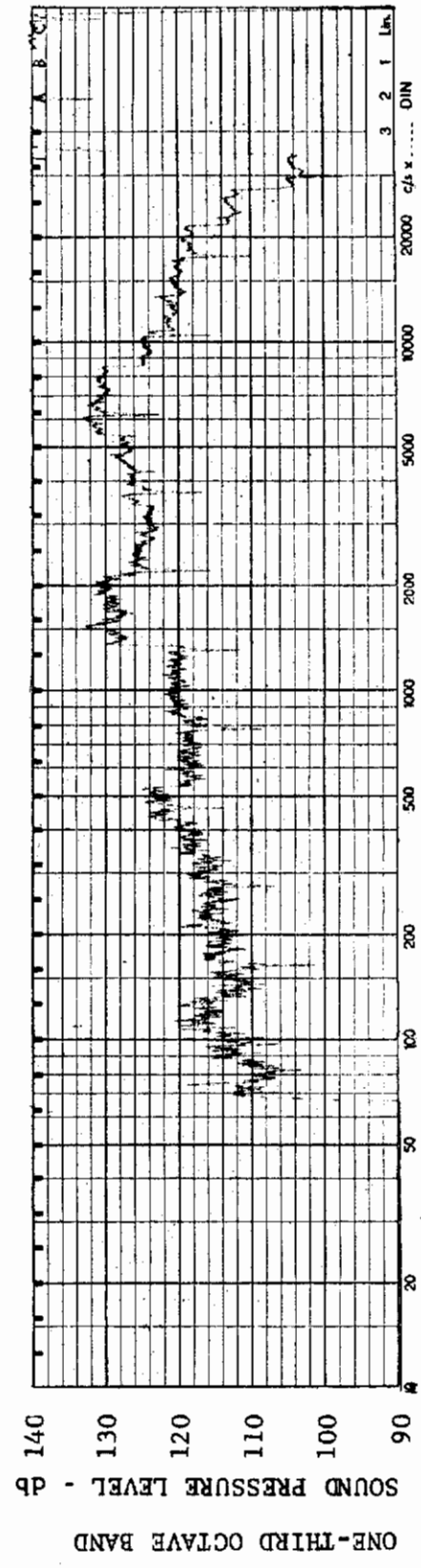

FIGURE 142 ONE-THIRD OCTAVE BAND SPECTRUM MODEL: FP 30

CHANNEL: 4 MACH NO.: 2 α: 0 ϕ: -90° Re_∞/FT.: 0.6×10^6 AEDC GROUP NO.: 16/115

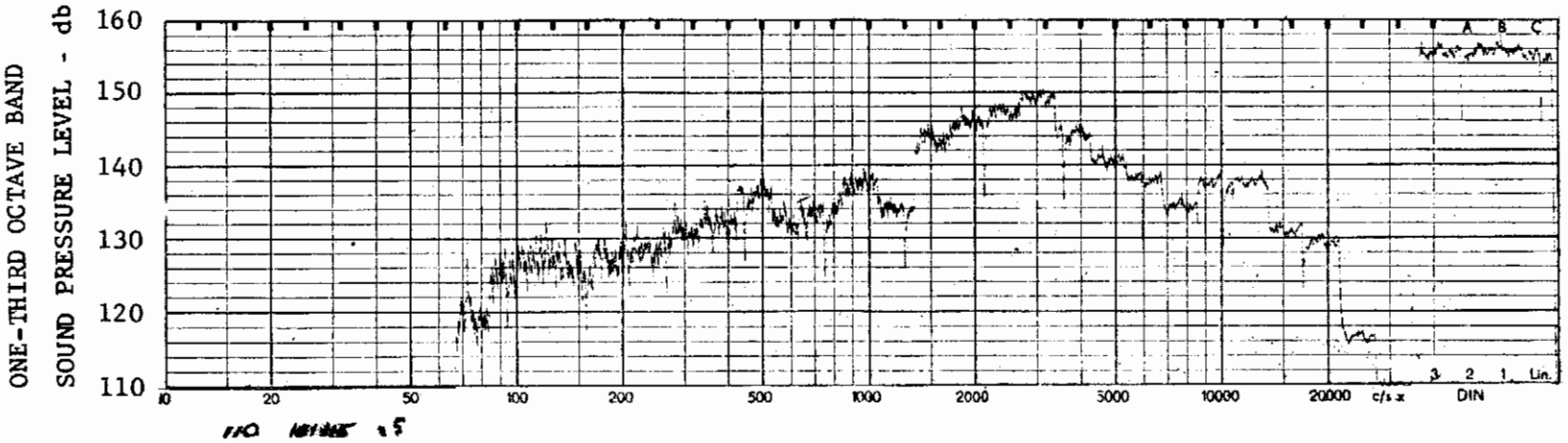

FIGURE 143 ONE-THIRD OCTAVE BAND SPECTRUM MODEL: FP 30

CHANNEL: 5 MACH NO.: 2 α: 0 ϕ: -90° Re_∞/FT.: 0.6×10^6 AEDC GROUP NO.: 16/115

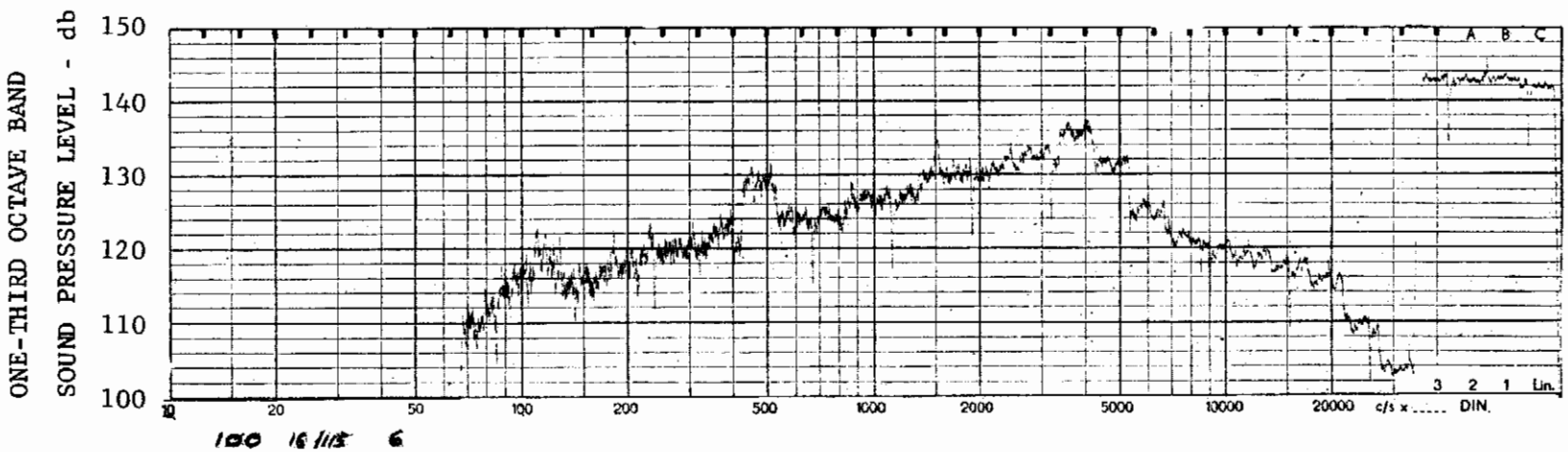

FIGURE 144 ONE-THIRD OCTAVE BAND SPECTRUM MODEL: FP 30

CHANNEL: 6 MACH NO.: 2 α: 0 ϕ: -90° Re_∞/FT.: 0.6×10^6 AEDC GROUP NO.: 16/115

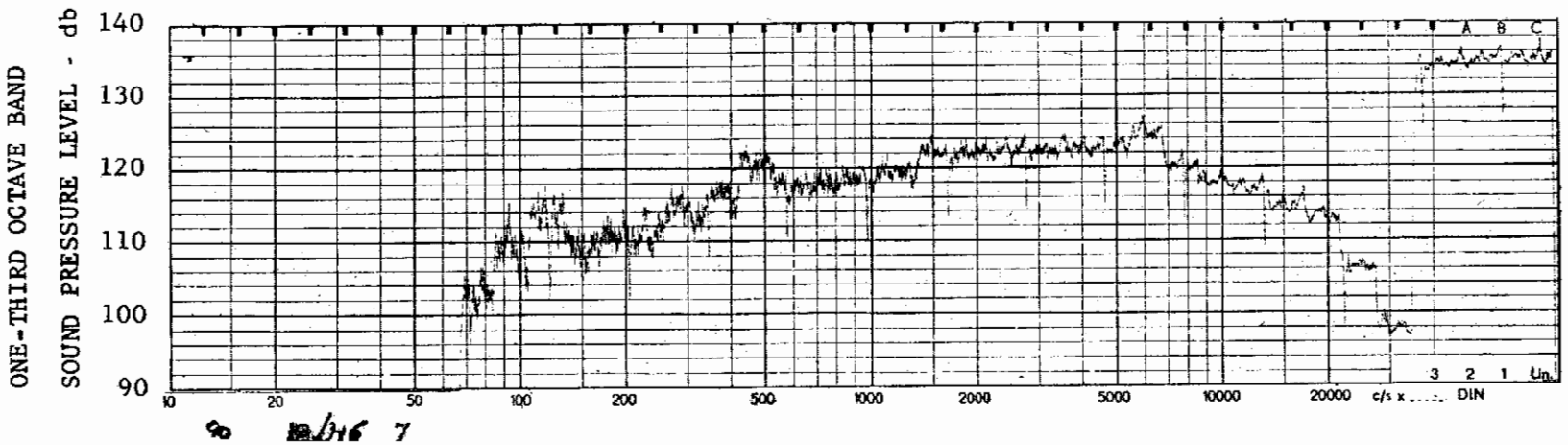

FIGURE 145 ONE-THIRD OCTAVE BAND SPECTRUM MODEL: FP 30

CHANNEL: - MACH NO.: 2 α: 0 ϕ: -90° Re_∞/FT.: 0.6×10^6 AEDC GROUP NO.: 16/115

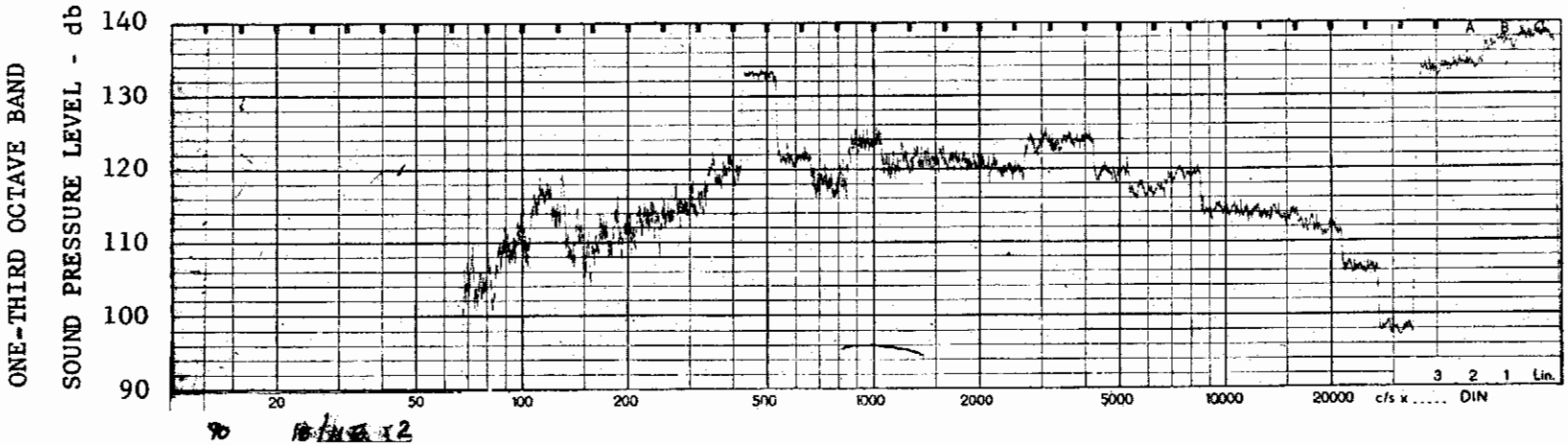

FIGURE 146 ONE-THIRD OCTAVE BAND SPECTRUM MODEL: FP 30

CHANNEL: 2 MACH NO.: 2 α: 0 ϕ: 0 Re_∞/FT.: 0.6×10^6 AEDC GROUP NO.: 16/116

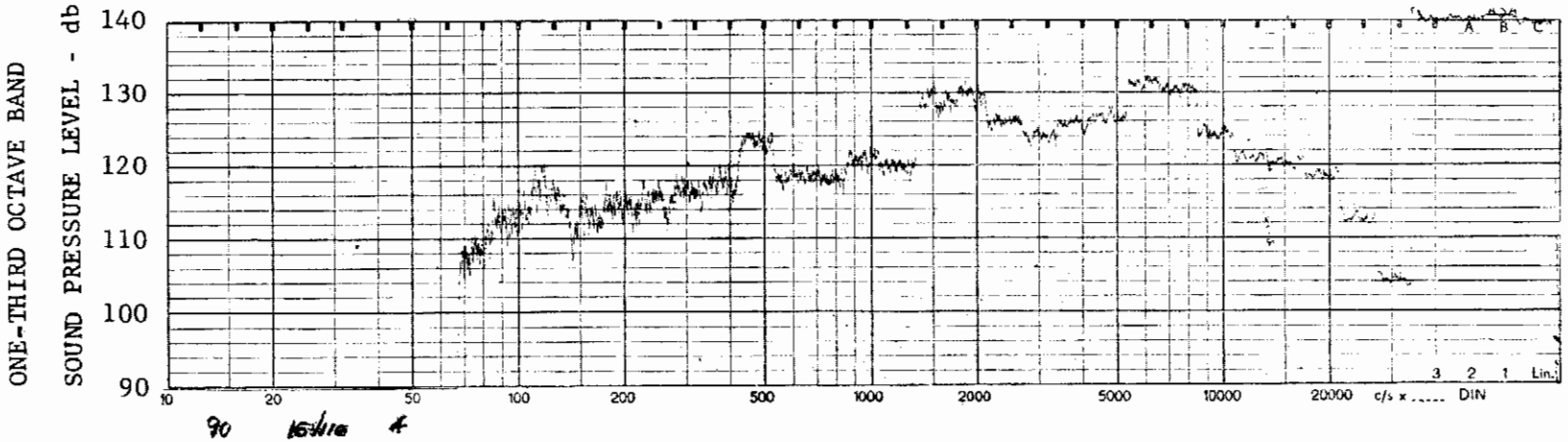

FIGURE 147 ONE-THIRD OCTAVE BAND SPECTRUM MODEL: FP 30

CHANNEL: 4 MACH NO.: 2 α: 0 ϕ: 0 Re_∞/FT.: 0.6×10^6 AEDC GROUP NO.: 16/116

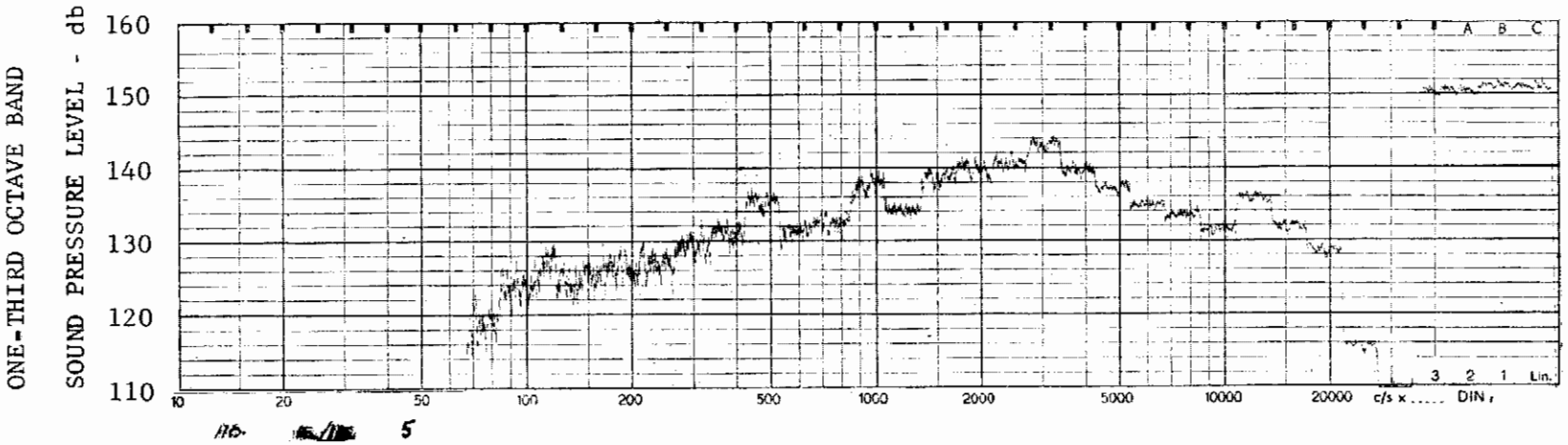

FIGURE 148 ONE-THIRD OCTAVE BAND SPECTRUM MODEL: FP 30

CHANNEL: 5 MACH NO.: 2 α: 0 ϕ: 0 Re_∞/FT.: 0.6×10^6 AEDC GROUP NO.: 16/116

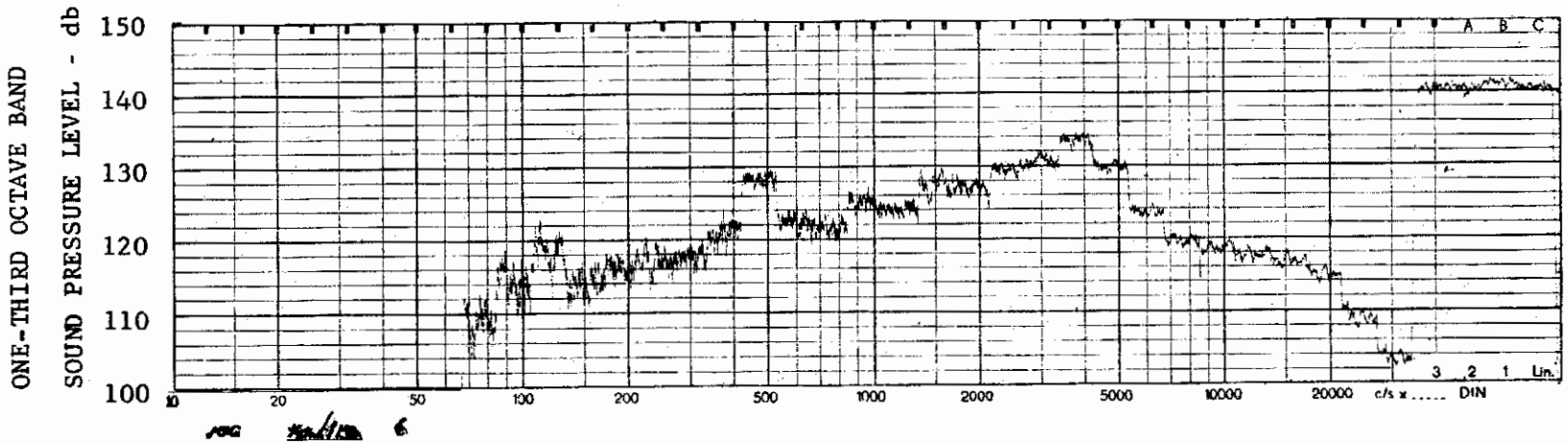

FIGURE 149 ONE-THIRD OCTAVE BAND SPECTRUM MODEL: FP 30

CHANNEL: 6 MACH NO.: 2 α: 0 ϕ: 0 Re_∞/FT.: 0.6×10^6 AEDC GROUP NO.: 16/116

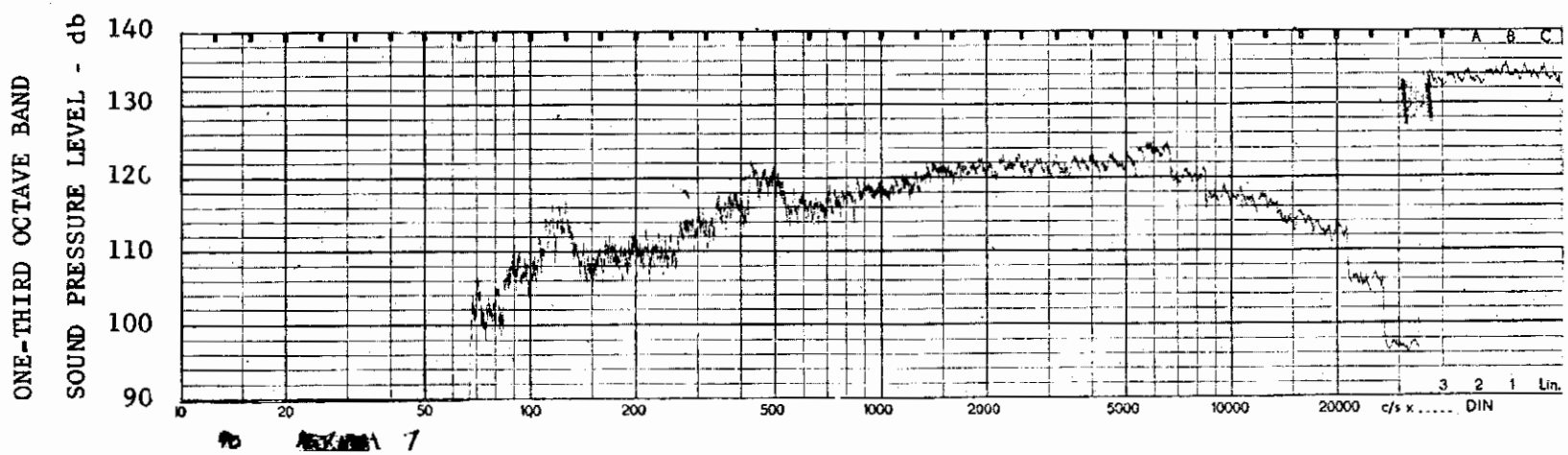

FIGURE 150 ONE-THIRD OCTAVE BAND SPECTRUM MODEL: FP 30

CHANNEL: 7 MACH NO.: 2 α: 0 ϕ: 0 Re_∞/FT.: 0.6×10^6 AEDC GROUP NO.: 16/116

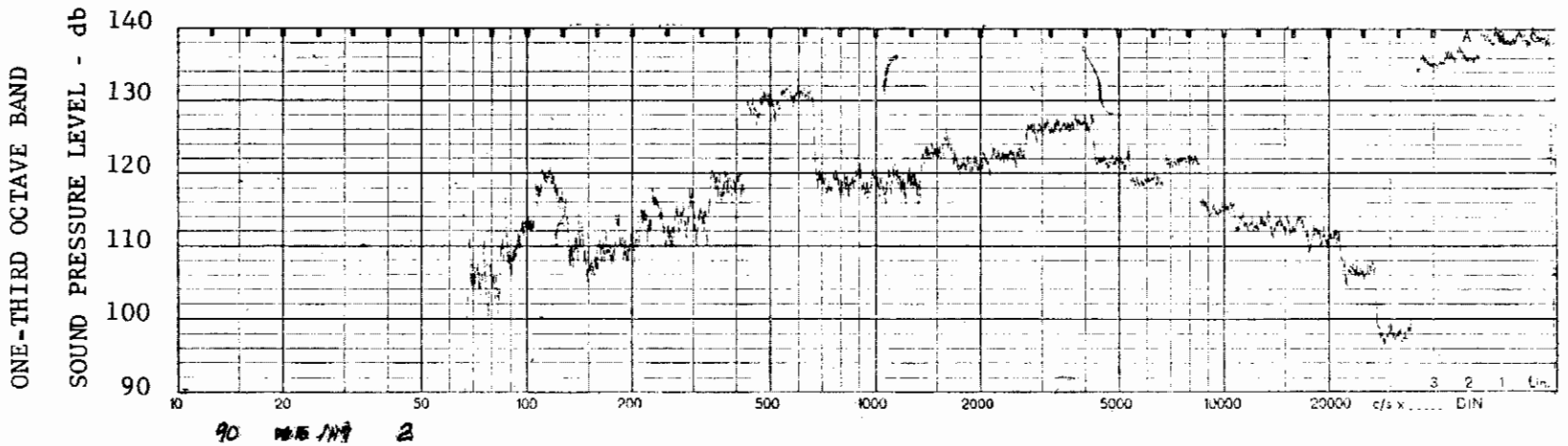

FIGURE 151 ONE-THIRD OCTAVE BAND SPECTRUM MODEL: FP 30

CHANNEL: 2 MACH NO.: 2 α: 0 ϕ: 0 Re_∞/FT.: 1.0×10^6 AEDC GROUP NO.: 16/117

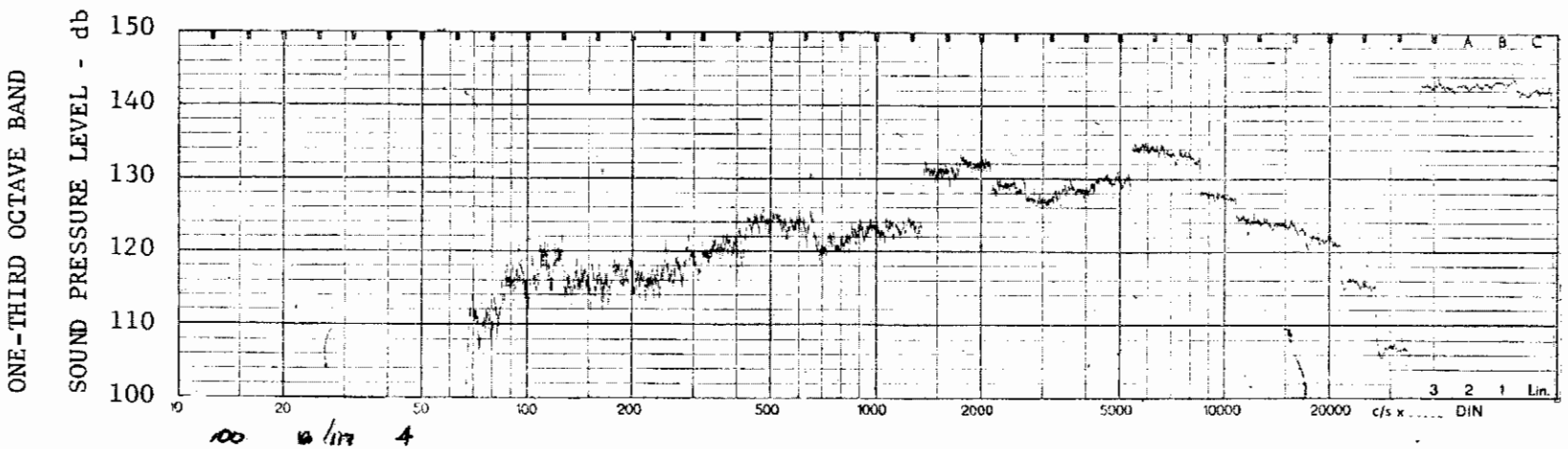

FIGURE 152 ONE-THIRD OCTAVE BAND SPECTRUM MODEL: FP 30

CHANNEL: 4 MACH NO.: 2 α: 0 ϕ: 0 Re_∞/FT.: 1.0×10^6 AEDC GROUP NO.: 16/117

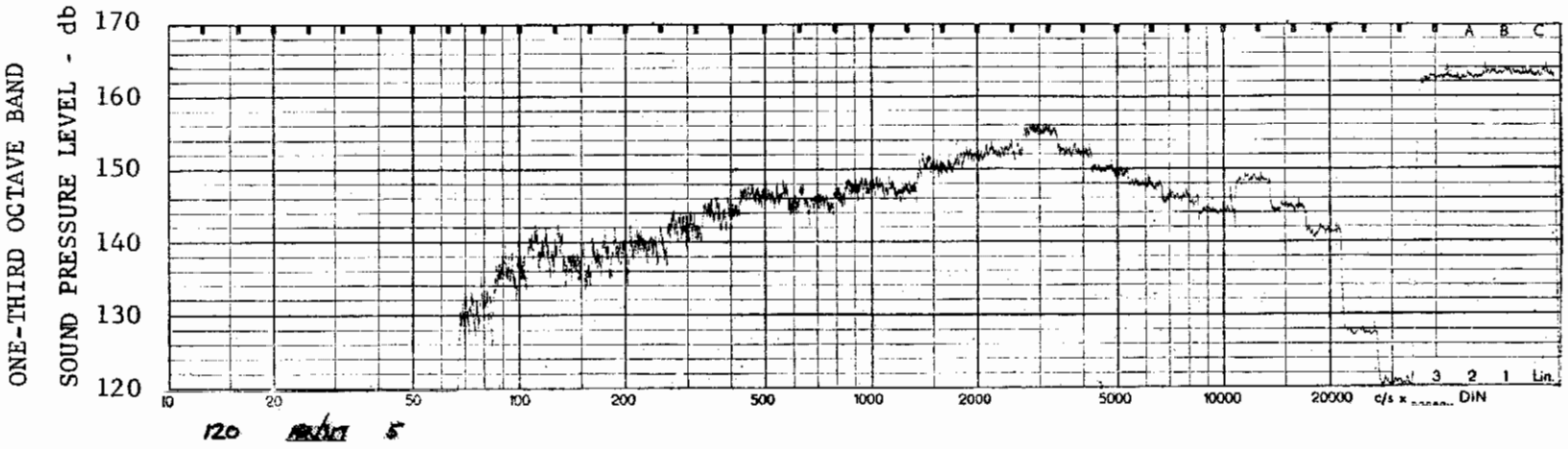

FIGURE 153 ONE-THIRD OCTAVE BAND SPECTRUM MODEL: FP 30

CHANNEL: 5 MACH NO.: 2 α: 0 ϕ: 0 Re_∞/FT.: 1.0×10^6 AEDC GROUP NO.: 16/117

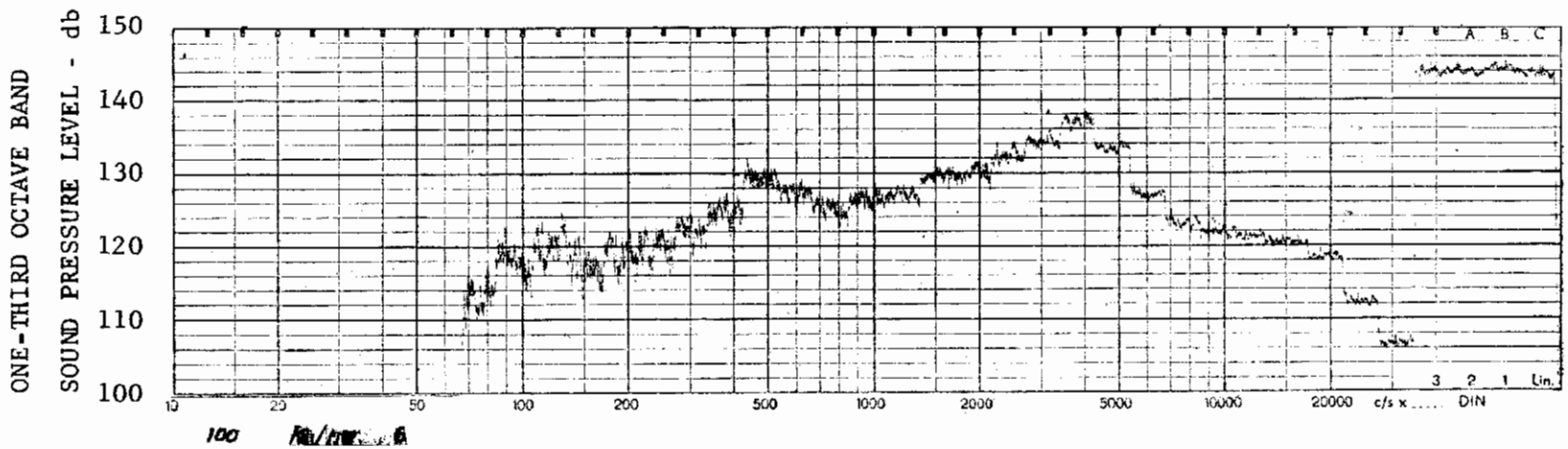

FIGURE 154 ONE-THIRD OCTAVE BAND SPECTRUM MODEL: FP 30

CHANNEL: 6 MACH NO.: 2 α: 0 ϕ: 0 Re_∞/FT.: 1.0×10^6 AEDC GROUP NO.: 16/117

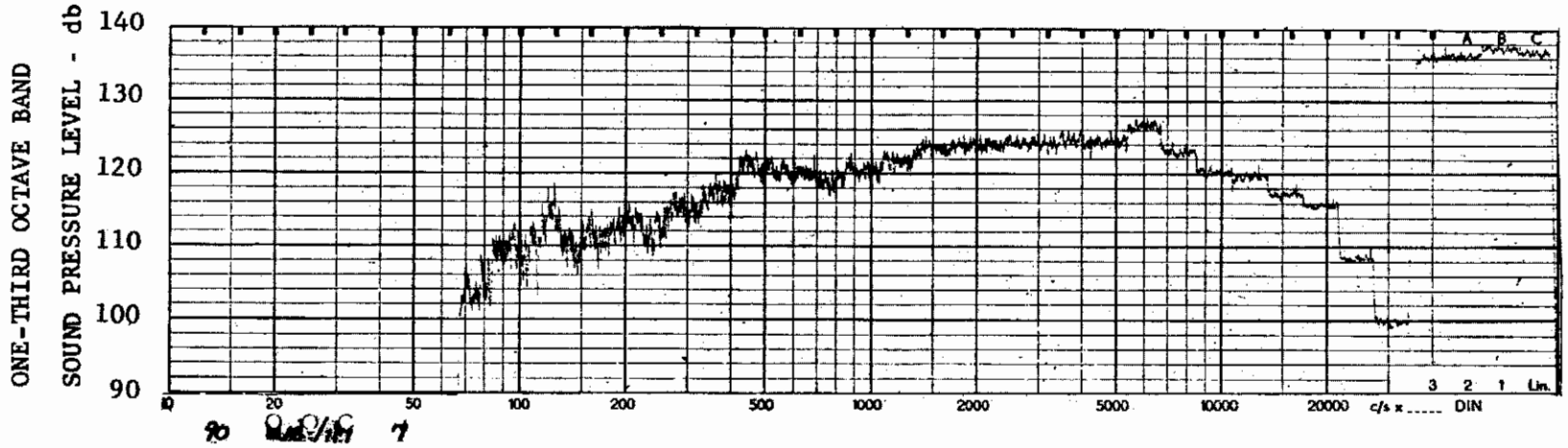

FIGURE 155 ONE-THIRD OCTAVE BAND SPECTRUM MODEL: FP 30

CHANNEL: 7 MACH NO.: 2 α: 0 ϕ: 0 Re_∞/FT.: 1.0×10^6 AEDC GROUP NO.: 16/117

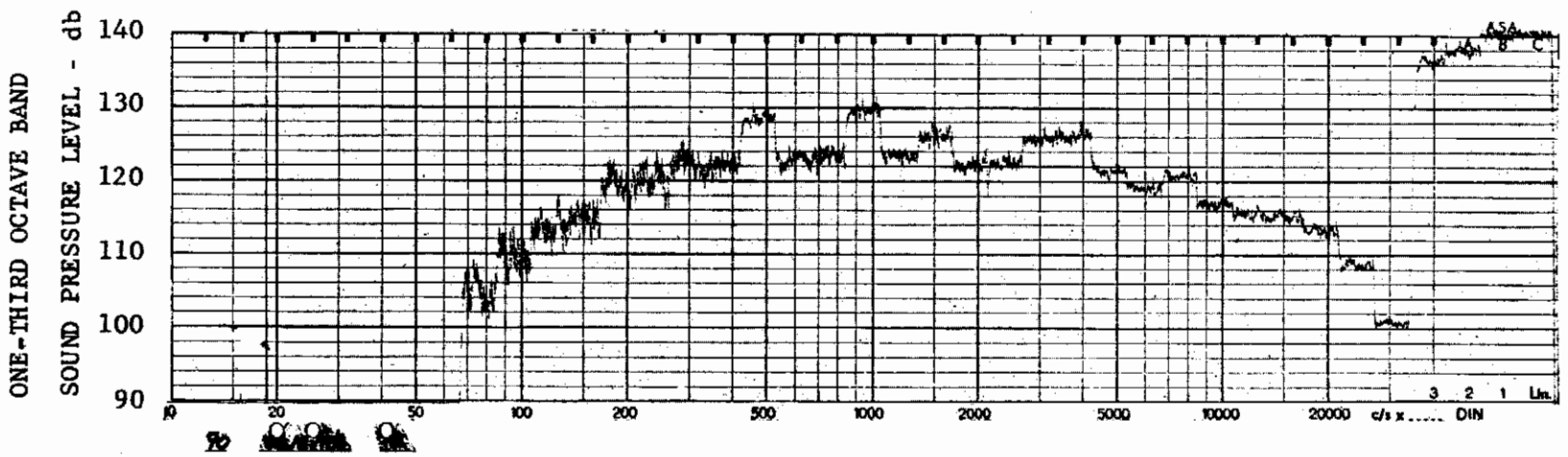

FIGURE 156 ONE-THIRD OCTAVE BAND SPECTRUM MODEL: FP 30

CHANNEL: 2 MACH NO.: 2 α: 5° ϕ: 0 Re_∞/FT.: 1.0×10^6 AEDC GROUP NO.: 16/118

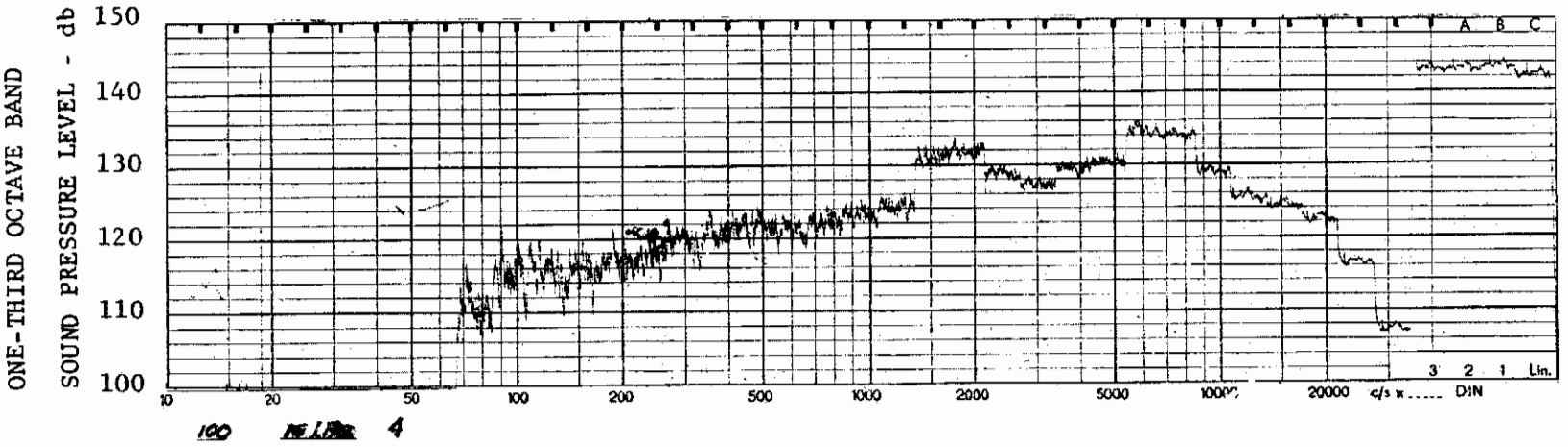

FIGURE 157 ONE-THIRD OCTAVE BAND SPECTRUM MODEL: FP 30

CHANNEL: 4 MACH NO.: 2 α: 5° ϕ: 0 Re_∞/FT.: 1.0×10^6 AEDC GROUP NO.: 16/118

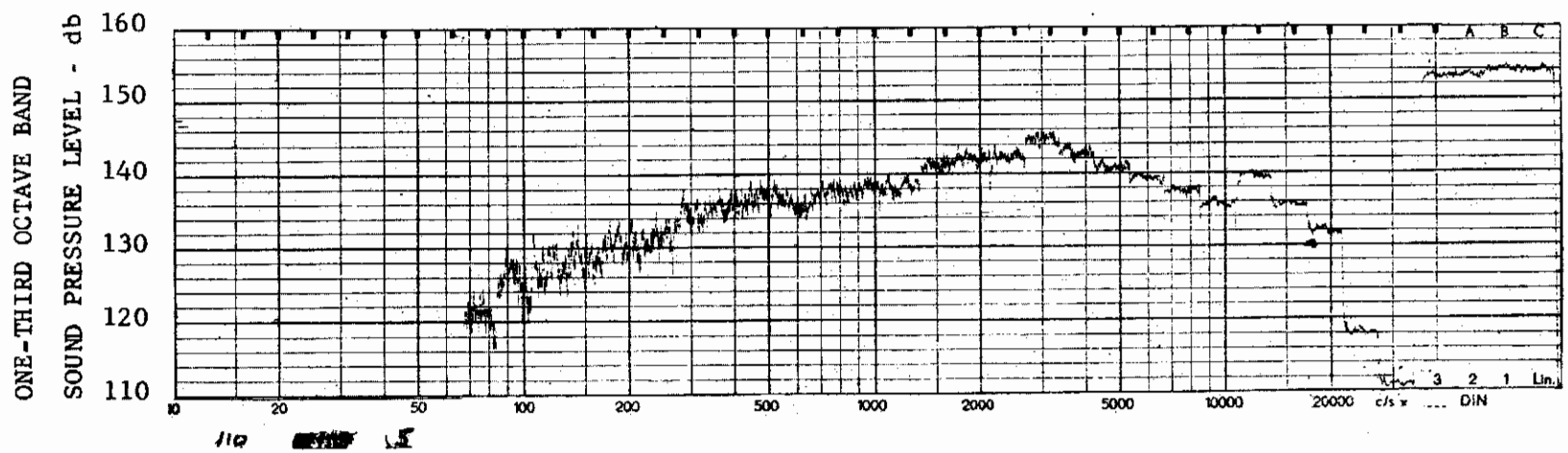

FIGURE 158 ONE-THIRD OCTAVE BAND SPECTRUM MODEL: FP 30

CHANNEL: 5 MACH NO.: 2 α: 5° ϕ: 0 Re_∞/FT.: 1.0×10^6 AEDC GROUP NO.: 16/118

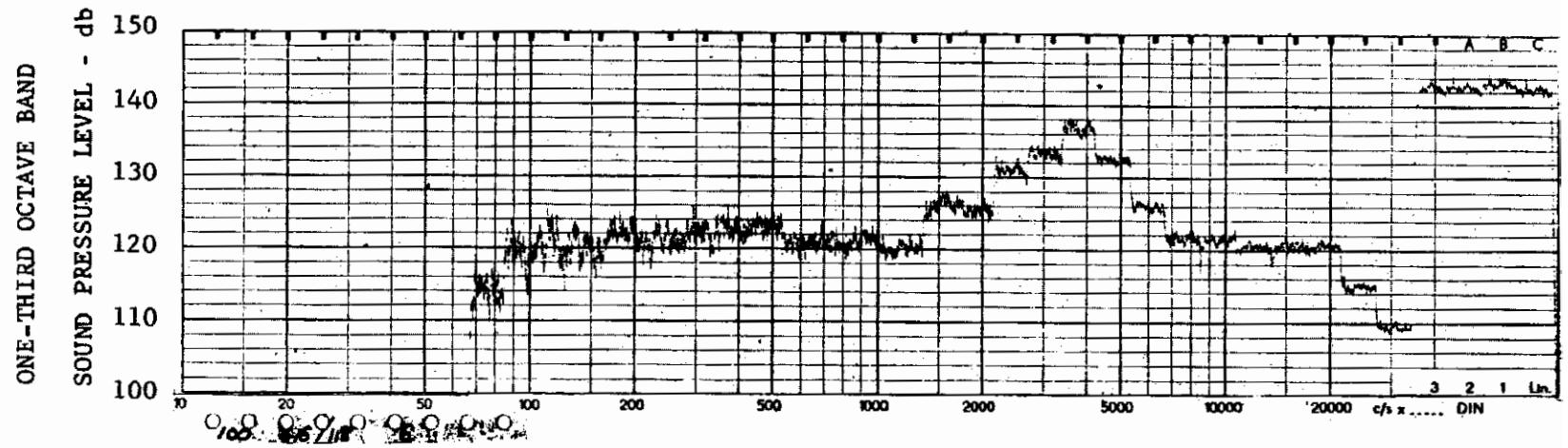

FIGURE 159 ONE-THIRD OCTAVE BAND SPECTRUM MODEL: FP 30

CHANNEL: 6 MACH NO.: 2 α: 5° ϕ: 0 Re_∞/FT.: 1.0×10^6 AEDC GROUP NO.: 16/118

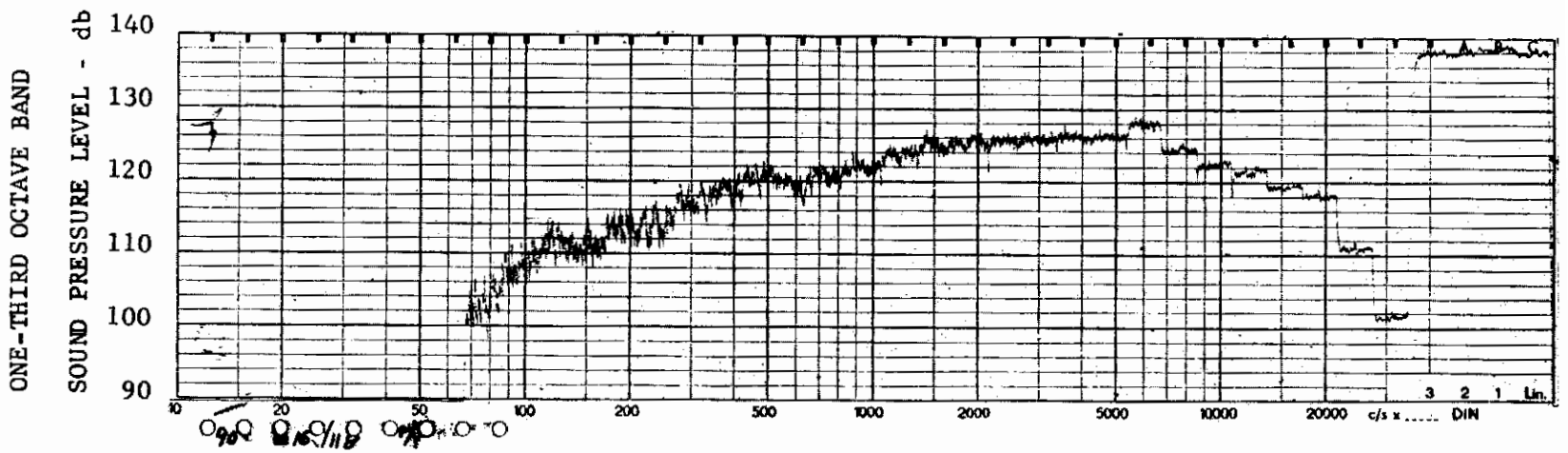

FIGURE 160 ONE-THIRD OCTAVE BAND SPECTRUM MODEL: FP 30

CHANNEL: 7 MACH NO.: 2 α: 5° ϕ: 0 Re_∞/FT.: 1.0×10^6 AEDC GROUP NO.: 16/118

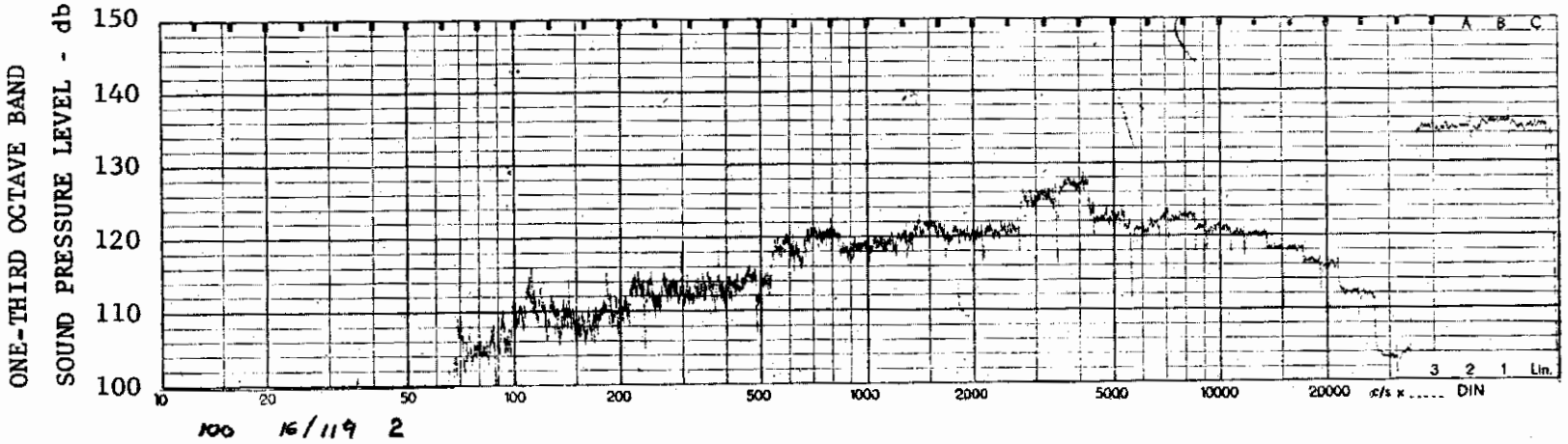

FIGURE 161 ONE-THIRD OCTAVE BAND SPECTRUM MODEL: FP 30

CHANNEL: 2 MACH NO.: 2 α: 15° ϕ: 0 Re_∞/FT.: 1.0×10^6 AEDC GROUP NO.: 16/119

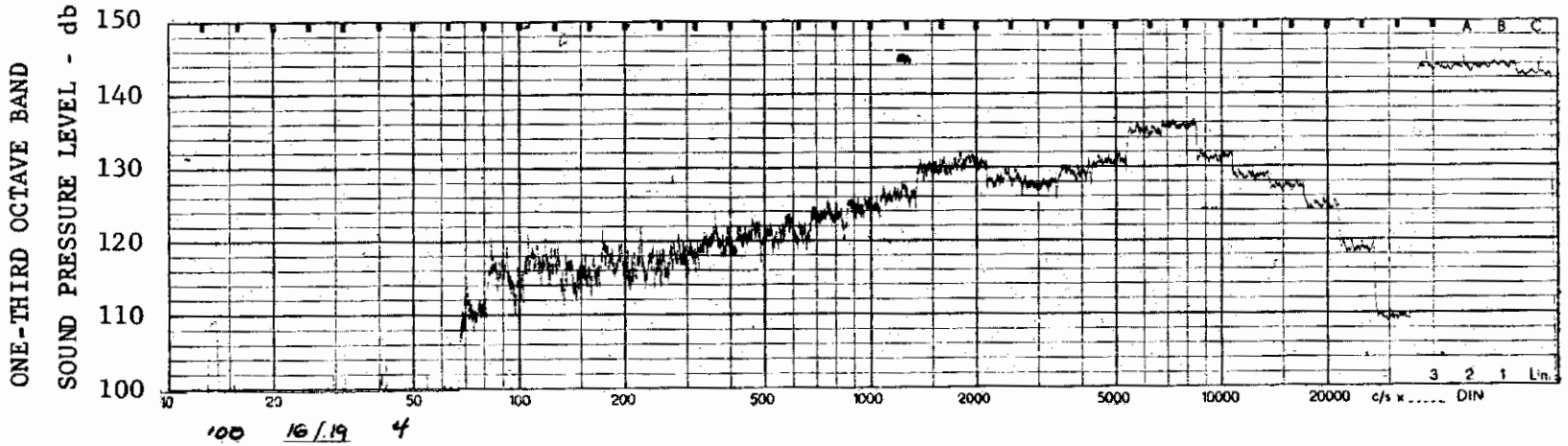

FIGURE 162 ONE-THIRD OCTAVE BAND SPECTRUM MODEL: FP 30

CHANNEL: 4 MACH NO.: 2 α: 15° ϕ: 0 Re_∞/FT.: 1.0×10^6 AEDC GROUP NO.: 16/119

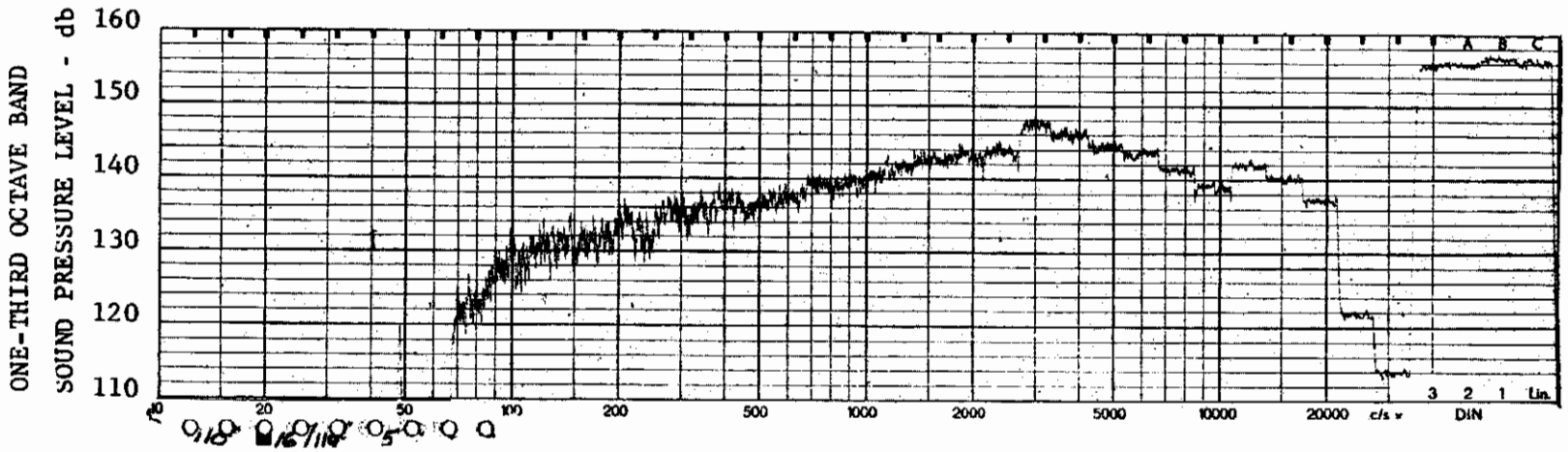

FIGURE 163 ONE-THIRD OCTAVE BAND SPECTRUM MODEL: FP 30

CHANNEL: 5 MACH NO.: 2 α: 15° ϕ: 0 Re_∞/FT.: 1.0×10^6 AEDC GROUP NO.: 16/119

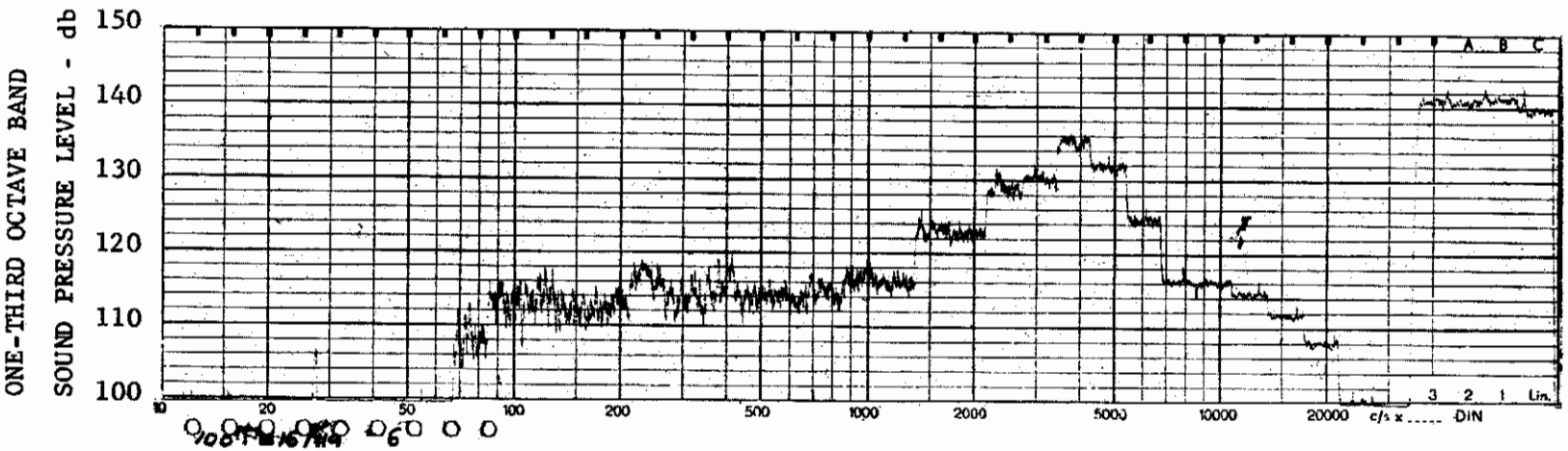

FIGURE 164 ONE-THIRD OCTAVE BAND SPECTRUM MODEL: FP 30

CHANNEL: 6 MACH NO.: 2 α: 15° ϕ: 0 Re_∞/FT.: 1.0×10^6 AEDC GROUP NO.: 16/119

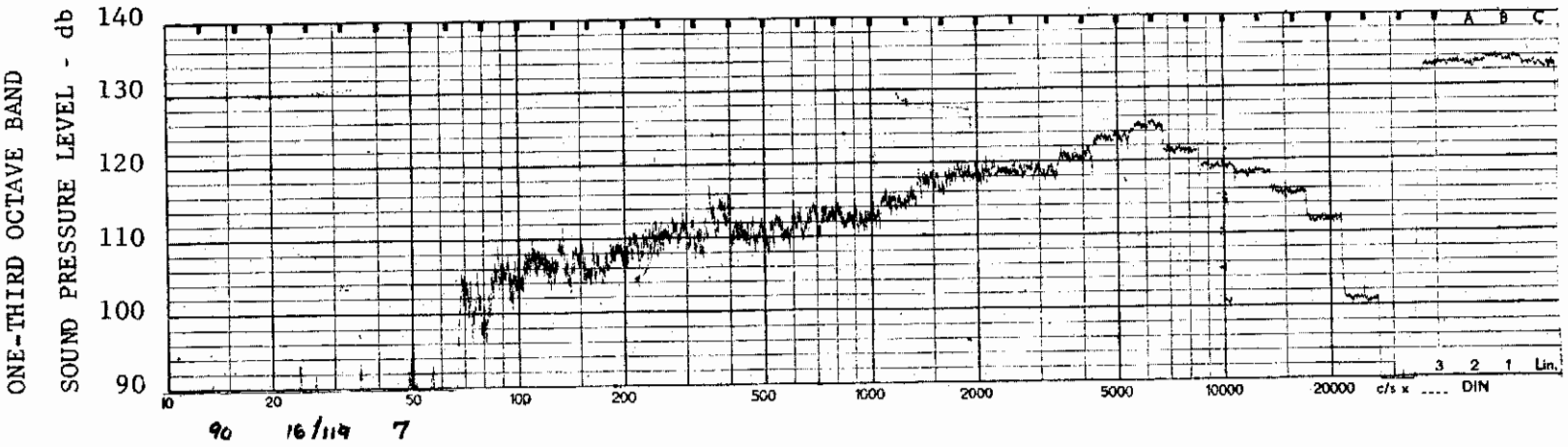

FIGURE 165 ONE-THIRD OCTAVE BAND SPECTRUM MODEL: FP 30

CHANNEL: 7 MACH NO.: 2 α: 15° ϕ: 0 Re_∞/FT.: 1.0×10^6 AEDC GROUP NO.: 16/119

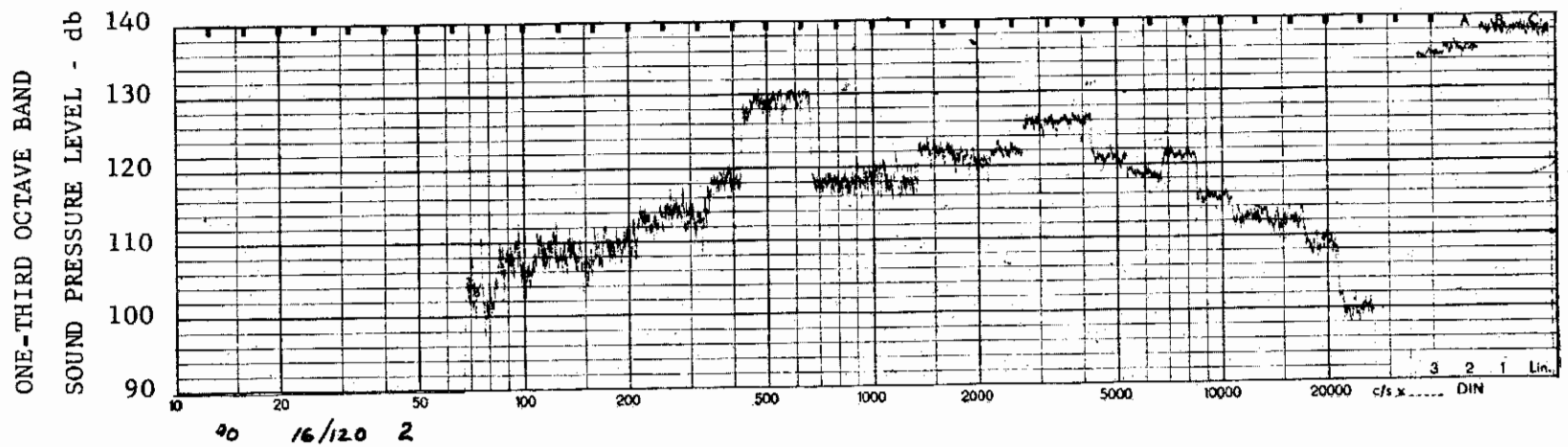

FIGURE 166 ONE-THIRD OCTAVE BAND SPECTRUM MODEL: FP 30

CHANNEL: 2 MACH NO.: 2 α: 0 ϕ: 0 Re_∞/FT.: 1.0×10^6 AEDC GROUP NO.: 16/120

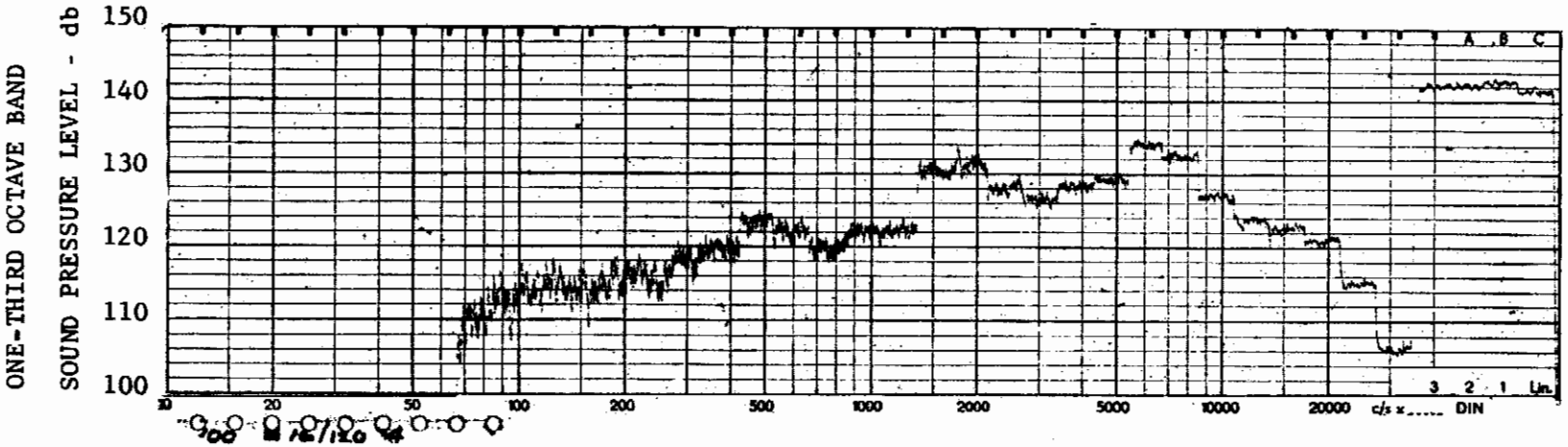

FIGURE 167 ONE-THIRD OCTAVE BAND SPECTRUM MODEL: FP 30

CHANNEL: 4 MACH NO.: 2 α: 0 ϕ: 0 Re_∞/FT.: 1.0×10^6 AEDC GROUP NO.: 16/120

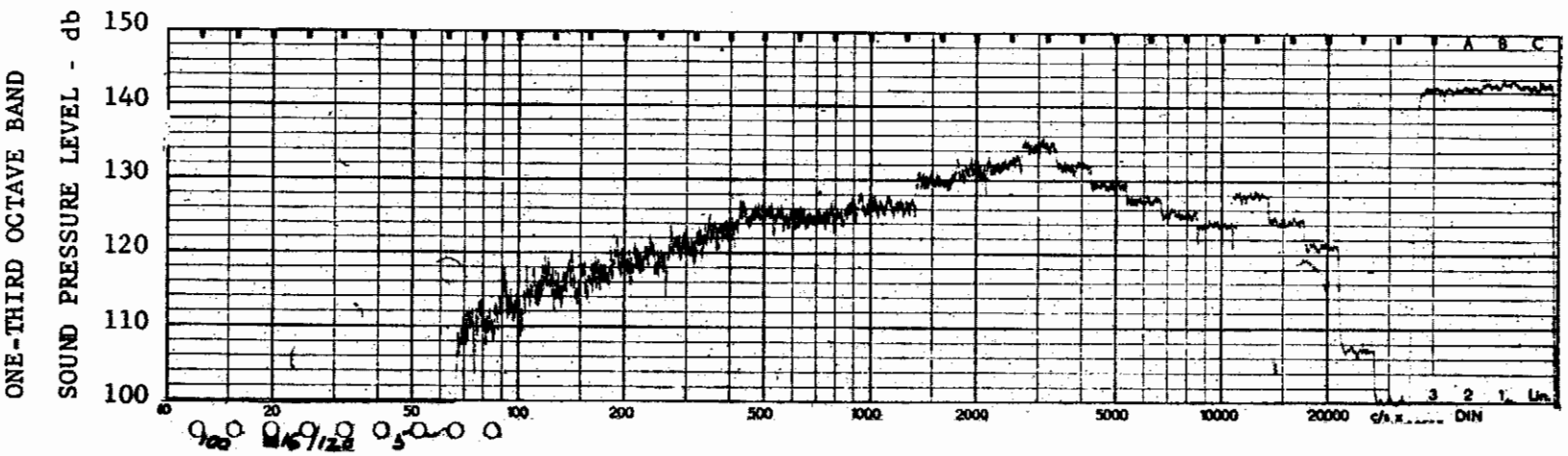

FIGURE 168 ONE-THIRD OCTAVE BAND SPECTRUM MODEL: FP 30

CHANNEL: 5 MACH NO.: 2 α: 0 ϕ: 0 Re_∞/FT.: 1.0×10^6 AEDC GROUP NO.: 16/120

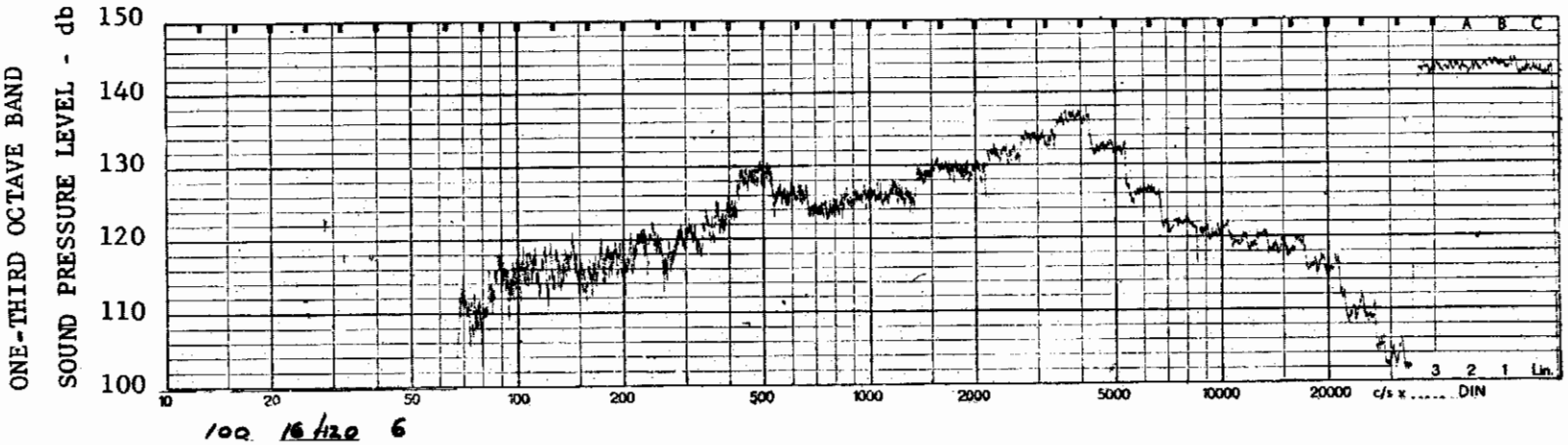

FIGURE 169 ONE-THIRD OCTAVE BAND SPECTRUM MODEL: FP 30

CHANNEL: 6 MACH NO.: 2 α: 0 ϕ: 0 Re_∞/FT.: 1.0×10^6 AEDC GROUP NO.: 16/120

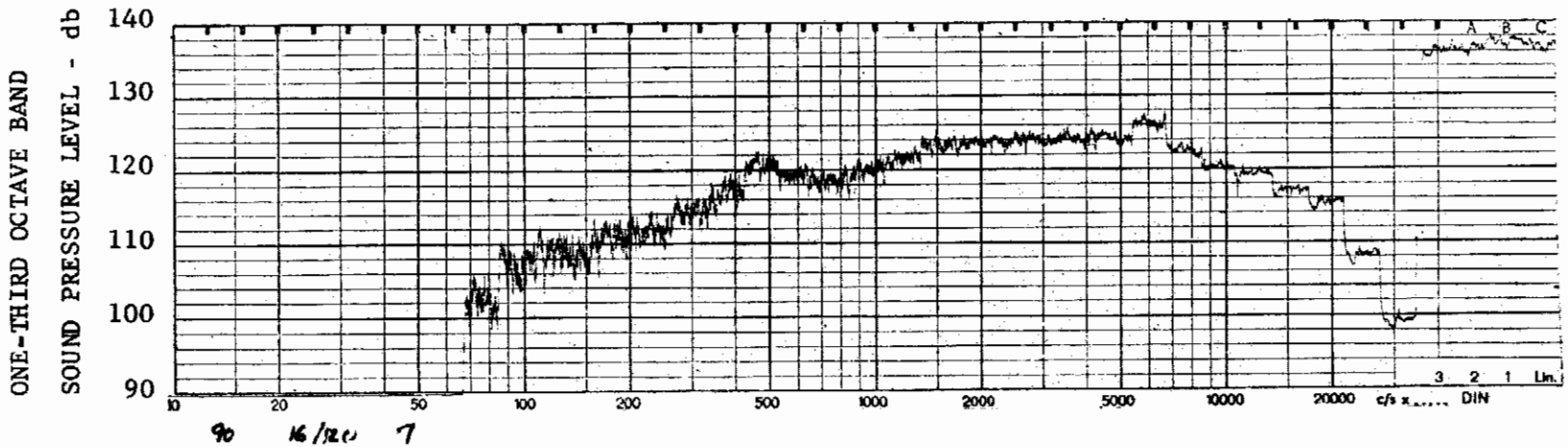

FIGURE 170 ONE-THIRD OCTAVE BAND SPECTRUM MODEL: FP 30

CHANNEL: 7 MACH NO.: 2 α: 0 ϕ: 0 Re_∞/FT.: 1.0×10^6 AEDC GROUP NO.: 16/120

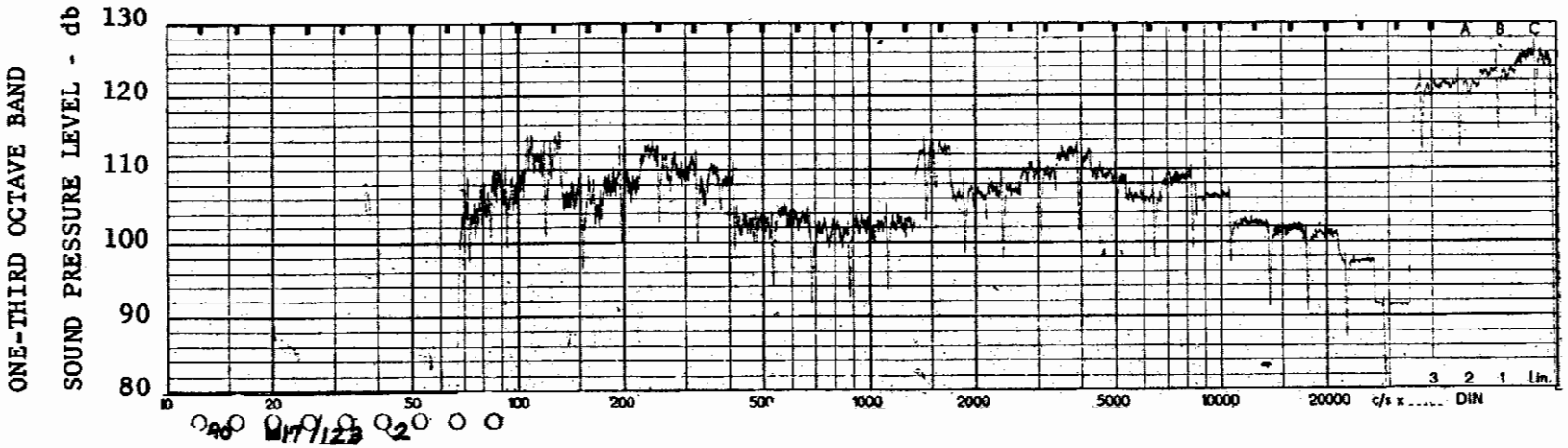

FIGURE 171 ONE-THIRD OCTAVE BAND SPECTRUM MODEL: FP 30

CHANNEL: 2 MACH NO.: 3.5 α: 0 ϕ: 0 Re_∞/FT.: 0.5×10^6 AEDC GROUP NO.: 17/123

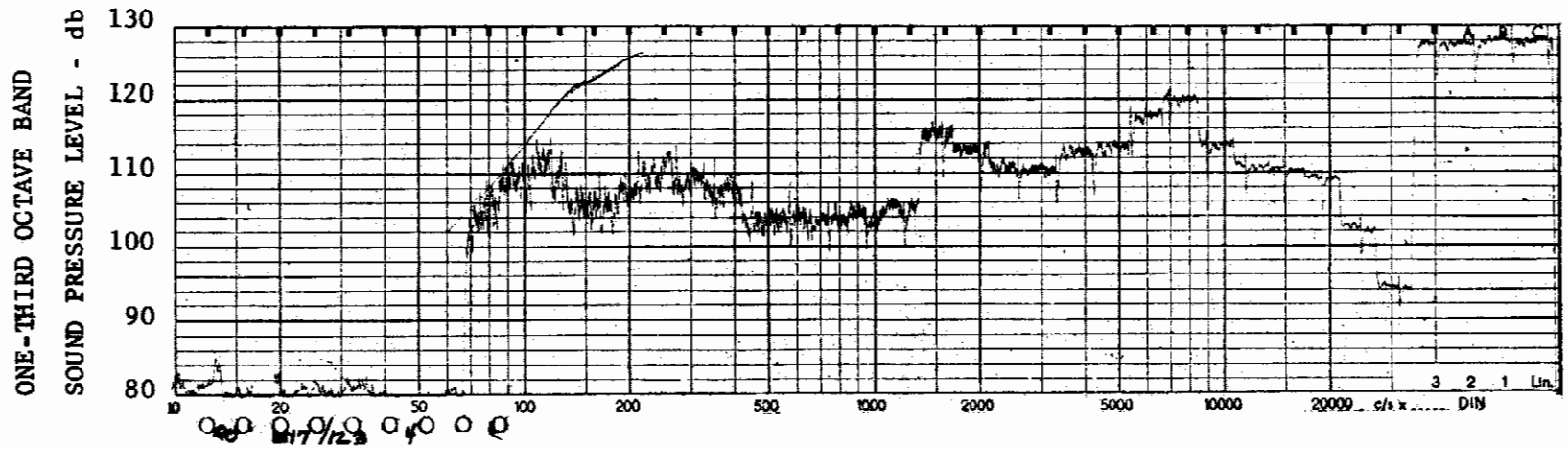

FIGURE 172 ONE-THIRD OCTAVE BAND SPECTRUM MODEL: FP 30

CHANNEL: 4 MACH NO.: 3.5 α: 0 ϕ: 0 Re_∞/FT.: 0.5×10^6 AEDC GROUP NO.: 17/123

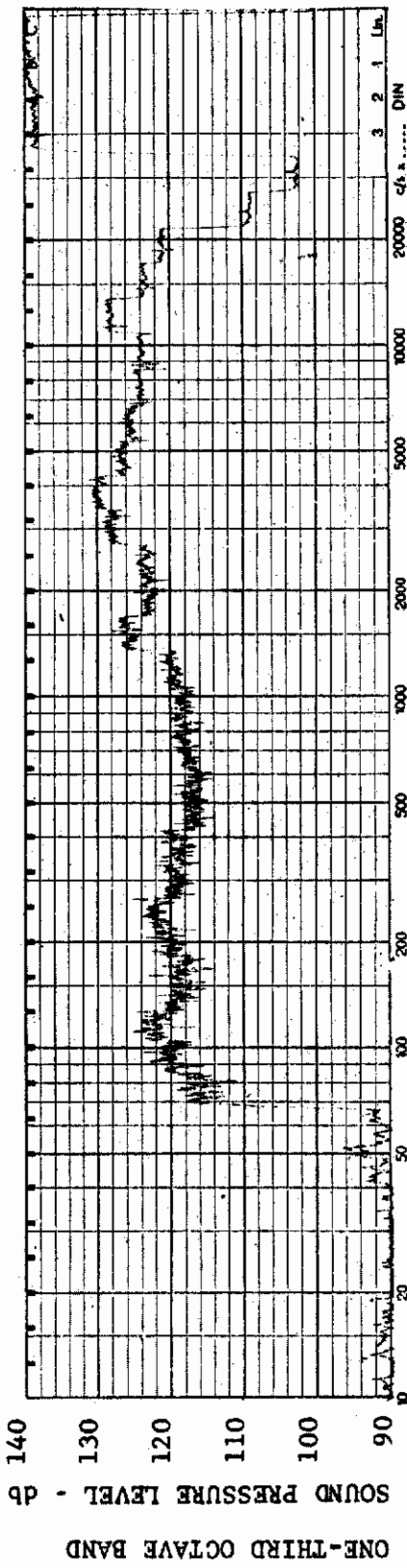

FIGURE 173 ONE-THIRD OCTAVE BAND SPECTRUM MODEL: FP 30

CHANNEL: 5 MACH NO.: 3.5 α: 0 ϕ: 0 Re_∞/FT.: 0.5×10^6 AEDC GROUP NO.: 17/123

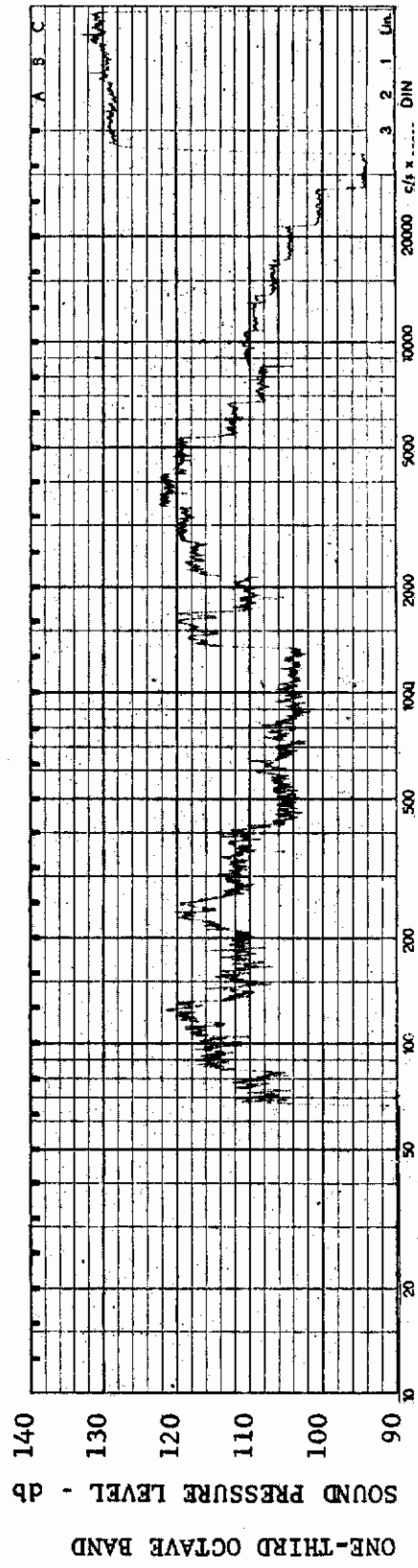

FIGURE 174 ONE-THIRD OCTAVE BAND SPECTRUM MODEL: FP 30

CHANNEL: 6 MACH NO.: 3.5 α: 0 ϕ: 0 Re_∞/FT.: 0.5×10^6 AEDC GROUP NO.: 17/123

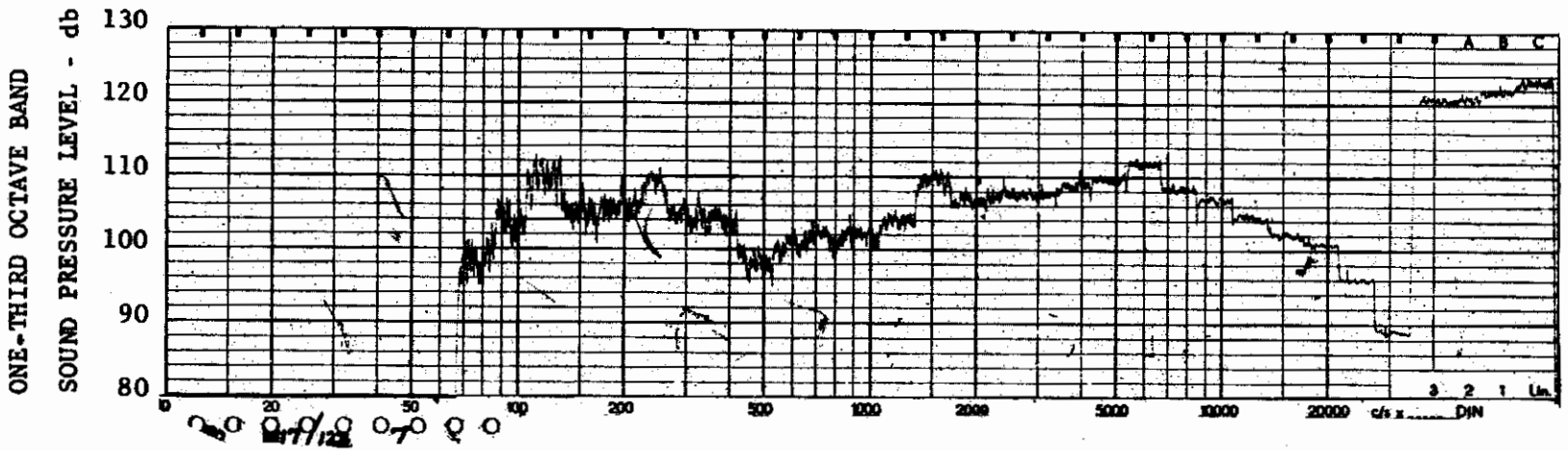

FIGURE 175 ONE-THIRD OCTAVE BAND SPECTRUM MODEL: FP 30

CHANNEL: 7 MACH NO.: 3.5 α: 0 ϕ: 0 Re_∞/FT.: 0.5×10^6 AEDC GROUP NO.: 17/123

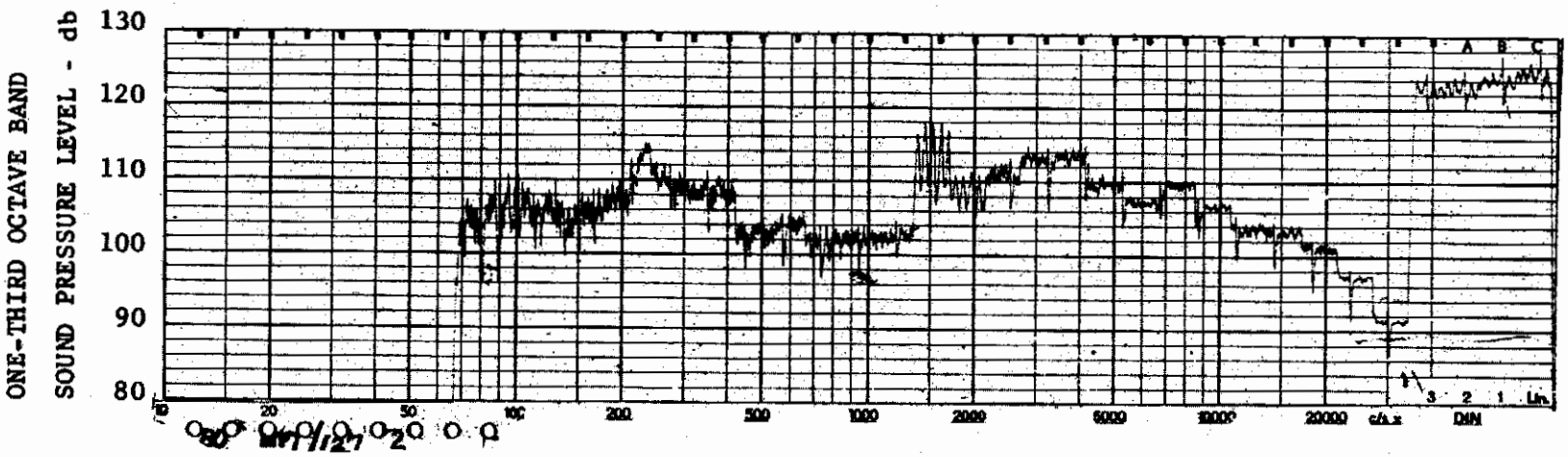

FIGURE 176 ONE-THIRD OCTAVE BAND SPECTRUM MODEL: FP 30

CHANNEL: 2 MACH NO.: 3.5 α: 0 ϕ: 0 Re_∞/FT.: 1.0×10^6 AEDC GROUP NO.: 17/127

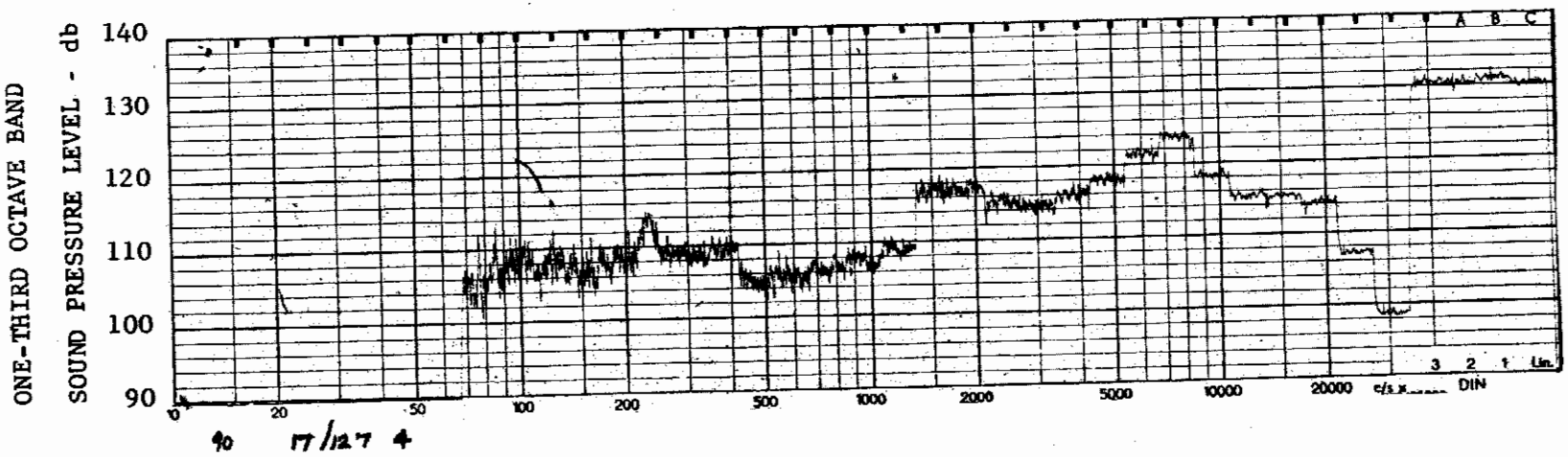

FIGURE 177 ONE-THIRD OCTAVE BAND SPECTRUM MODEL: FP 30

CHANNEL: 4 MACH NO.: 3.5 α: 0 ϕ: 0 Re_∞/FT.: 1.0×10^6 AEDC GROUP NO.: 17/127

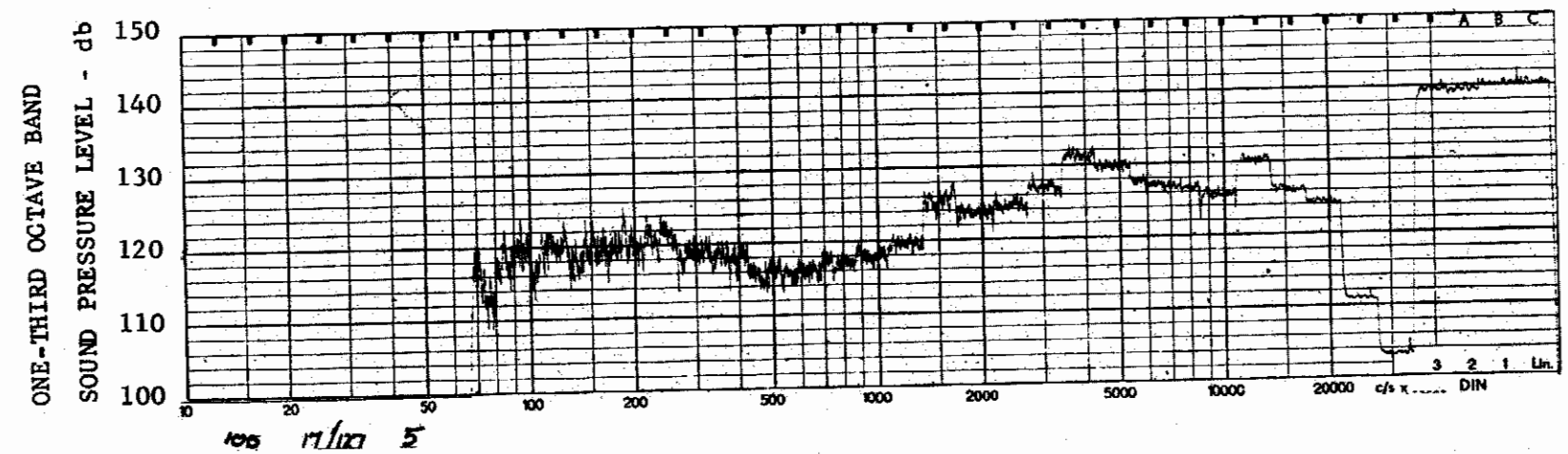

FIGURE 178 ONE-THIRD OCTAVE BAND SPECTRUM MODEL: FP 30

CHANNEL: 5 MACH NO.: 3.5 α: 0 ϕ: 0 Re_∞/FT.: 1.0×10^6 AEDC GROUP NO.: 17/127

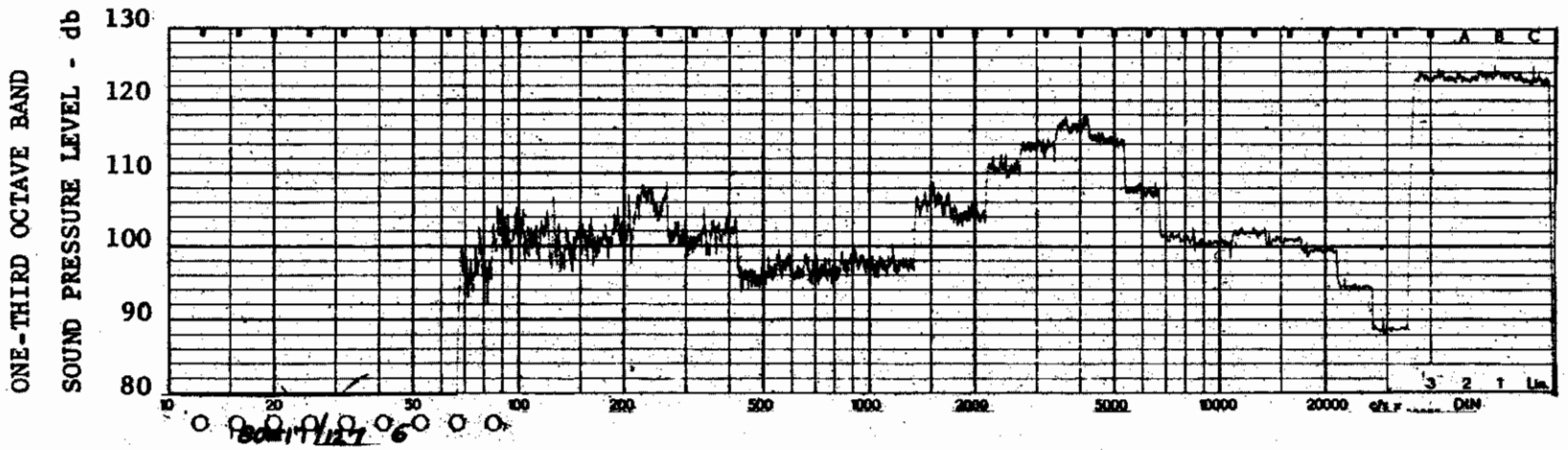

FIGURE 179 ONE-THIRD OCTAVE BAND SPECTRUM MODEL: FP 30

CHANNEL: 6 MACH NO.: 3.5 α: 0 ϕ: 0 Re_∞/FT.: 1.0×10^6 AEDC GROUP NO.: 17/127

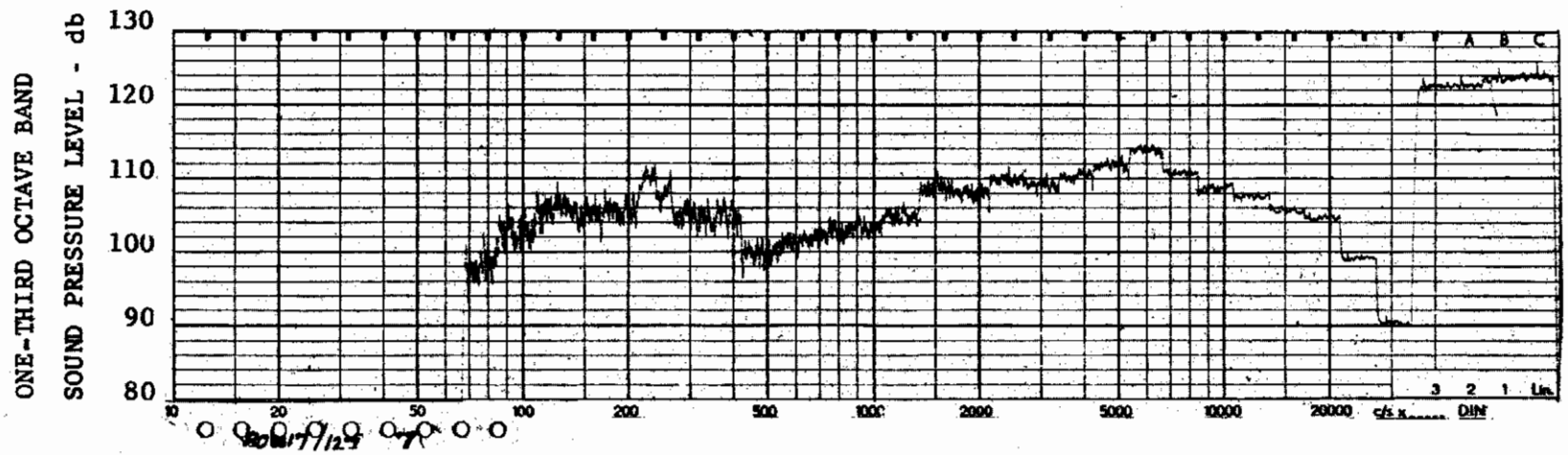

FIGURE 180 ONE-THIRD OCTAVE BAND SPECTRUM MODEL: FP 30

CHANNEL: 7 MACH NO.: 3.5 α: 0 ϕ: 0 Re_∞/FT.: 1.0×10^6 AEDC GROUP NO.: 17/127

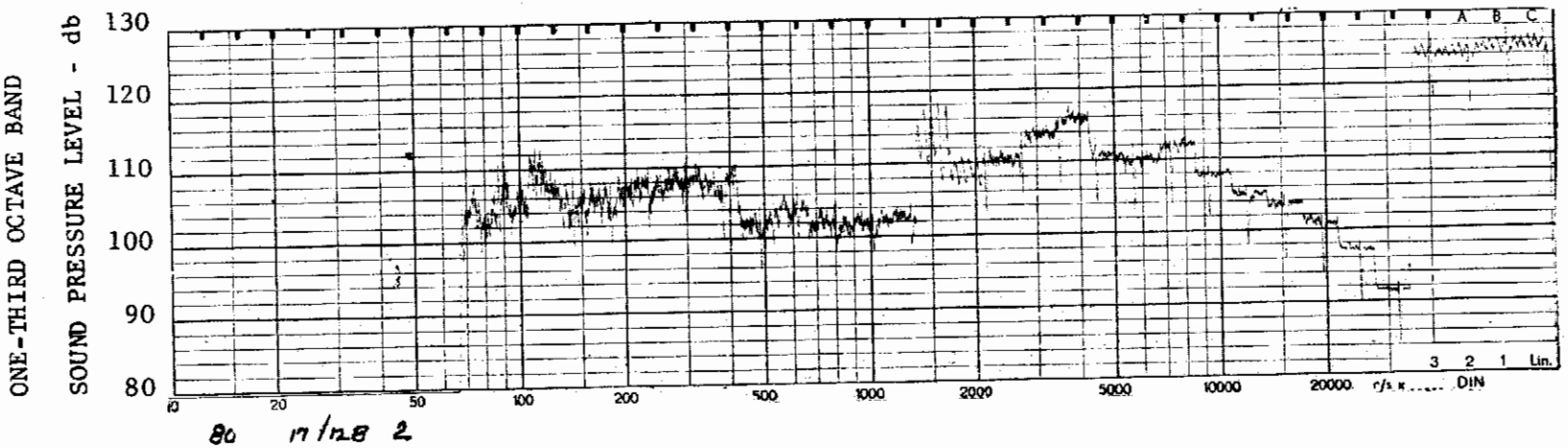

FIGURE 181 ONE-THIRD OCTAVE BAND SPECTRUM MODEL: FP 30

CHANNEL: 2 MACH NO.: 3.5 α: 5° ϕ: 0 Re_∞/FT.: 1.0×10^6 AEDC GROUP NO.: 17/128

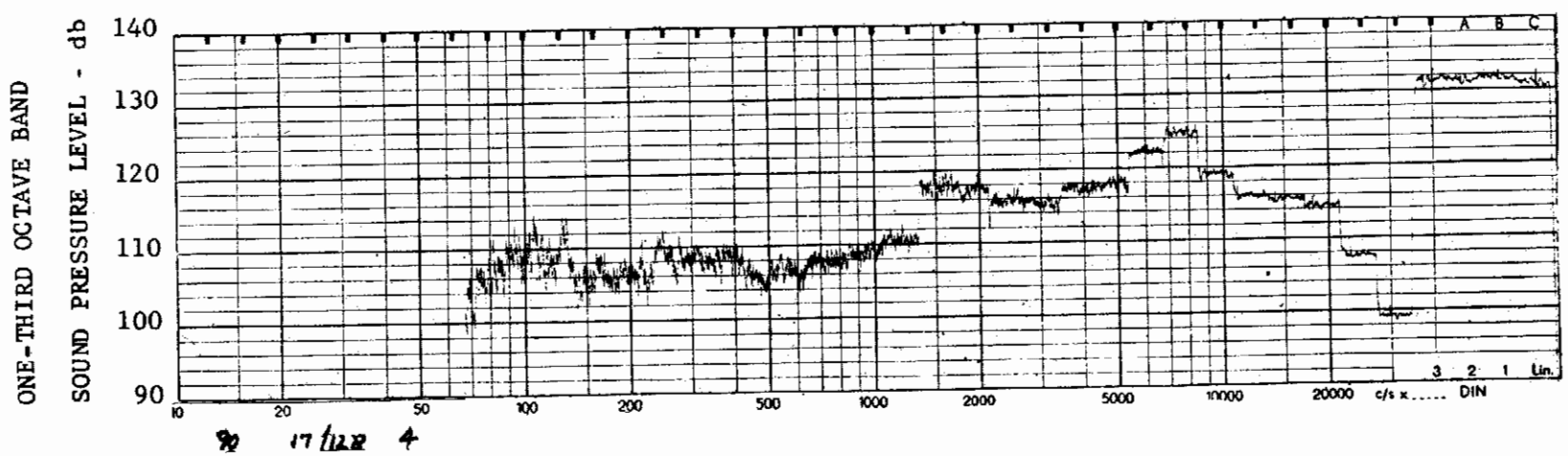

FIGURE 182 ONE-THIRD OCTAVE BAND SPECTRUM MODEL: FP 30

CHANNEL: 4 MACH NO.: 3.5 α: 5° ϕ: 0 Re_∞/FT.: 1.0×10^6 AEDC GROUP NO.: 17/128

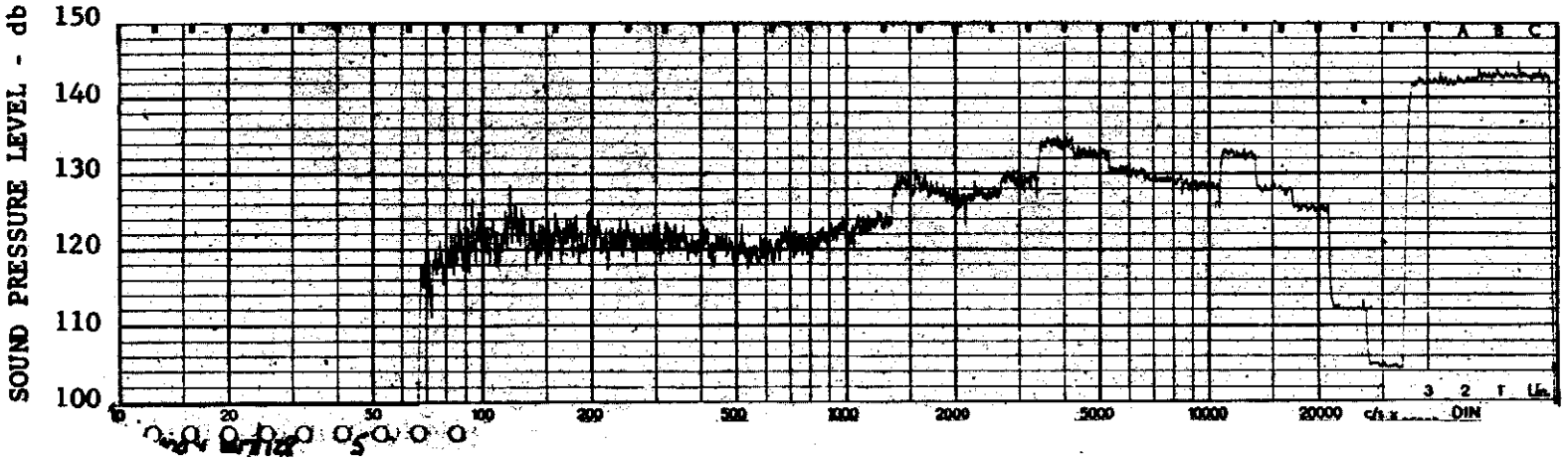

FIGURE 183 ONE-THIRD OCTAVE BAND SPECTRUM MODEL: FP 30

CHANNEL: 5 MACH NO.: 3.5 α: 5° ϕ: 0 Re_∞/FT.: 1.0×10^6 AEDC GROUP NO.: 17/128

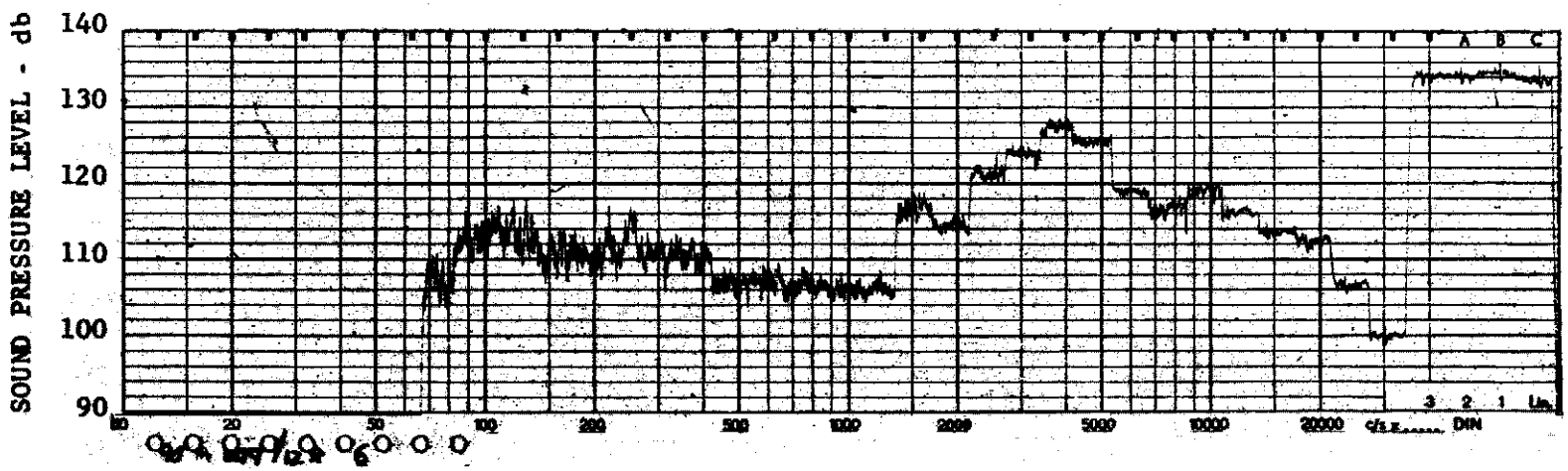

FIGURE 184 ONE-THIRD OCTAVE BAND SPECTRUM MODEL: FP 30

CHANNEL: 6 MACH NO.: 3.5 α: 5° ϕ: 0 Re_∞/FT.: 1.0×10^6 AEDC GROUP NO.: 17/128

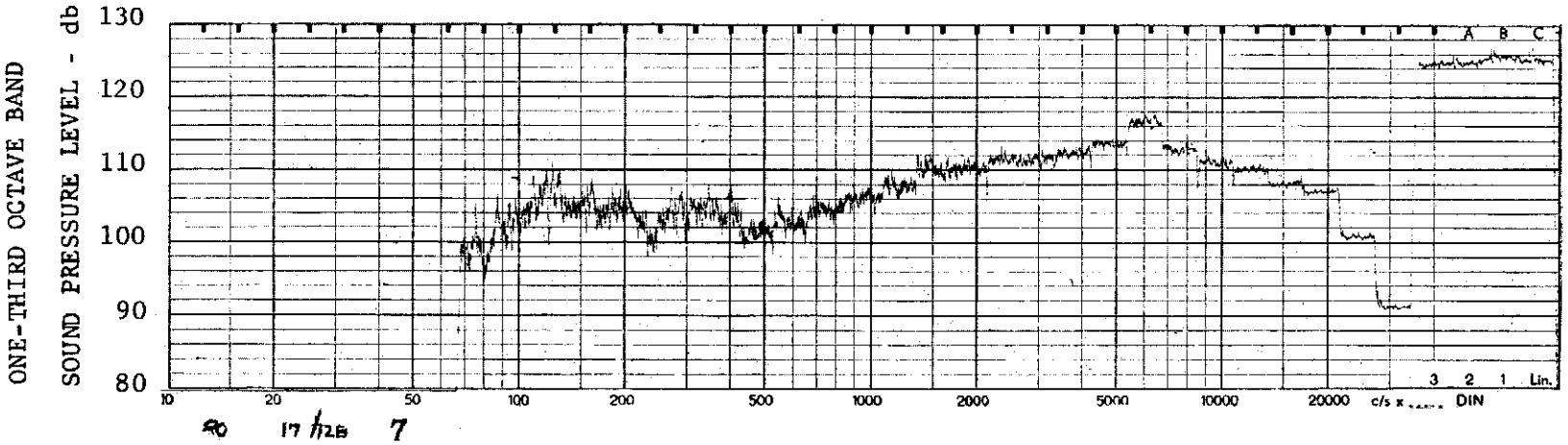

FIGURE 185 ONE-THIRD OCTAVE BAND SPECTRUM MODEL: FP 30

CHANNEL: 7 MACH NO.: 3.5 α: 5° ϕ: 0 Re_∞/FT.: 1.0×10^6 AEDC GROUP NO.: 17/128

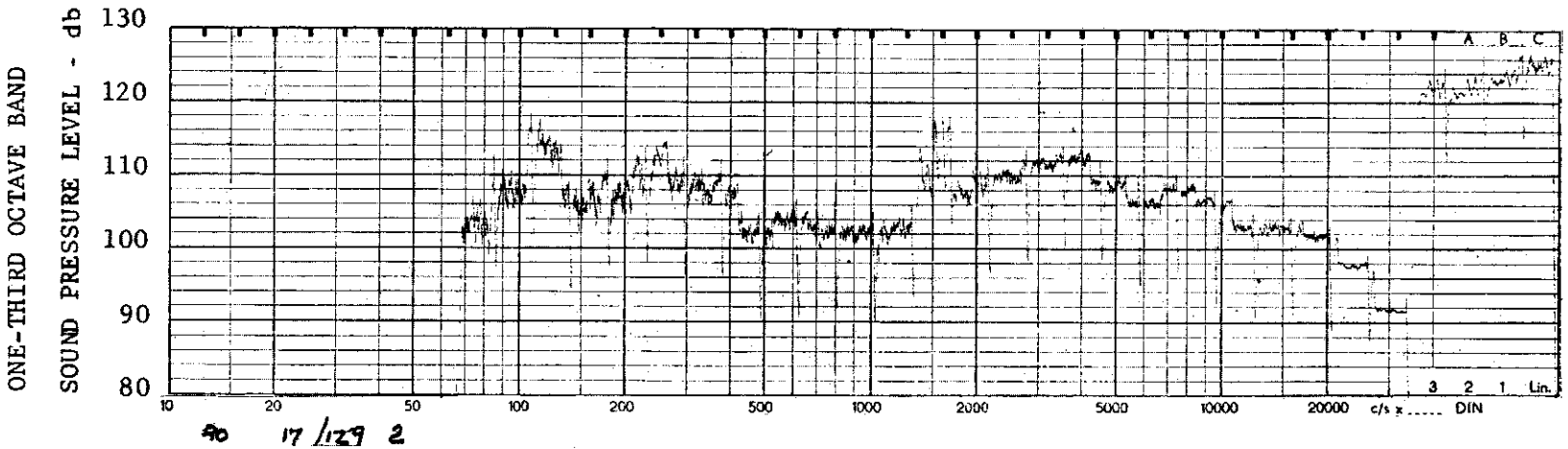

FIGURE 186 ONE-THIRD OCTAVE BAND SPECTRUM MODEL: FP 30

CHANNEL: 2 MACH NO.: 3.5 α: 15° ϕ: 0 Re_∞/FT.: 1.0×10^6 AEDC GROUP NO.: 17/129

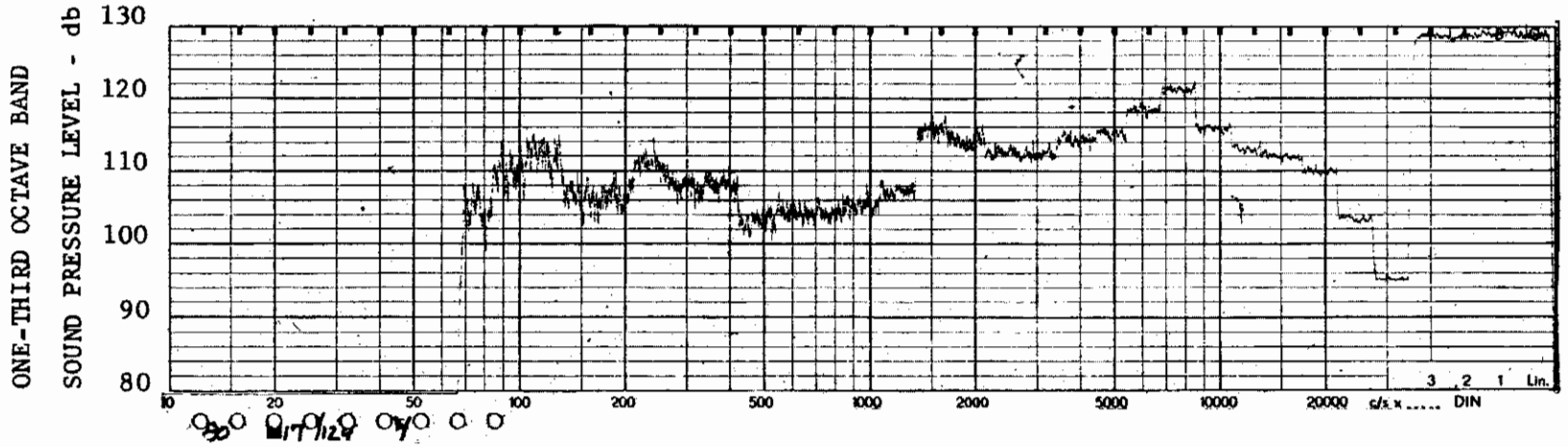

FIGURE 187 ONE-THIRD OCTAVE BAND SPECTRUM MODEL: FP 30

CHANNEL: 4 MACH NO.: 3.5 α: 15° ϕ: 0 Re_∞/FT.: 1.0×10^6 AEDC GROUP NO.: 17/129

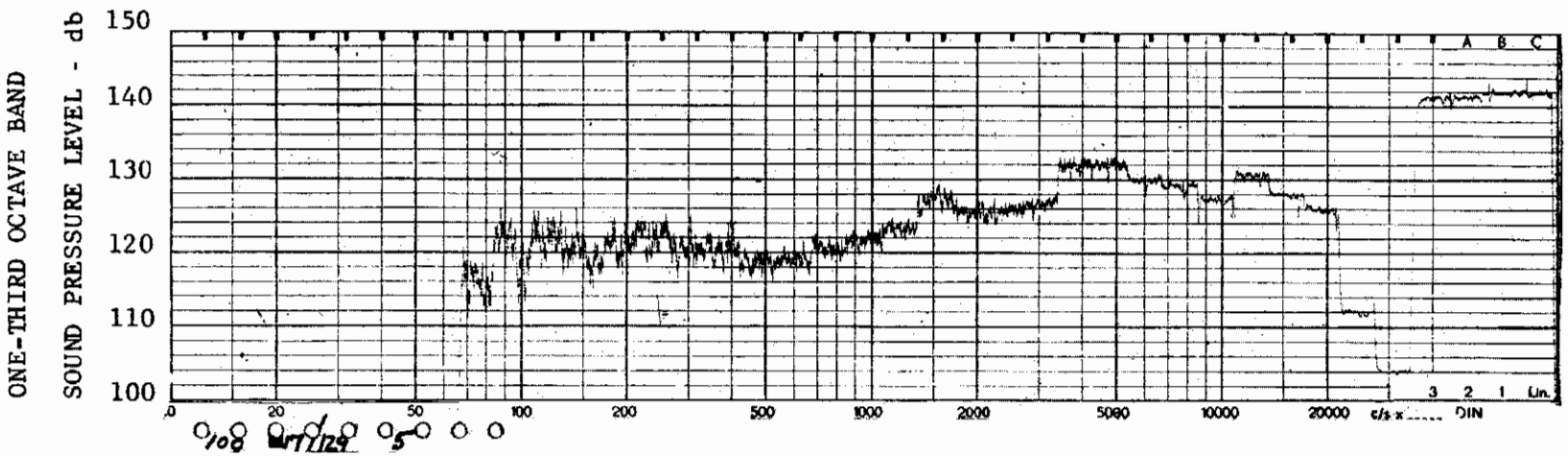

FIGURE 188 ONE-THIRD OCTAVE BAND SPECTRUM MODEL: FP 30

CHANNEL: 5 MACH NO.: 3.5 α: 15° ϕ: 0 Re_∞/FT.: 1.0×10^6 AEDC GROUP NO.: 17/129

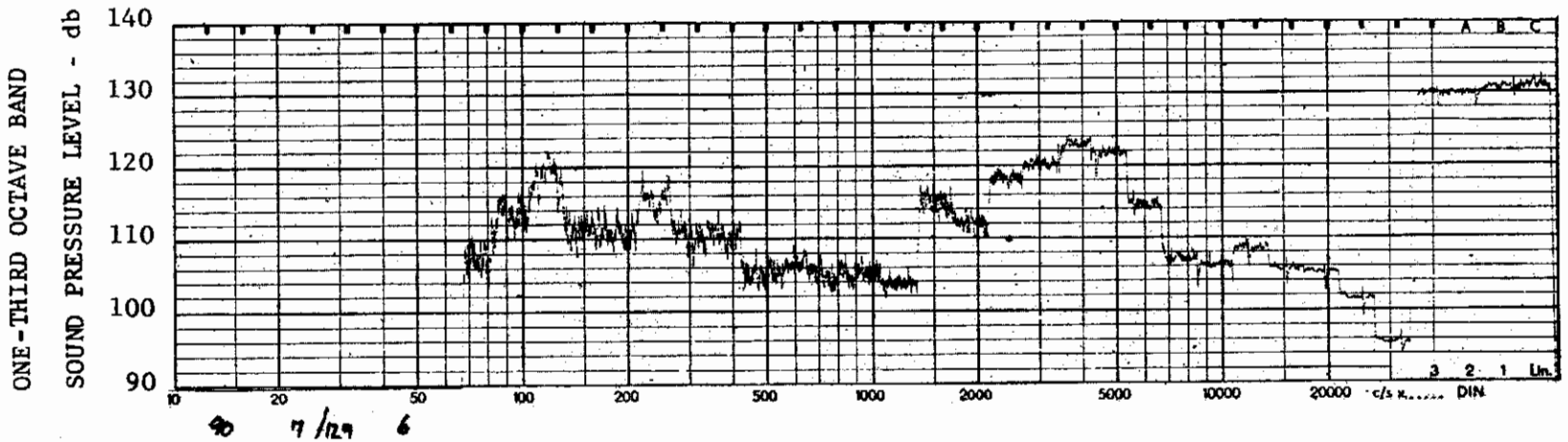

FIGURE 189 ONE-THIRD OCTAVE BAND SPECTRUM MODEL: FP 30

CHANNEL: 6 MACH NO.: 3.5 α: 15° ϕ: 0 Re_∞/FT.: 1.0×10^6 AEDC GROUP NO.: 17/129

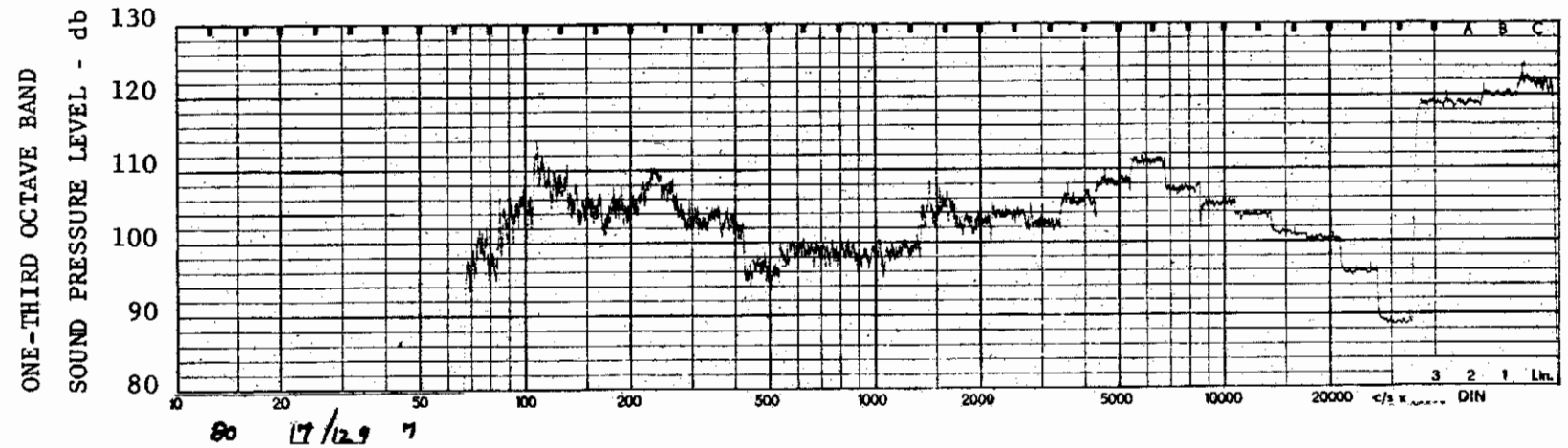

FIGURE 190 ONE-THIRD OCTAVE BAND SPECTRUM MODEL: FP 30

CHANNEL: 7 MACH NO.: 3.5 α: 15° ϕ: 0 Re_∞/FT.: 1.0×10^6 AEDC GROUP NO.: 17/129

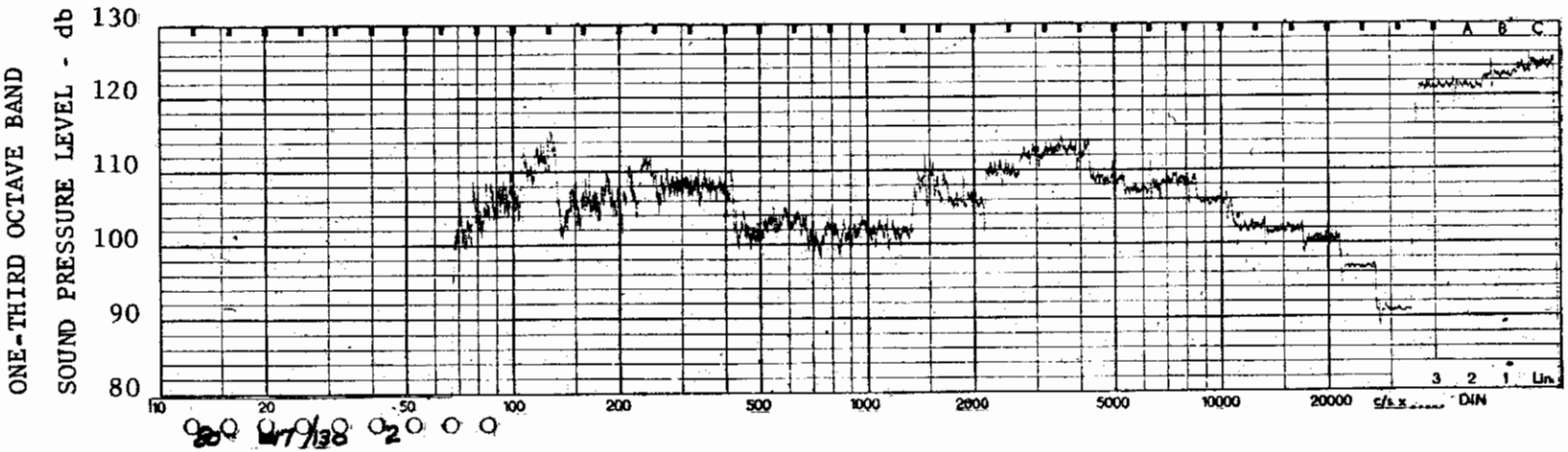

FIGURE 191 ONE-THIRD OCTAVE BAND SPECTRUM MODEL: FP 30

CHANNEL: 2 MACH NO.: 3.5 α: 0 ϕ: 0 Re_∞/FT.: 1.0×10^6 AEDC GROUP NO.: 17/130

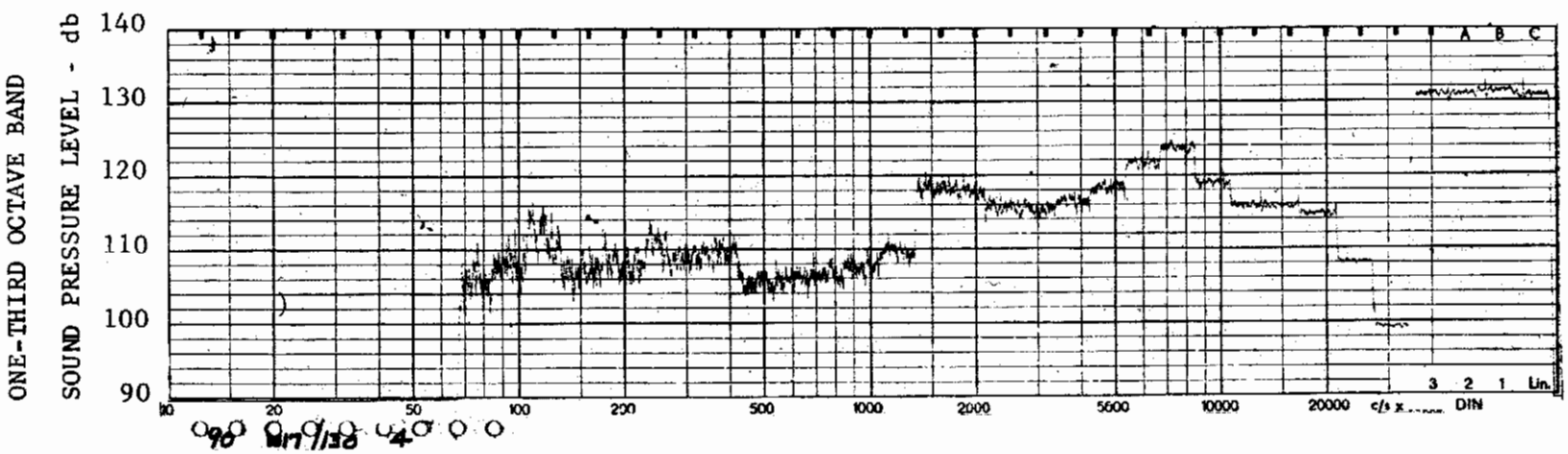

FIGURE 192 ONE-THIRD OCTAVE BAND SPECTRUM MODEL: FP 30

CHANNEL: 4 MACH NO.: 3.5 α: 0 ϕ: 0 Re_∞/FT.: 1.0×10^6 AEDC GROUP NO.: 17/130

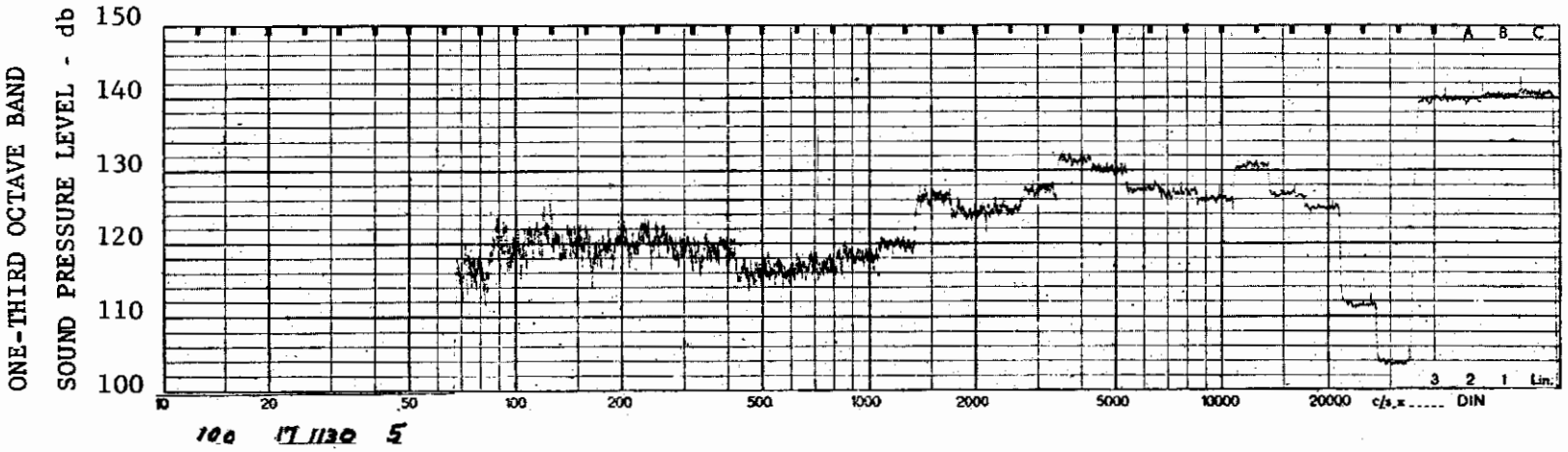

FIGURE 193 ONE-THIRD OCTAVE BAND SPECTRUM MODEL: FP 30

CHANNEL: 5 MACH NO.: 3.5 α: 0 ϕ: 0 Re_∞/FT.: 1.0×10^6 AEDC GROUP NO.: 17/130

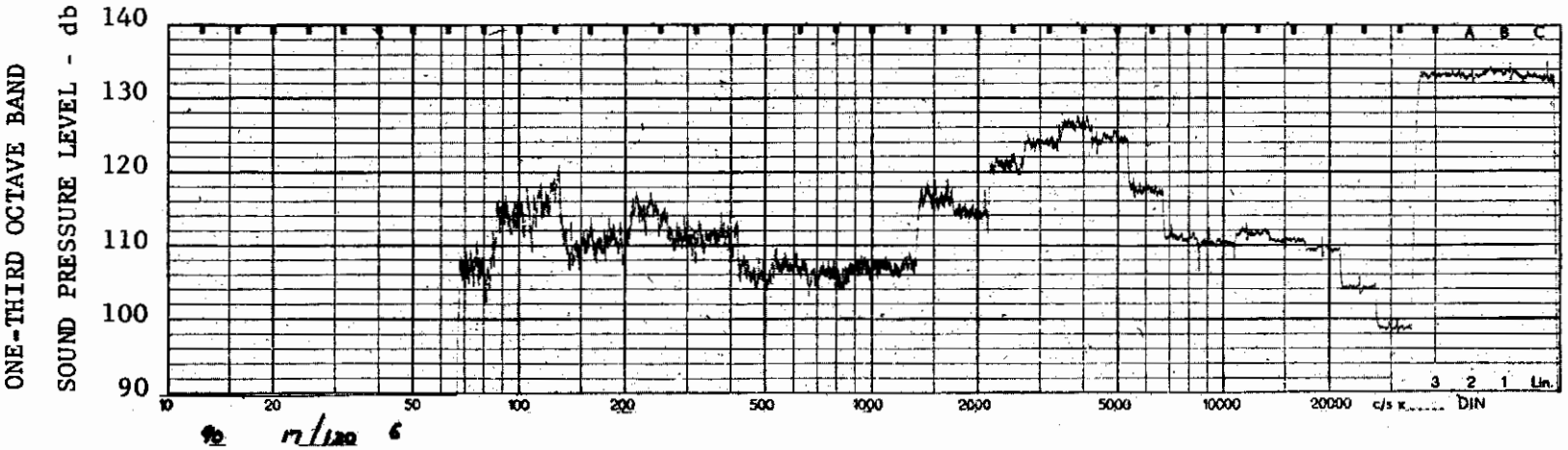

FIGURE 194 ONE-THIRD OCTAVE BAND SPECTRUM MODEL: FP 30

CHANNEL: 6 MACH NO.: 3.5 α: 0 ϕ: 0 Re_∞/FT.: 1.0×10^6 AEDC GROUP NO.: 17/130

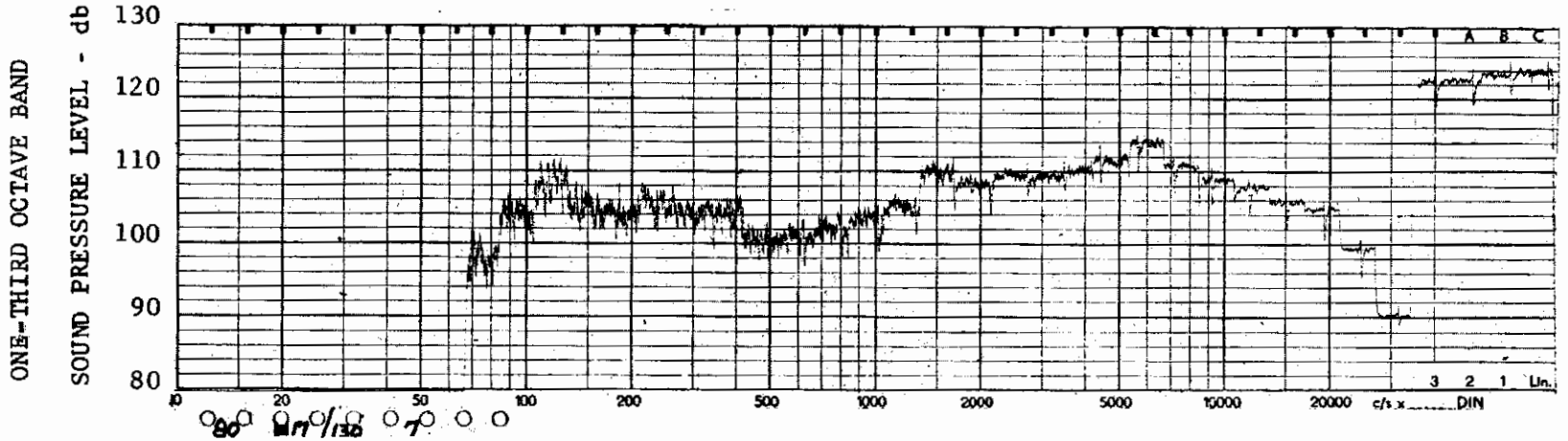

FIGURE 195 ONE-THIRD OCTAVE BAND SPECTRUM MODEL: FP 30

CHANNEL: 7 MACH NO.: 3.5 α: 0 ϕ: 0 Re_∞/FT.: 1.0×10^6 AEDC GROUP NO.: 17/130

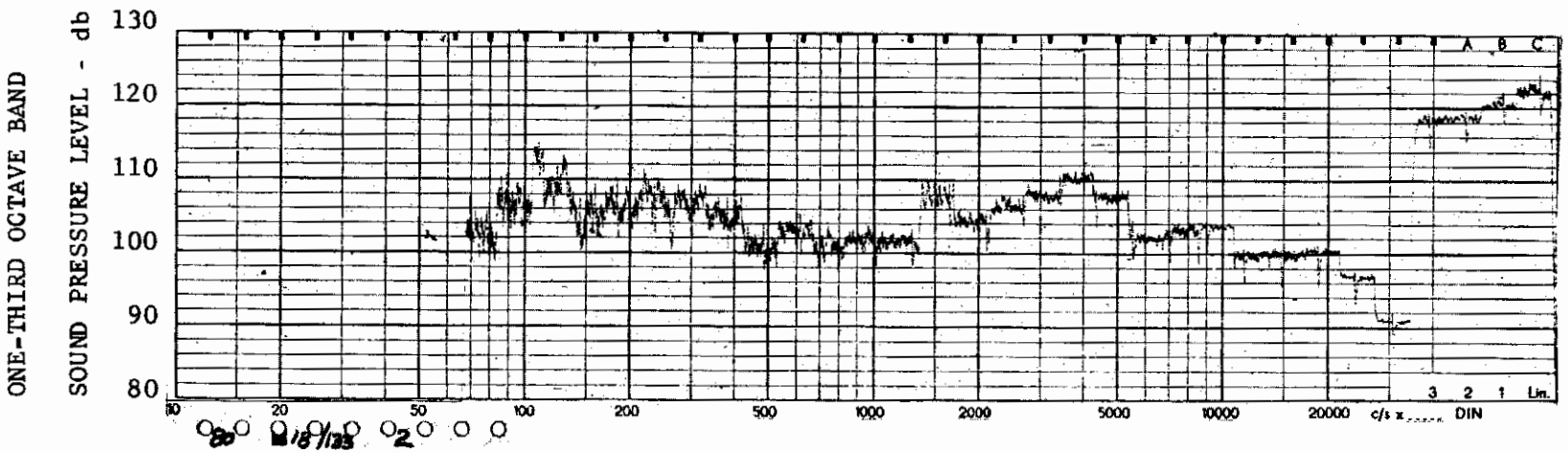

FIGURE 196 ONE-THIRD OCTAVE BAND SPECTRUM MODEL: FP 30

CHANNEL: 2 MACH NO.: 5 α: 0 ϕ: 0 Re_∞/FT.: 0.6×10^6 AEDC GROUP NO.: 18/133

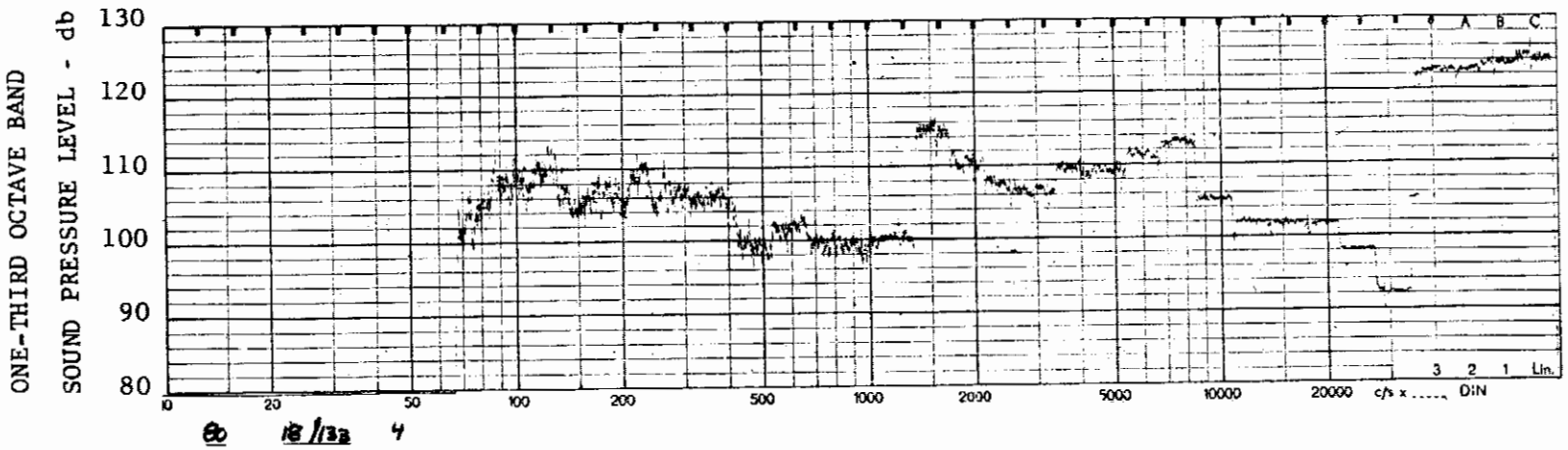

FIGURE 197 ONE-THIRD OCTAVE BAND SPECTRUM MODEL: FP 30

CHANNEL: 4 MACH NO.: 5 α: 0 ϕ: 0 Re_∞/FT.: 0.6×10^6 AEDC GROUP NO.: 18/133

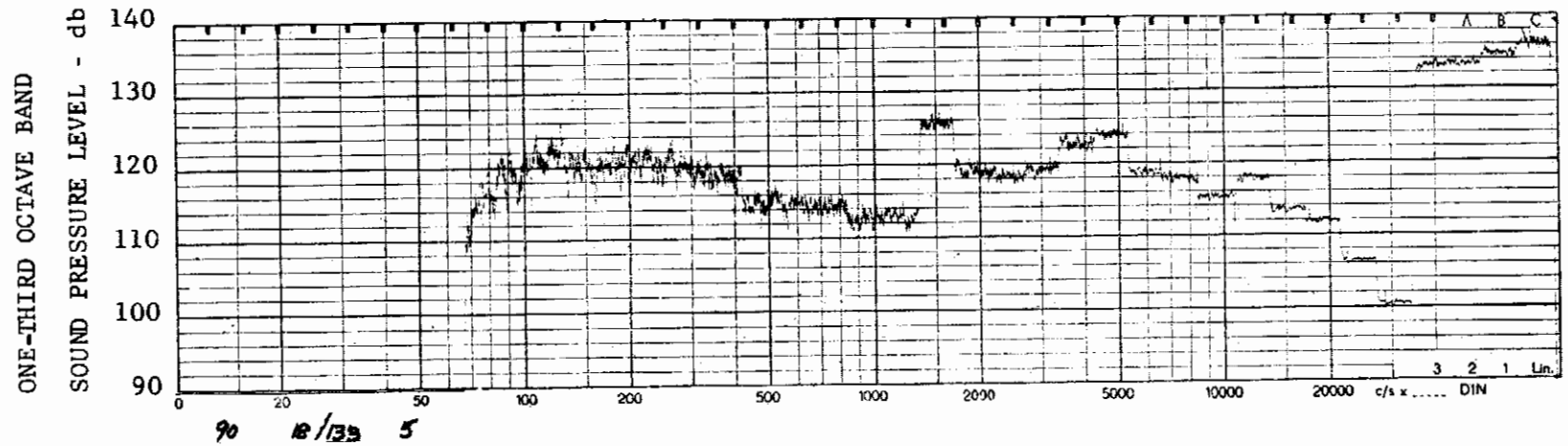

FIGURE 198 ONE-THIRD OCTAVE BAND SPECTRUM MODEL: FP 30

CHANNEL: 5 MACH NO.: 5 α: 0 ϕ: 0 Re_∞/FT.: 0.6×10^6 AEDC GROUP NO.: 18/133

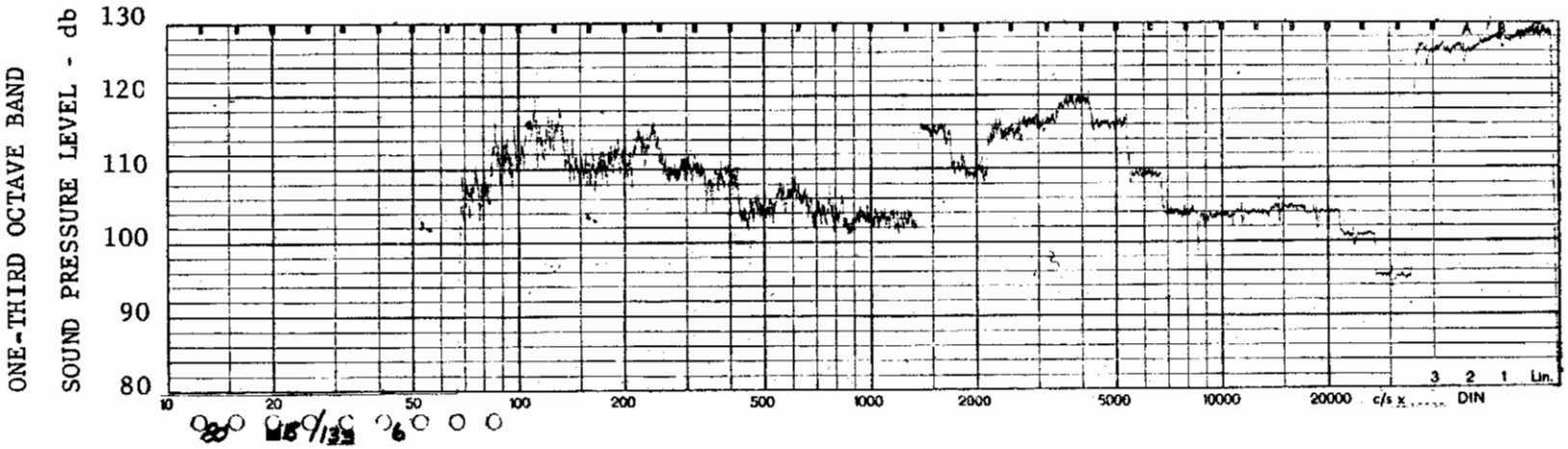

FIGURE 199 ONE-THIRD OCTAVE BAND SPECTRUM MODEL: FP 30

CHANNEL: 6 MACH NO.: 5 α: 0 ϕ: 0 Re_∞/FT.: 0.6×10^6 AEDC GROUP NO.: 18/133

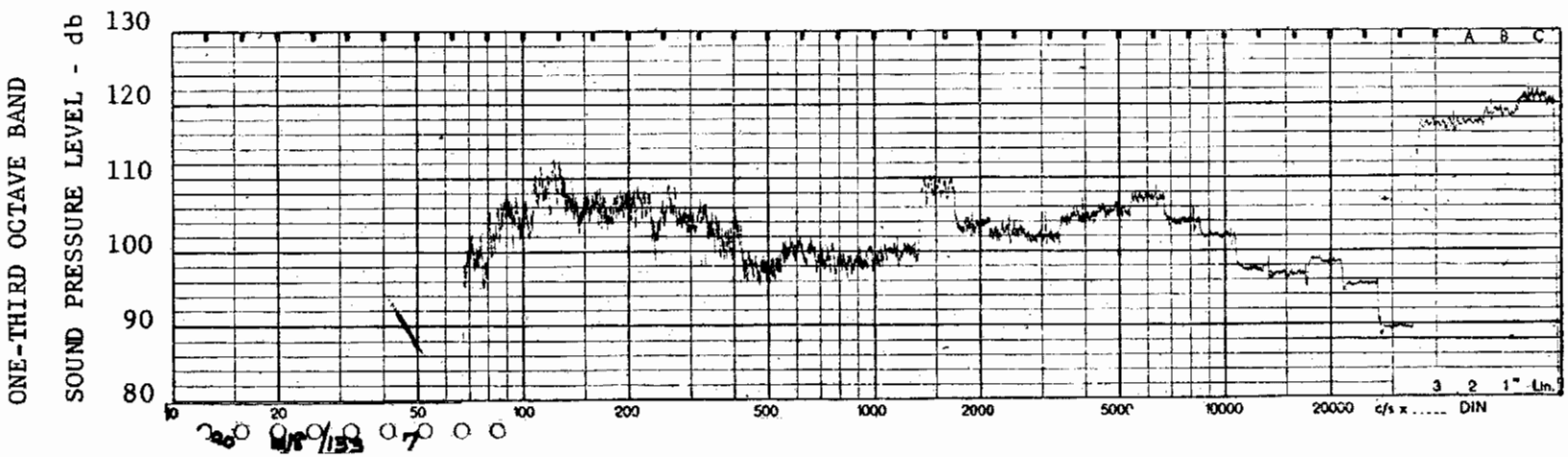

FIGURE 200 ONE-THIRD OCTAVE BAND SPECTRUM MODEL: FP 30

CHANNEL: 7 MACH NO.: 5 α: 0 ϕ: 0 Re_∞/FT.: 0.6×10^6 AEDC GROUP NO.: 18/133

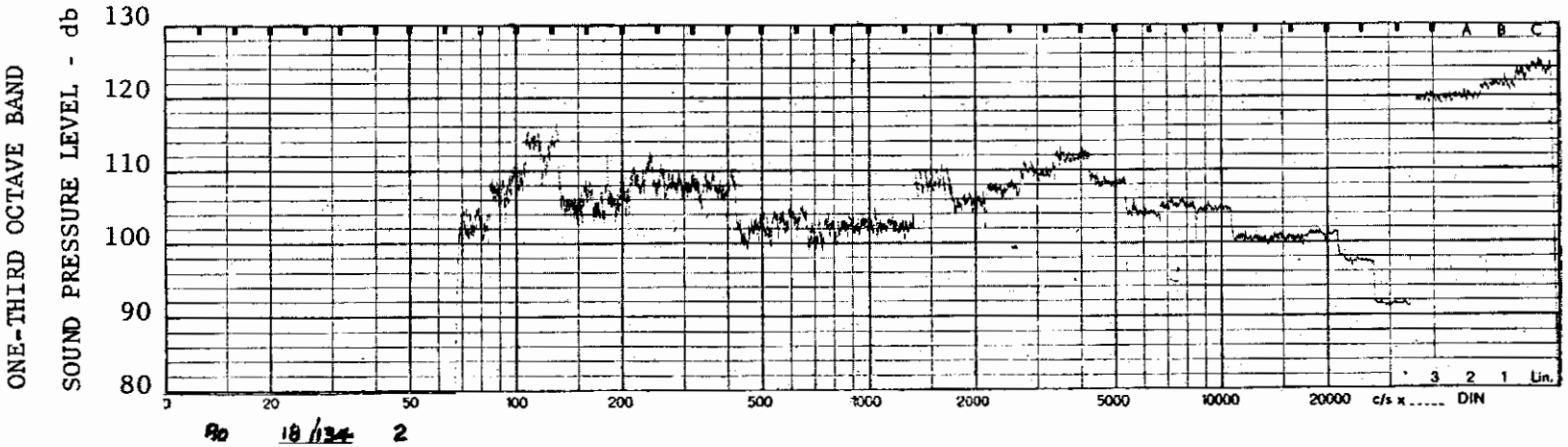

FIGURE 201 ONE-THIRD OCTAVE BAND SPECTRUM MODEL: FP 30

CHANNEL: 2 MACH NO.: 5 α: 0 ϕ: 0 Re_∞/FT.: 1.0×10^6 AEDC GROUP NO.: 18/134

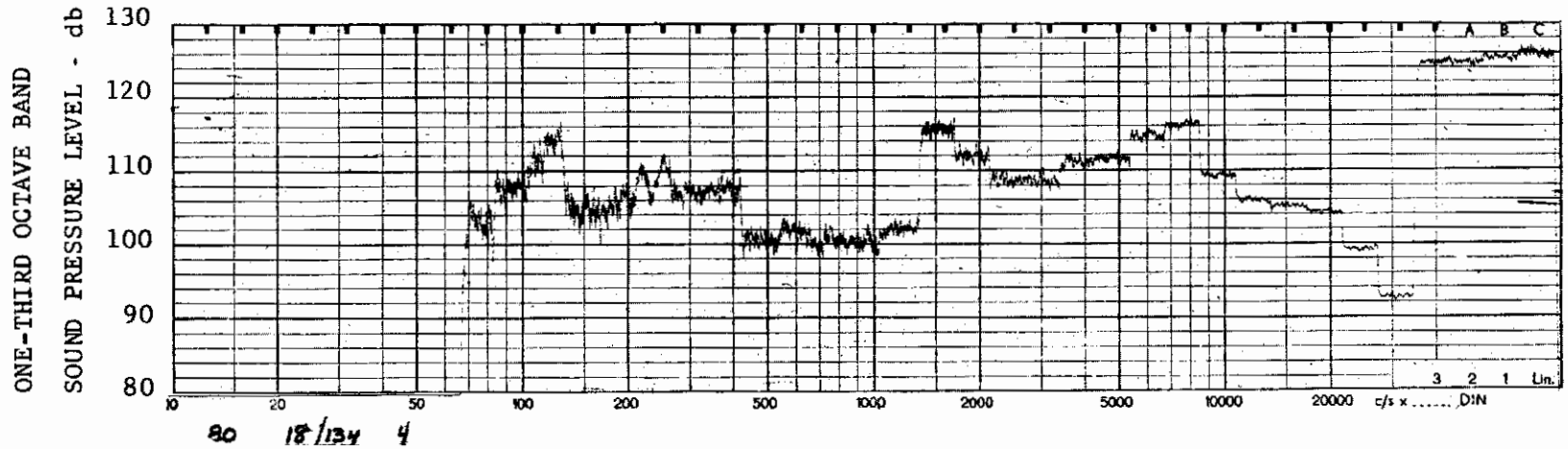

FIGURE 202 ONE-THIRD OCTAVE BAND SPECTRUM MODEL: FP 30

CHANNEL: 4 MACH NO.: 5 α: 0 ϕ: 0 Re_∞/FT.: 1.0×10^6 AEDC GROUP NO.: 18/134

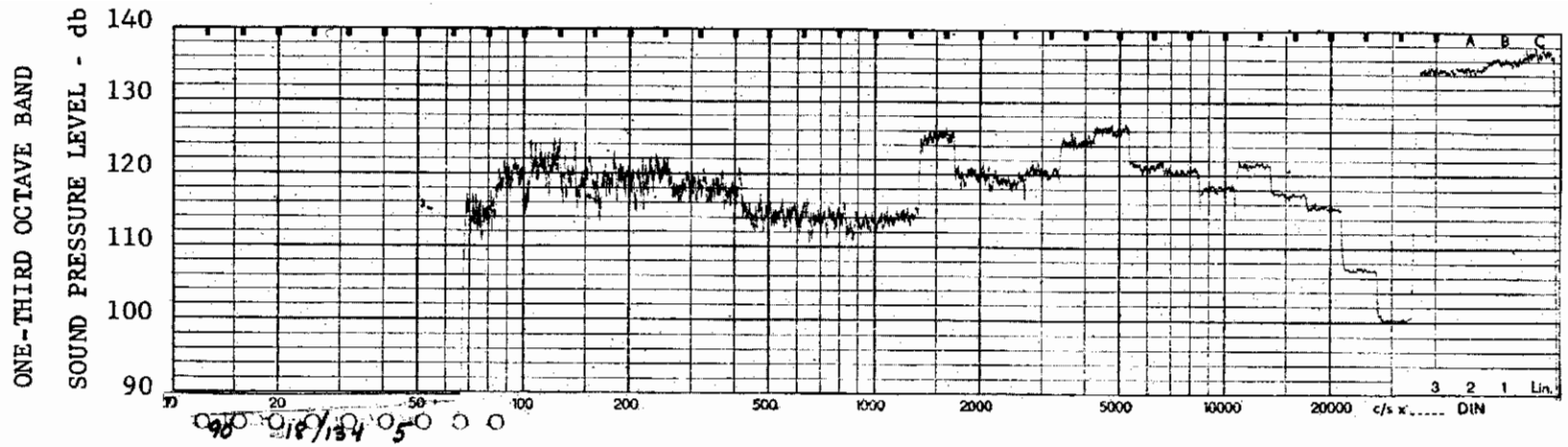

FIGURE 203 ONE-THIRD OCTAVE BAND SPECTRUM MODEL: FP 30

CHANNEL: 5 MACH NO.: 5 α: 0 ϕ: 0 Re_∞/FT.: 1.0×10^6 AEDC GROUP NO.: 18/134

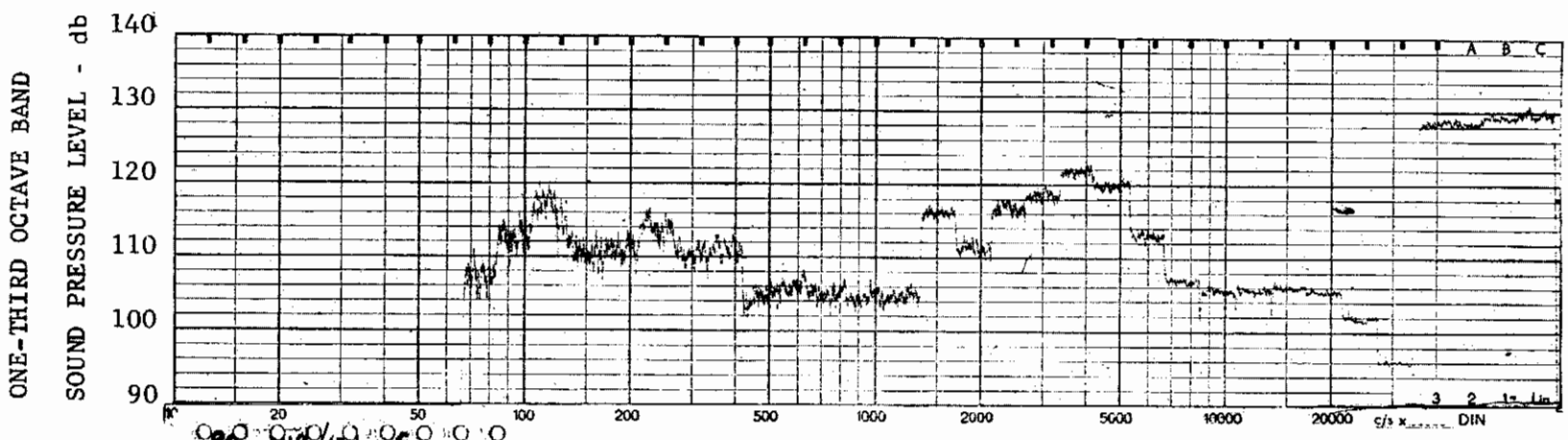

FIGURE 204 ONE-THIRD OCTAVE BAND SPECTRUM MODEL: FP 30

CHANNEL: 6 MACH NO.: 5 α: 0 ϕ: 0 Re_∞/FT.: 1.0×10^6 AEDC GROUP NO.: 18/134

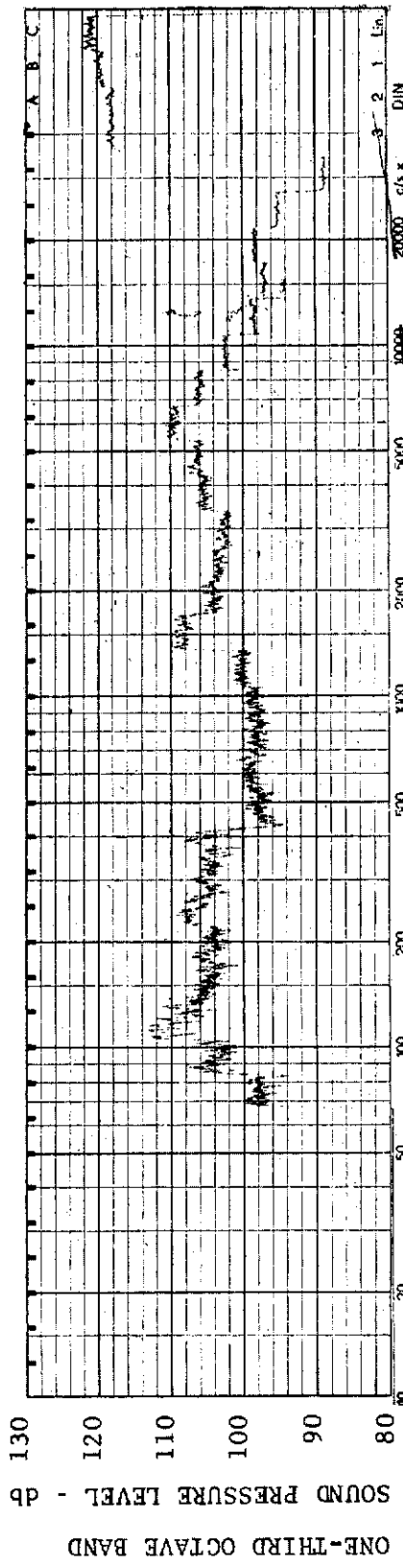

FIGURE 205 ONE-THIRD OCTAVE BAND SPECTRUM MODEL: FP 30

CHANNEL: 7 MACH NO.: 5 α: 0 ϕ: 0 Re_∞/FT.: 1.0×10^6 AEDC GROUP NO.: 18/134

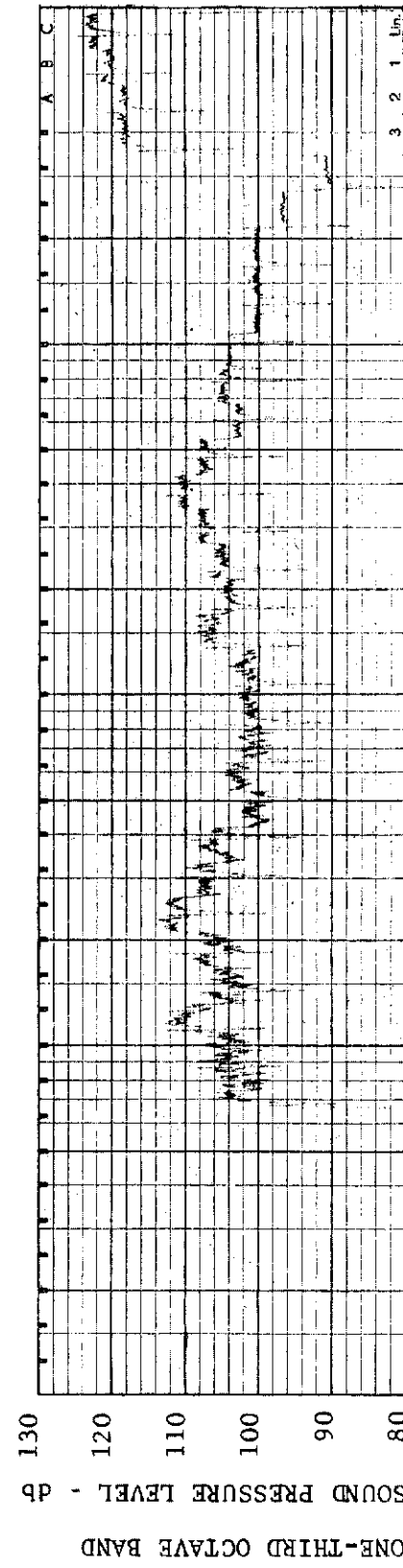

FIGURE 206 ONE-THIRD OCTAVE BAND SPECTRUM MODEL: FP 30

CHANNEL: 2 MACH NO.: 5 α: 5° ϕ: 0 Re_∞/FT.: 1.0×10^6 AEDC GROUP NO.: 18/135

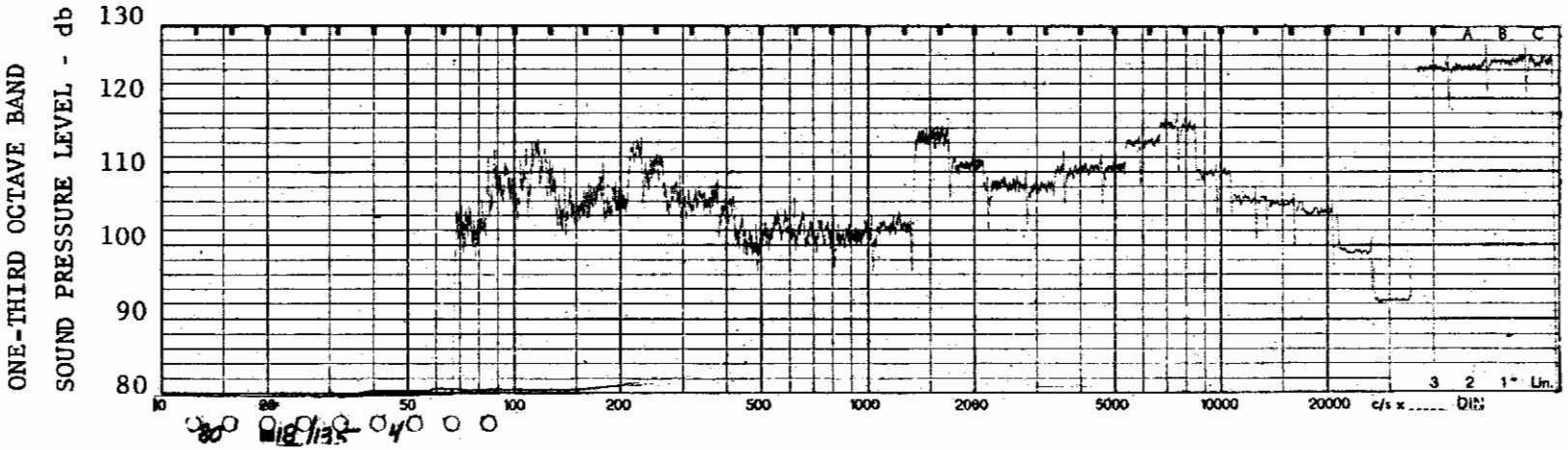

FIGURE 207 ONE-THIRD OCTAVE BAND SPECTRUM MODEL: FP 30

CHANNEL: 4 MACH NO.: 5 α: 5° ϕ: 0 Re_∞/FT.: 1.0×10^6 AEDC GROUP NO.: 18/135

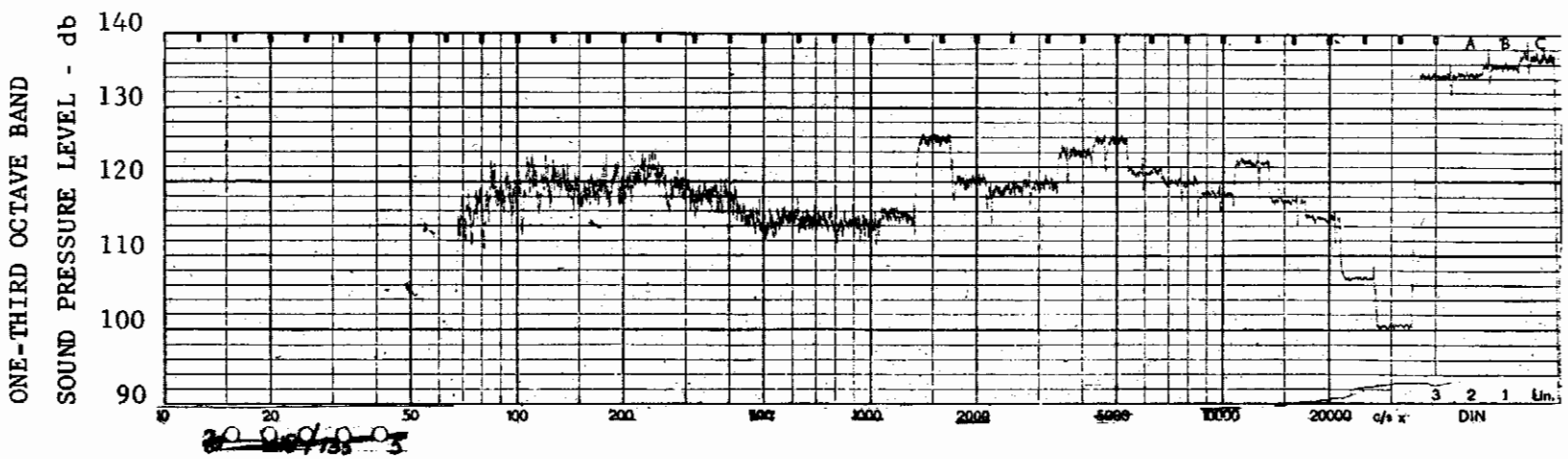

FIGURE 208 ONE-THIRD OCTAVE BAND SPECTRUM MODEL: FP 30

CHANNEL: 5 MACH NO.: 5 α: 5° ϕ: 0 Re_∞/FT.: 1.0×10^6 AEDC GROUP NO.: 18/135

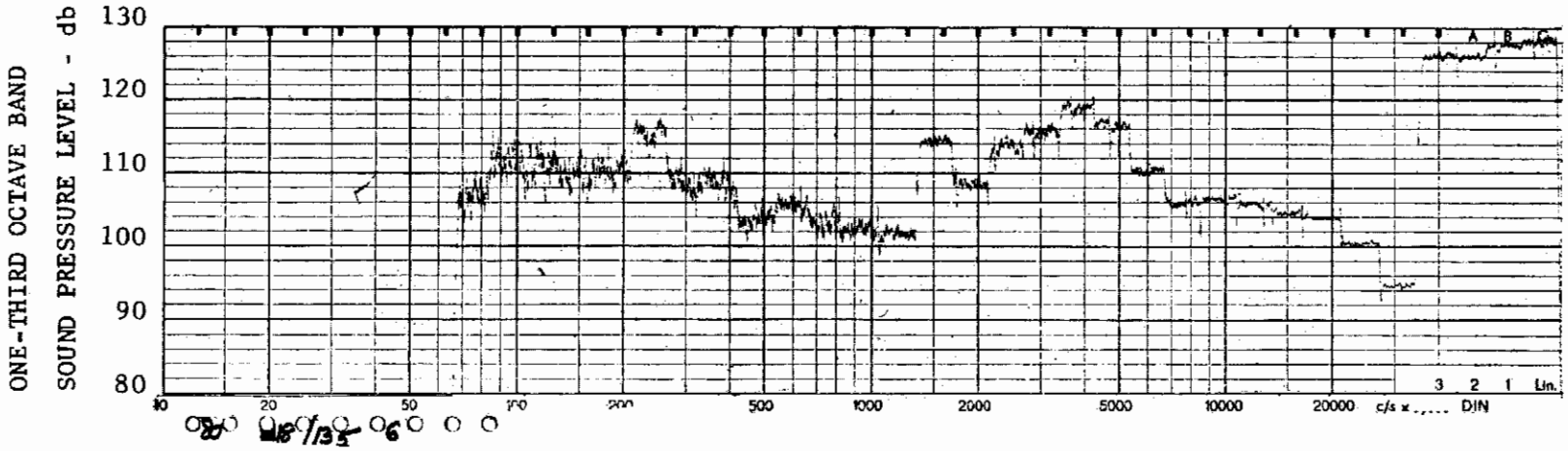

FIGURE 209 ONE-THIRD OCTAVE BAND SPECTRUM MODEL: FP 30

CHANNEL: 6 MACH NO.: 5 α: 5° ϕ: 0 Re_∞/FT.: 1.0×10^6 AEDC GROUP NO.: 18/135

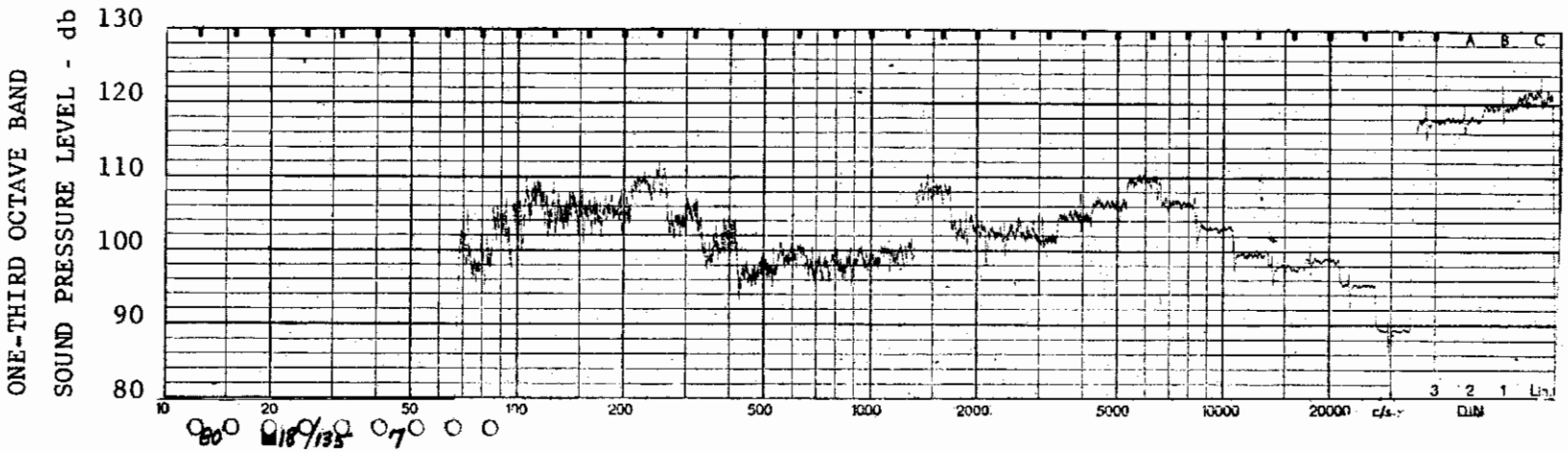

FIGURE 210 ONE-THIRD OCTAVE BAND SPECTRUM MODEL: FP 30

CHANNEL: 7 MACH NO.: 5 α: 5° ϕ: 0 Re_∞/FT.: 1.0×10^6 AEDC GROUP NO.: 18/135

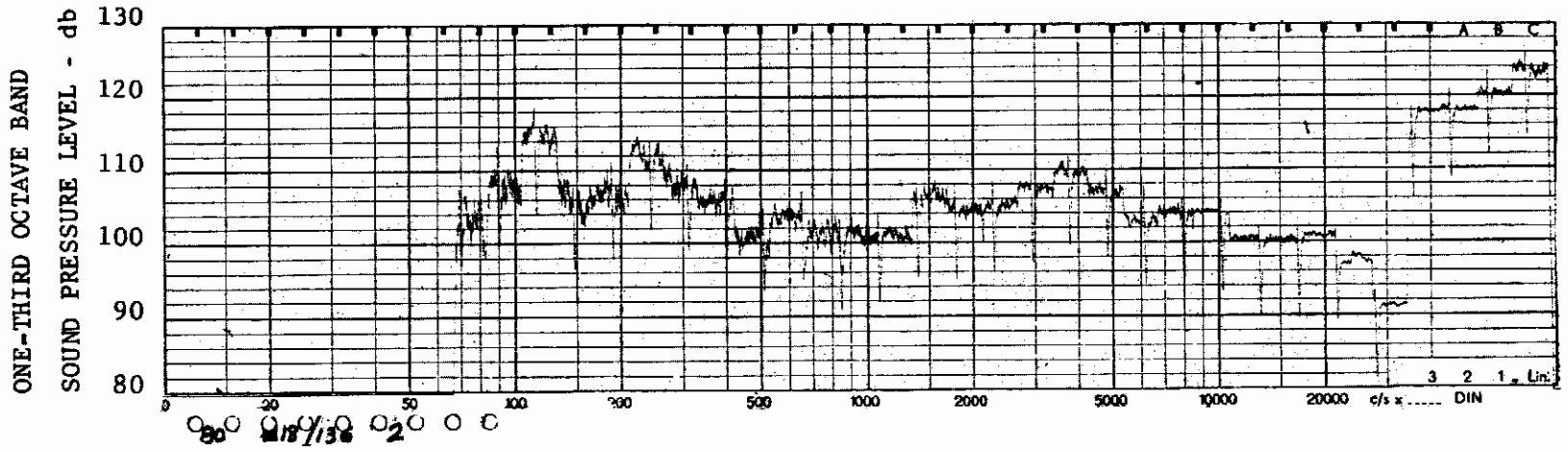

FIGURE 211 ONE-THIRD OCTAVE BAND SPECTRUM MODEL: FP 30

CHANNEL: 2 MACH NO.: 5 α: 15° ϕ: 0 Re_∞/FT.: 1.0×10^6 AEDC GROUP NO.: 18/136

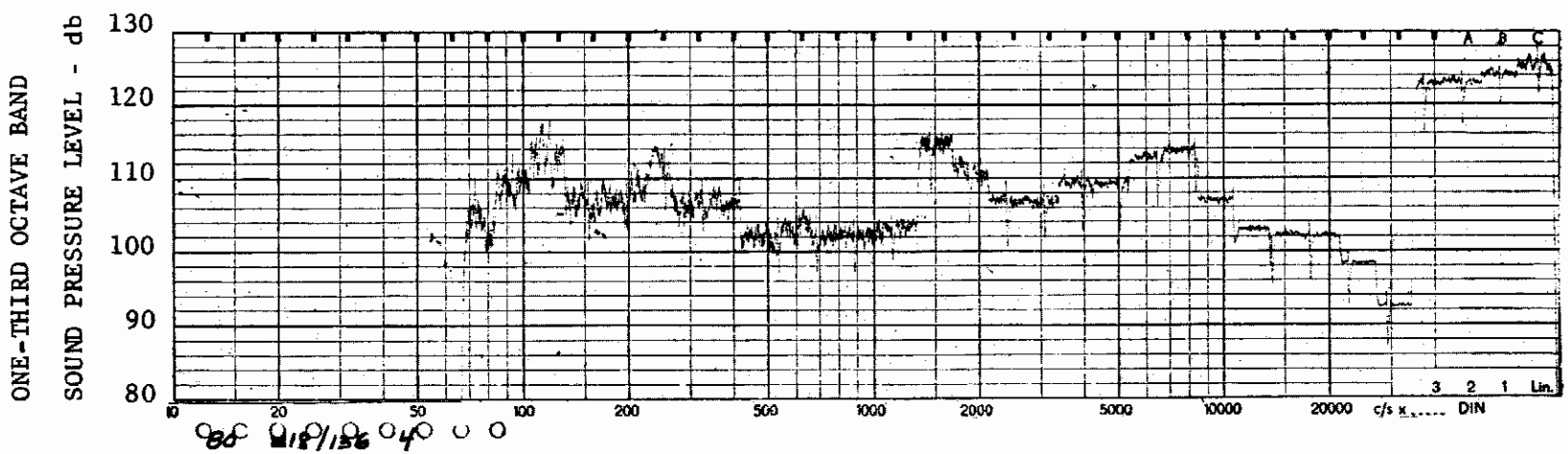

FIGURE 212 ONE-THIRD OCTAVE BAND SPECTRUM MODEL: FP 30

CHANNEL: 4 MACH NO.: 5 α: 15° ϕ: 0 Re_∞/FT.: 1.0×10^6 AEDC GROUP NO.: 18/136

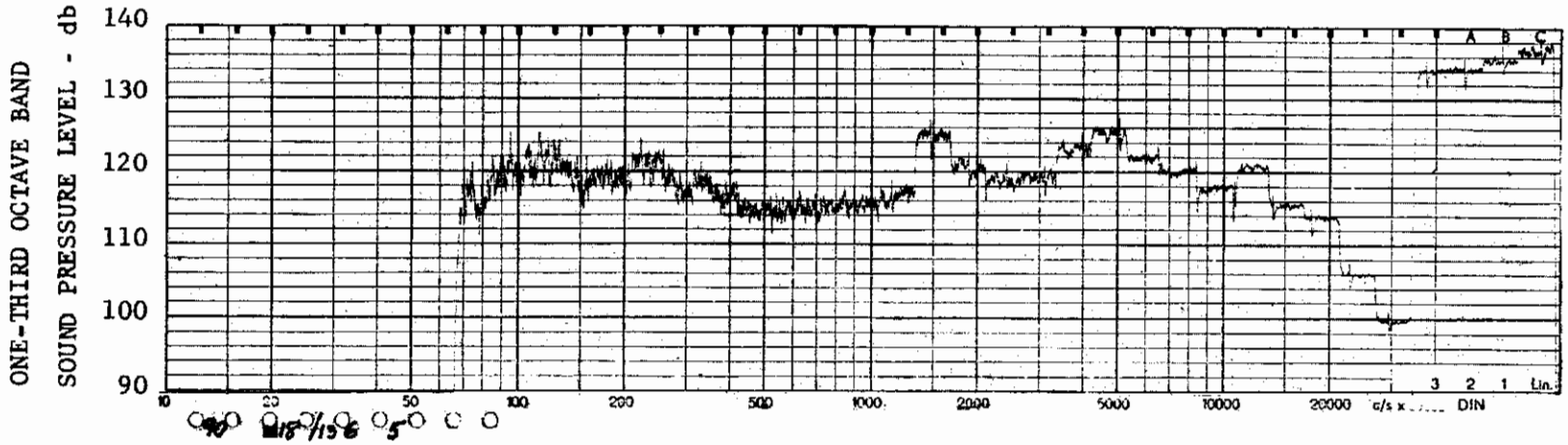

FIGURE 213 ONE-THIRD OCTAVE BAND SPECTRUM MODEL: FP 30

CHANNEL: 5 MACH NO.: 5 α: 15° ϕ: 0 Re_∞/FT.: 1.0×10^6 AEDC GROUP NO.: 18/136

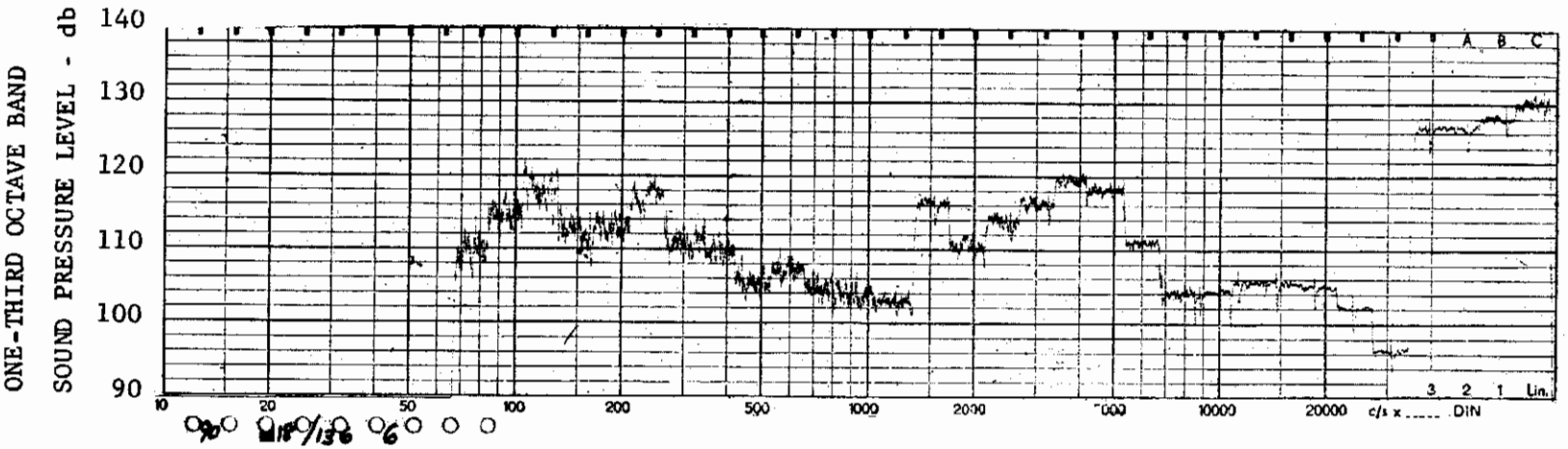

FIGURE 214 ONE-THIRD OCTAVE BAND SPECTRUM MODEL: FP 30

CHANNEL: 6 MACH NO.: 5 α: 15° ϕ: 0 Re_∞/FT.: 1.0×10^6 AEDC GROUP NO.: 18/136

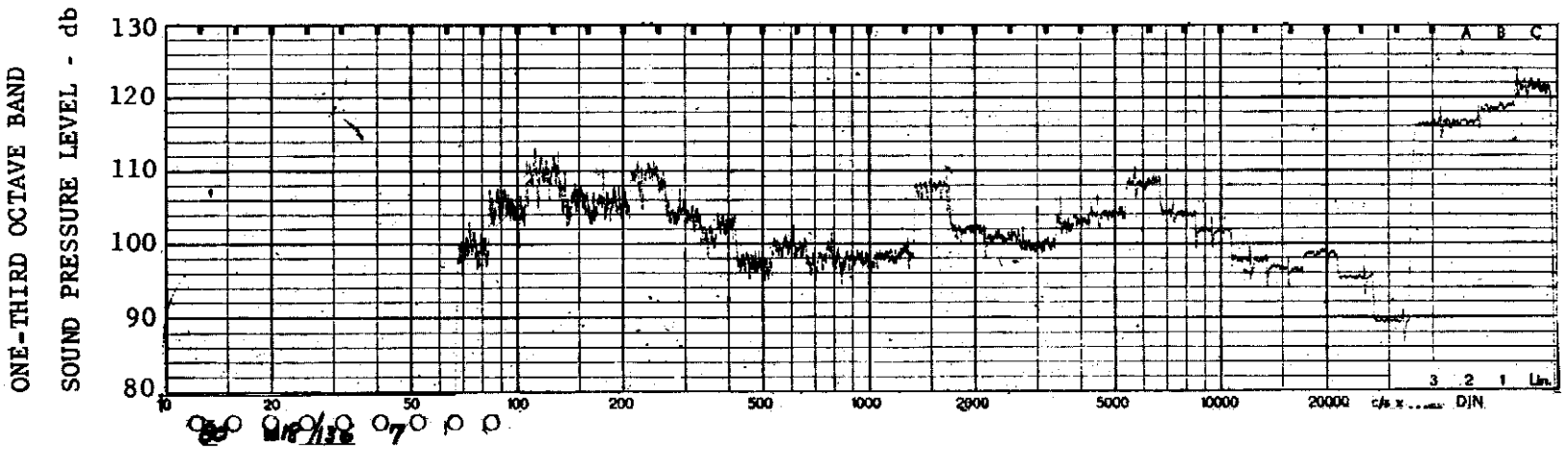

FIGURE 215 ONE-THIRD OCTAVE BAND SPECTRUM MODEL: FP 30

CHANNEL: 7 MACH NO.: 5 α: 15° ϕ: 0 Re_∞/FT.: 1.0×10^6 AEDC GROUP NO.: 18/136

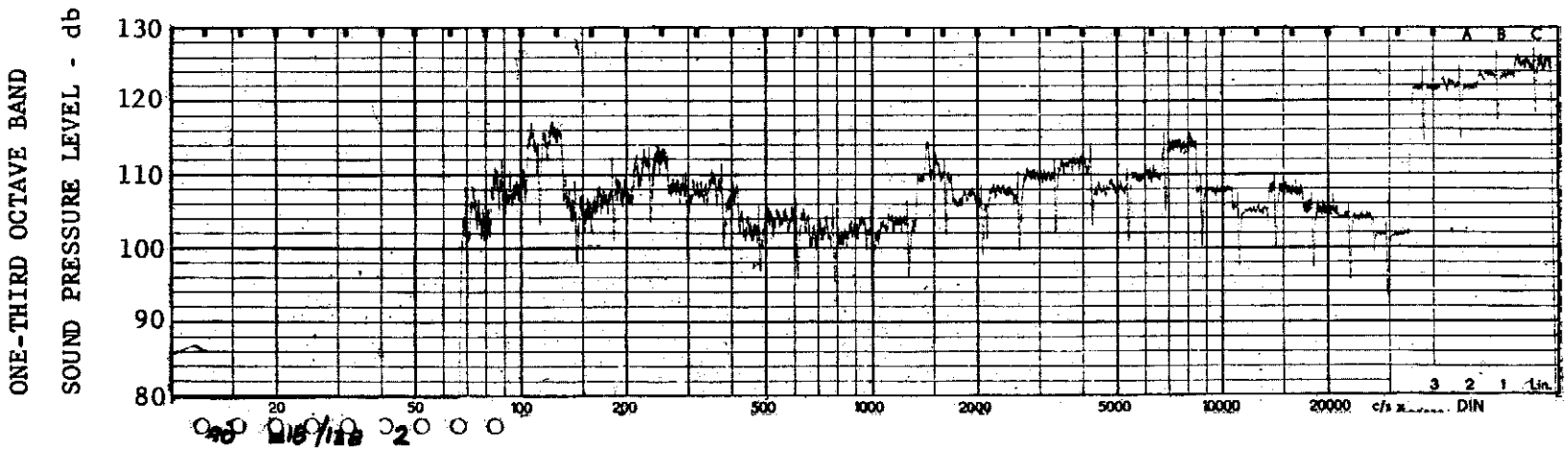

FIGURE 216 ONE-THIRD OCTAVE BAND SPECTRUM MODEL: FP 30

CHANNEL: 2 MACH NO.: 5 α: 0 ϕ: 0 Re_∞/FT.: 1.0×10^6 AEDC GROUP NO.: 18/138

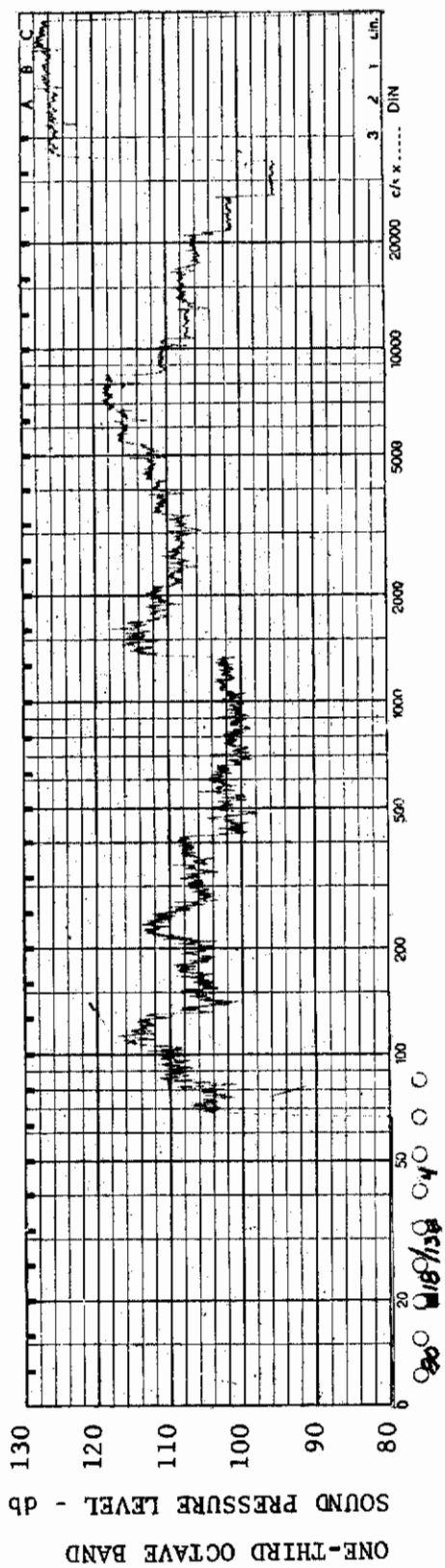

FIGURE 217 ONE-THIRD OCTAVE BAND SPECTRUM

MODEL: FP 30

CHANNEL: 4 MACH NO.: 5 α: 0 ϕ: 0 Re_∞/FT.: 1.0×10^6 AEDC GROUP NO.: 18/138

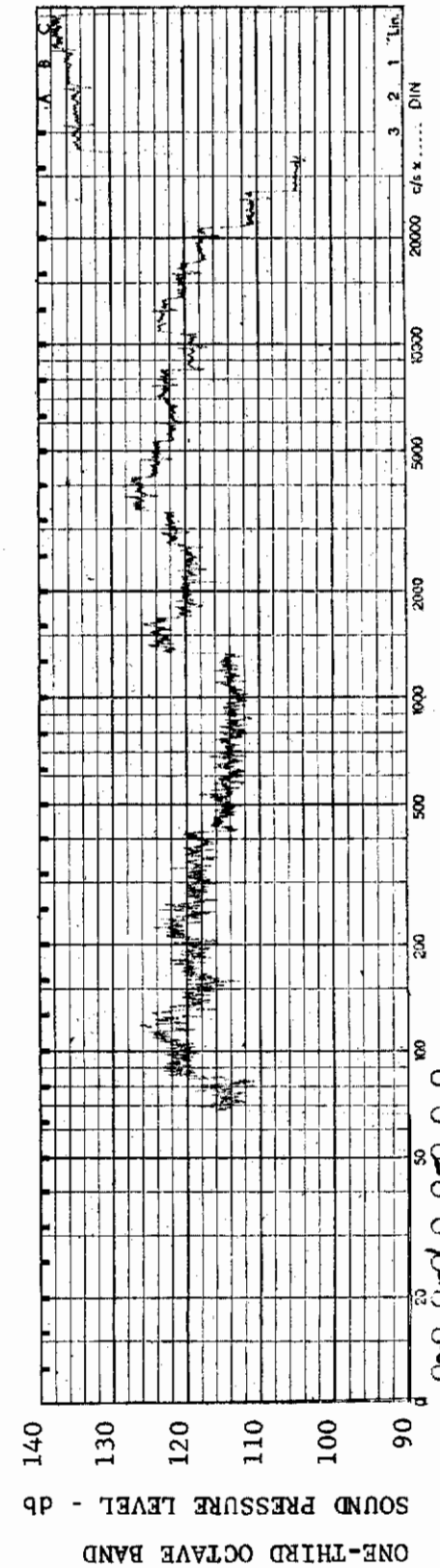

FIGURE 218 ONE-THIRD OCTAVE BAND SPECTRUM

MODEL: FP 30

CHANNEL: 5 MACH NO.: 5 α: 0 ϕ: 0 Re_∞/FT.: 1.0×10^6 AEDC GROUP NO.: 18/138

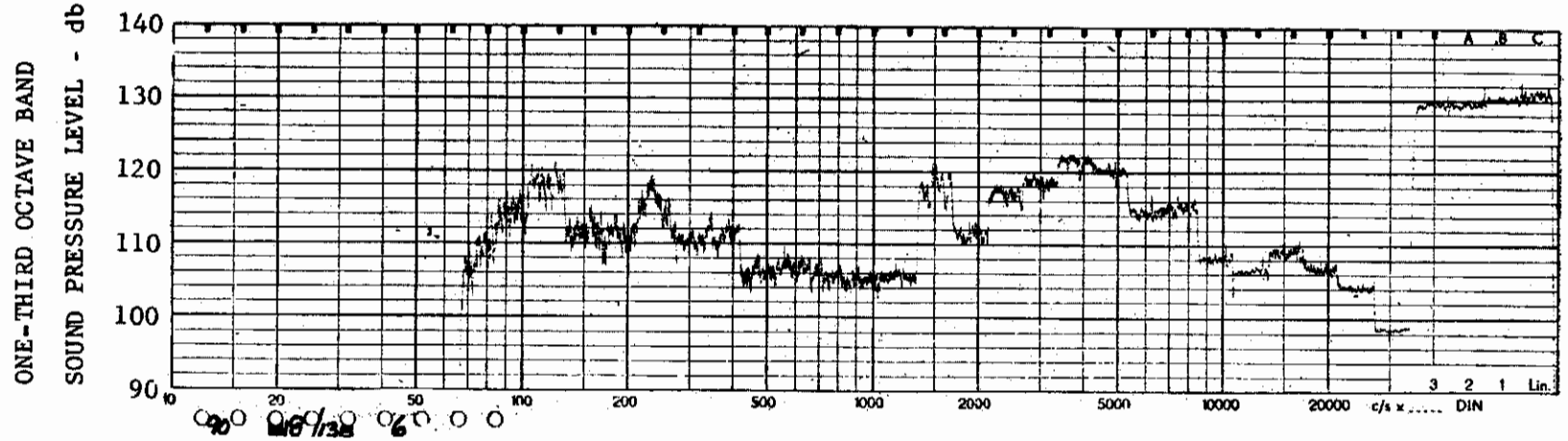

FIGURE 219 ONE-THIRD OCTAVE BAND SPECTRUM MODEL: FP 30

CHANNEL: 6 MACH NO.: 5 α: 0 ϕ: 0 Re_∞/FT.: 1.0×10^6 AEDC GROUP NO.: 18/138

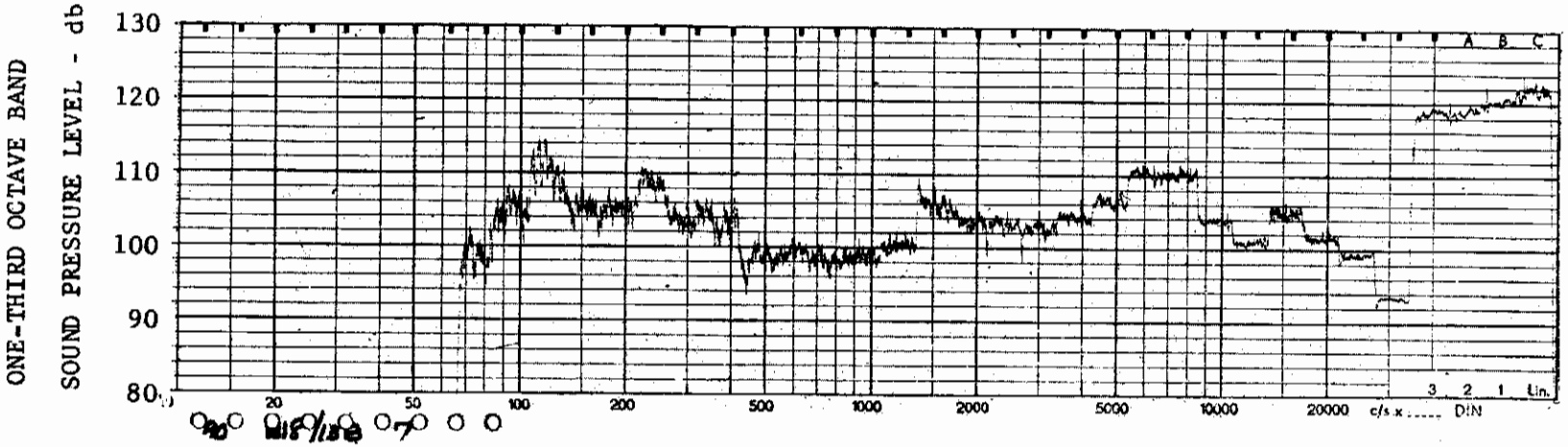

FIGURE 220 ONE-THIRD OCTAVE BAND SPECTRUM MODEL: FP 30

CHANNEL: 7 MACH NO.: 5 α: 0 ϕ: 0 Re_∞/FT.: 1.0×10^6 AEDC GROUP NO.: 18/138

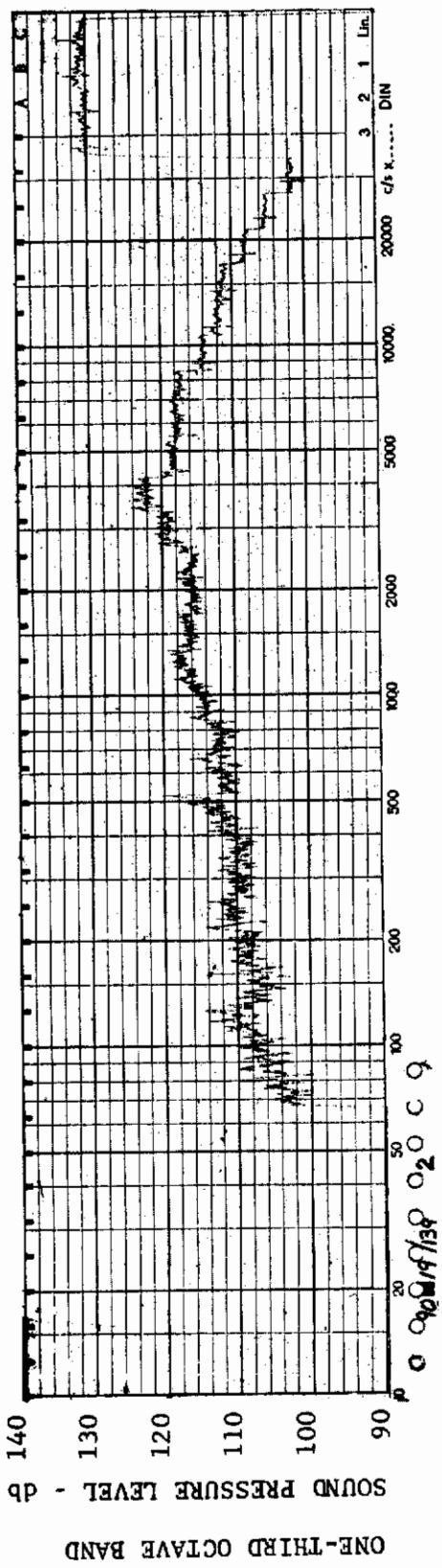

FIGURE 221 ONE-THIRD OCTAVE BAND SPECTRUM

MODEL: FP 60

CHANNEL: 2 MACH NO.: 5 α: 0 ϕ: 0 Re_∞ /FT.: 0.5×10^6 AEDC GROUP NO.: 19/139

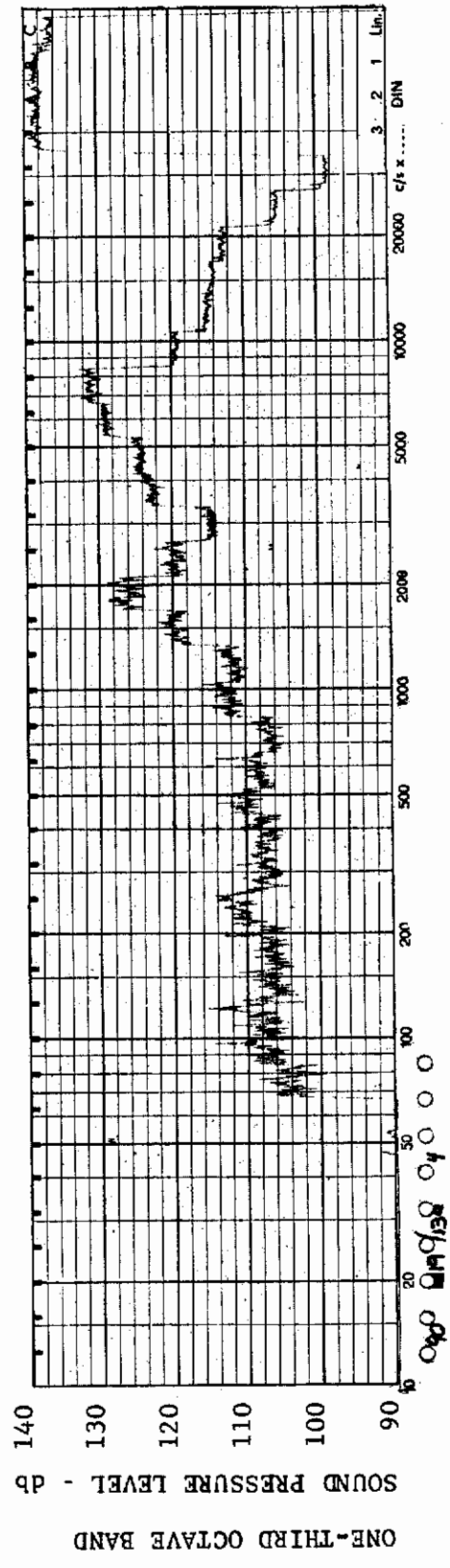

FIGURE 222 ONE-THIRD OCTAVE BAND SPECTRUM

MODEL: FP 60

CHANNEL: 4 MACH NO.: 5 α: 0 ϕ: 0 Re_∞ /FT.: 0.5×10^6 AEDC GROUP NO.: 19/139

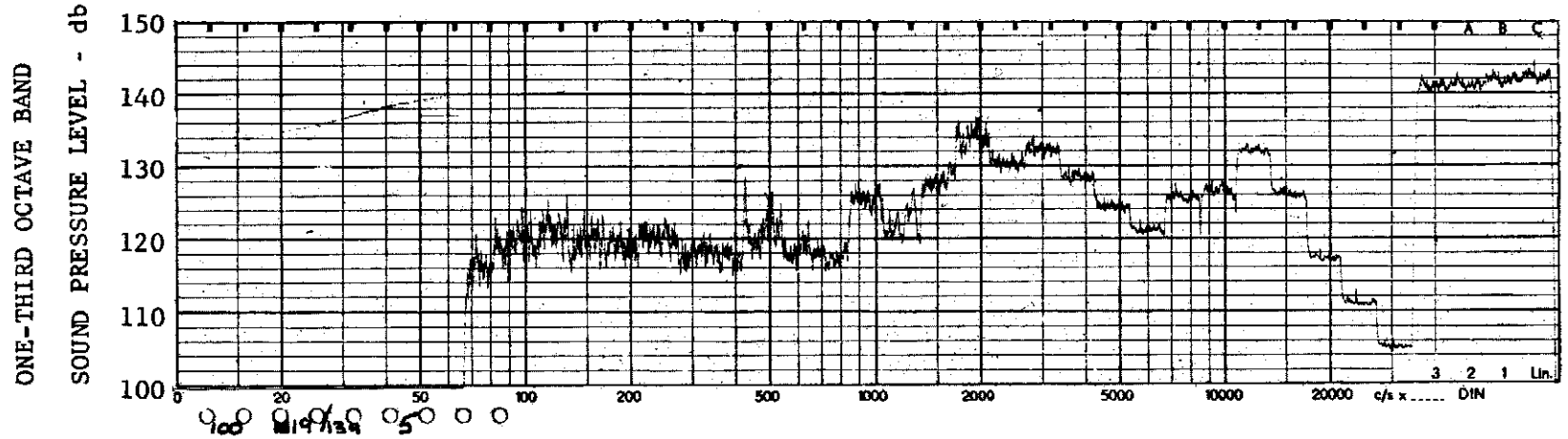

FIGURE 223 ONE-THIRD OCTAVE BAND SPECTRUM MODEL: FP 60

CHANNEL: 5 MACH NO.: 5 α: 0 ϕ: 0 Re_∞/FT.: 0.5 x 10^6 AEDC GROUP NO.: 19/139

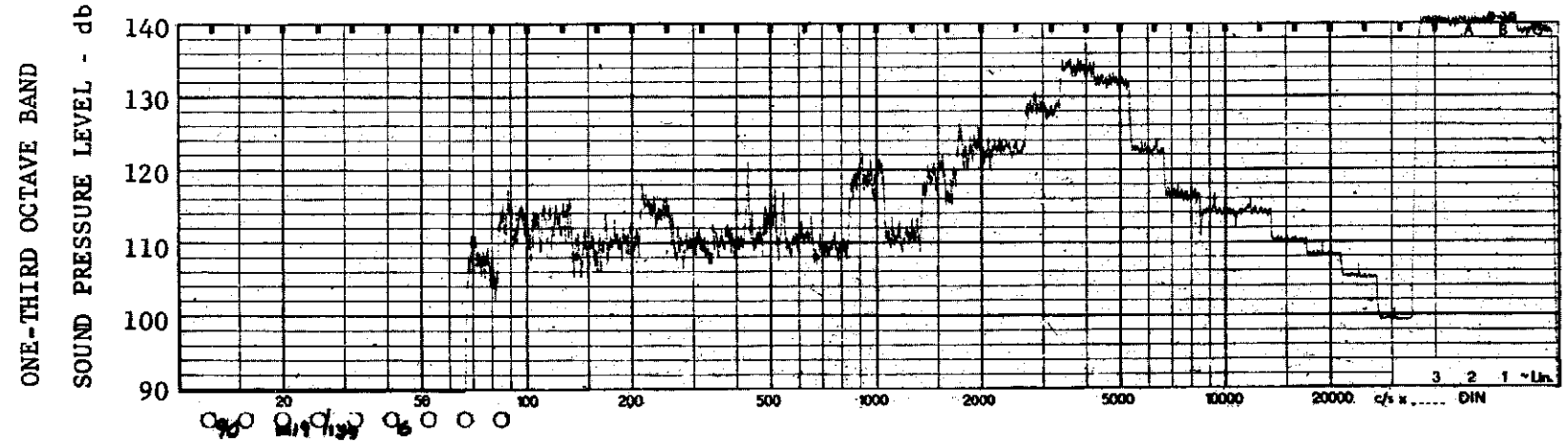

FIGURE 224 ONE-THIRD OCTAVE BAND SPECTRUM MODEL: FP 60

CHANNEL: 6 MACH NO.: 5 α: 0 ϕ: 0 Re_∞/FT.: 0.5 x 10^6 AEDC GROUP NO.: 19/139

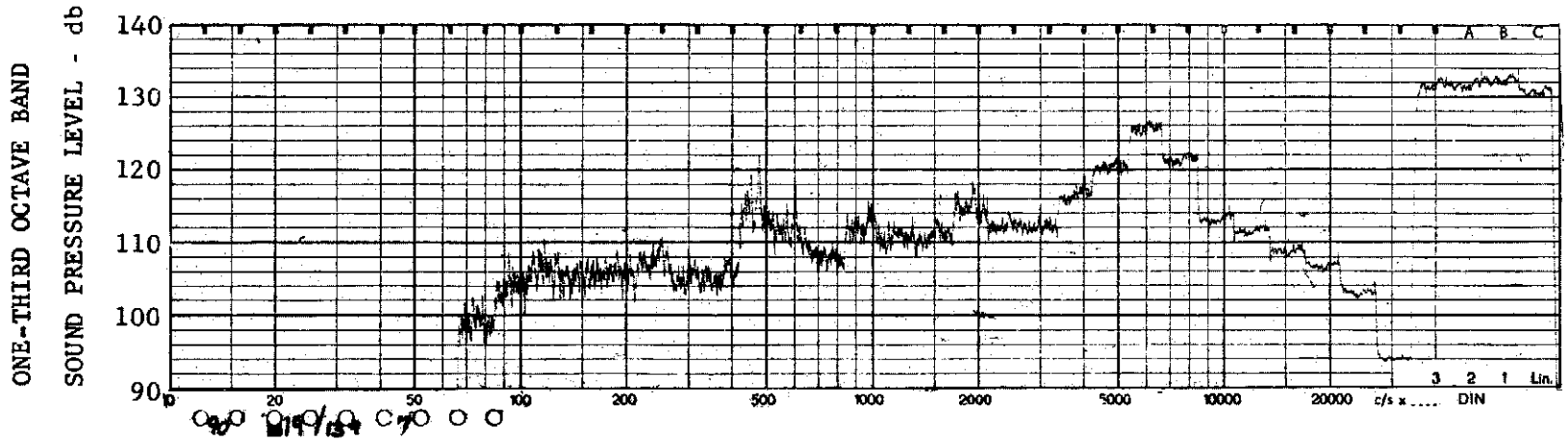

FIGURE 225 ONE-THIRD OCTAVE BAND SPECTRUM MODEL: FP 60

CHANNEL: 7 MACH NO.: 5 α: 0 ϕ: 0 Re_∞/FT.: 0.5 x 10^6 AEDC GROUP NO.: 19/139

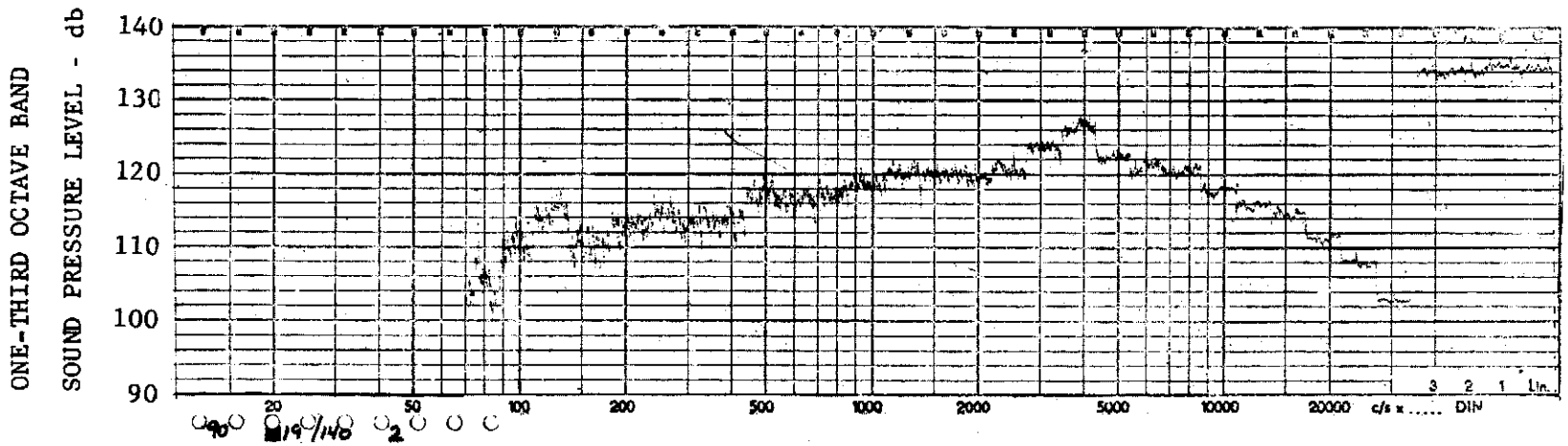

FIGURE 226 ONE-THIRD OCTAVE BAND SPECTRUM MODEL: FP 60

CHANNEL: 2 MACH NO.: 5 α: 0 ϕ: 0 Re_∞/FT.: 1.0 x 10^6 AEDC GROUP NO.: 19/140

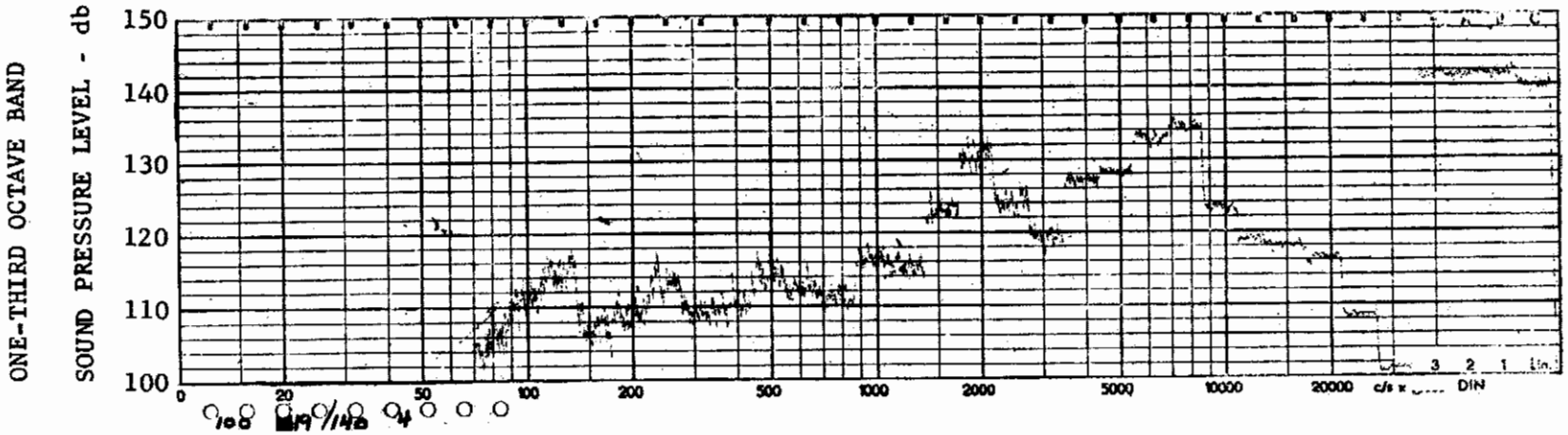

FIGURE 227 ONE-THIRD OCTAVE BAND SPECTRUM MODEL: FP 60

CHANNEL: 4 MACH NO.: 5 α: 0 ϕ: 0 Re_∞/FT.: 1.0×10^6 AEDC GROUP NO.: 19/140

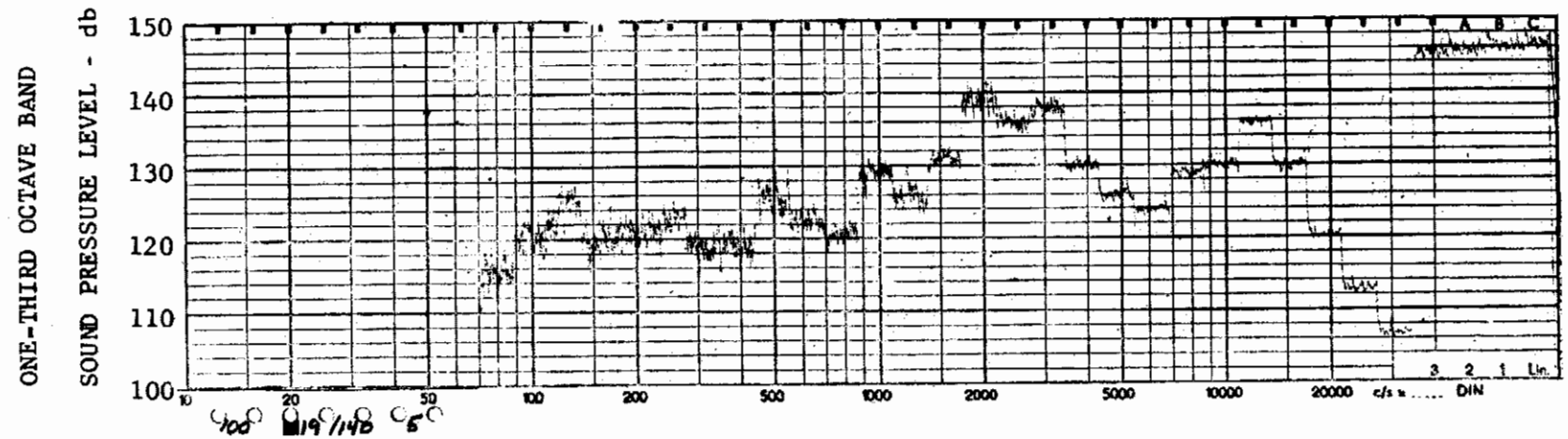

FIGURE 228 ONE-THIRD OCTAVE BAND SPECTRUM MODEL: FP 60

CHANNEL: 5 MACH NO.: 5 α: 0 ϕ: 0 Re_∞/FT.: 1.0×10^6 AEDC GROUP NO.: 19/140

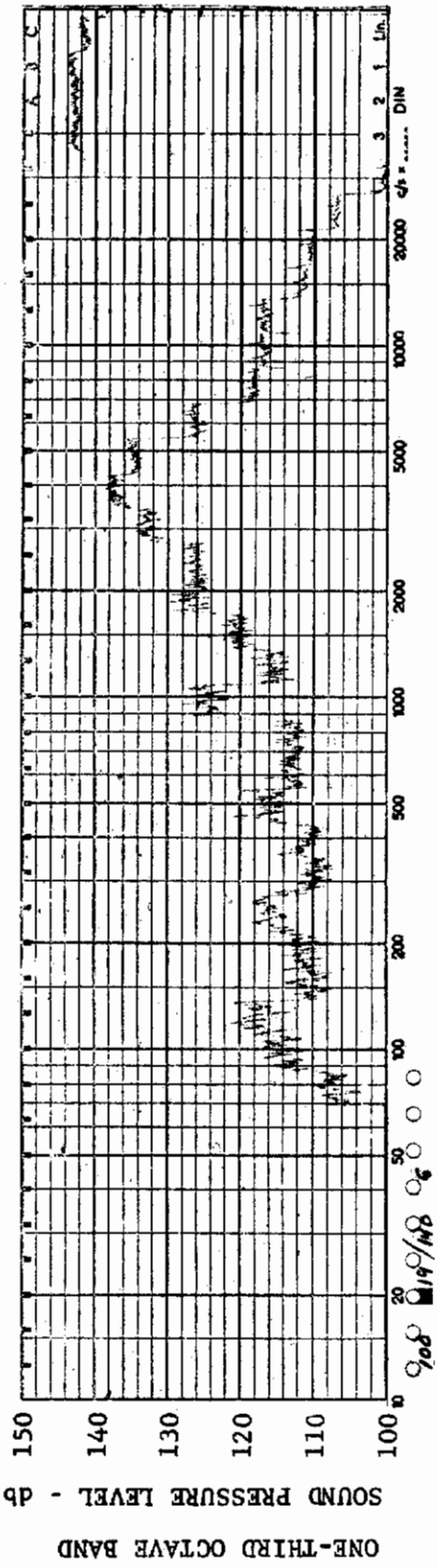

FIGURE 229 ONE-THIRD OCTAVE BAND SPECTRUM

MODEL: FP 60

CHANNEL: 6 MACH NO.: 5 α: 0 ϕ: 0 Re_∞/FT.: 1.0 x 10^6 AEDC GROUP NO.: 19/140

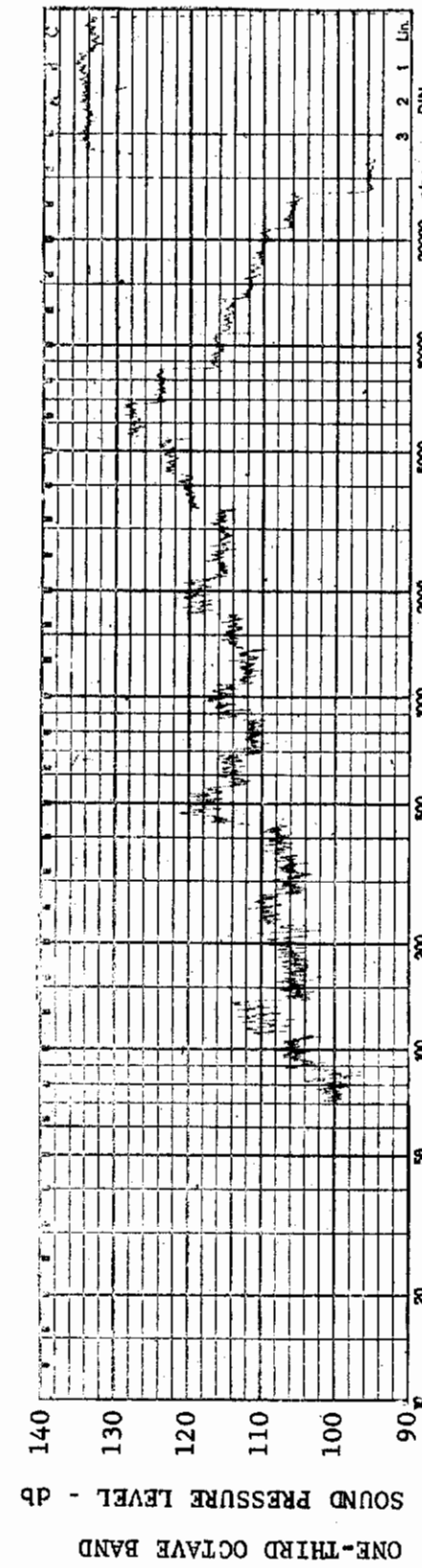

FIGURE 230 ONE-THIRD OCTAVE BAND SPECTRUM

MODEL: FP 60

CHANNEL: 7 MACH NO.: 5 α: 0 ϕ: 0 Re_∞/FT.: 1.0 x 10^6 AEDC GROUP NO.: 19/140

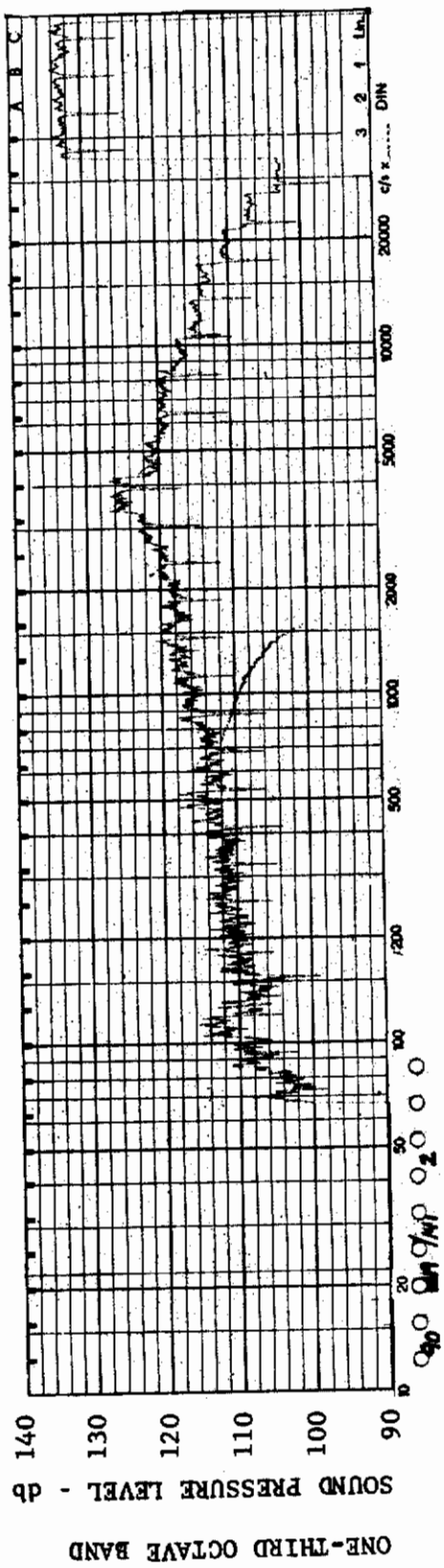

FIGURE 231 ONE-THIRD OCTAVE BAND SPECTRUM

MODEL: FP 60

CHANNEL: 2 MACH NO.: 5 α: 5° ϕ: 0 Re_∞/FT.: 1.0×10^6 AEDC GROUP NO.: 19/141

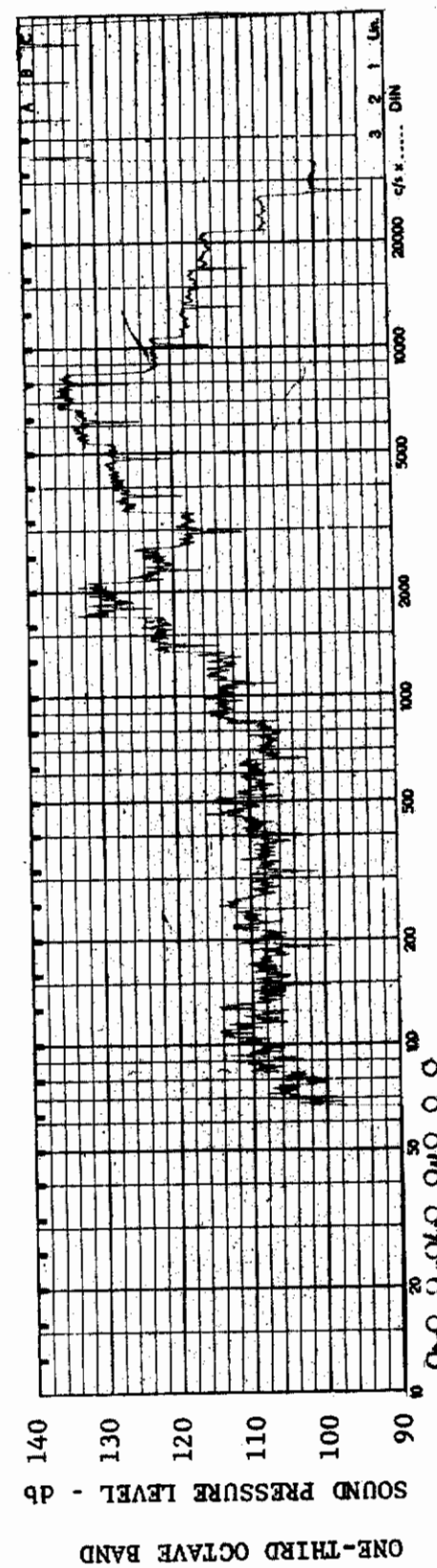

FIGURE 232 ONE-THIRD OCTAVE BAND SPECTRUM

MODEL: FP 60

CHANNEL: 4 MACH NO.: 5 α: 5° ϕ: 0 Re_∞/FT.: 1.0×10^6 AEDC GROUP NO.: 19/141

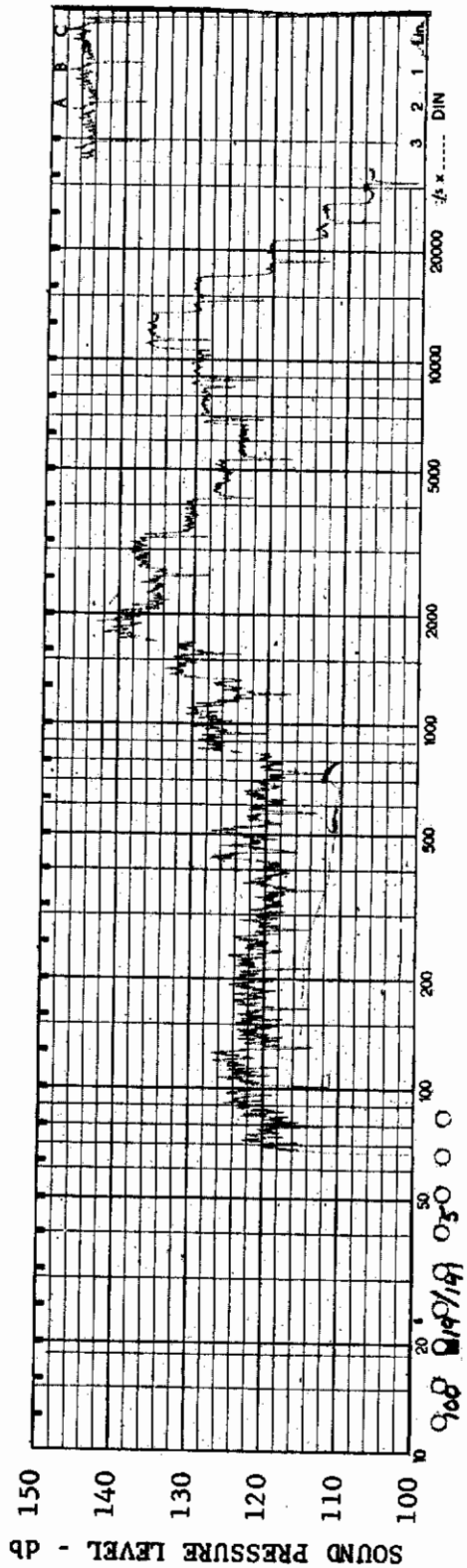

FIGURE 233 ONE-THIRD OCTAVE BAND SPECTRUM

MODEL: FP 60

CHANNEL: 5 MACH NO.: 5 α: 5° ϕ: 0 Re_∞/FT.: 1.0×10^6 AEDC GROUP NO.: 19/141

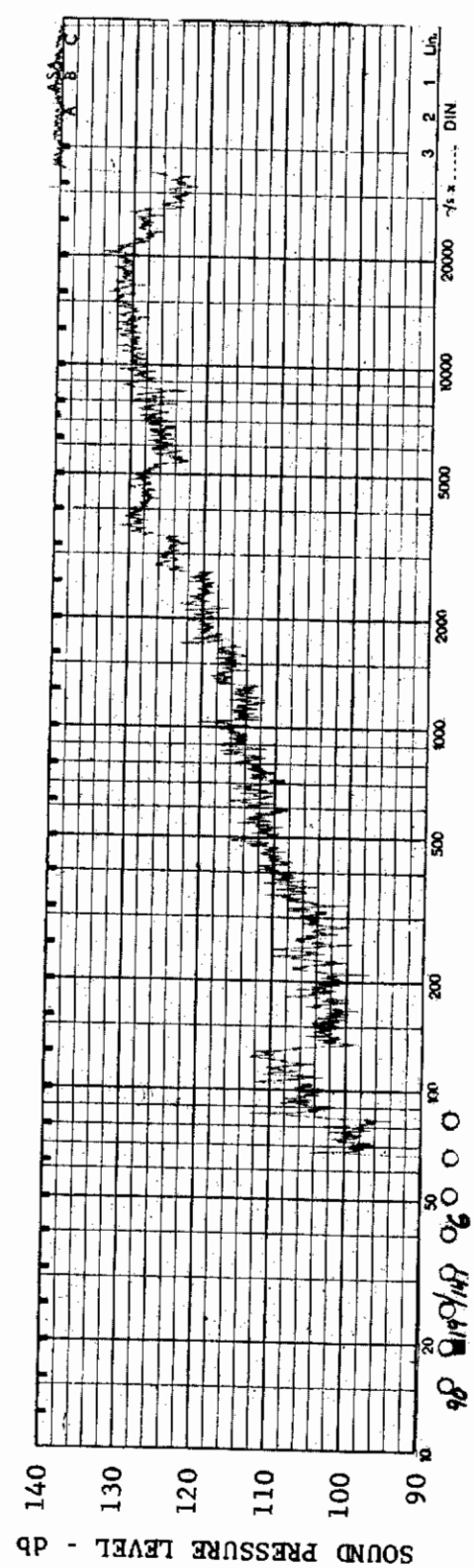

FIGURE 234 ONE-THIRD OCTAVE BAND SPECTRUM

MODEL: FP 60

CHANNEL: 6 MACH NO.: 5 α: 5° ϕ: 0 Re_∞/FT. 1.0×10^6 AEDC GROUP NO.: 19/141

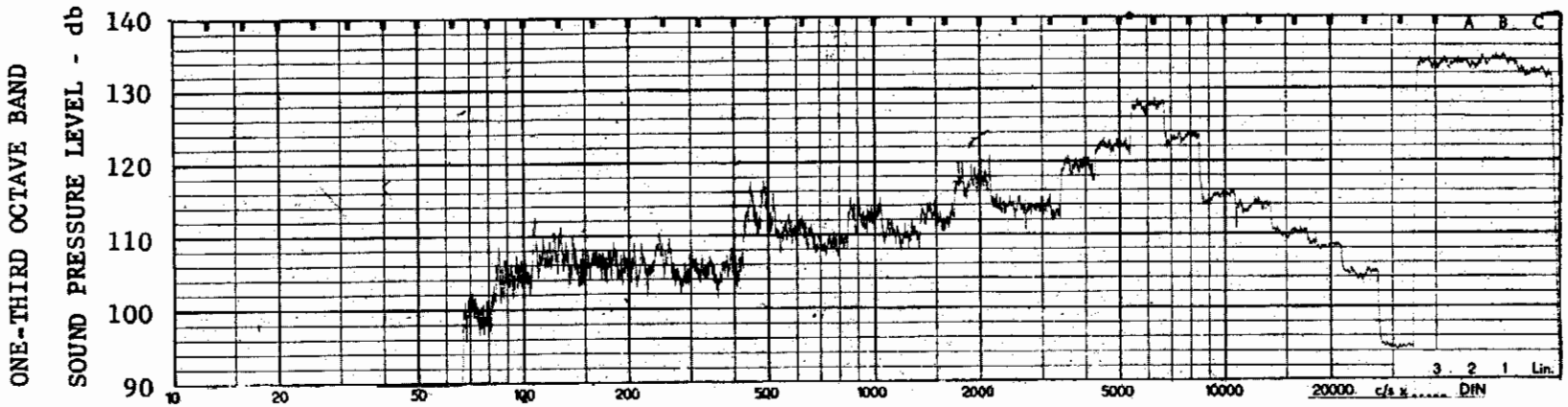

FIGURE 235 ONE-THIRD OCTAVE BAND SPECTRUM MODEL: FP 60

CHANNEL: 7 MACH NO.: 5 α: 5° ϕ: 0 Re_∞/FT.: 1.0×10^6 AEDC GROUP NO.: 19/141

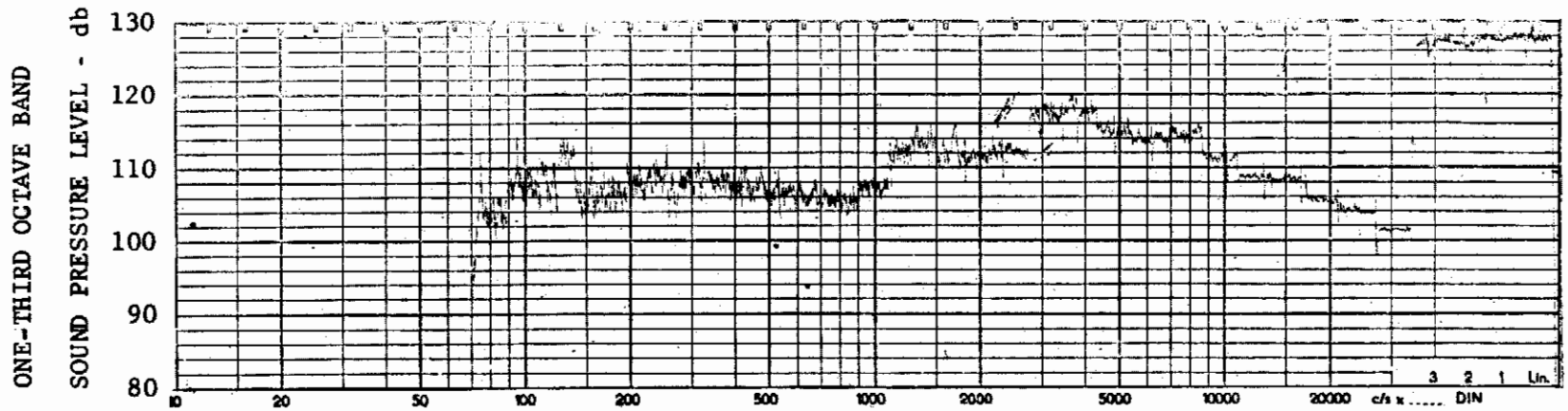

FIGURE 236 ONE-THIRD OCTAVE BAND SPECTRUM MODEL: FP 60

CHANNEL: 2 MACH NO.: 5 α: 15° ϕ: 0 Re_∞/FT.: 1.0×10^6 AEDC GROUP NO.: 19/142

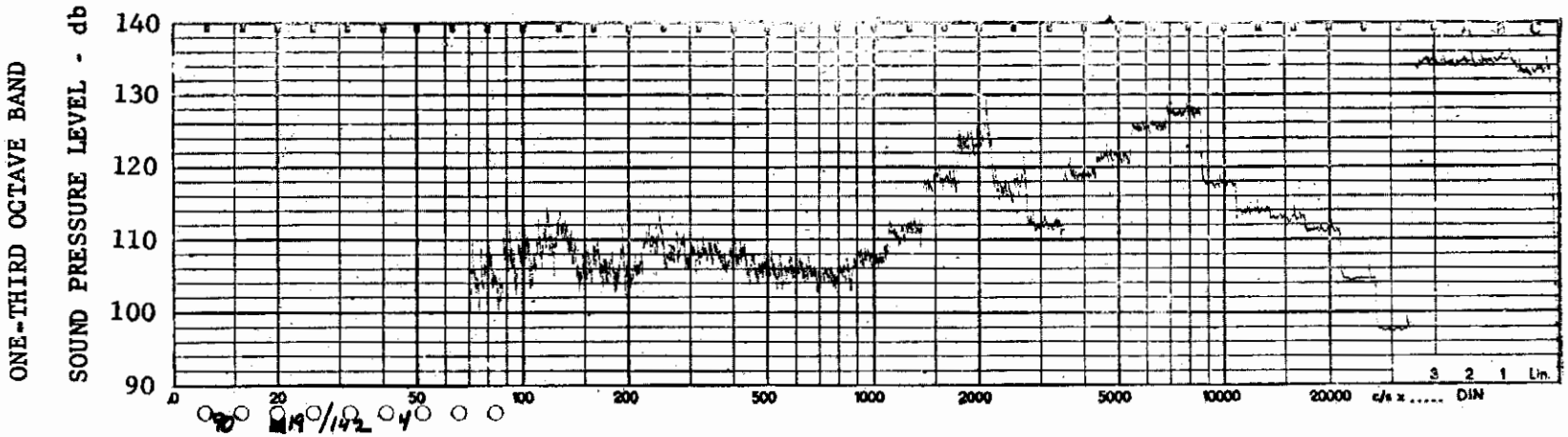

FIGURE 237 ONE-THIRD OCTAVE BAND SPECTRUM MODEL: FP 60

CHANNEL: 4 MACH NO.: 5 α: 15 ϕ: 0 Re_∞/FT.: 1.0×10^6 AEDC GROUP NO.: 19/142

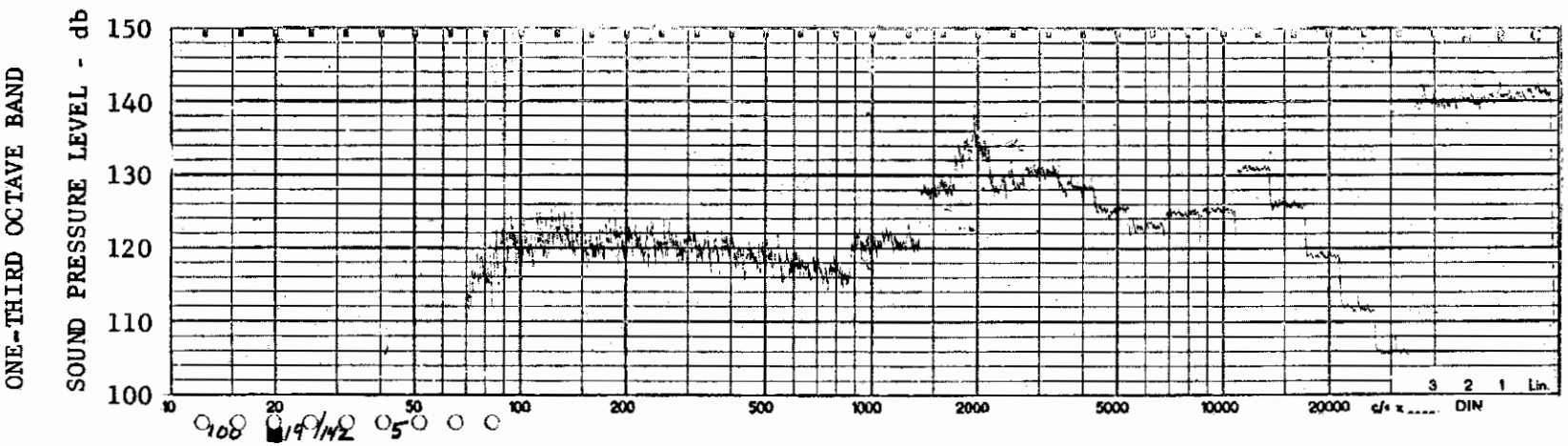

FIGURE 238 ONE-THIRD OCTAVE BAND SPECTRUM MODEL: FP 60

CHANNEL: 5 MACH NO.: 5 α: 15° ϕ: 0 Re_∞/FT.: 1.0×10^6 AEDC GROUP NO.: 19/142

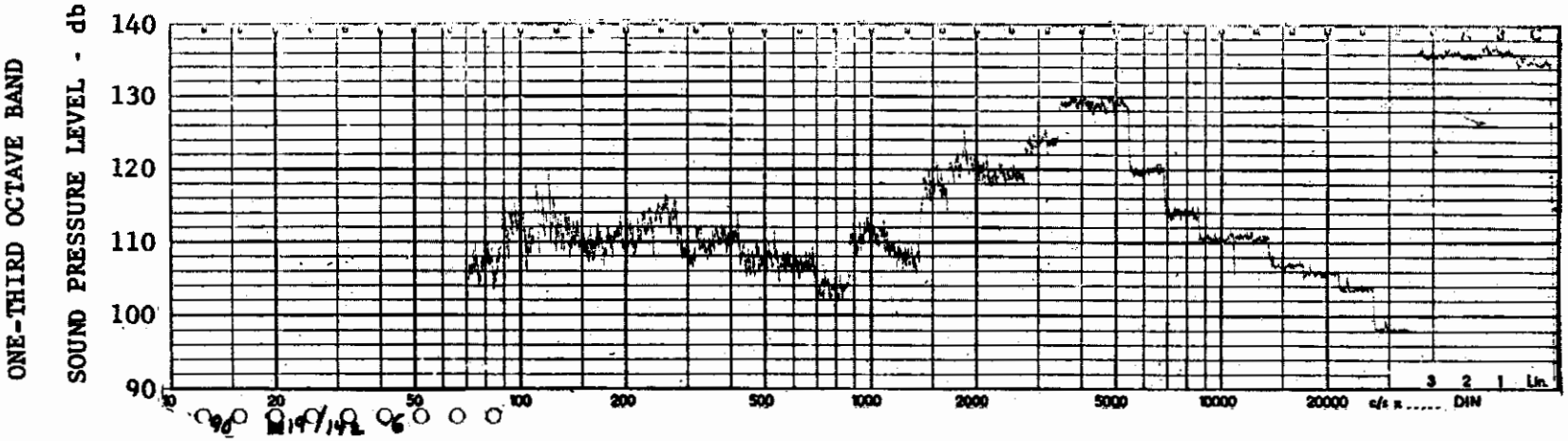

FIGURE 239 ONE-THIRD OCTAVE BAND SPECTRUM MODEL: FP 60

CHANNEL: 6 MACH NO.: 5 α: 15° ϕ: 0 Re_∞/FT.: 1.0×10^6 AEDC GROUP NO.: 19/142

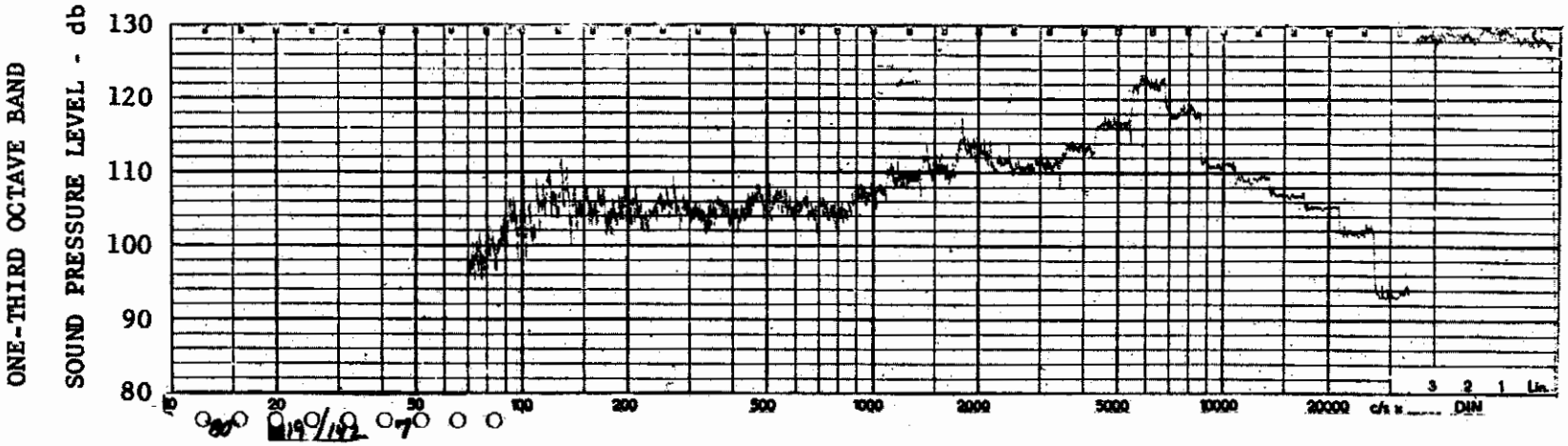

FIGURE 240 ONE-THIRD OCTAVE BAND SPECTRUM MODEL: FP 60

CHANNEL: 7 MACH NO.: 5 α: 15° ϕ: 0 Re_∞/FT.: 1.0×10^6 AEDC GROUP NO.: 19/142

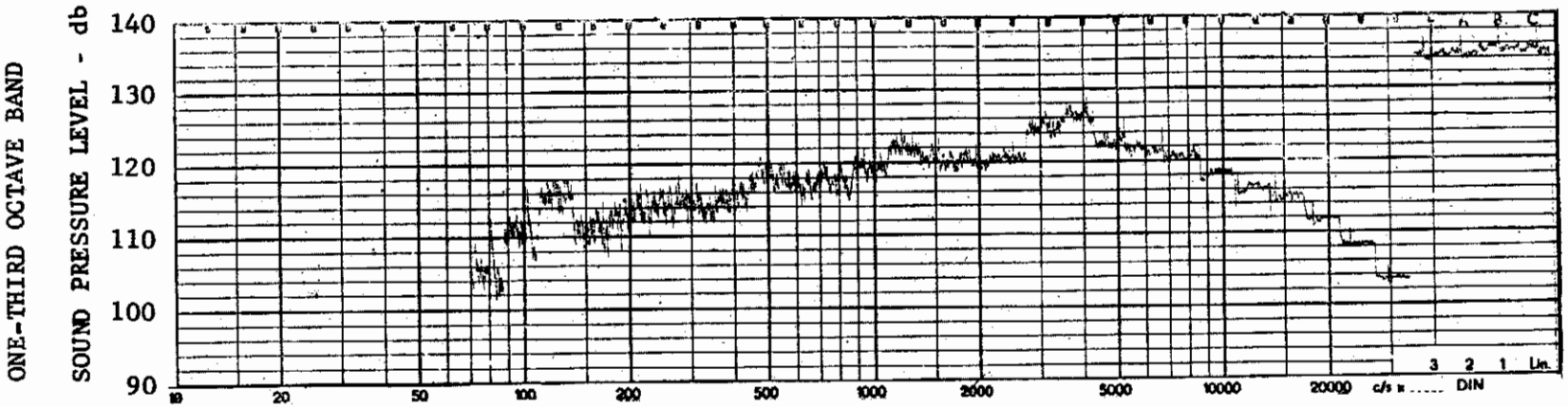

FIGURE 241 ONE-THIRD OCTAVE BAND SPECTRUM MODEL: FP 60

CHANNEL: 2 MACH NO.: 5 α: 0 ϕ: 0 Re_∞/FT.: 1.0×10^6 AEDC GROUP NO.: 19/143

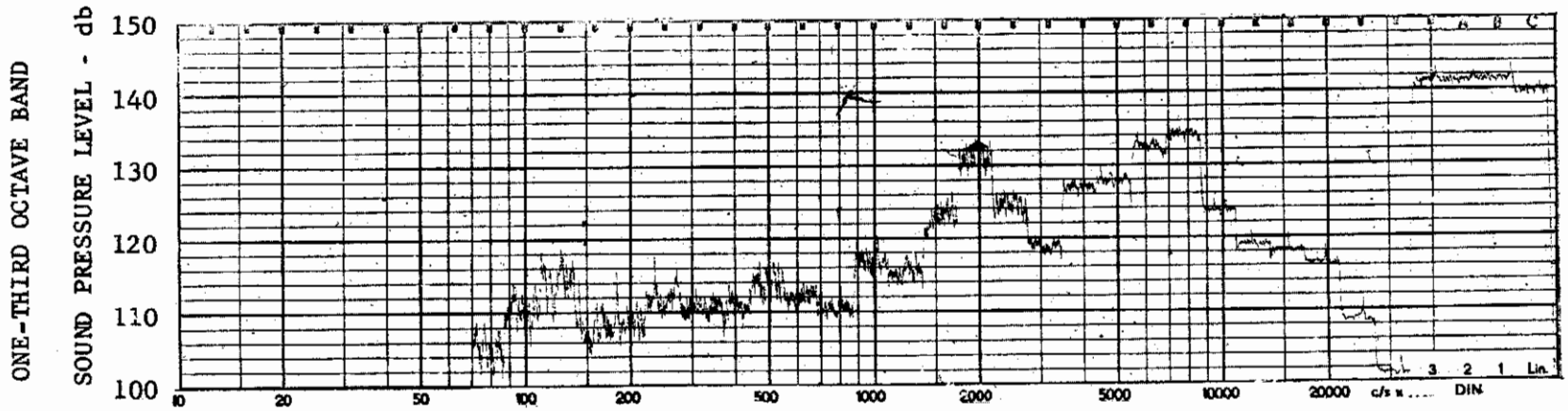

FIGURE 242 ONE-THIRD OCTAVE BAND SPECTRUM MODEL: FP 60

CHANNEL: 4 MACH NO.: 5 α: 0 ϕ: 0 Re_∞/FT.: 1.0×10^6 AEDC GROUP NO.: 19/143

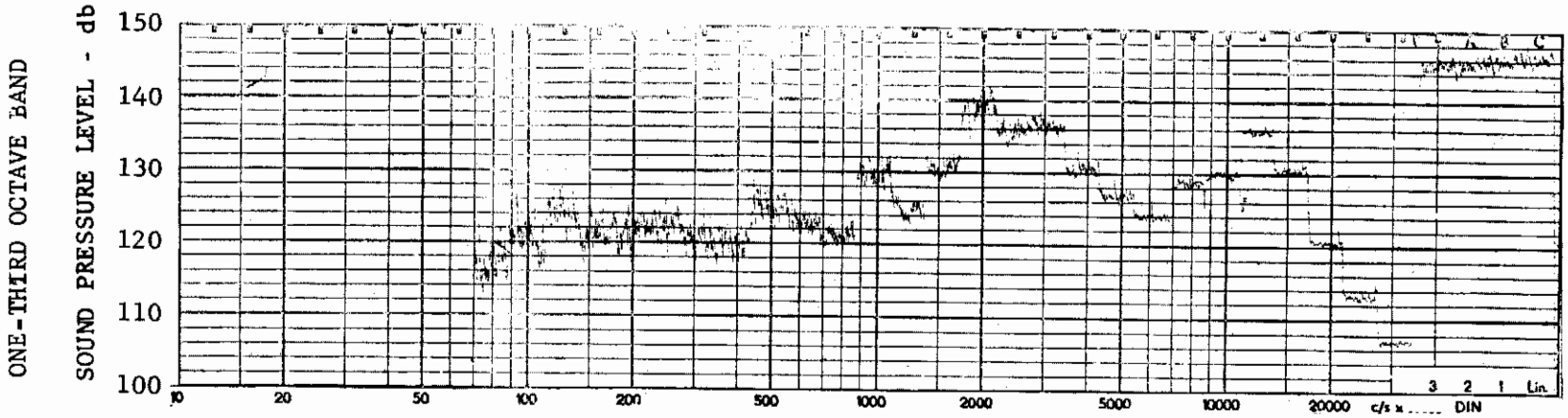

FIGURE 243 ONE-THIRD OCTAVE BAND SPECTRUM MODEL: FP 60

CHANNEL: 5 MACH NO.: 5 α: 0 ϕ: 0 Re_∞/FT.: 1.0×10^6 AEDC GROUP NO.: 19/143

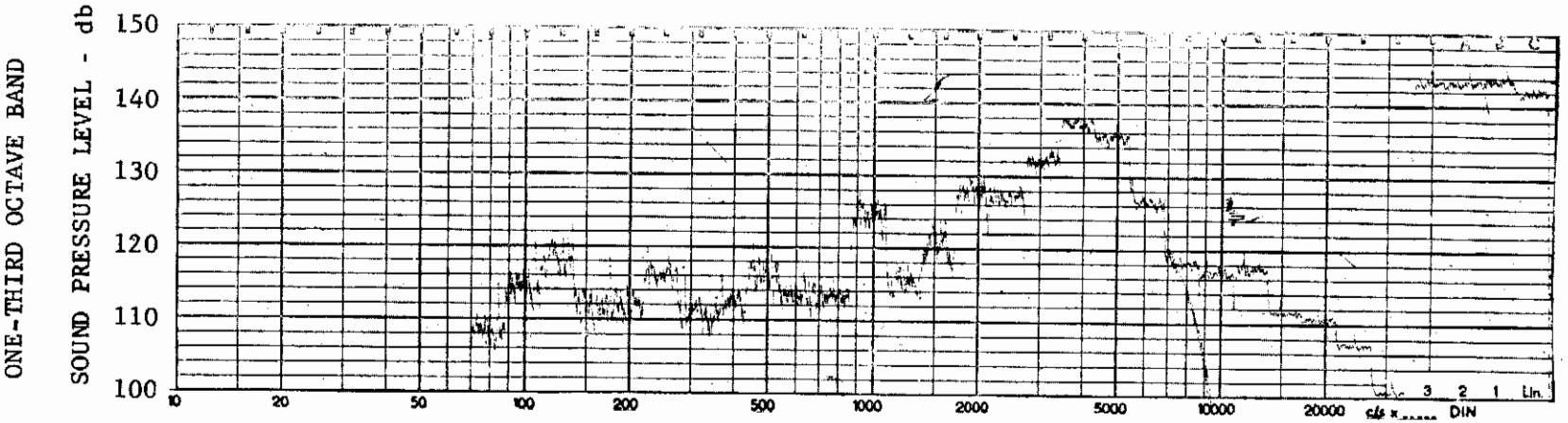

FIGURE 244 ONE-THIRD OCTAVE BAND SPECTRUM MODEL: FP 60

CHANNEL: 6 MACH NO.: 5 α: 0 ϕ: 0 Re_∞/FT.: 1.0×10^6 AEDC GROUP NO.: 19/143

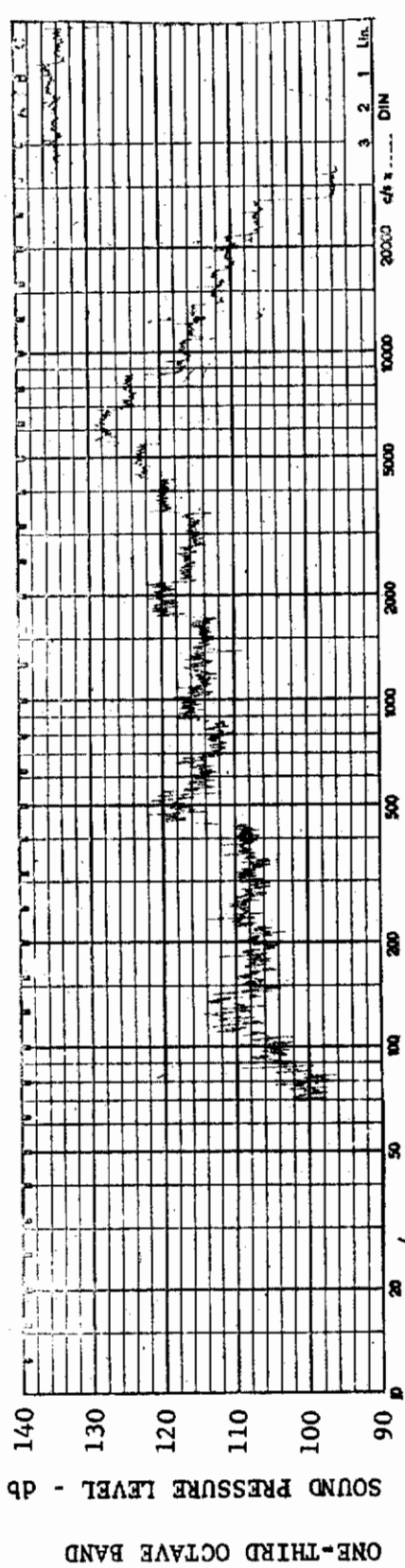

FIGURE 245 ONE-THIRD OCTAVE BAND SPECTRUM

MODEL: FP 60

CHANNEL: 7 MACH NO.: 5 α: 0 ϕ: 0 Re_∞/FT. 1.0×10^6 AEDC GROUP NO.:19/143

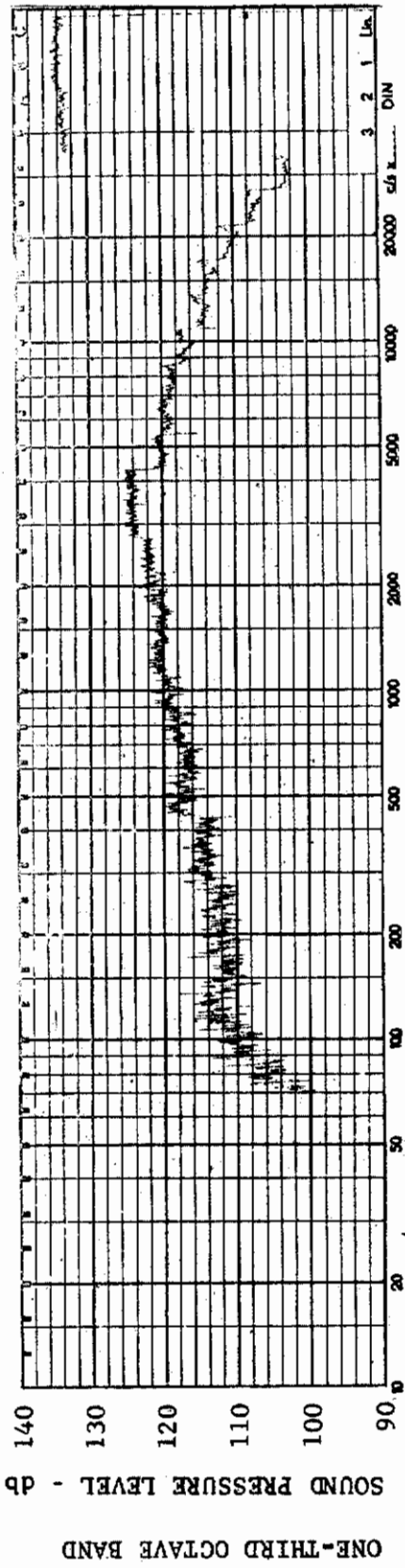

FIGURE 246 ONE-THIRD OCTAVE BAND SPECTRUM

MODEL: FP 60

CHANNEL: 2 MACH NO.: 3.5 α .0 ϕ :0 Re_∞/FT.: 0.5×10^6 AEDC GROUP NO.: 20/144

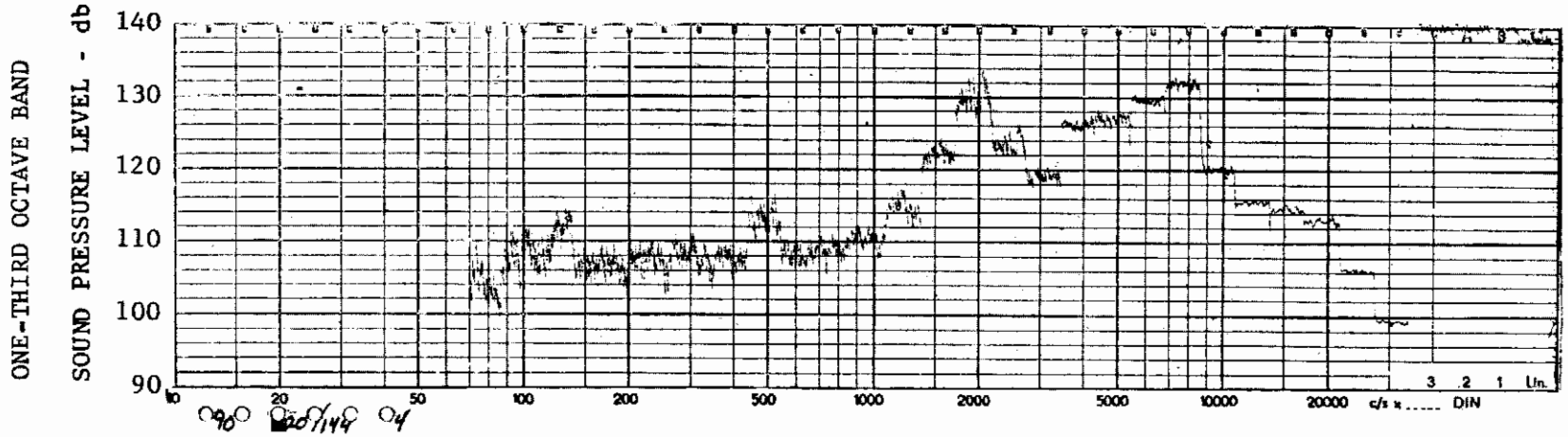

FIGURE 247 ONE-THIRD OCTAVE BAND SPECTRUM MODEL: FP 60

CHANNEL: 4 MACH NO.: 3.5 α: 0 ϕ 0 Re_∞/FT.: 0.5×10^6 AEDC GROUP NO.: 20/144

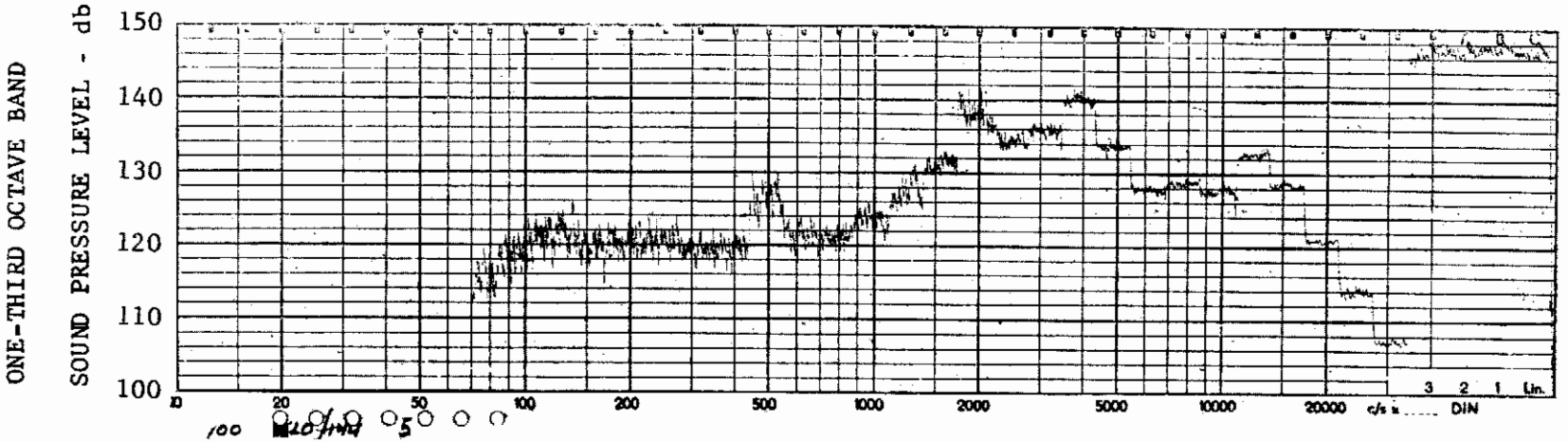

FIGURE 248 ONE-THIRD OCTAVE BAND SPECTRUM MODEL: FP 60

CHANNEL: 5 MACH NO.: 3.5 α: 0 ϕ: 0 Re_∞/FT.: 0.5×10^6 AEDC GROUP NO.: 20/144

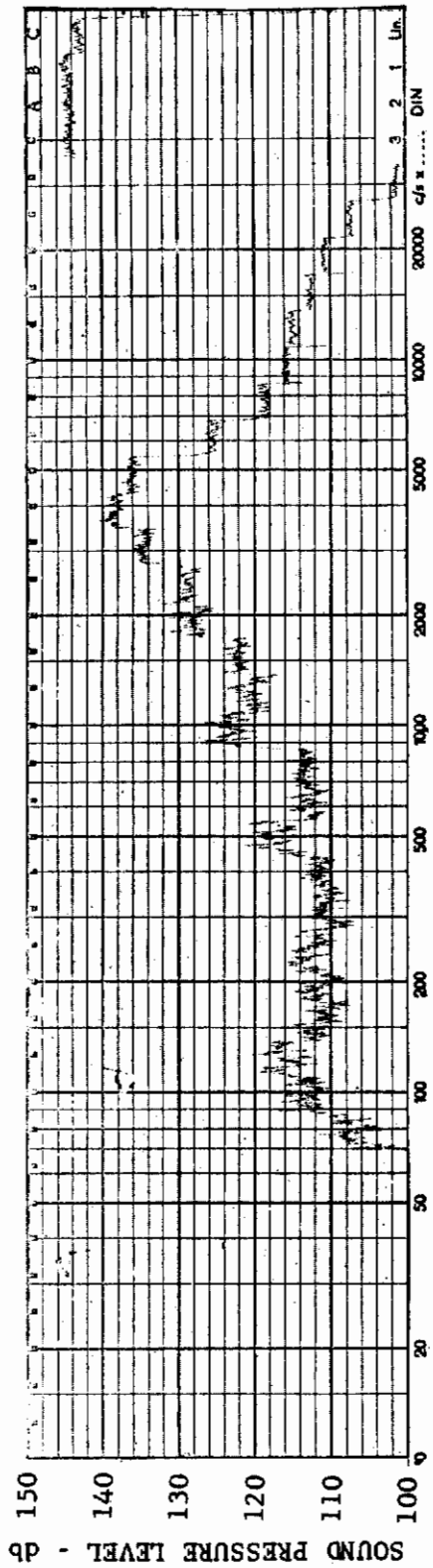

FIGURE 249 ONE-THIRD OCTAVE BAND SPECTRUM MODEL: FP 60

CHANNEL: 6 MACH NO.: 3.5 α: 0 ϕ: 0 Re_∞/FT.: 0.5×10^6 AEDC GROUP NO.: 20/144

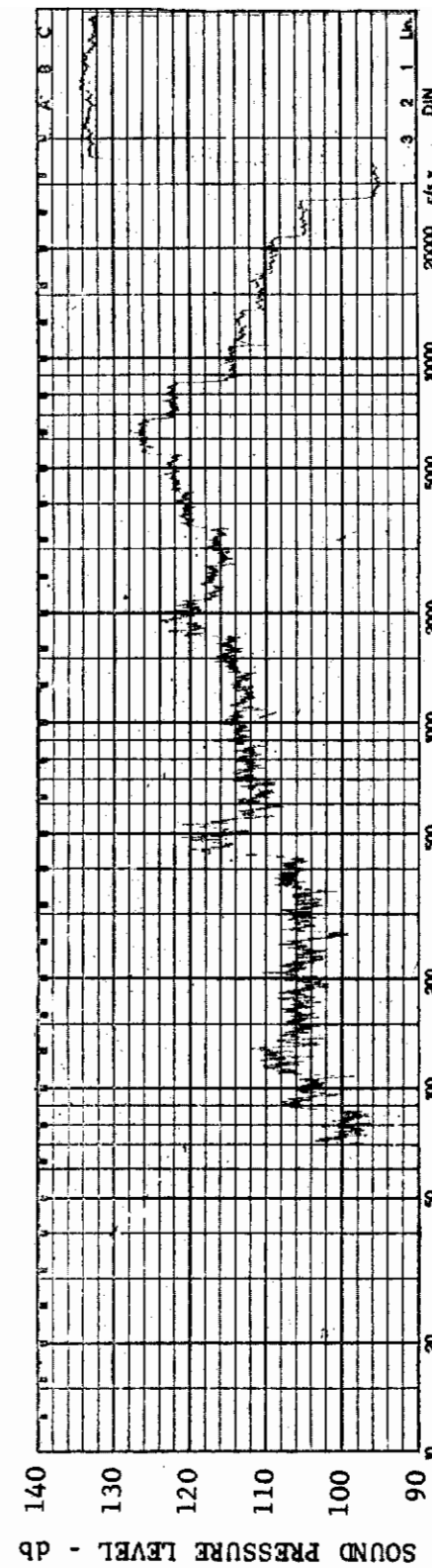

FIGURE 250 ONE-THIRD OCTAVE BAND SPECTRUM MODEL: FP 60

CHANNEL: 7 MACH NO.: 3.5 α: 0 ϕ: 0 Re_∞/FT.: 0.5×10^6 AEDC GROUP NO.: 20/144

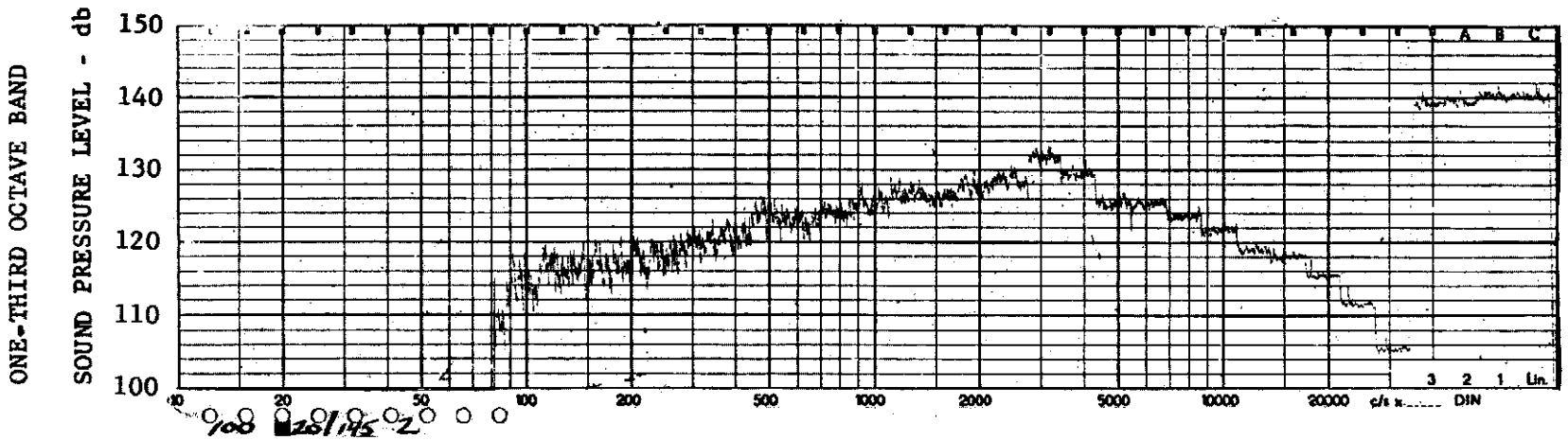

FIGURE 251 ONE-THIRD OCTAVE BAND SPECTRUM MODEL: FP 60

CHANNEL: 2 MACH NO.: 3.5 α: 0 ϕ: 0 Re_∞/FT.: 1.0×10^6 AEDC GROUP NO.: 20/145

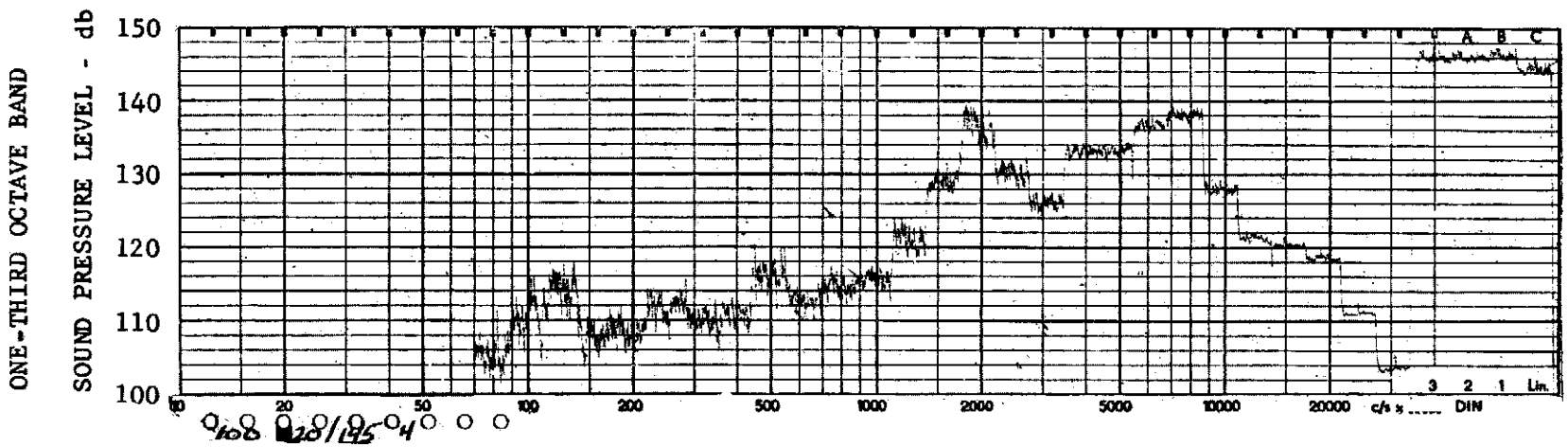

FIGURE 252 ONE-THIRD OCTAVE BAND SPECTRUM MODEL: FP 60

CHANNEL: 4 MACH NO.: 3.5 α: 0 ϕ: 0 Re_∞/FT.: 1.0×10^6 AEDC GROUP NO.: 20/145

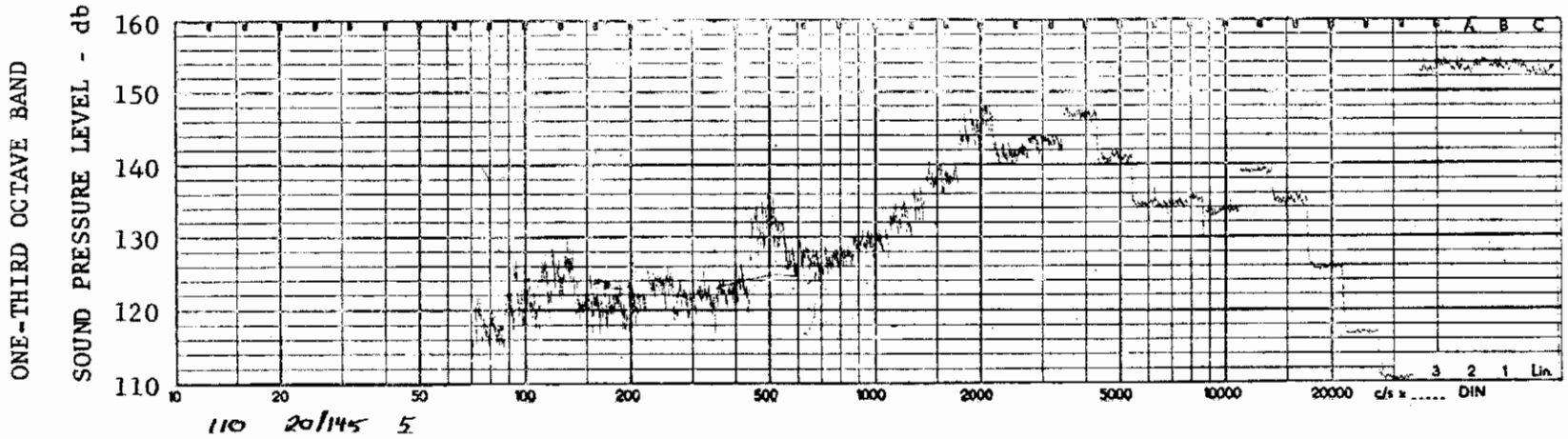

FIGURE 253 ONE-THIRD OCTAVE BAND SPECTRUM MODEL: FP 60

CHANNEL: 5 MACH NO.: 3.5 α: 0 ϕ: 0 Re_∞/FT.: 1.0×10^6 AEDC GROUP NO.: 20/145

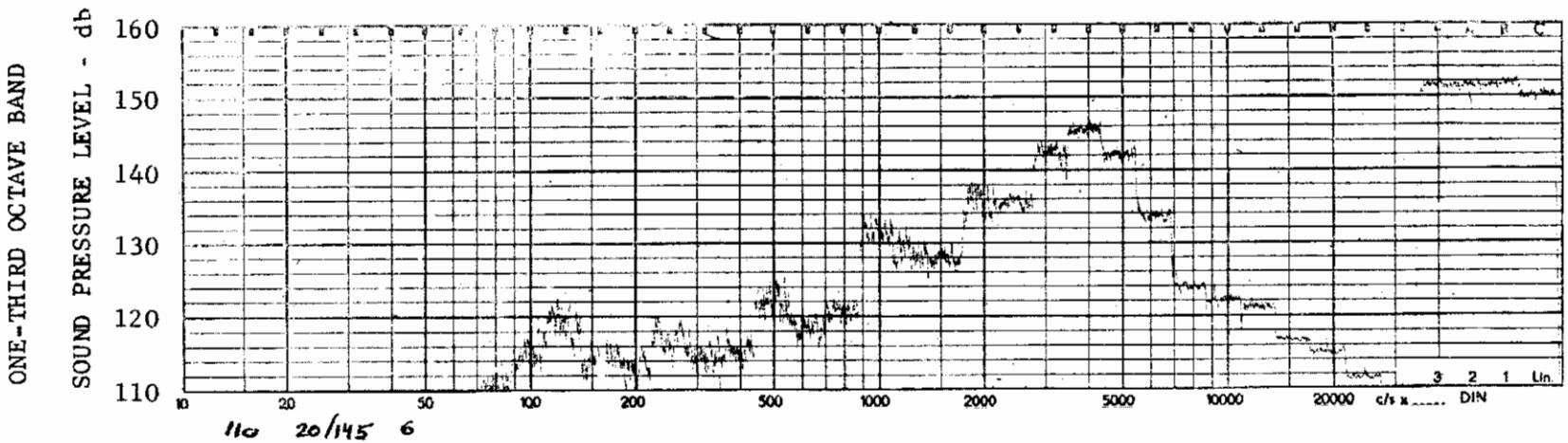

FIGURE 254 ONE-THIRD OCTAVE BAND SPECTRUM MODEL: FP 60

CHANNEL: 6 MACH NO.: 3.5 α: 0 ϕ: 0 Re_∞/FT.: 1.0×10^6 AEDC GROUP NO.: 20/145

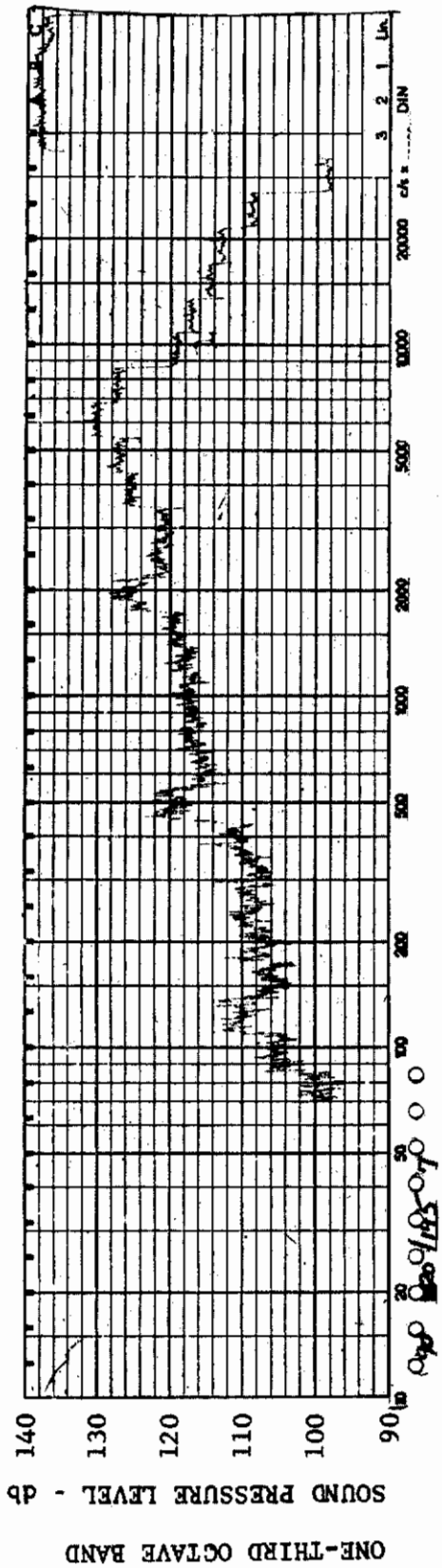

FIGURE 255 ONE-THIRD OCTAVE BAND SPECTRUM MODEL: FP 60

CHANNEL: 7 MACH NO.: 3.5 α: 0 ϕ: 0 Re_∞/FT.: 1.0×10^6 AEDC GROUP NO.: 20/145

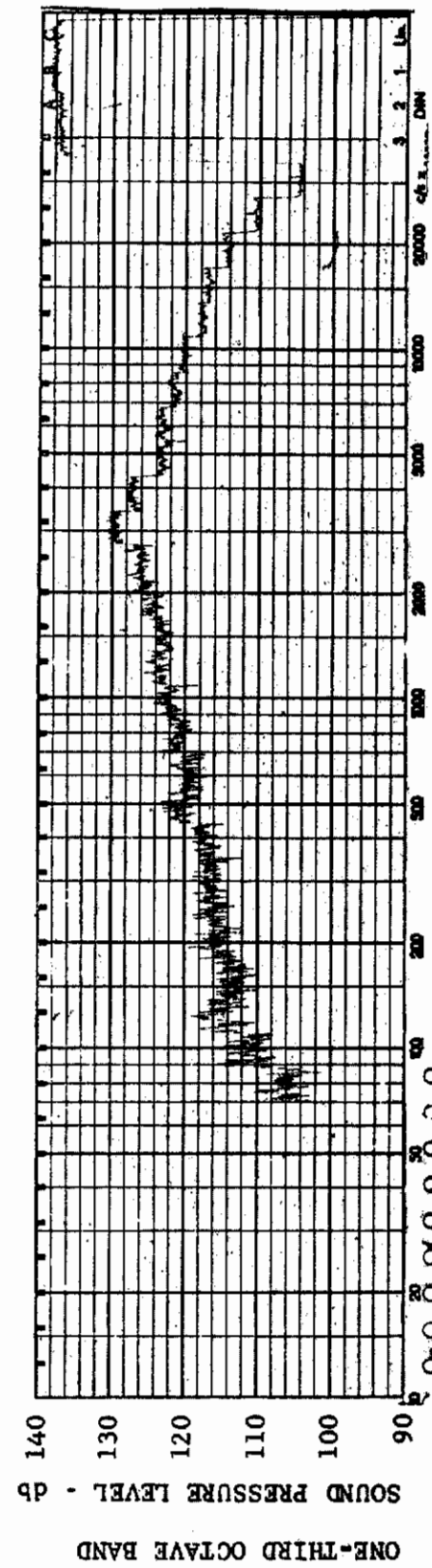

FIGURE 256 ONE-THIRD OCTAVE BAND SPECTRUM MODEL: FP 60

CHANNEL: 2 MACH NO.: 3.5 α: 5° ϕ: 0 Re_∞/FT.: 1.0×10^6 AEDC GROUP NO.: 20/146

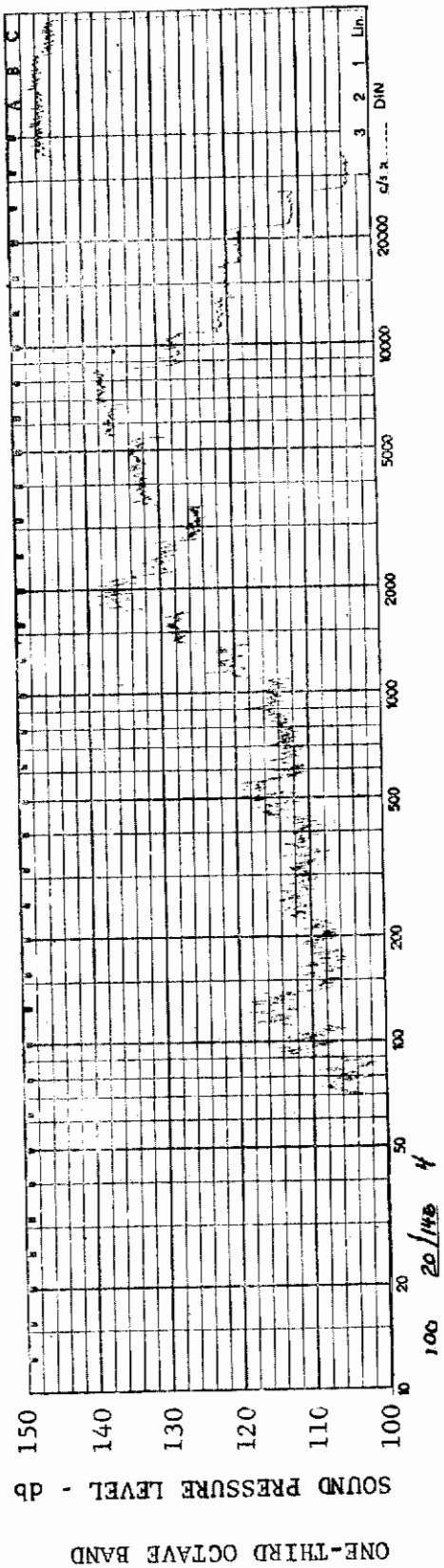

MODEL: FP 60

FIGURE 257 ONE-THIRD OCTAVE BAND SPECTRUM

CHANNEL: 4 MACH NO.: 3.5 α: 5° ϕ: 0 Re_∞/FT.: 1.0×10^6 AEDC GROUP NO.: 20/146

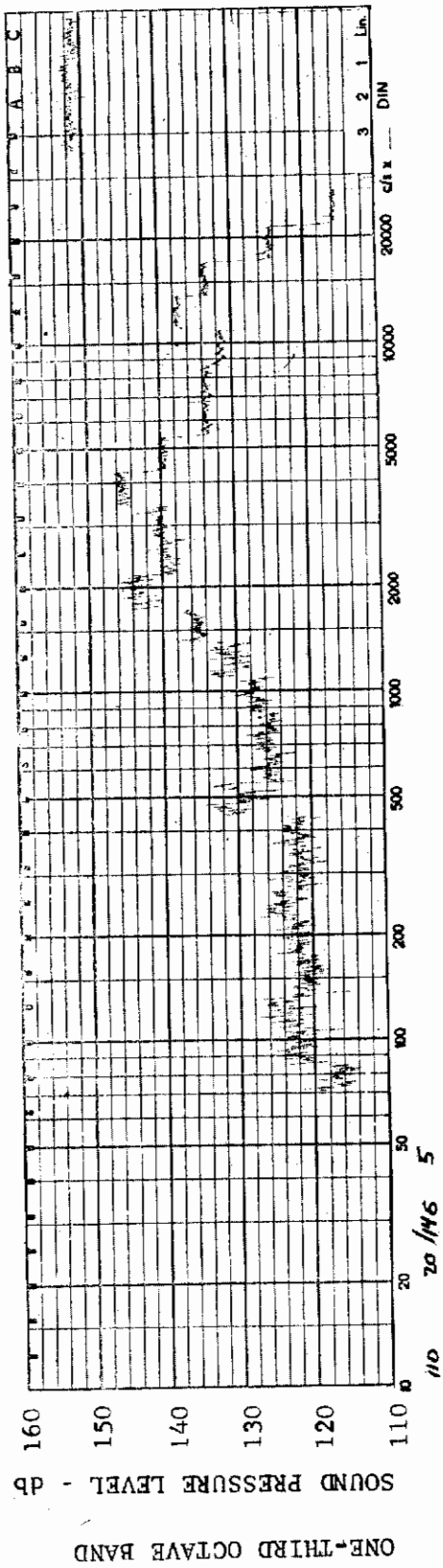

MODEL: FP 60

FIGURE 258 ONE-THIRD OCTAVE BAND SPECTRUM

CHANNEL: 5 MACH NO.: 3.5 α: 5° ϕ: 0 Re_∞/FT.: 1.0×10^6 AEDC GROUP NO.: 20/146

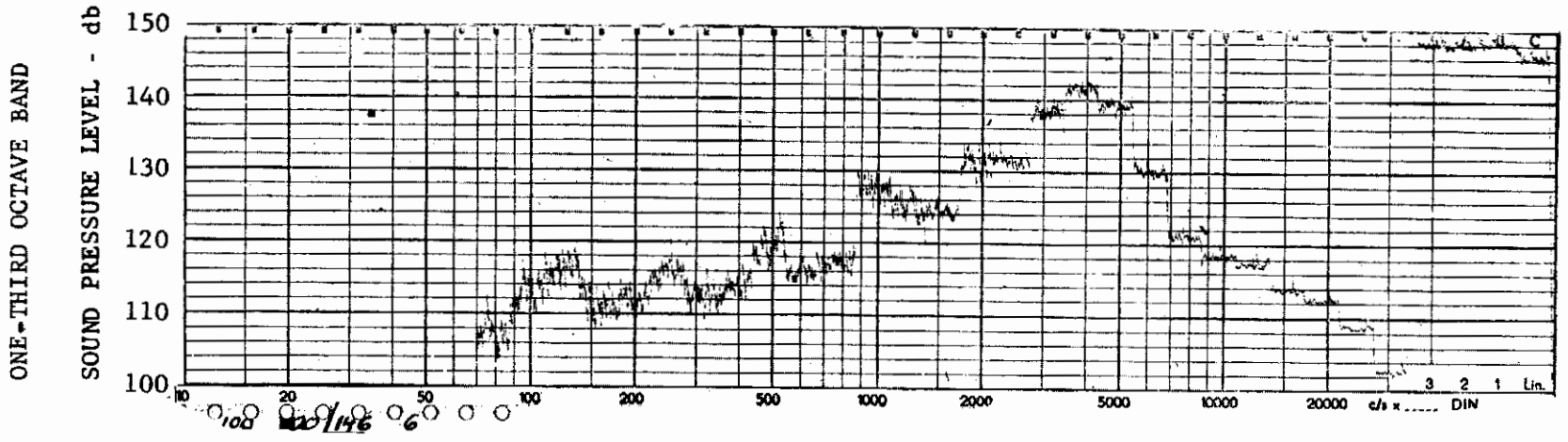

FIGURE 259 ONE-THIRD OCTAVE BAND SPECTRUM MODEL: FP 60

CHANNEL: 6 MACH NO.: 3.5 α: 5° ϕ: 0 Re_∞/FT.: 1.0×10^6 AEDC GROUP NO.: 20/146

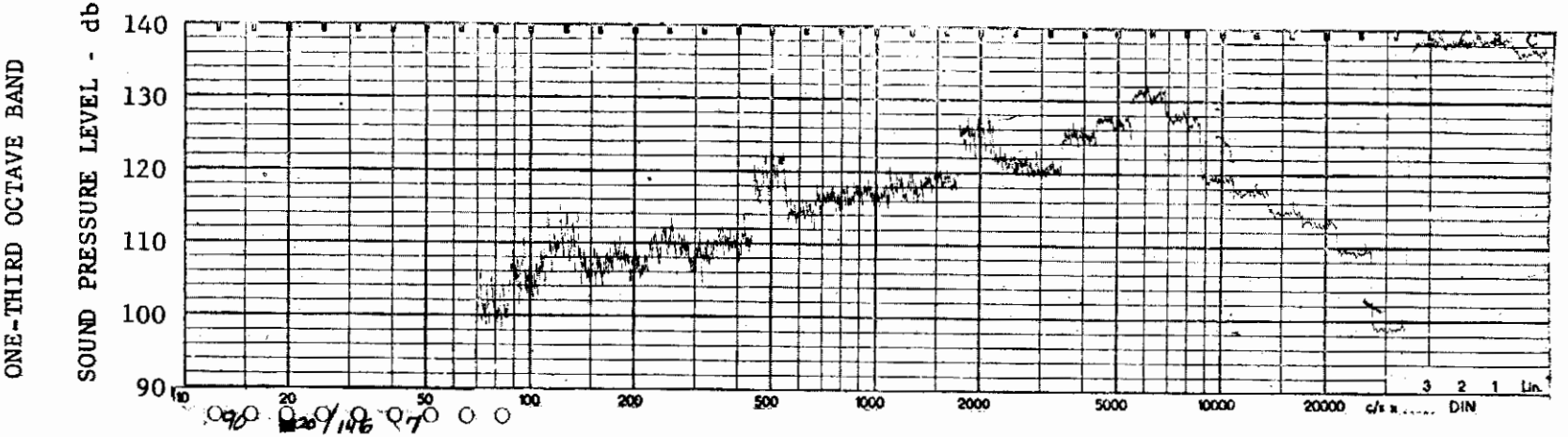

FIGURE 260 ONE-THIRD OCTAVE BAND SPECTRUM MODEL: FP 60

CHANNEL: 7 MACH NO.: 3.5 α: 5° ϕ: 0 Re_∞/FT.: 1.0×10^6 AEDC GROUP NO.: 20/146

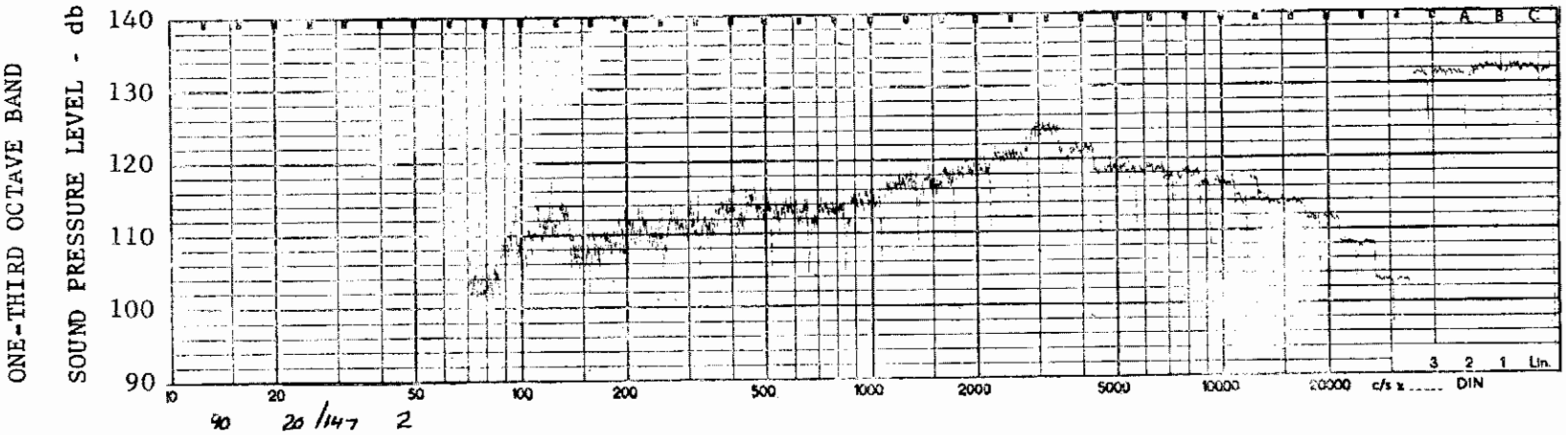

FIGURE 261 ONE-THIRD OCTAVE BAND SPECTRUM MODEL: FP 60

CHANNEL: 2 MACH NO.: 3.5 α: 15° ϕ: 0 Re_∞/FT.: 1.0×10^6 AEDC GROUP NO.: 20/147

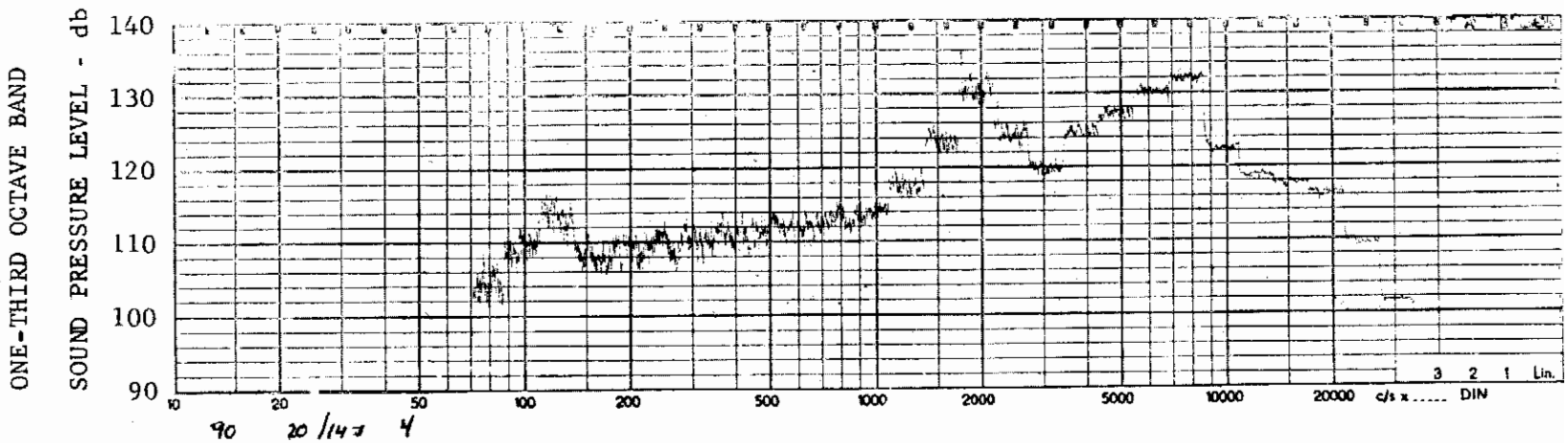

FIGURE 262 ONE-THIRD OCTAVE BAND SPECTRUM MODEL: FP 60

CHANNEL: 4 MACH NO.: 3.5 α: 15° ϕ: 0 Re_∞/FT.: 1.0×10^6 AEDC GROUP NO.: 20/147

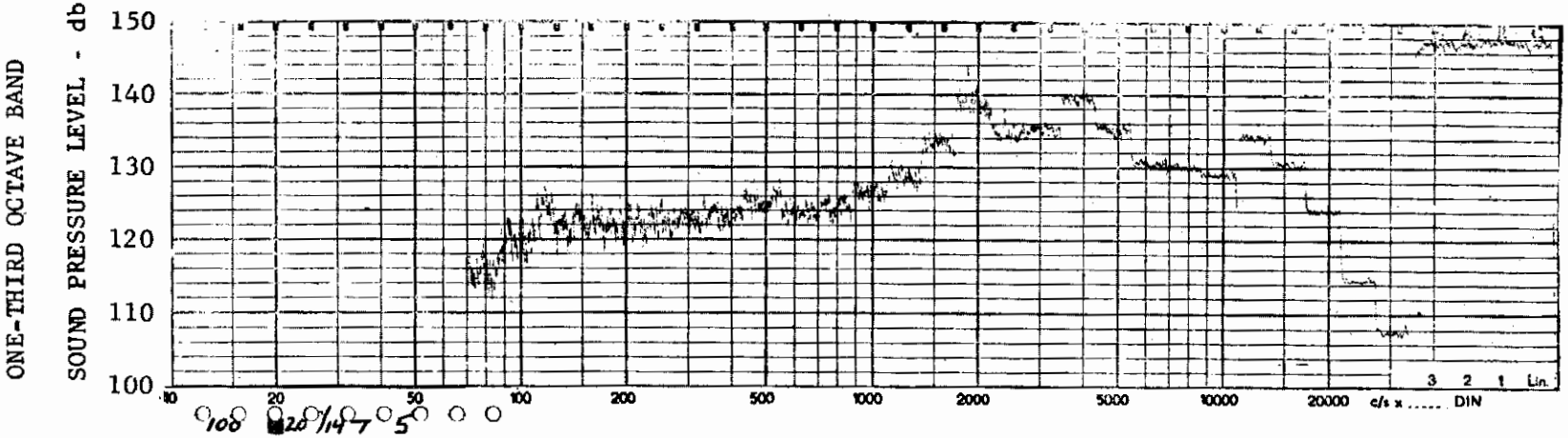

FIGURE 263 ONE-THIRD OCTAVE BAND SPECTRUM MODEL: FP 60

CHANNEL: 5 MACH NO.: 3.5 α: 15° ϕ: 0 Re_∞/FT.: 1.0×10^6 AEDC GROUP NO.: 20/147

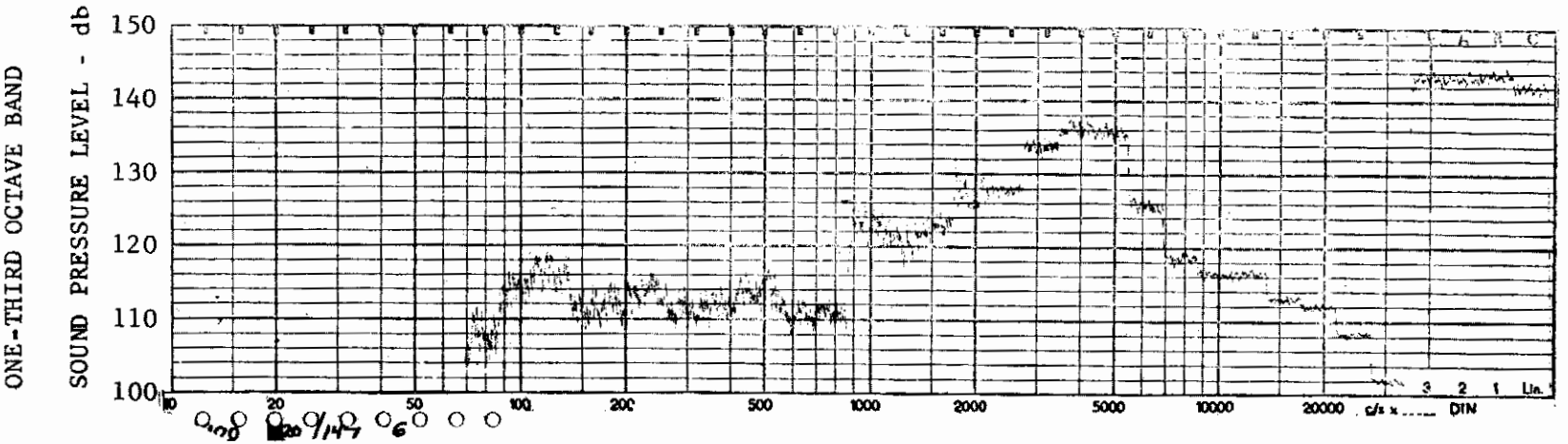

FIGURE 264 ONE-THIRD OCTAVE BAND SPECTRUM MODEL: FP 60

CHANNEL: 6 MACH NO.: 3.5 α: 15° ϕ: 0 Re_∞/FT.: 1.0×10^6 AEDC GROUP NO.: 20/147

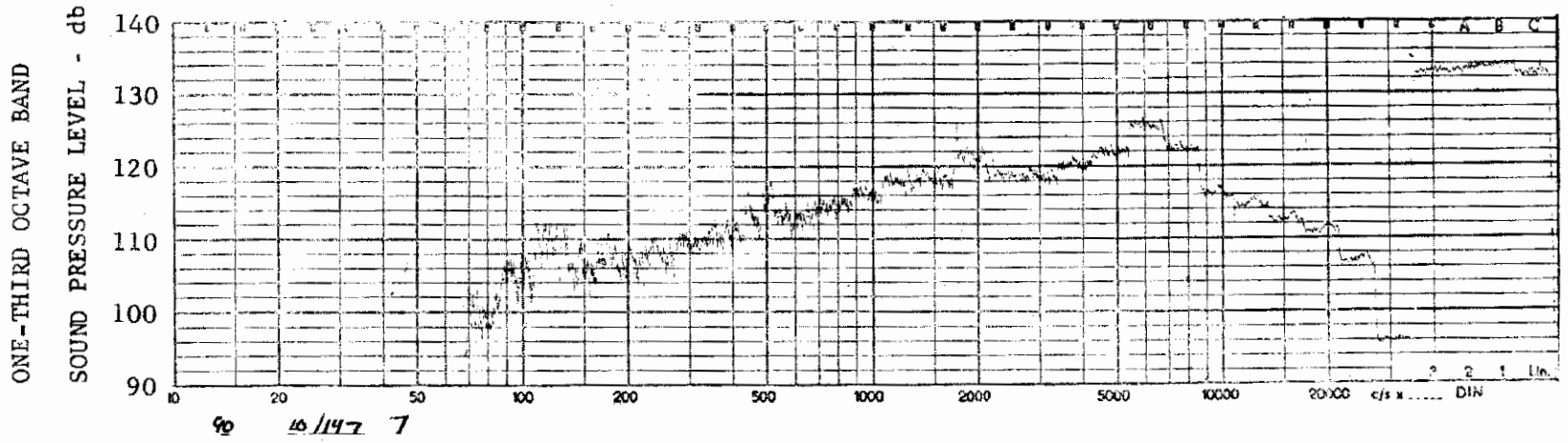

FIGURE 265 ONE-THIRD OCTAVE BAND SPECTRUM MODEL: FP 60

CHANNEL: 7 MACH NO.: 3.5 α: 15° ϕ: 0 Re_∞/FT.: 1.0×10^6 AEDC GROUP NO.: 20/147

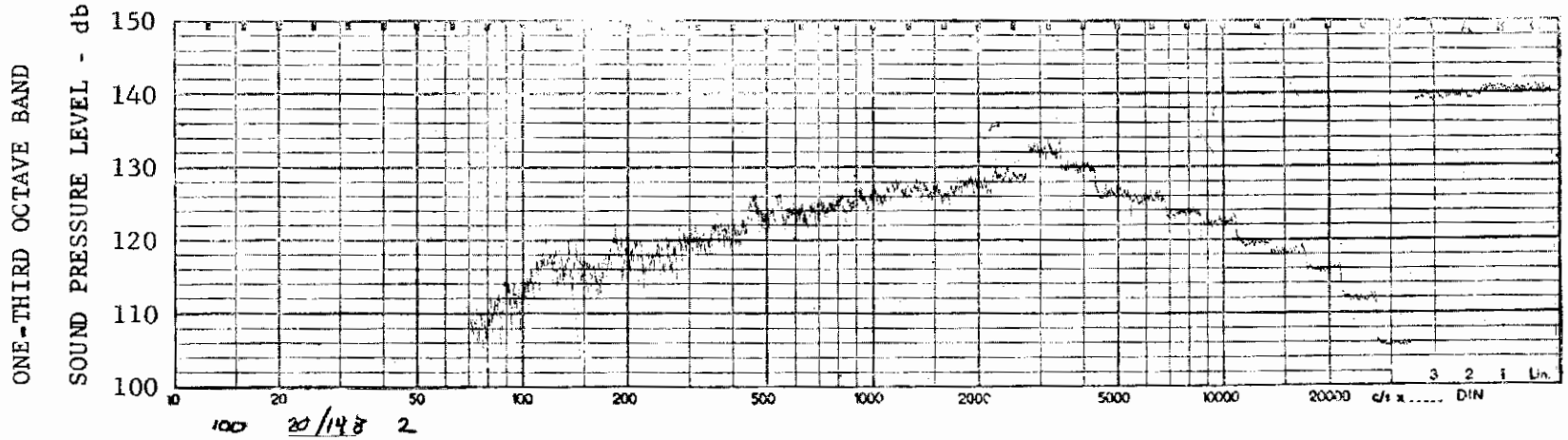

FIGURE 266 ONE-THIRD OCTAVE BAND SPECTRUM MODEL: FP 60

CHANNEL: 2 MACH NO.: 3.5 α: 0 ϕ: 0 Re_∞/FT.: 1.0×10^6 AEDC GROUP NO.: 20/148

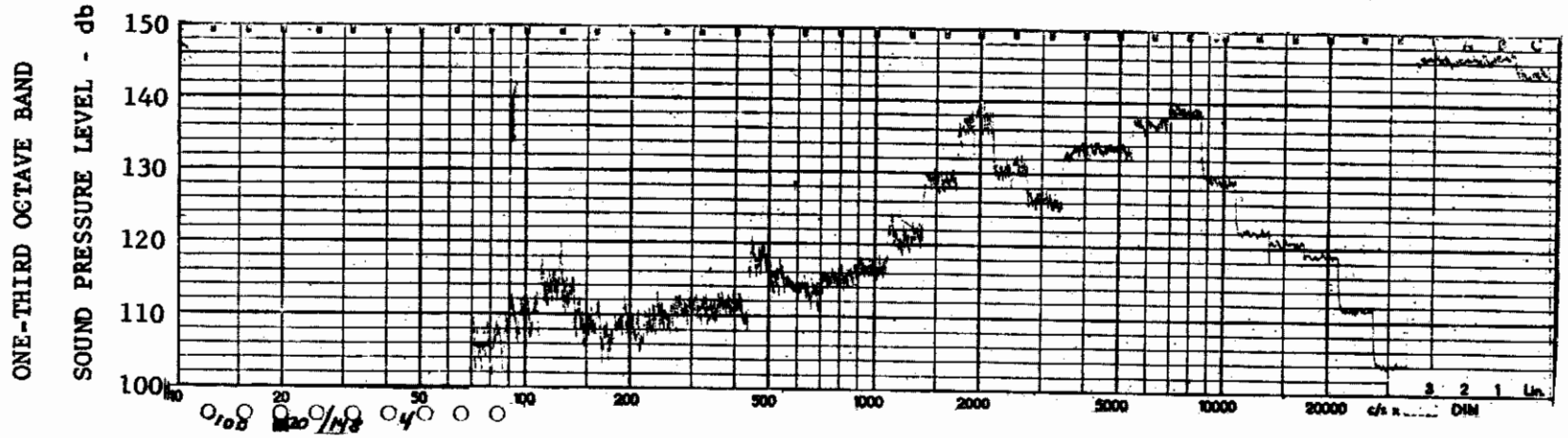

FIGURE 267 ONE-THIRD OCTAVE BAND SPECTRUM MODEL: FP 60

CHANNEL: 4 MACH NO.: 3.5 α: 0 ϕ: 0 Re_∞/FT.: 1.0×10^6 AEDC GROUP NO.: 20/148

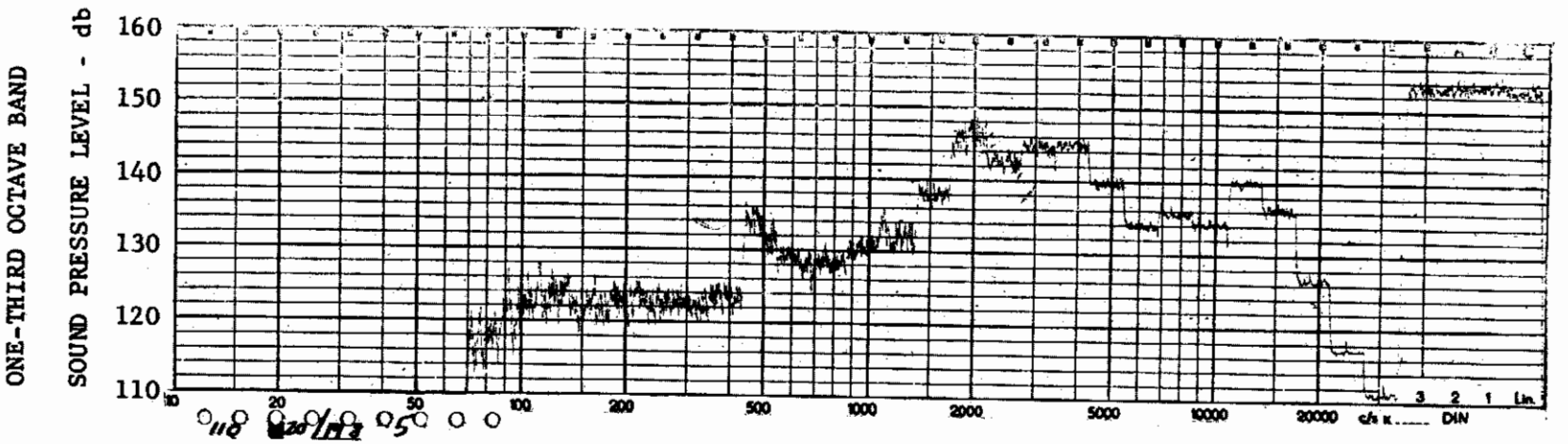

FIGURE 268 ONE-THIRD OCTAVE BAND SPECTRUM MODEL: FP 60

CHANNEL: 5 MACH NO.: 3.5 α: 0 ϕ: 0 Re_∞/FT.: 1.0×10^6 AEDC GROUP NO.: 20/148

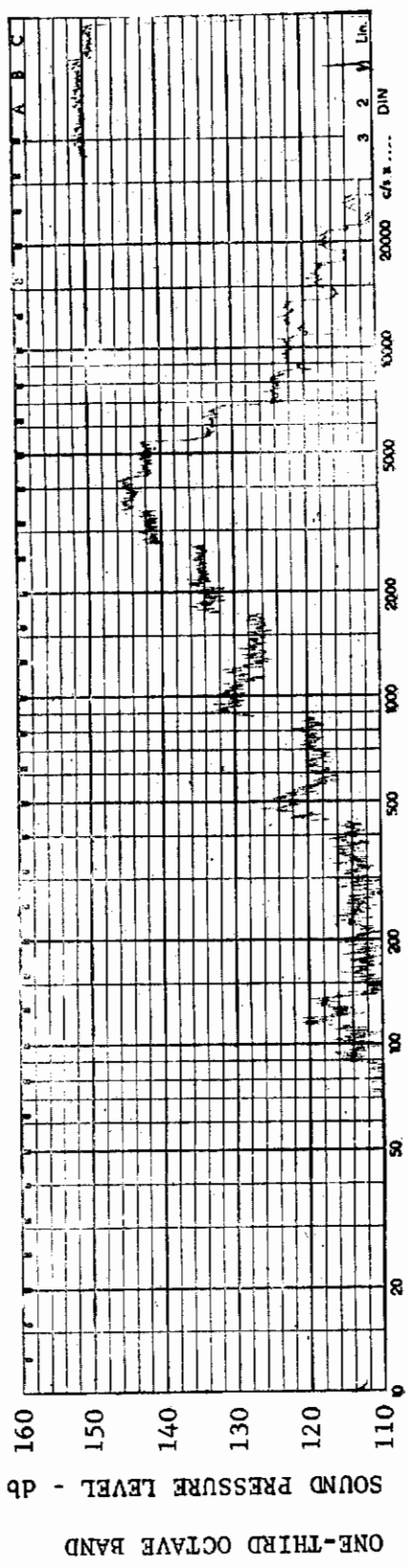

FIGURE 269 ONE-THIRD OCTAVE BAND SPECTRUM

MODEL: FP 60

CHANNEL: 6 MACH NO.: 3.5 α: 0 ϕ: 0 Re_∞/FT.: 1.0×10^6 AEDC GROUP NO.: 20/148

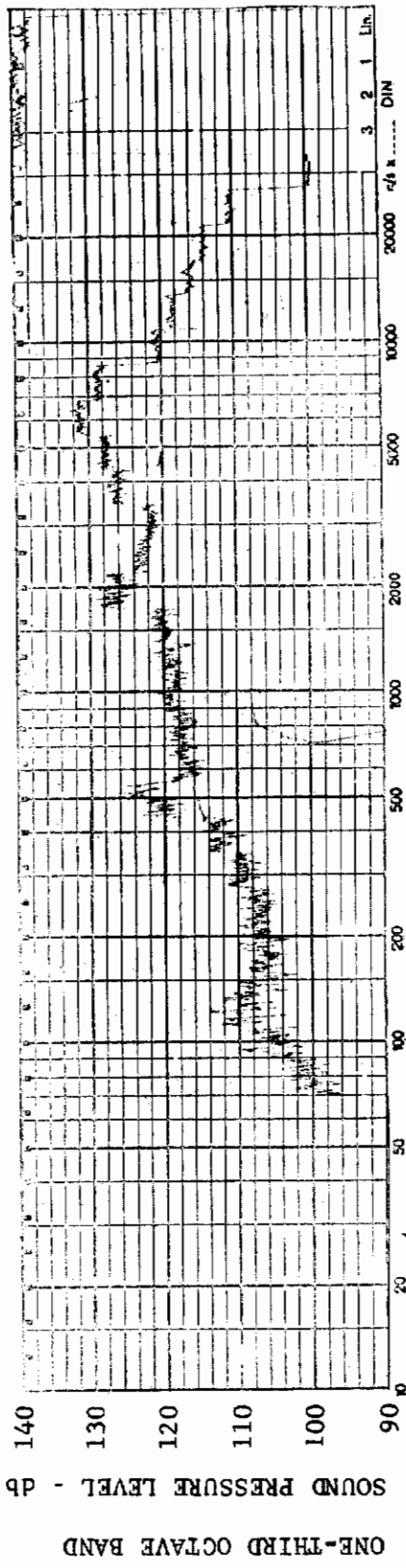

FIGURE 270 ONE-THIRD OCTAVE BAND SPECTRUM

MODEL: FP 60

CHANNEL: 7 MACH NO.: 3.5 α: 0 ϕ: 0 Re_∞/FT.: 1.0×10^6 AEDC GROUP NO.: 20/148

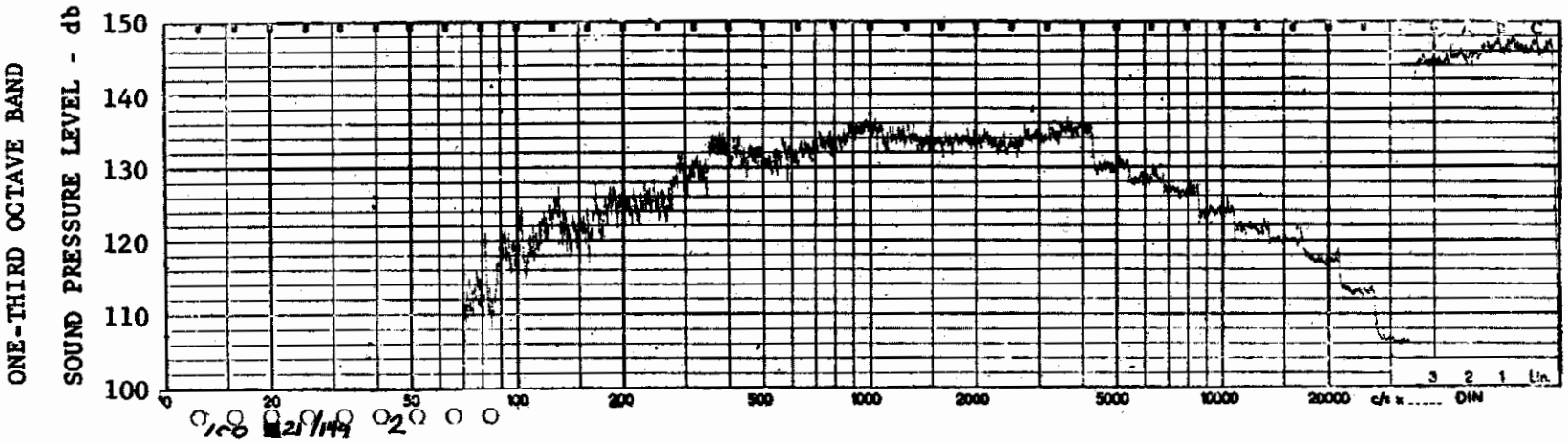

FIGURE 271 ONE-THIRD OCTAVE BAND SPECTRUM MODEL: FP 60

CHANNEL: 2 MACH NO.: 2 α: 0 ϕ: 0 Re_∞/FT. 0.75×10^6 AEDC GROUP NO.: 21/149

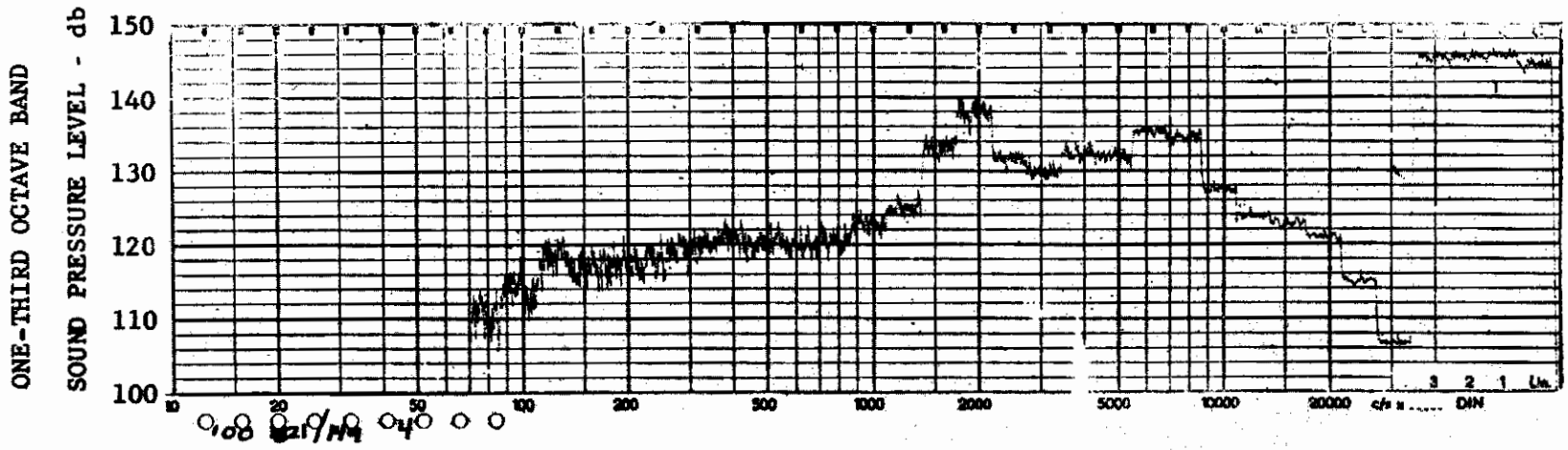

FIGURE 272 ONE-THIRD OCTAVE BAND SPECTRUM MODEL: FP 60

CHANNEL: 4 MACH NO.: 2 α: 0 ϕ: 0 Re_∞/FT. 0.75×10^6 AEDC GROUP NO.: 21/149

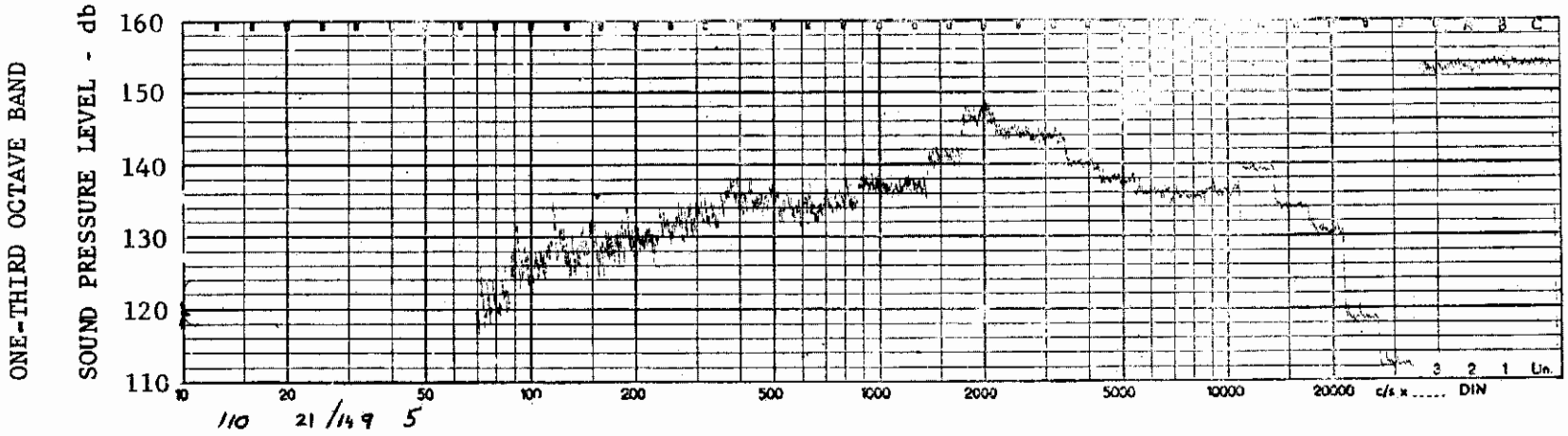

FIGURE 273 ONE-THIRD OCTAVE BAND SPECTRUM MODEL: FP 60

CHANNEL: 5 MACH NO.: 2 α: 0 ϕ: 0 Re_∞/FT. 0.75×10^6 AEDC GROUP NO.: 21/149

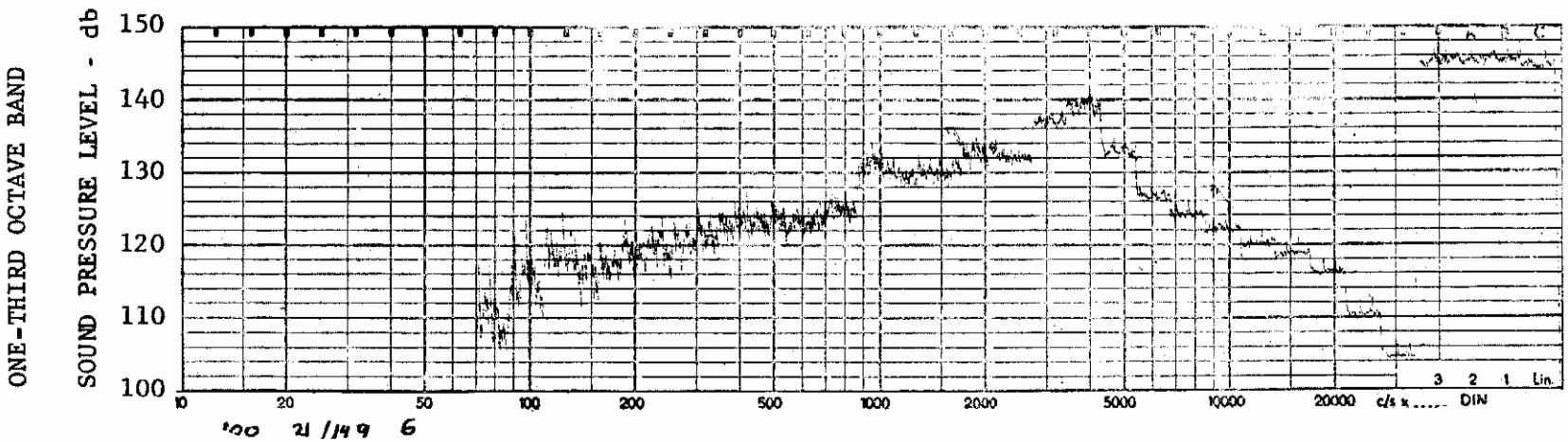

FIGURE 274 ONE-THIRD OCTAVE BAND SPECTRUM MODEL: FP 60

CHANNEL: 6 MACH NO.: 2 α: 0 ϕ: 0 Re_∞/FT. 0.75×10^6 AEDC GROUP NO.: 21/149

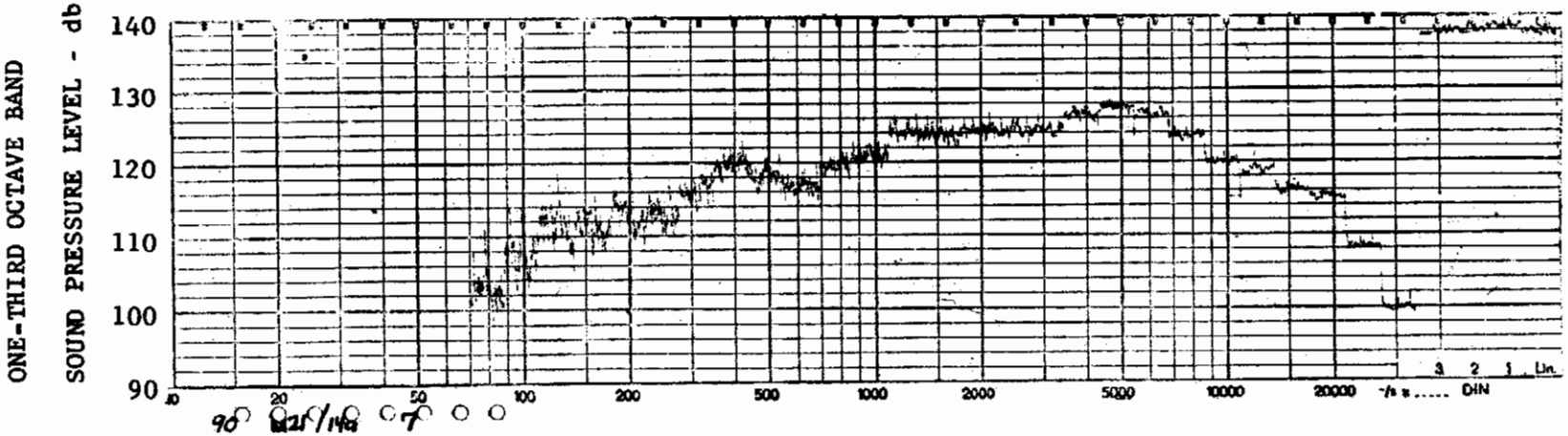

FIGURE 275 ONE-THIRD OCTAVE BAND SPECTRUM MODEL: FP 60

CHANNEL: 7 MACH NO.: 2 α: 0 ϕ: 0 Re_∞/FT. 0.75×10^6 AEDC GROUP NO.: 21/149

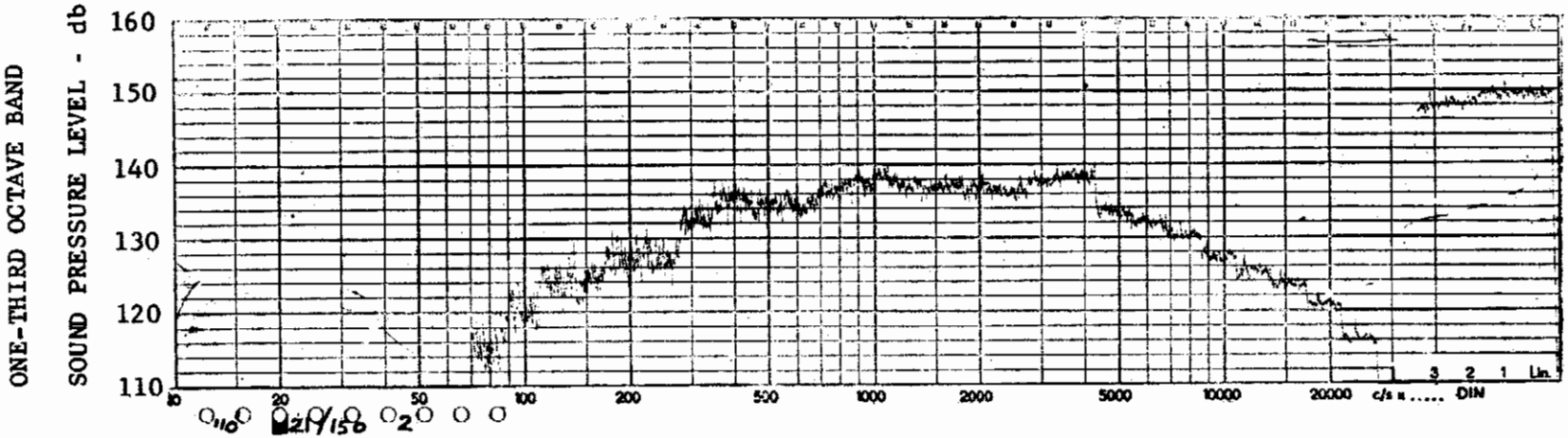

FIGURE 276 ONE-THIRD OCTAVE BAND SPECTRUM MODEL: FP 60

CHANNEL: 2 MACH NO.: 2 α: 0 ϕ: 0 Re_∞/FT. 1.0×10^6 AEDC GROUP NO.: 21/150

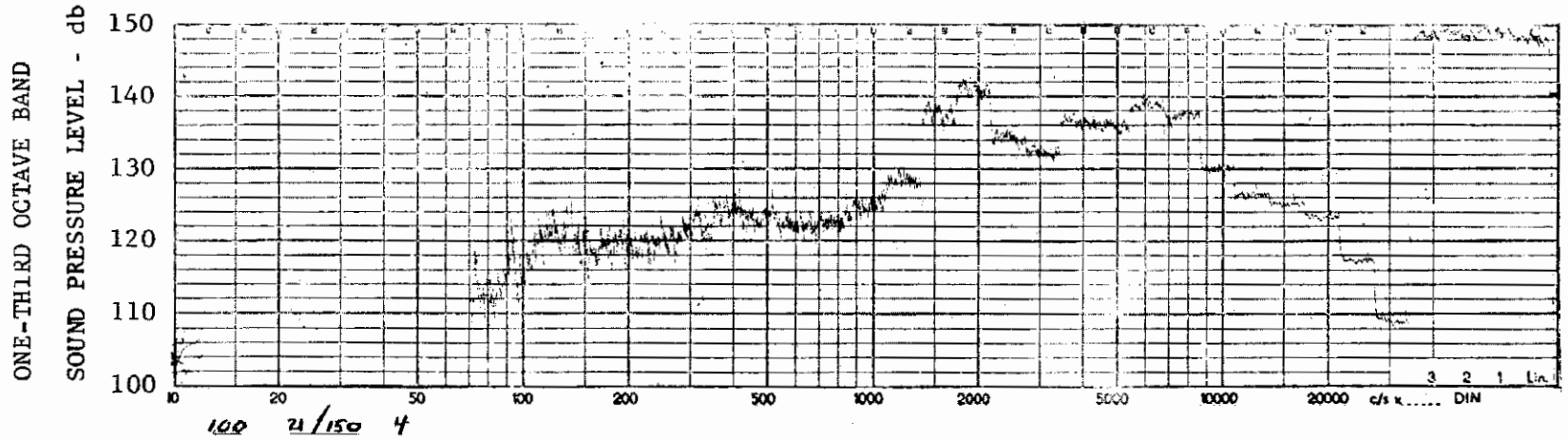

FIGURE 277 ONE-THIRD OCTAVE BAND SPECTRUM MODEL: FP 60

CHANNEL: 4 MACH NO.: 2 α: 0 ϕ: 0 Re_∞/FT.: 1.0×10^6 AEDC GROUP NO.: 21/150

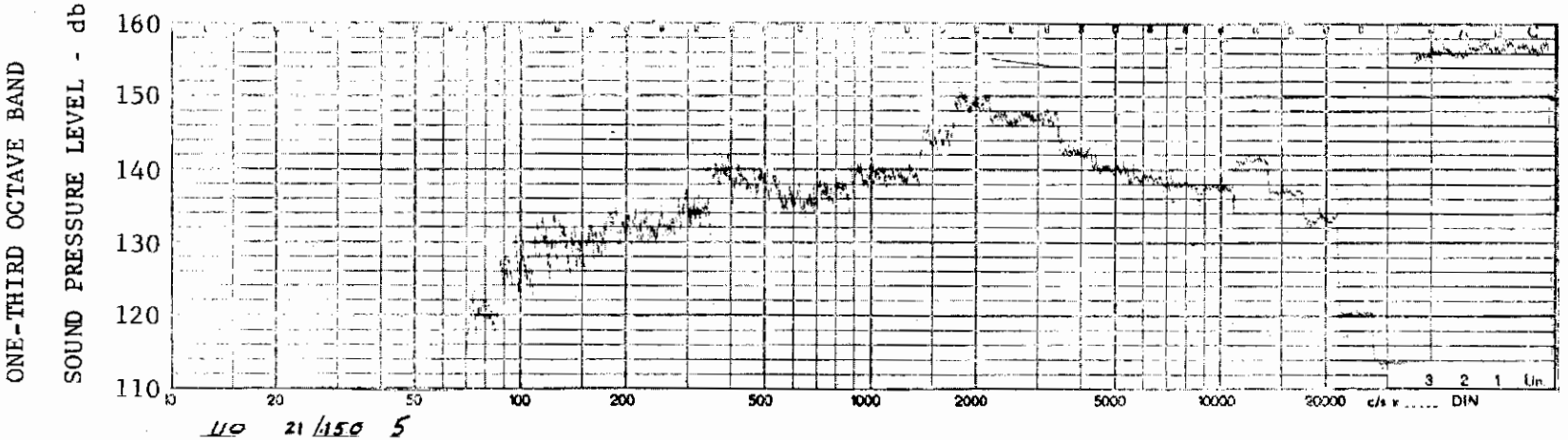

FIGURE 278 ONE-THIRD OCTAVE BAND SPECTRUM MODEL: FP 60

CHANNEL: 5 MACH NO.: 2 α: 0 ϕ: 0 Re_∞/FT.: 1.0×10^6 AEDC GROUP NO.: 21/150

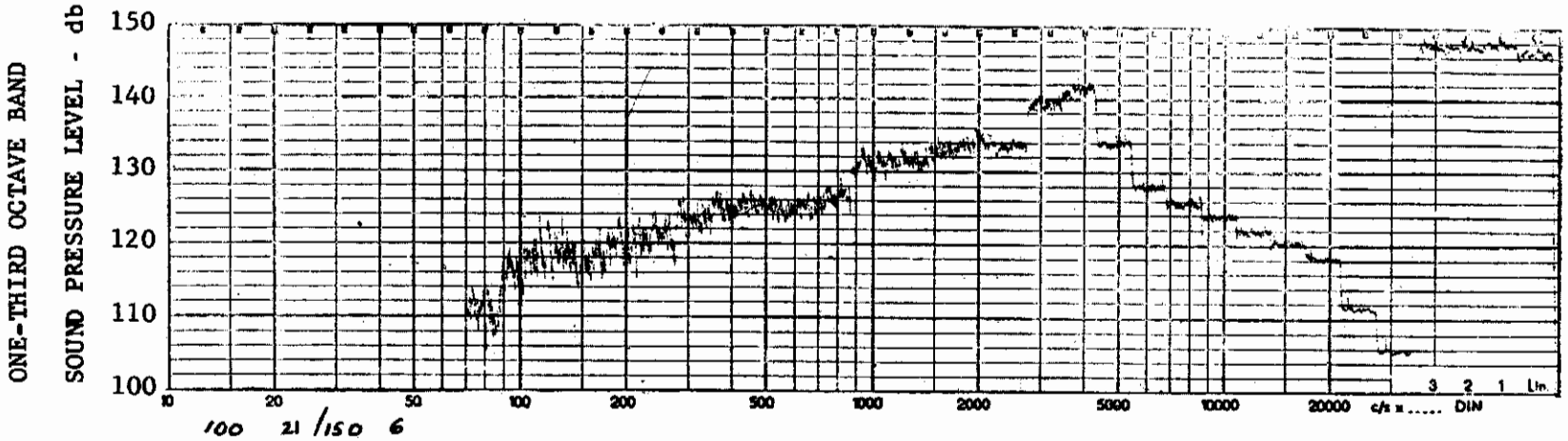

FIGURE 279 ONE-THIRD OCTAVE BAND SPECTRUM MODEL: FP 60

CHANNEL: 6 MACH NO.: 2 α: 0 ϕ: 0 Re_∞/FT.: 1.0×10^6 AEDC GROUP NO.: 21/150

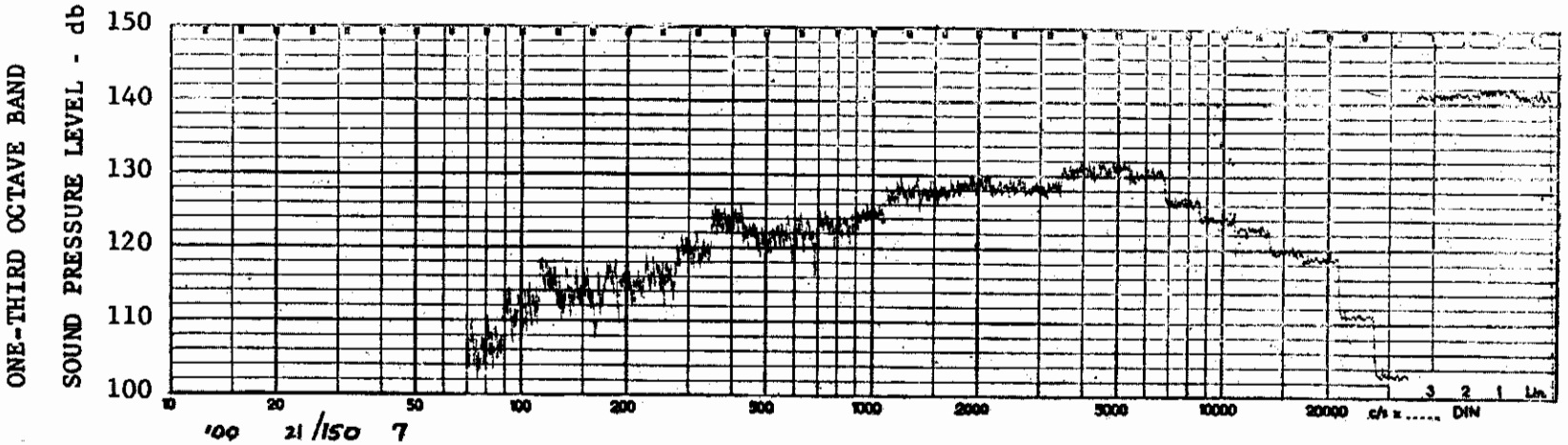

FIGURE 280 ONE-THIRD OCTAVE BAND SPECTRUM MODEL: FP 60

CHANNEL: 7 MACH NO.: 2 α: 0 ϕ: 0 Re_∞/FT.: 1.0×10^6 AEDC GROUP NO.: 21/150

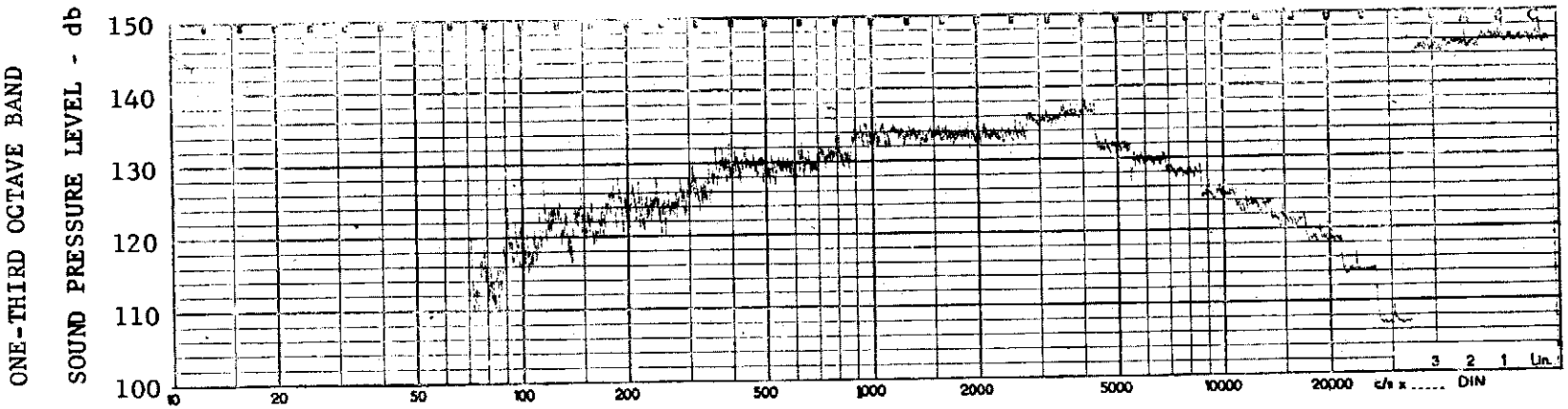

FIGURE 281 ONE-THIRD OCTAVE BAND SPECTRUM MODEL: FP 60

CHANNEL: 2 MACH NO.: 2 α: 5° ϕ: 0 Re_∞/FT.: 1.0×10^6 AEDC GROUP NO.: 21/151

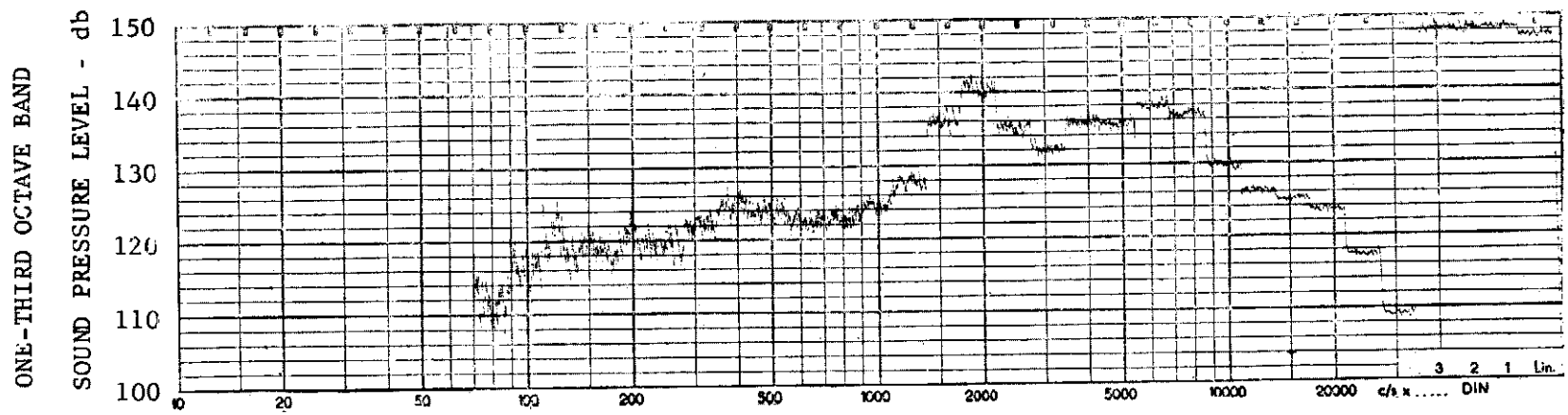

FIGURE 282 ONE-THIRD OCTAVE BAND SPECTRUM MODEL: FP 60

CHANNEL: 4 MACH NO.: 2 α: 5° ϕ: 0 Re_∞/FT.: 1.0×10^6 AEDC GROUP NO.: 21/151

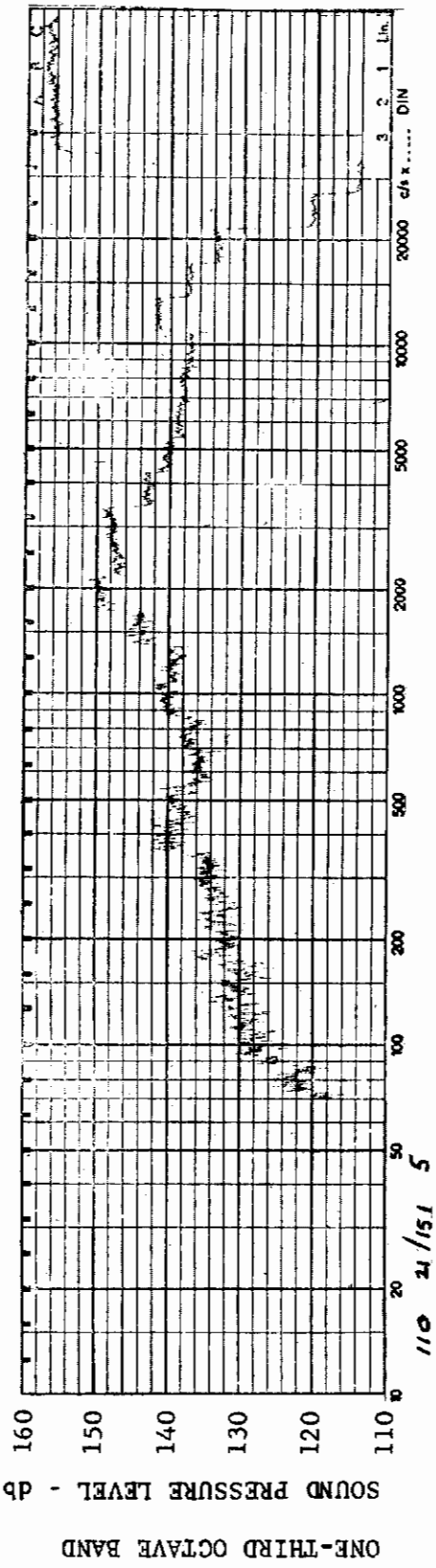

FIGURE 283 ONE-THIRD OCTAVE BAND SPECTRUM MODEL: FP 60

CHANNEL: 5 MACH NO.: 2 α: 5° ϕ: 0 Re_∞/FT.: 1.0×10^6 AEDC GROUP NO.: 21/151

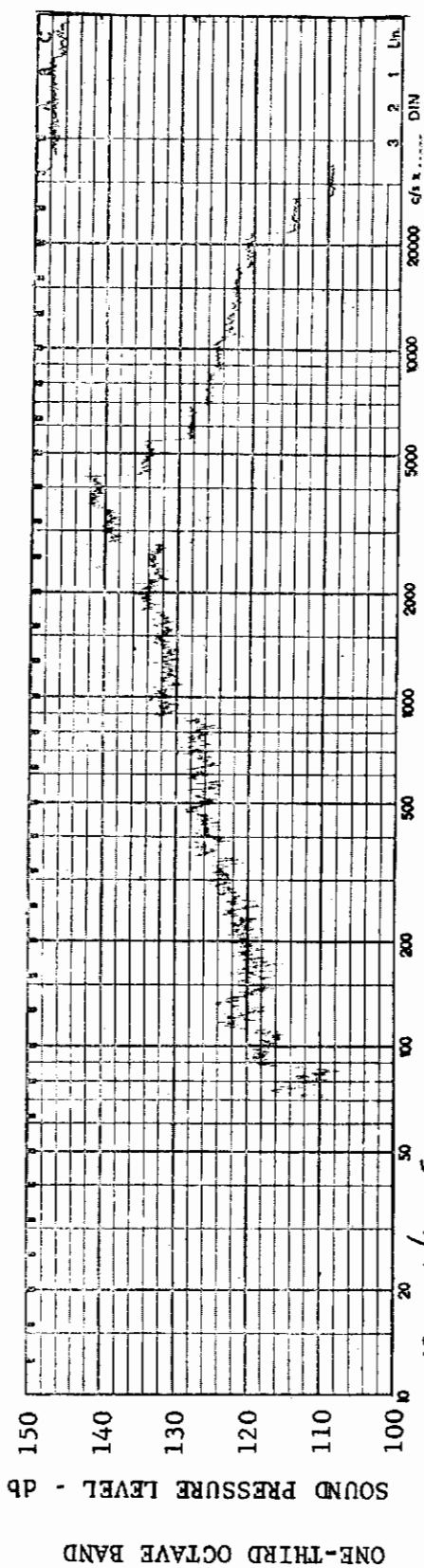

FIGURE 284 ONE-THIRD OCTAVE BAND SPECTRUM MODEL: FP 60

CHANNEL: 6 MACH NO.: 2 α: 5° ϕ: 0 Re_∞/FT.: 1.0×10^6 AEDC GROUP NO.: 21/151

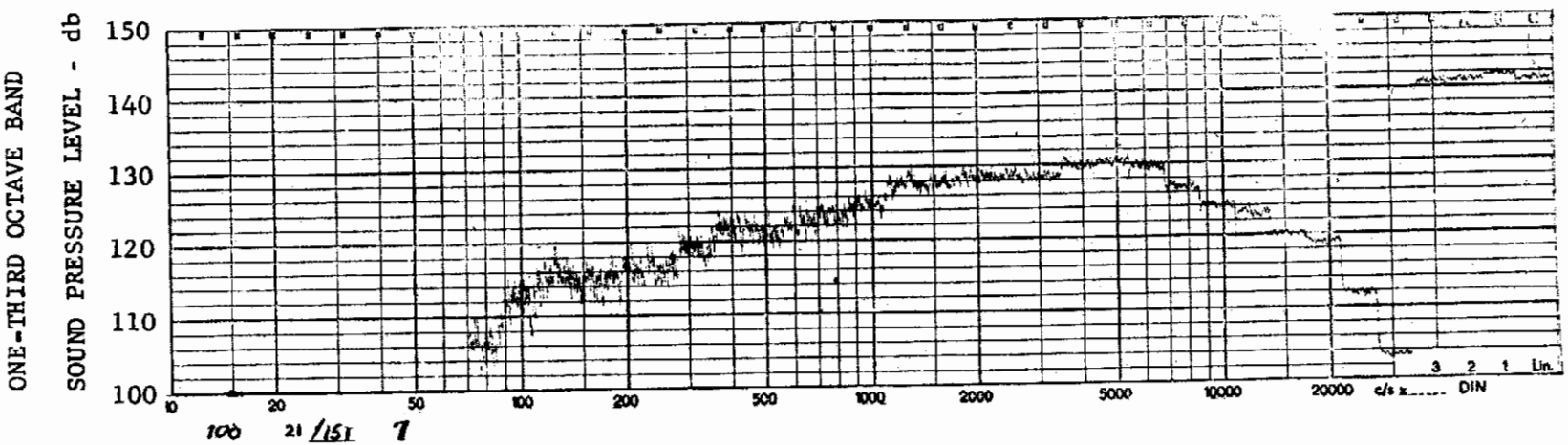

FIGURE 285 ONE-THIRD OCTAVE BAND SPECTRUM MODEL: FP 60

CHANNEL: 7 MACH NO.: 2 α: 5° ϕ: 0 Re_∞/FT.: 1.0×10^6 AEDC GROUP NO.: 21/151

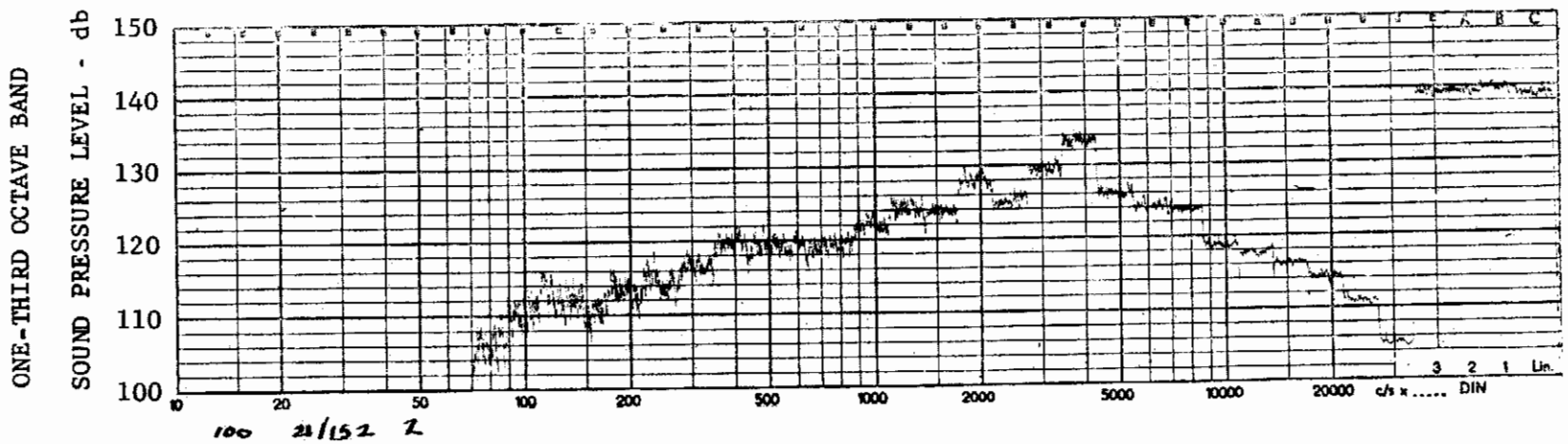

FIGURE 286 ONE-THIRD OCTAVE BAND SPECTRUM MODEL: FP 60

CHANNEL: 2 MACH NO.: 2 α: 15° ϕ: 0 Re_∞/FT.: 1.0×10^6 AEDC GROUP NO.: 21/152

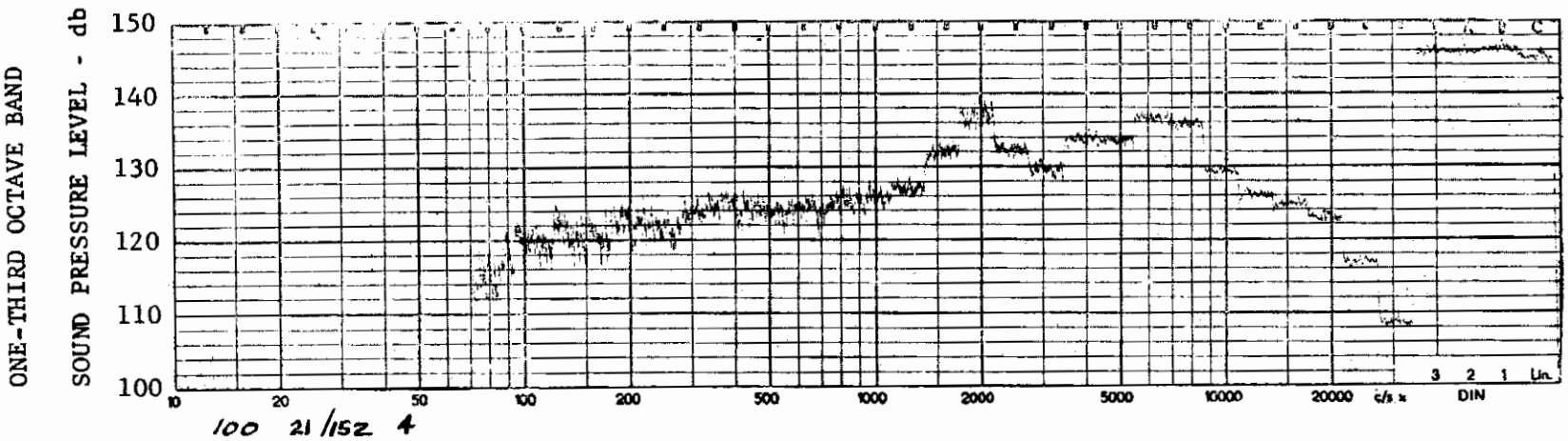

FIGURE 287 ONE-THIRD OCTAVE BAND SPECTRUM MODEL: FP 60

CHANNEL: 4 MACH NO.: 2 α: 15° ϕ: 0 Re_∞/FT.: 1.0×10^6 AEDC GROUP NO.: 21/152

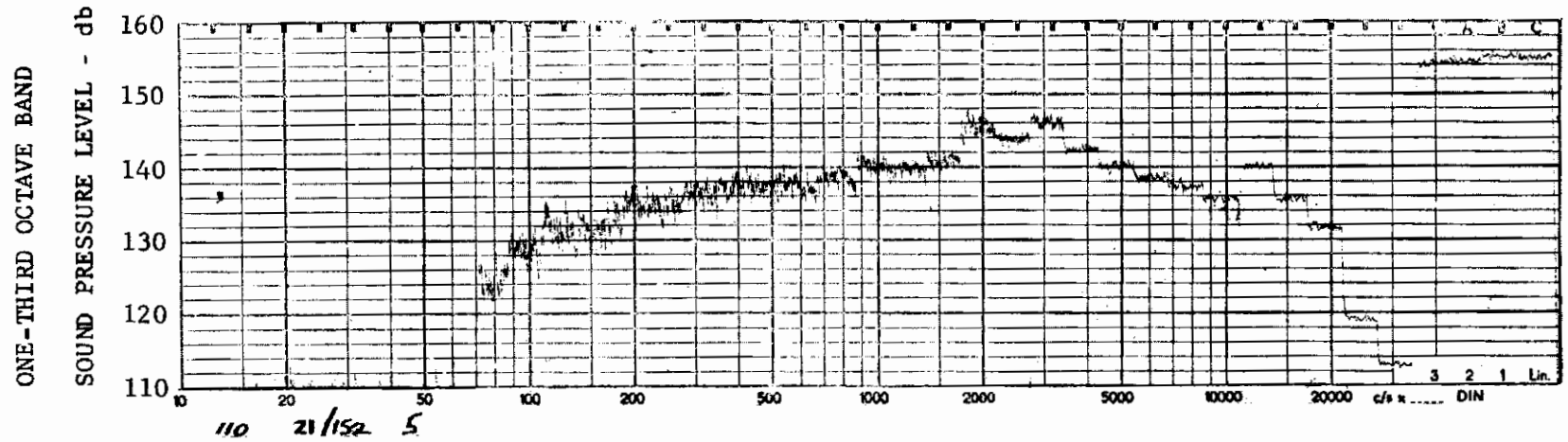

FIGURE 288 ONE-THIRD OCTAVE BAND SPECTRUM MODEL: FP 60

CHANNEL: 5 MACH NO.: 2 α: 15° ϕ: 0 Re_∞/FT. 1.0×10^6 AEDC GROUP NO.: 21/152

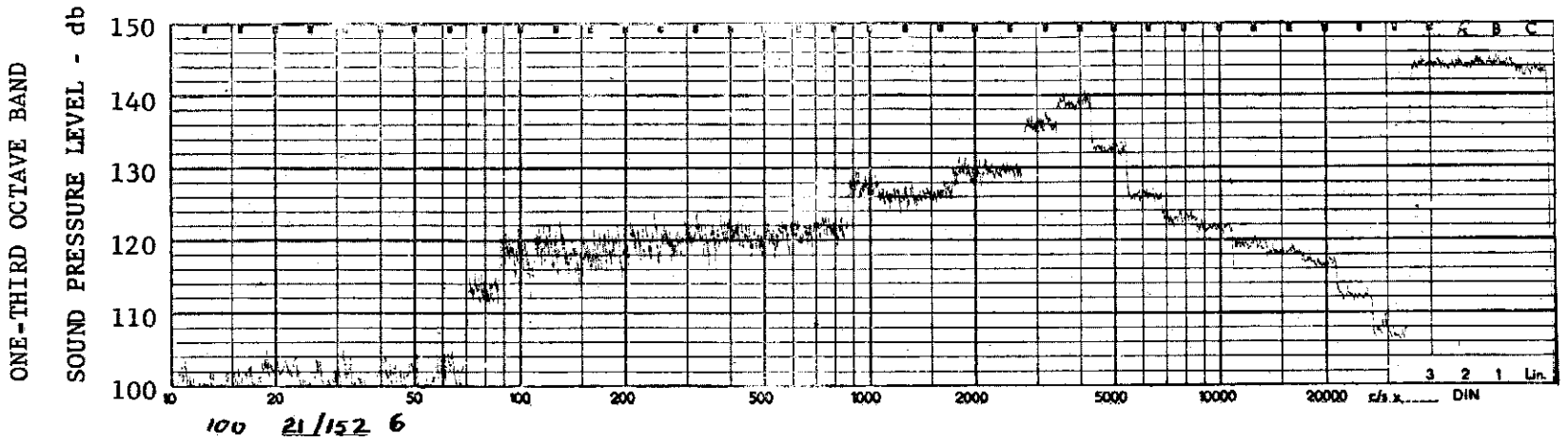

FIGURE 289 ONE-THIRD OCTAVE BAND SPECTRUM MODEL: FP 60

CHANNEL: 6 MACH NO.: 2 α: 15° ϕ: 0 Re_∞/FT.: 1.0×10^6 AEDC GROUP NO.: 21/152

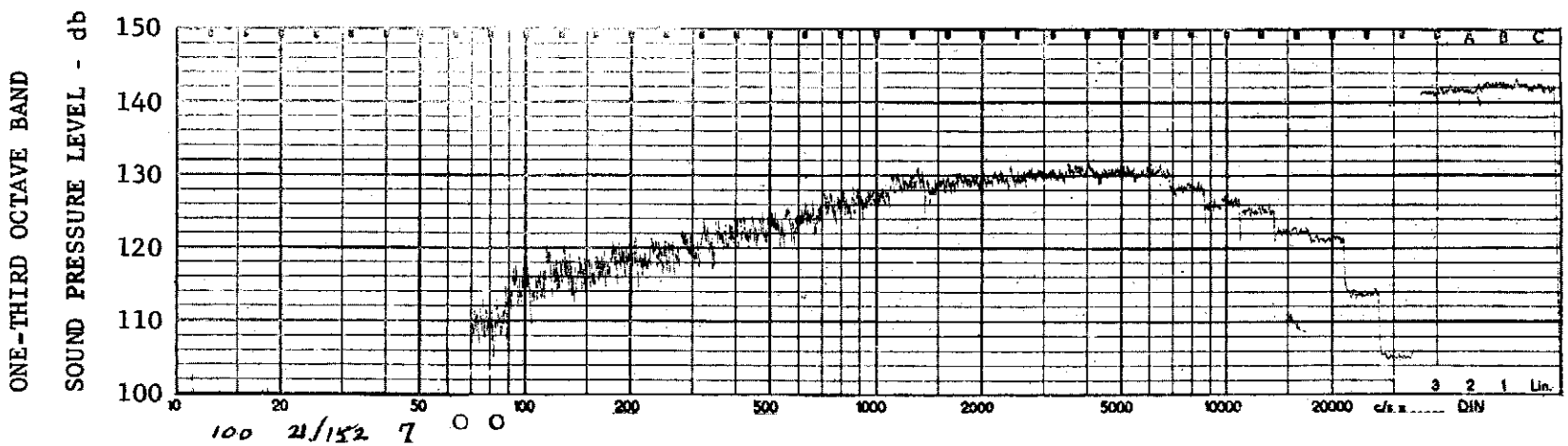

FIGURE 290 ONE-THIRD OCTAVE BAND SPECTRUM MODEL: FP 60

CHANNEL: 7 MACH NO.: 2 α: 15° ϕ: 0 Re_∞/FT.: 1.0×10^6 AEDC GROUP NO.: 21/152

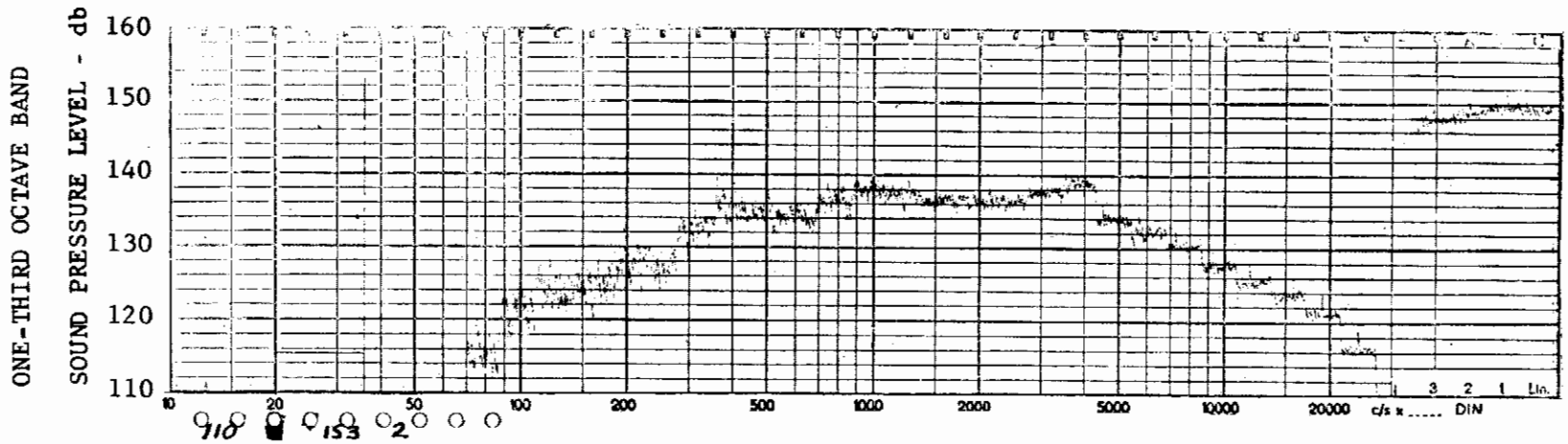

FIGURE 291 ONE-THIRD OCTAVE BAND SPECTRUM MODEL: FP 60

CHANNEL: 2 MACH NO.: 2 α: 0 ϕ: 0 Re_∞/FT.: 1.0×10^6 AEDC GROUP NO.: 21/153

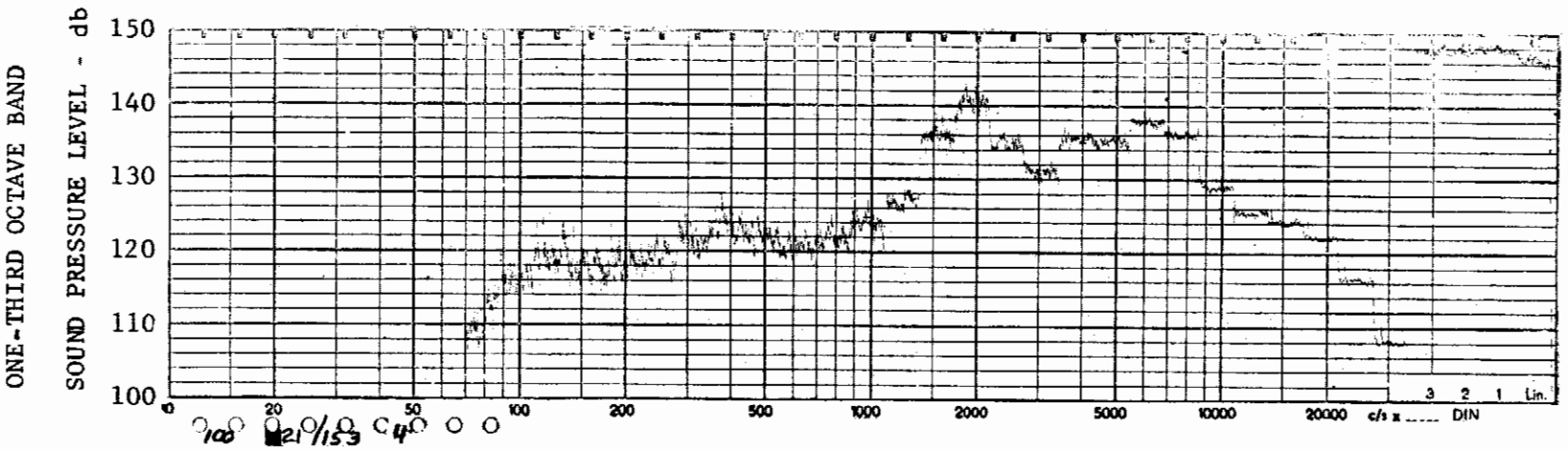

FIGURE 292 ONE-THIRD OCTAVE BAND SPECTRUM MODEL: FP 60

CHANNEL: 4 MACH NO.: 2 α: 0 ϕ: 0 Re_∞/FT.: 1.0×10^6 AEDC GROUP NO.: 21/153

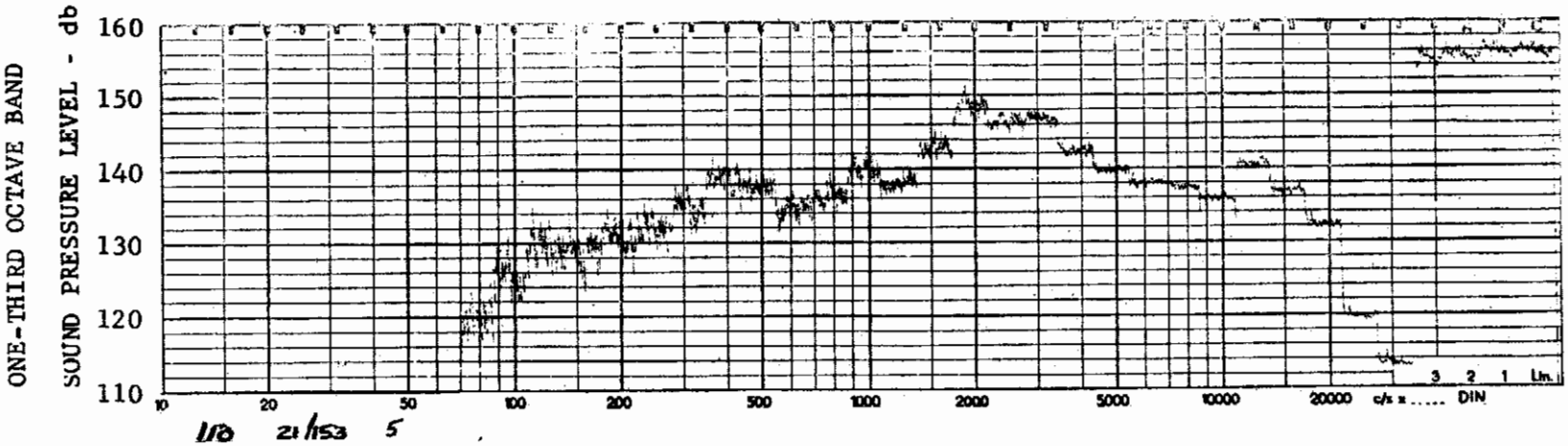

FIGURE 293 ONE-THIRD OCTAVE BAND SPECTRUM MODEL: FP 60

CHANNEL: 5 MACH NO.: 2 α: 0 ϕ: 0 Re_∞/FT.: 1.0×10^6 AEDC GROUP NO.: 21/153

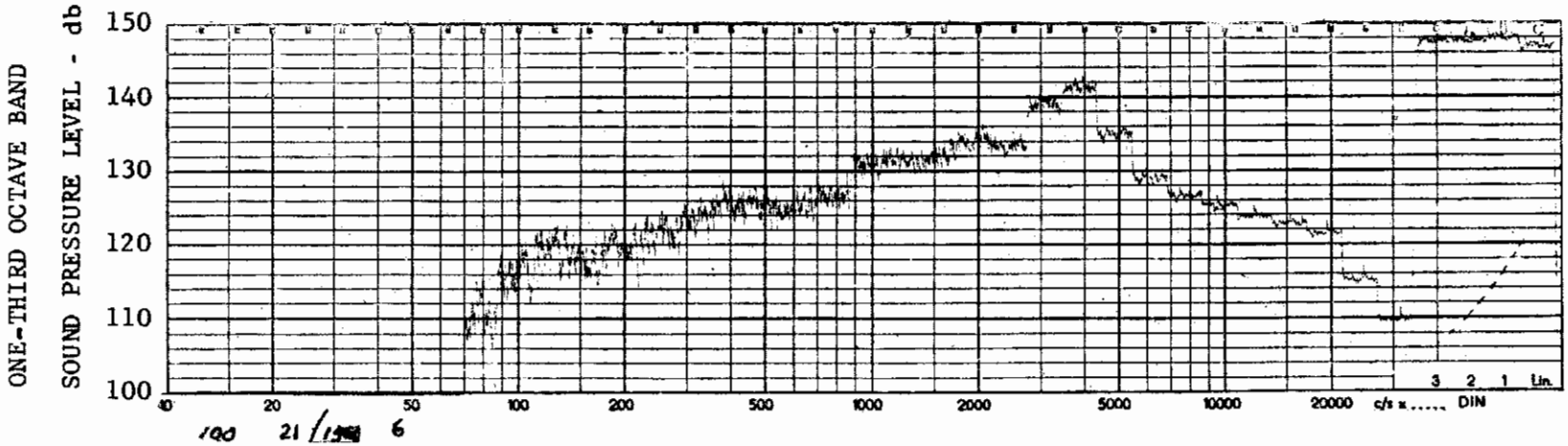

FIGURE 294 ONE-THIRD OCTAVE BAND SPECTRUM MODEL: FP 60

CHANNEL: 6 MACH NO.: 2 α: 0 ϕ: 0 Re_∞/FT.: 1.0×10^6 AEDC GROUP NO.: 21/153

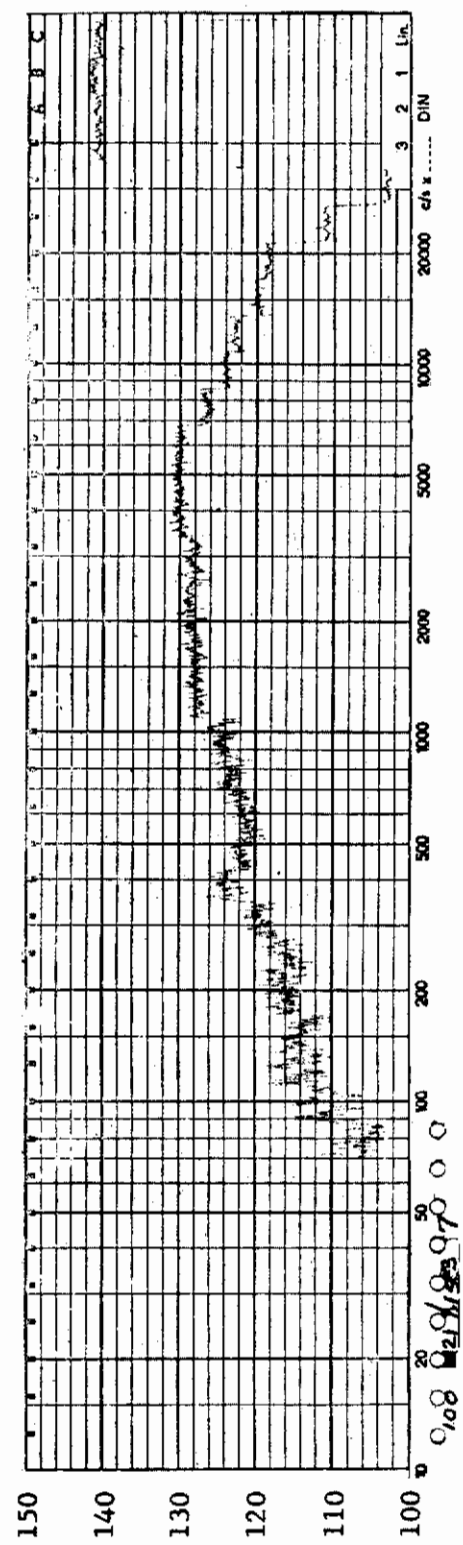

FIGURE 295 ONE-THIRD OCTAVE BAND SPECTRUM

MODEL: FP 60

CHANNEL: 7 MACH NO.: 2 α: 0 ϕ: 0 Re_∞/FT.: 1.0×10^6 AEDC GROUP NO.: 21/153

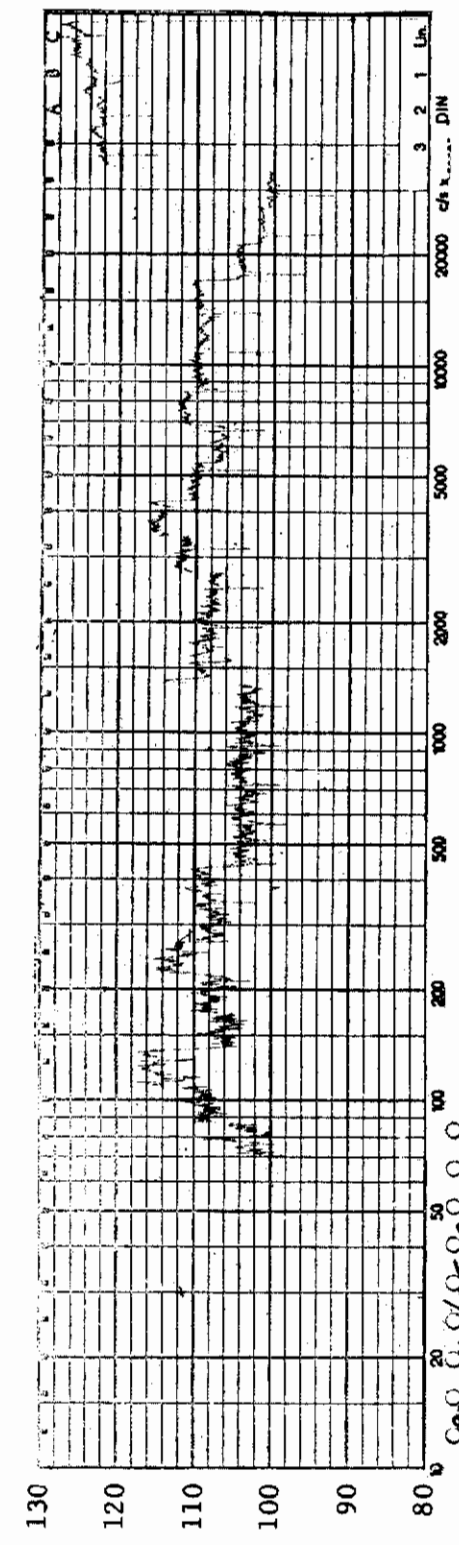

FIGURE 296 ONE-THIRD OCTAVE BAND SPECTRUM

MODEL: FP 0

CHANNEL: 2 MACH NO.: 2 α: 0 ϕ: 0 Re_∞/FT.: 0.75×10^6 AEDC GROUP NO.: 22/155

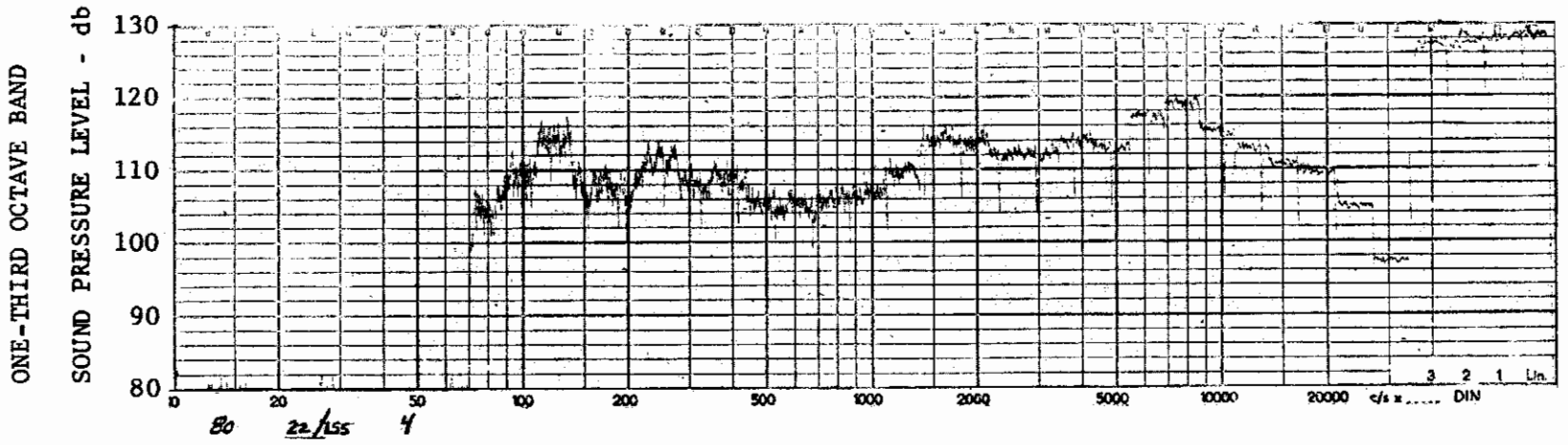

FIGURE 297 ONE-THIRD OCTAVE BAND SPECTRUM MODEL: FP 0

CHANNEL: 4 MACH NO.: 2 α: 0 ϕ: 0 Re_∞/FT.: 0.75×10^6 AEDC GROUP NO.: 22/155

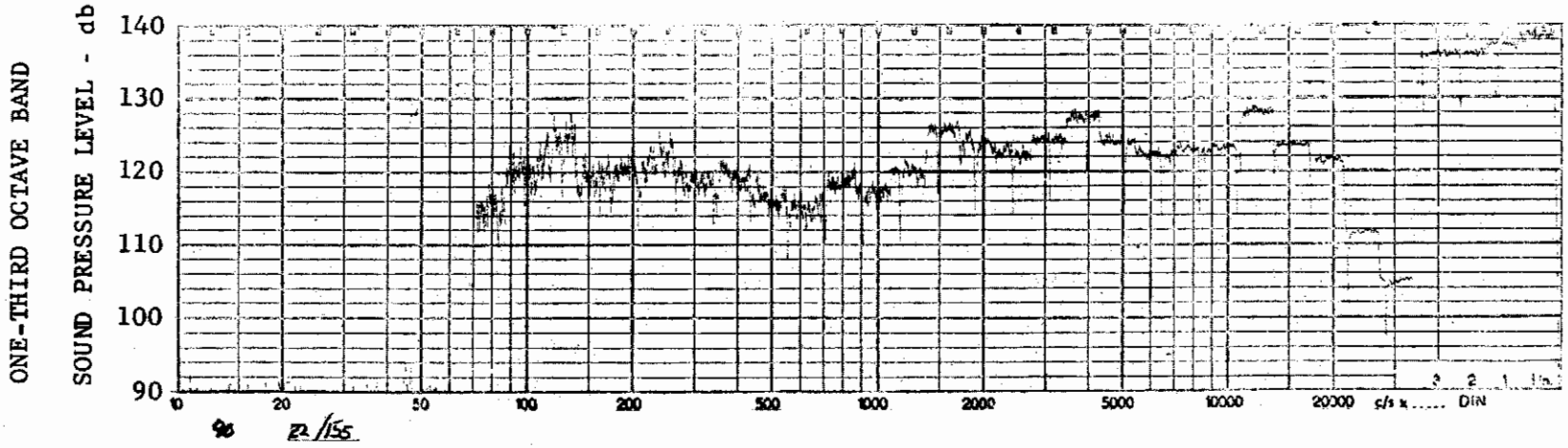

FIGURE 298 ONE-THIRD OCTAVE BAND SPECTRUM MODEL: FP 0

CHANNEL: 5 MACH NO.: 2 α: 0 ϕ: 0 Re_∞/FT.: 0.75×10^6 AEDC GROUP NO.: 22/155

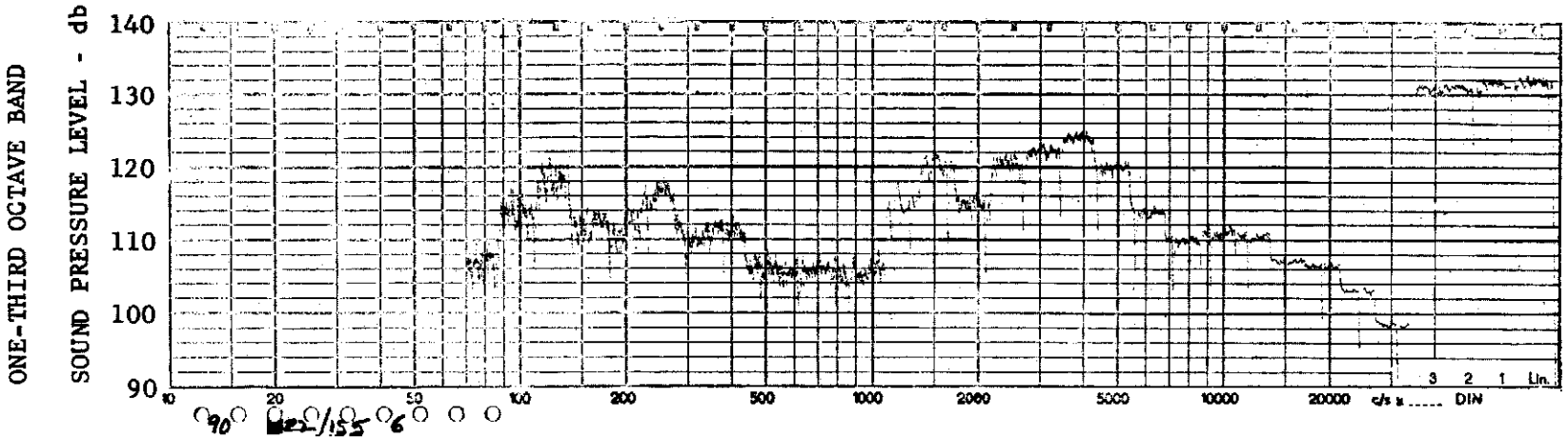

FIGURE 299 ONE-THIRD OCTAVE BAND SPECTRUM MODEL: FP 0

CHANNEL: 6 MACH NO.: 2 α: 0 ϕ: 0 Re_∞/FT.: 0.75×10^6 AEDC GROUP NO.: 22/155

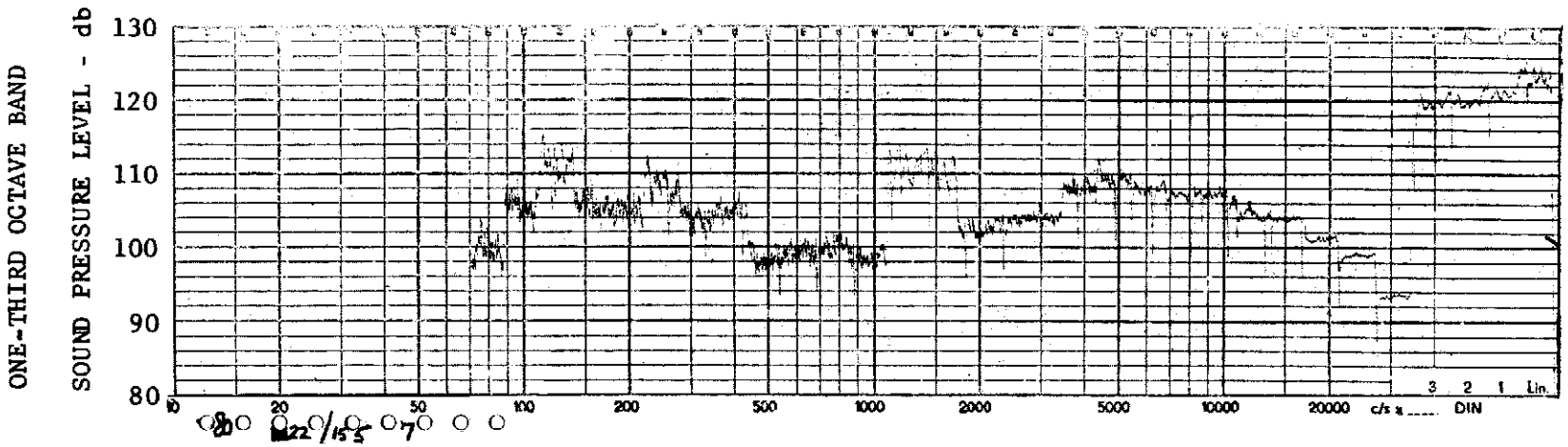

FIGURE 300 ONE-THIRD OCTAVE BAND SPECTRUM MODEL: FP 0

CHANNEL: 7 MACH NO.: 2 α: 0 ϕ: 0 Re_∞/FT.: 0.75×10^6 AEDC GROUP NO.: 22/155

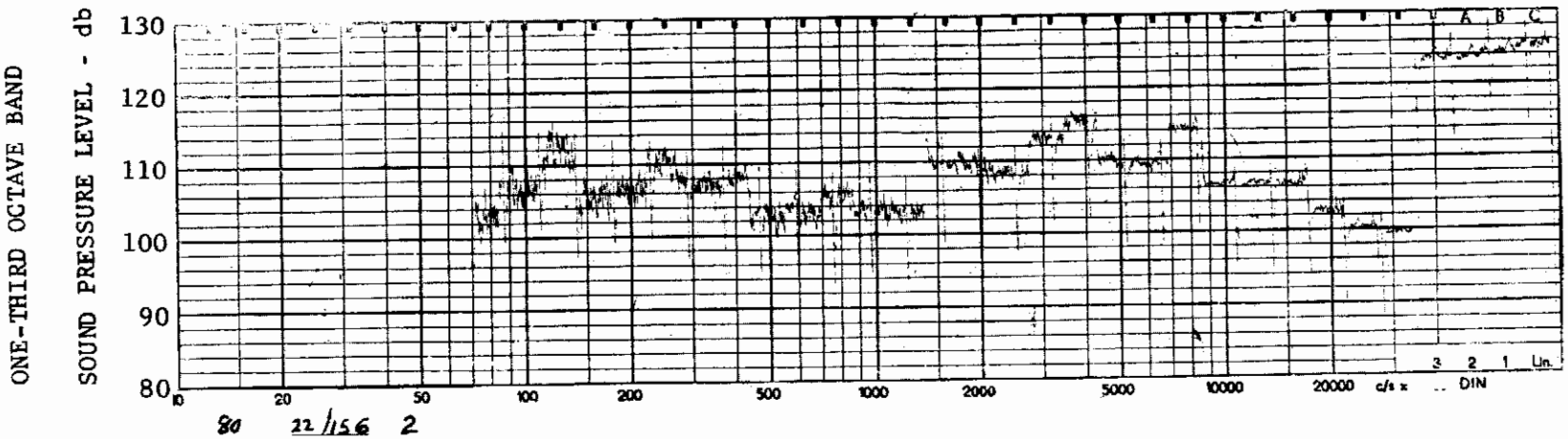

FIGURE 301 ONE-THIRD OCTAVE BAND SPECTRUM MODEL: FP 0

CHANNEL: 2 MACH NO.: 2 α: 0 ϕ: 0 Re_∞/FT.: 1.0×10^6 AEDC GROUP NO.: 22/156

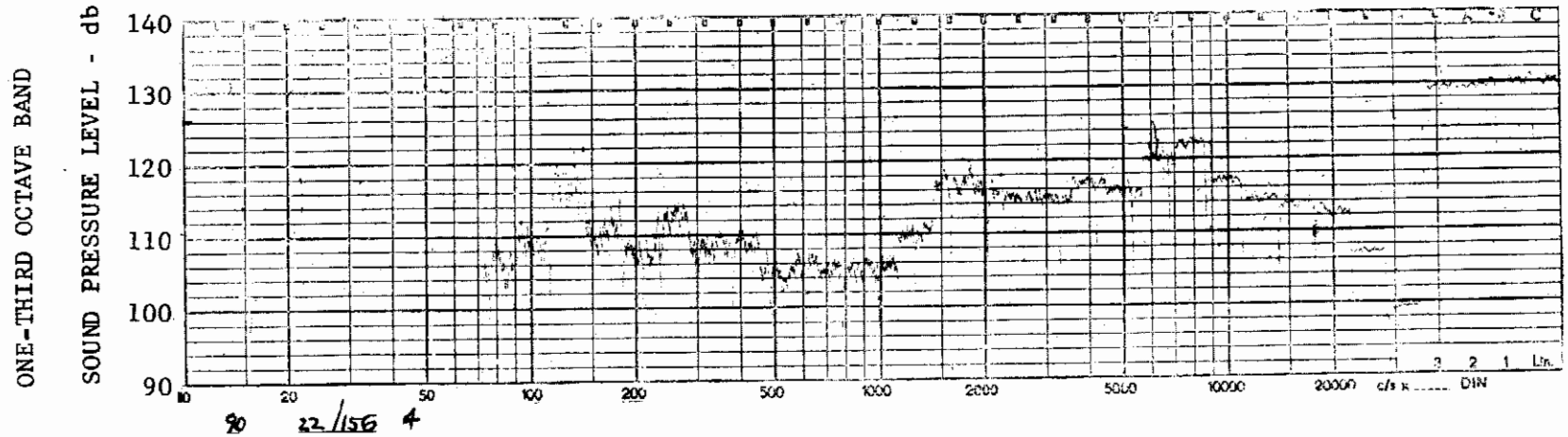

FIGURE 302 ONE-THIRD OCTAVE BAND SPECTRUM MODEL: FP 0

CHANNEL: 4 MACH NO.: 2 α: 0 ϕ: 0 Re_∞/FT.: 1.0×10^6 AEDC GROUP NO.: 22/156

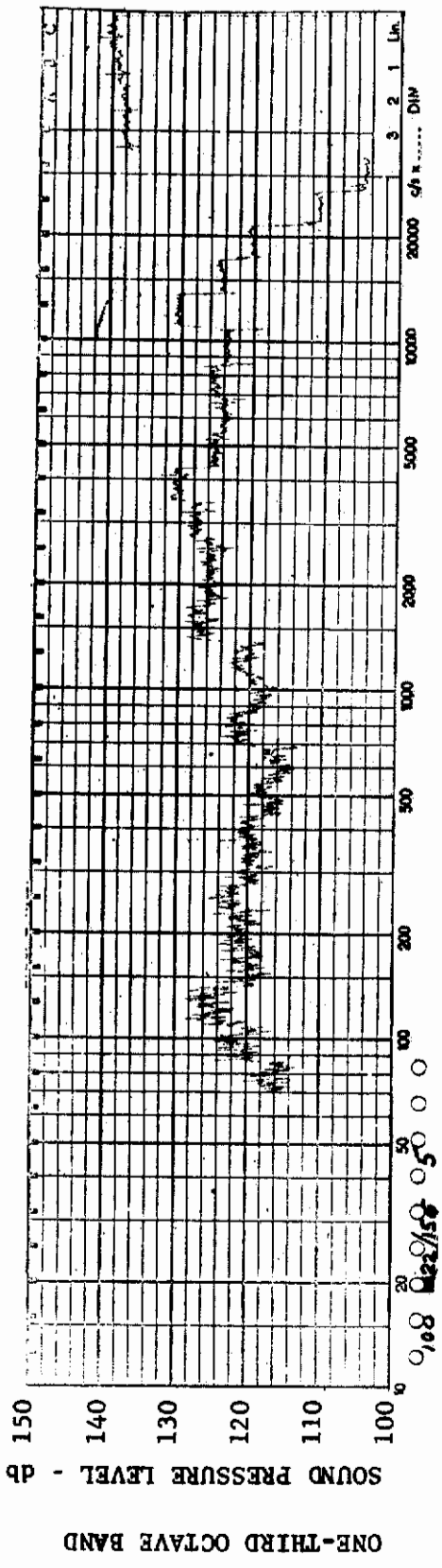

FIGURE 303 ONE-THIRD OCTAVE BAND SPECTRUM MODEL: FP 0

CHANNEL: 5 MACH NO.: 2 α: 0 ϕ: 0 Re_∞/FT.: 1.0×10^6 AEDC GROUP NO.:22/156

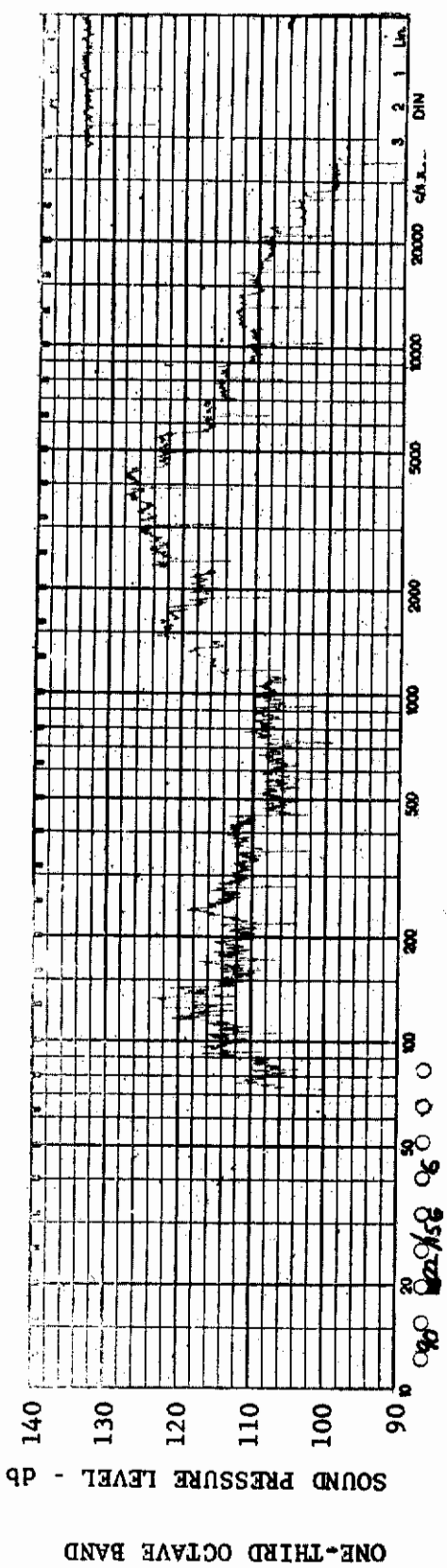

FIGURE 304 ONE-THIRD OCTAVE BAND SPECTRUM MODEL: FP 0

CHANNEL: 6 MACH NO.: 2 α: 0 ϕ: 0 Re_∞/FT.: 1.0×10^6 AEDC GROUP NO.: 22/156

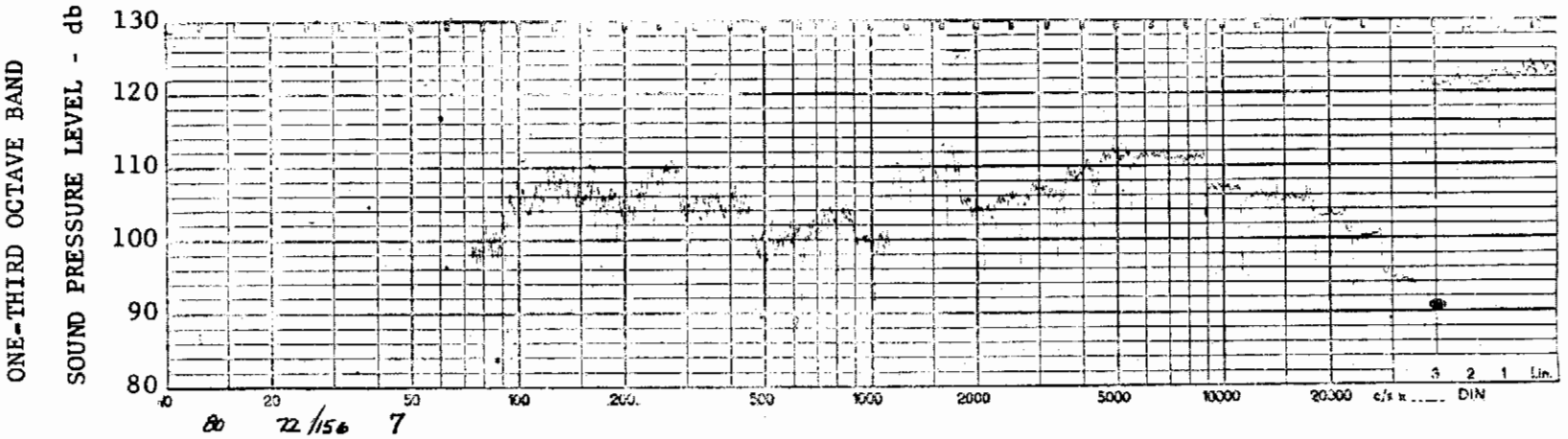

FIGURE 305 ONE-THIRD OCTAVE BAND SPECTRUM MODEL: FP 0

CHANNEL: 7 MACH NO.: 2 α: 0 ϕ: 0 Re_∞/FT.: 1.0×10^6 AEDC GROUP NO.: 22/156

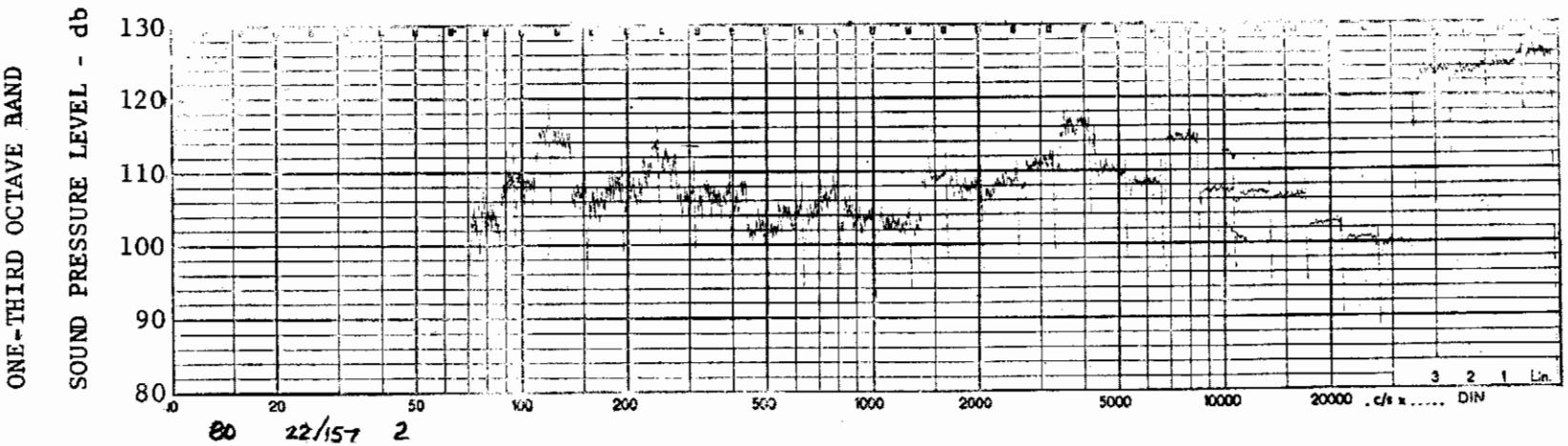

FIGURE 306 ONE-THIRD OCTAVE BAND SPECTRUM MODEL: FP 0

CHANNEL: 2 MACH NO.: 2 α: 5° ϕ: 0 Re_∞/FT.: 1.0×10^6 AEDC GROUP NO.: 22/157

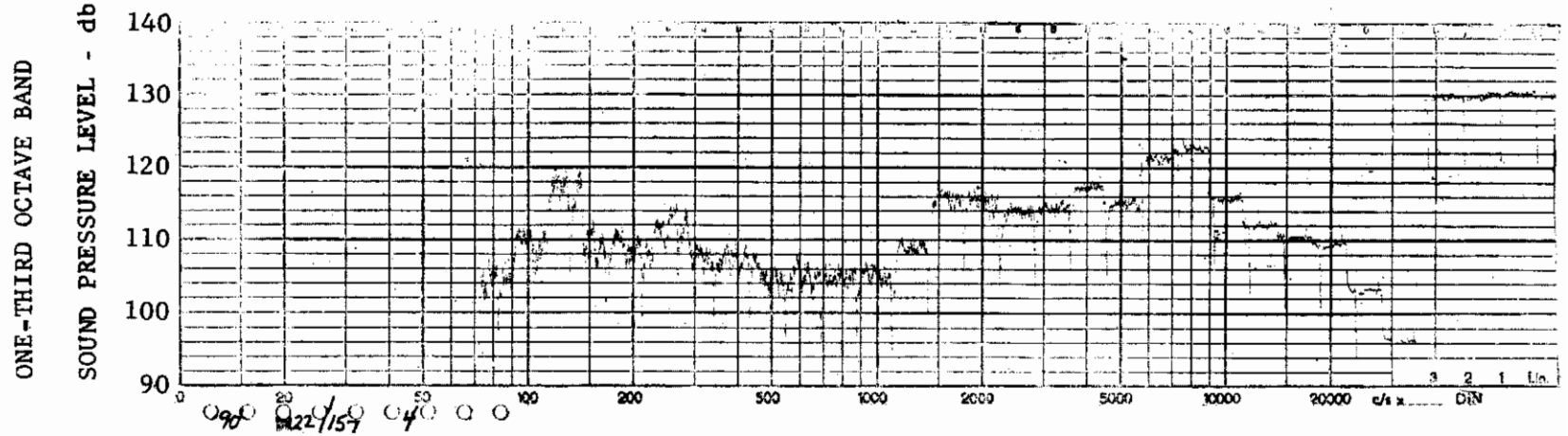

FIGURE 307 ONE-THIRD OCTAVE BAND SPECTRUM MODEL: FP 0

CHANNEL: 4 MACH NO.: 2 α: 5° ϕ: 0 Re_∞/FT.: 1.0×10^6 AEDC GROUP NO.: 22/157

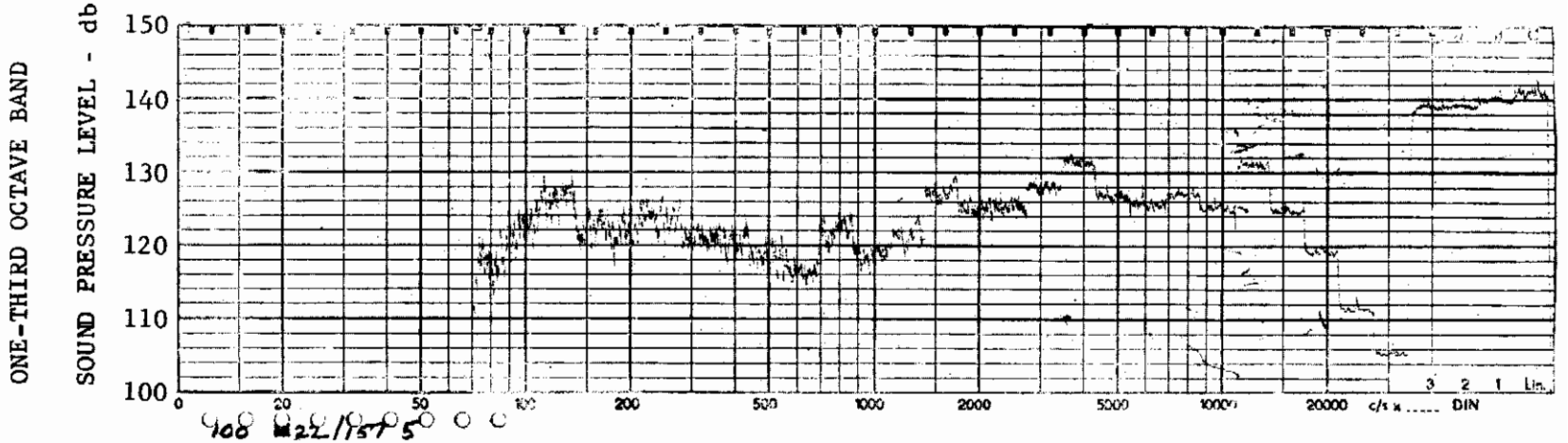

FIGURE 308 ONE-THIRD OCTAVE BAND SPECTRUM MODEL: FP 0

CHANNEL: 5 MACH NO.: 2 α: 5° ϕ: 0 Re_∞/FT. 1.0×10^6 AEDC GROUP NO.: 22/157

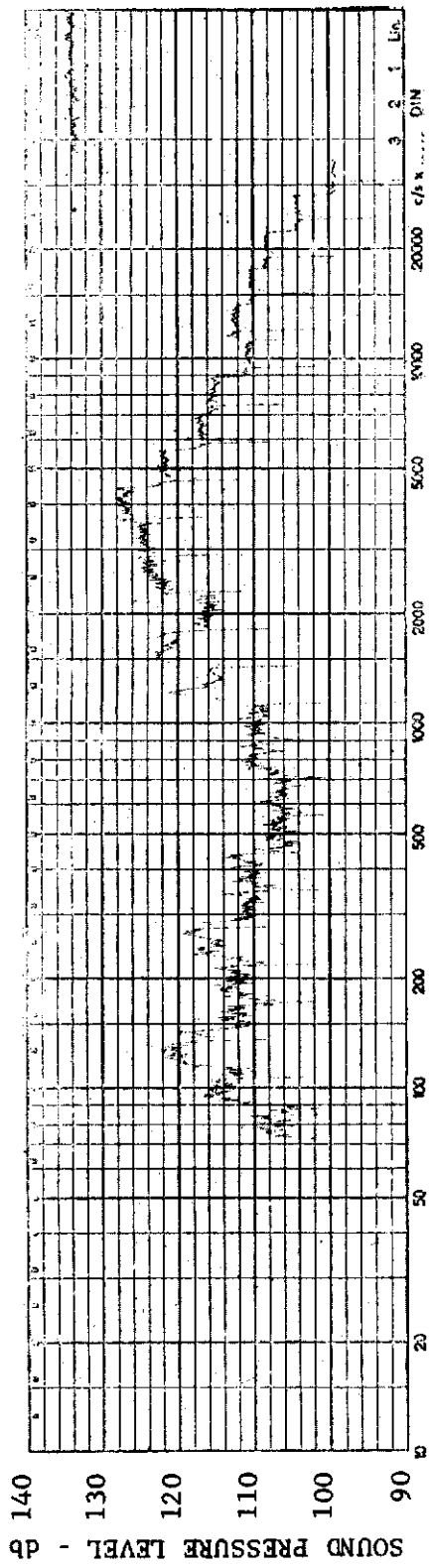

FIGURE 309 ONE-THIRD OCTAVE BAND SPECTRUM MODEL: FP 0

CHANNEL: 6 MACH NO.: 2 α: 5° ϕ: 0 Re_∞ /FT.: 1.0×10^6 AEDC GROUP NO.: 22/157

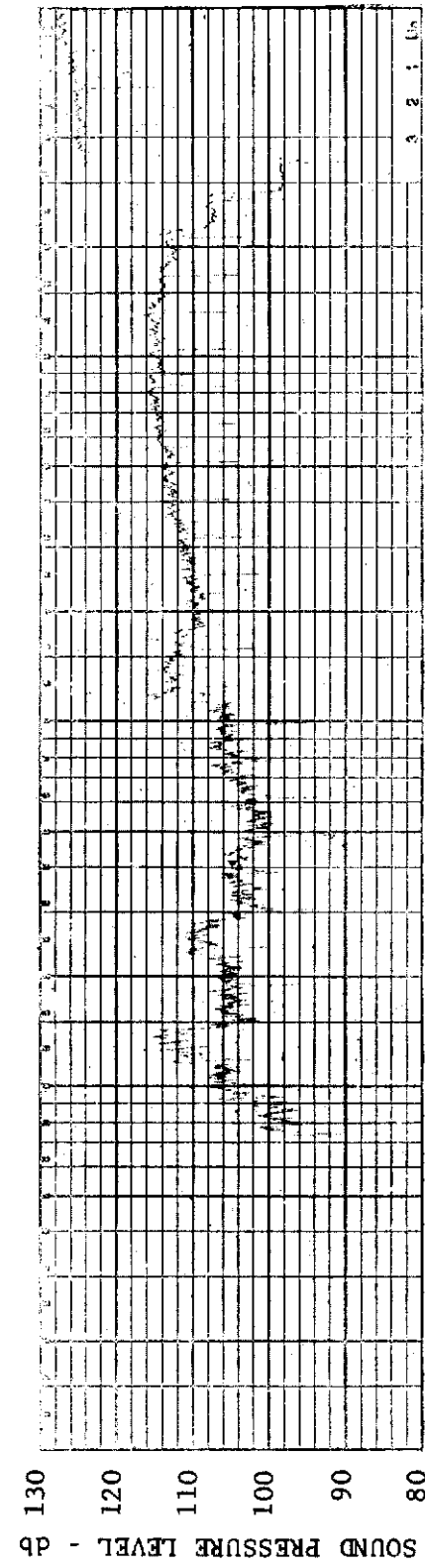

FIGURE 310 ONE-THIRD OCTAVE BAND SPECTRUM MODEL: FP 0

CHANNEL: 7 MACH NO.: 2 α: 5° ϕ: 0 Re_∞ /FT.: 1.0×10^6 AEDC GROUP NO.: 22/157

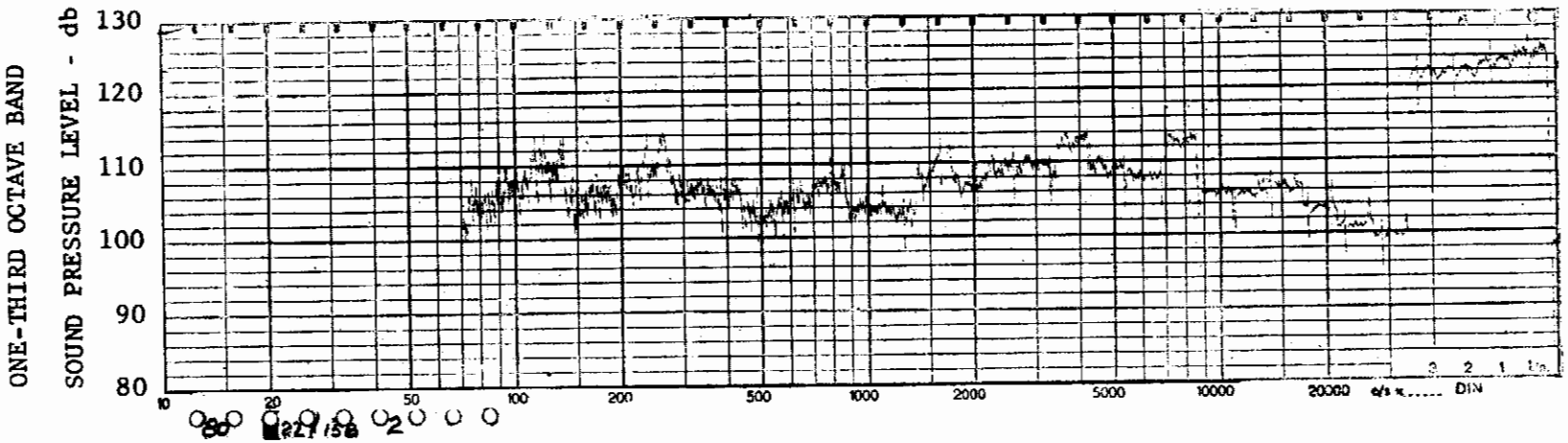

FIGURE 311 ONE-THIRD OCTAVE BAND SPECTRUM MODEL: FP 0

CHANNEL: 2 MACH NO.: 2 α: 15° ϕ: 0 Re_∞/FT.: 1.0×10^6 AEDC GROUP NO.: 22/158

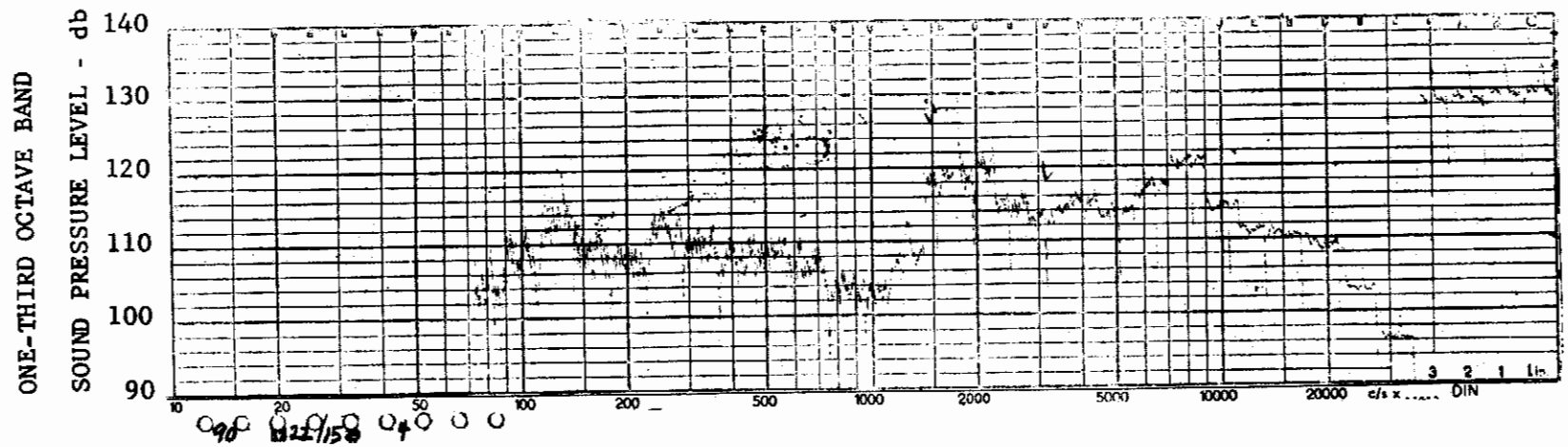

FIGURE 312 ONE-THIRD OCTAVE BAND SPECTRUM MODEL: FP 0

CHANNEL: 4 MACH NO.: 2 α: 15° ϕ: 0 Re_∞/FT.: 1.0×10^6 AEDC GROUP NO.: 22/158

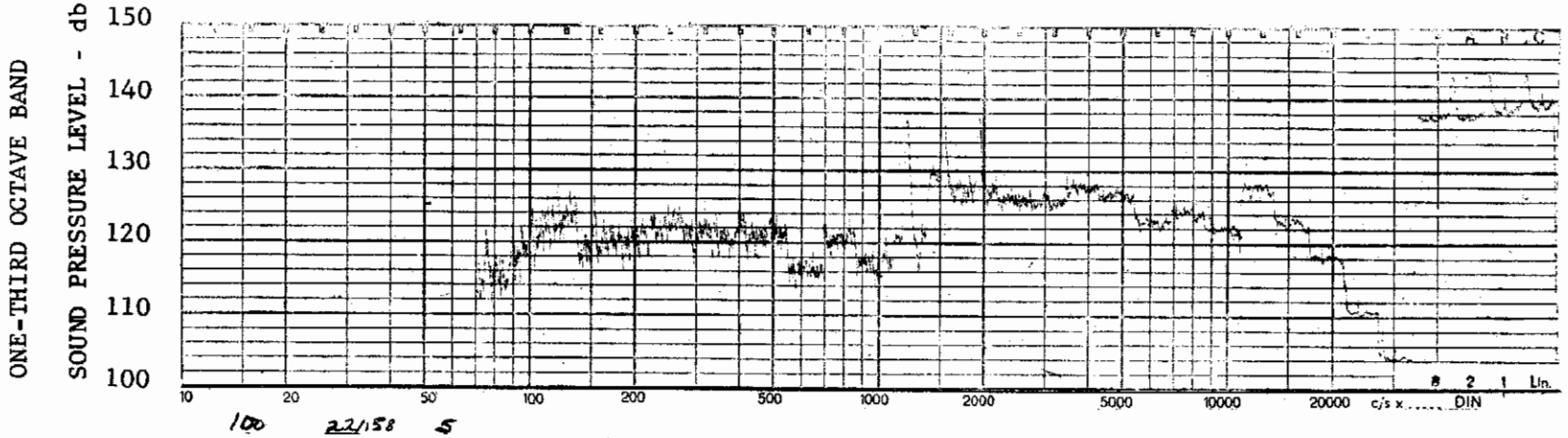

FIGURE 313 ONE-THIRD OCTAVE BAND SPECTRUM MODEL: FP 0

CHANNEL: 5 MACH NO.: 2 α: 15° ϕ: 0 Re_∞/FT.: 1.0×10^6 AEDC GROUP NO.: 22/158

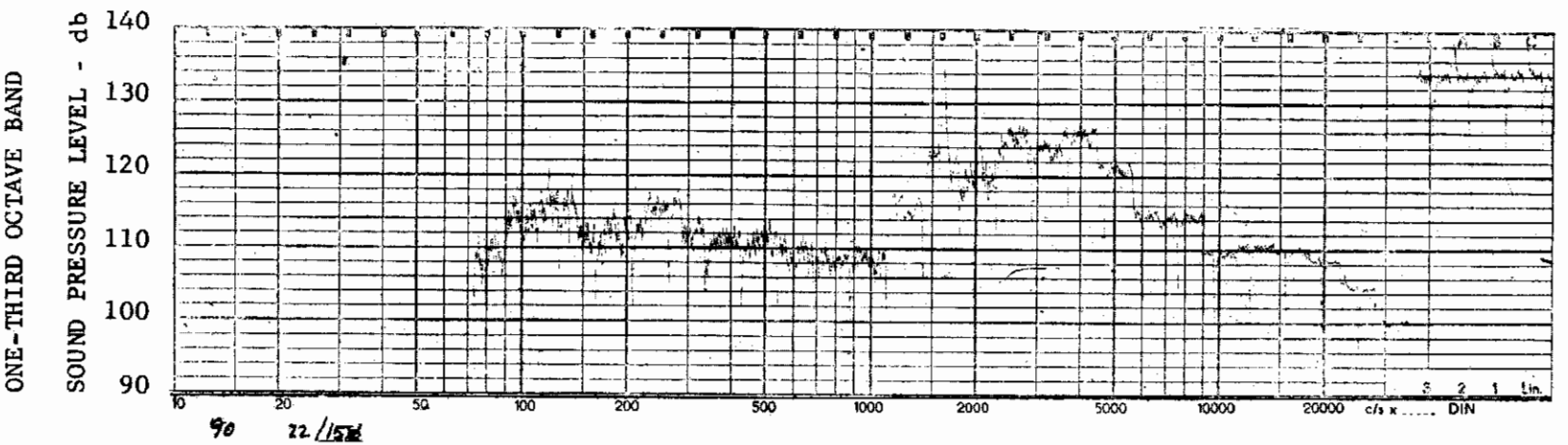

FIGURE 314 ONE-THIRD OCTAVE BAND SPECTRUM MODEL: FP 0

CHANNEL: 6 MACH NO.: 2 α: 15° ϕ: 0 Re_∞/FT.: 1.0×10^6 AEDC GROUP NO.: 22/158

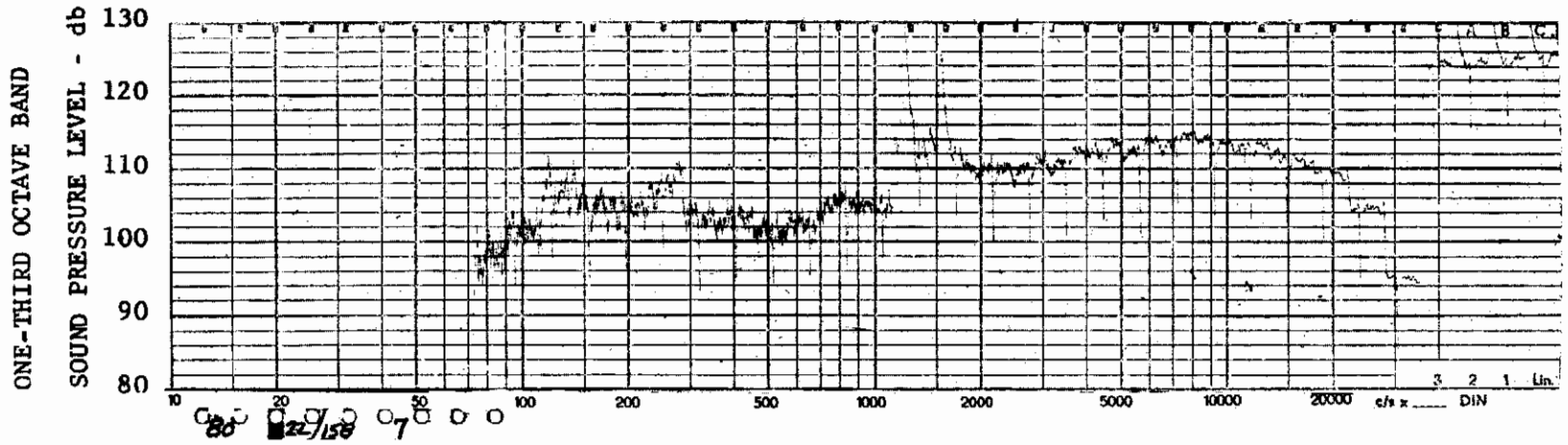

FIGURE 315 ONE-THIRD OCTAVE BAND SPECTRUM MODEL: FP 0

CHANNEL: 7 MACH NO.: 2 α: 15° ϕ: 0 Re_∞/FT.: 1.0×10^6 AEDC GROUP NO.: 22/158

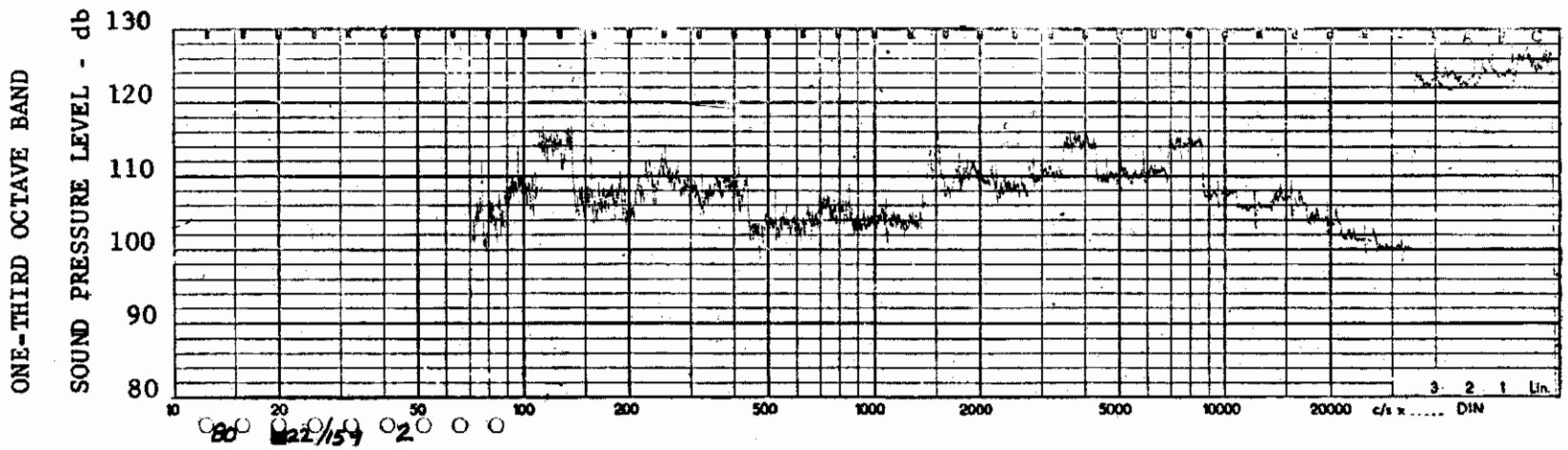

FIGURE 316 ONE-THIRD OCTAVE BAND SPECTRUM MODEL: FP 0

CHANNEL: 2 MACH NO.: 2 α: 0 ϕ: 0 Re_∞/FT.: 1.0×10^6 AEDC GROUP NO.: 22/159

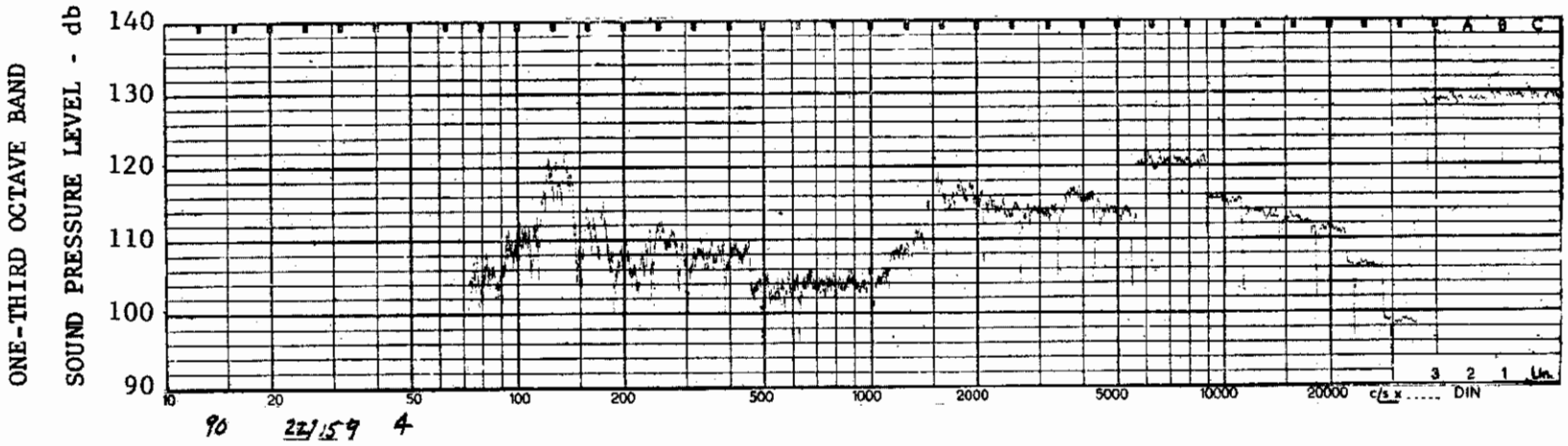

FIGURE 317 ONE-THIRD OCTAVE BAND SPECTRUM MODEL: FP 0

CHANNEL: 4 MACH NO.: 2 α: 0 ϕ: 0 Re_∞/FT.: 1.0×10^6 AEDC GROUP NO.: 22/159

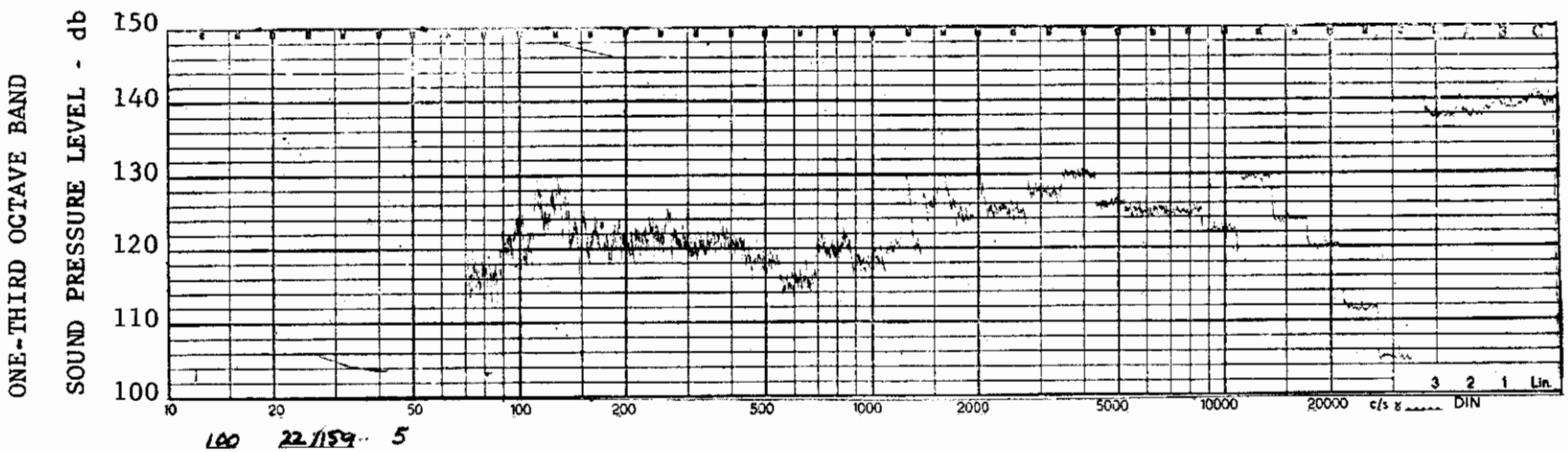

FIGURE 318 ONE-THIRD OCTAVE BAND SPECTRUM MODEL: FP 0

CHANNEL: 5 MACH NO.: 2 α: 0 ϕ: 0 Re_∞/FT.: 1.0×10^6 AEDC GROUP NO.: 22/159

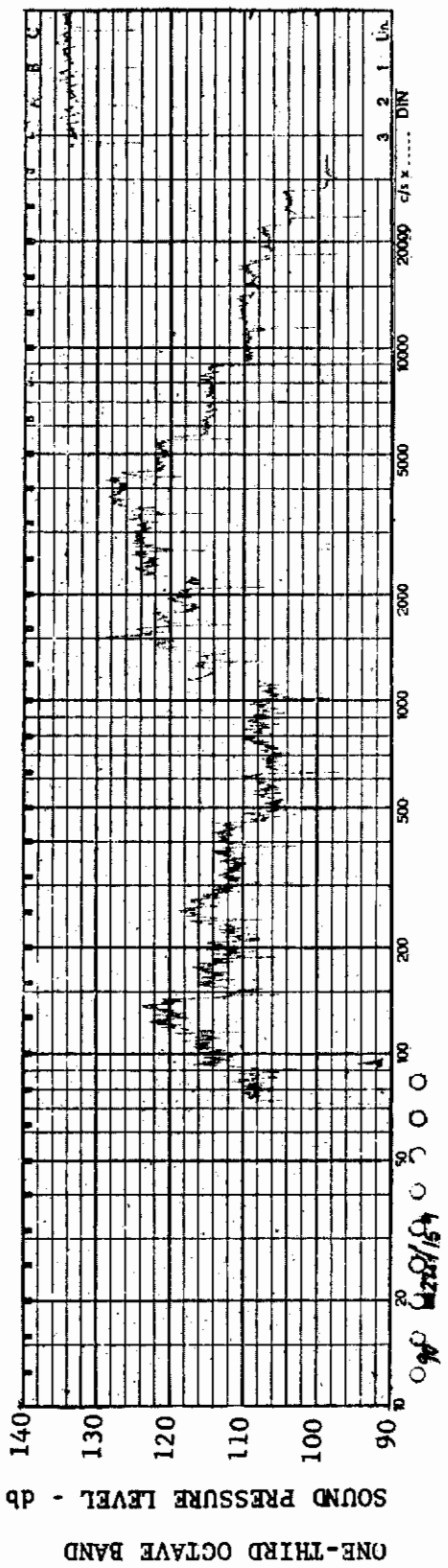

FIGURE 319 ONE-THIRD OCTAVE BAND SPECTRUM MODEL: FP 0

CHANNEL: 6 MACH NO.: 2 α: 0 ϕ: 0 Re_∞/FT.: 1.0×10^6 AEDC GROUP NO.: 22/159

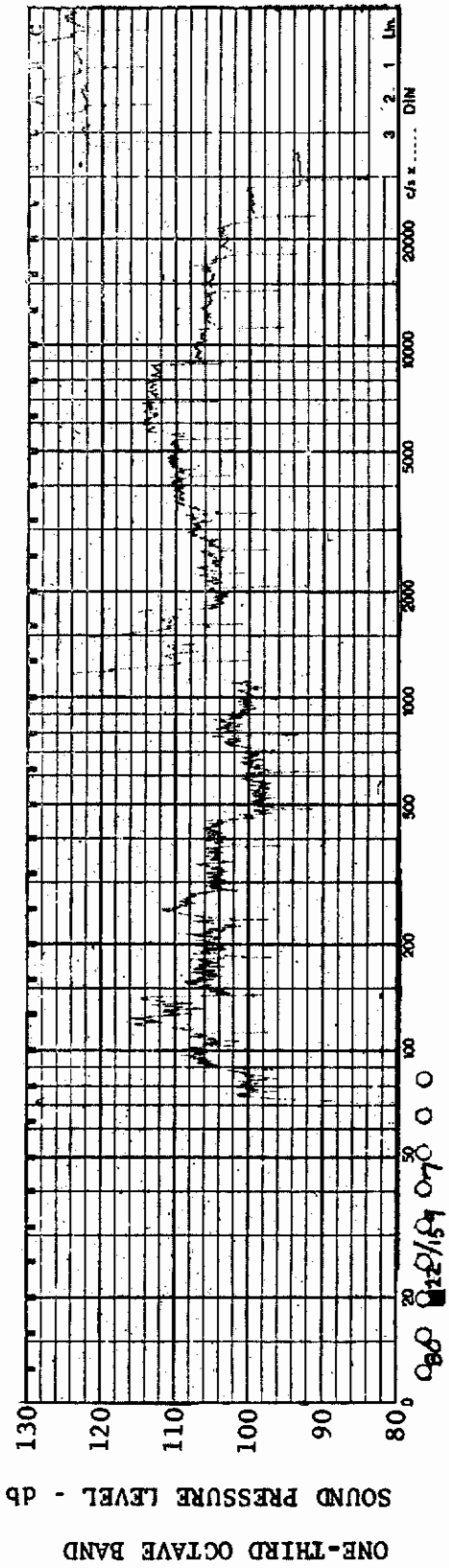

FIGURE 320 ONE-THIRD OCTAVE BAND SPECTRUM MODEL FP 0

CHANNEL: 7 MACH NO.: 2 α: 0 ϕ: 0 Re_∞/FT.: 1.0×10^6 AEDC GROUP NO.: 22/159

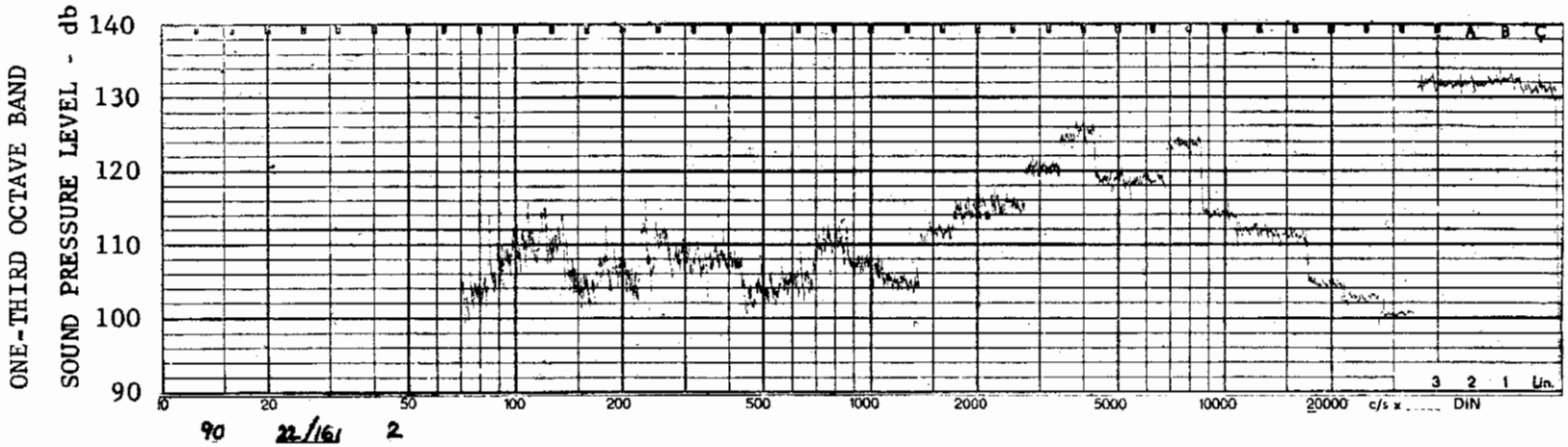

FIGURE 321 ONE-THIRD OCTAVE BAND SPECTRUM MODEL: FP 0

CHANNEL: 2 MACH NO.: 2 α: 0 ϕ: 0 Re_∞/FT.: 5.0×10^6 AEDC GROUP NO.: 22/161

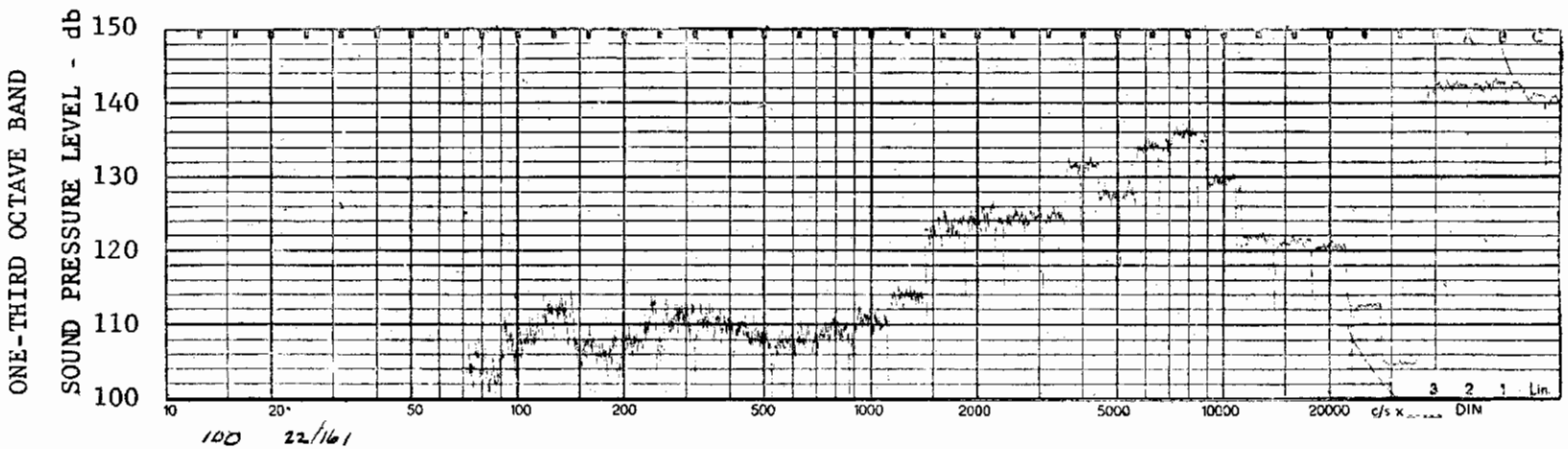

FIGURE 322 ONE-THIRD OCTAVE BAND SPECTRUM MODEL: FP 0

CHANNEL: 4 MACH NO.: 2 α: 0 ϕ: 0 Re_∞/FT.: 5.0×10^6 AEDC GROUP NO.: 22/161

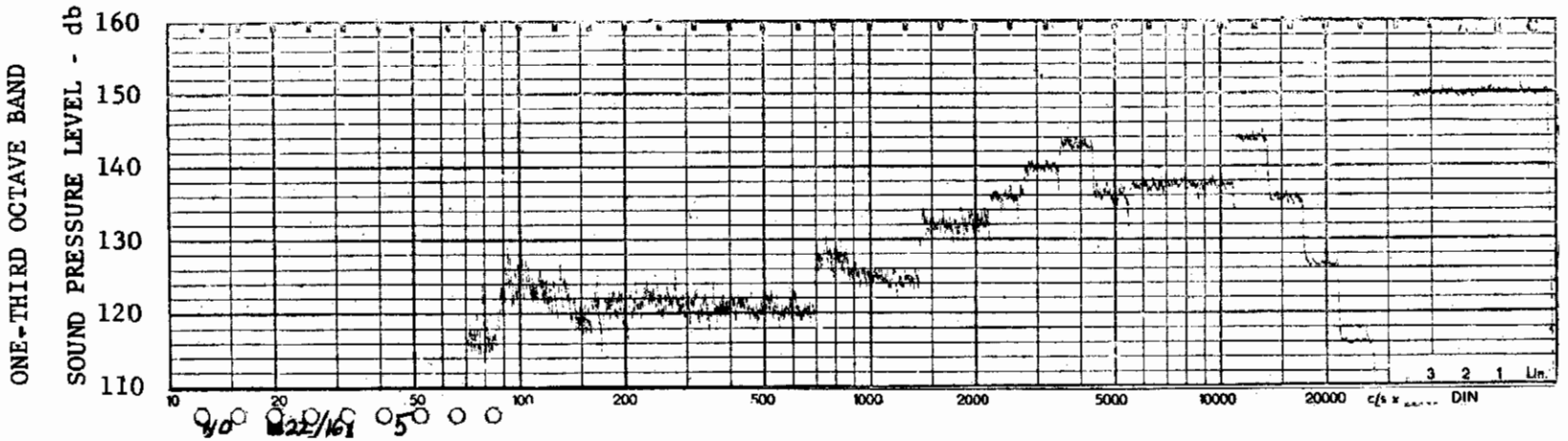

FIGURE 323 ONE-THIRD OCTAVE BAND SPECTRUM MODEL: FP 0

CHANNEL: 5 MACH NO.: 2 α: 0 ϕ: 0 Re_∞/FT.: 5.0×10^6 AEDC GROUP NO.: 22/161

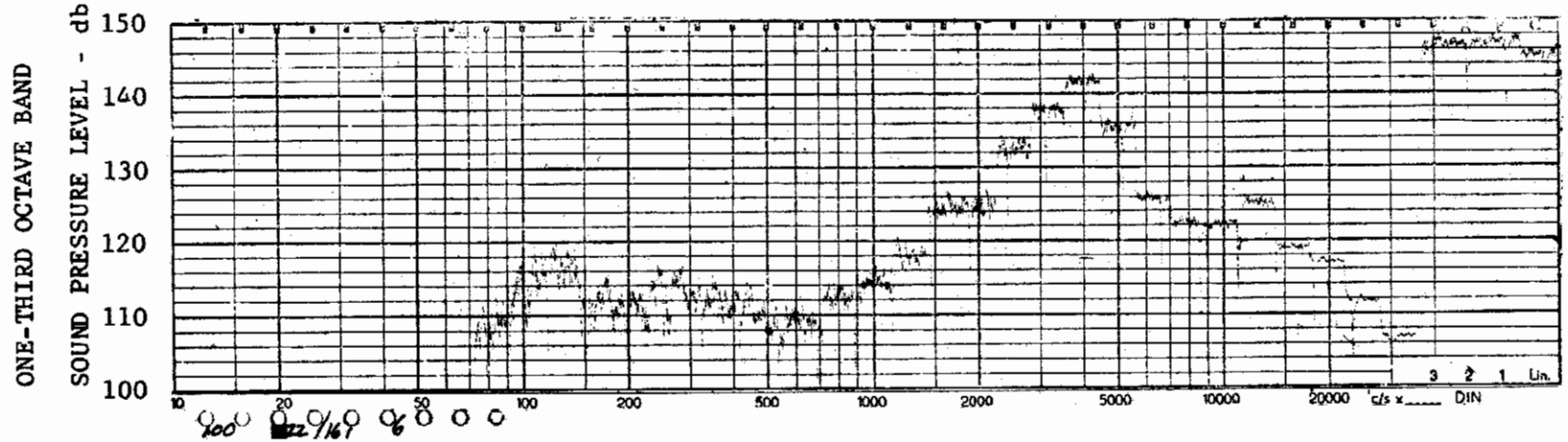

FIGURE 324 ONE-THIRD OCTAVE BAND SPECTRUM MODEL: FP 0

CHANNEL: 6 MACH NO.: 2 α: 0 ϕ: 0 Re_∞/FT.: 5.0×10^6 AEDC GROUP NO.: 22/161

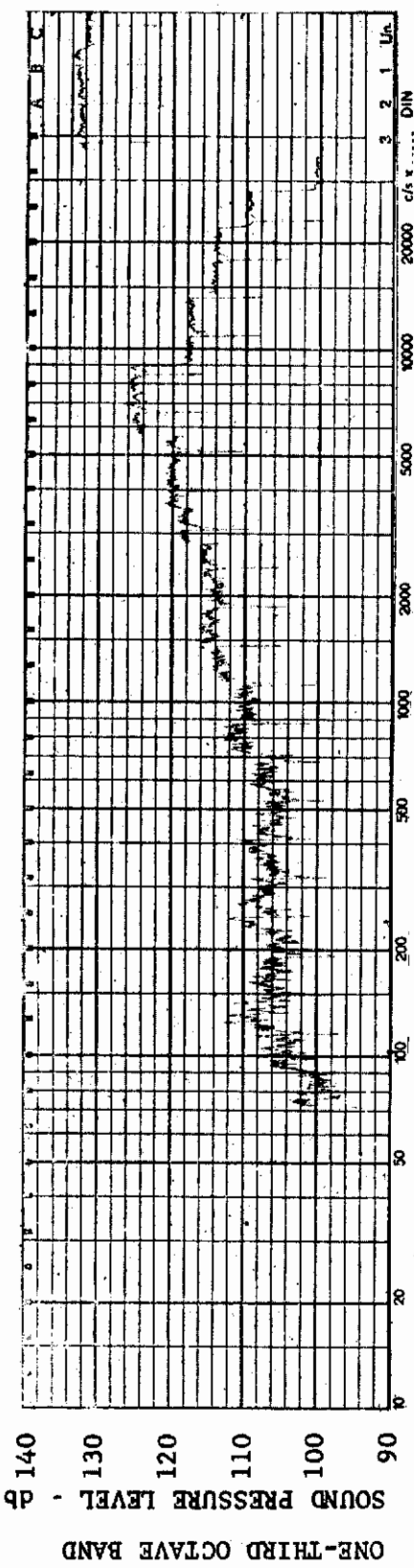

FIGURE 325 ONE-THIRD OCTAVE BAND SPECTRUM MODEL: FP 0

CHANNEL: 7 MACH NO.: 2 α: 0 ϕ: 0 Re_∞ /FT.: 5.0×10^6 AEDC GROUP NO.: 22/161

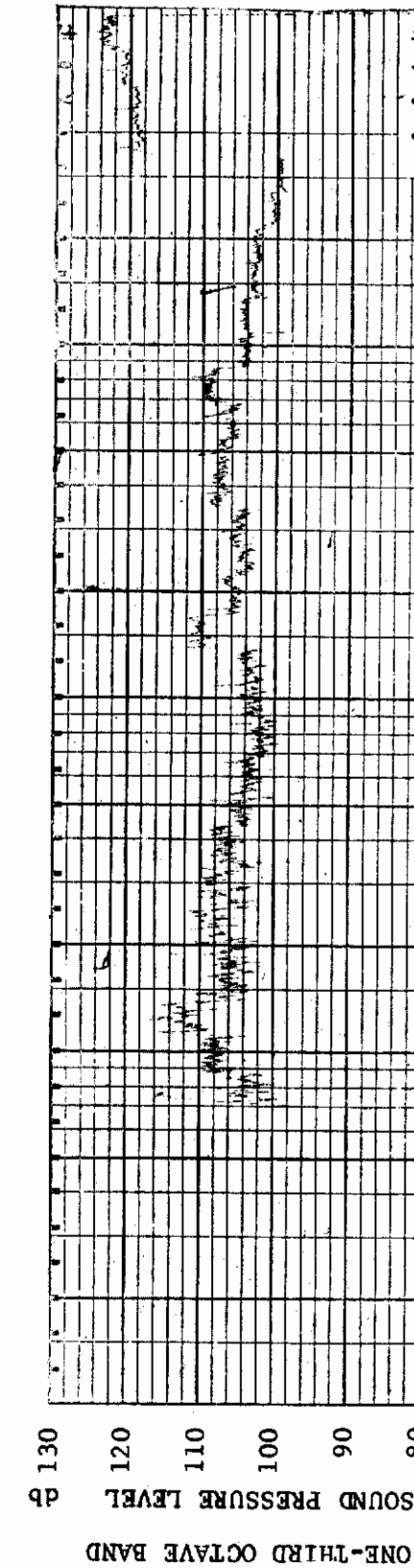

FIGURE 326 ONE-THIRD OCTAVE BAND SPECTRUM MODEL: FP 0

CHANNEL: 2 MACH NO.: 3.5 α: 0 ϕ: 0 Re_∞ /FT.: 0.5×10^6 AEDC GROUP NO.: 23/162

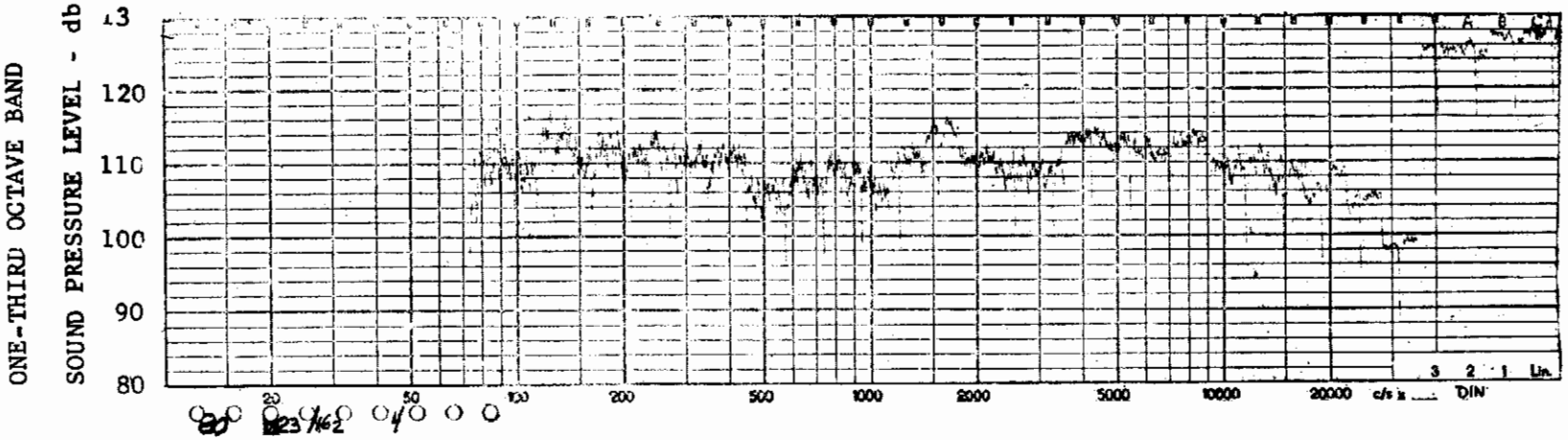

FIGURE 327 ONE-THIRD OCTAVE BAND SPECTRUM MODEL: FP 0

CHANNEL: 4 MACH NO.: 3.5 α: 0 ϕ: 0 Re_∞/FT.: 0.5 x 10^6 AEDC GROUP NO.: 23/162

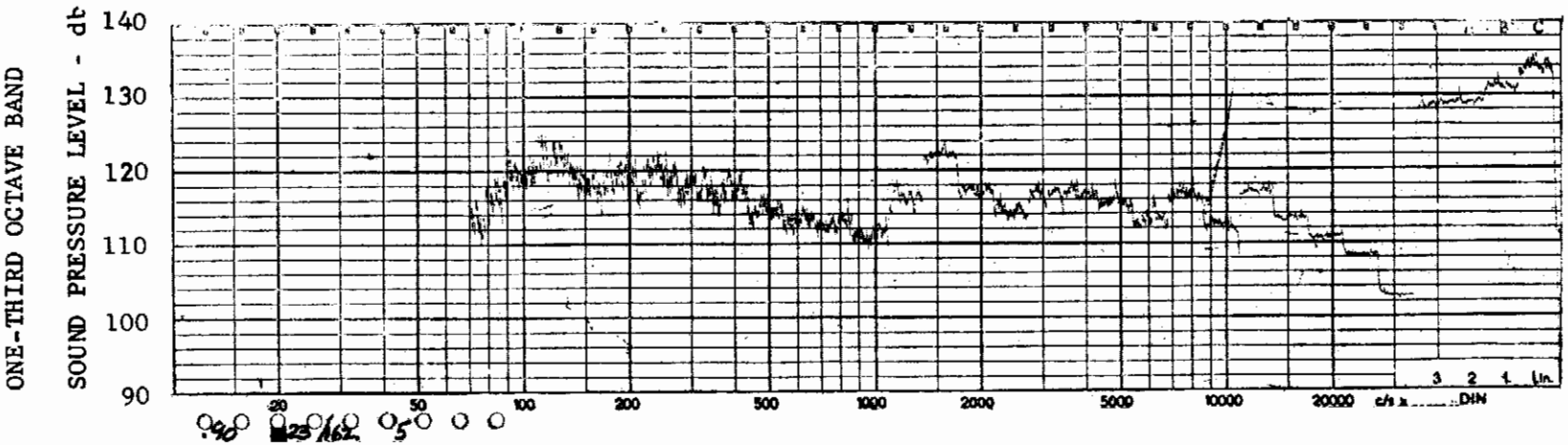

FIGURE 328 ONE-THIRD OCTAVE BAND SPECTRUM MODEL: FP 0

CHANNEL: 5 MACH NO.: 3.5 α: 0 ϕ: 0 Re_∞/FT.: 0.5 x 10^6 AEDC GROUP NO.: 23/162

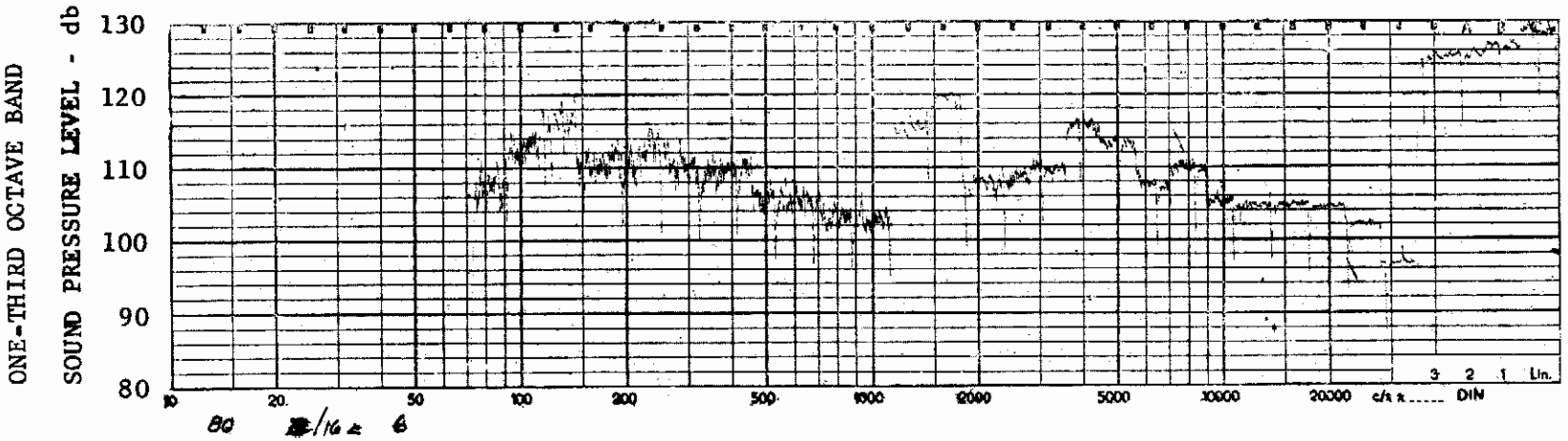

FIGURE 329 ONE-THIRD OCTAVE BAND SPECTRUM MODEL: FP 0

CHANNEL: 6 MACH NO.: 3.5 α: 0 ϕ: 0 Re_∞/FT.: 0.5 x 10^6 AEDC GROUP NO.: 23/162

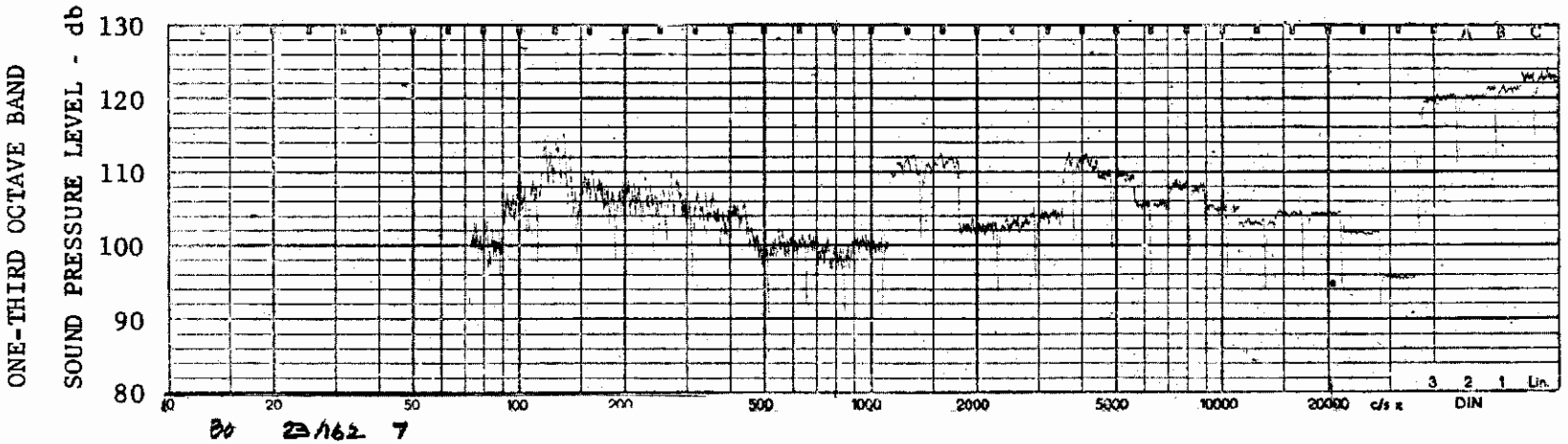

FIGURE 330 ONE-THIRD OCTAVE BAND SPECTRUM MODEL: FP 0

CHANNEL: 7 MACH NO.: 3.5 α: 0 ϕ: 0 Re_∞/FT.: 0.5 x 10^6 AEDC GROUP NO.: 23/162

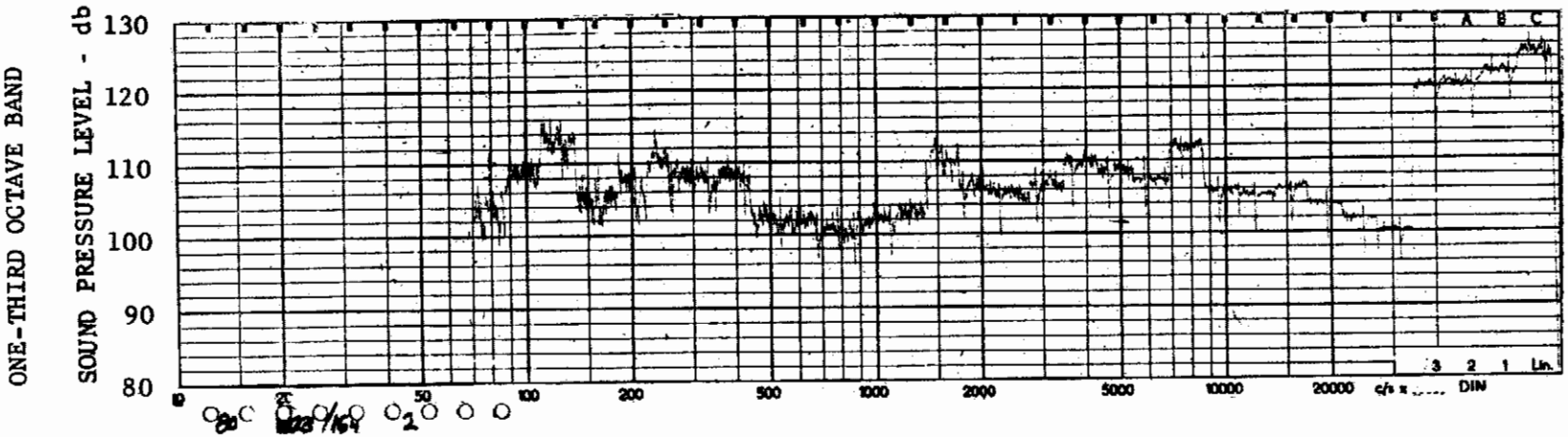

FIGURE 331 ONE-THIRD OCTAVE BAND SPECTRUM MODEL: FP 0

CHANNEL: 2 MACH NO.: 3.5 α: 0 ϕ: 0 Re_∞/FT.: 1.0×10^6 AEDC GROUP NO.: 23/164

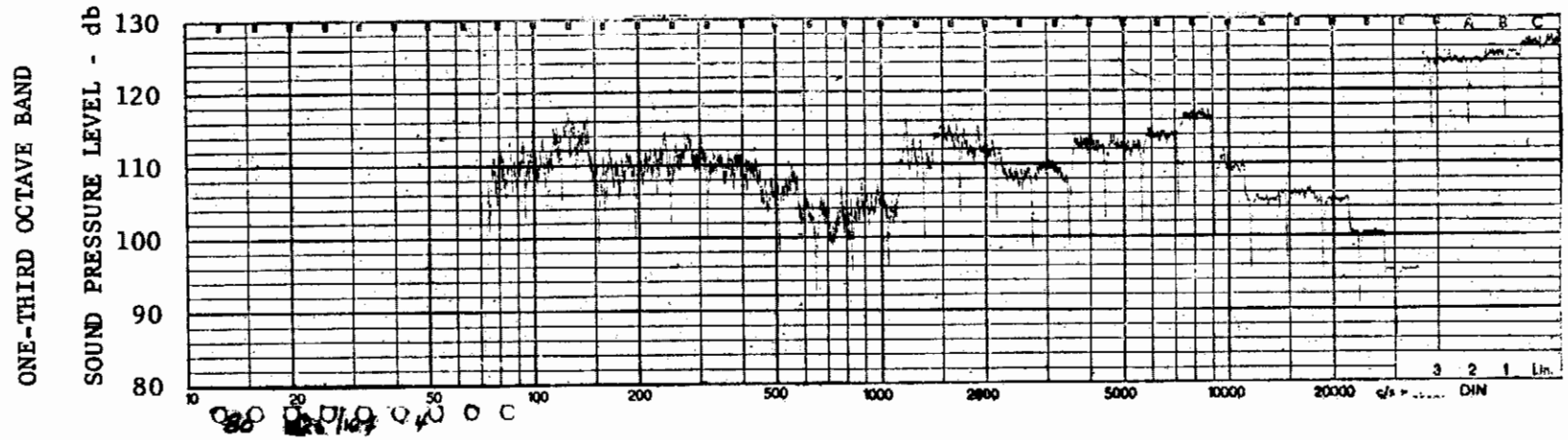

FIGURE 332 ONE-THIRD OCTAVE BAND SPECTRUM MODEL: FP 0

CHANNEL: 4 MACH NO.: 3.5 α: 0 ϕ: 0 Re_∞/FT.: 1.0×10^6 AEDC GROUP NO.: 23/164

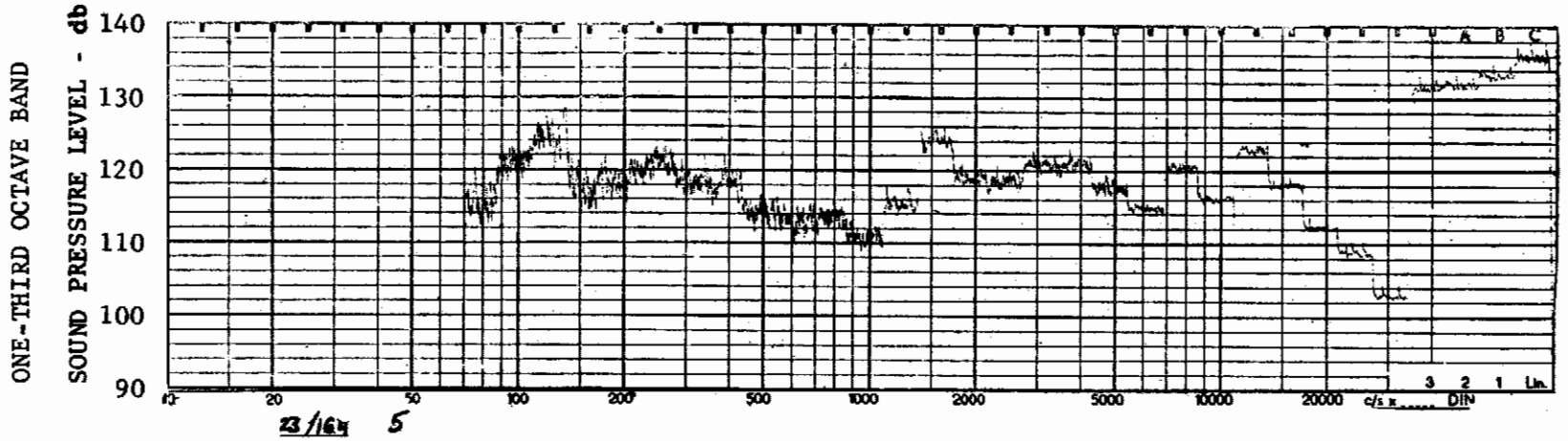

FIGURE 333 ONE-THIRD OCTAVE BAND SPECTRUM MODEL: FP 0

CHANNEL: 5 MACH NO.: 3.5 α: 0 ϕ: 0 Re_∞/FT.: 1.0×10^6 AEDC GROUP NO.: 23/164

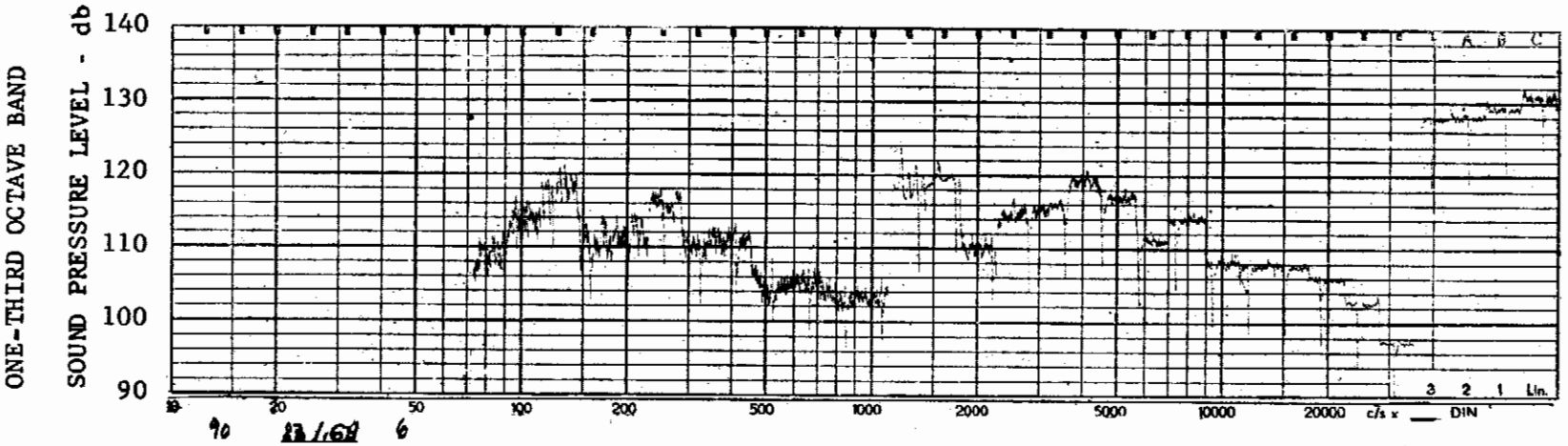

FIGURE 334 ONE-THIRD OCTAVE BAND SPECTRUM MODEL: FP 0

CHANNEL: 6 MACH NO.: 3.5 α: 0 ϕ: 0 Re_∞/FT.: 1.0×10^6 AEDC GROUP NO.: 23/164

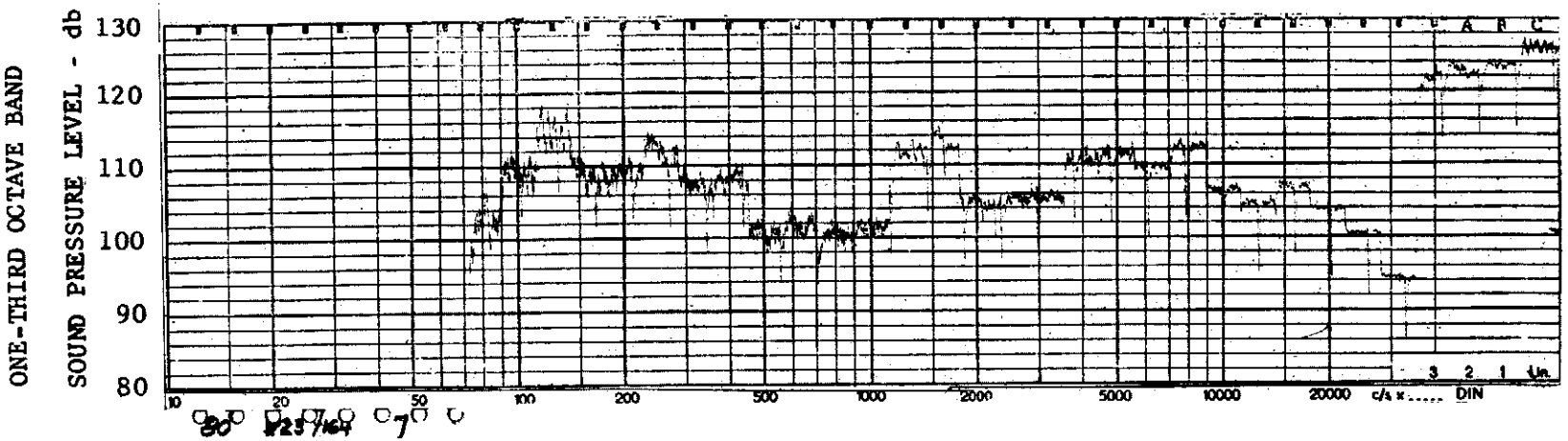

FIGURE 335 ONE-THIRD OCTAVE BAND SPECTRUM MODEL: FP 0

CHANNEL: 7 MACH NO.: 3.5 α: 0 ϕ: 0 Re_∞/FT.: 1.0×10^6 AEDC GROUP NO.: 23/164

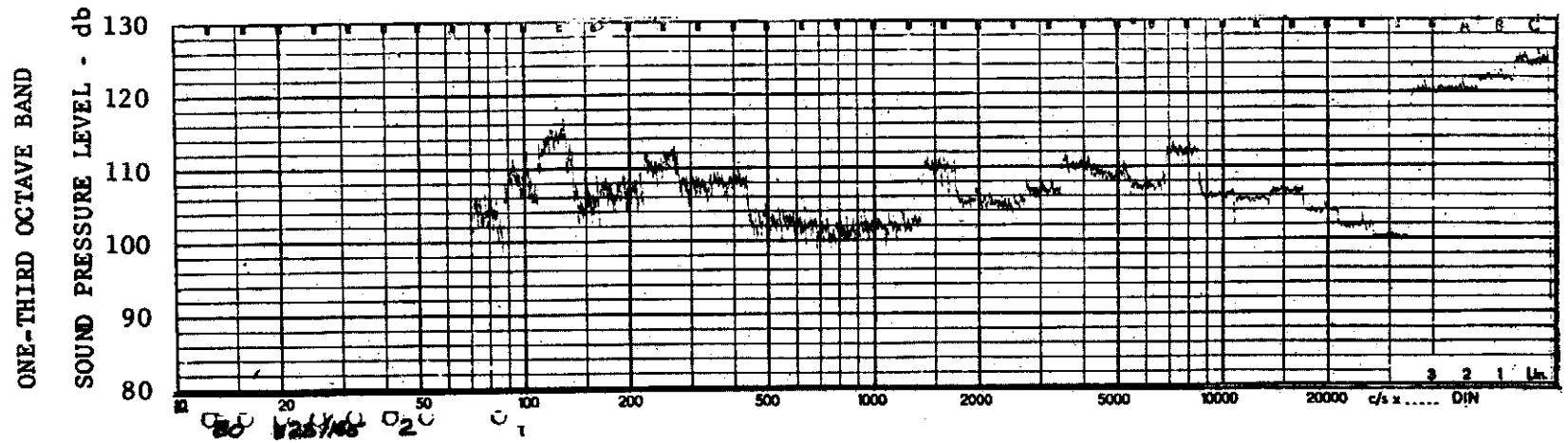

FIGURE 336 ONE-THIRD OCTAVE BAND SPECTRUM MODEL: FP 0

CHANNEL: 2 MACH NO.: 3.5 α: 5° ϕ: 0 Re_∞/FT.: 1.0×10^6 AEDC GROUP NO.: 23/165

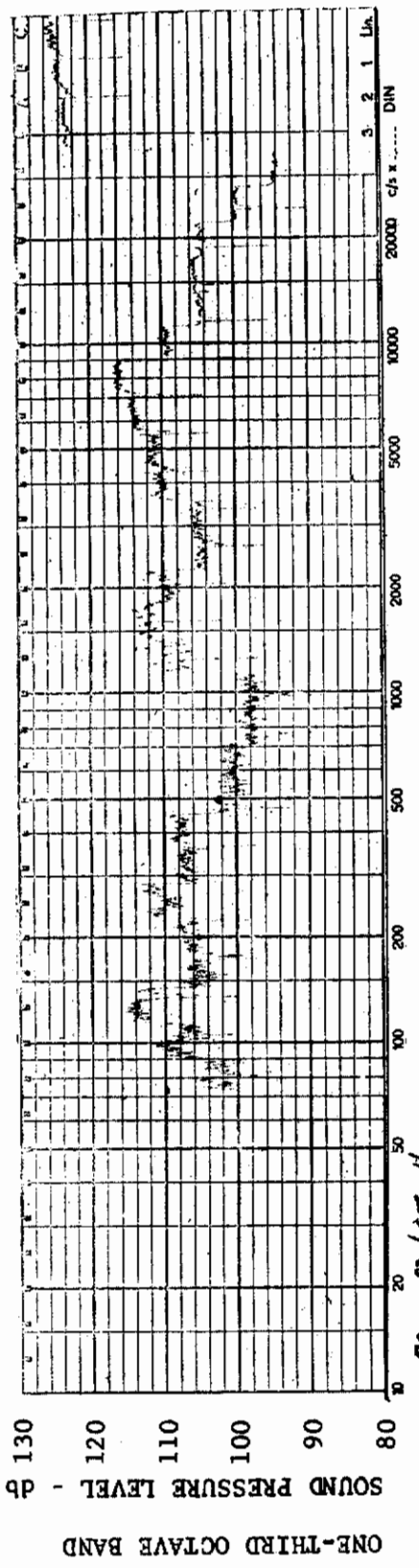

FIGURE 337 ONE-THIRD OCTAVE BAND SPECTRUM MODEL: FP 0

CHANNEL: 4 MACH NO.: 3.5 α: 5° ϕ: 0 Re_∞/FT.: 1.0×10^6 AEDC GROUP NO. 23/165

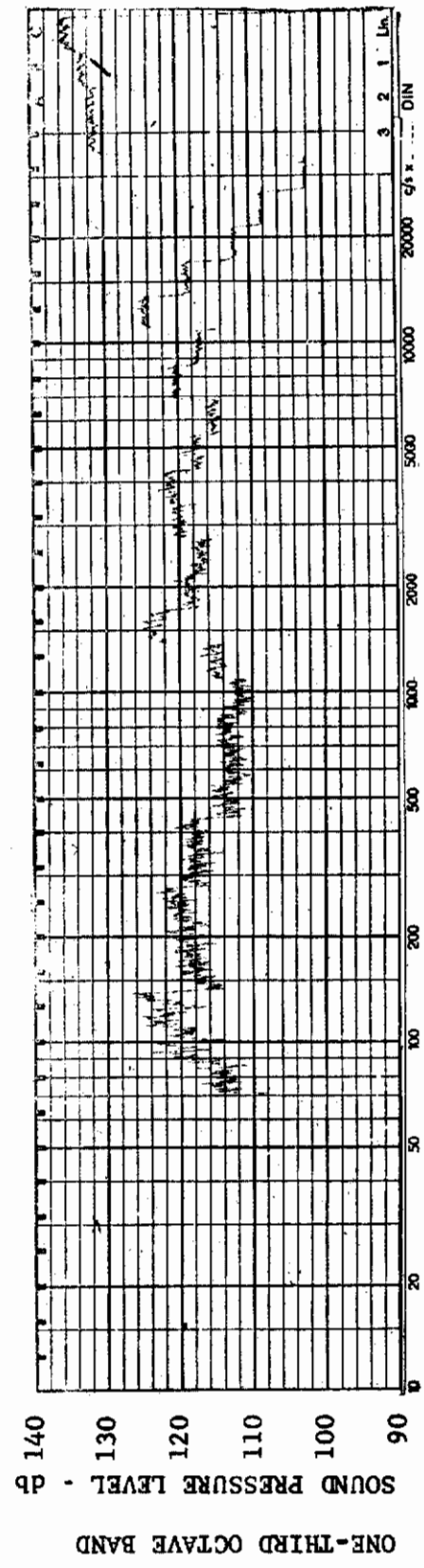

FIGURE 338 ONE-THIRD OCTAVE BAND SPECTRUM MODEL: FP 0

CHANNEL: 5 MACH NO.: 3.5 α: 5° ϕ: 0 Re_∞/FT.: 1.0×10^6 AEDC GROUP NO.: 23/165

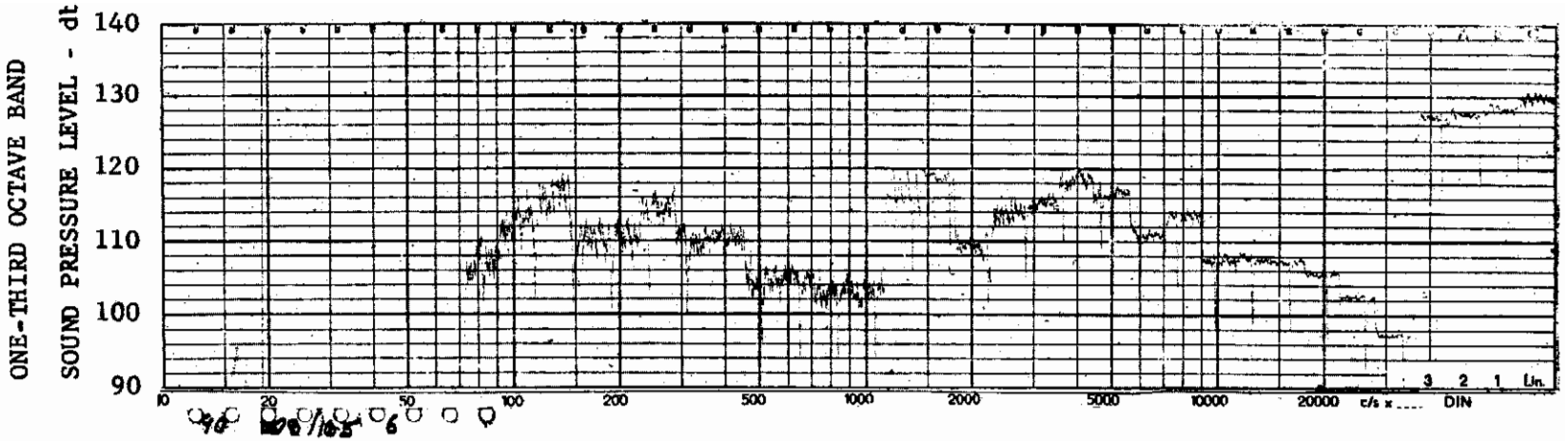

FIGURE 339 ONE-THIRD OCTAVE BAND SPECTRUM MODEL: FP 0

CHANNEL: 6 MACH NO.: 3.5 α: 5° ϕ: 0 Re_∞/FT.: 1.0×10^6 AEDC GROUP NO.: 23/165

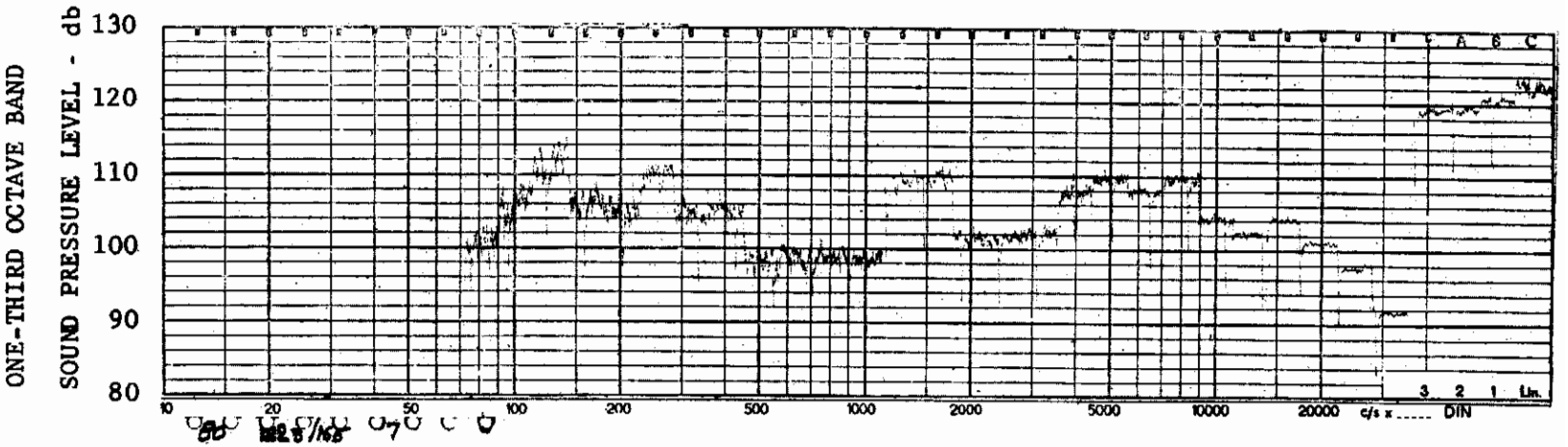

FIGURE 340 ONE-THIRD OCTAVE BAND SPECTRUM MODEL: FP 0

CHANNEL: 7 MACH NO.: 3.5 α: 5° ϕ: 0 Re_∞/FT.: 1.0×10^6 AEDC GROUP NO.: 23/165

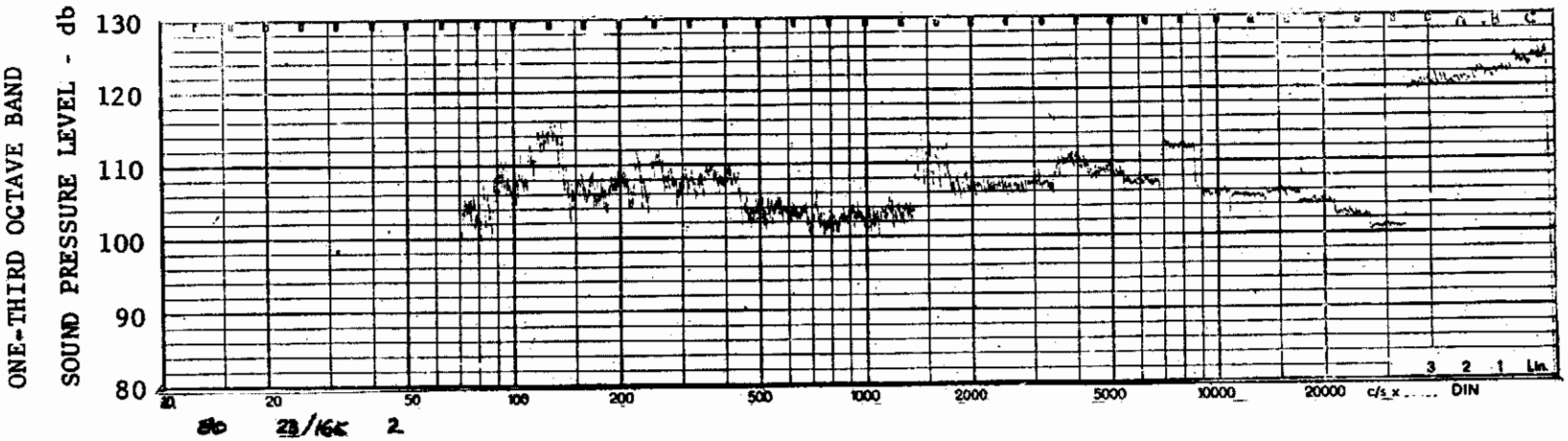

FIGURE 341 ONE-THIRD OCTAVE BAND SPECTRUM MODEL: FP 0

CHANNEL: 2 MACH NO.: 3.5 α: 15° ϕ: 0 Re_∞/FT.: 1.0×10^6 AEDC GROUP NO.: 23/166

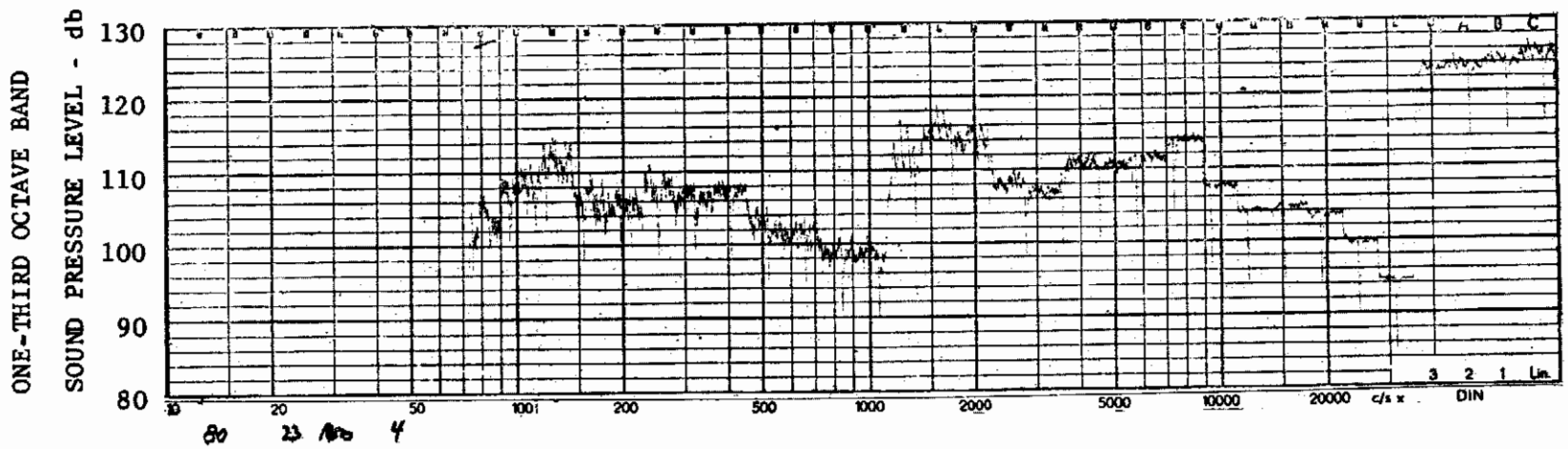

FIGURE 342 ONE-THIRD OCTAVE BAND SPECTRUM MODEL: FP 0

CHANNEL: 4 MACH NO.: 3.5 α: 15° ϕ: 0 Re_∞/FT.: 1.0×10^6 AEDC GROUP NO.: 23/166

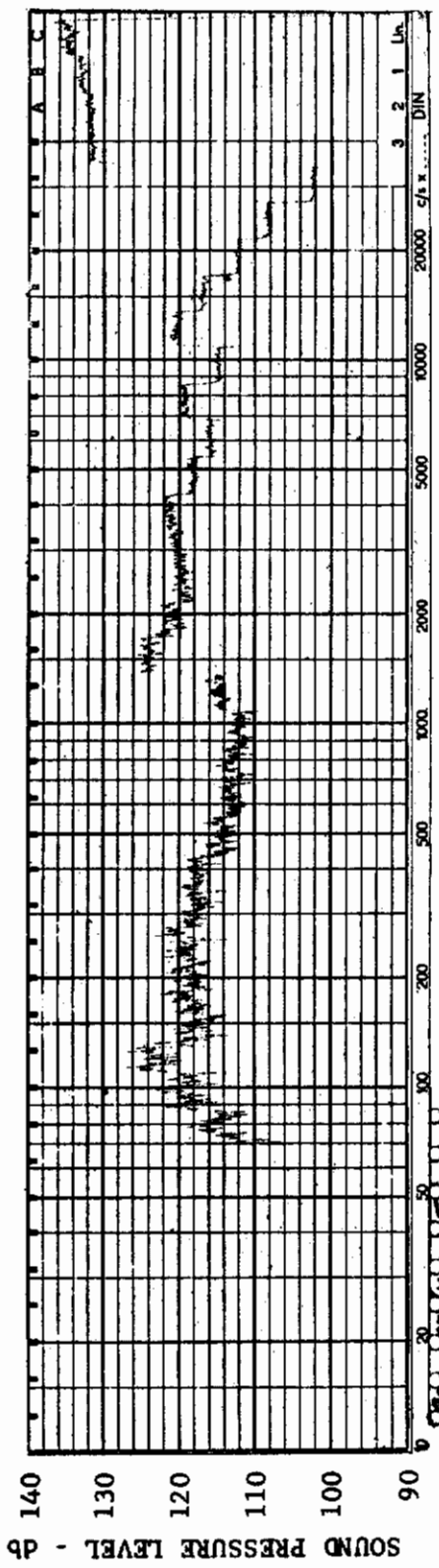

FIGURE 343 ONE-THIRD OCTAVE BAND SPECTRUM MODEL: FP,0

CHANNEL: 5 MACH NO.:3.5 α: 15° ϕ: 0 Re_∞/FT.: 1.0×10^6 AEDC GROUP NO.: 23/166

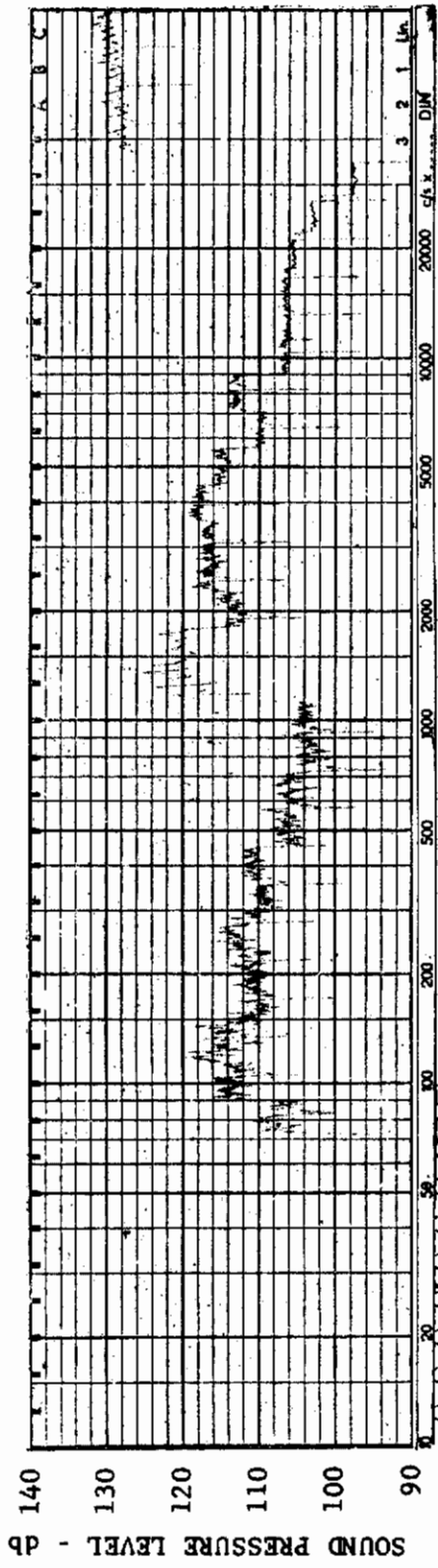

FIGURE 344 ONE-THIRD OCTAVE BAND SPECTRUM MODEL: FP 0

CHANNEL: 6 MACH NO.: 3.5 α: 15° ϕ: 0 Re_∞/FT.: 1.0×10^6 AEDC GROUP NO.: 23/166

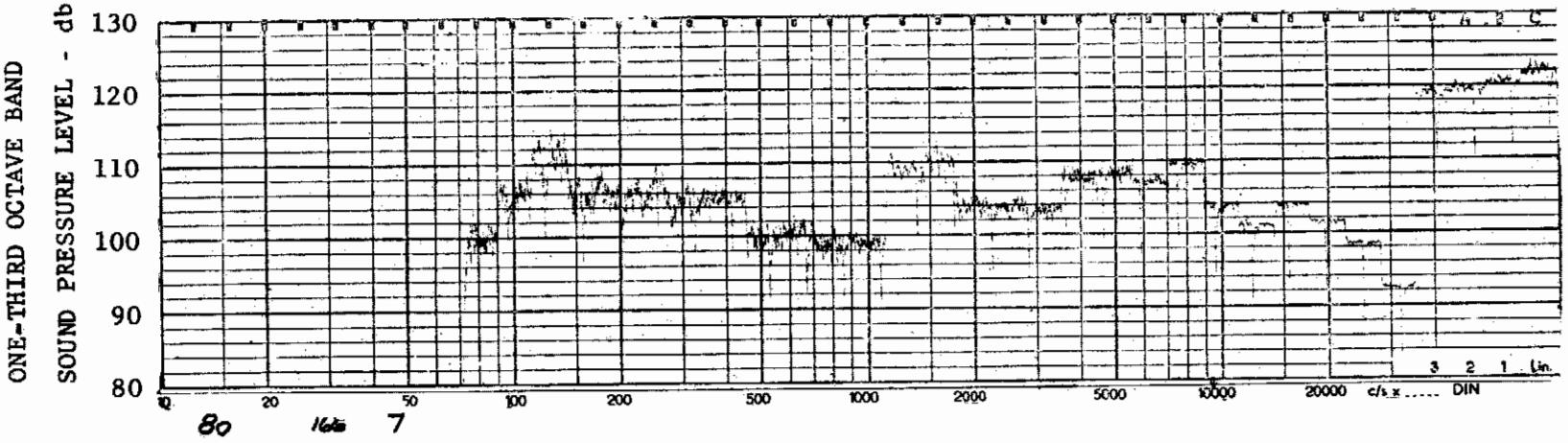

FIGURE 345 ONE-THIRD OCTAVE BAND SPECTRUM MODEL: FP 0

CHANNEL: 7 MACH NO.: 3.5 α: 15° ϕ: 0 Re_∞/FT.: 1.0×10^6 AEDC GROUP NO.: 23/166

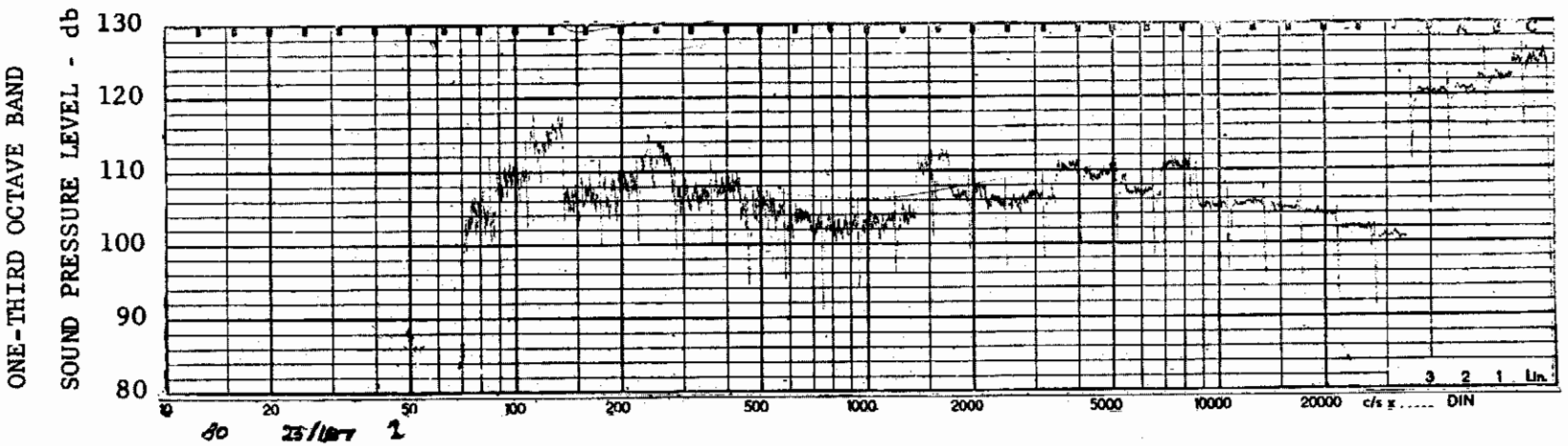

FIGURE 346 ONE-THIRD OCTAVE BAND SPECTRUM MODEL: FP 0

CHANNEL: 2 MACH NO.: 3.5 α: 0 ϕ: 0 Re_∞/FT.: 1.0×10^6 AEDC GROUP NO.: 23/167

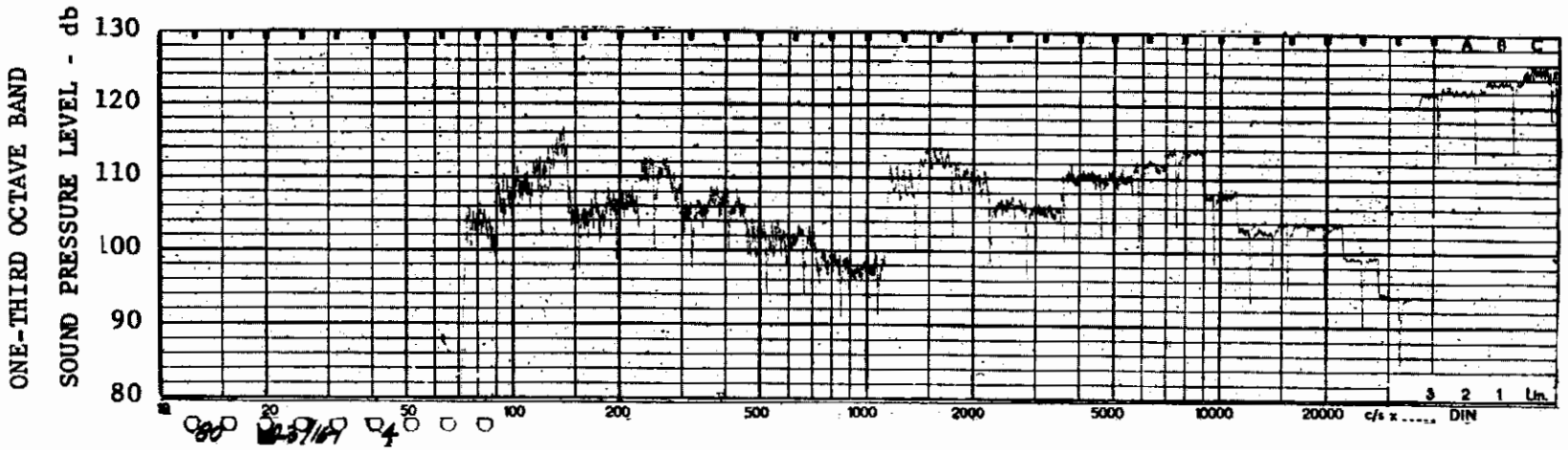

FIGURE 347 ONE-THIRD OCTAVE BAND SPECTRUM MODEL: FP 0

CHANNEL: 4 MACH NO.: 3.5 α: 0 ϕ: 0 Re_∞/FT.: 1.0×10^6 AEDC GROUP NO.: 23/167

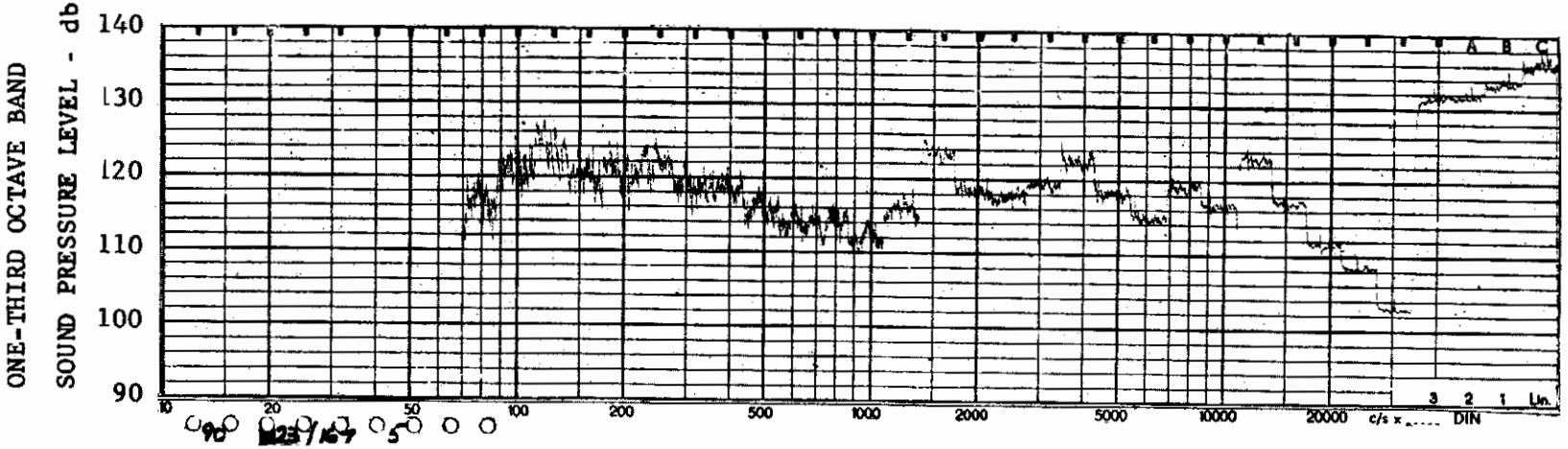

FIGURE 348 ONE-THIRD OCTAVE BAND SPECTRUM MODEL: FP 0

CHANNEL: 5 MACH NO.: 3.5 α: 0 ϕ: 0 Re_∞/FT.: 1.0×10^6 AEDC GROUP NO.: 23/167

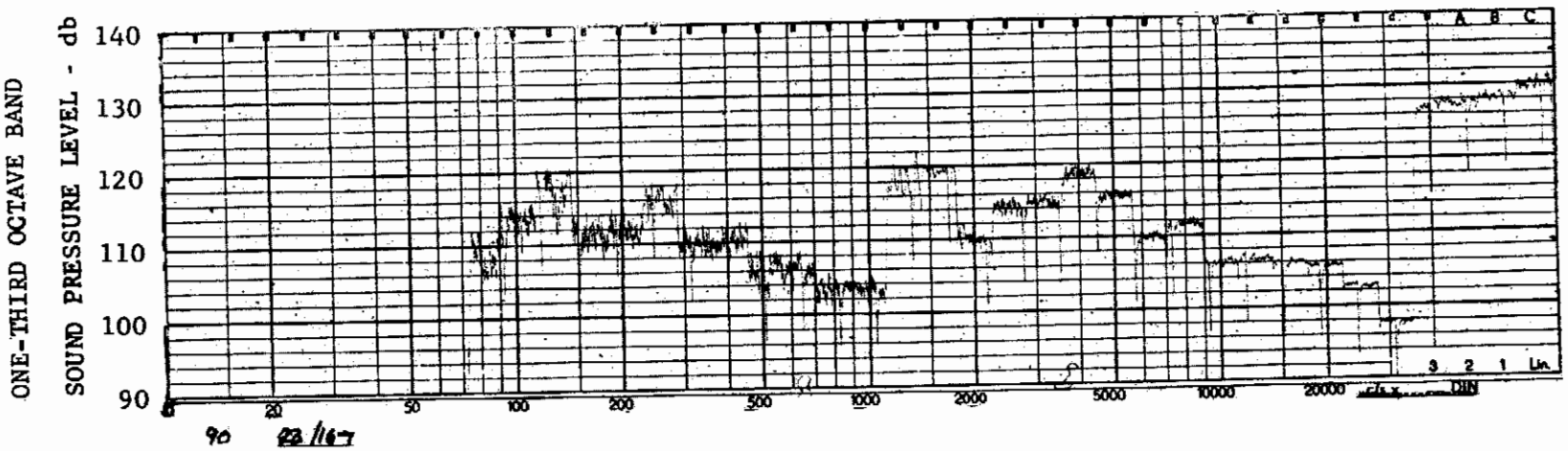

FIGURE 349 ONE-THIRD OCTAVE BAND SPECTRUM MODEL: FP 0

CHANNEL: 6 MACH NO.: 3.5 α: 0 ϕ: 0 Re_∞/FT.: 1.0×10^6 AEDC GROUP NO.: 23/167

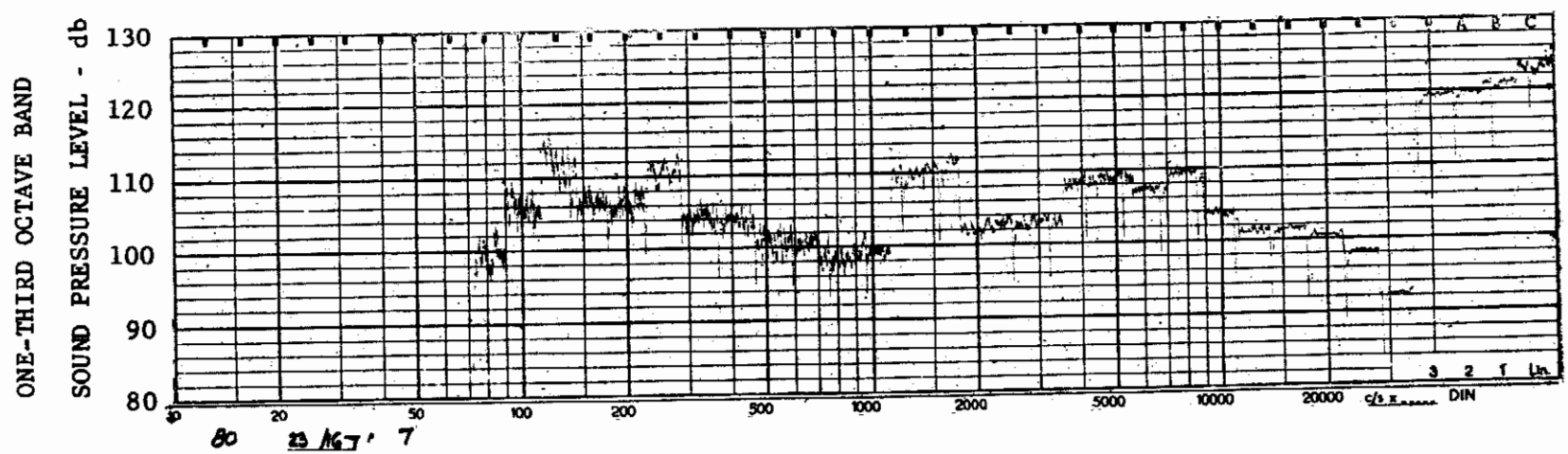

FIGURE 350 ONE-THIRD OCTAVE BAND SPECTRUM MODEL: FP 0

CHANNEL: 7 MACH NO.: 3.5 α: 0 ϕ: 0 Re_∞/FT.: 1.0×10^6 AEDC GROUP NO.: 23/167

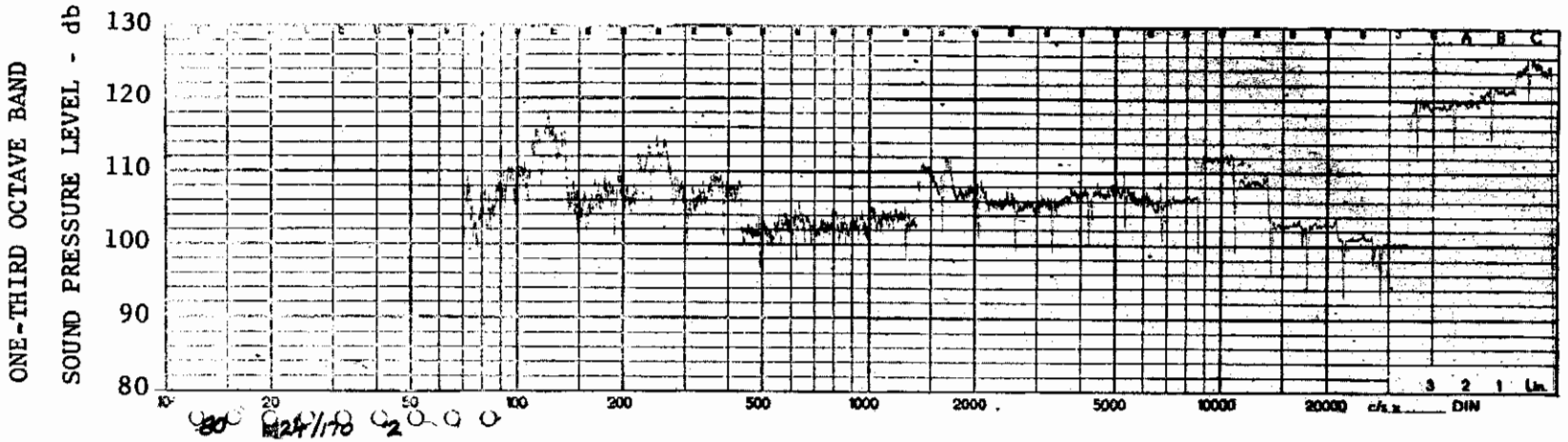

FIGURE 351 ONE-THIRD OCTAVE BAND SPECTRUM MODEL: FP 0

CHANNEL: 2 MACH NO.: 5 α: 0 ϕ: 0 Re_∞/FT.: 0.5×10^6 AEDC GROUP NO.: 24/170

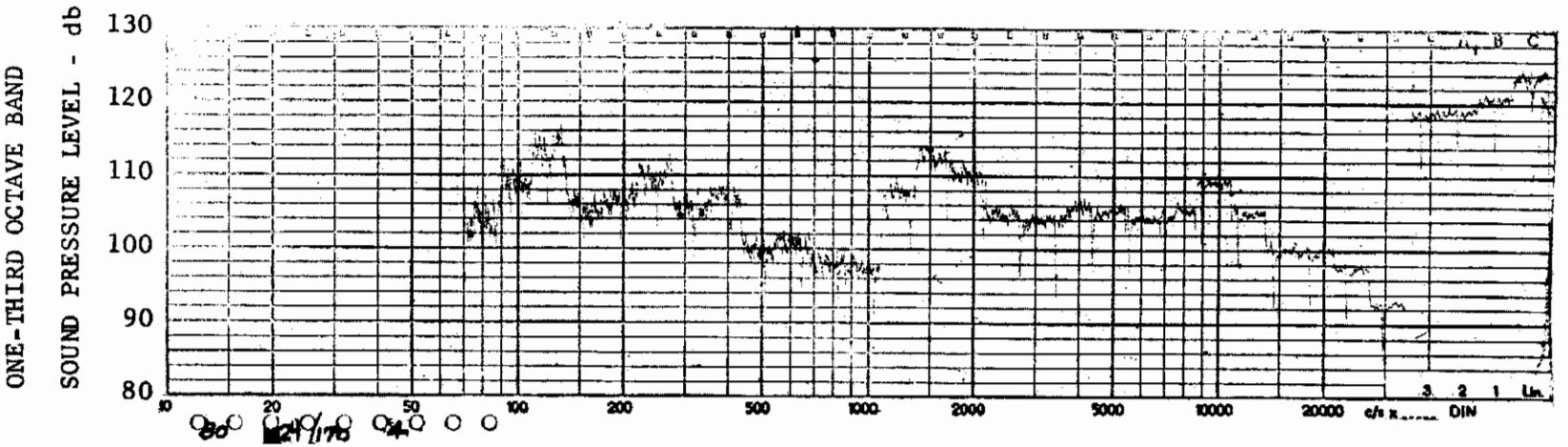

FIGURE 352 ONE-THIRD OCTAVE BAND SPECTRUM MODEL: FP 0

CHANNEL: 4 MACH NO.: 5 α: 0 ϕ: 0 Re_∞/FT.: 0.5×10^6 AEDC GROUP NO.: 24/170

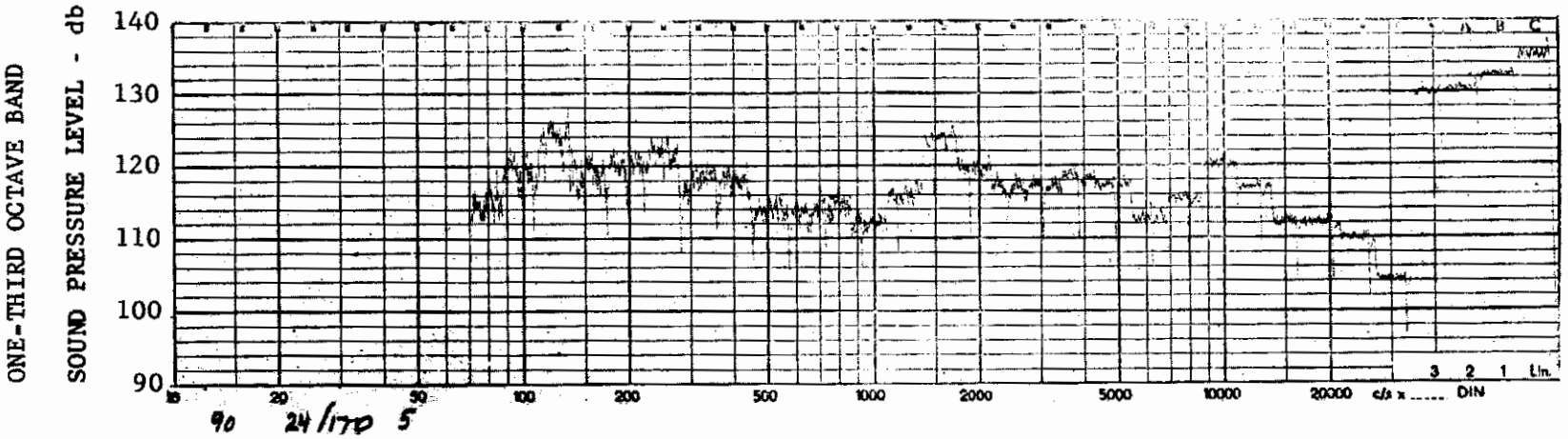

FIGURE 353 ONE-THIRD OCTAVE BAND SPECTRUM MODEL: FP 0

CHANNEL: 5 MACH NO.: 5 α: 0 ϕ: 0 Re_∞/FT.: 0.5×10^6 AEDC GROUP NO.: 24/170

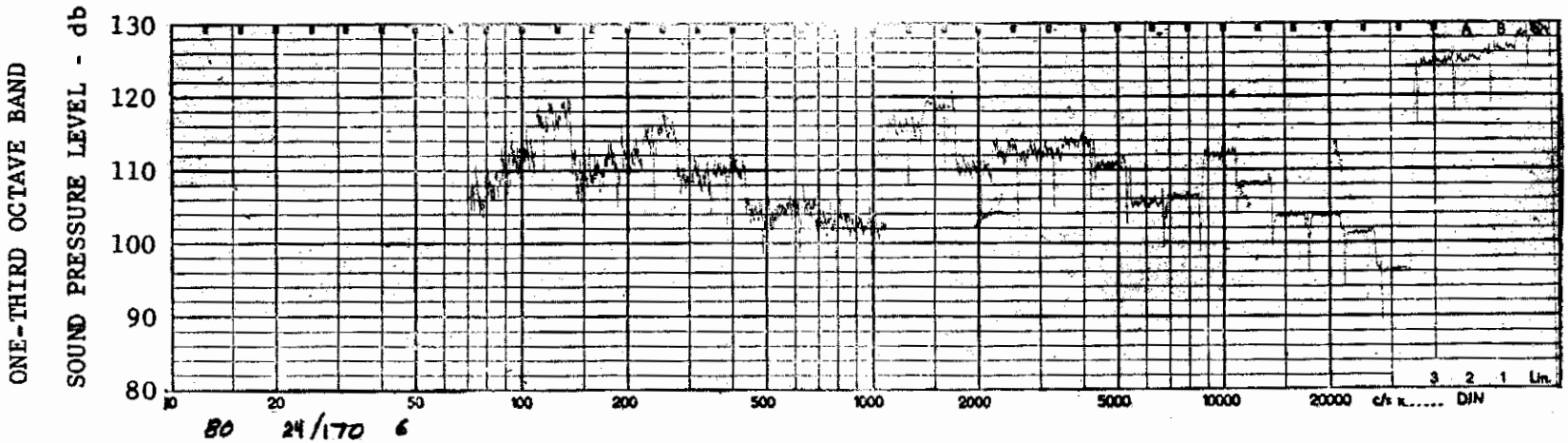

FIGURE 354 ONE-THIRD OCTAVE BAND SPECTRUM MODEL: FP 0

CHANNEL: 6 MACH NO.: 5 α: 0 ϕ: 0 Re_∞/FT.: 0.5×10^6 AEDC GROUP NO.: 24/170

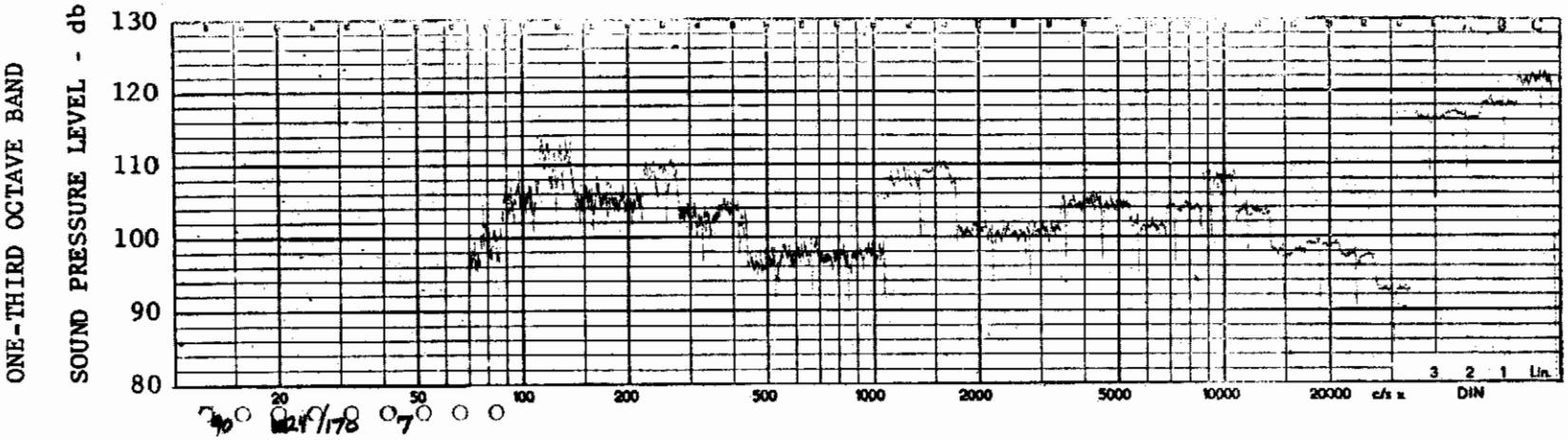

FIGURE 355 ONE-THIRD OCTAVE BAND SPECTRUM MODEL: FP 0

CHANNEL: 7 MACH NO.: 5 α: 0 ϕ: 0 Re_∞/FT.: 0.5×10^6 AEDC GROUP NO.: 24/170

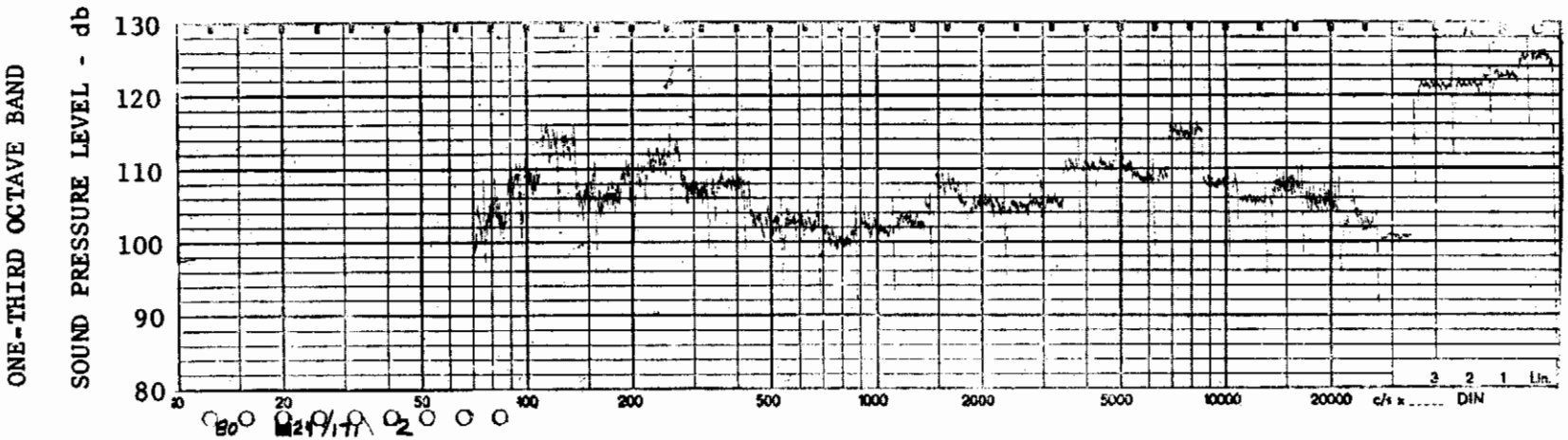

FIGURE 356 ONE-THIRD OCTAVE BAND SPECTRUM MODEL: FP 0

CHANNEL: 2 MACH NO.: 5 α: 0 ϕ: 0 Re_∞/FT.: 1.0×10^6 AEDC GROUP NO.: 24/171

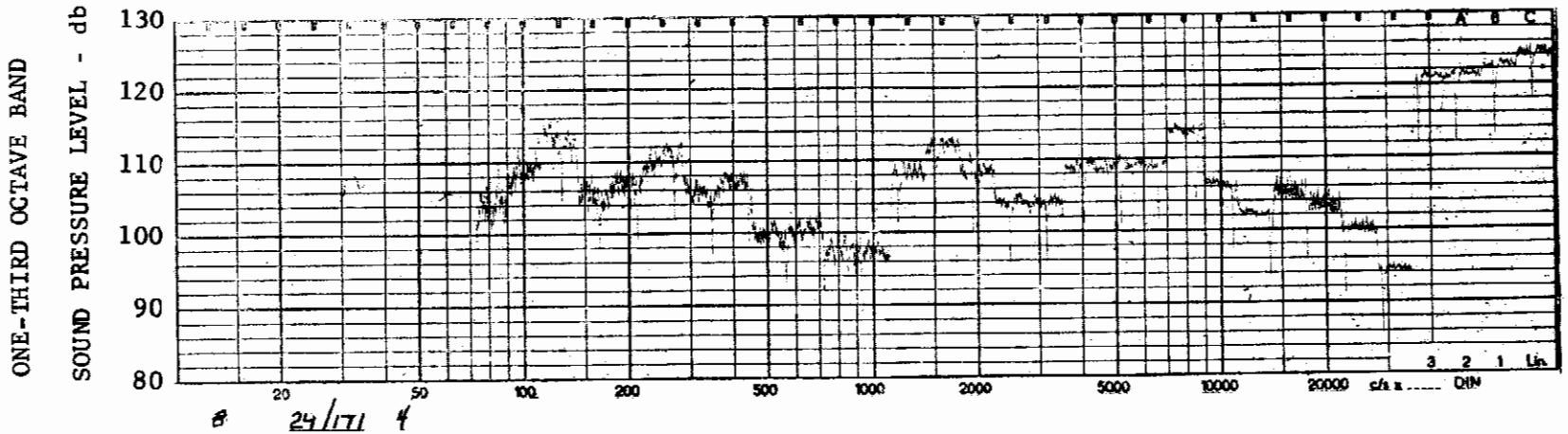

FIGURE 357 ONE-THIRD OCTAVE BAND SPECTRUM MODEL: FP 0

CHANNEL: 4 MACH NO.: 5 α: 0 ϕ: 0 Re_∞/FT.: 1.0×10^6 AEDC GROUP NO.: 24/171

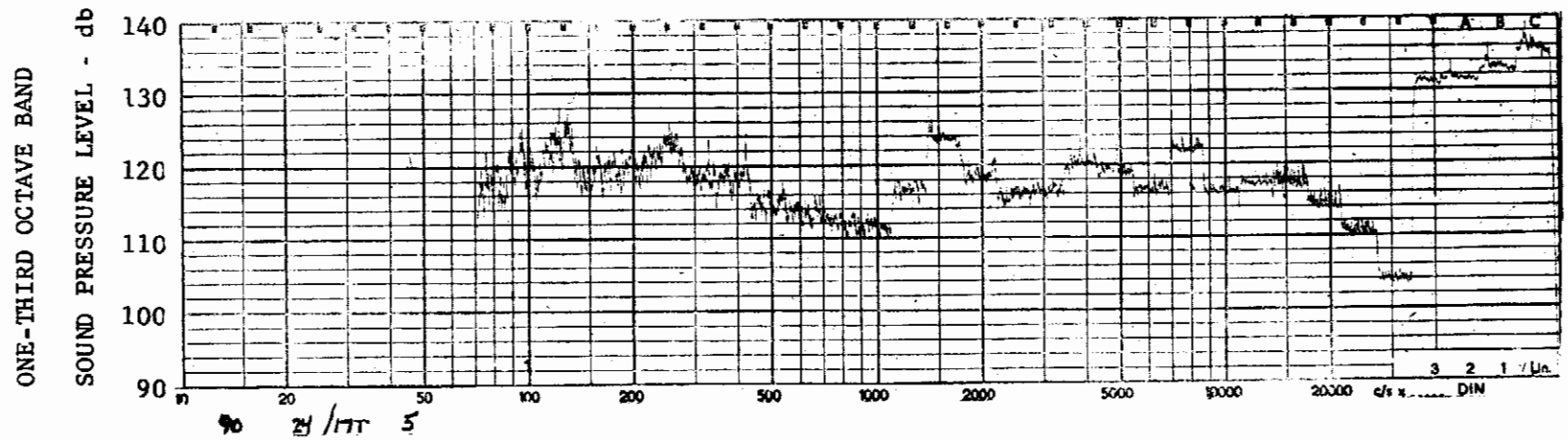

FIGURE 358 ONE-THIRD OCTAVE BAND SPECTRUM MODEL: FP 0

CHANNEL: 5 MACH NO.: 5 α: 0 ϕ: 0 Re_∞/FT.: 1.0×10^6 AEDC GROUP NO.: 24/171

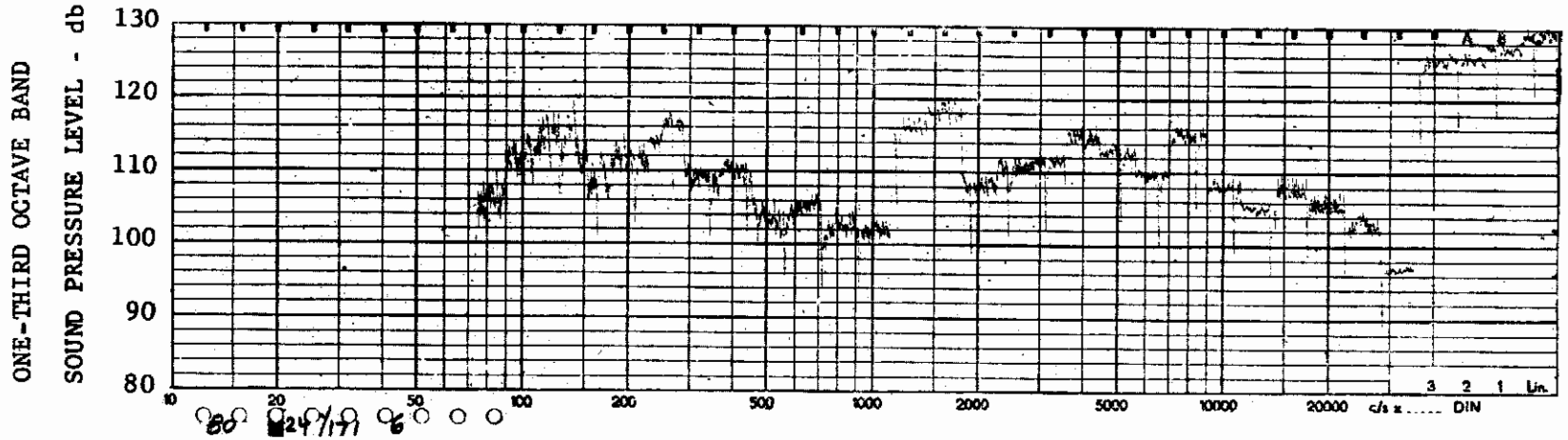

FIGURE 359 ONE-THIRD OCTAVE BAND SPECTRUM MODEL: FP 0

CHANNEL: 6 MACH NO.: 5 α: 0 ϕ: 0 Re_∞/FT.: 1.0×10^6 AEDC GROUP NO.: 24/171

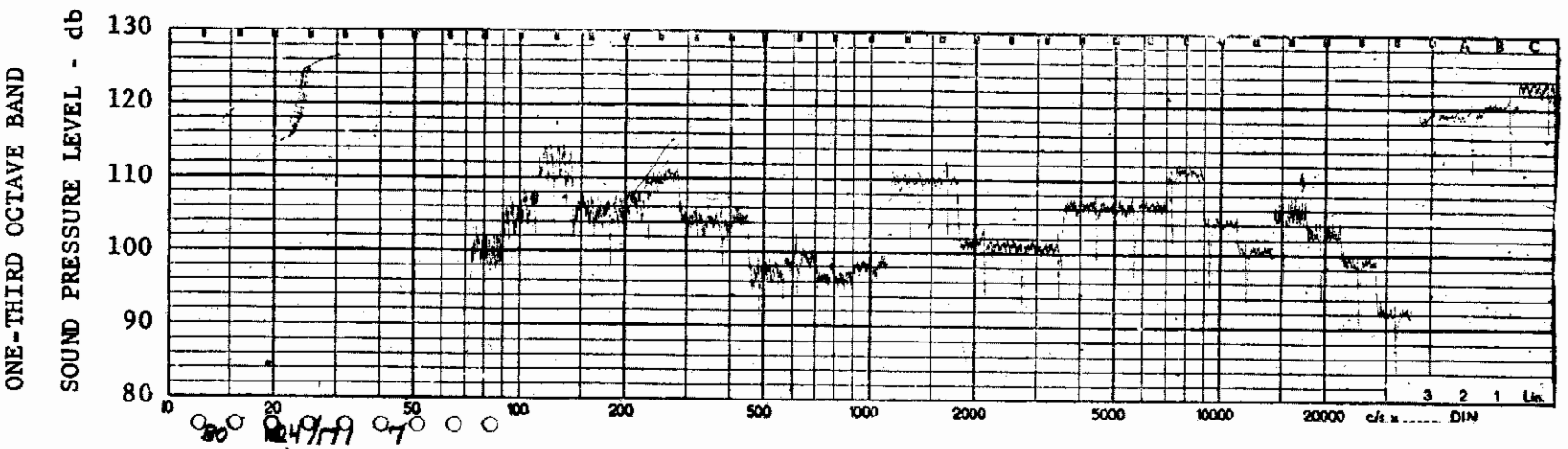

FIGURE 360 ONE-THIRD OCTAVE BAND SPECTRUM MODEL: FP 0

CHANNEL: 7 MACH NO.: 5 α: 0 ϕ: 0 Re_∞/FT.: 1.0×10^6 AEDC GROUP NO.: 24/171

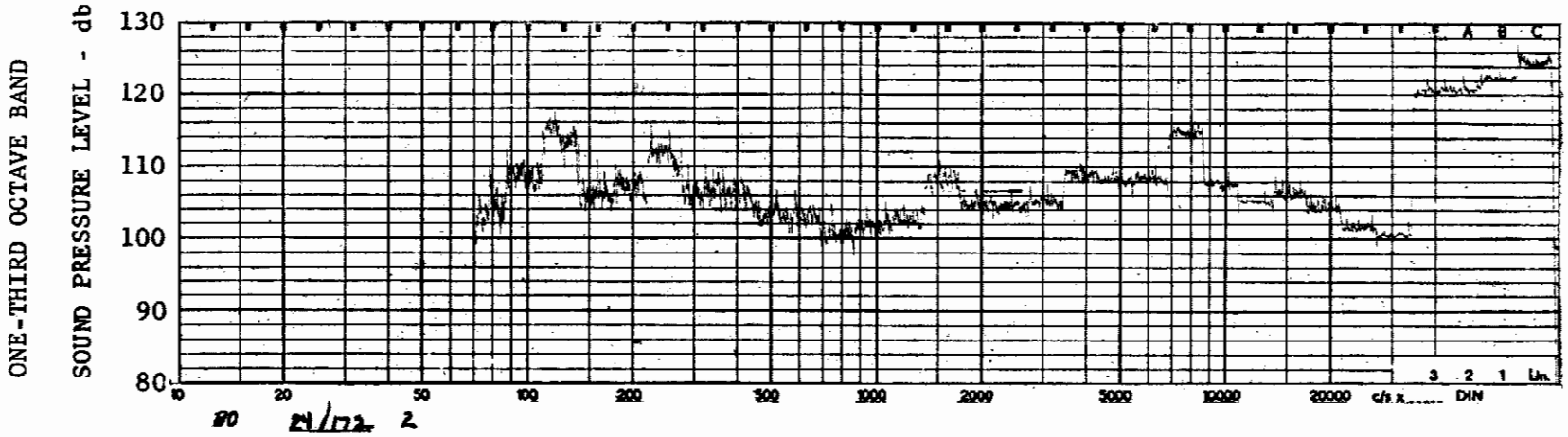

FIGURE 361 ONE-THIRD OCTAVE BAND SPECTRUM MODEL: FP 0

CHANNEL: 2 MACH NO.: 5 α: 5° ϕ: 0 Re_∞/FT.: 1.0×10^6 AEDC GROUP NO. 24/172

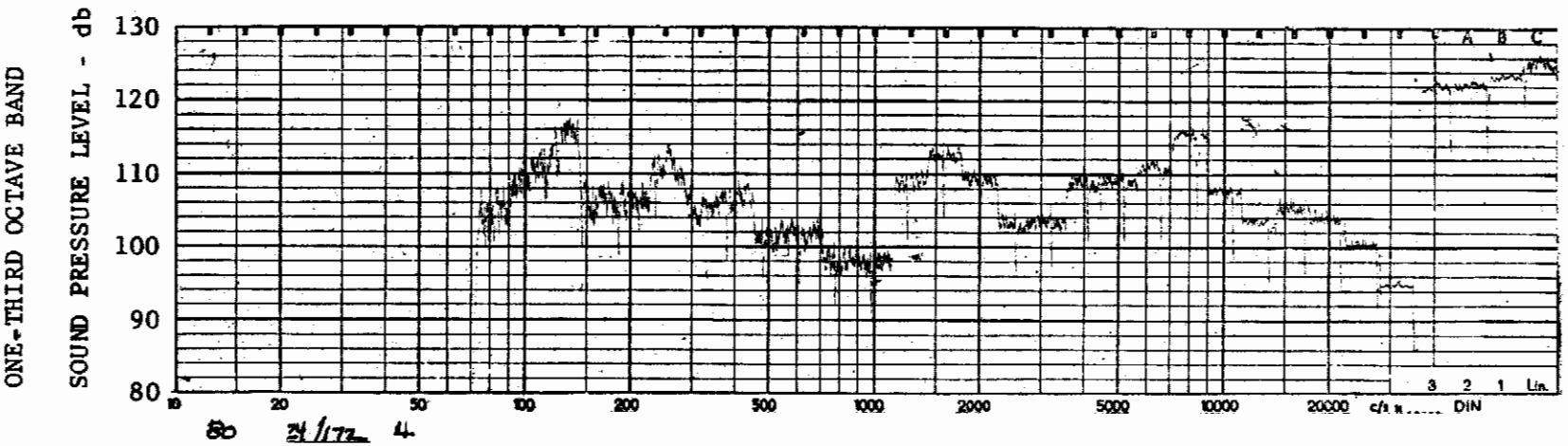

FIGURE 362 ONE-THIRD OCTAVE BAND SPECTRUM MODEL: FP 0

CHANNEL: 4 MACH NO.: 5 α: 5° ϕ: 0 Re_∞/FT.: 1.0×10^6 AEDC GROUP NO.: 24/172

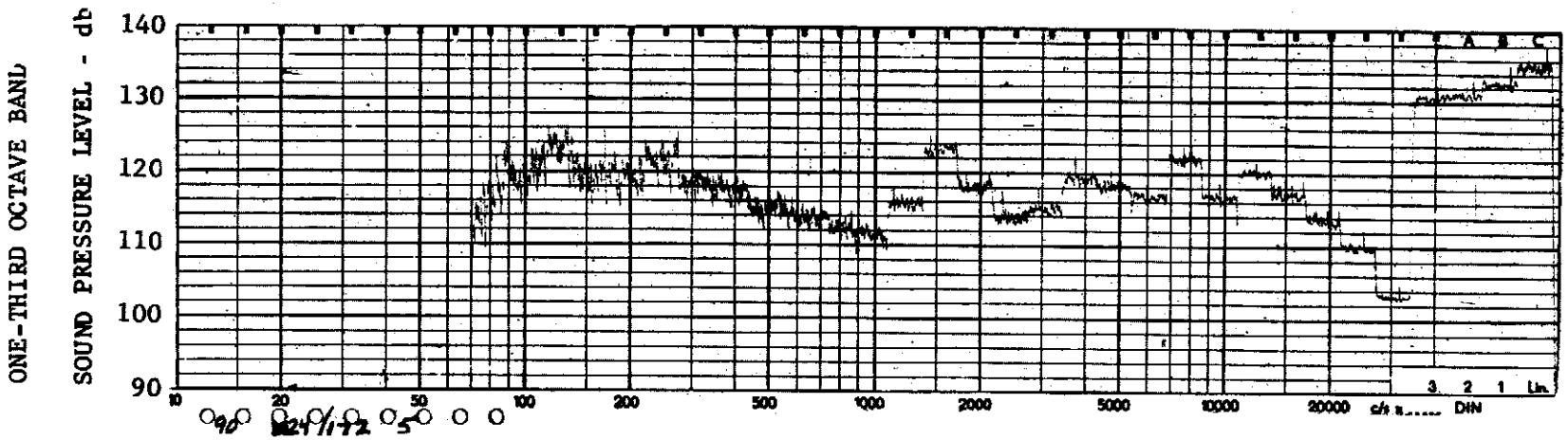

FIGURE 363 ONE-THIRD OCTAVE BAND SPECTRUM MODEL: FP 0

CHANNEL: 5 MACH NO.: 5 α: 5° ϕ: 0 Re_∞/FT.: 1.0×10^6 AEDC GROUP NO.: 24/172

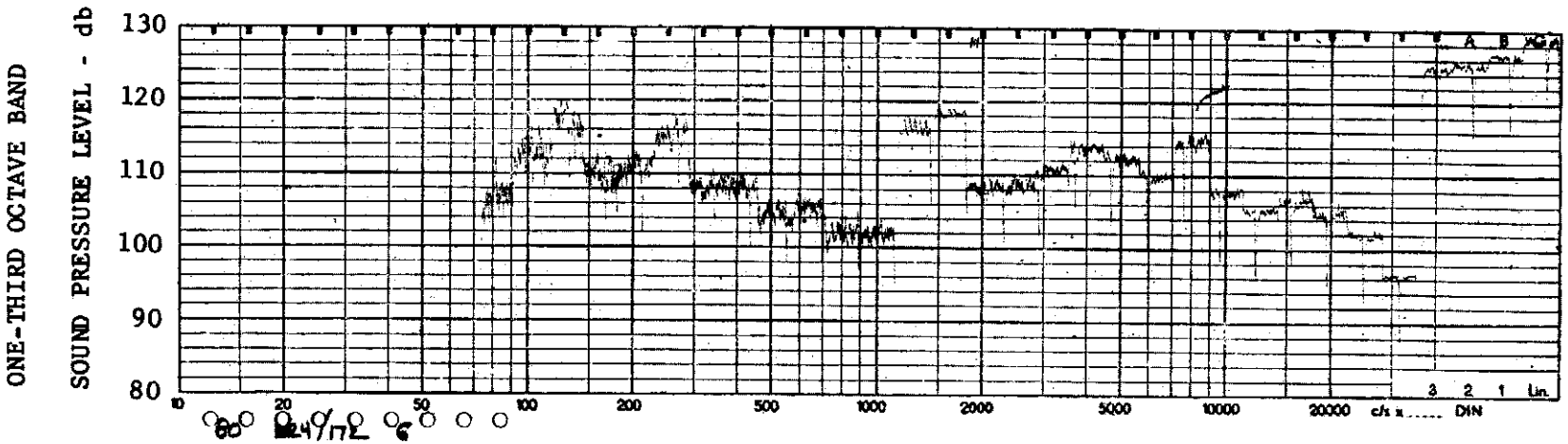

FIGURE 364 ONE-THIRD OCTAVE BAND SPECTRUM MODEL: FP 0

CHANNEL: 6 MACH NO.: 5 α: 5° ϕ: 0 Re_∞/FT.: 1.0×10^6 AEDC GROUP NO.: 24/172

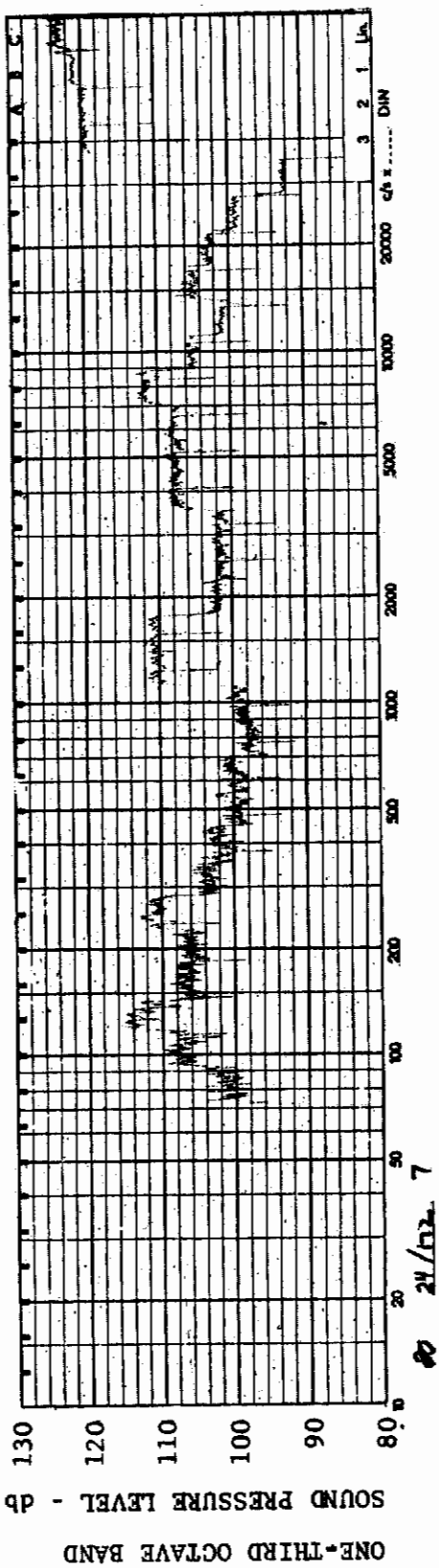

FIGURE 365 ONE-THIRD OCTAVE BAND SPECTRUM

MODEL: FP 0

CHANNEL: 7 MACH NO.: 5 α: 5° ϕ: 0 Re_∞/FT.: 1.0×10^6 AEDC GROUP NO.: 24/172

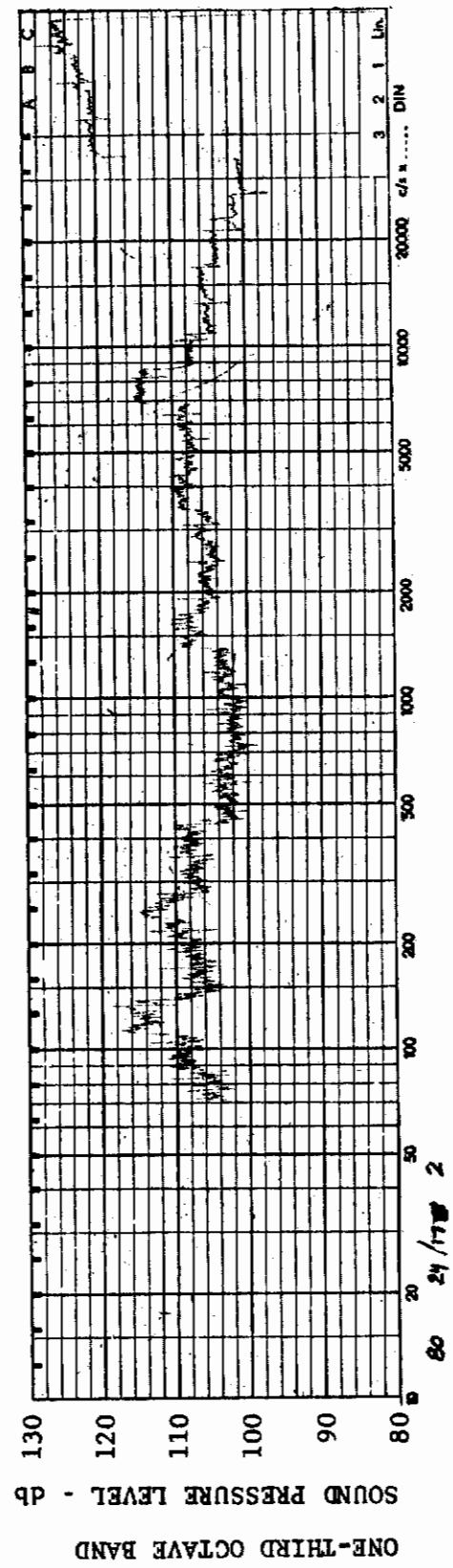

FIGURE 366 ONE-THIRD OCTAVE BAND SPECTRUM

MODEL: FP 0

CHANNEL: 2 MACH NO.: 5 α: 15° ϕ: 0 Re_∞/FT.: 1.0×10^6 AEDC GROUP NO. 24/173

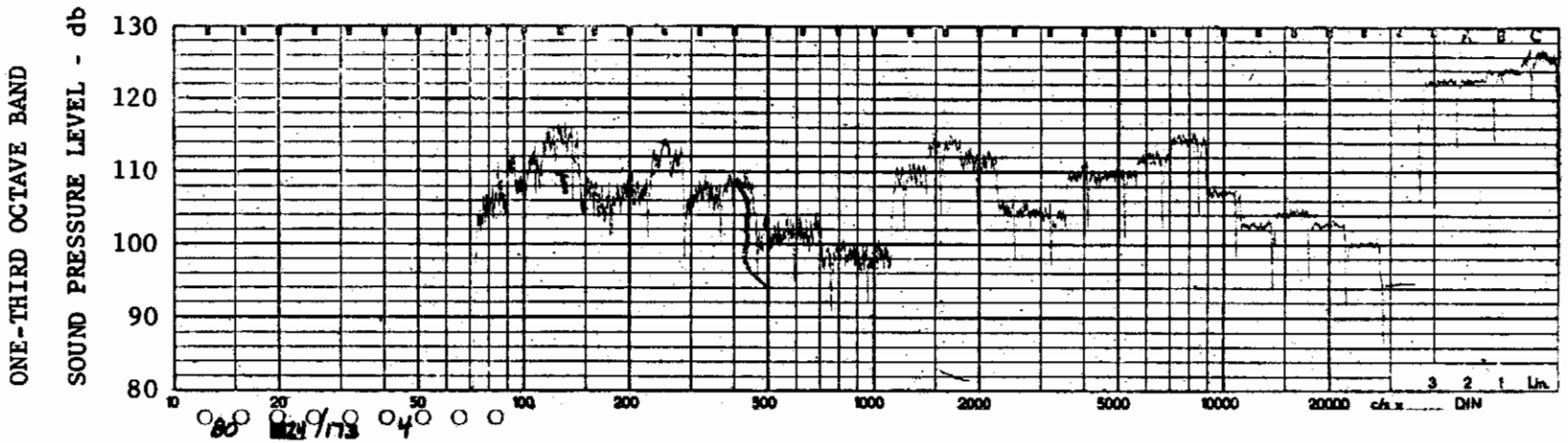

FIGURE 367 ONE-THIRD OCTAVE BAND SPECTRUM MODEL: FP 0

CHANNEL: 4 MACH NO.: 5 α: 15° ϕ: 0 Re_∞/FT.: 1.0×10^6 AEDC GROUP NO.: 24/173

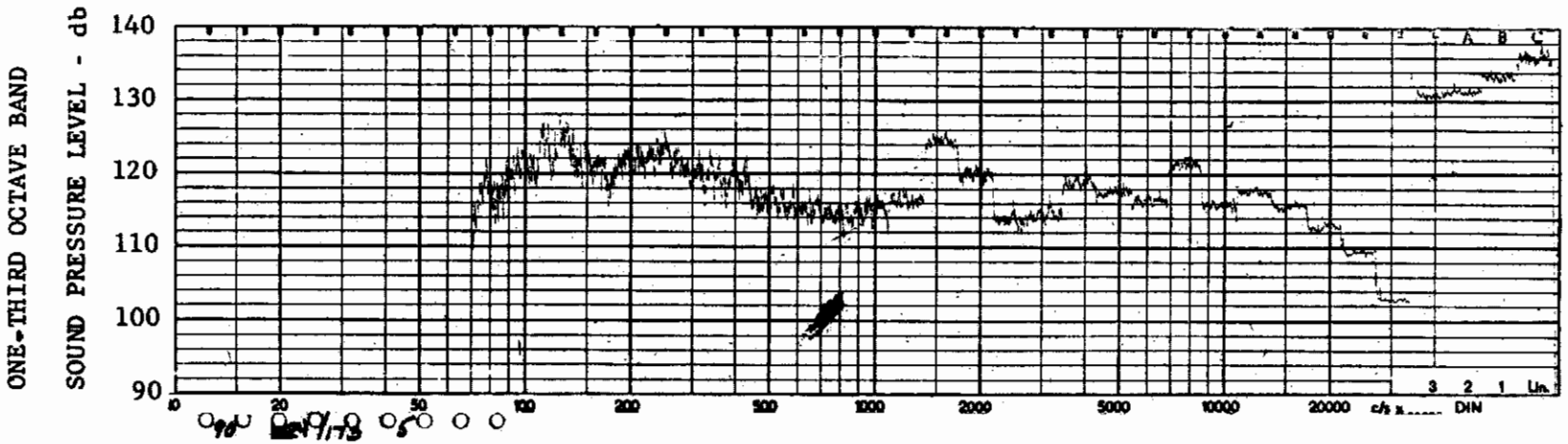

FIGURE 368 ONE-THIRD OCTAVE BAND SPECTRUM MODEL: FP 0

CHANNEL: 5 MACH NO.: 5 α: 15° ϕ: 0 Re_∞/FT.: 1.0×10^6 AEDC GROUP NO.: 24/173

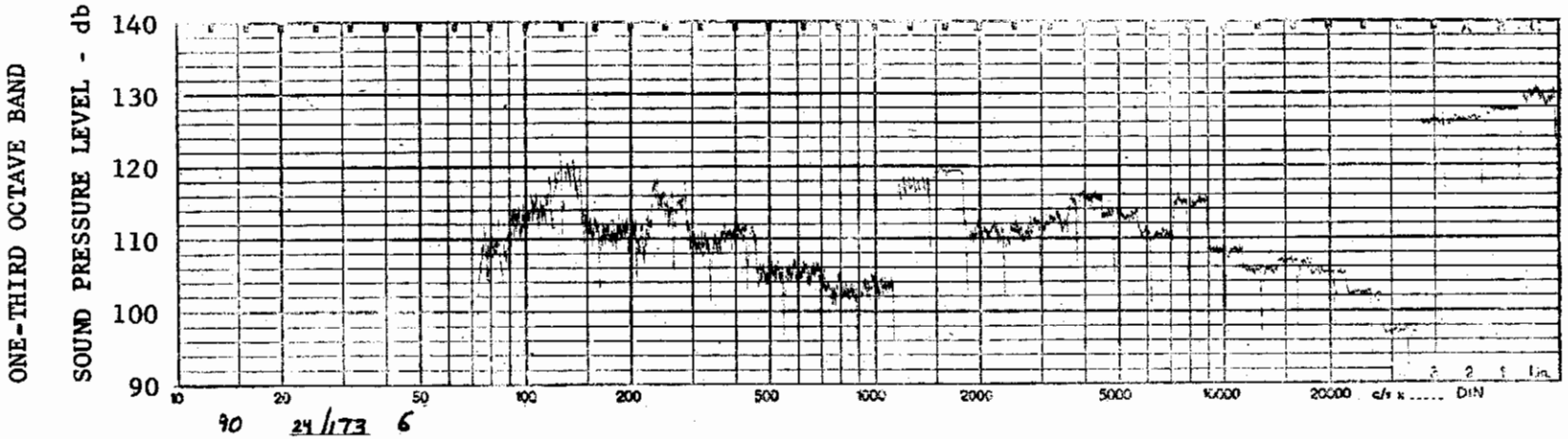

FIGURE 369 ONE-THIRD OCTAVE BAND SPECTRUM MODEL: FP 0

CHANNEL: 6 MACH NO.: 5 α: 15° ϕ: 0 Re_∞/FT.: 1.0×10^6 AEDC GROUP NO.: 24/173

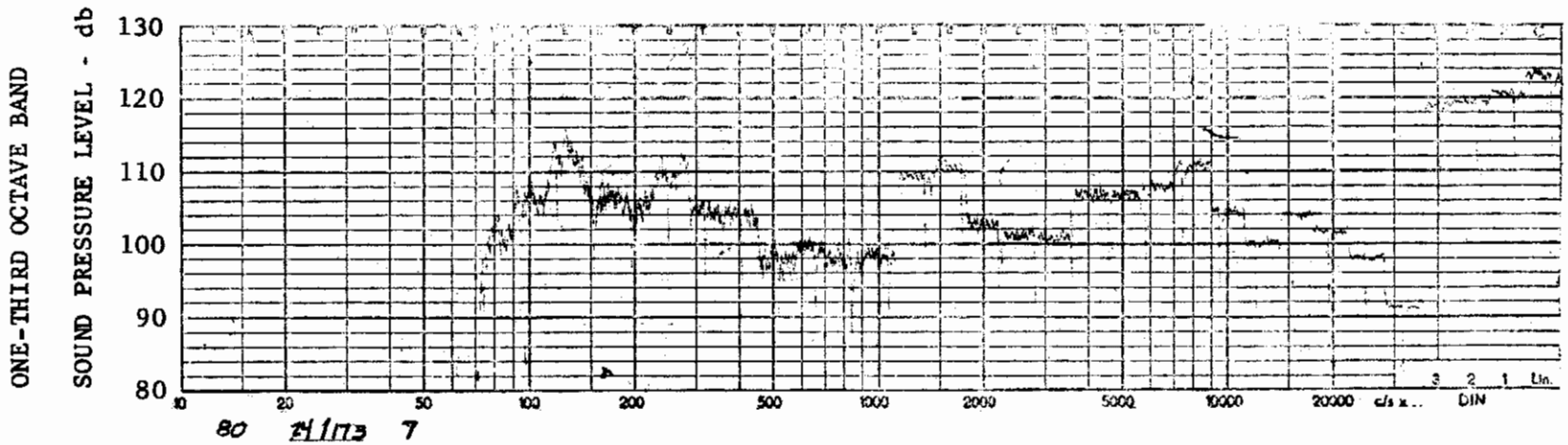

FIGURE 370 ONE-THIRD OCTAVE BAND SPECTRUM MODEL: FP 0

CHANNEL: 7 MACH NO.: 5 α: 15° ϕ: 0 Re_∞/FT.: 1.0×10^6 AEDC GROUP NO.: 24/173

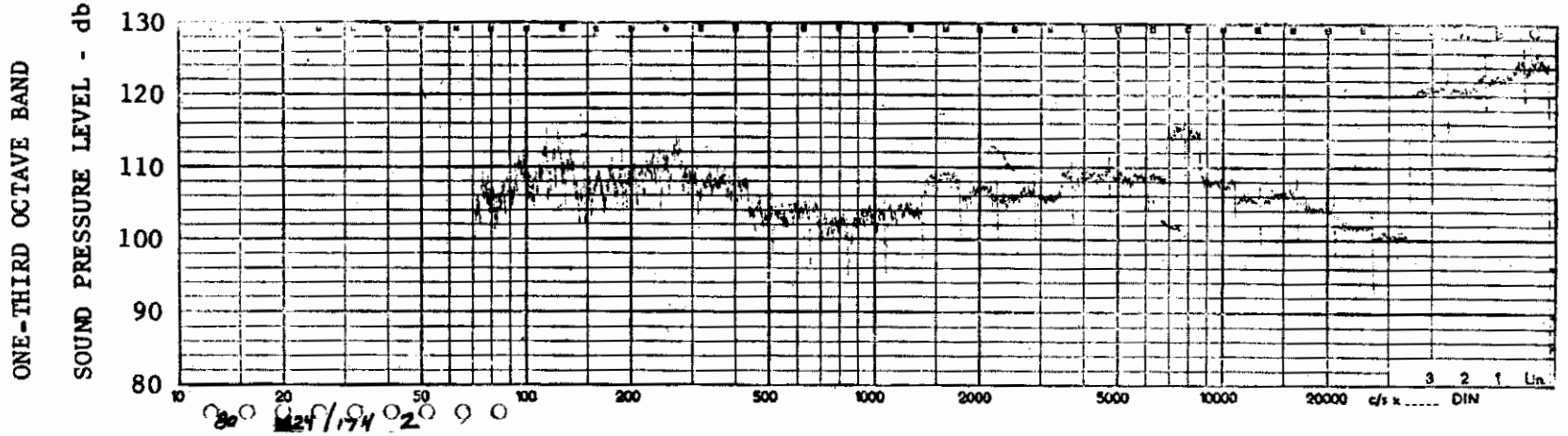

FIGURE 371 ONE-THIRD OCTAVE BAND SPECTRUM MODEL: FP 0

CHANNEL: 2 MACH NO.: 5 α: 0 ϕ: 0 Re_∞/FT.: 1.0×10^6 AEDC GROUP NO.: 24/174

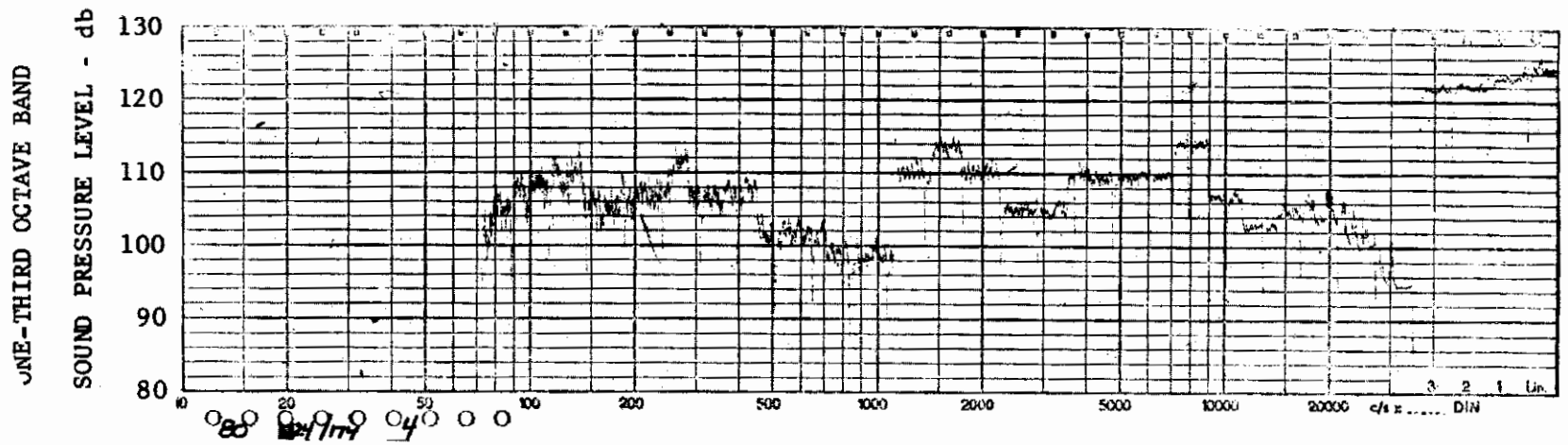

FIGURE 372 ONE-THIRD OCTAVE BAND SPECTRUM MODEL: FP 0

CHANNEL: 4 MACH NO.: 5 α: 0 ϕ: 0 Re_∞/FT.: 1.0×10^6 AEDC GROUP NO.: 24/174

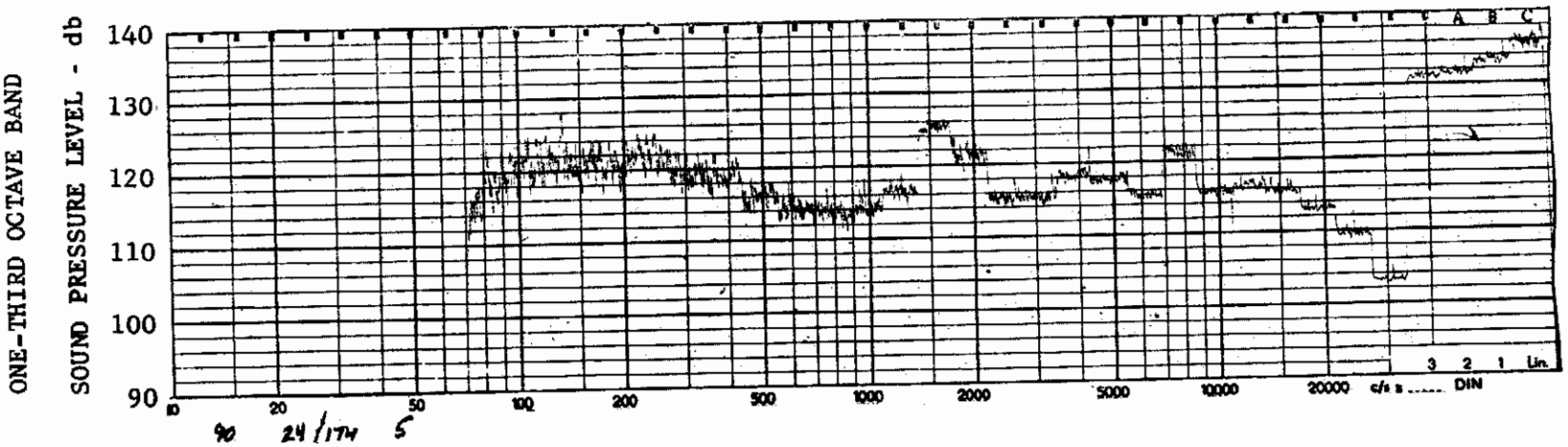

FIGURE 373 ONE-THIRD OCTAVE BAND SPECTRUM MODEL: FP 0

CHANNEL: 5 MACH NO.: 5 α: 0 ϕ: 0 Re_∞/FT.: 1.0×10^6 AEDC GROUP NO.: 24/174

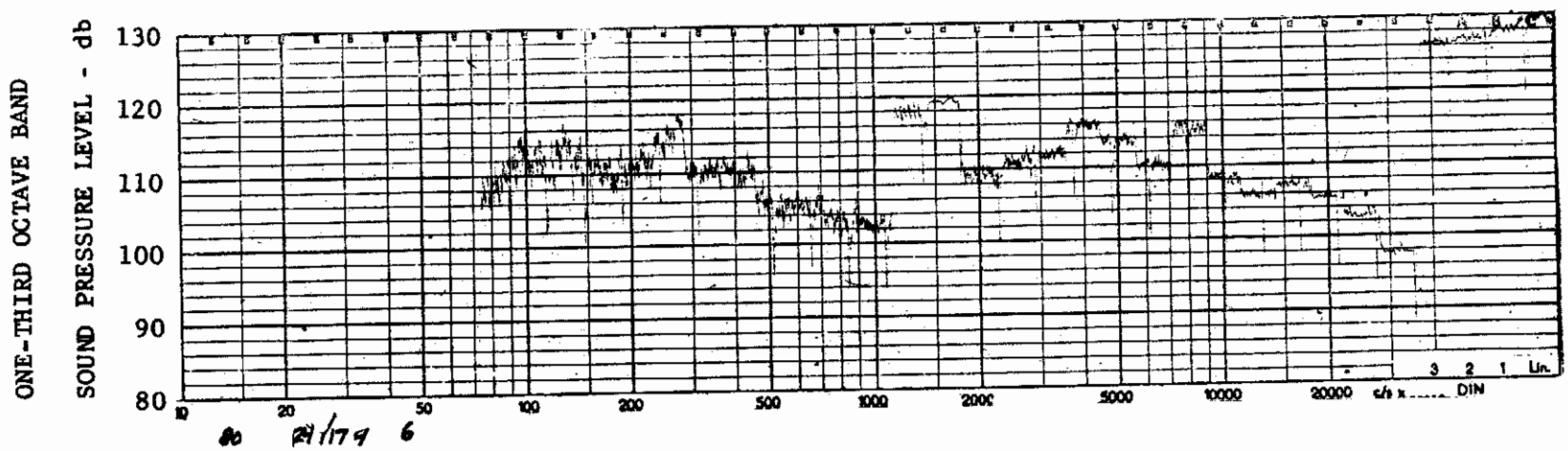

FIGURE 374 ONE-THIRD OCTAVE BAND SPECTRUM MODEL: FP 0

CHANNEL: 6 MACH NO.: 5 α: 0 ϕ: 0 Re_∞/FT.: 1.0×10^6 AEDC GROUP NO.: 24/174

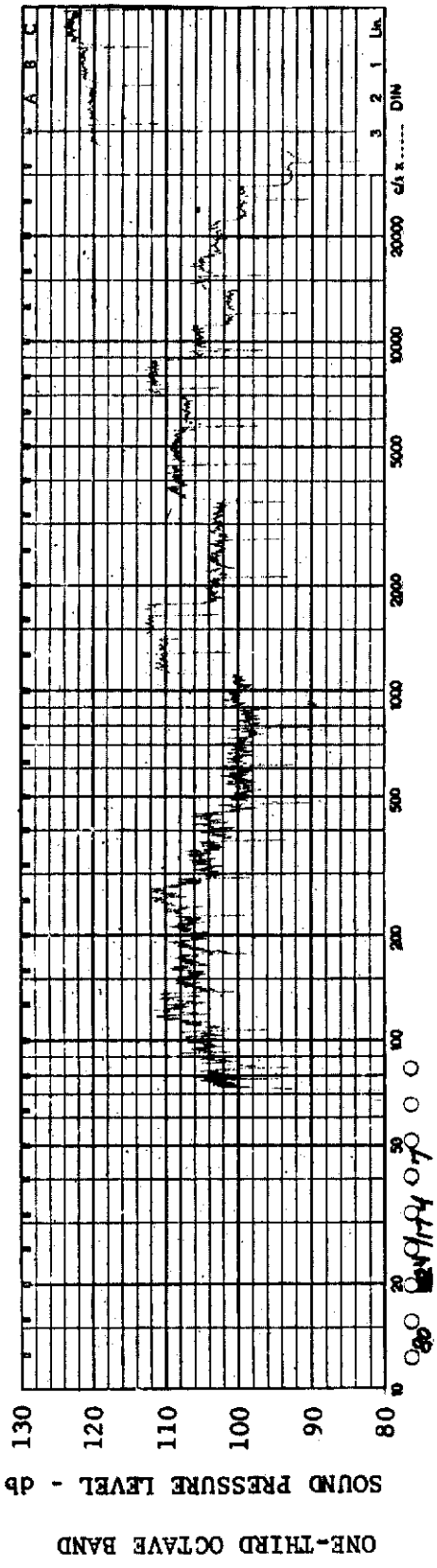

FIGURE 375 ONE-THIRD OCTAVE BAND SPECTRUM MODEL: FP 0

CHANNEL: 7 MACH NO.: 5 α: 0 ϕ: 0 Re_∞/FT.: 1×10^6 AEDC GROUP NO.: 24/174

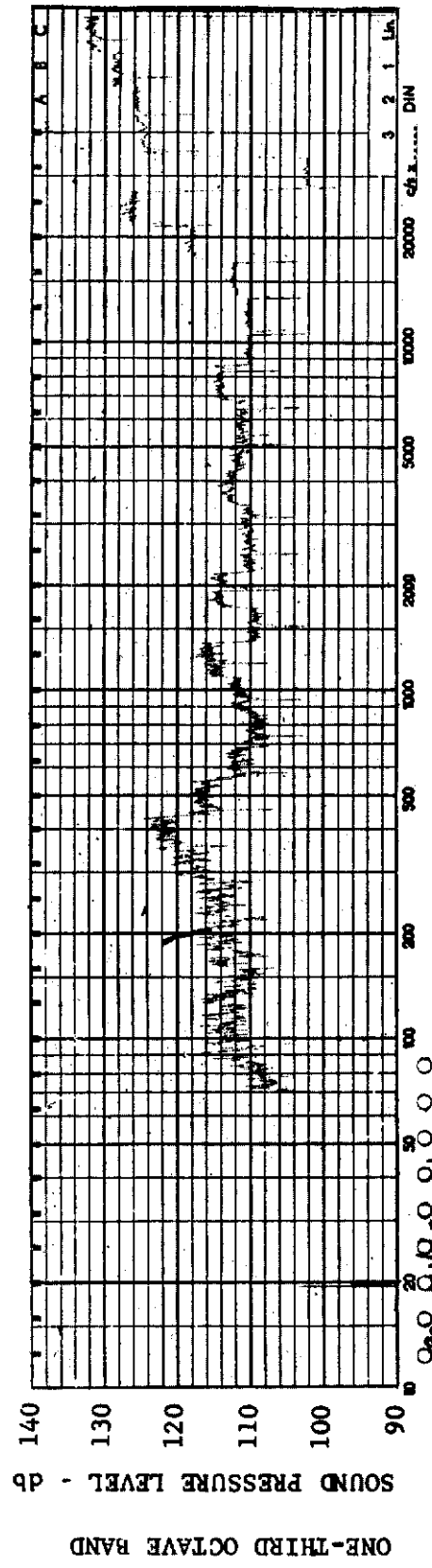

FIGURE 376 ONE-THIRD OCTAVE BAND SPECTRUM MODEL: FP 0

CHANNEL: 1 MACH NO.: 10 α: 0 ϕ: 0 Re_∞/FT.: 1×10^6 AEDC GROUP NO.: 1/1 C

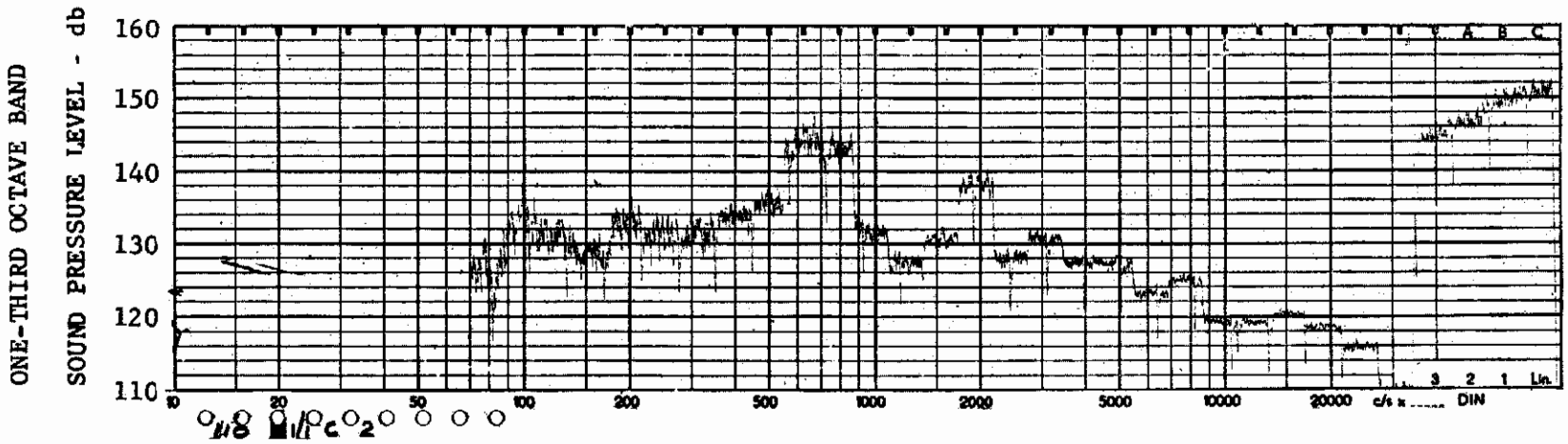

FIGURF 377 ONE-THIRD OCTAVE BAND SPECTRUM MODEL: FP 0

CHANNEL: 2 MACH NO.: 10 α: 0 ϕ: 0 Re_∞/FT.: 1×10^6 AEDC GROUP NO.: 1/1 C

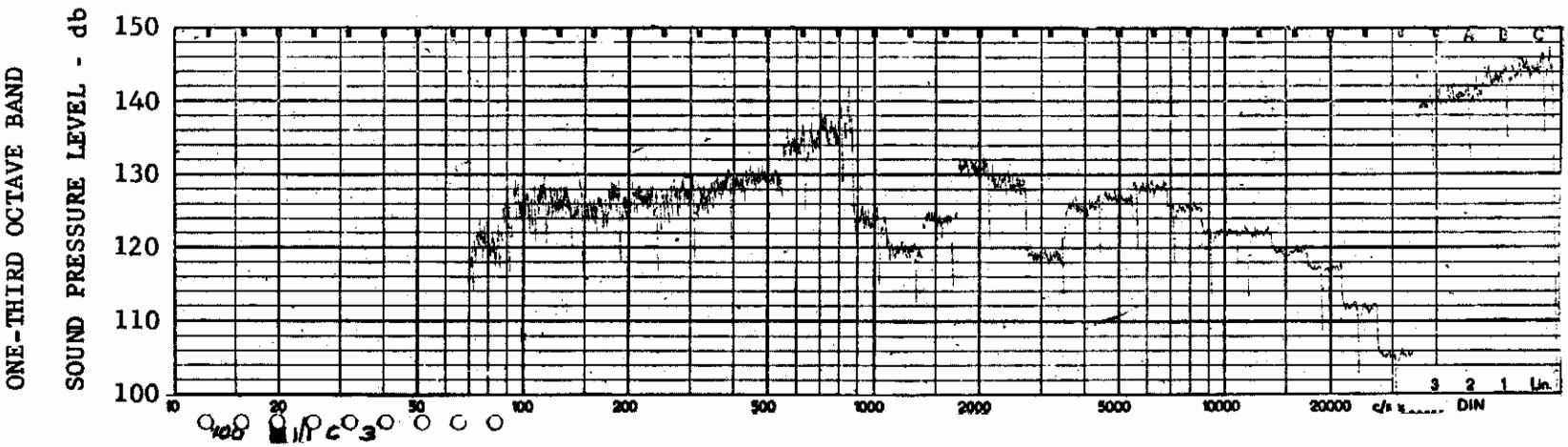

FIGURE 378 ONE-THIRD OCTAVE BAND SPECTRUM MODEL: FP 0

CHANNEL: 3 MACH NO.: 10 α: 0 ϕ: 0 Re_∞/FT.: 1×10^6 AEDC GROUP NO.: 1/1 C

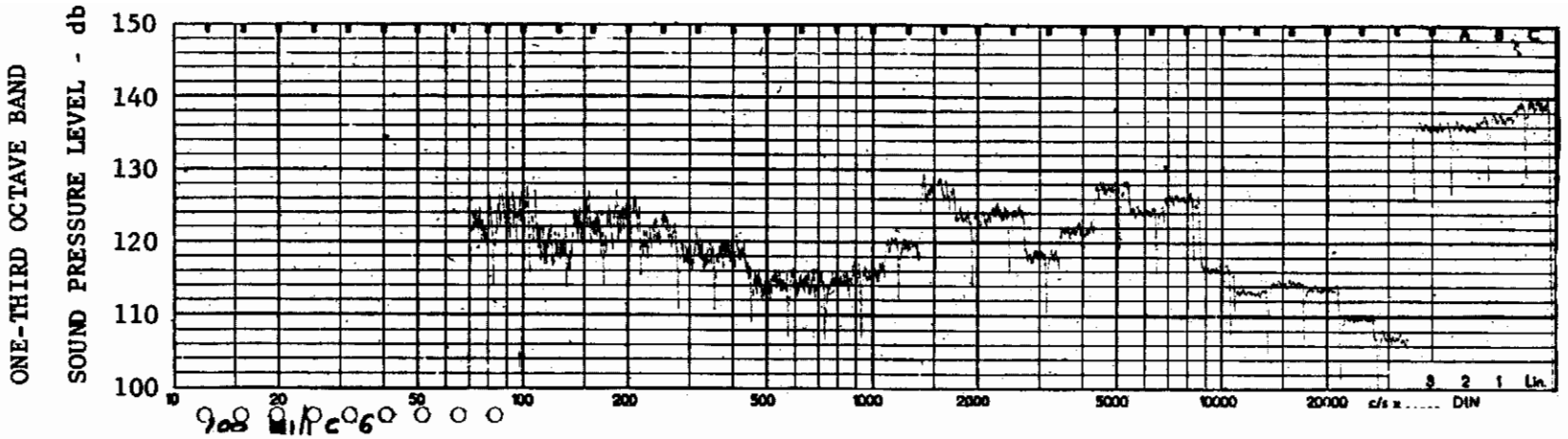

FIGURE 379 ONE-THIRD OCTAVE BAND SPECTRUM MODEL: FP 0

CHANNEL: 6 MACH NO.: 10 α: 0 ϕ: 0 Re_∞/FT.: 1×10^6 AEDC GROUP NO.: 1/1 C

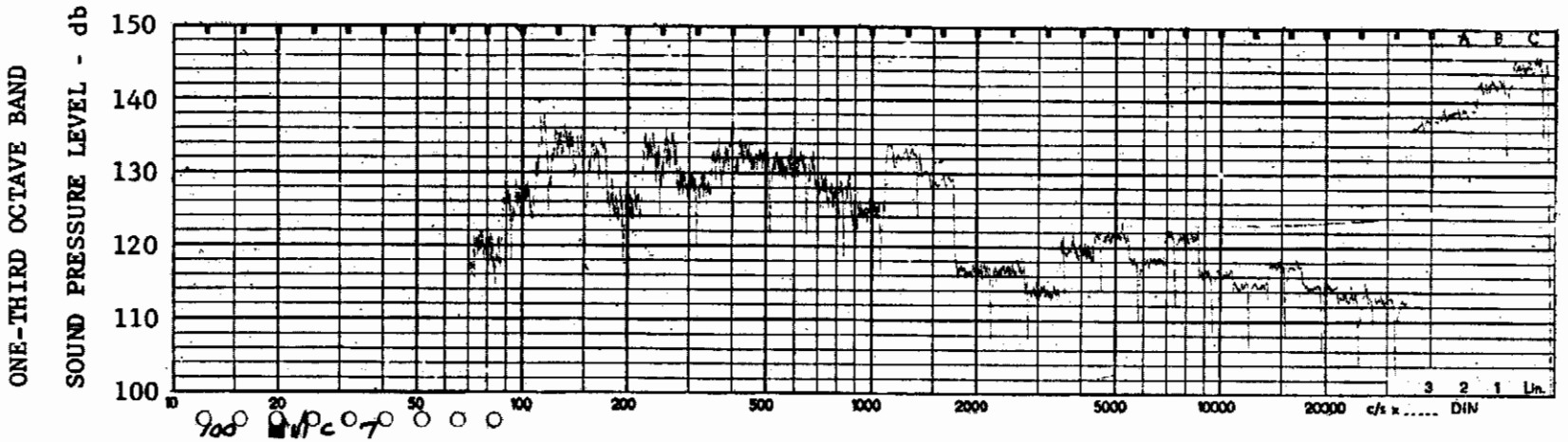

FIGURE 380 ONE-THIRD OCTAVE BAND SPECTRUM MODEL: FP 0

CHANNEL: 7 MACH NO.: 10 α: 0 ϕ: 0 Re_∞/FT.: 1×10^6 AEDC GROUP NO.: 1/1 C

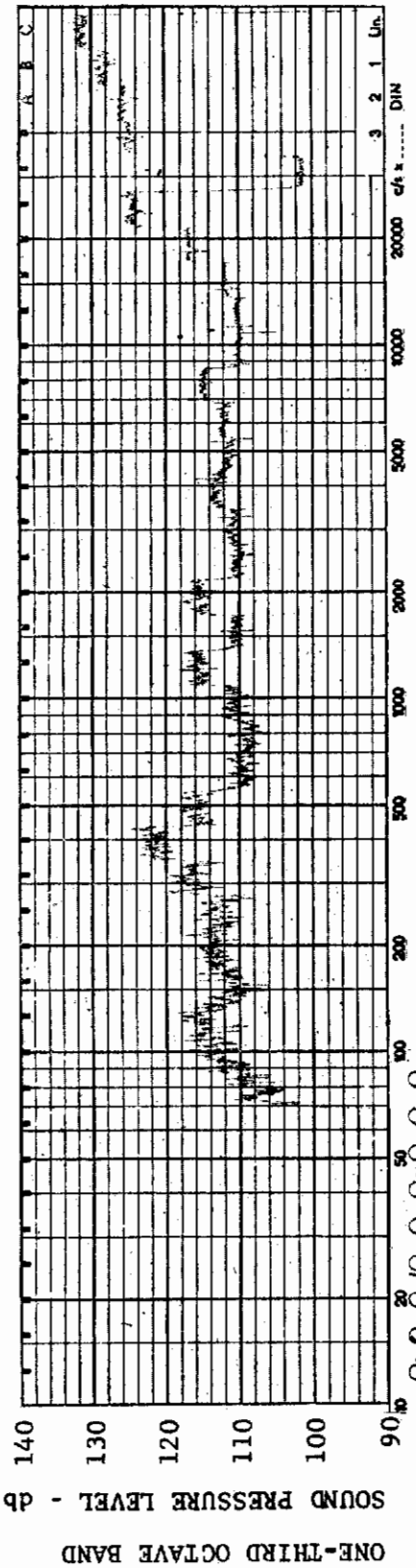

FIGURE 381 ONE-THIRD OCTAVE BAND SPECTRUM

MODEL: FP 0

CHANNEL: 1 MACH NO.: 10 α: 5° ϕ: 0 Re_∞/FT.: 1×10^6 AEDC GROUP NO.: 1/2 C

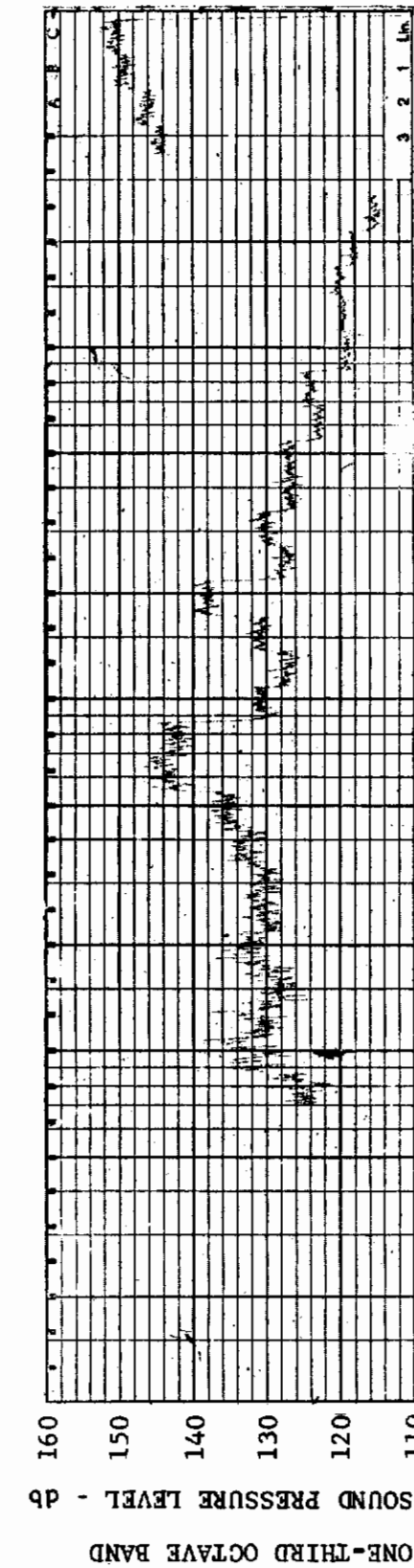

FIGURE 382 ONE-THIRD OCTAVE BAND SPECTRUM

MODEL: FP 0

CHANNEL: 2 MACH NO.: 10 α: 5° ϕ: 0 Re_∞/FT.: 1×10^6 AEDC GROUP NO.: 1/2 C

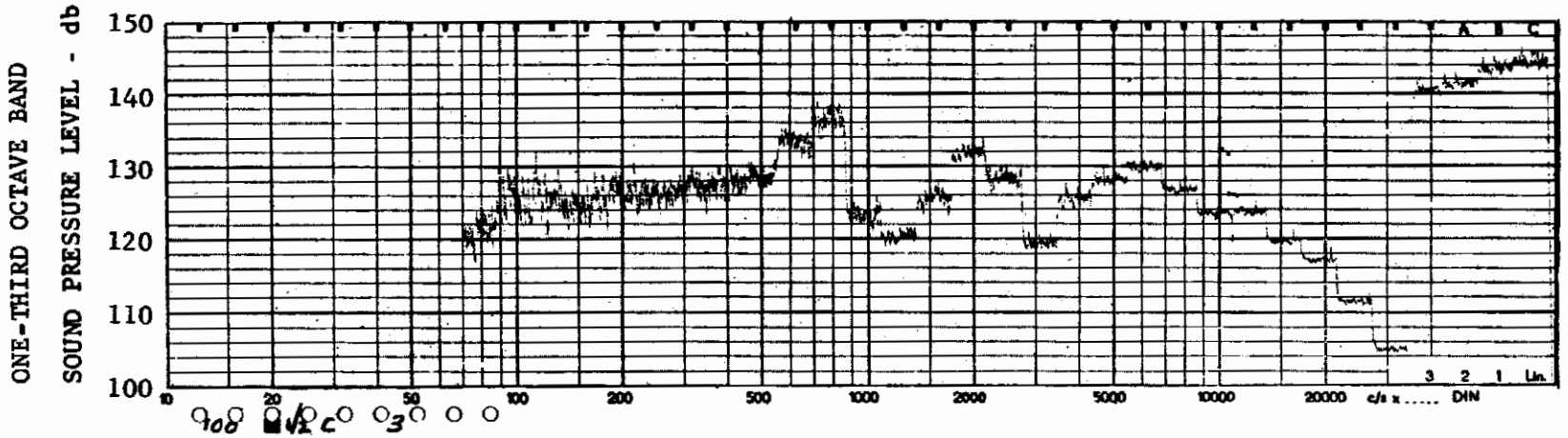

FIGURE 383 ONE-THIRD OCTAVE BAND SPECTRUM MODEL: FP 0

CHANNEL: 3 MACH NO.: 10 α: 5° ϕ: 0 Re_∞/FT.: 1×10^6 AEDC GROUP NO.: 1/2 C

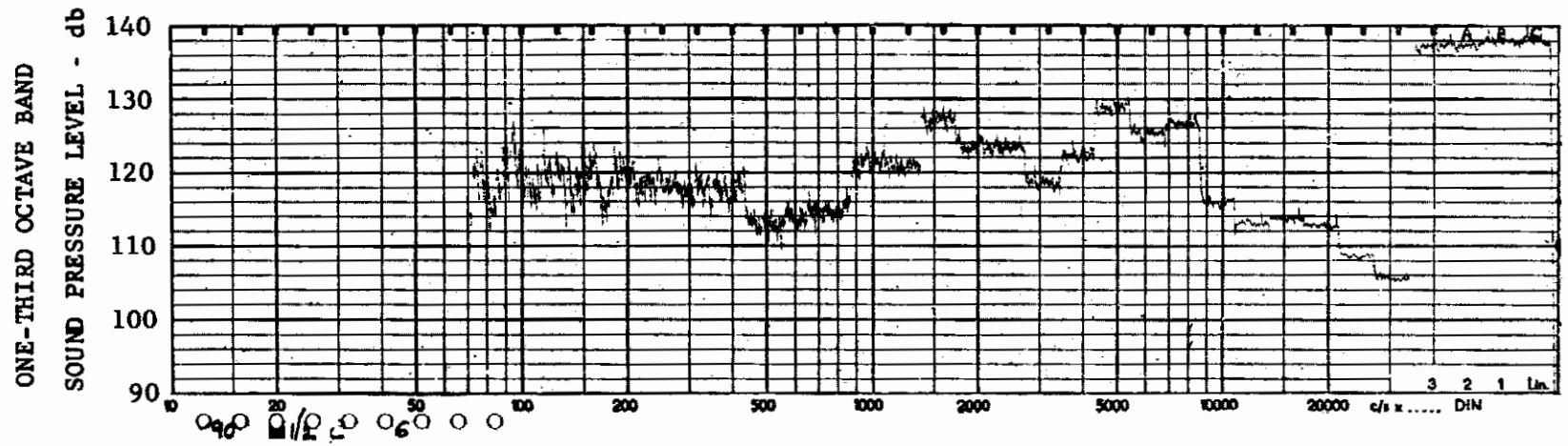

FIGURE 384 ONE-THIRD OCTAVE BAND SPECTRUM MODEL: FP 0

CHANNEL: 6 MACH NO.: 10 α: 5° ϕ: 0 Re_∞/FT.: 1×10^6 AEDC GROUP NO.: 1/2 C

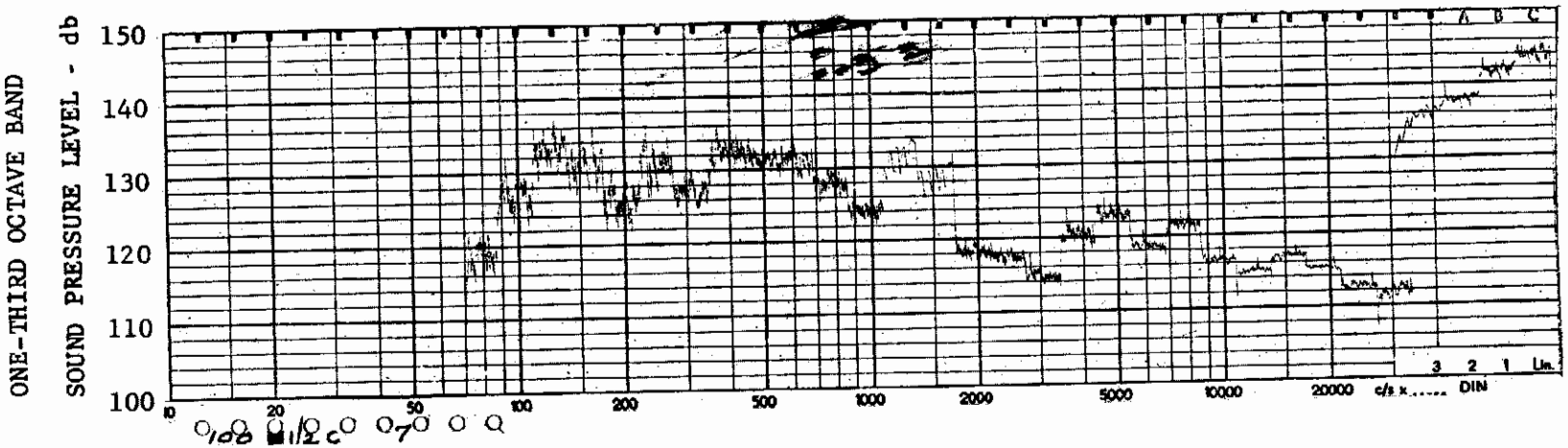

FIGURE 385 ONE-THIRD OCTAVE BAND SPECTRUM MODEL: FP 0

CHANNEL: 7 MACH NO.: 10 α: 5° ϕ: 0 Re_∞/FT.: 1×10^6 AEDC GROUP NO.: 1/2 C

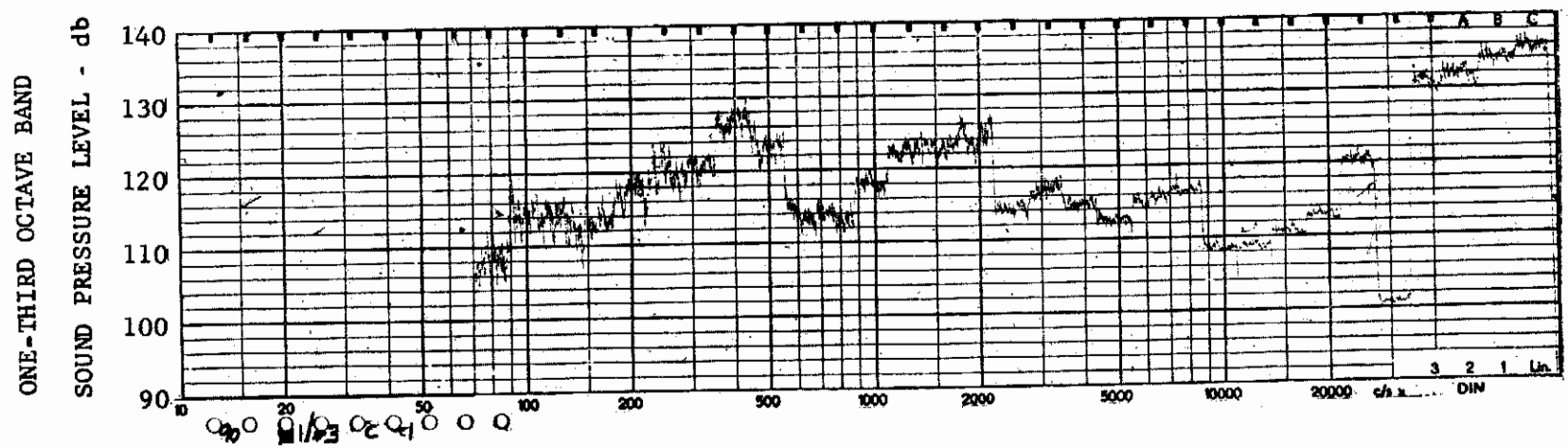

FIGURE 386 ONE-THIRD OCTAVE BAND SPECTRUM MODEL: FP 0

CHANNEL: 1 MACH NO.: 10 α: 13.7° ϕ: 0 Re_∞/FT.: 1×10^6 AEDC GROUP NO.: 1/3 C

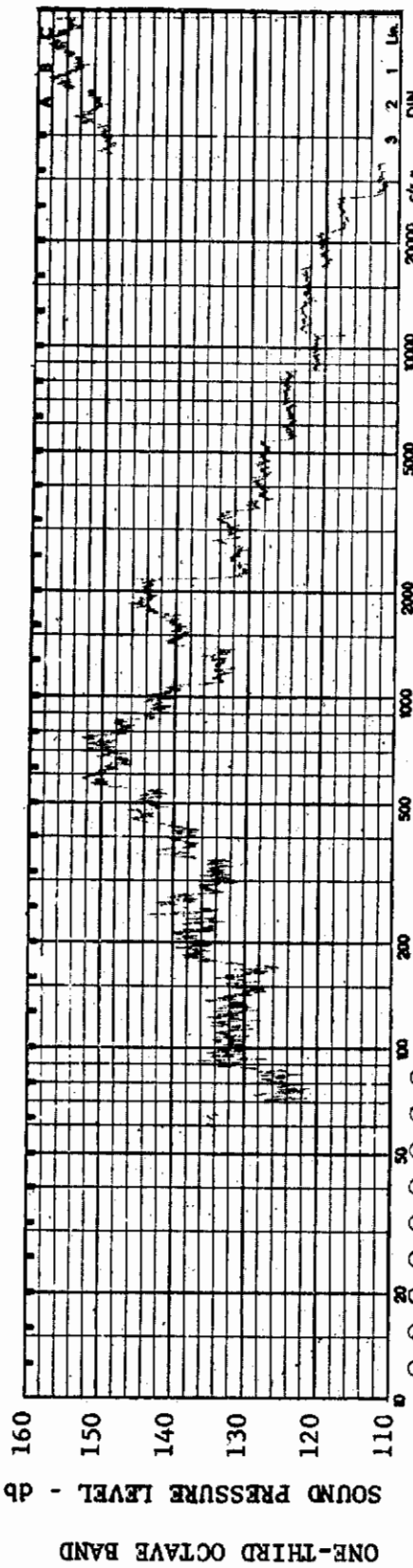

FIGURE 387 ONE-THIRD OCTAVE BAND SPECTRUM

MODEL: FP 0

CHANNEL: 2 MACH NO.: 10 α: 13.7° ϕ: 0 Re_∞ /FT.: 1×10^6 AEDC GROUP NO.: 1/3 C

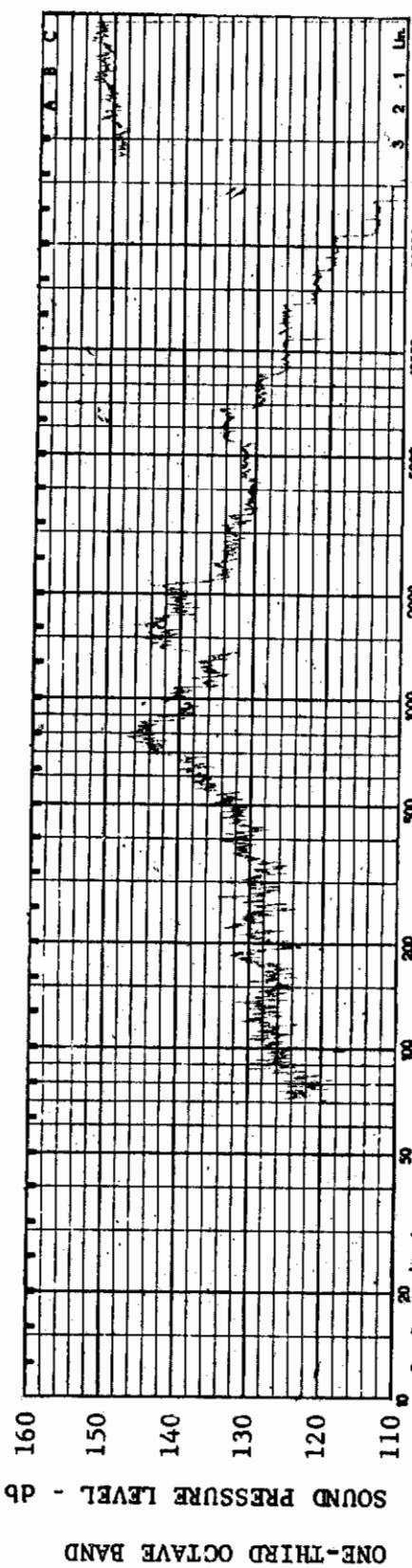

FIGURE 388 ONE-THIRD OCTAVE BAND SPECTRUM

MODEL: FP 0

CHANNEL: 3 MACH NO.: 10 α: 13.7° ϕ: 0 Re_∞ /FT.: 1×10^6 AEDC GROUP NO.: 1/3 C

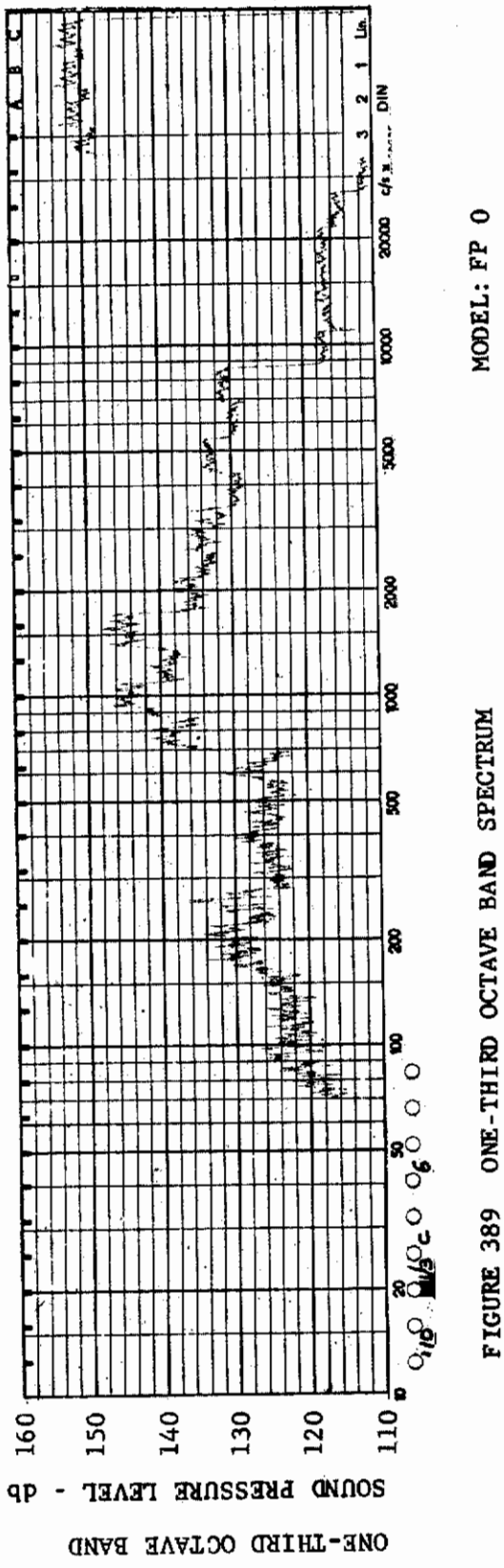

FIGURE 389 ONE-THIRD OCTAVE BAND SPECTRUM

MODEL: FP 0

CHANNEL: 6 MACH NO.: 10 α: 13.7° ϕ: 0 Re_∞/FT.: 1×10^6 AEDC GROUP NO.: 1/3 C

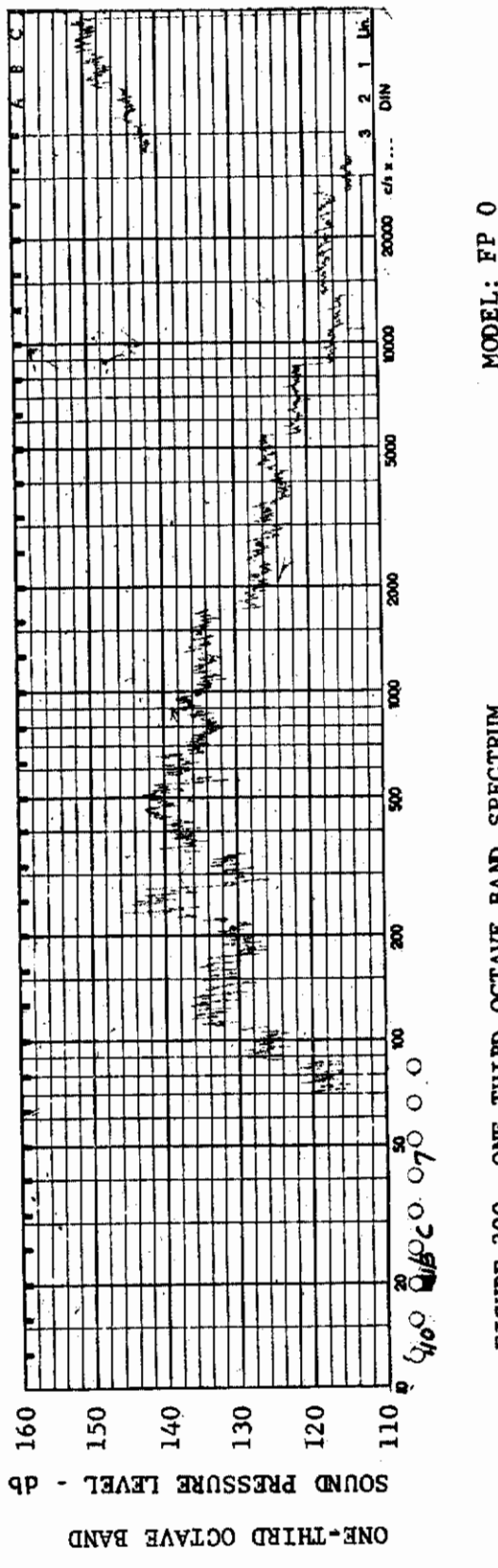

FIGURE 390 ONE-THIRD OCTAVE BAND SPECTRUM

MODEL: FP 0

CHANNEL: 7 MACH NO.: 10 α: 13.7° ϕ: 0 Re_∞/FT.: 1×10^6 AEDC GROUP NO.: 1/3 C

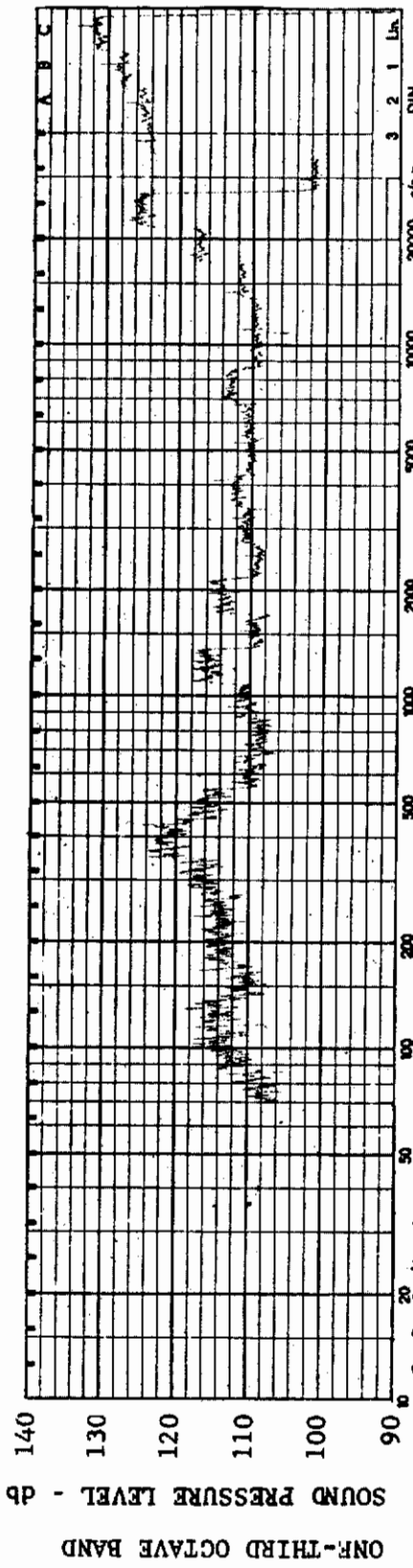

FIGURE 391 ONE-THIRD OCTAVE BAND SPECTRUM

MODEL: FP 0

CHANNEL: 1 MACH NO.: 10 α: 0 ϕ: 0 Re_∞/FT.: 1×10^6 AEDC GROUP NO.: 1/4 C

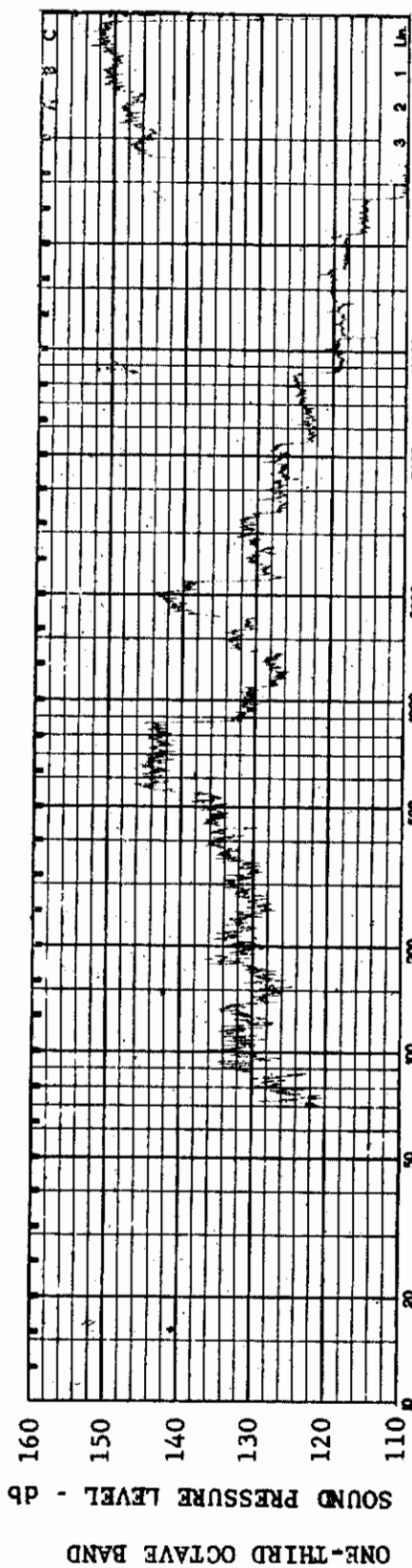

FIGURE 392 ONE-THIRD OCTAVE BAND SPECTRUM

MODEL: FP 0

CHANNEL: 2 MACH NO.: 10 α: 0 ϕ: 0 Re_∞/FT.: 1×10^6 AEDC GROUP NO.: 1/4 C

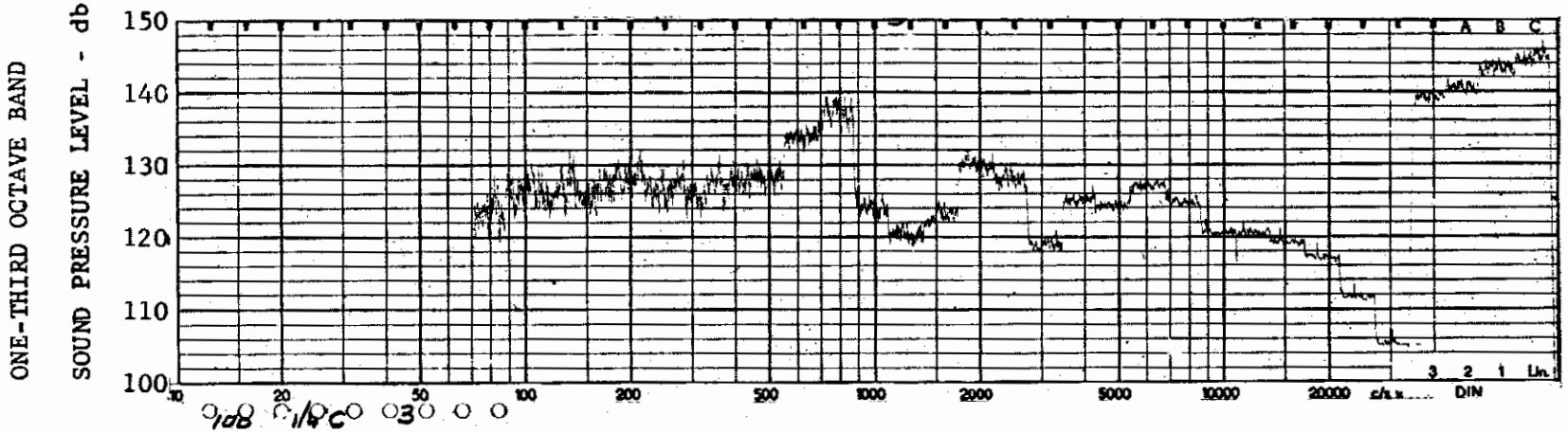

FIGURE 393 ONE-THIRD OCTAVE BAND SPECTRUM MODEL: FP 0

CHANNEL: 3 MACH NO.: 10 α: 0 ϕ: 0 Re_∞/FT.: 1×10^6 AEDC GROUP NO.: 1/4 C

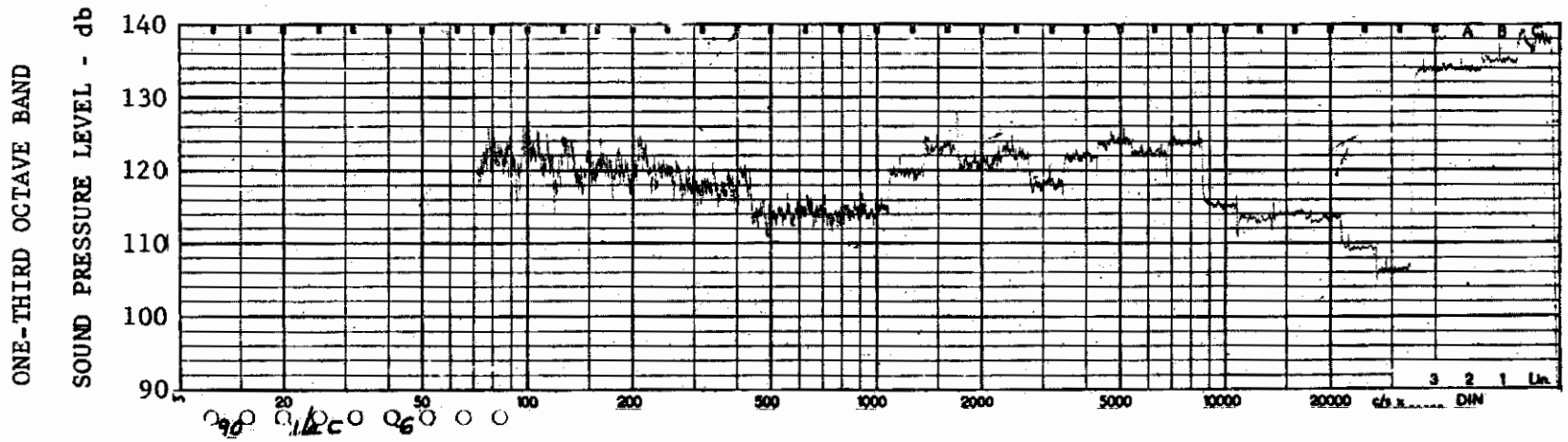

FIGURE 394 ONE-THIRD OCTAVE BAND SPECTRUM MODEL: FP υ

CHANNEL: 6 MACH NO.: 10 α: 0 ϕ: 0 Re_∞/FT.: 1×10^6 AEDC GROUP NO.: 1/4 C

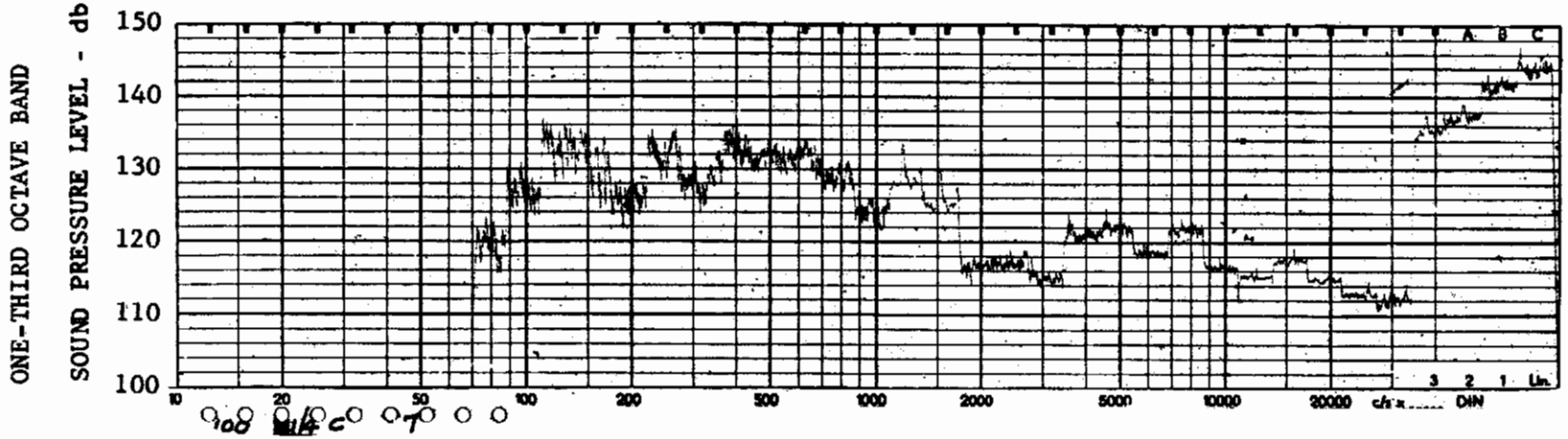

FIGURE 395 ONE-THIRD OCTAVE BAND SPECTRUM MODEL: FP 0

CHANNEL: 7 MACH NO.: 10 α: 0 ϕ: 0 Re_∞/FT.: 1×10^6 AEDC GROUP NO.: 1/4 C

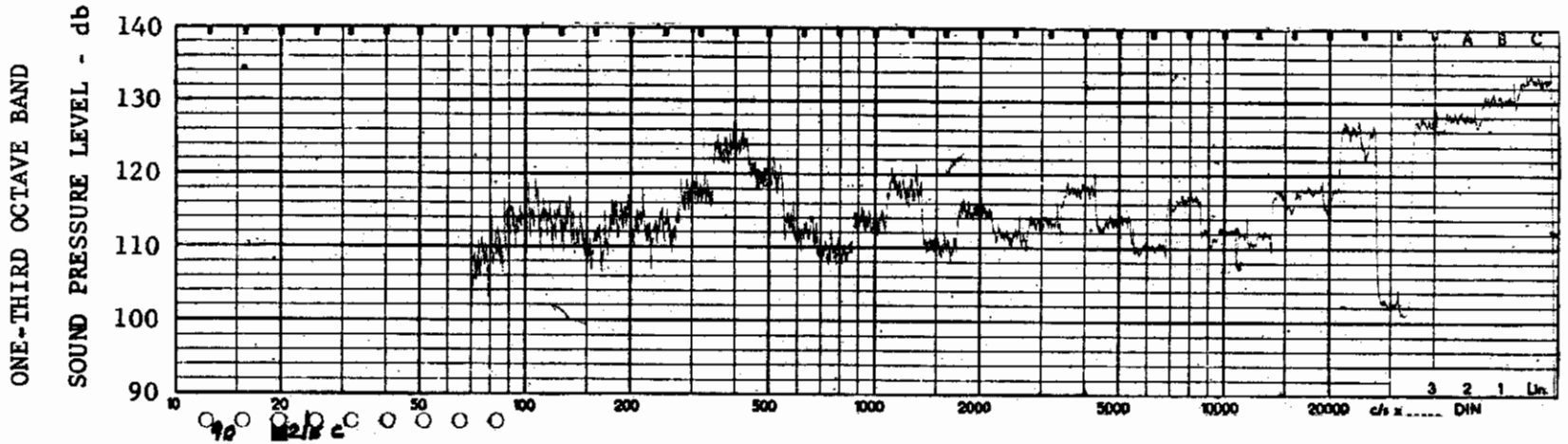

FIGURE 396 ONE-THIRD OCTAVE BAND SPECTRUM MODEL: FP 30

CHANNEL: 1 MACH NO.: 10 α: 0 ϕ: 0 Re_∞/FT.: 1×10^6 AEDC GROUP NO.: 1/5 C

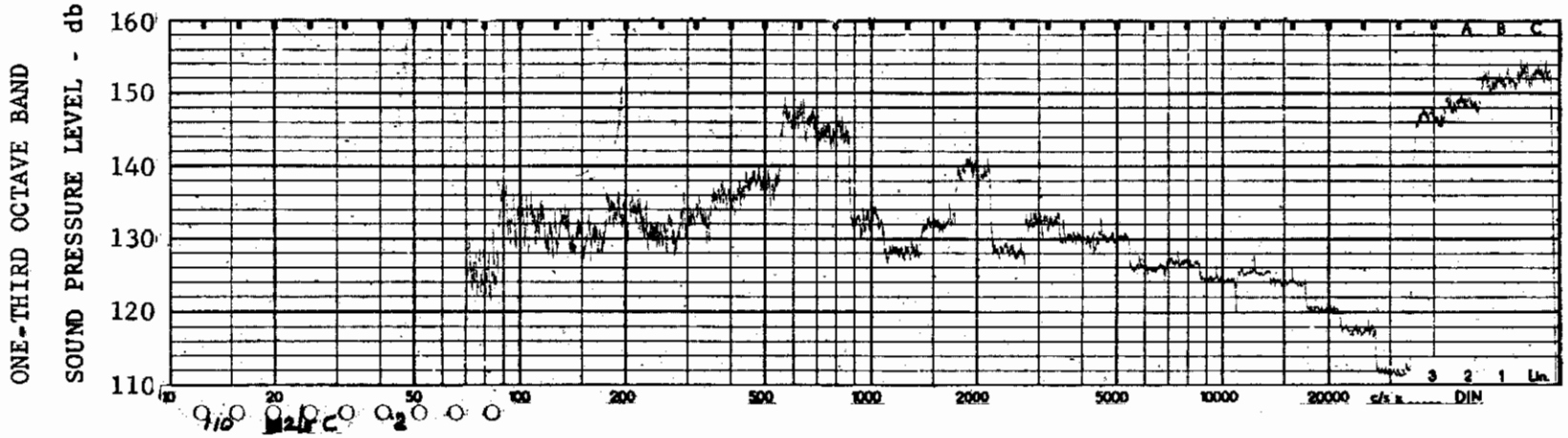

FIGURE 397 ONE-THIRD OCTAVE BAND SPECTRUM MODEL: FP 30

CHANNEL: 2 MACH NO.: 10 α: 0 ϕ: 0 Re_∞/FT.: 1×10^6 AEDC GROUP NO.: 1/5 C

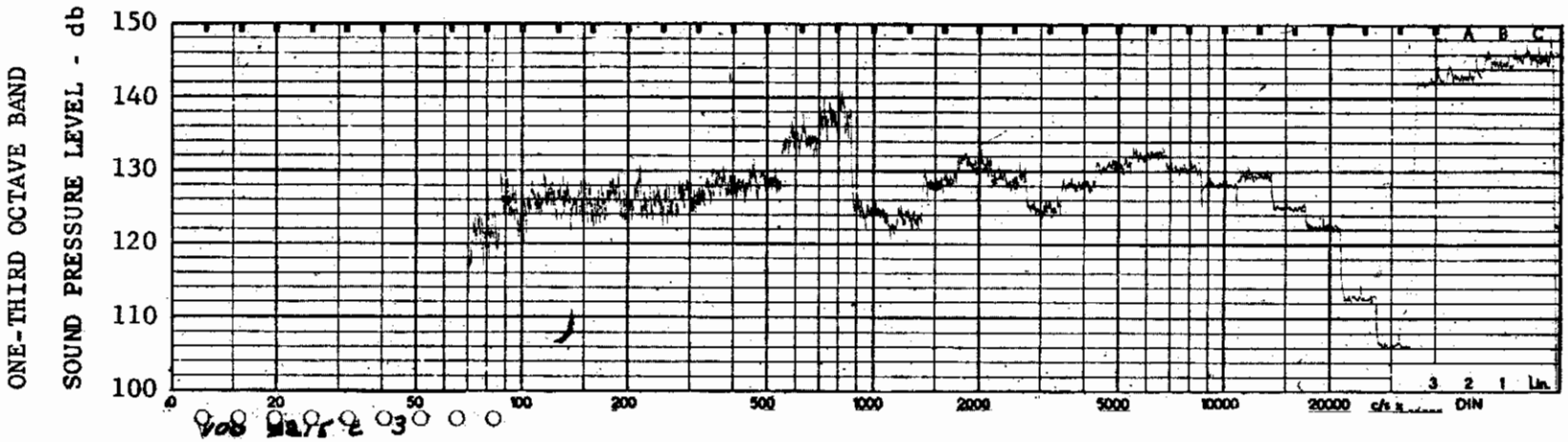

FIGURE 398 ONE-THIRD OCTAVE BAND SPECTRUM MODEL: FP 30

CHANNEL: 3 MACH NO.: 10 α: 0 ϕ: 0 Re_∞/FT.: 1×10^6 AEDC GROUP NO.: 1/5 C

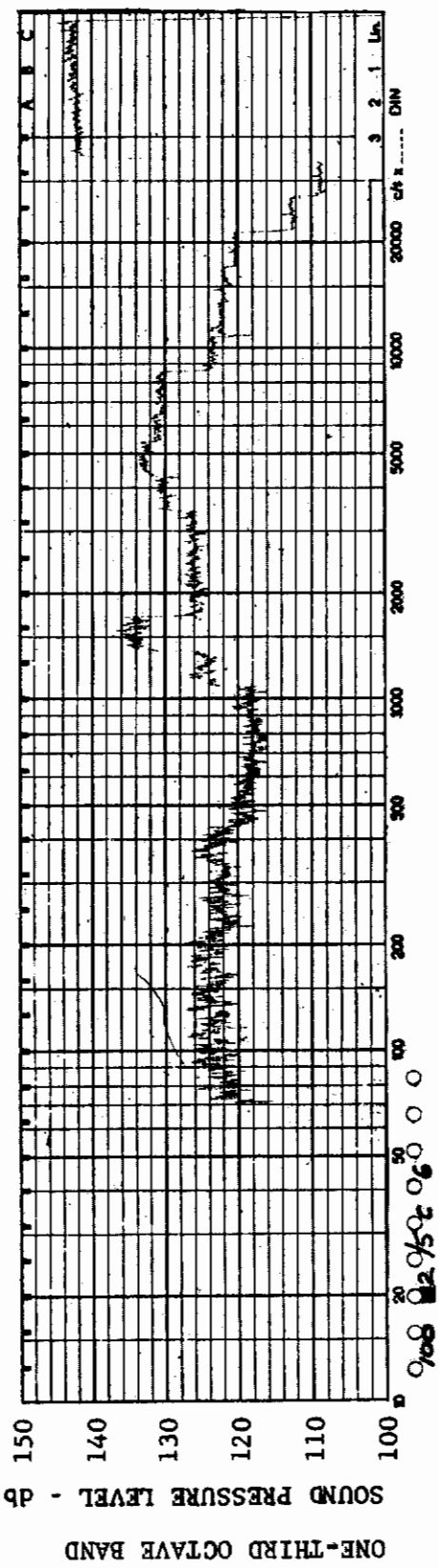

FIGURE 399 ONE-THIRD OCTAVE BAND SPECTRUM MODEL: FP 30

CHANNEL: 6 MACH NO.: 10 α: 0 ϕ: 0 Re_∞/FT.: 1×10^6 AEDC GROUP NO.: 1/5 C

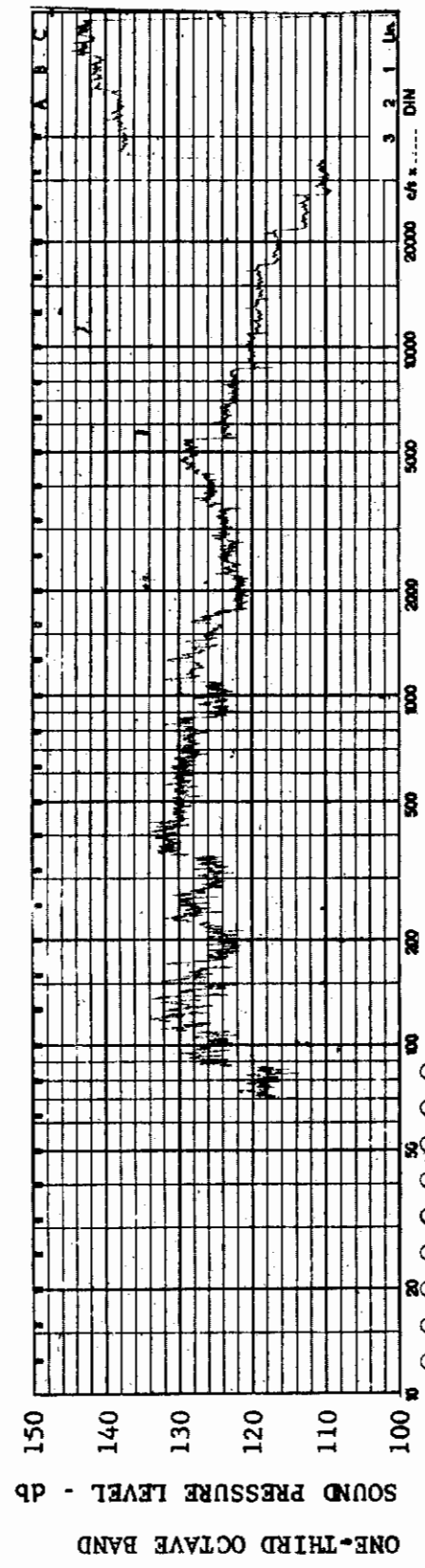

FIGURE 400 ONE-THIRD OCTAVE BAND SPECTRUM MODEL: FP 30

CHANNEL: 7 MACH NO.: 10 α: 0 ϕ: 0 Re_∞/FT.: 1×10^6 AEDC GROUP NO.: 1/5 C

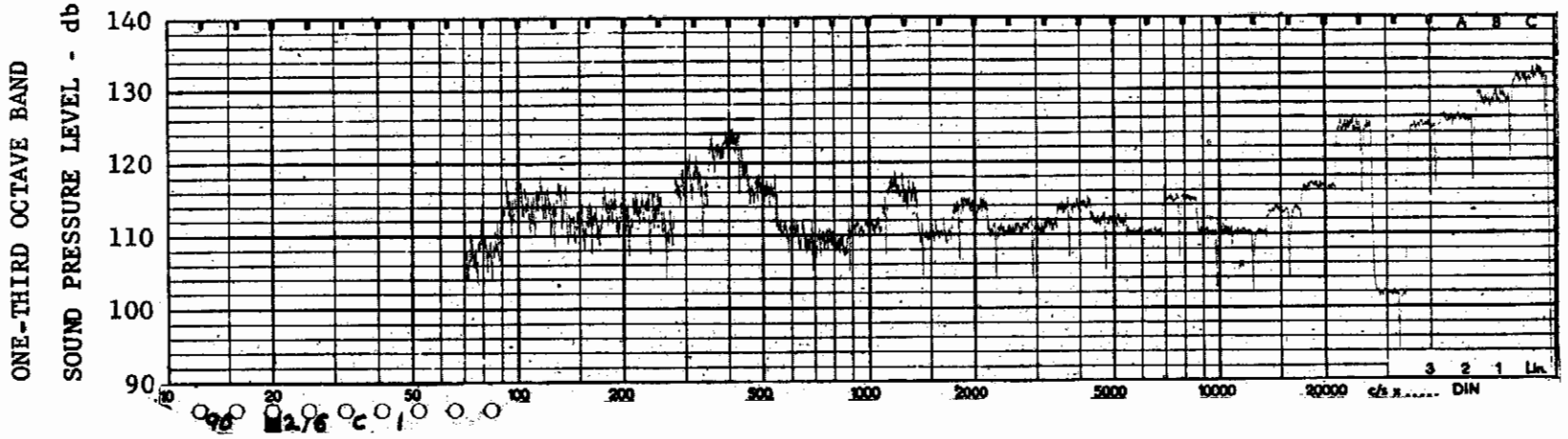

FIGURE 401 ONE-THIRD OCTAVE BAND SPECTRUM MODEL: FP 30

CHANNEL: 1 MACH NO.: 10 α: 5° ϕ: 0 Re_∞/FT.: 1×10^6 AEDC GROUP NO.: 1/6 C

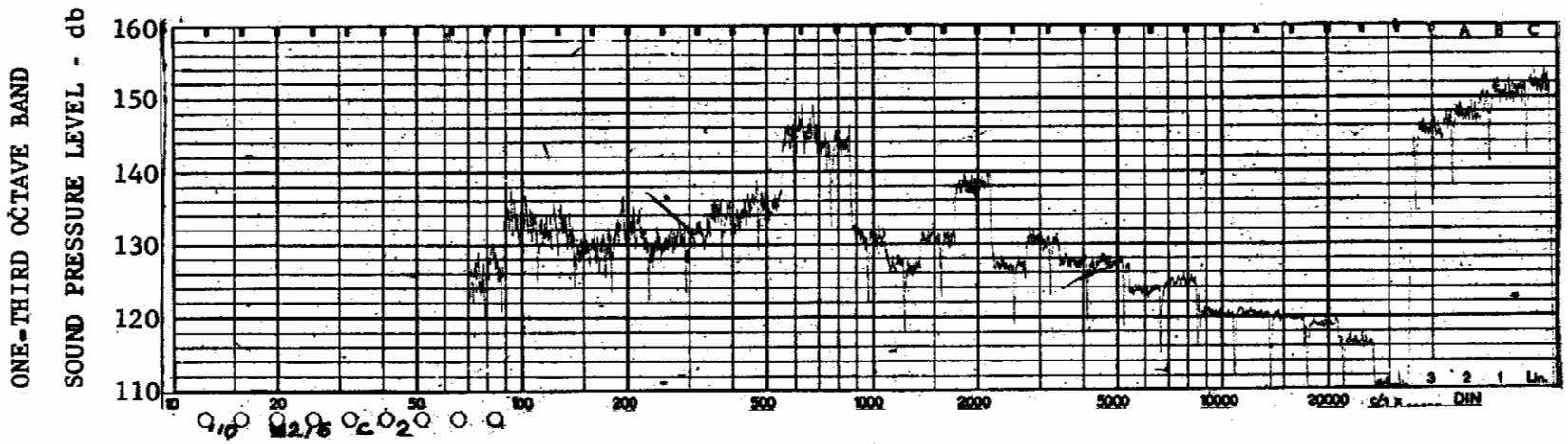

FIGURE 402 ONE-THIRD OCTAVE BAND SPECTRUM MODEL: FP 30

CHANNEL: 2 MACH NO.: 10 α: 5° ϕ: 0 Re_∞/FT.: 1×10^6 AEDC GROUP NO.: 1/6 C

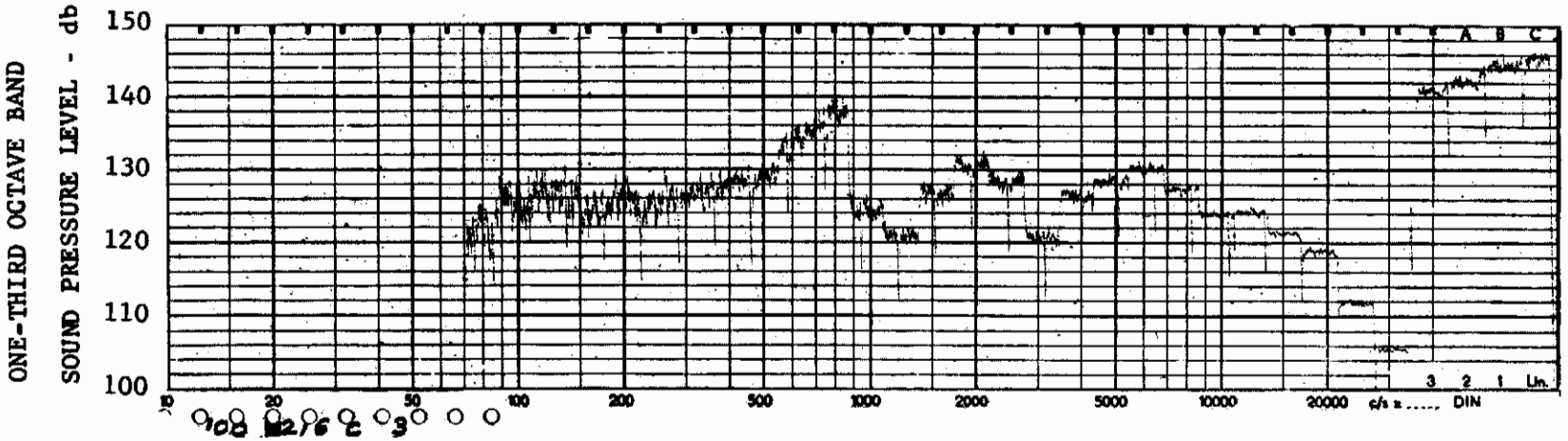

FIGURE 403 ONE-THIRD OCTAVE BAND SPECTRUM MODEL: FP 30

CHANNEL: 3 MACH NO. 10 α: 5° ϕ: 0 Re_∞ /FT.: 1×10^6 AEDC GROUP NO.: 1/6 C

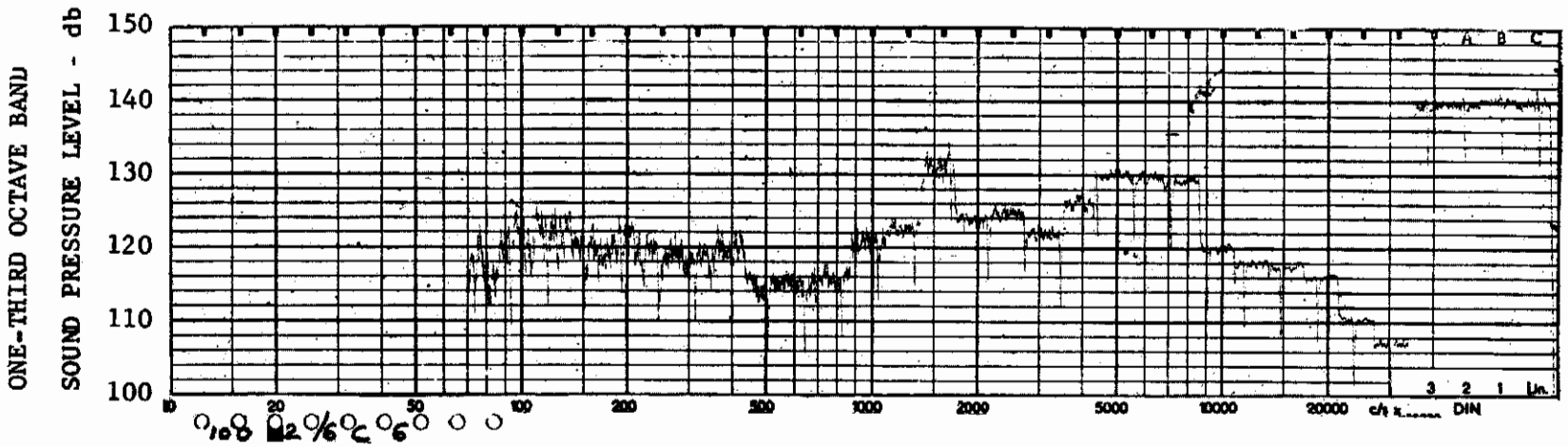

FIGURE 404 ONE-THIRD OCTAVE BAND SPECTRUM MODEL: FP 30

CHANNEL: 6 MACH NO.: 10 α: 5° ϕ: 0 Re_∞ /FT.: 1×10^6 AEDC GROUP NO.: 1/6 C

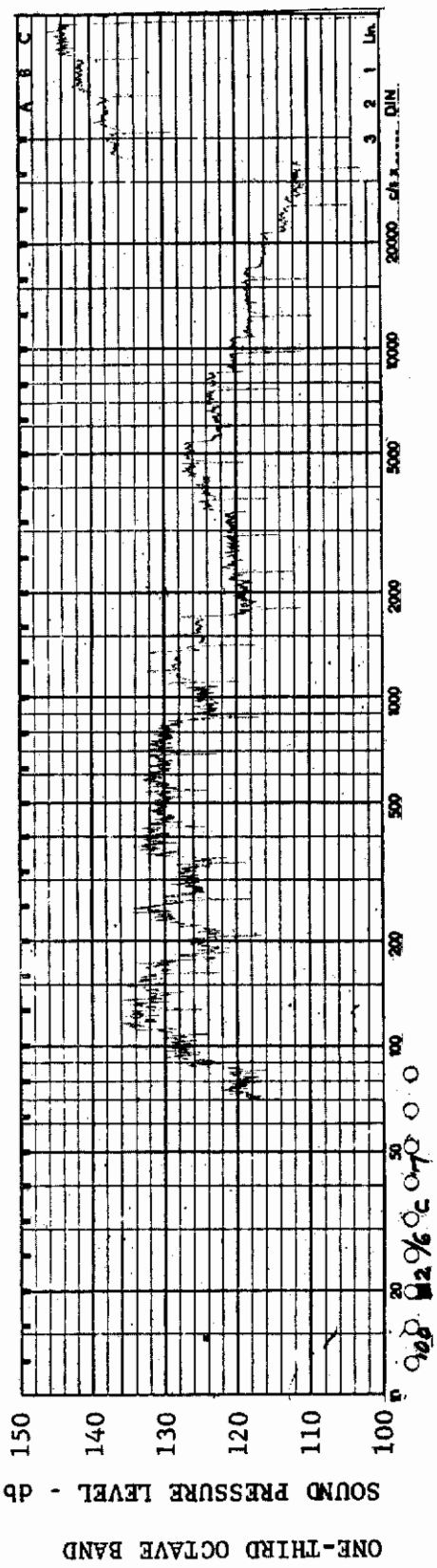

FIGURE 405 ONE-THIRD OCTAVE BAND SPECTRUM

MODEL: FP 30

CHANNEL: 7 MACH NO.: 10 α: 5° ϕ: 0 Re_∞/FT.: 1×10^6 AEDC GROUP NO.: 1/6 C

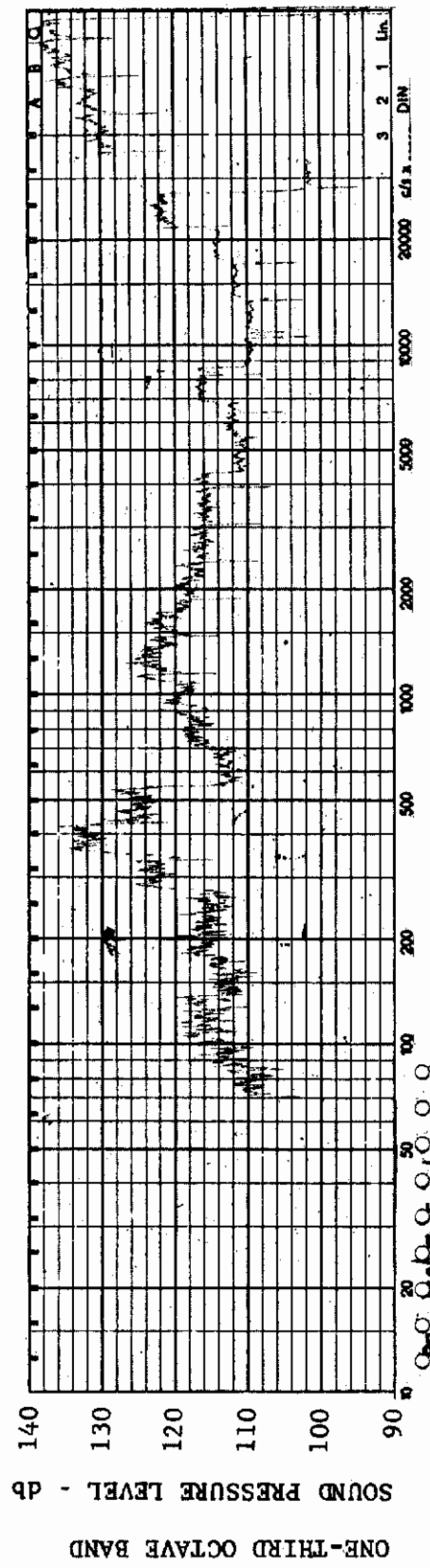

FIGURE 406 ONE-THIRD OCTAVE BAND SPECTRUM

MODEL: FP 30

CHANNEL: 1 MACH NO.: 10 α: 13.7° ϕ: 0 Re_∞/FT.: 1×10^6 AEDC GROUP NO.: 1/7 C

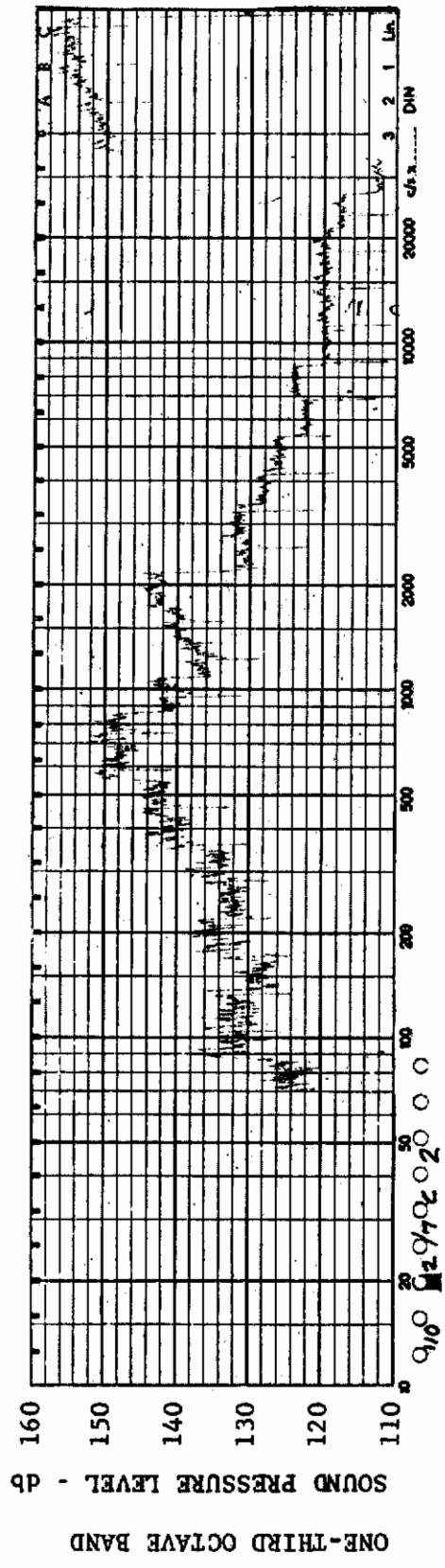

FIGURE 407 ONE-THIRD OCTAVE BAND SPECTRUM MODEL: FP 30

CHANNEL: 2 MACH NO. 10 α: 13.7° ϕ: 0 Re_∞/FT. 1×10^6 AEDC GROUP NO.: 1/7 C

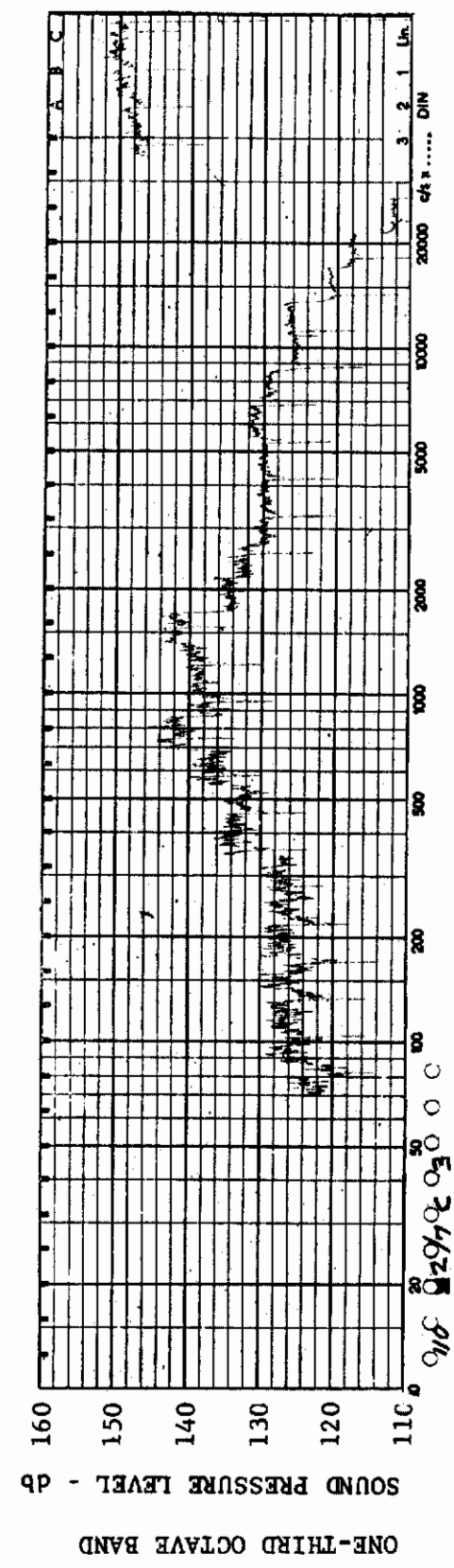

FIGURE 408 ONE-THIRD OCTAVE BAND SPECTRUM MODEL: FP 30

CHANNEL: 3 MACH NO.: 10 α: 13.7° ϕ: 0 Re_∞/FT.: 1×10^6 AEDC GROUP NO.: 1/7 C

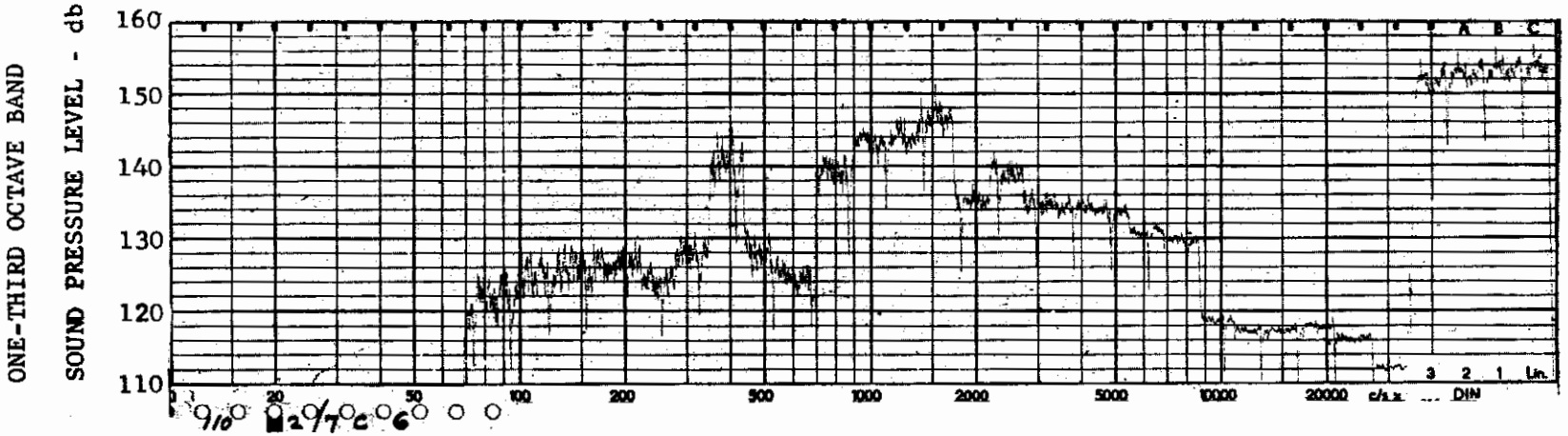

FIGURE 409 ONE-THIRD OCTAVE BAND SPECTRUM MODEL: FP 30

CHANNEL: 6 MACH NO.: 10 α: 13.7° ϕ: 0 Re_∞/FT.: 1×10^6 AEDC GROUP NO.: 1/7 C

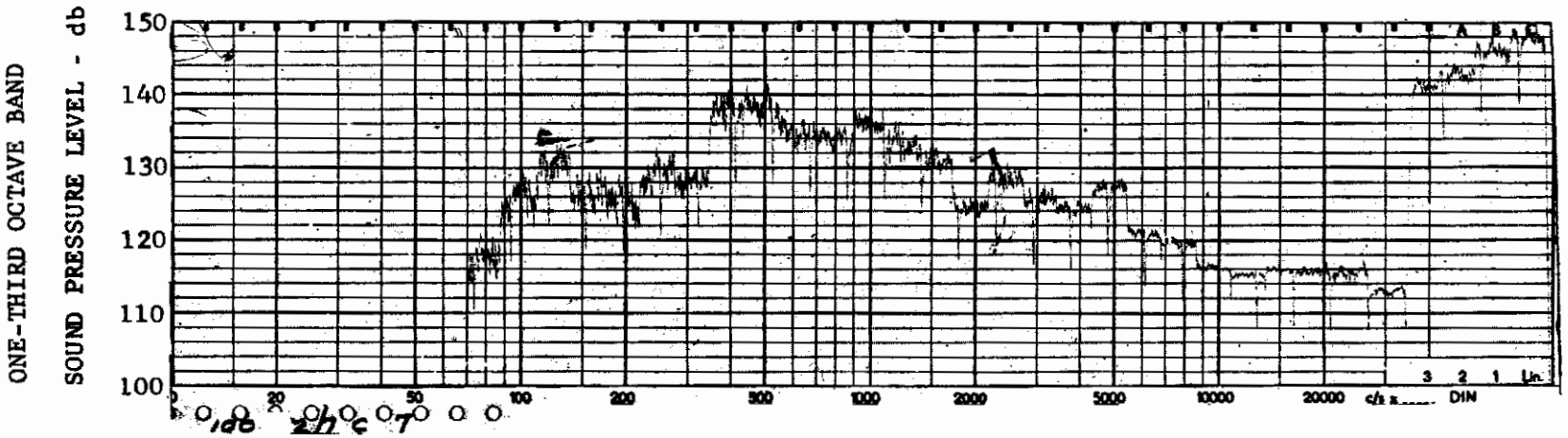

FIGURE 410 ONE-THIRD OCTAVE BAND SPECTRUM MODEL: FP 30

CHANNEL: 7 MACH NO.: 10 α: 13.7° ϕ: 0 Re_∞/FT.: 1×10^6 AEDC GROUP NO.: 1/7 C

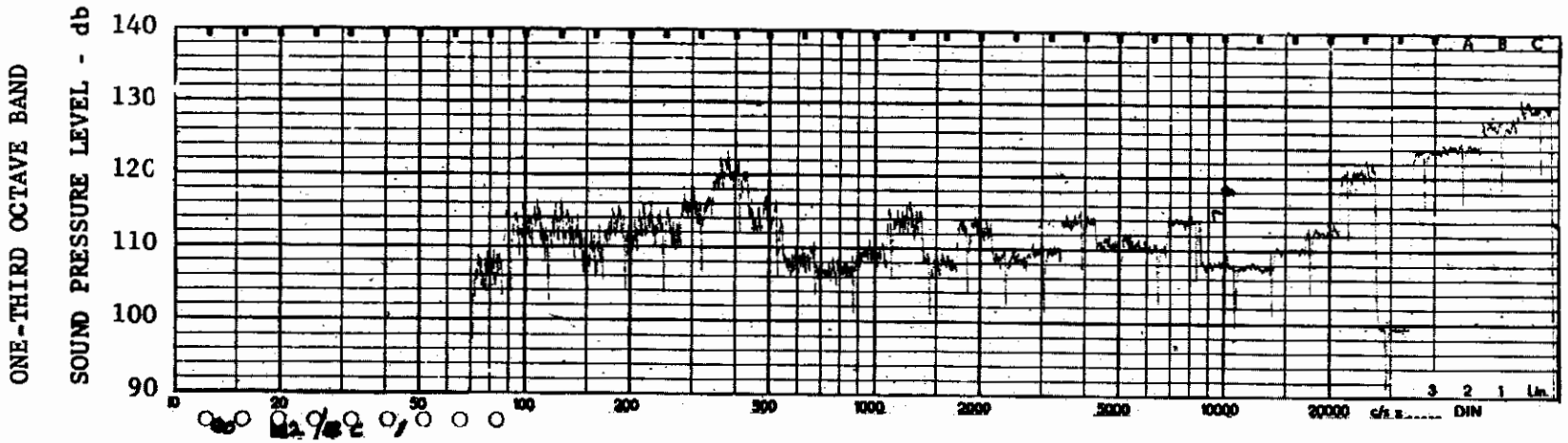

FIGURE 411 ONE-THIRD OCTAVE BAND SPECTRUM MODEL: FP 30

CHANNEL: 1 MACH NO.: 10 α: 10° ϕ: 0 Re_∞/FT.: 1x10^6 AEDC GROUP NO.: 1/8 C

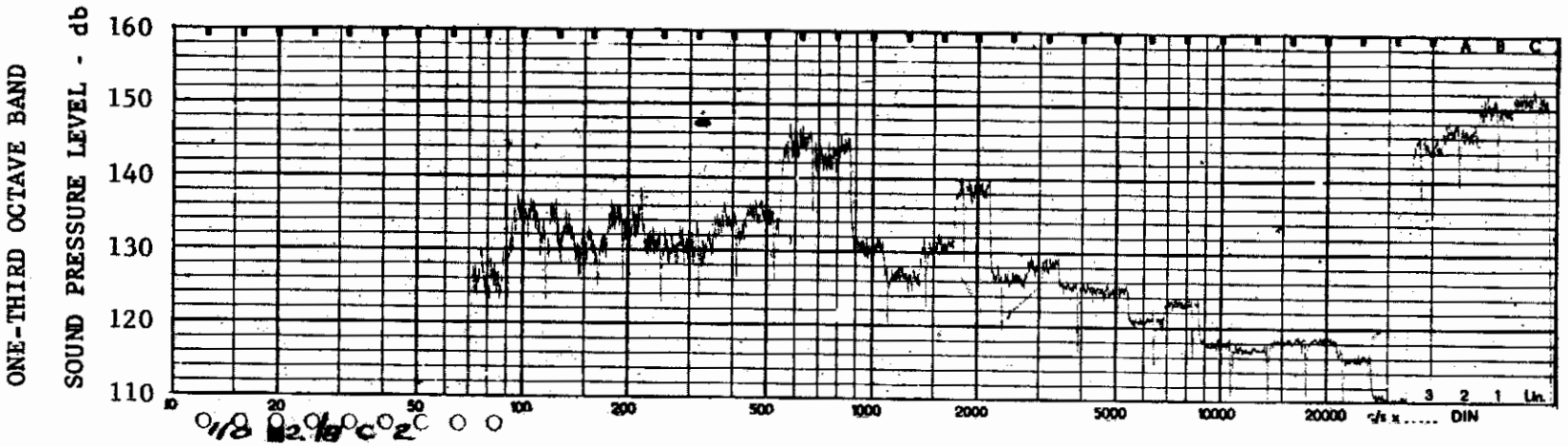

FIGURE 412 ONE-THIRD OCTAVE BAND SPECTRUM MODEL: FP 30

CHANNEL 2 MACH NO.: 10 α: 10° ϕ: 0 Re_∞/FT.: 1x10^6 AEDC GROUP NO.: 1/8 C

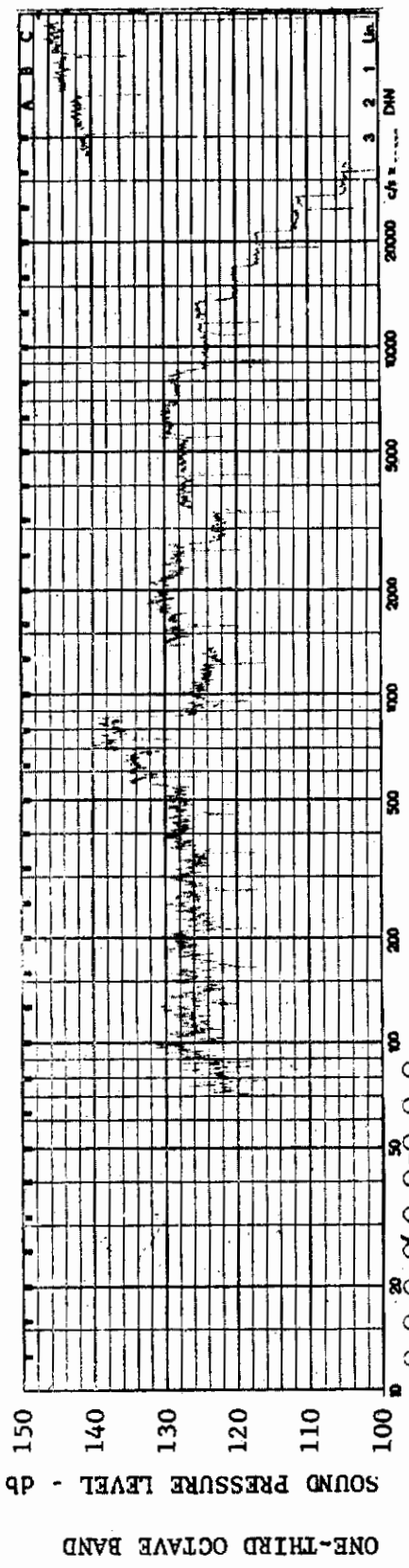

FIGURE 413 ONE-THIRD OCTAVE BAND SPECTRUM MODEL: FP 30

CHANNEL: 3 MACH NO.: 10 α: 10° ϕ: 0 Re_∞/FT.: 1×10^6 AEDC GROUP NO.: 1/8 C

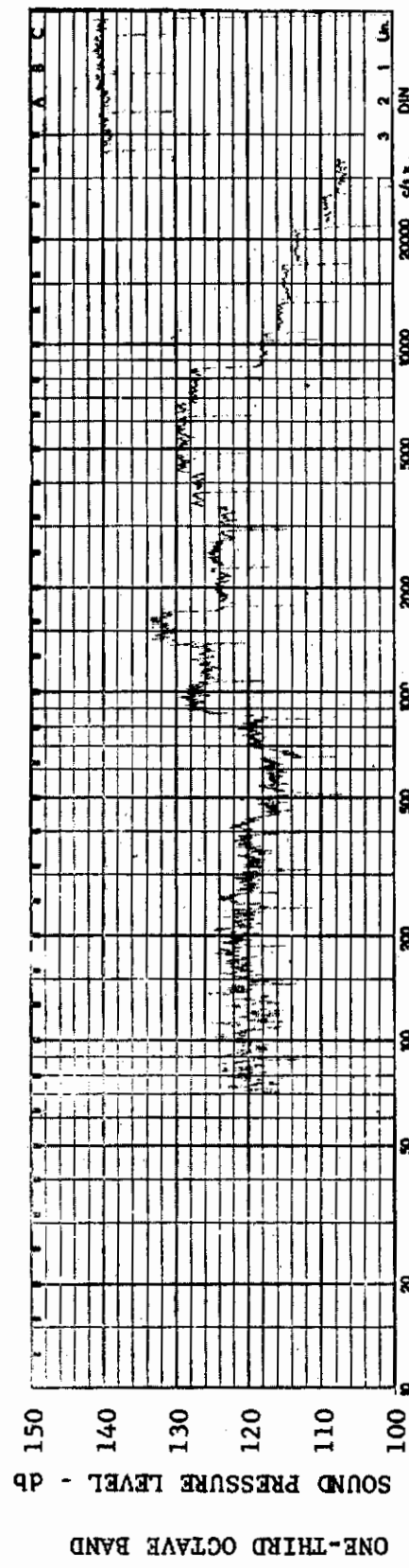

FIGURE 414 ONE-THIRD OCTAVE BAND SPECTRUM MODEL: FP 30

CHANNEL: 6 MACH NO.: 10 α: 10° ϕ: 0 Re_∞/FT.: 1×10^6 AEDC GROUP NO.: 1/8 C

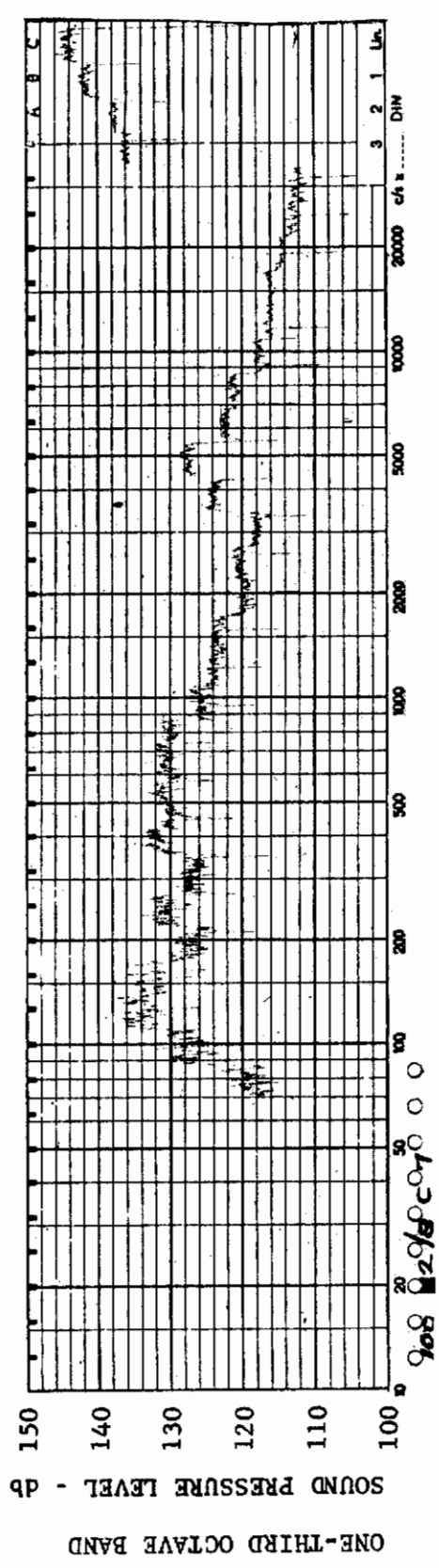

FIGURE 415 ONE-THIRD OCTAVE BAND SPECTRUM MODEL: FP 30

CHANNEL: 7 MACH NO.: 10 α: 10° ϕ: 0 Re_∞/FT.: 1×10^6 AEDC GROUP NO.: 1/8 C

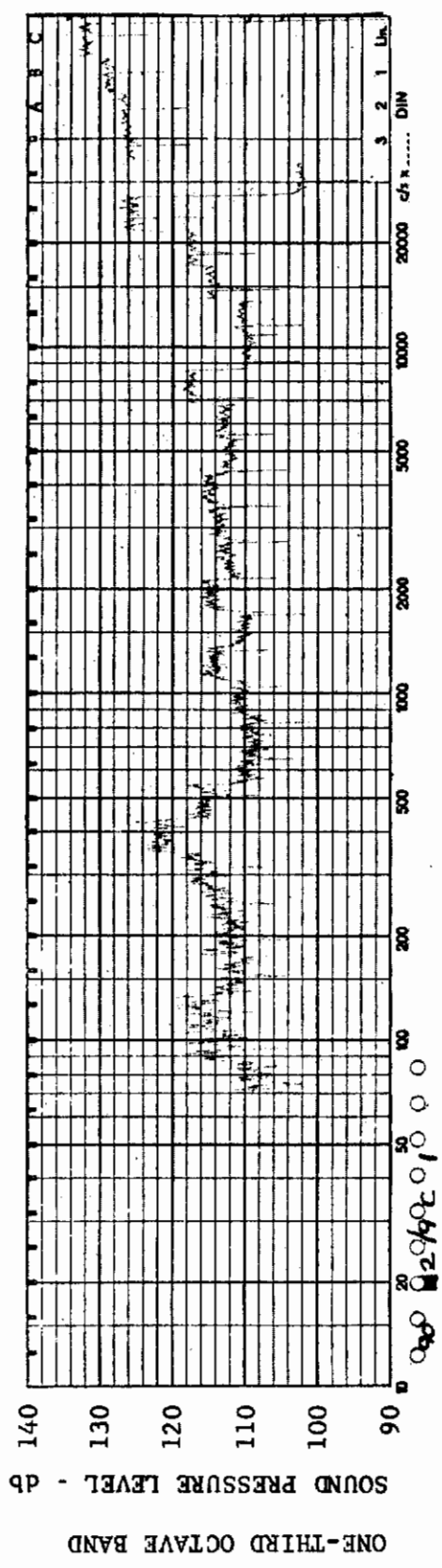

FIGURE 416 ONE-THIRD OCTAVE BAND SPECTRUM MODEL: FP 30

CHANNEL: 1 MACH NO.: 10 α: 0 ϕ: 0 Re_∞/FT.: 1×10^6 AEDC GROUP NO.: 1/9 C

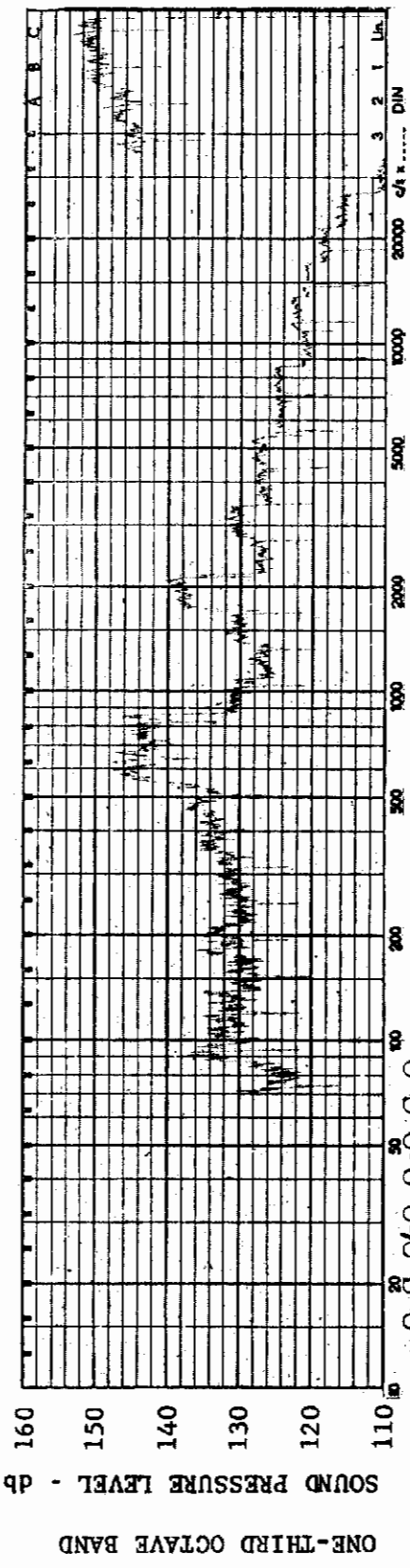

FIGURE 417 ONE-THIRD OCTAVE BAND SPECTRUM MODEL: FP 30

CHANNEL: 2 MACH NO.: 10 α: 0 ϕ: 0 Re_∞/FT.: 1×10^6 AEDC GROUP NO.: 1/9 C

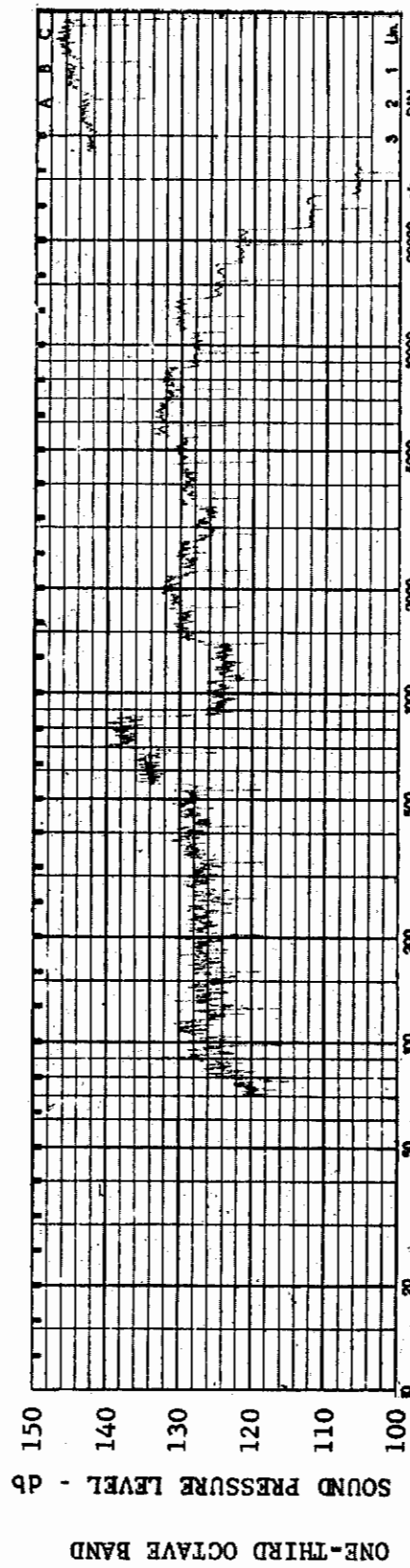

FIGURE 418 ONE-THIRD OCTAVE BAND SPECTRUM MODEL: FP 30

CHANNEL: 3 MACH NO.: 10 α: 0 ϕ: 0 Re_∞/FT.: 1×10^6 AEDC GROUP NO.: 1/9 C

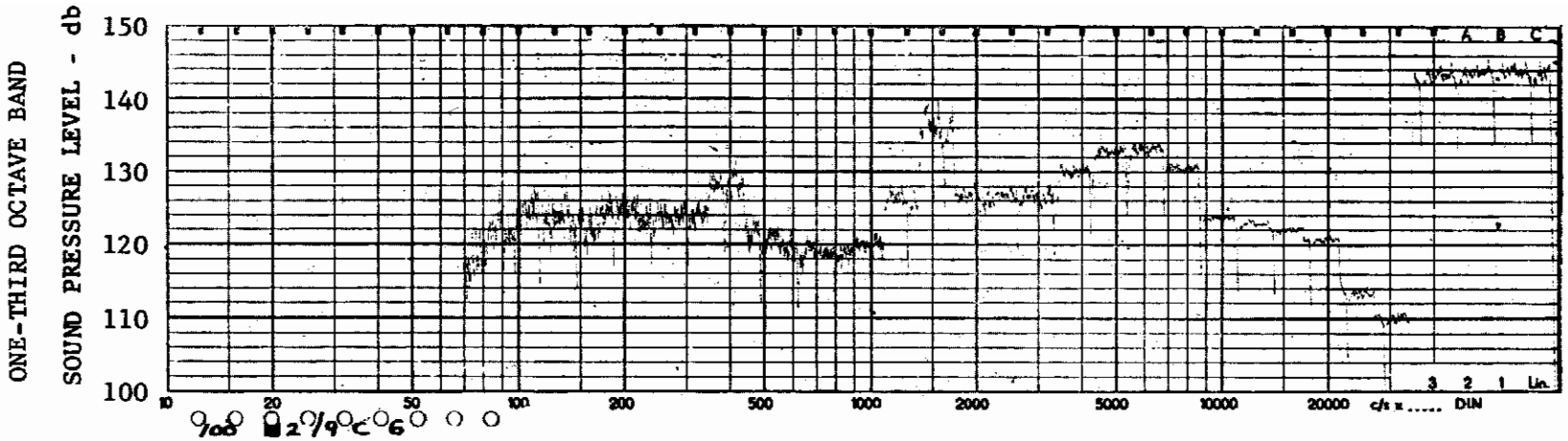

FIGURE 419 ONE-THIRD OCTAVE BAND SPECTRUM MODEL: FP 30

CHANNEL: 6 MACH NO.: 10 α: 0 ϕ: 0 Re_∞/FT.: 1×10^6 AEDC GROUP NO.: 1/9 C

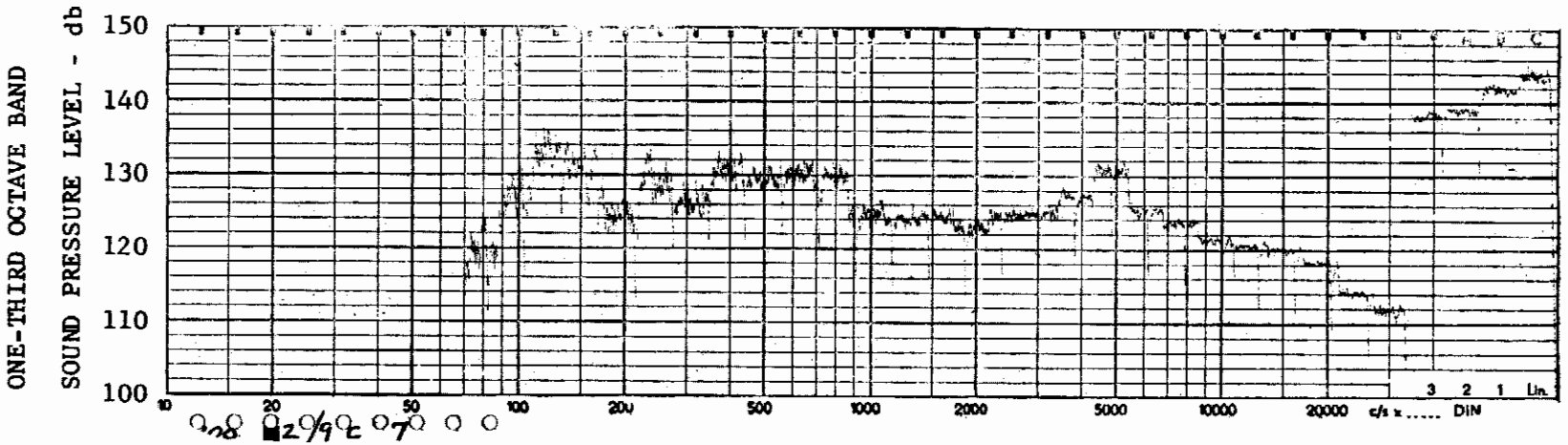

FIGURE 420 ONE-THIRD OCTAVE BAND SPECTRUM MODEL: FP 30

CHANNEL: 7 MACH NO.: 10 α: 0 ϕ: 0 Re_∞/FT.: 1×10^6 AEDC GROUP NO.: 1/9 C

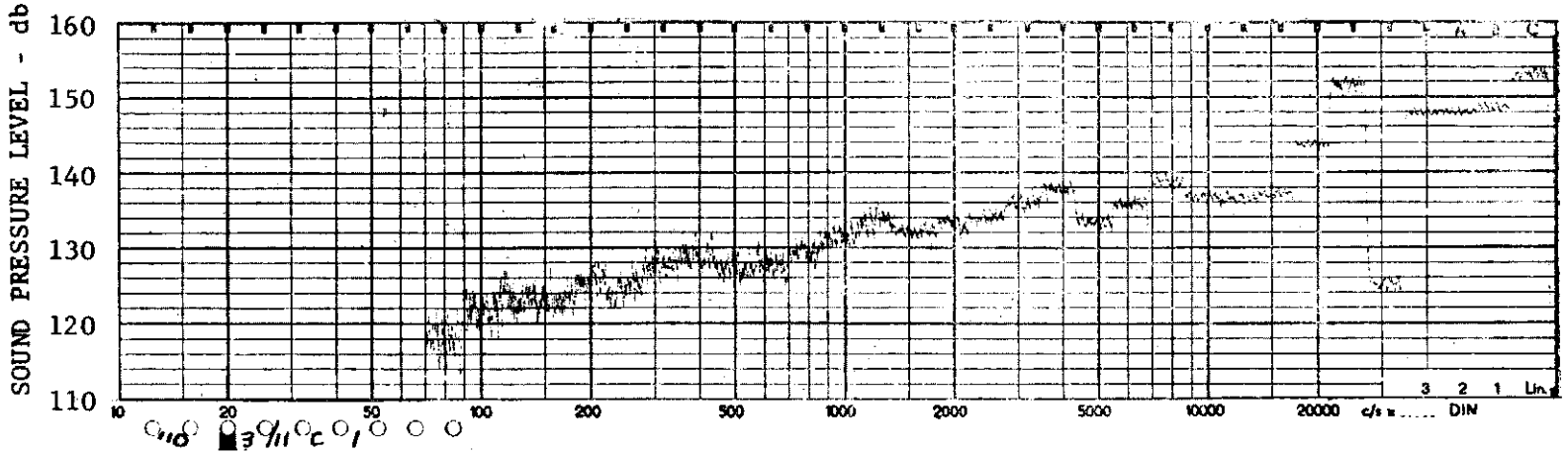

FIGURE 421 ONE-THIRD OCTAVE BAND SPECTRUM MODEL: FP 60

CHANNEL: 1 MACH NO.: 10 α: 0 ϕ: 0 Re_∞/FT.: 1×10^6 AEDC GROUP NO.: 1/11 C

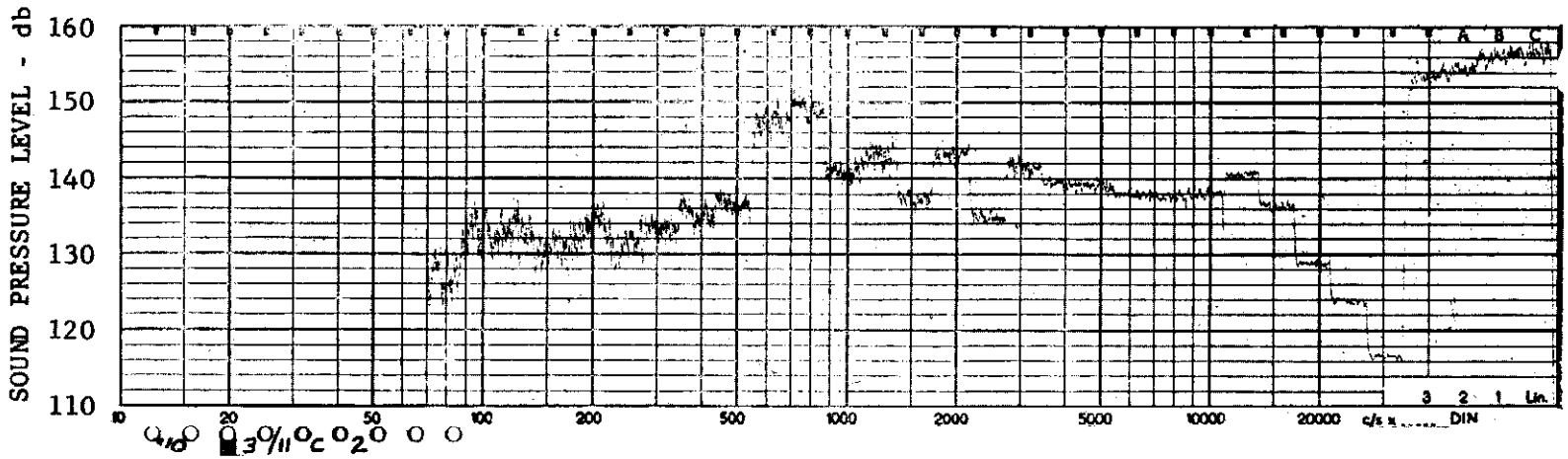

FIGURE 422 ONE-THIRD OCTAVE BAND SPECTRUM MODEL: FP 60

CHANNEL: 2 MACH NO.: 10 α: 0 ϕ: 0 Re_∞/FT.: 1×10^6 AEDC GROUP NO.: 1/11 C

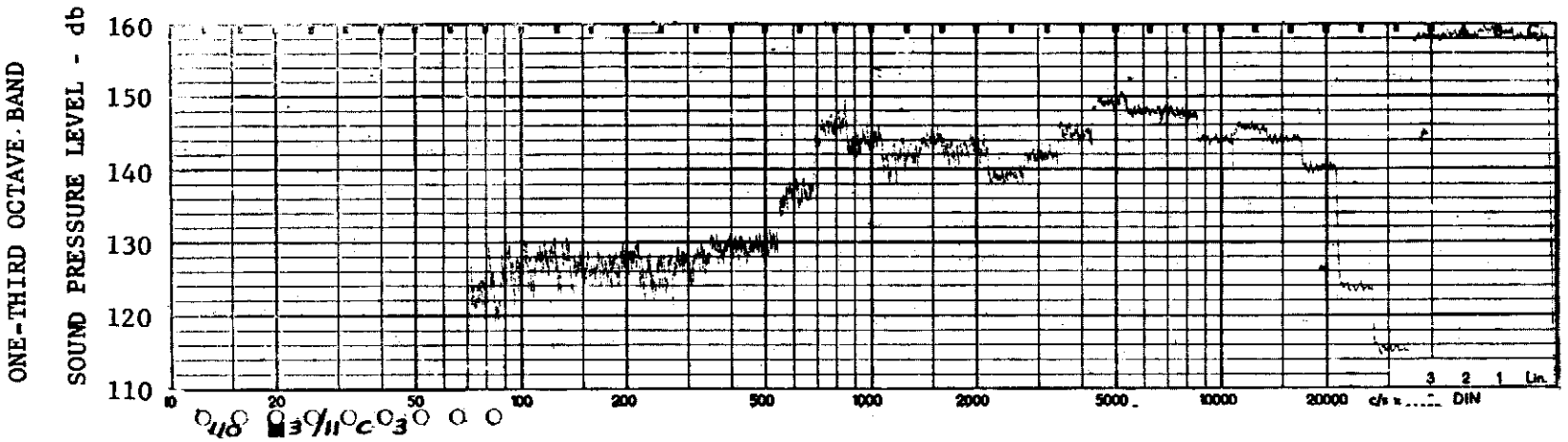

FIGURE 423 ONE-THIRD OCTAVE BAND SPECTRUM MODEL: FP 60

CHANNEL: 3 MACH NO.: 10 α: 0 ϕ: 0 Re_∞/FT.: 1×10^6 AEDC GROUP NO.: 1/11 C

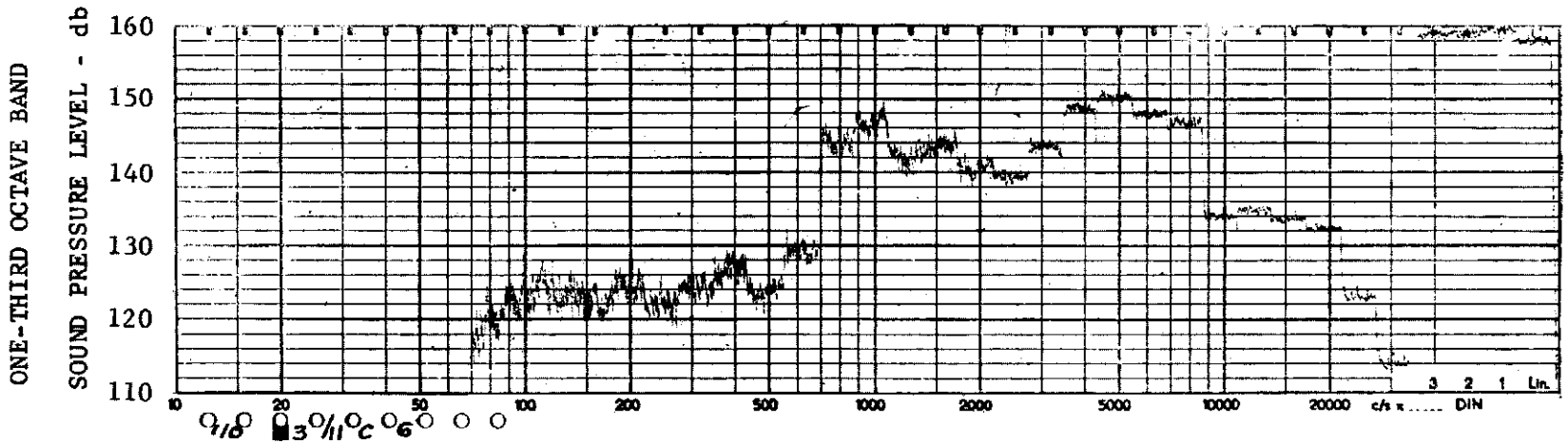

FIGURE 424 ONE-THIRD OCTAVE BAND SPECTRUM MODEL: FP 60

CHANNEL: 6 MACH NO.: 10 α: 0 ϕ: 0 Re_∞/FT.: 1×10^6 AEDC GROUP NO.: 1/11 C

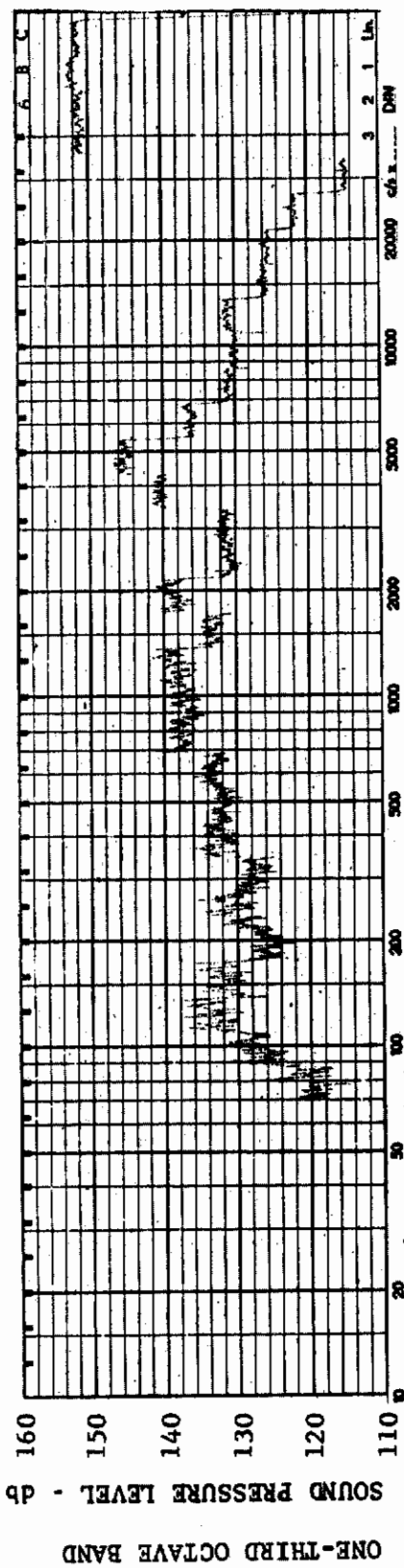

FIGURE 425 ONE-THIRD OCTAVE BAND SPECTRUM MODEL: FP 60

CHANNEL: 7 MACH NO.: 10 α: 0 ϕ: 0 Re_∞/FT.: 1×10^6 AEDC GROUP NO.: 1/11 C

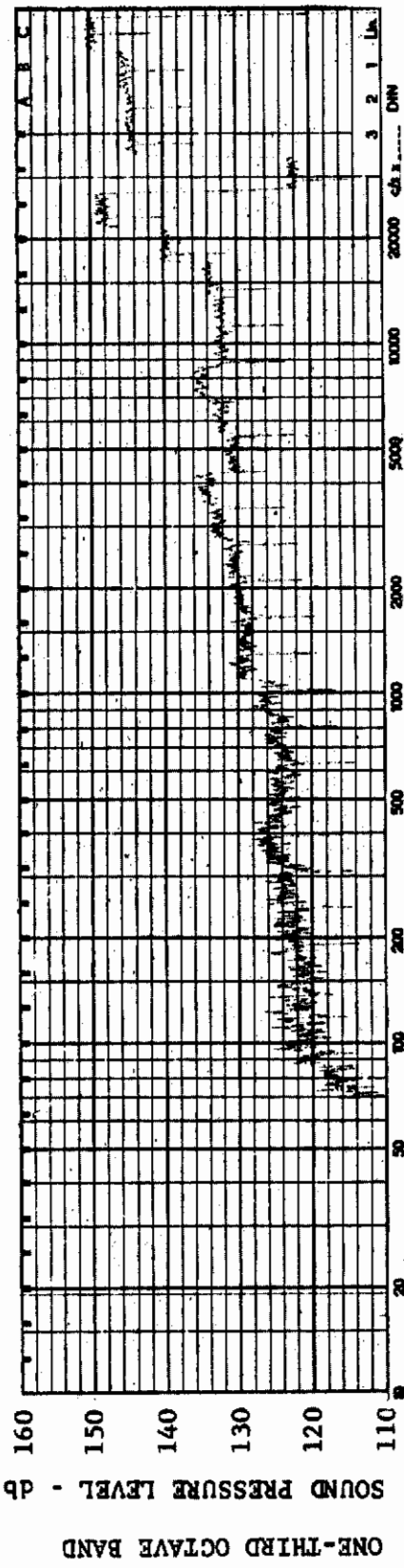

FIGURE 426 ONE-THIRD OCTAVE BAND SPECTRUM MODEL: FP 60

CHANNEL: 1 MACH NO.: 10 α: 5° ϕ: 0 Re_∞/FT.: 1×10^6 AEDC GROUP NO.: 1/12 C

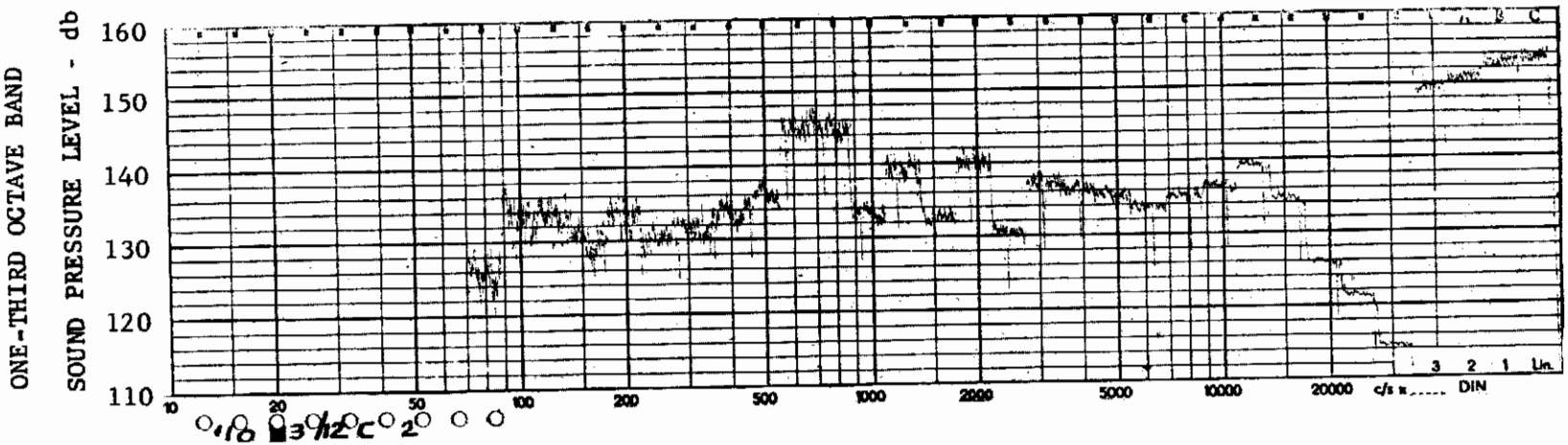

FIGURE 427 ONE-THIRD OCTAVE BAND SPECTRUM MODEL: FP 60

CHANNEL: 2 MACH NO.: 10 α: 5° ϕ: 0 Re_∞/FT.: 1×10^6 AEDC GROUP NO.: 1/12 C

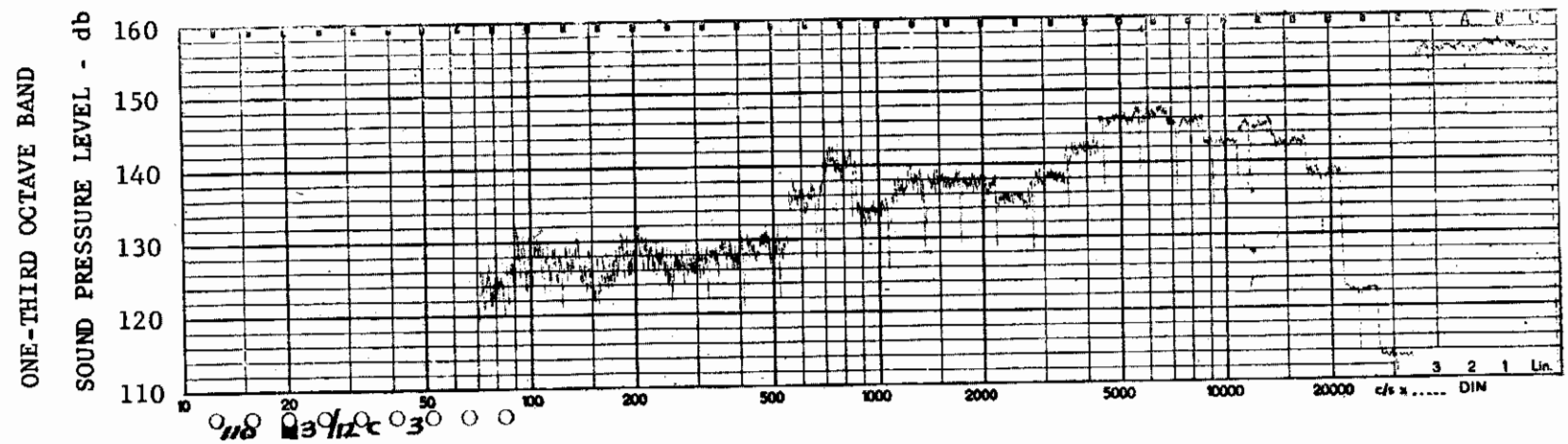

FIGURE 428 ONE-THIRD OCTAVE BAND SPECTRUM MODEL: FP 60

CHANNEL: 3 MACH NO.: 10 α: 5° ϕ: 0 Re_∞/FT.: 1×10^6 AEDC GROUP NO.: 1/12 C

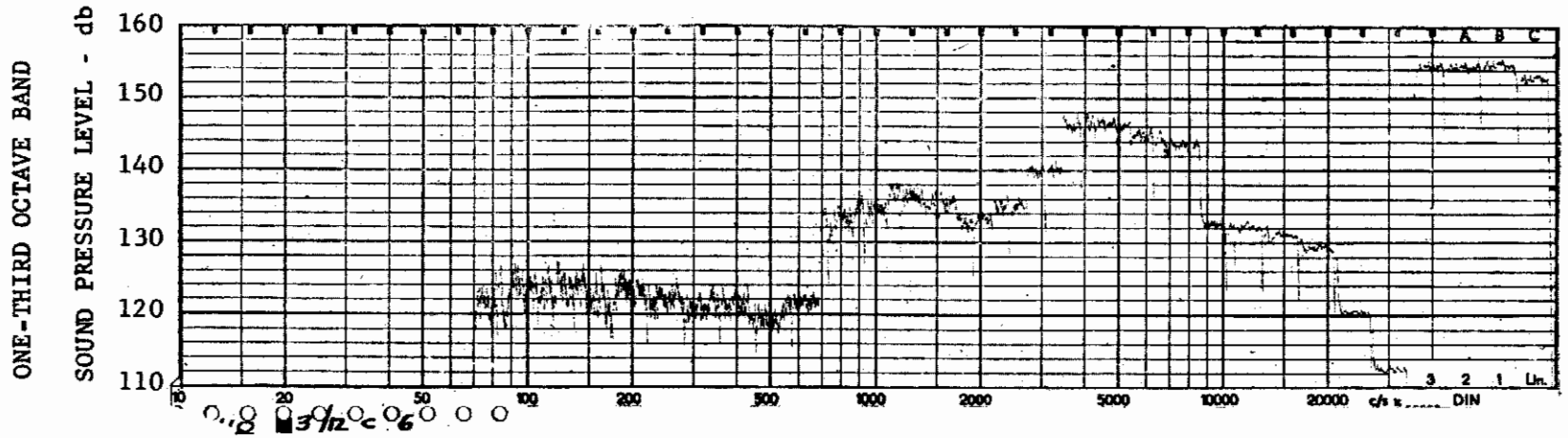

FIGURE 429 ONE-THIRD OCTAVE BAND SPECTRUM MODEL: FP 60

CHANNEL: 6 MACH NO.: 10 α: 5° ϕ: 0 Re_∞/FT.: 1×10^6 AEDC GROUP NO.: 1/12 C

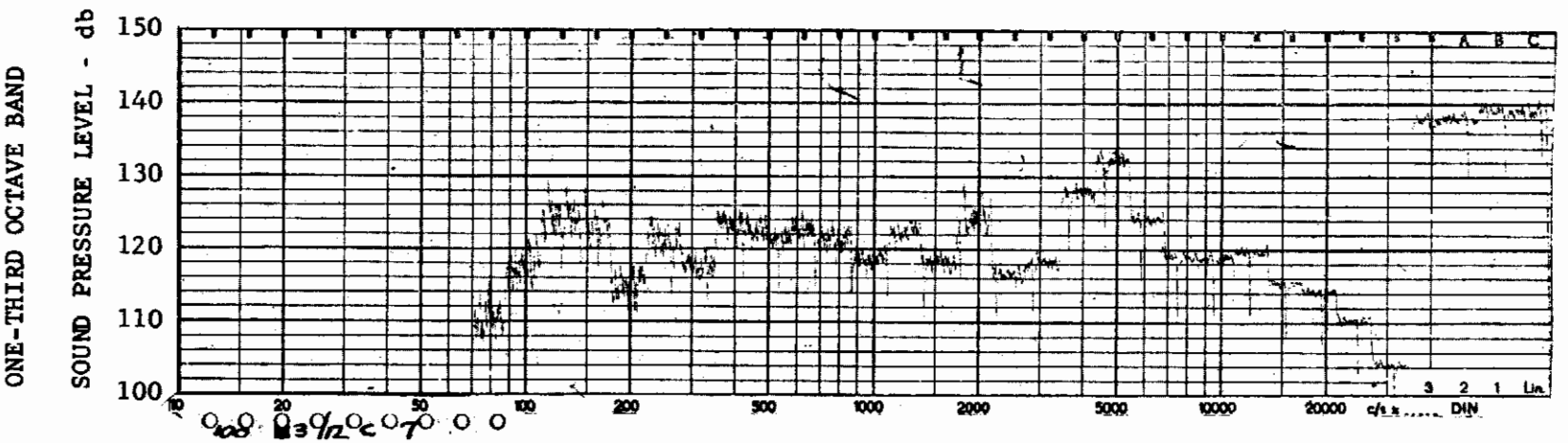

FIGURE 430 ONE-THIRD OCTAVE BAND SPECTRUM MODEL: FP 60

CHANNEL: 7 MACH NO.: 10 α: 5° ϕ: 0 Re_∞/FT.: 1×10^6 AEDC GROUP NO.: 1/12 C

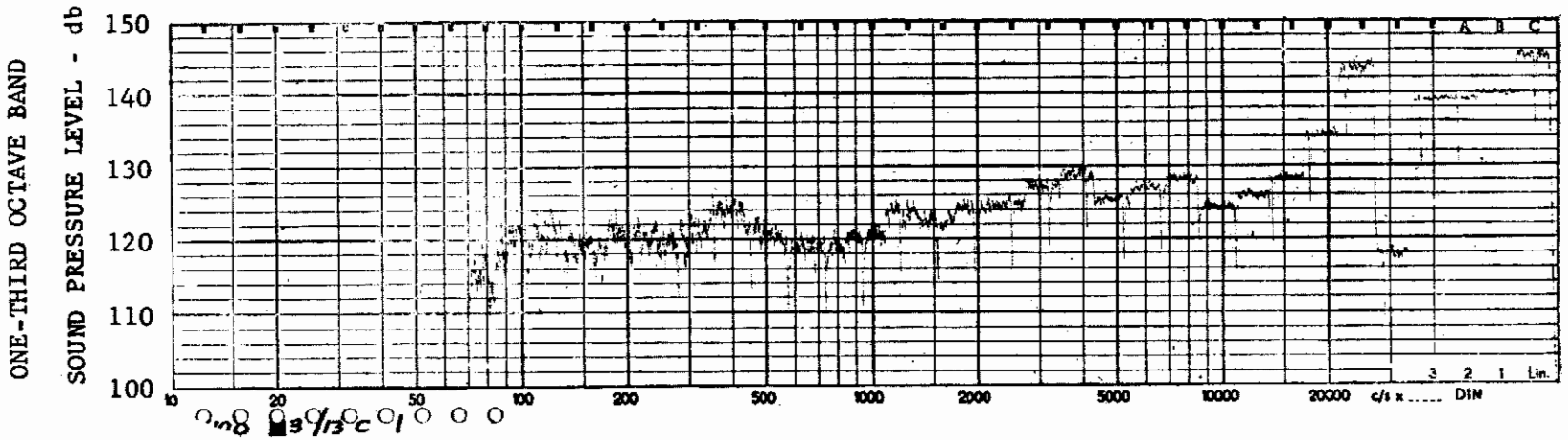

FIGURE 431 ONE-THIRD OCTAVE BAND SPECTRUM MODEL: FP 60

CHANNEL: 1 MACH NO.: 10 α: 10° ϕ: 0 Re_∞ /FT.: 1×10^6 AEDC GROUP NO.: 1/13 C

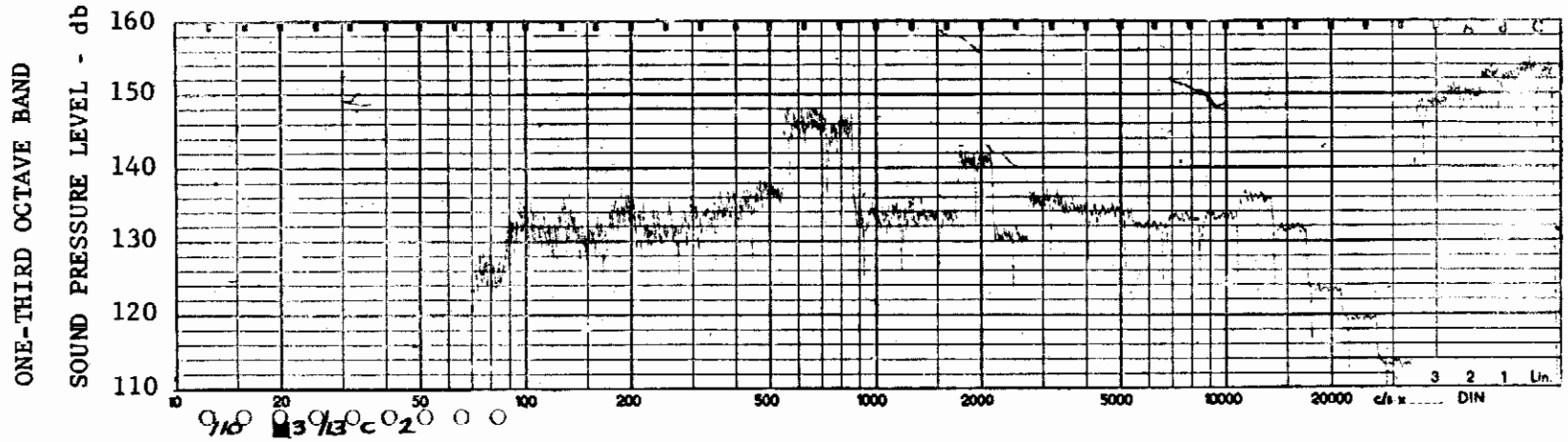

FIGURE 432 ONE-THIRD OCTAVE BAND SPECTRUM MODEL: FP 60

CHANNEL: 2 MACH NO.: 10 α: 10° ϕ: 0 Re_∞ /FT.: 1×10^6 AEDC GROUP NO.: 1/13 C

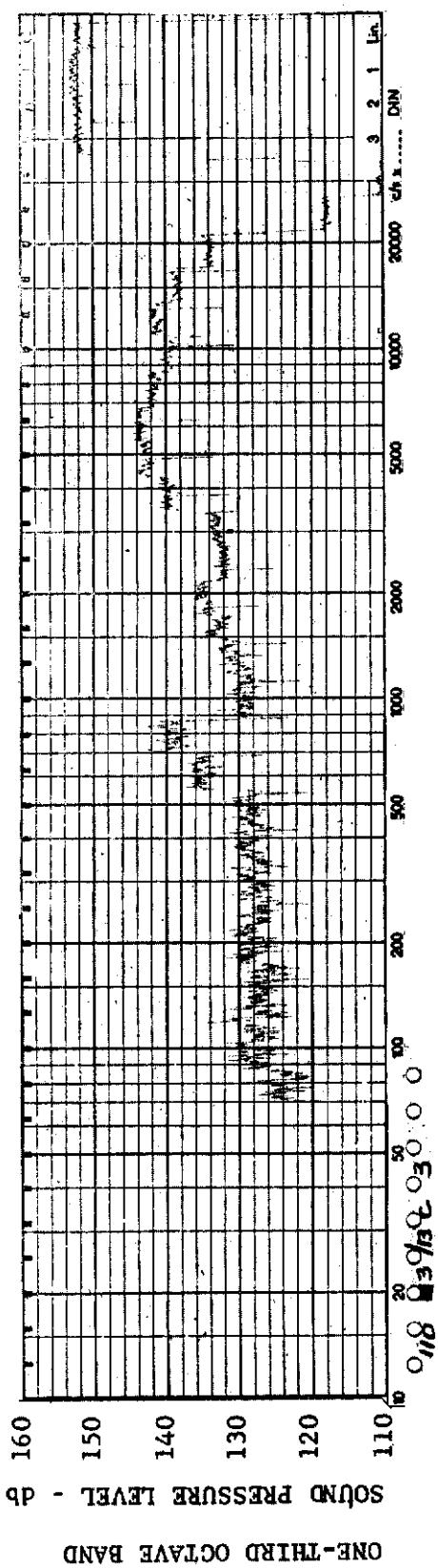

FIGURE 433 ONE-THIRD OCTAVE BAND SPECTRUM MODEL: FP 60

CHANNEL: 3 MACH NO.: 10 α: 10° ϕ: 0 Re_∞/FT.: 1×10^6 AEDC GROUP NO.: 1/13 C

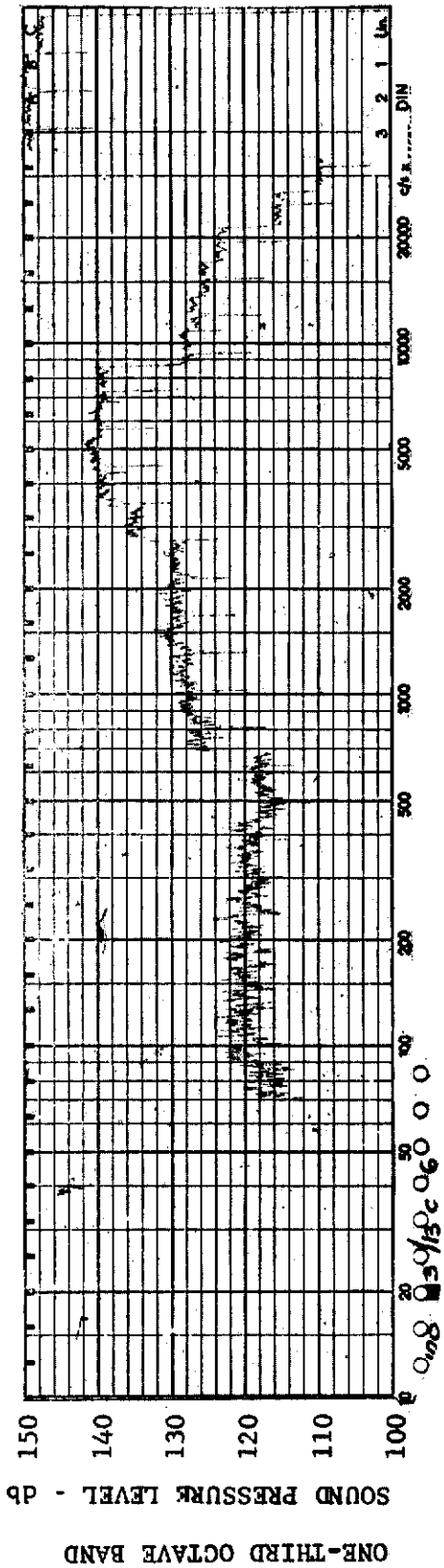

FIGURE 434 ONE-THIRD OCTAVE BAND SPECTRUM MODEL: FP 60

CHANNEL: 6 MACH NO.: 10 α: 10° ϕ: 0 Re_∞/FT.: 1×10^6 AEDC GROUP NO.: 1/13 C

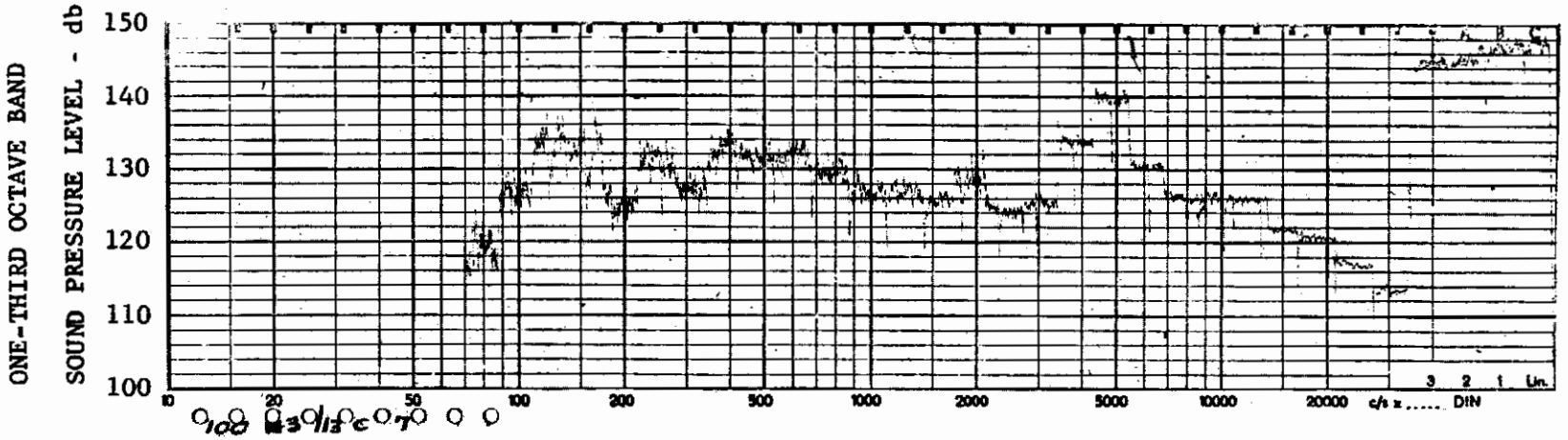

FIGURE 435 ONE-THIRD OCTAVE BAND SPECTRUM MODEL: FP 60

CHANNEL: 7 MACH NO.: 10 α: 10° ϕ: 0 Re_∞/FT.: 1×10^6 AEDC GROUP NO.: 1/13 C

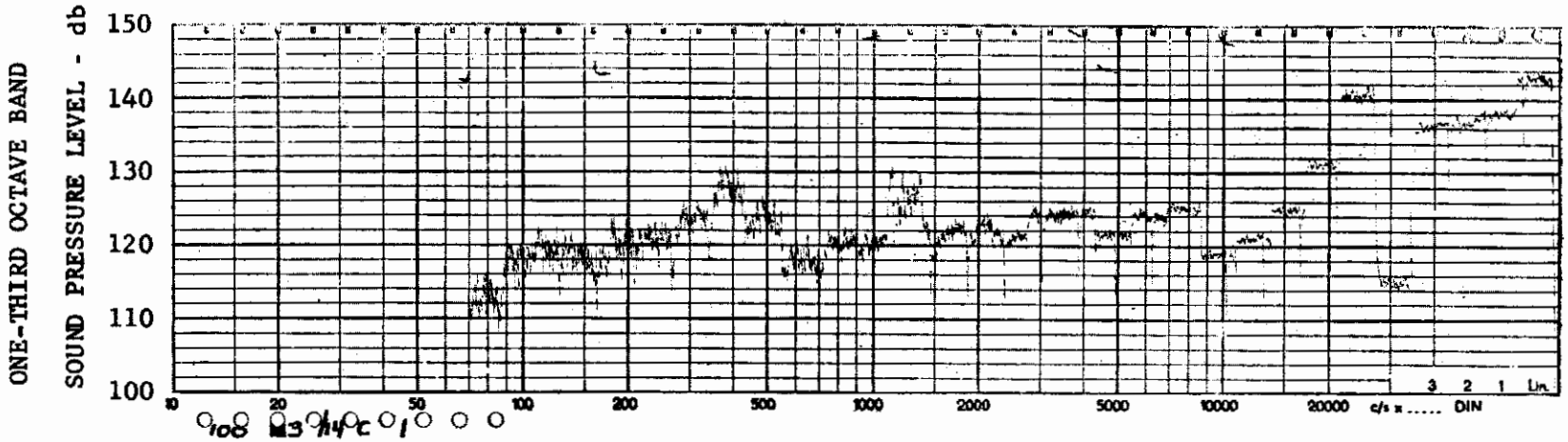

FIGURE 436 ONE-THIRD OCTAVE BAND SPECTRUM MODEL: FP 60

CHANNEL: 1 MACH NO.: 10 α: 13.7° ϕ: 0 Re_∞/FT.: 1×10^6 AEDC GROUP NO.: 1/14 C

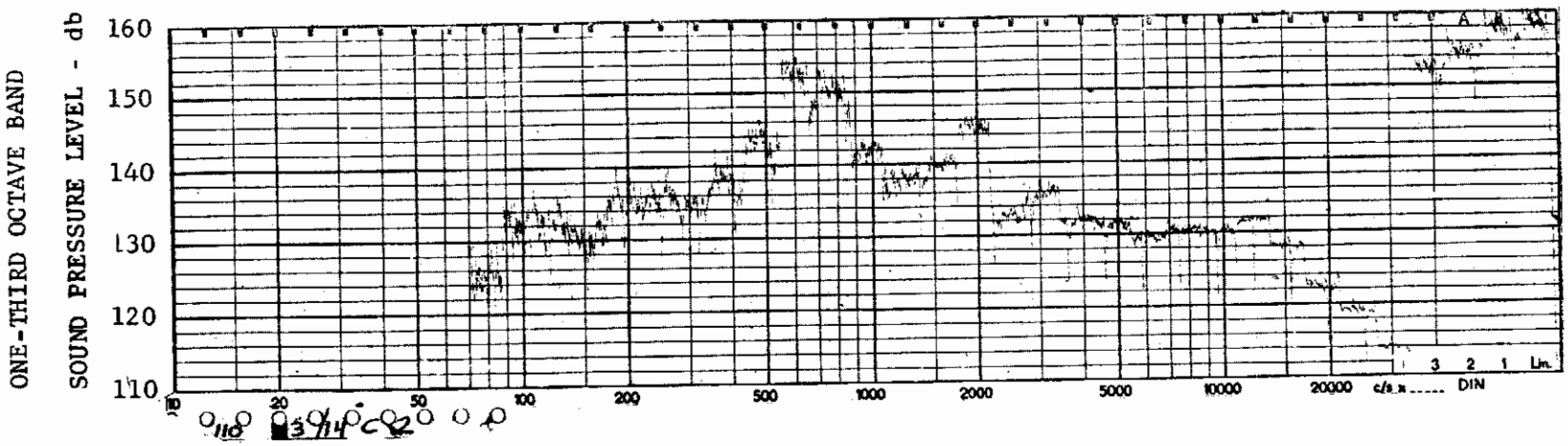

FIGURE 437 ONE-THIRD OCTAVE BAND SPECTRUM MODEL: FP 60

CHANNEL: 2 MACH NO.: 10 α: 13.7° ϕ: 0 Re_∞/FT.: 1×10^6 AEDC GROUP NO.: 1/14 C

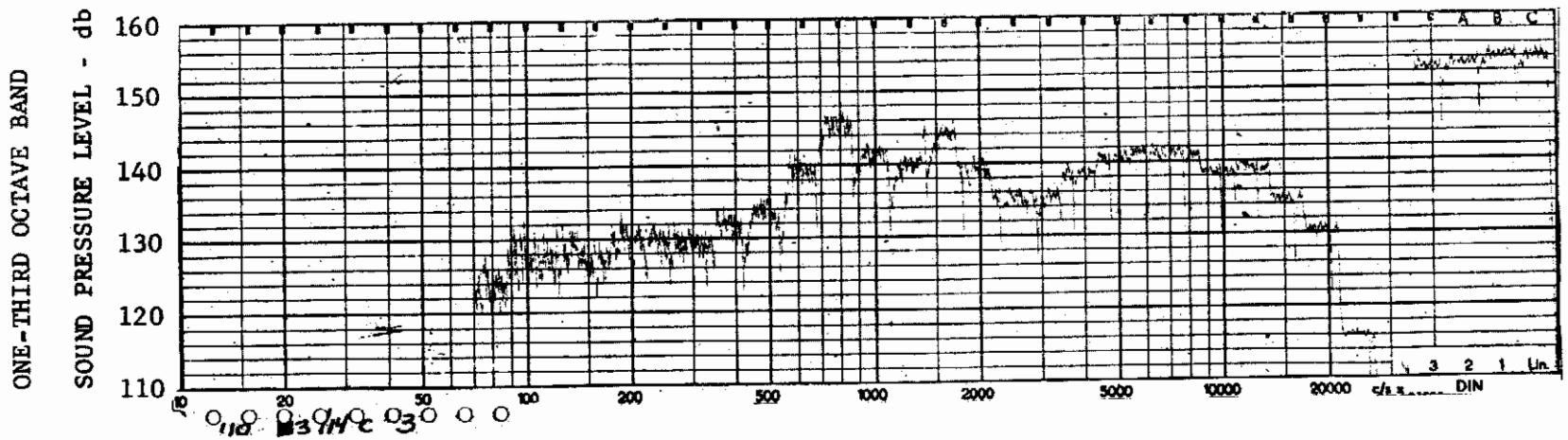

FIGURE 438 ONE-THIRD OCTAVE BAND SPECTRUM MODEL FP 60

CHANNEL: 3 MACH NO.: 10 α: 13.7° ϕ: 0 Re_∞/FT.: 1×10^6 AEDC GROUP NO.: 1/14 C

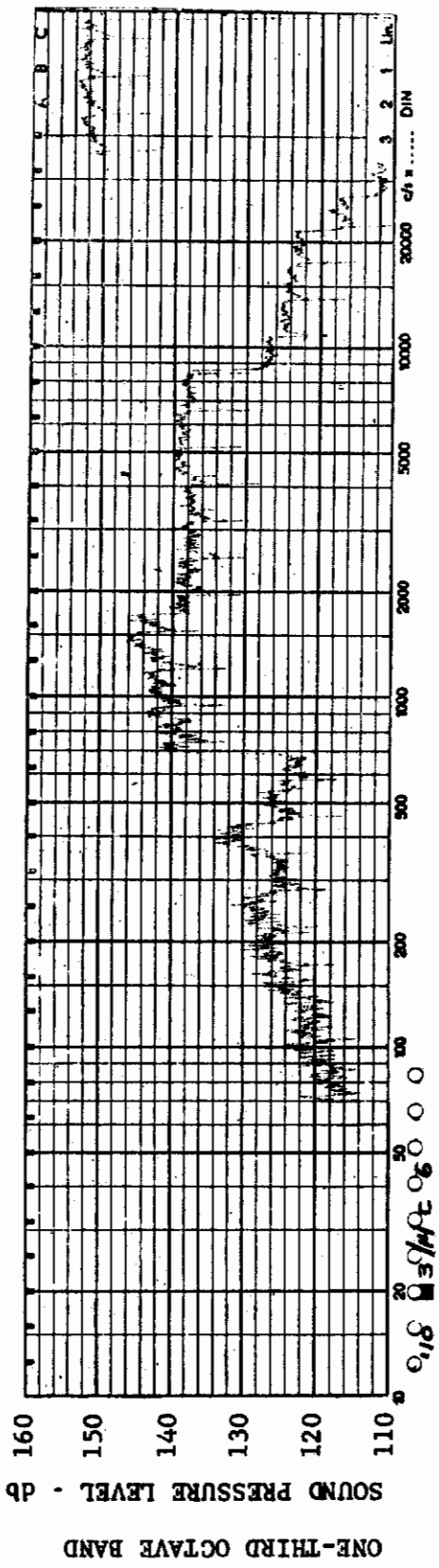

FIGURE 439 ONE-THIRD OCTAVE BAND SPECTRUM MODEL: FP 60

CHANNEL: 6 MACH NO.: 10 α: 13.7° ϕ: 0 Re_∞/FT.: 1×10^6 AEDC GROUP NO.: 1/14 C

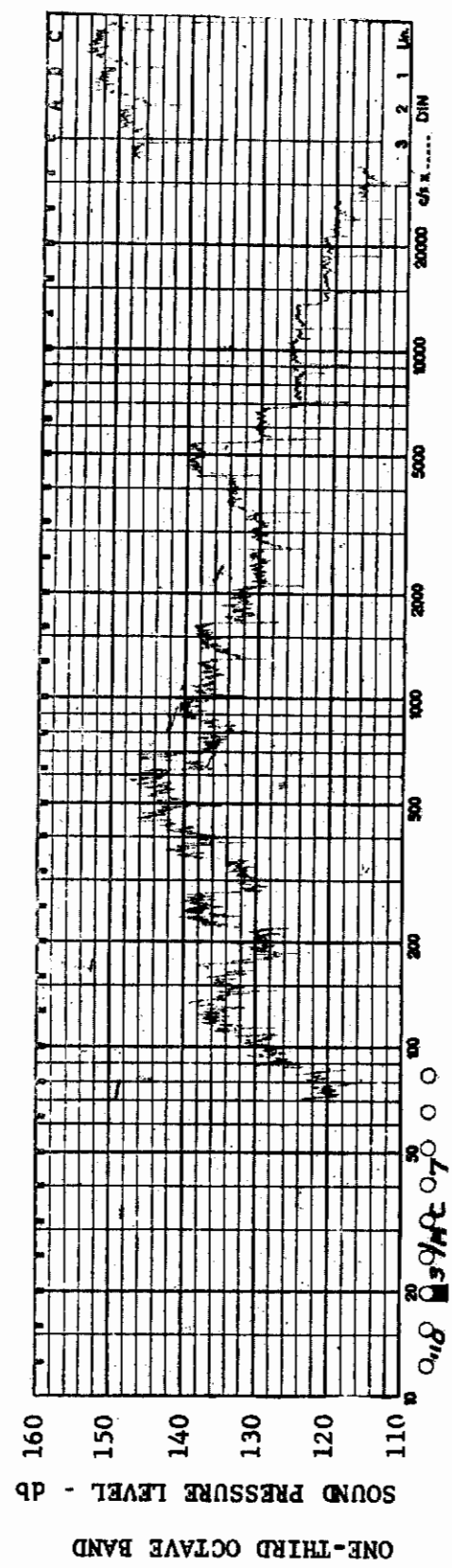

FIGURE 440 ONE-THIRD OCTAVE BAND SPECTRUM MODEL: FP 60

CHANNEL: 7 MACH NO.: 10 α: 13.7° ϕ: 0 Re_∞/FT.: 1×10^6 AEDC GROUP NO.: 1/14 C

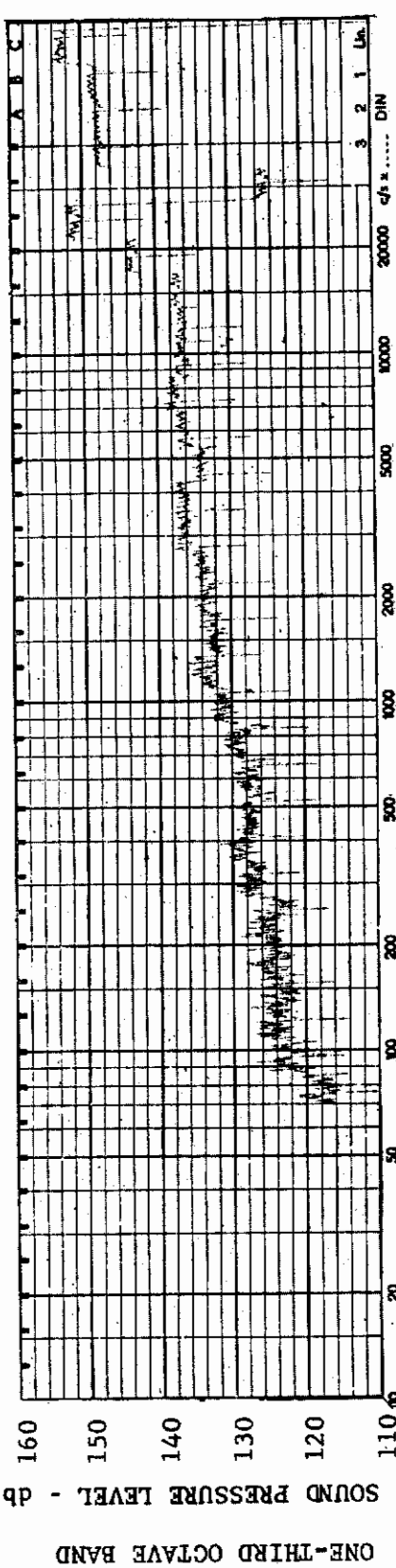

FIGURE 441 ONE-THIRD OCTAVE BAND SPECTRUM

MODEL: FP 60

CHANNEL: 1 MACH NO.: 10 α: 0 ϕ 0 Re_∞/FT.: 1×10^6 AEDC GROUP NO.: 1/15 C

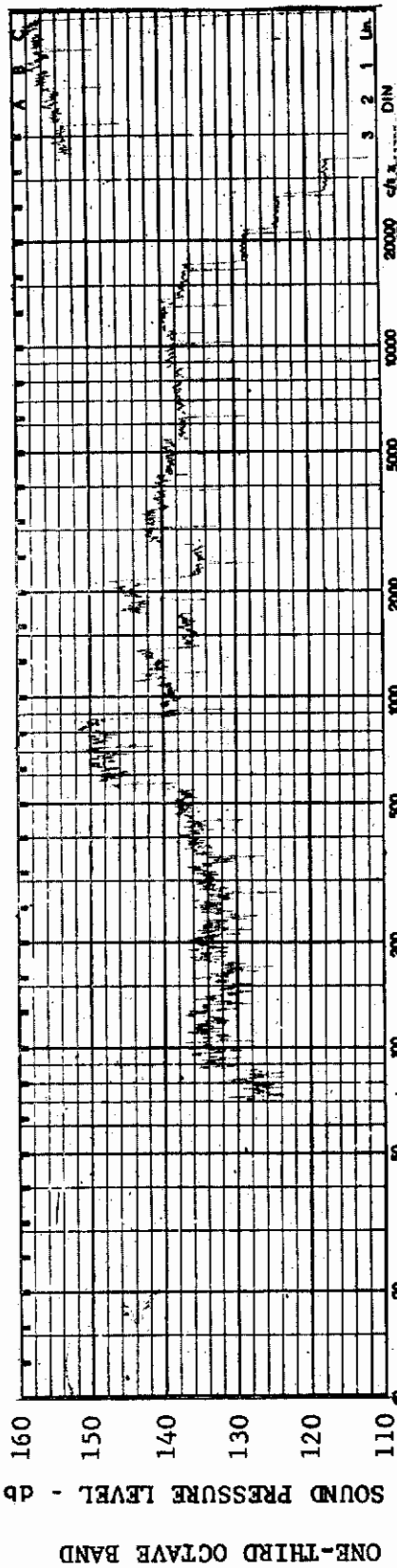

FIGURE 442 ONE-THIRD OCTAVE BAND SPECTRUM

MODEL: FP 60

CHANNEL: 2 MACH NO.: 10 α: 0 ϕ: 0 Re_∞/FT.: 1×10^6 AEDC GROUP NO.: 1/15 C

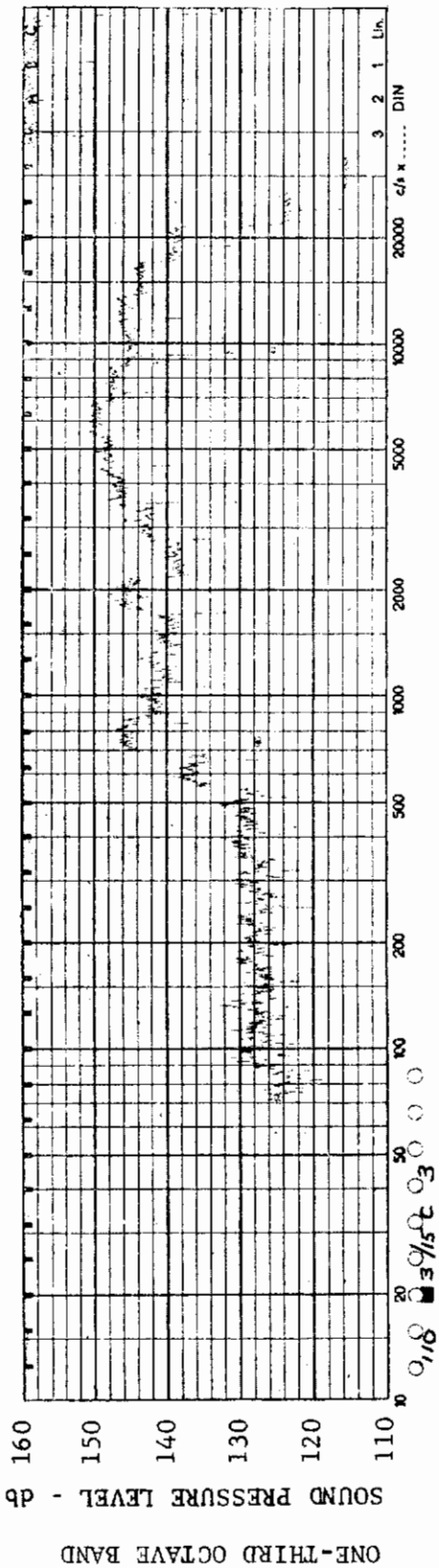

FIGURE 443 ONE-THIRD OCTAVE BAND SPECTRUM MODEL: FP 60

CHANNEL: 3 MACH NO.: 10 α: 0 ϕ: 0 Re_∞/FT.: 1×10^6 AEDC GROUP NO.: 1/15 C

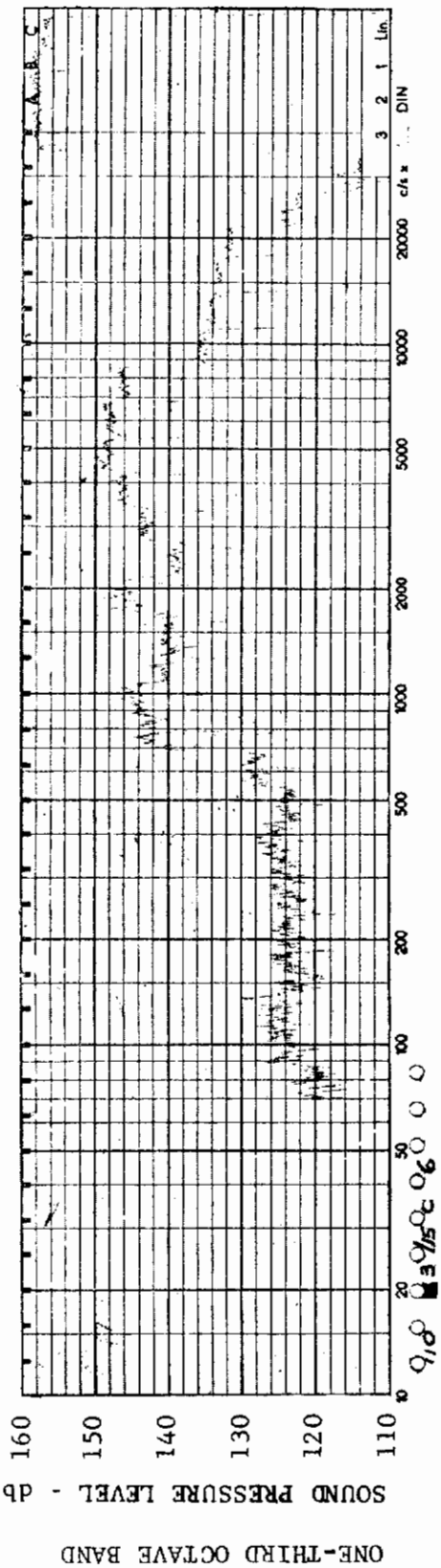

FIGURE 444 ONE-THIRD OCTAVE BAND SPECTRUM MODEL: FP 60

CHANNEL: 6 MACH NO.: 10 α: 0 ϕ: 0 Re_∞/FT.: 1×10^6 AEDC GROUP NO.: 1/15 C

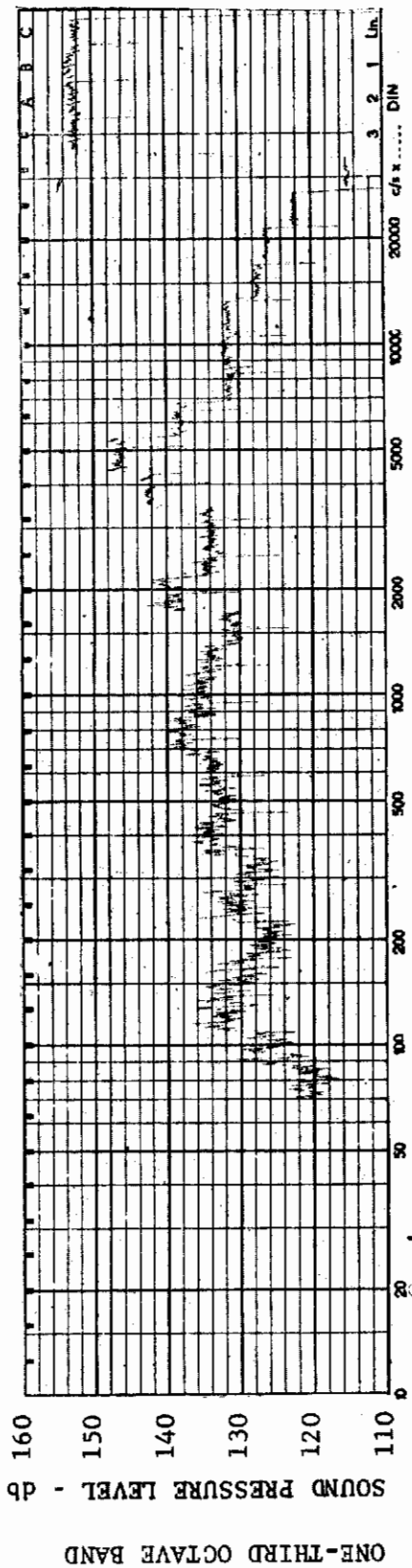

FIGURE 445 ONE-THIRD OCTAVE BAND SPECTRUM

MODEL: FP 60

CHANNEL: 7 MACH NO.: 10 α: 0 ϕ: 0 Re_∞/FT.: 1×10^6 AEDC GROUP NO :1/15 C

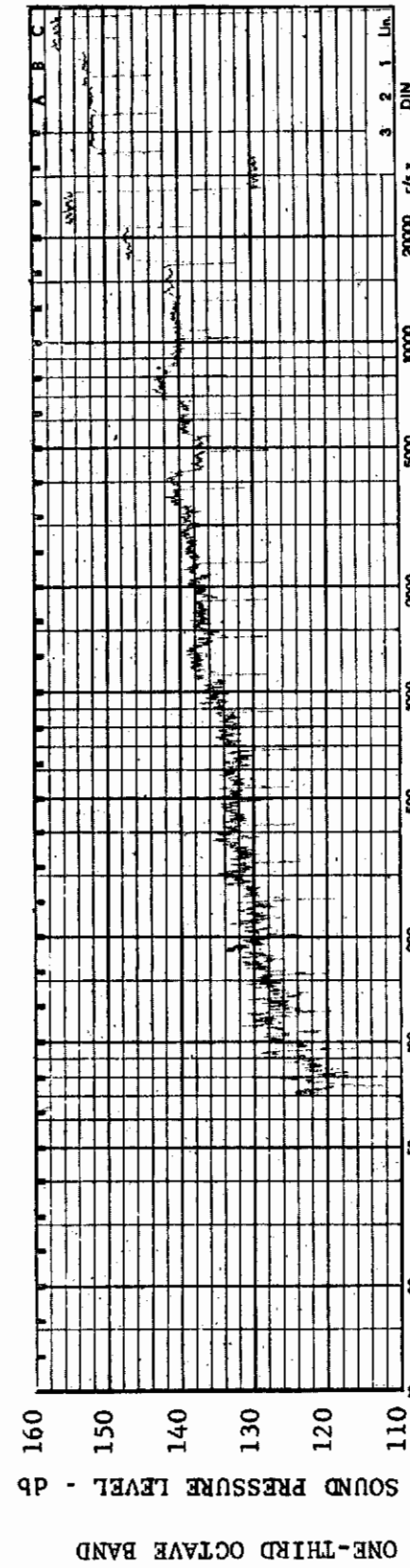

FIGURE 446 ONE-THIRD OCTAVE BAND SPECTRUM

MODEL: FP 60

CHANNEL: 1. MACH NO.: 10 α: -5° ϕ: 0 Re_∞/FT.: 2×10^6 AEDC GROUP NO.: 1/17 C

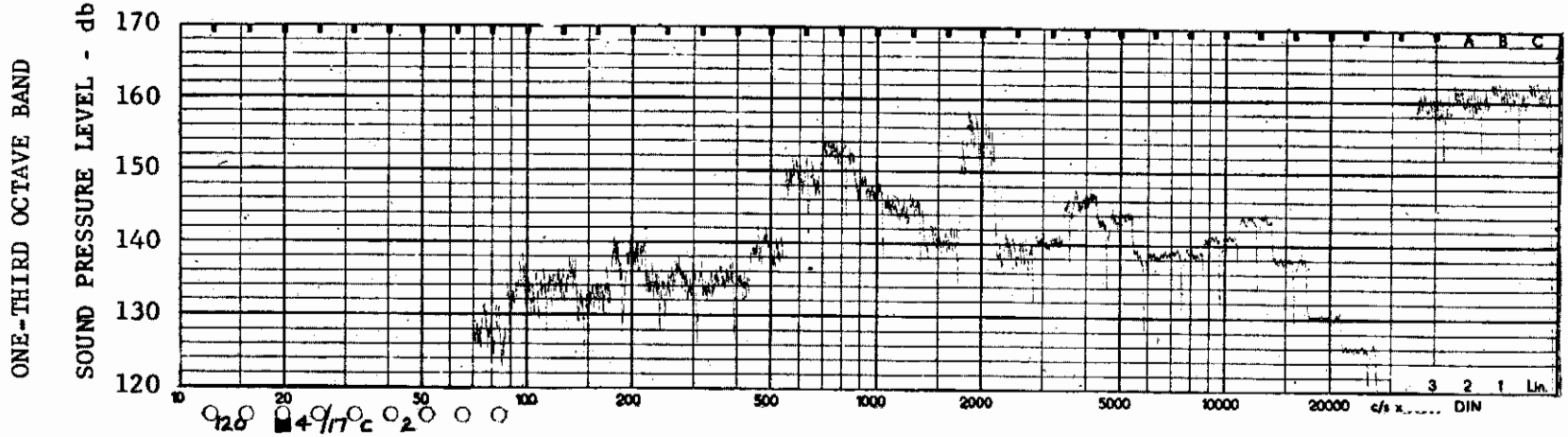

FIGURE 447 ONE-THIRD OCTAVE BAND SPECTRUM MODEL: FP 60

CHANNEL: 2 MACH NO.: 10 α: 5° ϕ: 0 Re_∞/FT.: 2×10^6 AEDC GROUP NO.: 1/17 C

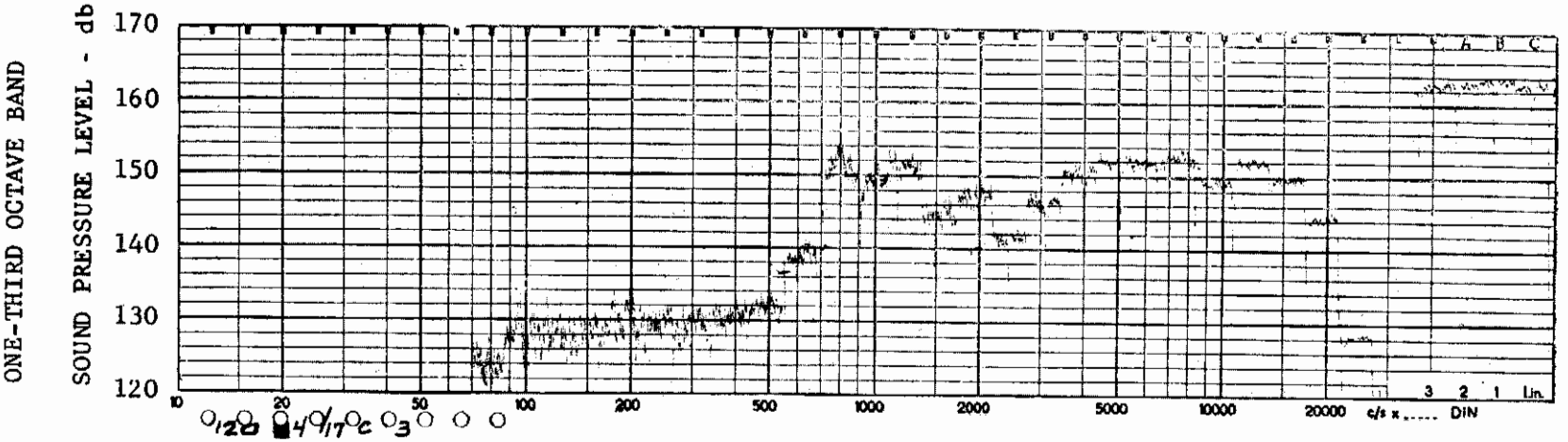

FIGURE 448 ONE-THIRD OCTAVE BAND SPECTRUM MODEL: FP 60

CHANNEL: 3 MACH NO.: 10 α: 5° ϕ: 0 Re_∞/FT.: 2×10^6 AEDC GROUP NO.: 1/17 C

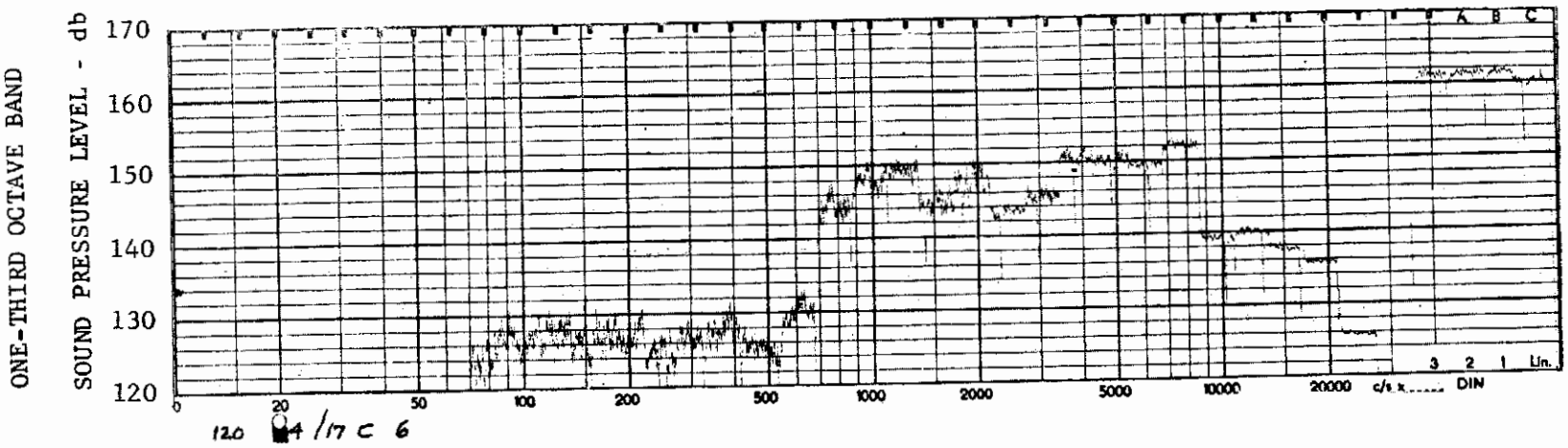

FIGURE 449 ONE-THIRD OCTAVE BAND SPECTRUM MODEL: FP 60

CHANNEL: 6 MACH NO.: 10 α: 5° ϕ: 0 Re_∞/FT.: 2×10^6 AEDC GROUP NO.: 1/17 C

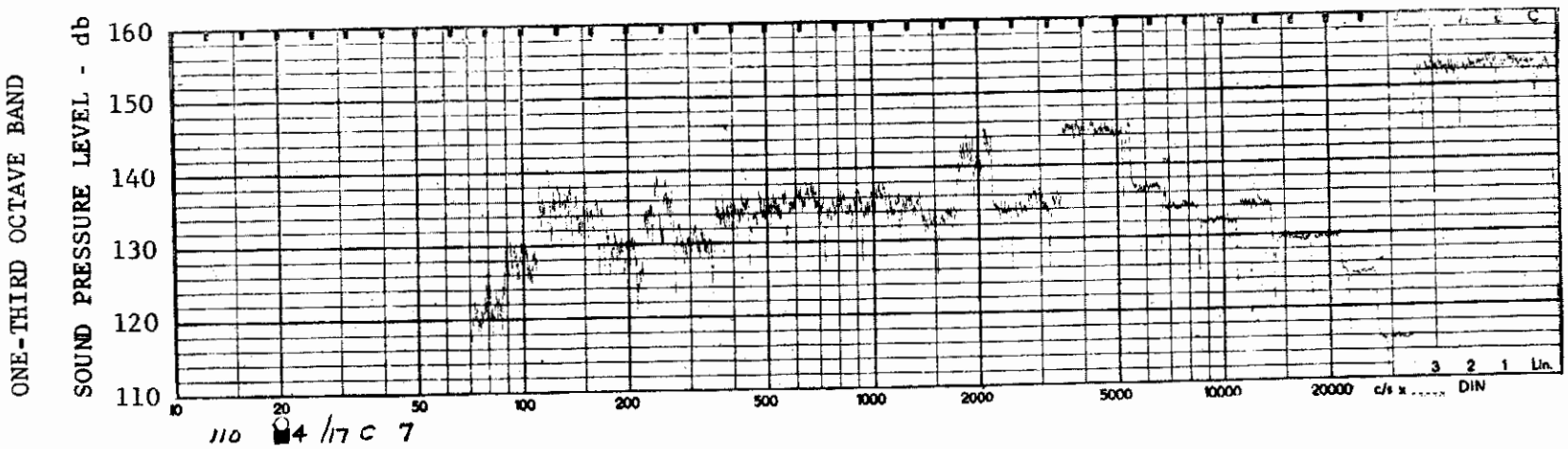

FIGURE 450 ONE-THIRD OCTAVE BAND SPECTRUM MODEL: FP 60

CHANNEL: 7 MACH NO.: 10 α: 5° ϕ: 0 Re_∞/FT.: 2×10^6 AEDC GROUP NO.: 1/17 C

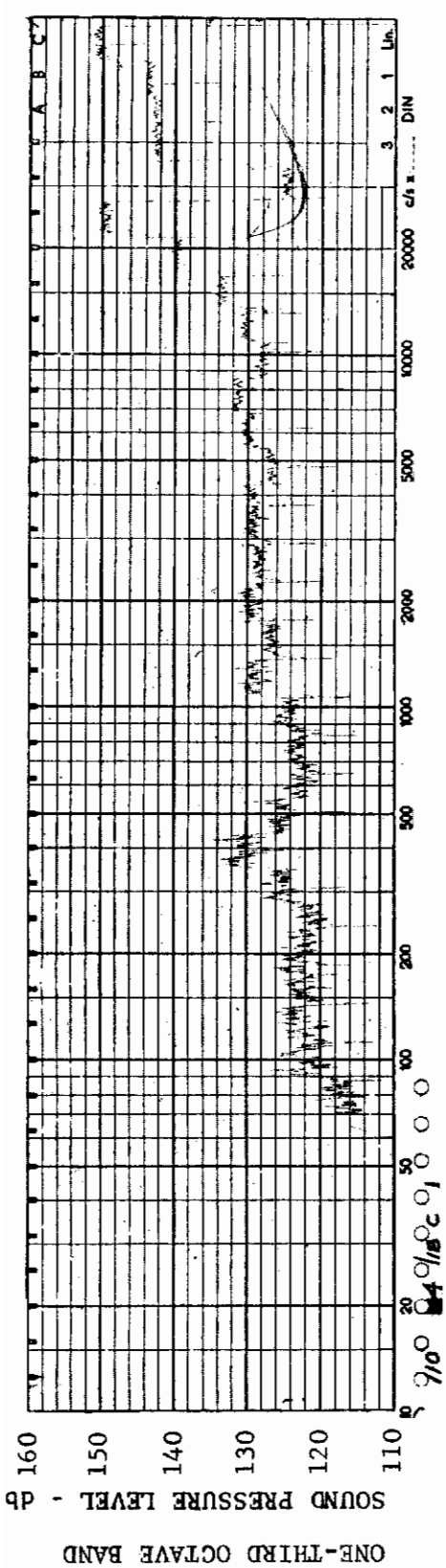

FIGURE 451 ONE-THIRD OCTAVE BAND SPECTRUM

MODEL: FP 60

CHANNEL: 1 MACH NO.: 10 α: 13.7° ϕ: 0 Re_∞/FT.: 2×10^6 AEDC GROUP NO.: 1/18 C

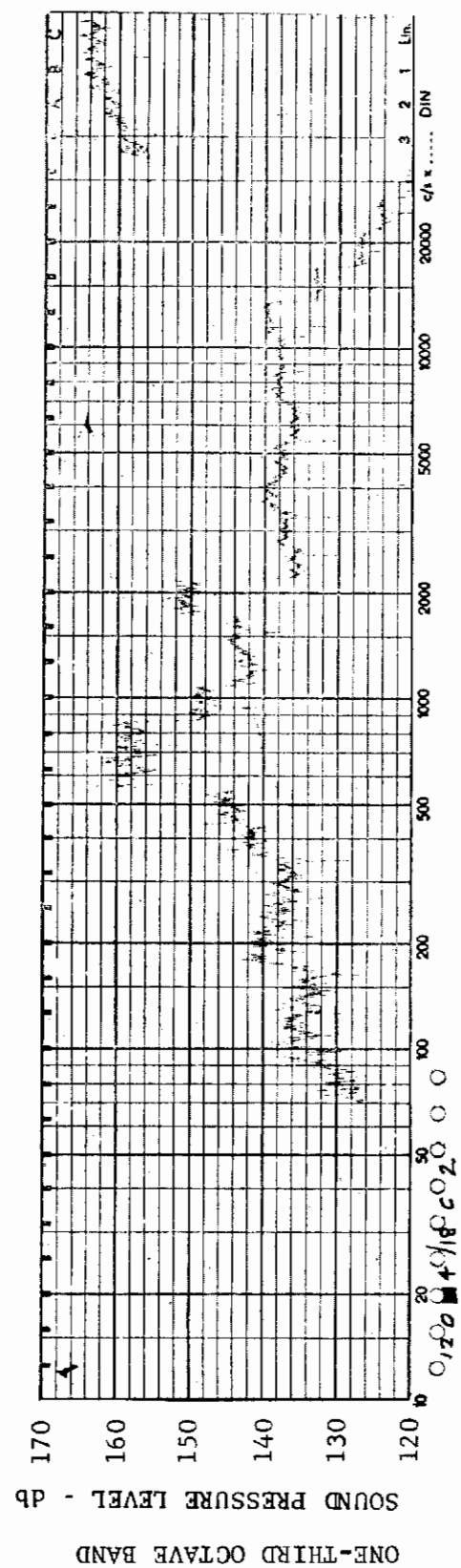

FIGURE 452 ONE-THIRD OCTAVE BAND SPECTRUM

MODEL: FP 60

CHANNEL: 2 MACH NO.: 10 α: 13.7° ϕ: 0 Re_∞/FT.: 2×10^6 AEDC GROUP NO.: 1/18 C

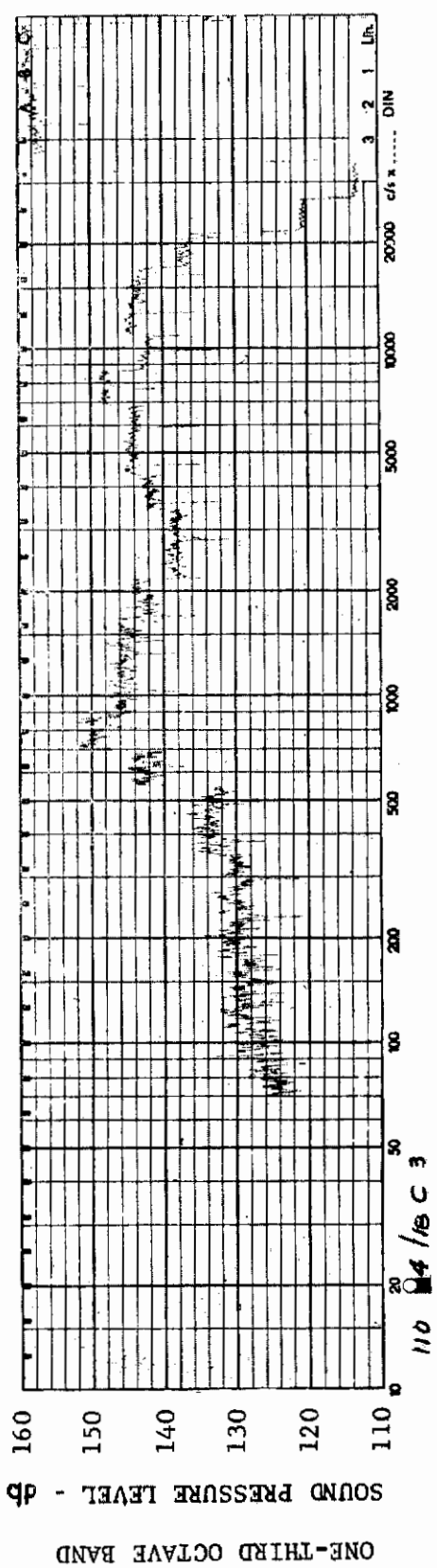

FIGURE 453 ONE-THIRD OCTAVE BAND SPECTRUM

MODEL: FP 60

CHANNEL: 3 MACH NO.: 10 α: 13.7° ϕ: 0 Re_∞/FT.: 2×10^6 AEDC GROUP NO.: 1/18 C

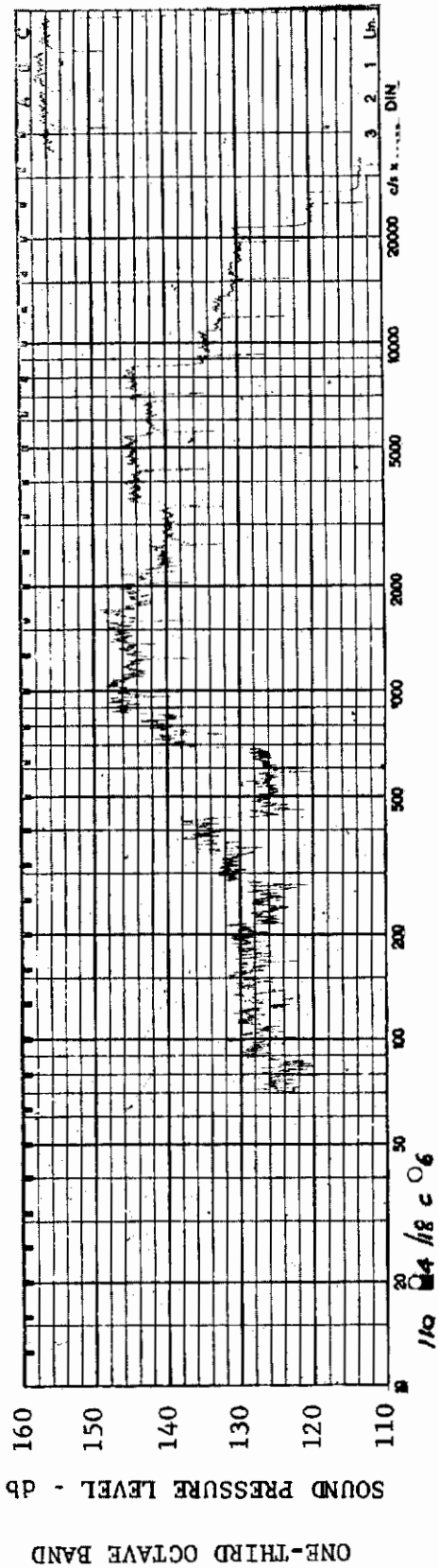

FIGURE 454 ONE-THIRD OCTAVE BAND SPECTRUM

MODEL: FP 60

CHANNEL: 6 MACH NO.: 10 α: 13.7° ϕ: 0 Re_∞/FT.: 2×10^6 AEDC GROUP NO.: 1/18 C

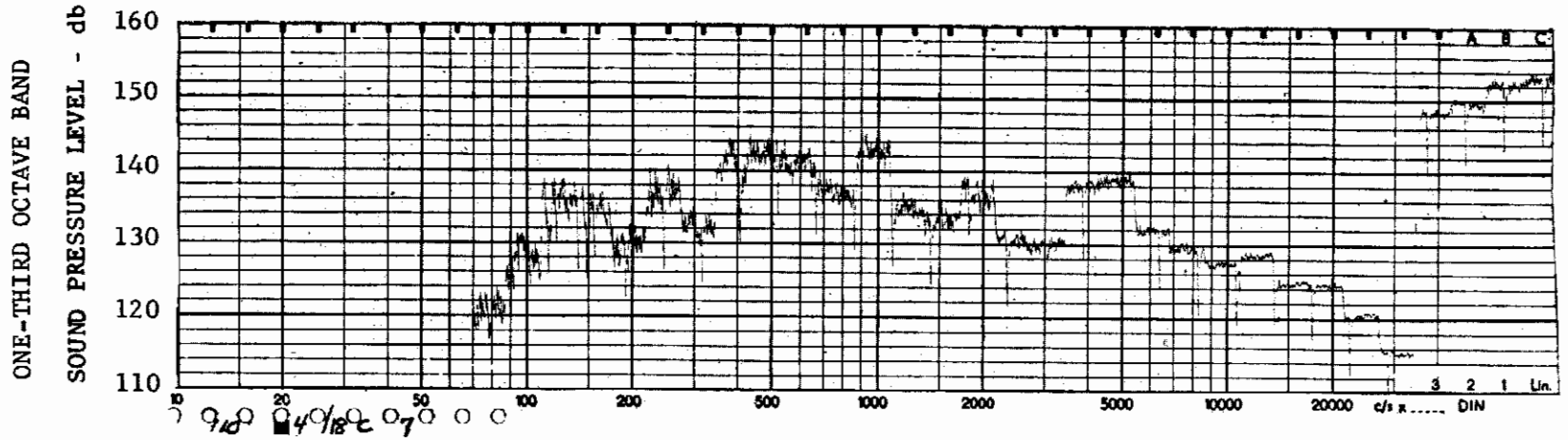

FIGURE 455 ONE-THIRD OCTAVE BAND SPECTRUM MODEL: FP 60

CHANNEL: 7 MACH NO.: 10 α: 13.7° ϕ: 0 Re_∞/FT.: 2×10^6 AEDC GROUP NO.: 1/18 C

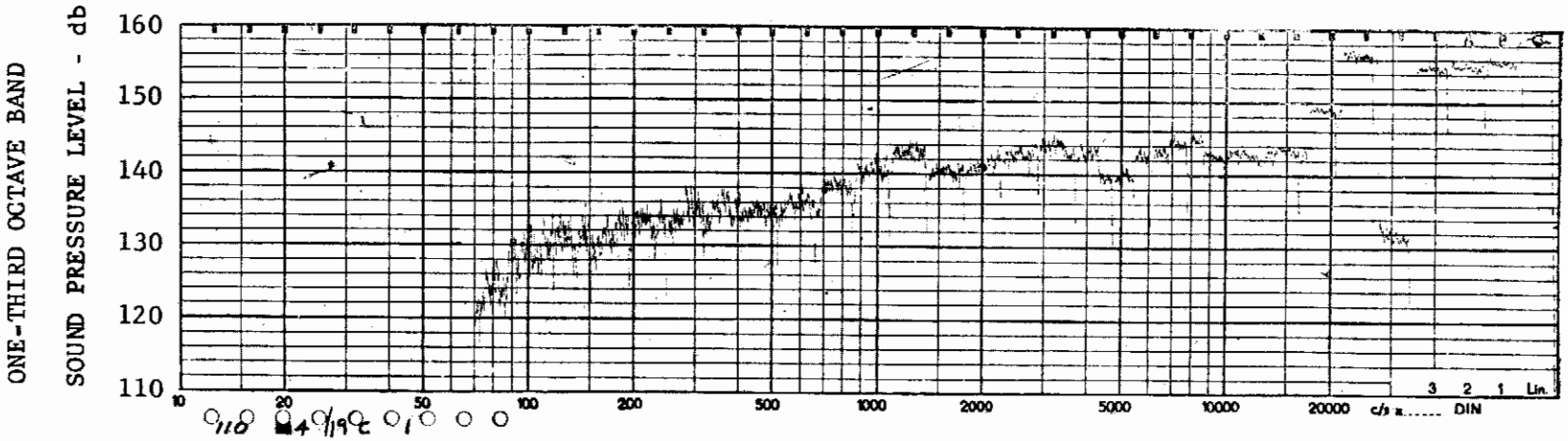

FIGURE 456 ONE-THIRD OCTAVE BAND SPECTRUM MODEL: FP 60

CHANNEL: 1 MACH NO.: 10 α: 0 ϕ: 0 Re_∞/FT.: 2×10^6 AEDC GROUP NO.: 1/19 C

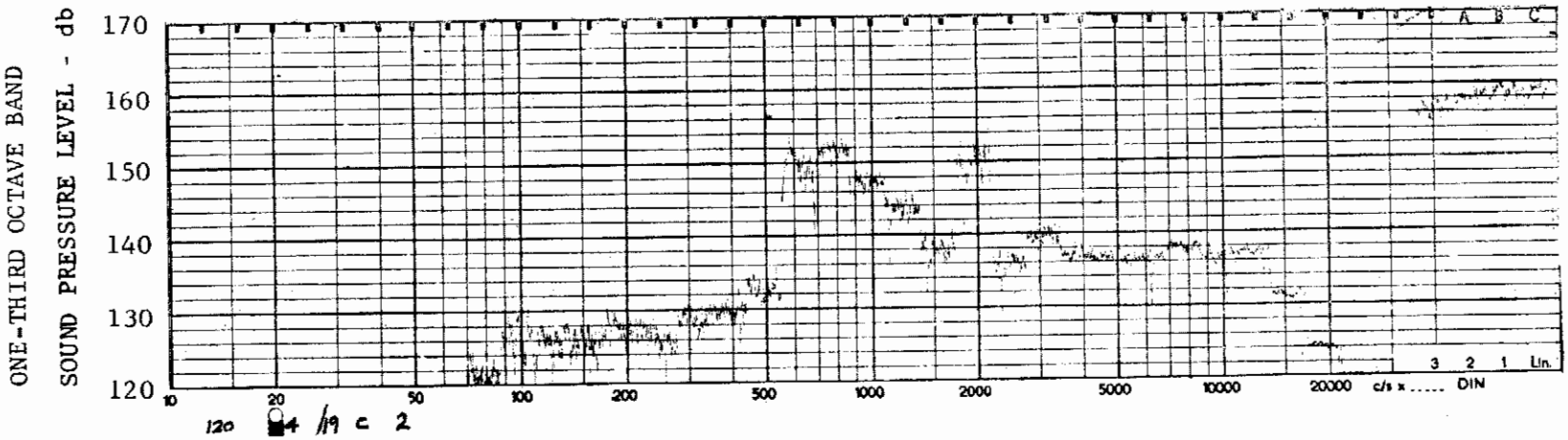

FIGURE 457 ONE-THIRD OCTAVE BAND SPECTRUM MODEL: FP 60

CHANNEL: 2 MACH NO.: 10 α: 0 ϕ: 0 Re_∞/FT.: 2×10^6 AEDC GROUP NO.: 1/19 C

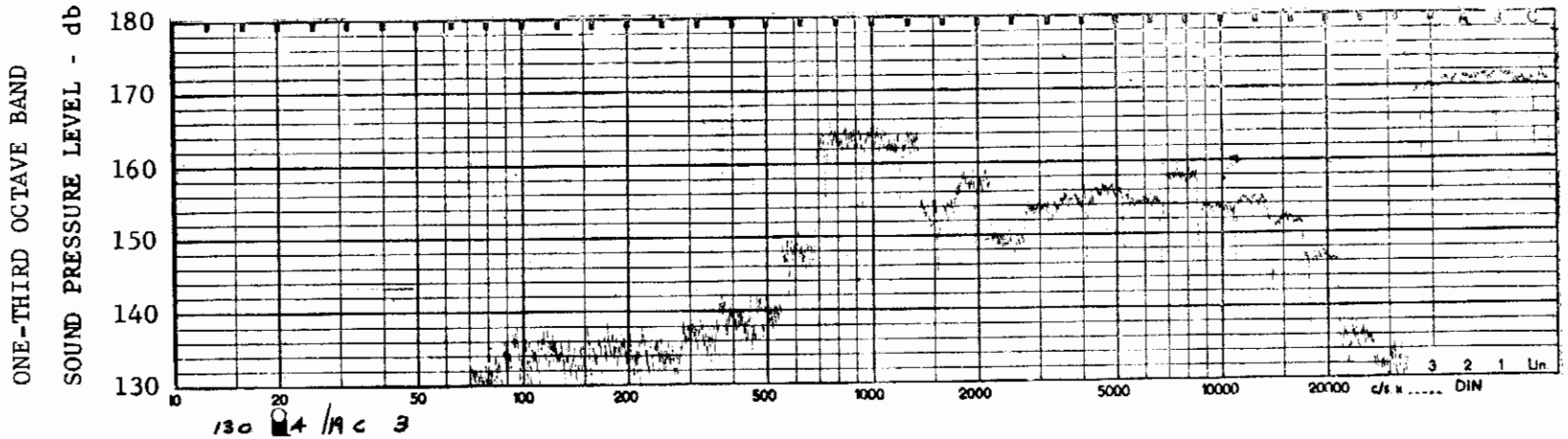

FIGURE 458 ONE-THIRD OCTAVE BAND SPECTRUM MODEL: FP 60

CHANNEL: 3 MACH NO.: 10 α: 0 ϕ: 0 Re_∞/FT.: 2×10^6 AEDC GROUP NO.: 1/19 C

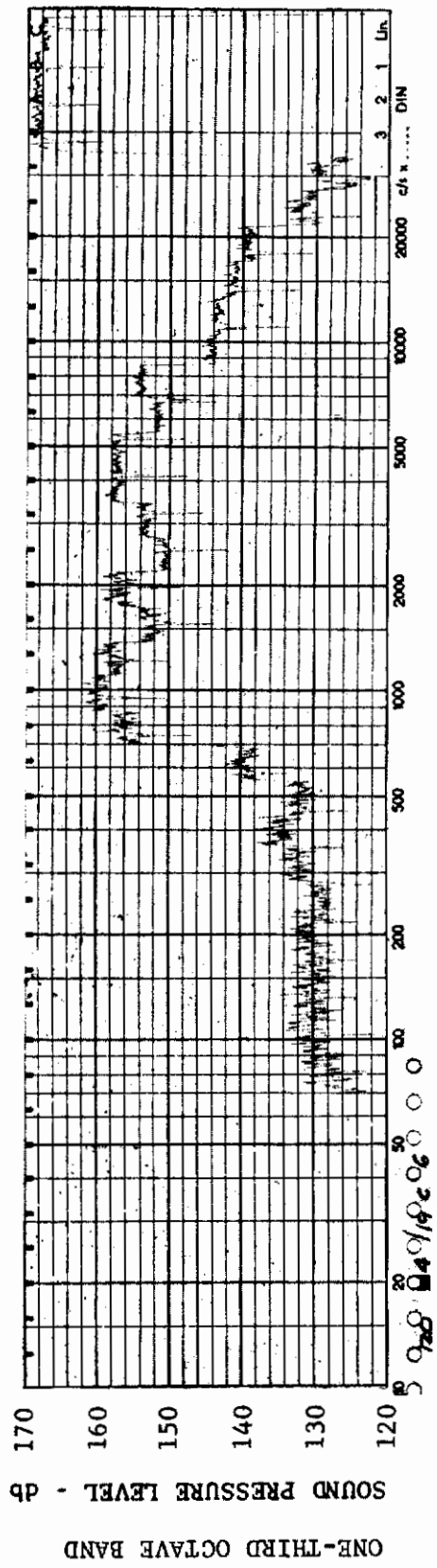

FIGURE 459 ONE-THIRD OCTAVE BAND SPECTRUM

MODEL: FP 60

CHANNEL: 6 MACH NO.: 10 α: 0 ϕ: 0 Re_∞/FT.: 2×10^6 AEDC GROUP NO.: 1/19 C

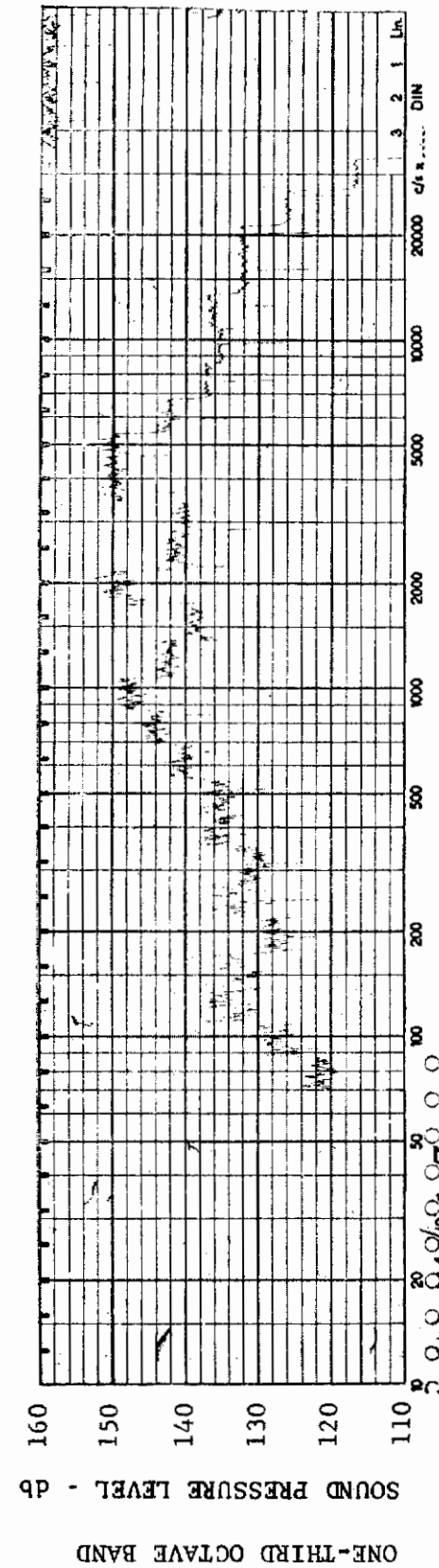

FIGURE 460 ONE-THIRD OCTAVE BAND SPECTRUM

MODEL: FP 60

CHANNEL: 7 MACH NO.: 10 α: 0 ϕ: 0 Re_∞/FT.: 2×10^6 AEDC GROUP NO.: 1/19 C

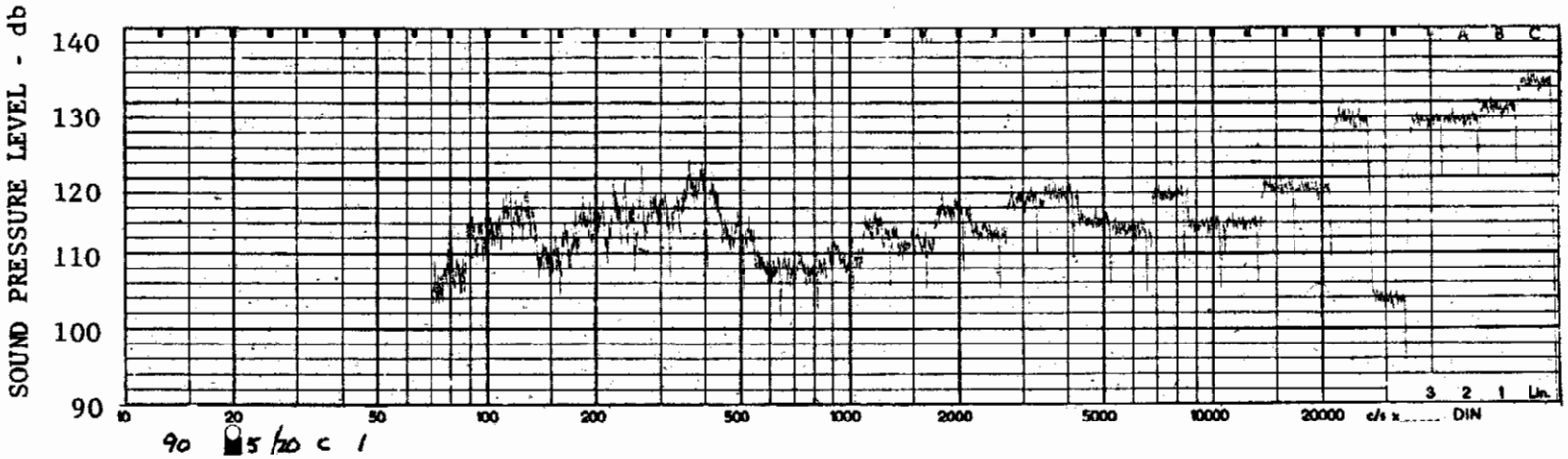

FIGURE 461 ONE-THIRD OCTAVE BAND SPECTRUM MODEL: FP 30

CHANNEL: 1 MACH NO.: 10 α: 0 ϕ: 0 Re_∞/FT.: 2×10^6 AEDC GROUP NO.: 1/20 C

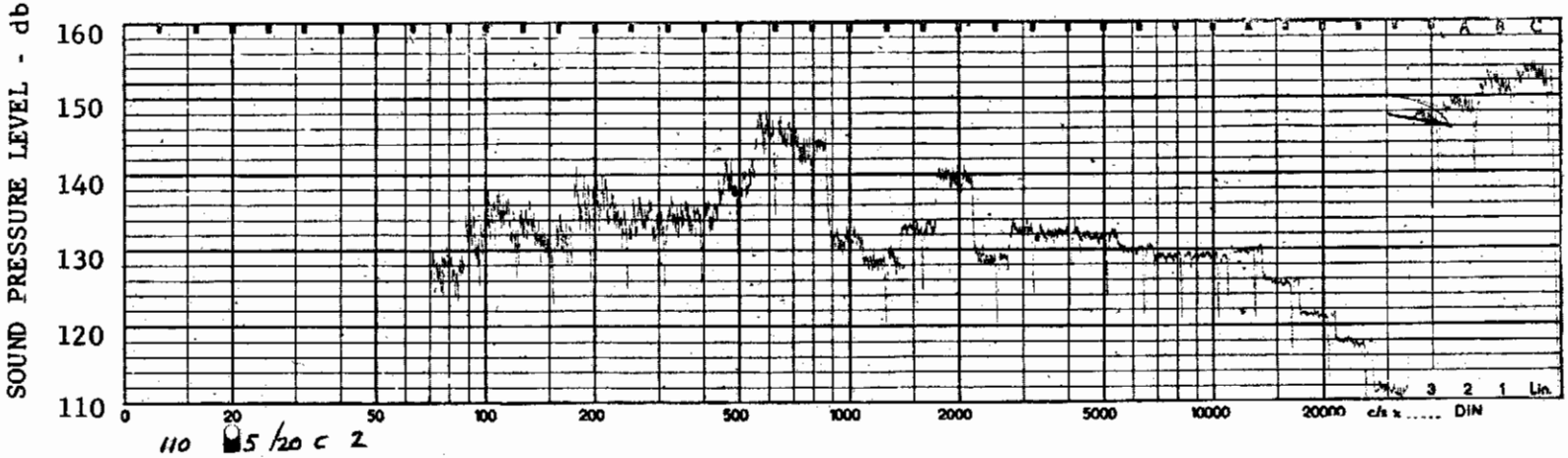

FIGURE 462 ONE-THIRD OCTAVE BAND SPECTRUM MODEL: FP 30

CHANNEL: 2 MACH NO.: 10 α: 0 ϕ: 0 Re_∞/FT.: 2×10^6 AEDC GROUP NO.: 1/20 C

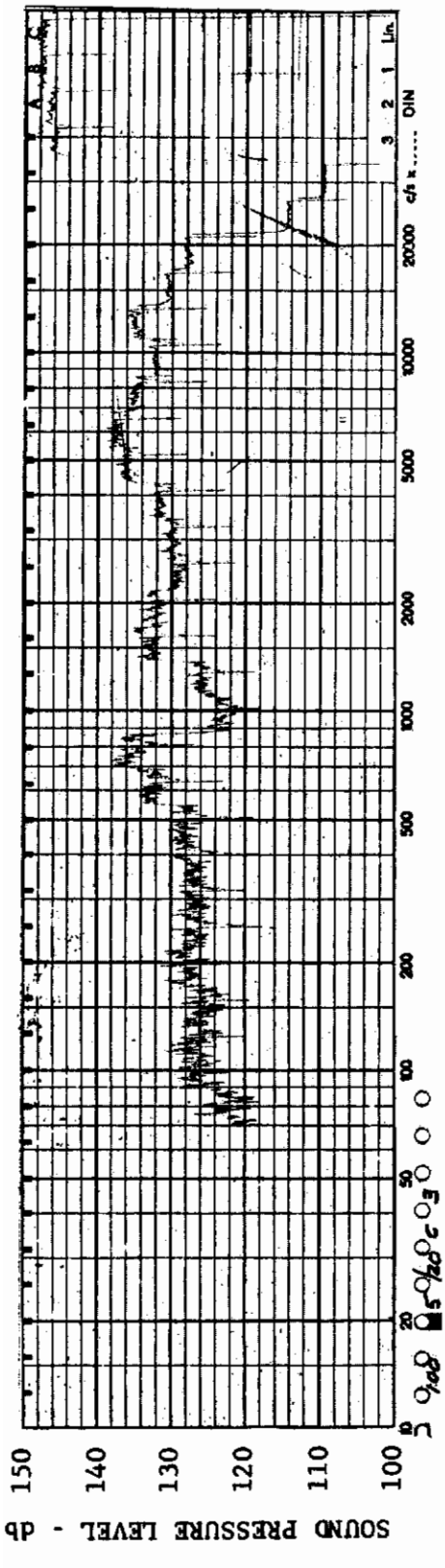

FIGURE 463 ONE-THIRD OCTAVE BAND SPECTRUM MODEL: FP 30

CHANNEL: 3 MACH NO.: 10 α: 0 ϕ: 0 Re_∞/FT.: 2×10^6 AEDC GROUP NO.: 1/20 C

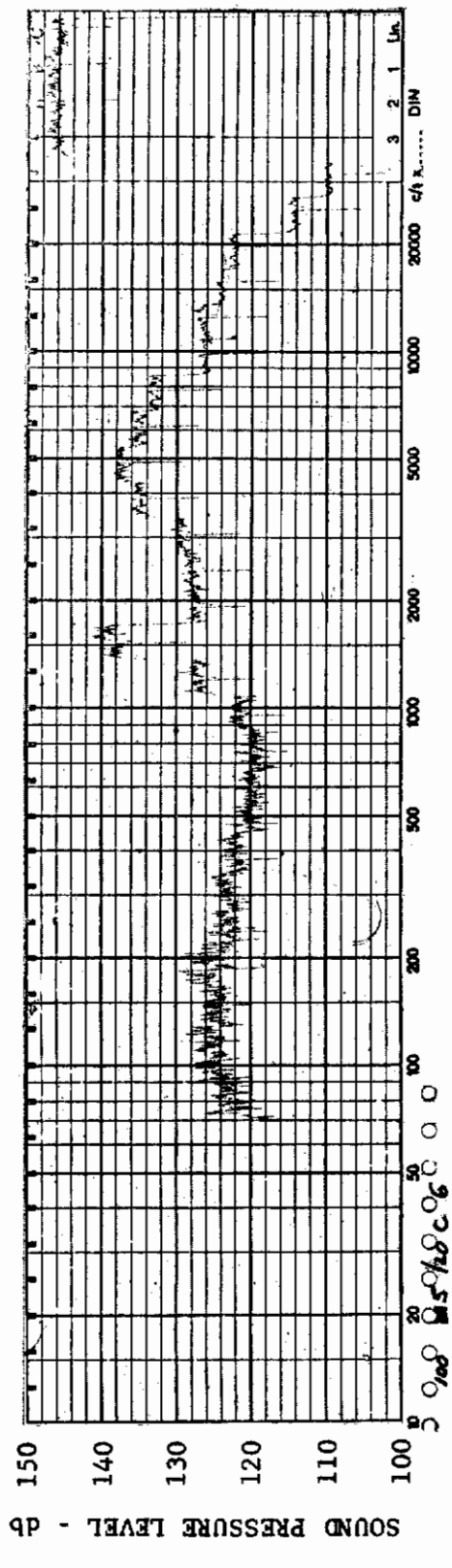

FIGURE 464 ONE-THIRD OCTAVE BAND SPECTRUM MODEL: FP 30

CHANNEL: 6 MACH NO.: 10 α: 0 ϕ: 0 Re_∞/FT.: 2×10^6 AEDC GROUP NO.: 1/20 C

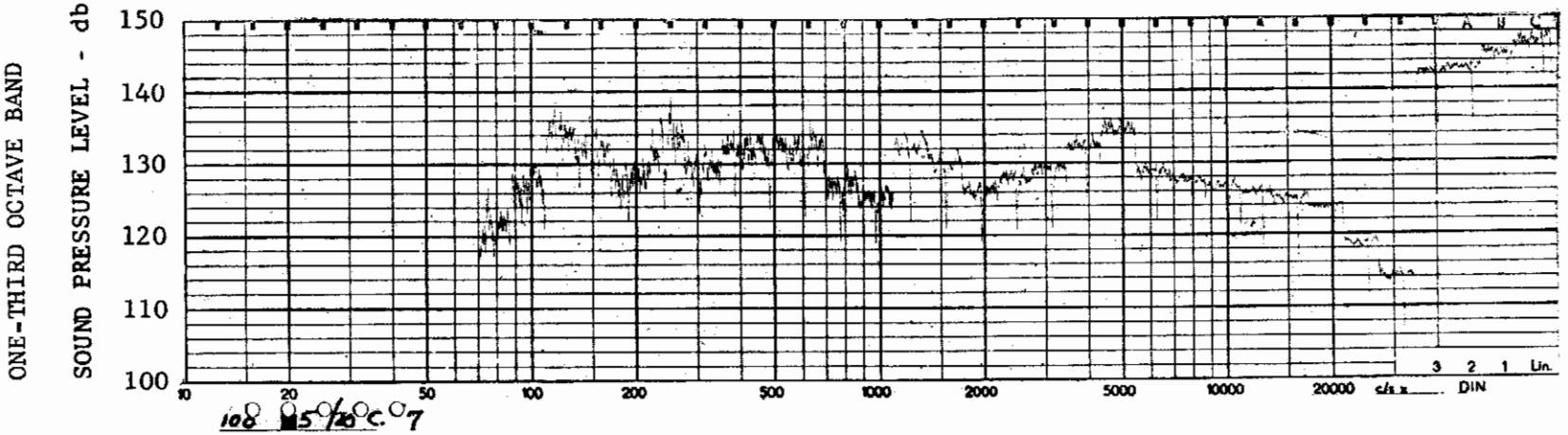

FIGURE 465 ONE-THIRD OCTAVE BAND SPECTRUM MODEL: FP 30

CHANNEL: 7 MACH NO.: 10 α: 0 ϕ: 0 Re_∞/FT.: 2×10^6 AEDC GROUP NO.: 1/20 C

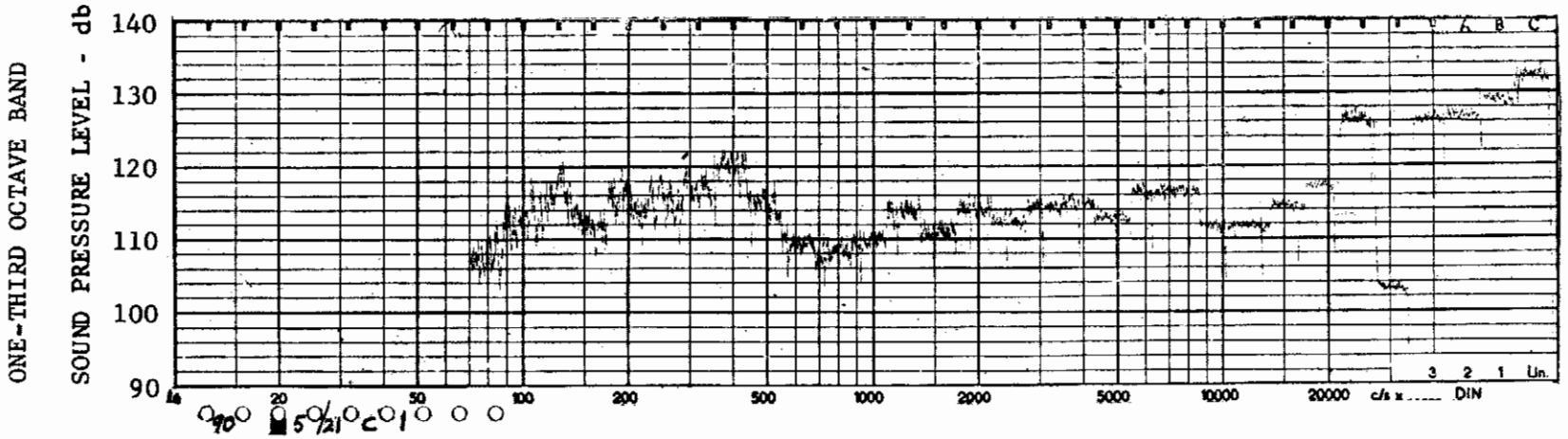

FIGURE 466 ONE-THIRD OCTAVE BAND SPECTRUM MODEL: FP 30

CHANNEL: 1 MACH NO.: 10 α: 5° ϕ: 0 Re_∞/FT.: 2×10^6 AEDC GROUP NO.: 1/21 C

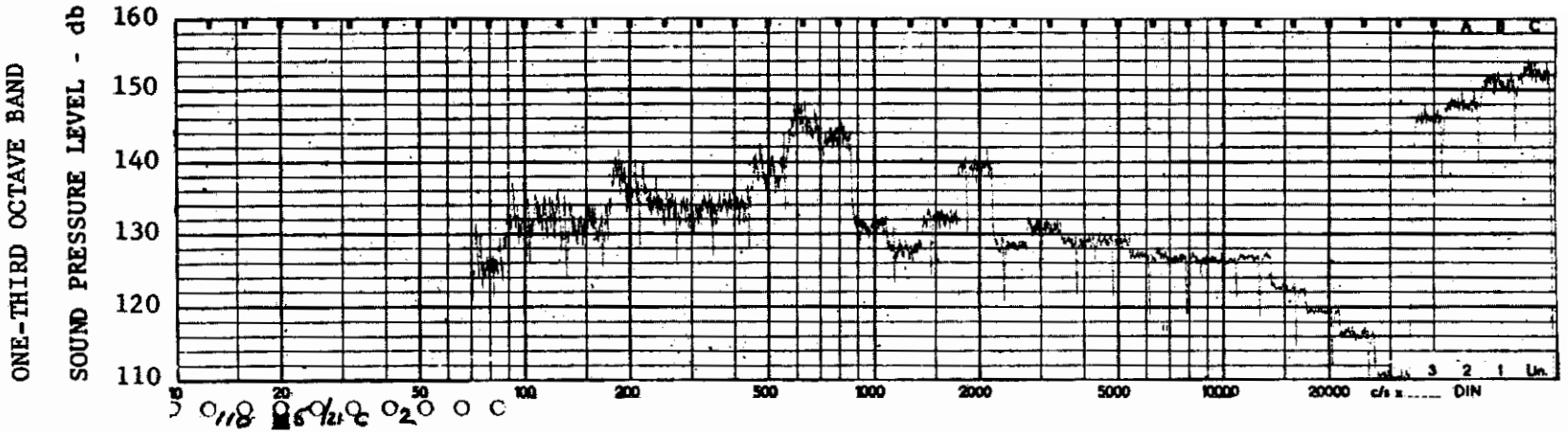

FIGURE 467 ONE-THIRD OCTAVE BAND SPECTRUM MODEL: FP 30

CHANNEL: 2 MACH NO.: 10 α: 5° ϕ: 0 Re_∞/FT.: 2×10^6 AEDC GROUP NO.: 1/21 C

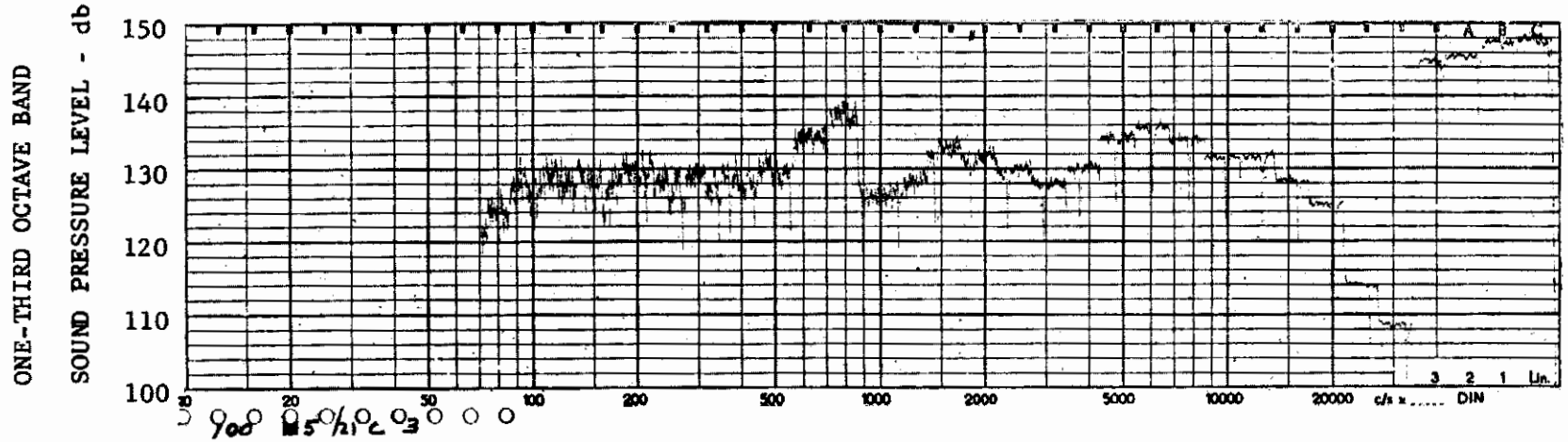

FIGURE 468 ONE-THIRD OCTAVE BAND SPECTRUM MODEL: FP 30

CHANNEL: 3 MACH NO.: 10 α: 5° ϕ: 0 Re_∞/FT.: 2×10^6 AEDC GROUP NO.: 1/21 C

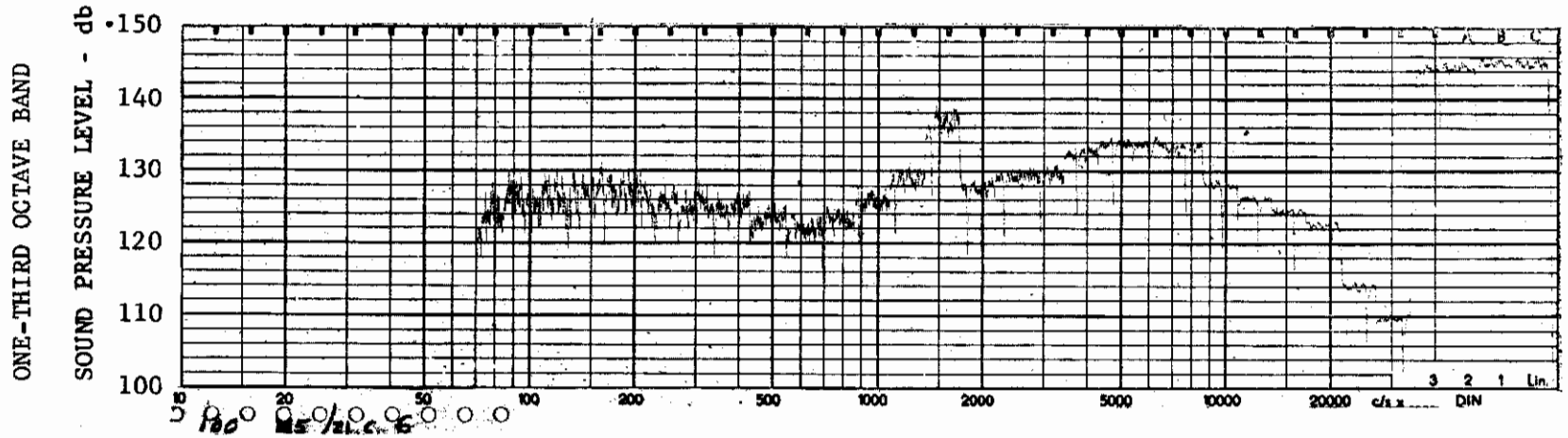

FIGURE 469 ONE-THIRD OCTAVE BAND SPECTRUM MODEL: FP 30

CHANNEL: 6 MACH NO.: 10 α: 5° ϕ: 0 Re_∞/FT.: 2×10^6 AEDC GROUP NO.: 1/21 C

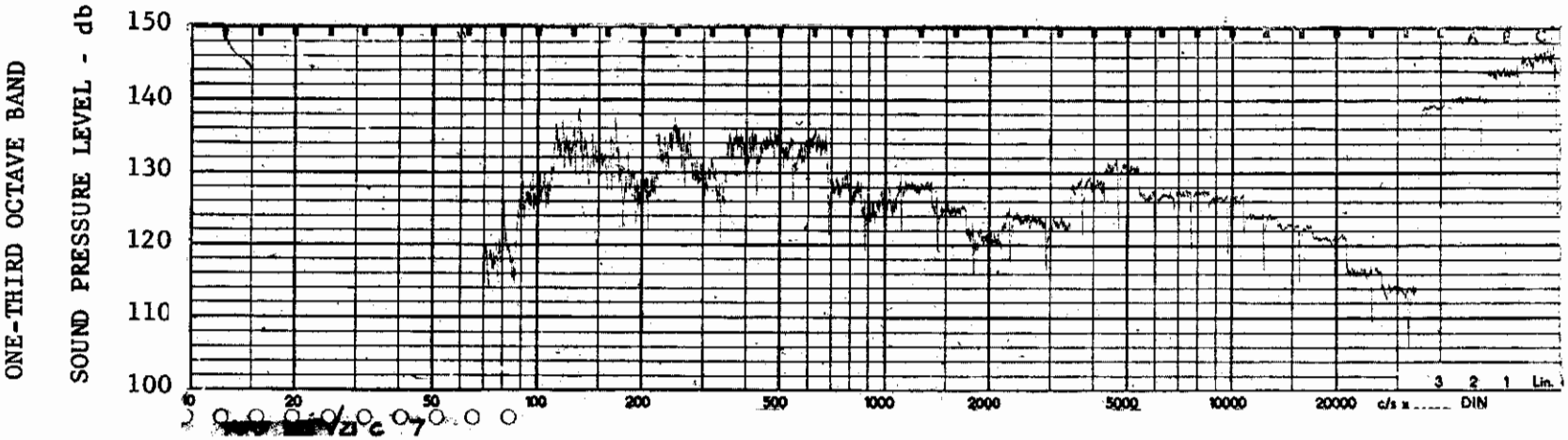

FIGURE 470 ONE-THIRD OCTAVE BAND SPECTRUM MODEL: FP 30

CHANNEL: 7 MACH NO.: 10 α: 5° ϕ: 0 Re_∞/FT.: 2×10^6 AEDC GROUP NO.: 1/21 C

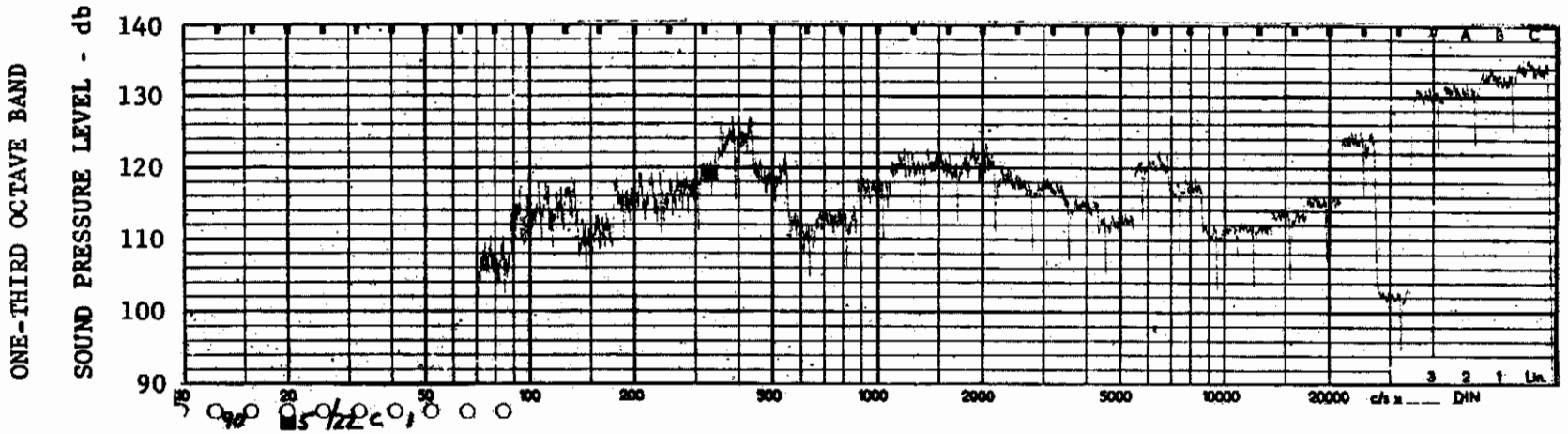

FIGURE 471 ONE-THIRD OCTAVE BAND SPECTRUM MODEL: FP 30

CHANNEL: 1 MACH NO.: 10 α: 13.7° ϕ: 0 Re_∞/FT.: 2×10^6 AEDC GROUP NO.: 1/22 C

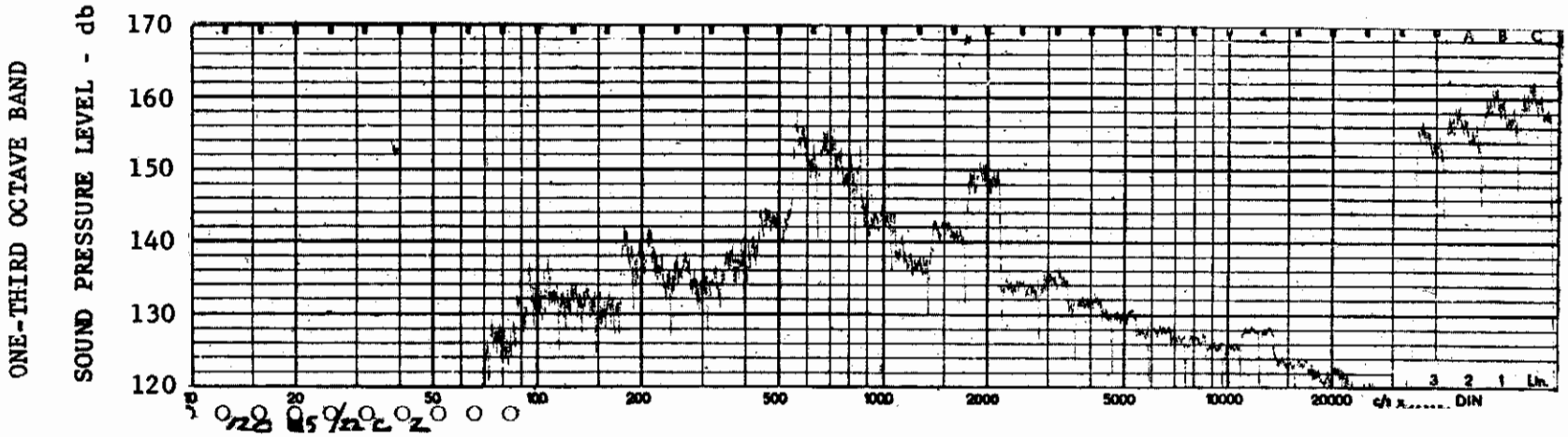

FIGURE 472 ONE-THIRD OCTAVE BAND SPECTRUM MODEL: FP 30

CHANNEL: 2 MACH NO.: 10 α: 13.7° ϕ: 0 Re_∞/FT.: 2×10^6 AEDC GROUP NO.: 1/22 C

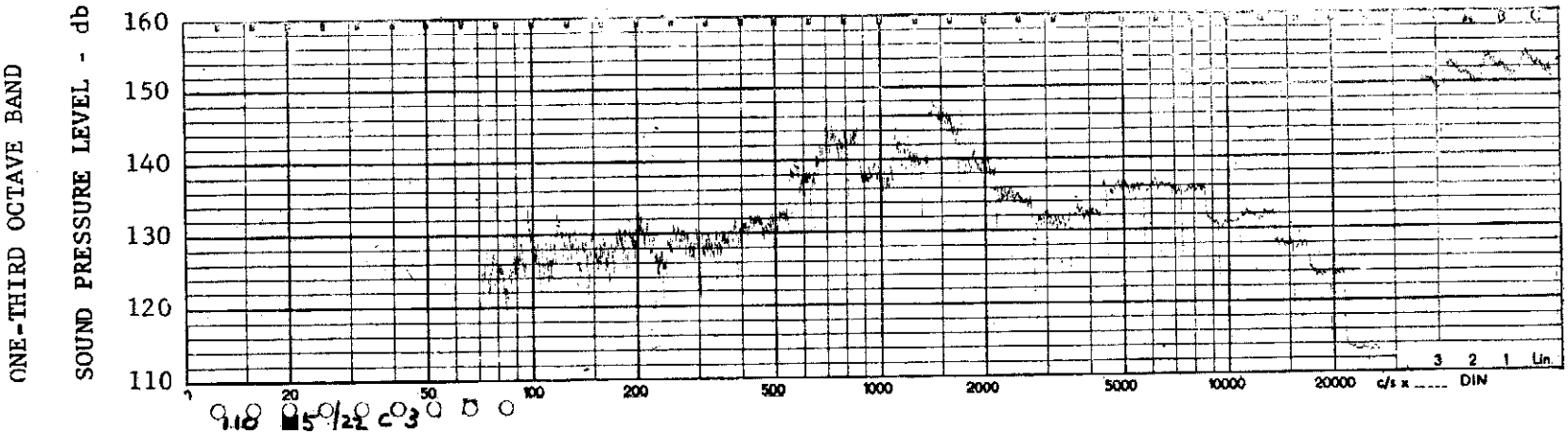

FIGURE 473 ONE-THIRD OCTAVE BAND SPECTRUM MODEL: FP 30

CHANNEL: 3 MACH NO.: 10 α: 13.7° ϕ: 0 Re_∞/FT.: 2×10^6 AEDC GROUP NO.: 1/22 C

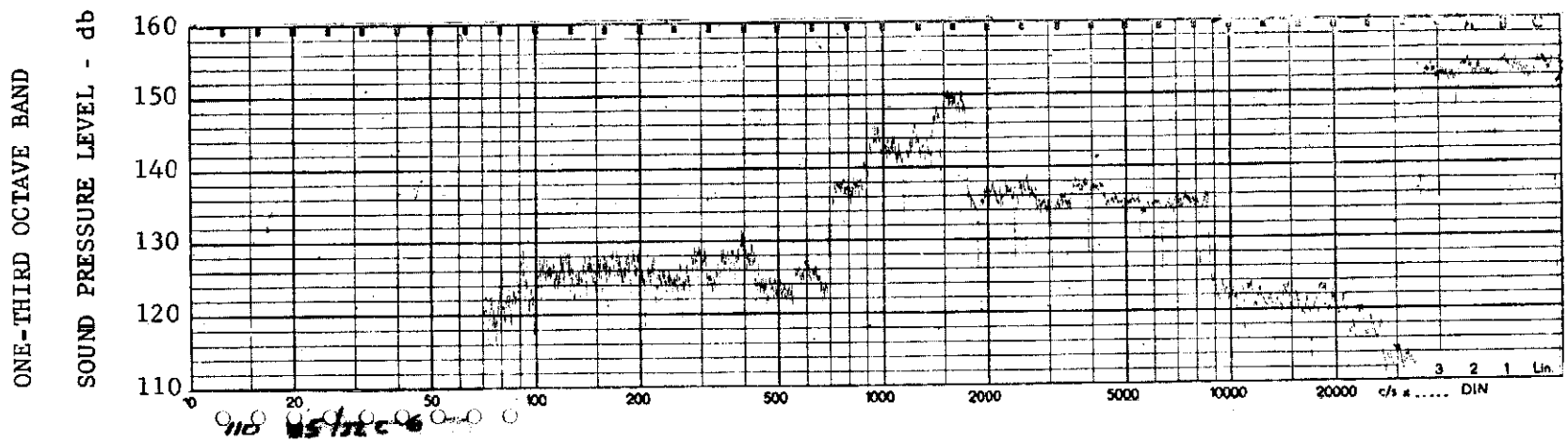

FIGURE 474 ONE-THIRD OCTAVE BAND SPECTRUM MODEL: FP 30

CHANNEL: 6 MACH NO.: 10 α: 13.7° ϕ: 0 Re_∞/FT.: 2×10^6 AEDC GROUP NO.: 1/22 C

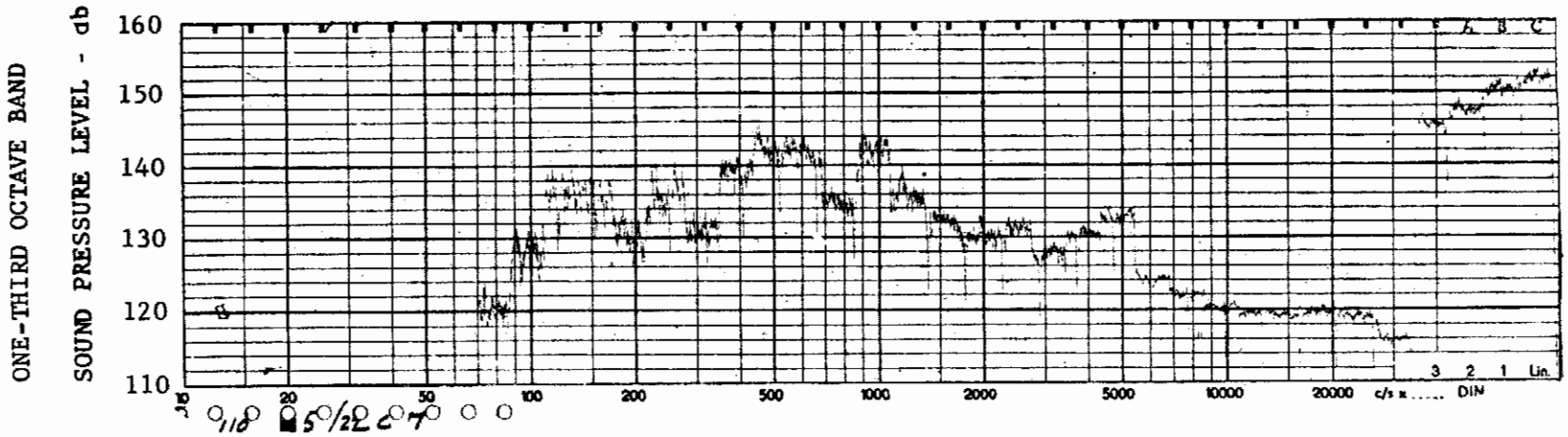

FIGURE 475 ONE-THIRD OCTAVE BAND SPECTRUM MODEL: FP 30

CHANNEL: 7 MACH NO.: 10 α: 13.7° ϕ: 0 Re_∞/FT.: 2×10^6 AEDC GROUP NO.: 1/22 C

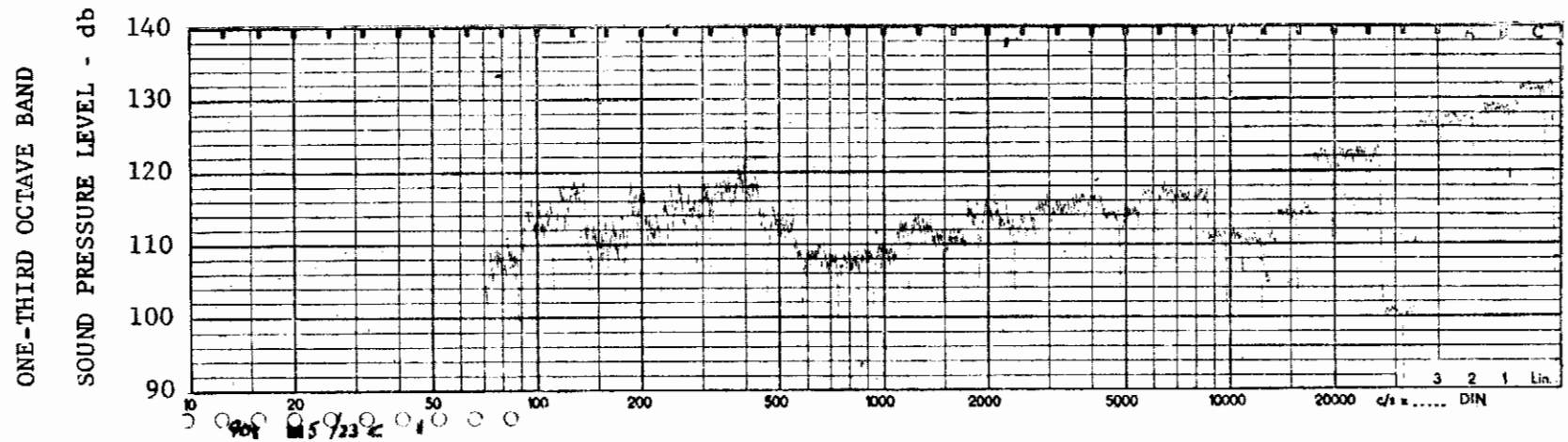

FIGURE 476 ONE-THIRD OCTAVE BAND SPECTRUM MODEL: FP 30

CHANNEL: 1 MACH NO.: 10 α: 0 ϕ: 0 Re_∞/FT.: 2.35×10^6 AEDC GROUP NO.: 1/23 C

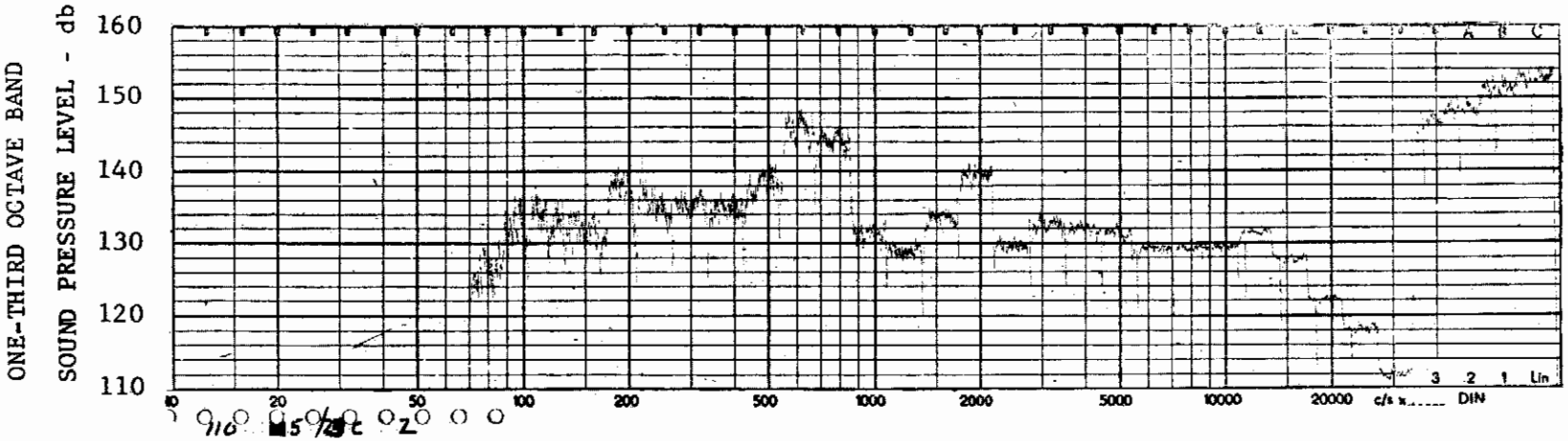

FIGURE 477 ONE-THIRD OCTAVE BAND SPECTRUM MODEL: FP 30

CHANNEL: 2 MACH NO.: 10 α: 0 ϕ: 0 Re_∞/FT.: 2.35×10^6 AEDC GROUP NO.: 1/23 C

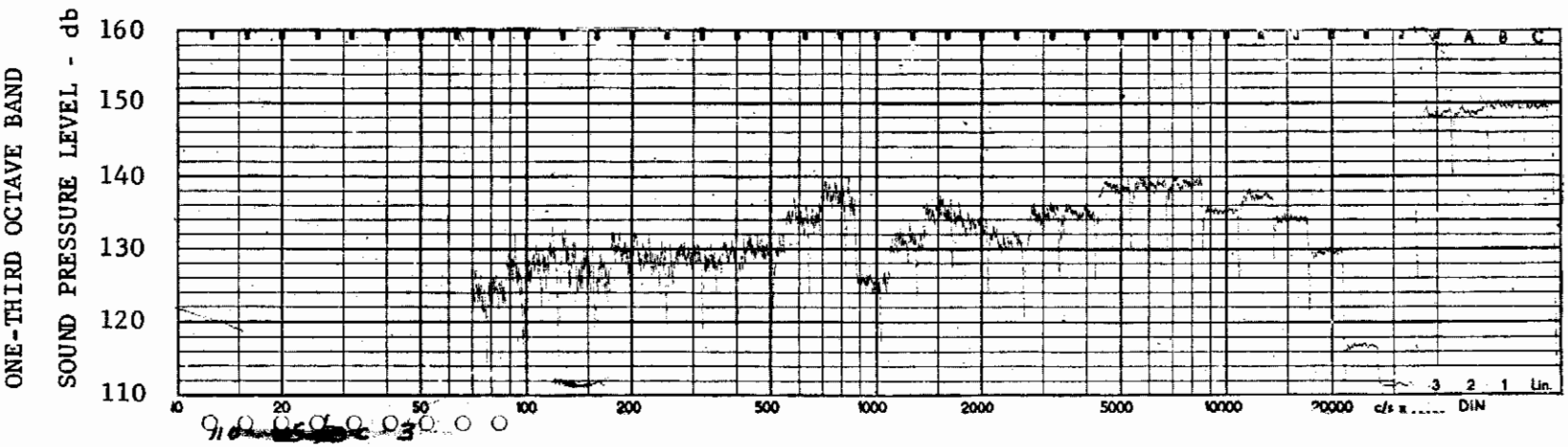

FIGURE 478 ONE-THIRD OCTAVE BAND SPECTRUM MODEL: FP 30

CHANNEL: 3 MACH NO.: 10 α: 0 ϕ: 0 Re_∞/FT.: 2.35×10^6 AEDC GROUP NO.: 1/23 C

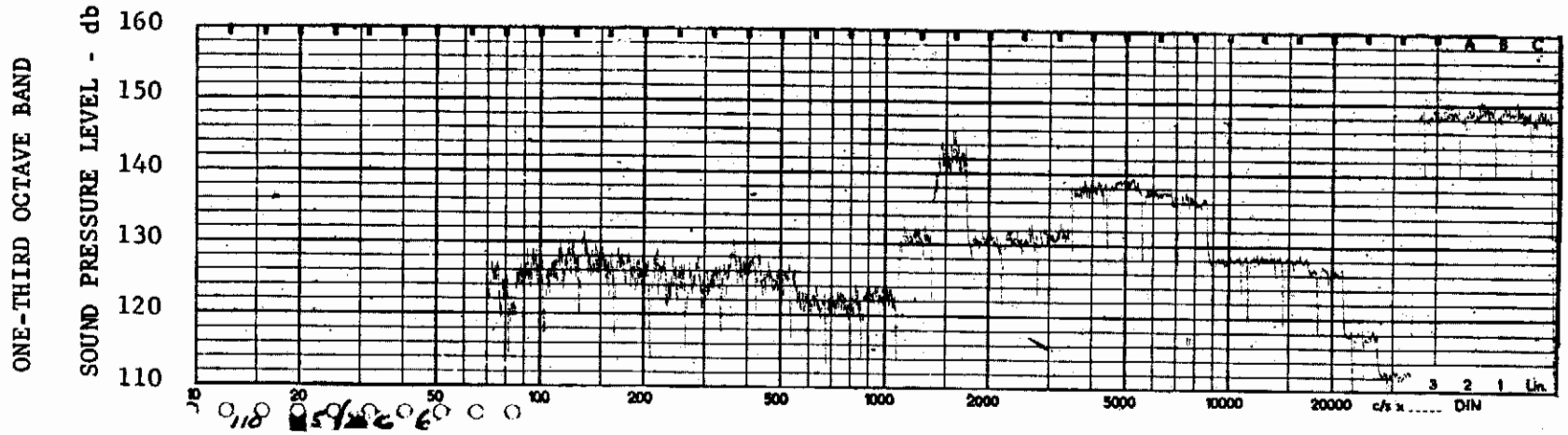

FIGURE 479 ONE-THIRD OCTAVE BAND SPECTRUM MODEL: FP 30

CHANNEL: 6 MACH NO.: 10 α: 0 ϕ: 0 Re_∞/FT.: 2.35×10^6 AEDC GROUP NO.: 1/23 C

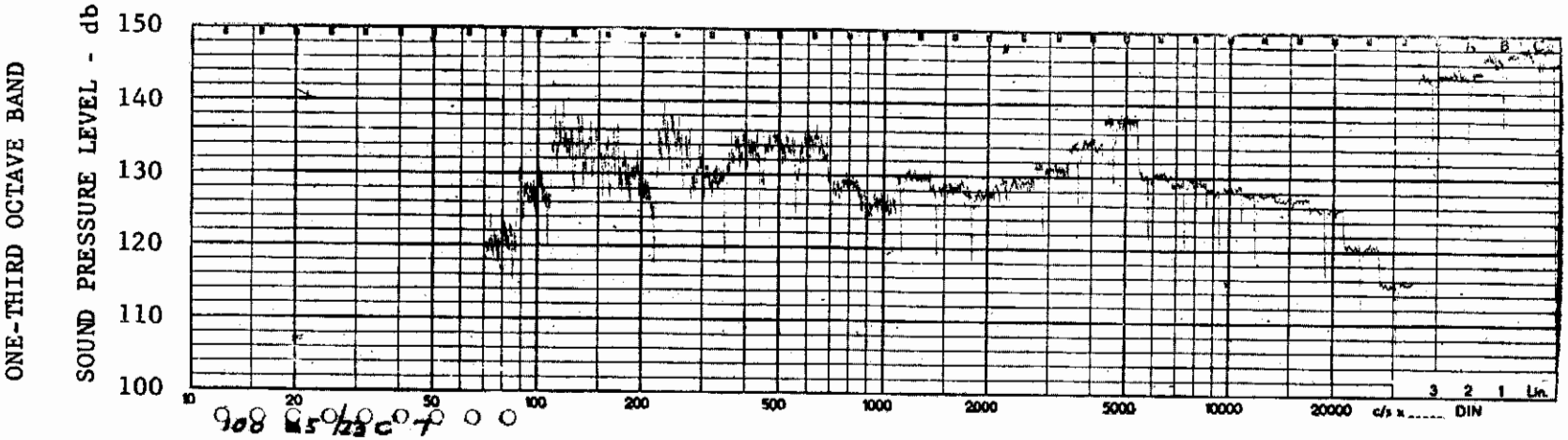

FIGURE 480 ONE-THIRD OCTAVE BAND SPECTRUM MODEL: FP 30

CHANNEL: 7 MACH NO.: 10 α: 0 ϕ: 0 Re_∞/FT.: 2.35×10^6 AEDC GROUP NO.: 1/23 C

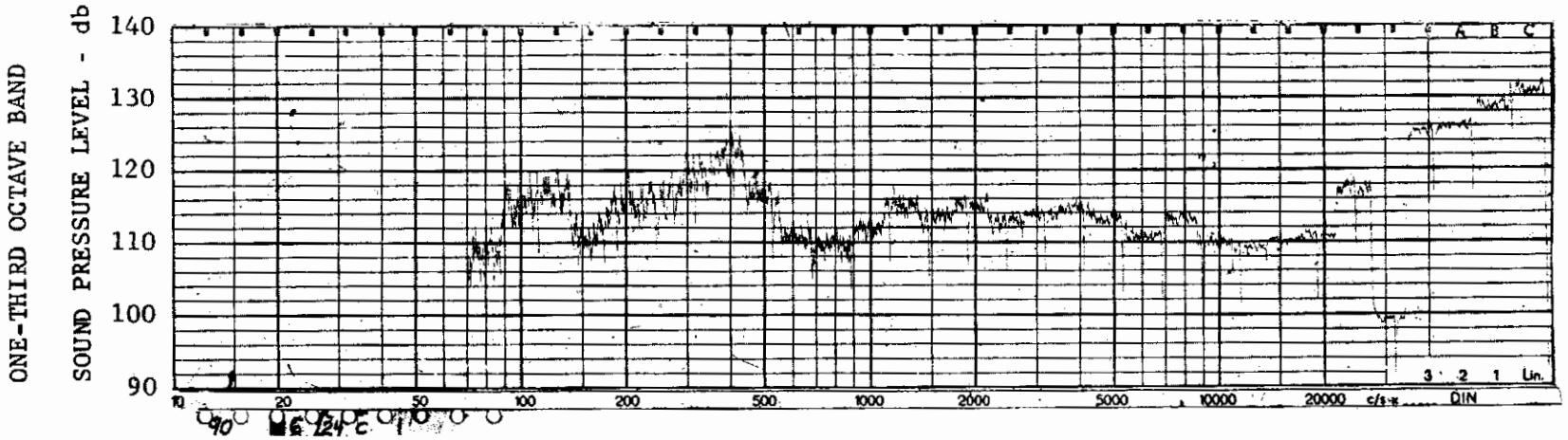

FIGURE 481 ONE-THIRD OCTAVE BAND SPECTRUM MODEL: FP 0

CHANNEL: 1 MACH NO.: 10 α: 0 ϕ: 0 Re_∞/FT.: 2.35×10^6 AEDC GROUP NO.: 1/24 C

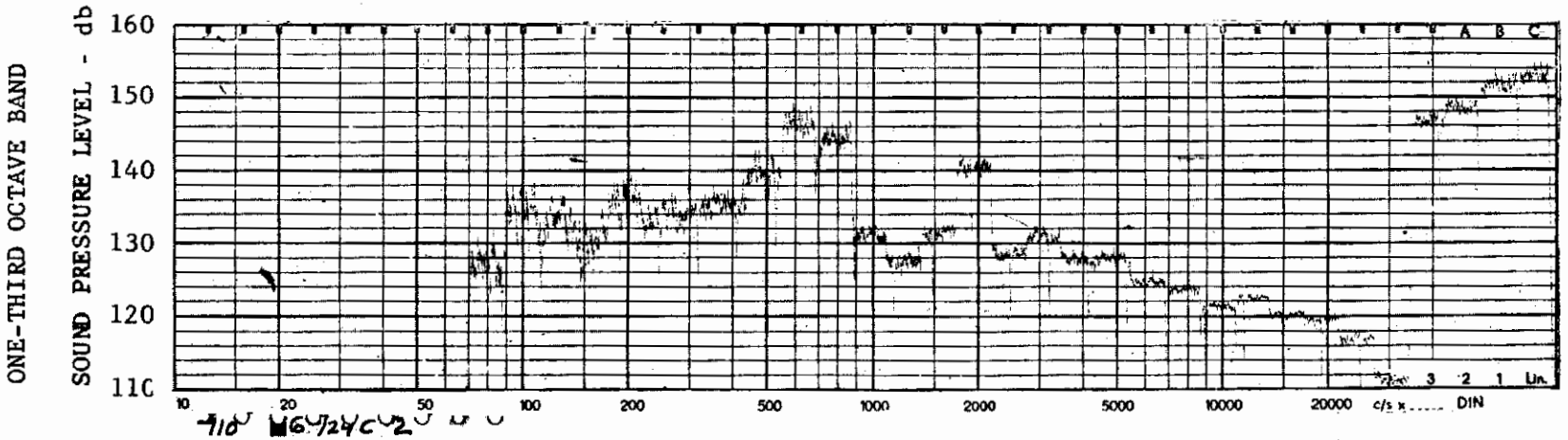

FIGURE 482 ONE-THIRD OCTAVE BAND SPECTRUM MODEL: FP 0

CHANNEL: 2 MACH NO.: 10 α: 0 ϕ: 0 Re_∞/FT.: 2.35×10^6 AEDC GROUP NO.: 1/24 C

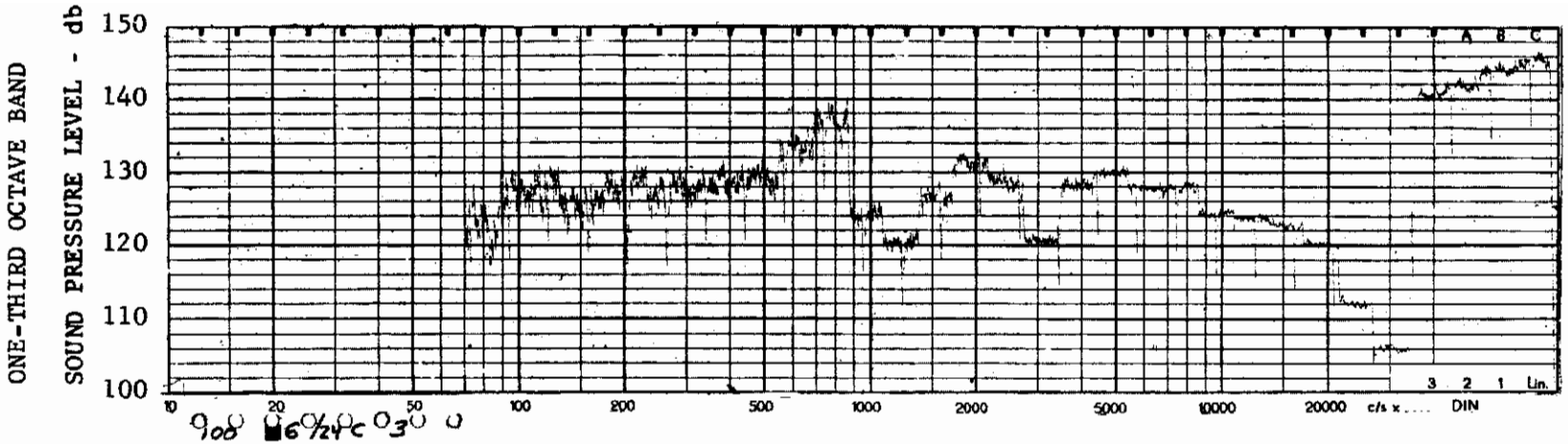

FIGURE 483 ONE-THIRD OCTAVE BAND SPECTRUM MODEL: FP 0

CHANNEL: 3 MACH NO.: 10 α: 0 ϕ: 0 Re_∞/FT.: 2.35×10^6 AEDC GROUP NO.: 1/24 C

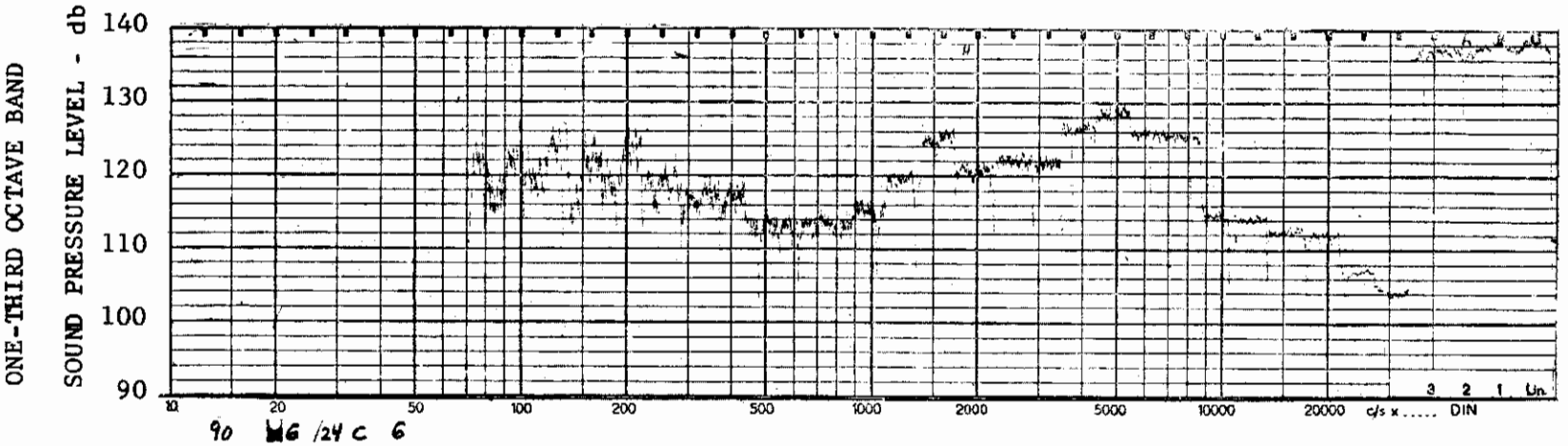

FIGURE 484 ONE-THIRD OCTAVE BAND SPECTRUM MODEL: FP 0

CHANNEL: 6 MACH NO.: 10 α: 0 ϕ: 0 Re_∞/FT.: 2.35×10^6 AEDC GROUP NO.: 1/24 C

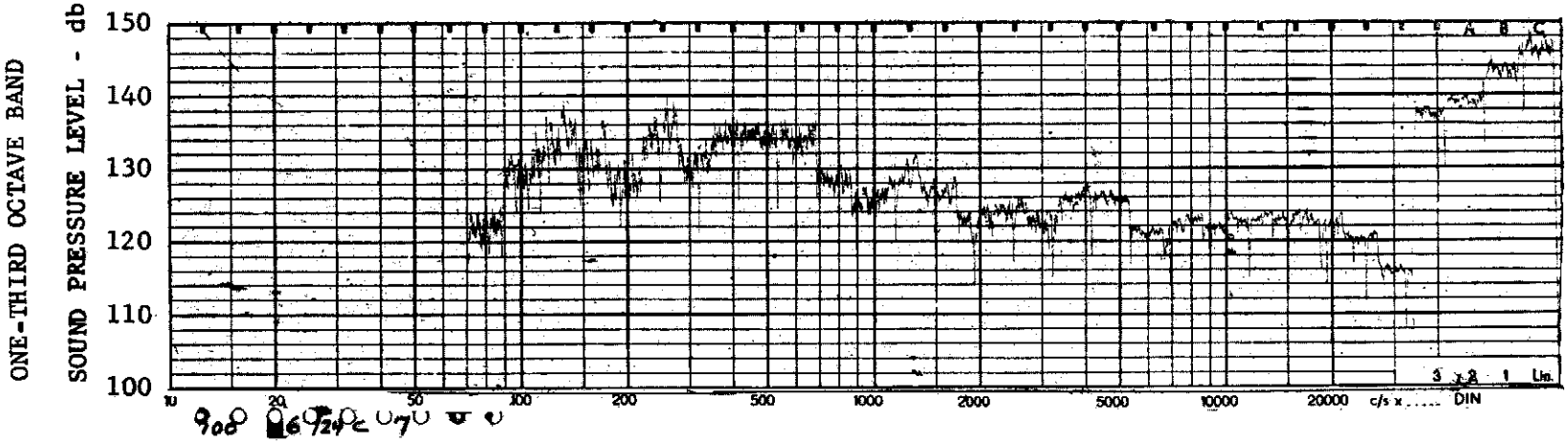

FIGURE 485 ONE-THIRD OCTAVE BAND SPECTRUM MODEL: FP 0

CHANNEL: 7 MACH NO.: 10 α: 0 ϕ: 0 Re_∞/FT.: 2.35×10^6 AEDC GROUP NO.: 1/24 C

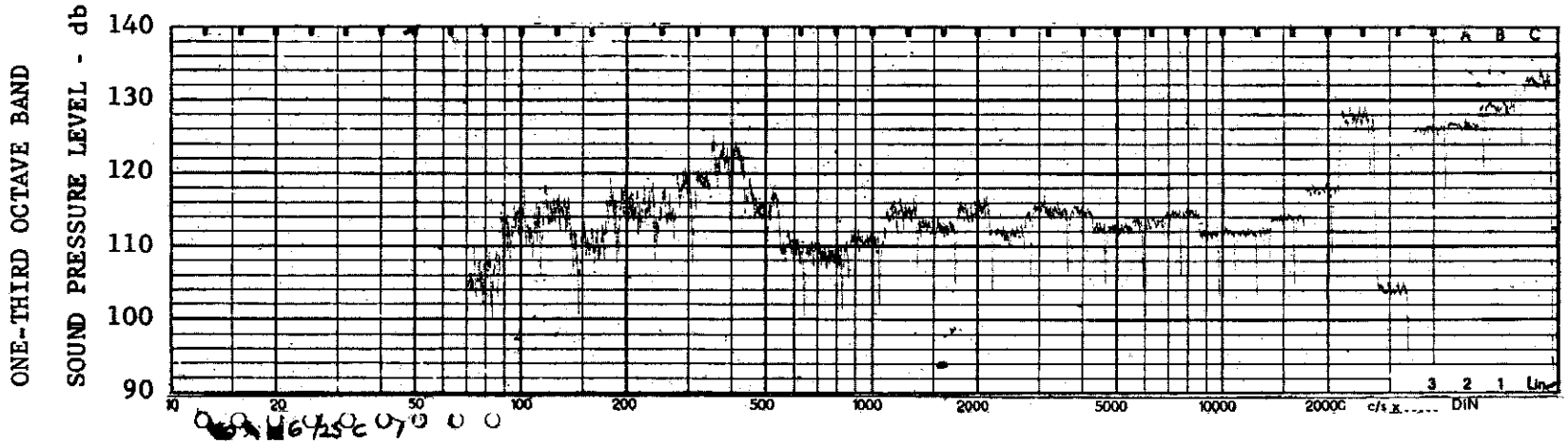

FIGURE 486 ONE-THIRD OCTAVE BAND SPECTRUM MODEL: FP 0

CHANNEL: 1 MACH NO.: 10 α: 5° ϕ: 0 Re_∞/FT.: 2.35×10^6 AEDC GROUP NO.: 1/25 C

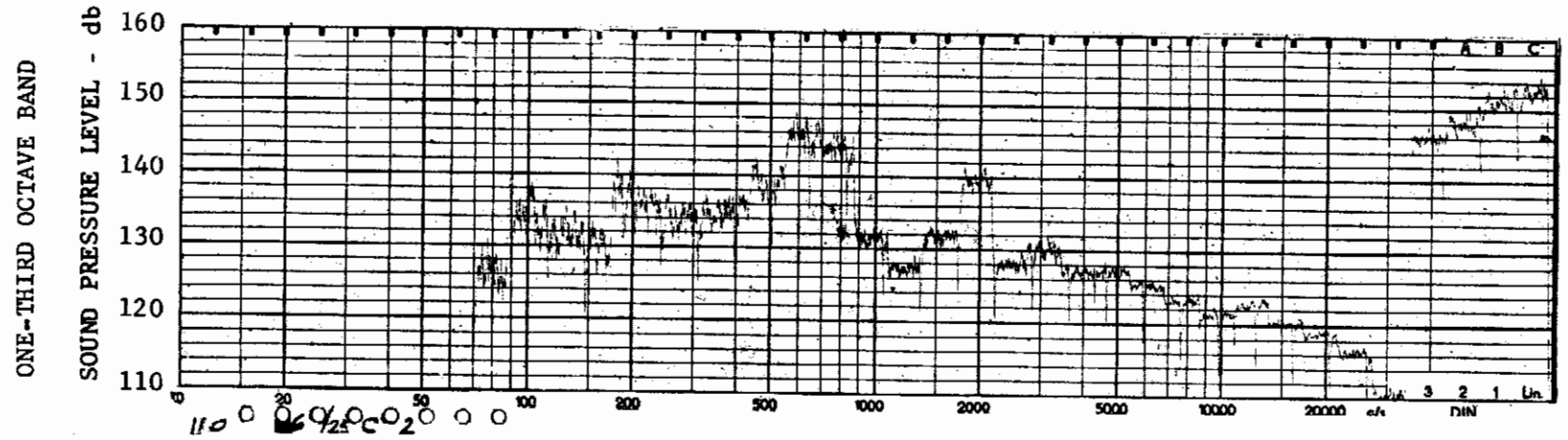

FIGURE 487 ONE-THIRD OCTAVE BAND SPECTRUM MODEL: FP 0

CHANNEL: 2 MACH NO.: 10 α: 5° ϕ: 0 Re_∞/FT.: 2.35×10^6 AEDC GROUP NO.: 1/25 C

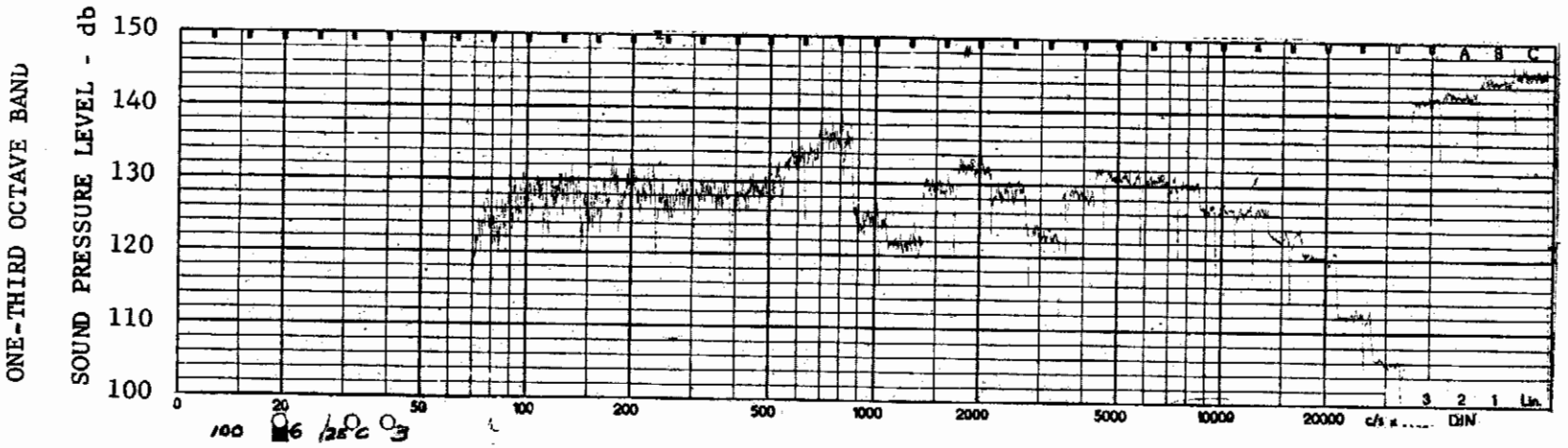

FIGURE 488 ONE-THIRD OCTAVE BAND SPECTRUM MODEL: FP 0

CHANNEL: 3 MACH NO.: 10 α: 5° ϕ: 0 Re_∞/FT.: 2.35×10^6 AEDC GROUP NO.: 1/25 C

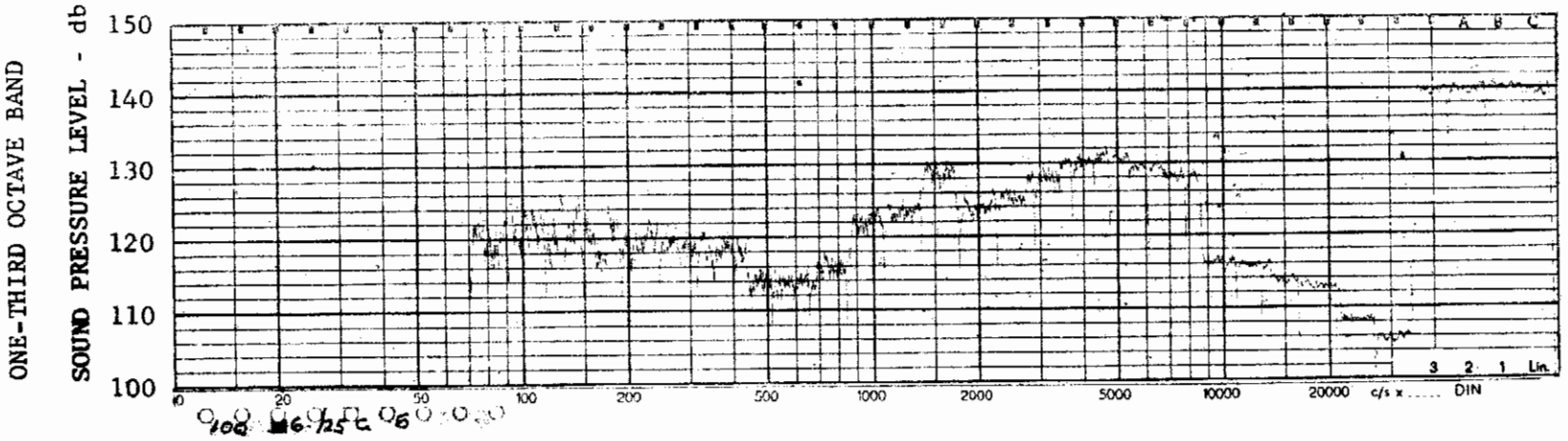

FIGURE 489 ONE-THIRD OCTAVE BAND SPECTRUM MODEL: FP 0

CHANNEL: 6 MACH NO.: 10 α: 5° ϕ: 0 Re_∞/FT.: 2.35×10^6 AEDC GROUP NO.: 1/25 C

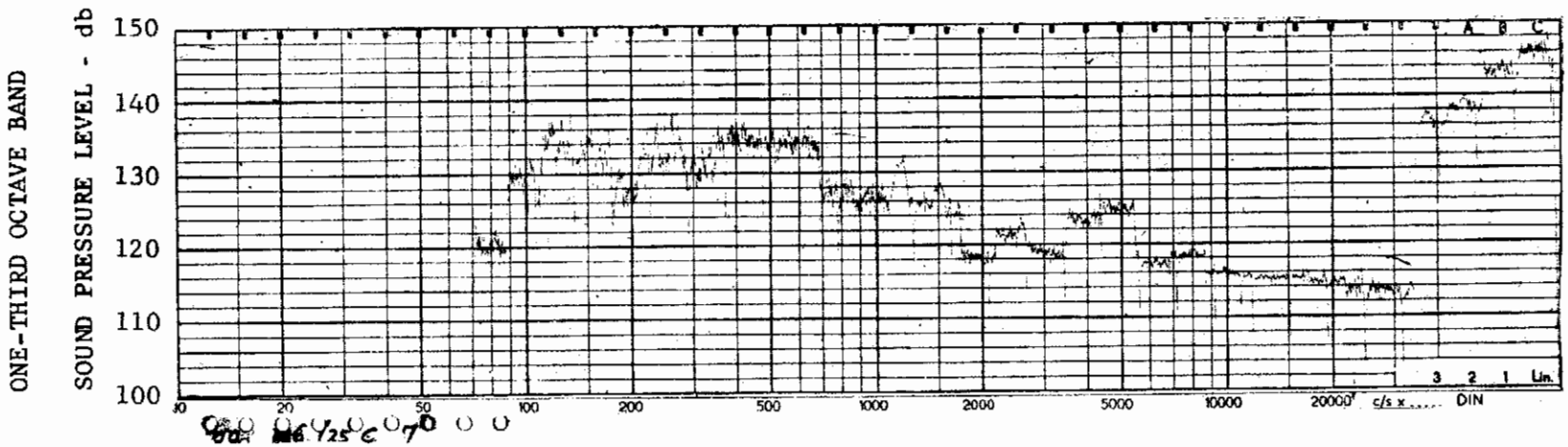

FIGURE 490 ONE-THIRD OCTAVE BAND SPECTRUM MODEL: FP 0

CHANNEL: 7 MACH NO.: 10 α: 5° ϕ: 0 Re_∞/FT.: 2.35×10^6 AEDC GROUP NO.: 1/25 C

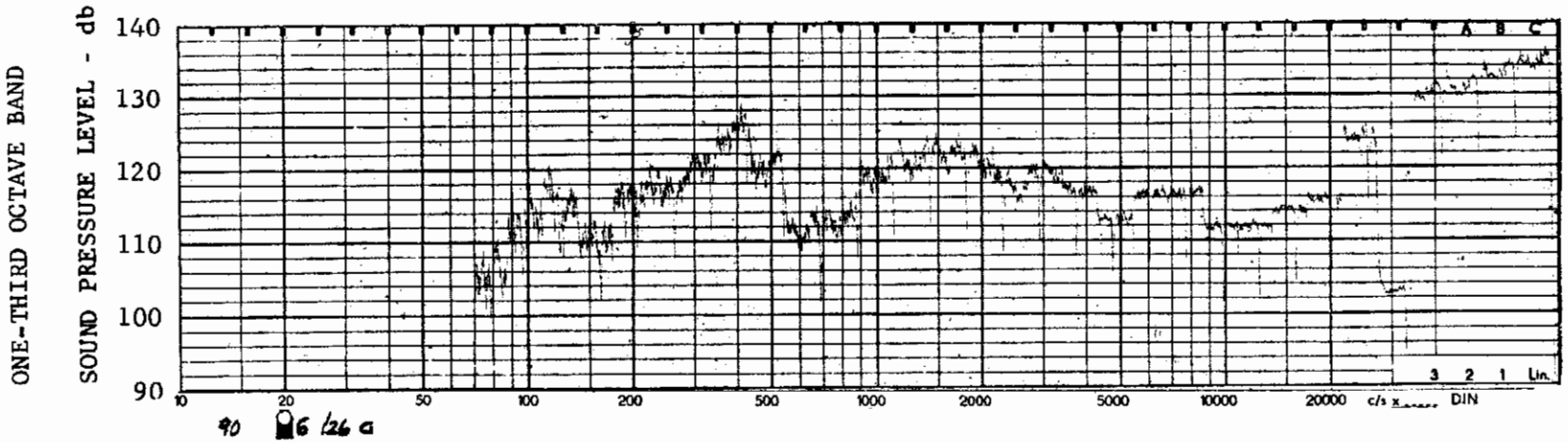

FIGURE 491 ONE-THIRD OCTAVE BAND SPECTRUM MODEL: FP 0

CHANNEL: 1 MACH NO.: 10 α: 13.7° ϕ: 0 Re_∞/FT.: 2.35×10^6 AEDC GROUP NO.: 1/26 C

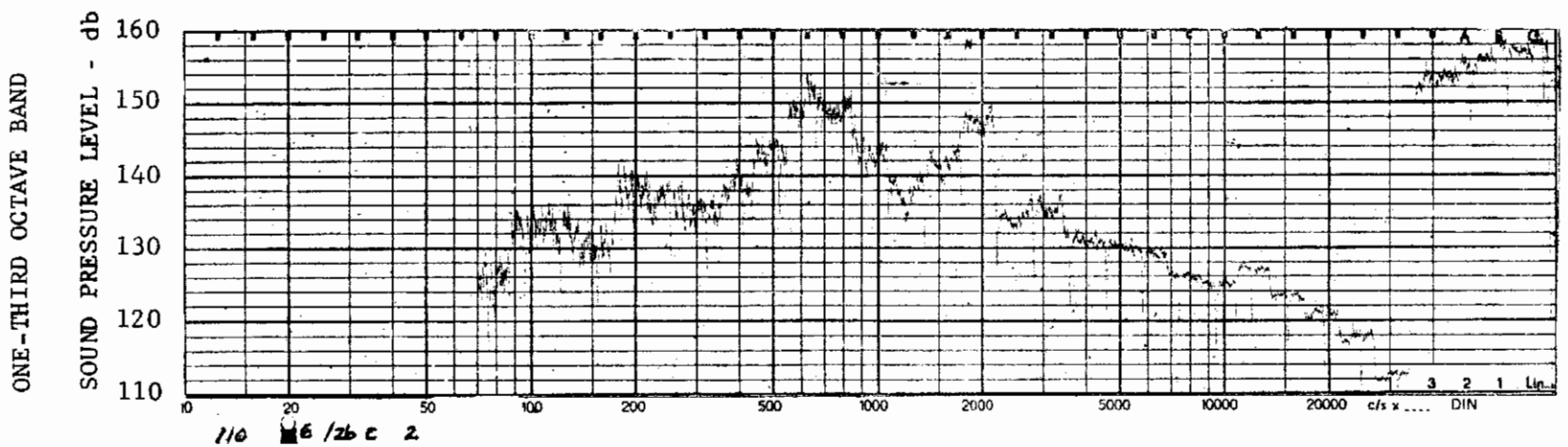

FIGURE 492 ONE-THIRD OCTAVE BAND SPECTRUM MODEL: FP 0

CHANNEL: 2 MACH NO.: 10 α: 13.7° ϕ: 0 Re_∞/FT.: 2.35×10^6 AEDC GROUP NO.: 1/26 C

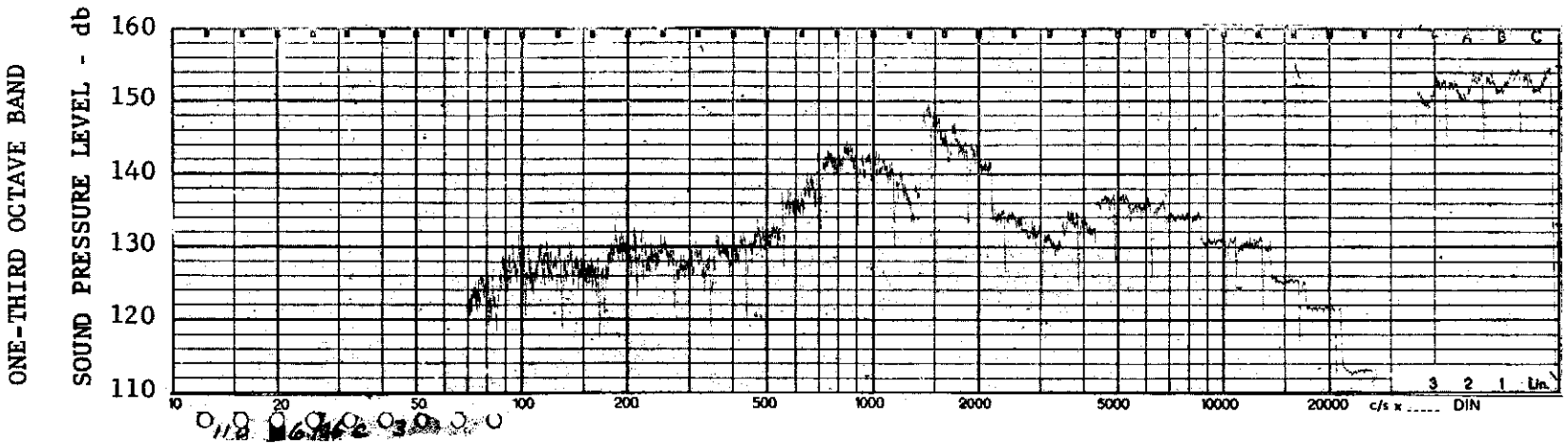

FIGURE 493 ONE-THIRD OCTAVE BAND SPECTRUM MODEL: FP 0

CHANNEL: 3 MACH NO.: 10 α: 13.7° ϕ: 0 Re_∞/FT.: 2.35×10^6 AEDC GROUP NO.: 1/26 C

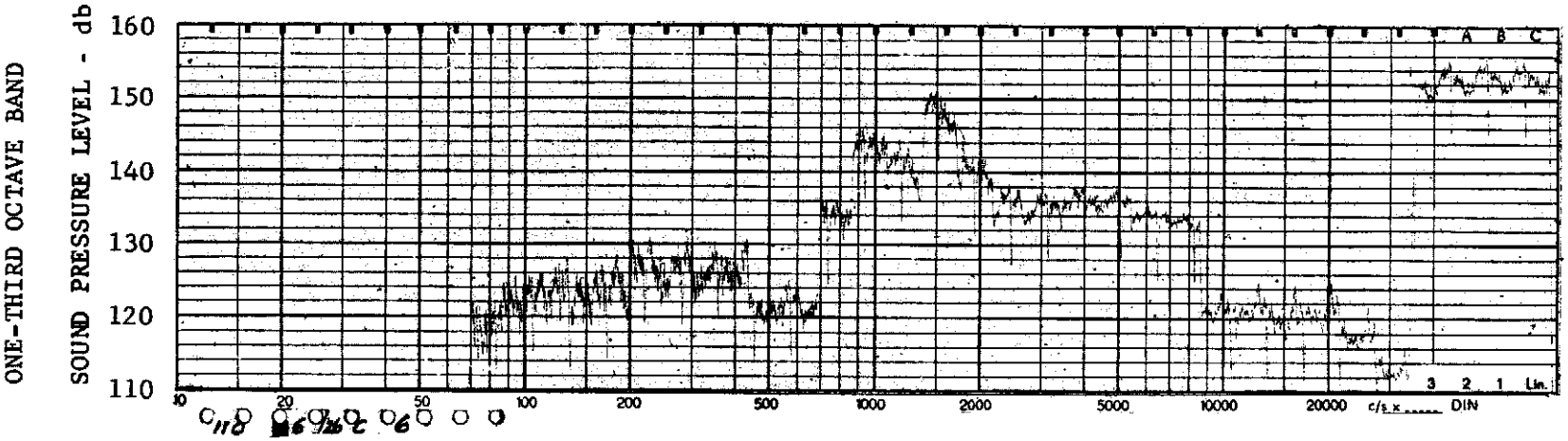

FIGURE 494 ONE-THIRD OCTAVE BAND SPECTRUM MODEL: FP 0

CHANNEL: 6 MACH NO.: 10 α: 13.7° ϕ: 0 Re_∞/FT.: 2.35×10^6 AEDC GROUP NO.: 1/26 C

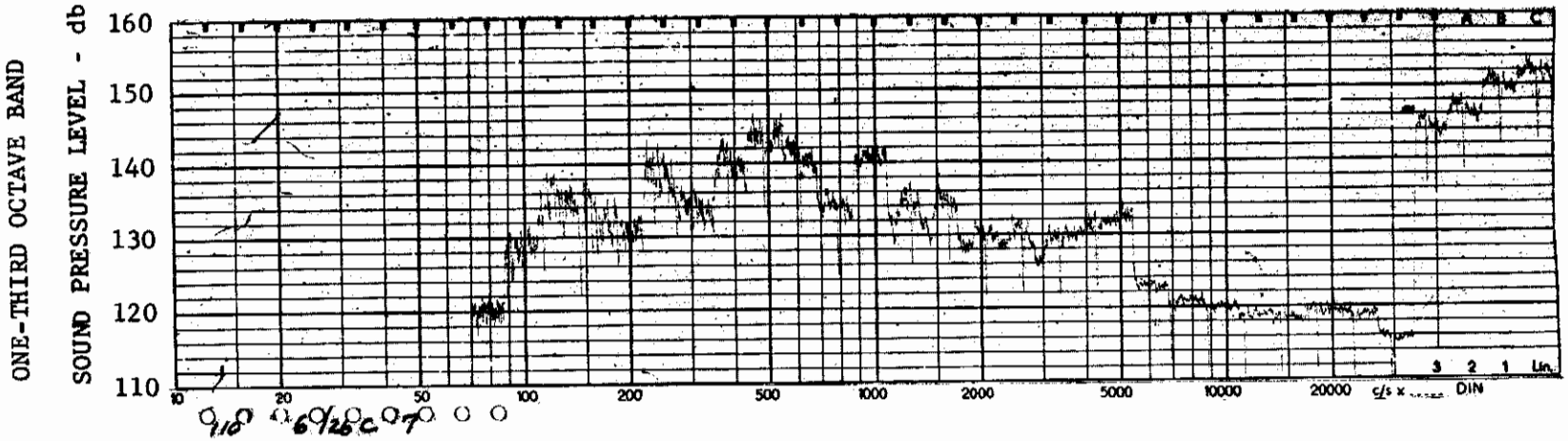

FIGURE 495 ONE-THIRD OCTAVE BAND SPECTRUM MODEL: FP 0

CHANNEL: 7 MACH NO.: 10 α: 13.7° ϕ: 0 Re_∞/FT.: 2.35×10^6 AEDC GROUP NO.: 1/26 C

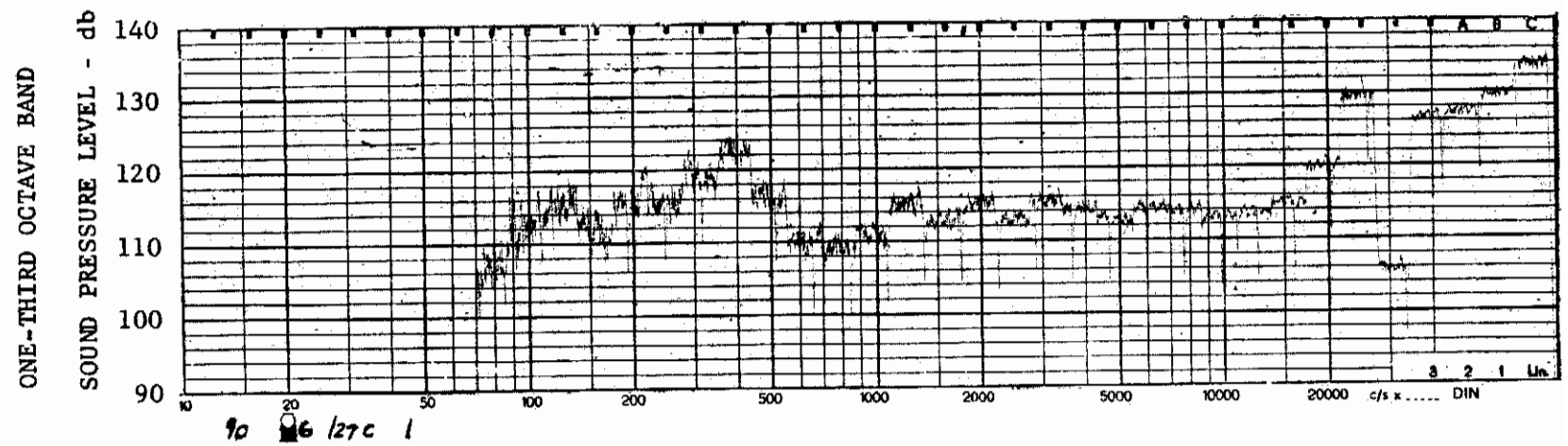

FIGURE 496 ONE-THIRD OCTAVE BAND SPECTRUM MODEL: FP 0

CHANNEL: 1 MACH NO.: 10 α: 0 ϕ: 0 Re_∞/FT.: 2.35×10^6 AEDC GROUP NO.: 1/27 C

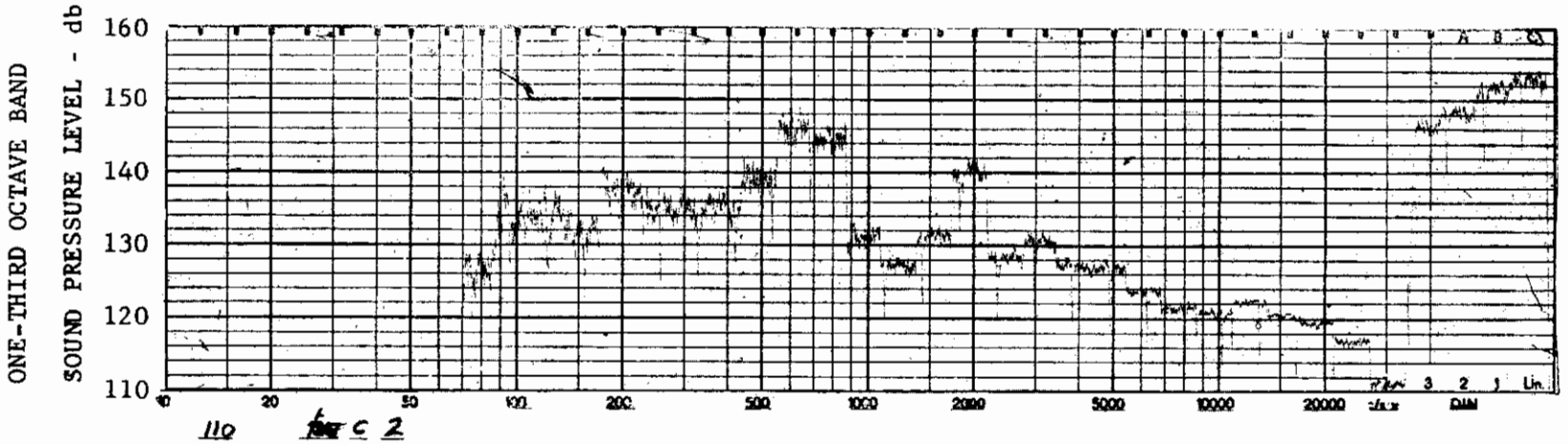

FIGURE 497 ONE-THIRD OCTAVE BAND SPECTRUM MODEL: FP 0

CHANNEL: 2 MACH NO.: 10 α: 0 ϕ: 0 Re_∞/FT.: 2.35×10^6 AEDC GROUP NO.: 1/27 C

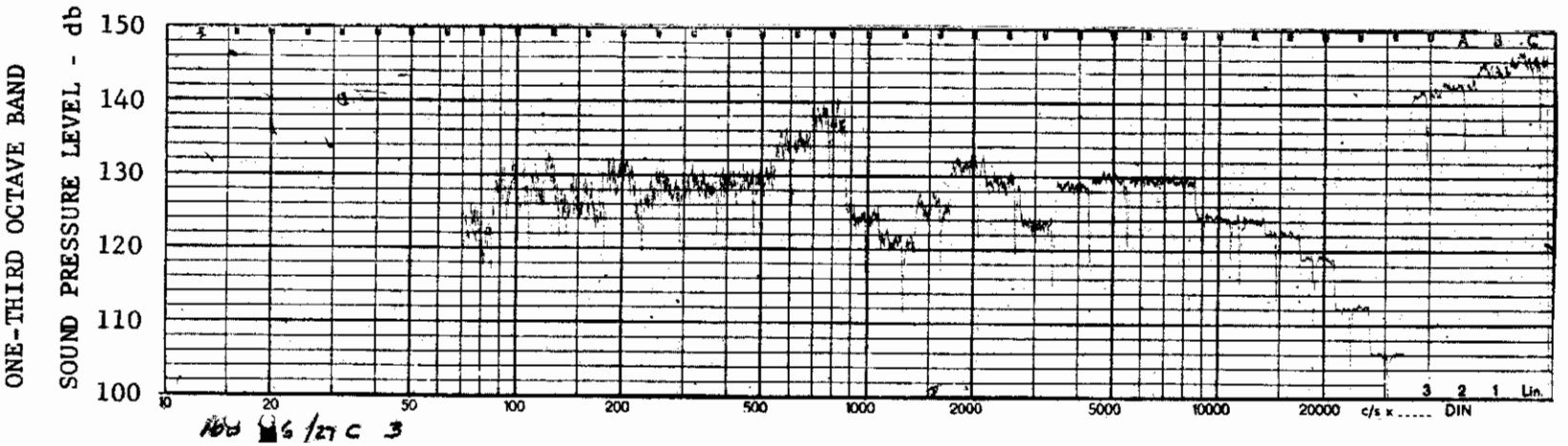

FIGURE 498 ONE-THIRD OCTAVE BAND SPECTRUM MODEL: FP 0

CHANNEL: 3 MACH NO.: 10 α: 0 ϕ: 0 Re_∞/FT.: 2.35×10^6 AEDC GROUP NO.: 1/27 C

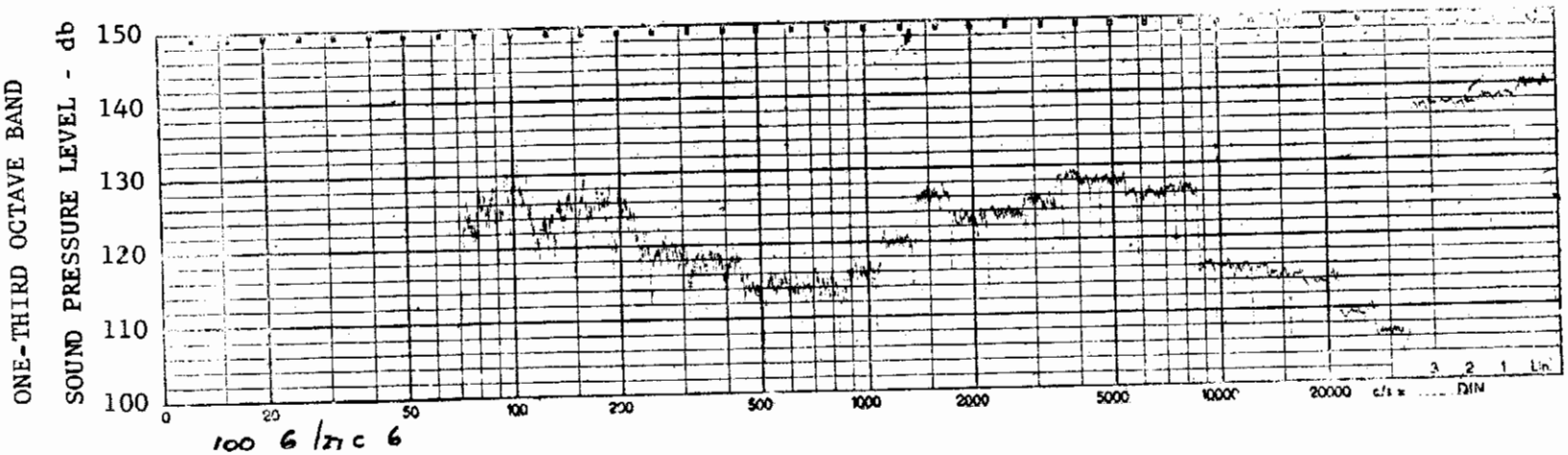

FIGURE 499 ONE-THIRD OCTAVE BAND SPECTRUM MODEL: FP 0

CHANNEL: 6 MACH NO.: 10 α: 0 ϕ: 0 Re_∞/FT.: 2.35×10^6 AEDC GROUP NO.: 1/27 C

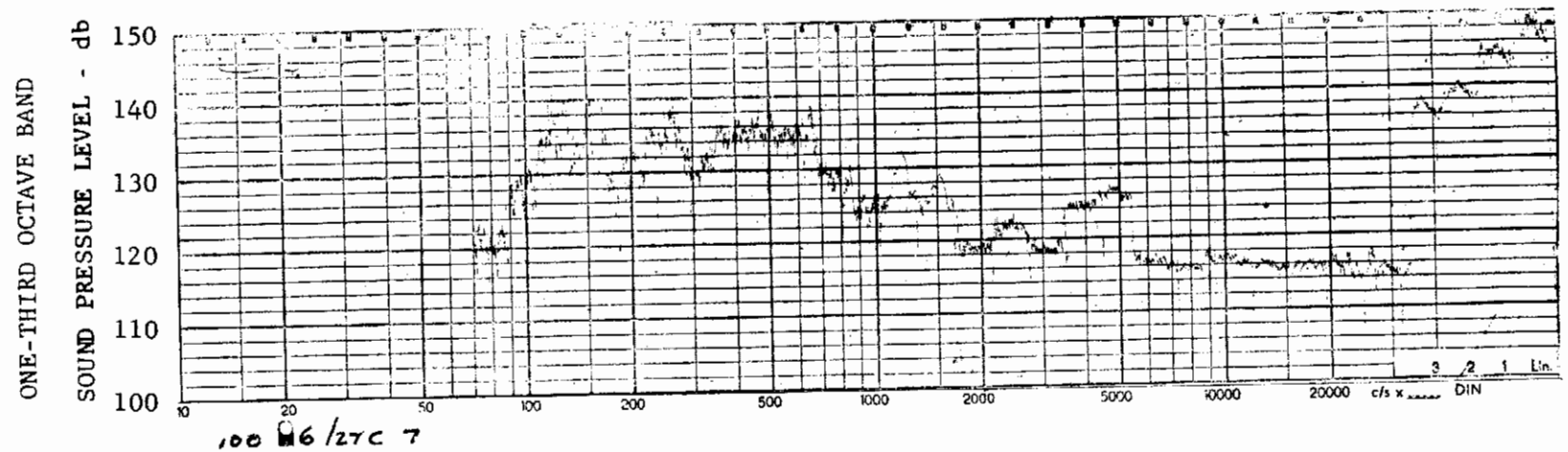

FIGURE 500 ONE-THIRD OCTAVE BAND SPECTRUM MODEL: FP 0

CHANNEL: 7 MACH NO.: 10 α: 0 ϕ: 0 Re_∞/FT.: 2.35×10^6 AEDC GROUP NO.: 1/27 C

UNCLASSIFIED
Security Classification

DOCUMENT CONTROL DATA - R&D

(Security classification of title, body of abstract and indexing annotation must be entered when the overall report is classified)

1. ORIGINATING ACTIVITY (Corporate author)	2a. REPORT SECURITY CLASSIFICATION
Northrop Corporation, Norair Division 3901 W. Broadway Hawthorne, California	Unclassified
	2b. GROUP N/A

3. REPORT TITLE

Turbulent Wall Pressure Fluctuations Under Separated Supersonic and Hypersonic Flows

4. DESCRIPTIVE NOTES (Type of report and inclusive dates)

Final Report - June 63 - March 65

5. AUTHOR(S) (Last name, first name, initial)

Revell, J. D.
Gleason, R. E.

6. REPORT DATE	7a. TOTAL NO. OF PAGES	7b. NO. OF REFS
August 1965	445	57

8a. CONTRACT OR GRANT NO.	9a. ORIGINATOR'S REPORT NUMBER(S)
AF 33(657)-11712 b. PROJECT NO. 1471 c. Task 147102 d.	AFFDL-TR-65-77
	9b. OTHER REPORT NO(S) (Any other numbers that may be assigned this report) NOR 65-4

10. AVAILABILITY/LIMITATION NOTICES

Qualified requestors may obtain copies of this report from DDC. This report will be furnished to CFSTI for sale to the public.

11. SUPPLEMENTARY NOTES	12. SPONSORING MILITARY ACTIVITY
	Air Force Flight Dynamics Laboratory Wright-Patterson AFB, Ohio 45433

13. ABSTRACT

The objective of this project was to conduct an exploratory and limited experimental program to obtain the parameters that are important in the occurance, magnitude, frequency content, and effective areas of forcing functions arising from separated flows, wakes, base pressure fluctuations, and oscillating shock waves.

Two wind tunnel models were used to obtain pressure fluctuation data. The data has been reduced in the form of one-third octave band power spectral densities. Data analyses and discussion of results are presented. Effects of Mach No., angle of attack, frequency, and Strouhal number on the pressure fluctuation levels generated are presented.

DD FORM 1 JAN 64 1473

UNCLASSIFIED
Security Classification

UNCLASSIFIED
Security Classification

14. KEY WORDS	LINK A		LINK B		LINK C	
	ROLE	WT	ROLE	WT	ROLE	WT
Aero-Acoustic Noise Separated Flow Wakes Base Pressure Fluctuations Oscillating Shock Waves						

INSTRUCTIONS

1. ORIGINATING ACTIVITY: Enter the name and address of the contractor, subcontractor, grantee, Department of Defense activity or other organization *(corporate author)* issuing the report.

2*a*. REPORT SECURITY CLASSIFICATION: Enter the overall security classification of the report. Indicate whether "Restricted Data" is included. Marking is to be in accordance with appropriate security regulations.

2*b*. GROUP: Automatic downgrading is specified in DoD Directive 5200.10 and Armed Forces Industrial Manual. Enter the group number. Also, when applicable, show that optional markings have been used for Group 3 and Group 4 as authorized.

3. REPORT TITLE: Enter the complete report title in all capital letters. Titles in all cases should be unclassified. If a meaningful title cannot be selected without classification, show title classification in all capitals in parenthesis immediately following the title.

4. DESCRIPTIVE NOTES: If appropriate, enter the type of report, e.g., interim, progress, summary, annual, or final. Give the inclusive dates when a specific reporting period is covered.

5. AUTHOR(S): Enter the name(s) of author(s) as shown on or in the report. Enter last name, first name, middle initial. If military, show rank and branch of service. The name of the principal author is an absolute minimum requirement.

6. REPORT DATE: Enter the date of the report as day, month, year; or month, year. If more than one date appears on the report, use date of publication.

7*a*. TOTAL NUMBER OF PAGES: The total page count should follow normal pagination procedures, i.e., enter the number of pages containing information.

7*b*. NUMBER OF REFERENCES: Enter the total number of references cited in the report.

8*a*. CONTRACT OR GRANT NUMBER: If appropriate, enter the applicable number of the contract or grant under which the report was written.

8*b*, 8*c*, & 8*d*. PROJECT NUMBER: Enter the appropriate military department identification, such as project number, subproject number, system numbers, task number, etc.

9*a*. ORIGINATOR'S REPORT NUMBER(S): Enter the official report number by which the document will be identified and controlled by the originating activity. This number must be unique to this report.

9*b*. OTHER REPORT NUMBER(S): If the report has been assigned any other report numbers *(either by the originator or by the sponsor)*, also enter this number(s).

10. AVAILABILITY/LIMITATION NOTICES: Enter any limitations on further dissemination of the report, other than those imposed by security classification, using standard statements such as:

(1) "Qualified requesters may obtain copies of this report from DDC."

(2) "Foreign announcement and dissemination of this report by DDC is not authorized."

(3) "U. S. Government agencies may obtain copies of this report directly from DDC. Other qualified DDC users shall request through _____."

(4) "U. S. military agencies may obtain copies of this report directly from DDC. Other qualified users shall request through _____."

(5) "All distribution of this report is controlled. Qualified DDC users shall request through _____."

If the report has been furnished to the Office of Technical Services, Department of Commerce, for sale to the public, indicate this fact and enter the price, if known.

11. SUPPLEMENTARY NOTES: Use for additional explanatory notes.

12. SPONSORING MILITARY ACTIVITY: Enter the name of the departmental project office or laboratory sponsoring *(paying for)* the research and development. Include address.

13. ABSTRACT: Enter an abstract giving a brief and factual summary of the document indicative of the report, even though it may also appear elsewhere in the body of the technical report. If additional space is required, a continuation sheet shall be attached.

It is highly desirable that the abstract of classified reports be unclassified. Each paragraph of the abstract shall end with an indication of the military security classification of the information in the paragraph, represented as *(TS), (S), (C), or (U)*.

There is no limitation on the length of the abstract. However, the suggested length is from 150 to 225 words.

14. KEY WORDS: Key words are technically meaningful terms or short phrases that characterize a report and may be used as index entries for cataloging the report. Key words must be selected so that no security classification is required. Identifiers, such as equipment model designation, trade name, military project code name, geographic location, may be used as key words but will be followed by an indication of technical context. The assignment of links, rules, and weights is optional.

UNCLASSIFIED
Security Classification